Structural and Geochemical Controls on Ore Formation at the New Occidental Gold Deposit, Cobar, New South Wales, Australia

New Occidental Opencut looking south to the Peak Mine

Craig Stegman, BSc (Hons)

Submitted as full requirement for Doctorate of Philosophy

University of Tasmania, Hobart, Australia.

October 2007

Declaration of originality

I declare that the material contained in this thesis is original and my own work, except where due acknowledgment is given, and has not been accepted for the award of any other degree or diploma.

Signed: 

Craig Stegman

26 September 2007

Statement of authority of access

This thesis may be made available for loan and limited copying in accordance with the *Copyright Act 1968*.

Dedicated to my father who inspired my interest in geology

ACKNOWLEDGEMENTS

The author gratefully acknowledges the support of Dr Robert Scott and Professor Ross Large from CODES who provided unstinting assistance and encouragement to the author during the initial research of this thesis and then during the equally demanding documentation of the research findings. Dr Scott's detailed review of early drafts of this document greatly improved my clarity of thinking and writing.

The assistance of a number of other parties is also duly acknowledged, including Dr Ivan Reynolds of Rio Tinto Advanced Technical Development, Bristol, who provided detailed mineralogical and petrological descriptions of ore samples; Sasha Pontual (AusSpec) and Mike Hornibrook (Rio Tinto Exploration), who undertook PIMA measurements and initial analysis of SWIR data; Dr Andrew Rae (UTAS) who assisted with collection of some of the fluid inclusion microthemometric data; Dr Khin Zaw (UTAS), who supervised the analysis and initial interpretation of fluid inclusion mass spectrometry; and Michael Blake (UTAS) who supervised the collection of sulfur isotope data by the Central Science Laboratory at UTAS. The CSIRO Division of Exploration and Mining undertook the lead isotope analyses cited in this study and also provided access to their database of previous lead isotope analyses of Cobar deposits.

Peak Gold Mines (PGM) provided initial support to this study when the author was employed at the Peak Mine. PGM allowed the author to access its detailed core library, mine workings and extensive geochemical databases and historical records for the purposes of this research.

Finally, my beautiful wife Therese is thanked for her unquestioning support she provided me over the years of this study.

SUMMARY

The 1.5 Moz New Occidental gold deposit is one of a number of Devonian fault-hosted gold-base metal deposits along the eastern margin of the Devonian Cobar Basin in the central belt of the Lachlan Orogen, western New South Wales. Cobar deposits do not easily conform to conventional ore deposit classifications, exhibiting characteristics of orogenic gold, intrusion-related, volcanic-hosted massive sulfide and epithermal gold deposits. This study has focussed on defining the relationship between formation of the New Occidental deposit and the structural evolution of the eastern margin of the Cobar Basin and characterising the composition and physical characteristics of hydrothermal fluids associated with deposit formation. The research has resolved many of the enigmatic aspects of Cobar deposits, including (i) mechanisms of deposit formation, (ii) the origins of their poly-metallic character and distinctive metal zoning evident at both the district scale and within individual deposits, and (iii) provides important new constraints on the source(s) of metals and sulfur in the deposits.

The New Occidental deposit is a steeply dipping pipe-shaped ore body with a strike length of 150–200m, width of 10–30m and vertical extent of more than 1200m. It is hosted within the Great Chesney Fault, a major north-northwest trending sub-vertical fault on the western flank of the south-plunging Chesney-Narri Anticline. Folding and faulting are interpreted to be the products of a single phase of deformation (D_1) during the Early Devonian, which was characterised by relatively constant orientation of regional stresses. Variation in the plunge and inter-limb angle of parasitic folds in the vicinity of the deposit (previously interpreted to indicate polyphase deformation), is here shown to reflect progressive fold development (with greater tightening and reorientation of earlier formed folds) in D_1 high-strain zones.

Analysis of fault zone kinematics and detailed stratigraphic reconstruction of the eastern Cobar Basin margin has resolved movement vectors on the Great Chesney Fault. Reverse dip-slip displacement on the fault (parallel to the prominent sub vertical stretching lineation on cleavage) is in the order of 1.5–2.5 km (east-block up), based on stratigraphic offsets across the fault. There is no evidence for significant syn-mineralisation strike-slip displacement on the fault, although many previous workers have postulated this as a means of explaining the sub-vertical pipe-like geometry of the orebody. The steep pitch of both the New Occidental deposit and of high-grade shoots within it (both parallel to the stretching lineation), are attributed to large-scale reverse movement on the fault, with vertical extent of the deposit and shoots a function of the amount of reverse displacement on the host fault.

Five texturally distinct stages of quartz veins and breccias have been recognised within the New Occidental deposit (Table 1). During Stages 1–4, successive stages of quartz veining and brecciation were localised along the footwall contact of the previous vein stage, resulting in an asymmetric distribution of the zones of maximum Stage 1 to 4 vein density from hanging wall to footwall across the deposit. This zonation is consistent over the full strike length (~200m) and known vertical extent (~1200m) of the deposit, reflecting the tendency for brecciation and dilation to be localised along rock mass boundaries where there is greatest competency contrast; principally the contact between the previously deposited vein arrays and more ductile siltstone/mudstone footwall.

Each of the five vein stages record cyclic episodes of sub-horizontal extensional fracturing followed by fault-rupture and slip on steeply dipping fault planes. Variably deformed quartz fault-fill veins are cut at high angles by arrays of sub-horizontal extension veins, which are in turn truncated by younger generations of fault-fill veins. The predominance of open-space filling vein and breccia textures in Stage 1–4 vein arrays indicates substantial fault-induced dilation accompanied displacement on the host Great Chesney Fault at the site of the New Occidental deposit. Similar features are not developed immediately along strike from the deposit, indicating it occupies a limited strike-length dilational jog formed progressively during the main phase of reverse displacement on the Great Chesney Fault system. Stage 2–3 veins exhibit the most intense implosive breccia textures, suggesting the bulk of dilation occurred during deposition of Stage 2–3 quartz veins. Stage 4 veins record a transition from predominantly brittle deformation (implosive brecciation and open-space vein fill) to a mixture of brittle and brittle-ductile deformation (e.g. crack-seal vein growth and cataclastic shear), indicating less dilation of the fault zone (and/or lower fluid fluxes) during displacement. A progressive decrease in the intensity of folds overprinting Stage 1–4 veins indicates significant fault-perpendicular shortening was broadly contemporaneous with fault displacement and vein development, with the greatest shortening occurring during deposition of Stage 2–3 veins. Significant displacement on the fault had largely ceased prior to deposition of Stage 5 veins.

The intimate association of sub-horizontal extension veins with each stage of fault-fill quartz veins and breccias, the latter characterised by vein textures indicating rapidly fluctuating physiochemical conditions during vein formation (colloform- and crustiform-banding), indicates fluid pressures alternated between supra-lithostatic and near hydrostatic values (i.e. extreme fault-valve behaviour) during slip on the Great Chesney Fault. Continued east-west shortening at the eastern margin of the Cobar Basin is interpreted to have rotated the fault from moderate dips (perhaps <60–70° initially) to progressively steeper dips. Once oriented at very high angles (>75°) to the maximum principal stress direction, supra-lithostatic fluid pressures were required to initiate slip on the fault. Additional criteria for fault-valve behaviour are also satisfied; specifically (i) the depth of deposit formation is of the order of 5-7 km, (ii) no more favourably oriented faults occur in the vicinity of the Great Chesney Fault, and (iii) upper basin siltstones and mudstones overlying the deposit appear to have formed a low permeability seal that limited the discharge of over-pressured fluids from depth.

The New Occidental deposit records a complex multi-stage paragenesis of alteration and ore mineral assemblages (Table 1). Overall there was a progression of ore mineral assemblages from magnetite-bearing (Stage 1), to native metal and S-deficient mineral-bearing (Stage 2) and finally to more S-rich mineral-bearing (Stage 3–7) assemblages. Significant gold was first introduced during development of the Stage 2–3 quartz veins, coincident with maximum dilation along the Great Chesney Fault. Subsequent mineralisation stages only contain appreciable gold where they overprint Stage 2 gold-bismuth bearing veins, suggesting that this is due to minor remobilisation of gold. Remobilised gold became progressively more silver-rich with time.

Table 1: New Occidental vein, ore mineral and alteration paragenesis.

Paragenetic Stage	Location	Quartz Vein Stage	Ore Mineralogy		Geochemistry		Gangue Minerals (Alteration + Vein)
			Major	Minor	Enrichments	Depletions	
1	Hanging wall	Stage 1: Strongly deformed coarsely crystalline quartz veins and breccia	Magnetite	Scheelite, wolframite	Fe-Mn-W	K-Be-Ba-Cs-Nb-Rb (destruction of white mica)	Fe-rich chlorite, calcite
2	Deposit core	Stage 2: Moderately-strongly deformed crystalline to cryptocrystalline crustiform and colloform-banded quartz veins and breccias	Gold, maldonite (Au_2Bi), native bismuth, Se-rich ikunolite (Bi_4Se_3-Bi_4S_3 solid solution series), clausthalite-galena (PbSe-PbS solid solution series)	Rare species of bismuth selenides, pyrrhotite, chalcopyrite	Fe-Mn-Au-Se-Bi-As-Ag-Sb		Fe-rich chlorite
3	Deposit core	Stage 3: Moderately-strongly deformed crystalline crustiform and colloform-banded quartz veins and breccias	Bismuthinite (Bi_2S_3), "newoccidentallite" (Bi_5AuS_4)	Gold	Fe-Mn-Au-Se-Bi-As-Ag-Sb with minor K-Ba-Rb-Sr		Stilpnomelane, minor biotite
4	Immediate Footwall and lesser Hanging wall	Stage 4: Weakly to moderately deformed microcrystalline quartz veins and breccias	Arsenopyrite		Mg-Fe-Mn-As-Ca-Sr-K-Ba-Rb-Al-Na	Si (dissolution of quartz)	Mg-rich iron chlorite
5	Footwall + local Hanging wall		Chalcopyrite, pyrrhotite	Silver-rich gold or electrum - cassiterite	Fe-Cu-Sn-In-K-Ba-Rb		Sericite
6	Deposit core		Sphalerite, galena, pyrrhotite		Fe-Zn-Pb-Ag-Cd		Greenalite, Fe-rich clay, calcite
7	Deposit core	Stage 5: Sparse undeformed quartz veins	Pyrite		Fe		Fe-rich clay

Alteration and vein gangue mineral assemblages are dominated by iron-rich minerals throughout the paragenesis, although chlorite compositions record minor Mg-enrichment during Stage 4 and sericite is locally developed during Stage 5 coincident with base metal deposition. Comparisons with documented metamorphic phase relations in the system K_2O-FeO-MgO-Al_2O_3-SiO_2-H_2O-CO_2 in the presence of quartz and magnetite suggest early alteration stages (1–3) in the New Occidental deposit were relatively high-temperature (up to 450°C), especially during Stage 3 where stilpnomelane and locally biotite replace Fe-chlorite. The formation of greenalite and Fe-rich clays during paragenetic Stages 6–7 (Table 1) indicates significantly lower temperatures (200–300°C).

Short wavelength infrared (SWIR) spectrometry studies reveal an extensive wallrock alteration halo around the New Occidental deposit related to the main stage of gold deposition. The degree of (Fe,Mg)Si substitution for Al in white mica and the Fe/(Fe+Mg) ratio of chlorite both increase towards the Great Chesney Fault at the New Occidental deposit. Similar mineralogical changes are absent around base metal-mineralised and unmineralised sections of the Great Chesney Fault, suggesting these features can be used to discriminate between barren and potentially gold-mineralised sections of the Great Chesney Fault and other similar fault zones in the Cobar Basin.

Mass balance calculations indicate major alteration stages in the New Occidental deposit were associated with well-defined variations in major element geochemistry (Table 1), the most pronounced being K-Ba-Rb depletion and Fe-Mn enrichment associated with progressive destruction of metamorphic white mica around the deposit and its replacement by Fe-chlorite (Paragenetic Stages 1–2). Subsequent stages of stilpnomelane and Fe-Mg chlorite alteration in the deposit (Paragenetic Stages 3 and 4 respectively) are characterised by successively stronger, albeit relatively subtle K-Mg-Na±Ca enrichment, which suggests a degree of wallrock buffering of the original hydrothermal fluid. Fe-Mg chlorite alteration is also associated with retrograde quartz solubility, which is tentatively attributed to pressure increases at relatively constant temperature during the transition from brittle to ductile deformation in the latter stages of deposit formation. The final stage of white mica alteration associated with late-stage chalcopyrite - pyrrhotite (Paragenetic Stage 5) is also associated with K-Rb-Ba enrichment. Ore element geochemistry suggests two different associations in the deposit comprising an early-stage gold-rich (Au-Ag-Bi-Sb-Se-W-Pb-As) association and a late-stage base metal-rich (Cu-In-Sn-Pb-Zn-Cd-Mo-Co) association.

Paragenetically constrained fluid inclusion studies of quartz in the New Occidental deposit indicate the deposit formed from weakly saline (1–5 wt% NaCl equivalent) H_2O-CO_2-H_2S-CH_4-bearing hydrothermal fluids with low to moderate CO_2 contents. Carbon dioxide contents are higher in early stages of quartz veins (Stages 1–3) whereas fluids associated with Stage 4 quartz-chalcopyrite are slightly more saline. Stage 3 quartz contains contemporaneous primary vapour-rich and liquid-rich inclusions homogenising to both the vapour or liquid phase at similar T_h values (350–390°C), indicating the hydrothermal fluid underwent phase separation at similar formation temperatures. Fluid inclusions in Stage 4 quartz homogenised to the liquid phase and yielded lower T_h values (270–350°C), consistent with the lower formation temperatures inferred from coeval alteration mineralogy. Abundant secondary fluid inclusions in all vein stages yielded considerably lower T_h values (100–300°C).

Lead mineralisation in the New Occidental deposit is characterised by a relatively narrow range of Pb isotopic ratios ($^{206}Pb/^{204}Pb$ ratios of 18.06–18.12; $^{207}Pb/^{204}Pb$ ratios of 15.59–15.64 and $^{208}Pb/^{204}Pb$ ratios of 38.13–38.27) that lie along or slightly above the Lachlan

Orogen crustal growth curve defined by Carr et al. (1995). Lead isotopic ratios are comparable to ratios recorded from other Cobar deposits and from Silurian stratabound and volcanic-hosted massive sulfide deposits in the Lachlan Orogen. The similarity indicates lead is sourced from a relatively homogenous crustal reservoir extending across both the Eastern and Central belts of the Lachlan Orogen. In detail, lead isotope initial ratios from the New Occidental and other Cobar deposits exhibit subtle variations that are interpreted to indicate that the New Occidental deposit and other gold deposits in the Cobar Basin contain a small component of mantle lead. This may reflect reworking of mantle lead contained in Ordovician mafic volcanics and intrusions that previous workers have postulated exist at depth beneath the Cobar Basin and which have been identified in basement to the east of the Cobar Basin. In comparison, gold-poor base metal deposits and deposits in basement rocks flanking the Cobar Basin are characterised by a stronger crustal lead isotopic signature. Cobar deposits yield Pb-model ages of 400–420 Ma, which indicate an Early Devonian age for mineralisation.

$\delta^{34}S$ values for sulfides from the New Occidental deposit are in the range of +4.2‰ to +11.4‰ (mean = 9.4‰), similar to those for sulfides from other Cobar deposits and from Silurian-Devonian volcanic-hosted massive sulfide deposits. No systematic spatial or temporal variation in $\delta^{34}S$ values of orebody sulfides is apparent. However, disseminated sulfides (syngenetic pyrite and metamorphic pyrrhotite) in the footwall of the New Occidental deposit have significantly higher $\delta^{34}S$ values (+16.4‰ to +18.6‰; mean ± 1 SD: 17.2 ± 0.9‰), similar to values previously recorded for syngenetic sulfides elsewhere in the Cobar Basin. The similarity of $\delta^{34}S$ values for the pyrite and overprinting pyrrhotite indicates little or no $\delta^{34}S$ fractionation during regional metamorphism. However, the large difference and abrupt transition between $\delta^{34}S$ values for orebody sulfides and syngenetic pyrite and metamorphic pyrrhotite in the footwall of the New Occidental deposit indicates a local (wall rock) sulfur source in the deposit is unlikely. The consistent sulfur isotopic signature of Cobar deposits and Silurian-Devonian volcanic-hosted massive sulfide deposits in the eastern Lachlan Orogen suggests a common sulfur source for the deposits. A predominantly igneous sulfur source is precluded on the basis that orebody $\delta^{34}S$ values are higher than expected values for igneous sulfur (0 ± 3‰). A homogenous crustal reservoir of sulfur (similar to orebody lead) is also unlikely given the expected range in basement composition, with lower $\delta^{34}S$ values expected from igneous sources and higher values from basement sedimentary rock-types. The most likely source of sulfur is contemporaneous late Silurian-Early Devonian seawater sulfate ($\delta^{34}S$ = 20‰), which has been inorganically reduced at elevated temperatures (>300–400°C) as it circulated through the crust.

The interpreted structural setting of the New Occidental deposit, together with the inferred sources of metals and sulfur in the deposit and composition of hydrothermal fluids associated with deposit formation, indicate that it and other Cobar deposits were products of large-scale fluid flow driven by Early Devonian (ca. 400Ma) regional deformation. The proposed model for formation of the New Occidental deposit invokes two hydrothermal fluids, which most likely represent different stages in the evolution of a single fluid system, that were largely sourced from crustal basement at or near the base of seismogenic zone (≥12km depth) under amphibolite facies conditions (400–500°C) where metal solubility, including gold, is relatively high. Basement is dominated by quartz-rich sedimentary rocks and granitoids (both S- and I-type), although mafic volcanics within the Girilambone Group are potentially an important component. Such rock-types have collectively contributed to the characteristic metal endowment (Au-Bi-W-Se-As-Cu-Pb-Zn-Ag-Sn) of the New

Occidental and other Cobar deposits. Discharge of the mineralising fluids was focussed along the more intensely deformed eastern margin of the Cobar Basin along early basin-forming faults re-activated during intense deformation of the eastern basin margin.

Early-stage hydrothermal fluids were high temperature (350–390°C), weakly saline CO_2-H_2S-minor CH_4-bearing aqueous fluids characterised by low sulfur fugacity. The fluids are interpreted to have transported gold as a bisulfide complex but their capacity to transport base metals was limited by their low salinity. Ore deposition was most likely triggered by cyclic decompression of the hydrothermal fluid in response to fault-valve behaviour along the Great Chesney Fault. Increasingly intense fault-valve activity in the centre of the deposit coincident with maximum fault zone dilation resulted in deposition of gold with Stage 2–3 crystalline to cryptocrystalline crustiform and colloform-banded quartz and implosive quartz vein breccias. The extreme fluid pressure fluctuations from supra-lithostatic to near-hydrostatic values initiated phase separation in the hydrothermal fluid and triggered gold deposition by partitioning H_2S to the vapour phase. Gold in the hydrothermal fluid was also preferentially partitioned into liquid native bismuth, which, on cooling, produced the characteristic intricate mixtures of gold, maldonite and native bismuth observed in the New Occidental deposit. Subsequent gold deposition during the latter stages of deposition of Stage 3 quartz was due to desulfidisation of the hydrothermal fluid in response to the formation of bismuthinite, newoccidentallite, ikunolite and pyrrhotite at the expense of native bismuth, maldonite and iron-rich silicates.

Late-stage fluids exhibit many similarities to the early-stage fluids, although they were lower temperature (300-350°C) than the early-stage fluids, more acidic and contained a component of connate or meteoric water derived from Late Silurian-early Devonian seawater, which increased the salinity, $a{Mg^{2+}}$ and sulfur fugacity of the fluids. The seawater was possibly drawn down into the upper crust in less-deformed areas peripheral to the highly deformed eastern margin of the Cobar Basin. As a result, early-stage hydrothermal fluids evolved from gold-bearing low salinity fluids to more saline gold-poor, base metal-bearing fluids as meteoric waters were introduced into the fluid system. Although gold-poor, the late-stage fluids remobilised previously deposited gold in the deposit. Deposition of base metal sulfides and silver-rich gold with Stage 4 quartz veins was triggered by further, albeit less intense, decompression of the late-stage fluids hydrothermal fluids, desulfidisation reactions and/or a decrease in fluid temperature in response to cooling of the hydrothermal fluid.

The influx of late-stage base metal-rich fluids in the New Occidental deposit also corresponded to a change from dominantly brittle to brittle-ductile deformation in the deposit associated with deposition of Stage 4 quartz veins. In part, this can be attributed to reduced fault-valve activity along the Great Chesney fault in the vicinity of the New Occidental deposit possibly as a consequence of decreasing strain rate (and lower time-averaged differential stresses) and lower fluid pressures due to decreased fluid flux along the fault. In addition, strain-softening of the fault through the development of weak cataclasite and phyllosilicate-rich layers may have promoted more ductile deformation.

This study has identified a number of factors critical to formation of gold and base metal deposits in the Cobar Basin and which provide a focus for renewed exploration in the region. Deposits are associated with major deep-seated fault systems that penetrate basement beneath the basin and which tapped and then focussed discharge of deep-sourced (>10km depth) or circulated hydrothermal fluids. They formed by repeated focussing of strain, dilation and fluid flow along relatively discrete (short strike-length) segments of

reverse dip-slip faults or shear zones, which accounts for the sub-vertical pipe-like shape of the New Occidental and other Cobar deposits. Fault-valve behaviour along such faults is a key determinant in formation of gold-rich deposits in the Cobar Basin, with gold deposition intimately liked to cyclic decompression of the hydrothermal fluid. The richest gold deposits are therefore predicted to occur in structural settings where the intensity of fault-valve behaviour is greatest, including:

- Along steeply-dipping major faults that were unfavourably oriented for slip (e.g. faults oriented at high angles to σ_1 which therefore require very high fluid pressures to slip).
- Where favourably oriented faults that would otherwise repeatedly slip and therefore prevent over-pressuring of hydrothermal fluids are absent.
- Beneath or within seals like the Great Cobar Slate that promote fluid over-pressuring.
- Within dilational sites along the fault which focus fluid flow and allow large fluid pressure drops from supra-lithostatic to near hydrostatic values during fault rupture events.
- Where fluid flux and fault zone permeability is high, which supports large-scale fluid flow from sources in basement beneath the Cobar Basin.

Evidence for fault-valve behaviour includes development of multiple sets of sub-horizontal extensional quartz veins exhibiting complex over-printing relationships with steeply dipping fault-fill veins, crystalline to cryptocrystalline crustiform and colloform-banded quartz and vein breccias and implosive-style breccia veins.

Recognition of two temporally and compositionally distinct hydrothermal fluids associated with formation of the New Occidental deposit (an early gold-rich fluid and a late-stage base metal-rich fluid that was capable of remobilising early-formed gold but did not contribute any further gold) provides an explanation for the district and deposit-scale metal zonation in the Cobar region. It further characterises those deposit features that indicate whether the first gold-bearing fluid was involved in deposit formation, including:

- Elevated levels of Bi-Se-W-As-Sb.
- Au/Ag ratios in the range 1-2.
- Higher temperature Fe-rich alteration mineral assemblages including Fe-chlorite ± stilpnomelane ± biotite.
- Subtle but distinctive trends of increasing chlorite and white mica content, increasing white mica crystallinity and phengicity and increasing Fe/(Fe+Mg) ratio and Fe^{3+}/Fe^{2+} ratio of chlorite in wallrock, which can readily be detected by SWIR spectrometry.

In contrast, late-stage base metal rich hydrothermal fluids produced Mg-chlorite ± talc and sericite alteration and ores containing elevated Cu-In-Pb-Zn-Cd-Ag-Sn-Co-Mn-S and Au/Ag ratios <1.

Table of Contents

List of Tables

List of Figures

List of Appendices

1 INTRODUCTION

The New Occidental gold deposit, located five kilometres south of Cobar in western New South Wales, was, until recently, the state's largest historical gold producer. Historical production from the New Occidental is estimated at 2.1 Mt @ 10.5 g/t Au (0.7 Moz gold) (Stegman and Stegman, 1996). Mining recommenced at the New Occidental deposit in 2001 based on a resource of 3.0 Mt @ 7.4 g/t Au (0.7 Moz gold) to a depth of 1050m from surface. Globally, the New Occidental deposit therefore contained approximately 1.5 Moz of gold. The New Occidental deposit is one of a number of gold – base metal deposits that occur in the Cobar Goldfield, a field that has produced in excess of 2.5 Moz of gold and contains a further 2.0 Moz of gold in resources. The field has also yielded in excess of 140,000 tonnes of copper and significant quantities of silver, lead and zinc (Stegman and Stegman, 1996).

The origin of and controls on the gold and base metal deposits in the Cobar Goldfield have been a source of contention since copper was first discovered at Cobar in 1870. Individual deposits have affinities with volcanic-hosted massive sulfide (VHMS) deposits, Mississippi Valley-type (MVT) deposits and the Au-Cu deposits at Tennant Creek (Lawrie, 1991a) whilst others clearly share many of the characteristics of mesothermal gold deposits. An epithermal origin for one of the gold deposits has also recently been proposed (Forster and Seccombe, 1999). Theories for the genesis of both the gold-rich and base metal-rich Cobar-style deposits have included hydrothermal replacement models (Andrews, 1913), sediment-hosted exhalative models with varying degrees of tectonically-induced remobilisation (Gilligan, 1974; Sangster, 1979) and structurally controlled deposits formed during basin inversion and de-watering (Glen, 1985, 1987a; de Roo, 1989a,b; Lawrie, 1991a; Hinman, 1992). In more recent times the controversies surrounding deposit genesis have largely been settled in favour of a syn-deformational epigenetic origin (Lawrie and Hinman, 1998).

However, much remains enigmatic about the genesis of Cobar deposits. The source of ore fluids, the mechanisms controlling ore formation in these deposits and ultimately, the controls on metal zoning within Cobar deposits have not been adequately resolved.

Extensive geological studies have been conducted on individual deposits in the Cobar Basin, including at the nearby Peak (Hinman, 1992; Jiang, 1996; Webster, 1999), Chesney (Jiang, 1996; Wilson, 1996), New Cobar (Wilson, 1996), CSA (Robertson, 1974; Brill, 1988a), Elura (de Roo, 1989a,b; Lawrie, 1991a,b) and McKinnons Tank (Forster, 1997) deposits. Glen (1985, 1987a,b, 1990, 1991, 1992, 1994, 1995) conducted detailed structural studies into controls on mineralisation within the Cobar Goldfield as part of regional mapping of the Cobar Basin. However, no recent research has focussed specifically on the New Occidental deposit.

1.1 Purpose of this Study

Whilst the various mineral deposits in the Cobar Goldfield have broad similarities, all differ slightly in detail (Stegman and Pocock, 1996; Lawrie and Hinman, 1998; Stegman, 2001a). Any model proposed for the genesis of mineralisation within the Cobar Goldfield must not only account for the broad similarities but must also explain the differences. The New Occidental deposit therefore represents an additional important source of geological data that can contribute to the development of a genetic model for deposits in the Cobar Gold Field.

This study aims to determine the nature and mode of gold mineralisation in the New Occidental deposit and resolve the geological, geochemical and structural controls on gold mineralisation through:

- Describing the nature and distribution of quartz veins, wallrock alteration and mineralisation within the deposit.
- Establishing an integrated paragenetic sequence for the various stages of quartz veins, wallrock alteration and mineralisation.
- Examining structural controls on the different stages of quartz veining, alteration and mineralisation within the deposit.
- Characterising the evolving chemistry of the ore fluids.

These studies provide structural and geochemical constraints for a model for the New Occidental deposit in terms of its tectonic setting within the Cobar Basin. The model provides the basis for assessing possible genetic models for mineralisation within the broader Cobar Goldfield.

1.2 Information Used in the Study

Research undertaken in this study is based upon:

- Surface geological exposure in the New Occidental deposit environs.
- Diamond drillcore obtained by Peak Gold Mines and Cobar Mines during their evaluation drilling programs at the deposit. Mineralised parts of the drillcore were routinely analysed for Au, Ag, As, Bi, Cu, Fe, Mn, Pb, Sb and Zn.
- Historical gold assay data from grade control drilling and underground sampling undertaken by New Occidental Gold Mines during mining operations over the period 1935–52 (data archived by Peak Gold Mines).

Specific studies that have been undertaken on the New Occidental deposit, and the author's input to data collection, are summarised in Table 2.

Table 2: Studies undertaken on the New Occidental deposit.

Study:	Data:	Data Collection:
Ascertaining the structural and geological setting of the New Occidental deposit	Surface geological mapping of the Cobar Goldfield from the New Cobar deposit in the north to Coronation-Beechworth deposits in the south	Author
Modelling the three dimensional structure of the deposit and that of its environs	Structural logging of New Occidental evaluation diamond drillcore (NO1–NO25)	Author
	Detailed structural mapping of the New Occidental deposit environs	Author
Determining both the nature and distribution of the various generations of quartz veins, alteration and the metal distribution within the New Occidental deposit	Detailed geological logging of New Occidental evaluation diamond drillcore (NO1–NO25)	Author
Mineralogical and structural studies to confirm and refine macroscopic mineral relationships identified during core logging	Microscopic studies of thin- and polished thin-sections	Author

Table 2 Continued

Detailing the nature of mineral associations within the broad framework identified by geological logging of the drillcore, including characterising the composition of fine-grained sulfides	Detailed geological logging of New Occidental evaluation diamond drillcore (NO1–NO25)	Author
	Detailed transmitted and reflected microscopy, in conjunction with both qualitative and quantitative scanning electron microscopy (SEM) on selected drillcore samples	Dr Ivan Reynolds, Rio Tinto Technology Development
Characterising the geochemistry of mineralisation and alteration within the deposit	Whole-rock and trace element geochemical analyses of drillcore samples collected from three traverses across the New Occidental deposit	Analyses performed by Amdel Laboratories, Thebarton, South Australia
Identifying changes in phyllosilicate alteration mineralogy throughout and peripheral to the New Occidental deposit	PIMA portable infra-red spectrometry of drillcore pulps and drillcore	Analyses and initial interpretation performed by M. Hornibrook (Rio Tinto Exploration) and then by S. Pontual (AusSpec International Ltd)
Fluid inclusion studies to help quantify the physiochemical conditions under which the deposit formed	Fluid inclusion petrology	Author
	Microthermometric analyses of fluid inclusion populations	Author (70%) and A. Rae (UTAS) (30%)
Mass spectrometry of fluid inclusions to determine the composition of gaseous phases in fluid inclusions	Mass spectrometry of crushed fluid inclusions in samples of mineralised quartz	Analyses and initial interpretation of spectrometric data by Dr Khin Zaw (UTAS)
Lead isotope studies to determine the age and likely source of metals in the various stages of mineralisation	Lead isotope analyses of selected drillcore samples	Analyses by CSIRO Division of Exploration and Mining, North Ryde
Sulfur isotope studies to determine the likely sources of sulfur in the various stages of mineralisation	Sulfur isotope analyses of selected drillcore samples	Initial sample preparation by M. Blake (UTAS) and analyses by Central Science Laboratory (UTAS)

1.3 History of Mining Operations at the New Occidental Deposit

The New Occidental deposit was first prospected for copper in 1871 not long after the discovery of copper at the Great Cobar in 1870. It was then named the United Mine. Initial prospecting, which included limited shaft sinking, was relatively unsuccessful. In 1889 the deposit was renamed the Occidental Mine and gold mining commenced from a steep-walled opencut and subsequently from levels underground. A 10-head stamper was erected onsite and began crushing oxide ore grading 10 g/t Au. By 1905 a 50-head stamper was operating, and this was expanded to a 60-head stamper in 1911. A cyanide recovery circuit was added to the mill and significantly improved gold recovery. However, following a decline in gold and copper prices at the end of World War I, the Occidental Mine ceased production in 1918 (Stegman and Stegman, 1996).

The rapid rise in the price of gold in the late 1920s and early 1930s lead to the formation of a syndicate to re-open the Occidental Mine in 1930. After a false start, the mine was eventually re-opened by New Occidental Gold Mines NL and commenced production in 1935. Renamed the New Occidental, the mine quickly established profitability and by 1937 was treating upwards of 80,000 tonnes of ore grading 12–13 g/t Au per annum. Production reached a peak

in 1942 but declined in the following years due to wartime shortages of manpower and restrictions on gold mining. Production ceased altogether in 1952 in response to increased cost of labour, declining head grade with depth, and a failure of the hanging wall in the main production stope (Stegman and Stegman, 1996).

From 1987 to 1988 Ranger Exploration re-treated the New Occidental tailing dumps (Stegman and Stegman, 1996).

In 1986, Cobar Mines Pty Ltd undertook a small exploration drilling program that highlighted the down-dip continuations of the New Occidental deposit to at least 1000m below surface. Peak Gold Mines commenced evaluation drilling of those extensions in early 1995 and also tested extensions of the New Occidental lode immediately to the north of the historical workings. A total of 18 diamond drillholes and 33 wedges (a total of 51 drillholes for approximately 22 kilometres of drilling) were completed at the New Occidental as part of this evaluation. These drillholes provide an overall drillhole spacing of approximately 50m in the north-south direction and 75m in the vertical direction (Figure 1).

In July 2000 Peak Gold Mines committed to re-opening the New Occidental mine. Construction of an underground drive from the nearby Peak mine to the 900m Level of the New Occidental orebody was completed in late 2001 and underground ore extraction of the orebody on the 92 Level (920m from surface) commenced soon afterwards.

Figure 1: Longitudinal section and plan of the New Occidental deposit showing PGM evaluation drilling.

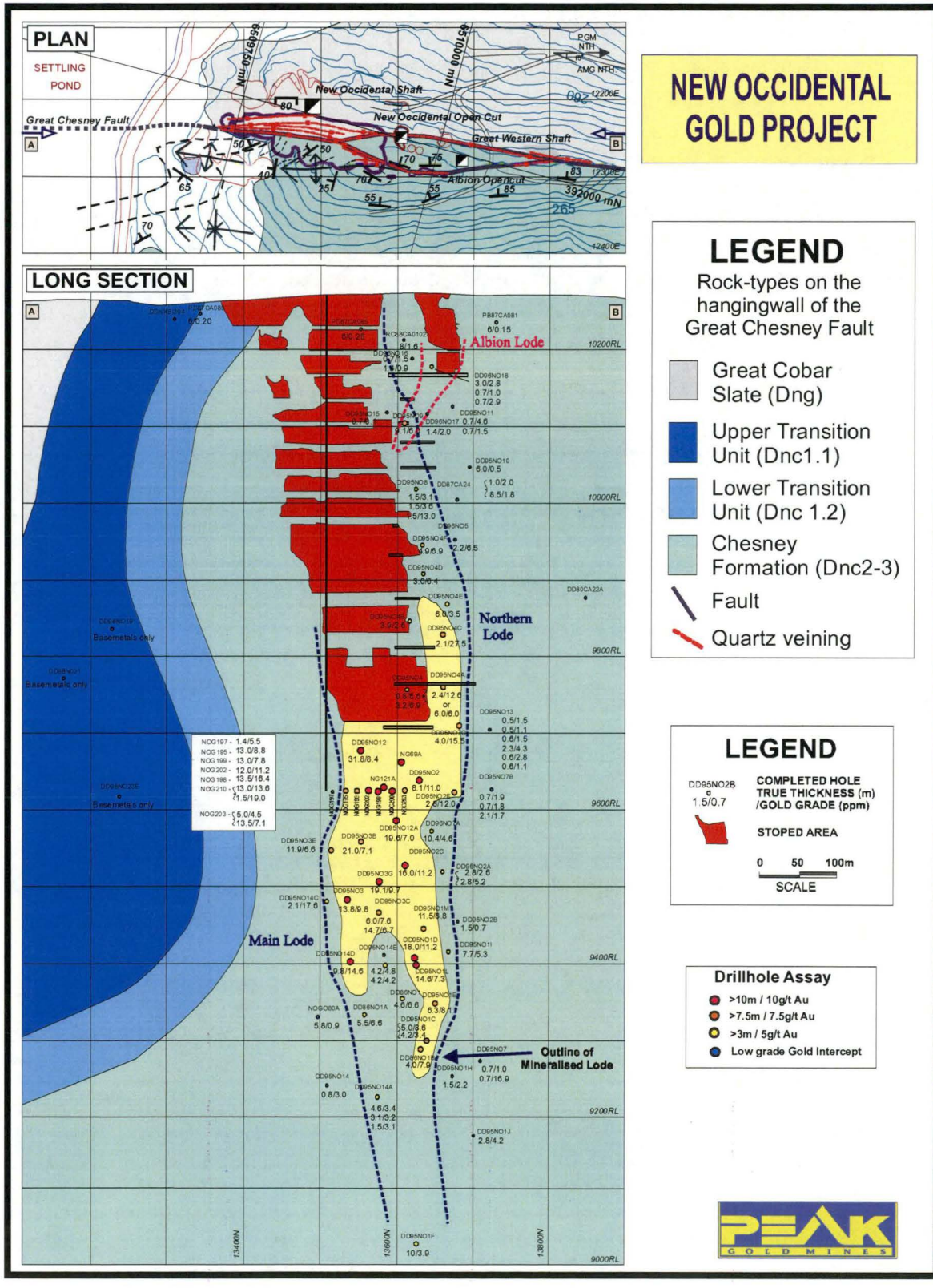

2 REGIONAL GEOLOGICAL SETTING - THE COBAR BASIN

2.1 Regional Geology and Mineralisation

The Early Devonian Cobar Basin lies within the northern part of the Central Belt of the Lachlan Orogen (Figure 2), as defined by Glen (1992, 1995). The Central Belt comprises Cambro-Ordovician sediments that have been intruded by an extensive suite of Silurian S-type granitoids of the Wagga Tin Belt, the latter cropping out over most of the length of this belt. Two smaller Devonian age basins, the Mt Hope and Rast Troughs, represent the southward continuation of the Cobar Basin. The Cobar Basin is associated with extensive gold-base metal mineralisation including the New Occidental, Peak and Mt Boppy gold deposits, the CSA copper deposit and the Elura zinc-lead-silver deposit. Apart from the Cobar deposits, the only other significant mineralisation within the Central Belt occurs at the Ardlethan tin deposit in the southern part of the belt (Glen, 1995)

Figure 2: Geology and mineralisation of the Lachlan Orogen (after Walshe et al., 1995; Glen, 1995).

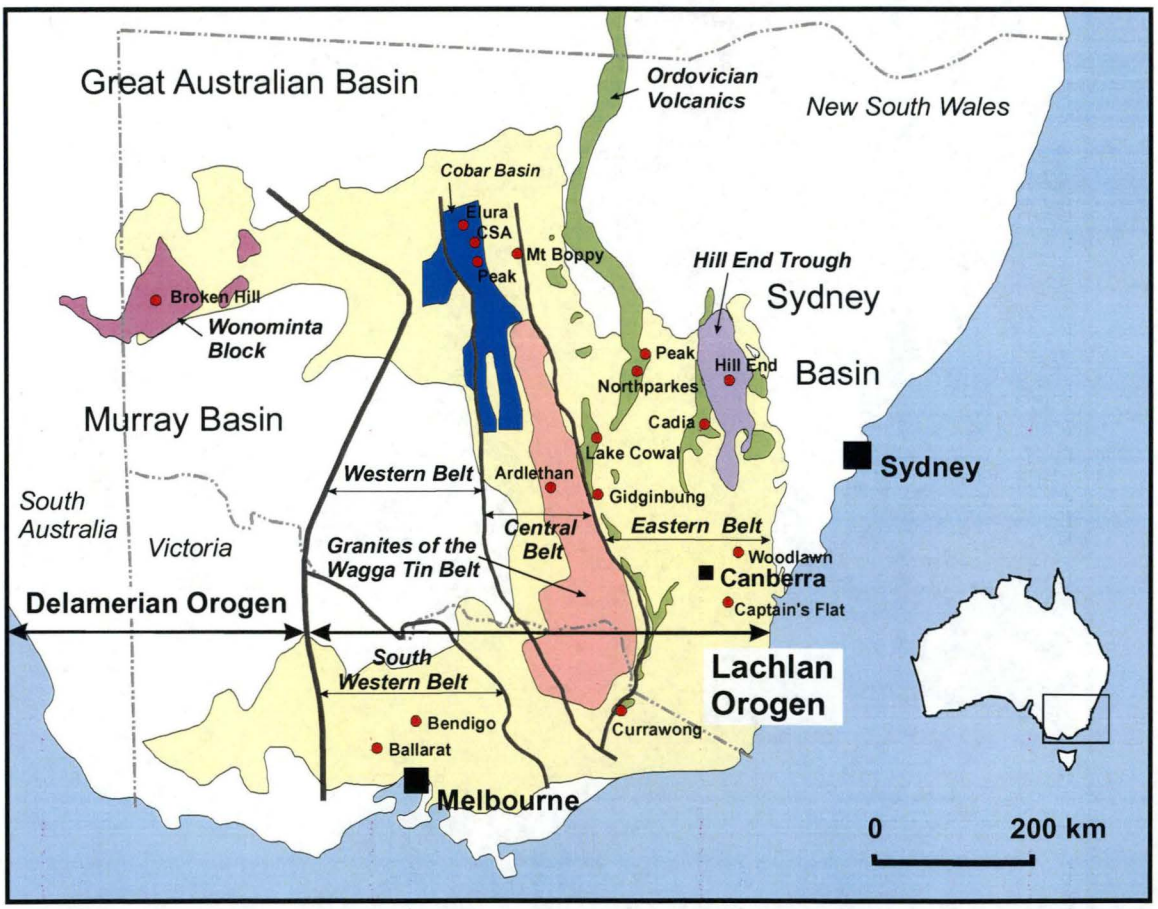

The Eastern Belt of the Lachlan Orogen is dominated by Ordovician quartz-rich turbidites and Siluro-Devonian granites and volcanics (Walshe et al., 1995). Lesser Early Devonian sediments are contained within the Hill End Trough in the eastern part of the belt (Glen, 1995). Copper-gold mineralisation is associated with Early Ordovician to Early Silurian volcanics and related granitoids including porphyry-style deposits at the Northparkes, Lake Cowal, Copper Hill and Cadia; skarn deposits at Browns Creek and Lucky Draw; and epithermal-style gold deposits at Gidginbung and Peak Hill. Volcanic-hosted massive sulfide (VHMS) deposits including the Woodlawn, Captains Flat and Currawong deposits are

associated with the Late Silurian volcanics present in the eastern part of the belt. Structurally controlled copper-minor gold mineralisation of probable Devonian age is present in the western part of the Eastern Belt at Girilambone and Tritton. The Hill End Trough, which is of a similar age to the Cobar Basin, contains structurally controlled gold mineralisation (Walshe et al., 1995; Glen, 1995; Perkins et al., 1995).

The Southwestern Belt is dominated by Ordovician and Devonian turbidites and contains the extensive structurally-controlled gold deposits of the Victorian gold fields (Walshe et al., 1995).

2.2 Cobar Basin Sedimentation

Regional crustal extension of the Lachlan Orogen in the latest Silurian is thought to have created a series of north-south trending basins in the Cobar region (Glen et al., 1996). These include the Cobar Basin in the north and the Rast and Mt Hope Troughs further to the south (Figure 3). Onset of extension was also marked by the emplacement of Late Silurian S- and I-type granitoids within the basement on both the eastern and western margins of the Cobar Basin (Glen, 1985). These include the S-type Thule Granite (c. 422 Ma) and Erimeran Granite (419 Ma) and the I-type Wild Wave Granodiorite (418 Ma) (Glen et al., 1996; Lawrie and Hinman, 1998).

The Cobar Basin was flanked by the Kopje Shelf to the east and the Winduck shelf to the west (Glen, 1991, 1995). Basin architecture was controlled by a series of internal and bounding WNW-trending extensional faults and internal northeast-trending transfer faults, (Glen et al., 1994; Glen, 1995). Drummond et al. (1992a,b) describe the pre-deformation shape of the Cobar Basin as asymmetric with the western margin of the basin steeper than the eastern margin.

Drummond et al. (1992a) suggested that the Cobar Basin formed by oblique northeast-southwest translation of an upper crustal plate above a major ramp-flat mid-crustal detachment during extension. The ramp is interpreted from seismic sections to be at about 12–16 kilometres depth in the west of the basin deepening to about 25 kilometres in the east. The strike of the ramp is northwest and sub-parallel to the strike of the basin. Glen et al. (1996) proposed that the Cobar Basin represents a trans-tensional basin that developed in response to a northeast-southwest direction of regional maximum extensional strain driven by left lateral movement on the Louth-Eumarra shear zone, an east-northeast-trending shear zone immediately north of the Cobar Basin. This shear contains syn-kinematic granites of inferred Siluro-Devonian age.

Cobar Basin fill comprises predominantly quartz-rich turbidites of the Early Devonian Cobar Supergroup. In contrast, the similar-aged Rast and Mt Hope Troughs to the south contain a significant component of rhyodacitic volcanics (Glen, 1985).

The Cobar Basin contains a two-stage fill, with the lower part characterised by coarser grained clastics and thicker bedded sediments than the upper part (Glen et al., 1996). Glen (1991) regarded the two fill sequences as representing syn- and post-rift stages, although Glen et al., (1996) highlighted the relatively subtle nature of this sub-division; based solely on the relative amounts of sandstone in the sequences. Average basin thickness is of the order of 6 kilometres (Glen et al., 1994).

Figure 3: Geology and mineralisation of the Cobar Region (after Glen, 1987a; 1994).

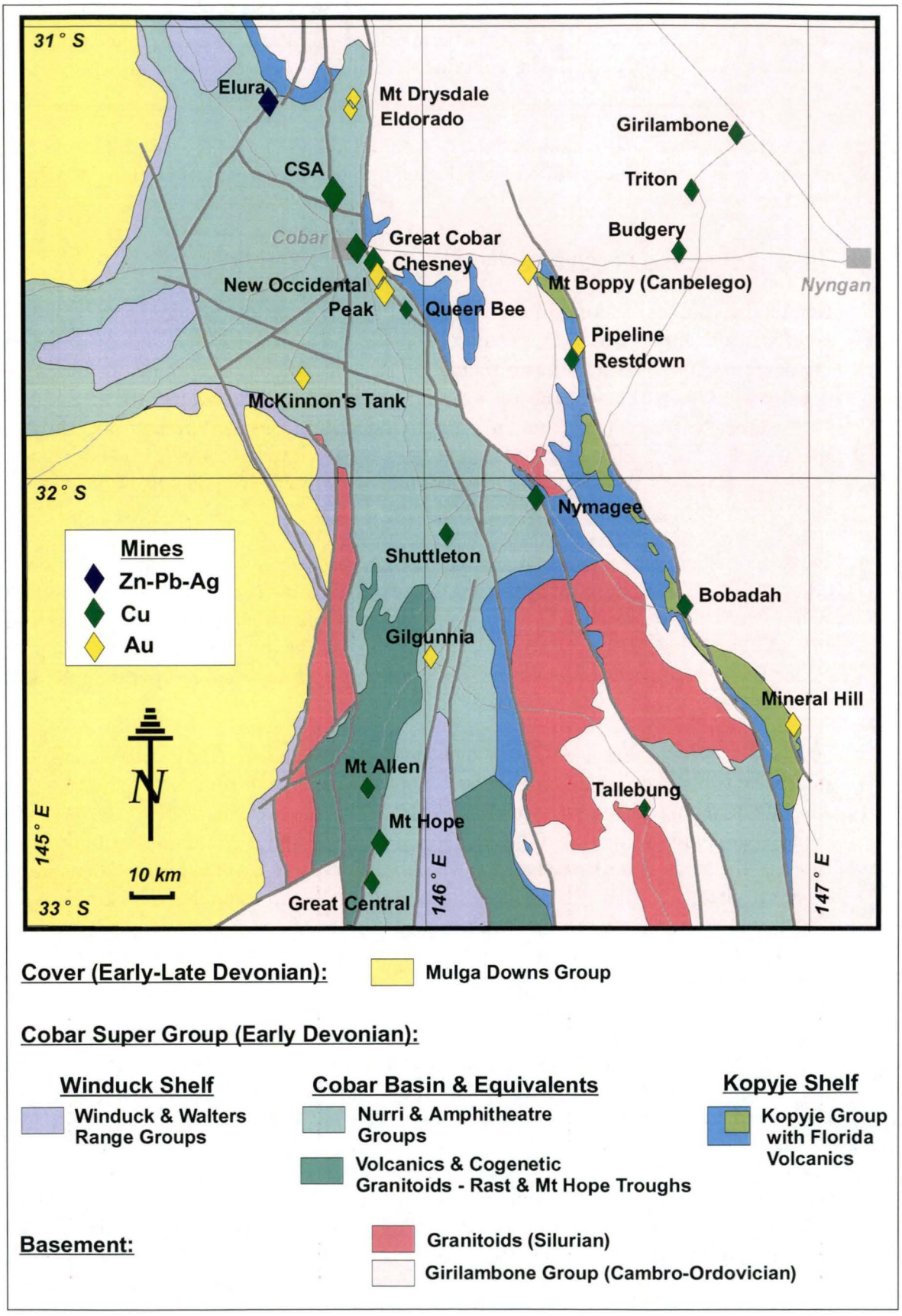

The lower unit of the Cobar Basin (the Nurri Group) is a fining upwards sequence comprising initial sandstone and conglomerate (the Chesney Formation) that passes abruptly up into more extensive fine-grained mudstone and siltstone (the Great Cobar Slate). The Great Cobar Slate is largely restricted to the eastern margin of the Cobar Basin, suggesting sediments were sourced from an eastern landmass. Less extensive sedimentation also occurred coevally on the Kopyje Shelf. The shelf sediments (the Kopyje Group) also comprise basal conglomerate and sandstone that grade upwards into finer grained sediments. However, in contrast to the Great Cobar Slate, the finer grained Kopyje Group sediments contain a significant calcareous component, including reefal limestone and marly mudstone (Glen, 1987a). Further east, a more extensive NNW-trending belt of Kopyje Group sediments crops out within an area known as the Canbelego-Mineral Hill trend. This belt contains a significant component of rhyolitic and lesser rhyodacitic and dacitic volcanics (Gilligan and Byrnes, 1994). The volcanic rocks interfinger with finer grained sediments near the top of the Kopyje Group sequence.

The upper unit of the Cobar Basin, the Amphitheatre Group, comprises much more extensive lower energy turbidite. The Amphitheatre Group consists of an upward coarsening cycle (lower Amphitheatre Group and CSA Siltstone) followed by an abrupt change to thinner-bedded and finer grained sediment (the upper Amphitheatre Group). Detritus is interpreted to have been sourced from an uplifted northwestern and western landmass (Glen, 1985). This unit occupies most of the Cobar Basin (Glen et al., 1996) and interfingers with sediments deposited on the western Winduck Shelf (Mulga Downs Group). Together, these sediments obscure the syn-rift original depositional western edge of the Cobar Basin.

Limestone is present within sediments deposited on both the Kopyje and Winduck Shelves and carbonate is increasingly recognised as a significant component of the clastic sedimentary rocks within the Cobar Basin. The McKinnons deposit located on the western margin of the Cobar Basin is hosted in a sequence of calcareous siltstone and mudstone within the lower Amphitheatre Group (Forster and Seccombe, 1999). Likewise, it is now recognised that the mudstone and siltstone within the upper parts of the Nurri Group contain appreciable carbonate detritus, possibly derived from erosion of limestone from the nearby Kopyje Shelf (Stegman, 1998). Reefal limestone and marly mudstone belonging to the upper part of the Kopyje Group have recently been discovered stratigraphically beneath the CSA Siltstone at the Elura deposit in the north of the Cobar Basin (Leevers, 2000).

Volcanics form only a small proportion of the exposed Cobar Basin, although volcanic units may be more prevalent at depth (Glen, 1991). Small bodies of felsic porphyry crop out near the Queen Bee mine at the southern end of the Cobar Gold Field and to the south of McKinnons mine (Glen, 1987a) and bodies of intrusive flow-banded rhyolite are exposed in the underground workings in the Peak mine (Stegman, 1998). These volcanics are compositionally similar to the extensive felsic volcanics present on the Kopyje Shelf along the Canbelego-Mineral Hill trend and also to volcanics in the Rast and Mt Hope Troughs to the south (Glen, 1990).

Syn-sedimentary faulting is inferred to have largely controlled patterns of sedimentation within the Cobar Basin (Glen, 1990; Gilligan & Byrnes, 1994). Syn-rift faulting is interpreted to have been active during deposition of both the Nurri Group and lower Amphitheatre Group. Glen (1990) has documented changes in turbidite cycle thickness and unit thickness across inferred syn-sedimentary faults. The transition from Nurri Group to Amphitheatre Group sedimentation in the Cobar Basin is considered by Glen (1990) to represent a disconformity on the basis of changes in sediment source area for these respective units. The presence of Kopyje Group sediments instead of Nurri Group sediments stratigraphically below the CSA

Siltstone at the Elura deposit (Leevers, 2000) points to a major facies change that itself probably reflects significant syn-sedimentary faulting associated with the transition from Nurri Group to Amphitheatre Group during basin sedimentation.

The geological framework of the Cobar region is outlined in Figure 4 and details of the basin stratigraphy are tabulated in Table 3.

Table 3: Cobar Basin Stratigraphy.

Age:	Setting:	Unit:	Composition:
Late-Mid Devonian	Cover	**Mulga Downs Group**	Sandstone, siltstone and shale
Early Devonian	Post-Rift Shelf	**Winduck Group**	Sandstone, siltstone
Early Devonian	Post-Rift Basin	**Amphitheatre Group**	
		Upper Amphitheatre Gp.	Sandstone, siltstone, mudstone
		Biddaburra Formation	Sandstone, siltstone, mudstone
		Alley Sandstone Member	Sandstone
		Lower Amphitheatre Gp.	Sandstone, siltstone, mudstone minor limestone, volcanics
		CSA Siltstone	Siltstone, mudstone
Early Devonian	Syn-Rift Basin	**Nurri Group**	
		Great Cobar Slate	Siltstone, mudstone
		Unnamed silicic volcanics	Porphyry, rhyolite
		Chesney Formation	Sandstone, siltstone
		Bee Conglomerate Member	Fan conglomerates, sandstones
Early Devonian	Syn-Rift Shelf	**Kopyje Group**	
		Meryula Formation	Siltstone, sandstone, conglomerate, limestone
Silurian	Basement	**Wild Wave Granodiorite**	Granodiorite
Cambro-Ordovician	Basement	**Girilambone Group**	Sandstones, siltstones, metasediments

Glen et al. (1994) suggest an overall thickness of basin fill in the Cobar Basin of up to six kilometres, although the effects of various syn-sedimentary growth faults cannot be easily quantified. Subsequent extensive deformation of the Cobar Basin sequence also contributes to the uncertainty surrounding this estimate.

Figure 4: Geology and mineralisation of the Cobar Basin (after Glen, 1991).

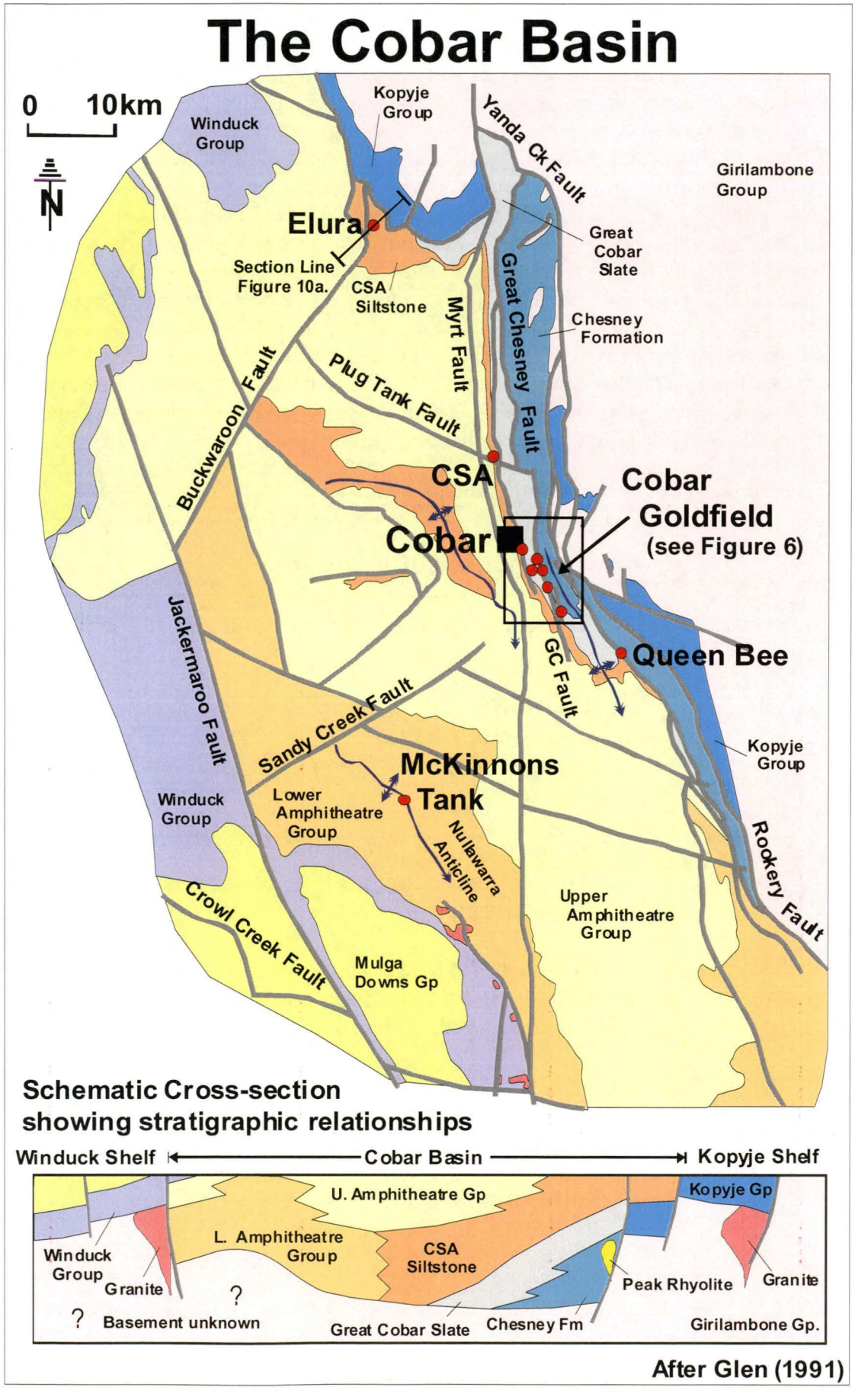

2.3 Cobar Goldfield Stratigraphy

The Cobar Gold Field is located along the eastern margin of the Cobar Basin within sediments of the Nurri Group. Detailed mapping of the Goldfield environs by Glen (1987a) has revealed that the Nurri Group comprises a relatively simple upward fining sequence of clastic sediments. Chesney Formation sandstones, which include basal conglomeratic phases, grade upwards into weakly calcareous silty mudstones and siltstones of the Great Cobar Slate. A distinctive sequence of moderately calcareous siltstones and fine grained sandstones informally known as the Transitional Unit marks the change from Chesney Formation to Great Cobar Slate and provides a useful marker horizon. This unit, whilst not described in Glen's (1987a) type section of the Chesney Formation, had been recognised in the southern part of the Gold Field by Enterprise Exploration during mapping of the area in the late 1940s. Hinman (1992) has also recognised this unit in his division of the Upper Chesney Formation in the Peak mine environs. The presence or absence of this Transition Unit between exposures of Chesney Formation and Great Cobar Slate has been used to help indicate conformable versus low-angle faulted contacts between these two units. A generalised stratigraphic column of the Cobar Basin stratigraphy present in the Cobar Gold Field is shown in Figure 5. The geology of the Cobar Gold Field is shown in Figure 6.

Figure 5: Basal Cobar Basin stratigraphic column.

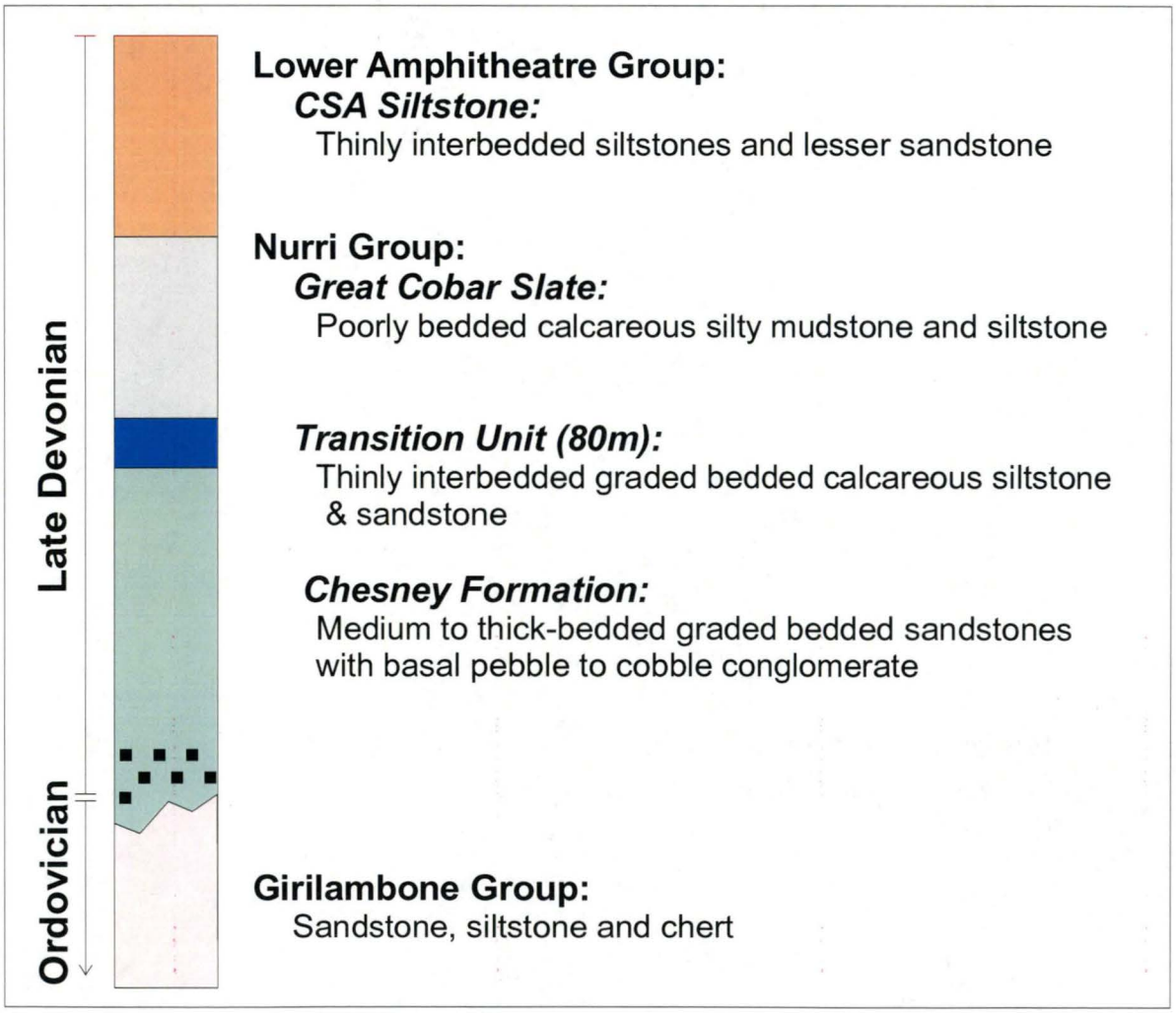

Figure 6: Geology of the Cobar Goldfield (modified from Stegman and Pocock, 1996).

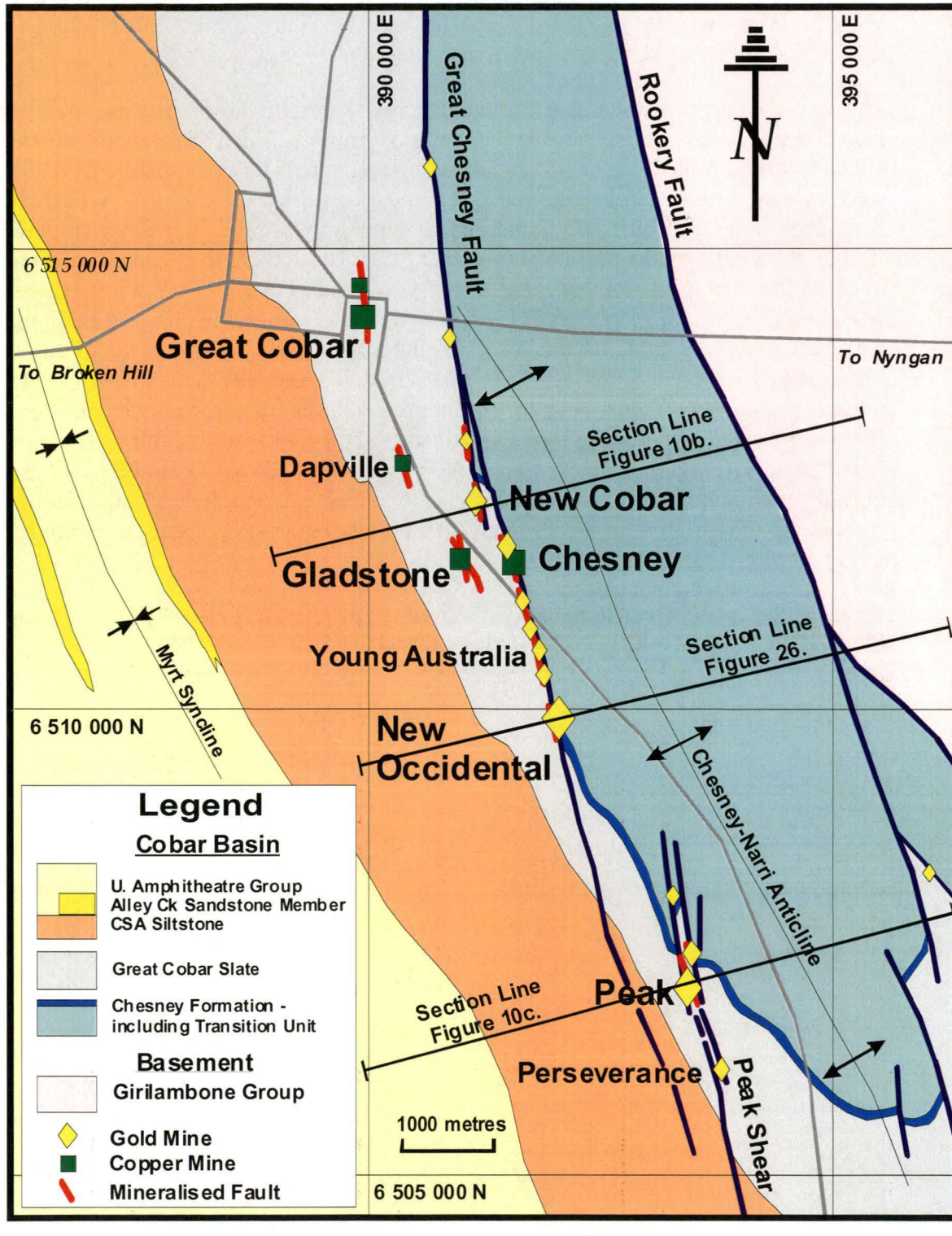

2.4 Cobar Basin Deformation

The Devonian basins were relatively short-lived features. The Cobar Basin was inverted in the late Early Devonian in response to northeast-southwest compression (Glen, 1992). Glen et al. (1996) suggested compression was associated with a reversal of strike-slip movement on the Louth-Eumarra shear zone to the north (Figure 2), and was partitioned into a high strain zone along the eastern margin of the basin and a low strain zone in the central and western parts of the basin. Deformation of the basin sedimentary strata was controlled by the re-

activation of the early basin-forming extensional faults and orthogonal transfer faults, and by the formation of new faults (Glen, 1990; Glen et al., 1994). Subsequent Carboniferous inversion of the western margin of the basin, after deposition of the Mulga Downs Group, was less intense than that along the eastern margin (Glen, 1991).

This eastern margin of the Cobar Basin comprises a north to north-northwest trending braided fault complex with internal fault-bound plates of strongly folded basin sediments (Figure 4). Glen (1990) described this fault complex as a positive half-flower structure developed above a steep-dipping inferred strike-slip fault. In comparison, Glen (1991) interpreted the fault complex as a linked thrust system merging at depth into a single floor thrust (Figure 7). On the basis of deep seismic profiling across the Cobar Basin this thrust is interpreted to underlie much of the eastern part of the Cobar Basin (Glen et al., 1994). The easternmost strand of the fault complex, the Rookery Fault, is interpreted to be a syn-sedimentary, west-dipping detachment fault along which the basin was initially extended. The Rookery Fault was subsequently re-activated during basin inversion as a thrust fault (Glen, 1991, 1994). The other more westerly fault strands are not interpreted to be basin-forming extensional faults. Rather, they are considered to have developed as short-cut structures during inversion as the major basin-forming faults locked up. These younger faults have both steep east and west dips, depending on their relative positions in the thrust complex (Glen et al., 1994). A component of left-lateral strike slip movement on these thrusts has also been inferred (Glen, 1991).

Figure 7: Schematic cross-sectional synthesis of the eastern margin of the Cobar Basin showing the relationship between faults and major mineral deposits (Glen, 1995).

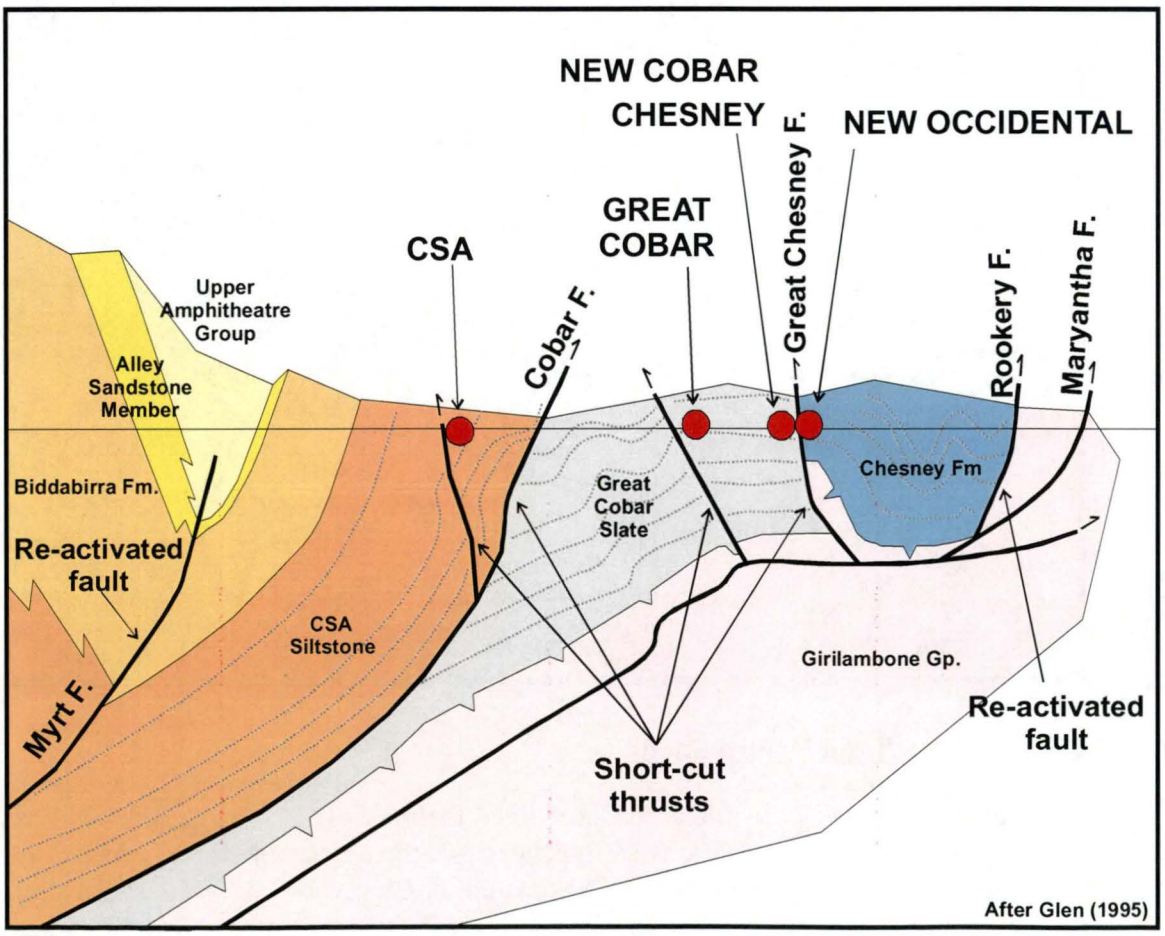

Transfer faults are interpreted in a number of places along the eastern margin of the basin, the most prominent being the Buckwaroon Fault in the north of the basin and the Sandy Creek Fault in the centre of the basin (Glen, 1994; Figure 4). The northeast trending Sandy Creek Fault is inferred from deep seismic reflection transects across the Cobar Basin (Glen et al., 1994) and both are interpreted to have been active during basin formation and inversion (Glen et al., 1994; Glen, 1995).

The fault-bounded sediment wedges are folded into open to tight, gentle to steep southeast-plunging folds with fold axis trends sub-parallel to the bounding faults. This folding is interpreted to be thrust-related, either as fault propagations or connected with bends in the thrust surfaces, (Glen, 1991). Variations in fold plunge are attributed to inhomogeneous strain during deformation rather than to an overprinting second deformation event (de Roo, 1989a; Hinman, 1992).

Deformation in the eastern high strain zone is marked by moderate to strong, penetrative, sub-vertical, white mica cleavage that is sub-parallel to the major faults and is associated with a prominent sub-vertical extension lineation (Glen, 1991). Cleavage intensity markedly increases in proximity to the major fault zones. The strike of the cleavage progressively rotates from a north-northwest trend south of Cobar to a north-northeast trend north of Cobar (Glen, 1985). In detail, cleavage transects the axial planes of folds in the Cobar Gold Field (Glen, 1985). Glen (1990) suggested that cleavage formed after folding in a rotating strain regime.

Glen (1990) concluded that the eastern margin of the Cobar Basin in the Cobar area was deformed during basin inversion under a right-lateral transpressive strain regime, with far field shortening oriented northeast-southwest. The main north-northwest-trending bounding faults to the Cobar Basin were reactivated as right lateral strike-slip/oblique slip faults whilst the west-northwest faults were reactivated as dip-slip faults (Glen, 1991). Smith (1992) argued that the closing direction during basin inversion was oriented more to the east-northeast than northeast on the basis of analogue modelling. However, structural interpretation of seismic data by Drummond et al. (1992a) supported Glen's (1990) interpretation of the orientation of basin closing.

The remainder of the Cobar Basin is characterised by less intense deformation. A sub-vertical cleavage and a steep extension lineation are locally developed and folds have variable plunges (Glen, 1990).

Cobar Basin sediments have been generally metamorphosed to chlorite grade during basin deformation (Glen, 1985). Brill (1988b) used illite crystallinity b_0 values and Si contents of K-white mica from basin sediments to constrain metamorphic conditions near Cobar township to be transitional between diagenesis and low-grade metamorphism. Further to the north at Elura, Brill (1988b) concluded that metamorphic conditions were equivalent to that of diagenesis. Brill (1988b)also suggested a change from low to intermediate pressure metamorphism from north to south, possibly reflecting the effect of increased strain on illite crystallinity. Samples from the Cobar township area were collected from near the CSA, Chesney, Peak and Queen Bee mines, all of which lie within a higher strain zone along the eastern margin of the Cobar Basin (Glen, 1985; 1990). Vitrinite reflectance studies also indicate that Cobar Basin sediments were heated to conditions of burial diagenesis, but were exposed to hotter fluids in the higher strain zones associated with mineralisation (Robertson and Taylor, 1987).

2.5 Structural Setting of the Cobar Goldfield

The bulk of the deposits in the Cobar Goldfield are located on the western margin of the Chesney-Narri Anticline, a moderate to tight south-plunging anticline cored by sandstones of the Chesney Formation (Glen, 1987). Mineralisation is associated with two principal shear zones, the Peak Shear and Great Chesney Fault, both of which juxtapose Chesney Formation with Great Cobar Slate. The structural setting of the Cobar Goldfield and the relationship of the Great Chesney Fault to the eastern basin margin fault complex are shown in Figure 7. The Great Chesney Fault is an east-dipping reverse fault (east block up) whilst the Peak Shear is a steep west-dipping reverse fault (west block up). Together, both faults bound an up-thrown wedge of Nurri Group strata (Glen, 1991; Stegman & Pocock, 1996).

Minor gold occurrences are also associated with shears on the eastern margin of the Chesney-Narri Anticline at the southern part of the Cobar Goldfield. The most prominent of these are the Coronation-Beechworth prospects, which are located on or about the Queen Bee Fault where the fault similarly juxtaposes Chesney Formation with the Great Cobar Slate.

2.6 Basin Mineralisation

The Cobar Basin contains a significant gold and base metal endowment within a relatively small area. The pre-mining resources present in each of the major Cobar deposits are summarised in Table 4 and the location of these deposits is shown in Figure 4 and Figure 6. The bulk of the mineral deposits are localised along the highly deformed eastern margin of the basin. Both the Elura and McKinnons Tank deposits are located within the less deformed westerly part of the Cobar Basin. The Elura deposit is located at the northern margin of the basin whilst the McKinnons Tank deposit is located at the western margin of the basin (Glen, 1995).

Table 4: Pre-Mining global resources of Cobar Deposits.

Deposit	Status	Resource (Mined and remaining Resource)						
		Mt	Au (g/t)	Cu (%)	Pb (%)	Zn (%)	Ag (g/t)	Bi (ppm)
Elura	Operating	42			5.4	8.6	96	
CSA	Operating	48		3.1	0.3	1.1	18	
Great Cobar	Closed	12	1.5	1.9				
New Cobar	Operating	4.4	6.8	0.8				
including	Unmined	1.4	6.4	0.6	0.02	0.07	4.1	70
Chesney	Closed	6	0.8	1.9				
Gladstone	Closed	2	0.5	2.5				
New Occidental	Reopened	5.4	8.8	0.2	0.07	0.07	4	450
Peak	Mined out	5.2	9.1	0.8	1.1	1.0	8.4	
Perseverance	Operating	1.9	11.3	0.85	0.14	0.11	8.8	60
Queen Bee	Closed	1.2		2.4				
McKinnons Tank	Closed	2.2	1.9					

Resources are based upon publicly available production data and released Resource statements

2.6.1 Metal Ratios and Zoning

Cobar deposits range from gold-rich types with only minor associated base metal mineralisation (Peak, New Occidental, New Cobar and McKinnons) to base metal-dominated examples with negligible precious metal credits (Elura, CSA and Queen Bee). Similarly, a full gradation exists between Pb-Zn rich and Cu-rich types. The base metal-only deposits are on average an order of magnitude larger that the largest gold-rich deposits whilst the Cu-Au

deposits tend to be of intermediate size. There is a crude concentric regional metal zoning of the mineral deposits along the eastern edge of the Cobar Basin centred on the cluster of Au-rich deposits located immediately south of Cobar township. Deposits progressively become more Au-poor and Cu-rich and ultimately Pb-Zn-Ag-rich to the north and south of the Au-rich deposits.

Cobar deposits also show an apparent zonation in relation to their stratigraphic setting within the Cobar Basin (Table 5). The gold-rich deposits, with the exception of McKinnons Tank, are located within or near the stratigraphically lowermost unit of the Cobar Basin sedimentary sequence, the Chesney Formation. The Cu-Au deposits are located within the Great Cobar Slate, the unit that overlies the Chesney Formation and which represents the top of the Nurri Group. In contrast, the base metal-rich, Au-poor deposits are consistently within the lower Amphitheatre Group sediments, specifically the CSA Siltstone. The McKinnons Tank deposit is located within lower Amphitheatre Group sediments on the western margin of the basin. The relative positions of the various Cobar deposits within the Cobar Basin sequence are shown in Figure 8.

Table 5: Metal Association and Host Stratigraphy of Cobar Deposits.

Deposit	Metal Association	Host Stratigraphy
Elura	Pb-Zn-Ag	CSA Siltstone
CSA	Cu-Pb-Zn-Ag	CSA Siltstone
Great Cobar	Cu-Au	Great Cobar Slate
New Cobar	Au-Cu	Great Cobar Slate
Chesney	Cu-Au	Great Cobar Slate
Gladstone	Cu-Au	Great Cobar Slate
New Occidental	Au	Chesney Formation & Great Cobar Slate
Peak	Au-Cu-Pb-Zn-Ag	Chesney Formation & Great Cobar Slate
Perseverance	Au-Cu	Chesney Formation
Queen Bee	Cu	CSA Siltstone
McKinnons Tank	Au (minor Pb-Zn)	Lower Amphitheatre Group

Within each deposit, metal zoning is less obvious, although much was initially made of variations in Cu/Pb-Zn ratios within the Cobar deposits in an attempt to determine the "stratigraphic top" of the mineralisation (Gilligan, 1974; Sangster, 1979). Cobar deposits commonly contain discrete Cu-rich and Pb-Zn-rich lenses. Discrete Pb-Zn-rich lenses are better developed in the western parts of several of the deposits (CSA, Great Cobar, Chesney, New Occidental, Peak and Queen Bee) (Sangster, 1979; Stegman & Pocock, 1996; Shi & Reed, 1990). Sangster (1979) interpreted this apparent zonation to be stratigraphic zoning consistent with westward-facing exhalative deposits. In detail, however, such an interpretation is opportunistic, and Pb-Zn and Cu mineralisation is developed in a variety of positions within the Cobar deposits. For example, the Pb-Zn mineralisation in the Peak gold deposit is present throughout the deposit but is best developed in the outer parts and within the Peak shear. In contrast, the Cu-rich mineralisation is best developed around and within the rhyolite core to the deposit (Stegman and Pocock, 1996; Figure 9a). In the Western system of the CSA deposit, Cu-rich mineralisation is associated with zones of strong quartz veining and whilst the Pb-Zn-rich mineralisation is largely restricted to chlorite-rich shears that anastomose through the core of the deposit (Stegman, 2001b; Figure 9b). In the deeper sections of the New Occidental gold deposit Pb-Zn-rich mineralisation occurs in the central part of the deposit whilst the Cu-rich mineralisation flanks the gold mineralisation along its western margin (Stegman, 2000; Figure 9c).

A trend of increasing Cu with depth has been noted in the CSA and Elura deposits (Lawrie, 1991b; Lawrie and Hinman, 1998) and is also apparent at the New Occidental deposit (Stegman, 2000). Gold mineralisation occurs within both Cu-rich and Pb-Zn-rich mineralisation, although a greater proportion of the Au deposits are Cu-rich rather than Pb-Zn-rich (Table 4).

Figure 8: Cobar deposits and their stratigraphic setting.

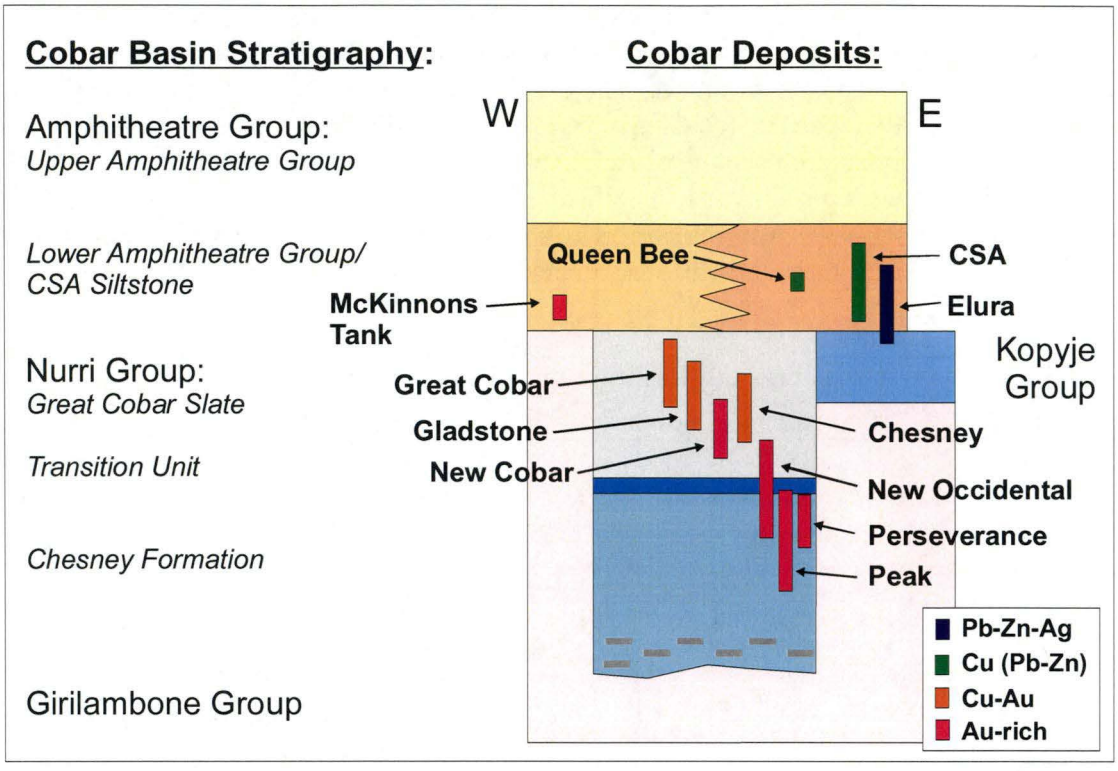

Figure 9: Detailed deposit-scale sections through the Peak, New Occidental and CSA deposits (modified from Stegman and Pocock, 1996; Stegman, 2000; Stegman, 2001b).

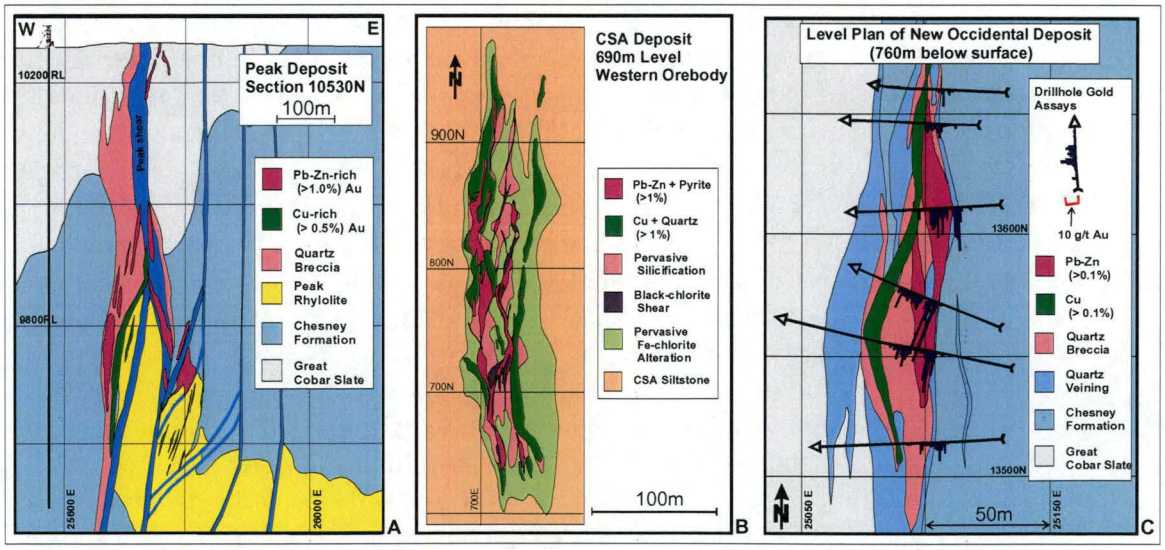

2.6.2 Structural Controls on Mineralisation

Cobar deposits demonstrate a strong structural control, both in terms of deposit location and shape. Individual deposits occur within higher strain zones, typically in intensely cleaved zones, shears and faults. In detail, mineral deposits occur within:

1. Dilational sites developed along zones of competency contrast (for example; faulted sandstone-slate contacts, sandstone-rhyolitic intrusive contacts and unaltered sediment-silicified sediment contacts).
2. Zones of more intense strain within high-strain zones (Lawrie and Hinman, 1998).
3. Hinge zones of anticlinal folds.
4. Intersections of two or more faults.

The structural setting of the major Cobar deposits is described in Table 6. Cross-sections through the Peak, New Cobar-Gladstone and Elura deposits are shown in Figure 10. Stratigraphic displacement across individual high-strain zones is apparently minor in the case of the shears that immediately host the Elura, CSA, Great Cobar, New Cobar, Chesney, Queen Bee and McKinnons Tank deposits. However, most of these deposits are proximal to major displacive faults (Table 6). In contrast, approximately 250m of dip-slip displacement have been documented on the Peak shear that hosts the Peak and Perseverance deposits and in excess of 1200m dip-slip displacement has been identified on the Great Chesney Fault, which hosts the New Occidental deposit (Stegman, 2000). All of these higher strain zones are uniformly characterised by a reverse sense of shear.

Table 6: Structural setting of individual Cobar deposits.

Deposit	Association with Major Structures	Structural Setting
Elura	Buckwaroon Fault	Deposit enveloped in sheath-type folds above a reactivated syn-sedimentary growth fault adjacent to major basin transfer fault (Buckwaroon Fault), (de Roo, 1989b)
CSA	Plug Tank Fault and Myrt Fault	Deposit localised within steep east-dipping shear zones developed in the hinge zone of a subvertical-plunging monoclinal fold adjacent to basin transfer fault (Plug Tank Fault), (Shi and Reed, 1998)
Great Cobar	Great Cobar Fault	Deposit located in an east-dipping shear zone transecting the hinge of a steeply north plunging anticline, (Stegman & Pocock, 1996)
New Cobar	Great Chesney Fault	Deposit located within an east-dipping second order splay fault associated with a dilational jog in the Great Chesney Fault, (Stegman & Pocock, 1996)
Chesney	Great Chesney Fault	Deposit within east-dipping shear zone in the immediate footwall of the Great Chesney Fault, (Stegman & Pocock, 1996)
Gladstone	Un-named fault	Deposit occurs at the intersection of two steep east-dipping shears, (Stegman & Pocock, 1996)
Peak & Perseverance	Peak Shear	Deposit located in dilational zones within the steep west-dipping dip-slip Peak Shear above/around fault-bound blocks of intrusive rhyolite. The immediate environs of Peak represent a zone of extreme strain within the Peak shear, (Stegman & Pocock, 1996)
Queen Bee	Queen Bee Fault	Deposit hosted in west-dipping shear zones in the hanging wall of the Queen Bee Fault (Company data)
New Occidental	Great Chesney Fault	Deposit located within a dilational jog in the steep east-dipping Great Chesney Fault, (Stegman, 2000)
McKinnons Tank	Un-named fault	Deposit localised in poorly developed shears in the hinge zone of the Nullawarra Anticline, which may overly a concealed reverse fault, (Forster & Seccombe, 1999)

The higher strain zones with which individual Cobar deposits are associated are transgressive to host stratigraphy, as illustrated in the examples presented in Figure 10. In addition, there is no evidence for precursor stratiform mineralisation within the Cobar Basin from which

individual deposits could have been remobilised. However, mineralisation is in places loosely stratabound, as evidenced by the regional zoning of deposits highlighted in Figure 8.

2.6.3 Internal Structure of Deposits

In detail, the Cobar deposits typically comprise multiple lenses that have characteristically steep-plunging pipe-like geometries with uniformly short strike lengths (less than 300m), narrow widths (10–30m) but great vertical extent (Stegman and Pocock, 1996). The Elura deposit has a vertical extent of 1000m (David, 2000); the New Occidental deposit has been traced from the surface down to a depth of 1200m and it is open at depth (Stegman, 2000); and the CSA deposit has been traced from the surface to a depth of 1800m (Shi and Reed, 1998). Deposit shape is elongate sub-parallel to the strong mineral lineation.

Individual lenses of mineralisation are localised within areas of higher strain within the deposit envelope. Lenses comprise sulfide mineralisation localised within zones of strong quartz veining and associated quartz-vein breccia and are often accompanied by strong alteration of the surrounding host rock. Some lenses consist largely of massive sulfide and chlorite and are relatively quartz-free. Lens boundaries are gradational and are often defined by grade cut-offs. The geometry of individual lenses reflects the interplay between the successive stages of mineralisation and alteration. For example, early stages of silicification and quartz veining localised within dilational zones along a fault subsequently became the sites for subsequent phases of mineralisation (Stegman and Pocock, 1996; Lawrie and Hinman, 1998). Later mineralisation occurred in dilational zones around and within sites of early mineralisation, consistent with formation during progressive deformation (Stegman, 2001a).

Cobar deposits are ubiquitously associated with voluminous amounts of quartz veining (Lawrie and Hinman, 1998; Stegman, 2001a). The geometry of the quartz veining within each deposit provides clear evidence for the nature of the associated deformation. Multiple overprinting vein sets are present and many of the early veins are strongly deformed, indicating a prolonged history of repeated fault displacement associated with vein formation (Glen, 1987b; Stegman & Pocock, 1996). Most quartz veins are steeply dipping and sub-parallel or slightly oblique to cleavage. These veins range from slip-fibred shear veins to cross-fibred extensional veins (Glen, 1987b). The cores of the gold-rich deposits (New Occidental, New Cobar and to a lesser extent Peak and Chesney) are characterised by the presence of well-developed quartz-vein breccia comprising both cleavage-parallel and lesser sub-horizontal colloform crystalline to cryptocrystalline quartz veins (Stegman, 2001a). A lesser but still significant number of veins comprise sub-horizontal extensional cross-fibred veins that both overprint and are overprinted by the various generations of sub-vertical cleavage-parallel veins (Stegman, 2001a).

2.6.4 Associated Alteration and Gangue Mineralogy

The Cobar deposits have a ubiquitous pervasive silicification and chlorite alteration. Silicification produces a bleached chert-like rock. Alteration chlorite is typically more iron-rich compared to metamorphic chlorite although discrete alteration zones of more Mg-rich chlorite also occur. Both Elura and McKinnons Tank deposits are characterised by carbonate alteration haloes, while zones of stilpnomelane $[(Fe, Mg)_8(Si, Al)_{12}(O, OH)_{12}]$ - trace biotite alteration are quite common in the Cu-Au deposits in the Cobar Gold Field. Sericite alteration is relatively rare although the rhyolite at Peak is pervasively sericite-altered. Forster and Seccombe (1999) describe quartz-sericite-adularia alteration associated with late-stage gold

mineralisation at McKinnons Tank, which they interpreted as an epithermal alteration assemblage.

Most deposits are characterised by the presence of pyrrhotite, with lesser pyrite developed at the deposit margins or in association with Zn-Pb-rich mineralisation. Queen Bee and McKinnons Tank appear to be the exceptions with pyrite developed in preference to pyrrhotite. Most of the Cu-Au and Au deposits in the Cobar Gold Field, with the exception of Peak, contain appreciable amounts of magnetite.

Table 7: Alteration and ore mineralogy of Cobar deposits.

Deposit	Major Ore Mineralogy	Associated Alteration
Elura	Ga, Sp, Po, lesser Py	Qz, Ch, Si, Ca, minor Se
CSA	Cp, Cb, Ga, Sp, Po, Py	Qz, Fe-Ch, Si, lesser Mg-Ch, minor Ta
Great Cobar	Mg, Cp, Cb, Po, minor Ga, Sp	Qz, Fe-Ch, St, lesser Mg-Ch
New Cobar	Mg, Cp, Po, Bm, Bi, minor Ga, Sp	Qz, Fe-Ch, St, lesser Mg-Ch
Chesney	Mg, Cp, Po, minor Bi	Qz, Fe-Ch, St, lesser Mg-Ch
Gladstone	Mg, Cp, Po	Qz, Fe-Ch
New Occidental	Mg, Cp, Bi, Bm, Po, minor Ga, Sp	Qz, Fe-Ch, St, lesser Mg-Ch
Peak	Cp, Ga, Sp, Po, Py	Qz, Fe-Ch, lesser Mg-Ch, Se, minor Ta-Ca
Perseverance	Cp, Cb, Po, minor Ga, Sp	Qz, Fe-Ch, lesser Se
Queen Bee	Cp, Py with lesser Ga, Sp, Po	Qz, Fe-Ch
McKinnons Tank	Py, Sp, Ga, trace Cp	Qz, Mg-Ch, Ca, Se, Ad

Ad - adularia, Bi - bismuth, Bm - bismuthinite, Ca - carbonate, Cb- cubanite, Fe-Ch - Fe-chlorite, Cp - chalcopyrite, Ga - galena, Mg-Ch - Mg-chlorite, Mg - magnetite, Po - pyrrhotite, Py - pyrite, Qz - quartz, Se - sericite, Si - silica, Sp - sphalerite, St - stilpnomelane, Ta - talc.

2.6.5 Igneous Associations

Most Cobar deposits show no obvious association with igneous rock-types. However, both I- and S-type granites are present within the basement immediately bounding the Cobar Basin. K-Ar dating of these granites indicates ages ranging from 418–440 Ma (Glen et al., 1992). Cobar Basin-equivalent sediments of the Kopyje Shelf unconformably overly these granites. Magnetic imagery indicates that these granites have only been partially unroofed by the current erosion surface. Forster and Seccombe (1999) argued that the McKinnons Tank deposit is genetically related to concealed granites that have intruded the Cobar Basin after the main phase of deformation. They infer the presence of these granites from regional magnetic data. However, the existence of these granites has not been confirmed, and no granites of similar age to the Cobar Basin strata are known in the region.

The Peak and Perseverance deposits are spatially associated with an intrusive rhyolite complex (Stegman and Pocock, 1996). The rhyolite intrusion comprises a flow-banded core with hyaloclastite and peperite margins (Stegman, 1998). It contains a weak to locally strong penetrative cleavage and has been extensively dismembered by the Peak Shear. Mineralisation is localised along fault contacts between sediment and rhyolite blocks and to a lesser extent along shears within the rhyolite. The rhyolite transgresses stratigraphy in the host Chesney Formation but as it does not appear to penetrate overlying stratigraphic units and has peperite margins it is interpreted to have been emplaced at a high level into wet sediments of the Chesney Formation during accumulation of the immediately overlying sequence (Stegman, 1998).

Figure 10: Cross-sections through the Elura, Gladstone-New Cobar and Peak deposits.

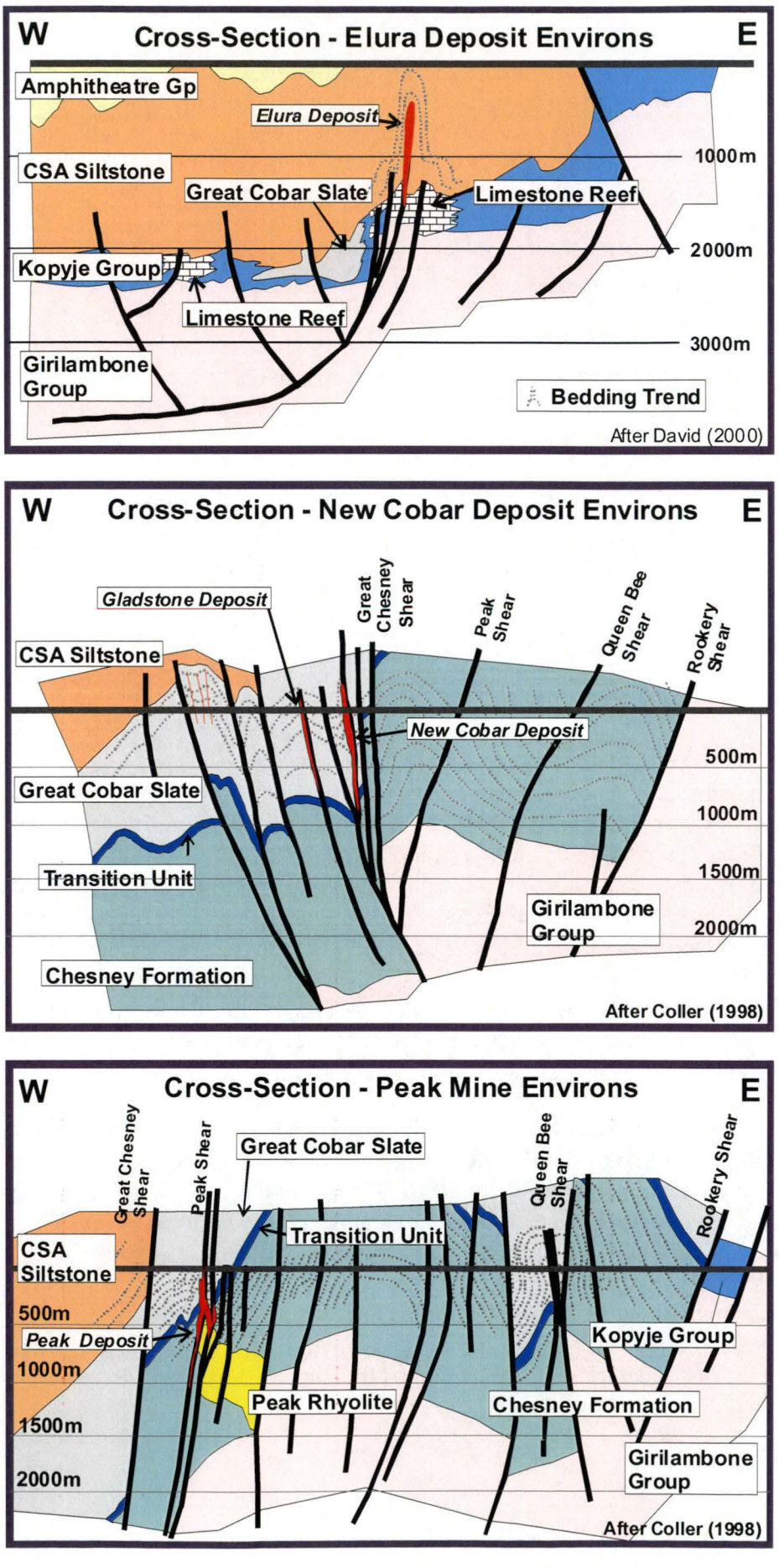

Small bodies of feldspar porphyry are present in the Queen Bee area and have been intersected in drillholes beneath the Queen Bee mine workings. They porphyry bodies are texturally and compositionally similar, comprising large 5–30mm K-feldspar and plagioclase phenocrysts set in a matrix of devitrified glass, sericite and chlorite (Glen, 1987a). Andrews (1913) regarded these bodies as intrusive. However, Kelso (1982) and Glen (1987a) concluded that these bodies were "rhyolitic crystal-vitric tuffs" that are concordant with their host Chesney Formation sandstones. A well-developed slaty cleavage is present within these rocks. However, more recent inspections of these units by the author indicate that they indeed intrude the Chesney Formation but are postdated by the regional cleavage. Whilst the porphyry bodies are generally elongate parallel to bedding, their relatively high height/width aspect ratios and their compositional and textural homogeneity preclude them being volcanic in origin.

Two small occurrences of flow-banded rhyolite and crystal-rich rhyolitic pyroclastics have been documented in the lower Amphitheatre Group on the western margin of the Cobar Basin near the McKinnons Tank deposit (Glen, 1987a). Both occurrences are associated with limestone in what is interpreted to be a shelf setting. However, these units are poorly exposed and their relationship to the enclosing sediments has not been established.

A thin, fine-grained bedded felsic pyroclastic unit has been identified within the CSA Siltstone in the vicinity of the CSA mine (Glen, 1994). It is described as a poorly bedded and weakly graded coarse siltstone to fine grained sandstone containing abundant microshards and devitrified cryptocrystalline quartzofeldspathic material. The unit appears to represent a distal, partially reworked airfall pyroclastic rock.

Igneous rock-types represent a very small part of the Cobar Basin sequence. Where present, they tend to be of felsic composition and have a volcanic to sub-volcanic affinity. They clearly predate cleavage and mineralisation and appear to be direct correlatives of the extensive rhyolitic and rhyodacitic volcanics developed in the Rast and Mt Hope Troughs to the south and the Canbelego-Mineral Hill trend to the east. These volcanic units also appear to be more common in the southern part of the basin.

2.6.6 Fluid Chemistry

Fluid inclusion studies have been undertaken on the Peak (Hinman, 1992; Jiang, 1996), Chesney (Jiang 1996), CSA (Brill, 1988a), Elura (Seccombe, 1990; Lawrie, 1991b; Lawrie et al. 1999a; Sun and Seccombe, 2000) and McKinnons Tank (Forster and Seccombe, 1999) deposits. Whilst each of these studies is based on very detailed deposit-specific paragenetic sequences, fluid inclusion data from the various deposits show many similarities. Primary fluid inclusions are uniformly two-phase and liquid-rich and most are relatively small (<20μm). However, many inclusions associated with the earlier paragenetic stages have clearly been modified by deformation. Inclusions associated with the stages of base metal mineralisation have relatively well preserved inclusion populations. In addition, a significant secondary inclusion population is usually present. Inclusions yield homogenisation temperatures in the range 150–420°C (generally 200–350°C). The higher temperature inclusions tend to occur in quartz associated with Au±Zn±Pb±Cu. Salinities are low to moderate in the range 2–15 wt. % NaCl (generally <10%) with higher salinities generally occurring in quartz veins associated with base metal sulfides. Sun and Seccombe (2000) documented very high salinities (maximum 63.4 wt. % NaCl, mean 16.1 wt. % NaCl) associated with the main stage of Zn-Pb mineralisation at Elura.

Microprobing and thermal-decrepitation mass spectrometry of inclusions from the Elura and Peak deposits indicates the presence of CO_2 and simple hydrocarbons, CH_4 and C_2H_6 (Lawrie et al., 1999b). Lawrie et al. (1999b) documented a progressive shift to higher hydrocarbon contents with increasing salinity and temperature through time in the Elura deposit.

2.6.7 Isotopic Constraints on Ore Fluids

A relatively comprehensive lead isotope database has been established for the Cobar deposits (Carr et al. 1995). All Cobar deposits show relatively homogenous lead isotope ratios and plot on or about the Lachlan Orogen crustal growth curve defined by Carr et al. (1995) (see Figure 11a).

Carr et al. (1995) have highlighted the very small variation in lead isotopic signature between Cobar deposits, other Lachlan Orogen deposits located in rocks of crustal origin (for example, the Silurian and Devonian VHMS deposits) and Devonian and Carboniferous granites in the Lachlan Orogen (see Figure 11b). They conclude that this homogeneity reflects the presence of isotopically homogenous source rocks or the homogenising effect of large-scale magmatic and hydrothermal processes.

Lawrie and Hinman (1998) noted that the Au-rich deposits (Peak and New Cobar) tend to be less radiogenic than the base metal-rich deposits (CSA and Elura). They concluded that the less radiogenic lead represented a basement-derived ore fluid whilst the more radiogenic lead represented a basinal fluid. Mixing of these two fluids has produced intermediate lead isotope signatures. Hinman (1992) concluded that the basement fluid is either metamorphic or magmatic in origin whilst the basinal fluid is derived from connate waters that have evolved in the basin during diagenesis and prograde thermal maturation of the basin sediments. Lawrie et al. (1999b) argued that changes in hydrocarbons documented in the fluid inclusions from Elura are also consistent with a connate source for the Pb-Zn-mineralising fluids, which was expelled from the basin in response to tectonic inversion.

Jiang and Seccombe (2000) argued that the distinction between basement and basinal ore-lead isotope data proposed by Lawrie and Hinman (1998) is within the analytical error of the measurements. Jiang and Seccombe have subsequently argued that the lead isotope signatures of the host sediments and basement rocks preclude these units from being the source of the ore lead. Rather, they considered that the ore-lead was pre-concentrated in the pre-Cobar Basin granites and then remobilised by later deep-seated hydrothermal fluids into the Cobar Basin sequences.

Initial sulfur isotope studies of the CSA, Elura and Cobar Gold Field deposits (Seccombe, 1990) suggested that the sulfur in these deposits is derived from Cobar Basin sediments. However, in a more detailed study of the Peak deposit, Jiang and Seccombe (2000) concluded that the $\delta^{34}S$ values for orebody sulfides are significantly different to both syngenetic and metamorphic pyrite and pyrrhotite. They argue that a trend towards heavier $\delta^{34}S$ values in the early stages of sulfide mineral precipitation indicates contamination of the hydrothermal S-signature by local syngenetic S digested during hydrothermal alteration and ore-formation. Large, apparently syn-sedimentary pyrite accumulations have been noted at several localities within the Cobar Basin, including at the Peak deposit (Stegman, 2001a), and these may have locally been a significant source of sulfur. Jiang and Seccombe (2000) further argue that the relative homogeneity of the $\delta^{34}S$ values for orebody sulfides for the different Cobar deposits indicates a deep-seated homogenous sulfur source.

Figure 11: Lead isotope ratio plots for Cobar deposits and other major deposit groups in the Lachlan fold belt.

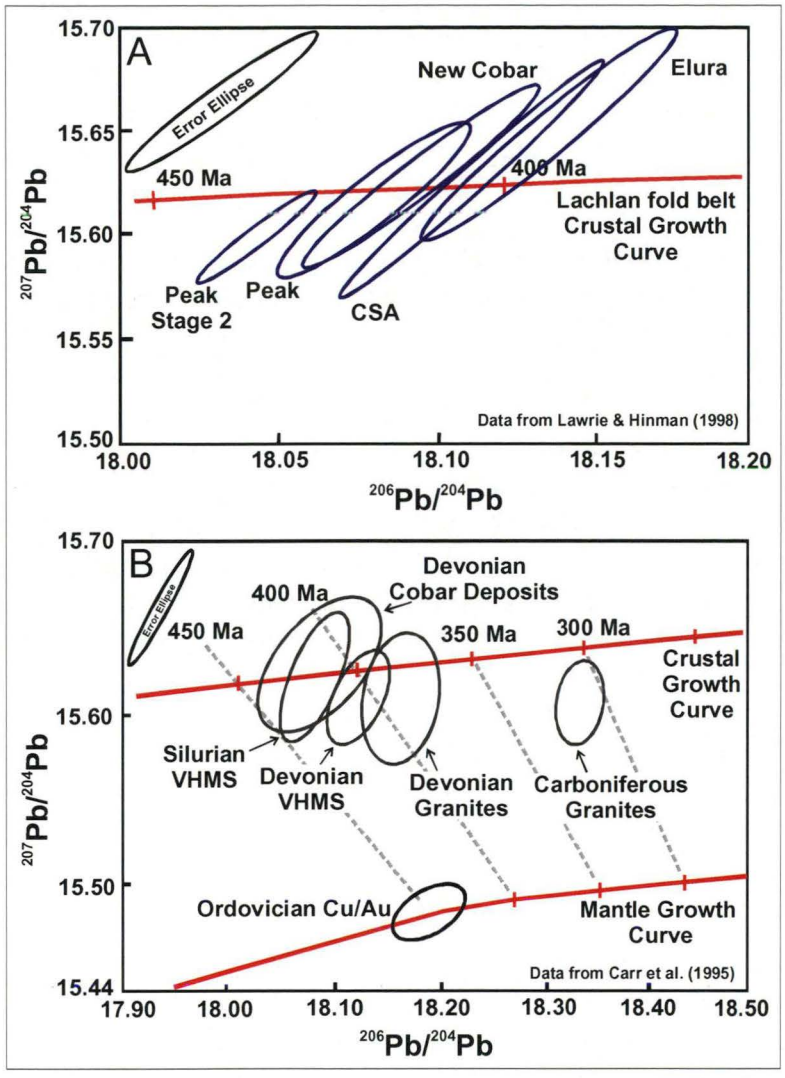

Oxygen and hydrogen isotope studies of the Peak (Jiang, 1996), Chesney (Jiang, 1996) and Elura (Sun and Seccombe, 2000) deposits have led these authors to conclude that fluids associated with the earliest stage of hydrothermal activity (chlorite alteration) were probably metamorphic in origin. However, subsequent ore fluids represent meteoric waters modified by deep circulation through basin and basement sequences. Both Jiang and Seccombe (2000) and Sun and Seccombe (2000) have suggested that the oxygen and hydrogen isotopes for Peak and Elura respectively provide evidence of significant isotope exchange between upwelling hydrothermal fluids and local host-rocks. The isotope data provides no direct evidence for a magmatic component to the hydrothermal system.

2.6.8 Depth of Formation

Metamorphic pressure estimates of 2–3 kb (Brill, 1988b Seccombe, 1990; Jiang, 1996; Sun & Seccombe, 2000) and stratigraphic thicknesses at the time of basin deformation indicate a depth of formation of the order of 5–10 kilometres. Hinman (1992) estimated a depth of formation for the Peak deposit of 3–4 kilometres based on fluid inclusion studies.

2.7 Age Dating of Cobar Basin Sedimentation, Deformation and Mineralisation

Timing of sedimentation in the Cobar Basin is poorly constrained. The maximum age of sedimentation is provided by field relations to the northeast of the Cobar Goldfield where Kopyje Shelf sediments (basal Cobar Basin equivalents) unconformably overlie the Wild Wave Granodiorite, which has been dated by Rb-Sr biotite-whole rock pairs at 418 ± 2 Ma (Glen et al., 1983). Sparse palaeontologic data poorly constrain basin sedimentation to the latest Silurian to early Devonian (Glen, 1994). The Kopyje Group sediments flanking the Cobar Basin are more fossiliferous than their basin equivalents and yield early Devonian ages (Glen, 1994). Glen et al. (1992) suggested that Cobar Supergroup sedimentation possibly continued until 402–397 Ma. K-Ar dating of biotite from the Florida Volcanics, which are intercalated with upper parts of the Kopyje Group sediments in the nearby Canbelego-Mineral Hill trend, indicates an age of volcanism of 391 ± 7 Ma. The pre-mineralisation Peak rhyolite, which intrudes lower Nurri Group sediments (Stegman, 1998), has been imprecisely dated at 430 ± 16 Ma using U-Pb dating of zircons (Perkins et al., 1994), and at 362 ± 25 Ma based on a whole-rock Rb-Sr isochron (Jiang and Seccombe, 1995). The age date suggested by Perkins et al. (1994) for the Peak rhyolite is clearly too old, based on the more precise and reliable age date for the Wild Wave Granodiorite. However, Perkins et al. (1994) regarded the 430 ± 16 Ma age as a maximum, arguing that the S-type Peak Rhyolite may have inherited much of its zircon and that little or no zircon may have precipitated during crystallisation of the rhyolite. Consistent with this line of argument, the zircons recovered from the Peak Rhyolite comprise multiply rimmed euhedral to subhedral grains and the cores of these zircons have returned dates as old as 1500 Ma (Perkins et al., 1994). In contrast, the Carboniferous age inferred by Jiang and Seccombe (1995) for the Peak Rhyolite appears too young compared to the age of the compositionally similar Florida Volcanics.

Glen et al. (1992) have used K-Ar and $^{40}Ar/^{39}Ar$ whole-rock age dating of white mica inferred to have formed during cleavage development in the higher strain zone along the eastern margin of the Cobar Basin to constrain the age of deformation in the Cobar Basin at 395–400 Ma. $^{40}Ar/^{39}Ar$ dating of sericite alteration assemblages at Peak Mine (Perkins et al., 1994) suggest two stages of mineralisation in this deposit occurred at 401.5 ± 1.0 Ma and 384.0 ± 1.4 Ma respectively. The main stage of mineralisation at 401.5 ± 1.0 Ma is approximately coeval with the 395–400 Ma timing of regional deformation and cleavage formation in the Cobar Basin proposed by Glen et al. (1992), whereas the late-stage mineralisation is approximately coeval with deposition of the Late Devonian Mulga Downs Group.

Sun et al. (2000a) reinterpreted the radiometric data of Glen et al. (1992) and Perkins et al. (1994) and suggested that deformation in the Cobar Basin occurred in the period 385–389 Ma. Sun et al. (2000a) argued that the older ages obtained by Glen et al. (1992) and Perkins et al. (1994) reflect the ages of detrital mica derived from reworking of Devonian volcanics during initial sedimentation in the Cobar Basin (e.g. Florida Volcanics), rather than micas formed during cleavage development. Accordingly, they argue that mineralisation at the Peak may have occurred over a much shorter period coincident with basin deformation. Sun et al. (2000a) also determined $^{40}Ar/^{39}Ar$ age dates of deformation and alteration assemblages for the Elura deposit ranging from 386–389 Ma to 376–379 Ma, the younger ages possibly highlighting a further stage of basin deformation.

Recently, Fergusson and Phillips (2001) documented examples of $^{40}Ar/^{39}Ar$ dates from the eastern part of the Lachlan Orogen being significantly influenced by recoil loss/redistribution of ^{39}Ar, leading to anomalously old $^{40}Ar/^{39}Ar$ ages. They also identified problems with inheritance of detrital muscovite, which also contribute to apparently older ages and argue that

low-grade metamorphism and recrystallisation do not eliminate inheritance. Fergusson and Phillips (2001) suggest that inheritance and recoil problems are significantly reduced for epizonal slates which have illite crystallinity values of <0.25.

In detail, Glen et al. (1992) determined $^{40}Ar/^{39}Ar$ ages for four samples from Glen's (1985) Zone 1 (three samples of CSA Siltstone from the CSA mine and one sample of Great Cobar Slate from near the Chesney mine). All four samples have illite crystallinity values of 0.25 or less and yielded ages of 389.2± 1.4 Ma, 399.6± 1.1 Ma, 403.8± 0.8 Ma and 395.6± 4.0 Ma respectively. Only two of the ages are within the Glen et al. (1992) 395–400Ma range for deformation in the Cobar Basin. In contrast, samples from Zone 2, which have illite crystallinity values of >0.25, yielded much older pre-Devonian ages as a consequence of significant inheritance (Glen et al., 1992). In contrast to the interpretation by Sun et al. (2000a) the low illite crystallinities of the samples from Zone 1 suggest it is unlikely they are significantly affected by inheritance. However, it is conceivable that some of those samples suffered ^{39}Ar loss and that the reported ages are maximum ages for deformation in the Cobar Basin.

The K-Ar whole rock ages determined by Glen et al. (1992), which are based on a sample of the Great Cobar Slate from the Chesney mine and two samples of the CSA Siltstone from the CSA mine, yielded ages of 402± 8 Ma, 402± 8 Ma and 405± 8 Ma respectively. Reuter and Dallmeyer (1989) concluded complete rejuvenation of the K-Ar system in micas is only achieved under upper anchizone, or higher, metamorphic grades. At lower metamorphic grades the K-Ar age determinations will reflect incomplete re-setting during metamorphism. Brill (1988b) determined that rocks in Zone 1 of the Cobar Basin, including the Chesney and CSA mines, are transitional between the anchizone and epizone, meaning that the K-Ar age dates obtained by Glen et al. (1992) should be reliable. Glen et al. (1992) concluded that any pre-deformational isotopic characters in these samples have probably been obliterated.

Glen et al. (1992) also conducted Rb-Sr analyses of specimens from Zone 1 (two samples of CSA Siltstone from CSA mine, one sample of Great Cobar Slate from Chesney Mine and one sample of Chesney Formation from near the Chesney mine). Analyses of all four samples yielded an indicated age of 442± 4 Ma, whilst selective analyses of the CSA Siltstone and Chesney Formation provided ages of 440± 15 Ma and 423± 7 Ma respectively. Glen et al. (1992) concluded that these ages represent inherited ages from basement metasediments and granitoids.

Finally, K-Ar dating of post-Au deposition K-feldspar veins in the Peak rhyolite yielded an age of 331 ± 11 Ma (Jiang & Seccombe; 1995). Based on this and their 362 ± 25 Ma Rb-Sr isochron age for the Peak rhyolite, they suggested that gold mineralisation at the Peak mine is Carboniferous (ca 340 Ma) in age.

In summary, current age dating of igneous activity, deformation and mineralisation undertaken in the Cobar Basin is ambiguous and spans a period of at least 70 Ma. It does not provide a clear indication of the relative ages of deposition, mineralisation and deformation in the Cobar Basin and based on this data, deformation and mineralisation apparently overlap with basin sedimentation (Glen et al., 1992). Age dating undertaken so far on the Peak rhyolite also appears unreliable and at odds with the more reliable K-Ar age dating of the pre-Cobar Basin age Wild Wave Granodiorite, the K-Ar dating of the compositionally similar Florida Volcanics on the Kopyje Shelf and the $^{40}Ar/^{39}Ar$ dating of overprinting hydrothermal mica.

2.8 Cobar Metallogeny: Summary and Unresolved Aspects

2.8.1 The Timing of Mineralisation

Considerable uncertainty remains as to the exact age of deformation and associated mineralisation in the Cobar Basin. Age dating undertaken thus far appears imprecise and contradictory.

Whilst age dating has failed to constrain the age of deformation and mineralisation in the Cobar Basin, it is, however, likely that the Cobar deposits are syn-deformational and developed during the Devonian deformation and inversion of the Cobar Basin. Earlier remobilised syngenetic models for these deposits (e.g. Gilligan, 1974; Sangster, 1979) are not supported by field relations and lack of precursor stratiform mineralisation elsewhere in the district. Furthermore, mineralisation in the Peak deposit overprints and clearly post-dates the Peak rhyolite, the latter apparently synchronous with deposition of the Cobar Basin sediments. The deposits described herein exhibit pronounced structural control and are generally associated with steep reverse faults.

2.8.2 Source of Metals and Sulfur

A variety of metal sources have been proposed for the Cobar deposits, including basin sediments and basement of varying composition and depth. The lead isotope data highlights the isotopic homogeneity of lead in the Cobar deposits and points to a crustal source for the metals (Carr et al., 1995). Critically, neither the mixing model involving the interaction of basinal Pb-Zn-bearing fluids and Au-Cu mineralising basement fluids proposed by Lawrie and Hinman (1998), nor Jiang and Seccombe's (2000) model of metamorphic remobilisation of metals from Silurian granitoids appear consistent with all of the data reviewed herein.

Seccombe (1990) initially proposed that sulfur in the Cobar deposits was sourced from sediments within the Cobar Basin. However, Jiang and Seccombe (2000) subsequently determined that for all Cobar deposits analysed to date, the orebody sulfur, whilst relatively isotopically homogenous, is isotopically different to the sulfur in the basin sediments.

The homogenous nature of both the ore-lead and sulfur within the Cobar deposits appears to favour a deep-seated hydrothermal system encompassing much of the Cobar Basin but extending beneath and beyond the Cobar Basin itself. Further detailed studies are required in order to resolve the likely source of metals and sulfur in the Cobar deposits.

2.8.3 Metal Zonation within the Cobar Basin

The metal zoning both between and within deposits in the Cobar Basin has previously been attributed to:

1. Differing degrees of mixing of basinal Pb-Zn rich fluids with basement-derived Cu-Au rich fluids (Lawrie and Hinman, 1998).
2. Differences in thrust geometry tapping different sources (Glen, 1991).
3. Temperature and depth of formation (Gilligan, 1974).

Each of these models only partly explains the data presented so far and do not adequately account for all of the observed variations within the Cobar deposits.

The mixing model proposed by Lawrie and Hinman (1998) is partly based on their interpretation of the lead isotope data from the Cobar deposits. Jiang and Seccombe (2000) rejected this interpretation on the grounds that much of the variation in lead isotope signature noted by Lawrie and Hinman (1998) is within the analytical error of the measurements. Furthermore, the common spatial separation of Cu and Au mineralisation both within and between the various Cobar deposits, including Cu-only deposits like the CSA deposit, cannot be simply explained by the concept of a single basement-derived Cu-Au fluid. Clearly, further analysis of the lead isotope data and of the mineralisation itself is required in order to resolve the origin of metals within the Cobar deposits.

The models proposed by Glen (1991) and Gilligan (1974) rely largely on physiochemical differences at the site of metal deposition to account for metal zonation with the Cobar field. These models have not been adequately assessed and require further review. Specifically, the possibility that significant time differences exist between various stages of mineralisation in the Peak deposit (Perkins et al., 1994) raises the concept of temporal zoning of mineralisation within the Cobar Basin. Further detailed studies of ore deposit paragenesis are required to determine the relative timing of different mineralisation types.

2.8.4 Transport Mechanisms

Fluid inclusion studies have established that base metals in the Cobar deposits are likely to have been dominantly transported as chloride complexes (Hinman, 1992; Jiang, 1996; Brill, 1988a; Seccombe, 1990; Lawrie, 1991b; Lawrie et al., 1999b; Forster & Seccombe, 1999; Sun & Seccombe, 2000). Although Forster & Seccombe (1999) have proposed that late-stage epithermal-style gold mineralisation in the McKinnons Tank deposit was transported in bisulfide complexes. Gold mineralisation in the Cobar Basin is intimately associated with magnetite, pyrrhotite and/or pyrite and with a variety of base metals. However, gold transport mechanism(s) for the Cobar deposits have not been adequately resolved. Further detailed studies into the nature of the gold deposition and its timing and relationship to the base metal mineralisation are required.

2.8.5 Mechanisms of Metal Deposition

Gold deposition may have occurred in response to rapid depressurisation and mixing of hydrothermal fluids during fault-valve behaviour along active fault zones (e.g. Sibson et al. 1988; Cox 1995) (Stegman, 2000). Stable isotope data and extensive chlorite- and carbonate-alteration haloes surrounding the various deposits both indicate considerable fluid-rock interaction during formation of deposits. Metal deposition may have occurred in response to mixing of early pulses of hydrothermal fluids that have undergone significant wallrock-buffering in the deposit environs, with later pulses of less-evolved hydrothermal fluids (e.g. Cox et al., 1995) (Stegman, 2000). Alternatively, metal deposition may have occurred as a result of mixing of basin- and basement-derived fluids as proposed by Lawrie & Hinman (1998). The lack of gas-rich fluid inclusions in those deposits, for which fluid inclusion data are available, does not support phase separation as a metal-precipitation mechanism (Lawrie & Hinman, 1998), and therefore appears to preclude gold deposition by a fault-valve model. Although Forster & Seccombe (1999) considered gold mineralisation at McKinnons Tank to have been the product of boiling, textural evidence for boiling and epithermal-style mineralisation at McKinnons Tank appears limited, based on descriptions of the deposit by Forster & Seccombe (1999). In some deposits, desulfidisation reactions associated with pyrite/pyrrhotite-chalcopyrite replacement of magnetite, chlorite and stilpnomelane may be locally important. Calcareous and pyritic units may have also locally played an important role in metal deposition.

Further research is required to determine the likely physiochemical conditions present within the various deposits during metal deposition as a prelude to identifying the likely mechanism for metal deposition. Any model for metal deposition within the Cobar deposits, assuming similar fluids and processes are involved in each case, must be able to explain the co-deposition of gold and base metals in some deposits and the absence of gold in other deposits.

2.8.6 Comparison with other Deposit Types

The Cobar deposits represent a distinct group of deposits that have structural affinities with mesothermal gold deposits like those in the Ballarat-Bendigo region of Victoria, Australia and the Abitibi Belt, Canada, although these deposits do not contain appreciable base metal mineralisation. Geochemically, the relative abundance of base metal mineralisation in the Cobar deposits, together with significant gold mineralisation, invites comparison with volcanic-hosted massive sulfide deposits like those in the Mt Read Volcanic Belt in Tasmania, Australia. Whilst volcanic rocks are relatively rare in the Cobar Basin, they are dominant in temporally equivalent basins to the south and east, although major mineral deposits are conspicuous by their absence in these basins. However, the syn-deformational age of the Cobar deposits indicates that volcanism is unlikely to be a key component in their genesis. Likewise, a direct intrusive magmatic component to the mineralisation is not supported by isotopic data and the field relationships between mineralisation and known granitoids. The presence of significant copper-gold in the Cobar deposits, and their higher temperatures of ore formation, distinguishes these deposits from MVT and SEDEX deposits.

The answer to understanding how Cobar deposits, and particularly the New Occidental deposit, fit into the spectrum of mineral deposit types lies in understanding the nature of the rocks from which the metals in these deposits have been sourced, the physiochemical conditions under which the metals have been mobilised, and the conditions under which the mineralisation has formed.

3 STRUCTURAL SETTING OF THE NEW OCCIDENTAL DEPOSIT

3.1 Introduction

Formation of Cobar deposits, including the New Occidental deposit, is linked to the structural evolution of the Cobar Basin (Glen, 1985, 1987a, 1990, 1994; de Roo, 1989a,b; Hinman, 1992; Wilson, 1996). In the case of deposits in the Cobar Goldfield, mineralisation formed along actively deforming faults that are a fundamental part of the structural architecture of the eastern margin of the Cobar Basin (Glen, 1987b, 1990, 1991).

However, despite those studies, there are a number of unresolved aspects of both the deformation history of the eastern basin margin and the relationship between deformation and mineralisation.

When did the Great Chesney Fault initiate? Glen (1991, 1994) argued the Great Chesney Fault initiated as a short-cut structure during basin inversion as the major basin-forming faults, the Myrt and Rookery Faults, locked up. Glen cited the absence of stratigraphic variations across the fault as further evidence it did not have a pre-inversion history. However, stratigraphic relations across the Great Chesney Fault are not well known and it is possible that the fault was an extensional fault formed during rifting of the Cobar Basin and was then reactivated during basin deformation (Coller, 1987). It is also unclear whether some major stratigraphic contacts within the Cobar Goldfield, including the Great Cobar Slate-CSA Siltstone contact west of the New Occidental and Peak deposits, are conformable or faulted. As a result, offsets on faults like the Great Chesney Fault have not been quantified.

What is the relative timing of fold and cleavage development? In a number of locations throughout the eastern part of the Cobar Basin dominant cleavage is apparently slightly oblique to axial traces of folds (Glen, 1985). This relationship prompted Glen (1985) and Hinman (1992) to propose fold development preceded cleavage formation. de Roo (1989b) and Hinman (1992) recognised an earlier axial planar cleavage to folds at the Elura and Peak deposits respectively that is slightly oblique to dominant cleavage. However, Glen (1994) argued the presence of an earlier cleavage throughout the eastern basin margin is equivocal and Wilson (1996) did not identify an earlier cleavage at the New Cobar and Chesney deposits. Whilst Glen (1985) proposed folding and cleavage formation occurred in single evolving deformation event, both Hinman (1992) and Wilson (1996) assigned folds to D_1 and dominant cleavage to D_2. Hinman also recognised a third stage of cleavage development involving reactivation of S_2 cleavage during D_3, which is restricted to a high-strain zone enveloping the Peak deposit.

Folds in the high-strain zone at the Peak deposit are doubly plunging and more open compared to folds in adjacent low-strain areas (Hinman, 1992). Hinman attributed those differences to the effects of $D_{2\text{-}3}$, arguing that fold axes rotated towards macroscopic cleavage, fold hinges rotated to both more gentle and steep plunges, and folds "unfolded" during $D_{2\text{-}3}$. However, Wilson (1996) suggested folds within high strain zones around the New Cobar and Chesney deposits have not been modified relative to folds marginal to those deposits. She also argued cleavage in those high strain zones simply reflected intensification of D_2 cleavage and not a subsequent generation of cleavage.

Structural controls on mineralisation along the major faults in the Cobar Goldfield are ambiguous. Whilst minor weak mineralisation is present along much of the length of Great Chesney Fault and other faults in the Cobar Goldfield, the major gold-copper deposits represent relatively discrete well-defined metal accumulations (Glen, 1985) that collectively

comprise less than 10% of the total strike length of those faults. Controls on localisation of mineralisation along the major fault zones in the Cobar Goldfield have not been resolved. Large-scale reverse displacement is inferred on the Great Chesney Fault, Great Cobar Fault and Peak Shear during development of macroscopic cleavage and an associated steeply north plunging stretching lineation (Glen, 1991; Hinman, 1992; Stegman & Pocock, 1996). Deposits associated with those faults are grossly parallel to dominant cleavage and elongate in the direction of the steeply north-plunging stretching lineation (Figure 12). Yet, some models of deposit formation in the Cobar Goldfield argue the sub-vertical pipe-like geometry of the deposits along the Great Chesney Fault, their location at flexures in the trace of the fault and the presence of components of strike-slip movement on both the Great Chesney Fault and Peak Shear are consistent with mineralisation forming with strike-slip (Figure 13) (Sullivan, 1947; Mullholland & Rayner, 1961; Glen, 1987b, 1991, 1995; Stegman & Pocock, 1996).

Figure 12: Longitudinal Sections of the Great Chesney and Great Cobar Faults (Peak Gold Mines data).

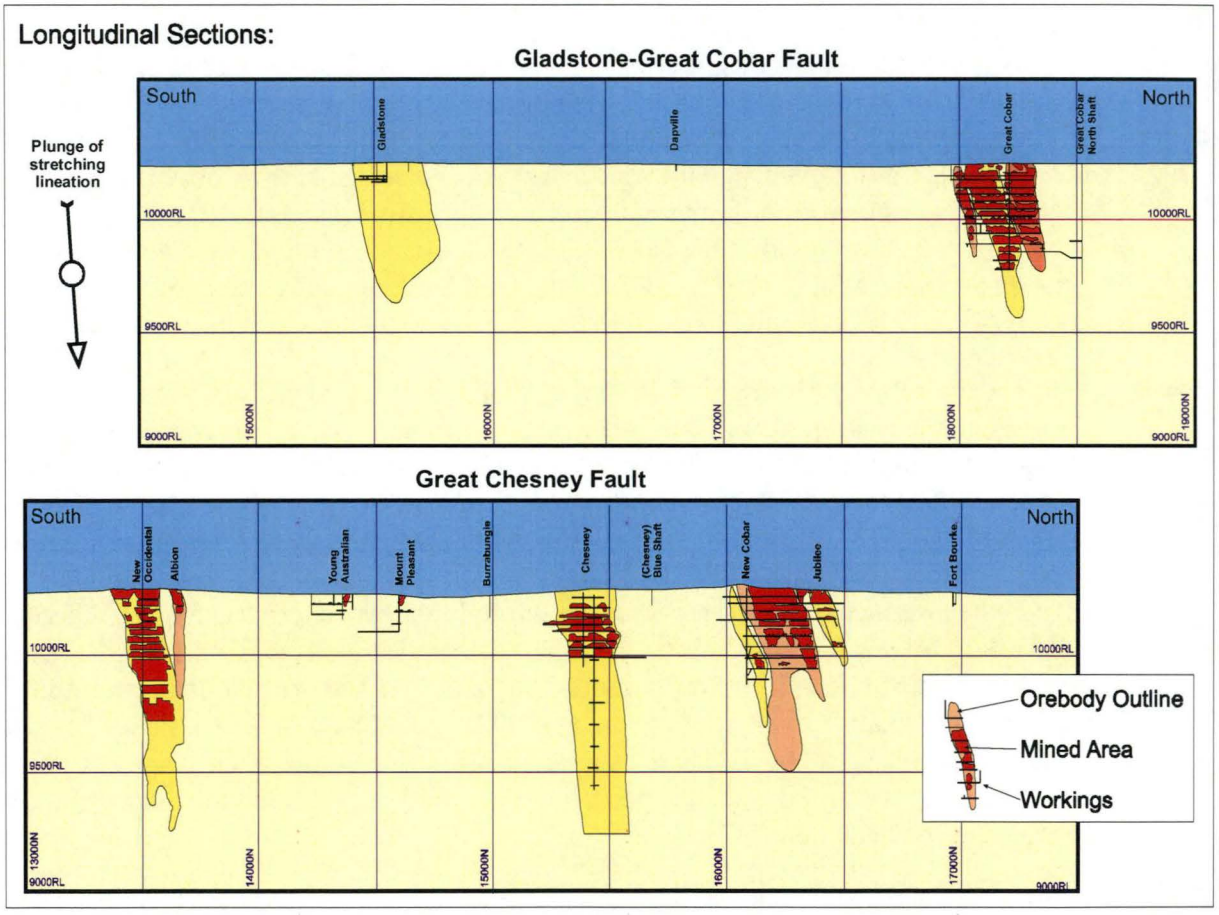

Consequently, the specific purposes of structural studies of the New Occidental deposit were to:

1. Clarify the structural setting of the deposits on the Great Chesney Fault and the history of the structural development of the eastern margin of the Cobar Basin.
2. Constrain timing and kinematics of Great Chesney Fault formation and thus its role in deformation of the eastern basin margin.
3. Identify controls on gold grade and resolve the geometry of high-grade gold shoots or lenses within the New Occidental deposit.

Towards those ends, regional mapping and structural analysis within the Cobar Goldfield has been used to determine the structural setting of the New Occidental deposit and its relationship to other major gold – base metal deposits in the Goldfield, including the Peak, New Cobar and Chesney deposits. At the prospect scale, both surface and sub-surface structural data were used to characterise the 3-dimensional geometry of the New Occidental deposit. The sub-surface data were entirely derived from reoriented diamond drillcore as old workings were not accessible and new underground development had not intersected the deposit at the time this work was conducted. Evaluation diamond drilling gold assays and close-spaced historical underground grade control assays were used to construct a 3-dimensional model of the New Occidental orebody. Close-spaced historical back sampling was then used to map out the distribution of high-grade mineralisation within the deposit.

Figure 13: Simplified geology of the Great Chesney Fault compared to the geometry of contractional and dilational jogs and bends in a left-lateral strike-slip fault zone.

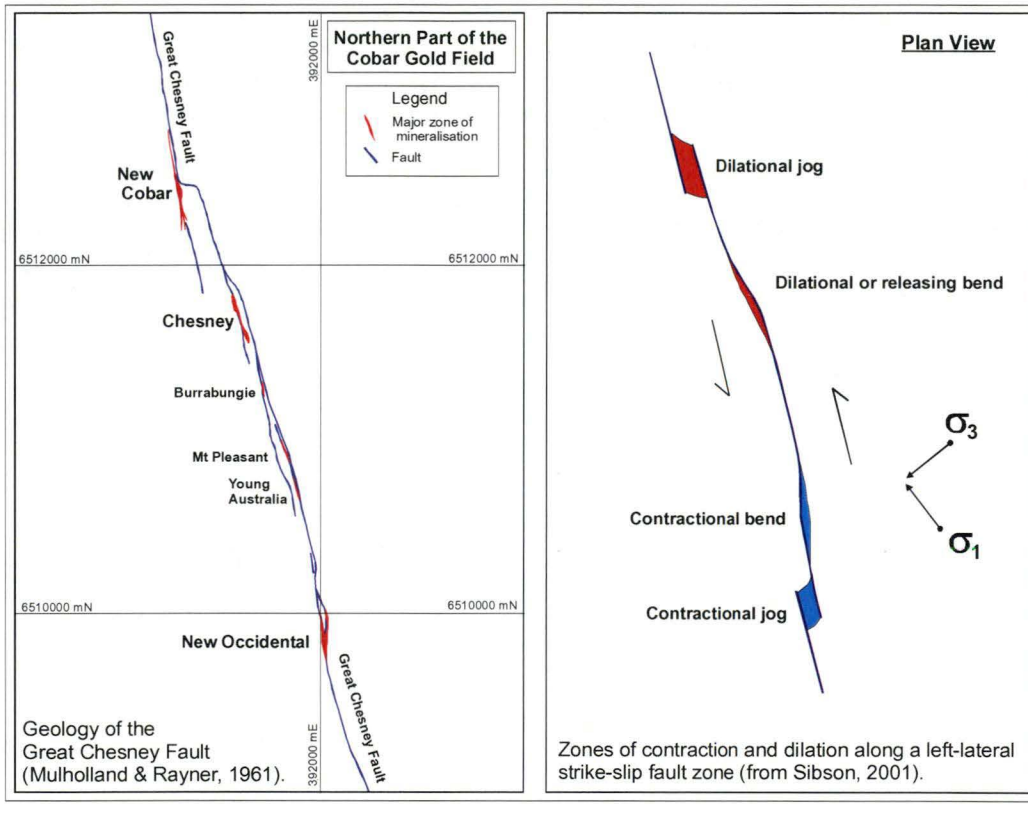

3.2 Previous Structural Studies

3.2.1 History of Basin Deformation

Glen (1985, 1987a, 1990, 1994) identified two major structural domains within the Cobar Basin; a high-strain Structural Zone 1 along the eastern margin of the basin and including the Cobar Goldfield, and a low-strain Structural Zone 2 in the central and western parts of the Cobar Basin, which are separated by the north-south trending Myrt Fault (Figure 14). He proposed both zones have been variably deformed during two episodes of deformation in the late Devonian and Carboniferous respectively (Glen, 1990). Within Structural Zone 1, D_1 deformation was high-strain and is characterised by a regional sub-vertical S_1 cleavage, a regional down-dip extension lineation, L_1, and F_1 south-southeast plunging meso- to macroscopic folds of variable appression. In contrast, D_1 deformation in Structural Zone 2 was low-strain and produced weakly developed open northwest-trending folds and thrusts (Table 8). D_2 deformation was mainly focussed on the western margin of the basin (Glen,

1987a). It produced small-scale folding and crenulations and kinks in S_1 cleavage in Structural Zone 1 and upright northeast-trending open folds with gentle and variable plunges and an axial planar cleavage in Structural Zone 2 (Glen, 1987a, 1990).

Glen (1985, 1987a) noted that S_1 is axial planar to the Chesney-Narri Anticline and other F_1 folds to the south of Cobar Goldfield. However, in the northern part of the Goldfield in the vicinity of the New Occidental and Great Cobar Mines, S_1 is interpreted to be slightly oblique to the axial traces of those folds, including the Chesney-Narri Anticline. Glen (1987a) recorded similar transected relationships between S_1 and F_1 elsewhere along the eastern margin of the Cobar Basin. As a consequence, Glen (1985) proposed D_1 deformation in Structural Zone 1 involved two stages of deformation, both part of a single progressive event. F_1 folds formed during an initial regime of left-lateral shear on bounding west-northwest trending faults, and S_1 and L_1 subsequently formed in response to increased shortening and high-angle reverse movement on those same bounding faults. Glen (1990) also suggested that F_1 fold plunges were steepened during the latter stage of D_1 deformation. Glen (1990) suggested that S_1 might overprint an earlier cleavage that was axial planar to the F_1 folds. However, Glen (1994) subsequently noted that whilst S_1 may overprint locally developed cleavages, especially given the prolonged history of faulting in the area, no unequivocal pre-S_1 cleavage was present.

In contrast, Hinman (1992) proposed a four-stage deformation history for the nearby Peak deposit (Table 8). He sub-divided Glen's (1985, 1987a, 1990, 1994) D_1 deformation into three separate stages of deformation. South-southeast plunging F_1 folds, including the Chesney-Narri Anticline and attendant parasitic folds, formed during D_1 in response to northwest-southeast shortening. Hinman identified a weak S_1 microscopic cleavage axial planar to those folds. S_2 is the macroscopic fabric present throughout the Cobar Goldfield and it apparently transects S_1 at a slight angle. A microscopic S_3 cleavage is developed in the higher strain zones at the Peak where it has variably deflected and reactivated S_2. According to Hinman (1992), S_2 and S_3 at the Peak are indistinguishable in outcrop and are essentially sub-parallel. F_1 folds were rotated towards the strike of S_2/S_3 during D_2/D_3 and locally unfolded in zones of high strain. Macroscopically, Hinman suggested that S_3 is indicated by doubly plunging folds whose axial planes are sub-parallel to S_2/S_3, north and south plunging S_0/S_2 intersection lineations and deformed pyrrhotite grains with length to width ratios of in excess of 10:1. D_2 and D_3 were regarded as progressive stages of a single intense deformation event that resulted in significant shortening of the eastern margin of the Cobar Basin. During deformation, the shortening direction rotated progressively to a direction that was slightly clockwise of east-west. D_4 is a late-stage, brittle, faulting event associated with relaxation of the earlier intense D_2 and D_3 deformations. D_4 produced local microscale crenulations of S_2/S_3 fabrics and is regarded as approximately equivalent to Glen's D_2.

At the New Cobar and Chesney deposits to the north of the New Occidental deposit, Wilson (1996) identified a three-stage deformation history (Table 8). The three stages are identical to D_1, D_2 and D_4 proposed by Hinman (1992). However, Wilson did not identify an early cleavage transected by the macroscopic cleavage and did not observe any overprinting and re-activation of S_2 consistent with Hinman's S_3, although an intense S_2 cleavage was interpreted to be analogous to Hinman's S_3 cleavage. Wilson observed a well-developed D_4, characterised by crenulations of S_2, locally developed S_4 cleavage, mesoscopic F_4 folding and reverse dip-slip conjugate brittle faulting. Wilson considered these structures to be inconsistent with a relaxation event as proposed by Hinman and instead argued D_4 reflects further shortening. Wilson proposed the Great Chesney Fault initiated late D_1 to early D_2.

Figure 14: Structural zones in the Cobar Basin (after Glen, 1985).

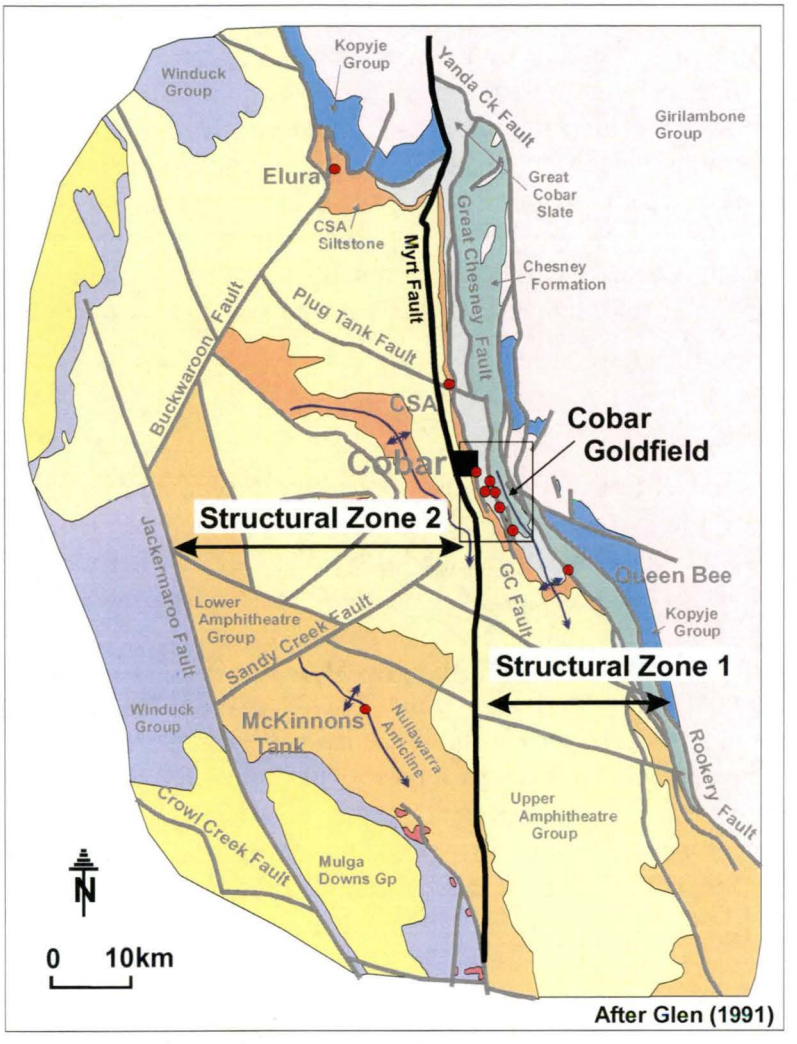

Table 8: Nomenclature of deformation events throughout the Cobar Goldfield.

Deformation	Glen (1985) Cobar Goldfield	Hinman (1992) Peak	Wilson (1996) New Cobar-Chesney
Gently NNE to steeply SSE plunging folds (e.g. Chesney-Narri Anticline)	"Possible early foliation" and F_1	D_1, S_1, F_1	D_1, S_1, F_1
Regional sub-vertical NNW-SSE striking cleavage and steep N plunging stretching lineation	D_1, S_1, L_1	D_2, S_2, L_2^2	D_2, S_2, L_2^2
Intense sub-vertical NNW-SSE striking cleavage associated with major shear zones including the Great Chesney Fault	S_1	S_3	Intense S_2
Reverse movement on gently to moderately WNW and ESE dipping brittle faults	D_2	D_4	D_4
Reverse movement on gently NNW and SSE dipping brittle faults; strike-slip re-activation of S^1 cleavage; strike-slip displacement on WNW and ESE dipping brittle faults; and gently N to NNW dipping kink bands	D_2	D_4	D_4

3.2.2 The Chesney-Narri Anticline

New Occidental deposit is located on the western limb of the south-southeast (150–160°) plunging Chesney-Narri Anticline. Bedding on the western limb of the anticline dips steeply west-southwest. The axis of the Chesney-Narri Anticline, which is located approximately one kilometre to the east of the New Occidental deposit, is defined by dip reversals within thc Chesney Formation. The anticline is upright and tight and both limbs of the anticline contain mesoscopic parasitic folds (Glen, 1987a). South of the Goldfield, the anticline is moderate to steeply south plunging (60–70°) but plunge decreases to the north and becomes north-plunging near Cobar township (Glen, 1987a). Glen attributes the variable plunge of the Chesney-Narri Anticline to either refolding during the latter stages of D_1 or to strain variations during D_1.

3.2.3 The Great Chesney Fault

The Great Chesney Fault is the largest of several north-northwest trending mineralised faults that are arranged in a left-stepping en-echelon pattern along the eastern margin of the Cobar Goldfield. From north to south, these shears included the Great Cobar, Gladstone, Great Chesney, Peak and Queen Bee Faults (Glen, 1985) (Figure 4 and Figure 6).

The Great Chesney Fault extends over a distance of approximately 30 km (Figure 4), although gold mineralisation is restricted to the southern eight km long section of the fault (Glen, 1987b). The Great Chesney Fault forms the Chesney Formation-Great Cobar Slate contact over much of its length. The contact is marked by a narrow (1–5m wide) zone of moderately to strongly sheared sandstone and siltstone and erratic zones of weak quartz veining and silicification that typically contain only minor associated mineralisation (Mullholland & Rayner, 1947; Glen, 1990; Stegman & Pocock, 1996). The fault is interpreted to terminate on the Yanda Creek Fault at the northern end of the Cobar Basin. At its southern end, the Great Chesney Fault diverges from the sandstone-slate contact and ramps laterally up-section into the Great Cobar Slate and Lower Amphitheatre Group before becoming lost in poorly outcropping monotonous siltstone (Glen, 1990). Glen (1990) argued slip on the Great Chesney Fault in this area was relayed to the Peak Shear in the east.

Whilst the Great Chesney Fault has long been recognised as having exerted the primary control on mineralisation in the central part of the Cobar Goldfield (Andrews, 1913), considerable uncertainty as to its origin is evident in the literature. Previously the Great Chesney Fault has been interpreted as:

- A disconformity caused by slumping (Sullivan, 1947).
- An unconformity subsequently modified by shearing (Sullivan, 1947).
- An early fault folded during later faulting (Sullivan, 1947).
- An attenuated underlimb of an anticline (Conolly, 1946; Thompson, 1953).
- A series of en echelon thrusts separated by linking thrusts developed along the conformable slate-sandstone contact (Mullholland and Rayner, 1961).
- A weakly faulted conformable stratigraphic contact (Gilligan and Suppel, 1978; Sangster, 1979).
- A high angle reverse fault comprising left stepping fault segments linked by cross-faults (Glen, 1987b).

Those various models have been influenced by the observation that over much of the trace of the fault bedding in the units either side of the fault has a similar strike to that of the fault. Estimates of fault displacement have also been hampered by the poorly bedded, relatively massive nature of the Great Cobar Slate and by the absence of any internal stratigraphic sub-division of the Chesney Formation.

The Great Chesney Fault strikes west-northwest (350–355°) within the Cobar Goldfield. Deep diamond drilling within the Goldfield (Andrews, 1913; Sullivan, 1951; Gilligan & Suppel, 1978; Peak Gold Mines data) indicates the fault consistently dips steeply (80–85°) east. The fault zone is grossly parallel to the prominent regional cleavage present throughout Glen's (1985) Structural Zone 1. The Great Chesney Fault is interpreted to be slightly oblique to the regional folds including the Chesney-Narri Anticline (Figure 6) and it truncates the western limb of the anticline (Glen, 1994). Glen (1987a) showed the Great Chesney Fault truncates bedding in both the hanging wall Chesney Formation and footwall Great Cobar Slate, although he did not quantify the amount of fault displacement.

In detail, the Great Chesney Fault contains numerous splays, which appear to be more prevalent in the footwall slates (Glen, 1990). These splays are interpreted to have minimal stratigraphic offsets (Stegman and Pocock, 1996).

A range of kinematic and stratigraphic data has been used to infer the sense of displacement on the Great Chesney Fault. Steeply north plunging (80–85°) striae on fault planes and the prominent mineral lineation on the regional cleavage indicate dominantly dip-slip movement on the fault (Sullivan, 1951; Glen, 1987a). Stratigraphic offsets confirm dominantly reverse (east block up) movement (Glen, 1987a; 1990). Glen (1990) interpreted a lesser component of dextral strike-slip movement associated with early phase high-angle reverse movement on the Great Chesney Fault based on quartz vein fibres. He also suggested a subsequent phase of dominantly left-lateral strike-slip movement, which accounted for left-stepping overlaps in fault segments, en echelon vein arrays, northwest-trending cross veins observed by Mullholland & Rayner (1961) and Glen (1987b), and sub-horizontal striae overprinting sub-vertical striae in the Blue Shear (a strand of the Peak shear).

Stegman and Pocock (1996) also proposed an early phase of large-scale reverse displacement on the Great Chesney Fault, followed by late-stage left-lateral strike-slip movement. Additional evidence for that strike-slip displacement included the presence of sub-vertical to steep north plunging folds in the Great Chesney Fault and marker units in the Great Cobar Slate at the New Cobar deposit (Figure 13), the apparent association of major ore deposits with left-stepping jogs and folds in the trace of the Great Chesney Fault (Figure 13), and the sub-vertical plunge of mineralisation associated with the Great Chesney Fault (Figure 12), consistent with sub-vertically plunging dilational jogs created by strike-slip faulting (Stegman and Pocock, 1996).

3.2.4 Structural characteristics of Deposits in the Cobar Goldfield

Sullivan (1947) and Glen (1990) have suggested that most hydrothermal alteration and mineralisation within the Goldfield is preferentially developed on splays off the Great Chesney Fault, particularly where these splays are entirely hosted within the footwall slates. Conversely, Stegman and Pocock (1996) argued that while the Chesney and New Cobar deposits are located on splays off the Great Chesney Fault, the New Occidental deposit, which accounts for over 50% of the contained gold in the northern part of the Goldfield, is located on the main fault. Similarly, most of the mineralisation in the Peak deposit is located within the Peak Shear (Stegman and Pocock, 1996).

The major deposits in the Cobar Goldfield have a number of distinctive structural features. The Peak (Hinman, 1992), New Cobar and Chesney (Wilson, 1996) deposits are associated with increases in fold intensity and frequency and changes in fold plunge. The greatest concentration of F_1 folds in the Peak area occurs within the Hinman's (1992) "high strain volume", which encompasses the Peak orebody. Likewise, fold plunges rotate from a consistent gentle southerly plunge (30°/170°) on the perimeter of the "high strain volume" to variable gentle south and north plunging folds (0–20°/170°) in the core. At the New Cobar and Chesney deposits, increases in fold frequency and intensity are not associated with changes in fold orientation (Wilson, 1996).

Hinman (1992) argued the distribution of L_0^2 bedding-cleavage intersection lineations at the Peak deposit confirms the presence of a high-strain zone in this area. Outside of the high-strain zone, Hinman determined L_0^2 intersection lineations have a relatively consistent gentle southerly plunge (average orientation of 36°/161°). Within the high-strain zone, the L_0^2 intersection lineations range from gently south and north plunging to steeply south plunging. Hinman argued redistribution of L_0^2 reflects heterogeneous rotation of bedding on cleavage planes due to variable extension in the direction of the stretching lineation L_2^2. In contrast, Wilson found that L_0^2 intersection lineations throughout the New Cobar-Chesney area have a relatively consistent gentle southerly plunge and do not appreciably vary in orientation within the high-strain zones encompassing those deposits.

Glen (1987b, 1991, 1995) proposed the locus for ore deposits along the Great Chesney Fault was left-stepping jogs in the Great Chesney Fault that formed either as tear faults during reverse faulting or as dilational jogs during left-lateral strike-slip movement. Similarly, Stegman and Pocock (1996) argued the main phases of alteration and mineralisation in the Goldfield were associated with late-stage left lateral strike slip fault movement. Deposits reportedly occur at the intersections of north-northwest and west-northwest trending major fracture systems (Sullivan, 1951; Mulholland & Rayner, 1961; Glen, 1987a). Those west-northwest trending fractures have been interpreted as gash fractures formed between the fault strands (Sullivan, 1951) and as reidel shears (Coller, 1987). In detail, the following structural settings have previously been suggested for these deposits:

1. The New Occidental deposit occurs around a left-stepping jog occupied by a west-northwest trending segment (Albion Fault) of the Great Chesney Fault (Glen, 1995).

2. The Chesney deposit is located within a shear zone in the footwall of the Great Chesney Fault immediately south of a subtle flexure in the trace of the fault (Stegman and Pocock, 1996). The high-grade gold-copper shoots are localised about the intersection of this footwall shear zone with west-northwest trending cross faults and quartz veins (Sullivan, 1951; Mulholland and Rayner, 1961; Glen, 1995).

3. The New Cobar deposit is also located along a shear zone in the footwall of the Great Chesney Fault about a left-lateral jog in this fault. Glen (1995) was unable to determine whether this jog formed in a relay between two fault segments or during strike-slip movement on the Great Chesney Fault.

Other potential controls on the localisation of significant mineralisation along the Great Chesney Fault that have been proposed include:

1. Early-formed broad zones of pervasive silicification within Chesney Formation sandstones adjacent to the Great Chesney Fault acted as rigid bodies during

deformation. The various deposits formed in pressure shadows about these bodies. These silicified zones are easily recognised as topographic highs, and all of the major deposits are invariably located about these features (Stegman and Pocock, 1996).

2. Releasing bends and offsets in the shear zones associated with strike changes in the Great Chesney Fault. These strike changes are related to inhomogenieties in the fault zone environs including in the footwall and hanging wall sediments (Coller, 1987).

3. The sandstone-slate competency contrast across the Great Chesney Fault (Sullivan, 1951; Glen, 1987b; Stegman & Pocock, 1996).

3.2.5 Gold Distribution in the New Occidental Deposit

Figure 15: Surface Plan of the New Occidental Deposit showing main lodes (Mulholland and Rayner; 1961).

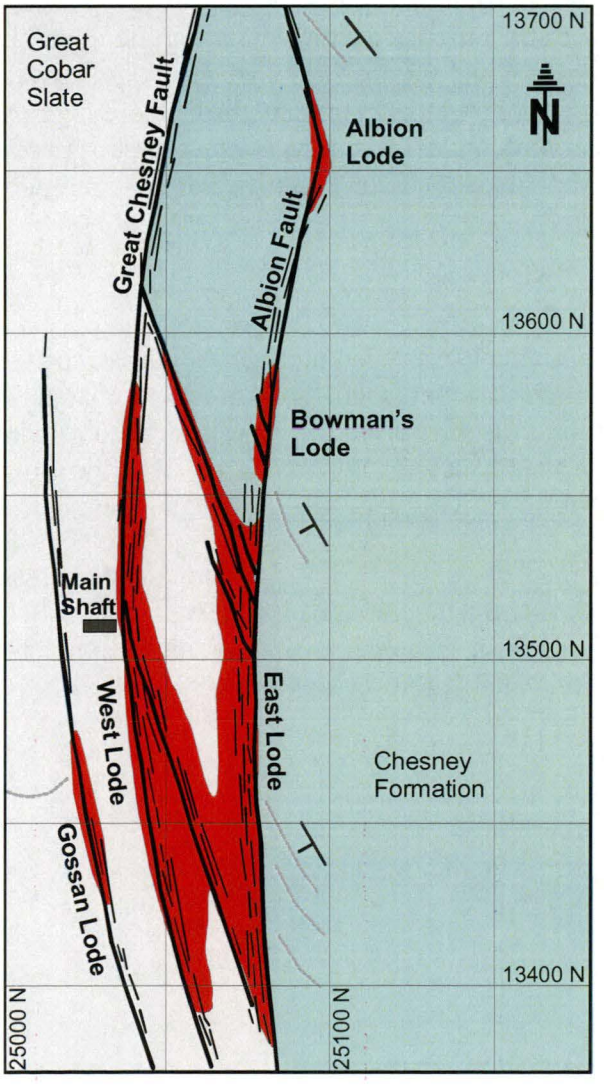

Gold mineralisation in the New Occidental deposit occurs within several discrete quartz-veined lenses that together define a disc-shaped orebody approximately 200m long and up to 25m wide that extends down dip at least 1200m. The orebody is parallel to and developed along the trace of the Great Chesney Fault and dips steeply to the east (85°) parallel to dominant cleavage. It plunges steeply to the north (80–85°) in the direction of the prominent stretching lineation (Sullivan, 1947; Mulholland & Rayner, 1961; Glen, 1985; Stegman & Pocock, 1996).

The New Occidental orebody was considered to comprise at least six lodes developed along a network of generally north-northwest to northwest trending curvi-linear shears (Mulholland & Rayner, 1961; Figure 15). The curvature of the shears is concave to the east. Most mineralisation occurs within two main north-northwest trending lenses, the Eastern and Western lodes, that together define a wishbone-shape, coalescing at the southern end of the orebody. Both lodes are 5–15m thick and, at the southern end of the orebody are collectively 25m thick. The Eastern lode is developed within a shear on the Chesney Formation-Great Cobar Slate contact whilst the Western lode occurs along a shear within the Great Cobar Slate. Mulholland and Rayner (1961) suggested the lodes possibly converge at depth to form a single but much thicker lode. A third 3–5m thick lens, the Gossan lode, occupies an additional parallel shear further to the west within the Great Cobar Slate. A fourth blind lens, the Galena - Sphalerite lode, has been intersected over narrow intervals

(<5m) in workings to the west of the Gossan lode and is apparently parallel to the other lodes. Peak Gold Mines' deeper drilling failed to find any indication of this lode below the present level of workings (approximately 560m below surface). This lode appears to be restricted to the top 200–300m of the deposit. Two other small lodes, the Bowman's and Albion lodes, occur within the Albion Fault, immediately north of the eastern lode. Those lodes are hosted entirely by Chesney Formation. The Albion lode reportedly occurs at the northern termination of the Albion Fault where it intersects a northwest trending cross-shear. Both the Bowman's and Albion lodes are 1–3m thick and less than 40m long. The Eastern, Western and Gossan lodes are vertically continuous over at least 1000m (Sullivan, 1947; Mulholland and Rayner, 1961; Stegman and Pocock, 1996).

3.3 Data Collection

3.3.1 Geological Mapping

The Cobar Goldfield has been previously mapped by Enterprise Exploration in the late 1940s; Mullholland & Rayner (1961); Glen (1987a); Hinman (1992); Wilson (1996) and by Peak Gold Mines' geologists in the late 1990s. The author compiled previous mapping data and then remapped much of the Goldfield with the purpose of differentiating the internal stratigraphy of Chesney Formation (Figure 16 and Figure 17). Drillhole logging was used to supplement surface mapping in areas of poor outcrop. In particular, drillcore logging was used to accurately locate the Great Cobar Slate - CSA Siltstone contact west of the Peak and Perseverance deposits and was used to determine the nature of many of the ambiguous lithological contacts in the Goldfield.

3.3.2 Surface Structural Data

Bedding and cleavage orientations were routinely recorded during mapping of the Cobar Goldfield to allow comparison of structure in the New Occidental area with that present in adjacent parts of the Goldfield. The bulk of the measurements were restricted to mineralised areas and within the Chesney Formation sandstone (i.e., the hanging wall of the Great Chesney Fault), due to the generally poor outcrop elsewhere.

Surface structural data collected during mapping of the New Occidental deposit environs was supplemented by extensive sub-surface structural data obtained from diamond drillcore from the New Occidental Project. Inclusion of sub-surface data provides a more complete three-dimensional view of the deposit than that available to previous workers.

Figure 16: Lithology legend for Cobar Goldfield geology.

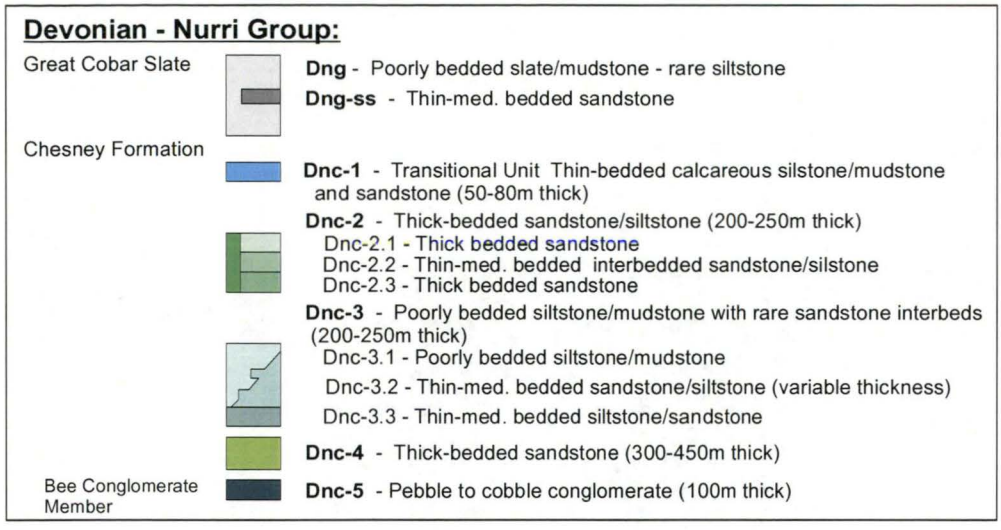

Figure 17: Geology of the Cobar Goldfield including the southern portion of the Great Chesney Fault.

(See Figure 16 for lithology legend)

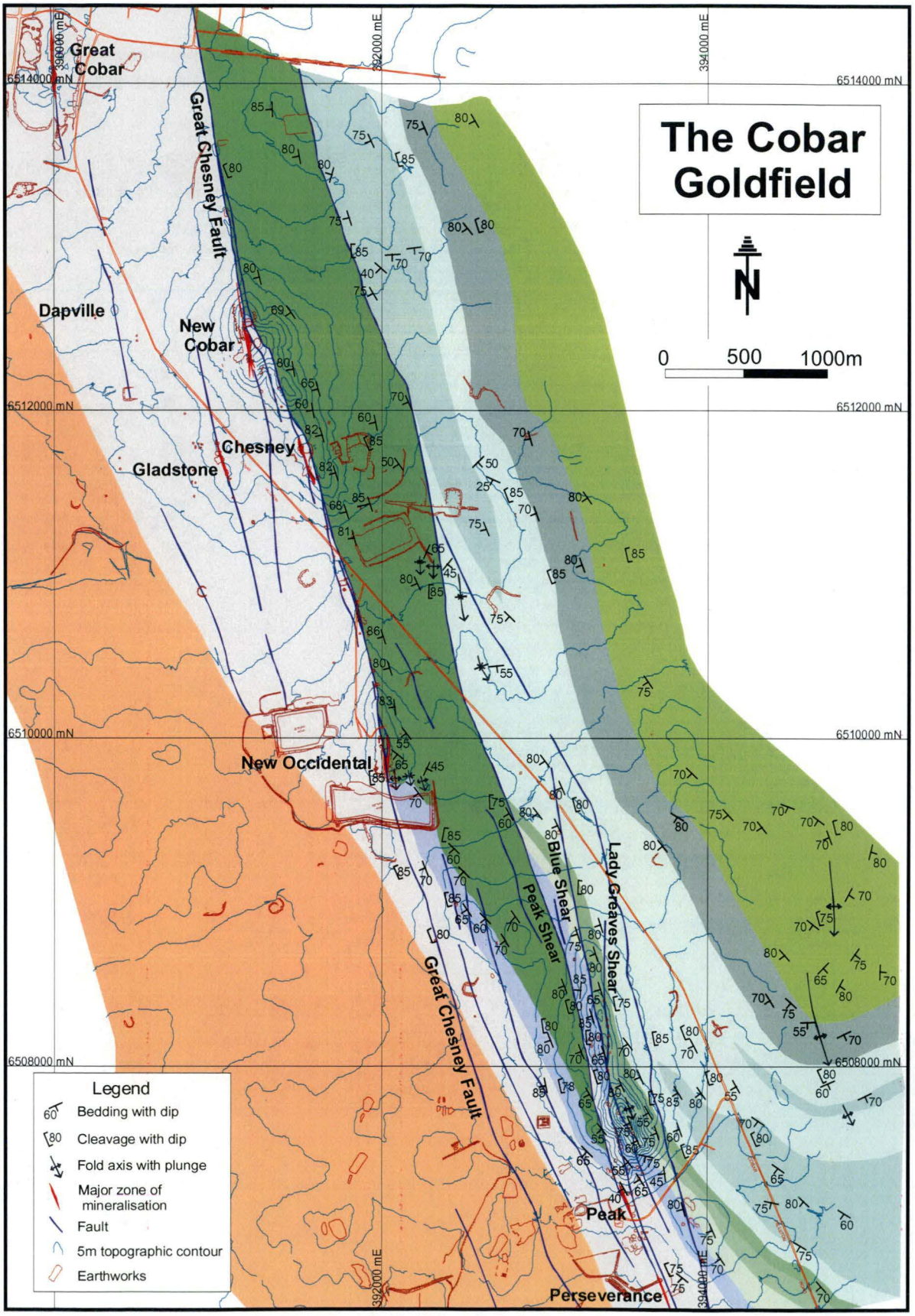

3.3.3 Sub-surface Structural Data

Schmidt (1980; 1990) first recognised that the relatively consistent orientation of the dominant cleavage throughout the eastern part of the Cobar Basin could be used to reliably re-orient drillcore, providing valuable constraints on the sub-surface structure. Where a structural element can be assumed to have a constant orientation, drillcore can be reoriented, enabling the calculation of the orientation of all other structural elements observed in the drillcore (Hinman, 1992). The drillholes must be accurately surveyed so that the axial orientations of the individual pieces of core are known. However, the pieces of drillcore do not need to be oriented within the hole (by means of spear test or similar) and only drilling direction need be known at the time the measurements are made. By manually reorienting drillcore so that the strike of cleavage was parallel to that in the northern part of the Cobar Basin, Schmidt was able to resolve the complex pattern of folds surrounding the Elura deposit. Subsequently, Hinman (1992) developed a computer-based spreadsheet to calculate the orientations of fabrics measured in core from their angular relations with respect to the cleavage and applied this technique to the resolution of the sub-surface structure of the Peak deposit.

Reorientation of drillcore structural measurements collected during this study was undertaken using the "Structural Calculator", an EXCEL-based program for determining foliation and lineation orientations from drill core (Scott and Berry, 2003). This software utilises different manipulation algorithms to those used by Hinman's (1992) spreadsheet model. Hinman's "fixed strike" methodology assumes a fixed average strike for the reference fabric, in this case cleavage, and "rotates" the core about its downhole axis to derive a best-fit solution for the orientation of cleavage. Where the plunge and azimuth of drillcore is known, Scott and Berry calculate the most likely orientation of the drillcore as the position where the angle between the reference fabric and its assumed regional orientation is at a minimum. In essence, the drillcore orientation is independent of the strike of the reference fabric. In addition, the technique can be used to determine the average orientation and degree of scatter in orientation of the reference fabric. Scott & Berry have shown the "fixed strike" method is prone to error when drillhole orientations are at steep angle to the reference fabric, for example, when drillholes are gently dipping and cleavage is steep-dipping. However, both methods achieve a similar level of accuracy when the drillhole orientations are at moderate to shallow angles to the reference fabric, for example, moderate-steeply inclined drillholes intersecting a steep-dipping cleavage. The latter scenario best matches the drilling undertaken in the New Occidental area, where drillholes range in dip from -35° to -90° and cleavage is sub-vertical.

The "Structural Calculator" uses downhole survey records for each drillhole to interpolate a plunge and trend of the drillcore axis for every point in the drillhole where structural measurements have been made. The dip direction of the reference fabric, in this case cleavage, has been constrained from surface structural measurements of cleavage in the New Occidental project area and is a fixed input to the model. The model calculates two orthogonal solutions for cleavage orientation, one of which can be dismissed as less likely. Cleavage dip and dip direction are then used in the subsequent calculation of the orientation of the other structural elements, including lineations on cleavage.

All drillholes from the New Occidental project have been accurately surveyed down the hole using an Eastman single shot camera. Selective intervals of drillcore were oriented using a downhole spear, which marks the bottom-of-core position on the core before it is broken from the bottom of the hole. These sections of oriented core confirm variation in both dip and dip direction of the cleavage is negligible. Subsequently, underground exposures have also confirmed that cleavage has a relatively consistent orientation throughout the New Occidental deposit.

Bedding and cleavage measurements were recorded on 10–15m intervals down every diamond drillhole completed as part of the New Occidental evaluation program (NO1C-NO26). Vein orientations were measured in the mineralised sections in each of these drillholes. A lesser number of shears were also measured. Subsequently, a more detailed investigation into the orientation of the different generations of quartz and sulfide veining in NO25 and NO26 was undertaken in order to assess whether the orientation of veining within the New Occidental deposit varied during deposit formation. Further bedding, shear and lineation orientations were also recorded from these two drillholes.

Conventions for recording structural measurements in core are shown in Table 9 and Figure 18. For each measurement of a structural fabric it is necessary to record:

1. The angle between the pole to the plane of the fabric and core axis **(δ)** for both the fabric of interest and the cleavage.
2. The angle between the positions of the long axis apical traces (high points) of the fabric of interest relative to the cleavage (reference fabric), measured around the core (perpendicular to the core axis) clockwise from cleavage to the fabric looking down hole **(α)**.
3. In the case of bedding measurements, the **facing** of the bedding is also recorded if it can be determined.

For lineations, it is necessary to measure:

1. The angle measured in the plane of cleavage between the long axis of the elliptical section of cleavage to the lineation **(β)** measured clockwise from the long-axis of cleavage looking downhole.
2. The delta angle **(δ)** of the cleavage plane containing the lineation.

Table 9: Drillcore Structural Measurement data conventions.

Hole Name	Depth	Cleavage	Fabric Type	Facing	δ Fabric	α Cleavage to Fabric	β Lineation
	(m)	(°)		(Up/Down)	(°)	(°)	(°)
Example:							
NO7C	670	60	S_0	Up	45	350	165
NO7C	690	60	V_1		55	10	015
NO25	180	85	L_{22}				205

Scott and Berry (2004) use a different measurement convention for those angles (Table 10). Angular measurements from core were converted for entry into "structural calculator" conventions.

Table 10: Comparison of structural measurement terminology between this study and Scott and Berry (2004)

Structural measurements (this Study)	Scott and Berry equivalent measurement
δ	90 – β
α	360 - Ω
β	δ

Both NO25 and NO26 are vertical drillholes drilled with the aid of directional navigation tools. As a consequence, the dip of these holes was maintained within 1.0° of vertical over their entire length. As a consequence, δ for the all fabrics in these drillholes equates to the dip of these fabrics in real space.

An average dip/dip direction of 84°/078° was applied for all structural reorientation calculations in the New Occidental deposit, with the exception of NO25–26, where a dip/dip direction of 84°/084° was assumed. Differences in the assumed orientation of the cleavage make little difference to the overall structural pattern (Hinman, 1992). Raw measurements and calculated structural re-orientations are tabulated in Appendix 1. Stereonets of structural data collected during this study are presented in Appendix 2.

Figure 18: Conventions for drillcore structural measurements (modified from Hinman, 1992).

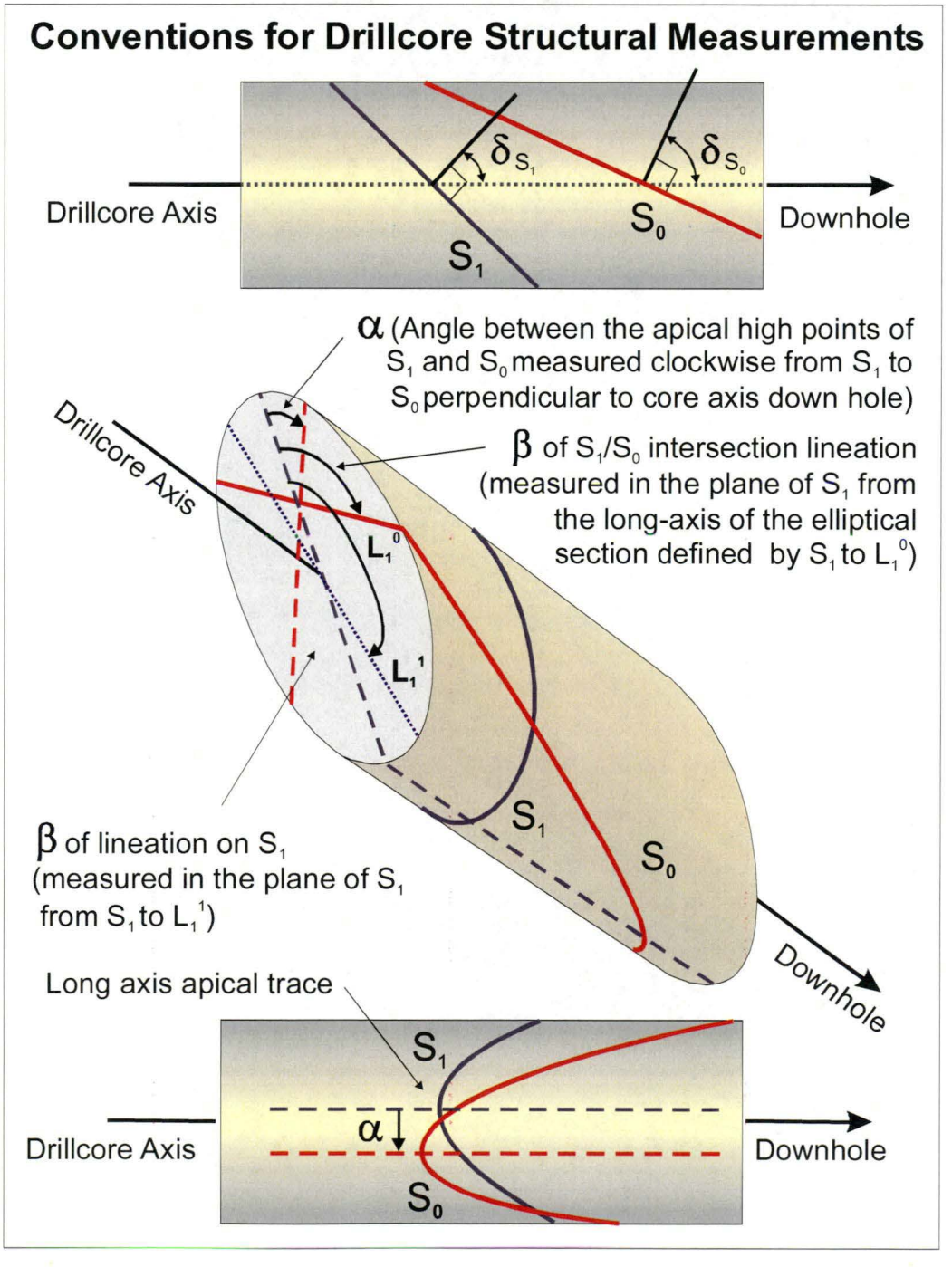

3.3.4 Gold Distribution Data

Evaluation diamond drilling gold assays and close-spaced historical underground grade control assays were used by the author to construct a three-dimensional model of the New Occidental orebody using a nominal >1 g/t Au cut-off. The close-spaced historical back sampling was then been used to map out the distribution of high-grade (>10 g/t Au) mineralisation within the deposit (Figure 19). Using approximately 12,250 back samples collected between 10080–9700m RL the author constructed a total of 15 discrete three-dimensional wire-frames of shoots of high-grade gold mineralisation.

Figure 19: 9880m RL Level plan (approx 390m below surface) through the New Occidental deposit showing the distribution of gold in historical back samples.

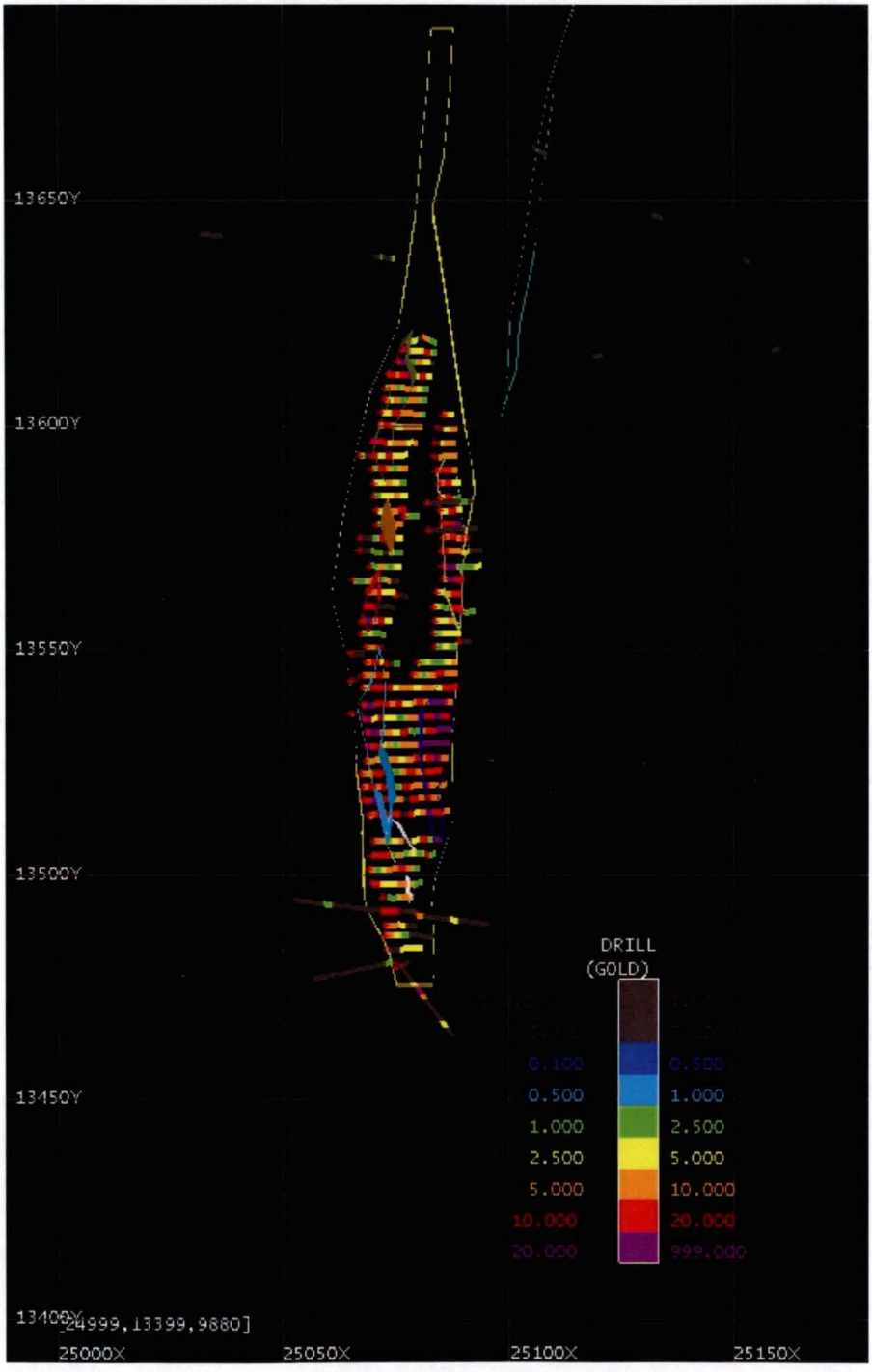

3.4 Stratigraphic relationships in the New Occidental Deposit Environs

3.4.1 Nature of Sedimentary Sequences in the New Occidental Deposit

Stratigraphic relations across the New Occidental deposit and host Great Chesney Fault provide important constraints on the origin of the fault. Regional and prospect scale geological mapping of the Cobar Goldfield, and geological logging of diamond drillcore by the author has been used to characterise the stratigraphic relationships across the Great Chesney Fault. This has enabled the development of a 3-dimensional stratigraphic framework for the New Occidental deposit environs.

In the New Occidental deposit environs, the Great Chesney Fault separates sandstones of the upper Chesney Formation (the lowermost unit of the Nurri Group) to the east from slates, siltstones and minor sandstones of the Great Cobar Slate (the uppermost unit of the Nurri Group) west of the fault (Sullivan, 1947; Glen, 1987a).

The upper Chesney Formation in the eastern hanging wall of the Great Chesney Fault is at least 500m thick. Bedding is discordant to the fault, and generally strikes north-northwest (340–345°) and dips moderately to steeply (50–85°) to the west (Figure 20 and Figure 21). The hanging wall sequence comprises medium-thick bedded, graded-bedded, coarse-grained lithic sandstone and muddy siltstone. Individual sand beds range in thickness from 0.05-2.0m with the thickest beds occasionally containing pebble bases (Figure 22a). Glen (1987a) described clasts in the sandstone as consisting of poorly sorted plutonic and subordinate metamorphic quartz, lesser quartz-veined massive and laminated sandstones, and minor chert. Glen tentatively identified felsic volcanic clasts in some sandstones and conglomerates. Rip-up clasts of siltstone and mudstone and flute marks at the base of sand beds are common primary sedimentalogical features. There is also evidence of soft-sediment deformation or slumping in parts of the sequence.

A 60-80m thick Transition Unit defines the contact between the Chesney Formation and overlying Great Cobar Slate. Thick-bedded sandstones of the Chesney Formation grade upwards through a sequence of thin to medium bedded graded sandstones and siltstones, thinly bedded to laminated calcareous siltstones and mudstones (Figure 22b) before passing into the Great Cobar Slate. The top of the Transition Unit, and hence the break between the Chesney Formation and overlying Great Cobar Slate is defined by the change from well-stratified mudstone and fine-grained siltstone to relatively poorly stratified mudstone and lesser siltstone.

The Great Cobar Slate, which also crops out along the western side of the Great Chesney Fault in the New Occidental mine environs, comprises relatively featureless and massive (poorly stratified) muddy siltstone and mudstone with rare carbonate nodules. Where present, bedding is defined by thin 1-2mm thick carbonate beds and/or fine-grained siltstone laminations. Bedding is largely west-southwest dipping.

Deep diamond drilling approximately 200-300m to the south of the New Occidental deposit has revealed that the poorly-stratified mudstones and siltstones of the Great Cobar Slate on the footwall of the Great Chesney Fault grade westwards into rhythmically interbedded, thin-medium bedded, graded fine- to coarse-grained siltstone of the CSA Siltstone. The contact between Great Cobar Slate and overlying CSA Siltstone is marked by a 30m wide transition from relatively massive mudstone/siltstone that grade into poorly-moderately stratified, thinly bedded mudstone/siltstone and then into well stratified and graded mudstone/siltstone (Figure 22c). The transitional nature of the contact between the Great Cobar Slate and CSA Siltstone

indicates the contact between the two units to the west of the New Occidental deposit is conformable. A similar transition has been observed between those two units in the Perseverance and Peak Mine areas, indicating the contact between Great Cobar Slate and CSA Siltstone in that part of the Goldfield is also conformable.

The CSA Siltstone contains up to 2–3% euhedral pyrite that is concentrated in the bases of individual siltstone beds. However, much of the original pyrite has been apparently altered to pyrrhotite and mobilised into the overprinting cleavage (Figure 22d).

Figure 20: Surface geology of the southern portion of the Great Chesney Fault in the vicinity of the New Occidental deposit.

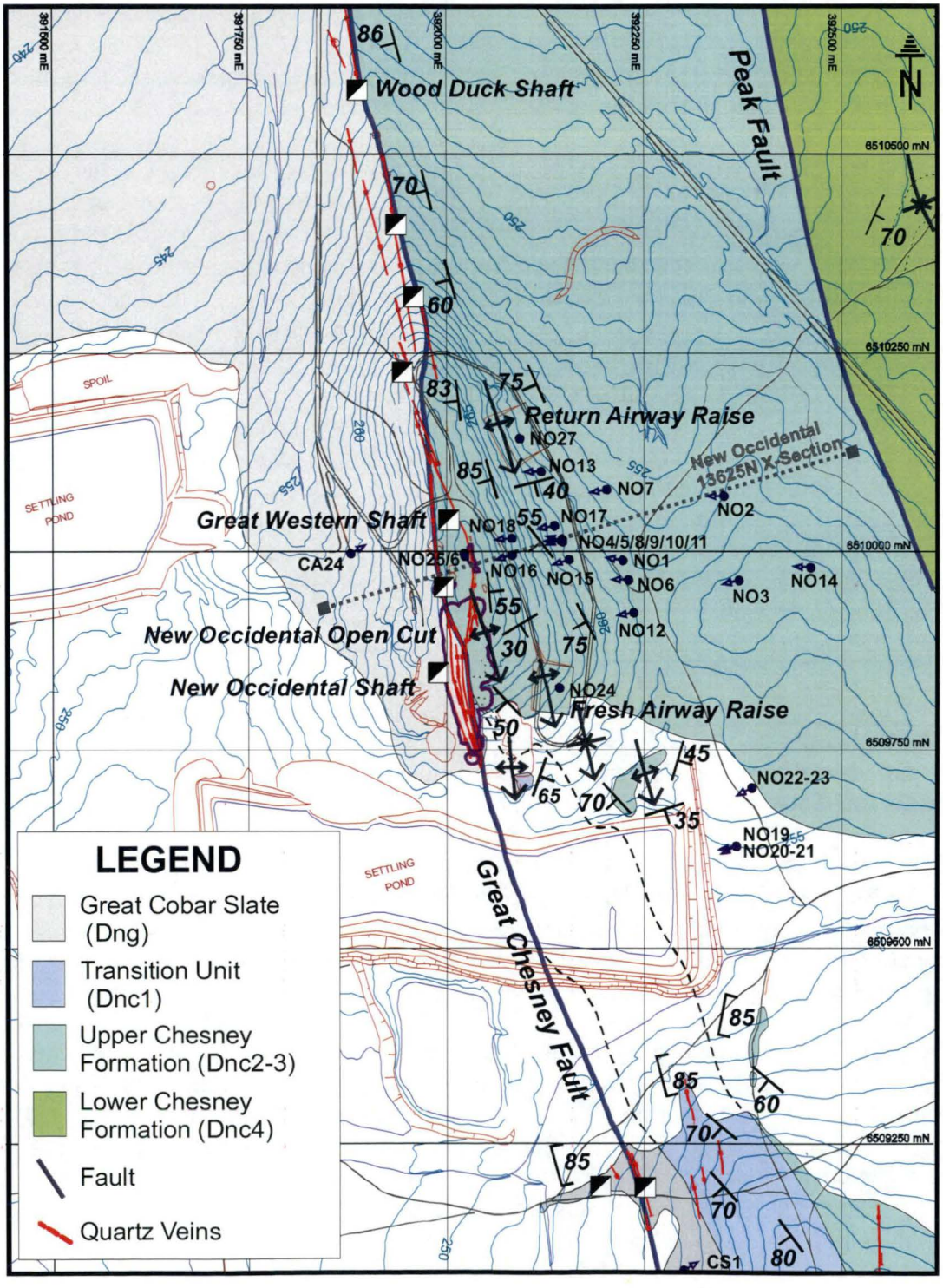

Figure 21: Detailed cross-section through the New Occidental deposit.

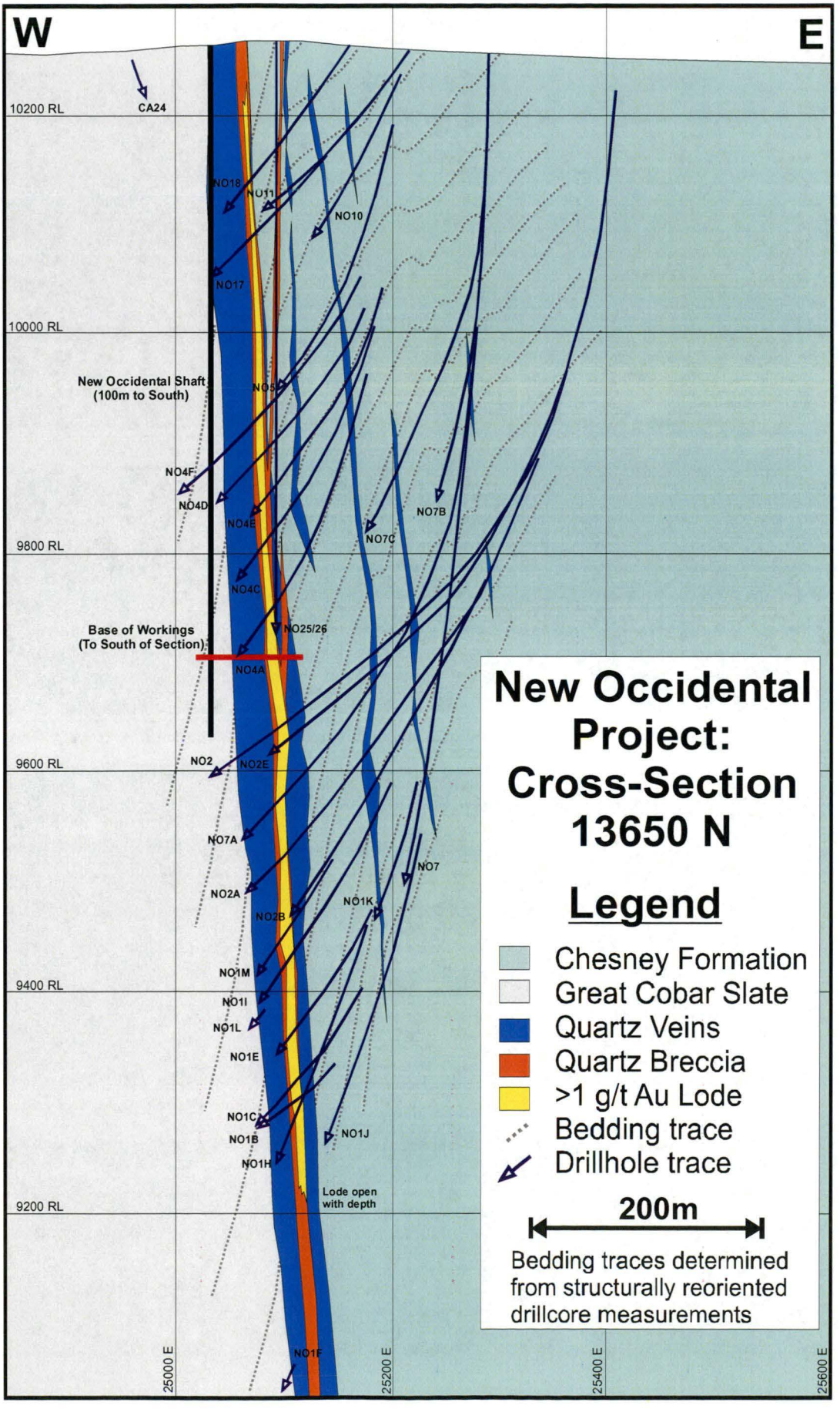

Figure 22: Rock-types present in the New Occidental deposit environs.

a) Pebbly base from thick-bedded sandstone from Chesney Formation.

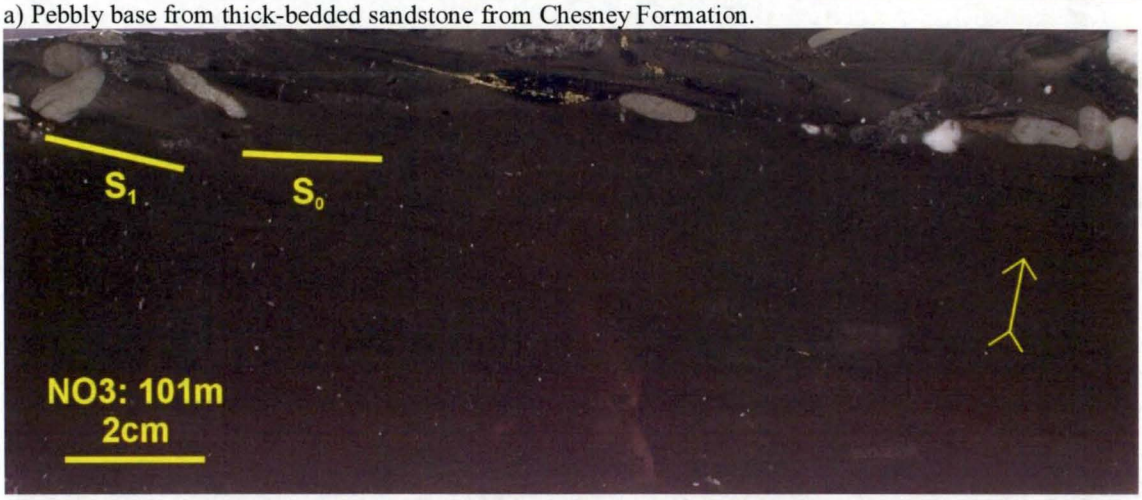

b) Thinly bedded siltstone with calcareous sandy interbeds from lower Transition Unit.

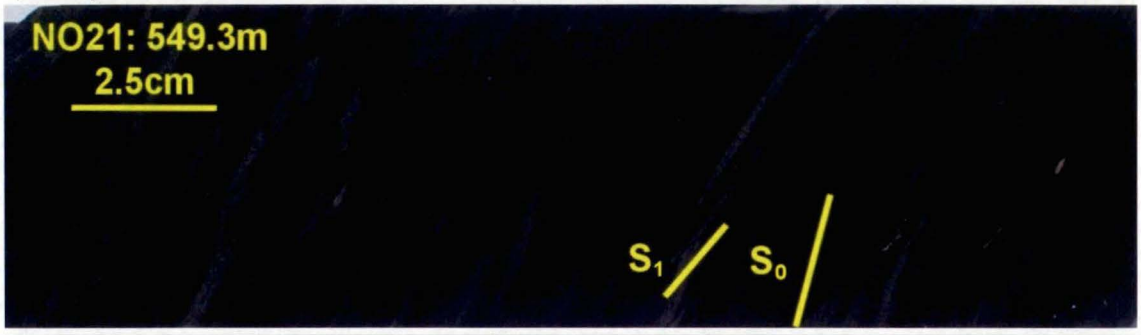

c) Thinly interbedded mudstone and siltstone from upper Great Cobar Slate (transitional to the overlying CSA Siltstone).

d) Rhythmically interbedded siltstones and mudstones of the CSA Siltstone. Pyrite present along the bases of siltstone beds has been partially converted to cleavage-parallel pyrrhotite.

3.4.2 Stratigraphic Relations Across the Great Chesney Fault

The contact between the Chesney Formation and Great Cobar Slate on the eastern side of the Great Chesney Fault is conformable from the New Occidental deposit south to the hinge of the Chesney-Narri Anticline where the fault is locally offset by faults including the Peak Shear (Figure 23). North of the New Occidental deposit to the New Cobar deposit, the Great Chesney Fault defines the contact between the Chesney Formation and Great Cobar Slate (Figure 24). At the New Cobar deposit, a conformable contact between the Chesney Formation and Great Cobar Slate has been mapped west of the Great Chesney Fault between that fault and a second parallel fault strand/splay, the Fort Bourke Fault (Peak Gold Mines data). North of the New Cobar deposit, the Chesney Formation-Great Cobar Slate contact is defined by the trace of the Fort Bourke Fault, although that fault and the Great Chesney Fault appear to merge further to the north.

South of the New Occidental deposit, the trace of the Great Chesney Fault is contained entirely in Great Cobar Slate. The fault trace is poorly defined in that area due in part to poor outcrop but also to the absence of a readily observable lithological contrast across the fault. However, deep diamond drilling at the New Occidental South and Comstock prospects south of the New Occidental deposit (Figure 25a–b) confirmed both the presence and location of the fault, with a faulted sandstone-slate contact present at depth. Glen's (1990) interpretation that the Great Chesney Fault dies out 1–2 km south of the New Occidental deposit is largely based on the lack of any discernible surface manifestation of the fault.

Sullivan (1947) estimated gross displacement on the Great Chesney Fault exceeds 300m. However, deep diamond drilling at the New Occidental deposit revealed Chesney Formation is still in fault contact with the Great Cobar Slate at 1500m depth (Peak Gold Mines data), indicating an apparent vertical offset of at least 1500m on the Great Chesney Fault. The presence of the Transition Unit either side of the Great Chesney Fault allows the offset on the Great Chesney Fault to be estimated, based on certain assumptions. The apparent horizontal offset of the Transition Unit across the Great Chesney Fault is approximately 3.0km. Assuming the intersection of the Transition Unit and the Great Chesney Fault dips 30° on average to the south, the apparent vertical displacement on the fault is of the order of 1500m. If the dip of that intersection is steeper (45°) then the apparent vertical displacement is approximately 2100m.

Likewise, the conformable CSA Siltstone-Great Cobar Slate contact that crops out to the west of the New Occidental Mine allows the vertical offset on the Great Chesney Fault to be determined if the thickness of the Great Cobar Slate in the New Occidental deposit environs is known. The type section of the Great Cobar Slate in the Great Cobar opencut is incomplete and marked by faulted contacts. The thickness of the Great Cobar Slate is thought to be in the range of 0.9–1.7 km with an average thickness of 1.0 km (Glen, 1987a). Diamond drilling at the Peak Mine and at the Perseverance prospect (Figure 25c–d) indicates the Great Cobar Slate is approximately 300m thick at those locations. The Great Cobar Slate appears to thicken to the north towards the location of the type section defined by Glen (1987a). The Great Cobar Slate also appears to thicken across the Great Chesney Fault (Figure 17). Assuming a minimum thickness of 400m for the Great Cobar Slate in the New Occidental Project area, and bedding attitudes adjacent to the Great Chesney Fault remain more or less constant, the Transition Unit - Great Cobar Slate contact west of the fault is approximately 1500m below surface, indicating an apparent vertical displacement on the Great Chesney Fault of approximately 1500m (Figure 26). The apparent vertical offset on the Great Chesney Fault could be as much as 2500m if the Great Cobar Slate is as thick (1000 m) as suggested by Glen (1987a).

Figure 23: Southern Cobar Goldfield geology with cross-section locations.

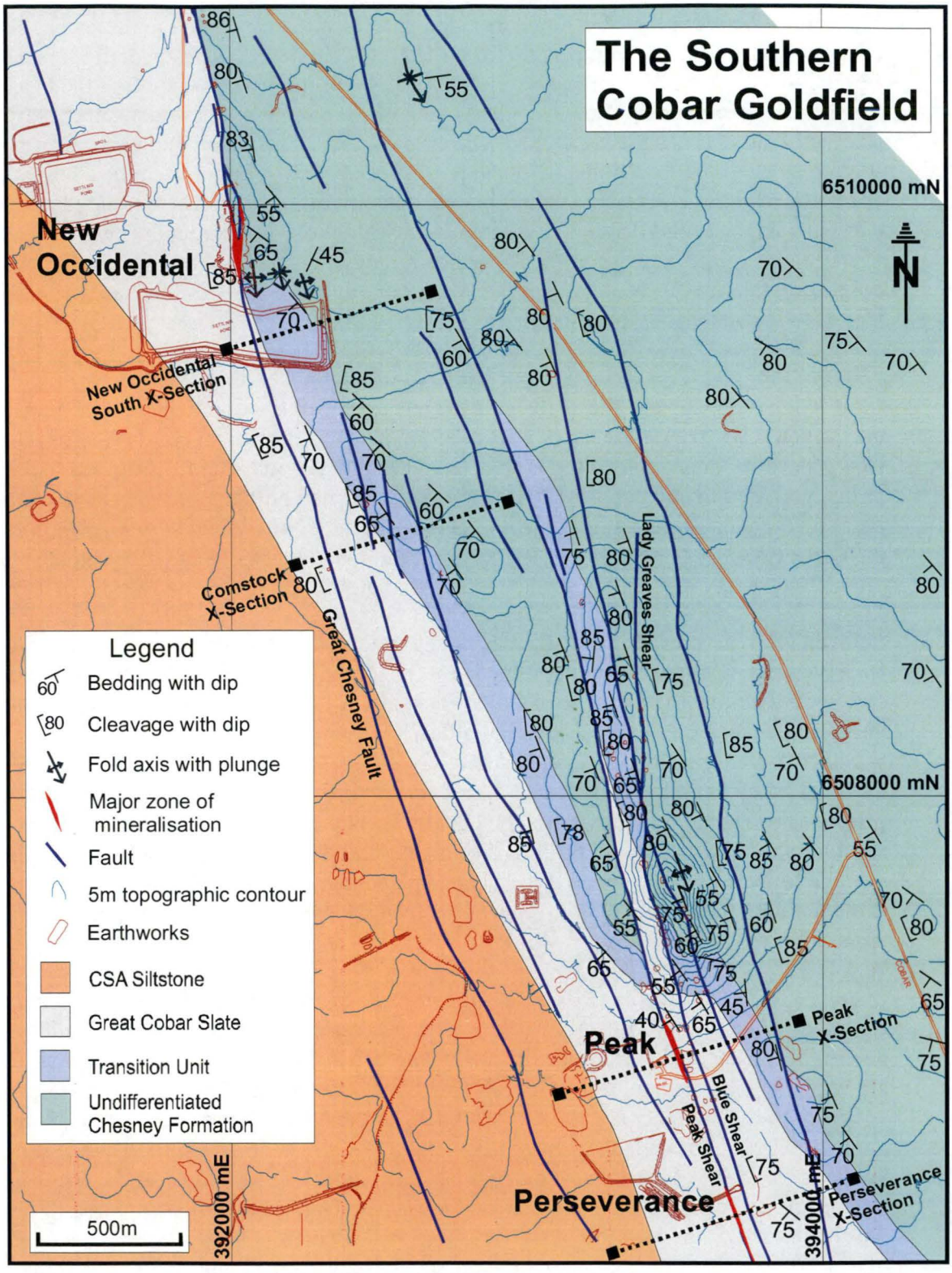

Figure 24: Northern Cobar Goldfield geology.

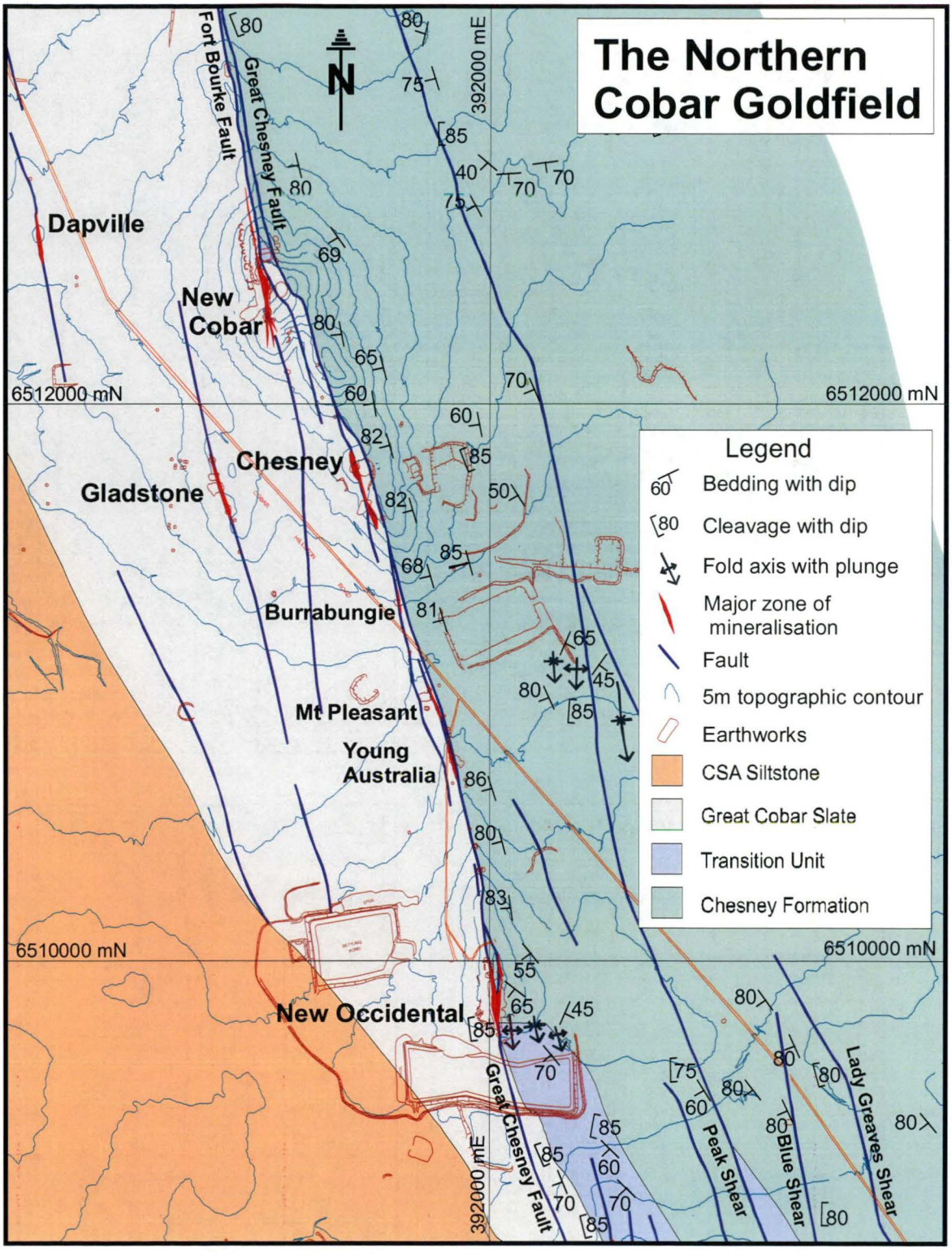

Figure 25: Cross-sections through the Southern Goldfield showing stratigraphic relationships in the Great Chesney Fault environs.

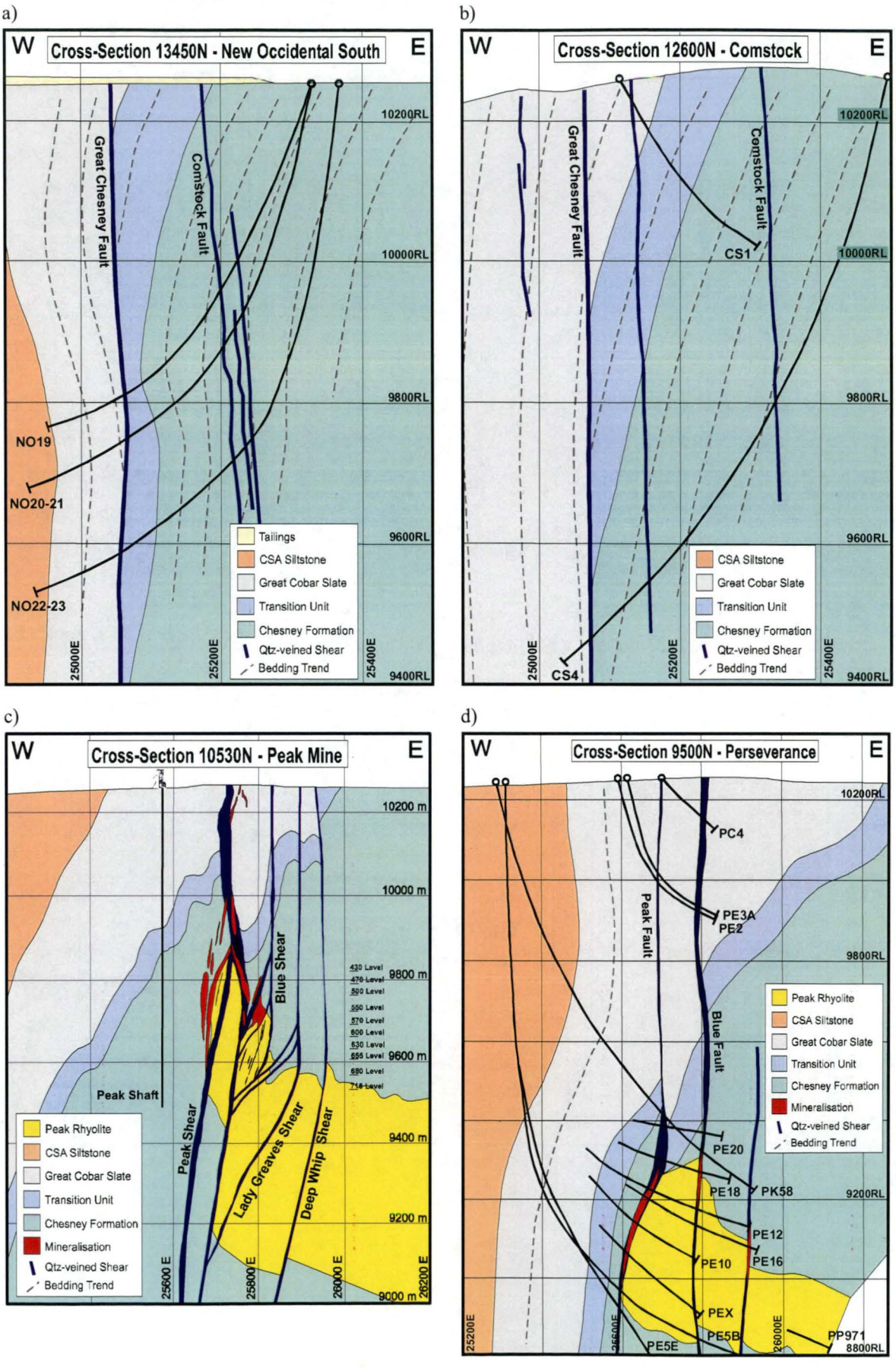

Figure 26: Cross-section through the New Occidental deposit environs.

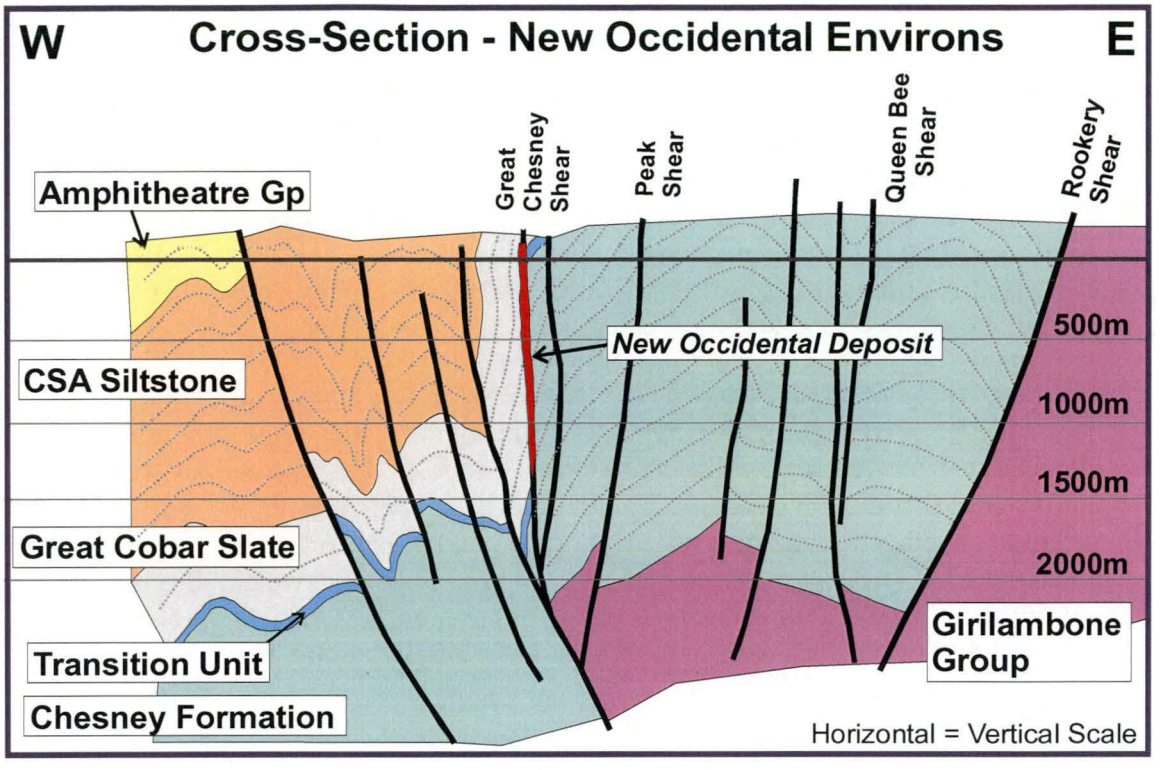

3.5 Macroscopic Structure

The structure of the New Occidental deposit environs can be divided into two domains separated by the Great Chesney Fault (and the New Occidental deposit). The eastern domain comprises a steeply west-dipping sequence of well-stratified sandstone and lesser siltstone. There is a high density of diamond drillcore data from this domain. In contrast, the western domain is less well resolved, reflecting both the paucity of drilling data and surface exposures in this area. However, the siltstone/mudstone sequence also appears to be largely west dipping. Both domains are located on the western limb of the south-southeast plunging Chesney-Narri Anticline and contain south-southeast plunging parasitic folds. The domains are transected by a prominent and ubiquitous mesoscopic steeply east-dipping cleavage and by numerous cleavage-parallel quartz-veined shears and faults, of which the Great Chesney Fault is the most significant. Cleavage intensifies around these faults without any appreciable change in orientation. Bedding on both sides of the Great Chesney Fault steepens towards the fault and is locally overturned (east-dipping) immediately adjacent to the fault. Minor small-scale gently dipping brittle faults and crenulations are locally present throughout the New Occidental area.

3.5.1 Cleavage

Macroscopic cleavage does not show any systematic variation in orientation throughout the Cobar Goldfield. Cleavage is consistently steep east dipping (80–90°/060–090°) with a weighted mean dip/dip direction of 85°/078° (Figure 27). This compares with an average S_1 orientation of 85°/076° recorded by Glen (1985) in the Cobar Goldfield, an average S_2 cleavage orientation of 84°/255° recorded by Hinman (1992) at the Peak deposit, 85°/060° in the Chesney deposit area (Wilson, 1996) and 85°/070° in the New Cobar deposit environs (Wilson, 1996). Cleavage within the Peak deposit is west dipping but is east dipping outside of the immediate deposit environs (Stegman and Pocock, 1996), reflecting inhomogeneous strain around the intrusive rhyolite core of the deposit (Hinman, 1992). Within the Cobar

Goldfield, cleavage therefore has a relatively consistent orientation and the progressive swing in cleavage orientation from east-northeast to east-southeast that Glen (1985) observed from south of Cobar township to north of town is not evident on the scale of the Goldfield.

The New Occidental deposit occurs within a high-strain zone characterised by a strongly developed cleavage. Distal to the Great Chesney Fault (>100m), cleavage is relatively weakly developed throughout the enclosing sediments of the Chesney Formation and Great Cobar Slate (Figure 29a). The intensity of this cleavage increases markedly within 30–50m of the fault. Bedding is partially dismembered and cleavage-parallel quartz veins becomes increasingly common (Figure 29b). Within 15m of the Great Chesney Fault bedding is largely dismembered by cleavage (Figure 22b).

Cleavage throughout the New Occidental deposit environs has relatively consistent orientation (Figure 28). Stereonets of cleavage measurements from locations within the New Occidental deposit environs (North Opencut; East Opencut, Fresh Air Raise pad and Return Air Raise pad) reveal that dip/dip directions of cleavage are in the range 80–90°/060–100° with a weighted average dip/dip direction of 86°/078° and a standard deviation in the dip direction of cleavage of 7° (based on 202 measurements of cleavage). However, cleavage in the northern part of the New Occidental Opencut has a slightly more easterly dip direction (85°/084°) compared to that of cleavage in the other sub-locations (Figure 28).

The dip of subsurface cleavage from the reoriented drillcore data ranges from steep east-dipping (50°/078°) to steep west-dipping (60°/258°) with an maximum orientation of 80°/078°. The greater spread in cleavage dip in the subsurface data compared to the surface cleavage data in part reflects uncertainties in measurements from core. A spatial analysis of the orientation of cleavage maxima in the sub-surface structural data reveals a subtle apparent shallowing in the average dip of cleavage from 85–89° at distances greater than 25m from the fault, to 82–84° within and immediately surrounding the Great Chesney Fault.

The variability in both dip and dip direction of cleavage between surface domains and in cleavage dip in the sub-surface drillcore data appears in part to reflect refraction of cleavage across bedding, particularly in the thick-bedded sandstones of the Chesney Formation. Underground exposures in the New Occidental Mine reveal cleavage is locally vertical or dips steeply to the west where it refracts along bedding in the siltstone tops of individual graded siltstone/sandstone beds. Cleavage refraction along bedding is more prevalent when cleavage is only moderately developed and bedding is still a dominant fabric in the rock, and is less well developed in the strongly cleaved margins of the New Occidental deposit where bedding has been strongly dismembered and overprinted. As a consequence, the maxima in stereoplots of cleavage data at distances greater than 25m from the Great Chesney Fault reflect the inclusion of a greater proportion of west-dipping cleavage data compared to data from the New Occidental deposit.

Figure 27: Variations in cleavage orientation throughout the Cobar Goldfield.

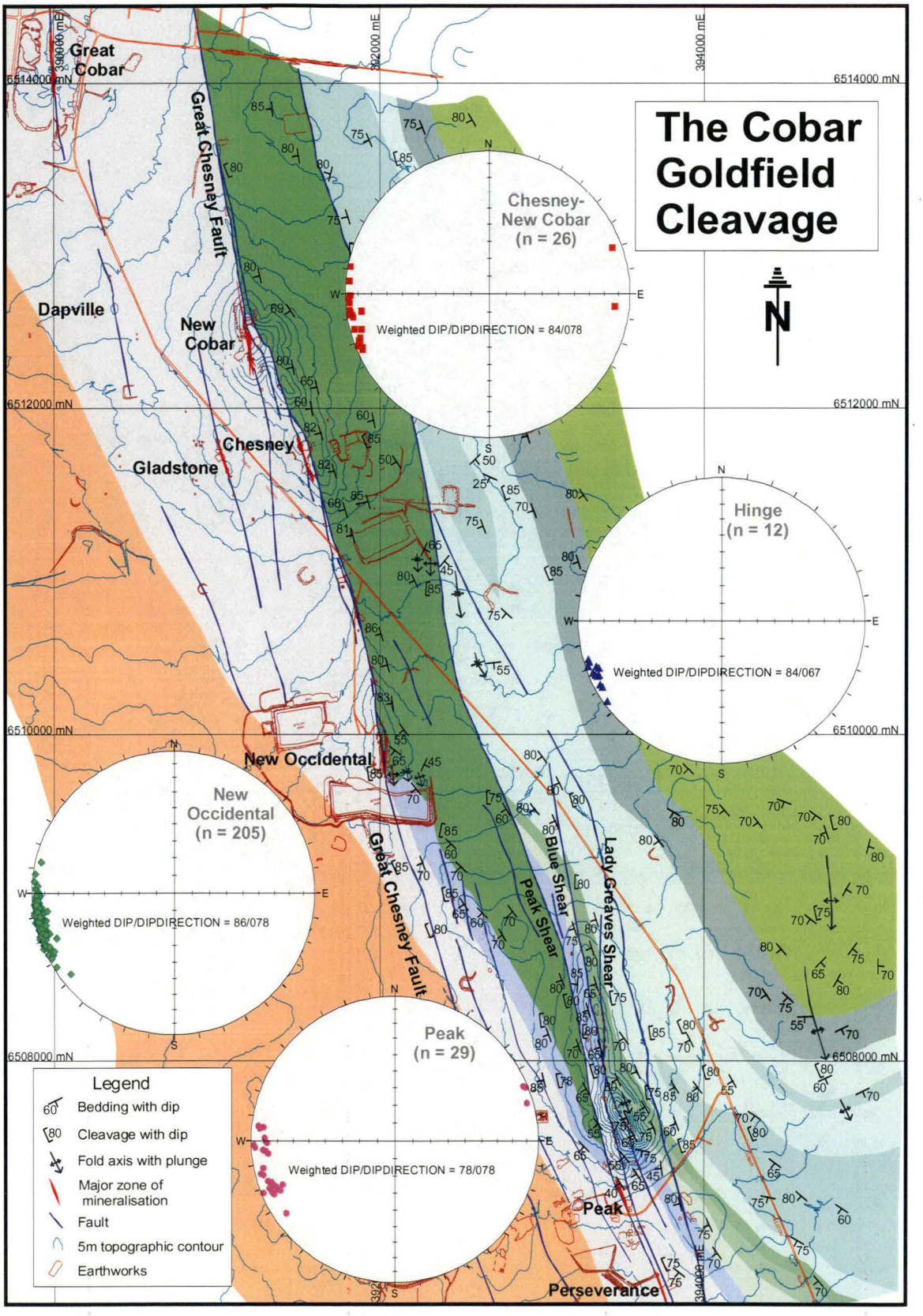

Figure 28: Variations in cleavage orientation throughout the New Occidental deposit environs.

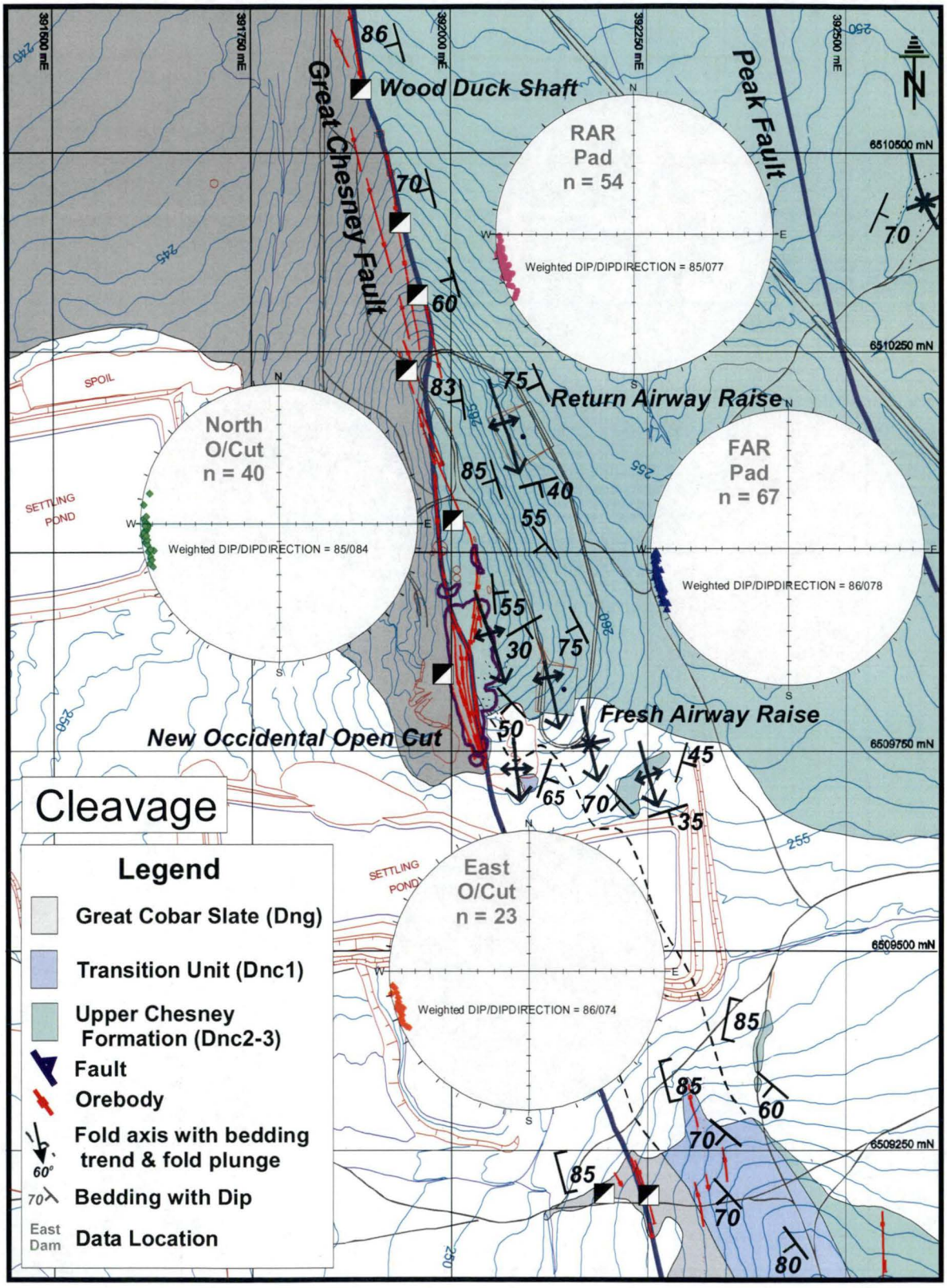

Figure 29: Examples of relations between bedding (S_0) and cleavage (S_2) in the New Occidental deposit.

a) Chesney Formation sandstones approximately 50m from the Great Chesney Fault.

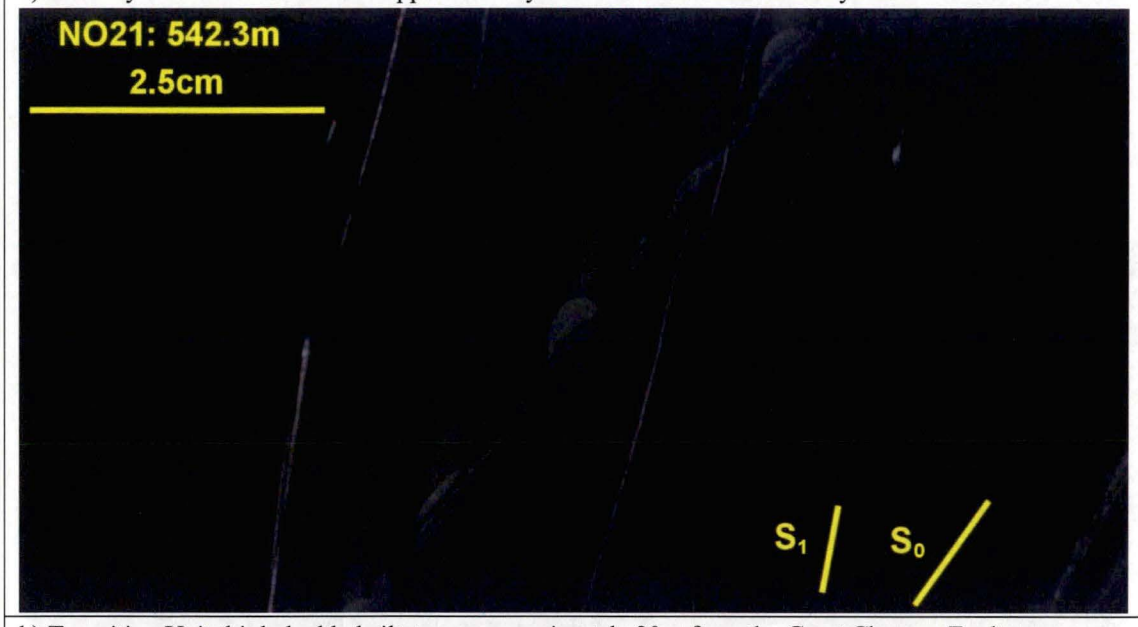

b) Transition Unit thinly bedded siltstones approximately 20m from the Great Chesney Fault.

3.5.2 Faulting

Geological mapping undertaken in this study, in conjunction with prospect mapping at the New Cobar deposit (Peak Gold Mines data, including mapping undertaken by Peter Leah) has revealed major faults in the Cobar Goldfield, including the Great Chesney Fault and Cobar Fault, consist of series of en-echelon left-stepping and overlapping fault segments (Figure 30), rather than single continuous northwesterly striking fault planes as defined by Glen (1985; 1987a; 1990; 1994). A series of north-northwest trending faults, including the various strands of the Peak Shear, the Queen Bee Fault and a number of lesser faults, variably offset the Chesney Formation - Great Cobar Slate stratigraphic contact around the hinge of the Chesney-Narri Anticline (Figure 30). Conformable stratigraphic contacts exist between each fault strand. Such relationships have now been recognised in a number of other locations in the Goldfield. For example, Peter Leah (pers comm.) determined that the Great Chesney Fault in the New Cobar area, which was previously interpreted by Mulholland & Rayner (1961) to be folded and offset by an east-west trending tear fault (Figure 31), comprises two sub-parallel faults, the Great Chesney Fault and the Fort Bourke Fault, separated by a conformable stratigraphic contact between Chesney Formation sandstones and overlying Great Cobar Slate.

It is also likely that many of the right-angle bends interpreted in the trace of the Great Chesney Fault north of Cobar (Glen, 1985; 1990 - Figure 30a) represent similar over-laps between parallel, and essentially separate, north-northwest trending faults (Figure 30b). Therefore, the Great Chesney Fault probably does not extend as far north as Glen (1985; 1990) proposed. Similarly, the Cobar Fault, which lies to the west of the Great Chesney Fault, is herein interpreted to consist of a series of parallel and partly overlapping north-northwest trending faults, rather than a single more northwesterly striking fault as interpreted Glen (1985; 1990). The north-northwest trending fault upon which the Great Cobar deposit is localised (previously Glen's Cobar Fault) may even be the southerly extension of a similarly oriented fault that offsets the Chesney Formation - Great Cobar Slate stratigraphic contact (previously the northern part of Glen's Great Chesney Fault) (Figure 30).

Figure 30: Major faults and folds in Structural Zone 1 (modified from Glen, 1990).

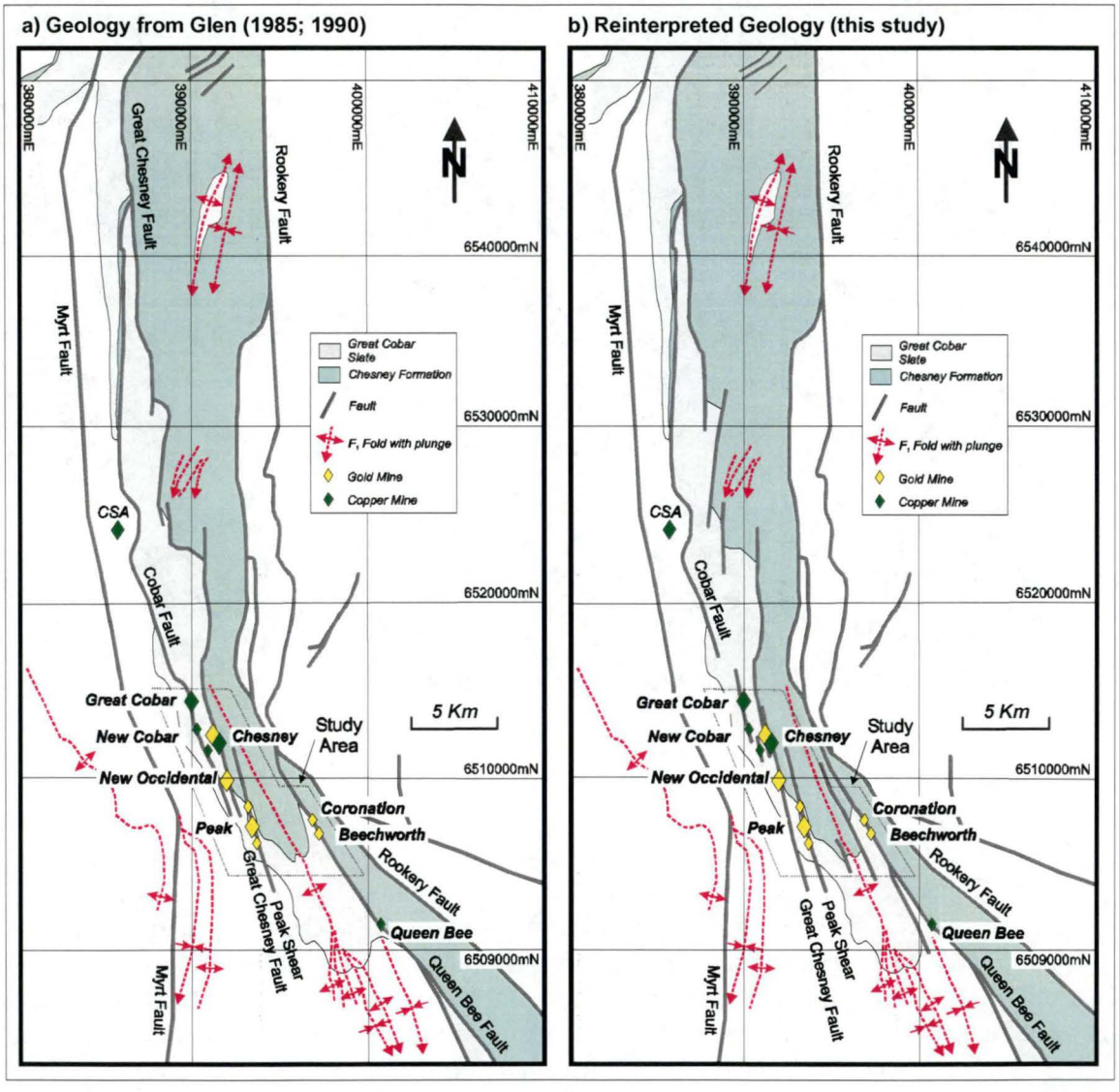

The Great Chesney Fault in the Cobar Goldfield is associated with numerous sub-parallel faults (Figure 23 and Figure 25). A number of those faults are splays off the main strand of the Great Chesney Fault that are either parallel to the Great Chesney Fault in plan but merge with the main fault at depth, or strike more northerly and merge with the Great Chesney Fault to the south along strike. At present levels of drilling and exposure some faults like the Peak Shear to the south, appear to be discrete separate faults, although the Peak Shear may merge with the Great Chesney Fault at greater depth (Figure 26).

Figure 31: New Cobar deposit geology showing revised fault interpretations.

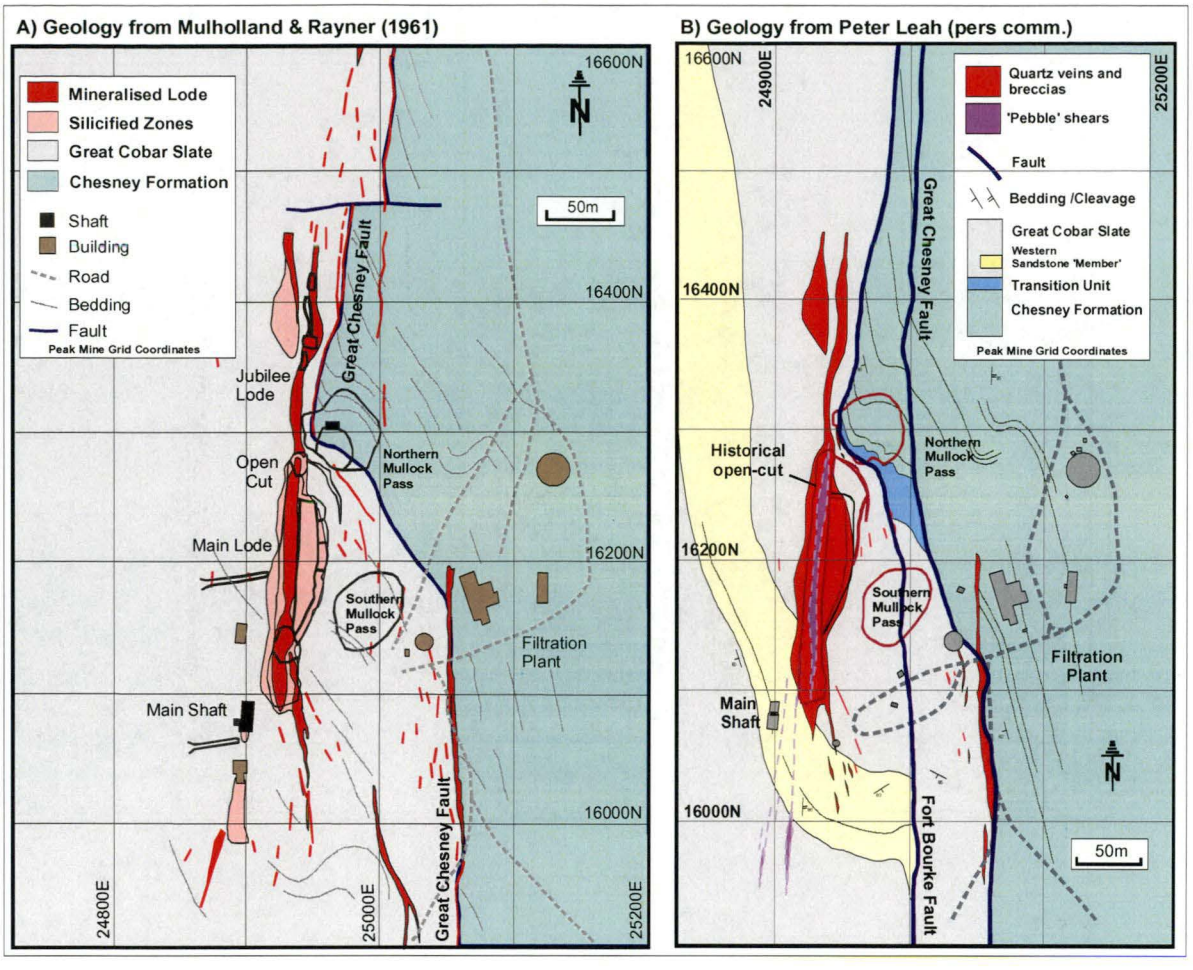

Within the New Occidental deposit environs, two subsidiary faults to the Great Chesney Fault have been identified:

1. The **Comstock Fault** is a north-northwest striking steeply east dipping fault located approximately 100m east and in the hanging wall of the Great Chesney Fault. The Comstock fault is best developed to the south of the New Occidental deposit where it is associated with a macroscopic-scale bedding flexure in the Comstock area. It is characterised by increased cleavage development and cleavage-parallel quartz veins. Bedding offset across that fault appears minor but is east block-up, consistent with reverse dip-slip fault displacement.

2. The **Albion Fault** is located in the immediate hanging wall of the Great Chesney Fault at the northern end of the New Occidental deposit. It forms a sigmoidal-shaped couple with the Great Chesney Fault (Figure 32a). In cross-section (Figure 32b), the Albion Fault has a sub-vertical to steep westerly dip (slightly oblique to cleavage) and merges with the Great Chesney Fault approximately 500m below the surface. The intersection of the Albion and Great Chesney Faults is steep north plunging and approximately parallel to the steeply north plunging stretching lineation. In detail, the fault zone is defined by zones of more intensely developed cleavage and zones of steeply to moderately east dipping quartz veins, including the Albion lode. Displacement across the Albion Fault appears to be relatively minor (<5m), although bedding steepens appreciably from east to west across the fault.

Figure 32: Relationship between the Great Chesney Fault and Albion Fault.

a) Plan of surface geology of the New Occidental area and location of cross-section.

b) Cross-section through the northern part of the New Occidental deposit.

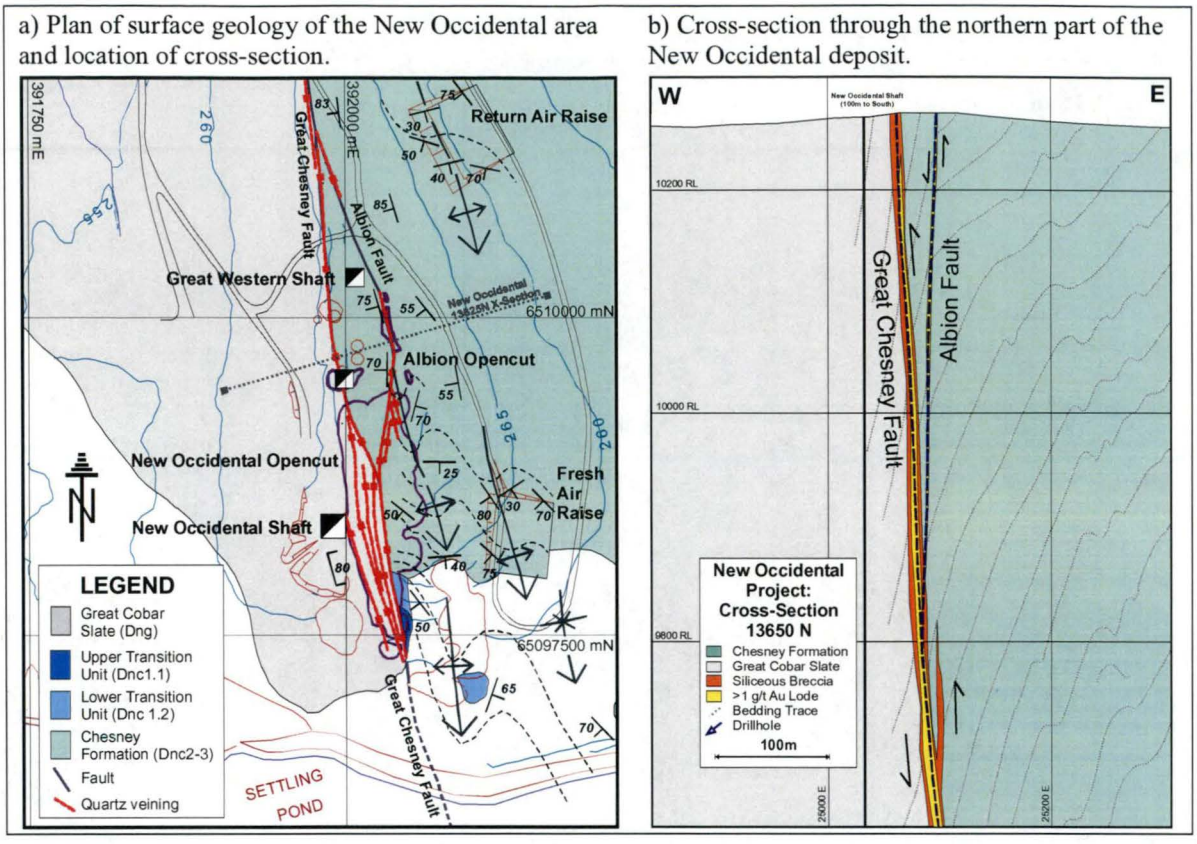

3.5.3 Folds

The Chesney-Narri Anticline dominates the gross structure of the Cobar Goldfield. Mapping during this study indicates the hinge line of the anticline in the Cobar Goldfield strikes north-northwest, parallel to dominant cleavage and major faults, including the Great Chesney Fault and Peak Shears (Figure 17, Figure 30b). Further north, the hinge line of the Chesney-Narri Anticline is inferred to lie east of the area mapped during this study and, importantly, 1–2km east of the location suggested by Glen (1985; 1987a) (Figure 30). Glen's positioning of the hinge line of the Chesney-Narri Anticline was based on inferred east-dipping strata in Chesney Formation east of the New Cobar deposit (Figure 5 in Glen; 1985). However, mapping of that area during this study revealed a largely west-dipping sequence of upper Chesney Formation sandstone and siltstone, truncated by the northern extension of the Peak Shear. Localised zones of south- and east-dipping strata are interpreted to reflect small-scale folds rather than the Chesney-Narri Anticline, as indicated by the continuity of the upper Chesney Formation stratigraphy through the area. Therefore, the Chesney-Narri Anticline does not terminate against the Great Chesney Fault as interpreted by Glen (1985; 1987a) but rather likely terminates against the Rookery Fault (Figure 30b).

Bedding throughout the Cobar Goldfield is consistently upward facing, based on younging directions inferred from graded beds. Stereographic projections of poles to bedding throughout the Cobar Goldfield are summarised in Figure 33.

In the Hinge area, which encompasses the hinge of the Chesney-Narri Anticline, bedding measurements define a single, relatively simple pole girdle that corresponds to moderate-steeply dipping fold axes (60°/170°). In contrast, the New Occidental, Peak and Chesney-New Cobar areas have more complex patterns of bedding orientations. Poles to surface

bedding in all three areas define much broader girdles that correspond to fold axes in the range 30–70°/170°.

Figure 33: Variations in bedding orientation throughout the Cobar Goldfield.

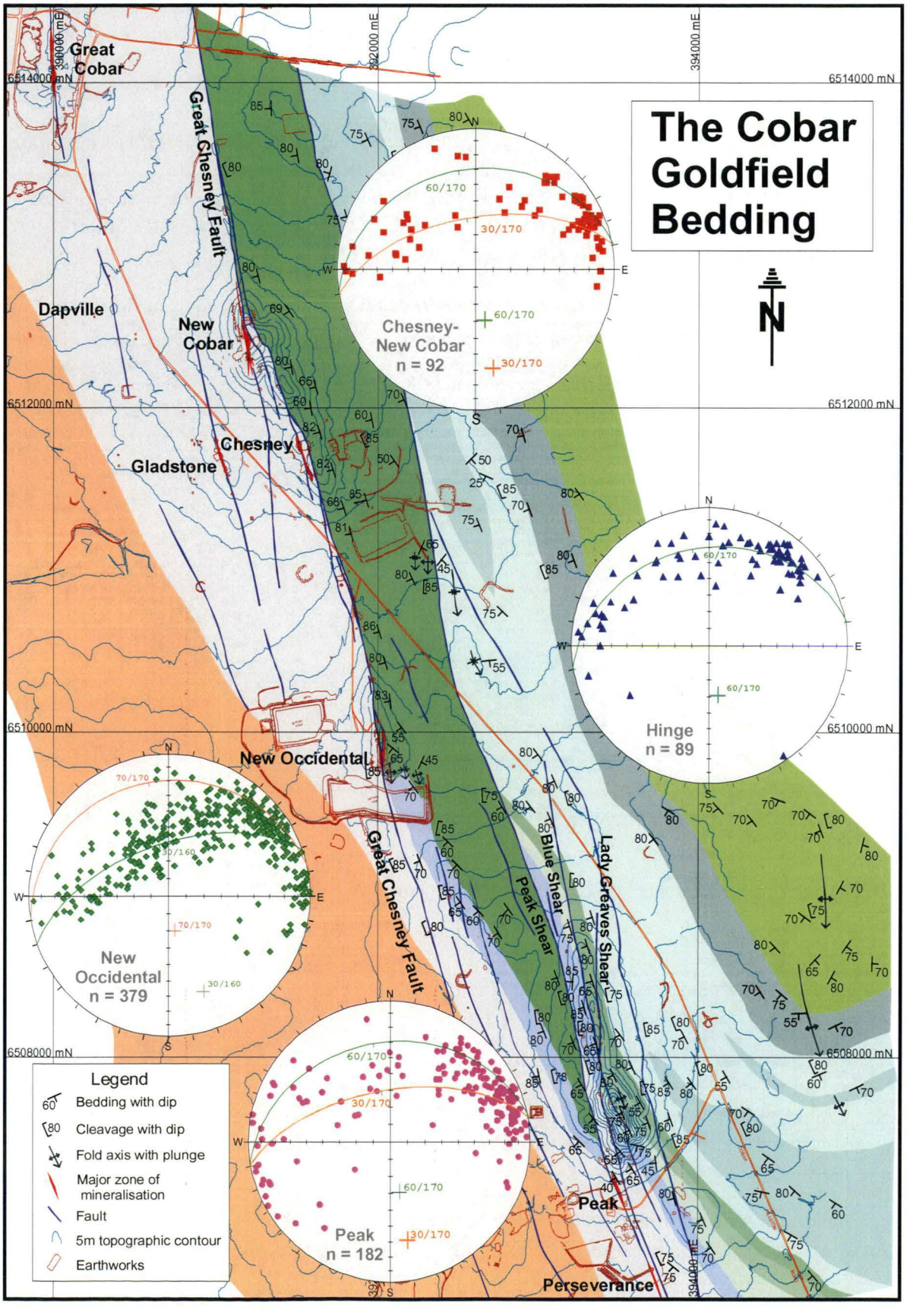

Mesoscopic folds parasitic to the Chesney-Narri Anticline are present throughout the Goldfield, being best developed in the Chesney Formation. These folds have wavelengths of the order of 5–20m and are typically open folds with inter-limb angles of ~90°. Mesoscopic fold hinges are present along the eastern wall of the opencut at New Occidental and on Fort Bourke hill around the New Cobar-Chesney deposits. Mesoscopic folds are also well developed on Peak ridge immediately to the north of the Peak deposit. Fold hinges recorded at those locations (this study) plunge gently to the south (15–45°/160–190°: average 28°/176°) (Figure 34a).

Within the New Occidental Opencut, the orientation of mesoscopic folds varies along the eastern wall of the Opencut. Fold hinges in the northeastern part of the Opencut plunge less steeply and trend more variably to the south (10–25°/155–180°) compared to folds in the eastern part of the Opencut (20–50°/160–170°) (Figure 34b). Folds are uniformly relatively open (inter-limb angles of ≥90°) and upward facing.

Figure 34: Equal area stereonets of poles to bedding and fold plunges in the Cobar Goldfield.

a) Poles to bedding define two great circles; one corresponding to mapped mesoscopic folds (20°/160°) and a second incomplete great circle that corresponds to a more steeply dipping fold axis orientation (70°/190°)

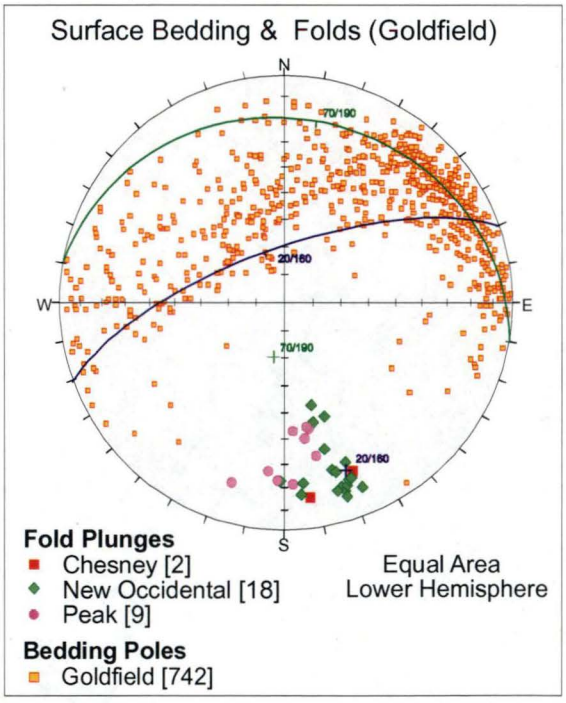

b) Poles to bedding define two great circles; one corresponding to mapped mesoscopic folds (15–50°/160°) and a second incomplete great circle that corresponds to a more steeply dipping fold axis orientation (70°/190°)

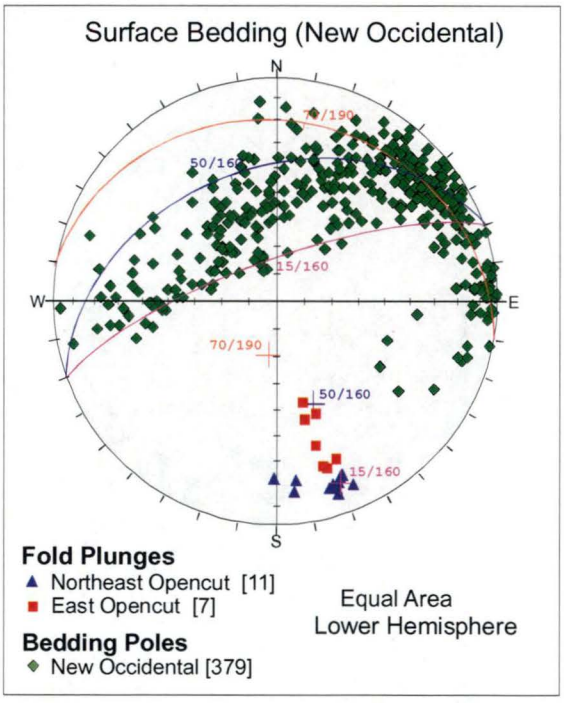

Stereonets of poles to bedding for all data collected at the New Occidental deposit (Figure 35 and Figure 36) contain relatively broad pole girdles corresponding to gently to steeply south plunging folds (15–70° to 160–170°). The pole girdle corresponding to gently south plunging folds (15–35°/160–170°) is almost complete, whereas the more steeply dipping pole girdle (70°/170°) is only partially defined.

Analysis of bedding data collected both from within and outside of the New Occidental Opencut reveals patterns of bedding orientation are less complicated with increasing distance from the New Occidental deposit. In areas >500m from the deposit (e.g. Comstock and East Regional areas, Figure 35), only the partially defined, more steeply plunging pole girdle

(70°/170°) is present. That girdle is most consistent with west-dipping, open, monoclinal folds or flexures that lack clearly defined hinges. A similar macro-scale bedding flexure has been mapped in the Comstock area (Figure 23: 392400E, 6509000N). This flexure has a half-wavelength of approximately 300m and is centred on the Comstock Fault. However, proximal to the New Occidental deposit, the partially defined, more steeply plunging pole girdle (70°/170°) and the almost complete gently plunging pole girdle (15–35°/160–170°) are both present. The 15–35°/160–170° pole girdle matches both the shape and orientation of the gently south plunging mesoscopic folds observed in the eastern wall of the New Occidental Opencut, thereby confirming the New Occidental deposit is located in an area of increased parasitic folding.

Within the New Occidental Opencut, the bedding pole girdle in the northeastern part of the Opencut corresponds to folds plunging 15–30°/160°, compared to poles to bedding from the East Opencut area, which define a girdle indicating folds plunging 20–50°/170° (Figure 36). These two inferred fold patterns match variations in the orientation of mesoscopic parasitic folds mapped along the eastern wall of the Opencut (Figure 34b).

The Opencut bedding data contains an anomalous population of very steep west-dipping beds that do not lie along the aforementioned pole girdles. These data are predominantly from within 10m of the trace of the Great Chesney Fault and indicate that although bedding is strongly dismembered by cleavage in close proximity to the fault, bedding is relatively planar and unfolded, very steeply west-dipping (>80°) and consistently west-facing.

Whilst bedding generally strikes north-northwest sub-parallel to the trend of the mesoscopic fold hinges, bedding in the northern part of the Opencut strikes north. Several mesoscopic fold hinges with more southerly plunges (180° compared to 160°) have also been recorded from this area (Figure 34b).

The reoriented drillcore data provides valuable information on the sub-surface structure of the New Occidental deposit and also provides critical data on the structure in the footwall of the Great Chesney Fault. Stereonets of poles to bedding from the reoriented drillcore data show a similar distribution of bedding poles to the surface data. A relatively broad pole girdle is well developed (Figure 38a), corresponding to fold axis orientations of 10–60°/160–170°. In detail, the data show an incomplete pole girdle that corresponds to a fold axis plunging 20°/170°, in addition to the more complete pole girdle corresponding to hinges of parasitic folds plunging 45°/160°. A very small number of bedding data correspond to a gently north-plunging fold orientation. Again, an anomalous population of steep west dipping bedding is present in the data. The small amount of data from the immediate footwall of the Great Chesney Fault indicates bedding is predominantly sub-vertical to steeply west-southwest dipping and west facing (Figure 37).

Bedding data from the South Occidental area (Figure 35) reveal a similar bedding pattern to that developed around the Occidental prospect. Bedding is predominantly steep west-southwest dipping and west facing. The data also reveals two well-developed bedding pole girdles corresponding to folds plunging 40°/160° and 0°/160° respectively. The latter girdle is anomalous in the context of the New Occidental area. Bedding in this girdle is from the lowermost part of the NO21 where it intersected CSA Siltstone in the footwall (western side) of the Great Chesney Fault (Figure 25a).

A spatial analysis of the sub-surface bedding data in relation to its proximity to the Great Chesney Fault reveals a systematic change in bedding patterns across the Great Chesney Fault (Figure 37). At distances greater than 100m from the Great Chesney Fault, pole girdles

corresponding to fold plunges of 10–45°/160° are well developed. The small population of bedding data that defines the pole girdle corresponding to the anomalous north-plunging folds is also located >100m from the fault. With the exception of the north-plunging fold pattern, these fold plunges are similar to those inferred from the surface bedding data. With increasing proximity to the Great Chesney Fault (distances of less than 100m from the fault) those bedding pole girdles become less complete. The girdles are largely absent at distances of less than 25m from the fault. In the footwall of the Great Chesney Fault, the subsurface bedding data indicates that folding is absent within 25m of the fault, but is again well developed in the footwall >25m from the fault. There is insufficient bedding data from the footwall to characterise variations in these folds.

Bedding also systematically steepens towards the Great Chesney Fault. In the hanging wall, bedding maxima steepens from 68°/249° at distances greater than 100m from the Great Chesney Fault to 77°/252° immediately adjacent to the fault. Similarly, in the footwall of the Great Chesney Fault, bedding maxima steepens from 60°/260° at distances greater than 100m from the fault to 85°/254° immediately adjacent to the fault.

Bedding measurements were also recorded from drillholes NO25/26, which are located to the north of the North Opencut area. NO25/26 are both vertical drillholes collared in the hanging wall of the New Occidental deposit 25m to the east of the Great Chesney Fault (Figure 36). Both holes intersect the Albion Fault at a depth of approximately 190m and terminate in the orebody at around 530m depth. Bedding data was reoriented assuming a cleavage dip/dip direction of 84°/084°, which is the average from surface measurements from the North Opencut area. The data indicate bedding in the footwall (east) of the Albion Fault is moderately east dipping (maxima of 69°/270°) and is steeper and dips in a more southwesterly direction in the hanging wall of the fault (maxima 78°/255°; Figure 38b). These drillholes did not intersect any parasitic folds, although several minor mesoscopic warps in bedding were noted. These warps are relatively short wavelength features (of the order of several metres) and are marked by a slight decrease in the dip of bedding (10–15°) without an appreciable change in dip direction.

In summary, folds present in the less intensely deformed parts of the Cobar Goldfield, like the Comstock area south of the New Occidental deposit and the Hinge area east of the Great Chesney Fault, are typically moderately to steeply plunging (60–70°/170°). These folds are large-scale long wavelength (200m to 500 m) relatively open structures. The more gently plunging mesoscopic folds (of the order of 30°/170°), which are characteristically tighter, shorter wavelength and more frequent than the moderately to steeply plunging folds, have only been observed in the more intensely deformed areas in the immediate vicinity of the major faults and gold-copper deposits in the Goldfield, including the vicinity of the New Occidental deposit. However, the more steeply plunging, more open folds also appear to be present in the more strongly deformed areas. Bedding data from each of the major deposit areas define broad pole girdles, indicating a continuum of fold plunges between 30–70° to the south.

The sub-surface reoriented structural data (Figure 37) reveal gently to moderately south-plunging parasitic folds, and the larger-scale, longer wavelength moderately south plunging folds, which are well developed in both footwall and the hanging wall of the Great Chesney Fault, both change shape within 100m of the Great Chesney Fault. The mesoscopic folds become progressively more open and monoclinal in shape as the east-dipping fold limbs assume a more sub-horizontal attitude and the west-dipping limbs become steeper and attenuated (Figure 39). Hinges of these folds are more gently plunging (of the order of 10° to the south) and oriented approximately orthogonal to the prominent stretching lineation on cleavage.

Within 25m of the Great Chesney Fault, folds are completely absent in the sub-surface environment, although macroscopic folds persist in the New Occidental Opencut to within 10–15m of the Great Chesney Fault. Subsurface reoriented structural data show that these folds gradually die out towards the fault. Concomitantly, bedding is steeper around the New Occidental deposit/Great Chesney Fault (Figure 36, Figure 37). Within this zone, bedding is also strongly dismembered by cleavage and is completely overprinted by cleavage within several metres of the fault.

Figure 35: Variations in bedding orientations in the New Occidental deposit environs (all data from surface measurements with the exception of the South Occidental area).

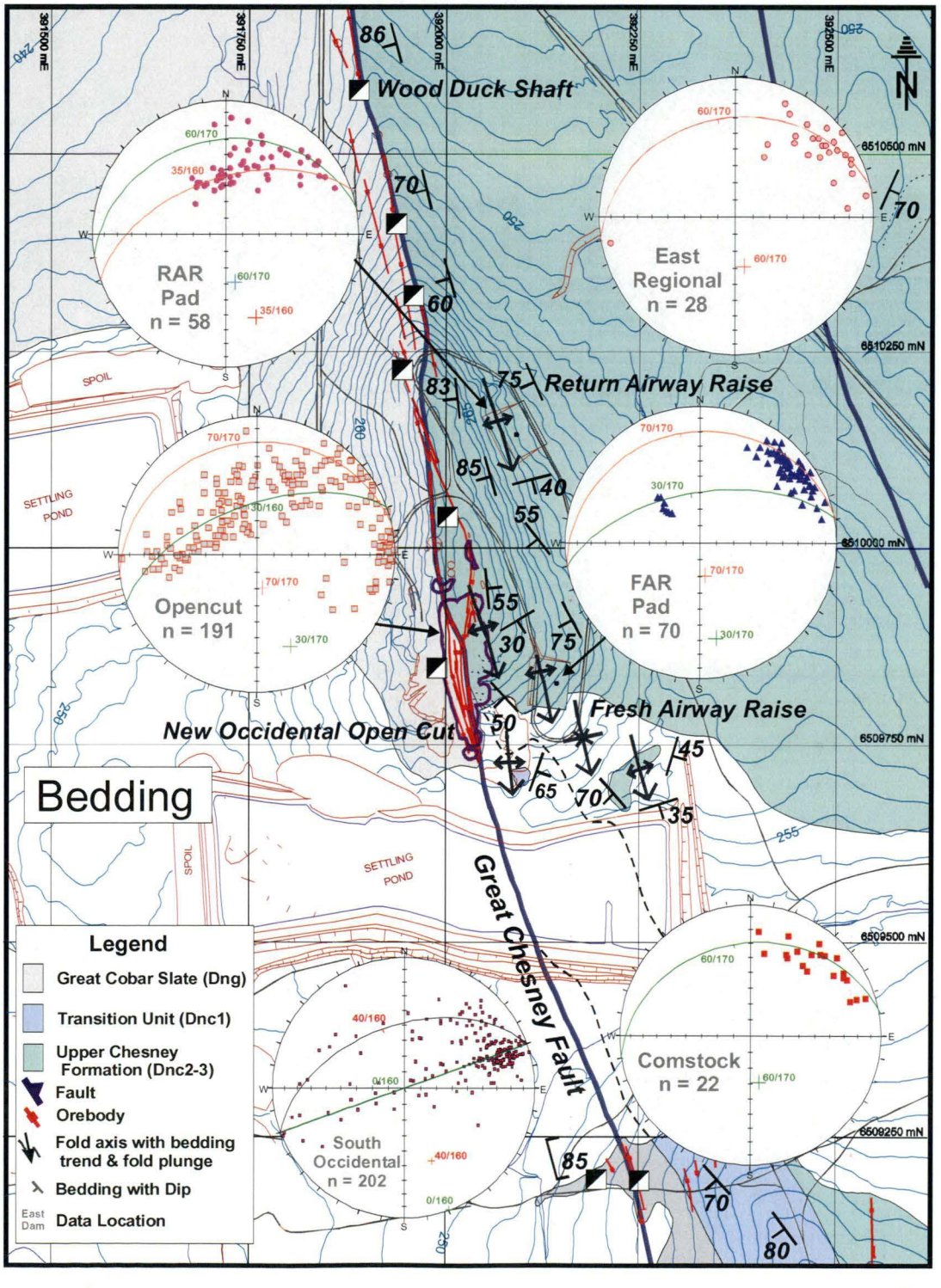

Figure 36: Variations in bedding orientations in the New Occidental Opencut (all data from surface measurements with the exception of NO25–26).

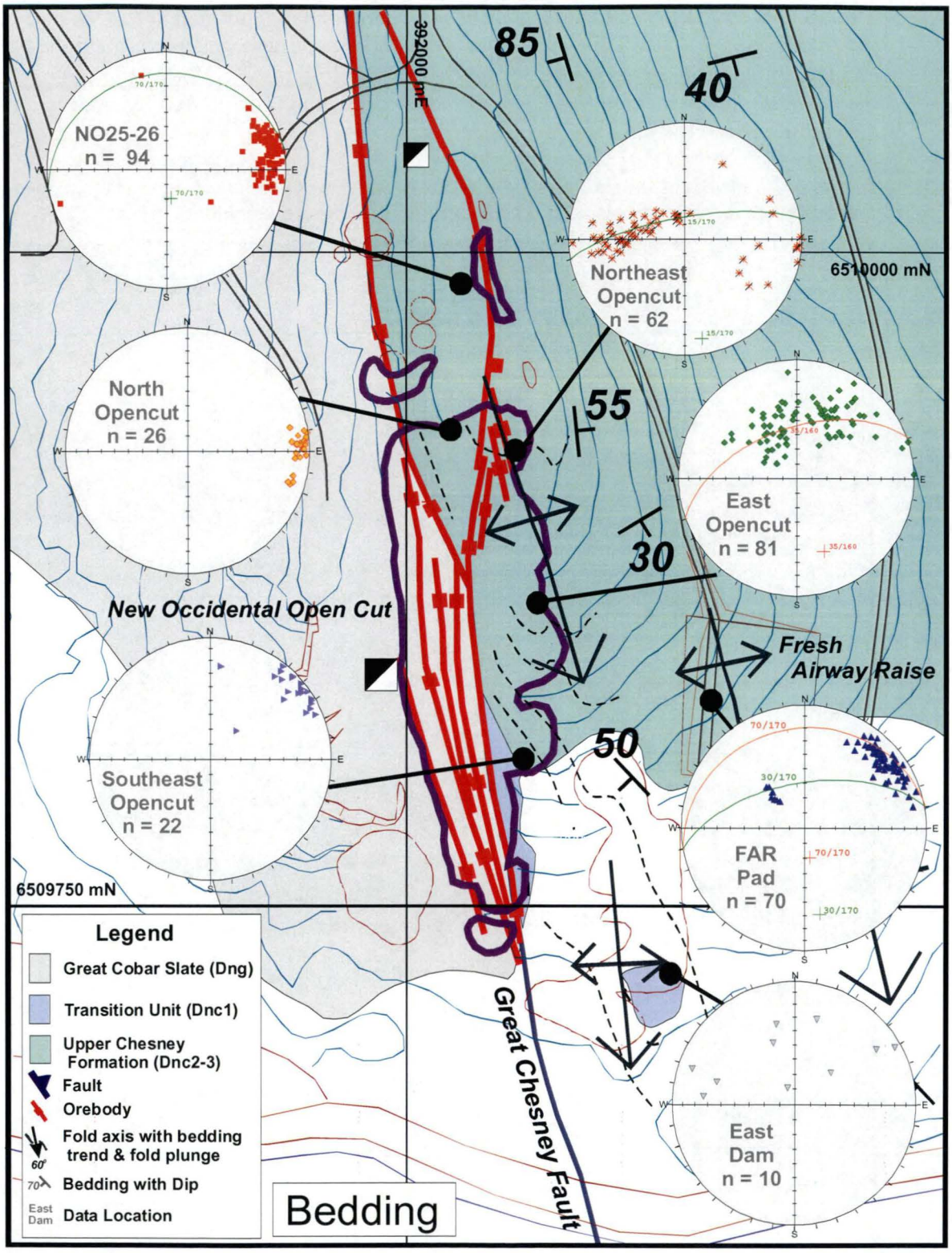

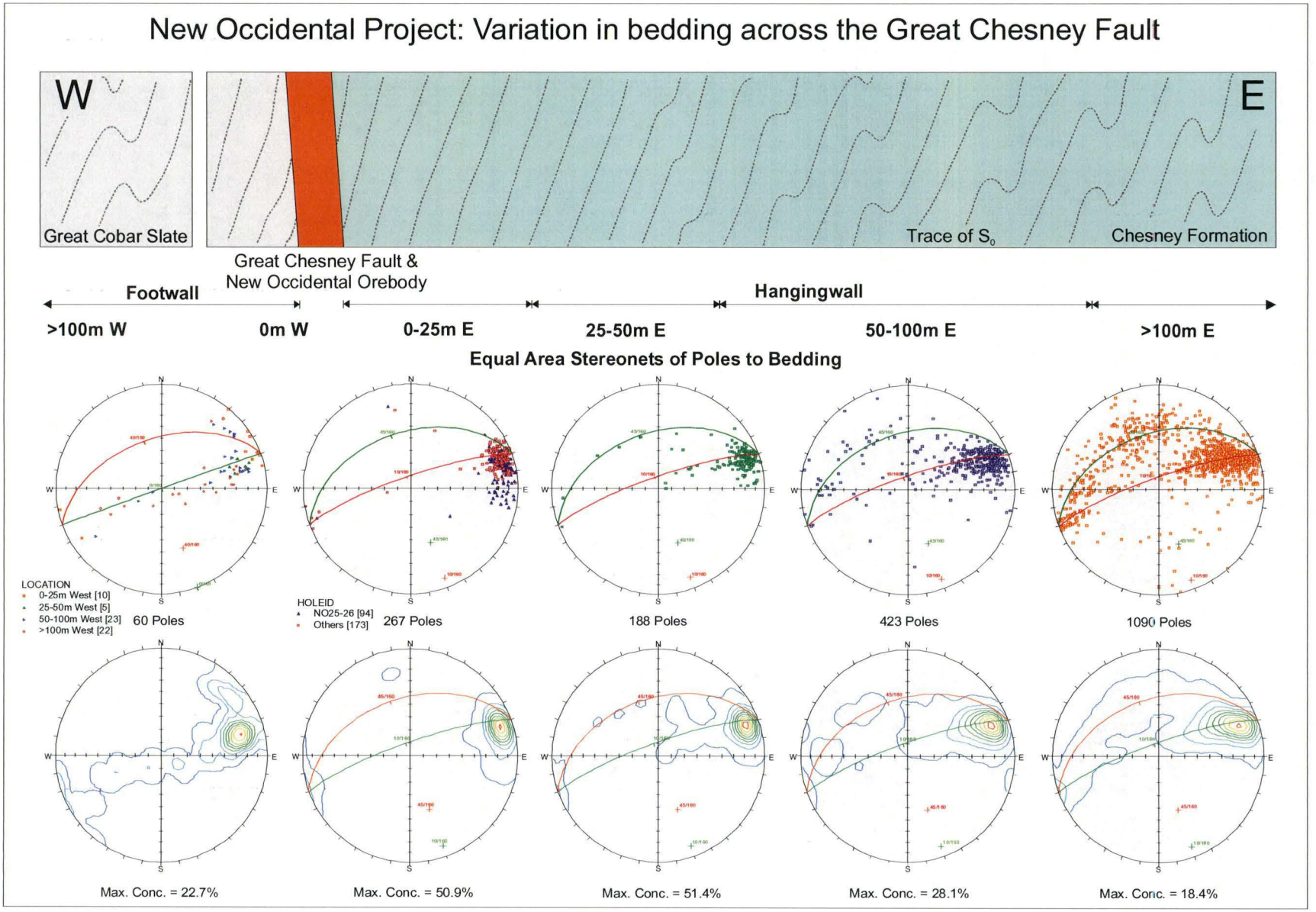

Figure 37: Variation in sub-surface bedding orientations across the Great Chesney Fault (data derived from reoriented drillcore measurements).

Figure 38: Equal area stereonets of reoriented bedding measurements from drillcore.

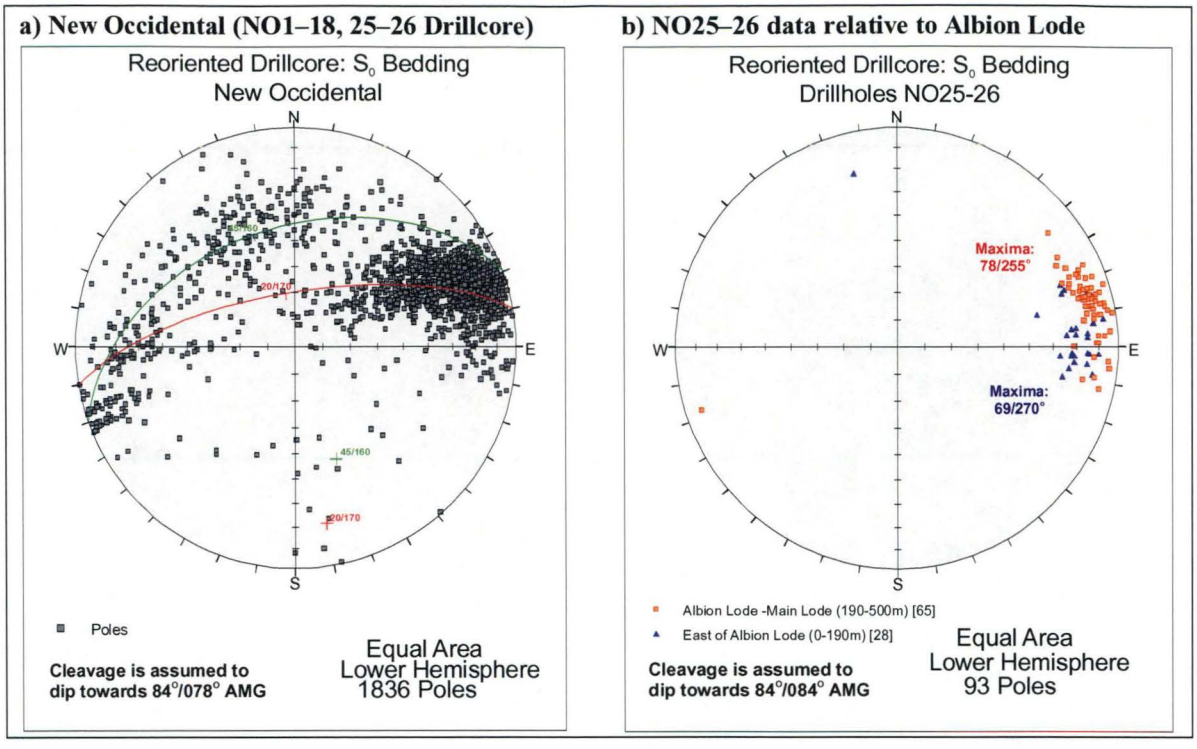

Figure 39: Interpreted shapes of parasitic folds distal and proximal to the Great Chesney Fault.

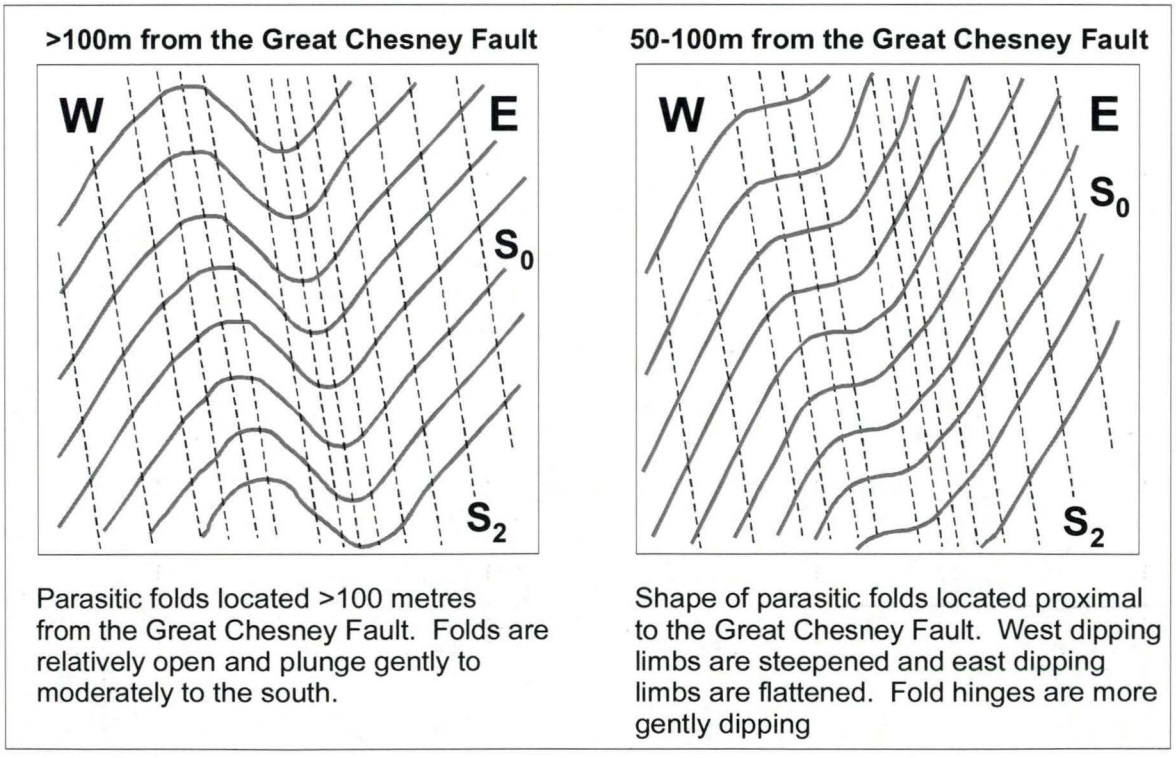

Folds have also been observed in gently dipping quartz veins in the New Occidental deposit (see Chapter 4 for more detail). Those folds are upright, relatively open (inter-limb angles of ≥90°) and dominant cleavage is axial planar to them. Fold hinges are uniformly sub-horizontal to gently plunging. Successively younger sets of sub-horizontal veins contain progressively more open folds with the last generation of quartz veins apparently unfolded.

The pattern of folds in the New Occidental deposit environs is summarised in Figure 40.

Figure 40: Fold patterns in the New Occidental area.

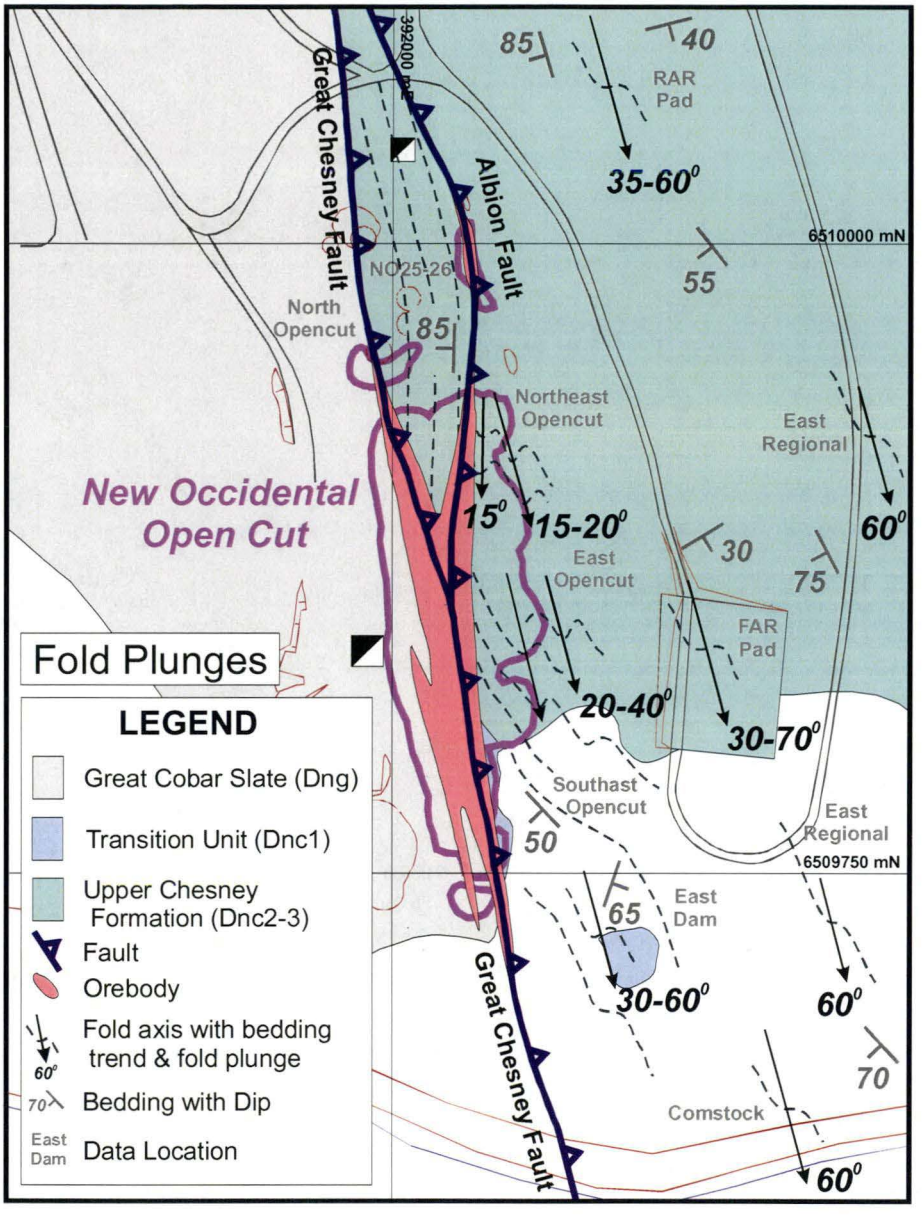

3.5.4 Lineations on Cleavage and Bedding

Re-oriented drillcore structural data was used to determine the orientation of the stretching lineation present on cleavage at depth. The alignment of chlorite and mica and the elongation of pyrrhotite grains along cleavage define this lineation. The lineation plunges steeply north (weighted plunge/trend = 78°/018°) and is best developed within 50m of the Great Chesney Fault (Figure 41a). Within 5m of the New Occidental deposit, where individual cleavage planes have been activated as discrete faults, the lineation is parallel to, and in part overprinted by, steeply north plunging striations on fault plane slickensides.

A similarly oriented lineation/striation is also developed on steeply west-dipping bedding surfaces immediately adjacent to the New Occidental deposit. The lineation is most prevalent in the North Opencut area, and particularly in NO25/26. This lineation also plunges steeply north (estimated plunge/trend = 75°/315°; Figure 41b).

Figure 41: Equal area stereonets of lineations on cleavage and bedding.

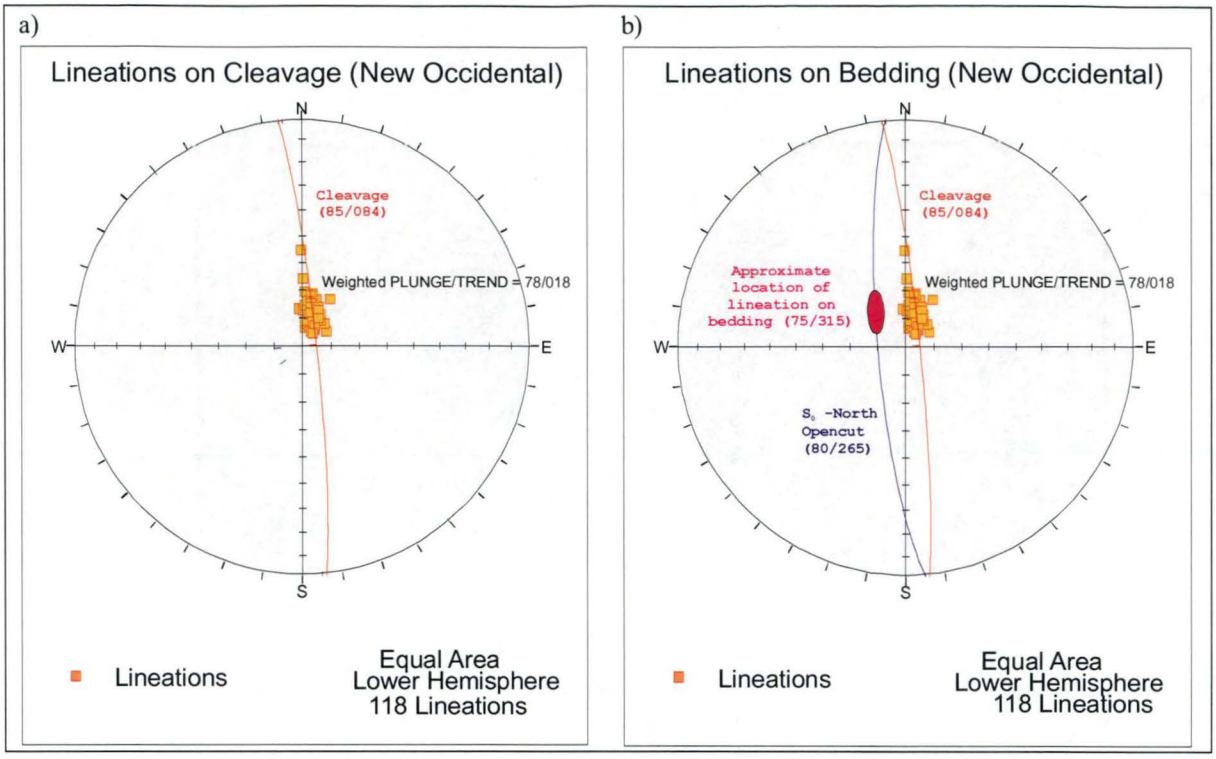

3.5.5 Bedding-Cleavage Intersection Lineations

Outside of the New Occidental Opencut, bedding-cleavage intersection lineations are consistently gently to moderately south plunging (mean = 45°/160°), approximately parallel to the plunge of parasitic folds in the deposit area. Within the Opencut, intersection lineations in the East Opencut and Southeast Opencut areas are similarly oriented. However, an anomalous population of north-plunging lineations is present in the northern part of the New Occidental Opencut extending northwards towards NO25/26. In the Northeast Opencut area the orientation of the lineation varies from a relatively gentle south plunge to a gentle north plunge; and in the North Opencut area is gently to moderately north plunging (Figure 43 and Figure 44).

The sub-surface data reveal a broad scatter in the orientation of bedding-cleavage intersection lineations in the New Occidental area from gently south to gently north plunging with the bulk of the intersection lineations having a relatively consistent gentle south plunge (22°/167°). Intersection lineations in the South Occidental area plunge more gently south (8°/167°), which in part reflects the presence of folds with a sub-horizontal plunge in NO21. Some of the apparent scatter in the orientation of the intersection lineation is probably caused by inaccurate measurements of the alpha angle between bedding and cleavage as well as real variation in strike of cleavage. In drillcore comprising coarse grained thick-bedded sandstone units, the position of the long axis apical trace (high point) of cleavage relative to that of bedding cannot always be precisely located. When the strike of bedding and cleavage are sub-parallel, a small error in the measurement of the alpha angle of the order of 5° can result in a 180° error in the trend of the lineation.

In NO25–26 the orientation of the bedding-cleavage intersection lineation varies either side of the Albion Lode (Figure 42). East of the Albion Lode, the intersection lineation has a dominantly gentle northerly plunge, consistent with the lineation plunge at surface in the

North Opencut area. Between the Albion and Main Lodes, the intersection lineation has a generally gentle south plunge, consistent with the plunge of the intersection lineation elsewhere in the New Occidental area.

A breakdown of subsurface intersection lineation data by proximity to the Great Chesney Fault (Figure 45) reveals no systematic variation in the orientation of the intersection lineation across the Great Chesney Fault. When data from NO21 is excluded from the analysis, the lineation orientation is remarkably constant, with data maxima from stereonets from each domain defining a narrow range of 20–27°/167–169°.

In summary, with the exception of the northern part of the New Occidental Opencut and the area around NO25–26, the orientation of the bedding-cleavage intersection lineation is relatively constant and plunges gently south (Figure 45). The orientation of intersection lineations does not appear to vary with depth or show any systematic variation across the Great Chesney Fault. However, an anomalous north-plunging intersection lineation is present in the North Opencut and NO25–26 areas between the Albion and Main Lodes (Figure 46).

Figure 42: Bedding-cleavage intersection lineation relationships from NO25–26.

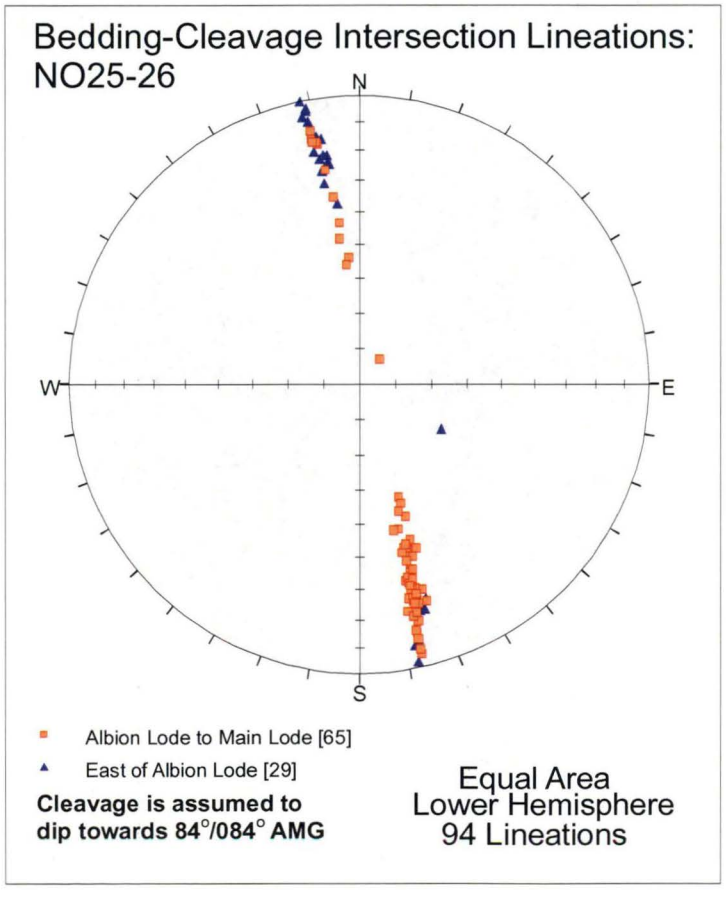

Figure 43: Variations in bedding-cleavage intersection lineation orientation throughout the New Occidental deposit environs (all data from surface measurements with the exception of the South Occidental area).

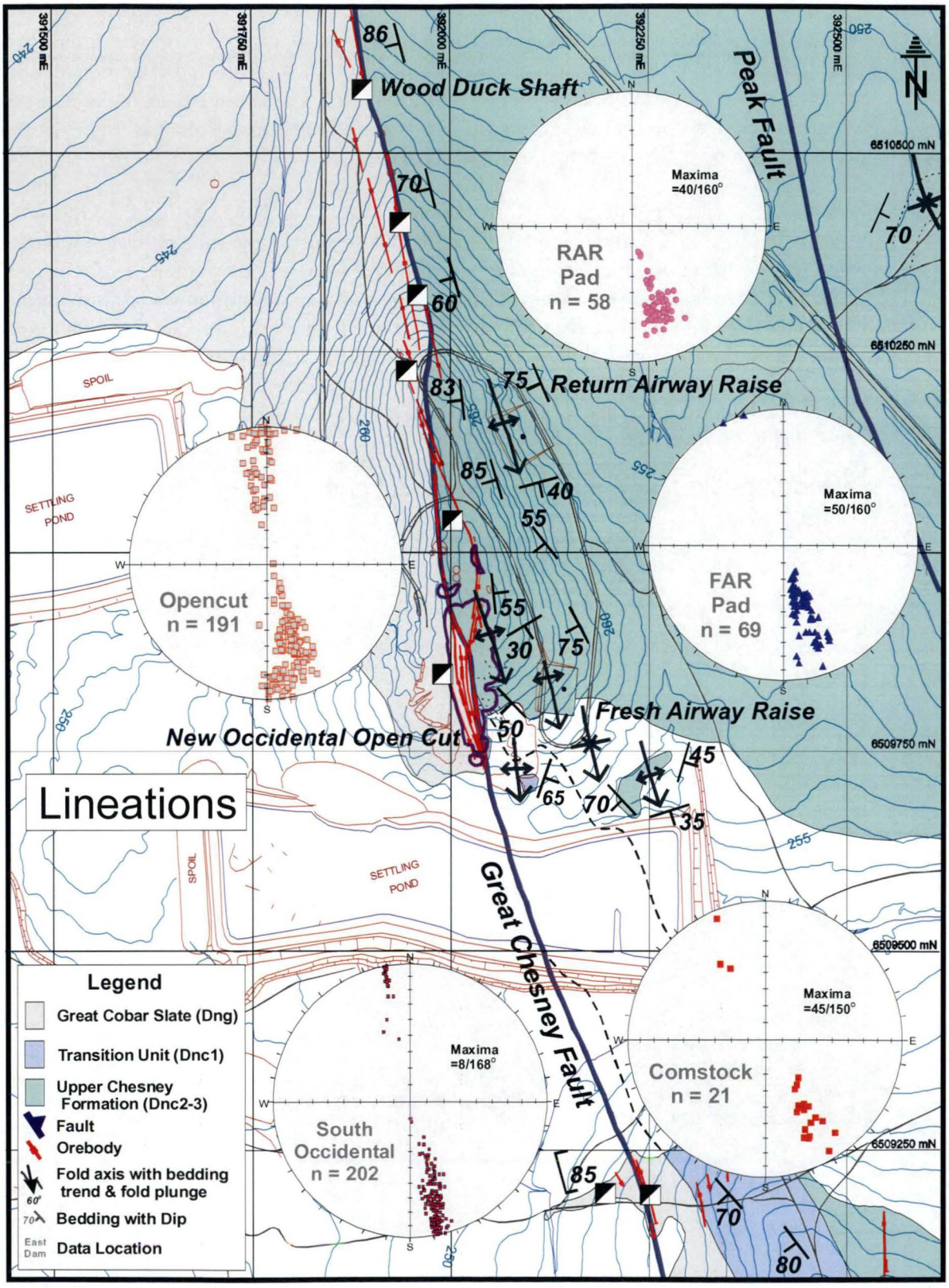

Figure 44: Variations in bedding-cleavage intersection lineation orientation in the New Occidental Opencut (all data from surface measurements with the exception of NO25–26).

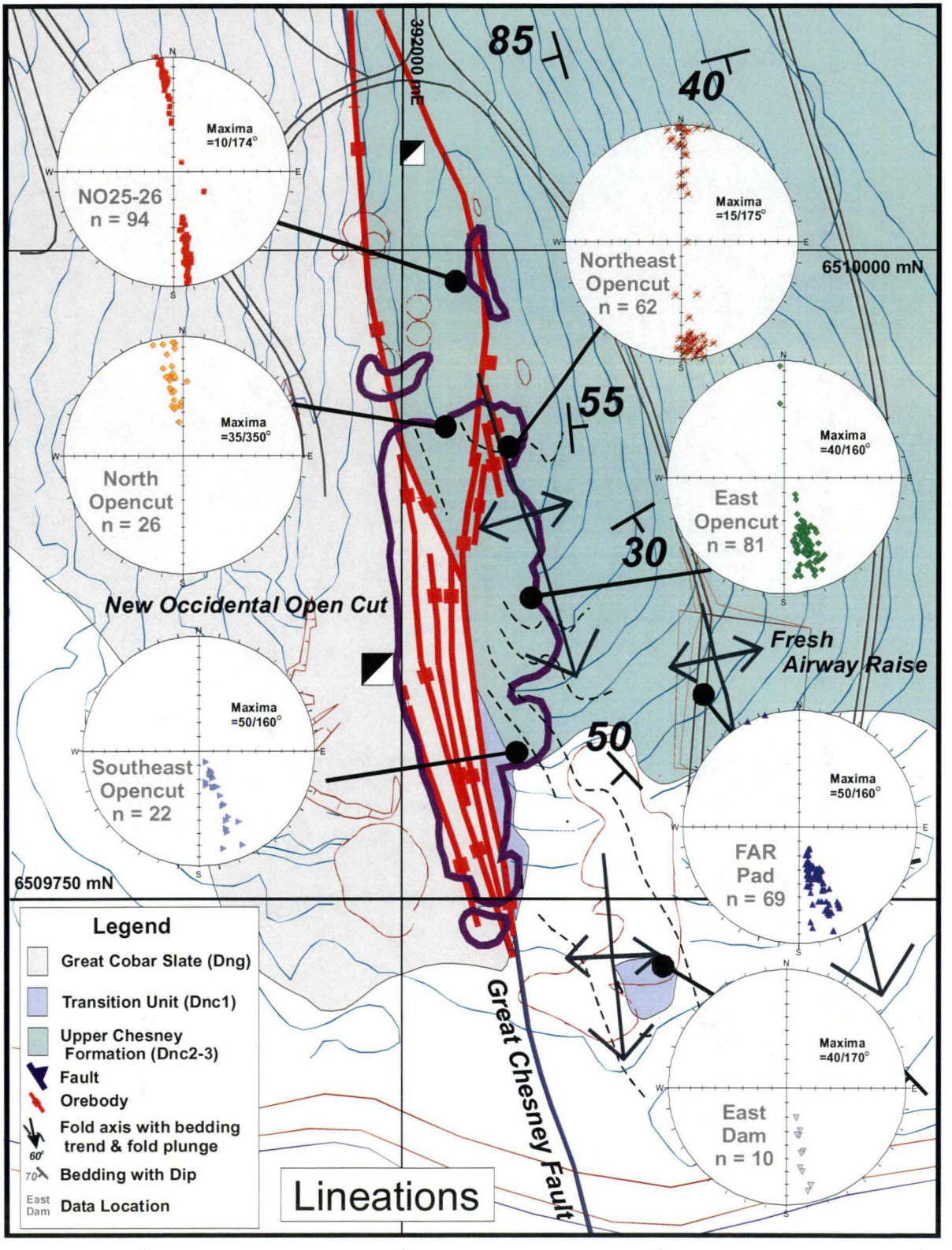

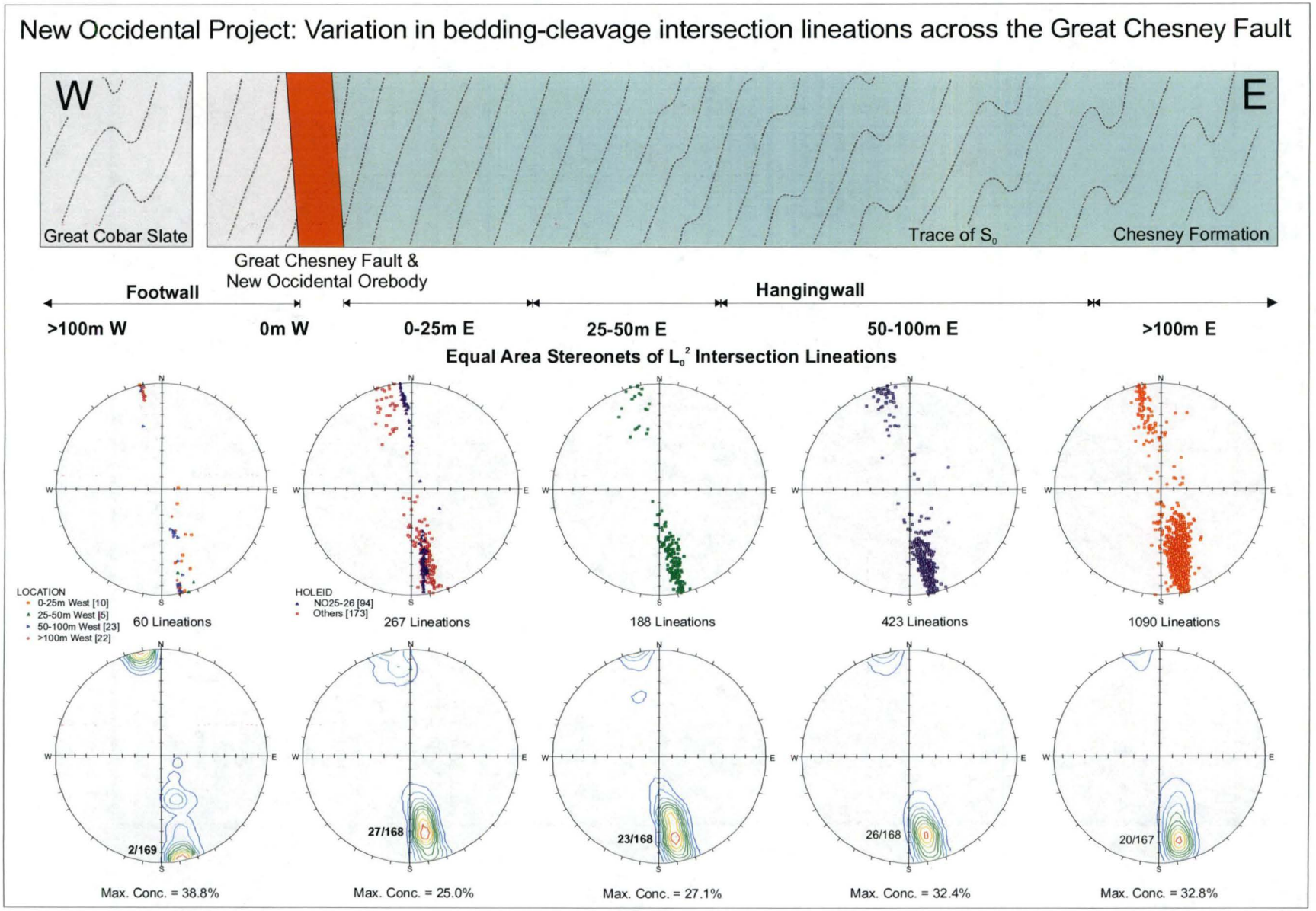

Figure 45: Variation in sub-surface bedding-cleavage intersection lineations across the Great Chesney Fault (data derived from reoriented drillcore measurements).

Figure 46: Variation in the plunge and trend of bedding-cleavage intersection lineations in the New Occidental area.

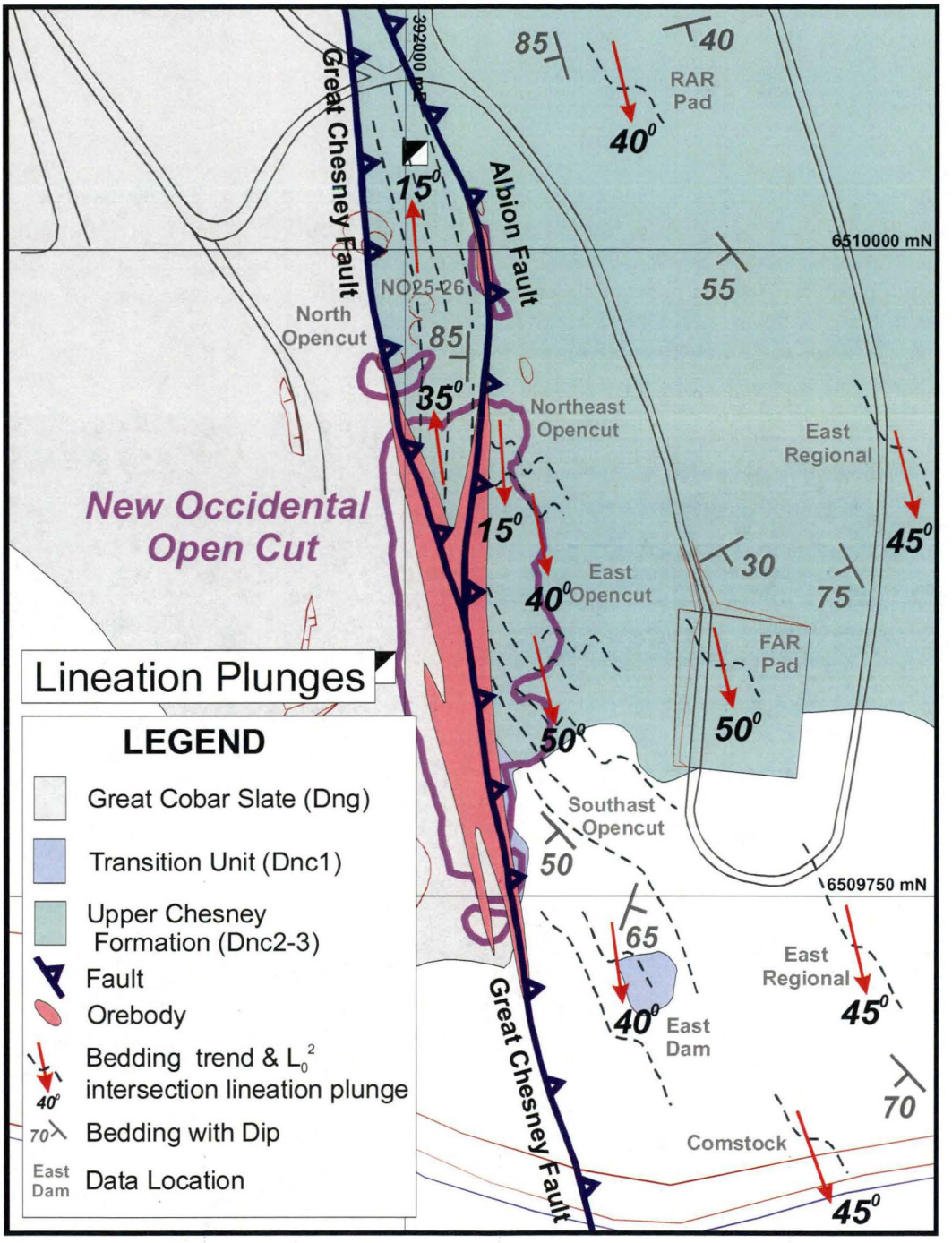

3.5.6 Late-Stage Faulting

Minor late-stage kink bands and brittle faults occur throughout the New Occidental deposit environs. Kink bands are relatively rare but are associated with minor late-stage quartz veins (Figure 47a). The faults are recognised by characteristic pale grey clay gouge, brittle deformation of cleavage and of associated mineralisation and alteration (Figure 47b–c).

In the reoriented drillcore data, stereonet plots of poles to the late-stage brittle faults indicate a range of orientations from cleavage-parallel shears (85°/078°) to gently to moderately west-southwest and east-northeast dipping shears (Figure 48a–b). One measurement of a kink band yielded a gentle south dipping orientation (Figure 48a). The cleavage-parallel shears are

predominantly at contacts between silicified and chlorite-altered sediments. Slickensides on shears and veins in NO25–26 (Figure 48c) show three contrasting senses of displacement:

1. 40°/090° (top to west).
2. 15°/245° (top to east).
3. 10°/360° (top to south).

The north plunging lineations are approximately parallel to a set of lineations observed on steep dipping cleavage planes, the latter overprinting prominent steep north-plunging lineations described in Section 3.5.4 (Figure 48d). Displacement along brittle faults is minimal (< 1–5 m) and offsets across all of the faults indicate a reverse sense of movement.

Figure 47: Late-stage brittle deformation fabrics.

a) Detail of kink band showing minor quartz vein infill localised in kink bands.

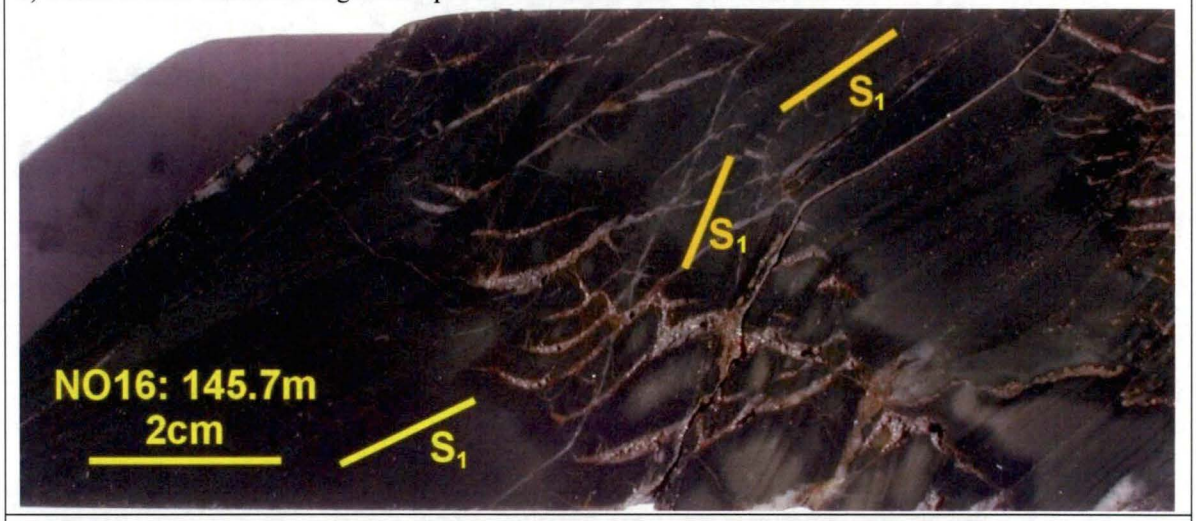

b) Moderately to steeply dipping brittle reverse fault sub-parallel to cleavage.

c) Gently west-dipping brittle reverse fault cross-cutting quartz veining associated with the New Occidental mineralisation.

Figure 48: Equal area stereonets of late-stage brittle fabrics.

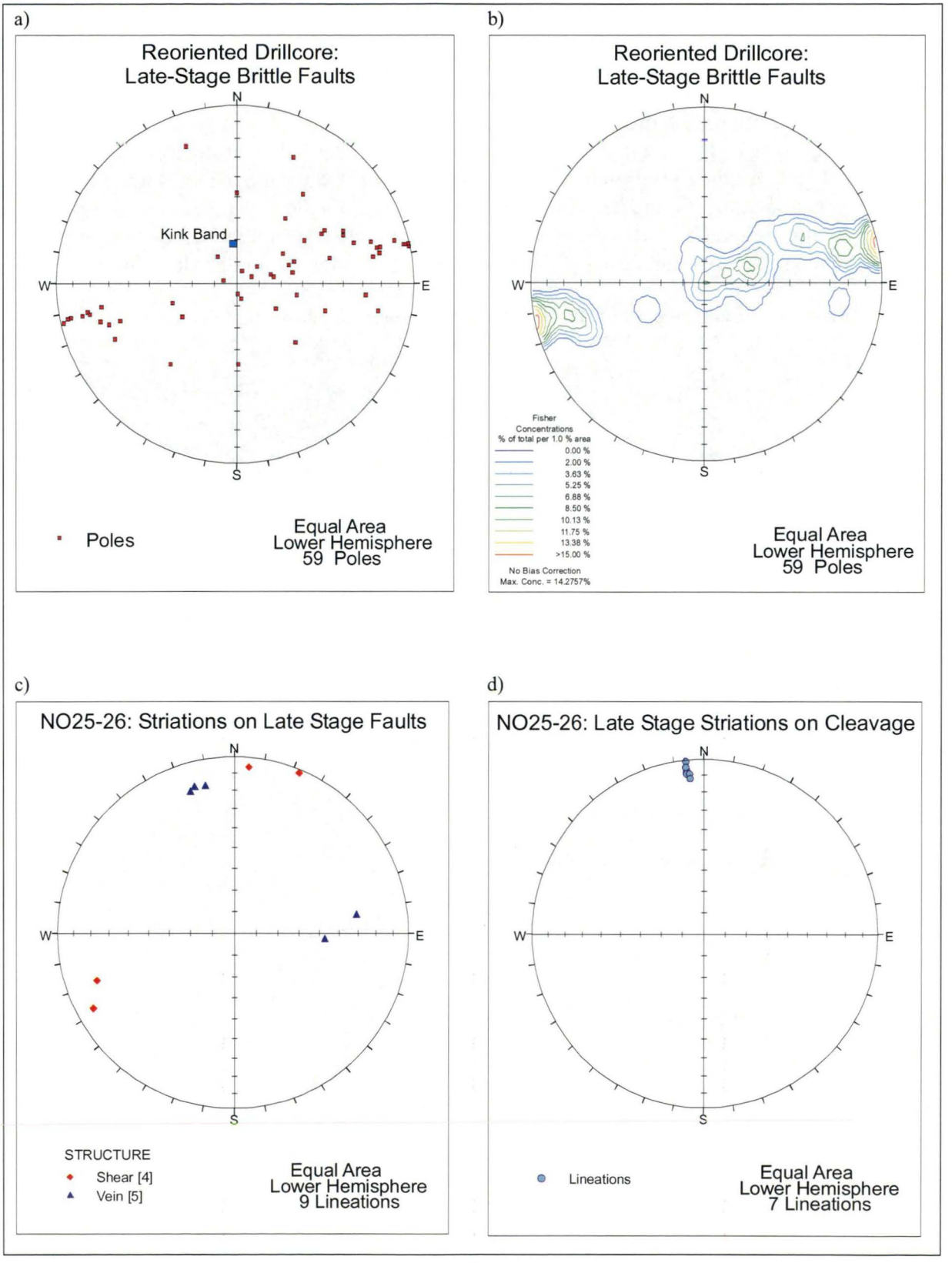

3.6 Gold Distribution in the New Occidental Deposit

Re-mapping of the New Occidental deposit environs, logging of deposit drillcore by the author and re-interpretation of historical grade control sampling by the author suggest a modified deposit configuration (Figure 49) to that described by Mulholland & Rayner (1961). The New Occidental deposit can be considered to consist of a Main lode, which is developed on and about the Great Chesney Fault, and the Albion lode, which is developed along the Albion Fault. Both the Main and Albion lodes have been defined by >1 g/t Au assay envelopes (Figure 50). The Main lode is characterised by a remarkably continuous and coherent zone of > 1 g/t Au mineralisation that contains only very narrow zones of low-grade (<1 g/t Au) mineralisation (Figure 51). In cross-section, the Main lode >1 g/t Au envelope pinches and swells appreciably. By comparison, the Albion lode is characterised by erratic zones of high-grade mineralisation developed intermittently along the Albion Fault.

Figure 49: Surface plan of the New Occidental deposit showing main lodes.

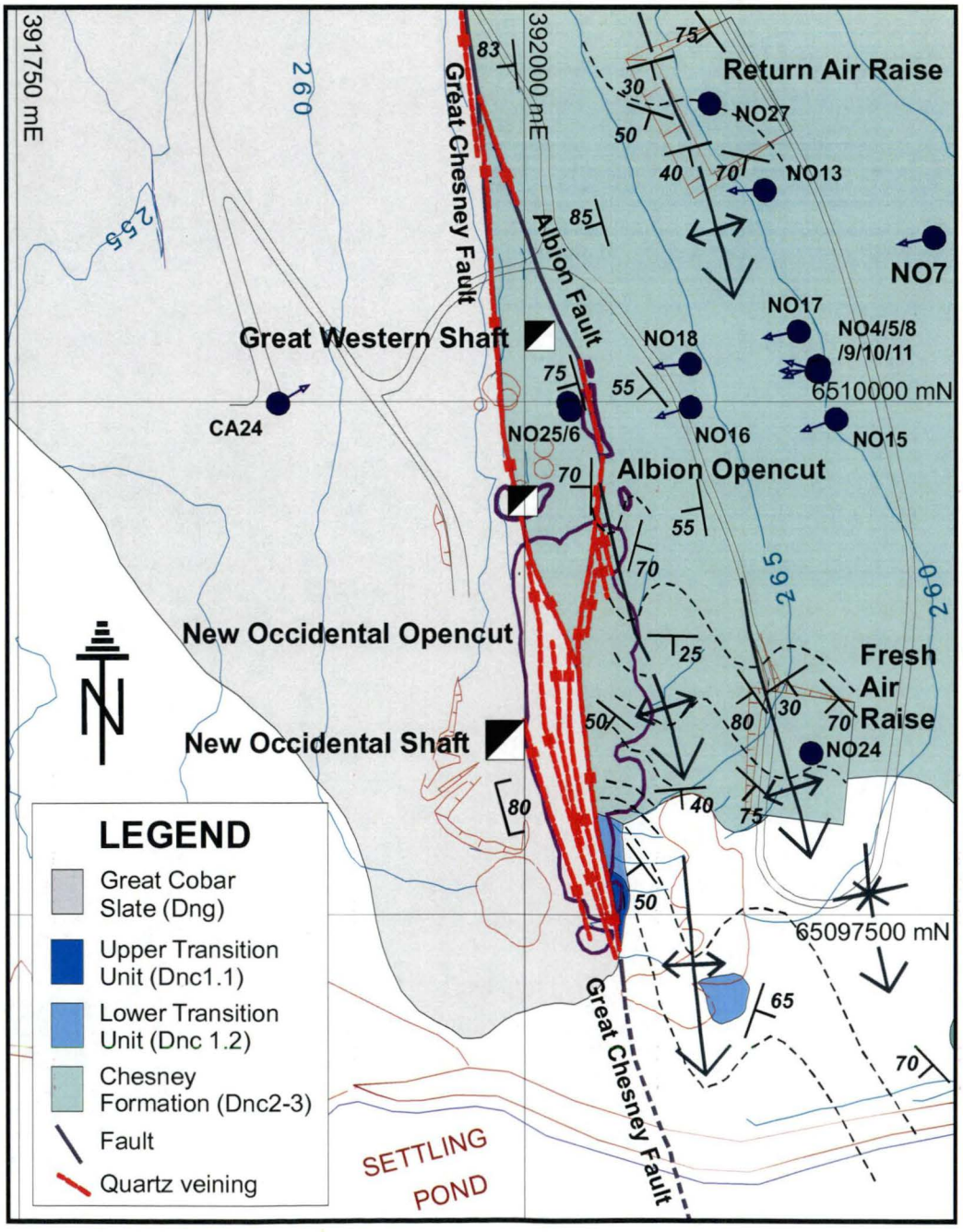

Figure 50: 3-dimensional plan view of the New Occidental deposit showing >1 g/t Au cut-off envelopes for the Main lode (yellow) and Albion lode (light blue).

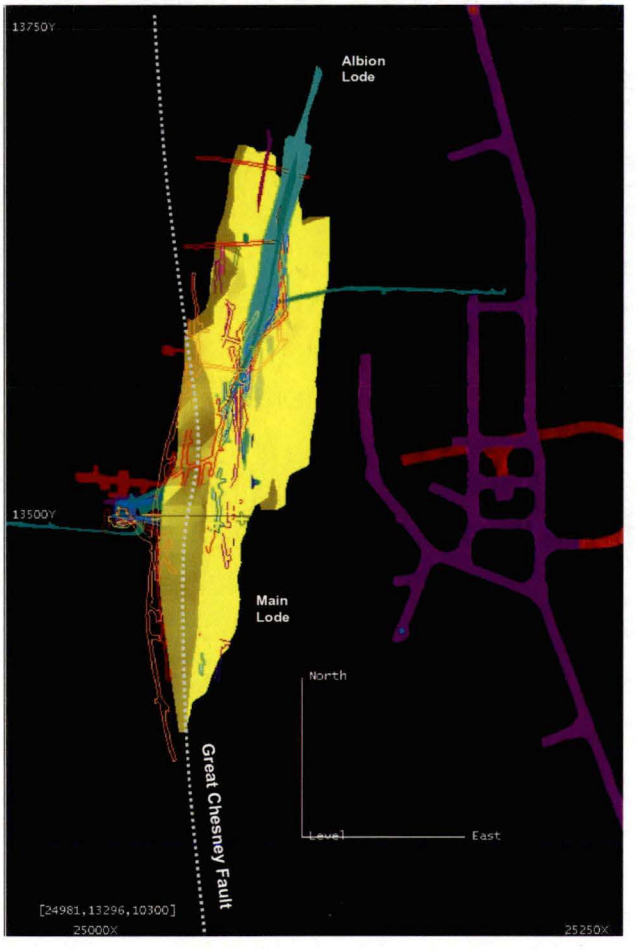

In plan view, the Main lode is thickest immediately south of the intersection of the Great Chesney and Albion Faults, and thins along the Great Chesney Fault north and south of this line of intersection. The Main Lode also appears to decrease in strike length and thin with depth (Figure 51). The >1 g/t Au assay envelope for the Main Lode is only 100m long and up to 10m wide at a depth of 1100m from surface, although drilling data is also more sparse on this level. This compares with an average strike length of 180m and a maximum width of 30m at a depth of 600m from surface. In addition to the decrease in the size of the >1 g/t Au envelop with depth, the grade of gold mineralisation also apparently decreases with depth. The Albion Lode comprises relatively narrow but high-grade mineralisation over widths of 1–10m and a strike length of up to 100m. The Albion Lode has been traced from surface to a depth of 500m where is appears to merge with the Main Lode.

Using wide-spaced drillhole assays alone, two discrete zones of high-grade gold mineralisation can be recognised within the Main Lode. Interpolation of those intersections both vertically and horizontally between adjacent drillholes gives the impression of parallel linearly extensive lodes in the sense of Mulholland & Rayner (1961). However, based on the closer-spaced underground sampling, the Main Lode can be seen to consist of a single relatively broad low-grade zone (0.1–1.0 g/t Au) containing smaller short strike length zones of high-grade gold. A zone of low-grade (<1 g/t Au) gold in the centre of the northern half of the Main Lode, which was poorly sampled by the back sampling, appears to represent a large block of poorly mineralised country-rock (Figure 19). That block was previously interpreted to separate the Eastern and Western Lodes (Mulholland & Rayner, 1961). However, drillholes reveal scattered low-grade and patchy high-grade mineralisation throughout this block.

Shoots of high-grade gold mineralisation interpreted within the Main Lode of the New Occidental deposit are on average 10–30m long and 5m wide and extend over vertical intervals of 50–400m (Figure 52). They are all sub-parallel to dominant cleavage and the bounding >1 g/t Au envelope for the Main Lode, and are elongated in the direction of steep north-plunging stretching lineation. The longer, more vertically continuous shoots pinch and swell considerably, which is consistent with the overall character of the bounding >1 g/t Au envelope for the Main Lode.

Figure 51: Distribution of gold mineralisation in the New Occidental deposit.

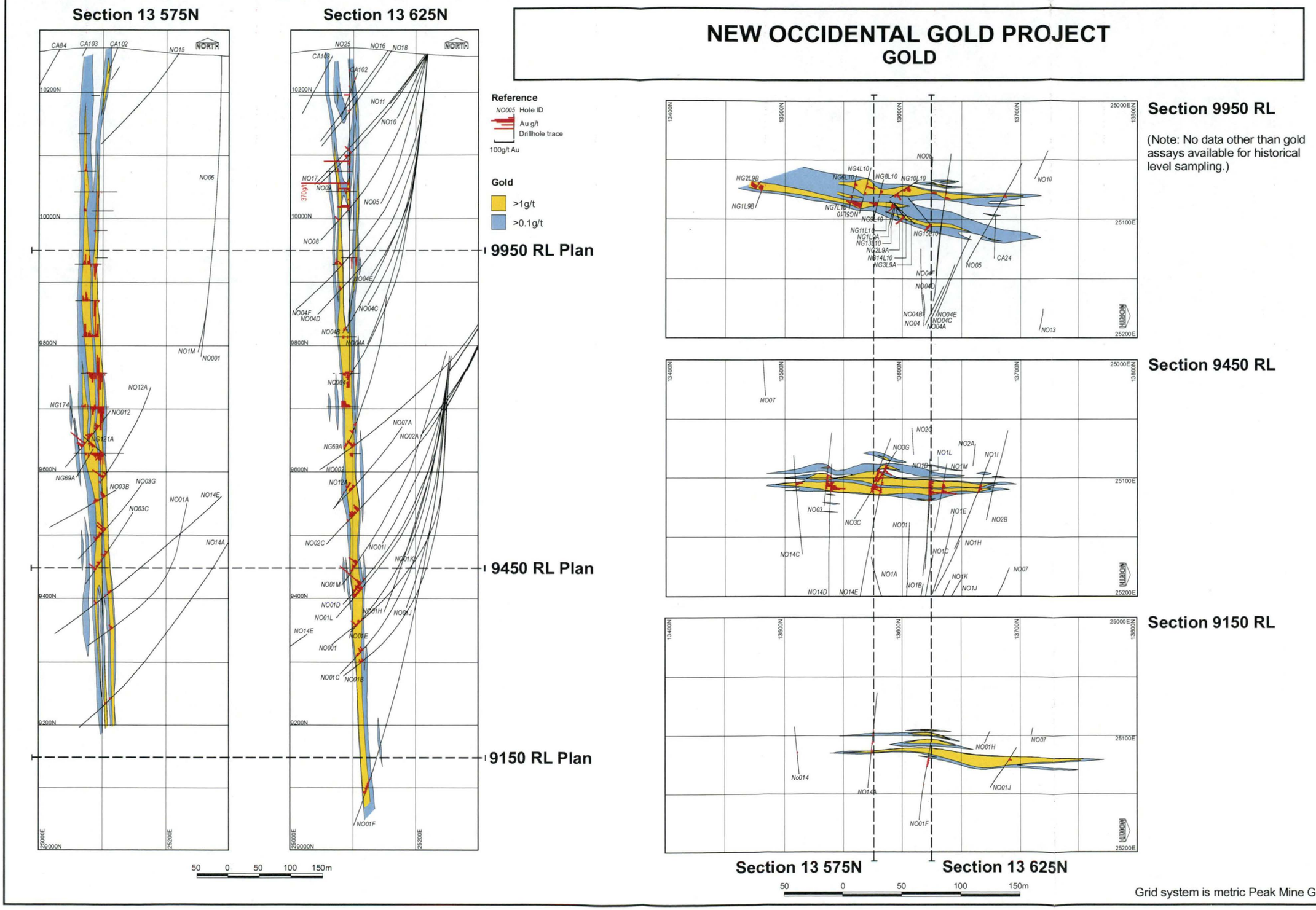

Figure 52: Three-dimensional long-sectional view of the New Occidental deposit showing the distribution of shoots of high-grade gold mineralisation.

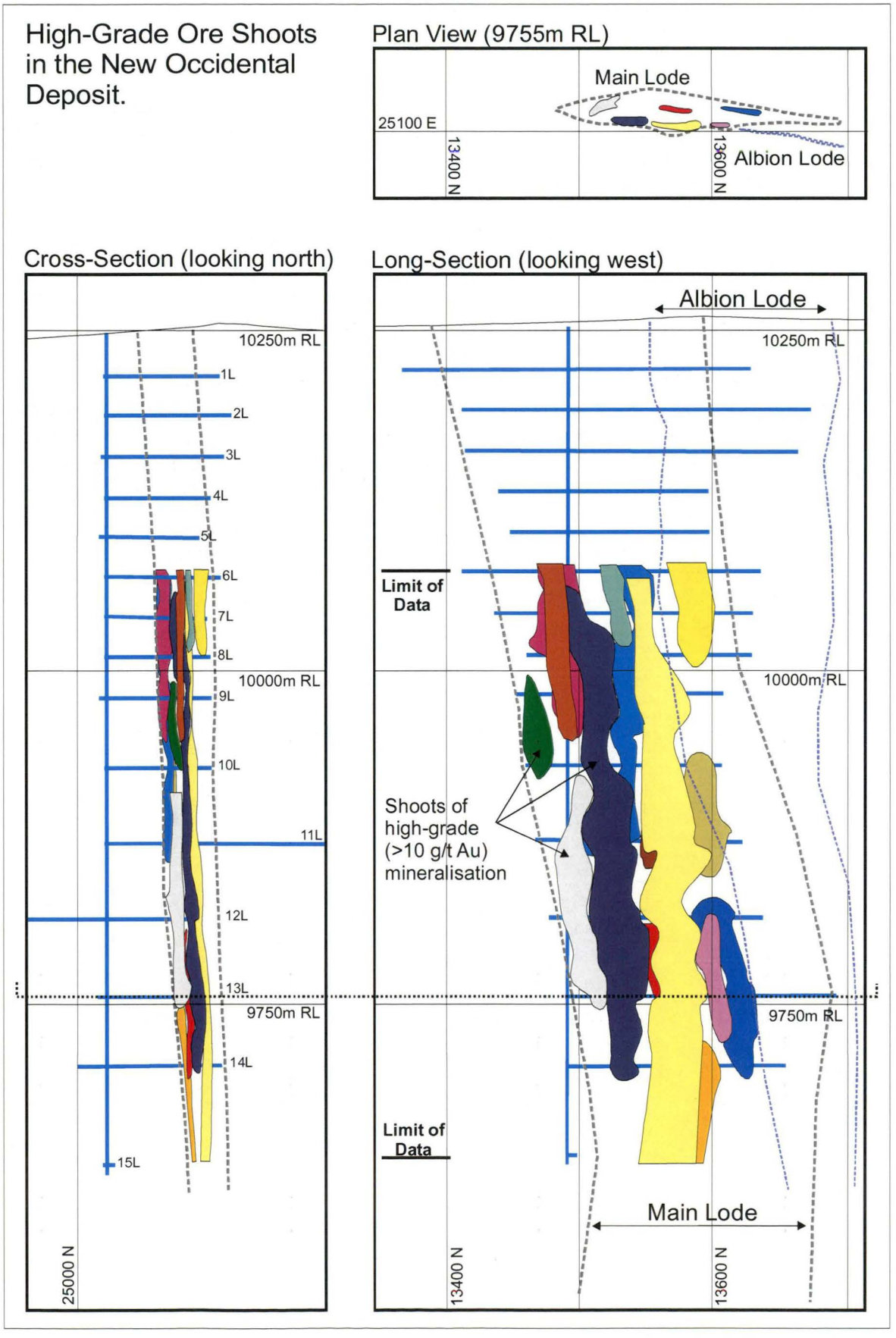

3.7 Structural Relationships in the Cobar Goldfield and New Occidental Deposit

3.7.1 Variations in Fold Geometry

Folds in the Cobar Goldfield have a relatively consistent strike, but typically variable plunge, ranging from gentle to steep south (Table 11). Based on the fold orientations recorded in this study and previously (Glen, 1985; Hinman, 1992; Wilson, 1996), it is concluded that there is little systematic variation in fold plunge over the length of the Goldfield. This contradicts Glen's (1987a) contention that the fold plunges in the Goldfield steepen from north to south.

Significant variation in fold plunge, comparable to fold plunge variations through the Cobar Goldfield, is evident at each of deposits investigated during this study (Table 11). While Hinman (1992) identified steeper and gentler dipping folds in the high-strain zone encompassing the Peak deposit compared to areas distal to the deposit, similar patterns are not evident at the New Occidental, Chesney and New Cobar deposits. Analysis of bedding pole girdles across the Great Chesney Fault at the New Occidental deposit (Figure 37; this study) indicates no systematic variation in fold plunge with increasing proximity to the Great Chesney Fault or New Occidental deposit. This is consistent with Wilson's (1996) observations of relatively constant fold plunge orientations across the New Cobar – Chesney deposits and host Great Chesney Fault. The presence of sub-horizontal folds in the South New Occidental area within an apparently low strain area >100m to the west of the Great Chesney Fault appears to contradict Hinman's (1992) suggestion that gently plunging folds are typically restricted to high strain zones proximal to major faults. The folds in the South Occidental area appear relatively symmetrical and characteristic of the less deformed parasitic folds from the hanging wall of the New Occidental deposit.

Table 11: Variation in measured fold plunges throughout the Cobar Goldfield.

Deposit:	Method:	Range of Fold Plunges	Average Fold Plunge
Cobar Goldfield - Zone 1c (Glen, 1985)	Macro-scale fold axes including Myrt Syncline and Chesney-Narri Anticline	20–70°/160°	
New Occidental (this study)	Mesoscopic fold axes	12–52°/148–172°	25°/165°
	Inferred from bedding pole girdles	15–70°/160–170°	30°/160°
	Bedding-cleavage intersection lineation		22°/167°
South Occidental (this study)	Inferred from bedding pole girdles	0–40°/160°	
	Bedding-cleavage intersection lineation		50°/160°
Peak (Hinman, 1992)	Mesoscopic fold axes	To 165–185°	
	Inferred from bedding pole girdles		36°/172°
	Bedding-cleavage intersection lineation		36°/161°
Peak (this study)	Mesoscopic fold axes		32°/177°
	Inferred from bedding pole girdles	30–60°/170°	40°/170°
New Cobar-Chesney (Wilson, 1996)	Mesoscopic fold axes		50°/150°
New Cobar-Chesney (this study)	Mesoscopic fold axes	15–20°/150–165°	
	Inferred from bedding pole girdles	25–70°/170°	40°/170°
Hinge (this study)	Inferred from bedding pole girdles	50–70°/170°	60°/170°

3.7.2 Relationship between Folds and Cleavage

Cleavage present in the New Occidental area is axial planar to mapped mesoscopic folds. No evidence of transected relationships between the folds and the cleavage has been observed during this study. Likewise, the trend of mesoscopic parasitic fold axes and those of fold axes inferred from surface and subsurface bedding pole girdles (Section 3.5.3) are within the plane of cleavage, allowing for the natural scatter in cleavage orientation (Figure 53). Several parasitic fold hinges in the Northeast Opencut area have a distinctly more southerly plunge (175–180°) compared to the remainder of folds in the New Occidental area (160–170°). Those south plunging fold hinges occur where cleavage has a more easterly dip direction (average dip direction of 084° compared to 078° in the remainder of the New Occidental area).

Figure 53: Angular relationships between cleavage and fold axis trends.

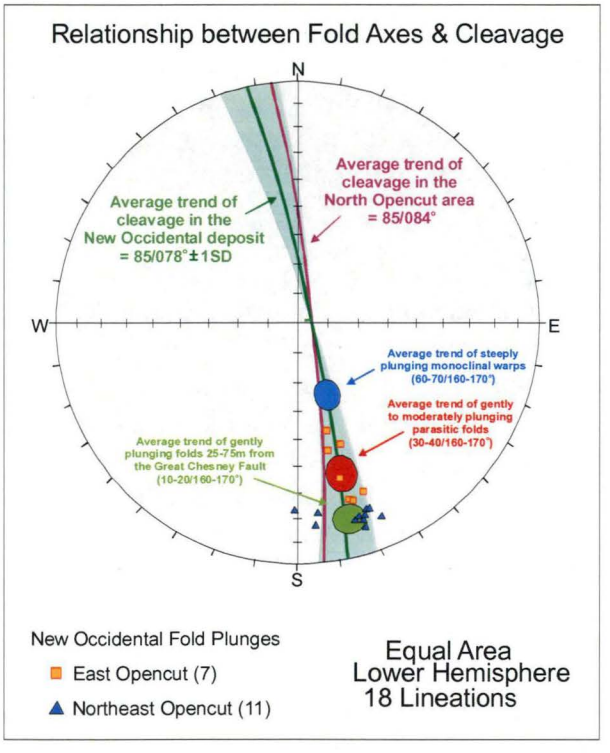

Glen (1985, 1987a) regarded the dominant cleavage in the Cobar Goldfield as being axial planar to folds like the Chesney-Narri Anticline, whilst Hinman (1992) and Wilson (1996) argued that the dominant cleavage transects those folds. Data collected in this study from throughout the Cobar Goldfield, including the Peak and Chesney-New Cobar deposits, does not support transection of fold axes by the dominant cleavage.

Evidence cited in support of transected relationships between cleavage and folds in the Cobar Goldfield include:

1. Apparent obliquities between cleavage and fold axes based on the orientation of fold axes inferred from both surface and reoriented sub-surface bedding pole girdles (Hinman, 1992; Wilson, 1996).

2. Measured obliquities between cleavage and mesoscopic fold axes on the Peak ridge (Hinman, 1992).

Using fold orientations inferred from bedding pole girdles, Hinman (1992) inferred an average obliquity of 7° between the trend of fold axes and the strike of the sub-vertical S_2

cleavage at the Peak deposit. Wilson (1996) inferred a maximum obliquity between those two fabrics in the New Cobar area of 10°. Those obliquities are not considered statistically significant. The natural variation in both cleavage and fold orientation is of a similar magnitude to the quoted obliquity between those two fabrics. For example, the standard deviation of dip direction of surface cleavage in the Cobar Goldfield and within individual deposits is approximately 7°. In the case of fold orientations inferred from bedding pole girdles in reoriented subsurface data, the use of an average dip/dip direction of cleavage in reorientation calculations compounds this error. The precision of fold axis plunges and trends inferred from bedding pole girdles in both surface and subsurface bedding data collected in this and other studies is estimated to be no better than ±10°.

Hinman (1992) mapped six south-plunging parasitic fold axes, consisting of syncline-anticline pairs, through the Peak ridge at the Peak deposit. Those fold axes are up to 250m long and are interpreted to be consistently transected by cleavage at angles of 5–15°. Re-examination of those folds during mapping of the Peak area in this study indicated that the transected relationship between dominant cleavage and fold axes is ambiguous at an outcrop scale. Some of the longer fold axes on Peak ridge were found to consist of a series of smaller en-echelon slightly offset fold axes. Whilst the gross trend of the fold axes is at a small angle to cleavage, cleavage is axial planar to individual fold axes.

3.7.3 Single versus Multiple Cleavages

Hinman (1992) identified an older discrete microscopic cleavage (S_1) in the Peak area that is axial planar to the F_1 folds and slightly oblique to dominant S_2 cleavage, and a younger S_3 cleavage that is parallel to and a reactivation of S_2. Hinman considered S_1 axial plane cleavage to be approximately sub-parallel to S_2 slaty cleavage and indistinguishable on a hand-specimen scale. Similarly, he argued that S_3 could only be microscopically distinguished from S_2. Neither a precursor fabric to the dominant cleavage nor a younger cleavage have been identified elsewhere in the Goldfield, including at the New Occidental deposit (Glen, 1994; Wilson, 1996; this study).

Hinman (1992) based his interpretation of multiple generations of cleavage on transected cleavage relationships in microlithons (S_2 transecting S_1) and reactivated cleavage in high strain zones (S_2 reactivated as S_3) in the Peak deposit. Similar overprinting relationships are locally present in the New Occidental deposit where early-formed cleavage is preserved in wallrock fragments in cleaved quartz breccias and where cleavage has been deformed and partially reactivated in high-strain zones. Any obliquity between cleavage in the wallrock fragments and that overprinting the enclosing quartz breccia appears largely a function of the degree to which those wallrock fragments have been rotated during brecciation, rather than to a different overall orientation of early cleavage. Hinman (1992) argued such overprinting relationships are systematically developed throughout the Peak deposit so that three distinctive cleavage generations are consistently recognisable (his S_1 to S_3). In the New Occidental deposit, however, apart from localised examples cited above, there is no evidence of consistent and systematic overprinting relationships between multiple generations of cleavage. Rather, cleavage appears to have been locally modified by shearing during ongoing coaxial shortening and deformation of the deposit.

If the dominant cleavage formed during large-scale displacement on the Great Chesney Fault is oblique to an earlier axial plane foliation, then a difference in the orientation of cleavage might be expected with increased distance from the Great Chesney Fault as the intensity of cleavage associated with the fault slip decreases and parasitic folds become more prevalent. However, the orientation of cleavage does not vary across the New

Occidental area to any significant degree (Figure 28). For example, the orientation of cleavage in the intensely sheared areas immediately surrounding the Great Chesney Fault where folds are absent is the same as that in folded areas less proximal to the fault that are characterised by lesser shearing (Section 3.5.1).

3.7.4 Timing and Mechanisms of Fold Formation

The consensus on timing of fold formation in the Cobar Goldfield is that folds formed in the initial stages of basin shortening, but that in the latter stages of deformation shortening has largely been accommodated by displacement on a network of north-northwest striking sub-vertical reverse faults and high-strain zones along the eastern margin of the basin, including the Great Chesney Fault (Glen, 1985, 1987a, 1990; Hinman, 1992; Wilson, 1996). Evidence for an early timing for fold formation is based on the apparent transected fold and cleavage relationships (previously discussed in Section 3.7.2) and fold patterns interpreted to be the product of deformation during subsequent stages of shortening. Deformation of early-formed folds has supposedly resulted in:

1. Fold hinges rotating to steeper and gentler plunges (Glen, 1990; Hinman, 1992).
2. Both tightening and opening ("unfolding") those folds (Hinman, 1992).
3. Rotating fold axes towards the dominant cleavage (Hinman, 1992).

Whilst steepening of fold plunges in response to ongoing shortening is expected (Glen, 1990), rotation of folds to gentler plunges during shortening is less common. Hinman (1992) argued heterogeneous, relatively intense sub-vertical extension (oriented parallel to the extension lineation) has caused significant rotation of F_1 fold axes and bedding-cleavage intersection lineations to both steeper south- and gentle north-plunges at the Peak deposit.

Rotation of bedding and fold hinges to both north- and south-plunging orientations in response to heterogeneous sub-vertical extension would be manifested as a broad pole to bedding girdle corresponded to both south- and north-plunging fold hinges. Likewise, bedding-cleavage intersection lineations would be similarly redistributed into a girdle that comprises both south- and north-plunging orientations (Figure 54). Folds would also be expected to have both south- and north-plunging fold hinges. The sense of bedding and fold hinges rotation would be both clockwise and anti-clockwise about a sub-horizontal axis orthogonal to S_1 cleavage (oriented approximately east-northeast – west-southwest). Both fold plunge and the orientation of the bedding-cleavage intersection lineations would also be expected to vary systematically across the Great Chesney Fault in response to intensifying strain with increasing proximity to the fault.

Although bedding-cleavage intersection lineations in the New Occidental deposit environs are largely south plunging an anomalous population of north plunging intersection lineations is present in the northern part of the New Occidental Opencut. Whilst those north plunging lineations potentially reflect the presence of a high strain zone enveloping the New Occidental deposit, Hinman's (1992) heterogeneous strain model is not supported by bedding, fold and bedding-cleavage intersection lineation data from the deposit. Poles to bedding in the New Occidental area show a relatively broad girdle indicative of heterogeneously deformed folds. However, bedding data does not define a girdle corresponding to north-plunging folding that would be consistent with a north plunging

bedding-cleavage intersection lineation. Likewise, no north-plunging folds were mapped at the New Occidental deposit, although some folds appear to have a gentler southerly plunge.

The orientation of bedding-cleavage intersection lineations in most high strain parts of the New Occidental deposit, for example, the Eastern Opencut and Southeastern Opencut areas, is relatively homogenous and consistently south plunging. It is indistinguishable from lineation orientations in the distal parts of the deposit environs, both in terms of average orientation and scatter of lineation orientations. Likewise, the sub-surface intersection lineation data does not reveal any systematic variation in the orientation of the intersection lineation across the Great Chesney Fault (Figure 45).

Figure 54: Bedding-cleavage relationships anticipated for heterogeneous extension of folds in the direction of the steep north-plunging extension lineation.

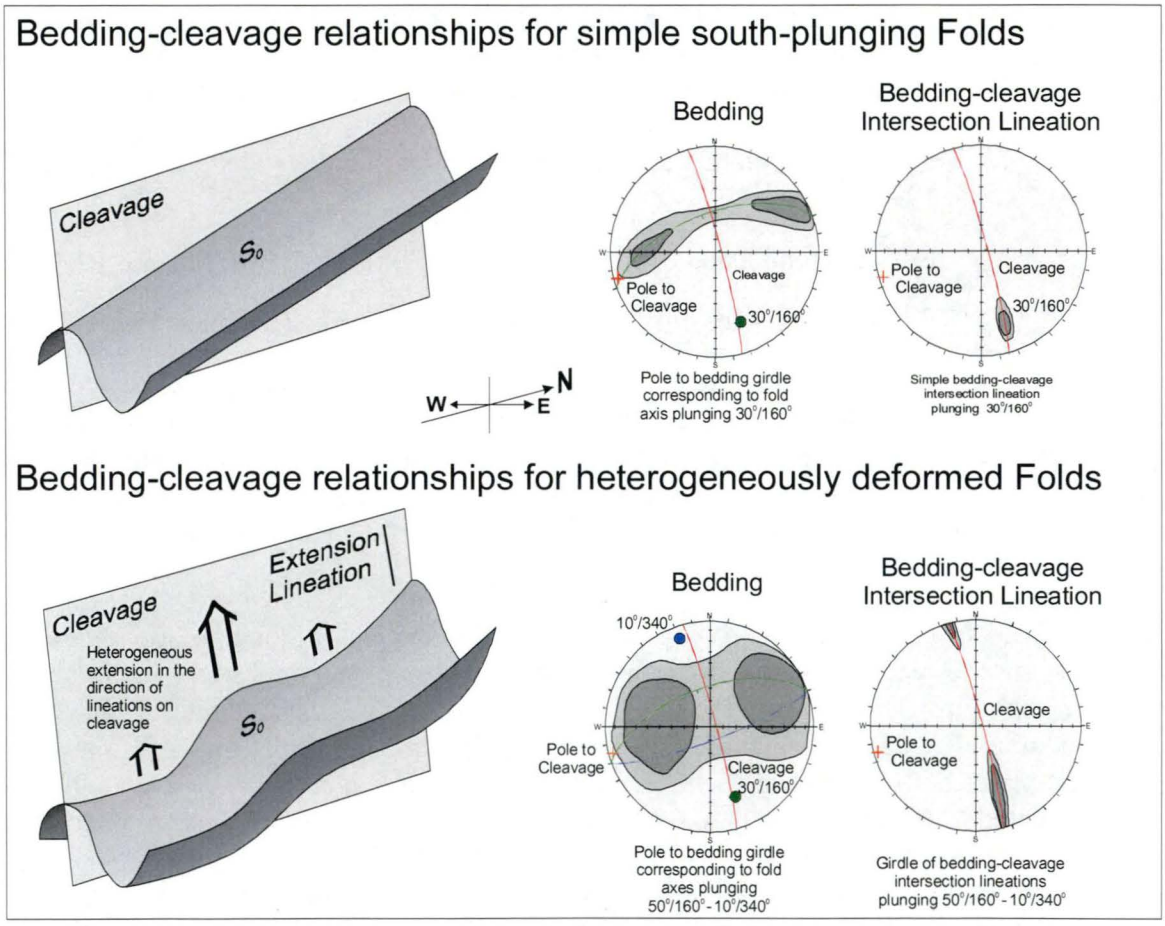

The anomalous north-plunging bedding-cleavage intersection lineations only occur in a relatively small part of the high strain zone surrounding the New Occidental deposit, being largely constrained to the fault bound wedge of Chesney Formation located between the Great Chesney and Albion Faults (Section 3.5.5). Bedding in that wedge is largely unfolded and very steeply dipping towards the west and west-southwest, whereas bedding in the remainder of the New Occidental area largely dips to the west-northwest. Similarly, cleavage is more northerly striking compared to in the remainder of the New Occidental deposit. Significantly, the strike of bedding is clockwise of the strike of cleavage, and therefore, bedding-cleavage intersection lineations are north plunging (Figure 55a). Elsewhere in the deposit, the strike of bedding is anticlockwise of the strike of cleavage and the resultant intersection lineations are south-plunging (Figure 55b). Given the relatively consistent steep easterly dip of cleavage in the New Occidental deposit, variations in plunge of bedding-cleavage intersection lineations in the New Occidental deposit can

simply be explained by relatively minor variations in the strike of bedding relative to that of cleavage.

Figure 55: Variations in bedding-cleavage relations across the New Occidental deposit.

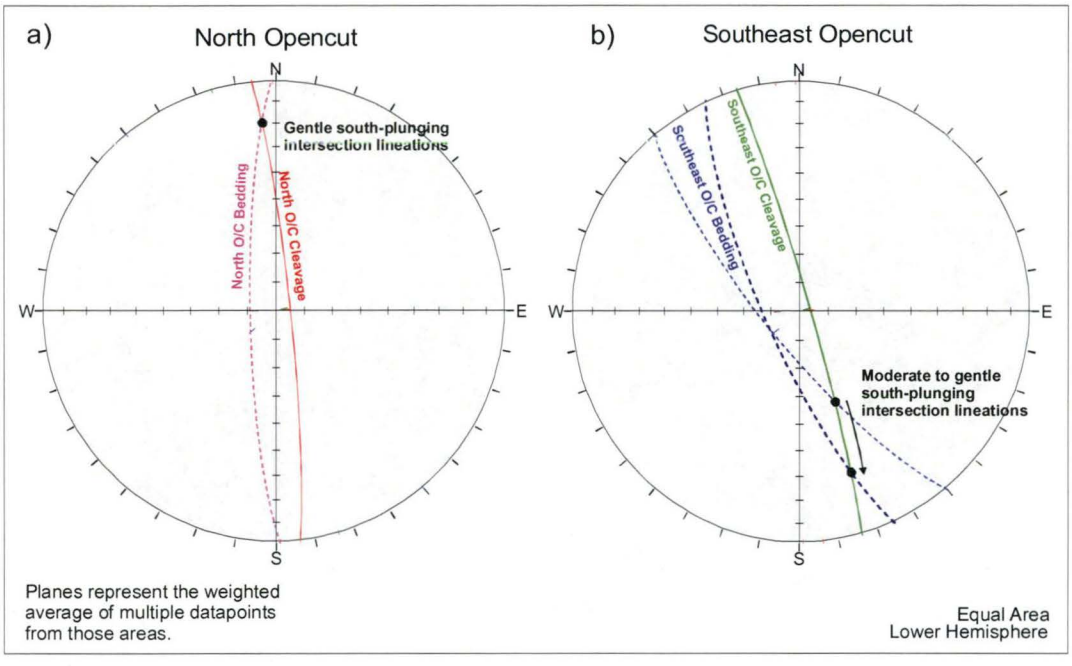

As noted previously (Section 3.7.1), gently and steeply south-plunging folds have been observed in both lower and higher strain environments through the Cobar Goldfield, suggesting folds with variable plunge are not restricted to high strain zones. An alternate explanation for the variable plunge of folds in the Goldfield is that parasitic folds have been superimposed on strata whose strike varies subtly in relation to the strike of cleavage/faults. For example, folds superimposed on bedding striking east of cleavage (as is the case immediately north of the New Occidental deposit) will have a northerly plunge whereas folds superimposed on bedding striking west of cleavage will plunge south (Figure 56). Folds formed when the strike of bedding and cleavage are parallel will have sub-horizontal hinges. The plunge of bedding-cleavage intersection lineations will behave in a similar way, although, because bedding and cleavage are both relatively steep dipping, relatively subtle changes in the strike of bedding relative to that of cleavage will produce large changes in the plunge of the bedding-cleavage intersection lineation (Figure 56). Therefore, variations in the plunge of folds throughout the Cobar Goldfield may in part reflect variations in the strike of bedding relative to that of cleavage rather than being entirely the result of heterogeneous sub-vertical extension.

Hinman (1992) argued tightening and unfolding of folds around the Peak deposit reflected the interplay of shortening and shearing, whereby coaxial shortening produced tighter folds and non-coaxial deformation (shearing) unfolded folds (Figure 57). Specifically, he attributed the change from symmetrical parasitic folds in low-strain margins of the Peak deposit to assymetrical folds in the high strain zone over the Peak deposit (with steeper long limbs and gentle dipping to subhorizontal short limbs) to unfolding during D_{2-3}. Implicit in Hinman's (1992) model for unfolding of folds at the Peak deposit is that deformation was partly non-coaxial. Hinman proposed that axes of F_1 folds were originally oriented at an angle to the dominant cleavage but were progressively rotated towards cleavage during ongoing shortening, thereby satisfying the condition for non-coaxial deformation. A similar change in the fold symmetry of parasitic folds has been observed at the New Occidental deposit with increasing proximity to the Great Chesney Fault (Section

3.5.3 – Figure 39), raising the question as to whether parasitic folds in the New Occidental deposit have been unfolded during ongoing deformation?

Figure 56: Relationship between bedding-cleavage intersection lineations associated with changes in the strike of bedding and the geometry of resultant superimposed parasitic folds.

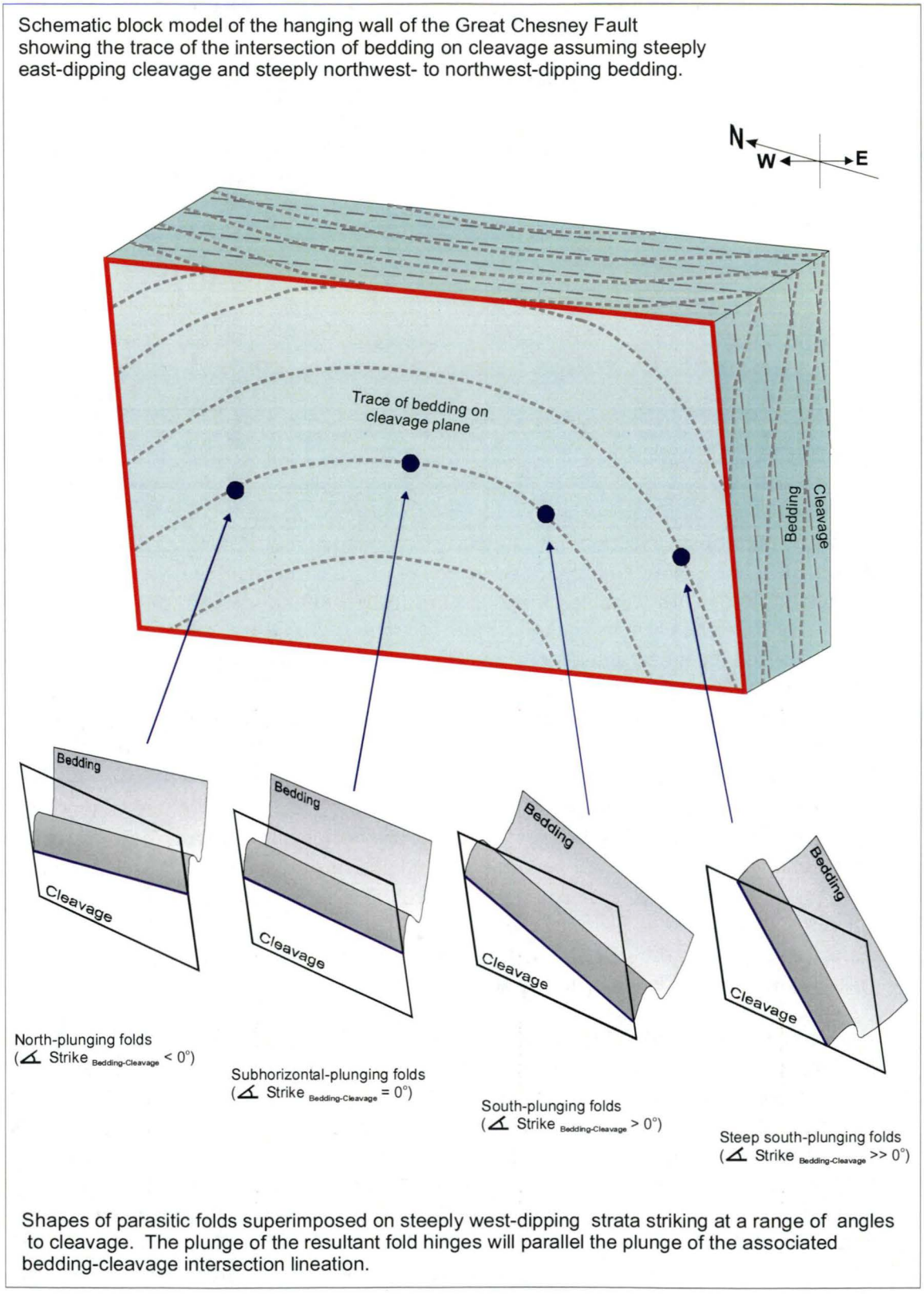

Glen (1985, 1987a, 1990) and Hinman (1992) argued folds formed early in the deformation history. However, the variable fold symmetry observed in the New Occidental deposit can

also be produced if, as previously proposed, some parasitic folds formed relatively late in the deformation cycle and were superimposed on strata with variable dip. Hobbs et al. (1976) highlighted fold initiation and fold symmetry in multilayered rocks is dependent on a range of parameters including the orientation of the layers with respect to the shortening direction. They noted layers oriented perpendicular to the direction of shortening are more likely to fold in response to shortening strain than layers oblique to the shortening direction. Therefore, folds can be expected to form more easily in strata inclined at a small angle to the shortening direction (for example, gentle to moderately dipping strata distant to the Great Chesney Fault in the hinge of the Chesney-Narri Anticline or strata striking at moderate to large angles to the Great Chesney Fault) compared to strata inclined at a steep angle to the shortening direction (steep-dipping strata in the immediate hanging wall of the Great Chesney Fault or strata striking parallel to the fault). Likewise, the asymmetry of folds likely increases as the angle between strata and shortening direction increases (Figure 58).

Figure 57: Coaxial versus non-coaxial deformation of early-formed folds (after Hinman, 1992).

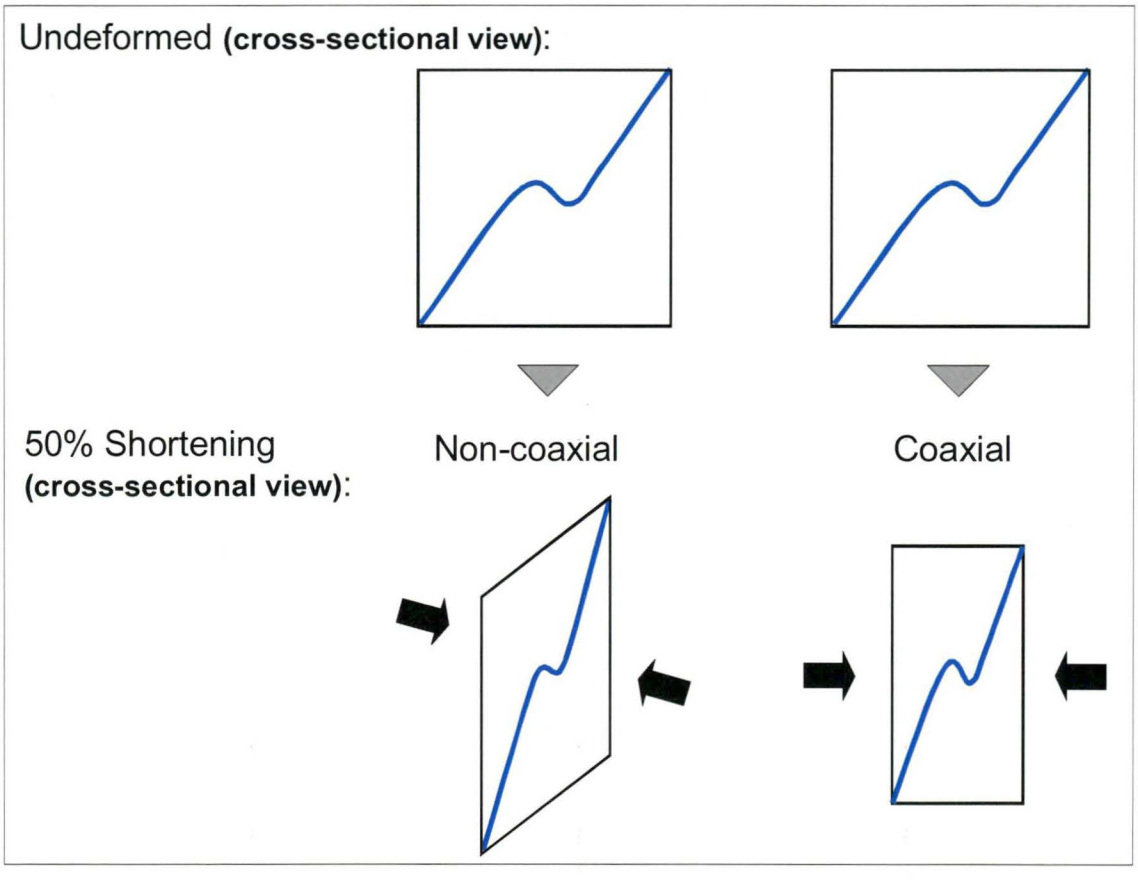

Finally, Hinman (1992) proposed axes of F_1 folds in the Cobar Goldfield had an initial northeast orientation but were rotated to northerly trends during east-northeast to west-southwest directed shortening (Figure 59). Hinman argued northeast trending F_1 fold axes in Glen's (1985) Structural Zone 2 have not been significantly deformed during D_{2-3} and therefore reflect the original orientation of F_1 folds in highly deformed Structural Zone 1. He suggested a shortening strain of 60%, which is similar to that inferred by Glen (1985) for Structural Zone 1, would produce a 25° anti-clockwise rotation of fold axes to a northerly trend, thereby preserving the transected relationships between fold axes and dominant cleavage he observed at the Peak deposit. The process is analogous to that described by Sanderson (1973) and Bell (1978) where fold axes oriented at some angle to a

stretching lineation direction have rotated towards, and ultimately into parallelism with the lineation direction during subsequent shortening.

Figure 58: Relationship between fold symmetry and the orientation of layering relative to the shortening direction.

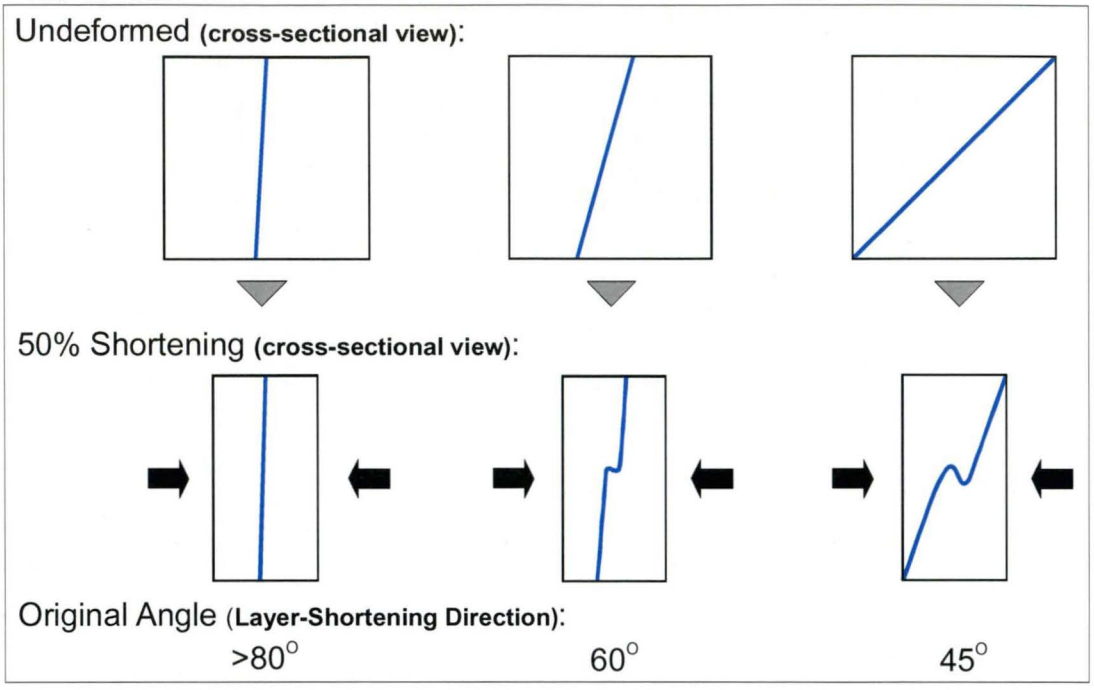

Figure 59: Passive rotation of fold axes assuming original folds were northeast trending under shortening strains of 60% (after Hinman, 1992).

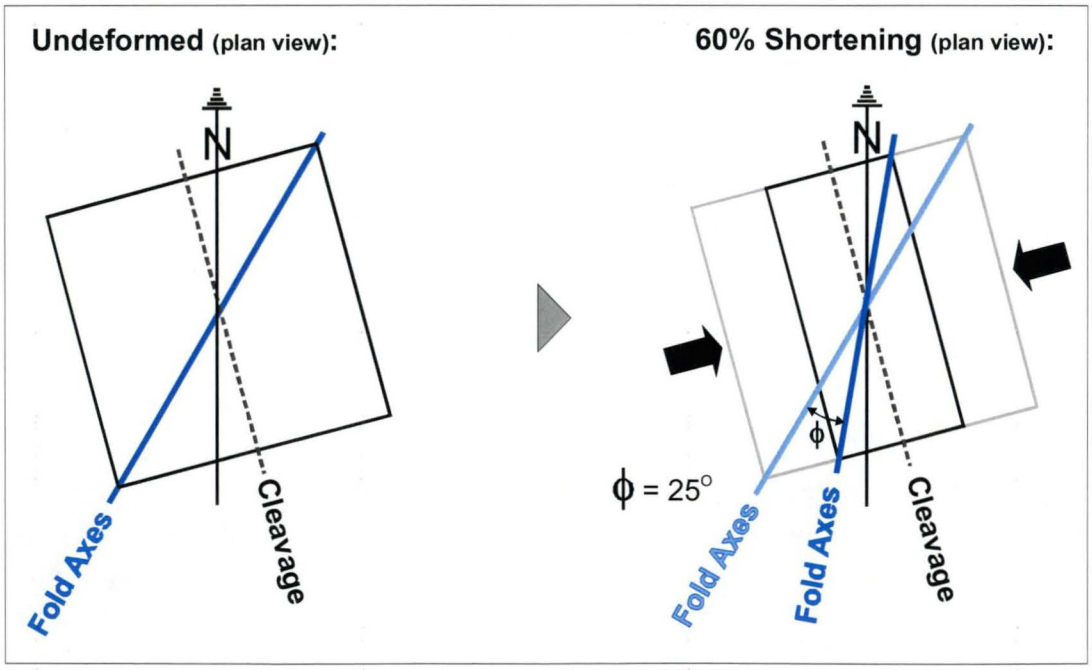

A number of significant flaws are evident in the model proposed by Hinman (1992). According to Glen (1985, 1987a, 1990), F_1 fold axes in Structural Zone 2 are consistently northwest trending, as opposed to the northeast trend cited by Hinman (1992):

> *In Zone 2, NW-trending F_1 folds developed initially ... Later F_1 folds trending west ... Further rotation of this local stress direction led to the formation of NE-trending F_2 folds* ... (Glen, 1985; page 301).

F_1 fold axes in Structural Zone 2 have a dominantly northwest trend except where they have been refolded to northwest trends during D_2 (Glen 1985).

If, as assumed by Hinman (1992), F_1 folds originally trended northeast and were rotated approximately 25° in an anticlockwise direction in response to 60% shortening strain, then fold axes would trend slightly east of north (Figure 59). Assuming a shortening direction of 078° (perpendicular to the strike of dominant cleavage) it is impossible to rotate a fabric with an original trend of 040° to a north-northwest trend (that is, parallel to cleavage and parallel to the observed trend of fold axes in the Cobar Goldfield). Similarly, if fold axes originally trended northwest (135°) as proposed by Glen (1985, 1987a, 1990), then a 60% shortening strain would rotate fold axes approximately 18° in a clockwise direction to a north-northwest trend of 153°, which is closer but still significantly different to the 160° to 180° trend of mapped fold axes.

The relative uniformity of fold axis trends throughout the Cobar Goldfield likewise does not support Hinman's (1992) model of fold axis rotation by shortening. No change in the trend of fold axes is evident between high- and low-strain zones in the Cobar Goldfield, as would be expected if the trend of fold axes was directly a function of shortening strain. In particular, the trend of fold axes remains relatively constant within the plane of cleavage, even though shortening strain likely increases dramatically towards the Great Chesney Fault. To demonstrate this point, shortening strains across the Great Chesney Fault have been estimated from the dip of bedding, which are likely to be minimum estimates. The expected change in strike of a fabric either originally oriented northeast or northwest has then been calculated for that range of shortening strains (Figure 60). Assuming an increase in shortening strain from 36% to 90% with increasing proximity to the Great Chesney Fault (steepening in dip of bedding from 50° to 85°), an originally northeast trending fabric would have rotated in an anticlockwise direction by 12° to 50° respectively. An originally northwest trending fabric would have rotated in a clockwise direction by 15° to 30° respectively. No such variation in the trend of fold axes is evident about the New Occidental deposit or elsewhere in the Cobar Goldfield.

Figure 60: Calculated variation in fold axis trends with increasing shortening strain with increasing proximity to the Great Chesney Fault.

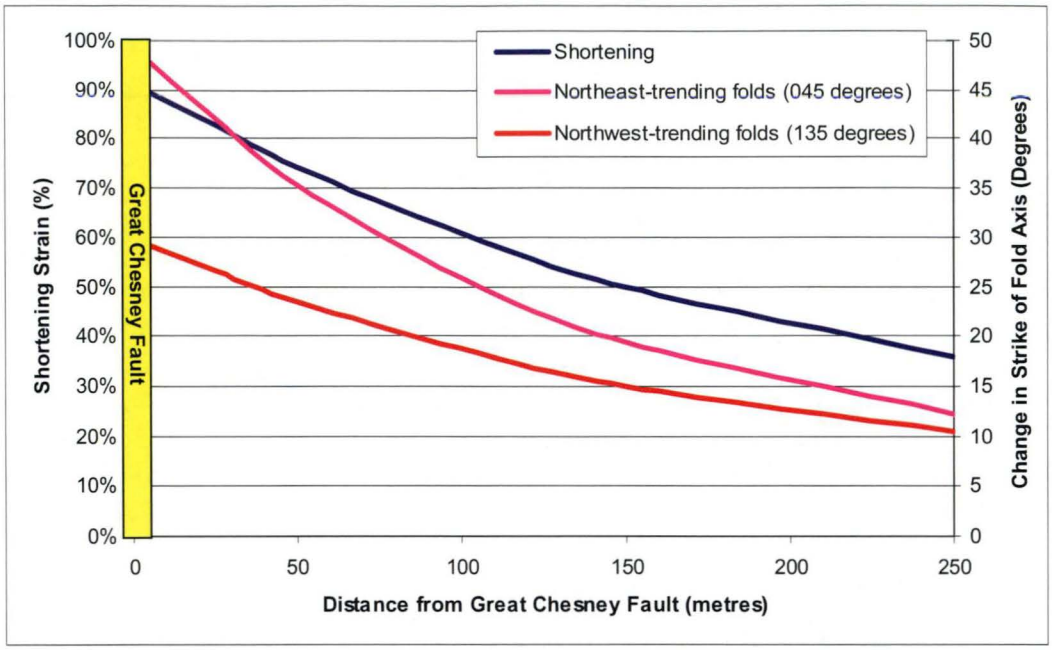

In summary, evidence for widespread and persistent deformation of folds, consistent with an exclusively early timing for fold formation in the New Occidental deposit and elsewhere in the Cobar Goldfield, is limited. Hinman's (1992) model of fold hinges rotating to both gentler and steeper orientations in response to heterogeneous subvertical extension is contradicted by the presence of variable fold plunges in both low- and high-strain areas. Rather, variation in the plunge of parasitic folds is attributed to two processes:

1. Steepening of fold plunges as early-formed folds were progressively tightened by ongoing deformation.

2. Superposition of folds on variably striking strata. Because bedding and cleavage are both steeply dipping, relatively subtle variations in the strike of bedding relative to cleavage have produced fold plunges ranging from gently north to steeply south. Significantly, axial planes of those folds are consistently parallel to dominant cleavage. Variations in strike of bedding relative to cleavage are potentially related to small-scale culminations on the hinges of major folds like the Chesney-Narri Anticline that have formed in response to heterogeneous subvertical strain. Glen (1987a) suggested strain variations during D_1 produced variable fold plunges in that anticline. Alternatively, they may reflect minor bedding flexures formed prior to main stage deformation.

Likewise, the folds patterns Hinman (1992) attributed to "unfolding" in response to non-coaxial shortening have herein also been interpreted to reflect folds forming in variably dipping strata. Finally, no evidence in support of rotated fold axes or folds transacted by cleavage was found during this study. The lack of any significant variation in fold axis orientation between early- and late-formed folds or between folds in low- or high-strain zones indicates the regional stress field has remained relatively constant throughout the main stage of basin deformation in the Cobar Goldfield.

Because variable fold plunges and variations in fold symmetry can largely be attributed to a superposition of parasitic folds on variably dipping and striking strata in the Cobar

Goldfield, some folds must have formed relatively late in the deformation history. The presence of progressively more open folds in successively younger sets of sub-horizontal quartz veins in the New Occidental deposit also indicates rocks in the immediate vicinity of the Great Chesney Fault underwent more or less continuous shortening by folding during displacement on the fault. Therefore, folds appear to have formed throughout the deformation history, and were not restricted to the initial stages of basin deformation as proposed by Glen (1985, 1987a, 1991), Hinman (1992) and Wilson (1996).

It is likely though that major folds, including the Chesney-Narri Anticline, initiated early in the deformation history when basin strata was oriented at a low angle to the northeast-southwest direction of shortening (Glen, 1985). Ongoing deformation continued to tighten early-formed folds with fold hinges rotating to steeper plunges. As strata progressively steepened, initiation of folds became increasingly difficult – for example, steep-dipping (>80°) strata adjacent to the Great Chesney Fault is largely unfolded – and deformation was increasingly accommodated by fault displacement and cleavage development. Later folds most likely formed in and about hinge zones of larger folds or where the strike of strata was at an angle to the strike of the Great Chesney Fault, that is, where bedding was oriented at a low angle to the shortening direction.

3.7.5 Relationship between steeply dipping Lineations on Cleavage and Bedding

Steeply north plunging lineations on bedding in the New Occidental deposit are stretching lineations formed synchronously with similarly oriented lineations on cleavage. They are most commonly observed in the North Opencut and NO25/26 areas occurs in an area where bedding and cleavage have a similar strike and the angle between those two planes is on average only 15°. However, where the angle between bedding and cleavage is >20° (for example, Southeast Opencut area) sub-vertical lineations on bedding are less common. The sub-vertical lineations on bedding therefore most likely formed when bedding and cleavage were similarly oriented so that some sub-vertical extensional strain was partitioned into bedding-parallel stretching and/or bedding plane surfaces were activated as slip planes during deformation. Hinman (1992) has also documented examples of favourably oriented bedding surfaces being activated as slip planes in the Peak deposit.

3.7.6 Structural Significance of Brittle Faults

Two contrasting styles of late-stage brittle deformation have been identified in the New Occidental environs (Figure 61):

1. Reverse movement on a conjugate series of low-angle west-southwest and east-northeast-dipping faults.
2. North-south movement on low-angle late-stage shears associated with strike-slip re-activation of dominant cleavage and cleavage-parallel shears.

The conjugate set of low-angle reverse faults that traverse the New Occidental deposit reflect east-northeast to west-southwest shortening. Although those faults locally offset the New Occidental deposit, they have probably formed in response to a regional stress field that is broadly similar to that associated with main stage of northeast-southwest directed compression. Thus, it is likely this phase of faulting represented the waning stages of that deformation, rather than younger Carboniferous deformation described by Glen (1985). In contrast, the north-south movement on low-angle shears, the accompanying strike-slip reactivation of cleavage and the gently north plunging kink bands documented in the New Occidental deposit environs are compatible with northwest-southeast compression and

therefore most likely correlate with the younger Carboniferous period of deformation that is widespread in the western part of the Cobar Basin (Glen, 1985).

Wilson (1996) identified a conjugate set of gently north-northwest and south-southeast dipping late-stage brittle faults in the New Cobar/Chesney area associated with a weak steep north-northwest dipping (80°/330°) mesoscopic cleavage (S_4) that is axial planar to a set of steep northeast plunging F_4 folds and crenulations. Wilson's S_4 cleavage is oriented approximately perpendicular to the dominant cleavage. Recent exposures in the New Cobar area in the newly constructed New Cobar Opencut (Peak Gold Mines company data) reveal conjugate sets of west-southwest and east-northeast dipping brittle faults as well as the north-northwest and south-southeast dipping faults previously documented by Wilson (1996). Offsets on the west-southwest and east-northeast dipping faults are largely reverse dip-slip, consistent with similarly oriented faults in the New Occidental deposit that are interpreted to have formed during the waning stages of northeast-southwest directed compression. Offsets on the north-northwest and south-southeast dipping faults are also largely reverse dip-slip, confirming those faults and associated steep north-northwest dipping cleavage and steep northeast plunging folds and crenulations formed in response to northwest-southeast compression.

Figure 61: Styles of brittle fault displacements in the New Occidental deposit.

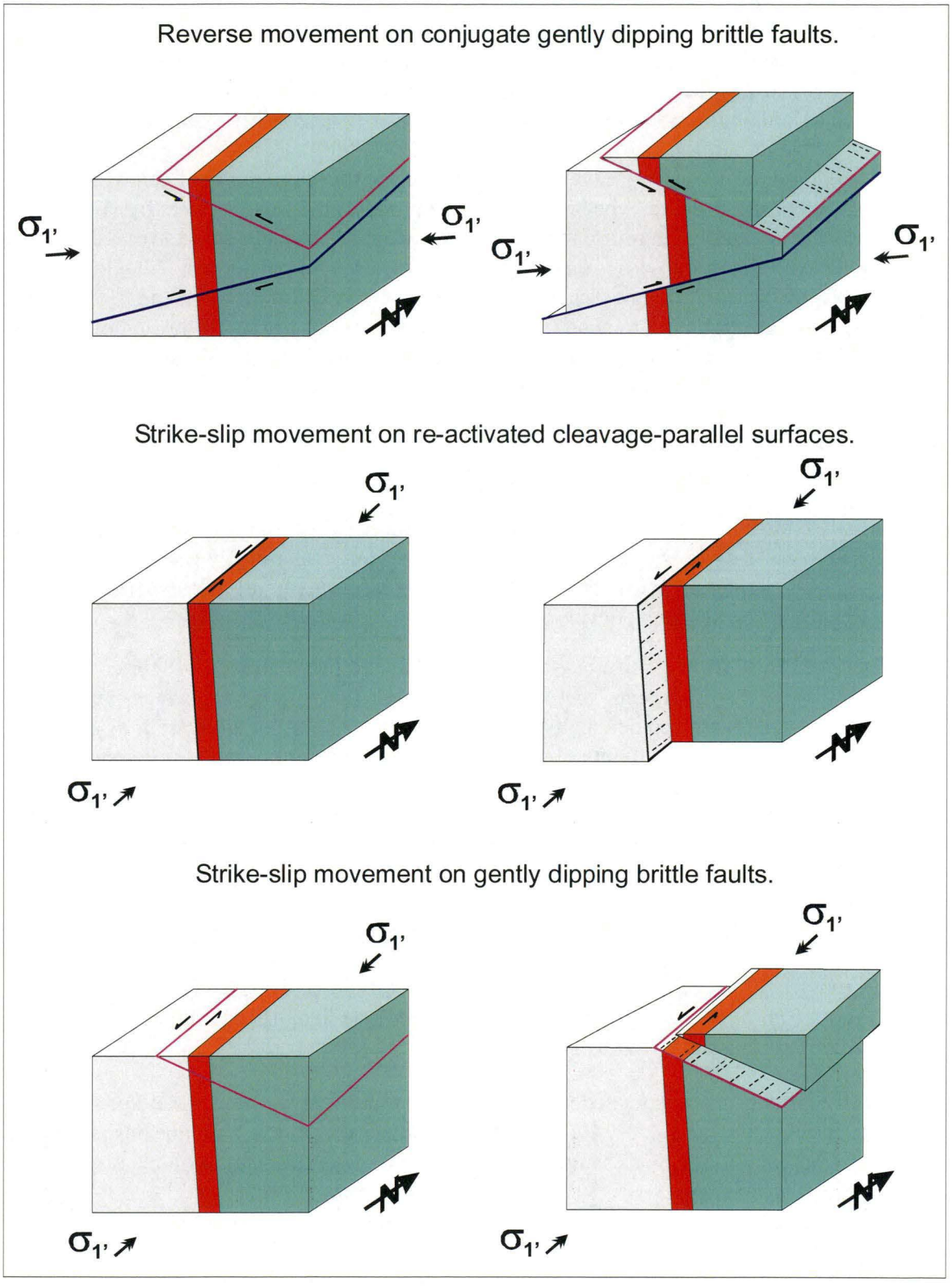

Hinman (1992) considered all brittle faults in the Peak area to be cleavage-parallel and associated with significant normal dip-slip displacement (of the order of 150–200m between the Peak and Blue Shears). Hinman argued that such faulting represented D_4 relaxation following D_1–D_3 shortening. The late-stage large-scale normal dip-slip displacement inferred by Hinman has been contradicted by more recent studies of the Peak deposit (Stegman and Pocock, 1996; Cook et al., 1998; Webster, 1999) and the

stratigraphic displacements inferred by Hinman (1992) as D_4, are interpreted to be syn-mineralisation in age, and hence by inference, most likely formed during the main stage of basin deformation associated with northeast-southwest shortening. Gently west-southwest dipping brittle reverse faults of the kind identified in the New Occidental and New Cobar/Chesney areas have subsequently been observed underground within the Peak Mine (Peak Gold Mines company data). Glen (1985; 1990) identified sub-horizontal striations on cleavage-parallel faults in the Blue lode area at the Peak and similarly oriented striations have been observed on cleavage and cleavage-parallel faults in the Peak Mine (Peak Gold Mines company data). The brittle cleavage-parallel faulting observed by Hinman (1992) in the Peak deposit is therefore most likely equivalent to the late-stage strike-slip reactivation of cleavage-parallel fabrics observed in the New Occidental deposit. The localised microscale crenulation of cleavage that Hinman (1992) identified in the Peak deposit is also likely to be equivalent to similarly oriented crenulations observed throughout the Cobar Goldfield by Glen (1985), in the New Cobar/Chesney deposits (Wilson, 1996) and in the New Occidental deposit (this study).

In conclusion, two distinct stages of late-stage predominantly brittle deformation are present in the Cobar Goldfield:

1. The waning stages of northeast-southwest shortening have produced reverse displacement on a conjugate set of gently west-northwest and east-southeast dipping brittle faults. In some deposits, only gently west-northwest dipping brittle faults developed.

2. Northwest-southeast shortening has produced a range of fabrics and fault displacements, including; strike-slip reactivation of cleavage-parallel fabrics (New Occidental and Peak deposits); strike-slip reactivation of gently west-northwest dipping brittle faults (New Occidental deposit); reverse displacement on a conjugate set of gently north-northwest and south-southeast dipping brittle faults (New Cobar/Chesney deposits), a weak steep north-northwest dipping cleavage and steep northeast plunging folds (New Cobar/Chesney deposits) and small-scale crenulations of cleavage (in all deposits).

3.8 Structural History of the Cobar Goldfield - A Revised Nomenclature

A modified structural history for the Cobar Goldfield is proposed herein (Table 12 and Figure 62). It is broadly similar to that outlined by Glen (1985), but simpler than Hinman's (1992) and Wilson's (1996) syntheses.

D_1 deformation is associated with northeast – southwest shortening, and produced gently north-northwest to steeply south-southeast-plunging F_1 folds, a ubiquitous steep east-dipping axial plane S_1 cleavage and a prominent mineral lineation on cleavage (L_1^1) and locally, on bedding (L_0^1). Sub-vertical extension parallel to L_1^1 and L_0^1 during D_1 appears to have been principally focussed along and immediately surrounding major faults, including the Great Chesney Fault. As a result, S_1, L_1^1 and L_0^1 fabrics are most intensely developed in the immediate vicinity of the New Occidental deposit and other deposits in the Cobar Goldfield. Bedding has been consistently steepened and rotated towards S_1 around the Great Chesney Fault. It has also been locally dismembered in closer proximity to the fault.

Late-stage brittle faults, characterised by minor clay fill, represent the last stages in the deformation history of the New Occidental deposit environs. These faults typically dip moderately-gently to the east-northeast and west-northwest and offset earlier structures,

including quartz veins in the New Occidental deposit and S_1 cleavage, by small amounts. Reverse dip-slip movement on those faults occurred during the waning stages of D_1 shortening. In contrast, minor strike-slip re-activation of S_1 cleavage-parallel faults, north-south displacement of the same gently dipping faults and reverse dip-slip on a further generation of gently north-northwest and south-southeast dipping brittle faults appears to represent a subsequent stage of deformation (D_2), which is equivalent to Glen's (1985) Carboniferous D_2 deformation in the western part of the Cobar Basin. That later fault displacement occurred in response to northwest – southeast oriented shortening, consistent with observations made by Glen (1985) and Wilson (1996), rather than in response to a relaxation event as proposed by Hinman (1992).

The changeover from D_1 deformation to D_2 deformation is marked by a change in the style of deformation. D_1 deformation predominantly comprises ductile deformation with spatially restricted zones of brittle deformation. The waning stages of D_1 consist of brittle reverse faults, which post-date mineralisation. D_2 deformation is manifested exclusively by brittle deformation with little or no associated hydrothermal alteration and mineralisation. It is clearly post-mineralisation in age.

Table 12: Nomenclature of deformation events throughout the Cobar Goldfield.

Deformation	Glen (1985) Cobar Goldfield	Hinman (1992) Peak	Wilson (1996) New Cobar-Chesney	This Study New Occidental
Gently NNE to steeply SSE plunging folds (e.g. Chesney-Narri Anticline)	"Possible early foliation" and F_1	D_1, S_1, F_1	D_1, S_1, F_1	D_1, S_1, F_1
Regional sub-vertical NNW-SSE striking cleavage and steep N plunging stretching lineation	D_1, S_1, L_1	D_2, S_2, L_2^2	D_2, S_2, L_2^2	S_1, L_1^1, L_0^1
Intense sub-vertical NNW-SSE striking cleavage associated with major shear zones including the Great Chesney Fault	S_1	S_3	Intense S_2	Intense S_1
Reverse movement on gently to moderately WNW and ESE dipping brittle faults	D_2	D_4		Late D_1
Reverse movement on gently NNW and SSE dipping brittle faults; strike-slip re-activation of S_1 cleavage; strike-slip displacement on WNW and ESE dipping brittle faults; and gently N to NNW dipping kink bands	D_2	D_4	D_4	D_2

Figure 62: Structural evolution of the New Occidental deposit area during D_1 deformation.

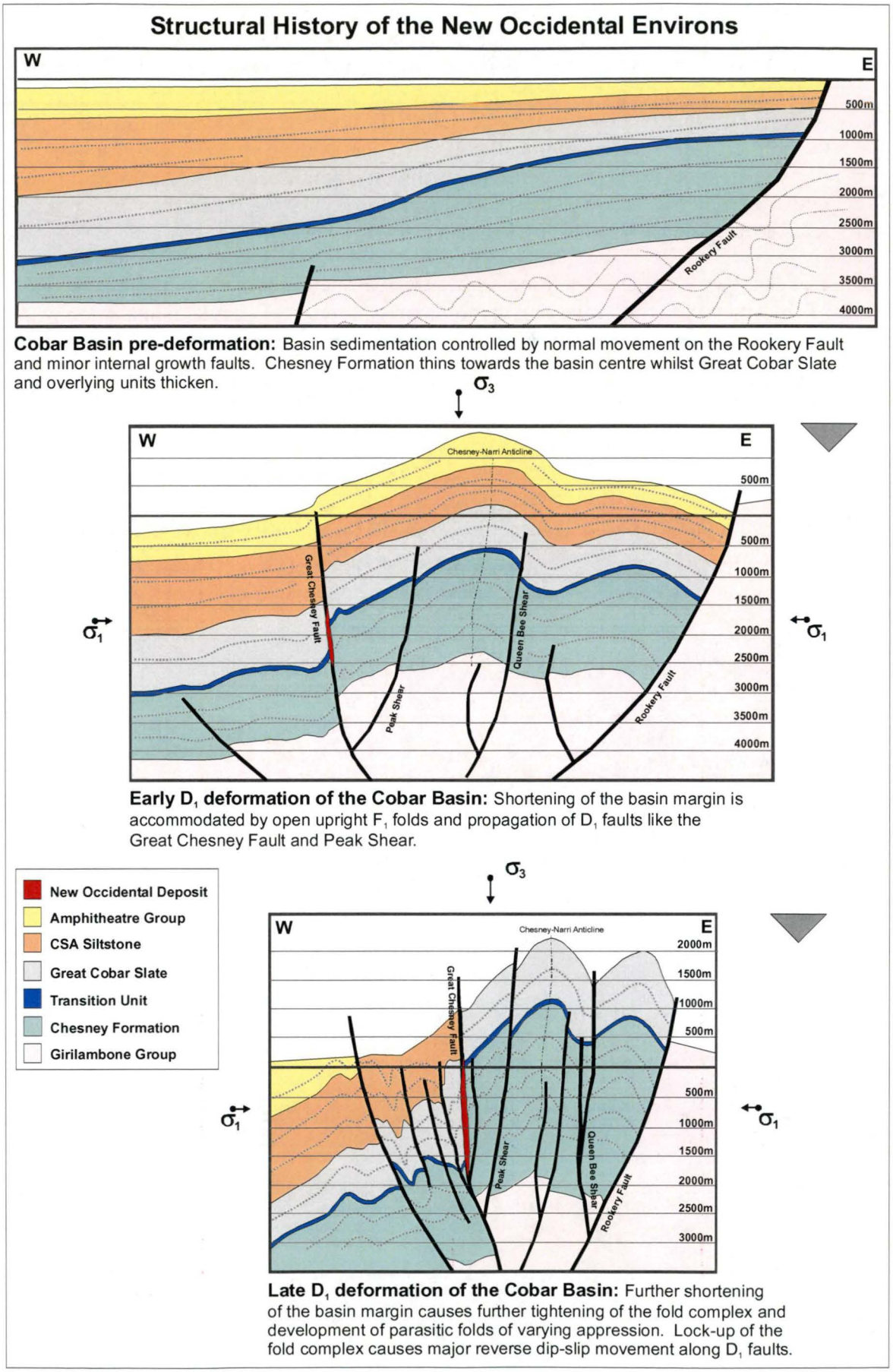

Cobar Basin pre-deformation: Basin sedimentation controlled by normal movement on the Rookery Fault and minor internal growth faults. Chesney Formation thins towards the basin centre whilst Great Cobar Slate and overlying units thicken.

Early D_1 deformation of the Cobar Basin: Shortening of the basin margin is accommodated by open upright F_1 folds and propagation of D_1 faults like the Great Chesney Fault and Peak Shear.

Late D_1 deformation of the Cobar Basin: Further shortening of the basin margin causes further tightening of the fold complex and development of parasitic folds of varying appression. Lock-up of the fold complex causes major reverse dip-slip movement along D_1 faults.

3.9 Structural History of the Great Chesney Fault

3.9.1 Displacement vectors and offset on the Great Chesney Fault

A large number of structural and stratigraphic observations from the New Occidental deposit consistently indicate east block-up reverse dip-slip displacement on the Great Chesney Fault during D_1:

1. The prominent steeply north-plunging stretching lineation on cleavage (L_1^1), and locally on bedding (L_0^1), which is best developed around the Great Chesney Fault, can be considered to parallel the direction of maximum finite elongation during D_1 (cf. Hobbs et al., 1976). As such, the steep northerly plunge of the lineation indicates the direction of stretching/extension during D_1 was essentially sub-vertical, consistent with dominantly dip-slip movement on the Great Chesney Fault. The presence of this lineation surrounding other deposits in the Cobar Goldfield indicates that sub-vertical extension and dip-slip displacement on host faults is a consistent feature of deformation in the Goldfield.

2. Apparent stratigraphic offsets of the order of 1.5–2.5 km across the Great Chesney Fault (Section 3.4.2) indicate an east block-up direction of movement on the fault.

3. Cleavage in the Cobar Goldfield is parallel to the fault, implying shortening has occurred at a very high angle to the fault.

4. The western limb of the Chesney-Narri Anticline has been subjected to large-scale sub-vertical stretching, which has resulted in steepening and attenuation of bedding in both the hanging wall and footwall of the Great Chesney Fault into the fault (Figure 62).

Stretched pyrrhotite grains have been used to quantify sub-vertical extension in the Peak deposit, with sub-vertical extensions of 200–350% estimated for the Peak area (Plibersek 1982) and much larger vertical extensions inferred in the core of the high-strain zone at the Peak deposit (Hinman, 1992). As this pyrrhotite formed along cleavage as a direct replacement of syngenetic pyrite during deformation, it is likely a component of the elongation of the pyrrhotite grains is due to oriented mineral growth (cf. Hobbs et al., 1976). Therefore, in this instance, elongation of pyrrhotite grains will not provide a reliable indication of the amount of extensional strain and it is likely extension in the Peak deposit is potentially significantly less than that estimated by Plibersek (1982) and Hinman (1992).

Was there a strike-slip component to displacement on the Great Chesney Fault during D_1?

A range of criteria have been cited as evidence for D_1 strike-slip displacement on the Great Chesney Fault, and by inference, a strike-slip control on mineralisation associated with the fault (Sullivan, 1947; Mulholland & Rayner, 1961; Glen, 1985, 1987a, 1990; Coller, 1987; Stegman & Pocock, 1996). These criteria have been contradicted in this study:

1. **Major D_1 faults traces contain flexures consistent with late-stage left-lateral strike slip displacement on the Great Chesney Fault** (Mulholland & Rayner, 1961; Coller, 1987; Stegman & Pocock, 1996) – previously mapped folds in the trace of the Great Chesney Fault in the New Cobar area (Mulholland & Rayner, 1961) have now been shown not to exist (Peak Gold

Mines data, Figure 31). Furthermore, the plan view of the Cobar Goldfield is parallel to the stretching lineation and dominant fault displacement, and, as a consequence, apparent lateral displacement associated with a dominantly reverse dip-slip fault can be contradictory. For example, the steep northerly plunge of the D_1 displacement vector on the Great Chesney Fault suggests a minor component of right-lateral strike-slip displacement will be associated with dominantly reverse dip-slip fault displacement. However, where subvertical extension was heterogeneous, a minor component of left-lateral strike slip displacement may also be evident. In any case, the amount of lateral displacement on the Great Chesney Fault during D_1 is insignificant compared to the magnitude of dip-slip displacement on the fault.

2. **Steeply plunging folds immediately adjacent to the Great Chesney Fault formed during strike-slip displacement on the Great Chesney Fault** (Sullivan, 1947; Stegman & Pocock, 1996) – steeply dipping folds adjacent to the Great Chesney Fault are interpreted to have formed in response to northeast-southwest oriented shortening of steeply dipping strata adjacent to the fault (Section 3.7.4). Had those folds formed in response to late-D_1 strike-slip fault displacement, S_1 cleavage should then be folded around their hinges. However, there is no evidence of folded S_1 cleavage in the steeply plunging folds adjacent to the Great Chesney Fault. Rather, cleavage maintains a constant axial planar relationship to all folds in the Goldfield (Glen, 1990; Wilson, 1996; this study).

3. **Sub-horizontal slicken-sides on fault planes indicate D_1 strike-slip displacement** (Glen, 1985, 1987a, 1990) – sub-horizontal slicken-sides on both the Great Chesney Fault and Peak Shear are herein interpreted to be associated with D_2 brittle faults, which are clearly post-mineralisation in age (Wilson, 1996; this study).

4. **Northwest trending cross-structures formed during strike-slip fault displacement** (Sullivan, 1951; Mulholland and Rayner, 1961; Glen 1985, 1987b; Coller, 1987) – no evidence of northwest-trending faults or cleavage was found during this study although some northwest trending quartz veins occur in both the hanging wall and footwall of the New Occidental deposit. Both the Great Chesney and Albion Faults locally strike northwest in the northern part of the New Occidental Opencut (Figure 49). The change in strike of the trace of the Great Chesney Fault occurs where the Albion Fault splits from the Great Chesney Fault. Further to the north where the Albion Fault rejoins the Great Chesney Fault, the trace of the Albion Fault also locally strikes northwest. Those northwest-striking fault segments do not appear to represent a discrete phase of northwest-trending faulting but rather are flexures associated with fault bifurcations.

5. **Ore deposits associated with the Great Chesney Fault are located in structural settings consistent with dilation during strike-slip fault displacement** (Coller, 1987; Stegman & Pocock, 1996) – application of a strike-slip fault model to mineralisation along the Great Chesney Fault indicates contradictory mechanisms for deposit localisation. Whilst the New Cobar and Chesney deposits are potentially located in strike-slip dilational bends and jogs along the trace of the Great Chesney Fault, other deposits like the New Occidental, Burrabungie, Mt. Pleasant and Young Australia deposits are located in apparently contractional sites along the Great Chesney Fault (Figure 13).

Minor strike-slip displacement on the Great Chesney Fault is therefore interpreted to be confined to D_2 and is unequivocally post-mineralisation in age (Section 3.7.6).

3.9.2 Origin of the Great Chesney Fault

The deformation history proposed herein for the Cobar Goldfield provides important constraints on both the timing and mode of formation of the Great Chesney Fault. In addition, stratigraphic relationships across the fault may also indicate the timing of fault initiation, especially if the Great Chesney Fault initiated as a syn-depositional fault.

The absence of equivalent Cobar Basin stratigraphy across the Great Chesney Fault in the Cobar Goldfield does not readily allow the possibility of stratigraphic changes across the fault to be assessed. In the Cobar Goldfield, Chesney Formation has only been observed in the footwall of the fault in a narrow fault-bound sliver immediately north of the New Cobar deposit. The sliver contains only a very small section of the uppermost part of the Chesney Formation and therefore does not allow Chesney Formation in the footwall and hanging wall of the Great Chesney Fault to be compared. Evidence of stratigraphic variations within Chesney Formation either side of the Great Chesney Fault may be present in the northern part of the Cobar Basin where the fault transects the Chesney Formation - Great Cobar Slate stratigraphic contact. That area is outside of the current study area.

Great Cobar Slate is present on both sides of the Great Chesney Fault in the Cobar Goldfield. No sedimentalogical differences in the Great Cobar Slate either side of the fault are evident, although the unit is relatively featureless and such differences would be difficult to discern. However, a difference in thickness of the Great Cobar Slate has been tentatively identified across the fault. The thickness of the Great Cobar Slate in the hanging wall of the fault in the Peak and Perseverance areas has been determined to be 300 to 400m. In contrast, Great Cobar Slate in the footwall of the Great Chesney Fault near Cobar is considered to be approximately 1000m thick (Glen, 1987a), although the section is incomplete (Section 3.4.2). This difference, if real, may reflect a major deepening of the basin across the Great Chesney Fault towards the basin centre as Great Cobar Slate was deposited. Alternatively, the change in thickness of the Great Cobar Slate may also reflect north to south thinning of the unit that is unrelated to the Great Chesney Fault.

While stratigraphic relationships across the Great Chesney Fault do not provide conclusive evidence on the timing of fault initiation, the structural setting of the fault is more revealing. The Great Chesney Fault is parallel to both S_1 cleavage and axial planes of F_1 folds, indicating shortening in the eastern margin of the Cobar Basin occurred at a very high angle to the fault. Given F_1 folds are interpreted to have formed in their present S_1-parallel orientations, it is unlikely the Great Chesney Fault formed at an angle to cleavage and fold axes and was then rotated into parallelism with those structures in response to basin shortening. Rather, the Great Chesney Fault must have initiated as a cleavage-parallel structure. The probability of a pre-D_1 deformation fault having the same north-northwest orientation as D_1 deformation fabrics is regarded as very low. This implies the fault was not a basin-forming extensional fault that has been re-activated and inverted during deformation of the eastern margin of the Cobar Basin. Instead, as previously proposed by Glen (1990), the Great Chesney Fault most likely formed contemporaneously with similarly oriented S_1 cleavage and F_1 folds during D_1.

Glen (1985) proposed shortening strains of 40–70% for the Chesney-Narri Anticline and remainder of Structural Zone 1. However, shortening strains in the immediate vicinity of the Great Chesney Fault are probably higher. Bedding has steepened to sub-vertical and locally over-turned attitudes, and a very strong steep-dipping cleavage is developed about

the fault. A shortening strain of as much as 90% is possible for the fault environs, assuming steepening of bedding is caused solely by shortening strain comprising both a sub-vertical stretching component (in the direction of L_1^1) and a flattening component orthogonal to the shortening direction. The pre-strain dip of the Great Chesney Fault is estimated at approximately 60–70° to the east, assuming the Great Chesney Fault formed in the earliest stages of basin shortening. Therefore, the Great Chesney Fault has probably always been a relatively steeply dipping structure.

Although the Great Chesney Fault is interpreted to be a D_1 fabric, its activation suggests that some form of precursor structure to the fault was present prior to initiation of D_1 deformation. Similarly, the zone of increased F_1 folding surrounding the Great Chesney Fault may reflect strain localisation above an existing weakness such as a basement fault. Glen (1990) discounted the presence of a precursor basement fault to the Great Chesney Fault, based partly on the apparent absence of sedimentalogical or facies variations in Cobar Basin stratigraphy across the fault. He argued the Great Chesney Fault and other steeply dipping faults in the eastern margin of the Cobar Basin flatten with depth and link into a west-dipping floor thrust (detachment) which underlies all of his Structural Zone 1 (Figure 7). The presence of this floor thrust was potentially substantiated by the seismic transect across the Cobar Goldfield (Glen et al., 1994). Although depth to the floor thrust is unconstrained, its depth is postulated by Glen (1990) to be approximately 2 km. The 1.5–2.5 km sub-vertical displacement herein inferred for the Great Chesney Fault, and its consistent sub-vertical dip to a depth of in excess of 1.5 km, cannot be easily reconciled with Glen's (1990, 1991) cross-sectional interpretation (Figure 7). Rather, it is more likely the Great Chesney Fault remains steeply dipping, propagates into underlying basement and substantially off-sets the Cobar Basin-basement contact (Figure 62). The seismic transect across the eastern margin of the Cobar Basin neither supports nor precludes this interpretation as the seismic transect did not image the Great Chesney Fault. Glen et al. (1994) noted the resolution of the seismic transect is relatively coarse and therefore could not resolve individual faults in the strongly faulted eastern margin of the Cobar Basin, especially if the faults were non-reflective and/or steeply dipping.

The interpreted geometry of faults within the eastern margin of the Cobar Basin (Figure 62) is akin to a positive flower structure with the Great Chesney Fault and other faults in the eastern margin of the Cobar Basin, including the Rookery and Queen Bee Faults, merging at depth in basement to the basin.

Figure 63: Fault geometry in Structural Zone 1 of the Cobar Basin (modified from Glen, 1990)

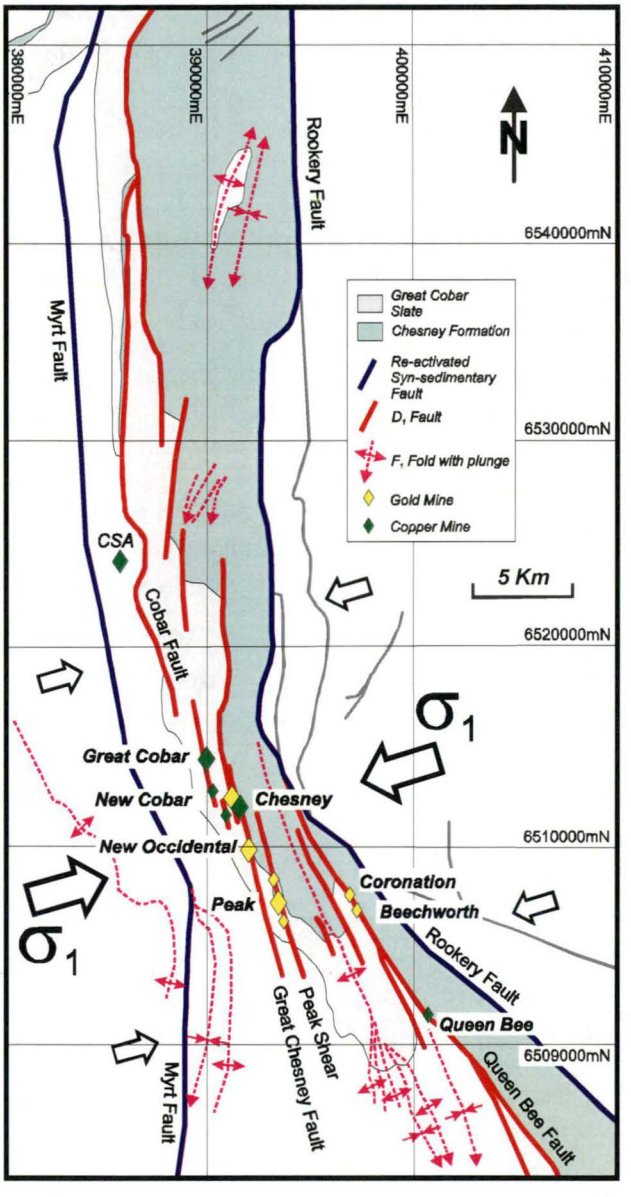

The mode of formation of the Great Chesney Fault proposed herein is consistent with Glen's (1990) model for formation of the Great Chesney Fault, and other faults in the Cobar Goldfield, including the Cobar Fault, Peak Shear and Queen Bee Fault. Glen (1990) argued those folds formed when the bounding Rookery and Myrt Faults, which were initially syn-depositional extensional faults, reactivated as oblique thrusts during compressional deformation of the eastern margin of the Cobar Basin (Figure 63). During ongoing D_1 deformation, strain in the zone between the Rookery and Myrt Faults was accommodated by formation of a series of internal short-cut reverse faults orthogonal to the shortening direction (Glen, 1990).

The curvature of D_1 structures in Structural Zone 1, from north-northeast striking north of Cobar to north-northwest striking south of Cobar, has previously been ascribed to the presence of a promontory (Glen, 1985) or indenter (Glen, 1990; Hinman, 1992) immediately east of Cobar. The apparent fanning of D_1 faults and F_1 folds south of Cobar, and the apparent along-strike termination of some of those D_1 faults in zones of F_1 folds both north and south of the Cobar Goldfield, suggest regional northeast-southwest directed shortening strain was greatest in and around the Goldfield, centred on Glen's (1990) indenter (Figure 63).

3.10 Controls on Mineralisation within the Cobar Goldfield

Mineralisation in the New Occidental deposit, like in other ore deposits in the Cobar Goldfield, including the New Cobar, Chesney and Peak-Perseverance deposits, demonstrates intimate relationships with D_1 structures (Figure 64 and Figure 65):

1. The gross outline of the New Occidental deposit is parallel to S_1 cleavage and elongate in the direction of the steeply dipping L_1^1 stretching lineation, lying within the plane of major D_1 fault zones.

2. High-grade ore shoots within the New Occidental deposit are also parallel to S_1 cleavage and elongate in the direction of the L_1^1 stretching lineation.

3. Multiple generations of quartz veins intimately associated with gold-base metal mineralisation in the New Occidental deposit are in part parallel to S_1 cleavage and have been variably deformed during D_1 deformation.

4. Mineralisation within the Cobar Goldfield is associated with D_1 faults, the largest of the deposits occurring within major fault zones. For example, the New Occidental deposit (1.5 Moz Au) is located on the Great Chesney Fault, the Peak and Perseverance deposits (collectively 2.0 Moz Au) are located within and immediately surrounding the Peak Shear. In contrast, the smaller New Cobar (0.9 Moz Au) and Chesney (0.2 Moz Au) deposits are both located in subsidiary fault strands parallel to and in the footwall of the Great Chesney Fault.

5. The intensity of S_1 cleavage and L_1[1] stretching lineation increases towards each deposit and is most intense immediately around the high-grade zones of mineralisation. However, both fabrics are also well developed within the zones of mineralisation.

6. Ore deposits are characterised by a halo of F_1 folds, those folds becoming tighter and more variably plunging with increasing proximity to individual deposits.

Such observations clearly indicate a syn-D_1 age of mineralisation in the Cobar Goldfield, consistent with previous syn-deformational epigenetic interpretations of the origin of Cobar deposits by Glen (1985, 1987a), de Roo (1989b) Lawrie (1991a), Hinman (1992) and Lawrie and Hinman (1998).

Figure 64: Summary Geology of the New Cobar, New Occidental and Peak deposits.

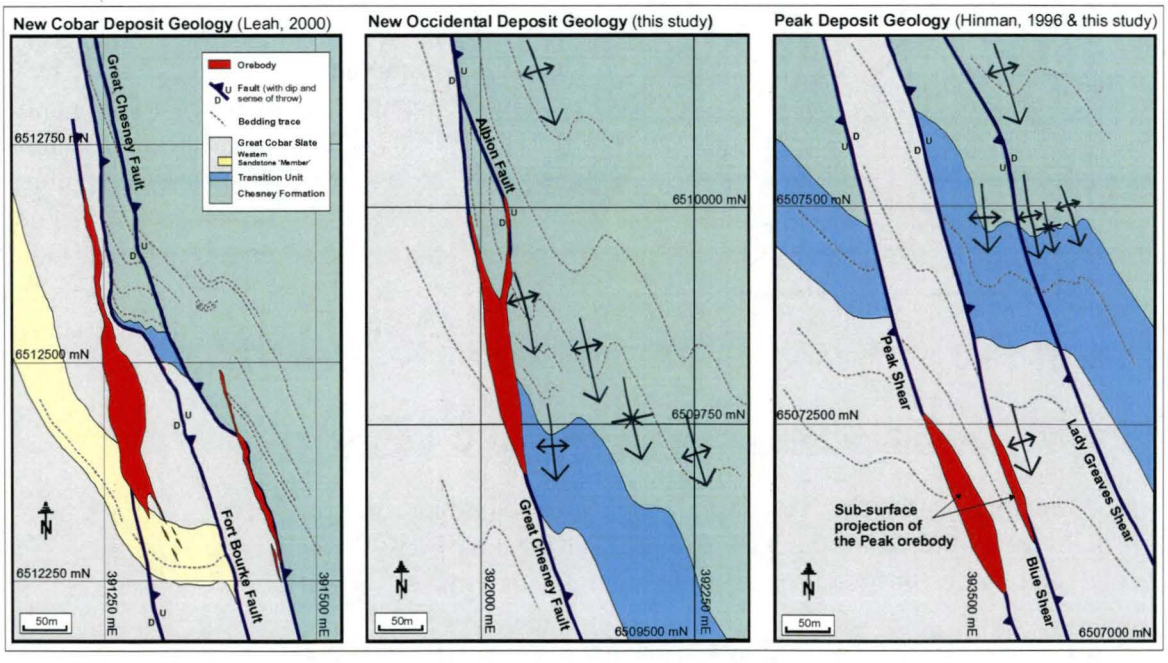

What controls localisation of mineralisation along fault zones in the Cobar Goldfield?

The increase in intensity of S_1 cleavage and L_1[1] stretching lineation, the halo of F_1 folds, and increase in F_1 fold appression around the various deposits in the Cobar Goldfield indicate deposits have formed in higher-strain zones. Hinman (1992) has argued the Peak deposit formed in a high-strain zone along the Peak Shear, a zone that is higher strain than elsewhere along the Peak Shear. The recognition the Peak deposit is associated with a

pronounced apophasis of rhyolite (Stegman, 2000) supports Hinman's conclusion. However, it is not unequivocal that deposits associated with the Great Chesney Fault have formed in higher-strain zones along that fault, although the halo of F_1 folds about each deposit associated with the Great Chesney Fault suggests that this may be so.

Deposits in the Cobar Goldfield are localised in areas where, on average, the angles between the strike of bedding and D_1 structures are relatively large (>20°) (Figure 65). In contrast, bedding strikes sub-parallel to the strike of D_1 faults and S_1 cleavage in unmineralised sections of major faults along strike from the deposits. This suggests deposits are associated with relatively long wavelength bedding flexures or warps. The flexures appear to represent subtle culminations on the F_1 Chesney-Narri Anticline and are interpreted to have formed in response to inhomogeneous strain during the initial stages of D_1 shortening as a result of interference between formation of the Chesney-Narri Anticline and reverse slip on D_1 faults. Because the flexures only occur about the major D_1 faults, they are unlikely to be pre-D_1 structures. The flexures appear to act as heterogeneities along the fault planes and have become the locus for subsequent deformation, including formation of parasitic F_1 folds.

It has also been suggested deposits in the Cobar Goldfield are localised by northeast-trending cross-structures, including megakinks (Sullivan, 1947; Mullholland & Rayner, 1961) or tear/transfer faults (Glen et al., 1994; Stegman & Pocock, 1996). However, such cross-structures have not been identified within the Cobar Goldfield, either in this study or previously. The northeast-trending Sandy Creek Fault was inferred from seismic studies (Glen et al., 1994), and while it may have controlled basin architecture, there is no indication this fault propagated through overlying Cobar Basin strata. Likewise, there is no evidence similar such structures were responsible for the previously described bedding flexures located along the major faults. The bedding flexures do not extend beyond the immediate environs of the associated fault zones, as might be expected were they related to northeast-trending structures.

Finally, many of the deposits in the Cobar Goldfield are located near the base of the Great Cobar Slate (Figure 65), raising the possibility mineralisation was in part controlled by stratigraphy. Great Cobar Slate and overlying Amphitheatre Group may represent a low permeability cap that allowed fluids in the underlying more permeable Chesney Formation to become over-pressured. Mineralisation then formed in response to fault-zone rupture of the seal and resultant fault-valve behaviour along the active fault zones (Stegman; 2000; e.g. Sibson et al. 1988; Cox 1995; Schaubs & Zhao, 2002). Great Cobar Slate forms the footwall to the New Occidental deposit, and Great Cobar Slate caps the deposit in its hanging wall (Figure 26). A similar relationship is evident at the Peak and Perseverance deposits where mineralisation is focussed in the hanging wall of the Peak Shear immediately beneath Great Cobar Slate (Figure 25). The relationship is less obvious at the New Cobar and Chesney deposits where mineralisation is contained entirely within Great Cobar Slate, although uppermost Chesney Formation crops out nearby.

In conclusion, deposits in the Cobar Goldfield are focussed in high-strain zones along the major reverse faults where subtle, long wavelength bedding flexures have created localised zones where angles between the strike of bedding and D_1 structures are relatively large. Such angles also favour formation of parasitic folds. The flexures are interpreted to have formed in the early stages of formation of the Chesney-Narri Anticline in response to strain heterogeneities caused by interference of those folds with synchronous reverse slip on D_1 faults like the Great Chesney Fault and Peak Shear. There also appears to be a stratigraphic control on mineralisation in the Goldfield. Deposits tend to be preferentially developed in

fault zones bound by Great Cobar Slate or within Chesney Formation immediately stratigraphically beneath Great Cobar Slate.

Figure 65: Simplified geology of the Cobar Goldfield showing interpreted bedding trends about the Great Chesney Fault and Peak Shear.

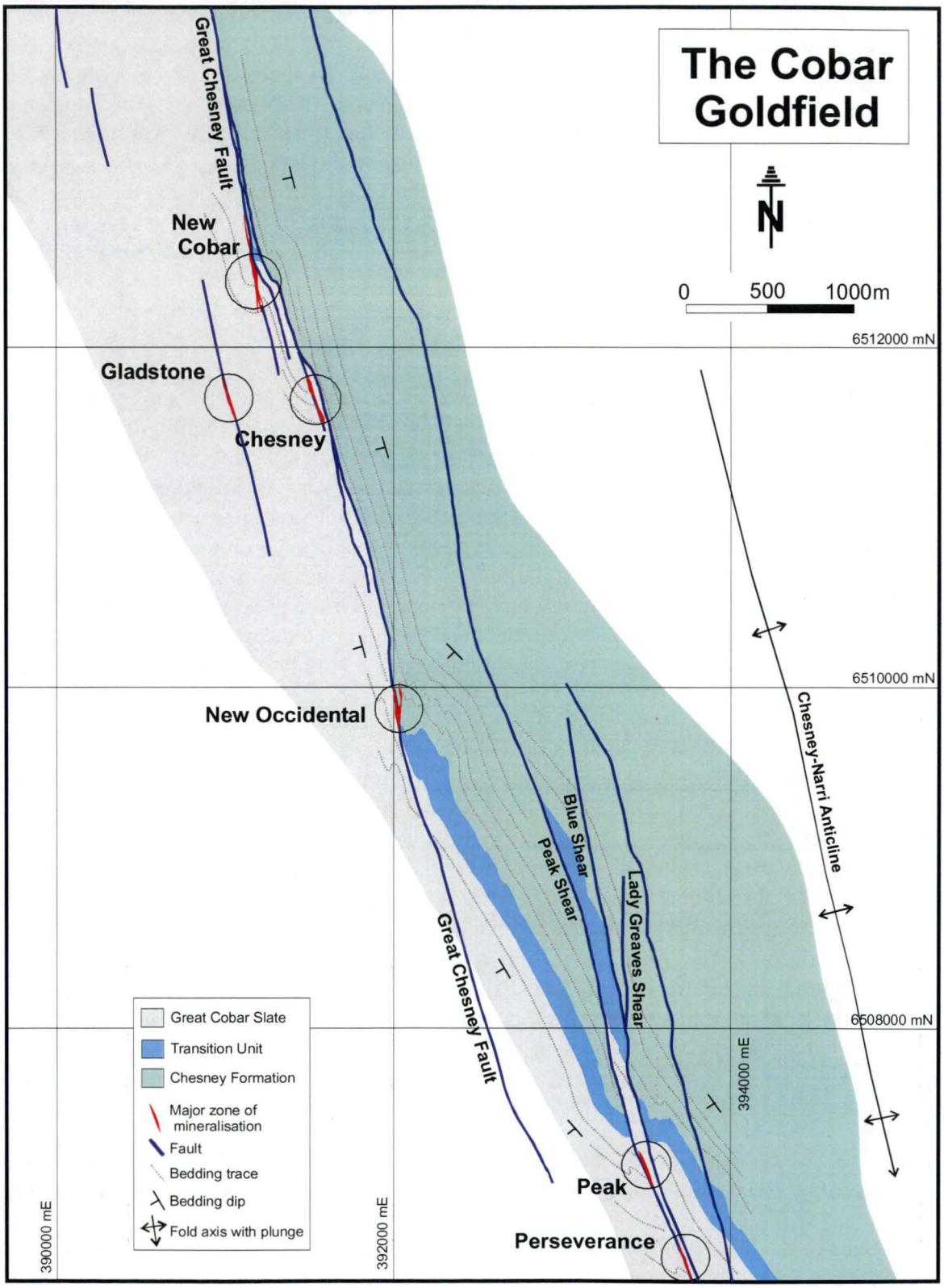

Why are deposits elongate in the direction of the sub-vertical stretching lineation and why do high-grade ore shoots also plunge sub-vertically rather than sub-horizontally?

Cox et al. (2001) argued strike-slip faulting will produce dilational jogs with a sub-vertical orientation, that is, parallel to the plunge of individual deposits and internal high-grade shoots and lenses, whereas reverse dip-slip faults will produce sub-horizontal dilational jogs in the plane of the fault zone (Figure 66). As a consequence, high-grade shoots in steeply dipping reverse fault zones have a sub-horizontal or gently dipping orientation, lying in the plane of cleavage but plunging orthogonal to the stretching lineation and sense of shear displacement (Sibson; 2001; Robert & Poulsen, 2001). However, a sub-horizontal control on the distribution of high-grade gold mineralisation is not evident in the New Occidental deposit or in other deposits in the Cobar Goldfield (Mullholland & Rayner, 1961; Glen, 1987a; Hinman, 1992; Lawrie & Hinman, 1998; Stegman & Pocock, 1996; this study).

Figure 66: Orientations of dilational jogs in contractional and wrench tectonic regimes (from Cox et al. 2001).

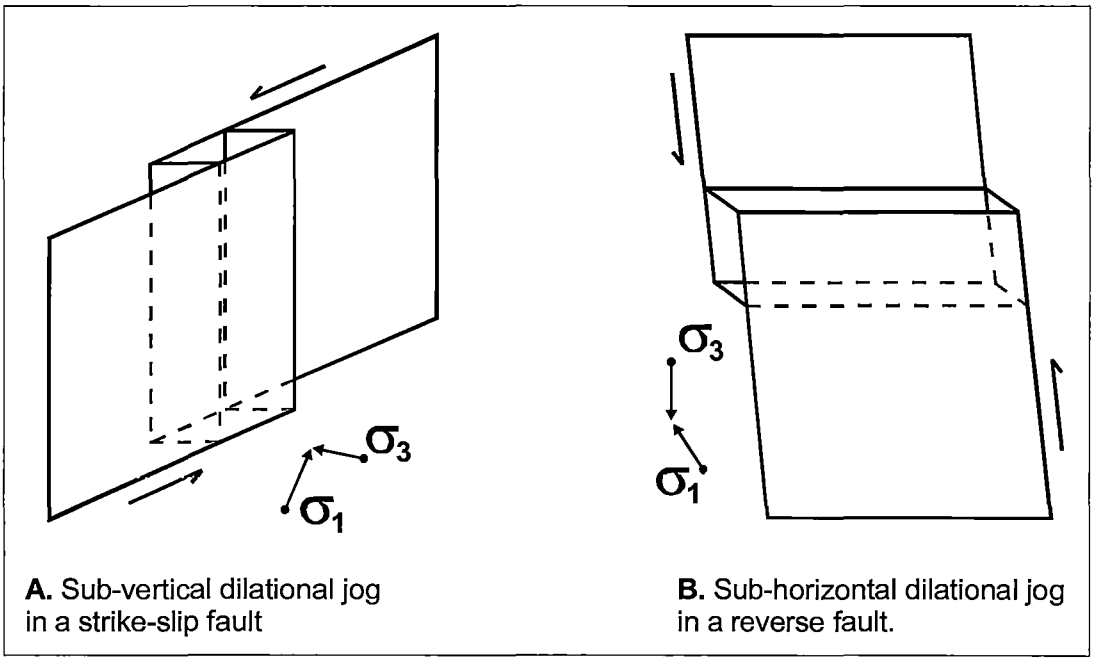

A. Sub-vertical dilational jog in a strike-slip fault

B. Sub-horizontal dilational jog in a reverse fault.

Three alternate models for formation of sub-vertically oriented orebodies and high-grade ore shoots in reverse faults are suggested:

1. **Large-scale slip and subvertical extension of an original sub-horizontally oriented dilation.** Whilst initial dilation in a reverse fault will have a sub-horizontal orientation, continued sub-vertical extension associated with fault slip will stretch that dilation sub-vertically, creating shoots and deposits with an overall sub-vertical orientation (Figure 67a).

2. **Dilation around more gently dipping sections of fault planes.** Reverse slip on a steep dipping fault will create elongate relatively narrow zones of dilation around more gently dipping fault sections (Figure 67b).

3. **Dilation above subtle flexures in the trace of fault planes.** Reverse slip on a steep dipping fault will create elongate zones of dilation above irregularities in the fault plane, including subtle flexures or pertubations in the fault plane (Figure 67c).

The New Occidental deposit, with a vertical extent of >1200m, is undoubtedly the most vertically continuous orebody in the Cobar Goldfield. It formed in a fault zone (Great Chesney Fault) with a sub-vertical displacement of >1500m. In contrast, other deposits in the Cobar Goldfield, like the Peak and New Cobar deposits, are associated with reverse faults with much smaller sub-vertical offsets (of the order of only 200–300m). While those deposits are elongate in a sub-vertical direction, they are not as vertically continuous as the New Occidental deposit, suggesting the vertical extent of deposits in the Goldfield and intensity of sub-vertical extension during deposit deformation is directly related to the magnitude of fault offset.

Figure 67: Mechanisms for creating sub-vertically oriented dilation in a reverse fault zone.

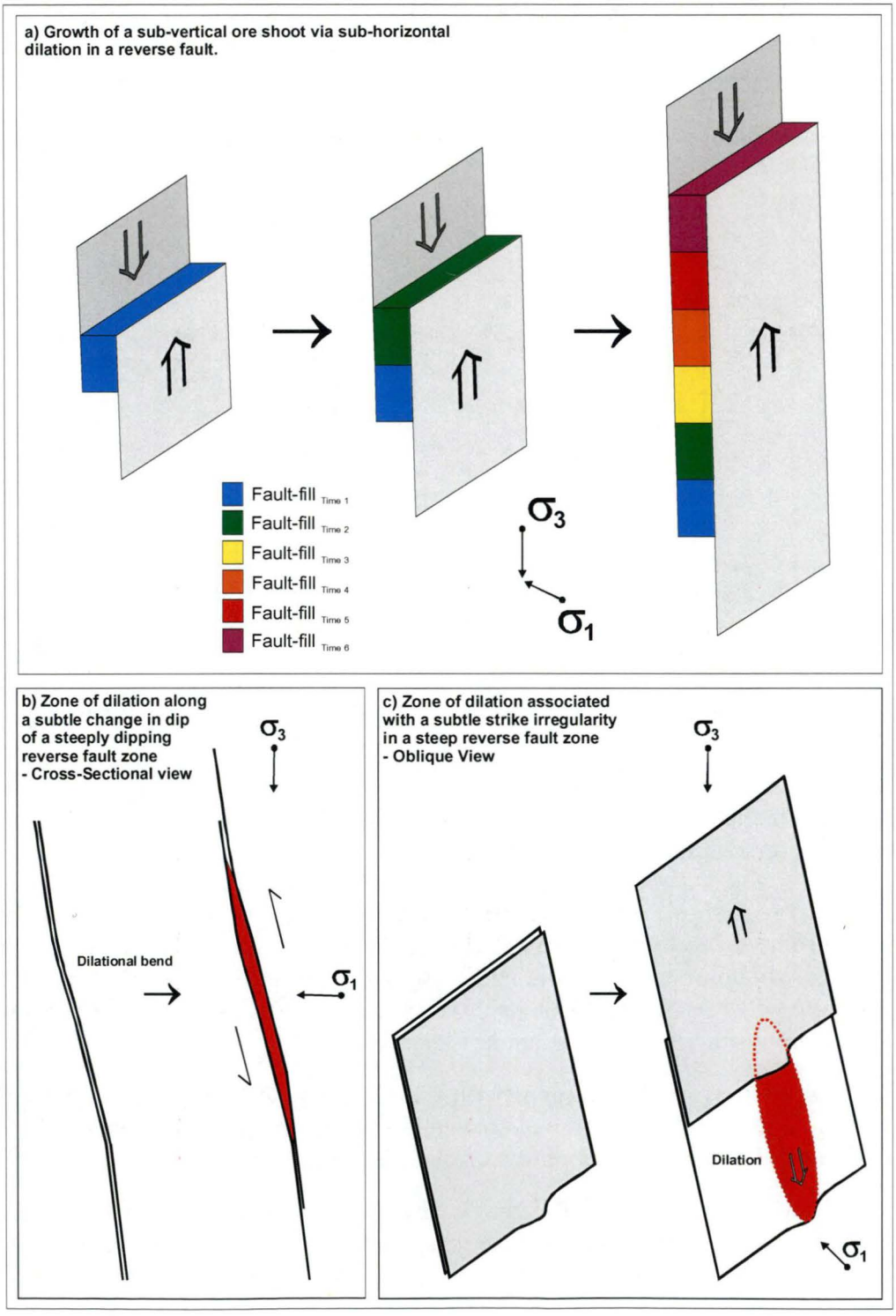

The dip of the Great Chesney Fault does not appear to vary in the vicinity of the New Occidental deposit. While the orientation of the Great Chesney Fault is not constrained beneath the deposit, it appears unlikely the New Occidental deposit formed in response to dilation about a more gently dipping section of the fault. Some variation in the strike of the Great Chesney Fault is evident in vicinity of the New Occidental deposit, particularly where the Albion Fault intersects the Great Chesney Fault, and the perturbation in the trace of the fault may have created some sub-vertical dilation during reverse fault slip. In contrast, the New Cobar deposit may have in part formed in a dilation associated with a change in the dip of the host fault. Below 500m from surface, the dip of the deposit and associated fault reportedly steepens and the deposit correspondingly thins below this level (Sullivan, 1947). In addition, the traces of the Great Chesney and Fort Bourke Faults are more irregular in the vicinity of the New Cobar deposit. The Peak deposit is located in dilations within the Peak Shear where it refracts around a rhyolite intrusive. The Peak Shear, which is normally sub-vertical to steeply west-dipping, is locally significantly more gently west-dipping around the rhyolite. Mineralisation is best developed in those more gently dipping sections of the shear (Hinman, 1992; Cook et al., 1998). Controls on mineralisation within the Chesney and other deposits in the Cobar Goldfield have not been adequately resolved during this or other studies.

In conclusion, deposits within the Cobar Goldfield appear to be localised about irregularities in fault planes. Relatively subtle changes in dip and strike of the host faults apparently create significant sub-vertically oriented dilation, especially in fault zones characterised by significant vertical displacement. Such irregularities may be difficult to detect, especially when they occur down-dip of mineralisation. In the case of the New Occidental deposit, the very large reverse displacement on the Great Chesney Fault, associated sub-vertical extension, has likely produced the pronounced sub-vertical elongation of both the deposit and of internal high-grade ore shoots. Lesser, but still relatively intense sub-vertical extension is also responsible for the vertical elongation of other deposits in the Cobar Goldfield.

What is the effect of synchronous sub-vertical extension on the geometry of the Cobar deposits?

The New Occidental deposit and internal high-grade ore shoots pinch and swell both vertically and along strike. This appears to be caused by ongoing D_1 reverse slip along the Great Chesney Fault during deposit formation. Sub-vertical extension associated with concurrent fault slip potentially impacts on deposit geometry in two ways:

1. Boudinage of early-formed mineralisation.
2. Creation of new sub-horizontal dilations within early-formed mineralisation.

Mineralised fault-fill deposited in the Great Chesney Fault in the early stages of D_1 deformation was subjected to significant sub-vertical extension as continued shortening of the eastern margin of the Cobar Basin was in part accommodated by slip on the Great Chesney Fault. As a consequence, early-stage mineralisation was likely stretched in a sub-vertical orientation and extensively boudinaged. Subvertical stretching of the early-stage mineralisation would also be associated with shortening of that mineralisation. Subsequent mineralisation potentially formed in dilational sites around and within early-formed boudinaged mineralisation (Figure 68). It is also likely that some of the apparent pinching and swelling of the New Occidental deposit is related to small-scale reverse offsets on conjugate sets of brittle D_2 faults.

Figure 68: Conceptualised effect of ongoing reverse fault slip and subvertical extension on early-formed fault-fill.

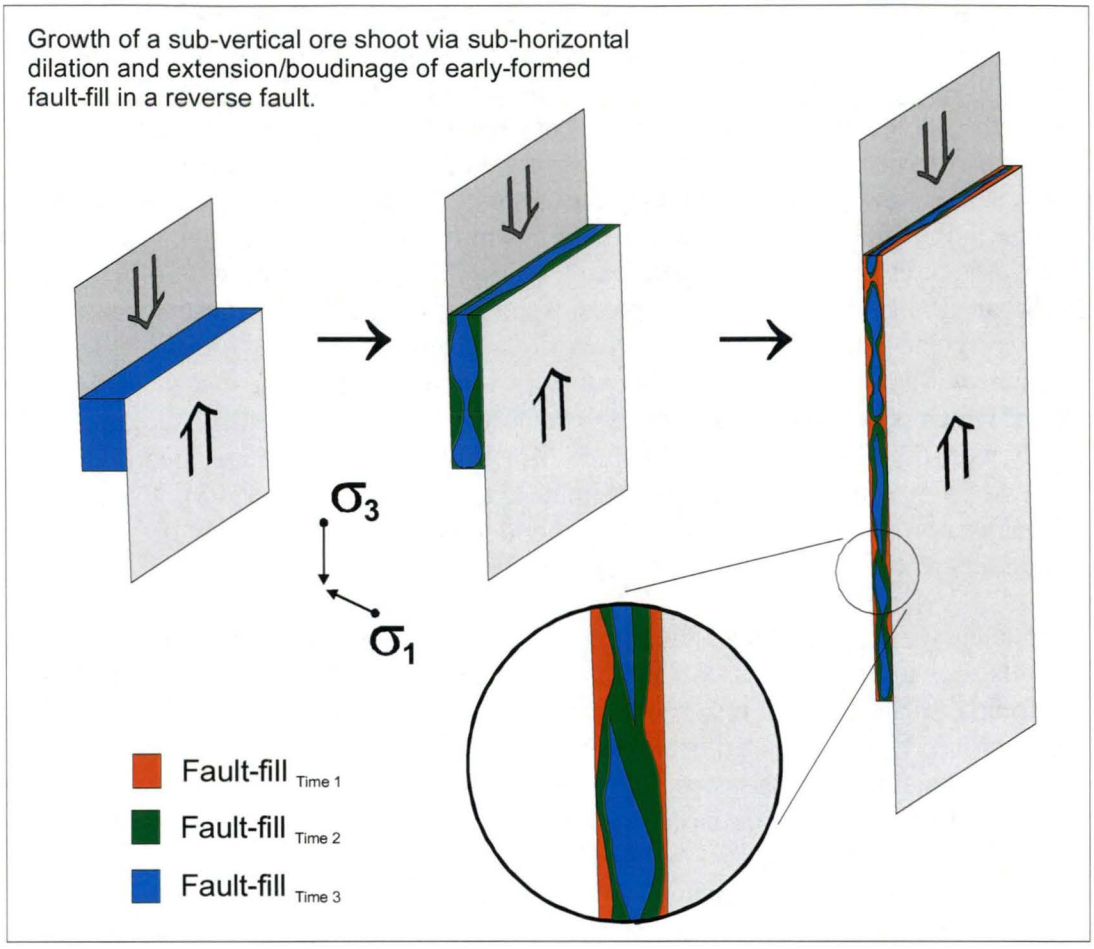

4 QUARTZ VEIN ASSEMBLAGES IN THE NEW OCCIDENTAL DEPOSIT

4.1 Introduction

In many ore deposits, particularly structurally hosted orogenic gold deposits, both the structural timing and style/texture of quartz veins provide important constraints on the mode of ore deposit formation (Robert and Poulsen, 2001). In particular, quartz vein studies have provided important constraints on timing of ore deposition in relation to host structures (Hodgson, 1989; Robert and Poulsen, 2001), controls on deposit geometry (Robert and Poulsen, 2001), likely depths of formation (Fournier, 1985; Dowling, 1989; Dowling & Morrison, 1988; Hodgson, 1989; Vearncombe, 1993; Groves et al., 1995; Hagemann & Cassidy, 2000) and physio-chemical conditions of ore formation (Sibson et al., 1988; Cox, 1995; Cox et al., 2001; Sibson, 2001).

The New Occidental deposit predominantly consists of quartz veins, which, in detail, comprise a complex sequence of veins characterised by variations in texture, morphology, orientation and spatial distribution. Analysis of those quartz veins has been used to resolve the following aspects of deposit formation.

How have quartz veins in the New Occidental deposit formed? Structural studies thus far have broadly characterised the structural evolution of the Great Chesney Fault in the context of D_1 deformation of the eastern margin of the Cobar Basin and have provided a general framework for interpreting the sequence of events leading to the formation and deformation of quartz veins in the deposit. However, the study of quartz veins in the deposit can provide much greater detail on the structural evolution of the New Occidental deposit, including its relationship to the host Great Chesney Fault.

What is the timing of the main stage(s) of ore deposition in relation to the structural evolution of the host Great Chesney Fault? Construction of a sequence of quartz vein stages in the New Occidental deposit can provide a paragenetic and structural framework in which mineralisation in the deposit can be constrained. This framework can also allow the timing of gold-base metal mineralisation in the deposit to be determined, including whether the gold and base metal mineralisation represent temporally discrete stages of mineralisation. The relative timing of gold and base metal mineralisation remains one of the major unanswered questions of ore genesis of Cobar deposits.

What ore deposit geometry, including geometry of high-grade ore shoots, can be inferred from quartz veins in the New Occidental deposit? The 3-dimensional geometry of the New Occidental deposit and of high-grade gold shoots in the deposit has been determined from gold assays of drillcore and underground sampling (Section 3.6). However, gold mineralisation in the New Occidental deposit is extremely fine-grained and generally invisible at hand-specimen scale (Mulholland and Rayner, 1961; Stegman & Pocock, 1996). If gold mineralisation in the deposit can be related to a discrete stage of quartz veins, then the geometry and distribution of gold mineralisation can be determined with increased confidence.

What is the likely depth of deposit formation and deposit style inferred from quartz vein textures and associations of textures in the New Occidental deposit? The textural and morphological features of the vein stages, both individually and collectively, may constrain the depth of formation of the New Occidental deposit. Similarly, those quartz vein textures can be used to determine whether the New Occidental and other deposits in

the Goldfield are epithermal or orogenic/mesothermal in origin (cf. Fournier, 1985; Dowling & Morrison, 1988; Dowling, 1989; Hodgson, 1989; Vearncombe, 1993; Groves et al., 1995).

What physiochemical conditions of ore formation are indicated by quartz vein textures in the New Occidental deposit? Quartz vein textures in the deposit may indicate possible mechanisms for ore deposition, including large-scale fluid pressure fluctuations, phase separation and decreases in temperature (cf. Sibson et al., 1988; Cox, 1995; Sibson, 2001).

Detailed geological logging and thin section examination of project drillcore has been used to identify and texturally characterise discrete stages of quartz veining within the New Occidental deposit. The 3-dimensional distribution of each stage of veining has then been established from drillcore logging. A comprehensive investigation of vein orientations in the New Occidental deposit was also collected as part of the structural characterisation of the quartz vein stages. Vein orientations were routinely recorded during geological logging of evaluation drillcore from the New Occidental deposit. Most of these measurements are from within the New Occidental orebody. In addition, detailed vein measurements have been undertaken on drillcore from NO25–26 for the immediate hanging wall of the orebody.

4.2 Previous Quartz Vein Studies of Cobar Deposits

4.2.1 Quartz Vein Nomenclature

A variety of nomenclature is currently employed to describe the texture, fabric and geometry of quartz veins (Ramsay & Huber, 1983; Cox & Etheridge, 1983; Dowling & Morrison, 1988; Hodgson, 1989; Vearncombe, 1993; Robert & Poulsen, 2001). The terms employed to describe the range of quartz vein textures observed in the New Occidental deposit are tabulated in Table 13. No genetic processes are implied by the use of these textural descriptors, although certain textures and associations of textures can be used to infer conditions of deposit formation.

Table 13: Quartz Vein Descriptors.

Quartz Grainsize	**Description**
Crystalline	Individual crystals are identifiable at hand-specimen scale.
Microcrystalline	Individual crystals are identifiable with the aid of a microscope.
Cryptocrystalline	Individual crystals are not identifiable with the aid of a microscope.
Quartz Textures	(from Ramsay & Huber, 1983; Dowling & Morrison, 1989; Hodgson, 1989; Vearncombe, 1993; Robert & Poulsen, 2001)
Buck	Milky white to vitreous quartz that consists of anhedral or euhedral tightly packed interlocking crystals of highly variable grain size and crystal orientation.
Saccharoidal	Loosely packed crystals which are uniform in grain-size and habit, with little or no matrix. Crystals may be euhedral, subhedral or anhedral, and of vitreous to milky quartz.
Fibred	Aggregate of parallel elongate quartz crystals typically with the crystallographic c-axis oriented at a high angle to the vein wall. Fibres are optically continuous and contain inclusion bands that are parallel to vein walls.
- Cross-fibred	Fibres oriented perpendicular to the vein walls.
- Slip-fibred	Fibred oriented parallel to sub-parallel to the vein walls.

Table 13: Continued.

Comb	Crystalline euhedral to subhedral quartz with crystallographic c-axis oriented perpendicular to the vein wall, cavity or other substrate. Crystals terminate in cavities or open-space, allowing rhombohedral crystal terminations. Uniform crystal size is typical, as is crystal zonation, which is caused by variations in inclusion abundance and contaminant content.
- Coarse	Comb crystals >4cm long with an a-axis to c-axis length ratio of 2:3.
- Medium	Comb crystals 2-4cm long with an a-axis to c-axis length ratio of 1:2 to 1:3.
- Fine	Comb crystals <2cm long with an a-axis to c-axis length ratio of 1:4.
Banded	Vein-parallel bands defined by variable mineral composition, grain form or grain size. Compositional changes include trace element content, solid and liquid inclusion abundance and mineral composition.
- Crustiform	Successive sub-parallel bands of variable mineral compositions, grain form and size. Bands are usually formed sub-parallel to vein walls.
- Colloform	Contorted bands on various scale which comprise successive bands defined by variable composition, grain form and size and combine spherical, botryoidal, reniform and mamillary forms of fine grained quartz.
- Cockade	Concentric bands on all scales developed on isolated fragments of wallrock or earlier formed quartz.
Radiating	Crystal growth from a single point.
- Rosette	Symmetrical radial crystal growth nucleated on fragments of wallrock or earlier formed quartz.
- Plumose	A feathery, radial, but patchy extinction pattern in quartz that has in places been interpreted to reflect the recrystallisation of amorphous silica to chalcedony or quartz.
Laminated	Layered veins comprising quartz bands or laminae that are generally parallel or sub-parallel to vein walls. Laminae may also be defined by subtle variations in the colour or texture of the quartz. Laminae are commonly separated by slivers of foliated wallrock or by millimetre-thick septa derived from the wall rock. They can also be separated by the slip-surfaces that are enhanced by presence of hydrothermal minerals like chlorite and sericite.
- Sheeted	Proportion of wallrock component ≥ vein component.
- Ribbon or book-textured	Proportion of vein component > wallrock component.
Stylolite	Defined by darker zones of relatively insoluble material such as phyllosilicates, clay and carbon, which cut across the interior of the interior of quartz veins. Stylolites are often developed at a slight angle to primary growth bands. They are characterised by a saw-toothed cross-section and are cone-shaped in three dimensions. Generally, the teeth are oriented parallel to the maximum compressive stress. The host minerals tend to be recrystallised with extensive sub-grain development around the stylolites.
Replacement	The deposition of a chemically or structurally new phase in the place of an older mineral, restricted to replacement of rock fragments or minerals within the vein.
- Lattice texture	Silica replacement of bladed calcite crystals.
Oriented mineral growth textures	
Syntaxial	Syntaxial veins are filled with mineral grains that are attached to, and in optical continuity with like mineral grains in the vein walls. Vein growth increments occur in the vein interiors defining an overall growth sense from wall to centre.
Antitaxial	Antitaxial veins are filled with minerals that are different to those in the vein walls. Fibres are usually in optical continuity across the vein and have grown from the vein centre outwards. Vein growth increments occur at the wallrock-vein interface. Veins commonly contain wall-parallel inclusion bands of slivers of wallrock.
Stretched crystal	Stretched crystal veins form like antitaxial veins, but the crack-seal process occurs in the vein interior. Vein growth occurs through one crystal linking the broken fragments of a wallrock crystal on either side of the vein.

4.2.2 Styles of Quartz Veins and Quartz Vein Breccias in Fault Zones

Quartz vein classification schemes were initially developed from detailed studies of quartz vein fabrics (Ramsay, 1980a, b; Ramsay & Huber, 1983; Cox & Etheridge, 1983; Cox, 1987). These schemes were refined through more holistic studies of quartz veins associated with structurally hosted gold mineralisation in a range of orogenic gold deposits (for example, the Val d'Or district, Abitibi belt, Canada – Hodgson, 1989; Boullier & Robert, 1990; Robert et al., 1995; Neumayr et al., 2000; Robert & Poulsen, 2001; the central Victorian gold deposits – Cox et al., 1991; Forde, 1991; Cox, 1995; Ramsay et al., 1998; and the Yilgarn Craton, Western Australia – Vearncombe, 1993; Groves et al., 1995; Hageman & Cassidy, 2000). Quartz vein classification schemes have also been developed from studies of North Queensland gold deposits, which include epithermal, porphyry, slate belt and plutonic environments (Dowling & Morrison, 1988; Dowling, 1989). Whilst early quartz vein classification schemes were based largely on textures and related fabrics (e.g. Dowling & Morrsion, 1989; Hodgson, 1989; Vearncombe, 1993), subsequent schemes attempted to relate vein styles and vein geometries to their structural/tectonic setting (Cox, 1995; Robert & Poulsen, 2001). These latter schemes provide a framework for interpreting the sequence of events leading to the formation and deformation of quartz vein-hosted ore deposits, for determining controls on mineralisation and ore-forming processes and for predicting the geometry of deposits and zones of mineralisation (Robert & Poulsen, 2001).

In contrast to the non-generic classification scheme developed to describe quartz vein textures (Table 13) the classification schemes proposed by Cox (1995) and Robert & Poulsen (2001) for vein types, vein arrays and breccia veins formed in active fault zones are based upon theoretical considerations of fracture opening and infer certain structural and tectonic processes. The Mohr-Coulomb theory of rock failure predicts the formation of extension, oblique-extension and fault-fill veins and dilational breccias in consistent orientations relative to the directions of principal stress, depending on the magnitude of the differential stress and fluid pressure. Within a particular rock unit, the mode of brittle failure is dependant on the differential stress ($\sigma_1 - \sigma_3$) and the tensile strength of the rock (T). In fluid-saturated rock, fluid pressure (P_f) reduces the principal stresses, such that the effective principal stresses $\sigma_{1,2,3}' = \sigma_{1,2,3} - P_f$ (Sibson, 2001; Robert and Poulsen, 2001). The three resultant modes of brittle failure are:

1. Extensional fractures form perpendicular to the least compressive stress (σ_3) when σ_3' equals or exceeds the tensile strength of the rock. This is only possible under conditions of low differential stress when $\sigma_3' \geq -T$ and $\sigma_1' - \sigma_3' \leq 4T$. Therefore, extensional fractures can only form in lithostatic environments under conditions of elevated fluid pressures, where $P_f \geq \sigma_3 + T$ (Sibson, 2001).

2. Shear fractures develop along planes containing the σ_2 axis at approximately 27 $\pm$ 5° to σ_1 when $(\sigma_1' - \sigma_3') > 5.66T$. Shear fractures associated with steep-dipping reverse faults often depart from their optimal gentle dipping orientation in compressional regimes. This typically occurs under conditions of high fluid pressures when pre-existing high angle structures and lithological contacts are re-activated in preference to the formation of new more optimally oriented low angle shear fractures (Sibson et al., 1988).

3. When $4T < \sigma_1' - \sigma_3' < 5.66T$ extensional-shear fractures form along planes containing the σ_2 axis, but at lower angles to σ_1 than shear fractures.

Hydrothermal filling of these three principal fracture-types can result in distinctive (diagnostic) internal textures, which can be used to infer fault zone kinematics and the

orientation of the regional stress field (Ramsay, 1980a). Specifically, where veins have grown by crack-seal mineral growth, the orientation of quartz fibres defines the direction of vein opening and extension (Ramsay, 1980a; Ramsay & Huber, 1983; Sibson, 1986; Sibson et al., 1988; Robert and Poulsen, 2001). The relationship between fracture and quartz vein type and the resultant orientation of quartz fibres is represented in Figure 69.

The principal vein orientations are associated with texturally and geometrically distinctive quartz veins and breccias (Cox, 1995; Robert & Poulsen, 2001). Breccia textures have been used to infer mechanisms of brecciation and associated dilation (Sibson, 1986; Taylor & Pollard, 1993; Forde & Bell, 1994; Robert & Poulsen, 2001). Sibson's (1986) classification scheme of fault zone breccias interprets breccia textures in terms of brecciation processes within active fault zones and relates those processes to the degree of associated dilation (Table 14). The main characteristics of vein and breccia types are summarised in Table 15.

Figure 69: Relationships between rock fracturing and quartz vein formation (Robert & Poulsen, 2001).

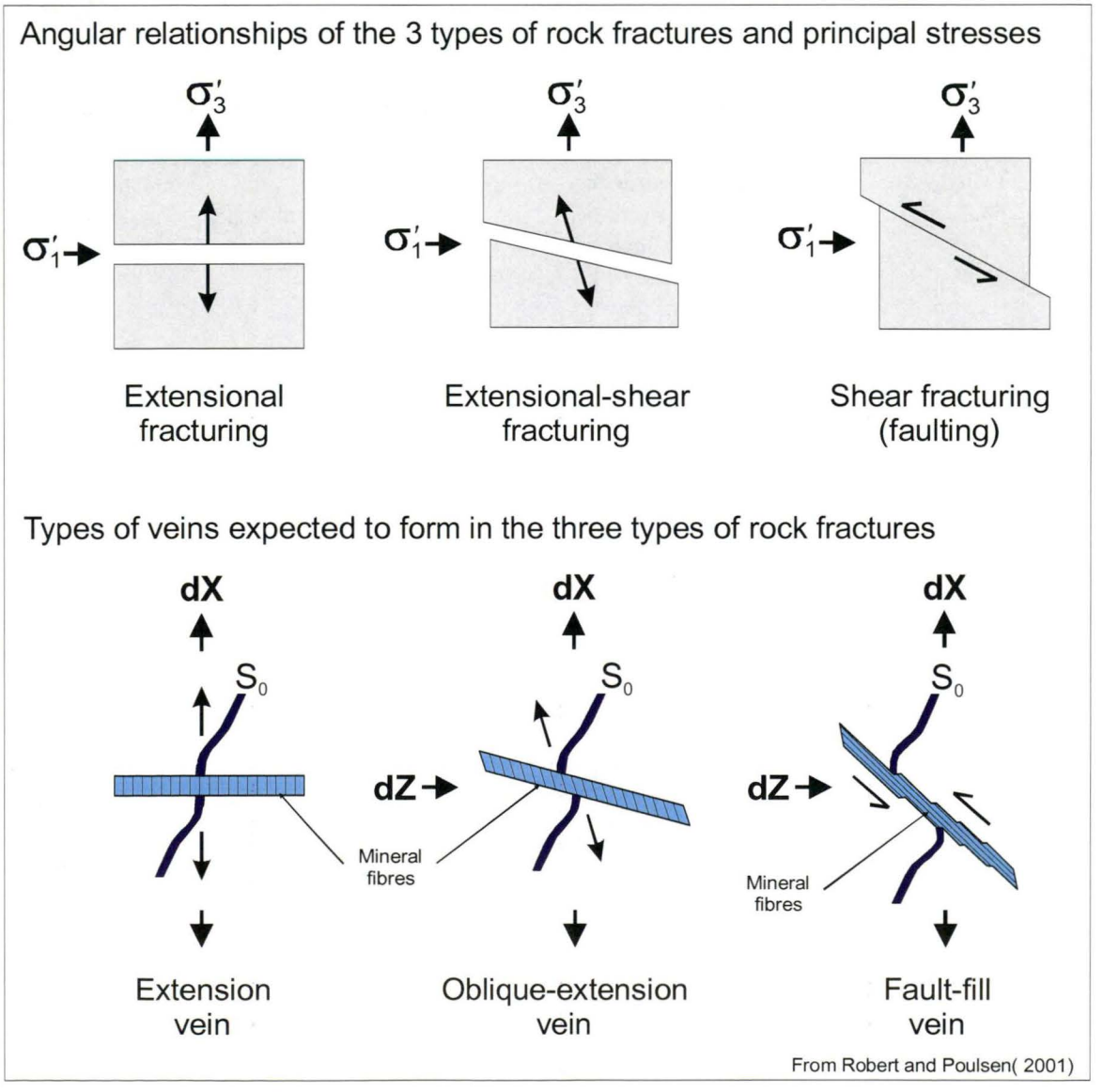

Table 14: Distinguishing characteristics of different fault breccia types (From Sibson, 1986).

	Brecciation Processes		
Distinguishing Characteristics	**Attrition**	**Crushing**	**Implosion**
	Increasing dilation 		
Structural Association	Tabular Principal Slip Surfaces. Major shear separations	Vicinity of antidilational jogs. Minor shear separations	Dilational jogs. Subsidiary extensional fractures
Textural Features	Extensively rolled clasts	Widespread pervasive microfracturing	Jigsaw puzzle textures
Internal Clast Deformation	High	Moderate-High	Low
Clast Size Distribution	Poor to moderately sorted	Poorly sorted	Often well sorted
Clast Composition	Often bimodal or polymict	Often unimodal	Often unimodal
Matrix Composition	Similar to clasts	Similar to clasts (minor hydrothermal)	Often exotic hydrothermal

Table 15: Classification and Main Characteristics of Different Types of Veins and Vein Arrays (Robert and Poulsen, 2001).

Vein Type	**Internal Features**	**Structural Site**	**Geometry**
Fault-fill vein	Laminated structure Foliated wallrock slivers Slip surfaces Fibres at low angle to vein walls	Shear zone or fault zone, especially at bends and dilational jogs Fold limbs and thrusts	Parallel or slightly parallel to host structure Lenticular veins common
Oblique-extension vein	Internal layering Open-space filling Mineral fibres at high (moderate) angle to vein walls Rock bridges Massive/buck quartz	Outside shear zones AC joints in folds At high (moderate) angles to competent units	Planar veins at moderate angle to shear zone Perpendicular (oblique) to fold hinge
Extension vein	Internal layering: multiple openings	Shear zones Competent layers	En echelon planar to sigmoidal veins Stacked planar veins At a high angle to foliation or competent layer
Vein Stockwork	Two or more oblique to orthogonal vein sets of extension or oblique-extension veins Breccia texture developed in intense stockworks	Non-specific but common at vein intersections Preferentially developed in competent lithologic units	Tabular to cigar-shaped zones
Breccia vein:			
Jig-saw (implosion) breccia	Angular wallrock un-rotated clasts in a hydrothermal matrix	Along faults	Parallel to host structure
Fault breccia	Rotated and abraded vein and wallrock clasts in a hydrothermal matrix	Fault or shear zone; component of fault-fill veins	Parallel to host structure

4.2.3 Studies of Quartz Veins in the Cobar Basin

Whilst descriptions of quartz veining in the various deposits in the Cobar basin are incomplete and often cursory, it can be reasonably concluded that most quartz veins in Cobar deposits are interpreted to have formed throughout the main D_1 stage of basin deformation. Veins are variously deformed with early sets strongly folded and/or boudinaged and later sets less deformed. The bulk of quartz veins appear to be steep dipping and cleavage-parallel veins and breccias, although sub-horizontal veins, including early-stage ptygmatic veins, are present in almost all deposits in the Cobar Basin (Robertson, 1974; Glen, 1987b; de Roo, 1989a; Brill, 1989; Hinman, 1992; Jiang, 1996; Stegman & Pocock, 1996; Wilson, 1996; Forster, 1997; Webster, 1999).

A variety of quartz vein textures have been documented including massive, fibrous, comb and colloform textures (Robertson, 1974; Glen, 1987b; de Roo, 1989a; Brill, 1989; Hinman, 1992; Stegman & Pocock, 1996). However, Glen (1987b) and de Roo (1989a) have undertaken the only studies that attempted to distinguish quartz veins in Cobar deposits in terms of whether they formed by open-space fill or crack-seal growth, although Robertson (1974) suggested many of the quartz veins in the various deposits in the Cobar Basin formed in dilational zones. de Roo (1989a) recorded both sub-horizontal and sub-vertical extension veins surrounding the Elura deposit, which he regarded as forming by crack-seal growth. However, he also suggested the massive sulfide pods in the core of the deposit formed in major zones of dilation.

Glen (1987b) identified steeply dipping quartz fibres in both sub-horizontal crack-seal extension veins and sub-vertical fault-fill veins in the Central Area of the Cobar Goldfield (New Cobar to New Occidental area). Fibre orientations are generally sub-parallel to S_1 cleavage and the $L_1{}^1$ stretching lineation. Glen concluded those fibre orientations track a sub-vertical to steep north-plunging fracture opening direction. Glen also concluded that some sub-vertical veins located throughout the New Occidental to New Cobar area that contain sub-horizontal quartz fibres formed during a phase of sub-horizontal extension associated with strike-slip movement on the Great Chesney Fault. Glen (1987b) concluded that the association of predominantly sub-horizontal cross-fibred extensional veins and sub-vertical slip-fibred fault-fill veins in the major deposits of the Cobar Basin, including the New Occidental, Chesney, New Cobar and CSA deposits, indicated the stress field active throughout the Cobar Goldfield during vein formation was predominantly defined by a sub-horizontal principal compressive stress (σ_1) and sub-vertical least compressive stress (σ_3) although σ_1 and σ_3 were both inferred to be sub-horizontal during formation of the steeply dipping extension veins (Glen, 1987b).

The grain size of vein minerals in Cobar deposits ranges from coarsely crystalline to cryptocrystalline (Robertson, 1974; Glen, 1987b; de Roo, 1989a; Brill, 1989; Hinman, 1992; Stegman & Pocock, 1996). A characteristic of Cobar deposits is the presence of cryptocrystalline quartz, referred to as "elvan" (Andrews, 1913; Sullivan, 1947; Mulholland and Rayner, 1961; Binns, 1983; Brooke, 1975; Binns & Appleyard, 1986). It has been considered to be either pervasive silicification of host siltstones and sandstones or discrete quartz veins infilling sites of dilation (Robertson, 1974; Binns, 1983; Binns & Appleyard, 1986). However a consistent paragenetic sequence of quartz vein textures has not been recognised in any of the deposits studied.

4.3 Quartz Vein and Vein Breccia Types in the New Occidental Deposit

Five sequential, overprinting, texturally distinct generations of quartz veins and breccias have been recognised within the New Occidental deposit during this study (Table 16), as

has a minor but discrete fault breccia that cannot be easily assigned to a particular vein stage.

These stages are recognised on the basis of a large number of consistent and repeated macroscopic and microscopic observations of vein and breccia mineralogy, morphology and textures and overprinting relationships between the different vein and breccia stages. Relative age relations have been established from one stage of veining truncating another and from inclusion of fragments of earlier formed quartz vein stages within later-formed stages of breccia veins. Definition of the various stages was complicated by a number of factors. The mode and magnitude of vein opening in the New Occidental deposit has produced a range of primary vein fabrics within a single stage of quartz veining, including crack-seal, open-space fill and breccia textures. Similarly, variable deformation of the early-formed stages of veining during development of subsequent vein stages has meant that individual stages are represented by contrasting undeformed and strongly deformed vein fabrics.

4.3.1 Stage 1 Quartz Veins

Stage 1 quartz veins are the earliest stage of quartz veins recognised in the New Occidental deposit and they are overprinted by all other vein stages. Stage 1 veins are largely restricted to the hanging wall of the New Occidental deposit where they are the dominant vein type (Figure 70). They have been documented over the full vertical extent of the hanging wall of the deposit (~1200m), although they are most strongly developed in the northern part of the deposit, extending northwards beyond the northern limit of the Main lode >1g/t Au mineralised envelope (Figure 70). Stage 1 veins also demonstrate a systematic increase in both vein density and vein thickness towards the centre of the New Occidental deposit. It is also likely that they extended into the core of the deposit. However, subsequent stages of veins in the core of the deposit have largely overprinted those early veins.

Stage 1 veins comprise largely translucent cross-fibred or fine to coarse comb quartz and lesser microcrystalline anhedral buck quartz with minor accessory magnetite and chlorite (Table 16, Figure 71a-f). Rare colloform quartz-magnetite veins, interpreted to be Stage 1 veins, have been observed in the core of the New Occidental deposit (Figure 71g). Veins show no obvious textural zonation over the vertical and horizontal extent of the deposit. They are characterised by minor chlorite wallrock alteration and a thin (0.5–1mm thick) layer of hydrothermal chlorite is commonly developed at the vein margins (Figure 71c, f).

Table 16: Quartz Vein characteristics in the New Occidental deposit.

	Stage 1	Stage 2	Stage 3	Stage 4	Stage 5
	Earliest				**Latest**
Quartz Grainsize	Fine grained crystalline/ micro-crystalline	Crystalline- cryptocrystalline. Fine comb bands are crystalline.	Fine grained crystalline/ micro-crystalline	Microcrystalline - minor localised crystalline	Fine grained crystalline - microcrystalline
Quartz Colour	Translucent - white to clear	Translucent - white to opaque - pale green	Translucent - white	Milky white, lesser translucent	Translucent - white
Associated Gangue Minerals	Magnetite, calcite, chlorite, minor scheelite	Chlorite	Stilpnomelane	Late-stage chlorite, calcite	Calcite
Associated Sulfides		Pb-Bi sulfides and selenides, minor pyrrhotite and chalcopyrite	Pb-Bi sulfides and selenides, minor pyrrhotite and chalcopyrite	Arsenopyrite, possibly chalcopyrite - pyrrhotite	
Relative Proportion of Stages in the deposit	10–15%	30–40%	30–40%	25–30%	<5%
Modal Orientation*	65°/090° *	81°/086° * (Steeply dipping veins only)	81°/086° * (Steeply dipping veins only)	72°/070° * (Steeply dipping veins only)	2°/230° *
Overprinting relationships		- Stage 2 and 3 vein breccias contain wallrock fragments hosting Stage 1 veins and vein breccias - Sub-horizontal veins in Stage 2–3 vein breccias are ptygmatically folded - Stage 1 veins infilled with Stage 2 quartz	- Stage 3 vein breccias contain abundant fragments of Stage 2 quartz and lesser Stage 2 veined wallrock - Stage 2 veins commonly infilled with Stage 3 quartz and Stage 2 cryptocrystalline quartz rimmed by crystalline comb Stage 3 quartz	- Stage 4 veins truncate Stage 1 veins in hanging wall - Stage 4 veins truncate Stage 2 and 3 veins - Stage 4 vein breccias contain abundant fragments of truncated Stage 2–3 quartz breccias - Stage 2 veins reopened and filled with Stage 4 quartz	- Stage 5 veins overprint Stage 1, 2, 3 and 4 veins and vein breccias
Timing	Formed within S_1 cleavage but strongly deformed by S_1: Early - D_1	Formed within S_1 cleavage but strongly deformed by S_1: Syn - D_1	Formed within S_1 cleavage but moderately deformed by S_1: Syn - D_1	Formed within S_1 cleavage but weak-moderately deformed by S_1: Late - D_1	Post main stage D_1

- **Based on measurements in drillhole NO25/26.**

Table 16 Continued: Quartz Vein characteristics in the New Occidental deposit.

	Stage 1	Stage 2	Stage 3	Stage 4	Stage 5
Steeply dipping Veins					
Average Orientation	Moderately to steeply east dipping				
Proportion of Stage	65%	10%	10%	50%	Absent
Vein Shapes	- Irregular lensoidal - Often in steeply dipping arrays of en echelon veins, individual veins dipping less steeply	Irregular lensoidal	Irregular lensoidal	- Irregular lensoidal to planar - Often in steeply dipping arrays of en echelon veins, individual veins dipping less steeply	
Vein Dimensions	0.1–5cm width 1–5m long	2–50cm width 1–5m long	0.5–5cm width 1–5m long	2–300cm width 1–20m long	
Textures	- Cross-fibred fine comb to anhedral buck - Rosette and cockade - Saw-toothed growth bands parallel to vein walls - Rare crustiform /colloform banded - Rare stylolites - Common boudinage	- Crustiform /colloform banded - Cockade with vugh infill	- Fine to coarse comb - Weak colloform banding - Cockade/rosette with vugh infill	- Laminated and ribbon-textured with chlorite septa - Planar growth bands - Stylolites - Slip-fibred to minor cross-fibred - Massive buck to localised euhedral	
Mineral Growth Orientation	Orthogonal to vein walls (~sub-horizontal)	Orthogonal to vein walls (~sub-horizontal)	Orthogonal to vein walls (~sub-horizontal)	Variable steep-dipping (parallel to S_1 cleavage)	
Location	Hanging wall (with rare remnants of crustiform /colloform banded veins in the centre of the deposit)	Core of deposit	Core of deposit	Throughout deposit environs but concentrated in the footwall and hanging wall (locally) of the deposit	
Origin	Open-space filling fault-fill veins	Open-space filling fault-fill veins	Open-space filling fault-fill veins	Crack-seal fault-fill veins	

Table 16 Continued: Quartz Vein characteristics in the New Occidental deposit.

	Stage 1	Stage 2	Stage 3	Stage 4	Stage 5
Gently dipping Veins					
Average Orientation	Gently east dipping				
Proportion of Stage	5%	10%	10%	10%	100%
Vein Shapes	- Lensoidal and ptygmatically folded	- Lensoidal and ptygmatically folded	- Lensoidal and ptygmatically folded	- Planar unfolded to weakly ptygmatically folded - Gently dipping arrays of sigmoidal/ lensoidal veins	- Planar unfolded - Gently dipping arrays of sigmoidal/ lensoidal veins
Shortening (-ϵ) (inferred from ptygmatically folded veins)	- Maximum 70% in Stage 1 veins from hanging wall of deposit (mean = 50%) - Maximum 65% in Stage 1 veins in wallrock fragments in Stage 2 vein breccias in the centre of the deposit (mean = 35%)	- Maximum 60% in Stage 2 veins from the centre of the deposit (mean = 55%)	- Maximum 40% in Stage 3 veins from the centre of the deposit (mean = 35%)	- Undeformed throughout the centre of the deposit - Maximum 20% in Stage 4 veins within deposit near footwall Stage 4 vein breccia (mean = 10%)	- Undeformed throughout the deposit
Vein Dimensions	0.1–0.5cm width <0.5m long	1–10cm width 1–2m long	0.5–5cm width 5m long	0.2–10cm width 1–5m long	0.1–1cm width 1–10cm long
Textures	- Cross-fibred	- Ptygmatic folded - Colloform banded	- Weak colloform banded - Cross-fibred	- Strongly cross-fibred - Planar growth bands	- Strongly cross-fibred - Planar growth bands
Mineral Growth Orientation	Orthogonal to vein walls (~sub-vertical)	Orthogonal to vein walls (~sub-vertical)	Orthogonal to vein walls (~sub-vertical)	Orthogonal to vein walls (~sub-vertical)	Orthogonal to vein walls (~sub-vertical)
Location	Hanging wall	Core of deposit	Core of deposit	Throughout deposit environs	Throughout deposit environs
Origin	Both crack-seal and open-space filling extension veins	Largely open-space filling extension veins	Largely open-space filling extension veins	Largely crack-seal extension veins with lesser open-space filling extension veins	Crack-seal extension veins

Table 16 Continued: Quartz Vein characteristics in the New Occidental deposit.

	Stage 1	Stage 2	Stage 3	Stage 4	Stage 5
Related Breccia Veins					
Average Orientation	Moderately to steeply east dipping				
Proportion of Stage	30%	80%	80%	40%	Absent
Vein Shapes	Lensoidal and typically pinching and swelling	Lensoidal and typically pinching and swelling	Lensoidal and typically pinching and swelling	Lensoidal, sheet-like with minor pinching and swelling	
Vein Dimensions	10–15cm width 1–10m long >100m high	1–25m width >50m long >300m high	1–10m width >50m long >500m high	1–8m width >50m long >500m high	
Textures	- Jigsaw breccias comprising angular unrotated fragments with high fragment to matrix ratios - Breccia fragments largely undeformed - Rosette and cockade	- Massive and lesser jigsaw breccias of largely chaotic rotated angular fragments with a low fragment to matrix ratio. - Breccia fragments largely undeformed.	- Massive and lesser jigsaw breccias of largely chaotic rotated angular fragments with a low fragment to matrix ratio. - Breccia fragments largely undeformed.	- Fault/shear breccias of stretched rotated strongly cleaved wallrock fragments with a low fragment to matrix ratio	
Mineral Growth Orientation	Open-space filling orthogonal to vein walls and nucleated on fragments	Open-space filling orthogonal to vein walls and nucleated on fragments	Open-space filling orthogonal to vein walls and nucleated on fragments	Open-space filling orthogonal to vein walls and nucleated on fragments	
Location	Hanging wall of deposit	Core of deposit	Core of deposit	Footwall of deposit	
Origin	Implosion brecciation	Mixture of implosion and fault brecciation	Mixture of implosion and fault brecciation	Mixture of implosion and fault brecciation	

Figure 70: Distribution of Stage 1 quartz veins in the New Occidental deposit.

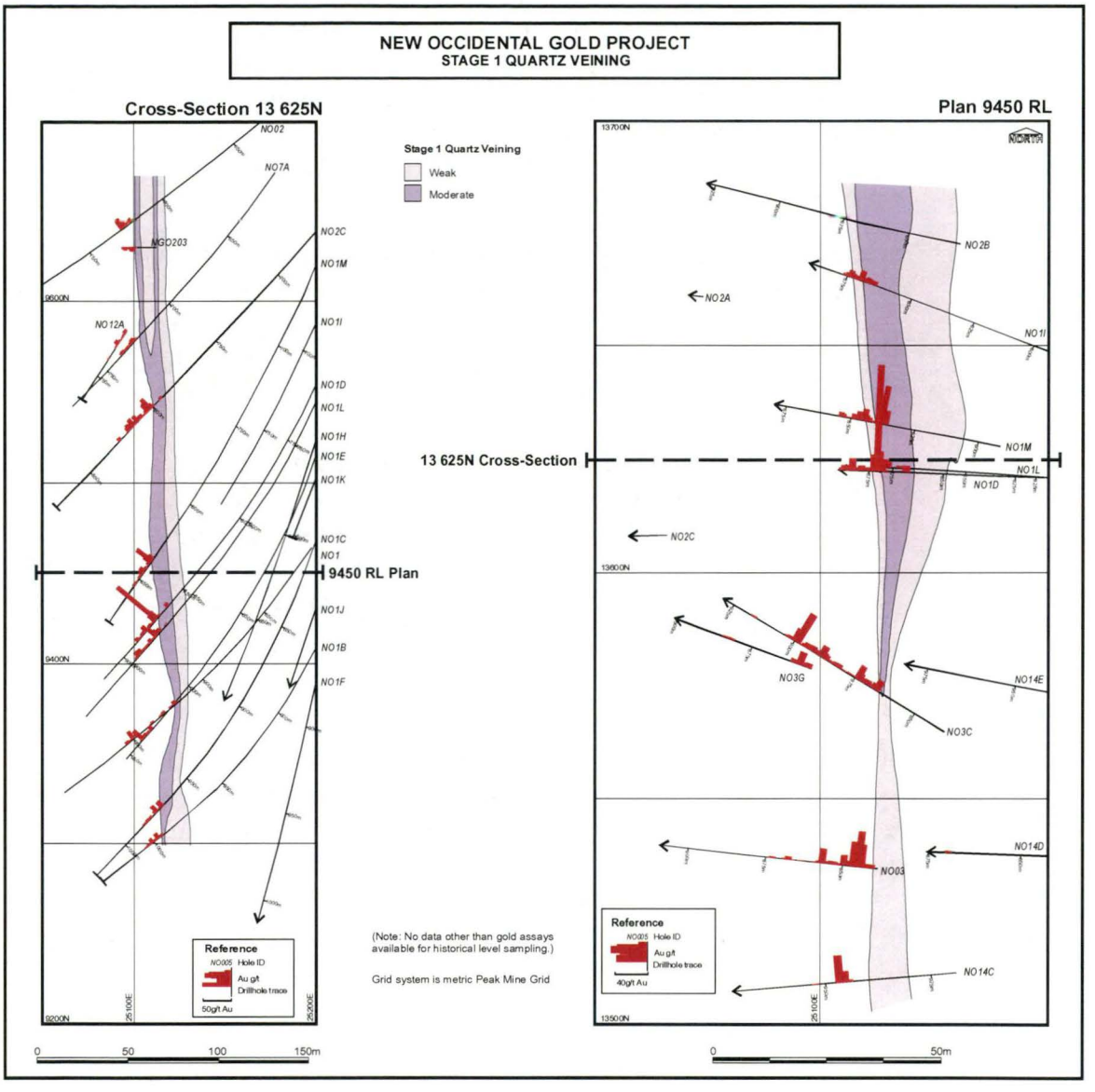

Three styles of Stage 1 veins are present in the New Occidental deposit:

1. **Ptygmatically folded sub-horizontal veins**, which are gently east-dipping and oriented approximately orthogonal to S_1 cleavage (Figure 71a–d). Cleavage is generally axial planar to folds in the veins but also locally transects and offsets folded veins (Figure 71a, d). Where veins have not been distorted by subsequent deformation, they have parallel vein walls and are often cross-fibred with fibres oriented approximately orthogonal to vein walls and parallel to the L_1[1] lineation (Figure 71c). Veins contain well-developed planar or occasionally saw-toothed growth bands defined by subtle changes in quartz grain size and colour and by common trails of chlorite and small wallrock inclusions. Growth bands are typically parallel to vein walls and mirrored across the individual veins.

2. **Moderately to steeply east dipping quartz veins**, which contain coarse comb quartz with quartz crystals usually oriented at right angles to vein walls and at variable high angles to S_1 cleavage (Figure 71b, e, f), although they may contain vuggy cores of rosette and cockade quartz. Zones of cockade quartz

correspond to localised bulges in the vein walls or zones of vein thickening (Figure 71e). Veins contain well-developed growth bands defined by changes in quartz grain size and colour and by common trails of chlorite and small wallrock inclusions. Growth bands are parallel to vein walls and mirrored across individual veins. However, in contrast to the planar form of the growth bands in the sub-horizontal veins, the growth bands in the steep-dipping veins have a saw-toothed shape, defined by rhombohedral crystal terminations on individual quartz grains (Figure 71e, f).

3. **Moderately-steeply east dipping quartz jigsaw breccia veins** (Figure 71h–j) form irregular elongate bodies parallel to S_1 cleavage. The breccias comprise abundant angular, largely unrotated elongate wedges of weakly sheared wallrock fragments (Figure 71h–j), which contain a weak to moderately well developed S_1 cleavage that parallels a more strongly developed cleavage in surrounding wallrock (Figure 71h–j). Breccia veins exhibit many of the microstructural textures characteristic of the associated steeply dipping veins, including saw-toothed growth banding. Quartz crystals have a variable orientation, including radiating crystals developed on vein walls and rosette to cockade textures where quartz crystals have nucleated on internal wallrock fragments (Figure 71h–j). These veins often contain vuggy vein centres that are occasionally filled with calcite (Figure 71i).

Stage 1 sub-horizontal veins often link into steep-dipping veins and vice-versa (Figure 71a, b), indicating veins in both orientations formed synchronously. In several instances, thin steeply dipping cleavage-parallel Stage 1 veins can be traced along strike into more moderately dipping and thicker zones of Stage 1 jigsaw breccia and/or veining. Elsewhere, localised zones of sub-horizontal Stage 1 veins have developed within zones of steeply dipping Stage 1 veins (Figure 71k). In Figure 71k, early steeply dipping quartz-magnetite veins have been dismembered and infilled with sub-horizontal veins consisting of sub-vertically fibred quartz and chlorite. Fibres locally have sigmoidal shapes, indicating a component of shear during vein opening/growth.

Vein growth in both the sub-horizontal and steep east-dipping veins is dominantly syntaxial with successive growth increments occurring in vein interiors. However, vein crystals are not in optical continuity with like minerals in the vein walls. Vein crystals are usually significantly more coarse-grained that the wallrock fragments (Figure 71c, f, k). Inclusion of thin slivers of foliated wallrock and chlorite-rich septa (the latter interpreted to have originally crystallised on the vein walls) at the vein margins indicate a component of antitaxial crack-seal vein growth where growth increments have also occurred along the vein-wallrock interface (Figure 71f).

Folds in ptygmatically folded sub-horizontal Stage 1 veins record shortening strains of up to 70% (mean = 50%), with highest strains in veins closest to the Main lode (Table 16). All Stage 1 veins, irrespective of style, are strongly sheared along planes parallel to S_1 cleavage. Steeply dipping veins are often strongly boudinaged and exhibit common sub-horizontal necking along the veins (Figure 71l). These boudinaged veins record sub-vertical extensions of up to 130% (mean = 80%). Magnetite crystals dismembered during sub-vertical extension and infilled with Stage 1 quartz-chlorite (Figure 71k) record similar sub-vertical extensions (mean = 90%). Some veins contain steeply dipping stylolites at low angles to cleavage that cut across primary growth bands (Figure 71e, m), indicating localised mineral dissolution and concentration of insoluble residue (mainly chlorite) along these dissolution planes. The disjointed and fragmented nature of many of the steep-dipping Stage 1 quartz veins indicates that significant mineral dissolution and shearing has

also occurred along cleavage planes (Figure 71b, m). Similarly, the chlorite-rich septa are strongly foliated, suggesting that they have been the loci for slippage during ongoing deformation (Figure 71f). Stage 1 veins near the centre of the New Occidental deposit are strongly over-printed by subsequent vein stages and fragments of these veins are commonly entrained in Stage 2–3 breccia veins (Figure 71d).

Figure 71: Stage 1 quartz veins and quartz vein breccias from the New Occidental deposit.

a) Stage 1 ptygmatically folded sub-horizontal quartz vein orthogonal to S_1 cleavage and coeval cleavage-parallel Stage 1 quartz veins.

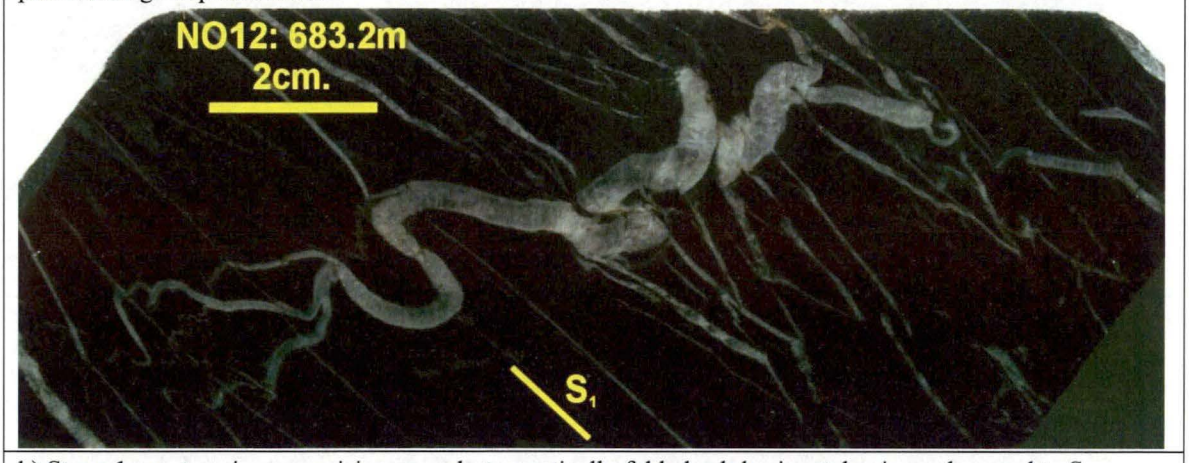

b) Stage 1 quartz veins comprising coeval ptygmatically folded sub-horizontal veins orthogonal to S_1 cleavage and steeply dipping quartz-chlorite veins sub-parallel to cleavage (PPL and XPL).

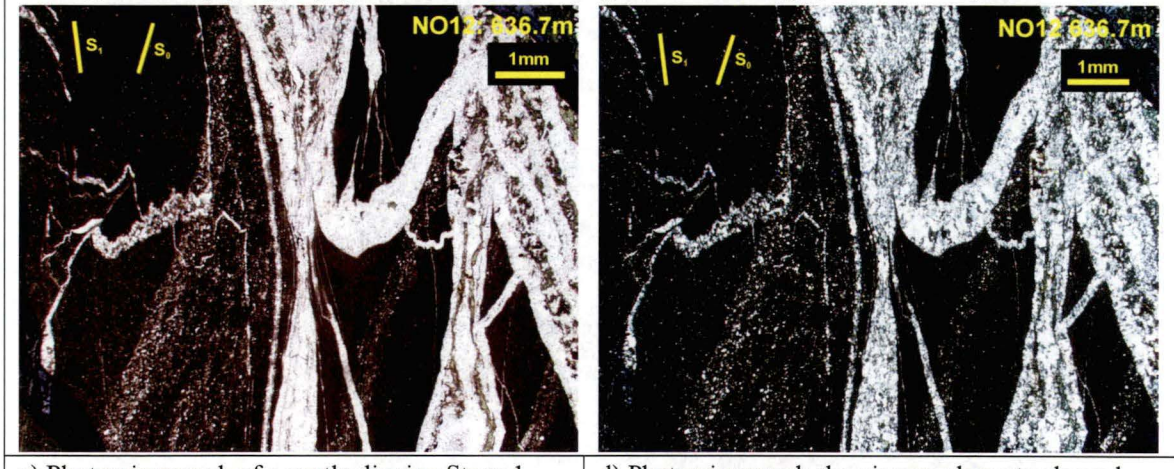

c) Photomicrograph of a gently dipping Stage 1 vein comprising chlorite (green) and magnetite (black) along vein margins and a core of cross-fibred quartz (PPL).

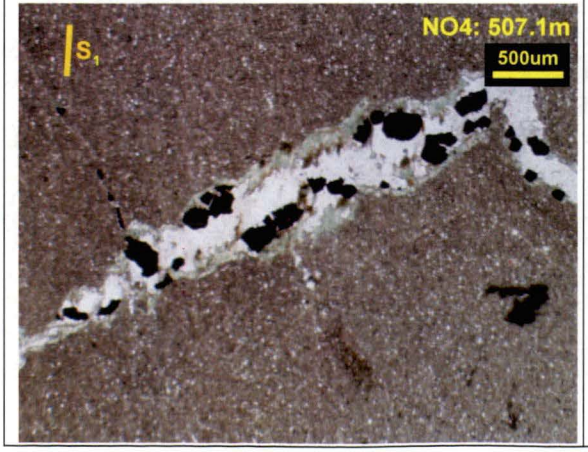

d) Photomicrograph showing an elongate cleaved sandstone fragment in a Stage 2–3 quartz breccia containing a sub-horizontal Stage 1 ptygmatically folded quartz vein (PPL).

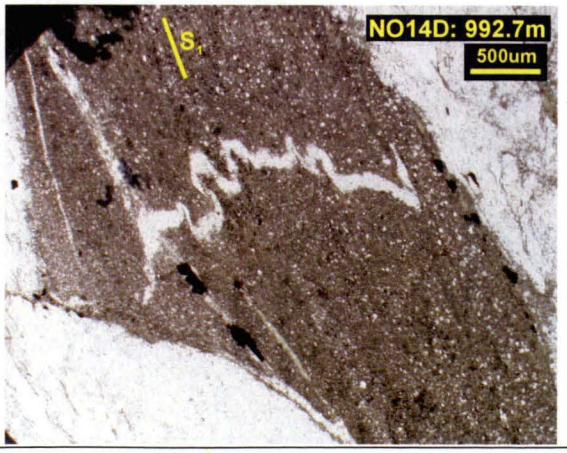

Figure 71: Continued.

e) Stage 1 cleavage-parallel comb quartz veins with trails of chlorite and wallrock inclusions parallel to vein walls. Growth bands are saw-toothed.

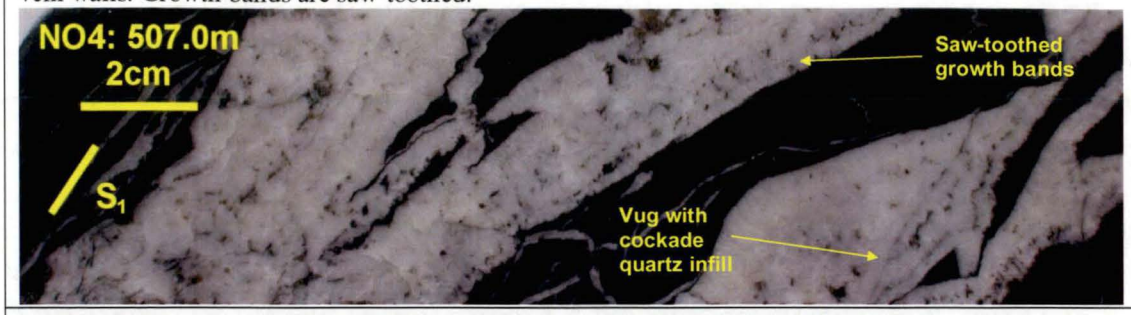

f) Photomicrographs of the margin of a Stage 1 vein showing coarsely crystalline comb quartz containing subtle saw-toothed growth banding. Foliated septa of hydrothermal chlorite (green) have detached from the vein wall during successive antitaxial crack-seal episodes (PPL and XPL).

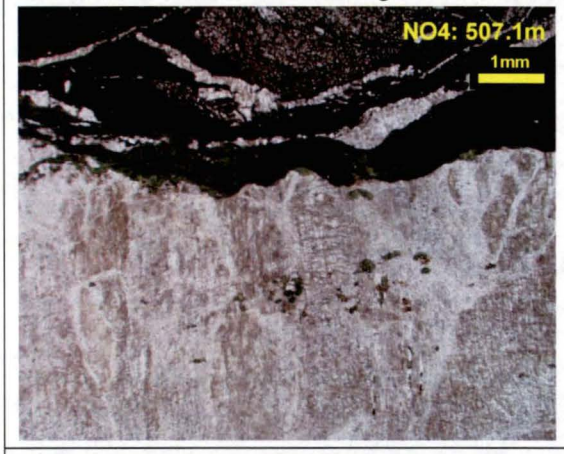

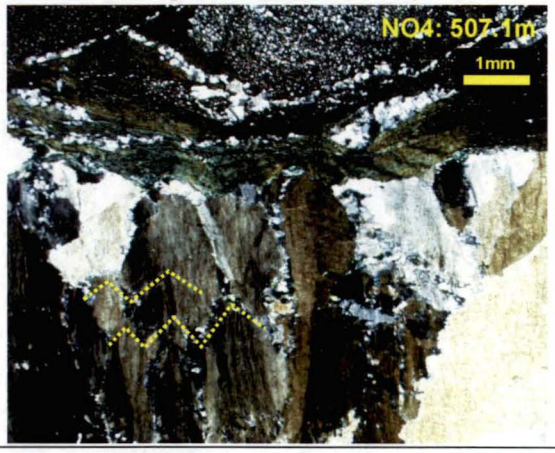

g) Remnant Stage 1 colloform-banded quartz-magnetite veining with chalcopyrite overprint.

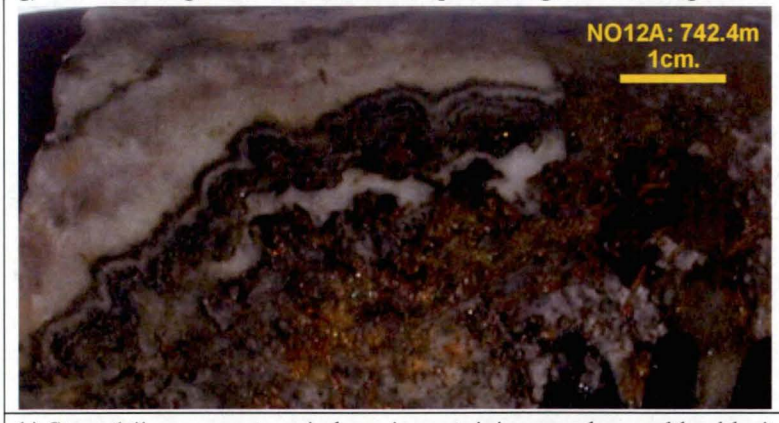

h) Stage 1 jigsaw quartz vein breccia containing angular weakly chlorite-altered sandstone fragments surrounded by cockade fine to coarse comb quartz that has nucleated on the wallrock fragments.

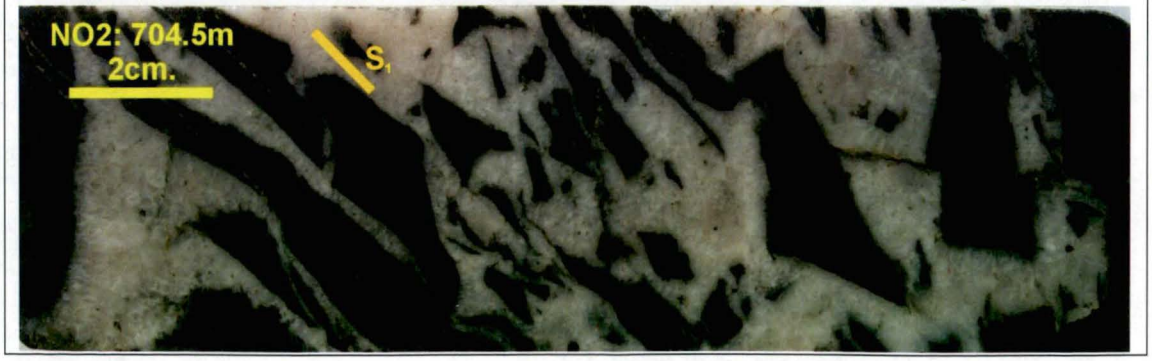

Figure 71: Continued.

i) Stage 1 jigsaw quartz vein breccia with cockade comb quartz fill. Growth bands are concentric about a vuggy more coarsely crystalline centre.

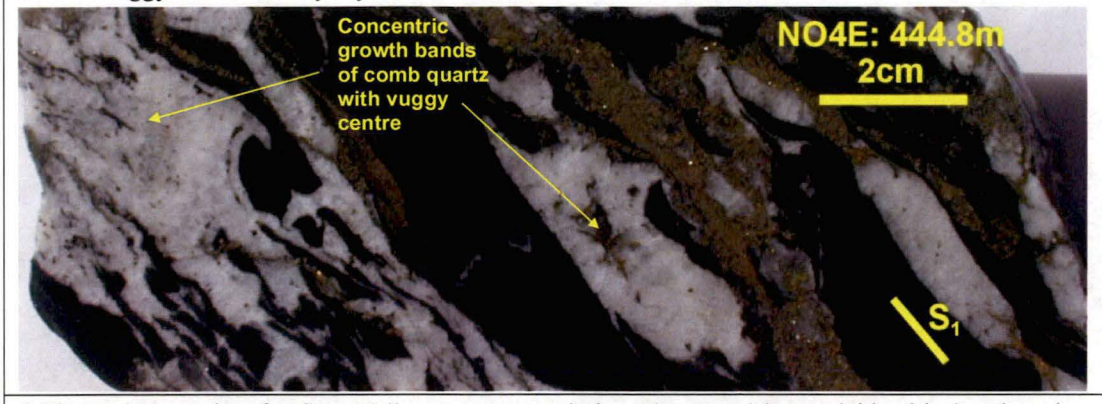

j) Photomicrographs of a Stage 1 jig-saw quartz vein breccia comprising variably chlorite-altered angular sandstone fragments in a comb quartz matrix (PPL and XPL).

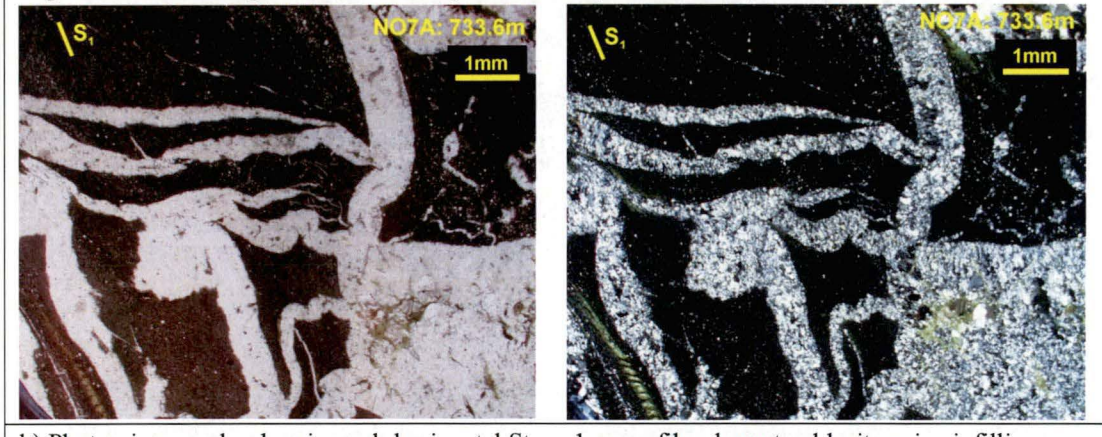

k) Photomicrographs showing sub-horizontal Stage 1 cross-fibred quartz-chlorite veins infilling steeply dipping Stage 1 quartz-magnetite (black) veins in cleaved sandstone. (PPL and XPL).

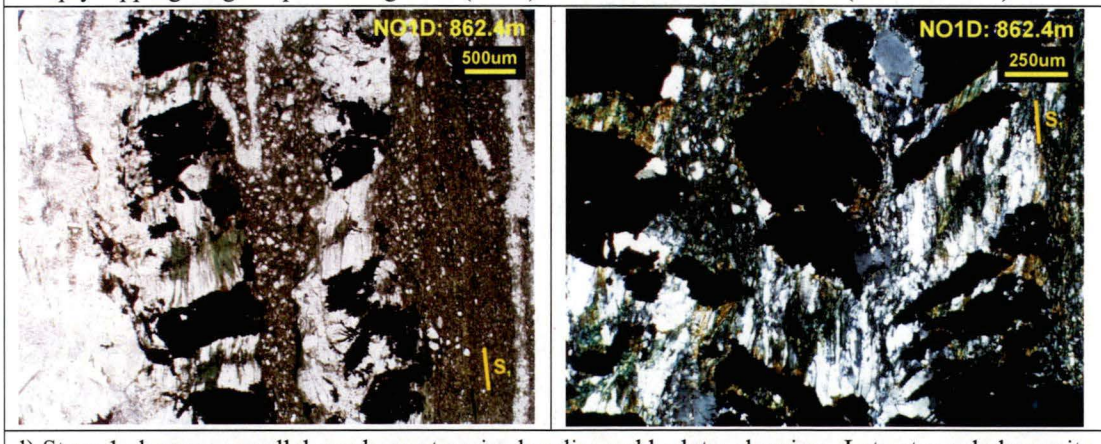

l) Stage 1 cleavage-parallel comb quartz veins boudinaged by later shearing. Late-stage chalcopyrite - pyrrhotite occurs in the necks of boudins.

Figure 71: Continued.

m) Shearing and mineral dissolution of Stage 1 quartz-magnetite veins along planes approximately parallel to cleavage (highlighted by yellow arrows).

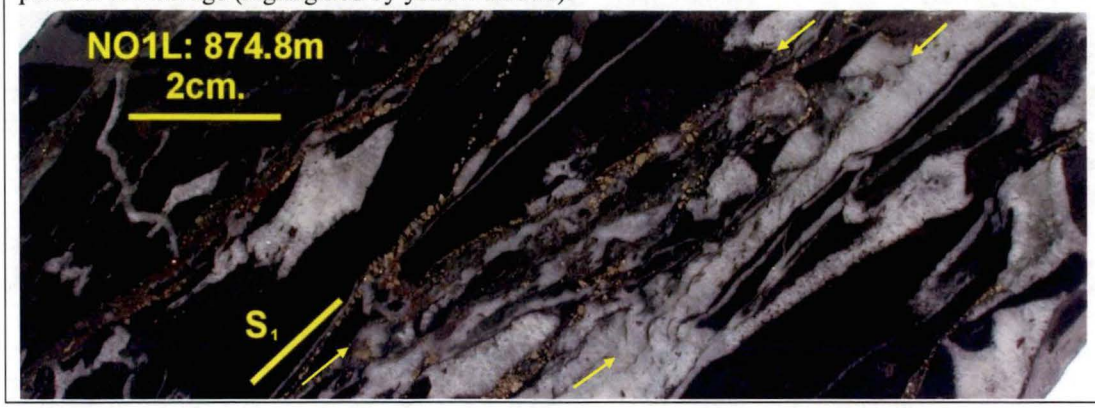

4.3.2 Stage 2 Quartz Veins

Stage 2 veins are largely restricted to the core of the New Occidental deposit and occur over the full vertical extent of Main lode (Figure 72). Minor occurrences of Stage 2 quartz veins are also present in the footwall of the New Occidental deposit (Figure 72) and as infill of Stage 1 veins in the gold-mineralised core of the Albion lode in the hanging wall of the deposit. Stage 2 veins are intimately spatially associated with gold mineralisation, although intensity of veining is not always directly proportional to the tenor of mineralisation (Figure 72).

The core of the Main lode of the New Occidental deposit consists of a relatively intense stockwork or network of steep east-dipping cleavage-parallel Stage 2 quartz veins and vein breccias and lesser ptygmatically folded sub-horizontal quartz veins. The stockwork of composite Stage 2 veins and vein breccias extends over the full strike length and vertical extent of the Main lode of the New Occidental deposit. This zone attains a maximum thickness of approximately 25m in the core of the deposit and narrows along strike to the north and south to less than 5m width. The intensity of veining also diminishes as the width of the stockwork zone decreases. The Stage 2 vein stockwork also decreases in thickness with depth. Based on relatively sparse drilling data, below a depth of approximately 900m from surface it abruptly thins to less than 10m.

Stage 2 veins consist of variably crustiform- to colloform-banded crystalline and cryptocrystalline quartz-chlorite-stilpnomelane with minor very fine-grained accessory pyrrhotite, chalcopyrite and Pb-Bi sulfides and selenides (Table 16, Figure 73). Cryptocrystalline quartz is usually pale green or black in colour, reflecting the presence of intergrown chlorite or stilpnomelane respectively, the latter having replaced chlorite. A crude textural zonation exists within Stage 2 veining through the New Occidental deposit. The most striking examples of colloform banded quartz veining occur in the centre of the deposit less than 900m below surface. At greater depth, and at the southern and northern extremities of the deposit, Stage 2 veins tend to be only weakly banded, the density of Stage 2 veins diminishes and complex breccia veins become less common. Stage 2 veins are associated with moderate to strong green chlorite wallrock alteration.

Figure 72: Distribution of Stage 2 quartz veins in the New Occidental deposit.

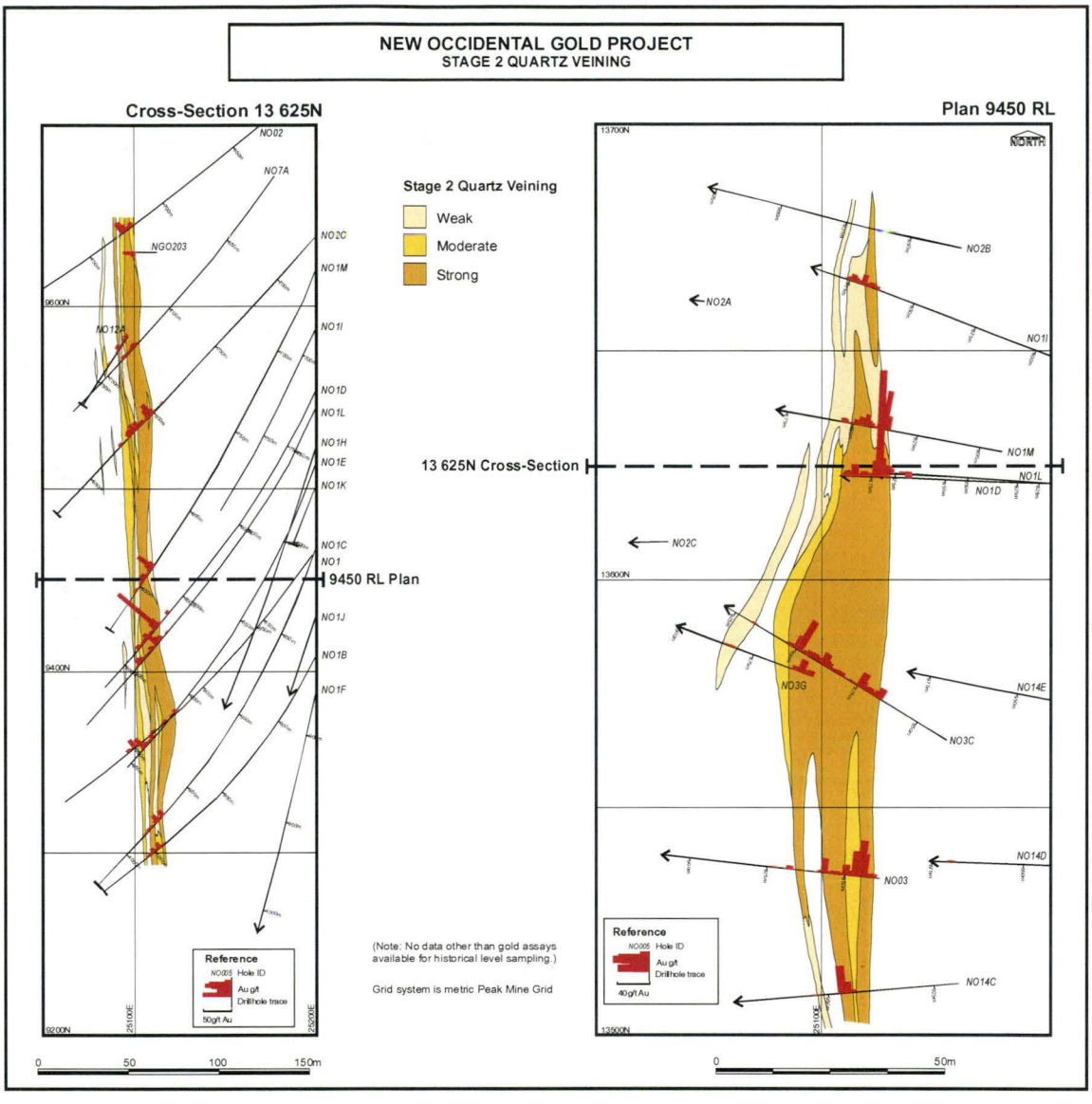

Three main styles of Stage 2 quartz veins are present in the New Occidental deposit:

1. **Ptygmatically folded sub-horizontal veins**, which are relatively rare and restricted to the core of the New Occidental deposit. These veins are gently east-dipping and oriented approximately orthogonal to S_1 cleavage (Figure 73a). S_1 cleavage is both axial planar to and transects and offsets the ptygmatically folded sub-horizontal veins (Figure 73a). Veins consist of colloform banded quartz and are either concentrically zoned with an outer zone of cryptocrystalline quartz and inner zone of crystalline quartz, or comprise separate zones of cryptocrystalline and crystalline quartz (Figure 73a). The concentrically zoned veins have formed by syntaxial vein growth whereas the second type formed by a combination of antitaxial and syntaxial vein growth.

2. **Moderately to steeply east dipping quartz veins and quartz vein breccias,** which form irregular complex vein stockworks sub-parallel to S_1 cleavage and elongate in the direction of L_1[1] lineation. In contrast to Stage 1 veins, discrete steeply dipping Stage 2 veins are relatively uncommon. Where present, many of the steeply dipping Stage 2 veins merge along strike and up/down dip into zones of steeply dipping Stage 2 quartz vein breccias. Stage 2 veins are

characterised by complex internal relations. Within an individual veins early-formed bands of colloform-banded quartz-chlorite are often incomplete and truncated by younger bands of quartz-chlorite. In extreme cases, younger colloform-banded quartz-chlorite is nucleated on fragments of early-formed colloform-banded quartz-chlorite material or wallrock (Figure 73b–f). This pattern of repeated vein truncation and overprinting by successive phases of the colloform-banded quartz-chlorite indicates earlier stages of vein material was repeatedly brecciated during vein growth.

Vein quartz is nucleated on numerous angular, rotated, elongate (in the direction of $L_1{}^1$ lineation), weakly to moderately cleaved and quartz veined fragments of chlorite-altered siltstone and sandstone and also on fragments of early stage vein chlorite (Figure 73b–j). Stage 1 quartz veins include both cleavage-parallel and ptygmatically folded sub-horizontal veins (Figure 73b, f, g, i). The crustiform/colloform-banded quartz veins comprise alternating layers 1–2mm thick pale grey-green cryptocrystalline to microcrystalline quartz, chlorite and lesser stilpnomelane and with occasional interlayers 2–5mm thick crystalline comb quartz (Figure 73b–j). In detail, individual quartz layers consist of initial cryptocrystalline quartz grading outwards into progressively more coarsely crystalline quartz (Figure 73h). Breccia fragments of wallrock or earlier formed quartz are usually also rimmed by cryptocrystalline quartz that grades outwards into more coarsely crystalline quartz (Figure 73b, c, f, I, j). Some vein centres are filled with irregular masses of pale green cryptocrystalline quartz (Figure 73b, d). The relative proportion of cryptocrystalline and crystalline quartz varies and some breccias are filled almost entirely by weakly banded cryptocrystalline quartz (Figure 73e) whilst others are dominated by banded crystalline quartz (Figure 73f).

3. **Moderately east dipping hybrid Stage 1-2 veins**, which comprise an outer rim of Stage 1 quartz veining with a relatively massive Stage 2 cryptocrystalline quartz-chlorite infill (Figure 73k), are present in the core of the Albion lode and in the hanging wall of the Main lode. The Stage 2 vein infill generally only occurs along more gently dipping sections of the Stage 1 veins.

Stage 2 gently dipping veins often link into steep-dipping veins and vein breccias and vice-versa (Figure 73a), indicating veins in both orientations formed synchronously.

Stage 2 veins are variably deformed, ranging from relatively intensely sheared and overprinted by subsequent stages of quartz veining to undeformed. Deformation of some Stage 2 quartz vein breccias has resulted in shortening perpendicular to S_1 cleavage, which has folded colloform bands oriented at high angles to cleavage (Figure 73i). Folds in Stage 2 sub-horizontal veins record shortening strains of up to 60% (mean = 55%), whereas folds in Stage 1 sub-horizontal veins contained in wallrock fragments in Stage 2 quartz vein breccias record shortening strains of up to 65% (mean = 35%) (Table 16).

Figure 73: Stage 2 quartz veins and quartz vein breccias from the New Occidental deposit.

a) Pytgmatically folded gently east-dipping colloform-banded quartz-chlorite Stage 2 vein in strongly sheared Stage 2 quartz vein breccia. The vein exhibits both antitaxial and syntaxial vein growth textures.

b) Colloform quartz breccia comprising angular sandstone fragments containing Stage 1 quartz veins (centre and top) that have been progressively rimmed by cryptocrystalline quartz-chlorite (in part replaced by stilpnomelane) and crystalline quartz. Cavities and vughs are infilled with pale green partly recrystallised cryptocrystalline quartz.

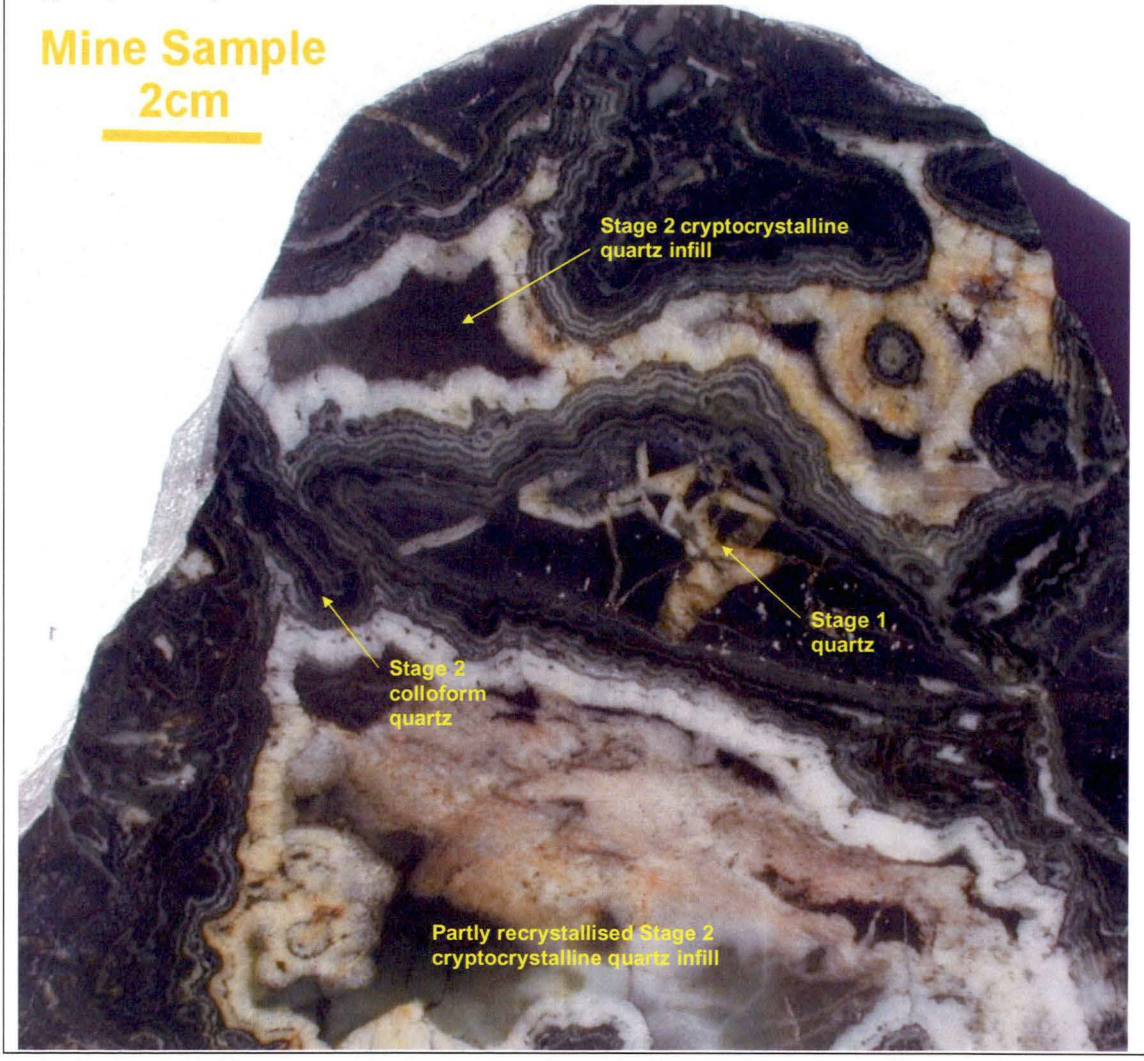

Figure 73: Continued.

c) Quartz breccia comprising quartz veined moderately sheared and cleaved sandstone/siltstone fragments rimmed by colloform quartz-chlorite veins. Chlorite is partly replaced by stilpnomelane. Some colloform quartz rims are truncated by younger stages of colloform quartz-chlorite.

d) Colloform quartz breccia comprising quartz veined sandstone fragments progressively rimmed by colloform quartz-chlorite veins and infilled with pale grey-green cryptocrystalline quartz.

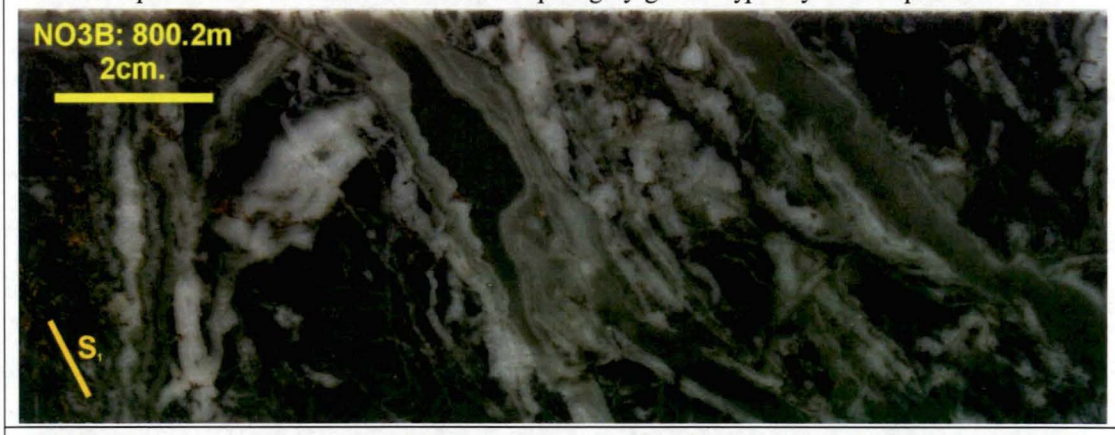

e) Quartz breccia comprising sandstone fragments with a pale grey-green cryptocrystalline quartz infill. Minor more coarsely crystalline Stage 3 quartz veining infills late stage vughs.

f) Stage 2 colloform banded microcrystalline - lesser cryptocrystalline quartz-chlorite veining in footwall breccia. The late-stage crystalline quartz is probably Stage 3 quartz. Veining has nucleated on moderately cleaved siltstone fragments.

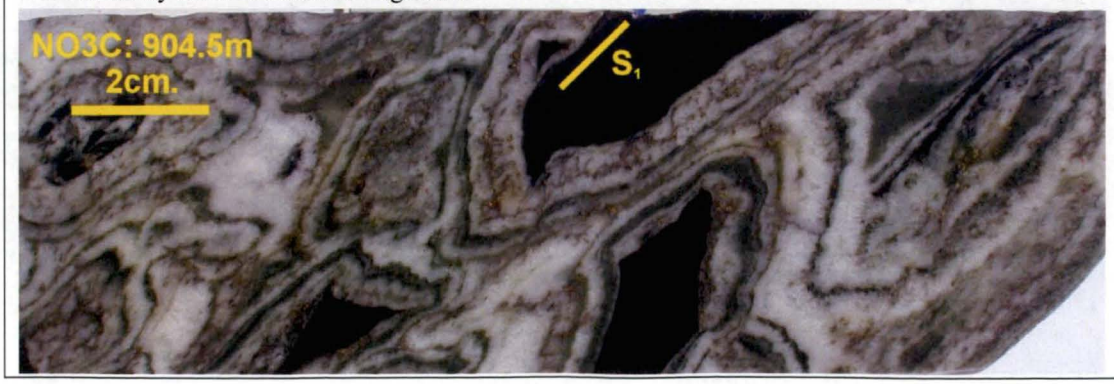

Figure 73: Continued.

g) Photomicrograph of folded Stage 1 quartz vein in a sandstone fragment, rimmed by Stage 2 colloform quartz-chlorite (PPL).

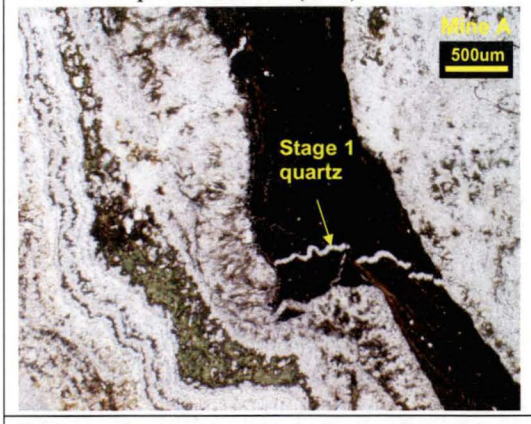

h) Photomicrograph of Stage 2 colloform-banded cryptocrystalline-microcrystalline quartz-chlorite-stilpnomelane (PPL).

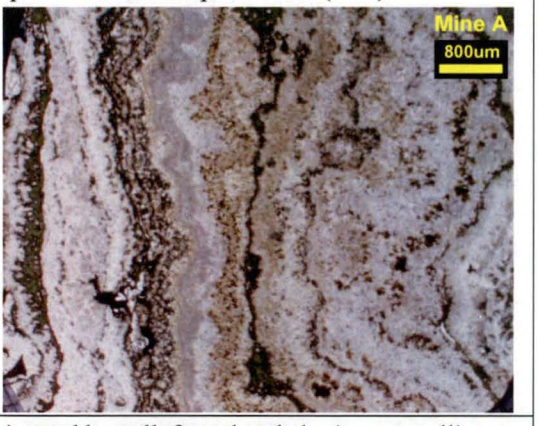

i) Photomicrographs of angular sandstone fragment rimmed by colloform-banded microcrystalline to cryptocrystalline Stage 2 quartz -chlorite. The vein has been folded (PPL and XPL).

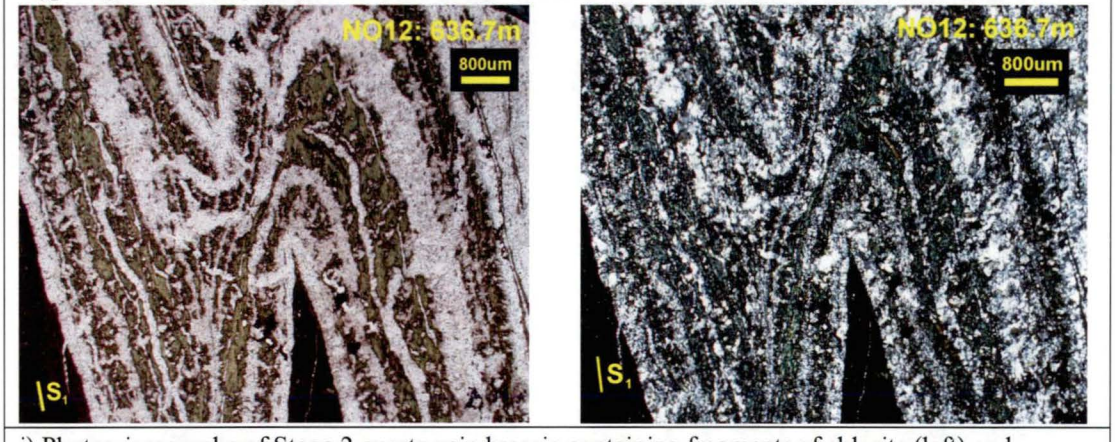

j) Photomicrographs of Stage 2 quartz vein breccia containing fragments of chlorite (left) and sandstone (right) rimmed successively by cryptocrystalline and crystalline quartz (PPL and XPL).

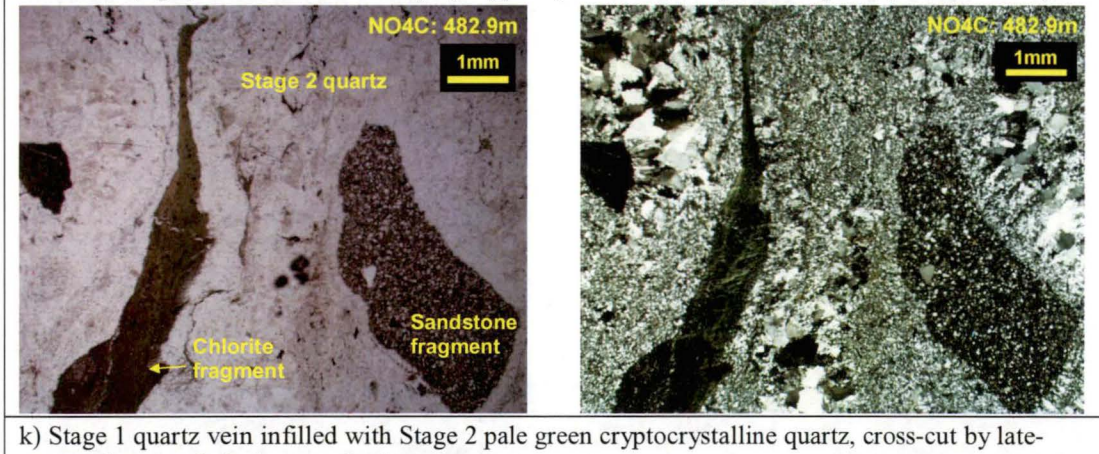

k) Stage 1 quartz vein infilled with Stage 2 pale green cryptocrystalline quartz, cross-cut by late-stage galena – sphalerite - pyrrhotite vein.

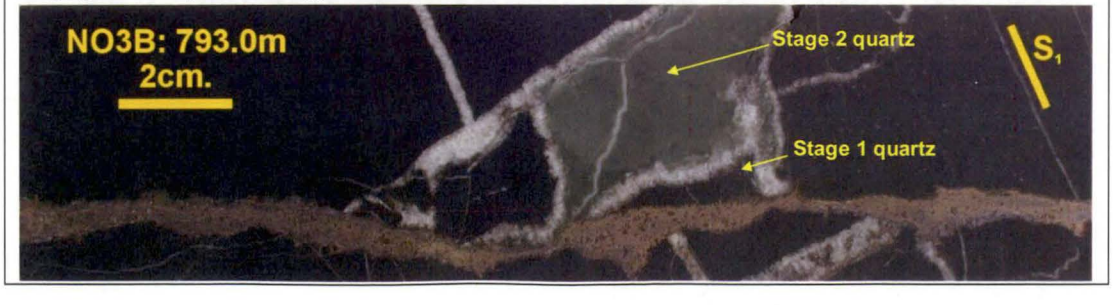

4.3.3 Stage 3 Quartz Veins

Stage 3 quartz veins are restricted to the core and immediate footwall of the New Occidental deposit (Figure 74). They occur over the full vertical extent of Main lode, largely as overprints on Stage 2 quartz veins, in zones of brecciation focussed along the margins of the stockwork of intense Stage 2 breccia veins. The zones of Stage 3 veins collectively define a broad envelope with a shape and overall dimensions similar to that of the Stage 2 breccia vein stockwork. Whilst Stage 2 and 3 veins are closely spatially related, there are zones of Stage 2 vein breccia, mainly in the core of the New Occidental deposit, that do not contain a Stage 3 overprint. Stage 3 veins also demonstrate a close spatial association with gold mineralisation. In contrast to Stage 2 veins, the density of Stage 3 veins appears to be proportional to the tenor of gold mineralisation within the Main lode.

Figure 74: Distribution of Stage 3 quartz veins in the New Occidental deposit.

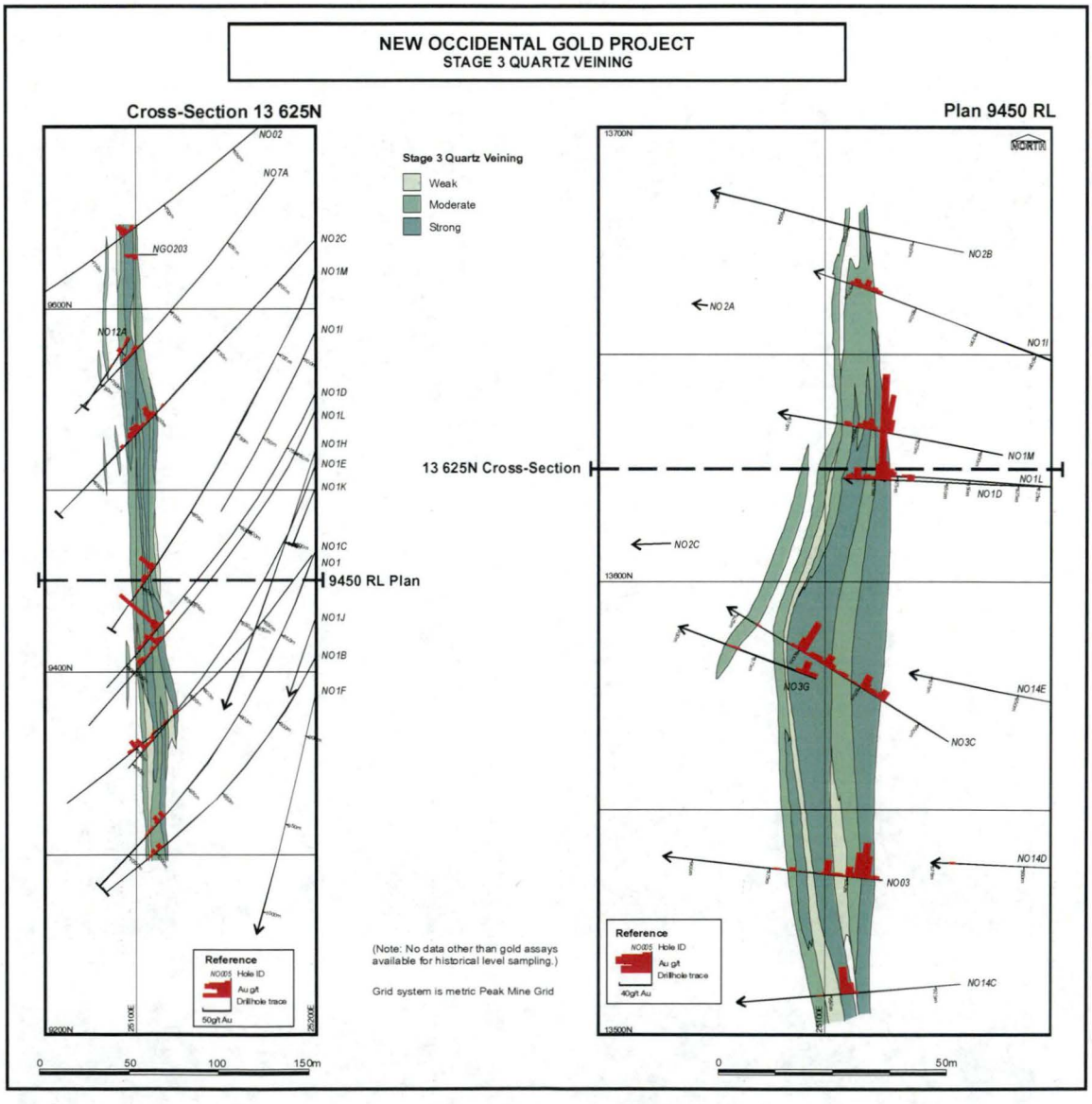

Stage 3 veins typically comprise white, weakly colloform microcrystalline to finely crystalline comb quartz that is intergrown with minor stilpnomelane and lesser chlorite. There is no obvious textural zonation in Stage 3 veins over the vertical and horizontal extent of the New Occidental deposit. Veins are characterised by little or no wallrock alteration or replacement at their margins (Table 16, Figure 75).

Three main styles of Stage 3 quartz veins are present in the New Occidental deposit:

1. **Ptygmatically folded sub-horizontal veins**, which are relatively rare and restricted to the core of the New Occidental deposit. Stage 3 quartz often occurs as syntaxial or antitaxial infills of sub-horizontal Stage 2 veins (Figure 75a–b). Veins are gently east-dipping orthogonal to S_1 cleavage and S_1 cleavage is both axial planar to and transects and offsets the ptygmatically folded veins (Figure 75a–b). Quartz vein fibres are weakly developed and are orthogonal to vein walls. Subtle planar growth bands are present and are parallel to vein walls.

2. **Steeply east dipping quartz veins and quartz vein breccias,** which form vein stockworks sub-parallel to S_1 cleavage and elongate in the direction of L_1^1 lineation (Figure 75c–e). Similar to Stage 2 veins, discrete steeply dipping Stage 3 veins are relatively uncommon and most steeply dipping Stage 3 veins consist of complex quartz vein breccias. Stage 3 quartz vein breccias are characterised by rotated, angular and elongate (in the direction in L_1^1 lineation) clasts exhibiting little or no evidence of attrition or rounding and by relatively high hydrothermal mineral matrix to wallrock clast ratios (Figure 75c–d). The breccias have a relatively strong shear fabric parallel to S_1 cleavage. Clasts consist largely of Stage 2 quartz veins and quartz vein breccias, with rare wallrock-only clasts. The Stage 2 quartz vein breccia fragments often comprise Stage 2 cryptocrystalline quartz rimming wallrock fragments that contain deformed Stage 1 quartz veins (Figure 75e). Breccia matrix consists of cockade and rosette textured comb quartz (Figure 75c–e) and occasionally, intergrown fibrous stilpnomelane (Figure 75c). Vuggy vein centres are common. The breccia matrix contains relatively common growth bands, which are concentrically zoned about vein walls and breccia fragments (Figure 75d). Growth bands have a saw-toothed shape, are approximately 0.5–3mm thick and defined by subtle variations in crystal colour and grain size and by trails of wallrock and stilpnomelane inclusions. Wallrock inclusion trails tend to be concentrated at the margins of the veins.

3. **Steeply east dipping hybrid Stage 2–3 quartz veins and vein breccias**, in which the vein walls are rimmed by Stage 2 cryptocrystalline quartz and the centre of the vein comprises fragments of wallrock and Stage 2 quartz vein breccia in a Stage 3 cockade and rosette textured comb quartz matrix (Figure 75f–g). Fragments of Stage 2 quartz vein breccia incorporated within Stage 3 vein breccia are equivalent to Stage 2 quartz-chlorite rimming vein walls (Figure 75g).

Sub-horizontal Stage 3 veins commonly merge with steeply-dipping veins and quartz vein breccias, indicating veins formed synchronously in both orientations (Figure 75a–b, f). The steeply dipping hybrid Stage 2–3 quartz veins and vein breccias merge along strike and up/down dip with the more common Stage 3 quartz veins/vein breccias.

Overall, Stage 3 veins are less deformed than the preceding quartz vein stages, although they may be intensely sheared and overprinted by subsequent stages of quartz veining locally. Folds in ptygmatically folded Stage 3 sub-horizontal veins record shortening strains of up to 40% (mean = 35%) (Table 16). Where deformed, steeply dipping veins are often boudinaged (Figure 75b).

Figure 75: Stage 3 quartz veins and quartz vein breccias from the New Occidental deposit.

a) Folded sub-horizontal Stage 2 colloform banded quartz-chlorite veining with overprinting Stage 3 veining in the fold axis and in the core of the sub-horizontal Stage 2 vein.

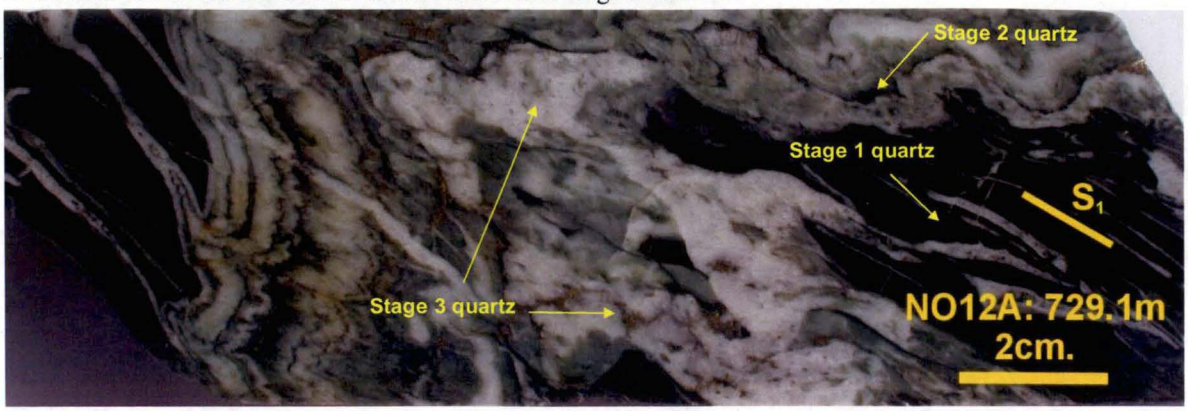

b) Strongly deformed cleavage-parallel Stage 1 quartz veins on the margin of composite steeply dipping and ptygmatically folded sub-horizontal Stage 2–3 quartz veins, the latter comprising an outer rim of Stage 2 cryptocrystalline quartz and an inner core of Stage 3 cockade comb quartz.

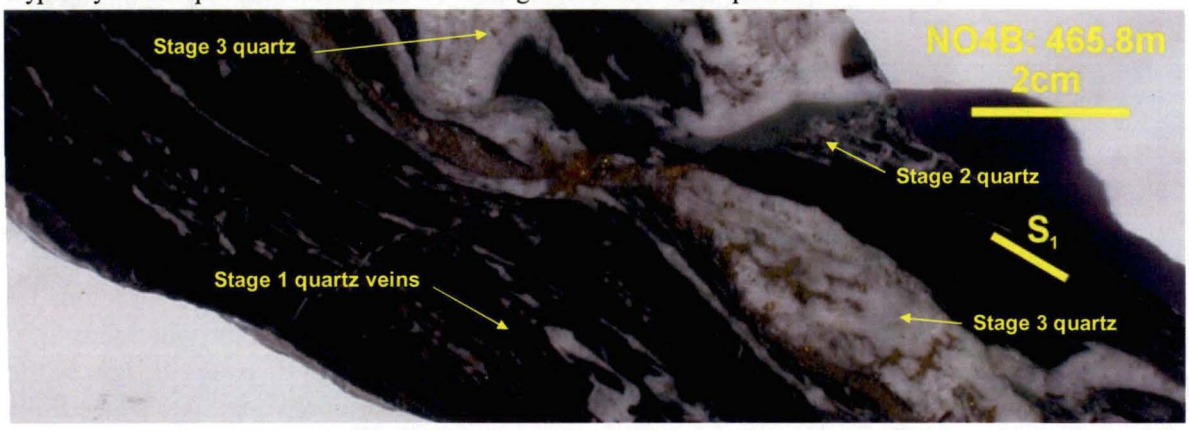

c) Quartz breccia comprising Stage 3 quartz-stilpnomelane veins rimming angular fragments of grey-green Stage 2 cryptocrystalline vein fill.

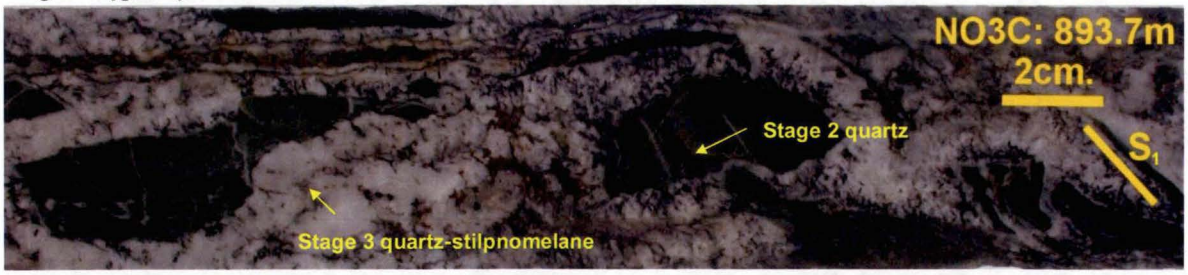

d) Quartz breccia comprising angular wispy fragments of sandstone and grey-green Stage 2 cryptocrystalline veins in a Stage 3 crystalline quartz vein matrix.

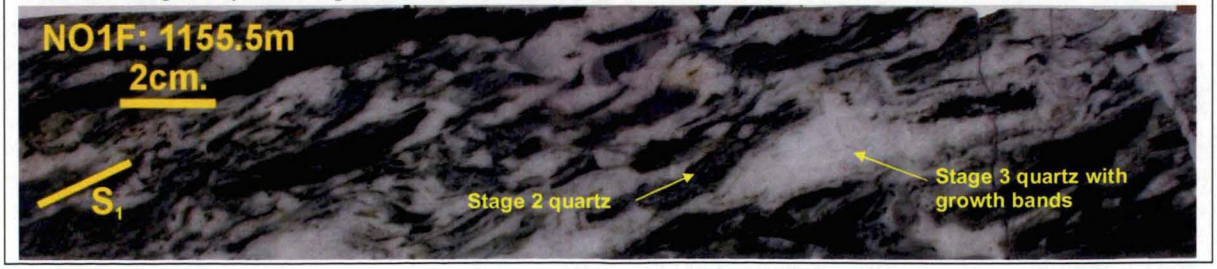

Figure 75: Continued

e) Photomicrographs of quartz breccia comprising fragments of Stage 2 quartz breccia consisting of cryptocrystalline quartz rimming sandstone/siltstone fragments, which contain Stage 1 veins. The breccia matrix comprises coarser grained Stage 3 crystalline comb quartz (PPL and XPL).

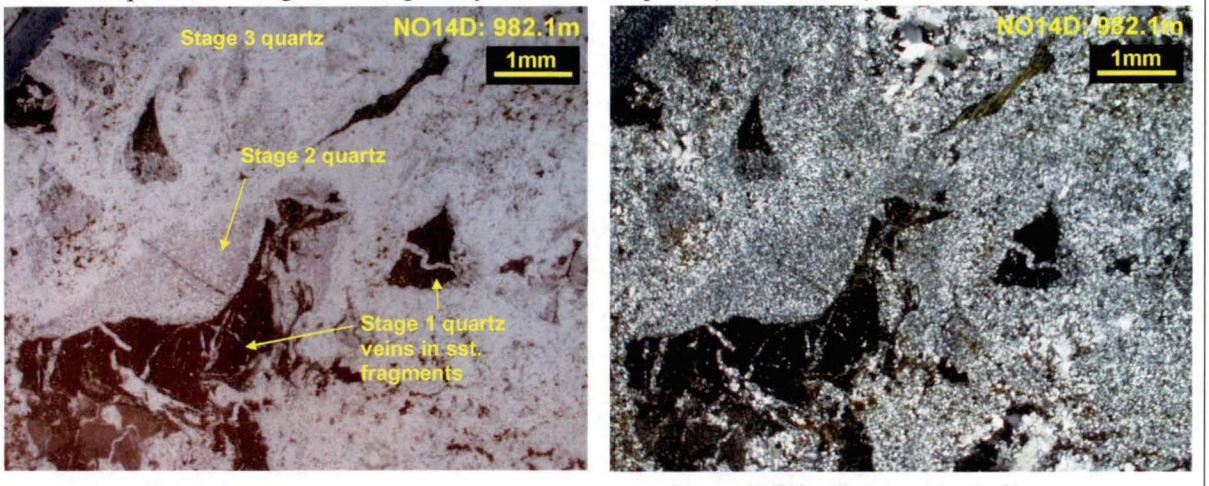

f) Stage 2–3 quartz vein breccia comprising Stage 2 cryptocrystalline quartz infilled with Stage 3 quartz veining nucleated on fragments of wallrock and Stage 2 quartz veining. Minor Stage 4 quartz infills the core of the vein at left.

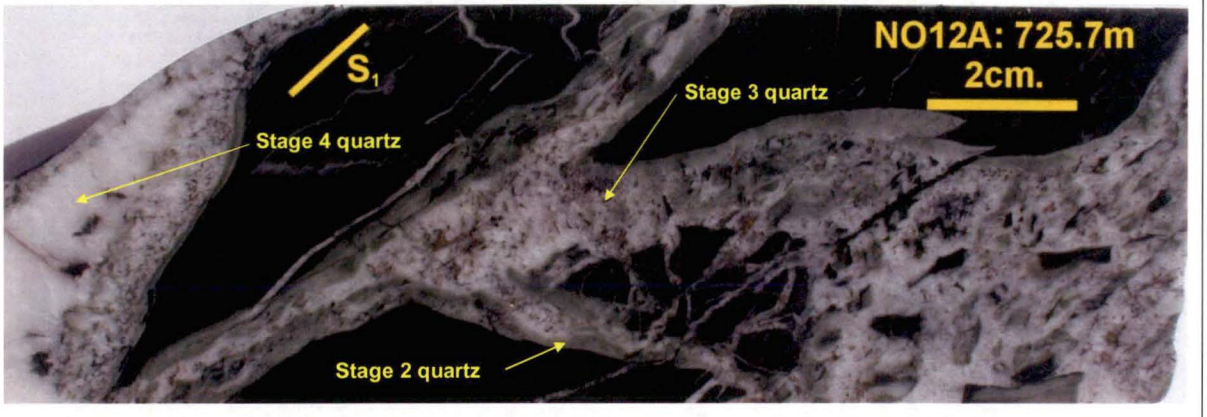

g) Photomicrograph of a hybrid Stage 2–3 quartz vein breccia. The vein wall has been progressively rimmed with Stage 2 cryptocrystalline quartz-chlorite and more coarsely crystalline Stage 3 comb quartz, which contains a fragment of the Stage 2 quartz-chlorite fill (top left). The Stage 2 quartz-chlorite rim contains a siltstone fragment (middle-right) hosting Stage 1 quartz veins (PPL and XPL).

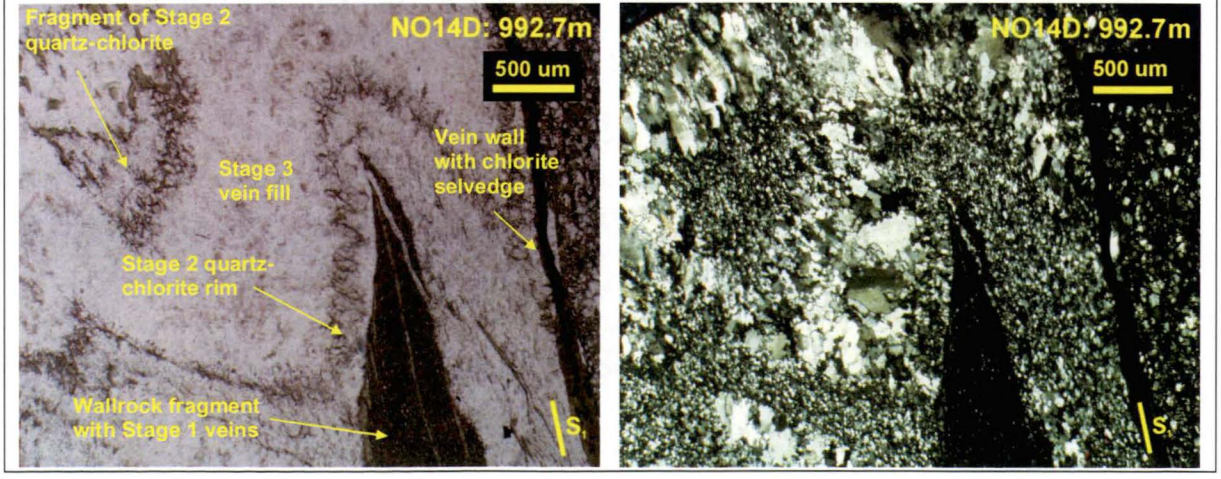

4.3.4 Stage 4 Quartz Veins

Stage 4 quartz veins are concentrated in the footwall of the Main lode of the New Occidental deposit, centred on a prominent strongly developed Stage 4 vein breccia at the footwall contact of the Main lode. An intense stockwork of Stage 4 veins extends outwards from this breccia zone into Great Cobar Slate footwall and to a lesser degree into the core of the New Occidental deposit. Lesser discrete zones of Stage 4 veins are also present in the hanging wall of the deposit and along the hanging wall contact of the Main lode (Figure 76). These veins and vein breccias extend over the full vertical and lateral extent of the New Occidental deposit. Stage 4 veins exhibit little or no spatial association with gold mineralisation in the New Occidental deposit.

Figure 76: Distribution of Stage 4 quartz veins in the New Occidental deposit.

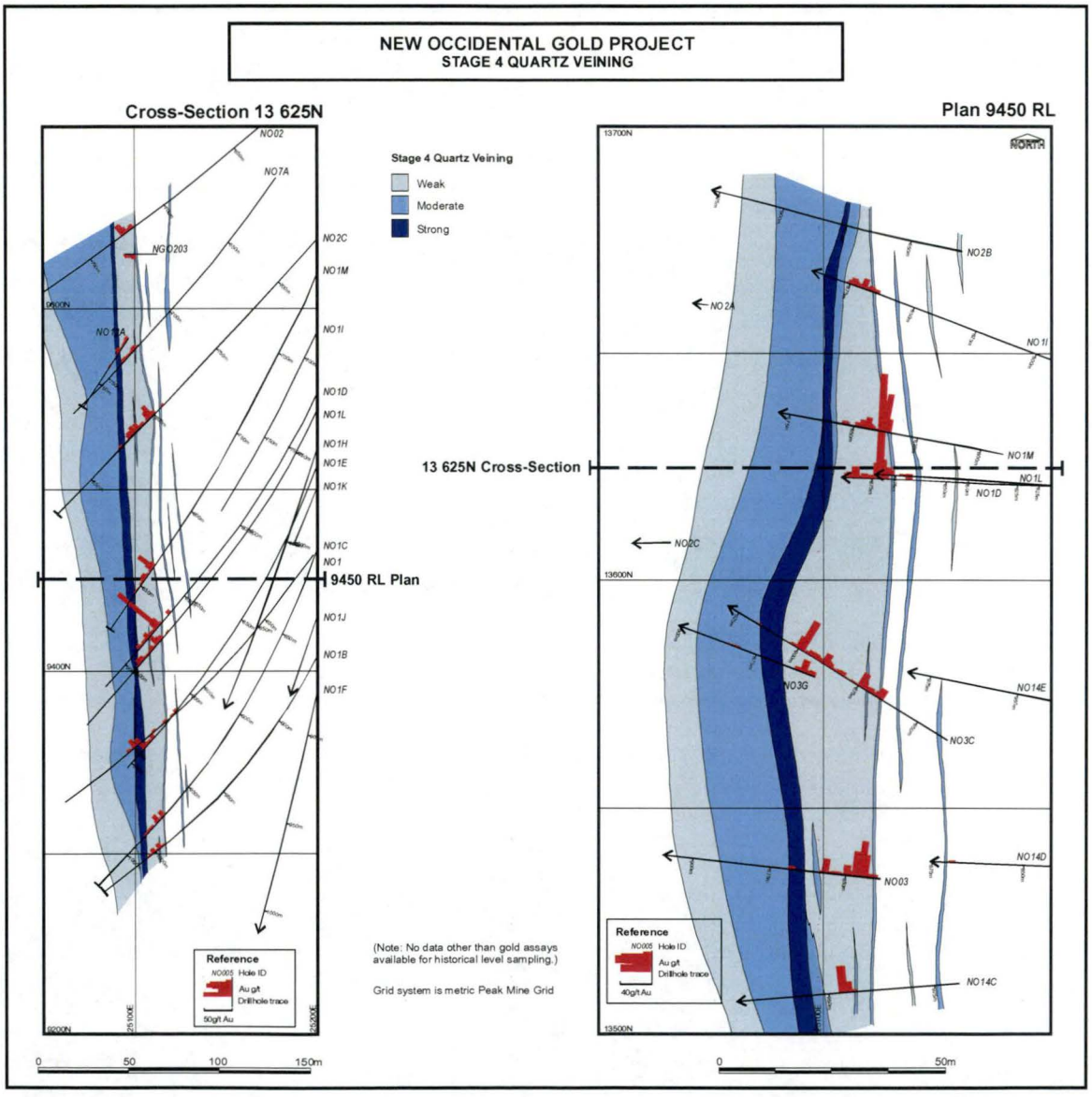

Stage 4 quartz veins are characterised by weakly to strongly fibred microcrystalline to crystalline milky quartz (Figure 77a–n). Occasionally, quartz in those veins can be coarsely crystalline and euhedral (Figure 77l). Stage 4 quartz veins in the New Occidental deposit do not exhibit any obvious textural zonation with depth or distance from the deposit. Quartz vein textures vary according to the style of veining. Stage 4 veins commonly contain a distinctive dark green chlorite and lesser carbonate and are associated

with relatively intense chlorite alteration of wallrock fragments. Minor arsenopyrite is preferentially developed in Stage 4 veins in and around the footwall breccia (Table 16, Figure 77).

Three main styles of Stage 4 quartz veins are present in the New Occidental deposit:

1. **Sub-horizontal veins** are relatively common in the centre and margins of the New Occidental deposit. There is no apparent variation in the intensity or frequency of these veins with depth in the New Occidental deposit although veins are thinner and less common away from the centre of the deposit. Overall, Stage 4 sub-horizontal veins are considerably thicker and more laterally extensive than sub-horizontal quartz veins in other vein stages in the New Occidental deposit (Figure 77a–c). Veins are sigmoidal to lensoidal in shape and are arranged in en echelon or stacked arrays that step progressively upwards to the west. They are generally fibrous with fibres oriented normal to vein walls and sub-parallel to the S_1 cleavage and L_1^1 lineation (Figure 77b–c). Some veins contain fibres oriented at high oblique angles to vein walls. Those veins are typically gentle-moderate dipping veins rather than sub-horizontal, although fibres are also oriented parallel to L_1^1 lineation. Stage 4 sub-horizontal veins are largely unfolded, although fibres may occasionally be buckled by subsequent deformation (Figure 77b–c). Veins generally have parallel vein walls and contain well-developed planar growth bands approximately 10–20 μm thick, which are defined by subtle changes in quartz grain size and colour and by common trails of dark green chlorite inclusions. Growth bands are typically parallel to vein walls. Veins also commonly contain chlorite-rich fibres that have apparently grown from chlorite-rich domains in the vein walls (Figure 77b), indicating syntaxial or stretched crystal vein growth. Vein chlorite is often optically continuous with the vein wall chlorites.

2. **Steeply east dipping quartz veins**, which are scattered throughout the New Occidental deposit and surrounds, although the intensity of veining increases around the Great Chesney Fault. Veins are typically planar and occur in sets that can be collectively traced over the full vertical extent of the New Occidental deposit. Whilst vein sets have an overall orientation parallel to S_1 cleavage, individual veins dip more gently to the east and appear to be arranged in en echelon stacked arrays within the sets (Figure 77c–e). Most veins typically have sub-parallel vein walls. In detail, however, vein walls can be quite irregular and non-matching. Offsets of bedding and earlier formed veins are common across these veins, confirming they formed by infill of fractures opened by fault slip. Veins are weakly to moderately laminated and ribboned, comprising vein-parallel quartz laminae separated by thin sub-planar foliated chlorite and chlorite-altered wallrock septa (Figure 77c–e). Septa, which define slip surfaces, form anastomosing networks through the veins. Quartz laminae comprise weakly buckled and deformed fibred quartz. Individual laminae may contain several domains of differently oriented fibred quartz. Fibres are mainly oriented parallel or slightly oblique to vein walls (Figure 77d) with a lesser proportion of weakly cross-fibred veins (Figure 77e). Veins contain only weakly developed, relatively subtle microscopic growth bands that are approximately 10–20 μm thick, defined by slight changes in the size and colour of quartz crystals. Growth bands are perpendicular to fibre orientations. In the slip-fibred veins growth bands are approximately perpendicular to vein

walls and S_1 cleavage. Growth bands are not obviously mirrored across individual veins. Stylolites are developed along many of the chloritic septa (Figure 77e). These stylolites parallel vein walls and S_1 cleavage.

Steeply dipping Stage 4 quartz veins have also formed along the margins of earlier formed steeply dipping quartz veins, apparently filling fractures developed along vein/wallrock contacts (Figure 77f), or as fill in the centres of earlier formed veins (Figure 77g).

3. **Steeply east dipping quartz vein breccias** focussed in the footwall of the Main lode and superimposed on the Great Chesney Fault. The breccia is present over the full strike length and vertical extent of the Main lode of the New Occidental deposit. It attains a maximum thickness of approximately 6–8m coincident with the thickest part of the New Occidental deposit (at about 600m below surface) and narrows along strike to the north and south to less than 1m widths. The breccia also thins with depth, decreasing to less than 4–5m thick below 900m from surface. The intensity of veining also diminishes as the width of the breccia zone decreases.

   The Stage 4 quartz vein breccias in the footwall of the Main lode of the New Occidental deposit comprise angular, generally rotated elongate fragments up to 10 cm long of wallrock and earlier stage quartz veining. Based on the composition of breccia clasts, two styles of breccia are recognised within the main breccia zone. The first breccia type occurs along the western margin of the Stage 2–3 quartz vein breccia and comprises rotated angular fragments of chlorite-altered Stage 2–3 quartz vein breccia in a matrix of rosette and cockade crystalline quartz (Figure 77h). Fragments comprise mainly sheared siltstone fragments (footwall Great Cobar Slate) partially rimmed by Stage 2 and 3 quartz veining (Figure 77h). Rarely, this breccia preserves fragments of colloform-banded Stage 2 quartz veins (Figure 77i). Quartz vein rims are often incomplete and truncated (Figure 77h). The breccia is often intensely chlorite altered (Figure 77j). Fragments decrease in both size and frequency as this breccia type grades westward into the core of the Stage 4 breccia zone. The core consists of sheared, chlorite-altered, weakly fibred, more massive buck quartz (Figure 77k) that contains localised zones of more crystalline, zoned euhedral quartz (Figure 77l). The massive quartz zone grades westwards into the second breccia type, which comprises predominantly rotated angular fragments of footwall Great Cobar Slate in a similar matrix of rosette and cockade-textured crystalline quartz (Figure 77m). Fragments increase in size, frequency and angularity towards the Great Cobar Slate footwall of the New Occidental deposit. The breccia in the immediate footwall of the breccia zone is characterised by jigsaw textures (Figure 77m). The immediate footwall to the Stage 4 quartz vein breccia consists of an intense stockwork of Stage 4 veins (Figure 77n). Both the density and thickness of veins in the stockwork gradually diminishes westwards into the footwall of the deposit.

The different styles of Stage 4 veins show ambiguous overprinting relationships with each other. The gently dipping Stage 4 veins commonly truncate the steeply dipping Stage 4 veins (Figure 77c) and elsewhere they have been clearly truncated by similar steeply dipping veins (Figure 77d). Similarly, individual steeply dipping veins are cut at high angles by arrays of sub-horizontal veins, which are in turn truncated by a younger generation of steeply dipping veins. The gently dipping veins are commonly nucleated about zones of steeply dipping veins and both sets are usually spatially associated with each

other (Figure 77c). In places, the thickness of gently dipping veins varies either side of a steeply dipping vein (Figure 77b). In these instances, sub-vertical vein opening has been in part accommodated by differential slip on the steeply dipping veins. Finally, both gently dipping and steeply dipping Stage 4 veins are concentrated about the main Stage 4 quartz vein breccia and reduce in frequency and intensity away from the breccia core. These relationships indicate that the various styles of Stage 4 quartz veining were formed synchronously and represent different failure modes rather than temporally distinct vein episodes.

Stage 4 veins and breccias are variably overprinted by brittle/ductile deformation fabrics including localised chlorite-rich septa defining slip-planes and stylolites and by base metal mineralisation. However, Stage 4 veins and breccias are considerably less deformed and dismembered than the earlier quartz vein stages. Folds in ptygmatically folded Stage 4 sub-horizontal veins record shortening strains of up to 20% (mean = 10%) (Table 16). The lack of significant deformation suggests they formed relatively late in the deformation history of the deposit.

Figure 77: Stage 4 quartz veins and quartz vein breccias from the New Occidental deposit.

a) Sub-horizontal cross-fibred Stage 4 veins overprinting a massive Stage 2 quartz vein breccia.

b) Sub-horizontal Stage 4 cross-fibred quartz vein overprinting Stage 2/3 quartz vein breccia. Chlorite domains continue into and across the Stage 4 vein. Note some buckling of fibres at the left of the vein.

c) Sub-horizontal Stage 4 cross-fibred veins overprinting a Stage 4 cleavage-parallel vein within a Stage 2–3 quartz vein breccia.

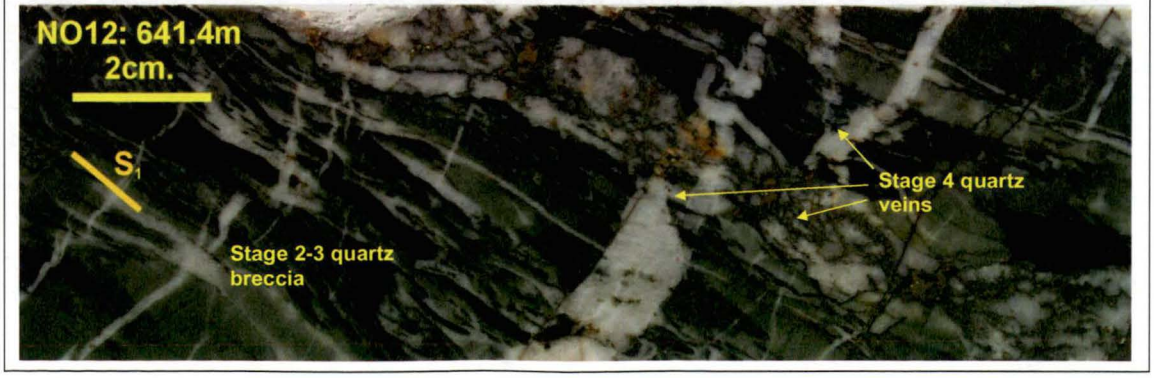

Figure 77: Continued

d) Stage 4 slip-fibred cleavage-parallel quartz veins and sub-horizontal cross-fibred veins cutting Stage 2 quartz vein breccia.

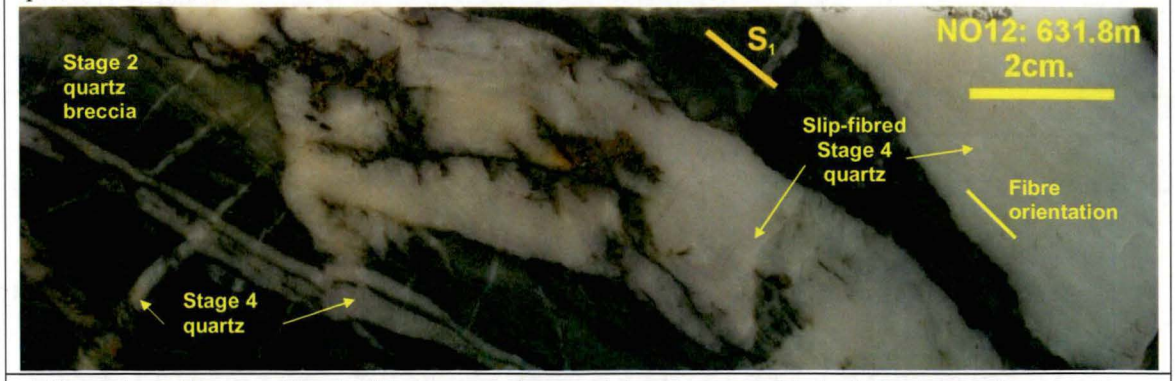

e) Stage 4 weakly cross-fibred milky quartz vein containing common chlorite inclusions and a central chloritic stylolite.

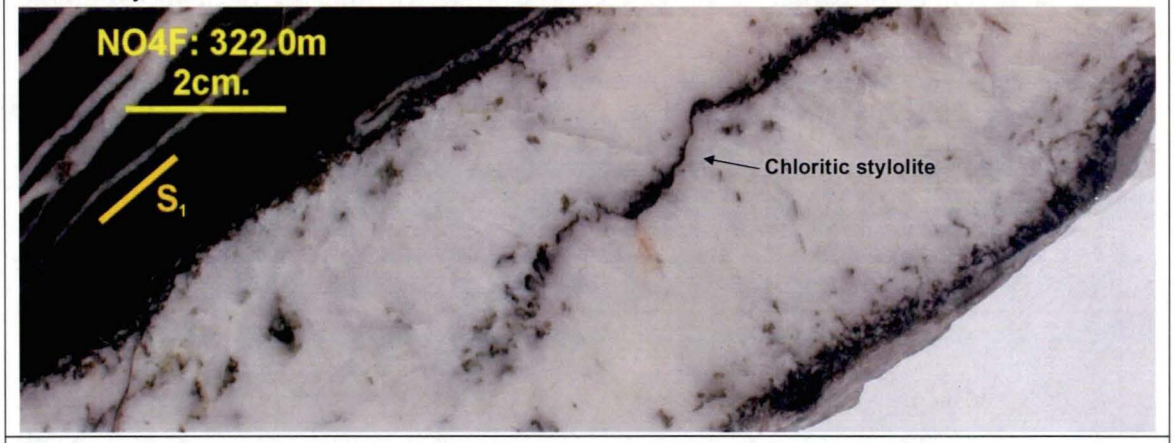

f) Composite vein comprising a steep-dipping open-spacing filling Stage 1 comb quartz-magnetite vein with saw-toothed growth bands (right) and a Stage 4 weakly cross-fibred milky quartz vein (left). The Stage 4 vein has formed along the contact between the Stage 1 vein and wallrock.

g) Cleavage-parallel colloform banded quartz-chlorite Stage 2 vein with Stage 4 quartz infill.

Figure 77: Continued

h) Stage 4 quartz vein breccia containing fragments of Stage 2–3 quartz vein breccia, the latter commonly containing wallrock cores.

i) Fragments of strongly chlorite-altered colloform Stage 2–3 quartz veining in a Stage 4 quartz breccia vein consisting of rosette and cockade textured open-spacing filling quartz.

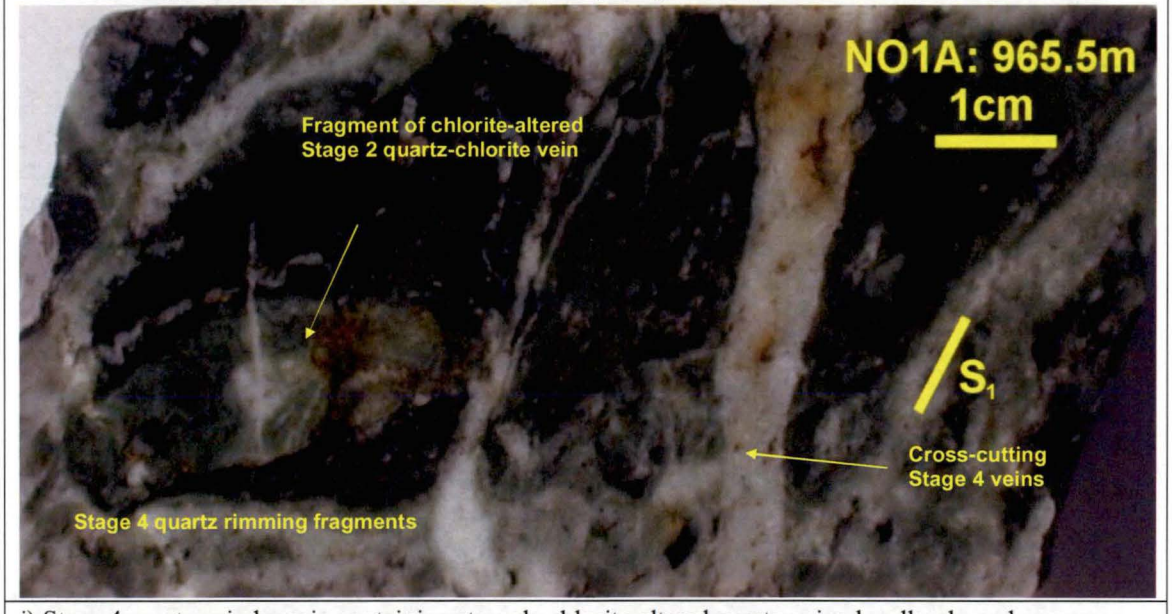

j) Stage 4 quartz vein breccia containing strongly chlorite-altered quartz-veined wallrock and precursor Stage 2/3 breccia fragments. Minor Stage 5 veins overprint the breccia.

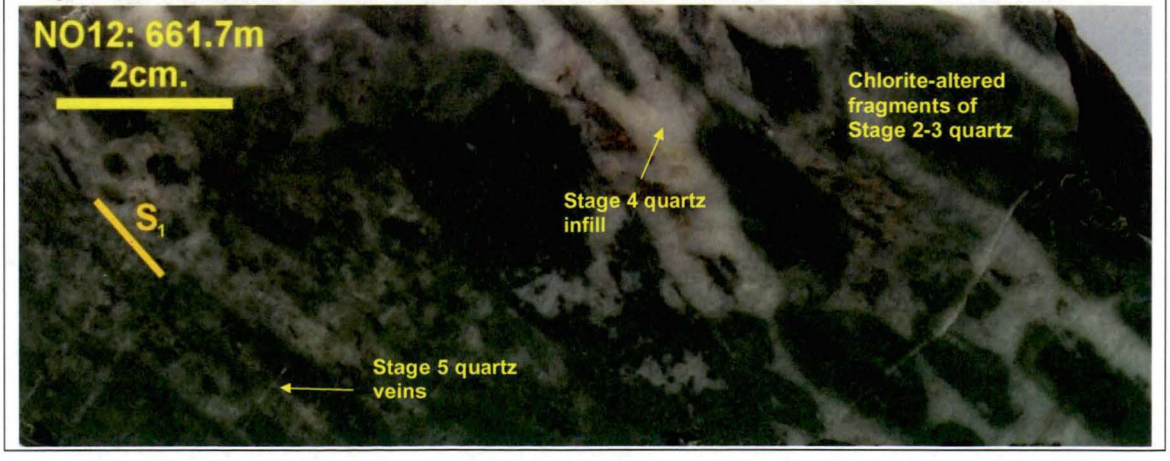

Figure 77: Continued

k) Strongly sheared Stage 4 quartz from the centre of the main Stage 4 footwall breccia containing numerous wisp-like inclusions of chlorite and occassional chlorite-altered wallrock fragments.

l) Stage 4 quartz milky quartz vein from the centre of the main Stage 4 footwall breccia containing irregular chlorite stylolites and remnant zones of coarsely crystalline euhedral quartz (right).

m) Stage 4 quartz vein breccia from the footwall of the New Occidental deposit containing largely angular slate/siltstone fragments

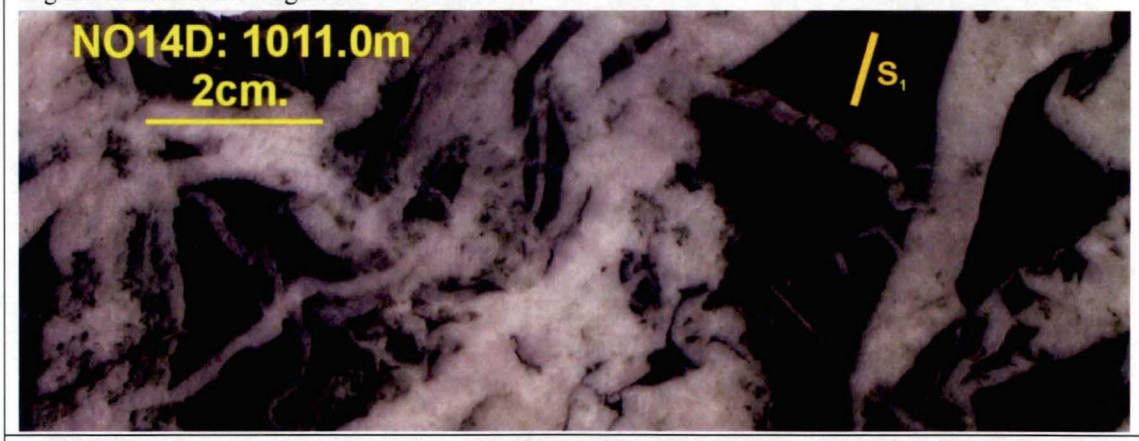

n) Typical Stage 4 cleavage-parallel vein stockwork in the footwall of the Great Chesney Fault.

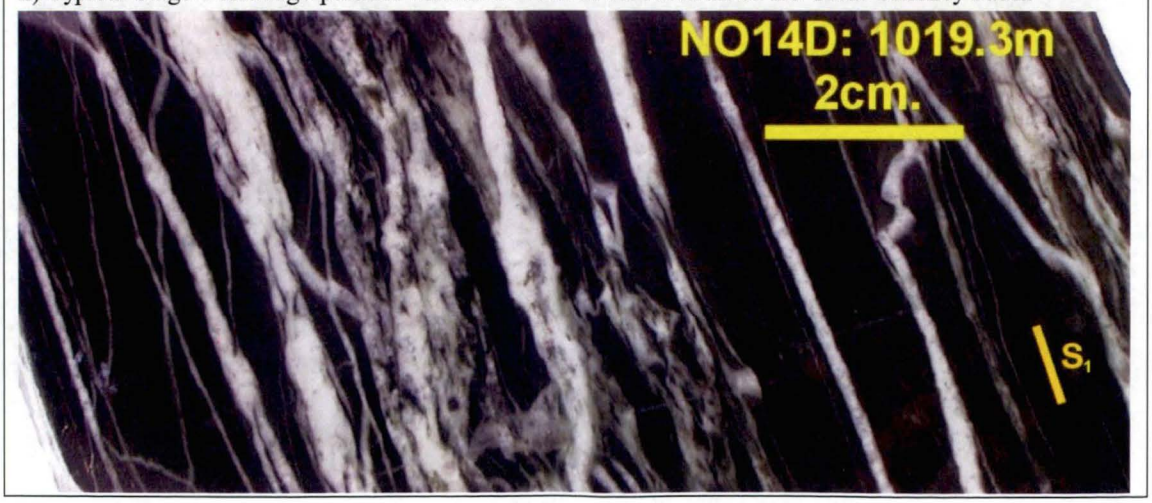

A distinctive fault breccia characterised by the absence of quartz vein matrix occurs along the footwall of the New Occidental deposit in the upper northern parts of the deposit (Figure 78). This breccia contains angular Stage 2-3 vein fragments up to 10 cm in diameter, entrained within a matrix of finer-grained crushed and strongly sheared siltstone/mudstone fragments (Figure 79a, b). The breccia is matrix-supported and poorly sorted. The breccia forms a 1–2m wide zone that extends laterally for approximately 30–40m and down dip for 150–200m. It is localised along the immediate footwall of the Stage 2-3 quartz vein and breccia stockwork that forms the Main lode where the Main lode is slightly more gently dipping (Figure 78). This breccia therefore has a similar clast composition to the Stage 4 quartz vein breccia. Its timing of formation is somewhat ambiguous relative to the Stage 4 quartz vein breccia as Stage 4 veins do not overlap the breccia. The breccia is however overprinted by Stage 5 quartz veins.

Figure 78: Distribution of Foot Wall Fault Breccia in the New Occidental deposit.

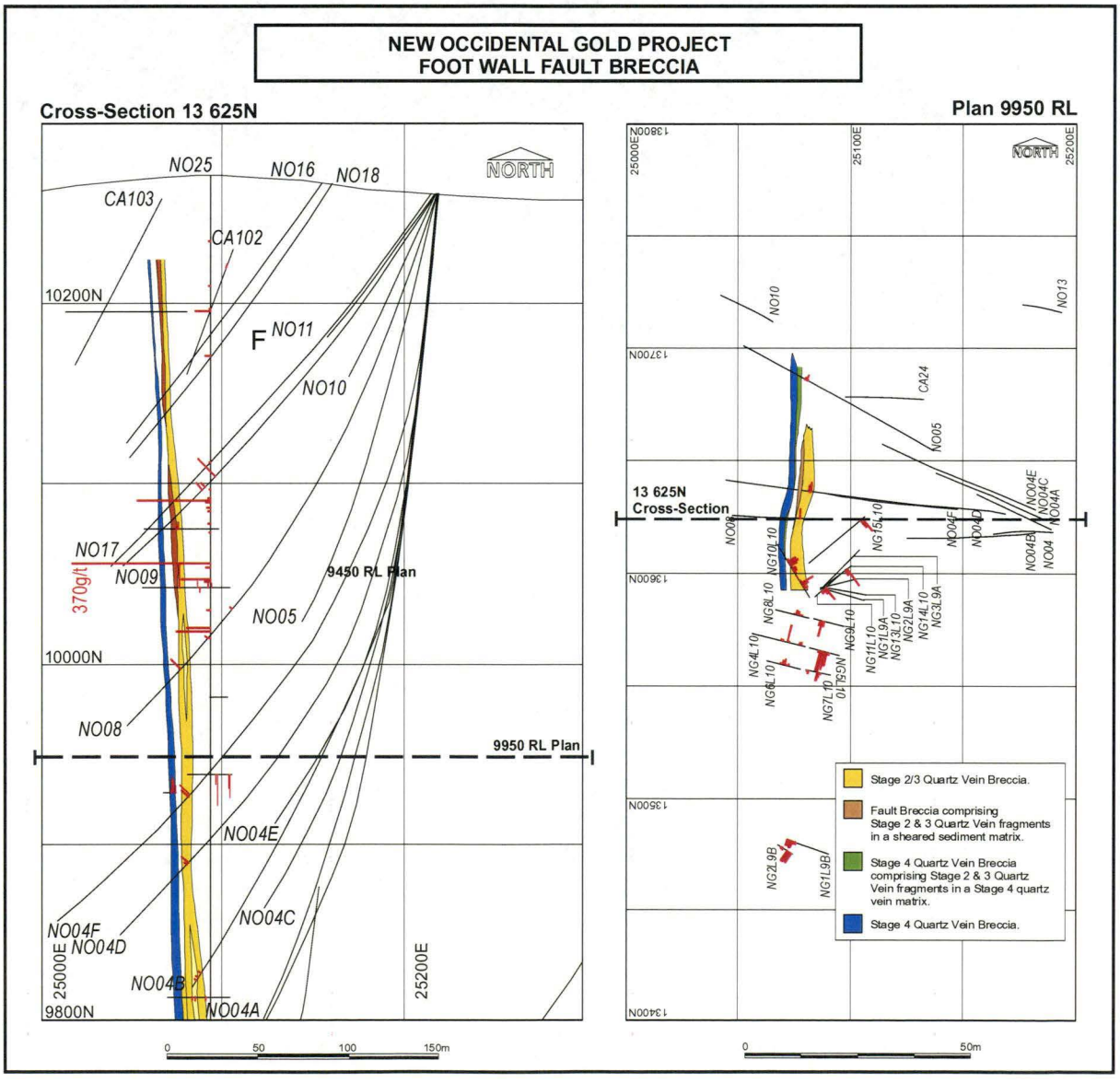

Figure 79: Examples of fault breccias from the footwall of the main Stage 2–3 quartz vein breccia in the New Occidental deposit.

a) Fault breccia comprising angular fragments of Stage 2 and 3 quartz entrained in a fine-grained cataclastic matrix.

b) Fault breccia comprising angular fragments of Stage 2 and 3 colloform-banded quartz entrained in a fine grained cataclastic matrix. Chalcopyrite mineralisation overprints the fault breccia.

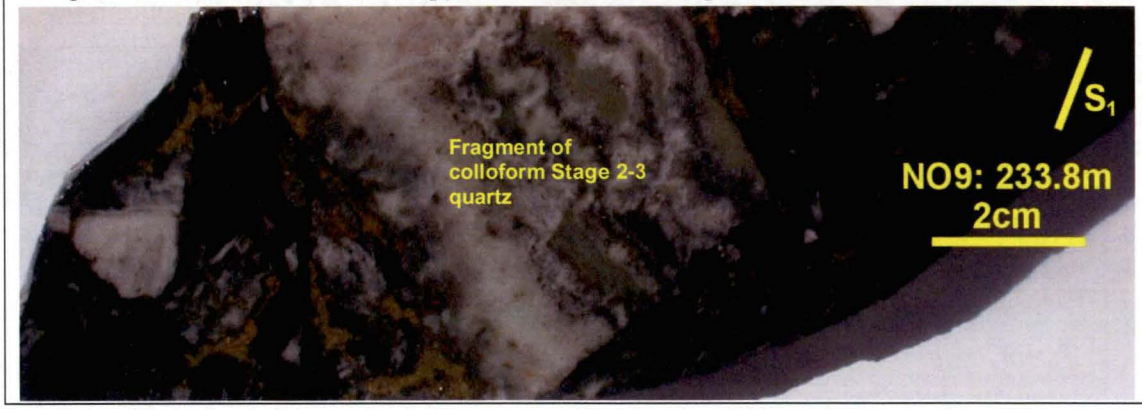

4.3.5 Stage 5 Quartz Veins

Stage 5 quartz veins comprise gently dipping to sub-horizontal veins orthogonal to the S_1 cleavage. They represent a relatively minor phase of quartz veining in the New Occidental deposit and are most commonly developed in the central part of the deposit but also occur in more highly deformed zones within the footwall and hanging wall.

Stage 5 veins consist predominantly of quartz, although minor calcite and trace sulfides, predominantly chalcopyrite and pyrite, may occur in some veins (Figure 80a–d). There is no obvious wallrock replacement and alteration associated with this vein set.

Stage 5 quartz veins are undeformed and overprint and slightly offset all other vein types including the steeply dipping Stage 4 veins (Figure 80a–d). These veins tend to be much narrower than the Stage 4 veins. They are sigmoidal to lensoidal in shape and often arranged in en echelon or conjugate arrays stepping progressively upwards to the west. Individual veins are commonly only 1–10 cm long, but the vein arrays extend laterally over several metres.

Veins are weakly to moderately cross-fibred with fibres oriented normal to vein walls and sub-parallel to the S_1 cleavage and L_1^1 lineation. Growth bands, where present, are typically planar and defined by subtle quartz colour variations. Wallrock inclusions are relatively uncommon. Veins may have locally vuggy centres characterised by euhedral quartz vein terminations. Veins are occasionally mineralogically zoned from quartz at the margins to calcite within the interiors (Figure 80b).

Figure 80: Examples of Stage 5 quartz veins from the New Occidental deposit.

a) Minor late Stage 5 sub-horizontal veins overprinting both Stage 2–3 quartz breccia and Stage 4 quartz veining (right). Minor chalcopyrite also infills late Stage 5 veins.

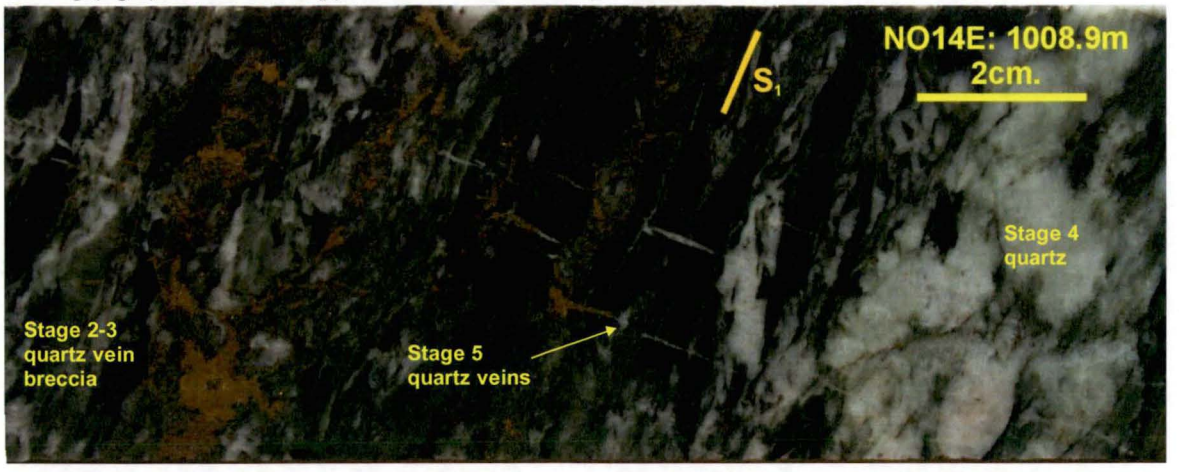

b) Photomicrograph of Stage 5 sub-horizontal quartz-calcite (clear)-sulfide (black) veins cross-cutting a strongly cleaved Stage 2–3 quartz-chlorite vein breccia (PPL).

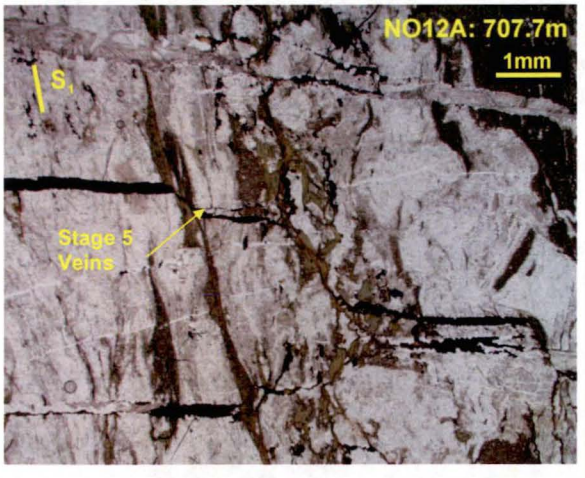

c) Photomicrograph of sandstone fragment containing ptygmatically folded Stage 1 quartz veins in a Stage 2–3 quartz breccia overprinted by unfolded Stage 5 sub-horizontal veins (PPL).

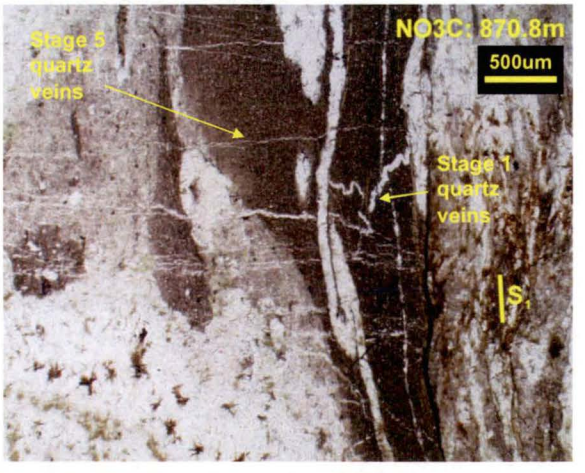

d) Sub-horizontal Stage 1 and 5 quartz veins exhibiting differential deformation. Stage 1 veins are ptygmatically folded whilst Stage 5 veins are unfolded.

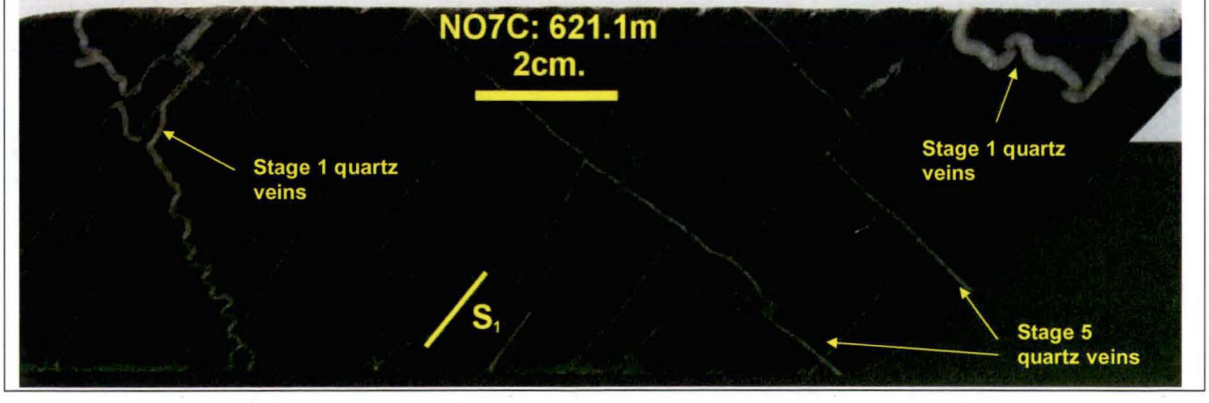

4.3.6 Spatial Distribution of Vein Types

Quartz vein types within the New Occidental deposit exhibit a remarkably consistent spatial distribution relative to the Great Chesney Fault. Spatially, the locus of quartz veining and brecciation, from early to late-stage, progressively shifts from the hanging wall of the New Occidental deposit to the footwall. Whilst vein density and thickness varies along strike and with depth, the zonation of individual vein stages across the deposit is consistently developed over the full strike length (~200m) and known vertical extent (~1200m) of the deposit (Figure 82 and Figure 81).

The progressive shift in the focus of quartz vein stages from the hanging wall to the footwall of the New Occidental deposit as the deposit formed provides a quartz-vein "stratigraphy" with a "younging direction" to the west that can be used to constrain the paragenesis of the associated mineralisation. It has also minimised the degree of overlap between the four successive stages of breccia veining in the New Occidental deposit and has resulted in these quartz breccias commonly containing only one to two stages of quartz veins as clasts. For example, Stage 4 breccias containing fragments of all three previous stages of quartz veins have not been observed.

Figure 81: Detailed spatial distribution of vein stages in the New Occidental deposit.

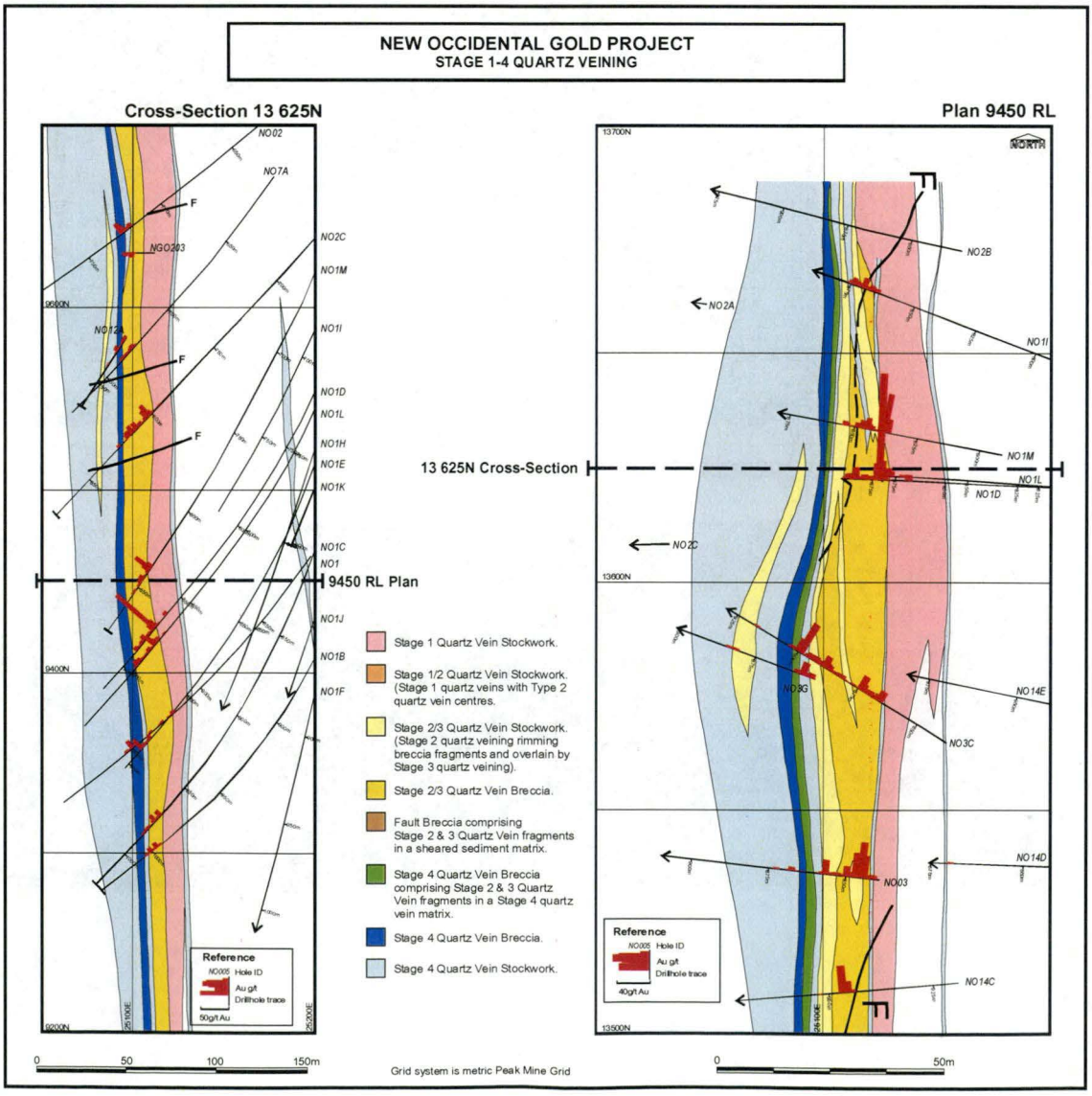

Figure 82: Spatial distribution of vein stages in the New Occidental deposit.

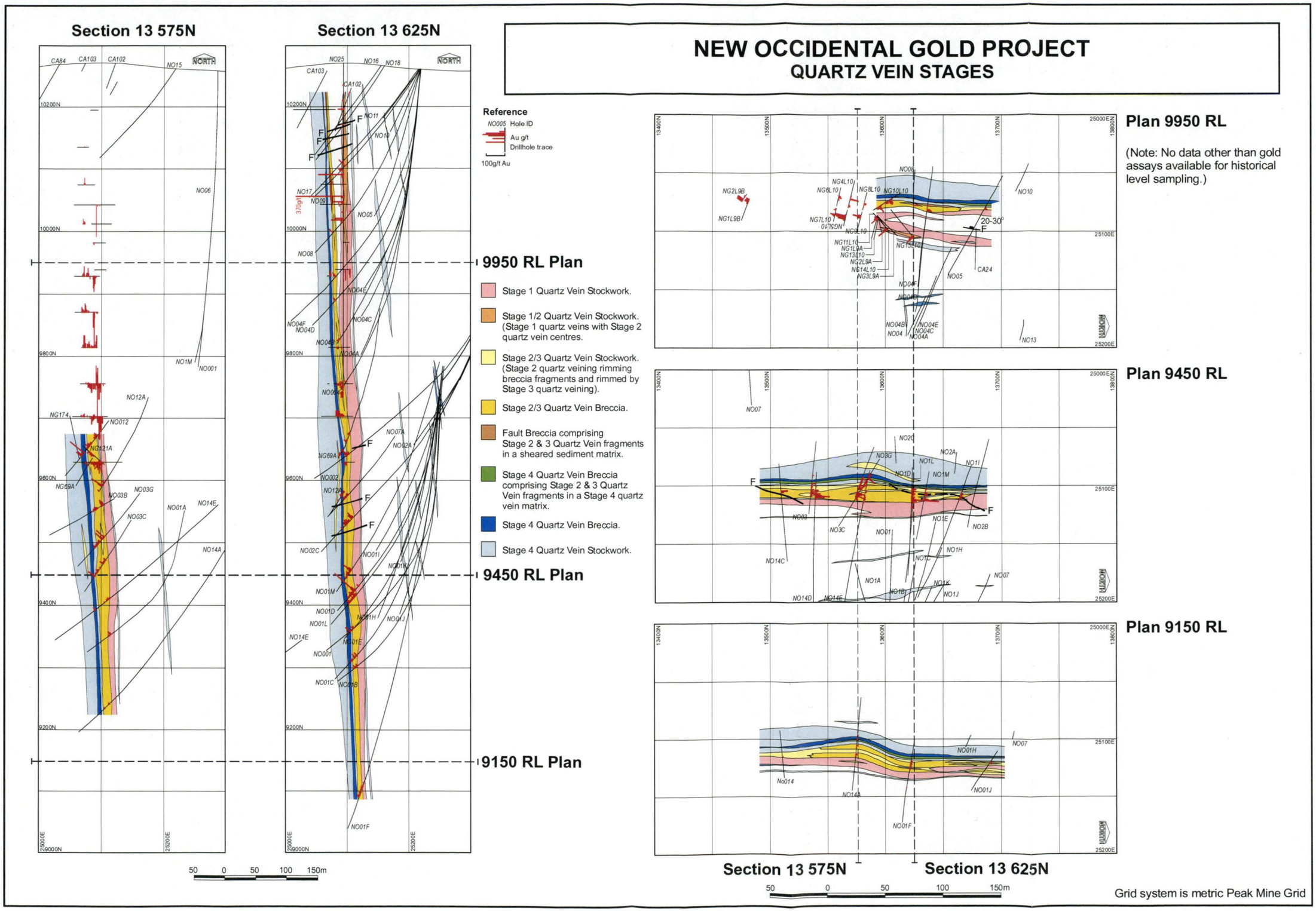

4.3.7 Vein Thickness and Gold Distribution

The true thickness of Stage 2–3 quartz veins and quartz vein breccias in the New Occidental deposit (i.e. thickness of the Stage 2–3 quartz vein stockwork measured perpendicular to deposit strike * density of Stage 2–3 quartz veins and breccias in the stockwork) correlates strongly with the tenor of gold mineralisation (i.e. thickness of the >1 g/t Au envelope measured perpendicular to the deposit strike * gold grade) within the New Occidental deposit (Figure 83). For example, the >15m true thickness contour of the Stage 2–3 quartz vein stockwork is approximately coincident with the >100 Au gram*metre contour and the >5m true thickness contour of the Stage 2–3 quartz vein stockwork is approximately coincident with the >10 Au gram*metre contour in Figure 83.

Although the Stage 4 quartz vein breccia is located in the footwall of the Main lode, the true thickness of this breccia (i.e. thickness of the Stage 4 quartz vein breccia and associated stockwork measured perpendicular to deposit strike * density of Stage 4 quartz veins and breccias) is also strongly correlated with the tenor of gold mineralisation (i.e. thickness of the >1 g/t Au envelope measured perpendicular to the deposit strike * gold grade) in the deposit (Figure 84). For example, the >100 gram metre contour in Figure 84 is approximately coincident with the >5m true thickness contour of the Stage 4 breccia.

4.3.8 Vein Orientations

Using reoriented drillcore measurements of vein orientations from drillholes NO01–18, in which the stage of quartz veining was not distinguished, three principal quartz vein orientations are recognised within and immediately surrounding the New Occidental orebody (Figure 85a–b):

1. Moderate-steeply east dipping and sub-parallel to S_1 cleavage (equivalent to Glen, 1987b's Set 2, 4, 5 and 6 veins).
2. Steeply west dipping and parallel to S_0 bedding.
3. Sub-horizontal to gentle west dipping and orthogonal to S_1 cleavage (equivalent to Glen, 1987b's Set 1 and 3 veins).

Approximately 80% of all veins are moderate-steeply east dipping. Stereonet plots of poles to S_1-cleavage parallel veins indicate an average vein orientation of 82°/078° (Figure 85a), which is slightly less steeply dipping than S_1 cleavage but of a similar strike. Glen (1987b) also recognised the slight angular divergence between the dip of veins and S_1 in the Chesney and New Cobar deposits. The gently dipping veins, which have an average vein orientation of 06°/194°, are best developed within and immediately adjacent to the deposit.

Figure 86 shows the density of veins from the five stages in NO25–26. The bulk of veins in the hanging wall of the New Occidental deposit comprise mainly Stage 1 veins with lesser Stage 4 veins. Composite Stage 1–2 veins are present in the area of the Albion lode whilst Stage 2–4 quartz veins define the Main lode. Stage 5 veins are scattered around and within the Main lode. Sulfide-only veins represent a minor proportion of the total vein population in NO25–26 and tend to be scattered throughout the zone between the Albion and Main lodes, extending into the Main lode.

Figure 83: Relationship between true thickness of Stage 2–3 quartz veining and gold mineralisation in the New Occidental deposit.

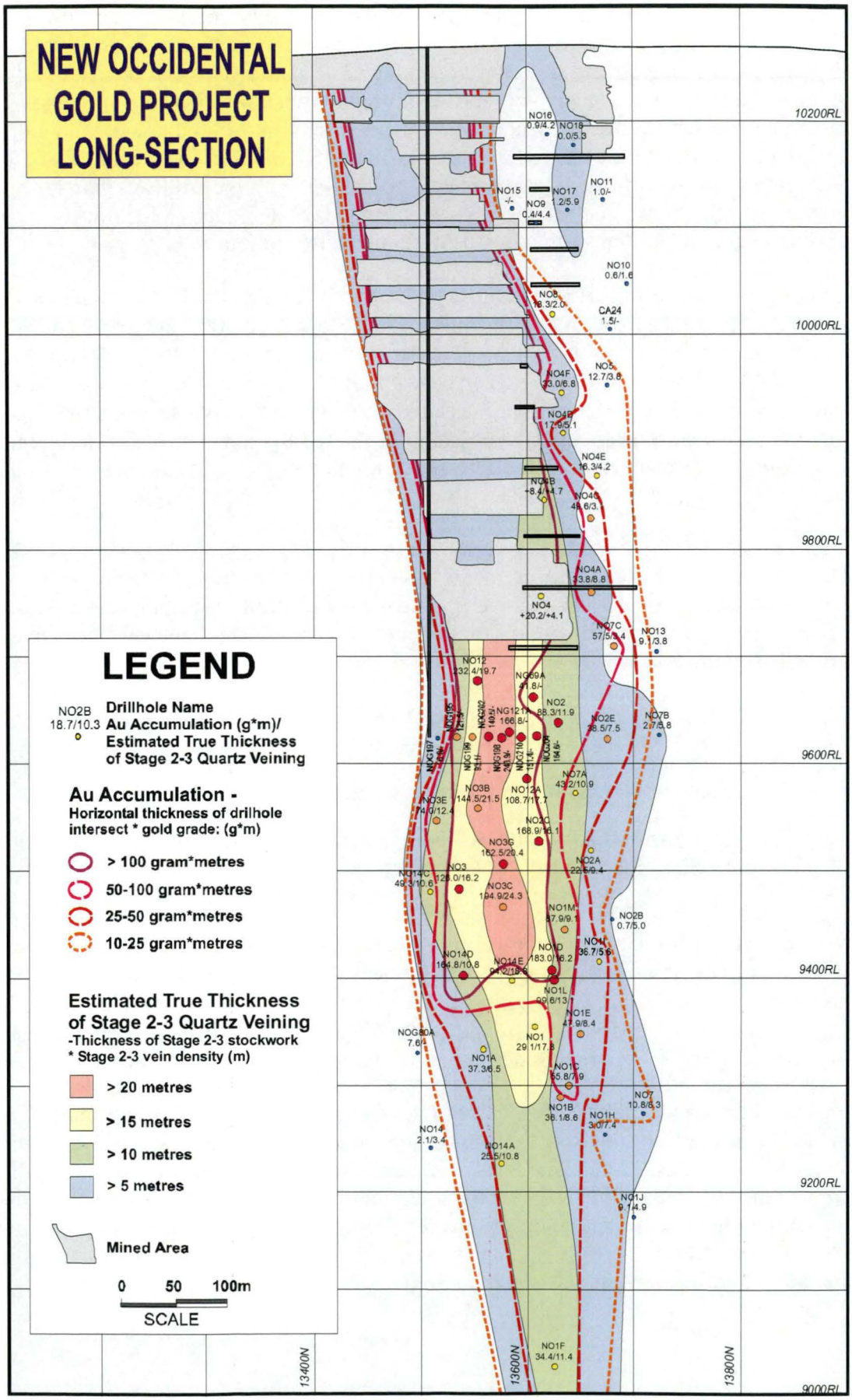

Figure 84: Relationship between true thickness of Stage 4 quartz veining and gold mineralisation in the New Occidental deposit.

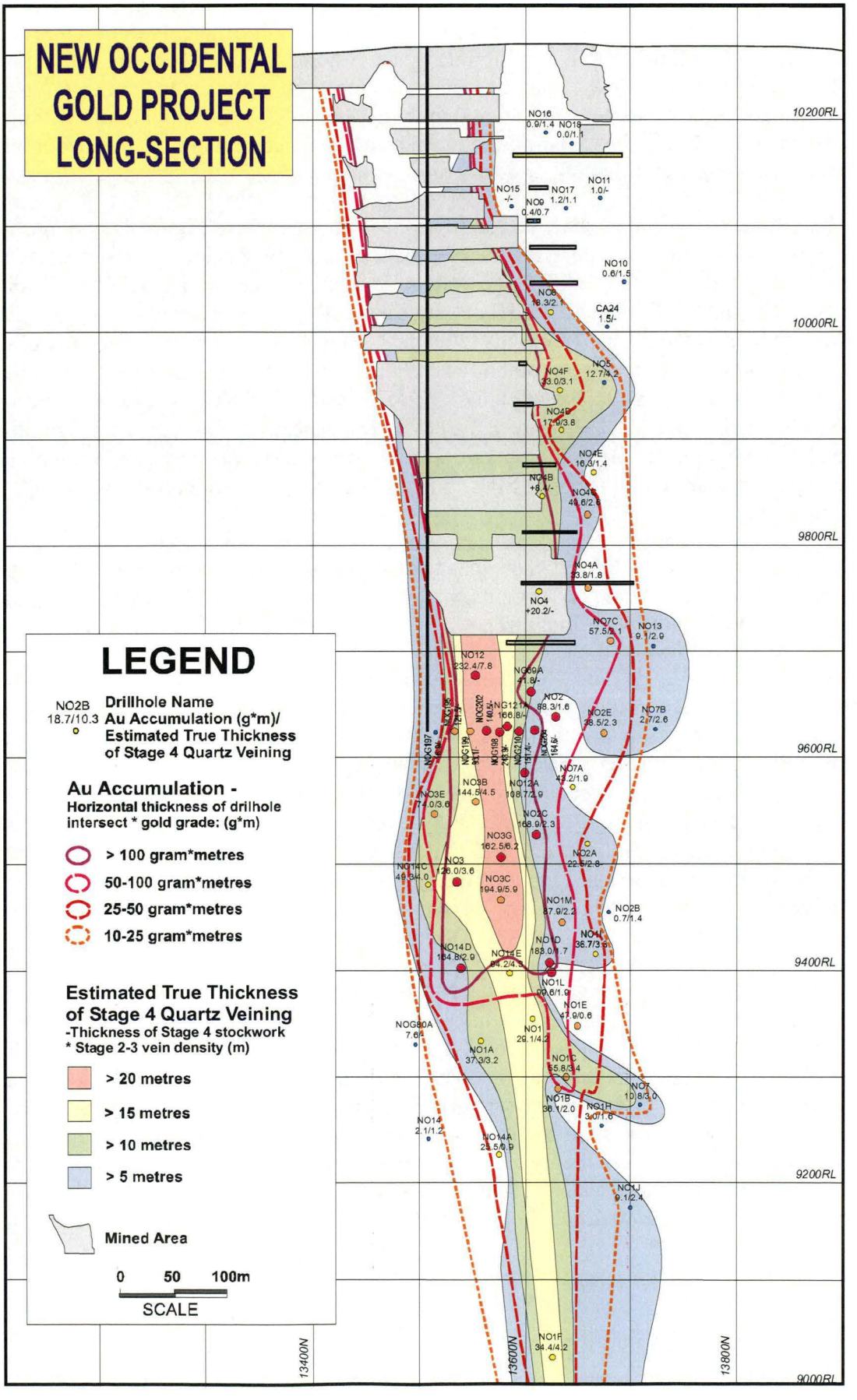

The reoriented vein measurements from NO25–26 drillcore (Figure 85c–d) demonstrate that quartz veins in the hanging wall of the New Occidental deposit are more randomly oriented compared to veining within the orebody (Figure 85a–b). Hanging wall veins in the upper sections of NO25–26 (0–400m) show a continuum from steeply dipping through moderately east dipping to gentle dipping veins. The strike of the hanging wall veins is also more variable, with vein dip directions ranging from northeast to southeast. Immediately above the New Occidental orebody (NO25–26: 400–500m) and within the orebody (NO25–26: 500–530m) quartz vein orientations have a bimodal distribution; they are either steeply east dipping or gently dipping (Figure 87).

The different vein stages show subtle differences in orientation (Figure 87). Stage 1 veins, the most common vein type in the hanging wall of the New Occidental deposit, have a modal orientation of 65°/090°. Hybrid Stage 1–2 veins, which comprise Stage 1 veins with a Stage 2 quartz infill, have a modal orientation of 60°/094° and are slightly more gently dipping than Stage 1 veins. Composite Stage 2–3 quartz veins make up the bulk of the veining in the New Occidental orebody and have a modal orientation of 81°/086°. Stage 4 quartz veins have a modal orientation of 72°/070° and thus strike more northwesterly than the other vein types. Sulfide-only veins have a broad scatter of orientations with little evidence of preferred orientation, ranging from gently to steeply east dipping, with an average orientation of 48°/086°. Stage 5 quartz veins have a modal orientation of 2°/230° (Figure 87).

A breakdown of all NO25–26 veins into sulfide-mineralised versus unmineralised veins demonstrates that all vein orientations, with the exception of the sub-horizontal veins, appear to be mineralised (Figure 87).

Vein geometries in the New Occidental deposit define a relatively simple and consistent pattern. Within the orebody, veins are predominantly sub-parallel to S_1 cleavage with a lesser sub-horizontal population orthogonal to cleavage and L_1[1]. On the margins of the orebody, veins, whilst more randomly oriented, typically dip more gently to the east than cleavage. Most of these veins strike parallel to cleavage, with the exception of Stage 4 veins, which strike in a more northwesterly direction. Veins to a lesser extent are also developed along bedding planes. Sub-horizontal veins decrease in frequency away from the New Occidental deposit, and are largely absent at distances greater than 15m horizontally from the orebody. The three dimensional relationship between the different stages of quartz veins within the New Occidental deposit is shown in Figure 88.

Quartz veins in the hanging wall of the New Occidental deposit are commonly associated with small scale bedding offsets. Whilst most of these offsets are east block-up and consistent with reverse displacement (Figure 89a–c), several examples of small-scale west block-up or normal offsets of bedding have been documented (Figure 89d–g). Both normal and reverse offsets have been recorded across the same stage of quartz veins, indicating normal offsets are not associated with a particular vein stage. Similar normal west block-up offsets on steeply east dipping veins have also been observed in underground exposures in the New Occidental mine. Those offsets are clearly anomalous in the context of the overwhelming evidence for an east block up, reverse sense of movement on the Great Chesney Fault.

Figure 85: Equal Area Stereonet of poles to quartz veins from the New Occidental deposit determined from reorientation of drillcore data.

a) All drillcore (excluding NO25–26)

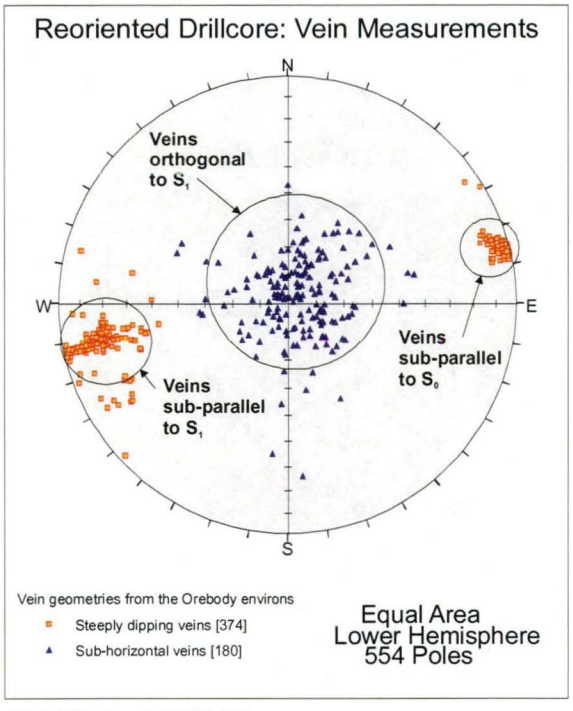

b) All drillcore (excluding NO25–26)

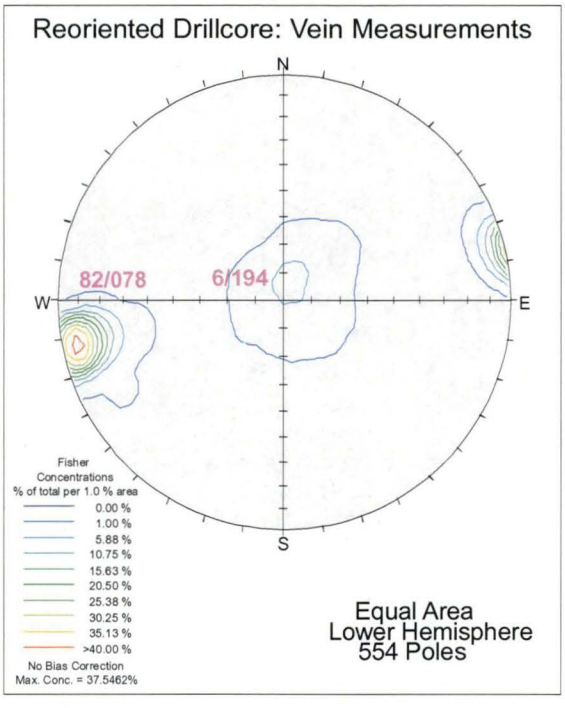

c) Drillholes NO25–26

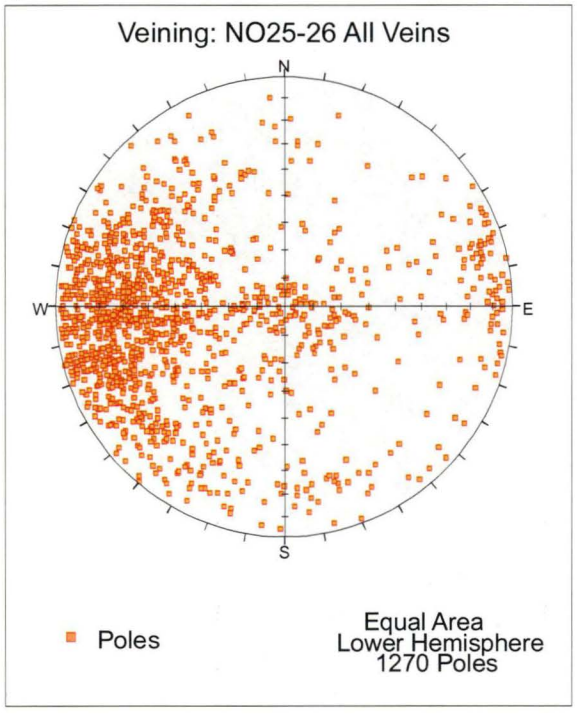

d) Drillholes NO25–26

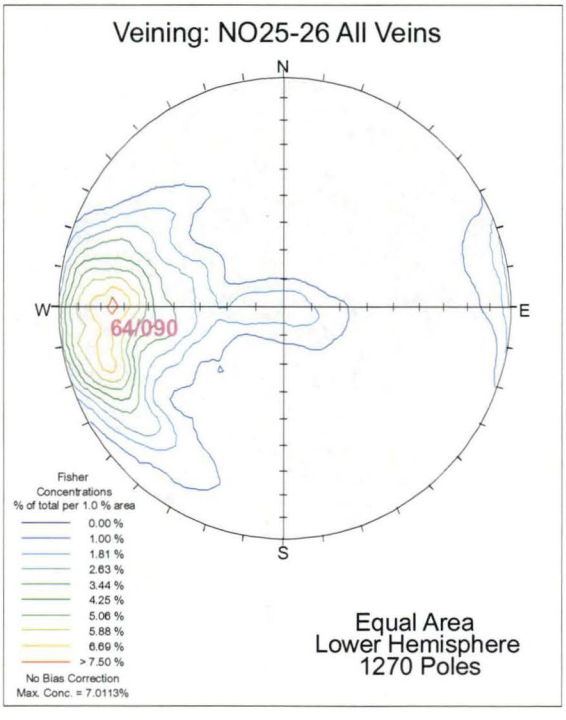

Figure 86: Distribution and frequency of different vein stages in NO25–26.

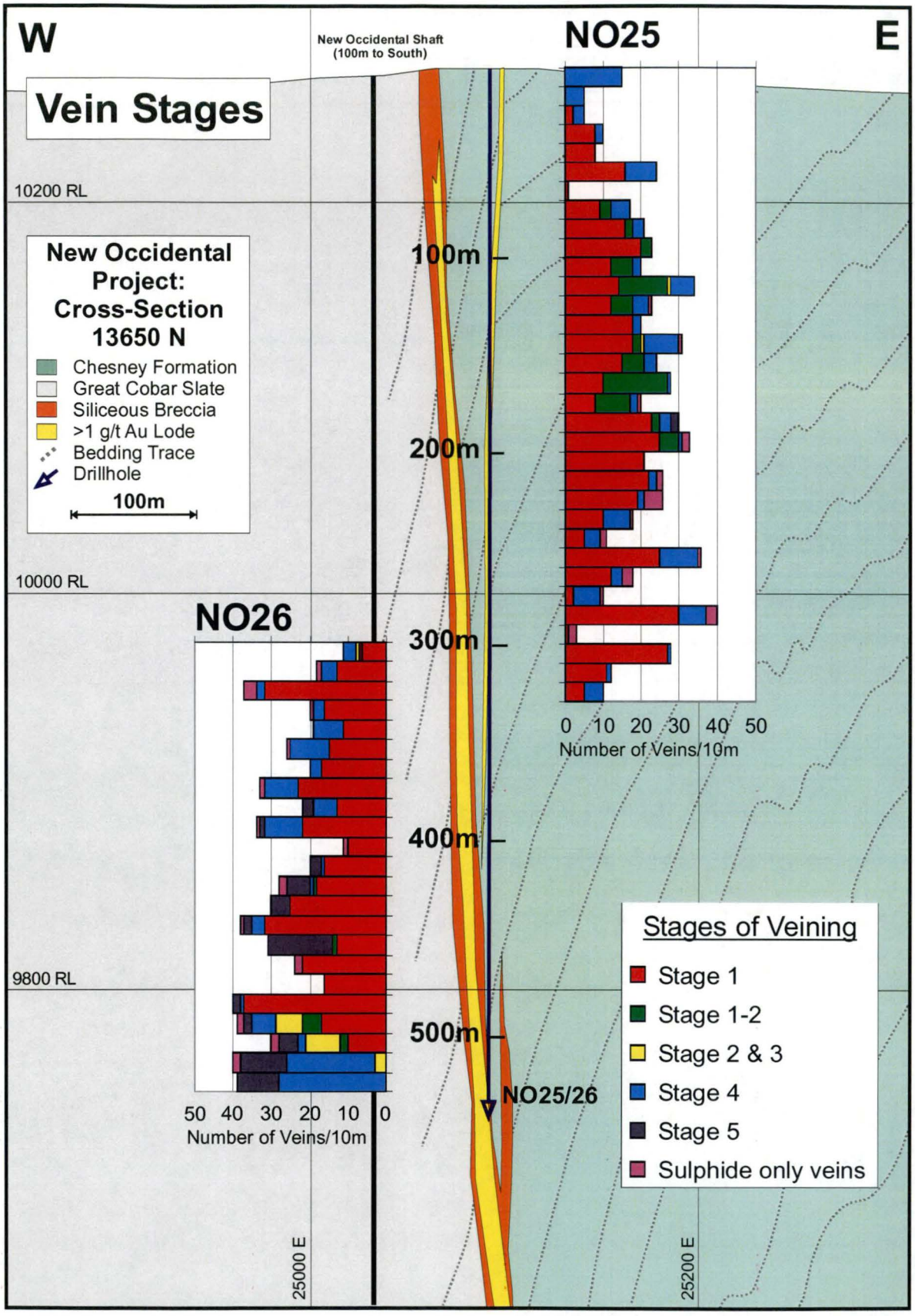

Figure 87: Equal area stereonets of poles to reoriented vein measurements from NO25–26.

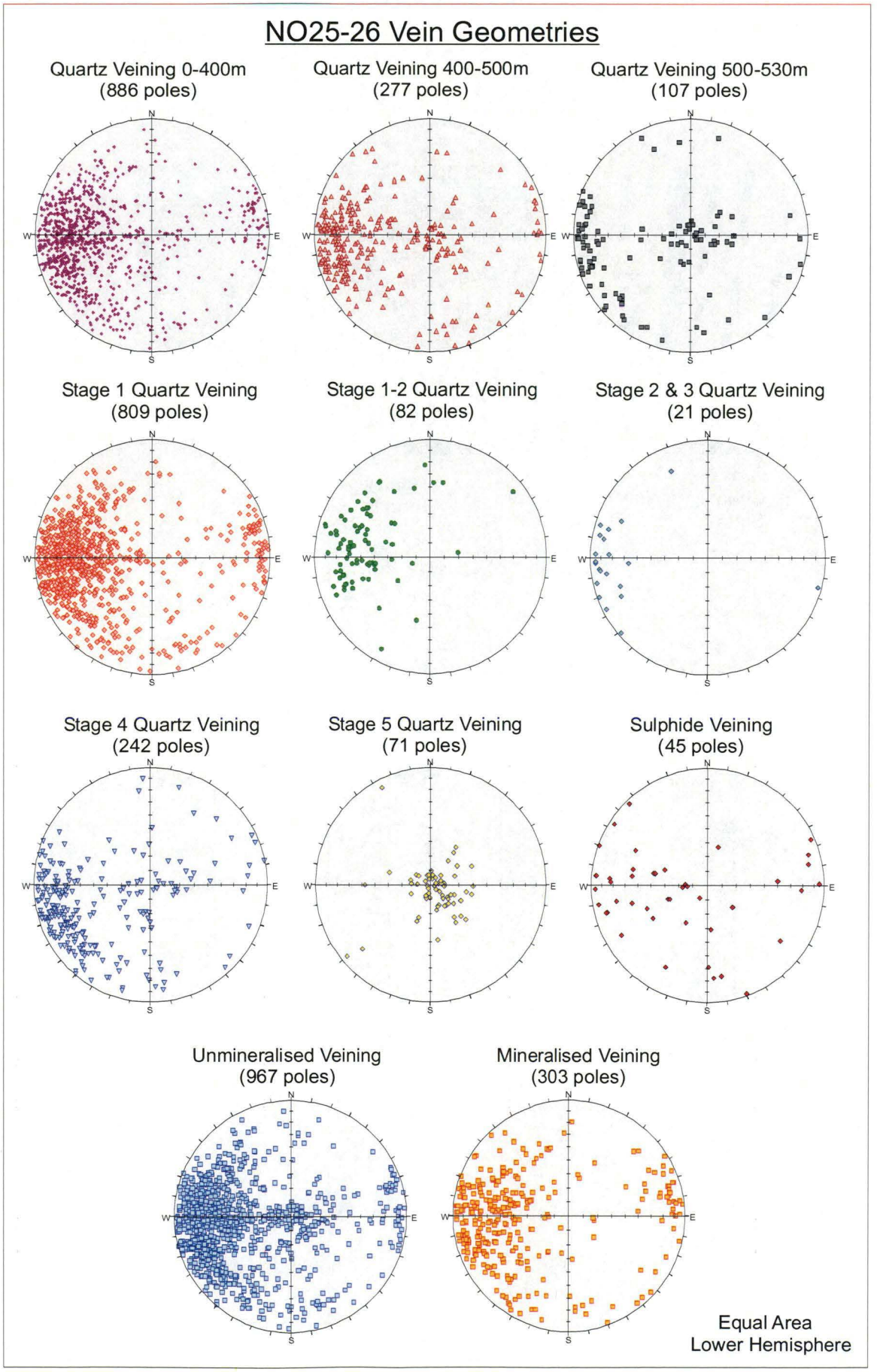

Figure 88: Schematic block model showing relationships between the 5 stages of quartz veining in the New Occidental deposit.

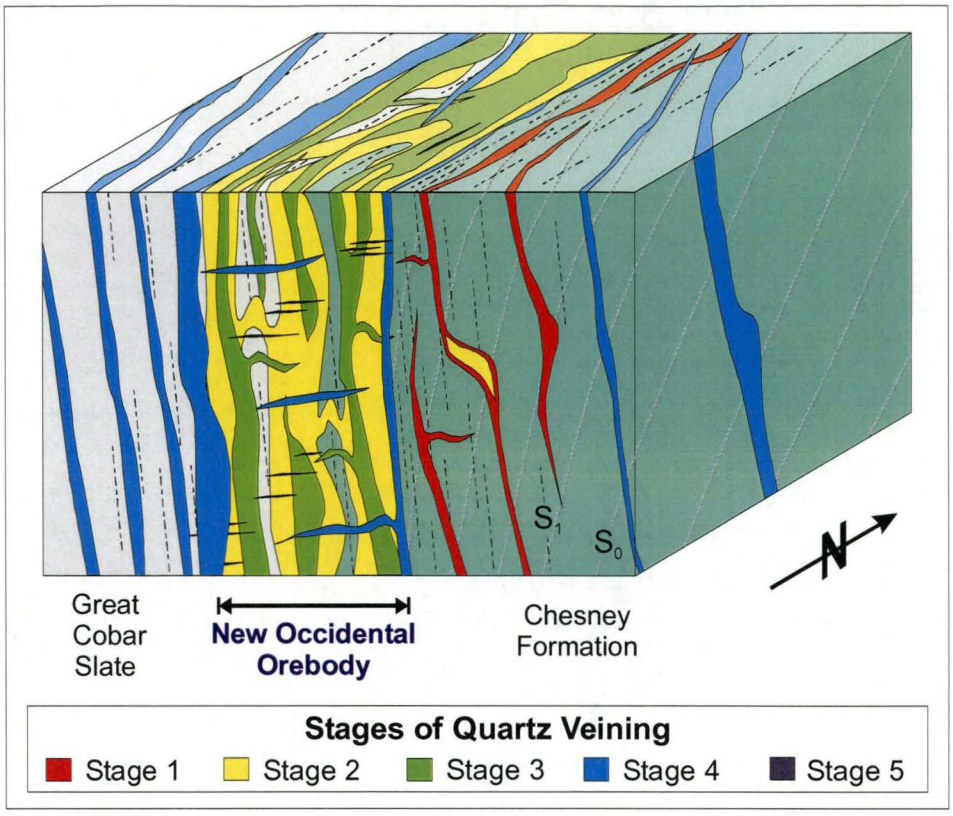

Figure 89: NO25 Drillcore structural relationships.

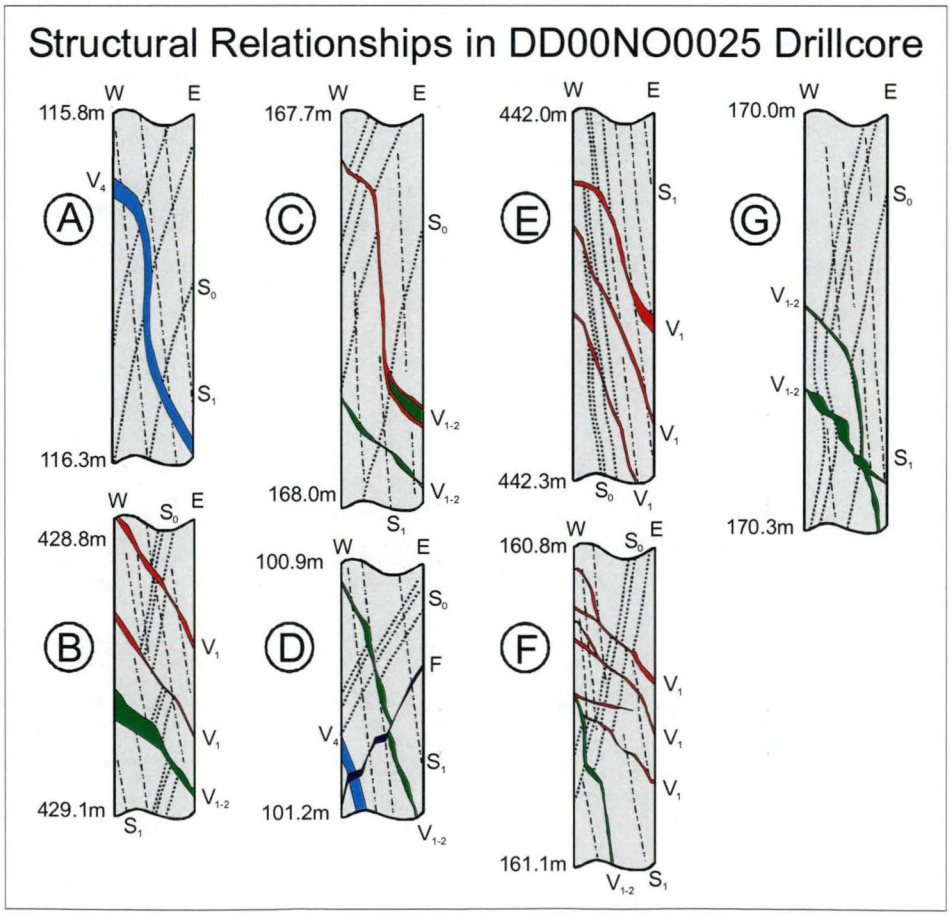

4.4 Stress Regimes and Fault Zone Dynamics Inferred from Quartz Vein Systematics

Quartz veins and breccias within the New Occidental deposit provide important constraints on the displacement history of the host Great Chesney Fault. Similarly, they also constrain the regional stress field under which the deposit and the Great Chesney Fault formed. The five stages of quartz veins and vein breccias identified within the New Occidental deposit are intimately spatially associated with the Great Chesney Fault zone and their formation spans most of the D_1 event.

4.4.1 Relationship between Vein Stages and D_1 Deformation

Of the five vein stages in the New Occidental deposit Stage 1 veins are generally most strongly deformed. Steeply dipping Stage 1 veins have been extensively dismembered by slip and dissolution along S_1 cleavage whilst sub-horizontal Stage 1 veins have been extensively ptygmatically folded. The average shortening strain of 50% estimated for the folded sub-horizontal Stage 1 veins in the hanging wall of the New Occidental deposit is comparable to the 60% shortening strain Glen (1985) estimated for Structural Zone 1 in the eastern margin of the Cobar Basin, although much less than the 90% shortening estimated herein for the immediate hanging wall of the Great Chesney Fault. Stage 1 vein breccias contain wallrock fragments that possess a weak to moderately developed S_1 cleavage. As cleavage in clasts is much weaker than in surrounding rock, Stage 1 veins are interpreted to have formed in the early stages of S_1 cleavage development. The absence of uncleaved wallrock fragments in Stage 1 vein breccias indicates deposition of Stage 1 veins does not predate S_1 cleavage.

Stage 2 veins are also strongly deformed and sub-horizontal Stage 2 veins are also ptygmatically folded. Folds in sub-horizontal Stage 2 veins record an average shortening strain of 60%; the highest for all vein stages. The apparent contradiction of Stage 2 veins recording higher shortening strains than Stage 1 veins is interpreted to reflect the increased proximity of Stage 2 veins to the Great Chesney Fault. Ptygmatically folded Stage 2 veins are from the high strain core of the New Occidental deposit, whereas ptygmatically folded Stage 1 veins are from the less deformed margins of the deposit. Ptygmatically folded Stage 1 veins in wallrock fragments contained within Stage 2–3 breccias record shortening strains of only 35%. In addition, wallrock fragments within Stage 2 breccia veins contain a moderate to strongly developed S_1 cleavage, which is typically more strongly developed than cleavage in wallrock fragments in Stage 1 vein breccias. Both features are consistent with Stage 2 veins forming later than Stage 1 veins during ongoing D_1 deformation.

Stage 3 veins are less deformed than previous vein stages, although veins are deformed locally and sub-horizontal Stage 3 veins are also ptygmatically folded. However, folds in sub-horizontal Stage 3 veins record an average shortening strain of 35%, which is significantly lower than in previous vein stages.

Stage 4 veins are relatively planar and less deformed internally than previous vein stages. Sub-horizontal Stage 4 veins are weakly folded and record an average shortening strain of only 10%. Wallrock fragments within Stage 4 vein breccias are more strongly cleaved and altered than those in earlier generations of breccias. Cleavage-parallel stylolites are common in steeply dipping Stage 4 veins, particularly in deformed chlorite-rich veins. The stylolites, which formed in response to localised relatively intense mineral dissolution and concentration of insoluble residue (mainly chlorite) along dissolution planes, indicate

further shortening at a high angle to the veins. Such relationships indicate that the Stage 4 veins formed during the latter stages of D_1 deformation and cleavage formation.

Stage 5 veins are undeformed and formed in the waning stages of S_1 cleavage development.

All stages of quartz veins have been overprinted by brittle late-stage D_1 and D_2 faults (Figure 47b–c) with which little or no quartz deposition is associated.

Figure 90: Quartz Vein textures recognised within the New Occidental deposit and their relationship to D_1 deformation.

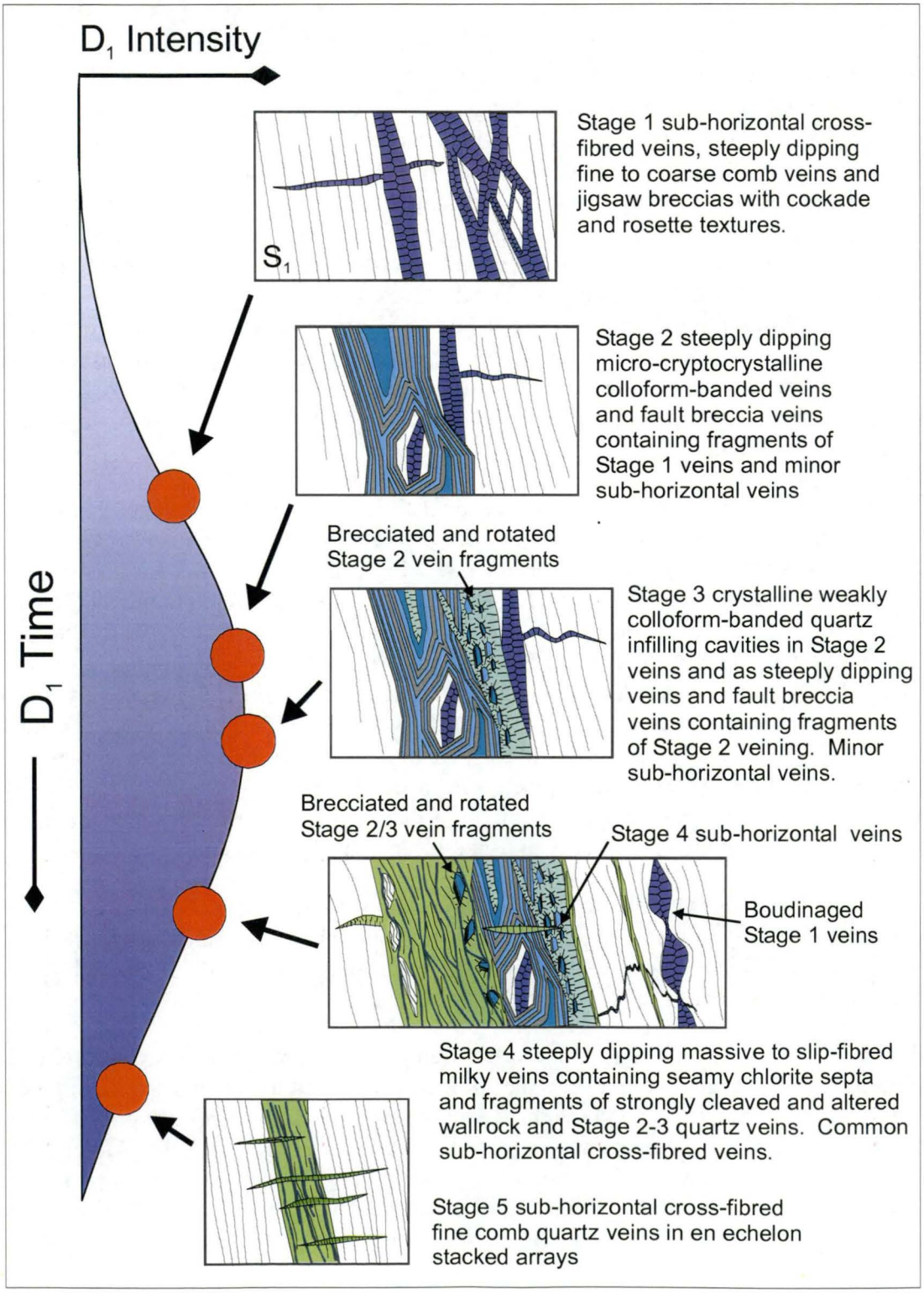

4.4.2 Interpretation of Crack-Seal and Open-Space Filling Quartz Vein Textures

The direction of fracture opening can be inferred from matching irregularities or deflections in vein walls across the vein and by the relative offset of geological markers or pre-existing veins (Robert and Poulsen, 2001). In addition, mineral fibre orientations in crack-seal veins also generally track the direction of vein opening (Ramsay, 1980; Ramsay & Huber, 1983; Cox & Etheridge, 1983). Whilst Vearncombe (1993) has suggested that the geometry of inclusions in crack-seal veins provides a more powerful means of determining the history of incremental vein opening, highlighting examples where fibre orientations are apparently oblique to the direction of vein opening, the critical issue appears to be one of distinguishing between crack-seal and open-space filling vein growth. Free growth of a crystal, that is, open-space filling vein growth, results in apparent fibre orientations that do not track the incremental displacement history of the fracture, but rather grow sub-perpendicular to the vein wall (Cox and Etheridge, 1983), whereas fibre orientations in crack-seal veins are reliable indicators of the direction of fracture opening.

Glen (1987b) documented both sub-vertical and sub-horizontal directions of fracture opening in deposits in the Cobar Goldfield, including the New Occidental deposit. He argued cross-fibred sub-horizontal veins and slip-fibred steeply dipping veins indicate a sub-vertical vector of fracture opening, whereas cross-fibred steeply dipping veins in the Goldfield indicate a sub-horizontal phase of fracture opening. However, whilst a sub-vertical vector of fracture opening was confirmed for the New Occidental deposit, this study indicates Glen's sub-horizontal quartz fibres are not true fibres formed during incremental fracture opening but are narrow comb-textured crystals formed during open-space filling vein growth.

Steeply dipping veins from the first three stages of quartz veins in the New Occidental deposit (Stages 1–3) exhibit a variety of quartz vein textures consistent with open-space filling vein growth where the rate of vein opening exceeded the rate of vein growth. Those include colloform/crustiform banding, cavity-filling inwardly radiating comb quartz containing saw-toothed growth bands, cockade- and rosette-textured quartz and quartz crystals with c-axes oriented orthogonal to vein walls irrespective of the orientation of the veins (c.f. Dowling & Morrison, 1988, Hodgson, 1989; Cox 1987). In contrast, steeply dipping Stage 4 veins are often strongly laminated and ribbon-textured and contain well-developed slip-fibres (parallel to vein walls and the L_1^1 stretching lineation) with planar growth bands perpendicular to fibre orientations. The development of quartz vein fibres sub-parallel to the host shear zone is induced by incremental slip on steeply dipping slip surfaces during crack-seal vein growth (Ramsay, 1980a; Ramsay & Huber, 1983; Cox & Etheridge, 1983; Hodgson, 1989). Such textures are typical of veins in which the rate of vein mineral growth has exceeded the rate of vein opening (Cox, 1995; Robert & Poulsen, 2001). A lesser number of steeply dipping Stage 4 quartz veins on the margins of the main Stage 4 quartz vein breccia in the footwall of the New Occidental deposit contain more coarsely crystalline cavity-filling comb quartz, indicative of open-space filling vein growth.

The five stages of sub-horizontal veins in the New Occidental deposit (Stages 1–5), which formed synchronously with steeply dipping veins of the same stage, define a similar history of vein growth to that described above. Stage 1 and 3 sub-horizontal veins contain comb quartz and are generally weakly fibred with fibres oriented orthogonal to vein walls. They contain planar and saw-toothed growth bands indicating both crack-seal and open-space filling vein growth. The colloform- and crustiform-banded nature of Stage 2 sub-horizontal veins suggests they developed by open-space filling vein growth. In contrast, Stage 4 and 5 sub-horizontal veins are consistently strongly cross-fibred (fibres parallel to the L_1^1 stretching lineation) and show evidence of syntaxial and/or stretched crystal vein growth

(Section 4.3.4), textures characteristic of veins formed by repetitive incremental crack-seal (Ramsay, 1980a; Cox and Etheridge, 1983). Like the equivalent steeply dipping veins, earlier formed sub-horizontal quartz veins (Stages 1–3) record predominantly open-space growth where the rate of vein opening exceeded vein growth, whilst the later stages (Stages 4–5) have clearly formed by crack-seal vein growth where the rate of vein growth has exceeded the rate of vein opening.

Fibre orientations in those veins in the New Occidental deposit that have demonstrably formed by crack-seal growth, including some Stage 1 and 3 sub-horizontal veins, all Stage 4 and 5 sub-horizontal veins and most Stage 4 steeply dipping veins, are all consistently sub-vertical and parallel to the L_1^1 stretching lineation. Steeply dipping quartz veins in the New Occidental deposit equivalent to Glen's (1987b) steeply dipping cross-fibred veins (all Stage 1 and 3 quartz veins and a lesser number of Stage 4 veins) have formed by open-space filling vein growth rather than of incremental crack-seal growth. Importantly, sub-horizontal crystal orientations in these veins do not indicate the vector of fracture opening and, consequently, do not provide evidence for a phase of sub-horizontal fracture opening in the New Occidental deposit. Quartz fibre orientations in veins in the New Occidental deposit therefore indicate a consistent sub-vertical direction of fracture opening in the deposit throughout its history of vein deposition.

4.4.3 Significance of Quartz Vein and Fibre Orientations

The consistent pattern of both gently dipping quartz veins (orthogonal to cleavage) and steeply dipping (cleavage-parallel) quartz veins and breccias in the New Occidental deposit is characteristic of quartz veins formed in active reverse fault zones (c.f. Cox, 1995; Robert & Poulsen, 2001; Figure 91). Both the geometry and internal textures of gently dipping quartz veins in the New Occidental deposit are consistent with those veins being extension veins, whereas the steeply dipping quartz veins in the deposit are interpreted to be fault-fill veins. Evidence for the gently dipping veins in the New Occidental deposit being **extension veins** includes:

1. Veins lie at high angles to both S_1 cleavage and associated L_1^1 stretching lineation
2. Veins are typically planar with parallel veins walls and occur in stacked arrays throughout the deposit
3. Quartz fibres in gently dipping quartz veins, which are oriented perpendicular to vein walls and parallel to the L_1^1 stretching lineation, indicate a sub-vertical direction of fracture opening during vein deposition

Evidence for the steeply dipping quartz veins and vein breccias being **fault-fill veins** includes:

1. Veins and vein breccias are parallel or slightly oblique to S_1 cleavage and the host Great Chesney Fault
2. Veins are strongly foliated parallel to S_1 cleavage
3. Veins contain abundant cleavage-parallel slickensides, anastomosing chlorite septa and foliated wallrock slivers, indicating significant post-deposition cleavage-parallel shearing of those veins

4. Veins form elongate complex stockworks within the host shear that parallel cleavage and are elongate in the direction of the L_1^1 stretching lineation

5. Some veins (mainly Stage 4 veins) are slip-fibred with fibres sub-parallel to the L_1^1 stretching lineation, indicating sub-vertical fracture opening during vein deposition

6. Offsets across steeply dipping veins are common, and, where bedding can still be observed, readily quantified

Figure 91: Characteristic vein geometries in a steeply dipping fault zone (from Robert & Poulsen, 2001).

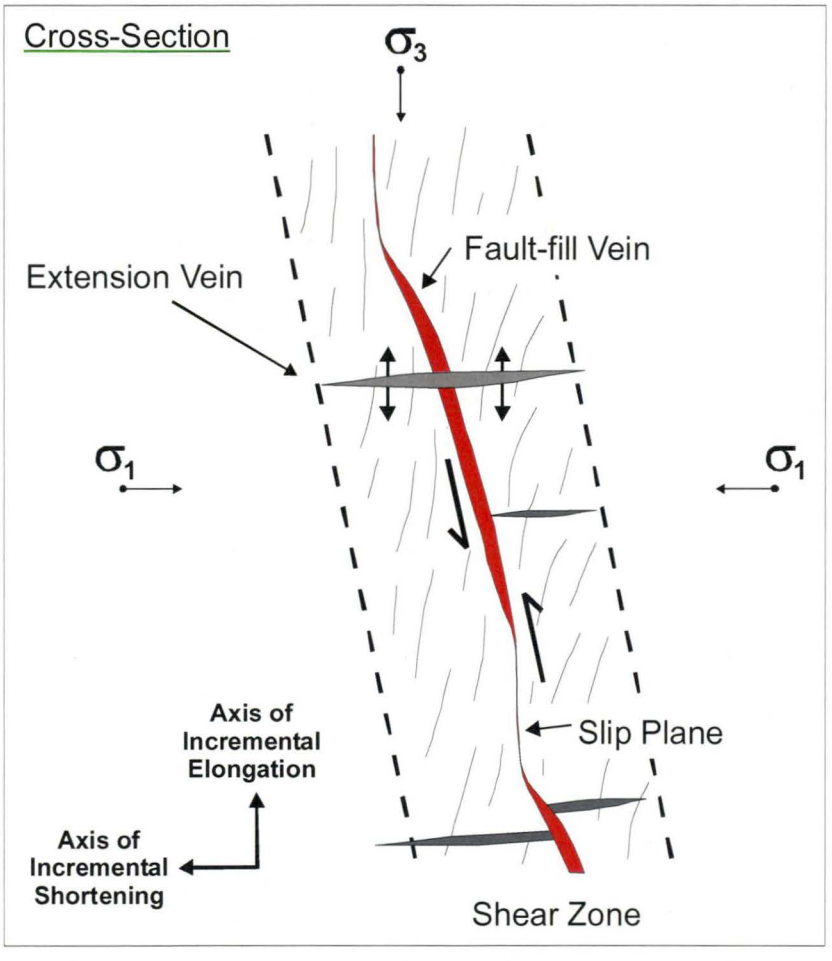

Formation of steeply dipping fault-fill and sub-horizontal extension veins in the New Occidental deposit during reverse slip on the steeply dipping Great Chesney Fault indicates the regional stress field during deposit formation comprised a sub-horizontal maximum compressive stress (σ_1), which is orthogonal to strike of the shear zone, and a sub-vertical the least compressive stress (σ_3) (e.g. Ramsay, 1980; Ramsay & Huber, 1983; Sibson, 1986; 2001; Sibson et al., 1988; Robert & Poulsen, 2001). Glen (1987b) also inferred similar stress field orientations for the broader Cobar Goldfield based on this pattern of vein orientations.

Development of sub-horizontal extension veins in all five stages of quartz veining in the New Occidental deposit indicates the orientation of σ_3 remained relatively constant throughout the period bracketed by the five vein stages. Further, the widespread presence of sub-horizontal extension veins throughout other deposits of the Cobar Basin (Section

4.2.3) indicates the stress field orientation interpreted for the New Occidental deposit in this study, and also by Glen (1987b) for the Cobar Goldfield, is a basin-wide phenomenon.

The relatively constant orientation of the steeply dipping fault-fill veins through time also suggests that the orientation of the far-field stresses remained relatively constant through D_1 time. The four stages of fault-fill quartz veins (Stages 1–4) in the New Occidental deposit predominantly strike sub-parallel to S_1 but dip less steeply towards the east. Stages 1–3 quartz veins have similar modal dip/dip directions in the range 50–80°/085–095°, whereas the Stage 4 quartz veins have a modal dip/dip direction of 72°/070°. This compares with a cleavage orientation of 85°/078–084° in the New Occidental area. These orientations are consistent with the principal compressive stress (σ_1) having an east-northeast – west-southwest orientation. The small difference in strike between the Stage 4 veins and the other vein types may reflect a small-scale anti-clockwise rotation of the orientation of the regional stress field through D_1 time from east-northeast – west-southwest during deposition of Stages 1-3 quartz veins to northeast-southwest during deposition of Stage 4 veins.

4.4.4 Significance of Crustiform- and Colloform Banded Quartz Veins

The presence of crustiform- and colloform-banded quartz veins and vein breccias in the New Occidental deposit is evidence that both the veins and the interclast space of the breccia veins remained open for the length of time required to precipitate all infilling vein minerals (Hodgson; 1989). Whilst such textures are more typical of epithermal vein systems formed at shallow crustal levels, crustiform- and colloform-banded quartz veins have also been observed in vein systems formed at relatively deeper crustal levels (Hodgson, 1989) of the order of 2–5 km (Vearncombe, 1993; Groves et al., 1995; Hageman & Cassidy, 2000) where they are interpreted to have formed in zones of significant dilation.

Crustiform- and colloform-banded quartz is best developed in the Stage 2 quartz veins where it comprises multiple alternating bands of cryptocrystalline and crystalline quartz. Colloform- and crustiform-banding is best developed in Stage 2 veins in the centre of the New Occidental deposit in the thickest part of the fault dilation associated with this vein stage. Lesser colloform- and crustiform-banding is also developed in Stage 3 veins and rarely in Stage 1 veins. The colloform-banded Stage 1 quartz-magnetite veins are best developed in the centre of the deposit, coincident with the Great Chesney Fault where vein density is greatest. In contrast, Stage 1 veins in the hanging wall of the deposit comprise only weakly banded cockade and comb quartz. Accordingly, development of colloform- and crustiform-banded quartz veins in the New Occidental deposit appears directly related to the degree and rate of dilation along the Great Chesney Fault.

In detail, individual quartz bands in the colloform- and crustiform-banded quartz veins consist of initial cryptocrystalline quartz grading outwards into progressively more coarsely crystalline quartz. This pattern is consistently developed along individual bands and is cyclically repeated in successive bands, suggesting that the gradational coarsening in quartz crystal size within each band is a primary feature and is not caused by subsequent recrystallisation. A likely mechanism for formation of the colloform and crustiform veins in the New Occidental deposit involves a cyclic pattern of:

1. Slip on the host Great Chesney Fault initiates dilational brecciation and causes a significant drop in fluid pressure, which triggers silica supersaturation in the hydrothermal fluids contained within the fault zone and deposition of cryptocrystalline quartz on vein walls and on breccia fragments. While

chalcedony and amorphous silica are relatively common in shallow-level epithermal systems, they are less common in deeper deposits (Fournier, 1985; Vearncombe, 1993). However, Fournier (1985) proposed that sudden decreases in fluid pressure, possibly from nearly lithostatic to nearly hydrostatic or lower, cause fluids at relatively high temperatures (300°C) to become supersaturated with silica, resulting in the precipitation of very fine grained or cryptocrystalline silica.

2. As hydrothermal precipitation begins to seal the fault zone, fluids entering the fault do not experience the same magnitude of pressure drop. Fluid pressures in and around the fault begin to stabilise and gradually increase, and the hydrothermal fluid becomes progressively less supersaturated with silica. As a consequence, the rate of growth for favourably oriented quartz crystals exceeds the rate of nucleation, resulting in deposition of progressively more coarsely crystalline comb-textured quartz crystals oriented at high angles to substrate.

3. Cyclic growth zones suggest the process is re-initiated during episodic slip on the host fault.

When fault slip is relatively minor and the corresponding drop in fluid pressure is of a lesser magnitude, then the new band of quartz will likely commence with crystalline or microcrystalline quartz rather than finer-grained cryptocrystalline quartz. Alternatively, when fault slip is relatively major but only small voids or open spaces are created then the cryptocrystalline quartz deposition may be sufficiently prolonged to completely fill or seal the void. Each successive band in the colloform/crustiform veins in the New Occidental deposit is therefore interpreted to represent a new slip event on the Great Chesney Fault, in much the same way as each growth increment in crack-seal veins does (Ramsay, 1980a; Cox and Etheridge, 1983).

4.4.5 Mechanisms of Breccia Formation

The range of breccia textures in the New Occidental deposit indicates widespread relatively intense implosive brecciation associated with large-scale dilation along the Great Chesney Fault. The presence of well-developed jigsaw breccias and zones of open-space filling rosette/cockade quartz crystal vein growth in steeply dipping Stage 1 breccia veins and along the margins of the main Stage 4 quartz vein breccia is indicative of vein formation in an implosive extensional setting (Sibson, 1986; Robert and Poulsen, 2001) and open-space filling environments (Hodgson, 1989). The angular, internally undeformed nature of clasts within these breccias is also consistent with brittle extensional deformation rather than shear brecciation (Hodgson, 1989). The occurrence of jigsaw breccia in the thicker and less steeply dipping parts of Stage 1 fault-fill veins is also consistent with breccia formation in dilational jogs in active fault zones (Robert and Poulsen, 2001; Table 15).

Stage 2 and 3 quartz vein breccias and the core of the main Stage 4 quartz vein breccia in the footwall of the Main lode of the New Occidental deposit are characterised by rotated, angular and elongate breccia fragments exhibiting little or no evidence of attrition or rounding, an abundance of well-developed open space fill quartz vein growth textures and higher hydrothermal mineral matrix to wallrock clast ratios than the Stage 1 and 4 jigsaw breccias, indicating formation in a more highly dilational implosive environment (e.g. Sibson, 1986; Hodgson, 1989). Clast compositions reflect the composition of the opposing walls of the breccia zones. For example, fragments in Stage 2–3 quartz vein breccias in the hanging wall side of the Main lode consist predominantly of Stage 1 veined sandstone, whereas Stage 3 quartz vein breccias contain largely fragments of Stage 2 quartz veins and

Stage 2 quartz veined wallrock. In the hanging wall side of the main Stage 4 quartz vein breccia, Stage 2–3 quartz vein and vein breccia fragments predominate while the footwall side contains almost exclusively fragments of Great Cobar Slate.

Whilst the bulk of the quartz vein breccias in the New Occidental deposit formed by implosive brecciation associated with dilation along the Great Chesney Fault, a minor component of the breccia veins in the deposit has formed by attrition and fault brecciation. Some Stage 4 breccia veins and, in particular, the fault breccia developed in the footwall of the New Occidental deposit in the upper part of the deposit (Section 4.3.4; Figure 79) are characterised by high matrix to fragment ratios, reduced hydrothermal mineral contents, little or no hydrothermal open-space filling mineral growth and strong shear fabrics, including slip-fibred and laminated quartz. For example, the breccia in the footwall of the New Occidental deposit contains virtually no hydrothermal mineral component, consisting instead of angular rotated fragments within a matrix of crushed and strongly sheared siltstone/mudstone fragments. Those characteristics, especially the paucity of hydrothermal minerals, the absence of open-space fill quartz vein textures and the strong shear fabrics, indicate the breccias formed mainly by shearing and fault displacement and were associated with little or no dilation during breccia formation (e.g. Sibson, 1986; Hodgson, 1989; Robert and Poulsen, 2001).

The first four stages of quartz vein formation (Stages 1–4) in the New Occidental deposit therefore all record cyclic slip and dilation along and adjacent to the Great Chesney Fault. Stage 1 breccias, which comprise mainly jigsaw breccias, indicate dilation in the hanging wall of the deposit was less intense than in the core of the deposit, both in terms of the rate and extent of dilation, but also suggest that the intensity of dilation increased towards the fault. Stage 2–3 breccias represent a more intense phase of brecciation and open-space filling veining within the Great Chesney Fault, consistent with their location in the centre of the New Occidental deposit where dilation was maximised. The main Stage 4 breccia also formed as a result of implosion into a large-scale dilation along the Great Chesney Fault in the footwall of the Main lode. The presence of jigsaw breccia along its hanging wall and footwall contacts is consistent with reduced dilation along the margins of the breccia. However, some Stage 4 breccias and the distinctive fault breccia in the immediate footwall of the Main lode have formed by fragmentation, plucking and abrasive wear during slip. These latter breccias have most likely formed along contractional fault planes (e.g. Sibson, 1986; Table 14).

Estimates of the volume of each vein stage across the New Occidental deposit allow the magnitude of dilation associated with each stage of quartz veining to be quantified (Section 4.3.7). In the centre of the deposit the Stage 2–3 quartz breccia complex that defines the Main Lode is estimated to have a maximum true thickness of approximately 24m (Figure 83). In contrast, the maximum thickness of the Stage 4 breccia is estimated to be only 7–8m thick (Figure 84). The Stage 2–3 breccia development clearly records the main stage of fault dilation along the Great Chesney Fault. The apparent increase and subsequent decline in fault zone dilatancy may reflect the rate and amount of displacement during each vein stage, hydrothermal fluid supply and evolving fault geometry. Sibson (2001) suggested that in the early stages of fault movement, fault surfaces are highly irregular, favouring higher degrees of dilation. Progressive smoothing of the fault surface with ongoing fault displacement reduces the effective size of the resultant dilation.

4.4.6 Displacement Vectors on the Great Chesney Fault inferred from Quartz Veins

Previously cited structural and stratigraphic observations from the New Occidental deposit indicate consistently east-block up dip-slip displacement on the Great Chesney Fault (Section 3.9.1). Analysis of quartz vein textures and orientations provide further supporting evidence of east-block up displacement on the fault (Figure 92):

1. Fracture opening directions inferred from quartz fibres in crack-seal veins indicate a consistent sub-vertical extension direction (Section 4.4.2).
2. Steeply dipping Stage 1 and 4 quartz veins form steeply dipping arrays of en-echelon steeply to moderately dipping veins within and surrounding the Great Chesney Fault/New Occidental deposit, consistent with east block-up reverse dip-slip fault movement. Veins in these arrays typically dip less steeply to the east than cleavage (Section 4.3.8).
3. Small-scale east-block up offsets of bedding occur across all stages of steeply dipping veins (Section 4.3.8).
4. Steeply dipping sections of quartz veins are commonly attenuated and boudinaged. Necks in individual boudins have a sub-horizontal plunge (Section 4.3.1).
5. Flatter sections of quartz veins are generally thicker, indicating greater dilation. In some cases, only the flat segments of veins include later-stage vein-fill (Section 4.3.2).

Figure 92: Schematic cross-section through the New Occidental deposit showing kinematic indicators of displacement on the Great Chesney Fault.

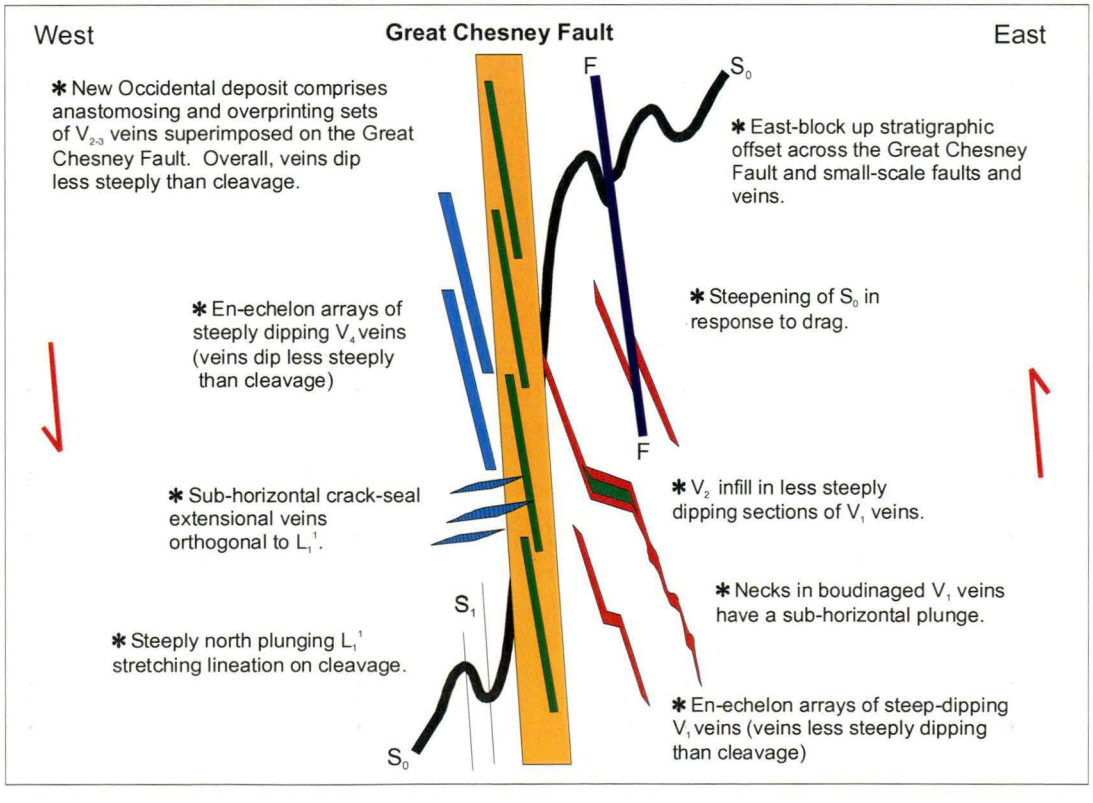

The only kinematic indicators of a contrary sense of fault displacement on the Great Chesney Fault are the apparent normal bedding and vein offsets on some steep-dipping

fault-fill veins (Section 4.3.8). A possible explanation is that they formed during restricted periods of relaxation associated with local reversals of the stress field. Such phenomena have been described from the Sigma mine in the Val d'Or district of the Abitibi Belt, Canada (Boullier & Robert, 1992) and in the Wattle Gully deposit, Victoria (Cox, 1995). Cox (1995) suggested that those normal fault offsets are the product of total relief of shear stress and transient reversal in stress orientations after some (major) slip events on the faults. Zoback and Beroza (1993) cite evidence of similar near-total relief of shear stress associated with the main rupture event of the modern (1989) Loma Prieta earthquake.

4.4.7 Implications of Regional Stress Field Orientation for Activation of the Great Chesney Fault

The very steeply dipping Great Chesney Fault was unfavourably oriented for slip given the prevailing stress field inferred during D_1 in the New Occidental deposit area. Reverse faults have been determined to ideally form at angles of $27 \pm 5°$ to σ_1, which is also the optimal orientation for re-activation of pre-existing fault surfaces (Sibson, 2001). As the orientation of an existing structure becomes progressively less favourable for re-activation, in this case steeper, the ratio of effective stresses (σ_1'/σ_3') required for re-activation increases, reaching infinity or frictional lock-up at angles of 50–60° (Sibson, 2001). As σ_1 was sub-horizontal east-northeast – west-southwest trending during D_1, steeply dipping structures in the New Occidental deposit were severely mis-oriented for slip (Figure 93). For example, the Great Chesney Fault and the bulk of the associated minor faults, veins and breccias dip between 60–87° and are unfavourably oriented for slip. Significantly, the Great Chesney Fault initiated as a relatively steeply dipping fault (not less than 60° - Section 3.9.2) and continued to slip throughout D_1, as it steepened in response to ongoing shortening. Slip on the Great Chesney Fault and other steeply dipping surfaces was only possible under special circumstances when the least compressive stress, $\sigma_3 < 0$. Such a condition, which Sibson (2001) refers to as the tensile overpressure condition, is only satisfied when fluid pressure (P_f) is greater than $\sigma_3 + T$ (tensile strength of the rock) (Sibson, 2001).

Figure 93: Ratio of greatest to least effective stresses (σ_1'/σ_3') required for reshear of a cohesionless fault plotted against the reactivation angle (θ_r). θ_r^* is the optimum angle for reactivation at which the stress ratio reaches a positive minimum (from Sibson, 2001).

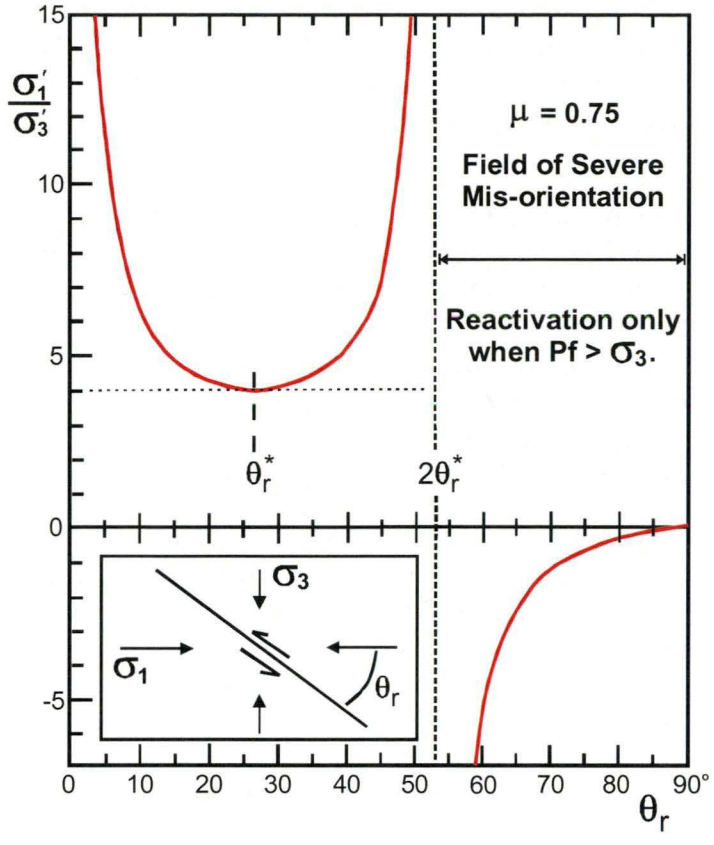

Sibson (2001) noted that favourably oriented faults within the prevailing stress field would re-activate in preference to any other form of brittle failure. Similarly, the tensile over-pressure condition required for pure extension fracturing and extensional shear failure is unlikely to have been attained if a favourably oriented structure already existed. By inference, the presence of widespread extension veins throughout the New Occidental deposit indicates that favourably oriented faults were absent from the deposit environs and that the Great Chesney Fault was unlikely to have initiated as a favourably oriented fault that subsequently rotated into its current unfavourable orientation.

4.4.8 Fluid Pressure Regimes inferred for the New Occidental deposit

The geometry, distribution and texture of quartz veins and vein breccias within the New Occidental deposit provide a number of constraints on the fluid pressure regime within the deposit during vein deposition:

1. The presence of widespread sub-horizontal extension veins throughout the deposit indicates that the tensile overpressure condition of $\sigma_3 < 0$ was intermittently attained throughout development of the deposit (e.g. Cox, 1995; Sibson, 2001 – Figure 94).

2. Because the Great Chesney Fault and sub-parallel structures like bedding and cleavage are severely mis-oriented relative to the prevailing stress field, slip on these structures requires very high to supra-lithostatic fluid pressures during D_1. However, pre-existing planes of weakness in the New Occidental deposit that

are characterised by lower cohesive strength than intact rock were preferentially activated (Figure 94).

3. The four main stages of quartz veining in the New Occidental deposit (Stages 1–4) all contain significant volumes of quartz breccia veins that are interpreted to have formed by implosive brecciation. Implosive brecciation typically occurs in response to high fluid pressures in the wallrock causing spalling of wallrock into the dilational zones where fluid pressures are significantly lower (Sibson, 1986; Cox, 2000).

4. The widespread occurrence of dilational quartz vein breccias in Stages 1–4, and particularly in Stages 2–3 where open space filling quartz vein breccias comprise over two-thirds of the total vein population, indicates both high fluid pressures to promote fracturing and high fluid flux/supply to keep vein walls apart during hydrothermal mineral deposition. Similarly, the greater proportion of open-space filling vein textures in the early stages of veining in the New Occidental deposit, compared to the latter stages, indicates that fault dilation and fluid supply was greatest in the earliest stages of deposit formation.

5. The presence of abundant well-developed sub-horizontal Stage 4 extension veins in the core of the New Occidental deposit (overprinting the complex stockwork of steeply dipping Stage 2–3 veins and vein breccias) is interpreted to reflect a declining strain rate and/or fluid supply within that part of the deposit. However, fluid pressures remained sufficiently high in the core of the deposit to initiate extensional fracturing. Therefore, the shift in locus of fault slip to the footwall of the New Occidental deposit during Stage 4 (where the bulk of Stage 4 veins and vein breccias have deposited) resulted in lower overall strain rates in the core of the deposit, promoting formation of sub-horizontal extension veins over steeply dipping fault-fill veins (Figure 94).

6. Thinner and more sparse sub-horizontal extension veins in Stage 5, and the total absence steeply dipping fault-fill veins in this Stage, indicates reduced fluid pressures, albeit still occasionally transiently higher than σ_3, and greatly reduced strain rates/fluid supply, consistent with cessation of slip on the Great Chesney Fault (Figure 94).

7. Extension veins decrease in both frequency and intensity away from the New Occidental deposit and the host Great Chesney Fault, indicating transiently higher fluid pressures in the centre of the fault zone compared to the wallrock. Cox (1995) has previously noted that the decrease in both frequency and intensity of extension veins away from the Wattle Gully Fault Zone indicated transiently higher fluid pressures rather than increasing stress gradients in the fault zone, i.e. hydrothermal fluids were concentrated in and around zones of most intense deformation where time-integrated and structurally enhanced permeability were greatest.

Quartz vein textures and geometries within the New Occidental deposit suggest that much of the deposit has formed under relatively high fluid pressures that have transiently exceeded lithostatic fluid pressure conditions. The extensive implosive breccias and a range of open-space filling vein textures indicate large-scale fault dilations resulted in high fluid fluxes and extreme fluid pressure variations within the Great Chesney Fault.

4.4.9 The Role of Competency Contrast in Quartz Vein Formation

Quartz veins in the New Occidental deposit are preferentially developed at the boundaries of and within more competent units. Stage 1 quartz veins are largely developed in the sandstone hanging wall of the Great Chesney Fault rather than in the less competent siltstones and mudstones in the footwall of the fault. Stage 2 veins and vein breccias are similarly developed along the boundary between competent Stage 1 veined sandstones (hanging wall) and less competent siltstones/mudstones (footwall). In this case, Stage 1 quartz veins have effectively silicified the hanging wall sandstones, thereby enhancing the hanging wall – footwall competency contrast. Stage 3 veins are focussed within the margins of the strongly siliceous Stage 2 quartz breccias whilst Stage 4 veins have been subsequently preferentially focussed along the boundaries of the stockwork of Stage 2–3 quartz veins and vein breccias. In particular, Stage 4 veins and breccia veins are best developed at the footwall boundary between the very siliceous and very competent stockwork of Stage 2–3 quartz veins/vein breccias and less competent siltstone/mudstone footwall. The competency contrast across this boundary has been further enhanced by pervasive chlorite alteration of the footwall siltstones/mudstones. Stage 4 and 5 extension veins are localised within the same stockwork of Stage 2–3 quartz veins and vein breccias.

Figure 94: Mohr diagrams illustrating relationships between principal stresses, shear stress and differential stress for the different quartz vein stages in the New Occidental deposit.

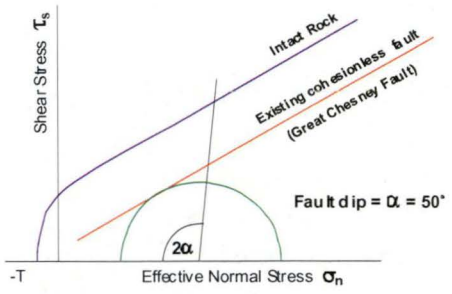

Pre-Stage 1

Low-moderate fluid pressure, high differential stress and Great Chesney Fault moderately highly misoriented for slip under the prevailing regional stress field:
- Intact rock did not fail
- Shear failure did not occur on the Great Chesney Fault

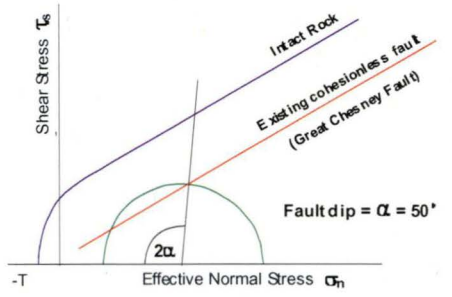

Stage 1

High fluid pressure and high differential stress:
- Intact rock did not fail
- Shear failure occurred on the Great Chesney Fault
- Cohesive strength of fault is low

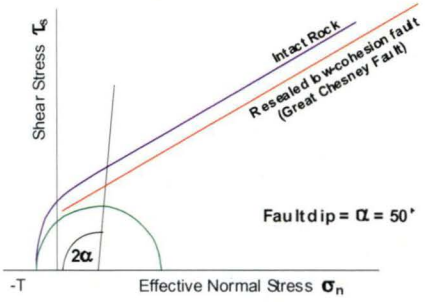

Stage 1 (Post-rupture)

Very high fluid pressure, lower differential stress and the Great Chesney Fault has been resealed with hydrothermal minerals (increased cohesion on the fault):
- Intact rock did not fail
- Differential stresses were low
- Shear failure did not occur on the Great Chesney Fault
- Sub-horizontal extension veins formed
- Note that the Great Chesney Fault must have regained appreciable cohesion before sub-horizontal extension veins could form.

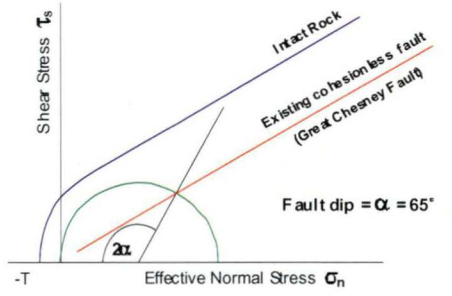

Stage 2-4

Intermittently developed near lithostatic to supralithostatic fluid pressure (pore fluid pressure greater than lithostatic pressure at failure), high differential stress and the Great Chesney Fault highly misoriented for slip under the prevailing regional stress field:
- Intad rock did not fail
- Shear failure occurred on the Great Chesney Fault only at higher fluid pressures.

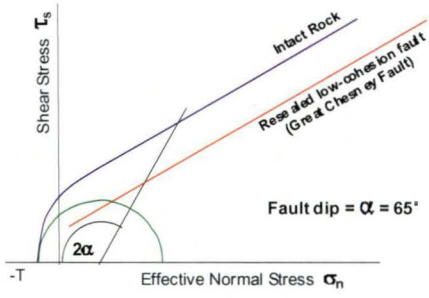

Stage 2-4 (Post-rupture)

Intermittently developed supralithostatic fluid pressure, lower differential stress and the Great Chesney Fault had been resealed with hydrothermal minerals (increased cohesion on the fault):
- Intact rock did not fail
- Shear failure did not occur on the Great Chesney Fault
- Sub-horizontal extension veins formed
- Note that, in comparison to Stage 1, when the fault dip is interpreted to have been lower, the fault needed to regain only moderate cohesion prior to sub-horizontal extension veins forming in the fault environs.

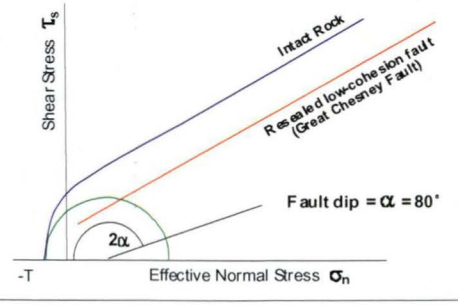

Stage 5

Very high fluid pressure, lower differential stress and the Great Chesney Fault severely misoriented for slip under the prevailing regional stress field:
- Intact rock did not fail
- Shear failure did not occur on the Great Chesney Fault
- Only sub-horizontal extension veins formed.

Two parallel processes appear to have been operated during formation of the New Occidental deposit:

1. **Deposition of veins and breccias along the boundaries between competent and less competent rock masses.** Oliver et al. (2001) argued deformation of rock packages consisting of bodies of strong rocks in a matrix of weaker, less competent rock causes stress and strain to localise around those more competent /stronger rock bodies, with dilation preferentially occurring along hard/soft rock boundaries oriented at a high angle to the maximum compressive stress (σ_1). They argued significant variations in P_f and large fluid pressure gradients resulting from fluid infiltration along the hard/soft rock boundaries may ultimately dilate the boundaries, and give rise to implosive brecciation. Such situations are more readily attained along the boundaries of rock masses of contrasting competency than between more homogenous rock types (Oliver et al., 2001).

2. **Deposition of veins preferentially within more competent rock masses.** Cox et al. (2001) argued that competency contrasts within rock masses localise fracturing. Where strong rock masses occur within a weaker matrix, with boundaries between the two rock-types oriented at a high angle to the shortening direction (~90° in the case of the New Occidental deposit) viscous or frictional drag along these boundaries reduces the minimum principal stress in the competent rock mass. As a consequence, brittle failure in the form of hydraulic extension fractures and/or shear failure will occur first in the zone of decreased effective principal stress in the competent rock masses (Cox et al., 2001). Sibson (2001) have similarly noted that hydrothermal silicification, by increasing the tensile strength of the rock mass, may also increase the depth range over which extension fractures may occur.

The progressive shift in the locus of quartz veining from the hanging wall to the footwall of the New Occidental deposit during deposit formation can therefore be explained by repeated cycles of brecciation and dilation focussing along rock mass boundaries with the greatest competency contrast. The process of sealing dilations with quartz and other hydrothermal minerals largely eliminated the competency contrast across those boundaries, resulting in subsequent dilation along other competency contrasts in the deposit including the boundary between the newly deposited stage of veins and footwall siltstone/mudstone. The net result was that successive stages of quartz veins and vein breccia were accreted to the previously formed zones of quartz veins/vein breccias, thereby progressively enlarging the more competent zone of quartz-veined rock within the New Occidental deposit (Figure 95).

Figure 95: Spatial evolution of quartz veins in the New Occidental deposit.

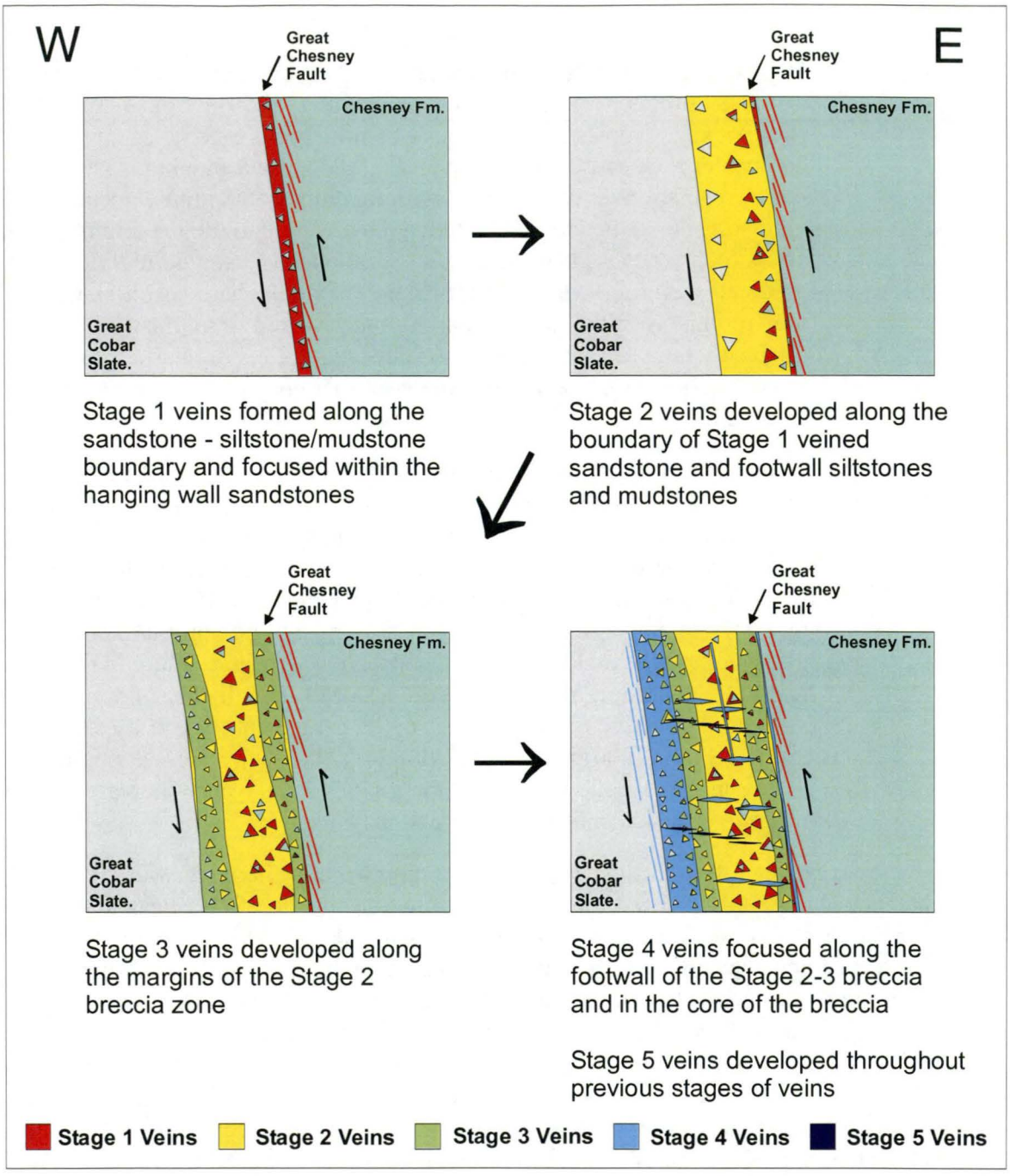

4.4.10 Depth of Deposit Formation inferred from Quartz Vein Textures

Quartz vein textures have been used to infer depths of ore formation (Dowling & Morrison, 1988; Dowling, 1989; Hodgson, 1989; Vearncombe, 1993; Groves et al., 1995; Hageman & Cassidy, 2000). Quartz vein textures in the New Occidental deposit do not indicate deposit formation in a shallow-level (<1000m) epithermal environment. Bladed carbonate and quartz-adularia (after carbonate) and other epithermal vein textures are absent in the deposit. Rather, quartz vein textures in the New Occidental deposit are indicative of deeper (>1000m) levels of deposit formation characteristic of orogenic gold deposits.

Based on an analysis of vein textures in orogenic gold deposits of the Yilgarn Craton, Western Australia, Vearncombe (1993) suggested that whilst a variety of factors control quartz morphology, depth of formation is the major indirect control on vein quartz textures.

Groves et al. (1995) subsequently developed the concept of a depth continuum for Archaean orogenic gold deposits of the Yilgarn Craton, recognising a series of critical trends in quartz vein textures that correspond to increasing depth of formation and grade of metamorphism, including trends from:

- More brittle to more ductile structures
- Breccias and discordant quartz veins to foliation-parallel veins and shear-zone replacement deposits
- Plumose, comb, cockade and vuggy quartz textures through massive or laminated veins to veins with coarse-grained granoblastic quartz

Hageman & Cassidy (2000) refined the depth continuum model of Groves et al. (1995) and suggested a threefold classification of orogenic gold deposits based on depth of formation and characteristic quartz vein textures and structures (Table 17).

Table 17: Characteristics of orogenic gold deposits in relation to depth of deposit formation (after Hageman and Cassidy, 2000).

	Physiochemical Conditions	Quartz Vein Types and Structures	Gold Deposits
EPIZONAL	250–400° C <1–2 Kbar <5–8 km	Fault zones and cataclasites Jigsaw breccias Open-space filling quartz textures including comb, cockade, crustiform and colloform quartz Precursor cryptocrystalline quartz Sheeted veins Pressure solution cleavage	Golden Mile Wiluna Campbell, Ontario Kirkland Lake, Ontario
MESOZONAL	375–550° C 2–3 Kbar 7–12 km	Ductile to brittle-ductile shear zones Fault-fill and extension veins Breccias Pressure solution cleavage Sheeted and stockwork veining Massive white quartz	Defiance Lodes, Kambalda Mt Charlotte Lancefield Sons of Gwalia Sigma-Lamarque, Ontario
HYPOZONAL	525–650° C 3–4 Kbar 10–15 km	Ductile to brittle-ductile shear zones Fault-fill and cleavage-parallel veins Minor breccia Laminated to massive veins	Marvel Loch Norseman Lupin Westonia Nevona Kolar, India

Based on the criteria cited by Vearncombe (1993), Groves et al. (1995) and Hageman & Cassidy (2000), the New Occidental deposit contains a number of quartz vein textures that can be used to infer likely depths of formation, including:

1. **The relative proportions of open-space filling and crack-seal quartz veins.** The New Occidental deposit is characterised by abundant open-space filling quartz veins and vein breccias and by a relatively high proportion of open-space filling veins compared to other orogenic gold deposits (e.g. Groves et al., 1995). Formation of open-space fill vein textures require a high fluid flux and fluid supply sufficient to maintain fracture openings during hydrothermal mineral deposition, conditions that are most likely to occur at shallower crustal levels

(Vearncombe, 1993; Groves et al., 1995) of the order of <5–8 km where confining pressure is lower (Hagemann & Cassidy, 2000). As a further point of reference, Fischer et al. (2003) recorded open fissures coated with comb quartz crystals at a depth of 2.6km in a drillhole testing an active magma chamber in the Long Valley caldera, California.

2. **The relative abundance of open-space fill breccias, including jigsaw breccias.** Open-space fill vein breccias constitute the bulk of veins in the New Occidental deposit and their relative abundance is higher than in most other orogenic gold deposits (e.g. Groves et al., 1995; Hageman & Cassidy, 2000). Predominance of brittle breccia textures relative to ductile breccia textures indicates a shallower level of deposit formation (Groves et al., 1995; Hageman & Cassidy, 2000).

3. **The presence of cryptocrystalline quartz in Stage 2 veins.** As outlined in Section 4.4.4, cryptocrystalline quartz deposited as chalcedony/amorphous silica is relatively common in shallow <1km depth hydrothermal deposits. It is not possible to conclusively determine whether the cryptocrystalline quartz in the Stage 2 veins at New Occidental originally deposited as amorphous silica and subsequently recrystallised to very fine-grained quartz or whether it was originally crystalline. Critical textures like plumose textures indicative of amorphous silica have not been observed in the New Occidental deposit. Similarly, lattice-textured quartz (as replacement of lattice-textured carbonate) and quartz-adularia mineral assemblages that are indicative of boiling (Fournier, 1985), and hence conditions that favour precipitation of amorphous silica or chalcedony, are also absent. Fournier (1985) proposed that very fine grained or cryptocrystalline silica can precipitate from relatively high temperature fluids (300°C) characteristic of shallow-level orogenic gold deposits when these fluids become supersaturated with silica in response to rapid, large decreases in fluid pressure. This is consistent with observations of very fine grained quartz in open fissures in the previously described drillhole in the Long Valley caldera, California, which is interpreted to have crystallised at 300–350°C during periods on silica supersaturation initiated by seismic activity (Fischer et al., 2003). Hagemann et al. (1992) described crustiform cryptocrystalline quartz bands in open-space fill breccias in the Wiluna gold deposits in Western Australia, deposits that are inferred to have formed at depths of approximately 5 km (Hagemann & Cassidy, 2000). However, cryptocrystalline quartz has not been observed in orogenic gold deposits inferred to form at depths greater than 7–8 km (Hagemann & Cassidy, 2000).

4. **The presence of crustiform- and colloform-banded crystalline and cryptocrystalline quartz-chlorite in Stage 2 veins.** Crustiform- and colloform-banded vein textures are generally regarded as having formed in the near-surface environment (Dowling and Morrison, 1988; Vearncombe, 1993). However, colloform veining has been noted in a number of shallow-level orogenic deposits including the Campbell and Dickenson mines of the Red Lake area, Abitibi Belt, Canada (Hodgson, 1989), in the Central Victorian gold deposits (Cox, 1995) and in the Kalgoorlie, Wiluna and Racetrack gold deposits in the Yilgarn Craton, Western Australia (Clout et al., 1990; Hagemann et al., 1992; Vearncombe, 1993). Crustiform- and colloform banded vein textures develop where rapidly fluctuating fluid pressure gradients and/or significant changes in fluid chemistry cause rapid oscillating patterns of mineral precipitation (Fournier, 1985; Cox et al., 1986; Taylor, 1992). In the case of the

New Occidental deposit, crustiform- and colloform-banded veins are interpreted to have formed in zones of maximum fault dilation under conditions of rapidly fluctuating fluid pressure and fluid flux in the centre of the deposit (Section 4.4.4). Therefore, formation of crustiform- and colloform-banded veins, like other open-space fill vein textures, are most likely to form in shallower crustal levels where confining pressures are lower (Vearncombe, 1993; Groves et al., 1995; Hagemann & Cassidy, 2000).

5. **The occurrence of laminated fault-fill veins in Stage 4 veining.** Laminated veins are considered to be characteristic of deeper crustal levels (Vearncombe, 1993; Groves et al., 1995). Groves et al. (1995) suggested that laminated veins are most likely to form under lower greenschist to amphibolite facies metamorphic grades at or below the brittle to ductile transition and at depths greater than 7 km. Formation of laminated quartz veins in the New Occidental deposit reflects a reduction in the amount of fault dilation during fault slip, which can be caused by greater depth of formation (higher confining pressure); a reduction in the amount of incremental fault slip; and/or fault smoothing, the latter occurring in response to progressive smoothing of the surface of the Great Chesney Fault with ongoing fault displacement (Sibson, 2001). Laminated veins in the New Occidental deposit, which occur only in Stage 4, are interpreted to have formed in the latter stages of deposit formation when differential stresses and fluid supply were decreasing and irregularities in the surface of the Great Chesney Fault had been largely smoothed out. As a consequence, their presence in the New Occidental deposit does not provide a reliable constraint of depth of deposit formation.

Whilst the morphology of quartz veins in the New Occidental deposit is broadly similar to that documented in orogenic gold deposits from the Yilgarn Craton, Western Australia, the Abitibi belt, Canada and the Central Victorian gold deposits, the New Occidental deposit can be distinguished by:

- Multiple phases of large-scale dilation, resulting in a greater proportion of fault-fill quartz veins and quartz vein breccias and an abundance of open-space fill vein textures
- More variable vein textures, ranging from open-space fill textures (colloform- and crustiform-banded, cockade, comb) to crack-seal textures (laminated, cross-fibred and slip-fibred) and more variable quartz crystal size (ranging from crystalline to cryptocrystalline)
- Less strongly laminated or foliated quartz veins
- A better temporal spatial variation in textural types.

These differences indicate the scale of dilation and open-space fill in the New Occidental deposit was greater than in most of the deposits described above, and that there was less reworking and deformation of earlier formed quartz veins in the New Occidental deposit. This can in part be explained by the progressive shift in the locus of quartz vein deposition from the hanging wall to the footwall of the New Occidental deposit through time, whereas deformation and vein deposition in the many of the other deposits remained focussed within the same structure through time. It also indicates the New Occidental deposit formed at a shallower-level, where open-space fill vein textures, including breccias, are most likely to form. In comparison to the gold deposits of the Yilgarn Craton in Western Australia and the Abitibi belt, Canada, the New Occidental deposit is most similar to those

deposits inferred to have formed at the shallowest levels, including the Racetrack, Wiluna, Golden Mile and Campbell/Red Lake gold deposits. A relatively shallow (5–7km) depth of formation is inferred for the New Occidental deposit, in the context of formation depths suggested for similar orogenic gold deposits (Table 17 and Figure 96).

Figure 96: Schematic outline of characteristics of Yilgarn Block gold deposits in relation to depth of deposit formation (after Groves et al., 1995).

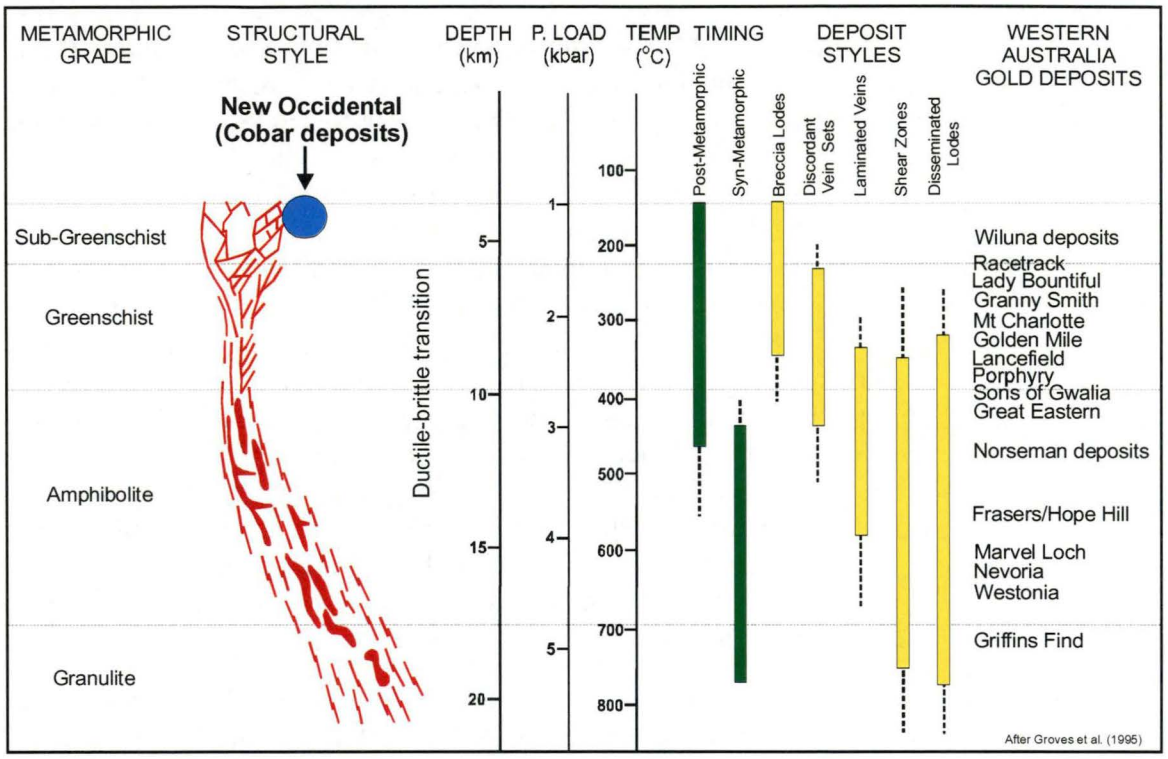

4.5 Synthesis of Quartz Vein Deposition in the New Occidental Deposit

The history of vein deposition proposed herein for the New Occidental deposit is remarkably similar to patterns of vein formation recognised in orogenic gold deposits from central Victoria, Australia (Forde & Bell, 1994; Cox, 1995; Cox et al., 1991; Cox et al. 1995), the Yilgarn Craton, Western Australia (Vearncombe, 1993; Groves et al., 1998; Vearncombe, 1998; Hagemann & Cassidy; 2000) and the Abitibi Belt, Canada (Robert and Brown, 1986a; Hodgson, 1989; Robert, 1990; Robert et al., 1995; Robert & Poulsen, 2001).

Spatial and temporal variations in quartz vein textures exhibited by the 5 vein stages in the New Occidental deposit outline a complex history of evolving deformation intimately linked to displacement on the Great Chesney Fault. Based on vein relationships and interpreted modes of quartz vein formation, the following history of vein and breccia formation in the New Occidental deposit is indicated:

Stage 1: marked the onset of significant dilation along the Great Chesney Fault in the vicinity of the New Occidental deposit. Transiently high fluid pressures ($P_f \geq \sigma_3 + T$) along the fault resulted in the formation of sub-horizontal extension veins throughout the hanging wall of the deposit, predominantly by crack-seal growth. High fluid pressures were periodically relieved in response to initiation of reverse dip-slip on the Great Chesney Fault, which produced a range of steeply east dipping fault-fill quartz veins and vein breccias. The veins and vein breccias contain exclusively open-space fill vein textures, including cockade and comb quartz and jigsaw breccia, indicating significant dilation and

implosive brecciation accompanied fault slip. While minor colloform-banded quartz-magnetite vein breccias were deposited in the core of the deposit during Stage 1, the bulk of Stage 1 veins were deposited in the hanging wall of the deposit. The intensity of internal vein brecciation, and the thickness and density of those veins and vein breccias increase towards the Great Chesney Fault, indicating that while fluid pressure fluctuations were highest along the fault, maximum dilation occurred in the competent sandstones in the immediate hanging wall of the fault. Stage 1 veins were extensively deformed during subsequent vein stages.

Stage 2: represents peak vein deposition in the New Occidental deposit. Steeply dipping fault-fill veins and vein breccias, along with minor sub-horizontal extension veins, formed in major zones of dilation along the Great Chesney Fault. Dilation induced large-scale implosive brecciation along the fault and, as a consequence, many of the fault-fill veins comprise relatively thick and vertically continuous breccia veins characterised by low fragment to matrix ratios. Breccia fragments are dominated by sandstone clasts containing Stage 1 veins, consistent with spalling of competent hanging wall into the dilatant fault zone. Dilation was accompanied by major fluid pressure fluctuations, resulting in extreme silica supersaturation of pore fluids and deposition of distinctive crustiform- and colloform-banded cryptocrystalline and microcrystalline quartz-chlorite.

Stage 3: steeply dipping fault-fill veins and vein breccias, together with minor sub-horizontal extension veins, formed in major zones of dilation developed along the margins of the Stage 2 vein complex in the core of the Great Chesney Fault. Again, many of the fault-fill veins formed as result of implosive brecciation and contain abundant fragments of Stage 1–2 veins and veined sandstone. However, fluid pressure fluctuations were less extreme than in Stage 2 and only weakly colloform banded microcrystalline to crystalline quartz was deposited. Stage 3 veins formed by open-space fill vein growth and are characterised by cockade and comb textured quartz with minor intergrown stilpnomelane.

Stage 4: represents a final stage of implosive dilation focussed along the Great Chesney Fault in the footwall of the Stage 2–3 vein complex, resulting in the formation of a steeply dipping fault-fill vein breccia containing abundant fragments of Stage 2–3 veins in a matrix of weakly crystalline quartz-chlorite. The breccia is flanked by stockworks of steeply dipping Stage 4 fault-fill veins and jigsaw breccias which extend outwards into the Stage 2–3 vein stockwork in the deposit centre and into the footwall mudstones/siltstones of the Great Cobar Slate. Stage 4 veins in the core of the deposit reflect reduced differential stresses in response to the shift in locus of dilation to the footwall of the deposit. Extensive arrays of steeply dipping fault-fill veins and sub-horizontal extension veins formed contemporaneously throughout the main Stage 2–3 vein complex. The fault-fill veins, which formed by both crack-seal and open-space fill vein growth, are characterised by weakly to strongly slip-fibred microcrystalline to crystalline milky quartz laminae separated by slip surfaces defined by chlorite-rich septa. The veins are associated with an anastomosing network of more ductile shears that overprinted the core of the New Occidental deposit. These veins record the transition from mainly brittle deformation (Stage 1–3) to ductile deformation in the core of the deposit, reflecting reduced strain rates in that part of the deposit. Deposition of crack-seal strongly cross-fibred sub-horizontal extension veins in the core of the deposit was relatively common during Stage 4, indicating continued ongoing intermittently high fluid pressures in the fault environs. A distinctive fault breccia in the immediate footwall of the Stage 2–3 vein complex, which consists of angular rotated fragments of Stage 2–3 veins in a crushed and strongly sheared siltstone/mudstone matrix, is interpreted to represent a component of non-dilational or contractional slip along the Great Chesney Fault.

Stage 5: narrow and relatively sparse late-stage sub-horizontal crack-seal extension veins formed throughout the New Occidental deposit and immediate environs during the waning stages of deformation. The planar undeformed nature of these veins indicates they post-date most shortening and cleavage development in the deposit, although they also indicate continued intermittent high fluid pressures.

Gold mineralisation in the New Occidental deposit is intimately spatially associated with Stage 2–3 quartz veins. The Main lode of the deposit is defined by the intense stockwork of Stage 2–3 veins, whereas gold mineralisation in the Albion lode is spatially associated with Stage 2 quartz infilling the centres of moderately dipping sections of Stage 1 veins scattered in and around the Albion Fault. Little or no gold mineralisation is associated with Stage 1 veins in the hanging wall of the deposit. Likewise, gold mineralisation is also not associated with Stage 4 veins, the only exception being minor gold mineralisation in the eastern (hanging wall) side of the main Stage 4 quartz vein breccia, which occurs where the Stage 4 quartz vein breccia contains abundant fragments of Stage 2–3 quartz. The predominance of steeply dipping fault-fill veins in Stages 2 and 3 indicates gold mineralisation in the Main lode of the New Occidental deposit is relatively continuous and elongate in a sub-vertical direction, although it pinches and swells where Stage 2–3 veins have been deformed and boudinaged. In contrast, gold mineralisation in the Albion lode is extremely discontinuous and erratic in its distribution.

Collectively, the range of vein and breccia textures in the New Occidental deposit indicate that the majority of displacement on the host Great Chesney Fault system was associated with multiple events of extensive fault-induced dilation. Whilst Stage 1 veins imply the presence of widespread and moderate-scale dilation in the hanging wall of the deposit, Stage 2–3 veins record a far more intense and extensive phase of dilation in the core of the deposit. A final phase of more moderate-scale dilation occurred in the footwall of the New Occidental deposit during Stage 4. Deposition of Stage 1 veins is interpreted to have taken place when the Great Chesney Fault first began to slip. Ptygmatically folded Stage 1 sub-horizontal extension veins in the hanging wall of the New Occidental deposit record comparable shortening strains to those estimated for host rocks. Based on the relative magnitude of fault dilation, the bulk of slip on the Great Chesney Fault occurred during Stage 2–3. Slip on the fault ceased prior to deposition of Stage 5 veins.

The five vein stages in the New Occidental deposit all record a complex pattern of overprinting vein orientations that indicate a cyclic process of sub-horizontal extensional fracturing followed by fault-failure and slip on steeply dipping fault planes. Variably deformed quartz fault-fill veins are cut at high angles by arrays of sub-horizontal extension veins, which are in turn truncated by younger generations of fault-fill veins. The intimate association of extension veins with each stage of fault-fill quartz veins and quartz vein breccias, the latter characterised by vein textures indicating rapidly fluctuating physiochemical conditions during vein formation (colloform- and crustiform-banding), indicates that formation of the New Occidental deposit is characterised by alternating periods of supra-lithostatic fluid pressures and periods of rapid and large-scale fluid pressure decreases to near hydrostatic accompanying fault-slip.

Dilation along the Great Chesney Fault within the New Occidental deposit was accompanied by ongoing deformation and shortening of earlier formed veins. Early stage (Stage 1–3) sub-horizontal extension veins have been extensively folded whilst the steep-dipping fault-fill veins (Stage 1–4) have been dismembered, boudinaged and overprinted by stylolites at a low angle to vein margins. Fragments of wallrock preserved in Stage 2 breccia veins contain ptygmatically folded Stage 1 veining, whilst overprinting Stage 2

extension veins are also folded, inferring that shortening occurred throughout the early stages of the formation of the New Occidental deposit when significant dilation of the fault zone was also taking place. Boudinage is present at all scales, ranging from boudinage of individual quartz veins through to boudinage at the deposit scale. The network of anastomosing Stage 4 shearing and fault brecciation that overprints the main Stage 2–3 vein complex is interpreted to have transformed the core of the New Occidental deposit into a series of en-echelon mega-boudins. Stage 4 veins themselves have also been progressively deformed during their formation, as demonstrated by buckling of slip fibres, shear-induced brecciation and lamination of these veins and variable offsets across overprinting sub-horizontal and sub-vertical Stage 4 veins. The presence of contrasting undeformed and strongly deformed vein fabrics within the one vein stage and in adjacent sections of individual veins indicate that fault dilation, quartz vein deposition, fault-slip and shortening at high angles to the fault were all part of a cyclic process in which early-stage quartz veins became progressively more deformed during evolution of the fault system.

Stage 4 veins in the core of the New Occidental deposit also record the transition in the fault system from predominantly implosive brecciation and open-space fill veining to crack-seal vein growth in a tighter, less-open system where fault brecciation processes were more prevalent. In a gross sense, deformation changed in character from largely brittle to a mixture of brittle-ductile in response to a decrease in fluid supply and reduced differential stresses.

Deformation fabrics recorded in the New Occidental deposit indicate the deposit has undergone extensive shortening (at a high angle to S_1 cleavage) and sub-vertical extension (parallel to L_1^1 stretching lineation) more or less continuously throughout its history of formation. Early stage veins (Stage 1 veins from the hanging wall of the deposit and Stage 2 veins from within the deposit) record shortening strains of in excess of 60% and sub-vertical extensions of greater than 100%, consistent with large-scale reverse (east-block up) displacement on the Great Chesney Fault. Shortening strains measured for successive vein stages indicate the majority of deposit shortening occurred during deposition of Stage 1–3 veins, reaching a maximum during Stage 2; which corresponds to the period of maximum dilation of the fault (Figure 97).

The history of fluctuating fluid pressure within the New Occidental deposit is demonstrably cyclic in nature, which is consistent with fault-valve behaviour along active fault zones as proposed by Sibson et al. (1988) and Cox (1995). The Great Chesney Fault and New Occidental deposit environs satisfies Sibson's (2001) criteria for extreme fault-valve behaviour. The Great Chesney Fault is unfavourably oriented relative to the prevailing compressional stress field (the fault is oriented at ~90 to σ_1); favourably oriented faults appear to be absent from the deposit environs, and the depth of deposit formation is of the order of 5 km. Slip on the Great Chesney Fault under such circumstances would have required supra-lithostatic fluid pressures (e.g. Sibson, 2001; Cox et al. 2001).

An additional pre-requisite for fault-valve activity in the Great Chesney Fault is the presence of a seal that allowed fluids in the fault to reach supra-lithostatic pressures (especially at the relatively shallow crustal levels inferred during formation of the New Occidental deposit) before fault rupture facilitated rapid depressurisation of the fault zone. The upper part of the Chesney Formation (Transition Unit) and overlying Great Cobar Slate, which comprise dominantly massive fine-grained siltstones and mudstones, provide such a seal to the more permeable and porous sandstones of the underlying Chesney Formation (Figure 97). The location of many of the major gold deposits in the Cobar

Goldfield, including the New Occidental deposit, immediately beneath or within the Great Cobar Slate supports this interpretation (see Section 3.10).

Figure 97: Synthesis of the relationship between vein deposition in the New Occidental deposit and displacement on the Great Chesney Fault.

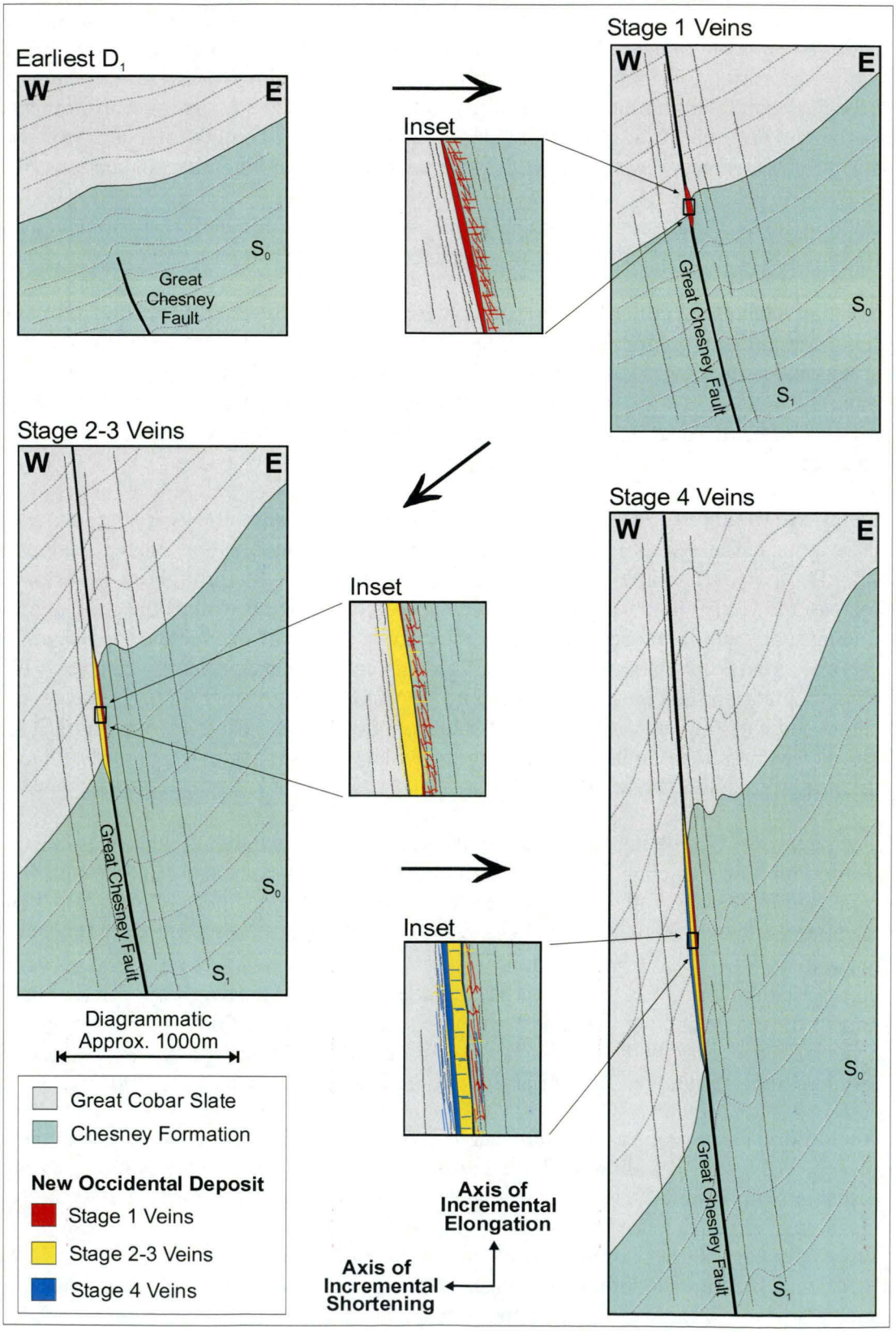

4.6 Comparisons with Vein Types in other Cobar Deposits

The orientation of quartz veins in the various deposits throughout the Cobar Basin appear to be relatively consistent, comprising largely cleavage-parallel fault-fill quartz veins and breccias with lesser sub-horizontal extension veins (Robertson, 1974; Glen, 1987b; de Roo, 1989a; Brill, 1989; Hinman, 1992; Jiang, 1996; Wilson, 1996; Webster, 1999).

Whilst quartz vein orientations are relatively consistent, the style and internal texture of quartz veins varies significantly between deposits. The author has identified veins equivalent to Stage 1 in the New Occidental deposit in the New Cobar and Chesney deposits, and possibly in the Peak and Perseverance deposits. Similarly, Stage 2 colloform-banded cryptocrystalline and microcrystalline quartz veins have also been identified in the New Cobar, Chesney, Peak and Perseverance deposits. Stage 2 quartz veins are potentially equivalent to the chert-like quartz identified by Robertson (1974) in most of the major Cobar deposits, including the New Cobar, Chesney, Peak, Great Cobar, CSA and Queen Bee deposits. Although widespread, the chert-like quartz is best developed in the gold deposits of the Cobar area (Robertson, 1974). Colloform-textured veining also appears to be a characteristic of the gold-rich deposits, being particularly well developed in the New Occidental and New Cobar deposits and to a lesser extent in the Peak and Chesney deposits, and is absent from the Elura (de Roo, 1989a), Great Cobar, CSA and Queen Bee deposits (Robertson, 1974). Stage 3 veins in the New Occidental deposit are difficult to identify without crosscutting relations with more distinctive vein types its presence or absence in the other Cobar deposits, apart from the New Cobar and Peak deposits, cannot be proved from the data available. However, Stage 4 veins are well represented in all of the Cobar deposits, where they constitute the bulk of quartz veins in the base metal-rich deposits like the CSA, Elura, Great Cobar and Queen Bee. The New Cobar, Peak and Perseverance deposits also contain a very strong Stage 4 quartz vein overprint. Stage 5 veins are a relatively minor phase and appear to be present in most of the Cobar deposits.

Quartz vein sequences in the other major gold deposits in the Cobar Goldfield also appear to be broadly similar to that outlined at the New Occidental deposit. For example, quartz vein development at the New Cobar deposit is similar to that at the New Occidental deposit, although the relative abundance of the different quartz vein stages differs between deposits:

1. Early-stage crustiform to colloform crystalline quartz-magnetite veins and quartz vein breccias, which are more abundant than in the New Occidental deposit (Equivalent to Stage 1 at the New Occidental deposit) (Figure 98a).
2. Early-stage grey-green cryptocrystalline quartz veins, often preserved as breccia fragments in younger quartz vein breccias (Equivalent to Stage 2 at the New Occidental deposit).
3. Cockade to weakly crustiform comb quartz veins and quartz vein breccias (Equivalent to Stage 3 at the New Occidental deposit) (Figure 98b).
4. Late-stage overprinting massive to weakly cross-fibred buck to milky quartz veins (Equivalent to Stage 4 at the New Occidental deposit).

Based on the author's observations of drillcore, a similar quartz vein paragenesis to that in the New Cobar deposit is recognised at the nearby Chesney deposit, with colloform quartz-magnetite veining and veined breccias in the gold-rich parts of the deposit.

The Peak and Perseverance deposits contain the following quartz vein stages (from oldest to youngest):

1. Minor rare strongly ptygmatically folded sub-horizontal extension veins (equivalent to Stage 1 at the New Occidental deposit) (Figure 98c).
2. Early-stage crustiform- and colloform-banded cryptocrystalline to microcrystalline quartz veins (equivalent to Stage 2 at the New Occidental deposit) (Figure 98d).
3. Weakly crustiform to cockade comb quartz veins and quartz vein breccias containing fragments of early-stage cryptocrystalline grey-green quartz (equivalent to Stage 3 at the New Occidental deposit) (Figure 98e–g).
4. Late-stage massive to weakly fibred milky quartz in fault-fill, oblique-extension and extension veins that overprint the two previous stages of quartz veining (equivalent to Stage 4 at the New Occidental deposit) (Figure 98e–h).

The Peak deposit is characterised by a strong base metal sulfide overprint, which is particularly strongly developed in the Polaris Lens. As a consequence, many of the original primary quartz textures in this deposit have been overprinted by sulfide mineralisation and associated deformation.

The transition from abundant open-space filling quartz vein textures in early veins to a predominance of crack-seal textures in the later vein stages at New Occidental is repeated in the Peak, Perseverance, New Cobar and Chesney deposits. Early vein stages include abundant quartz-fill implosion breccias and open-space filling vein textures as well as massive colloform- and crustiform-banded cryptocrystalline and microcrystalline quartz. As at the New Occidental deposit, such features indicate brecciation and fault dilation were accompanied by large decreases in fluid pressure, suggesting fault-valve behaviour as a common mechanism for formation of gold-rich deposits in the Cobar Goldfield.

Stage 4 and possibly Stage 5 veins are developed in all Cobar deposits, but appears to be especially well developed in the base metal-rich deposits. Apart from early-stage cryptocrystalline quartz (elvan) in the CSA, Great Cobar and CSA deposits, the most veins in those deposits appear to be equivalent to Stage 4 veins in the New Occidental deposit. In the case of the Peak deposit, which contains appreciable base metal mineralisation in addition to gold mineralisation, Stage 4 veins are also strongly developed.

In summary, the gold-rich deposits of the Cobar Basin appear to be characterised by the presence of well-developed Stage 1–3 quartz veins, whereas those vein stages appear to be only weakly developed in the base metal-only deposits (Robertson, 1974; Brill, 1989; de Roo, 1989a). Gold-rich deposits of the Cobar Basin are therefore distinguished from the base metal-rich gold-poor Cobar deposits by the presence of widespread open-space filling veins and vein breccias that are indicative of significant fault-induced dilation, whereas the base metal-rich deposits contain more crack-seal veins indicative of lower differential stresses and fluid supply.

Figure 98: Examples of quartz veins from gold deposits in the Cobar Goldfield.

a) Steeply dipping vein breccia comprising wallrock fragments in a colloform-banded crystalline quartz-magnetite matrix at New Cobar (equivalent to Stage 1 - New Occidental deposit).

b) Quartz breccia comprising clasts of early formed grey-green cryptocrystalline quartz (equivalent to Stage 2 - New Occidental deposit) within a matrix of cockade to comb quartz (~ Stage 3 - New Occidental deposit) and overprinted by chalcopyrite - pyrrhotite mineralisation (New Cobar deposit).

c) Quartz breccia comprising strongly deformed clasts containing ptgmatically folded quartz veins (equivalent to Stage 1 - New Occidental deposit) in a strongly deformed quartz-chalcopyrite-gold matrix (~ Stage 4 - New Occidental deposit) (Perseverance deposit).

d) Colloform- and crustiform-banded cryptocrystalline to crystalline quartz vein containing replacive bands of galena - sphalerite-pyrite at Peak (equivalent to Stage 2 - New Occidental deposit).

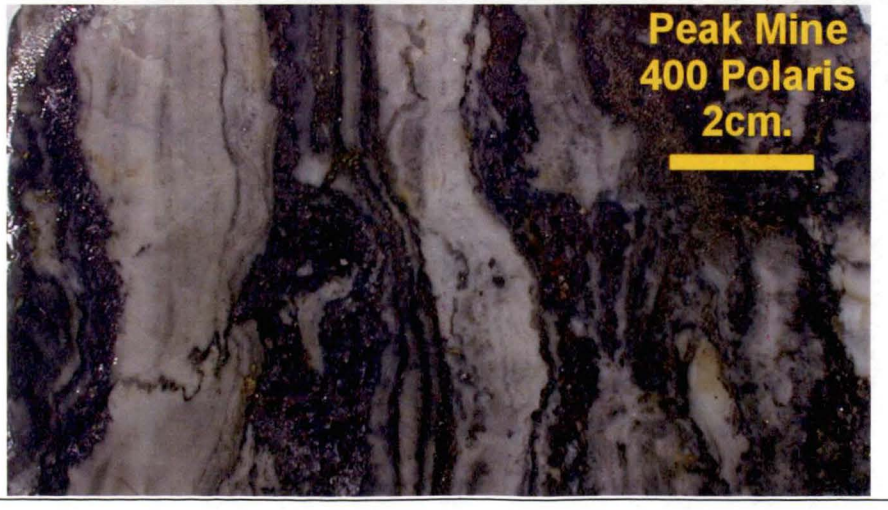

Figure 98: Continued.

e) Laminated cleavage-parallel quartz breccia containing sheared sediment clasts in a matrix of cryptocrystalline to microcrystalline quartz (equivalent to Stages 2–3 - New Occidental deposit) cut by weakly fibred sub-horizontal extension veins (~ Stage 4 - New Occidental deposit) at Peak.

f) Breccia comprising angular clasts of early formed grey-green cryptocrystalline quartz (equivalent to Stage 2 - New Occidental deposit) partly rimmed by more crystalline quartz (~ Stage 4 - New Occidental deposit) in a galena – sphalerite - pyrite matrix at Peak.

g) Quartz breccia comprising remnant clasts of early formed grey-green cryptocrystalline quartz (equivalent to Stage 2 - New Occidental deposit) within a matrix of more crystalline milky quartz (~ Stages 3–4 - New Occidental deposit) and overprinted by chalcopyrite - pyrrhotite (Peak deposit).

h) Sub-horizontal cross-fibred extension quartz-calcite veins in rhyolite breccia at Peak (equivalent to Stage 4 - New Occidental deposit).

5 ALTERATION ASSEMBLAGES WITHIN THE NEW OCCIDENTAL DEPOSIT

5.1 Introduction

The paragenetic sequence of quartz vein stages in the New Occidental deposit (Section 4) provides a framework by which the complex pattern of overlapping silicate and lesser carbonate wallrock alteration assemblages in the deposit (Table 7) can be resolved, thereby providing an answer to the following question:

What is the nature of temporal and spatial variations in phyllosilicate alteration and gangue mineralogy, including chlorite chemistry in the New Occidental deposit?
Previous alteration studies have not adequately resolved the significance of the various phyllosilicate alteration assemblages present in Cobar deposits and, in particular, why deposits with differing metal associations have inconsistent alteration mineral associations (Table 7). In addition, systematic variations in the chemistry (Fe/Fe+Mg ratios) of metamorphic, alteration and vein chlorite in both space and time have previously been documented in a number of Cobar deposits (Robertson, 1974; Binns & Appleyard, 1986; Brill, 1988a; Scott & Phillips, 1990; Hinman, 1992; Jiang, 1996; Forster, 1997; Stegman, 2000). Those variations have been used in a number of studies to determine physiochemical conditions of ore formation including temperatures of formation, thereby providing important constraints on ore fluid chemistry (Brill, 1988a; Hinman, 1992; Jiang, 1996; Forster, 1997).

Consequently, the purpose of this part of the study is to:

1. Establish a paragenetic sequence of alteration assemblages that are temporally related to the five quartz vein stages in the New Occidental deposit
2. Document the three-dimensional distribution of those alteration assemblages
3. Quantify variations in chlorite chemistry within the New Occidental deposit, compare those variations with that previously observed in other Cobar deposits and determine the significance of those differences.

5.2 Previous Alteration Studies of Cobar Deposits

Studies of alteration mineral chemistry have been undertaken at a number of Cobar deposits, including the CSA (Robertson, 1974; Binns & Appleyard, 1986; Robertson & Taylor, 1987; Brill, 1988a), New Occidental (Robertson, 1974), New Cobar (Robertson, 1974), Great Cobar (Robertson, 1974), Peak (Hinman, 1992; Jiang, 1996), Chesney (Jiang, 1996) and McKinnons (Forster, 1997) deposits.

Studies have shown the Fe/(Fe+Mg) ratio of alteration and vein chlorites increases with increasing intensity of mineralisation (Robertson, 1974; Brill, 1988a; Hinman, 1992; Hornibrook 1998a, b), although Robertson (1974) also identified zones of distinctly Mg-rich chlorite within ore zones in a number of deposits, including the New Occidental deposit. Chlorite compositions in Cobar deposits have also been shown to vary temporally. Typically, early-stage chlorite is Fe-rich whereas chlorite associated with late stage shears is Mg-rich (Brill, 1988a; Hinman, 1992). In contrast, Forster (1997) and Forster & Seccombe (1999) argued early-stage mineralisation in the McKinnons gold deposit is associated with Mg-rich chlorites while Fe-rich chlorites are predominantly associated with late-stage mineralisation. Brill (1988a) and Jiang (1996) used the Walshe (1986) chlorite

geothermometer to conclude trends of increasing Mg-content of chlorites from the CSA and Peak deposits respectively correspond to a general decrease in formation temperature.

Robertson (1974) demonstrated muscovite, which is usually abundant in unaltered wallrock, is less abundant with increasing proximity to deposits in the Cobar Goldfield and is usually absent from the chlorite-rich deposit centre. Analysis of short wave infrared (SWIR) spectra from the New Occidental deposit (Hornibrook, 1998a, b) confirmed those trends but also showed white mica became more phengitic towards the ore zone. Hornibrook (1998b) concluded Fe-rich chlorite alteration has destructively overprinted broad early-formed zones of phengitic white mica and Mg-intermediate chlorite alteration.

5.3 Data Collection & Analytical Techniques

Alteration mineralogy was logged in 51 diamond drillcores from the New Occidental deposit by the author to establish 3-dimensional distribution of each alteration assemblage developed.

In order to constrain the chemistry of key alteration minerals in the deposit 22 samples of chlorite from within and surrounding the New Occidental deposit (Figure 99) and 10 samples of stilpnomelane from the deposit were collected for analysis. Semi-quantitative scanning electron microbeam (SEM) analysis of those samples (Appendix 3 and Appendix 4) was performed by Dr Ivan Reynolds, Rio Tinto Technology Development (Reynolds, 1998; 1999a; 2001). Because SEM is unable to distinguish Fe^{2+} from Fe^{3+}, total iron was determined for all samples. TiO_2, Cr_2O_3 and CaO contents were uniformly at or near detection and were not recorded.

SWIR spectrometry of New Occidental deposit drillcore and drillcore pulps was undertaken to characterise compositional variations and relative abundances of phyllosilicate alteration minerals, including chlorite, white mica and stilpnomelane, within and peripheral to the deposit (Figure 100). Hornibrook (1998a, b) acquired the bulk of spectral data analysed during this study using a PIMA II instrument (drillholes NO1F, NO1H, NO3, NO3B, NO3C, NO4C, NO14/14E and NO14D). AusSpec International Pty Ltd acquired spectra from additional samples (drillholes NO1M, NO3C) using a PIMA 12 instrument as part of the current study to compliment previous data. The spectra acquired from NO14/14E were of particular interest to this study as it sampled significant intervals of the hanging wall and footwall of the deposit. In addition, SWIR spectra were also collected from drillcore cuttings from CS4A, which intersected a poorly mineralised section of the Great Chesney Fault zone at the Comstock prospect approximately 800m south of the New Occidental deposit. Some variation is evident between spectra acquired using the PIMA II and PIMA 12 instruments with the PIMA 12 spectra typically characterised by deeper absorption features compared to those in the PIMA II spectra. Spectral data was processed using *The Spectral Geologist version 2.0*. Spectra acquired in the main mineralised zones are relatively noisy and poor quality, reflecting the relative abundance of non-reflective quartz and sulfide in those zones.

Figure 99: Location of chlorite samples for semi-quantitative microbeam analysis.

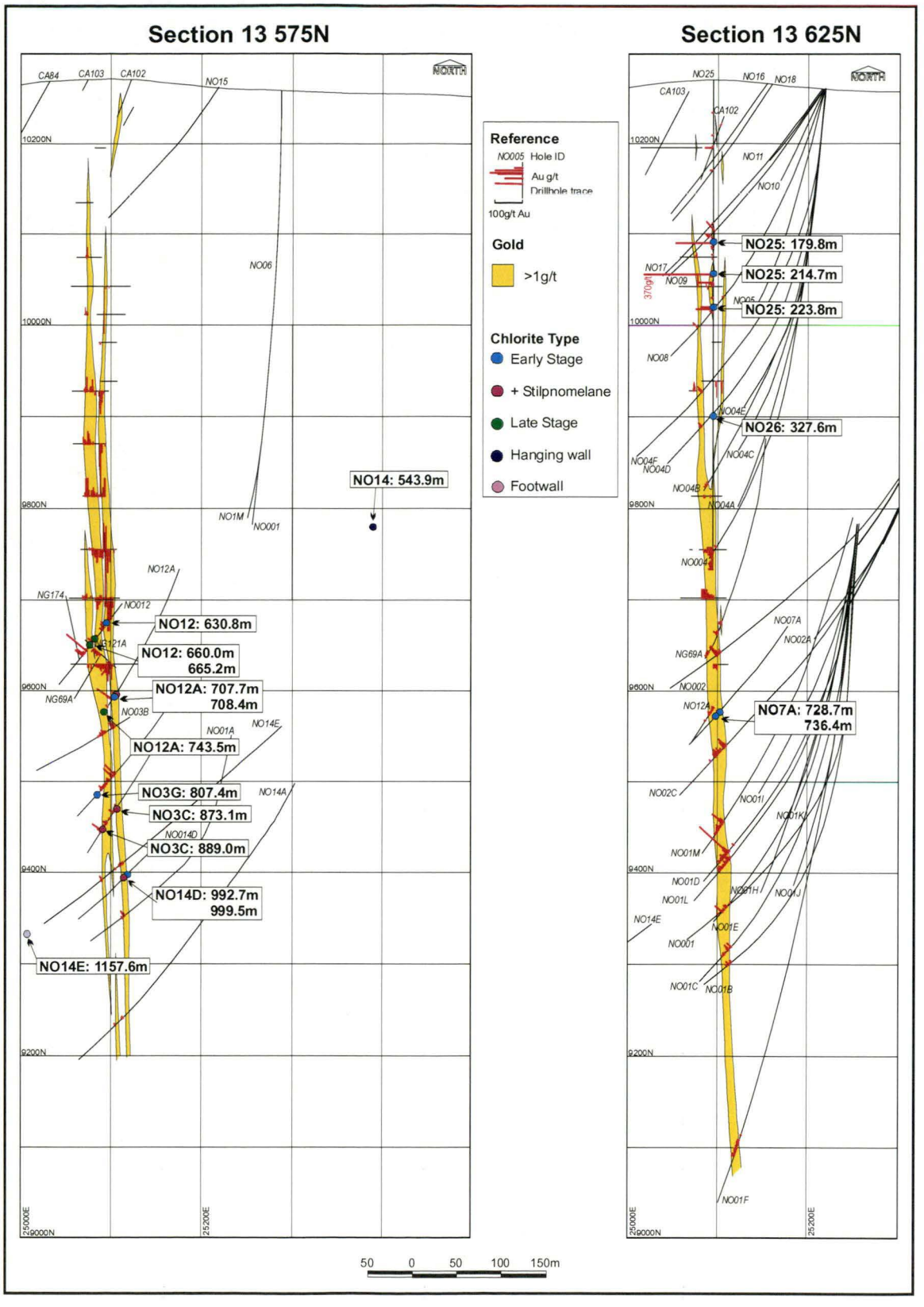

Figure 100: Location of SWIR traverses in the New Occidental deposit.

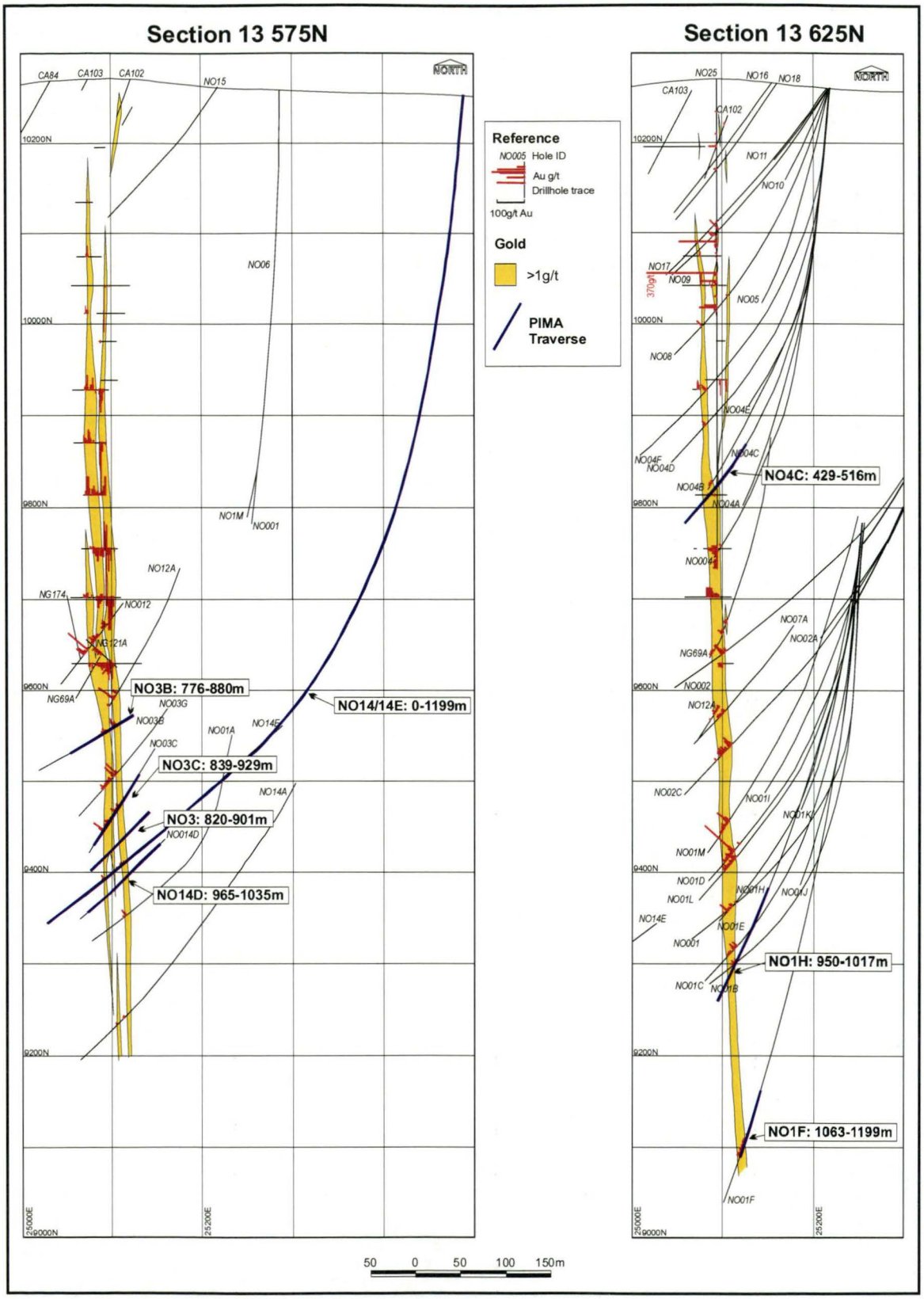

5.4 Wallrock Alteration Associated with the New Occidental Deposit

Sedimentary rocks along the eastern margin of the Cobar Basin, including wallrock to the New Occidental deposit, were metamorphosed to chlorite grade (Glen, 1985) and have a

simple mineral assemblage of quartz-muscovite-chlorite-minor carbonate-pyrrhotite. Muscovite and chlorite flakes and elongate pyrrhotite grains are oriented parallel to the strong penetrative S_1 cleavage present in all rocks throughout the Cobar Goldfield (Figure 101).

Figure 101: Wallrock to the New Occidental deposit.

Chesney Formation sandstone/siltstone comprising a simple mineralogy of quartz - chlorite - muscovite. Muscovite and chlorite forms elongate laths parallel to S_1 cleavage (PPL and XPL).

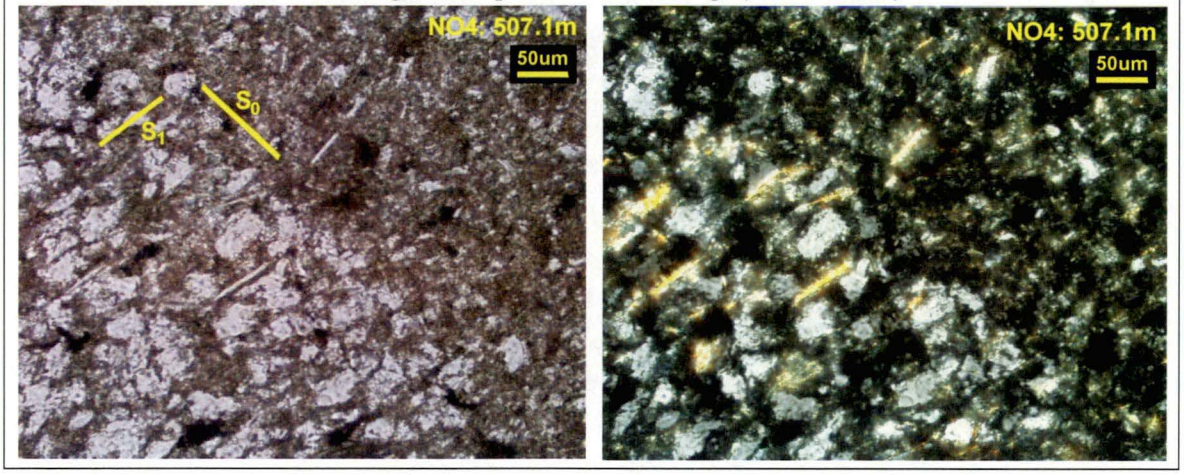

Five temporally discrete, spatially constrained stages of phyllosilicate-dominated wallrock alteration and corresponding vein gangue assemblages have been identified at the New Occidental deposit:

1. Widespread early-stage pervasive chlorite - minor biotite
2. Stilpnomelane in the central part of the deposit
3. Late-stage chlorite, predominantly in the deposit footwall
4. Minor locally developed sericite - minor chlorite in the deposit footwall
5. Localised minor greenalite (Fe-hydrous silicate) - iron-rich clay - calcite in the centre of the deposit.

The five stages define an alteration paragenesis intimately linked to quartz vein paragenesis in the deposit (Figure 102). Similarly, the spatial distribution of the different alteration stages within the deposit is also closely correlated to the distribution of quartz vein stages, with alteration intensity matching zones of increased quartz vein density (Figure 103). Their mineralogy and relation to vein stages and deformation fabrics are summarised in Table 18. Their spatial distribution in the New Occidental deposit is depicted in Figure 104 to Figure 106.

Figure 102: Alteration paragenesis at the New Occidental deposit.

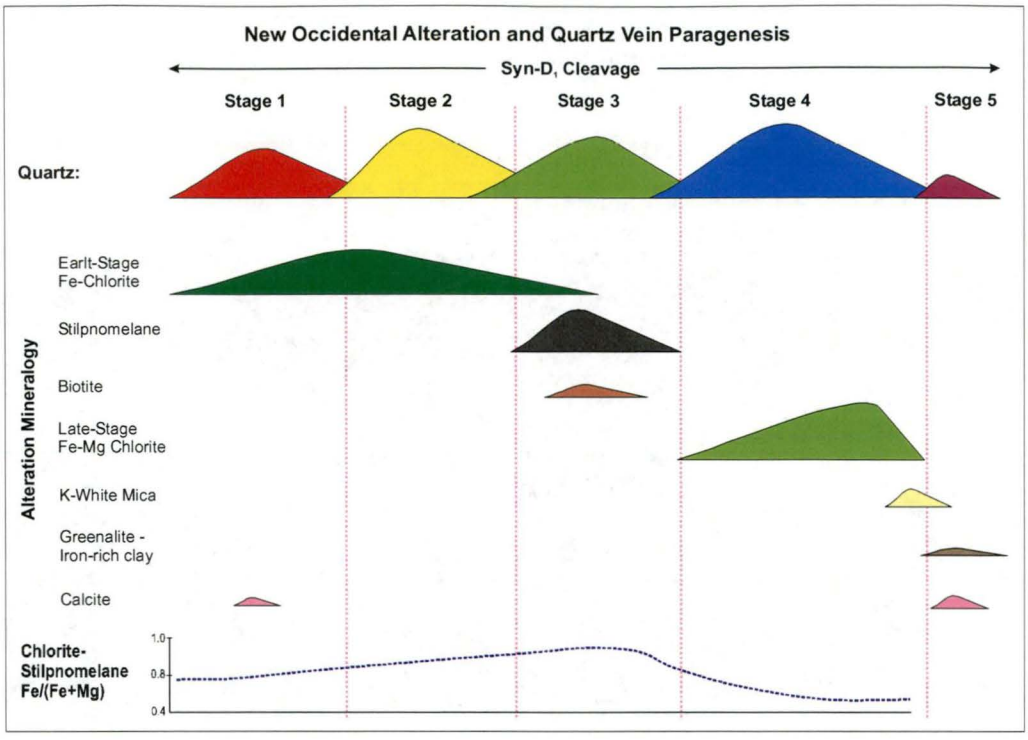

Figure 103: Spatial distribution of alteration stages in the New Occidental deposit.

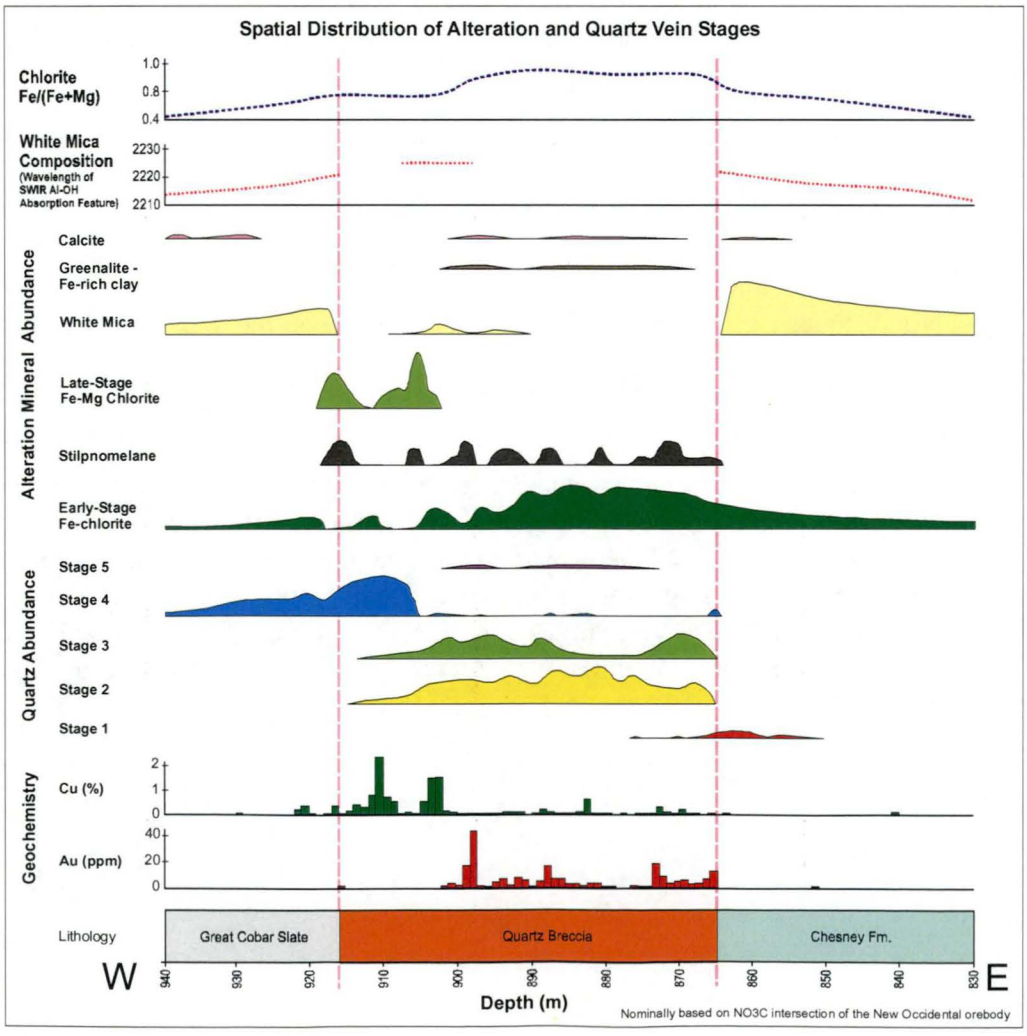

Table 18: Alteration assemblages in the New Occidental deposit.

Alteration Assemblage	Early-Stage Iron Chlorite	Stilpnomelane	Late-Stage Chlorite	Sericite	Greenalite
Mineralogy	Fe-chlorite - minor biotite - calcite	Stilpnomelane	Fe-Mg-Chlorite	Sericite	Greenalite - minor Fe-rich clay - calcite
Associated Ore Minerals	Magnetite, pyrrhotite, native bismuth, maldonite, gold and (Bi-Pb)(Se-S) minerals	Bismuth sulfides, gold and Au-Bi sulfide	Arsenopyrite	Chalcopyrite, pyrrhotite and pyrite	Sphalerite, galena, pyrrhotite and pyrite
Location	- Broad pervasive alteration halo around the deposit and extending along the trace of the Great Chesney Fault - Alteration intensity increases towards the centre of the deposit	- Elongate steeply dipping bands within the Main Lode	- Intensely developed in the footwall of the Main Lode, centred on the Stage 4 quartz vein breccia and the trace of the Great Chesney Fault - Locally in the hanging wall of the deposit	- Patchy zones in the footwall of the Main Lode and along the Albion Lode	- Minor fracture- and grain boundary-controlled alteration throughout the core of the Main Lode - Largely restricted to vicinity of sphalerite-galena veins
Overprinting Relationships	- Overprinted by all other alteration assemblages	- Predominantly replaces early-stage chlorite	- Replaces stilpnomelane, early-stage chlorite and quartz	- Preferentially replaces both metamorphic white mica and chlorite, and late-stage chlorite	- Localised replacement of stilpnomelane and late-stage chlorite
Relationship to Quartz Vein Stages	- Gangue mineral in Stage 1–2 quartz veins, often forming narrow selvedges on vein walls and wallrock breccia fragments	- Replaces Fe-chlorite in Stage 1–2 quartz veins but occurs as a primary gangue mineral in Stage 3 quartz veins - Overprinted by Stage 4 & 5 quartz veins	- Replaces Stage 2–3 quartz veins but appears as a primary component of Stage 4 quartz veins - Overprinted by Stage 5 quartz veins	- Developed around sheared zones containing brecciated fragments of Stage 4 quartz - Apparently overprinted by Stage 5 quartz veins	- Cross-cut Stage 2–4 quartz veins - Relationship to Stage 5 quartz veins not clearly established
Relationship to Deformation Fabrics	- Intensity increases with increasing intensity of S_1 cleavage development	- Elongate zones parallel to S_1 cleavage and L_1^1 lineation - Infills sub-horizontal extension fractures (perpendicular to L_1^1)	- Elongate zones parallel to S_1 cleavage and L_1^1 lineation	- Along fractures and quartz veins that are parallel to S_1	- Often infills sub-horizontal extension fractures (perpendicular to L_1^1)

Figure 104: Distribution of early-stage chlorite in the New Occidental deposit.

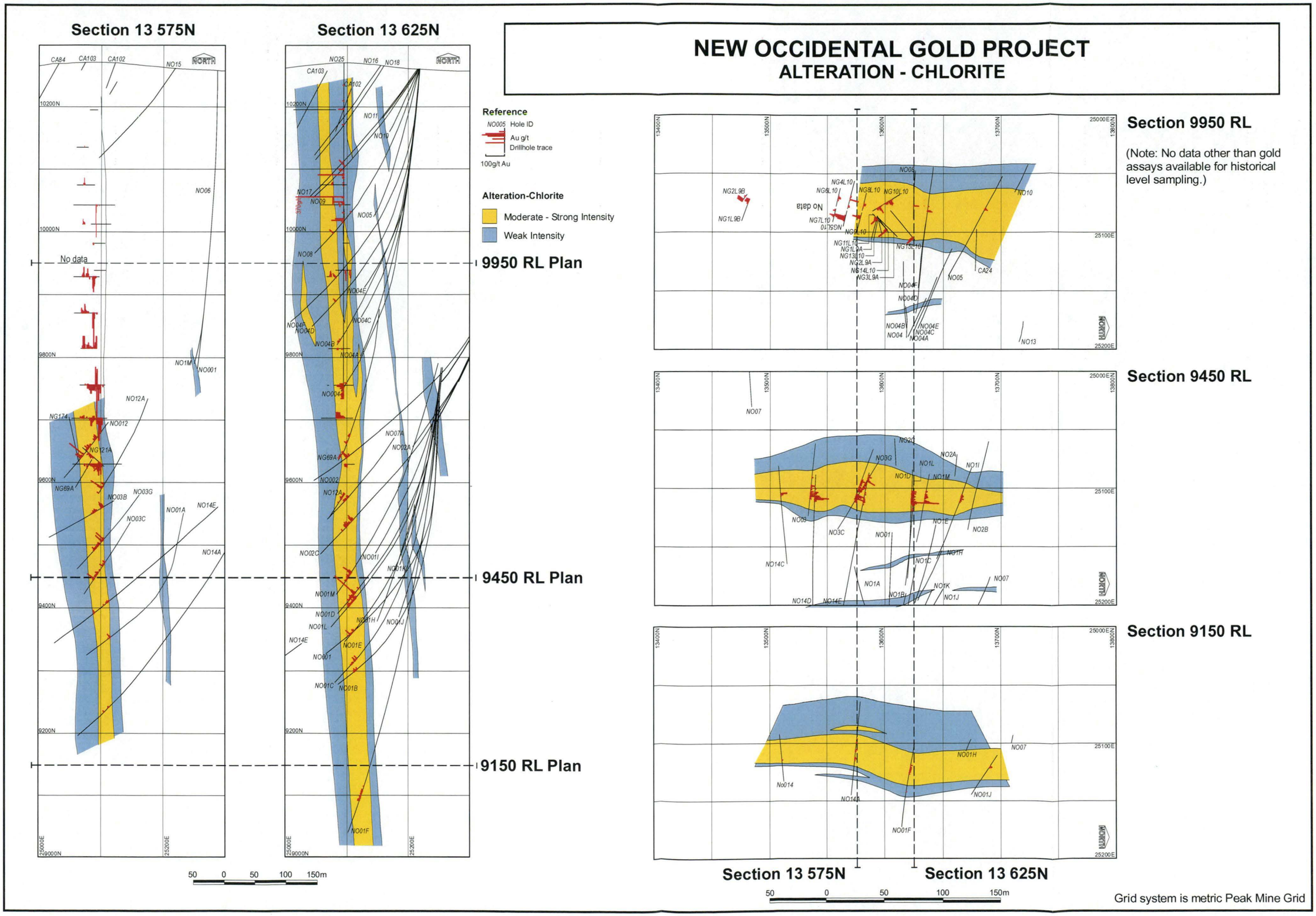

Figure 105: Distribution of stilpnomelane alteration in the New Occidental deposit.

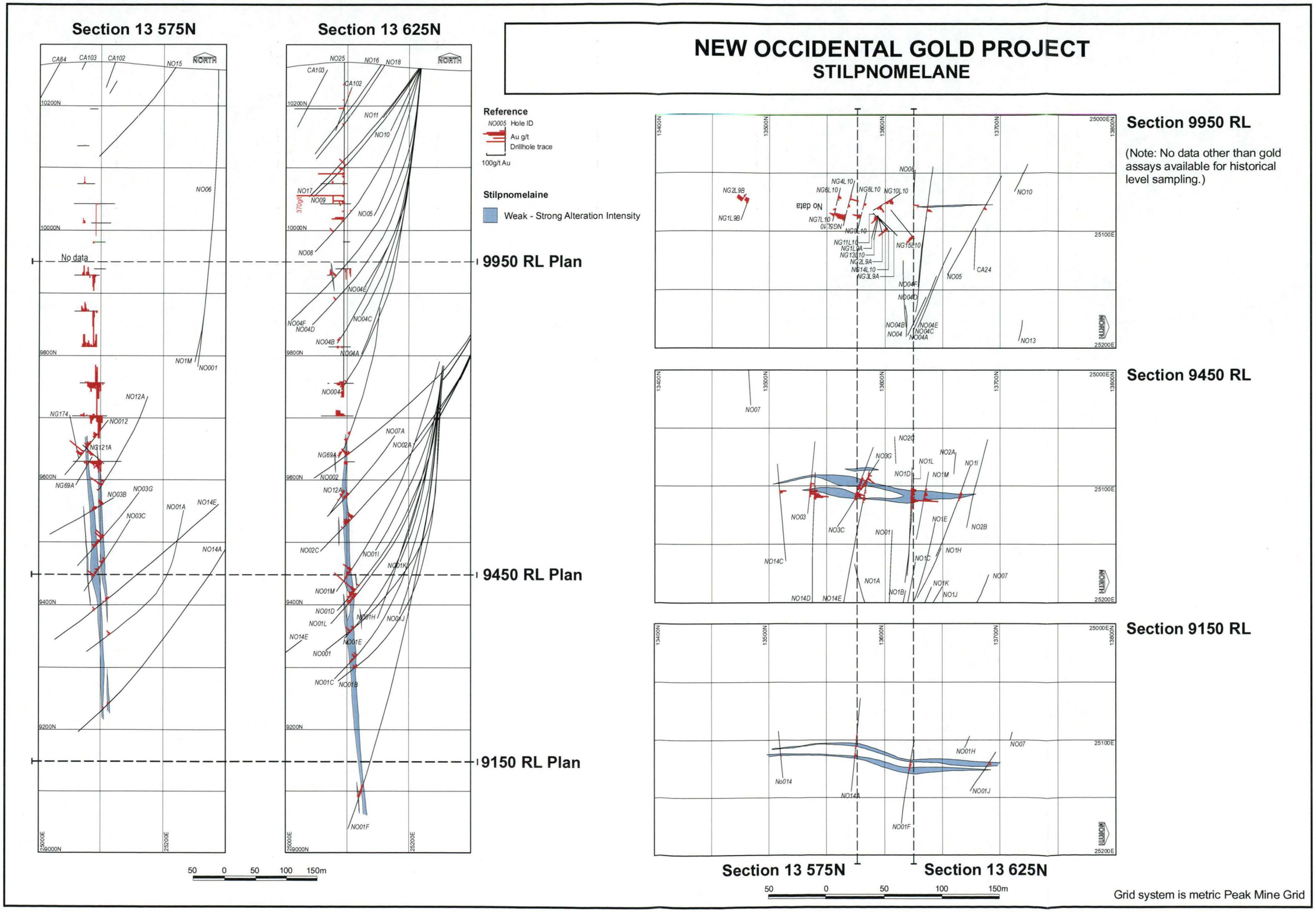

Figure 106: Distribution of late-stage chlorite alteration in the New Occidental deposit.

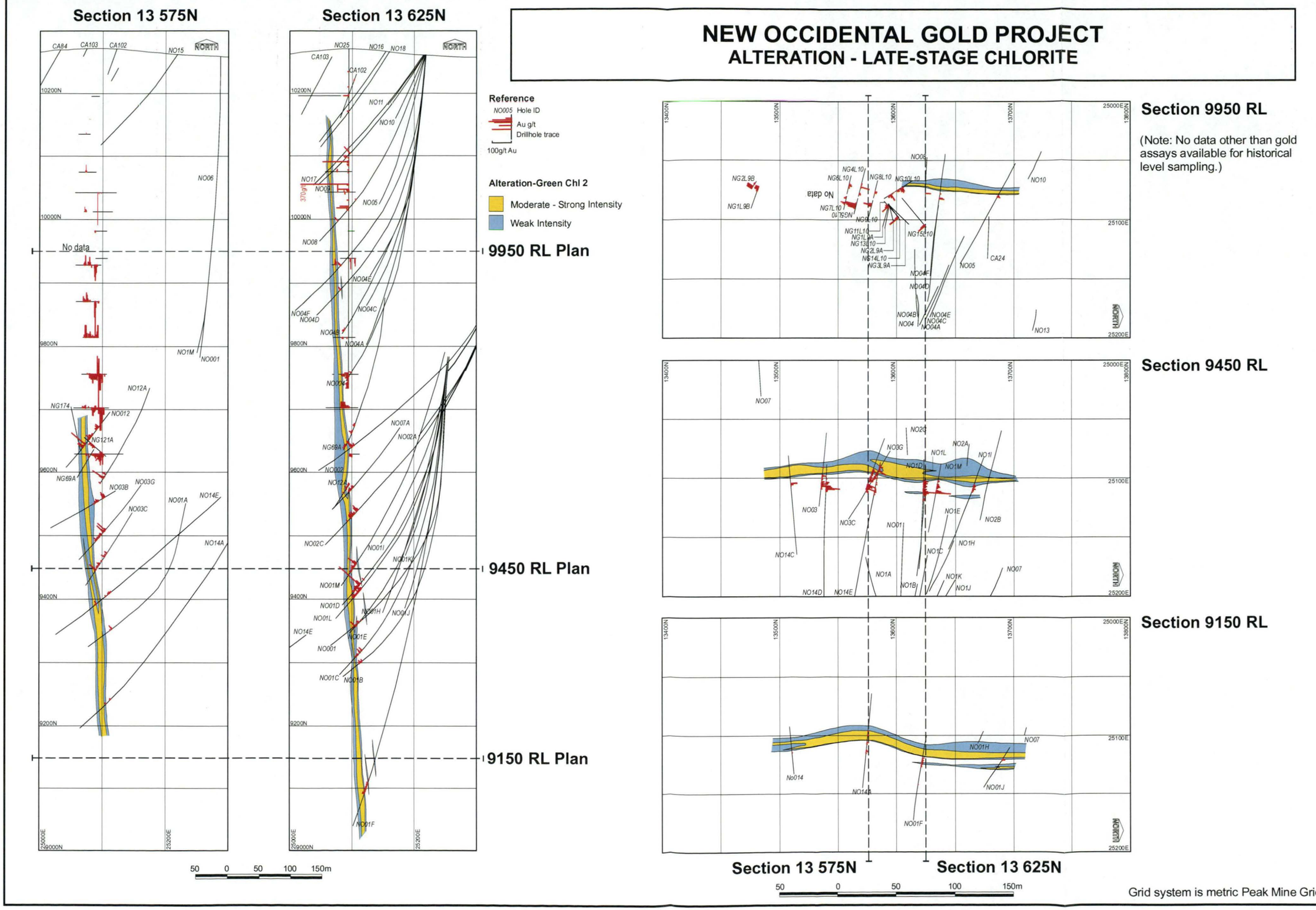

5.4.1 Early-Stage Iron Chlorite

Early-stage Fe-chlorite is dark green in colour in both hand specimen and thin section. In altered wallrock it is typically fine-grained and strongly fibrous whereas compositionally identical chlorite in quartz veins is fine to medium-grained.

Extensive semi-quantitative microprobe analyses of both early-stage chlorite in pervasively altered wallrock and in quartz veins indicates a relatively consistent chemistry characterised by low MgO (3–6 wt%) and high iron FeO (35–45 wt% expressed as FeO) with Fe/(Fe+Mg) cation ratios in the range 0.75 to 0.93 (Appendix 3).

Figure 107: Plot of Fe/(Fe+Mg) cation ratio against number of tetrahedral Al cations in early- and late-stage chlorite.

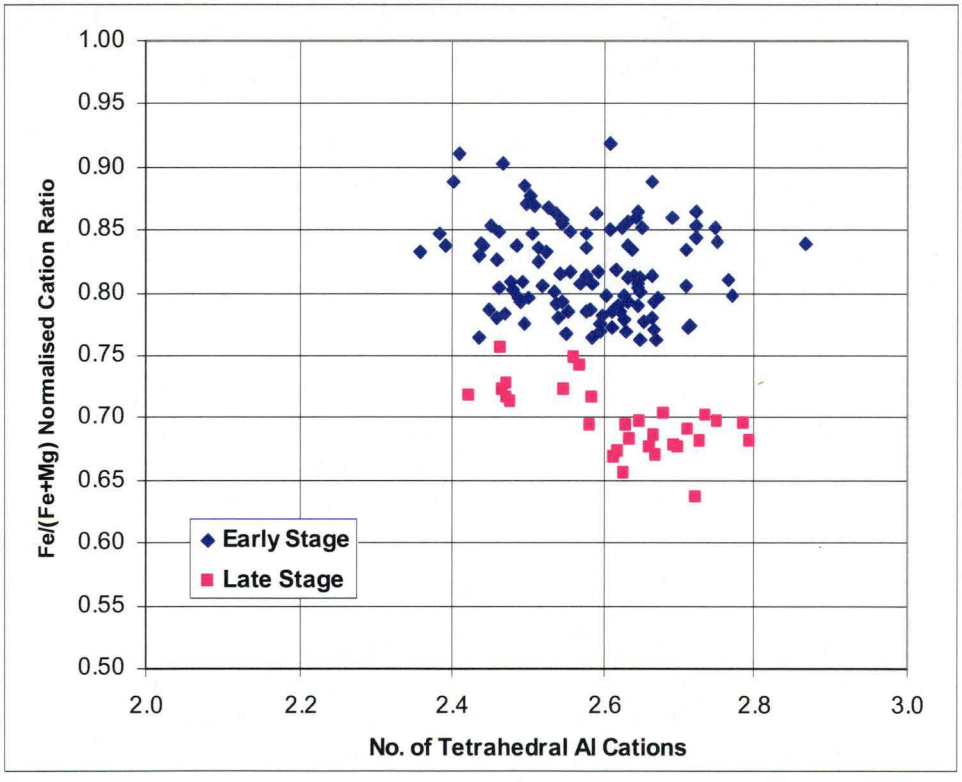

Chlorite alteration intensity visually increases with proximity to New Occidental deposit and is strongest in the deposit core (Figure 104). The halo of early-stage Fe-chlorite alteration (determined from geological logging) extends up to 30m into both the hanging wall and footwall of the deposit. The size of the chlorite alteration halo and intensity of alteration within the halo remain relatively constant over the known vertical extent of the deposit (>1500 m). Strong chlorite wallrock alteration extends approximately 100m north and south of the deposit along the trace of the Great Chesney Fault. Weak to moderate intensity chlorite alteration extends >400m further south and >1km north to the Mt Pleasant and Young Australian deposits.

Early-stage Fe-chlorite is also a common constituent of early quartz vein stages in the deposit (Stages 1–2), occurring in several different forms including selvedges in Stage 1 veins (Figure 71c, f, k), rimming wallrock fragments in Stage 1 and 2–3 quartz veins (Figure 108), as alternating layers in Stage 2 colloform-banded quartz veins (Figure 73g–i) and as fragments in Stage 2 quartz vein breccias (Figure 73j).

Figure 108: Early-stage vein Fe-chlorite.

Fe-chlorite rimming angular sandstone fragments in a cryptocrystalline and crystalline Stage 2–3 quartz vein breccia (PPL and XPL).

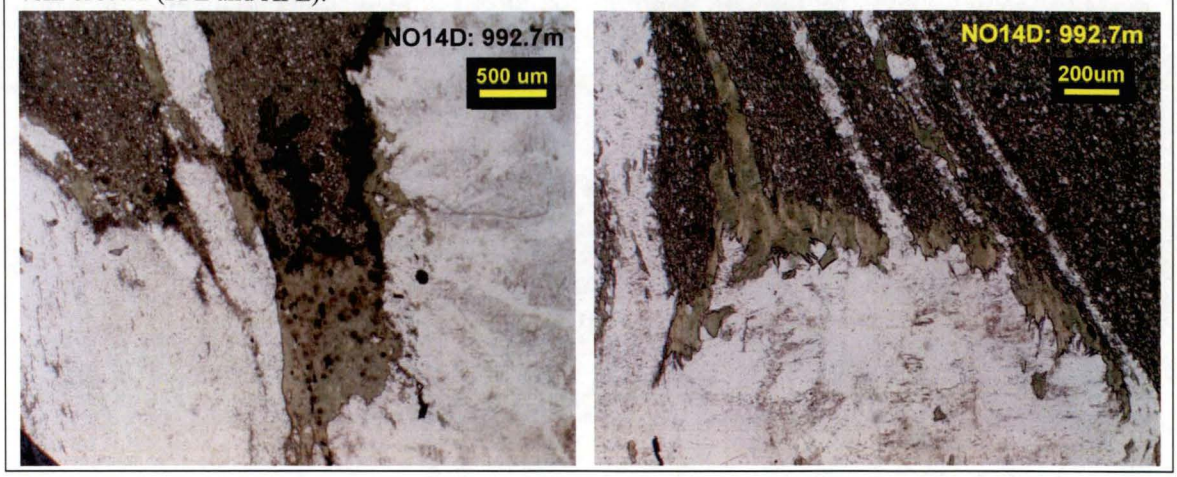

5.4.2 Stilpnomelane

In hand-specimen, stilpnomelane [$(Fe, Mg)_8(Si, Al)_{12}(O, OH)_{12}$] is black to dark green and relatively fine grained. In thin-section, it is strongly fibrous and typically forms felted masses.

Semi-quantitative microprobing of both fine and coarse-grained stilpnomelane grains indicates that the stilpnomelane has a relatively consistent chemistry with low MgO (0.1–1.3 wt%) and high total iron (32.2–37.2 wt% as FeO) (Appendix 4). Low analytical totals indicate significant amounts of water (up to 6–7 wt %) in the crystal structure. However, as all iron is expressed as FeO, failure to account for the additional oxygen in Fe_2O_3 may also contribute to low totals.

Stilpnomelane alteration occurs in several cleavage-parallel bands within the gold-mineralised core of the New Occidental deposit. Alteration is developed over the full vertical extent of the deposit, although the intensity appears to diminish with depth (Figure 105). Stilpnomelane has predominantly replaced early-stage Fe-chlorite in Stage 1–2 quartz veins (Figure 109a–e) and in adjacent wallrock although it is a minor primary component of Stage 3 veins (Figure 75c). Although stilpnomelane replacement of Fe-chlorite often appears complete in hand-specimen (Figure 73b–c), remnant cores of unaltered chlorite are readily apparent in thin-section (Figure 109b–d). Stilpnomelane often infills sub-horizontal extension fractures in chlorite (Figure 109c–d) and may extend outwards from the chlorite grains along sub-horizontal fractures (Figure 109d). Stilpnomelane alteration of chlorite is often strongest in areas of precursor magnetite mineralisation.

Figure 109: Stilpnomelane alteration in the New Occidental deposit.

a) Selective stilpnomelane alteration of Fe-chlorite-rich rims on fragments in a Stage 2–3 quartz vein breccia, including along cleavage planes in breccia fragments. The stilpnomelane-altered Stage 2–3 quartz breccia has been overprinted by a Stage 5 quartz vein (right).

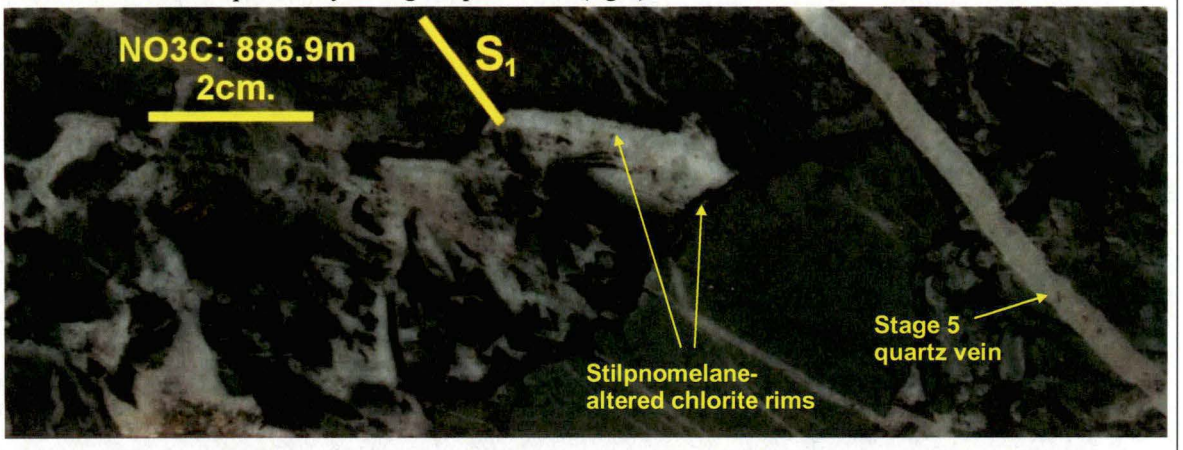

b) Photomicrograph showing partial stilpnomelane (brown) replacement of Fe-chlorite (green) bands along quartz-chlorite band boundaries in a Stage 2 colloform quartz-chlorite vein (PPL).

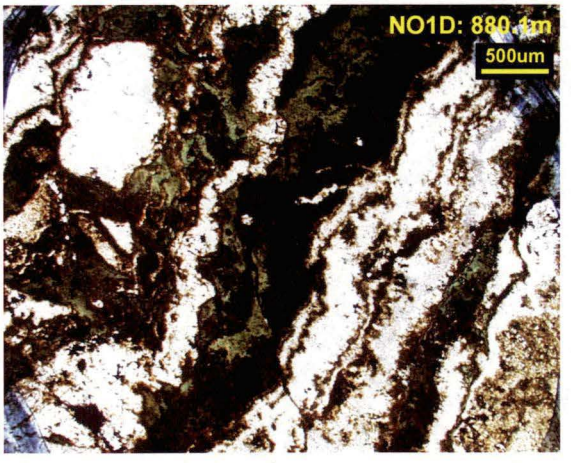

c) Photomicrograph showing partial stilpnomelane (brown) replacement of Fe-chlorite (green) along horizontal fractures, cleavage and grain boundaries in a Stage 2–3 quartz vein breccia. Stilpnomelane extends along quartz crystal boundaries (PPL).

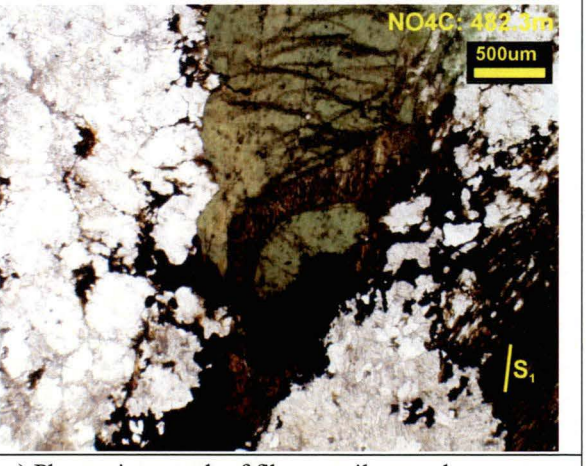

d) Photomicrograph showing advanced stilpnomelane (brown) replacement of Fe-chlorite (green) in Stage 2 quartz vein breccia. Note sub-horizontal tails of stilpnomelane emanating from the chlorite grains (PPL).

e) Photomicrograph of fibrous stilpnomelane (brown), formed by replacement of chlorite, in a Stage 2 quartz vein breccia. Stilpnomelane has the same sub-vertical crystallographic orientation as the primary chlorite (PPL).

5.4.3 Late-stage Fe-Mg Chlorite

Late-stage chlorite is distinguished from early-stage Fe-chlorite by its hand-specimen appearance and optical properties. Late-stage chlorite has an apple-green colour in hand-specimen (Figure 110a), a light green colour under plane polarised light and is characterised by anomalous blue birefringence under cross-polarised light (Figure 110b).

Figure 110: Late-stage Fe-Mg chlorite alteration in the New Occidental deposit.

a) Pervasive intense late-stage chlorite alteration overprinting stilpnomelane-altered Stage 2–3 quartz vein breccia.

b) Photomicrographs of finely crystalline late-stage chlorite incipiently replacing surrounding quartz crystals in a Stage 2–3 quartz vein breccia (PPL and XPL).

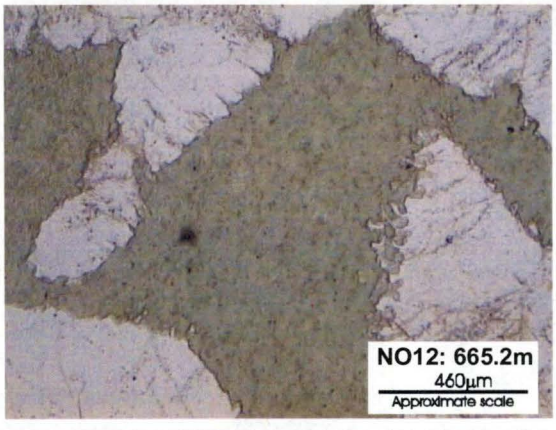

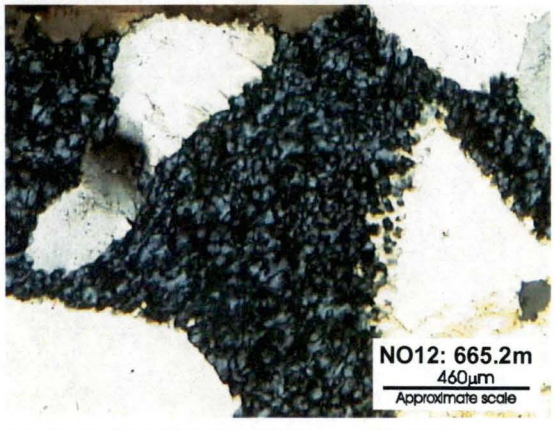

Semi-quantitative microbeam analyses of late-stage chlorite indicate a relatively consistent chemistry with low-moderate MgO (6.5–8.4 wt%), moderate-high iron (32.6–35.9 wt% as FeO) and moderate Fe/(Fe+Mg) cation ratios in the range 0.64 to 0.76 (Figure 107).

The Fe-Mg chlorite consistently overprints the Fe-rich chlorite and stilpnomelane alteration (Figure 110a) and is apparently quartz-destructive (Figure 110b). It is largely restricted to the footwall of the New Occidental deposit where it forms a well-defined zone that is continuous over the full length of the orebody. The zone partially overlaps the western side of the Main Lode, where it locally overprints zones of stilpnomelane alteration. Weakly developed late-stage chlorite alteration is also locally developed in the hanging wall of the New Occidental orebody (Figure 106).

The Fe-Mg chlorite alteration is spatially correlated with Stage 4 quartz veins, and is best developed throughout the Stage 4 quartz vein breccia in the footwall of the Main Lode. It overprints Stage 1–3 quartz veins and quartz vein breccias (Figure 77i–j; Figure 110a) and is a common constituent of Stage 4 veins (Figure 77a–c). Deformation of Stage 4 veins,

including localised buckling of vein fibres and the development of stylolites, also effects fibres and bands of late-stage chlorite (Figure 77b).

5.4.4 Sericite - Minor Chlorite

Sericite close to the theoretical end-member muscovite composition (Reynolds, 1999a) is a relatively minor alteration phase in the New Occidental deposit. It occurs as narrow (1–5mm thick) selvedges of wallrock bleaching around chalcopyrite - pyrrhotite ± galena - quartz veins (Figure 111a) in isolated patches throughout the immediate footwall of the Main Lode and along the Albion Lode. Sericite replaces metamorphic white mica and chlorite in the host siltstones and mudstones and locally overprints late-stage Fe-Mg chlorite (Figure 111b). Sericite alteration and associated base metal sulfide mineralisation overprint Stage 4 quartz (Figure 111a) but have been overprinted by Stage 5 quartz veins.

Figure 111: Sericite alteration in the New Occidental deposit.

a) Coarse-grained chalcopyrite - pyrrhotite mineralisation overprinting sheared siltstone of the Great Cobar Slate in the footwall of the orebody. Fragments of Stage 4 quartz are contained within the sulfide veins. Distinctive bleaching of the siltstone immediately adjacent to the chalcopyrite fracture-fill reflects incipient sericite alteration.

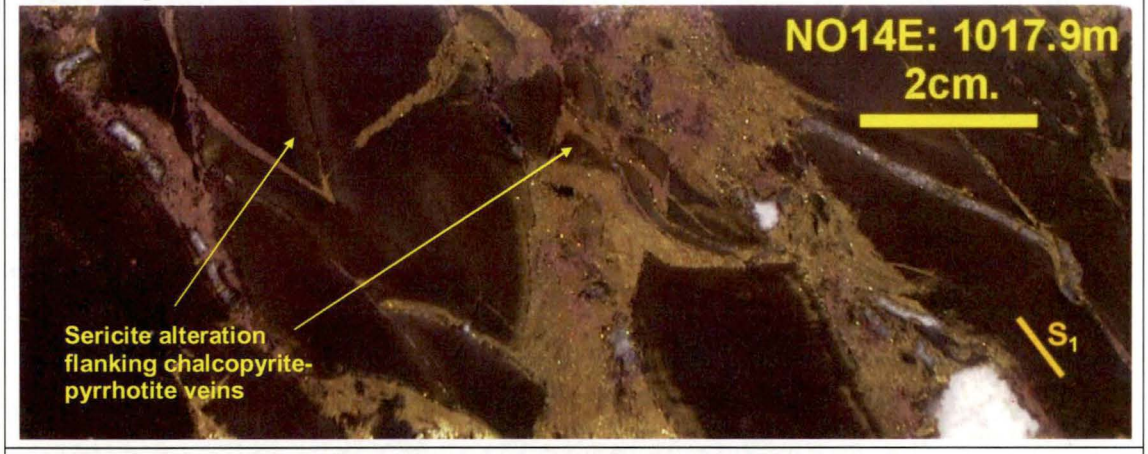

b) NO12 - 666.0m: False colour backscattered electron image showing preferential sericite alteration of chlorite associated with chalcopyrite-minor pyrrhotite intergrowths in a quartz-rich area.

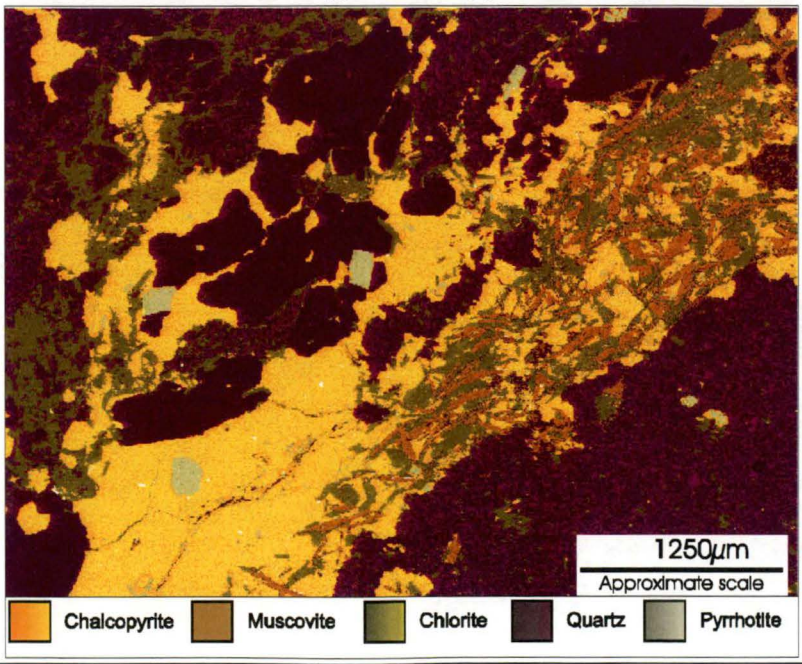

5.4.5 Greenalite-Fe-rich Clay-Calcite

Minor amounts of a reddish-brown mineral forming narrow alteration selvedges and sub-horizontal veinlets on late-stage Fe-Mg chlorite and stilpnomelane (Figure 112a–d) throughout the centre of the New Occidental deposit have been identified by Reynolds (1999a) as an Fe-rich hydrous silicate with a composition approximating that of greenalite [$(Fe^{2+}, Fe^{3+})_{2-3}Si_2O_5(OH)_4$] with a small amount of cronstedtite [$(Fe^{2+}{}_2Fe^{3+}(SiFe^{3+})O_5(OH)_4$] in solid solution. Reynolds (1999a) also identified small amounts of iron-rich clay (Figure 112b–d) associated with greenalite and concluded this phase either represents a poorly crystalline variety of greenalite or an Fe-rich member of the smectite clay group.

Minor amounts of calcite are also commonly associated with greenalite-Fe-rich clay veins (Figure 112d). Those veins are spatially associated with Stage 5 quartz veins and appear to have formed coevally with those quartz veins.

Figure 112: Greenalite and Fe-rich clay alteration in the New Occidental deposit.

a) Photomicrographs of Fe-rich clay (reddish-brown seams) over-printing and rimming late-stage Fe-Mg chlorite in a quartz breccia (light green) (PPL).

b) NO12A: 708.4m - False colour, backscattered electron image of greenalite alteration of late-stage chlorite vein cross-cutting stilpnomelane-altered quartz.

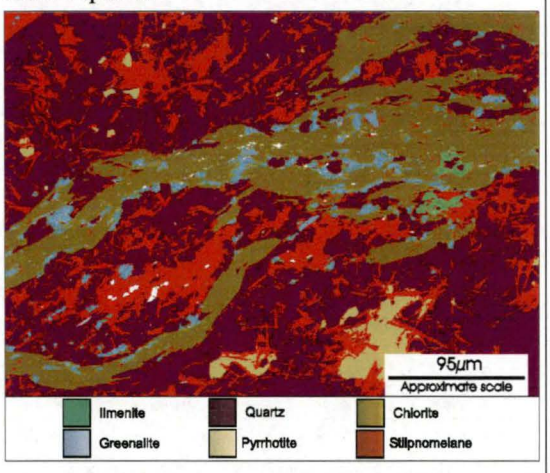

c) NO12A: 707.7m - Photomicrographs of late-stage poorly crystalline Fe-rich clay (brown) developed along a sub-horizontal fracture and overprinting late-stage chlorite (green) (PPL).

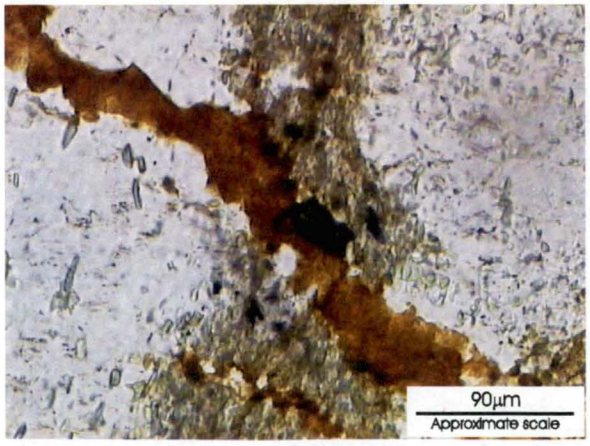

d) NO12A: 708.4m - False colour, backscattered electron images of sphalerite - galena - Fe-rich clay vein overprinting a younger quartz vein.

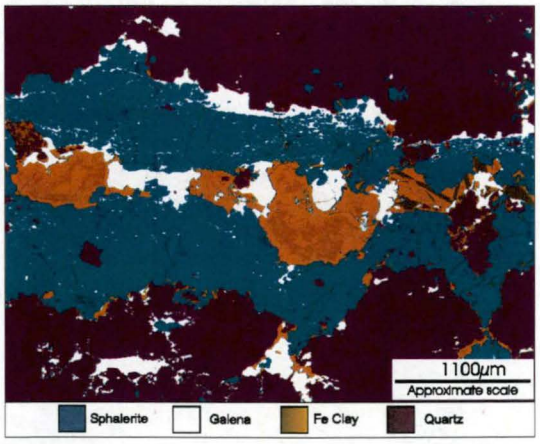

5.5 Compositional Variations in Chlorite Chemistry

5.5.1 Variations in Chlorite Chemistry within the New Occidental Deposit

Chlorites in the New Occidental deposit exhibit significant chemical compositional variation. Composition of early-stage chlorites varies subtly depending on location within the deposit and associated alteration mineralogy (Table 19). Assuming an ideal chlorite structural formula of $(Mg,Al,Fe)_{12}[(Si,Al)_8O_{20}](OH,O)_{16}$ (Deer et al., 1966), principal variations in chlorite chemistry in the New Occidental deposit are the relative proportions of Fe and Mg in octahedral structural sites and the relative proportions of Si and Al in tetrahedral structural sites. Most New Occidental chlorites are thuringites according to the standard chlorite classification scheme, as outlined by Deer et al. (1966). Early-stage orebody chlorites are predominantly daphnites (Fe-rich thuringite) whereas late-stage orebody chlorites and wallrock chlorites fall within the ripidolite (Fe-Mg thuringite) composition field (Figure 113).

Figure 113: Hey Diagram with plots of analyses of New Occidental chlorites.

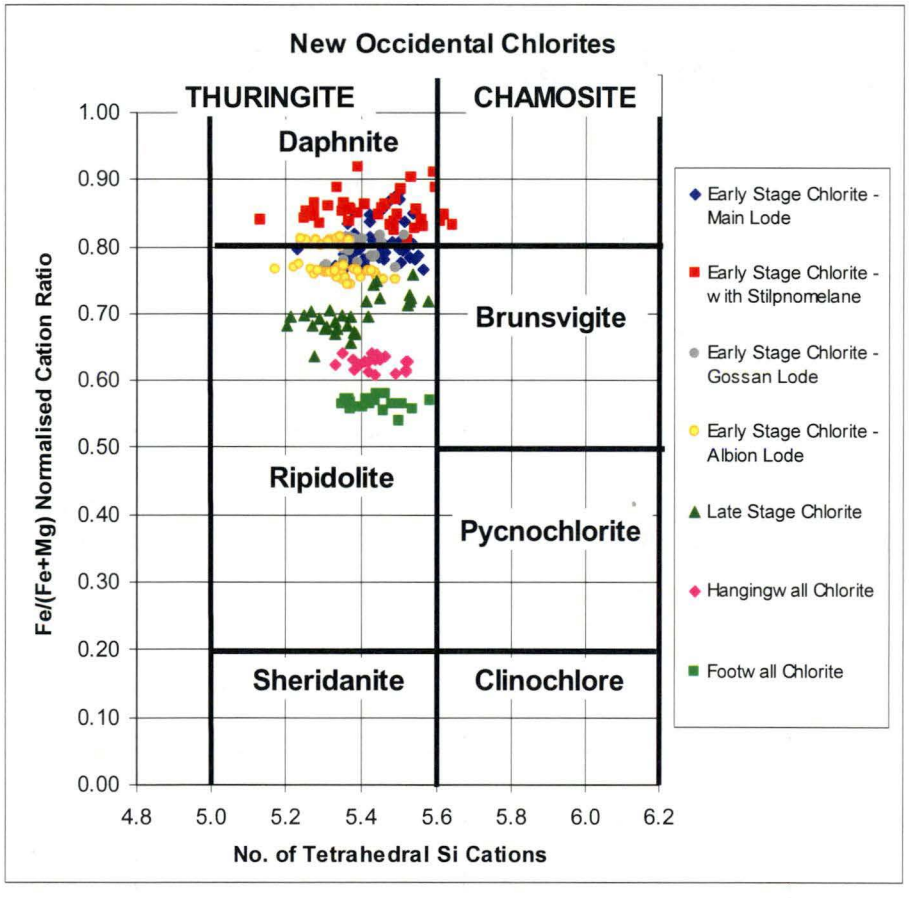

Both early- and late-stage vein and alteration chlorites from the New Occidental deposit are more Fe-rich than chlorites in the hanging wall and footwall of the New Occidental deposit, which is consistent with the systematic increases in Fe/(Fe+Mg) ratio of alteration and vein chlorites with increasing intensity of mineralisation in the New Occidental deposit described by Robertson (1974). The number of tetrahedral Al cations in chlorites in the New Occidental deposit is relatively constant and is on average subtly higher than for footwall and hanging wall chlorites (Table 19). Correspondingly, the number of octahedral Al cations in orebody chlorites is slightly lower than in footwall and hanging wall chlorites.

Composition of orebody chlorite stages does not vary either along the strike or with increasing depth in the deposit.

Table 19: Average chemical compositions of New Occidental chlorites.

Description	Early Stage Main Lode	Early Stage +Stilpnomelane	Early Stage Gossan	Early Stage Albion Lode	Late Stage	Hanging wall	Footwall
# Analyses	50	40	20	40	30	20	20
Weight %							
SiO_2	24.54	24.21	23.47	23.57	24.87	24.86	25.15
TiO_2	bld	bld	bld	bld	bld	bld	bld
Al_2O_3	20.56	19.83	20.53	20.62	21.17	20.97	21.52
Cr_2O_3	bld	bld	bld	bld	bld	bld	bld
FeO	38.33	40.98	37.15	36.57	34.47	30.67	27.65
MnO	0.27	0.21	0.50	0.47	0.43	0.32	0.33
MgO	5.32	3.93	5.34	6.06	8.40	10.28	11.94
CaO	bld	bld	bld	bld	bld	bld	bld
Na_2O	0.58	0.72	nd	nd	0.49	nd	nd
K_2O	0.32	0.36	nd	nd	0.25	nd	nd
H2O							
TOTAL	**89.92**	**90.22**	**86.98**	**87.29**	**90.07**	**87.10**	**86.60**
Normalised Cation Distribution*							
Si	5.44	5.44	5.36	5.34	5.38	5.44	5.44
Ti	0.00	0.00	0.00	0.00	0.00	0.00	0.00
Al (Tetrahedral)	2.56	2.56	2.64	2.66	2.62	2.56	2.56
Al (Octahedral)	2.80	2.68	2.88	2.84	2.77	2.84	2.92
Fe	7.10	7.70	7.09	6.93	6.23	5.61	5.00
Mn	0.05	0.04	0.10	0.09	0.08	0.06	0.06
Mg	1.75	1.31	1.82	2.04	2.71	3.35	3.85
Ca	nd	nd	nd	nd	nd	nd	nd
Na	0.25	0.31	nd	nd	0.20	nd	nd
K	0.09	0.10	nd	nd	0.07	nd	nd
Total	**20.05**	**20.15**	**19.88**	**19.91**	**20.06**	**19.86**	**19.82**
Site Occupancy#							
Sum IV	8.00	8.00	8.00	8.00	8.00	8.00	8.00
Sum VI	12.05	12.15	11.88	11.91	12.06	11.86	11.82
VI Vacancy	-0.05	-0.15	0.12	0.09	-0.06	0.14	0.18
Fe/(Fe+Mg)	0.80	0.85	0.80	0.77	0.70	0.63	0.57
Cation Ratio							
2Ca+Na+K	0.34	0.42	nd	nd	0.27	nd	nd

bld - below level of detection of 0 1%

nd - not determined due to low concentrations

* - calculated on the basis of $O_{20}(OH)_{16}$ (Deer et al. 1966) and Fe treated as Fe^{2+}

- based on normalising to 8 octahedral cations

Relatively high levels of K_2O and Na_2O are evident in the microprobe analyses of New Occidental chlorites, which most likely reflect the presence of contaminant minerals including biotite, corrensite, saponite, illite, muscovite or smectite-like layers within chlorite (e.g. de Caritat et al., 1993; Jiang et al., 1994). A subtle decrease in the number of 2Ca+Na+K cations with increasing Al^{IV} occupancy is evident in those New Occidental chlorites for which Na and K probe analyses are available. The number of 2Ca+Na+K

cations in New Occidental chlorites decreases with increasing octahedral site vacancies but increases with increasing Fe/(Fe+Mg) ratio.

5.5.2 Variations in Chlorite Chemistry amongst Cobar Deposits

A comparison of chemical compositions of New Occidental chlorites with those of orebody chlorites in the Peak, Chesney, CSA, McKinnons and Perseverance deposits (Figure 114) indicates Perseverance chlorites are compositionally similar to New Occidental chlorites (especially chlorites from near the bottom of the Perseverance deposit), but that Chesney, CSA and Peak deposit chlorites are consistently characterised by lower Fe/(Fe+Mg) ratios. In particular, Peak chlorites show a very large range in Fe/(Fe+Mg) ratio, with decreasing ratios associated with decreasing number of tetrahedral Al cations. Chlorites characterised by moderate Fe/(Fe+Mg) ratios are typically associated with Cu-Au mineralisation in the deposit, whereas the Mg-rich chlorites are associated with late-stage Pb-Zn-Ag mineralisation (Figure 114b). The small number of samples of extremely Fe-rich chlorites from the CSA deposit (Figure 114a) is located in the footwall of the Western ore system and is interpreted by Brill (1988a) to represent a very early stage in the paragenetic sequence of that deposit. Compositionally, they are characterised by very low number of Al^{IV} cations but relatively high CaO, K_2O and Na_2O contents, which is interpreted to be in part due to the presence of illite and/or smectite interlayers in the chlorite (Brill, 1988a).

Figure 114: Variations in chlorite chemistry in Cobar deposits.

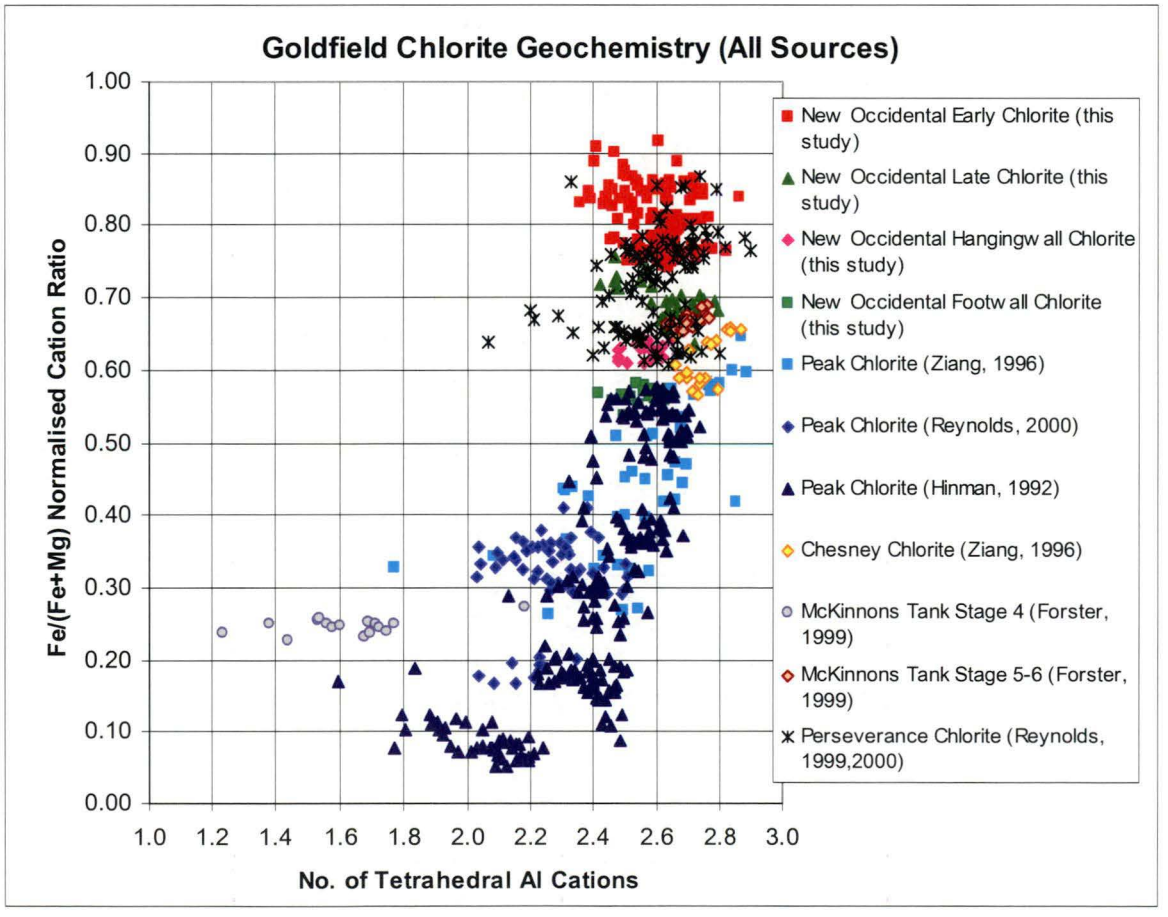

5.6 Short Wavelength Infrared (SWIR) Spectrometry of the New Occidental Deposit

5.6.1 SWIR Spectral Parameters

A number of specific SWIR spectral parameters based upon hull quotient spectra have been used to identify mineralogical changes within and surrounding the New Occidental deposit. These parameters, which were developed by Hornibrook (1998a, b) and AusSpec (2000), are summarised in Appendix 5.

5.6.2 SWIR Spectrometry of the New Occidental Deposit

SWIR spectra from the New Occidental deposit (Figure 115 – Figure 116, Appendix 5) confirm the deposit contains a relatively simple mineralogy comprising varying proportions of white mica (sericite), chlorite and minor carbonate. Stilpnomelane was identified in a number of drillhole traverses, but only within the strongly mineralised zones within the deposit. The weathered zone intersected by drillholes NO14/14E contains a mineral assemblage of illite, kaolinite and minor carbonate.

The key SWIR spectral characteristics of the New Occidental deposit include:

White mica (sericite)

- Al-OH absorption features are strongly developed in spectra from the hanging wall and footwall of the New Occidental deposit but are relatively weakly developed in spectra from the orebody and its immediate margins, indicating white mica is widespread throughout the deposit hanging wall and footwall but is largely absent from the orebody and immediate surrounds (Figure 115 – Figure 116).
- White micas are increasingly phengitic with increasing proximity to the New Occidental orebody and orebody white mica is strongly phengitic. The wavelength of the Al-OH absorption feature that correlates with the composition of white mica progressively shifts from lower values of the order of 2210–2215nm (muscovitic to phengitic) in relatively unaltered wallrock to 2215–2230nm (strongly phengitic) in the orebody. The transition typically occurs over 10–20m wide zones at the margins of the orebody (Figure 115 – Figure 116).
- Decreasing depth and increasing wavelength of the Al-OH absorption feature with increasing Au and Cu grade (Figure 117) confirm white mica, although largely absent from the orebody, becomes more phengitic with increasing Au-Cu grade.
- The muscovitic to weakly phengitic character of the white mica in the Chesney Formation hanging wall persists beyond the limits of sampling (>400m horizontally perpendicular to the orebody), including a very broad zone of more phengitic mica approximately 200–400m from the orebody, whereas, at relatively short distances into the Great Cobar Slate footwall of the deposit (approximately 50m), the Al-OH absorption feature progressively shifts to even lower values of the order of 2200–2205nm (muscovitic) (Figure 116).

- The *Sericite Crystallinity Index* decreases in proximity to the New Occidental orebody (Figure 116), indicating crystallinity of the white mica increases towards the deposit (low values within the orebody are likely due to the relative absence of white mica in the orebody and the presence of water-bearing minerals like stilpnomelane, water in fluid inclusions and chlorite in the orebody).

Chlorite

- The ratio of the depth of the Al-OH and Fe-OH absorption features are consistently less than one throughout the orebody, indicating chlorite predominates over white mica (Figure 115 – Figure 116). Many spectra from the orebody returned null values indicating white mica is absent.

- Chlorite is increasingly Fe-rich in proximity to the New Occidental deposit. The wavelength of the Fe-OH absorption feature associated with relatively unaltered wallrock is typically in the range of 2255–2257nm in comparison to chlorite in the orebody which has values in the range 2260–2266nm. The transition from background values to those typical of the orebody occurs over a horizontal width of approximately 20–30m (Figure 115). Spectra from NO14/14E (Figure 116) indicate that the transition is locally much wider (approximately 100m). The spectra from those drillholes also highlight the presence of a broad zone of longer Fe-OH wavelength values (~2260nm), and hence locally more Fe-rich chlorite, in the hanging wall of the New Occidental orebody approximately coincident with the zone of elevated Al-OH wavelength values.

- The depth and area of the Fe-OH absorption feature reflecting chlorite abundance typically increases towards the New Occidental orebody itself. Data for drillholes NO14/14E (Figure 116) indicate chlorite content increases within the orebody (c.f. NO3C) but this is an artefact of the way in which spectra from NO14/14E were collected. Those spectra were acquired by direct measurement of phyllosilicate-rich sections of half-drillcore, rather than from homogenised drillcore pulps used in the other drillcore traverses. Isolated higher values of both depth and area of the Fe-OH absorption feature within the New Occidental orebody likely reflect localised intervals of chlorite-rich veins or altered wallrock.

- Decreasing depth and increasing wavelength of the Fe-OH absorption feature with increasing Au grade (Figure 117) confirm chlorite is less abundant in the orebody compared to the wallrock but that it is more Fe-rich.

- The wavelength of the Mg-OH absorption feature exhibits a subtle increase towards the New Occidental orebody but is either strongly reduced or not developed in spectra from the orebody (Figure 115 – Figure 116). The subtle increase in wavelength reflects a trend of increasing Fe/(Fe+Mg) ratio of chlorite towards the orebody. The abrupt decrease in the wavelength of the Mg-

OH absorption feature in the orebody reflects the low abundance of Mg-bearing minerals (e.g. Mg-chlorite, carbonate) within the orebody. Again, the increase in wavelength of the Mg-OH absorption feature in spectra from the orebody in NO14/14E reflects the mode of data acquisition for those drillholes and highlights the Fe-rich nature of the orebody chlorite.

- Normalised reflectance values at 1350nm typically decrease towards the New Occidental orebody and are most negative on the immediate margins of the orebody. Values are generally less negative or >0 within the orebody. Such trends indicate that Fe^{2+}-bearing minerals, most likely chlorite, increase in abundance towards the New Occidental orebody, and are most abundant on the immediate margins of the orebody. The decrease in normalised reflectance values towards the orebody may also reflect increasing Fe^{2+} content of minerals like chlorite. Again, variable reflectance values in the New Occidental orebody most likely partly reflect variable chlorite and quartz contents of the orebody. Zones of Cu mineralisation in drillhole NO3C are associated with positive (>0) normalised reflectance values (Figure 115), indicating those zones are characterised by the absence of Fe^{2+}-bearing minerals

Stilpnomelane

- The occurrence of stilpnomelane, as mapped by the *Stilpnomelane Index*, is restricted to the New Occidental orebody (Figure 115). Index values in excess of 0.3 appear to reliably indicate the presence of stilpnomelane.

SWIR spectra for a poorly mineralised section of the Great Chesney Fault in the Comstock area 900m to the south of the New Occidental deposit (drillhole CS4A; Figure 118) show little difference between quartz breccia developed along the Great Chesney Fault and the adjacent wallrock. The rock units either side of the Great Chesney Fault, however, are spectrally distinct. White mica in the Great Chesney Formation is both more phengitic and more crystalline than the mica in the Great Cobar Slate. Chlorite composition is equivalent to that of chlorite from unmineralised wallrock in the New Occidental deposit environs, with Fe/(Fe+Mg) ratios of <0.8.

Figure 115: SWIR spectral characteristics of drillhole NO3C.

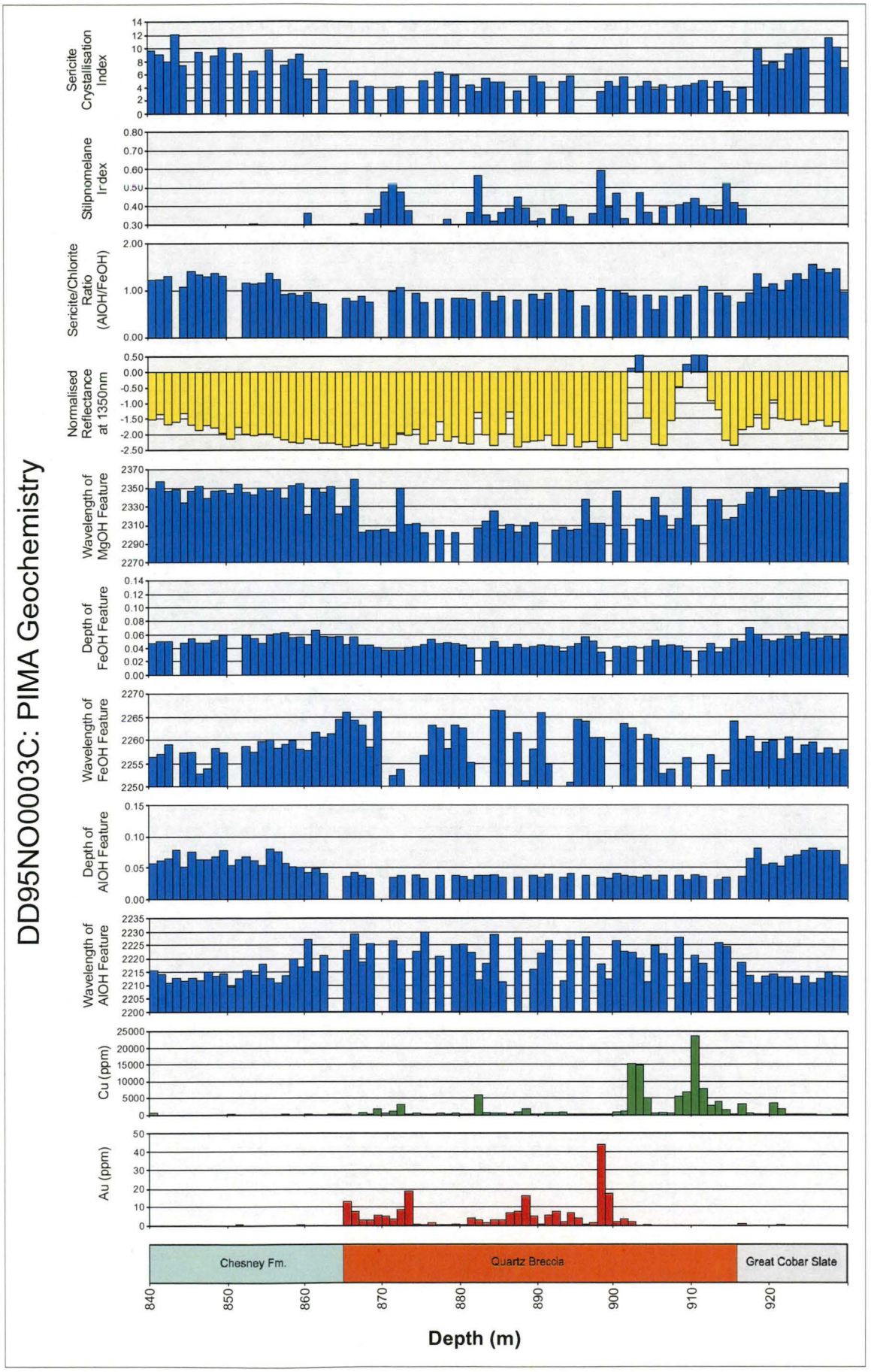

Figure 116: SWIR spectral characteristics of drillholes NO14/14E.

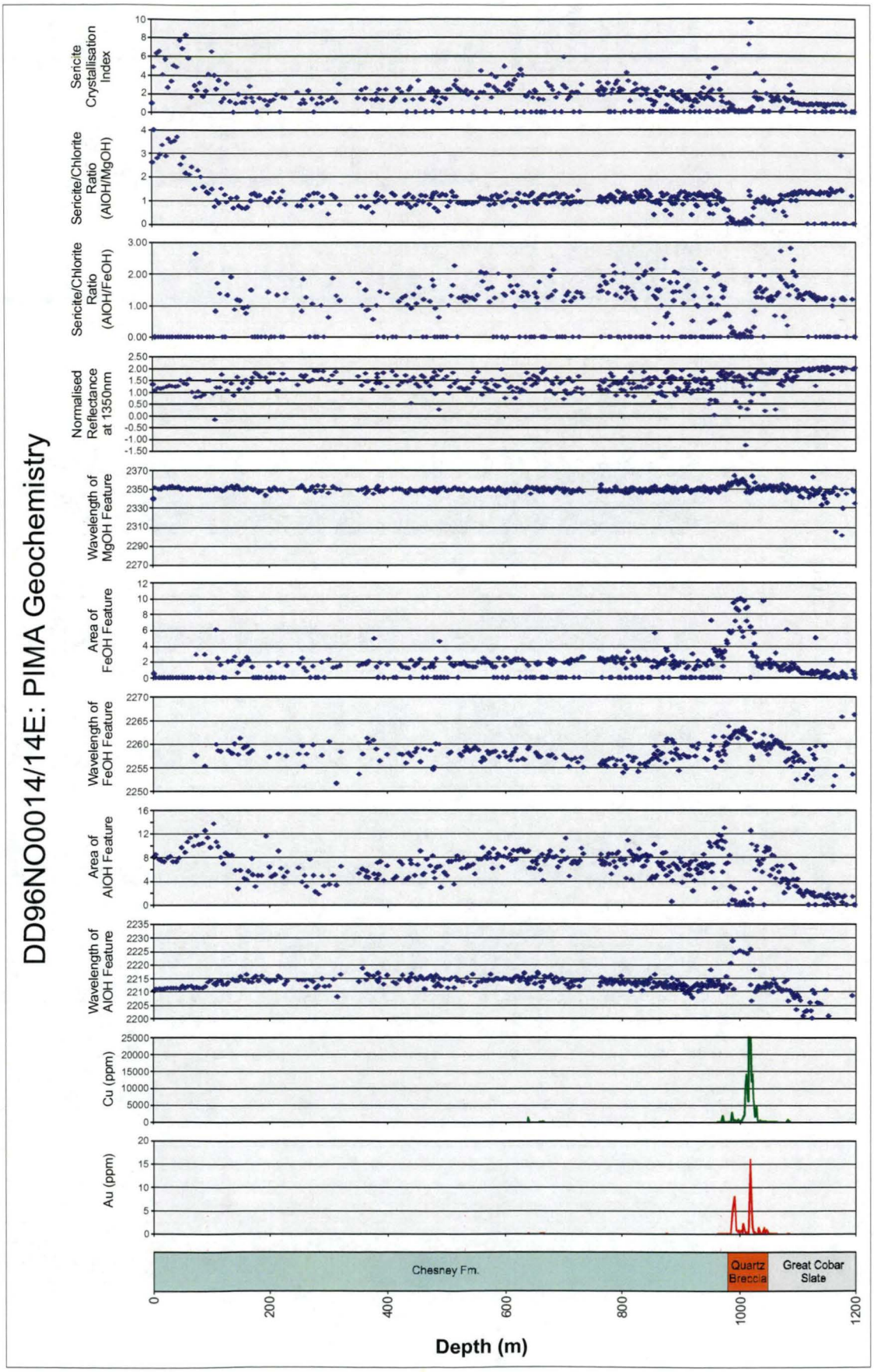

Figure 117: Plots of SWIR spectral parameters and Au and Cu assays (all SWIR spectra from 8 drillholes outlined in Figure 100).

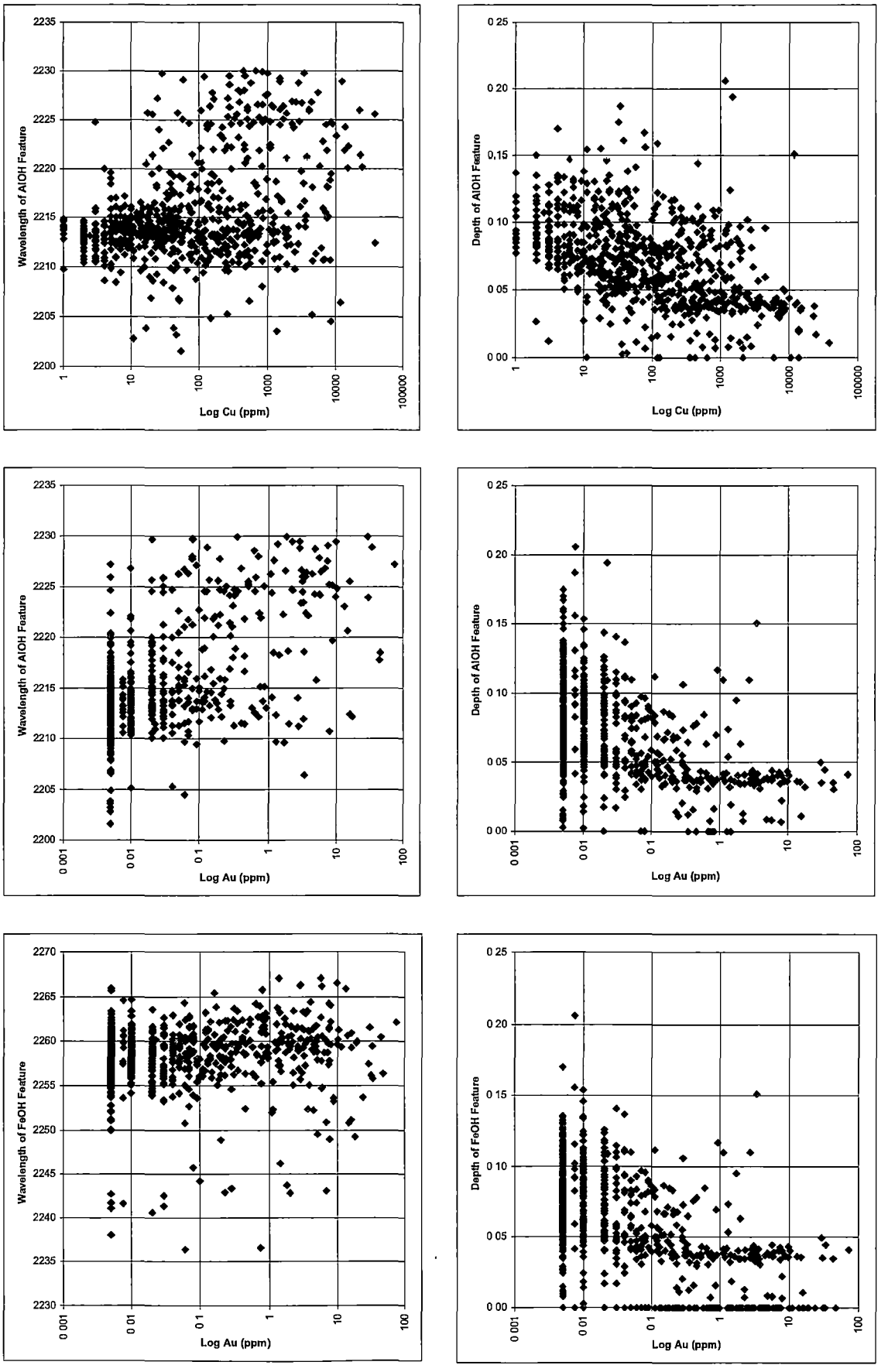

Figure 118: SWIR spectral characteristics of drillhole CS4A, Comstock area.

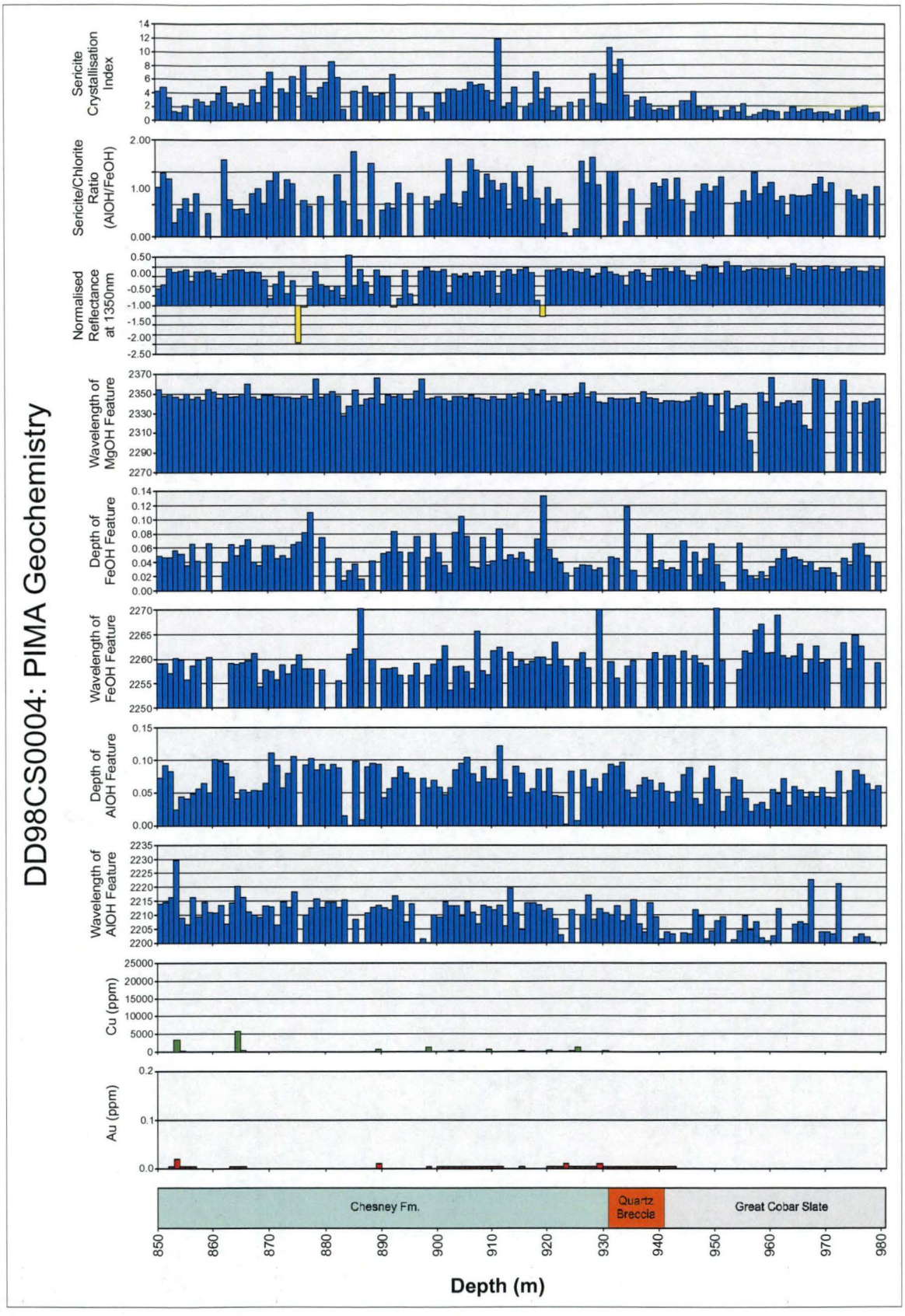

5.7 Evolution of the New Occidental Hydrothermal Fluid Inferred from Alteration Mineral Paragenesis - And Unresolved Aspects!

5.7.1 Nature and Extent of Wallrock Alteration around the New Occidental Deposit

The most likely explanation for the mineralogical changes observed about the New Occidental deposit is that the pre-existing metamorphic mineral assemblage of muscovitic to weakly phengitic white mica and chlorite $_{Fe/(Fe+Mg)\ 0.6-0.7}$ has been replaced by a hydrothermal mineral assemblage comprising extremely Fe-rich chlorite $_{Fe/(Fe+Mg)\ =\ 0.7-0.9}$, stilpnomelane and minor phengitic white mica. The presence of white mica in altered wallrock immediately flanking the orebody and its absence (by and large) within the deposit is interpreted to reflect fluid/rock ratios within and peripheral to the Great Chesney Fault. Within the fault zone, fluid/rock ratios were relatively high and white mica was extensively replaced by chlorite. However, fluid/rock ratios on the margins of the fault zone were lower and wallrock buffering of the hydrothermal fluid maintained the stability of white mica. This is consistent with coincident changes in white mica and chlorite composition with increased proximity to the New Occidental deposit.

The presence of wide zones (>400m) of increased chlorite content and more phengitic and crystalline white mica in Chesney Formation hanging wall, compared to the relatively narrow zones in Great Cobar Slate (<50m) in the immediate footwall of the New Occidental deposit, suggest fluid flow and attendant hydrothermal mineral growth was greatest in the hanging wall of the deposit. This most likely reflects enhanced porosity and permeability of the Chesney Formation sandstones compared to the relatively impermeable siltstones and mudstones of the Great Cobar Slate. Zones of more phengitic and crystalline white mica within the Chesney Formation, often associated with better developed cleavage and minor base metal mineralisation, most likely represent localised zones of increased fluid flow in the hanging wall of the deposit.

Trends of increasing chlorite and white mica content, increasing white mica crystallinity and phengicity (increasing Fe/Mg/Si and decreasing Al content of white mica) and increasing Fe/(Fe+Mg) ratio of chlorite towards the Great Chesney Fault at the New Occidental deposit (Section 5.6) are consistent with increasing intensity of hydrothermal alteration about the deposit. Absence of similar mineralogical changes about the Great Chesney Fault in the Comstock area (e.g. drillhole CS4A) indicate such changes can be used to discriminate between barren and potentially mineralised sections of the Great Chesney Fault and other similar fault zones.

5.7.2 Chlorite Compositional Variations and Implications for Their Use as Geothermometers

The widespread occurrence of compositionally variable hydrothermal and metamorphic chlorite in Cobar deposits suggests studies of chlorite composition have the potential to provide important insights into the physiochemical conditions of ore formation. In particular, systematic temperature-dependent compositional variations, including increases in Al^{IV} occupancy and decreases in Si^{IV} and Al^{VI} content, octahedral vacancies and Fe/Mg ratio have been used by a number of authors (Brill, 1988a; Jiang, 1996; Forster, 1997) to derive temperatures of formation for the various stages of chlorite alteration and associated mineralisation in Cobar deposits

A simple correlation between Al^{IV} content of Cobar chlorites and temperature of formation is unlikely. Geothermometers based upon empirical calibrations of chlorite Al^{IV} content in

chlorites with measured formation temperatures (e.g. Cathelineau and Nieva, 1985; Cathelineau, 1988), including models accounting for the effects of bulk rock composition, mainly Fe:Mg ratio, of the host rock (Hillier & Velde, 1991) have been shown to yield widely varying temperature estimates that were often significantly different (>150°C) from independently measured temperatures of formation (de Caritat et al., 1993). Rather, Al^{IV} content appears to be dependent on a wide range of parameters including Al-content and Fe/(Fe+Mg) ratio of host rock and/or hydrothermal fluid (Kranidiotis and MacLean, 1987; de Caritat et al., 1993; Hutcheon et al., 1994), the abundance of mixed layers of contaminant minerals (de Caritat et al., 1993) and a range of physiochemical parameters including temperature, pressure and water/rock ratio (Vidal et al., 2001).

Although the Walshe (1986) 6-component chlorite solid solution model has been applied to a number of Cobar deposits to determine temperatures of formation (e.g. Brill, 1988a; Jiang, 1996; Forster, 1997) and have yielded temperatures consistent with temperatures measured in fluid inclusion studies (Table 20), the reliability of this geothermometer and others has been questioned in a number of studies (de Caritat et al., 1993; Hutcheon et al., 1994; Jiang et al., 1994; Xie et al., 1997; Zane et al., 1998; Schmidt et al., 1999; Vidal et al., 2001). In addition to the limitations Walshe (1986) himself imposed on the model, including that it could not be used to calculate formation temperatures for Fe-rich chlorites (like the early stage chlorites from the New Occidental deposit) and that significant errors may arise from poor quality microprobe analyses of chlorites intergrown with other minerals, Kavalieris et al. (1990) and de Caritat et al. (1993) concluded the Walshe (1986) geothermometer could only be used where bulk rock composition and physiochemical conditions are relatively constant. Therefore, the key temperature-dependent substitutions underpinning the Walshe (1986) geothermometer may also driven by variations in the composition of host rocks and the hydrothermal fluid.

de Caritat et al. (1993) tested the thermodynamic geothermometer of Walshe (1986) on a range of chlorites and found that estimated temperatures were still up to 100°C different from independently measured temperatures of formation. Similarly, although Brill (1988a), Jiang (1996) and Forster (1997) claimed the Walshe geothermometer has provided robust temperature estimates for the range of Cobar deposits tested, temperatures of formation estimated for the Peak and Chesney deposits are apparently ~60–90°C lower than fluid inclusion temperature estimates (Table 20). The Walshe (1986) geothermometer is therefore unlikely to provide accurate and unequivocal temperature estimates for the various stages of chlorite alteration and associated mineralisation in Cobar deposits.

Vidal et al. (2001) claimed their thermodynamic chlorite model offers a further refinement over the Walshe (1986) geothermometer by accounting for the bulk of observed substitutions in chlorite. Whilst the accuracy of this model has not been independently assessed and its applicability to studies of Cobar deposits may represent an opportunity for further research, their model also assumes key chlorite substitutions are predominantly controlled by temperature and pressure and not by variations in bulk-rock/hydrothermal fluid chemistry.

Table 20: Temperatures of deposit formation calculated using Walshe's (1986) chlorite geothermometer and fluid inclusion homogenisation temperatures from co-existing quartz.

Deposit	Chlorite Type	Walshe Chlorite Temperature (°C)	Fluid Inclusion Temperature Th (°C)
CSA (Brill, 1988a)	Chlorite associated with Cu-Pb-Zn mineralisation	243–365 °C	199–389 °C
Peak (Jiang, 1996)	Ore	230–285 °C	283–393 °C
	Metasediments	221–310 °C	
	Rhyolite	140–284 °C	
Chesney (Jiang, 1996)	Ore	288–316 °C	285–381 °C
McKinnons (Forster, 1997)	Stage 5–6 mineralisation	124–260 °C	157–269 °C

It therefore appears variations in bulk-rock/hydrothermal fluid chemistry during formation of the New Occidental deposit, particularly of Fe:Mg ratio, have been the primary control on chlorite composition, rather than temperature.

5.7.3 The Significance of Iron-rich Alteration Minerals

The predominance of hydrothermal Fe-Mg-K-rich aluminosilicates such as Fe-chlorite, stilpnomelane and greenalite in orogenic gold deposits is relatively rare. Stilpnomelane has only been documented in more than trace amounts in the Magdala deposit, Stawell, central Victoria (Fredericksen & Gane, 1998; Bierlein et al., 2000) and in the Agnico-Eagle gold deposit, Quebec, Canada (Wyman et al. 1986). At Stawell, stilpnomelane is present in both auriferous quartz-sulfide-magnetite veins and peripheral hydrothermally altered siliceous wallrock in the Magdala deposit (Fredericksen & Gane, 1998) where it is inferred to reflect large-scale Fe-enrichment during deposit formation. In comparison, formation of stilpnomelane in the Agnico-Eagle gold deposit is associated with alteration of host sedimentary iron formation (Wyman et al. 1986). Stilpnomelane has also been occasionally recorded in metamorphosed volcanic hosted massive sulfide deposits in association with magnetite (e.g. Phelps Dodge deposit, Quebec – Kranidiotis & MacLean, 1987; Currawong deposit, Benambra, Victoria – Bodon & Valenta, 1995).

Hydrothermal alteration reactions within the New Occidental deposit are best approximated by phase relations in the system K_2O-FeO-MgO-Al_2O_3-SiO_2-H_2O-CO_2 in the presence of quartz and magnetite. Phase relations for this system are limited to studies of aluminosilicate-rich bands in metamorphosed iron-formations (e.g. Brown, 1971; Miyano & Klein, 1989), or metamorphosed Fe-rich pelitic assemblages (e.g. Brown, 1975). However, more extensive studies of phase relations of both metamorphic and hydrothermal chlorite have been undertaken (Cathelineau & Nieva, 1985; Walshe, 1986; Kranidiotis & MacLean, 1987; Cathelineau, 1988; Hutcheon, 1991; Hutcheon et al., 1994; Jiang et al., 1994; Xie et al., 1997; Zane et al., 1998; Schmidt et al., 1999; Vidal et al., 2001).

Chlorite is a relatively ubiquitous mineral in hydrothermal and metamorphic environments and forms under a wide range of temperature (150–450°C) and pressure (up to several kbars) conditions (Cathelineau & Nieva, 1985). Jenkins & Chernosky (1986) measured maximum thermal stabilities for Mg-chlorite in the range 650–850°C over a range of pressures (1–14kb). The presence of chlorite therefore, by itself, provides little constraint on the chemistry of the New Occidental ore fluid. Chlorite similarly coexists with muscovite under a variety of hydrothermal and greenschist facies metamorphic conditions

(Brown, 1971; Beane & Titley, 1980; Cathelineau & Nieva, 1985; McCuaig & Kerrich, 1998). However, chlorite formation at the expense of muscovite does indicate increasing $a(Fe^{2+})/ a(H^+)$ and potentially decreasing $a(K^+)/ a(H^+)$ in the hydrothermal fluid, although not changes in temperature (Beane & Titley, 1980; Beane, 1994). Similarly, although variation in the Fe/(Fe+Mg) ratio of hydrothermal chlorite has been attributed to a number of factors including changes in water/rock ratio, oxygen and sulfur fugacity and *pH* (Kranidiotis & MacLean, 1987), most studies have concluded the dominant cause of variation in chlorite Fe/(Fe+Mg) ratio is varying Fe-Mg contents of the host rock or hydrothermal fluid, with the chlorite Fe/(Fe+Mg) ratio closely matching the Fe/(Fe+Mg) ratio of the host rock (Cathelineau & Nieva, 1985; Kranidiotis & MacLean, 1987; de Caritat et al., 1993; Xie et al., 1997; Zane et al., 1998; Wyman, 2001). SWIR spectral parameters show wallrock metamorphic chlorite is characterised by relatively consistent Fe/(Fe+Mg) ratios, indicating wallrock composition is unlikely to be the source of Fe-enrichment of hydrothermal chlorites. Rather, formation of chlorite $_{Fe/(Fe+Mg) = 0.8}$ at the expense of muscovite and metamorphic chlorite $_{Fe/(Fe+Mg) = 0.6}$ in the New Occidental deposit most likely indicates the primary hydrothermal fluid was characterised by high $a(Fe^{2+})$.

Stilpnomelane has been documented in metamorphosed Precambrian iron formations (Deer et al. 1966; Eggleton & Chappell, 1978; Miyano & Klein, 1989) and in Fe-rich schists (Brown, 1971; 1975), where it is indicative of low- to medium-grade metamorphism (Miyano & Klein, 1989). In studies of metamorphosed iron-formations stilpnomelane is stable over a wide range of temperatures (200–470°C and 5–6 kbars; Figure 119a). At higher temperatures and higher $a(K^+)/a(H^+)$ values stilpnomelane is replaced by biotite whilst it decomposes to chlorite in response to lower $a(K^+)/a(H^+)$ (Figure 119b). Stilpnomelane stability is also restricted to reduced conditions where magnetite is stable instead of haematite (Miyano & Klein, 1989). Under oxidising conditions, the assemblage Fe oxide – chlorite appears to be stable instead (Brown, 1971). The stability field of stilpnomelane is also diminished with increasing $a(Mg^{2+})/a(Fe^{2+})$ and X_{CO_2} (Miyano & Klein, 1989); stilpnomelane reacts to form biotite and siderite with increasing X_{CO_2}.

Figure 119: Stability diagrams for stilpnomelane (Miyano & Klein, 1989).

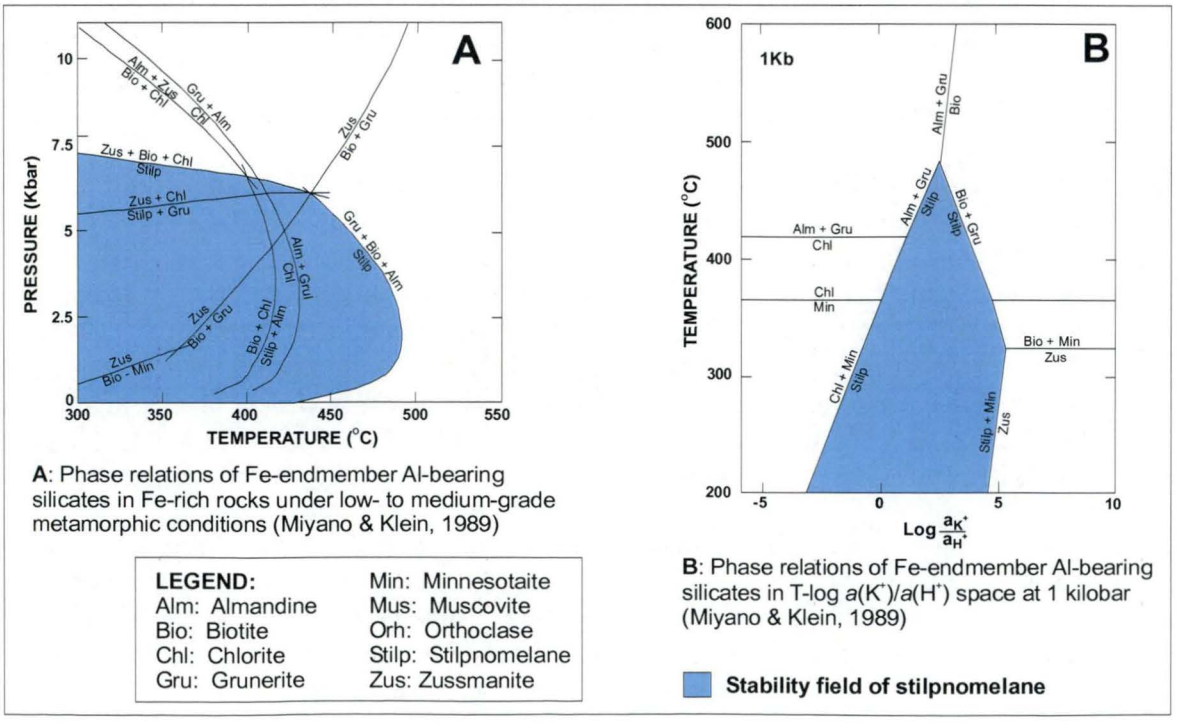

A: Phase relations of Fe-endmember Al-bearing silicates in Fe-rich rocks under low- to medium-grade metamorphic conditions (Miyano & Klein, 1989)

LEGEND:	
Alm: Almandine	Min: Minnesotaite
Bio: Biotite	Mus: Muscovite
Chl: Chlorite	Orh: Orthoclase
Gru: Grunerite	Stilp: Stilpnomelane
	Zus: Zussmanite

B: Phase relations of Fe-endmember Al-bearing silicates in T-log $a(K^+)/a(H^+)$ space at 1 kilobar (Miyano & Klein, 1989)

Stability field of stilpnomelane

The presence of stilpnomelane in the New Occidental deposit can therefore be used to infer the hydrothermal fluid was characterised by increased $a(K^+)/a(H^+)$ and/or $a(Fe^{2+})/a(H^+)$ and low X_{CO_2}. Increased $a(K^+)/a(H^+)$ potentially reflects increased $a(K^+)$ in the fluid in response to associated destruction of K-white mica, especially as only minor amounts of liberated K^+ would have been incorporated into chlorite. A number of factors also indicate increased $a(Fe^{2+})$ including higher Fe/(Fe+Mg) ratios of stilpnomelane and coexisting chlorite compared to early-stage chlorite and that stilpnomelane has only been observed in Cobar deposits containing appreciable precursor magnetite. Stilpnomelane replacement of chlorite may also correspond to when wallrock surrounding the New Occidental deposit was no longer capable of buffering the hydrothermal fluid due to the effects of ongoing alteration.

Greenalite has been documented in metamorphosed Precambrian iron formations where it is indicative of lowest-grade metamorphism (Deer et al. 1966; Miyano & Klein, 1989). Greenalite and Fe-rich clays formed in the New Occidental deposit as a direct replacement of stilpnomelane and chlorite and most likely represent a lower-temperature alteration mineral assemblage.

Unfortunately, the range of Fe-rich hydrothermal alteration minerals present at the New Occidental deposit cannot be used to adequately constrain the temperature of the hydrothermal fluids. As already noted, chlorite and stilpnomelane are stable over a wide range of temperatures. Replacement of stilpnomelane by biotite in the deposit may reflect either localised higher temperatures (>400–470°C) or increased $a(K^+)/a(H^+)$, whereas greenalite replacement of chlorite and/or stilpnomelane provides only a qualitative indication of reduced fluid temperature.

5.7.4 Potential Causes of Mg-Enrichment

Replacement of stilpnomelane by late-stage chlorite$_{FFM=0.7}$ in the New Occidental deposit is potentially caused by a number of factors including decreasing $a(K^+)/a(H^+)$, $a(Fe^{2+})/a(Mg^{2+})$ and/or increasing X_{CO_2} in the hydrothermal fluid (e.g. Miyano & Klein, 1989), whereas concurrent replacement of early-stage Fe-chlorite$_{FFM=0.8–0.9}$ by late-stage chlorite$_{FFM=0.7}$ suggests decreasing $a(Fe^{2+})/a(Mg^{2+})$ in the ore fluid is the most likely factor. The absence of appreciable carbonate minerals associated with in this alteration stage suggests increasing X_{CO_2} was not a significant factor.

Potential causes of a decrease in $a(Fe^{2+})/a(Mg^{2+})$ include mixing of the primary hydrothermal fluid with Mg-rich meteoric water (e.g. as proposed for the Phelps Dodge deposit by Kranidiotis & MacLean, 1987) and/or ongoing buffering of the hydrothermal fluid by wallrock containing chlorite$_{FFM=0.6}$. The possibility of such a change being caused by change in temperature of the hydrothermal fluid alone (in the case of reduced chlorite Fe/(Fe+Mg) ratios) has already been discounted (Section 5.7.2). At this stage, further studies, including whole rock geochemistry and fluid inclusion studies, are required to determine whether a second fluid was involved in the formation of the New Occidental deposit. However, wallrock buffering is consistent with reduced fluid flow along the Great Chesney Fault post deposition of Stage 4 quartz veins and during the main stage of late-stage chlorite alteration (Section 4.5).

5.7.5 Quartz Dissolution Mechanisms

Quartz dissolution associated with late-stage chlorite$_{FFM=0.7}$ alteration in the footwall of the New Occidental deposit indicates a change from silica saturation to undersaturation in the ore fluid. Potential causes for silica undersaturation include heating of the fluid (possibly as a result of mixing with a hotter fluid as proposed by Hinman (1992) at the Peak

deposit), retrograde quartz solubility as a consequence of decreasing temperature (e.g. when the fluid cools below about 500°C at 500 bars), and/or a period of increased pressure at relatively constant temperature (e.g. Fournier, 1985; Figure 120).

Again, there is insufficient data at this stage to determine the existence or otherwise of a second hotter hydrothermal fluid, or whether fluid temperatures increased – such evidence will be sought in subsequent fluid inclusion studies. Retrograde quartz solubility in response to decreasing temperature appears unlikely given the relatively high fluid temperatures required (e.g. Fournier, 1985; Figure 120). More tightly constrained fluid temperatures are required to establish whether such a mechanism for quartz dissolution is applicable to the New Occidental deposit. Finally, quartz dissolution due to pressure increases at relatively constant temperature is plausible, especially during fault valve activity on the Great Chesney Fault immediately after slip following resealing of the fault zone. However, such pressure increases would likely be transitory in nature. Significantly, quartz dissolution associated with late-stage chlorite alteration occurs immediately after deposition of the last major quartz vein stage (Stage 4; Table 18), which corresponds to the waning stages of fault zone dilation (and onset of local contractional slip) and the transition from brittle to ductile deformation in the deposit. Fluid pressures were still relatively high as evidenced by ongoing deposition of Stage 5 crack-seal sub-horizontal extension veins, although absence of significant fault zone dilation suggests less intense cyclic decompression of the fluid. The average fluid pressure could therefore reasonably be expected to show an overall increase in such an environment (e.g. Figure 121).

Figure 120: Calculated solubilities of quartz in water at the indicated pressures showing the region of retrograde quartz solubility (Fournier, 1985)

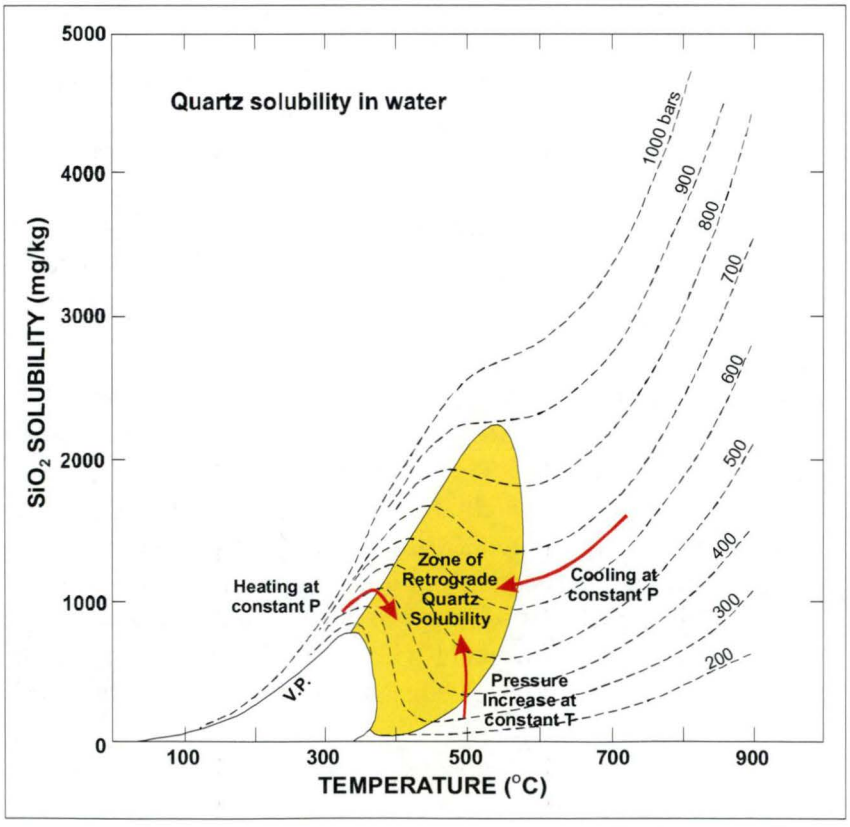

Figure 121: Schematic pressure variations along the Great Chesney Fault during quartz vein deposition.

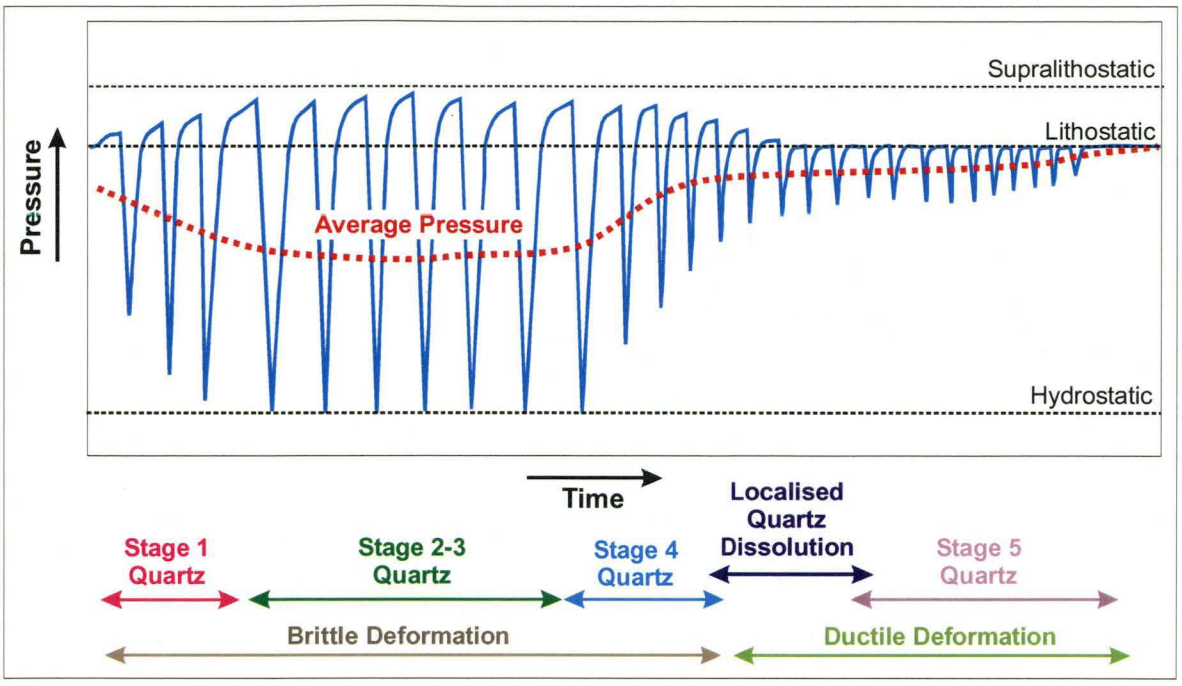

5.7.6 Sericite Alteration - An Indicator of a Second Hydrothermal Fluid?

Sericite replacement of chlorite $_{FFM = 0.7–0.9}$ according to the reaction:

$$Chlorite_{\ FFM = 0.7} \rightarrow Sericite + Quartz$$

$$2(Mg_3,Al_2,Fe_7)[(Si_{5.5},Al_{2.5})O_{20}](OH,O)_{16} + 3K^+ + 37H^+ \rightarrow 3KAl_2(AlSi_3O_{10})(OH)_2 + 2SiO_2 + 6Mg^{2+} + 14Fe^{2+} + 23½H_2O + 16O_2$$

requires decreasing $a(Fe^{2+})/a(H^+)$ and $a(Mg^{2+})/a(H^+)$, and possibly increasing $a(K^+)/a(H^+)$ in the hydrothermal fluid (Figure 122), but is unlikely to be caused by temperature changes alone (Beane & Titley, 1980; Beane, 1994). Possible explanations for sericite alteration in the deposit include ongoing wallrock buffering (as a continuance of wallrock buffering that initially produced chlorite $_{FFM = 0.7}$-stable alteration mineralogy; Section 5.7.4) or introduction of a second more acidic hydrothermal fluid.

Ongoing wallrock buffering of the New Occidental hydrothermal fluid is unlikely to produce conditions under which sericite replaces chlorite, given it is more likely the fluid would revert to conditions under which chlorite and sericite coexist (as is the case in unaltered wallrock on the immediate margins of the deposit). Wallrock buffering is also unlikely to produce decreasing $a(Fe^{2+})/a(H^+)$ and $a(Mg^{2+})/a(H^+)$ given the geochemistry (Mg-Fe content) of wallrock to the deposit. Introduction of a second more acidic fluid characterised by lower $a(Fe^{2+})$ and $a(Mg^{2+})$ but higher $a(K^+)$ into the deposit is plausible, although data analysed to this point does not provide evidence of a second hydrothermal fluid. Whole rock geochemistry and fluid inclusion studies are required to determine whether a second hydrothermal fluid was involved in formation of sericite alteration in the New Occidental deposit.

Figure 122: Activity-activity diagram [a(K+)/a(H+) versus $a(Mg^{2+})/a(H^{+})$] showing the stability of silicate minerals at 350°C, 500 bars pressure and quartz saturation (Beane & Titley, 1981)

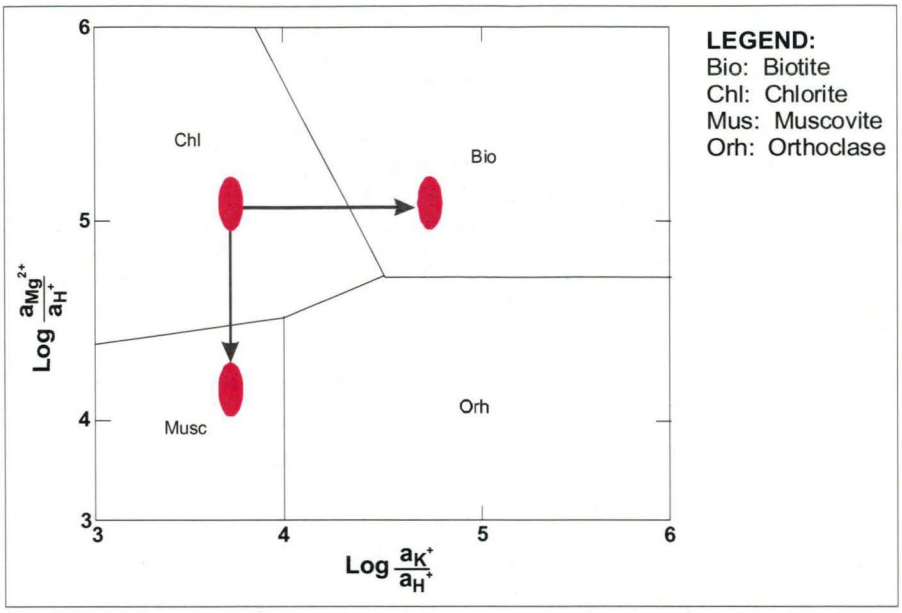

5.8 Comparison with Alteration Paragenetic Sequences in other Cobar Deposits

The alteration mineral paragenesis outlined for the New Occidental deposit has a number of distinctive features both common and different to parageneses proposed for other deposits in the Cobar Basin, including:

1. The New Occidental alteration mineral paragenesis is dominated by Fe-rich hydrothermal minerals, which is a characteristic of Cobar deposits. For example, all Cobar deposits contain abundant Fe-chlorite and occasional stilpnomelane, whereas deposits containing appreciable lead-zinc (Elura, CSA and McKinnons deposits) are also characterised by abundant Fe-carbonate (Table 7). Stilpnomelane is relatively abundant in gold-copper deposits of the northern Cobar Goldfield (Great Cobar deposit south to the New Occidental deposit). Only trace amounts of stilpnomelane are present in the Peak and Perseverance deposits to the south (Cook et al., 1998) and it has not been observed in either the CSA or Elura deposits to the north (Table 7).

2. The New Occidental deposit contains relatively minor sericite alteration compared to the Peak and Perseverance deposits where sericite alteration is strongly developed throughout the Peak Rhyolite (e.g. Cook et al., 1998).

3. Many Cobar deposits are characterised by Mg-enrichment in the later stages of their alteration mineral parageneses, which is mostly manifested as black (Mg-rich) chlorite replacement of green (Fe-rich) chlorite (Lawrie & Hinman, 1998; Stegman, 2001). In the case of the New Occidental deposit, such enrichment is relatively subtle but such enrichment is much stronger in other Cobar deposits including the Peak, Perseverance and CSA deposits (Table 21).

Table 21: Mg-enrichment trends in Cobar deposits.

Deposit	Mg-Enrichment Trends	Source
New Occidental	$Chlorite_{FFM=0.8-0.9}$ + Stilpnomelane → $Chlorite_{FFM=0.6-0.7}$	This Study
Peak	$Chlorite_{FFM=0.4-0.6}$ + Biotite + Stilpnomelane → $Chlorite_{FFM=0.1-0.4}$ + Talc + Mg-carbonate	Hinman (1992); Cook et al. (1998)
Perseverance	$Chlorite_{FFM=0.7-0.9}$ + Biotite → $Chlorite_{FFM=0.6-0.7}$	Reynolds (1999b, 2000b)
CSA	$Chlorite_{FFM=0.7-0.95}$ → $Chlorite_{FFM=0.3-0.6}$ + Talc	Brill (1988b)
Elura	Chlorite + Fe-carbonate → Chlorite + Mg-carbonate	Lawrie & Hinman (1998)

6 ORE MINERAL ASSEMBLAGES WITHIN THE NEW OCCIDENTAL DEPOSIT

6.1 Introduction

The New Occidental deposit, like many Cobar deposits, contains a complex pattern of primary oxide, native element and sulfide mineral assemblages (Table 7). Constraints on the relative timing of the various ore mineral assemblages are provided by the paragenetic sequence of quartz vein stages and alteration assemblages in the New Occidental deposit (Section 4 and Section 5 respectively), allowing the metallogenesis of Cobar deposits to be addressed. The focussing question is:

What is the timing and metal association of gold relative to hydrothermal alteration and vein development in the New Occidental deposit? Previous paragenetic models for the major ore deposits in the Cobar Goldfield provide contrasting interpretations of both the timing and mineral association of gold mineralisation in the various deposits. For example, gold mineralisation has been interpreted to be late in the paragenetic sequence of the Peak (Hinman, 1992; Jiang, 1996), Chesney (Jiang, 1996) and McKinnons deposits (Forster and Seccombe, 1999) but relatively early in that of the New Occidental and New Cobar deposits (Stegman and Pocock, 1996; Sullivan, 1947; Mulholland and Rayner, 1961). Gold mineralisation is often associated with base metal mineralisation but many base metal deposits are relatively gold-poor and base metal mineralisation in the gold-rich deposits is not consistently gold-mineralised. Gold may also be associated with magnetite and/or bismuth ore minerals (Mulholland and Rayner, 1961; Glen, 1985; Stegman & Pocock, 1996; Lawrie & Hinman, 1998). The variety of gold associations in Cobar's gold deposits suggest either multiple stages of gold mineralisation and/or remobilisation of gold during subsequent stages of mineralisation. For example, Hinman (1992) identified at least two separate stages of gold mineralisation in the Peak deposit with a component of earlier-formed gold remobilised during the second stage. The timing and nature of gold mineralisation in Cobar deposits has not been adequately constrained, and rather, has often been assumed to the same as that of co-existing mineral phases.

Consequently, the purpose of this part of the study is to:

1. Establish a paragenetic sequence of ore mineral assemblages in relation to the quartz vein and alteration stages in the New Occidental deposit
2. Document the three-dimensional distribution of the different ore mineral assemblages
3. Determine the timing of gold mineralisation in the New Occidental deposit
4. Assess the metallogenesis of Cobar deposits in light of paragenetic sequence developed for mineralisation and alteration in the New Occidental deposit.

6.2 Previous Ore Mineral Studies of Cobar Deposits

6.2.1 Ore Mineral Assemblages

A synthesis of ore deposit studies of Cobar deposits (Table 22) shows two dominant mineralisation-types are present:

1. Early-stage **siliceous mineralisation:** associated with abundant quartz veins, Fe-chlorite and comprising either:
   - ❖ Gold-rich: (chalcopyrite - gold - pyrrhotite - pyrite - magnetite with subordinate galena - sphalerite - arsenopyrite - bismuth minerals); or
   - ❖ Gold-poor: (chalcopyrite - pyrite - arsenopyrite - marcasite)
2. Late-stage **massive sulfide mineralisation:** typically overprinting the bulk of quartz veins in the deposits and comprising chalcopyrite - cubanite - pyrrhotite - magnetite - pyrite - galena - sphalerite - marcasite - Mg-chlorite - calcite.

Thompson (1953) argued varying proportions of the two types in an individual deposit explains differences in mineralisation styles between deposits with, for example, the New Occidental deposit comprised predominantly of siliceous mineralisation.

Table 22: Ore deposit studies of Cobar deposits.

Deposit:	Studies:
Cobar deposits	Andrews (1913); Sullivan (1947); Thompson (1953); Robertson, 1974; Gilligan (1974); Brooke (1975); Glen (1987b); Stegman & Pocock (1996); Lawrie & Hinman (1998)
CSA	Brill (1988a); Scott & Phillips (1990); Shi & Reed (1998)
Peak	Hinman (1992); Jiang (1996); Stegman & Pocock (1996)
Chesney	Jiang (1996)
New Cobar	Stegman & Pocock (1996)
New Occidental	Stegman & Pocock (1996)
Elura	de Roo (1989b); Sun & Seccombe (2000)
McKinnons	Forster (1998); Forster and Seccombe (1999)
Perseverance	Priestly (2000); Reynolds (1999b, 2000b)

Stegman & Pocock (1996) presented a generalised interpretation of the paragenetic sequence of mineralisation in the New Occidental and New Cobar deposits, recognising the following stages, from oldest to youngest:

1. Magnetite
2. Native bismuth - bismuthinite - gold, associated with stilpnomelane (possibly after magnetite) or within strongly silicified quartz - chlorite breccias
3. Chalcopyrite - pyrrhotite in the deposit centre grading outwards to pyrite - chalcopyrite
4. Galena - sphalerite - pyrrhotite - pyrite

They argued the first three mineralisation stages formed during the main period of regional cleavage formation whilst the last stage post-dated or formed towards the end of cleavage formation.

Hinman (1992) proposed a 5-stage ore and gangue mineral paragenesis for the nearby Peak deposit (Figure 123), which the last 3 stages containing the bulk of ore minerals:

1. Stage 3: Quartz - sphalerite - galena associated with intense cleavage-parallel silicification of host sediments

2. Stage 4: Quartz - electrum - pyrrhotite - chalcopyrite with minor sphalerite - galena, associated with chlorite - muscovite wallrock alteration

3. Stage 5: Quartz-absent/replacive black chlorite - minor muscovite with Ag-rich sphalerite - galena - pyrrhotite - pyrite - minor chalcopyrite

Hinman (1992) regarded Stages 3 and 4 to be synchronous with regional cleavage formation and the main phase of deformation at the Peak (Hinman's D_{2-3}) whereas Stage 5 was more closely associated with his D_4. Jiang (1996) subsequently proposed a similar paragenesis for the Peak deposit.

Figure 123: Paragenetic sequence proposed for the Peak deposit (Hinman, 1992).

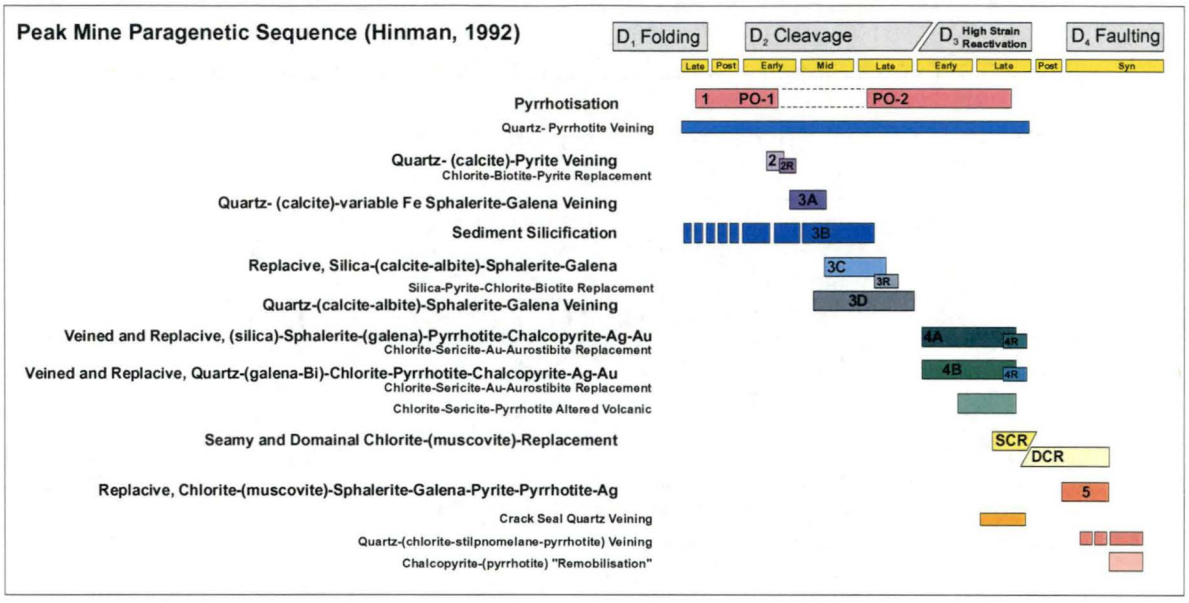

6.2.2 Character of Gold

Gold is spatially associated with a range of ore minerals (Table 23). However, it is unclear whether gold was deposited synchronously with spatially associated minerals, as has been inferred in previous studies. Mineralogical studies undertaken by Reynolds (1998; 1999a, b; 2000a, b) demonstrate a pattern of consistent and significant silver enrichment of gold through the paragenetic sequence of the New Occidental, Peak and Perseverance deposits, whereas Hinman (1992) concluded gold became progressively more silver-poor at the Peak deposit.

6.3 Data Collection

The three-dimensional distribution of ore minerals and ore mineral assemblages was determined from detailed geological logging of 51 diamond drillcore intersections from the deposit. Multi-element assays of drillcore samples (Au by fire assay and for Ag, As, Bi, Cu, Fe, Mn, Pb, Sb and Zn by atomic absorption spectrometry) performed by Amdel Laboratories, Adelaide have been used to confirm ore mineral associations. Representative samples of the ore mineral assemblages identified during this study were provided to Dr Ivan Reynolds (Rio Tinto Research & Technology, Clevedon, United Kingdom) for detailed mineral identification and qualitative and quantitative scanning electron microscopy (SEM). Some of the material used in this chapter, including SEM images and microprobe analyses, was sourced from personal communications with and reports prepared by Dr Reynolds and is duly acknowledged. However, delineation of those

assemblages, mapping of their three-dimensional distribution and interpretations of timing of deposition and relationships to alteration minerals and quartz veins are the work of the author.

Table 23: Gold associations in Cobar deposits.

Association:	Deposit (Study):
Au - bismuth minerals	**New Occidental** (Andrews, 1913; Stegman & Pocock, 1996), **New Cobar** (Sullivan, 1947; Mulholland & Rayner, 1961), **Perseverance** (Reynolds, 2000b)
Au - magnetite	**New Occidental** (Andrews, 1913; Mulholland & Rayner, 1961); **New Cobar** (Sullivan, 1947; Mulholland & Rayner, 1961);
Au (electrum) - chalcopyrite - pyrrhotite (minor Bi)	**New Occidental** (Mulholland & Rayner, 1961); **Peak** (Hinman, 1992; Jiang, 1996); **New Cobar** (Sullivan, 1947; Mulholland & Rayner, 1961); **Chesney** (Jiang, 1996); **Perseverance** (Reynolds, 2000b)
Au (electrum) - sphalerite - galena	**Peak** (Jiang, 1996; Stegman & Pocock, 1996)
Au - pyrite	**McKinnons** (Forster, 1998; Forster and Seccombe, 1999)

6.4 Ore Mineral Assemblages within the New Occidental Deposit

Seven partly overlapping stages of ore mineral deposition have been recognised within the New Occidental deposit during this study:

1. Oxides comprising magnetite - minor scheelite - trace wolframite - calcite
2. Gold - bismuth minerals comprising a sulfur-poor assemblage of extremely fine-grained gold - maldonite (Au_2Bi) - native bismuth - Se-rich ikunolite (Bi_4Se_3-Bi_4S_3 solid solution series) - clausthalite-galena (PbSe-PbS solid solution series) - rare bismuth selenides - minor pyrrhotite - chalcopyrite
3. Bismuthinite (Bi_2S_3) - "newoccidentallite" (Bi_5AuS_4) - minor gold
4. Arsenopyrite
5. Chalcopyrite - pyrrhotite - minor silver-rich gold/electrum - cassiterite
6. Sphalerite - galena - pyrrhotite - calcite
7. Pyrite.

Each stage demonstrates a consistent temporal and spatial relationship with previously identified quartz vein and alteration stages in the deposit, thereby allowing the timing of each ore mineral stage to be related to the structural evolution of the host Great Chesney Fault. Their mineralogy and relation to vein and alteration stages and deformation fabrics are summarised in Table 24 and Figure 125, and their spatial distribution is shown in Figure 126 to Figure 135.

Key features of the New Occidental ore mineral paragenesis are:

1. Temporal progression from an oxide-only ore mineral assemblage, through native metals and S-poor, Se-rich assemblages to sulfide ore minerals, including:

   Magnetite → pyrrhotite → pyrite

Native bismuth + maldonite → bismuthinite + newoccidentallite

Se-ikunolite → S-ikunolite

Clausthalite → galena

2. Progressive shift in the locus of ore mineral and alteration stages from the hanging wall of the New Occidental deposit to the footwall with time, which matches the shift in locus of quartz vein stages across the deposit (Figure 127).

3. Gold in the New Occidental deposit became progressively more silver-rich with time (Figure 124). Decreasing Au fineness of metallic gold through paragenetic sequence corresponds to an increase in whole-rock Ag/Au ratio (Figure 127).

Figure 124: Variations in Au/(Au +Ag) ratios of gold within the New Occidental deposit.

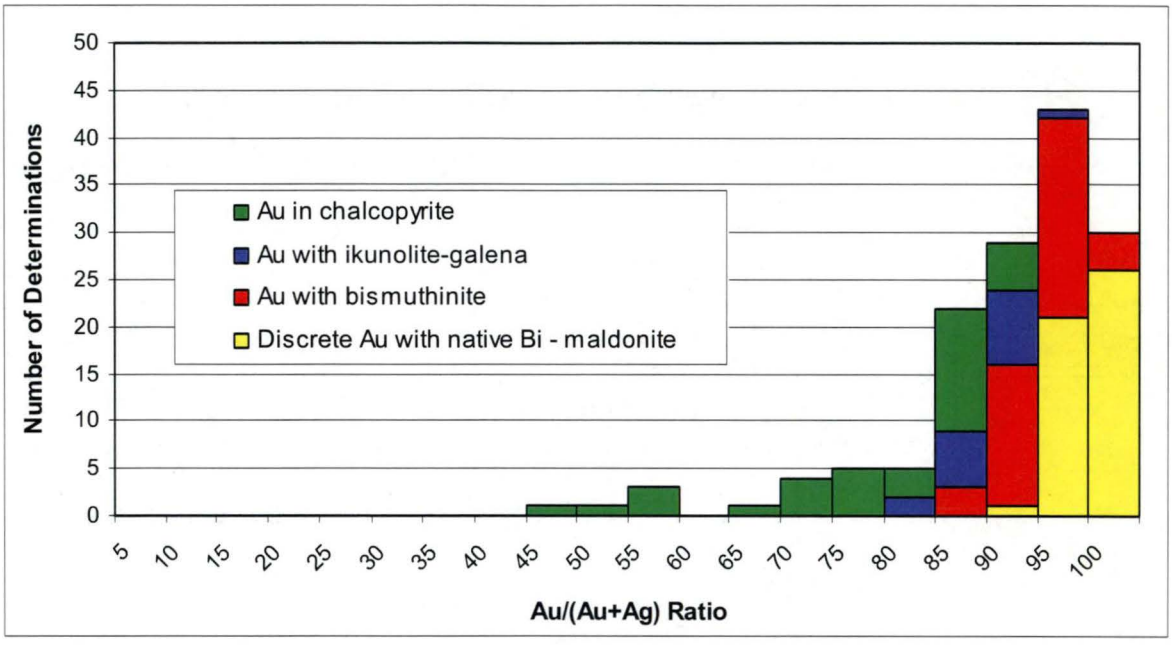

Table 24: Ore mineral assemblages in the New Occidental deposit.

Assemblage	1	2	3	4	5	6	7	
Major ore minerals	Magnetite - scheelite	Gold (Ag-poor) - native bismuth - maldonite - pyrrhotite - Se-ikunolite	Bismuthinite - "newoccidentallite" (Bi_5AuS_4)	Arsenopyrite	Chalcopyrite - pyrrhotite - electrum	Sphalerite - galena - pyrrhotite	Pyrite	Pyrrhotite replacement of syngenetic pyrite
Minor ore minerals	Wolframite	Galena-clausthalite, chalcopyrite	Ag-poor gold		Galena - sphalerite			
Alteration mineralogy	Early-stage Fe-chlorite in wallrock and Fe-chlorite - calcite veins	Early-stage Fe-chlorite in wallrock and veins	Stilpnomelane	Late-stage Mg-Fe chlorite in wallrock and veins	Minor sericite - chlorite	Greenalite - Fe-rich clay - minor calcite	Minor Fe-rich clay	Associated with metamorphic assemblage of muscovite-chlorite
Form	Lenses parallel to S_1 and elongate along L_1[1]	Fine-grained interstitial to quartz, forming elongate lenses parallel to S_1 and L_1[1]	Fine-grained overprinting Stage 2 gold-bismuth	Coarse-grained aggregates disseminated along S_1-parallel shears	Sub-horizontal (perpendicular to S_1) and S_1-parallel splashes forming elongate lenses parallel to S_1 and L_1[1]	Scattered sub-horizontal (perpendicular to S_1) and S_1-parallel veins	Scattered sub-horizontal (perpendicular to S_1) and S_1-parallel veins	Elongate flakes concentrated around zones of syngenetic pyrite
Location	Mainly Main lode hanging wall, with minor remnants in deposit core	Core of Main Lode and locally along the Albion Lode	Mainly the core of the Main Lode where stilpnomelane overprints previous gold-bismuth	Immediate footwall of Main Lode, locally in the hanging wall of the Main Lode and minor zones transecting the northern part of the Main Lode	Mainly Main Lode footwall and, to a lesser extent, in Albion Lode	Mainly the core of Main Lode 500–900 metres from surface with lesser zones in the footwall of the Main Lode coincident with chalcopyrite-pyrrhotite	Preferentially developed outside of the Main Lode, including in the Albion Lode Scattered veins are present within the Main Lode.	Broad stratabound zones coincident with major shear zones, usually spatially separate from mineralised zones
Relationship to Quartz Vein Stage	Stage 1 quartz veins	Stage 2 quartz, particularly colloform-banded cryptocrystalline quartz	Stage 3 quartz veins	Stage 4 quartz veins	Overprints Stage 1–4 quartz veins and cross-cut by Stage 5 quartz veins	Overprints Stage 1–4 quartz veins and cross-cut by Stage 5 quartz veins	Overprints Stage 1–4 quartz veins, and possibly Stage 5 quartz veins	Un-related to quartz veins
Relationship to Deformation Fabrics	Strongly deformed and boudinaged along S_1 in the direction of L_1[1]	Moderately deformed and boudinaged along S_1 in the direction of L_1[1]	Moderately deformed and boudinaged along S_1 in the direction of L_1[1]	Weakly-moderately deformed. Arsenopyrite grains are commonly fractured Preferentially located in zones of late-stage cleavage-parallel shearing.	Weakly deformed Located in zones of late-stage shearing and brecciation, forming in sub-horizontal extension fractures and in sub-horizontal necks of boudinaged cleavage-parallel veins	Largely undeformed Located in unfolded sub-horizontal extension fractures and in cleavage-parallel veins	Largely undeformed Located in sub-horizontal extension fractures and in cleavage-parallel veins	Developed in zones of strong cleavage development Pyrrhotite grains developed along S_1 cleavage and are elongate parallel to L_1[1]

Figure 125: New Occidental deposit paragenetic sequence.

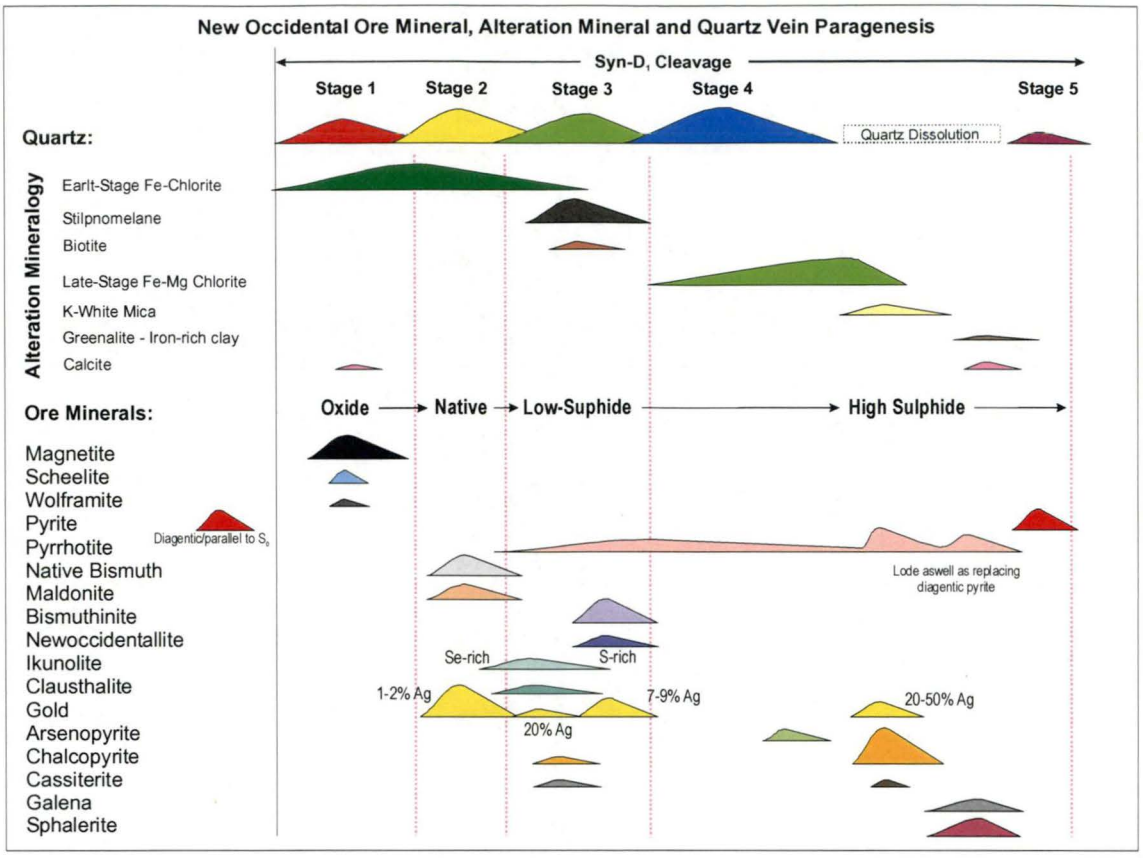

Figure 126: Schematic block model of ore mineral assemblages in the New Occidental deposit.

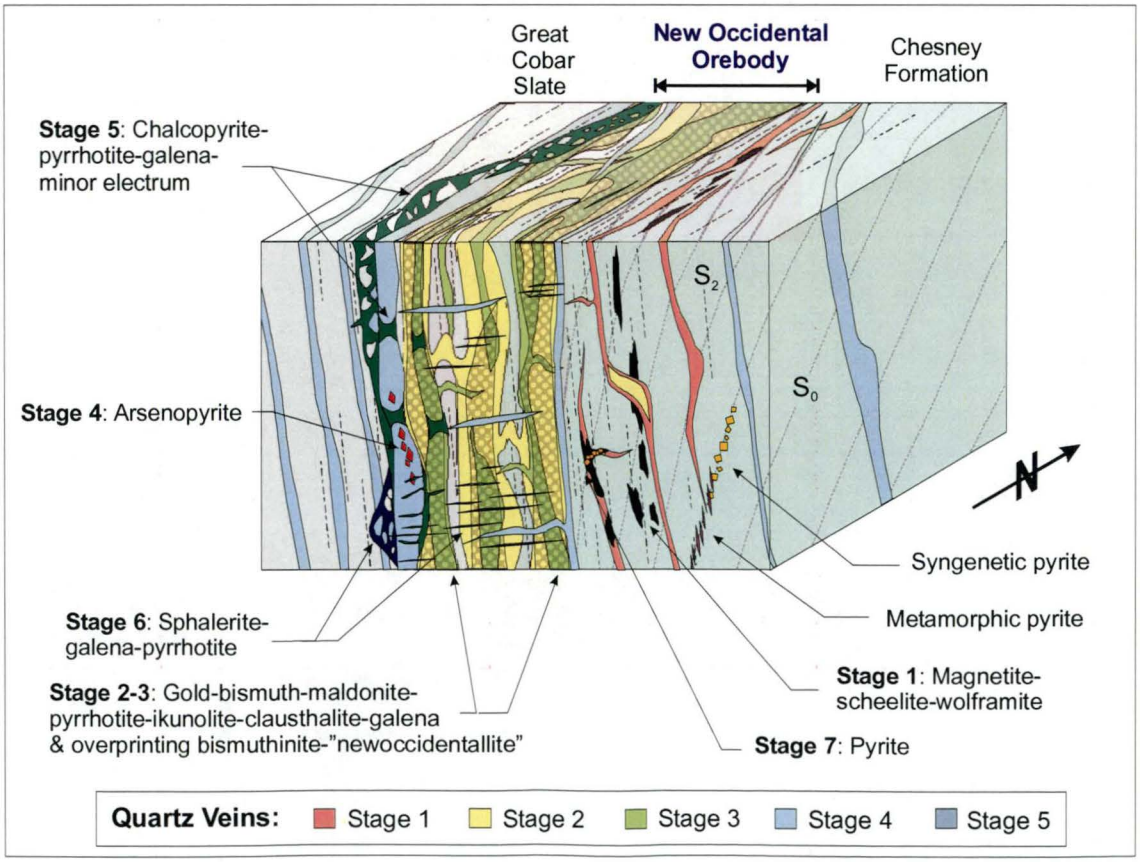

Figure 127: Spatial distribution of mineralisation stages in the New Occidental deposit.

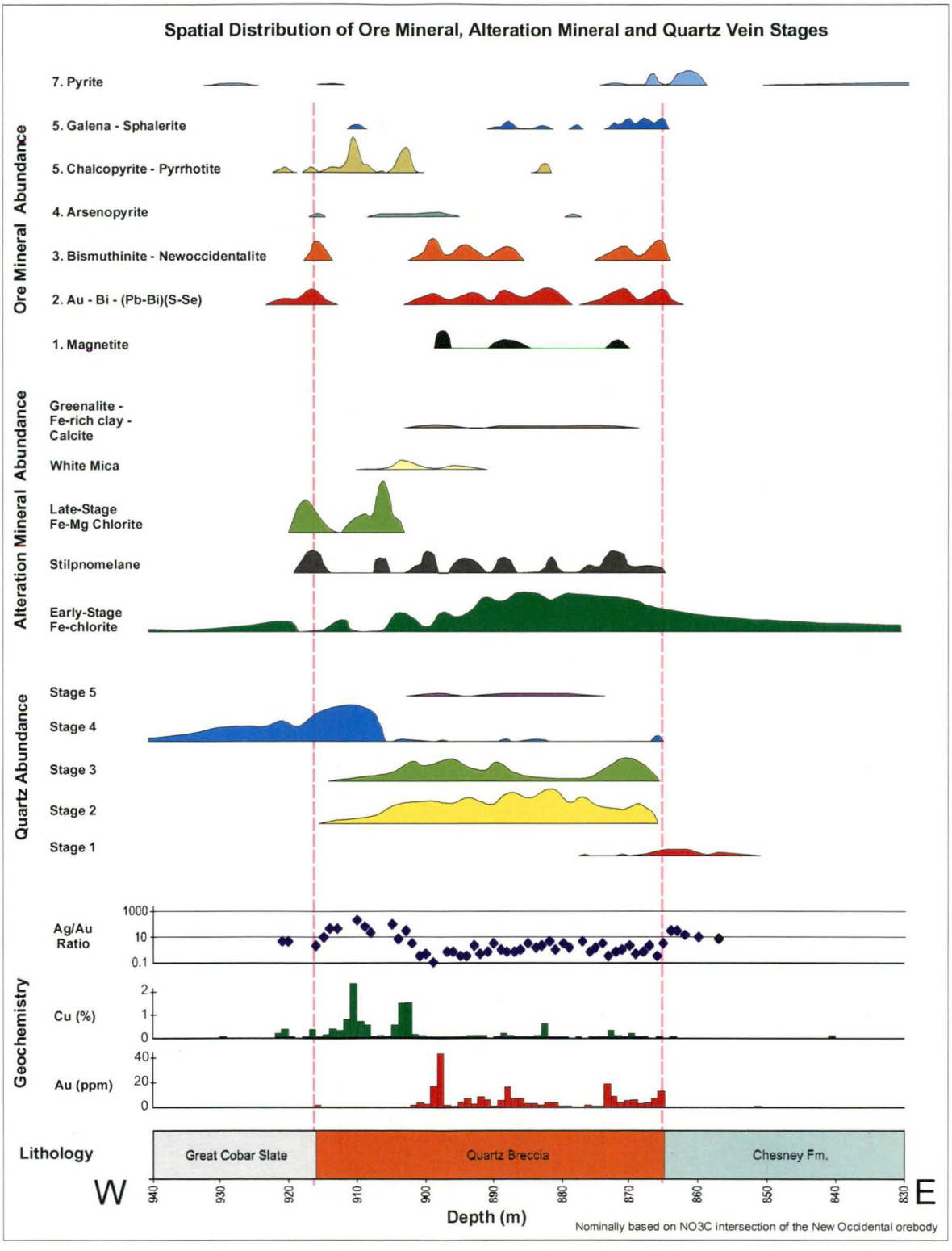

Figure 128: Magnetite distribution in the New Occidental deposit.

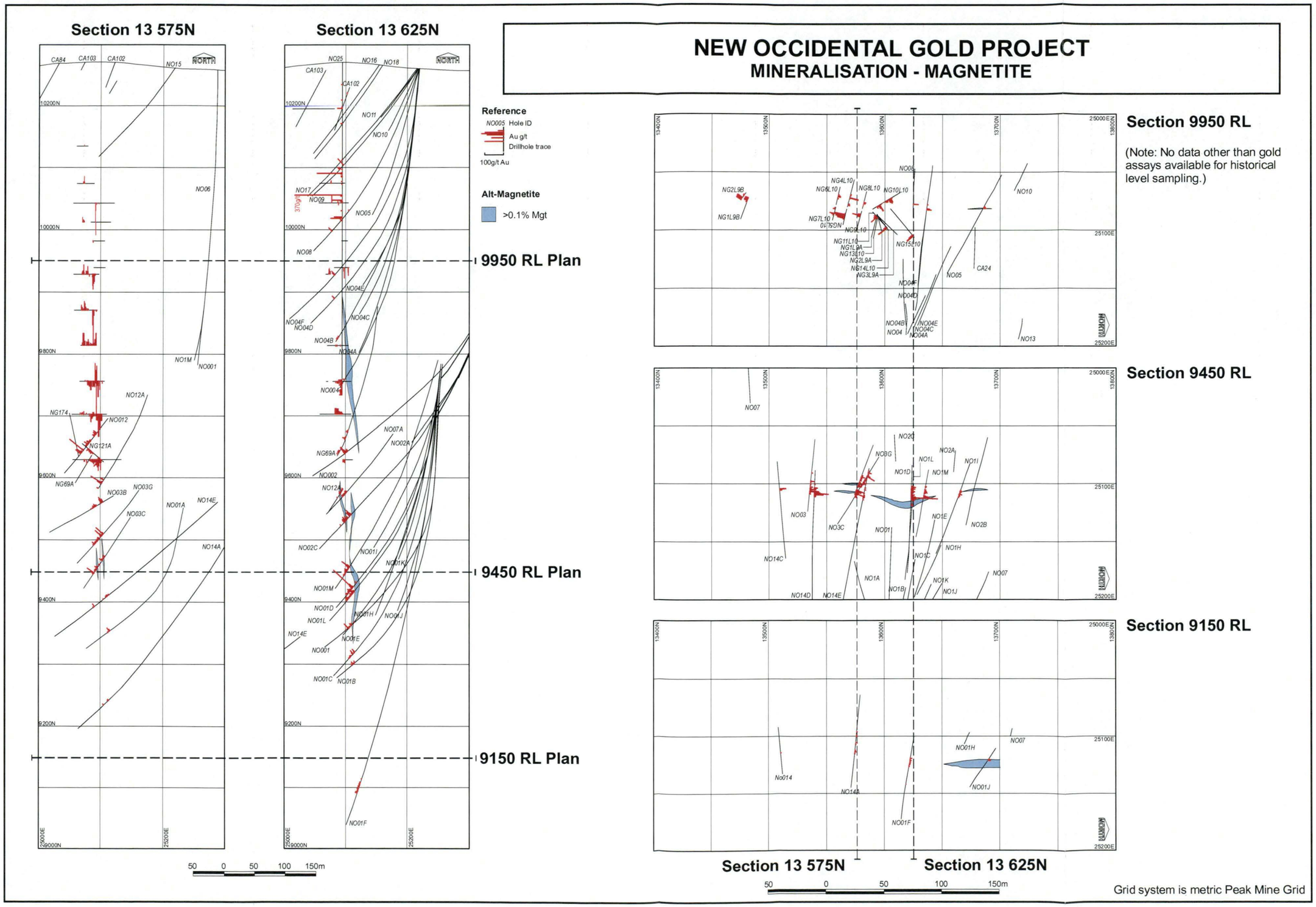

Figure 129: Bismuth distribution in the New Occidental deposit.

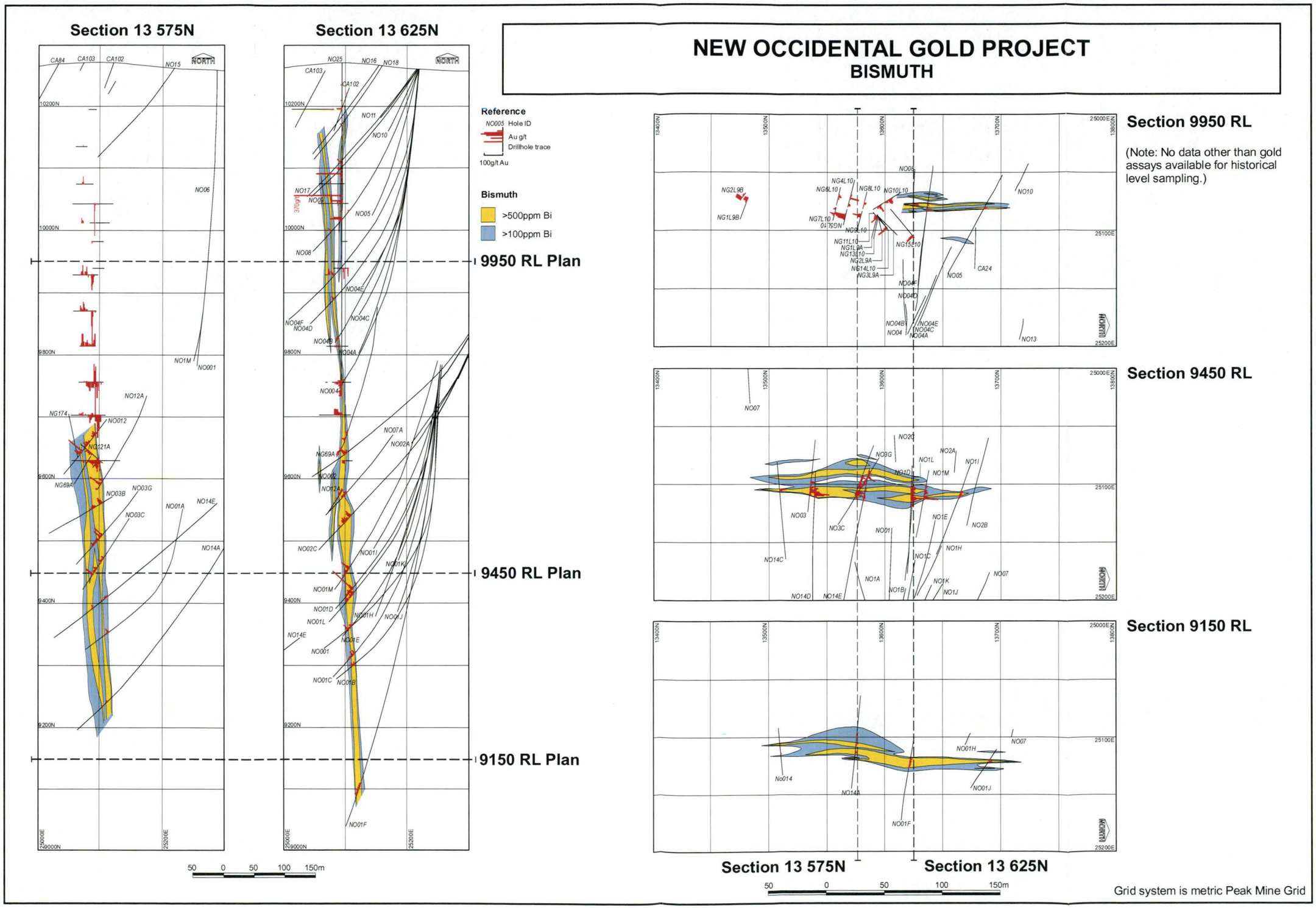

Figure 130: Pyrrhotite distribution in the New Occidental deposit.

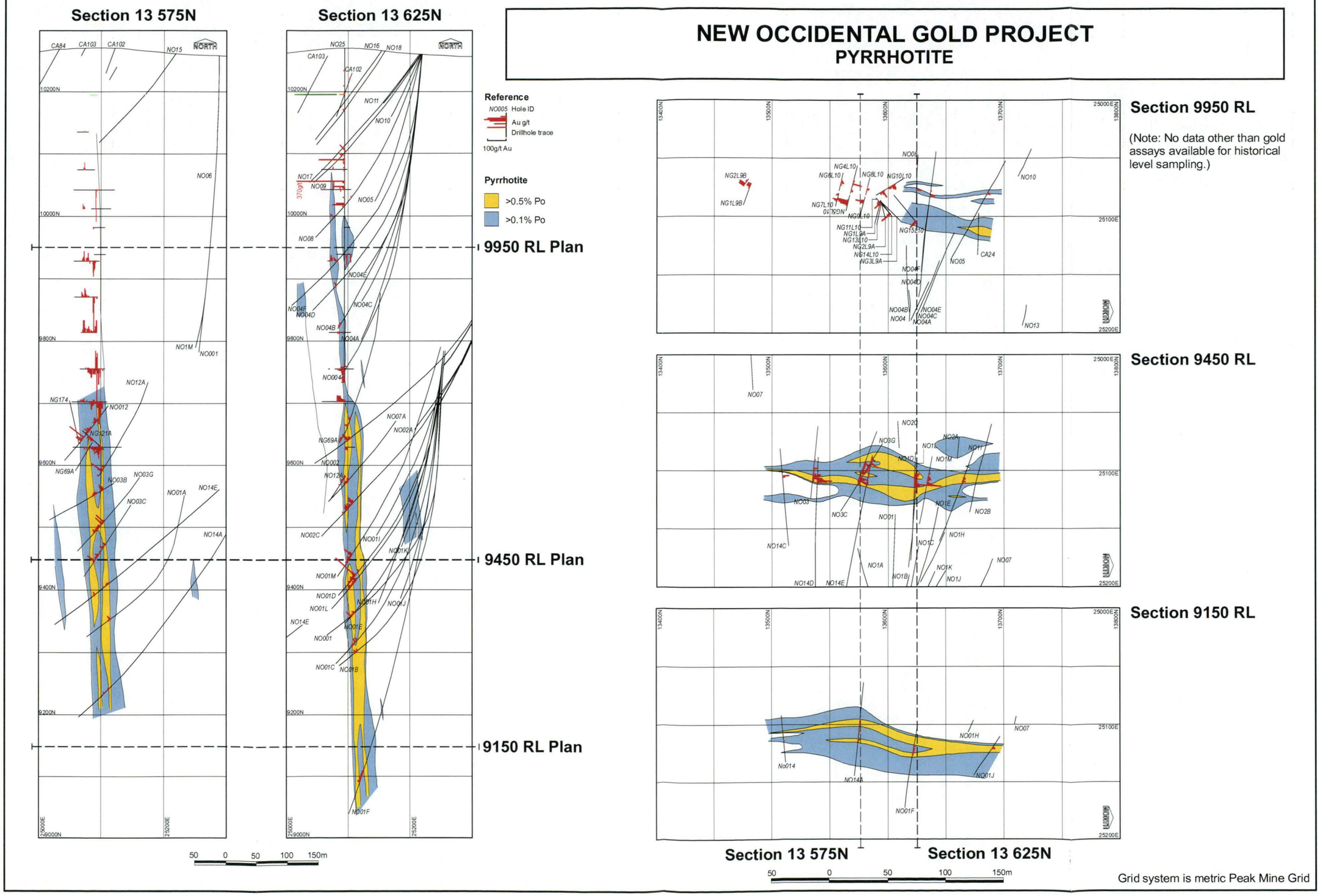

Figure 131: Arsenic distribution in the New Occidental deposit.

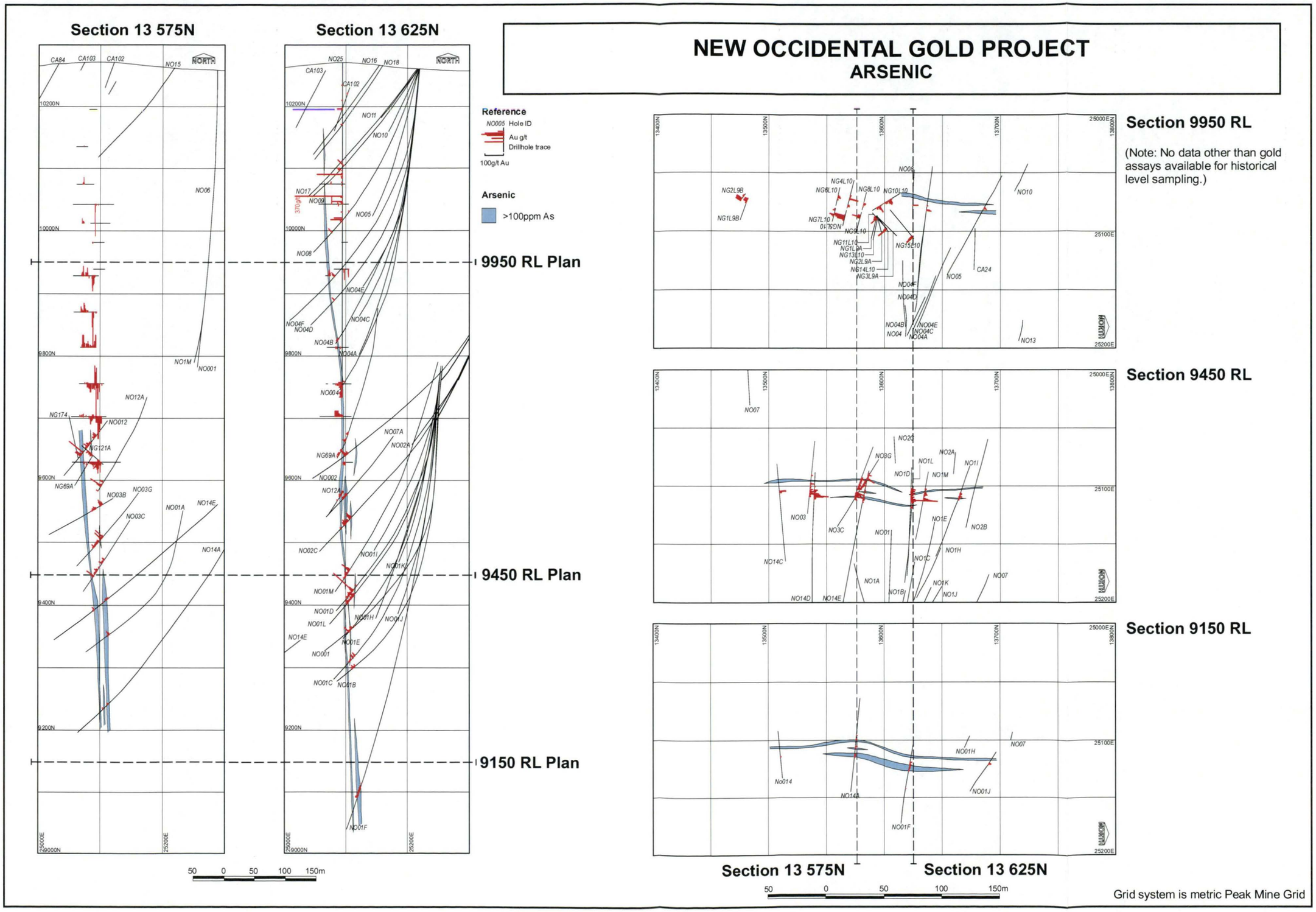

Figure 132: Copper distribution in the New Occidental deposit.

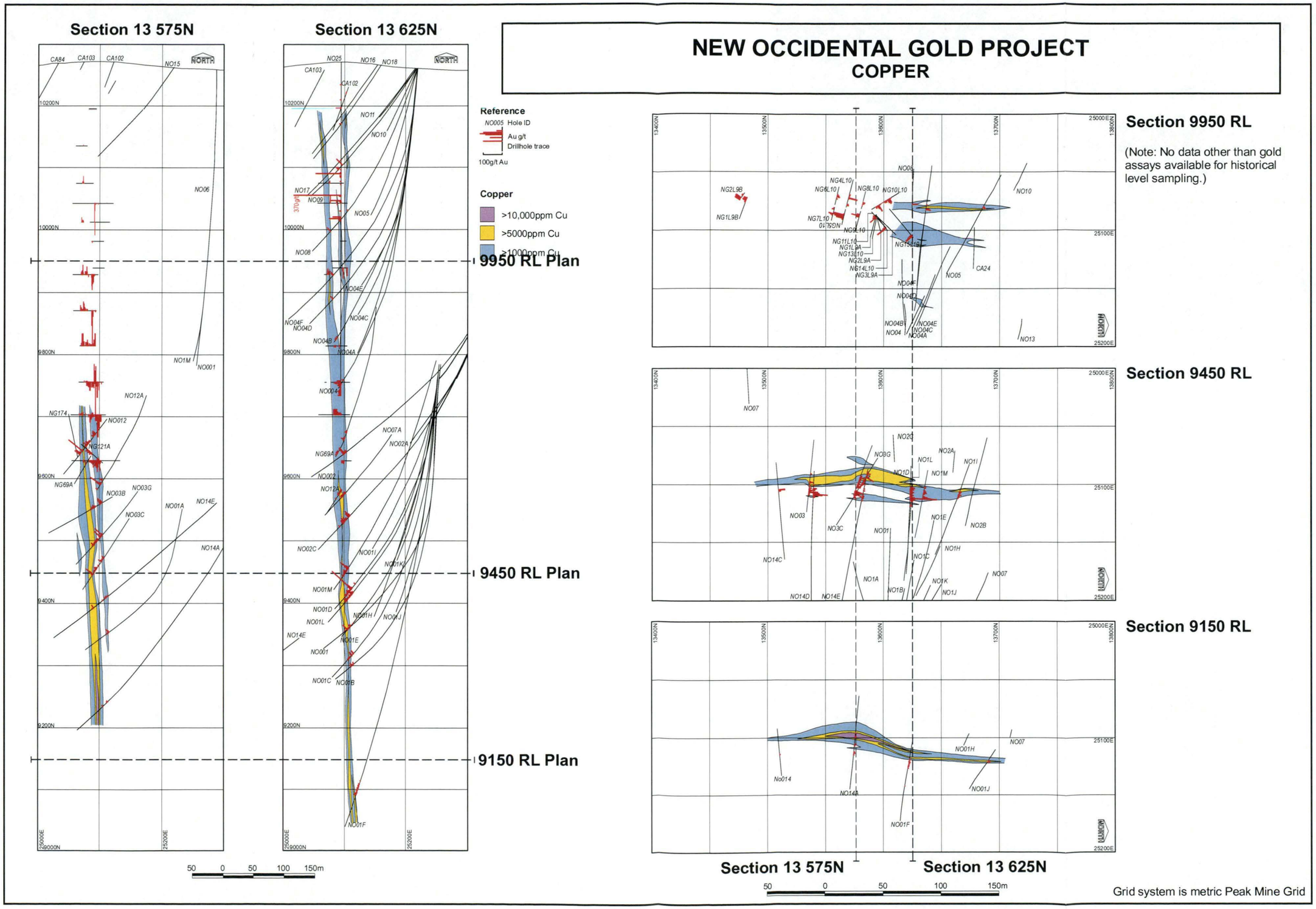

Figure 133: Lead distribution in the New Occidental deposit.

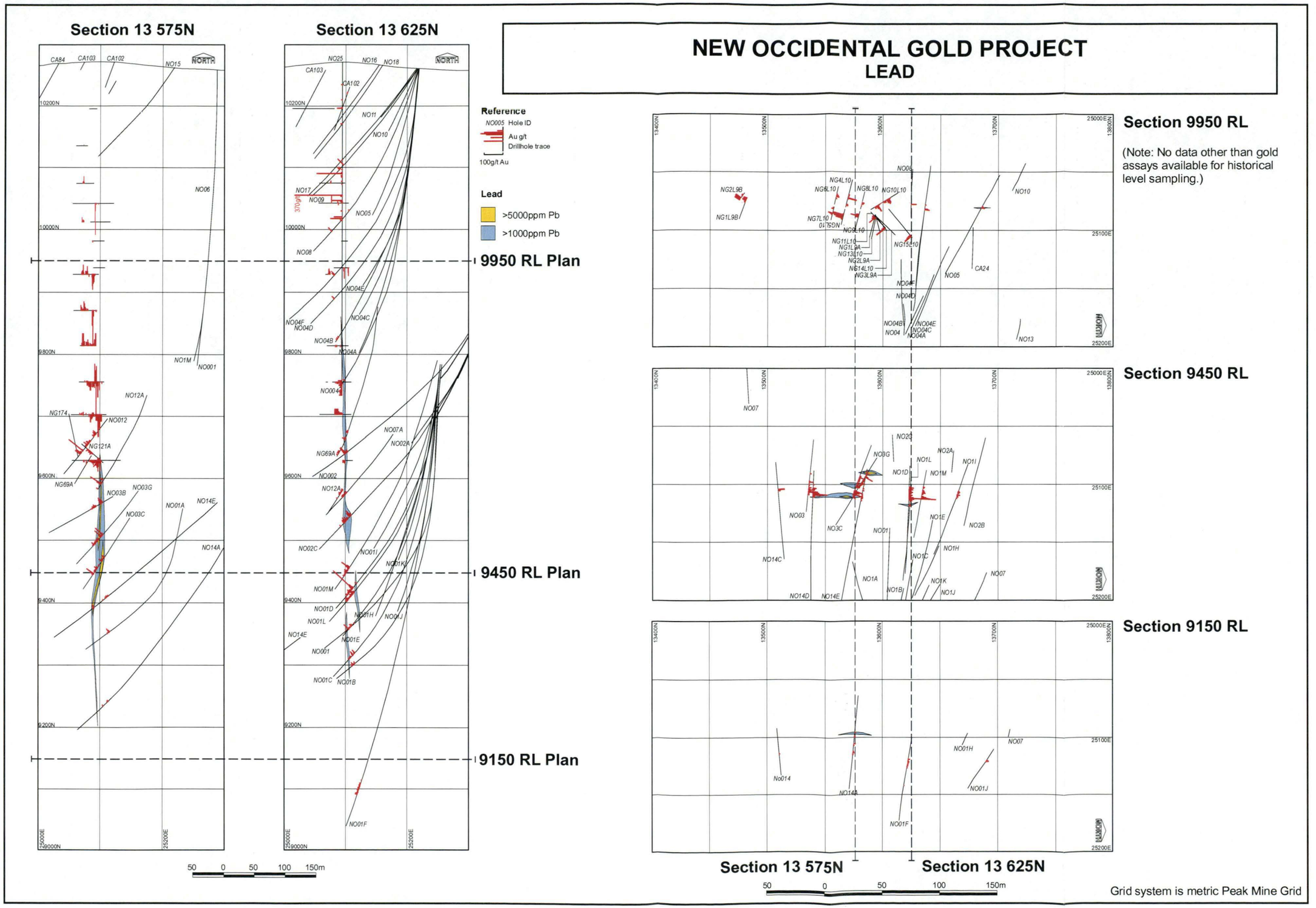

Figure 134: Zinc distribution in the New Occidental deposit.

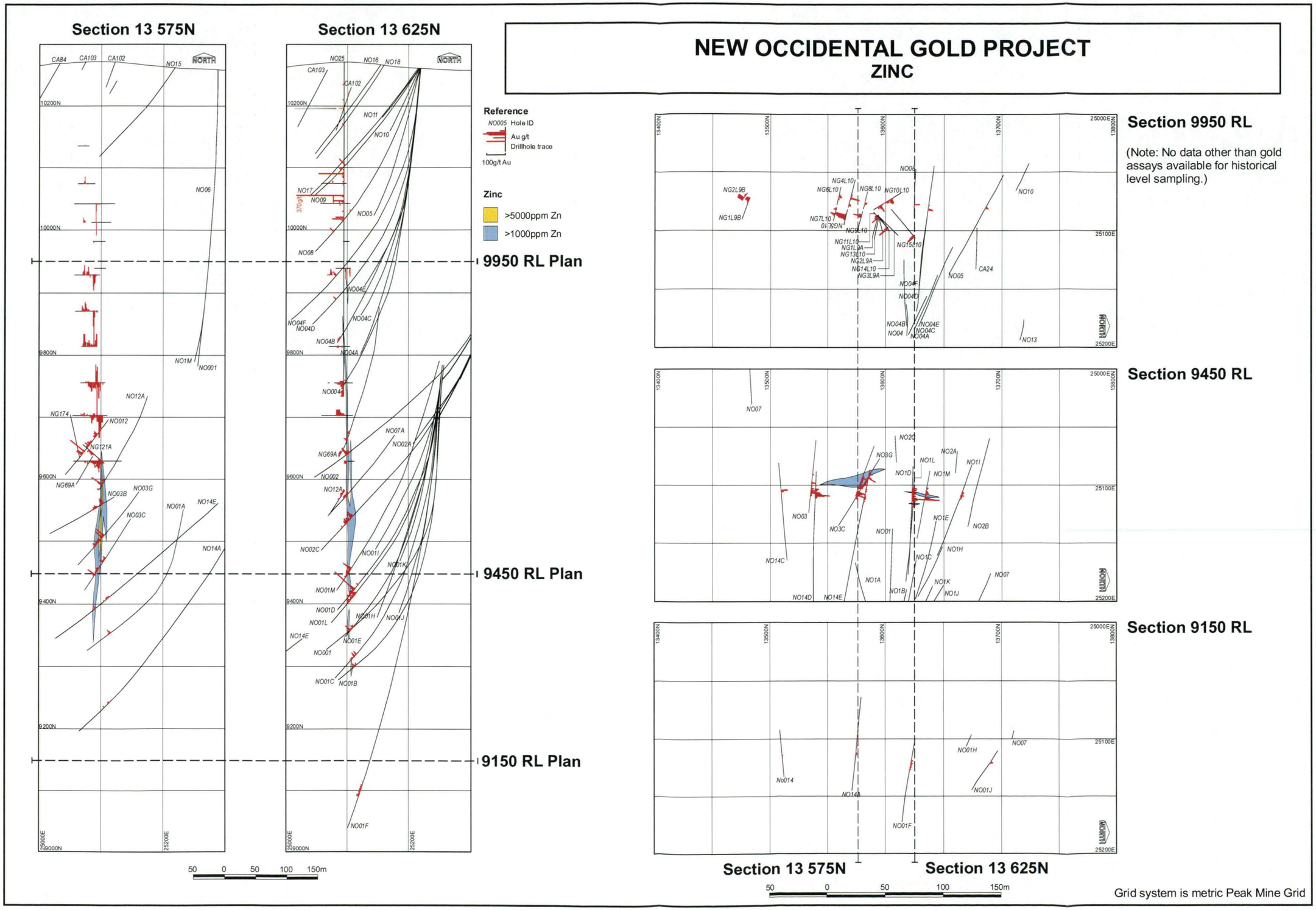

Figure 135: Pyrite distribution in the New Occidental deposit.

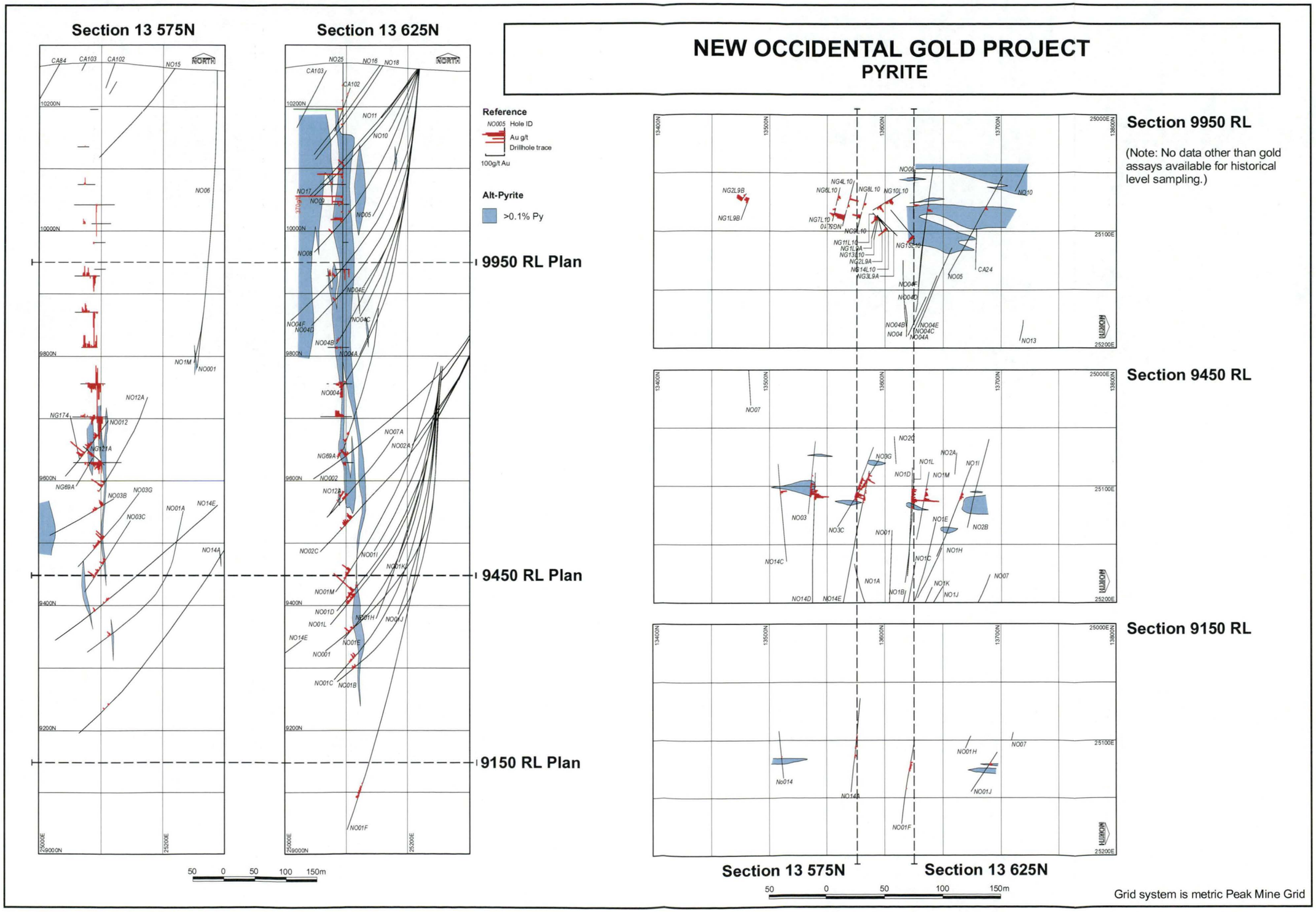

6.4.1 Stratiform Pyrite

Bedding-parallel layers of probable syngenetic pyrite are locally present in finer grained siltstone and mudstone beds within the Chesney Formation, Great Cobar Slate and CSA Siltstone. Pyrite is typically coarse grained (1–5 mm) and euhedral (Figure 136).

Figure 136: Stratiform pyrite mineralisation.

Thinly interbedded siltstone and sandstone from the Chesney Formation in the Peak area showing bedding-parallel pyrite and cross-cutting cleavage-parallel pyrrhotite.

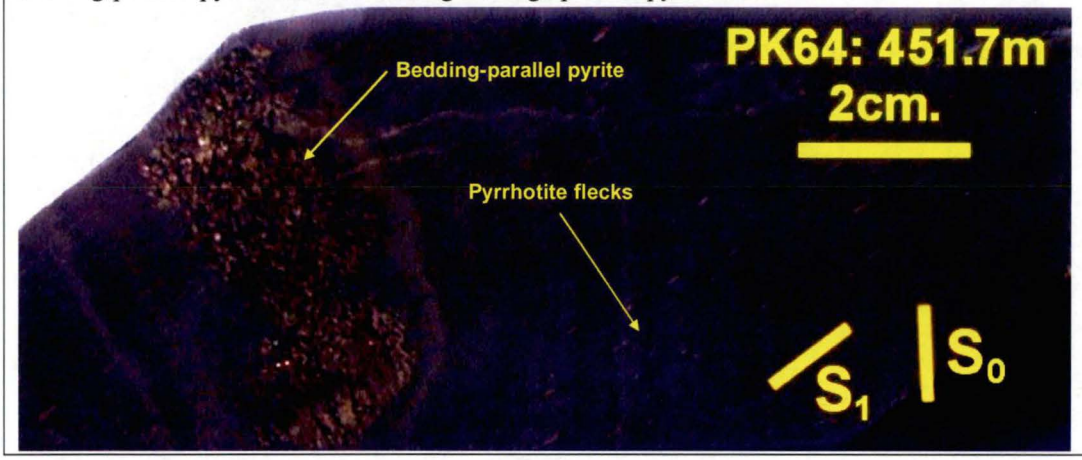

6.4.2 Magnetite - Scheelite

The earliest formed metalliferous assemblage recognised in the New Occidental deposit comprises:

Magnetite - scheelite - minor wolframite

Magnetite occurs largely as stringers and veinlets of discrete crystals 1–5mm in diameter. Scanning electron microscopy (Reynolds, 1999a) revealed individual magnetite crystals contain numerous <20μm inclusions of scheelite and rarer, but slightly larger, inclusions of wolframite (Figure 137a, b).

The magnetite assemblage is mainly developed in the hanging wall of the New Occidental deposit where it is intimately associated with Stage 1 quartz veins (Figure 128). The assemblage is commonly best developed in areas of more abundant Stage 1 quartz veins. Minor remnants of the assemblage are locally preserved in colloform Stage 1 quartz veins in the core of the deposit.

In detail, a complex relationship exists between magnetite and Stage 1 quartz veins. Not all Stage 1 quartz veins contain magnetite and some of the thickest sections of Stage 1 quartz veins are devoid of magnetite. Conversely, magnetite occurs in relatively quartz-poor areas in the hanging wall of the New Occidental deposit. Magnetite appears to predate quartz in some Stage 1 veins but elsewhere is intergrown with or cross-cuts Stage 1 quartz. For example, magnetite is present as monominerallic cleavage-parallel stringers cross-cut by Stage 1 quartz veins, as selvedges along vein walls in Stage 1 quartz veins and as fragments in Stage 1 veins upon which cockade and crustiform-banded quartz was deposited (Figure 71m, Figure

137c). Magnetite selvedges are commonly brecciated, or cut by sub-horizontal extensional quartz-chlorite fibre veins (Figure 71k). Elsewhere, magnetite is intergrown with comb and crustiform/colloform-banded quartz (Figure 71g), including as fine grained magnetite crystals developed along saw-toothed growth bands in a Stage 1 quartz veins (Figure 77f).

Individual magnetite crystals are usually fractured and disaggregated and crystal margins are often strongly corroded. Magnetite exhibits varying degrees of replacement by pyrrhotite, pyrite, chalcopyrite, stilpnomelane, chlorite or bismuth minerals. Relations between small inclusions of bismuth minerals (including native bismuth and clausthalite) and the host magnetite (Figure 137a) are not obvious in thin section but there is a clear association of the bismuth minerals with subsequent ore mineral assemblages, suggesting these minerals also replaced magnetite.

Magnetite has mutual overprinting relationships with Fe-chlorite (Figure 137b, d) and magnetite is usually closely spatially associated with Fe-chlorite wallrock alteration. These relationships suggest that magnetite broadly formed synchronously with Fe-chlorite. Magnetite-bearing quartz veins also commonly contain minor amounts of calcite as a late stage infill of the interstices or remnant voids in the veins.

6.4.3 Early-Stage Gold - Bismuth

Detailed electron microscopy of early-stage gold mineralisation in the New Occidental deposit (Reynolds, 1998; 1999a; 2001) identified a diverse suite of very fine-grained sulfur-poor gold-bismuth-lead ore minerals:

Ag-poor gold$_{(760\text{-}990\ fine)}$ - pyrrhotite - native bismuth - maldonite (Au_2Bi)- Se-rich ikunolite ($Bi_4Se_3 - Bi_4S_3$ solid solution series) with minor clausthalite - galena (PbSe – PbS solid solution series), other rare bismuth-lead minerals and trace chalcopyrite

The most common bismuth minerals include native bismuth, maldonite (Au_2Bi), with subordinate ikunolite solid solutions [$Bi_4(Se,S)_3$] and members of the galena-clausthalite solid solution series (PbS – PbSe) (Reynolds, 1998; 1999a). Microbeam analyses of ikunolite and clausthalite indicate that both minerals are relatively Se-rich (Table 25; Appendix 7). Reynolds (1998; 1999a) also tentatively identified other minor Pb-Bi phases conforming to the general formula $(Bi,Pb)_5(S,Se)_6$, and which do not correspond directly to any known minerals but are similar to lillianite ($Pb_3Bi_2S_6$). These phases appear to represent a complex solid solution series between Bi – Pb and Se – S. It is likely trace amounts of Bi-telluride and Te-Se-bearing bismuth minerals occur within the New Occidental ore (Reynolds, 1999a).

Table 25: Microbeam analyses of ikunolite and galena – clausthalite.

	Ikunolite			Galena-clausthalite		
	Minimum	Maximum	Average	Minimum	Maximum	Average
Selenium (wt%)	7.4	17.7	11.4	6.8	22.7	10.9
Sulfur (wt%)	1.8	6.6	4.9	2.2	10.2	8.2
Lead (wt%)				72.9	82.3	79.6
Bismuth (wt%)	81.0	84.8	83.5	0.2	1.6	1.0
Ideal Formula	$Bi(S_{0.4-0.6}Se_{0.4-0.6})$			$(Pb_{0.95-1.00}Bi_{0.00-0.02})(S_{0.2-0.8}Se_{0.2-0.8})$		

Figure 137: Magnetite - scheelite mineralisation.

a) NO7A - 733.6m: False colour, backscattered electron image of magnetite intergrown with chlorite and lesser stilpnomelane and containing numerous wolframite inclusions and a larger aggregate of scheelite.

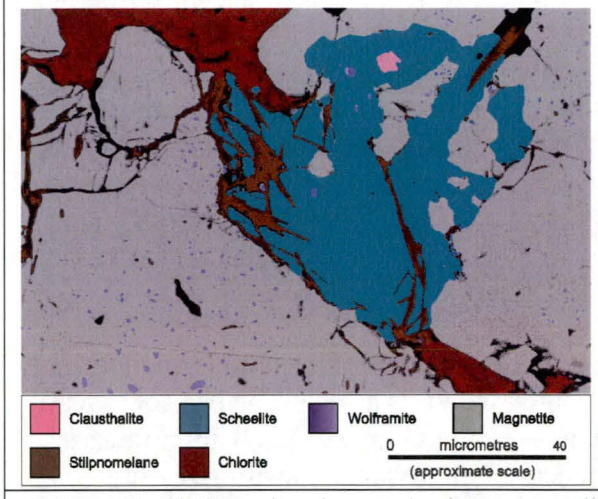

b) NO7A - 736.4m: False colour backscattered electron image of fractured and corroded grains of relict magnetite partially replaced by pyrrhotite. Abundant small scheelite inclusions are present within the magnetite.

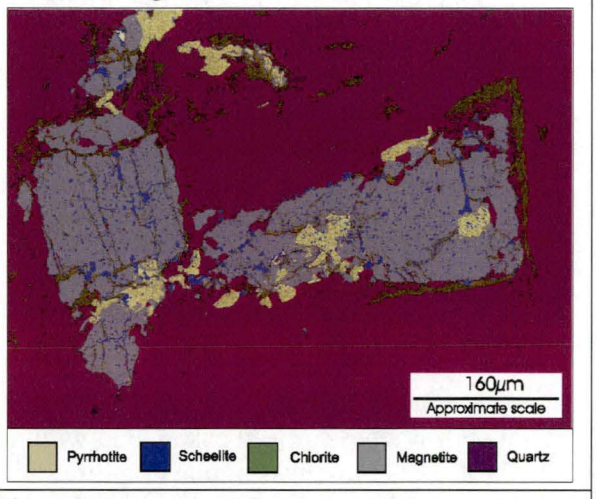

c) Magnetite (dark-grey) and quartz in cleavage-parallel Stage 1 quartz veins. Note some veins comprise only magnetite (left). Chalcopyrite - pyrrhotite has replaced some magnetite.

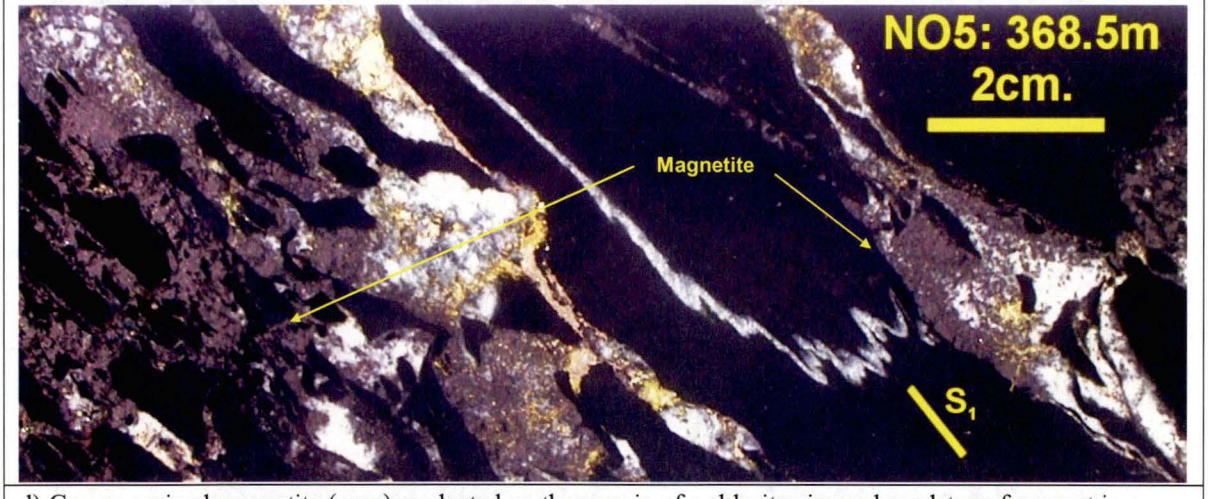

d) Coarse-grained magnetite (grey) nucleated on the margin of a chlorite-rimmed sandstone fragment in a Stage 1 quartz vein. Finer-grained magnetite is disseminated through the sandstone (reflected PPL).

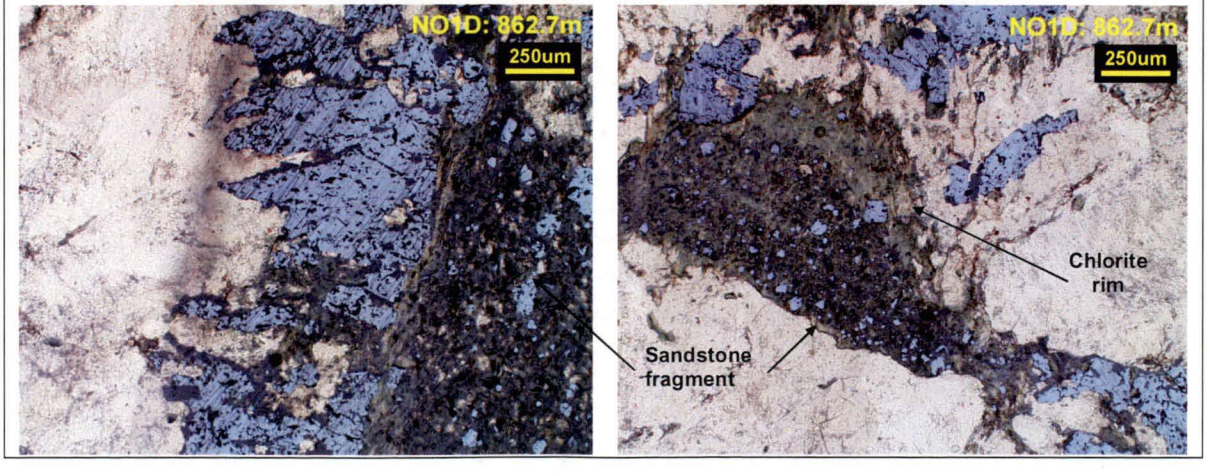

The gold-bismuth minerals are generally extremely fine grained (<5μm), although they form complex intergrowths that are slightly more coarse-grained (<25–100μm) (Figure 138a–e). Some coarser-grained (100–1000μm) bismuth-gold intergrowths are present in the Albion Lode. Grain boundary relationships between the gold-bismuth minerals are relatively simple, indicating a degree of recrystallisation. Typically, gold, native bismuth and maldonite form complex intergrowths in the cores of the gold-bismuth mineral aggregates. Occasionally, gold and native bismuth intergrowths exhibit myrmekitic textures (Figure 138a). Pyrrhotite, ikunolite and galena-clausthalite tend to rim or cluster around the margins of gold, native bismuth and maldonite grains, suggesting that they have formed at the expense of these minerals (Figure 138b–c). Galena-clausthalite in particular commonly contains abundant native bismuth, which exhibit ex-solution like textures with the host galena (Figure 138d–e). Some gold is also intergrown with the pyrrhotite, ikunolite and galena-clausthalite.

Electron microbeam analyses of gold grains associated with the various bismuth minerals (Appendix 6) indicate gold associated with this assemblage has consistently high fineness. Gold associated with native bismuth has an extremely high fineness (900–990 fineness and averaging 960 fineness); gold associated with ikunolite typically has a slightly lower fineness (840–900 fineness and averaging 860 fineness) whilst gold associated with galena-clausthalite tends to have an even lower fineness (760–890 fineness and average 820 fineness) (Reynolds; 1999a).

The gold-bismuth association is confirmed at both the deposit and microscopic scale. The distribution of bismuth determined from drillhole Bi assays strongly correlates with the distribution of high-grade gold in the New Occidental deposit (Figure 129). Similarly, correlation coefficients calculated from drillcore assays (Section 7) reveal gold is only strongly correlated with Bi. Detailed electron microscopy also revealed a consistent spatial association of bismuth minerals with gold. Gold is usually intimately intergrown with bismuth minerals, or, when gold is present as monominerallic grains, bismuth minerals are typically in close proximity (Reynolds, 1999a). However, the relative abundance of bismuth minerals provides only a semi-quantitative guide to gold abundance.

The gold-bismuth assemblage is developed throughout the centre of the deposit, occurring within zones of colloform-banded Stage 2 crystalline and cryptocrystalline quartz. It is best developed in zones of strongly colloform-banded quartz. In detail, mineralisation is interstitial to quartz grains (Reynolds, 1998; 1999a). It is notably absent from the more coarsely crystalline Stage 3 and 4 quartz veins. Gold-bismuth is also developed along fractures and grain boundaries within earlier-formed magnetite and locally replaced magnetite. The presence of fine-grained scheelite inclusions in pyrrhotite associated with gold-bismuth suggests some pyrrhotite was formed by replacement of magnetite during this stage of mineralisation (Figure 138f). These overprinting relations indicate this stage of mineralisation post-dates the magnetite-scheelite mineralisation, and formed concurrently with the Stage 2 quartz veins.

Gold-bismuth mineralisation is also spatially associated with early stage Fe-chlorite alteration. At the deposit scale the distribution of gold-bismuth mineralisation in the New Occidental deposit matches that of Fe-chlorite (Figure 127), and microscopically, gold-bismuth is intergrown with Fe-chlorite in Stage 2 quartz veins, (Figure 138b, d–f).

Figure 138: False colour, backscattered electron images and photomicrographs of polished sections of gold - bismuth mineralisation.

a) NO25 - 179.8m: Eutectic-like intergrowth between gold and native bismuth rimmed by bismuthinite within a pyrite.

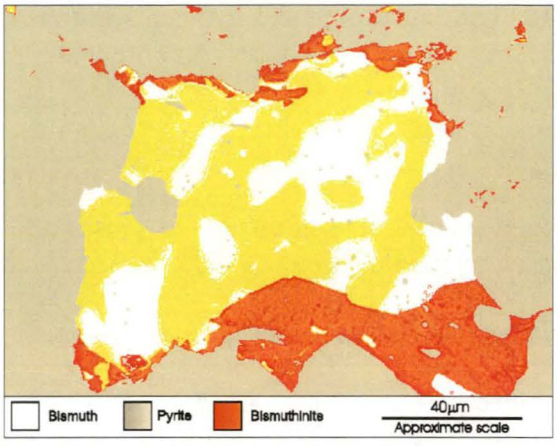

b) NO14D - 992.7m: Intergrowths of gold, native bismuth, galena, ikunolite, pyrrhotite, maldonite and chlorite along grain boundaries in quartz.

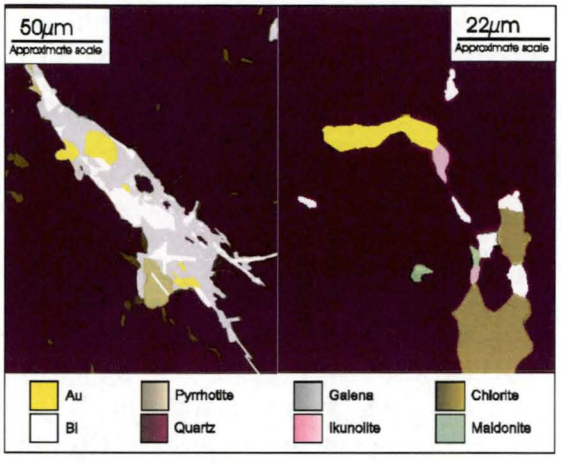

c) NO14D - 992.7m: Intergrowths of maldonite, native bismuth, galena-clausthalite and ikunolite along grain boundaries in quartz.

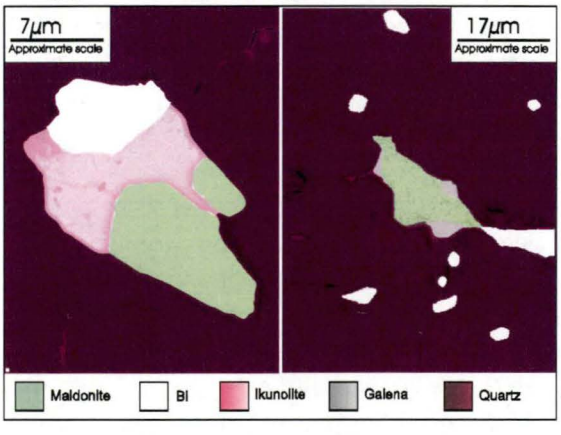

d) NO12A - 743.5m: Intergrowths of native bismuth, pyrrhotite and galena in quartz - Fe-chlorite.

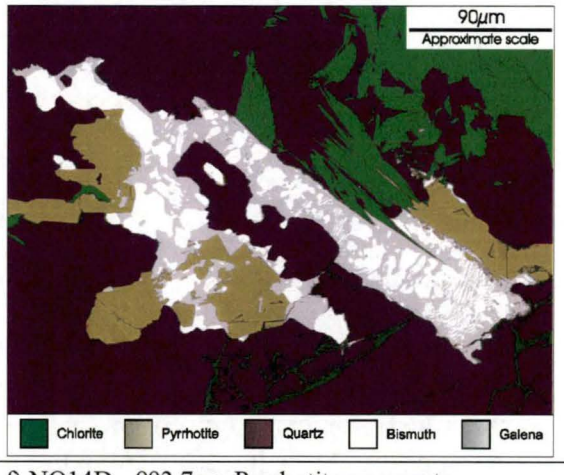

e) NO14D - 993.5m. Fine-grained gold, native bismuth, ikunolite and PbSe present along grain boundaries within quartz-rich aggregates.

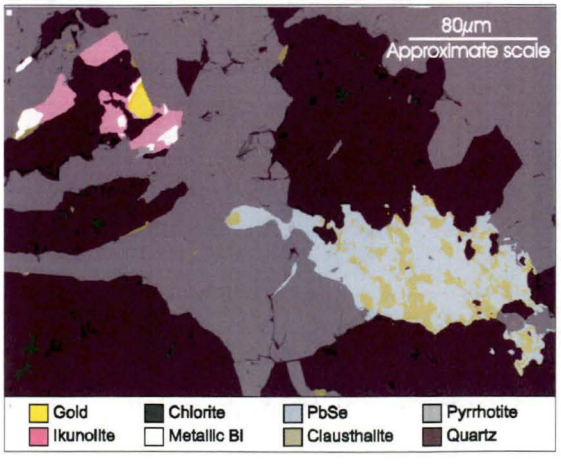

f) NO14D - 992.7m: Pyrrhotite aggregate containing numerous tiny inclusions of scheelite. Small grains of maldonite, native bismuth and ikunolite are developed along grain boundaries.

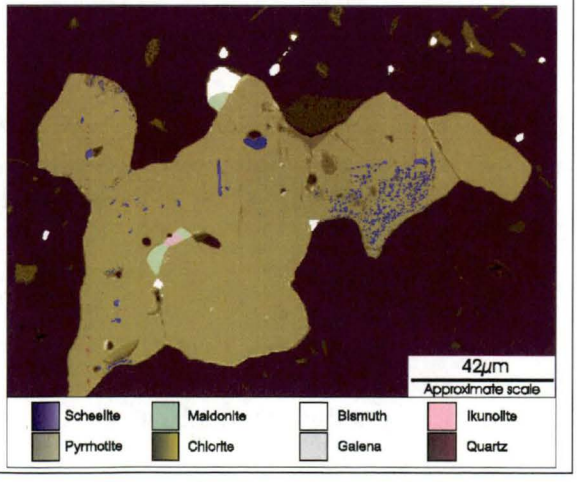

In summary, early gold-bismuth mineralisation is associated with initial cryptocrystalline phases of Stage 2 quartz veins and with Fe-rich chlorite alteration in the core of the deposit. Within this assemblage, mineralisation progressively evolves from predominantly native minerals (gold, maldonite, native bismuth) and Se-rich ikunolite and clausthalite, to a more S-rich assemblage (S-rich ikunolite, galena, chalcopyrite and pyrrhotite). Gold associated with maldonite and native bismuth is extremely high fineness (900–990 fine) whilst gold associated with ikunolite and clausthalite-galena is of a lower fineness (760–900 fine).

6.4.4 Bismuthinite - "Newoccidentallite" - Gold

The New Occidental deposit contains a second stage of fine-grained gold - bismuth sulfide mineralisation consisting of the following assemblage:

Bismuthinite (Bi_2S_3) - "newoccidentallite" (Bi_5AuS_4) - minor gold $_{(820–900\ fine)}$

"Newoccidentallite" is the name herein assigned to a bismuth-gold sulfide with an ideal stoichiometry of Bi_5AuS_4 (Reynolds, 1998; 1999a). Newoccidentallite is relatively fine-grained (<5μm in diameter) and has similar optical properties to bismuthinite, with which it is intimately intergrown (Reynolds, 1999a). Newoccidentallite from the New Occidental deposit has not been able to be characterised sufficiently to allow it to be formally recognised as a new mineral by the International Mineralogical Association (Reynolds pers comm.), although W Paar, Institute of Mineralogy, University Salzburg, Austria has reportedly been able to formally identify the mineral (Paar pers comm.).

Bismuthinite and newoccidentallite are preferentially developed as rims around the margins of pre-existing gold, maldonite, native bismuth, ikunolite and other bismuth mineral particles. Bismuthinite and newoccidentallite have also extensively replaced those earlier-formed minerals, which often remain as corroded remnants in the cores of bismuthinite and newoccidentallite grains (Figure 139a–d). Bismuthinite preferentially replaced gold, maldonite and native bismuth but replaced ikunolite to a much lesser extent (Figure 139a–b). Newoccidentallite preferentially replaced gold, maldonite and to a lesser extent, ikunolite (Figure 139c–d).

Gold associated with the bismuthinite-newoccidentallite is slightly more silver-rich (820–900 fine) than gold associated with the early stage gold-bismuth mineralisation. Some of this gold represents relict early-stage higher-fineness gold associated with precursor native bismuth and maldonite. Some lower-fineness gold is also relict gold similar to that associated with early-stage ikunolite and galena - clausthalite. However, a component of the lower fineness gold also appears to have formed coevally with bismuthinite and newoccidentallite. Reynolds (1999a) documented more silver-rich margins on the remnant gold grains rimmed by bismuthinite. An anomalous concentration of coarse-grained (0.1–2mm) gold mineralisation is present in the Albion Lode. Gold is intergrown with coarse-grained laths of ikunolite and partially rimmed by equally coarse-grained bismuthinite and lesser newoccidentallite. Microbeam analyses of gold grains indicate the gold is 890–930 fine, consistent with the range of gold fineness identified from gold associated with bismuthinite - newoccidentallite mineralisation.

Figure 139: False colour, backscattered electron images of stilpnomelane - bismuthinite - newoccidentallite mineralisation.

a) NO12 - 628.4m: Gold particle intergrown and partly rimmed with bismuthinite. The particle occurs in Stage 2 quartz with stilpnomelane overprint.

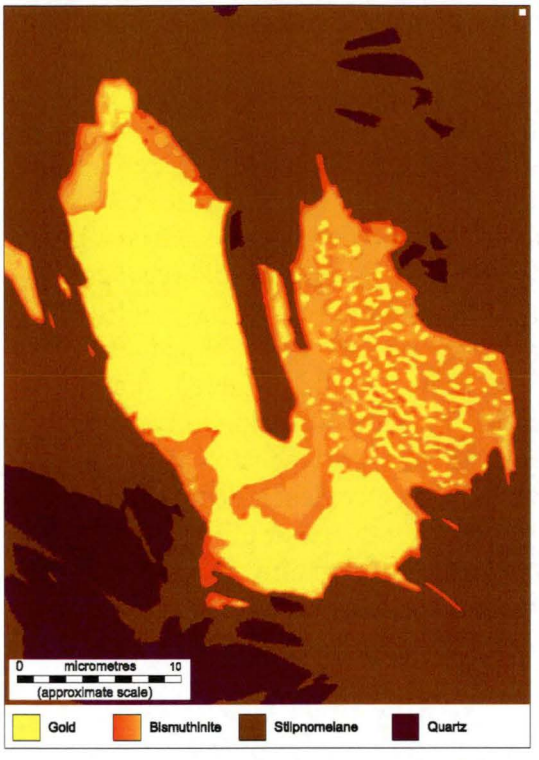

b) NO12 - 670.0m: Discrete particles of maldonite, gold and native bismuth rimmed by bismuthinite in a quartz - chlorite groundmass. The ikunolite particle is not rimmed by bismuthinite.

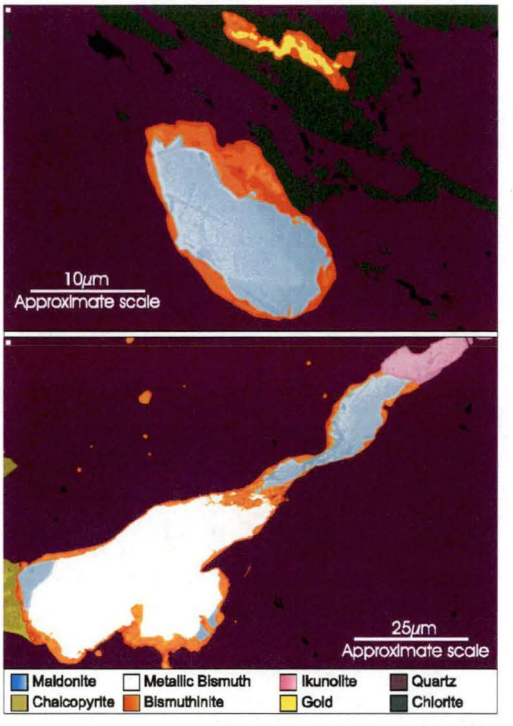

c) NO7A - 733.6m: Complex intergrowth of gold, native bismuth, ikunolite, bismuthinite, Bi_5AuS_4 phase and pyrrhotite within stilpnomelane-quartz.

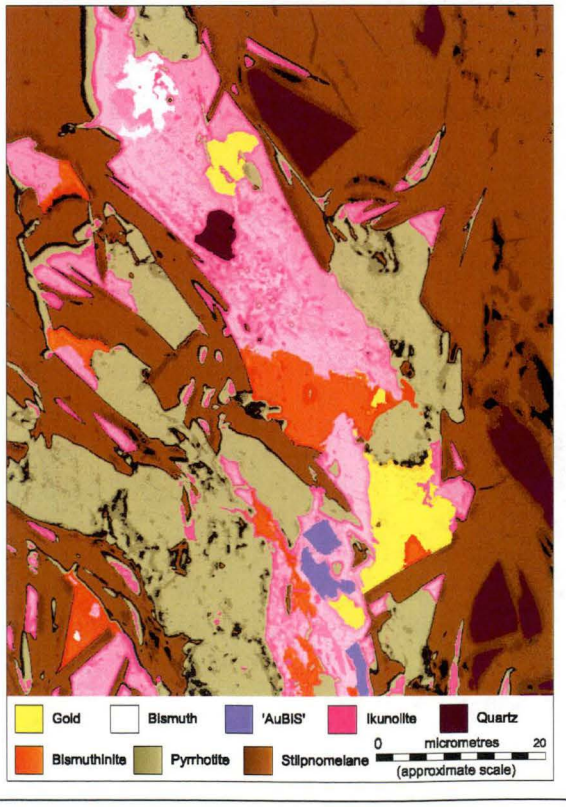

d) NO25 - 223.8m: Complex intergrowths of gold, bismuthinite and ikunolite and Bi_5AuS_4 in quartz.

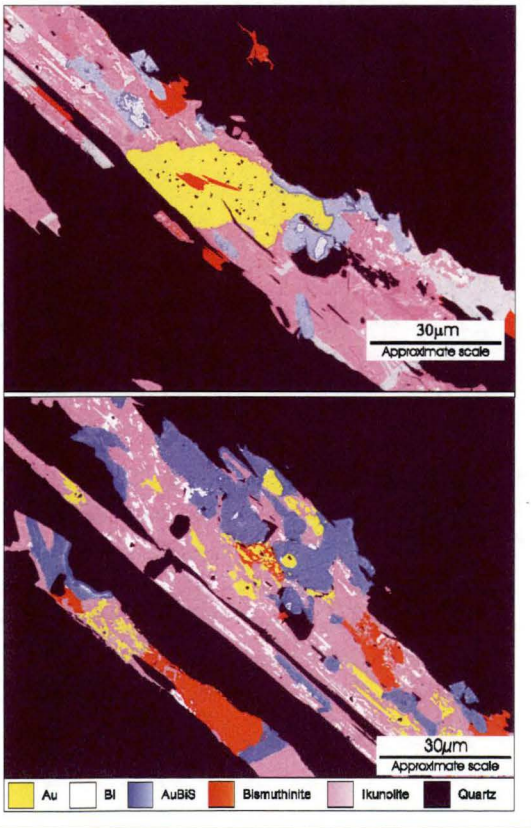

The bismuthinite - newoccidentallite - gold overprint of precursor gold - bismuth has produced mineralogically complex aggregates with a typical grainsize in the range 5–50μm. Electron microscopy has therefore been required to resolve the individual minerals within such grains and therefore determine the extent of this overprint. Reynolds (1998, 1999a) has identified this stage of mineralisation throughout the gold-mineralised sections of the Main Lode and, to a lesser extent, the Albion Lode of the New Occidental deposit.

Bismuthinite - newoccidentallite - gold is ubiquitously associated with stilpnomelane and is usually restricted to zones of strong stilpnomelane alteration (Figure 139a, c). Correlation of bismuthinite-newoccidentallite with stilpnomelane alteration was confirmed by metallurgical studies of the New Occidental ores (data analysed by the author for this study). These data show decreasing cyanide-leach gold recovery correlates with increasing intensity of stilpnomelane alteration. Reynolds (1999a) subsequently noted an increase in the refractory components of the New Occidental ore, specifically, encapsulation of gold and maldonite within insoluble bismuthinite and the development of refractory newoccidentallite with increasing intensity of stilpnomelane alteration. However, whilst bismuthinite - newoccidentallite - gold is consistently associated with stilpnomelane in the New Occidental deposit, the degree to which stilpnomelane is gold-mineralised depends on the tenor of coincident early-stage gold-bismuth; that is, zones of stilpnomelane alteration only contain appreciable gold where the stilpnomelane overprints early-stage gold-bismuth.

6.4.5 Arsenopyrite

Arsenopyrite is a relatively minor but widespread phase in the New Occidental deposit. The average arsenic content of the deposit based on 1-metre drillcore assays is 140 ppm with a maximum assay of 1.57% As. Reynolds (1999a) reports trace amounts of cobaltite (CoAsS) in the New Occidental deposit. However, as cobalt assays for the deposit are uniformly low, the bulk of the As is most likely in arsenopyrite. Intervals of elevated As in the deposit consistently correlate with zones of coarse-grained arsenopyrite.

Arsenopyrite usually occurs as clusters of coarse-grained (1–20mm) euhedral to subhedral crystals dispersed along zones of more intense S_1 cleavage within Stage 4 quartz veins and vein breccias and associated with late-stage Mg-Fe chlorite alteration and veins. Individual arsenopyrite grains are often deformed and contain sub-horizontal fractures (Figure 140a–b). Arsenopyrite is best developed in the footwall of the Main Lode, occuring along the contact between the footwall Stage 4 quartz vein breccia and Main Lode. Narrow zones of arsenopyrite are also erratically developed in the immediate hanging wall of the Main Lode associated with the scattered Stage 4 quartz veins and minor Mg-rich iron chlorite.

Arsenopyrite is largely absent from zones of gold mineralisation in the New Occidental deposit, except in the northern part of the deposit where several narrow zones of arsenopyrite are associated with cross-cutting Stage 4 quartz veins that transect the Main Lode (Figure 141 and Figure 142). Arsenopyrite overprints both stages of gold-bismuth mineralisation (Figure 140b–c).

Figure 140: Examples of arsenopyrite mineralisation.

a) Coarse-grained fractured arsenopyrite developed in cleavage-parallel Mg-rich iron chlorite layers either side of a deformed sub-horizontal Stage 4 quartz-chlorite extension vein.

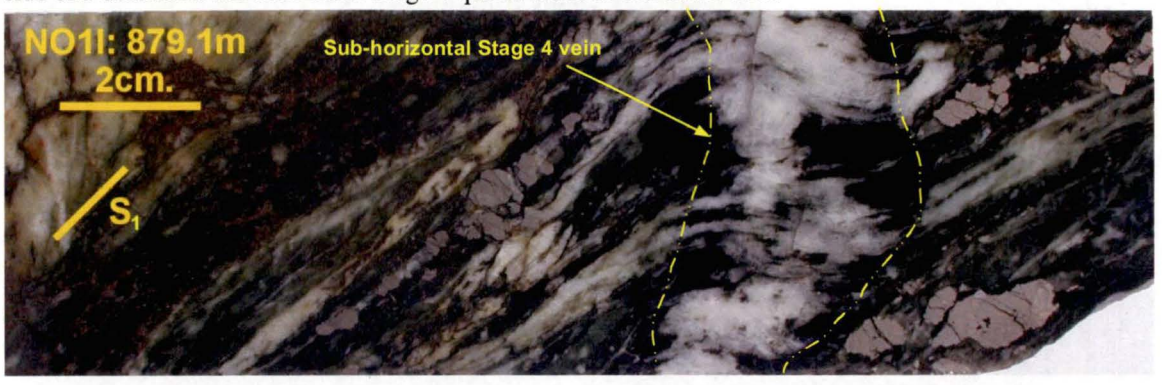

b) NO12 - 665.2m: False colour backscattered electron image of early stage gold-bismuth mineralisation partially replaced by arsenopyrite.

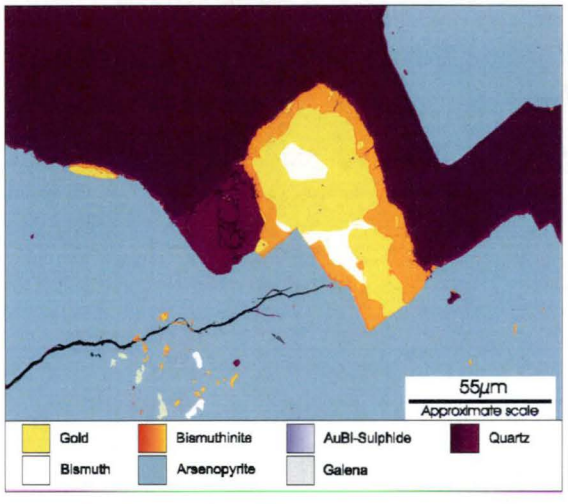

c) NO12 - 665.2m: False colour backscattered electron image of bismuthinite-galena-Bi_5AuS_4 mineralisation partially replaced by arsenopyrite.

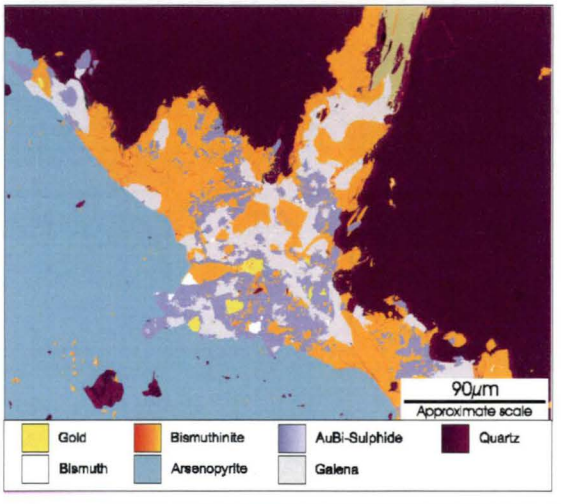

6.4.6 Chalcopyrite - Pyrrhotite - Electrum

A discrete zone of coarse-grained chalcopyrite-rich mineralisation is developed as a late-stage overprint in the New Occidental deposit. It consists of the assemblage:

Chalcopyrite - pyrrhotite - electrum$_{(450–820\ fine)}$ with minor galena - sphalerite - cassiterite

Coarse-grained chalcopyrite - pyrrhotite mineralisation forms a more or less continuous sub-vertical cleavage-parallel zone 1–5m wide in the footwall of the New Occidental deposit (Figure 132 and Figure 143). Subsidiary 1–2m wide cleavage-parallel zones of similar coarse-grained chalcopyrite - pyrrhotite - pyrite mineralisation are also present in the Albion Lode, although the pyrite in this assemblage formed by replacement of pyrrhotite. Minor galena and iron-rich sphalerite is intergrown with the chalcopyrite - pyrrhotite (Reynolds, 1999a). Collectively, this mineralisation stage accounts for the bulk of the copper in the deposit with Cu assays over 1-metre intervals of the order 0.1 – 5.8% Cu.

Figure 141: Distribution of Stage 4 quartz veins and arsenic mineralisation.

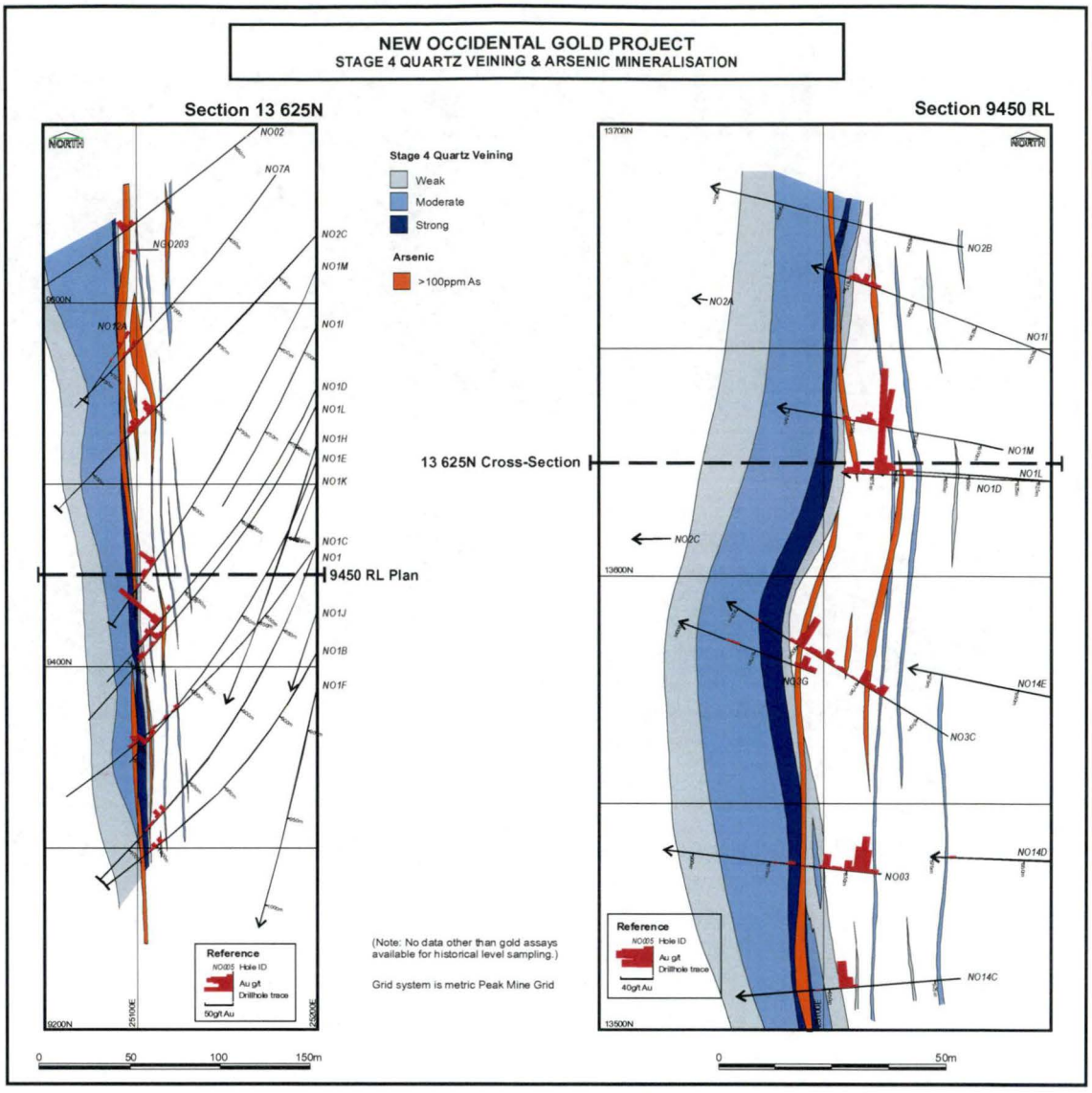

Most chalcopyrite - pyrrhotite mineralisation contains little or no gold, except where it cross-cuts earlier stages of gold mineralisation (e.g., along the western margin of the Main Lode where it overprints gold-bismuth mineralisation associated with Stage 2–3 quartz vein breccias and in the Albion Lode where it overprints earlier gold-bismuth mineralisation). This gold is typically coarse-grained (up to 1–2mm in diameter) and is the most silver-rich gold in the New Occidental deposit with an average fineness of 650 (range 450–820 fineness) (Reynolds, 2001) (Figure 144a). Reynolds (1999a) also identified small amounts of fine-grained high fineness gold associated with metallic bismuth and other bismuth minerals, including Se-rich ikunolite, developed along grain boundaries within the chalcopyrite - pyrrhotite (Figure 144b), which most likely represent early-stage gold-bismuth that has been incorporated into the chalcopyrite - pyrrhotite assemblage.

The chalcopyrite - pyrrhotite assemblage typically infills sub-horizontal extensional fractures in pre-existing quartz veins and quartz vein breccias (Figure 144c–f). Localised coarse-grained chalcopyrite - pyrrhotite overprint Stage 1 colloform quartz-magnetite veins in the centre of the Main Lode (Figure 144c) and preferentially

replaced magnetite in Stage 1 quartz veins in the hanging wall of the deposit (Figure 138c). Cleavage-parallel zones of chalcopyrite-pyrite (pyrite replacing pyrrhotite) overprint composite Stage 1–2 quartz veins in the Albion Lode. Chalcopyrite - pyrrhotite also occurs in pressure shadows around boudinaged cleavage-parallel Stage 1–4 quartz vein fragments and brecciated Stage 2–3 quartz vein fragments in the footwall fault breccia (Figure 144d and Figure 79a, c). It occasionally overprints intense stilpnomelane alteration and also overprints deformed Stage 4 quartz-Mg-rich iron chlorite veins that host similarly deformed arsenopyrite mineralisation (Figure 144e). Stage 5 quartz veins overprint the chalcopyrite - pyrrhotite assemblage.

Where coarse-grained chalcopyrite - pyrrhotite mineralisation is developed in brecciated siltstones and sandstones on the margin of the deposit, it is commonly associated with narrow selvedges approximately 1–5mm wide of sericite alteration (Figure 144f).

Figure 142: Distribution of Mg-rich Fe-chlorite alteration and arsenic mineralisation.

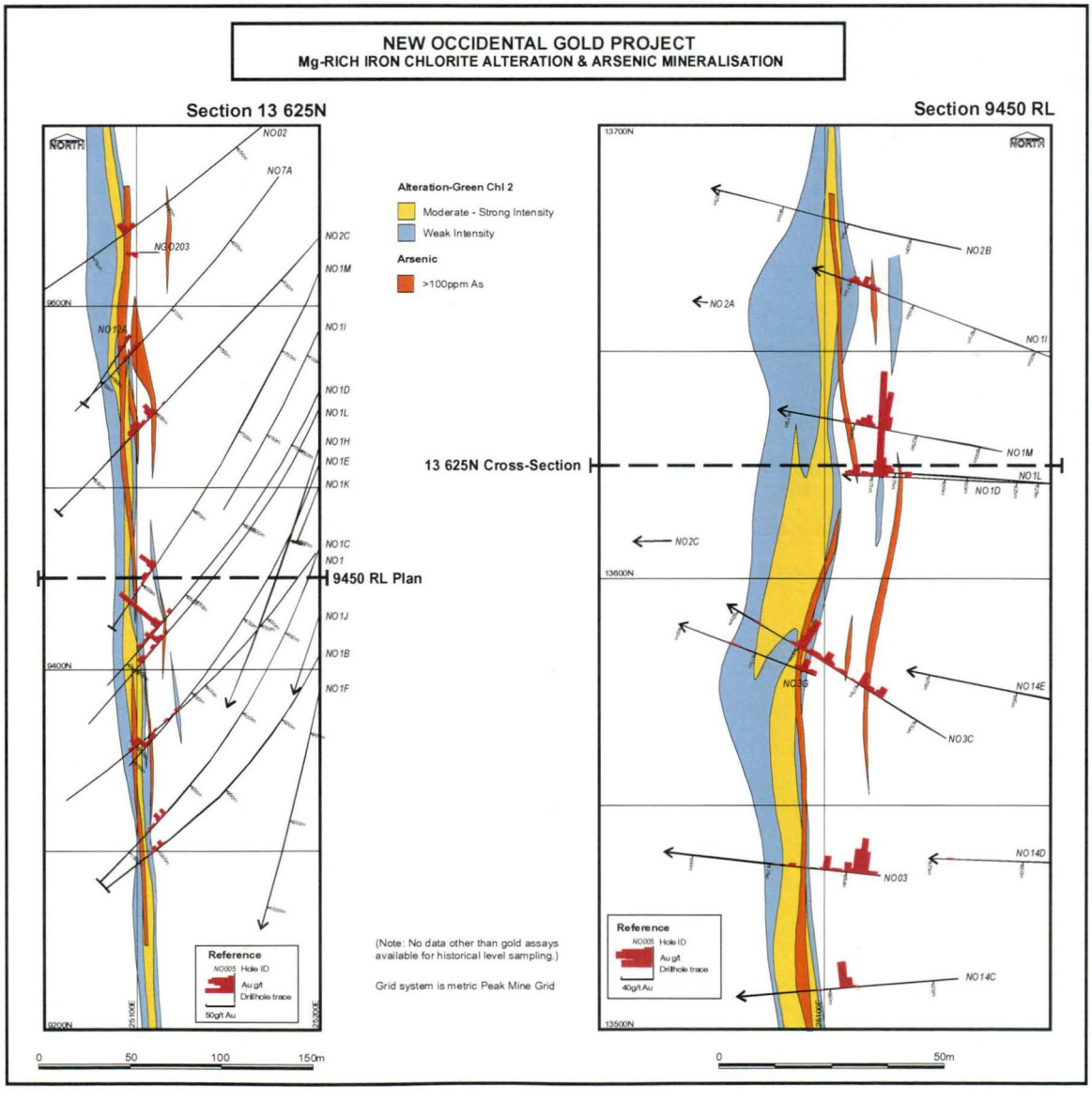

Figure 143: Distribution of Stage 4 quartz veins and copper mineralisation.

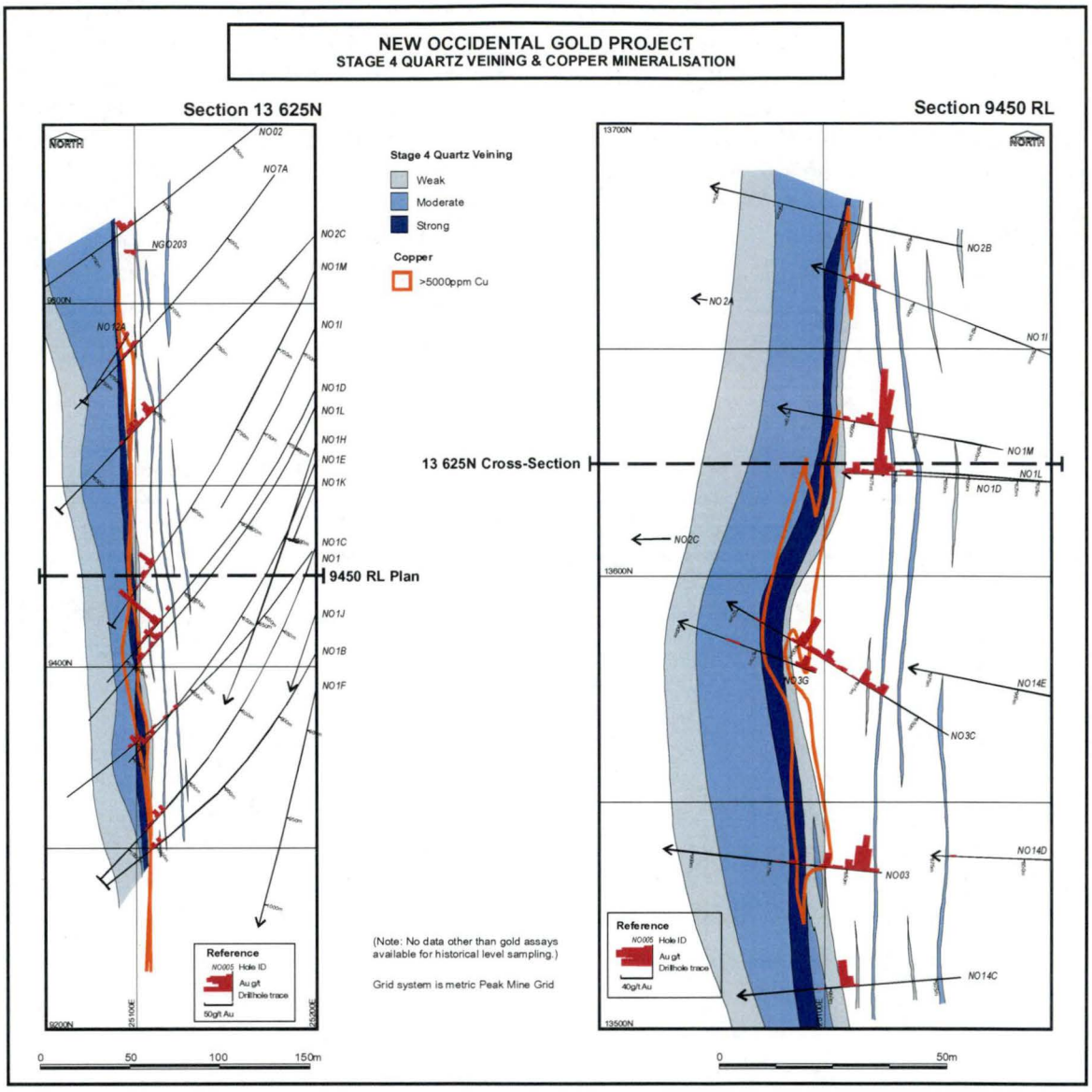

Figure 144: Examples of chalcopyrite - pyrrhotite mineralisation.

a) NO12 Gravity Concentrate: A false colour, backscattered electron image of electrum partially intergrown with chalcopyrite. An extremely Ag-rich rim is present on one side of the largest electrum grain.

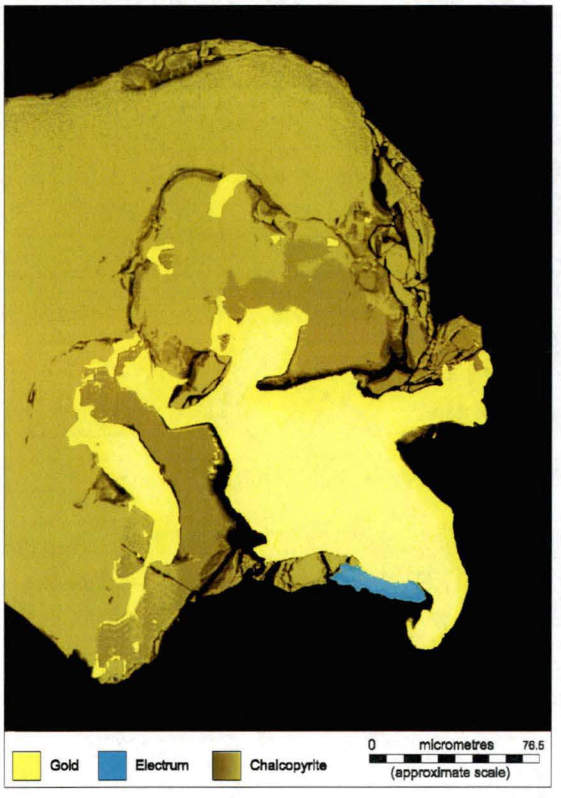

b) NO1M - 837.0m: A false colour, backscattered electron image of chalcopyrite intergrown with pyrrhotite, quartz and lesser sphalerite and galena. Fine-grained inclusions of gold/electrum and native bismuth occur along grain boundaries within the chalcopyrite and to a lesser extent pyrrhotite.

c) Coarse-grained chalcopyrite - pyrrhotite infilling sub-horizontal (perpendicular to cleavage) and cleavage-parallel fractures in sheared Stage 1 colloform quartz - magnetite vein breccias from the core of the Main Lode.

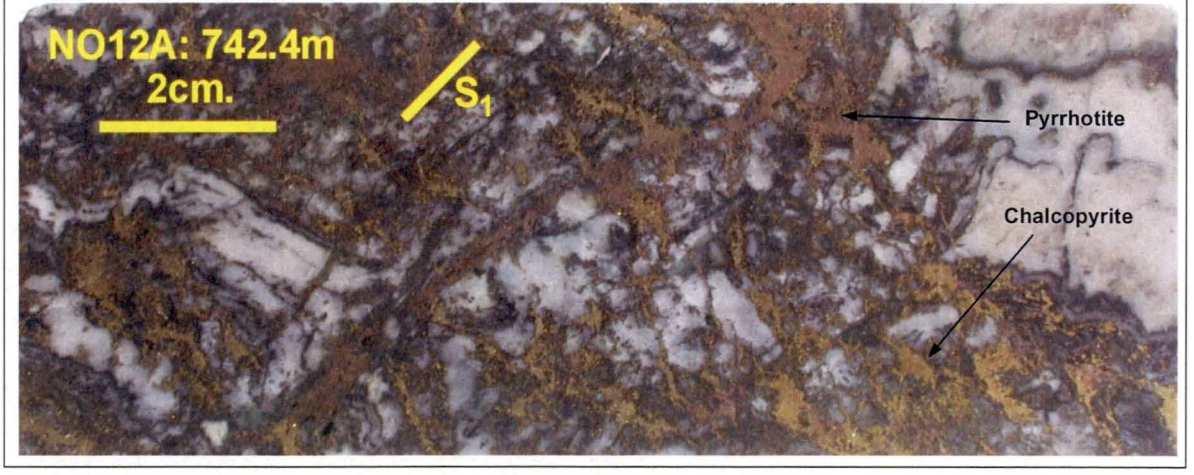

Figure 144 Continued.

d) Coarse-grained chalcopyrite - pyrrhotite developed in fractures in sheared siltstone and Stage 4 quartz vein breccias in the footwall of the Main Lode.

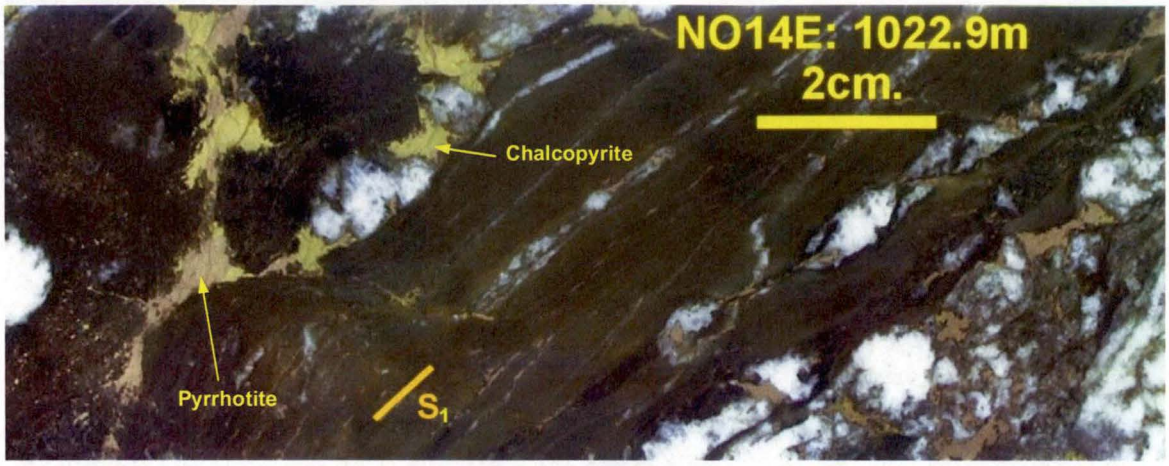

e) Coarse-grained chalcopyrite infills sub-horizontal fractures perpendicular to S_1 cleavage within sheared Stage 4 quartz-chlorite-arsenopyrite vein.

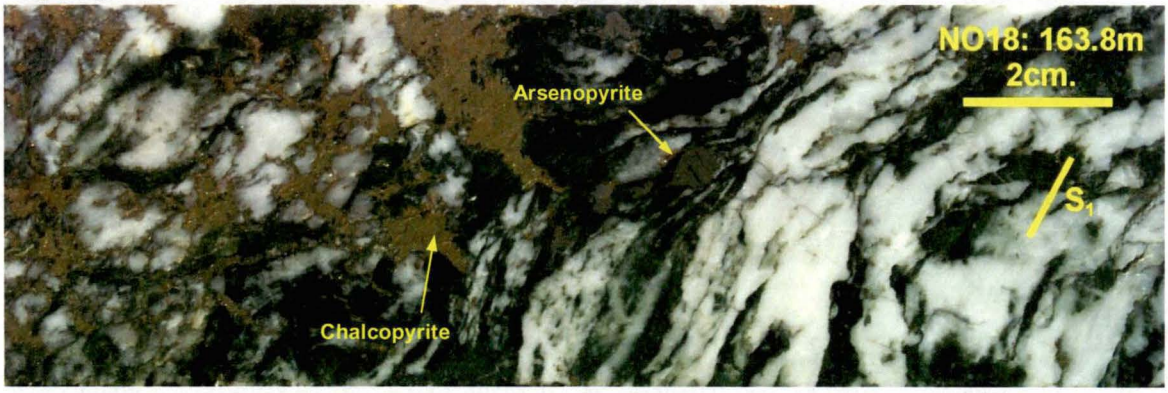

f) Late-stage galena – sphalerite - pyrrhotite overprinting chalcopyrite - pyrrhotite in brecciated siltstones of the Great Cobar Slate. Distinctive bleaching of the siltstone immediately adjacent to the chalcopyrite reflects sericite alteration.

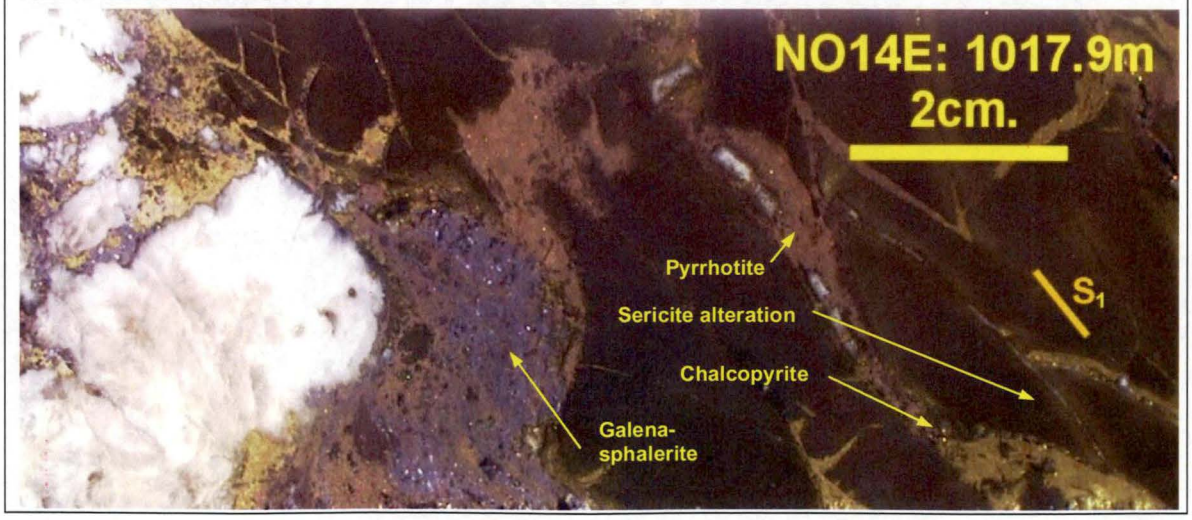

6.4.7 Sphalerite - Galena - Pyrrhotite

Whilst small amounts of galena and lesser sphalerite are associated with earlier stages of mineralisation within the New Occidental deposit, discrete late stage sphalerite-galena mineralisation is also evident. This mineralisation consists of the following assemblage:

Sphalerite - galena - pyrrhotite

Overall, Zn and Pb contents of the New Occidental deposit are in the range 0.0 – 2.4% (average 0.06%) and 0.0 – 5.7% (average 0.06%) respectively based on 1-metre drillcore assays. Whilst some of the Pb content of the New Occidental deposit is related to galena-clausthalite solid solution series and to other Pb-Bi phases associated with the early stage gold-bismuth mineralisation, intervals of elevated (>0.1%) Pb-Zn are usually associated with the late-stage sphalerite-galena-pyrrhotite mineralisation. Sphalerite-galena mineralisation is best developed between 9400–9800m RL (500–900m from surface) within the Main Lode of the New Occidental deposit, coincident with the thickest sections of the deposit (Figure 133 and Figure 134).

Semi-quantitative microbeam analysis of sphalerite by Reynolds (1999a) reveal it is relatively iron-rich with 7.0 – 9.3 wt% Fe and 57.1 – 59.3 wt% Zn and contains only minor amounts of cadmium (0.12 – 0.16 wt% Cd) (Appendix 8).

The sphalerite-galena-pyrrhotite ore assemblage is associated with minor greenalite, Fe-rich clay and calcite (Figure 145a) and occurs in both sub-horizontal and steeply dipping cleavage-parallel sulfide-rich veins in the core of the Main Lode (Figure 145b–d). The veins crosscut Stage 1–4 quartz veins (Figure 145b–c) but are cross-cut by Stage 5 quartz veins. Sphalerite-galena-pyrrhotite also overprints the chalcopyrite - pyrrhotite assemblage in the footwall of the Stage 4 quartz vein breccia (Figure 144f, Figure 145b–c).

Figure 145: Examples of sphalerite - galena - pyrrhotite mineralisation.

a) NO12A: 708.4m - False colour, backscattered electron images of sphalerite - galena - Fe-rich clay vein overprinting a younger quartz vein.

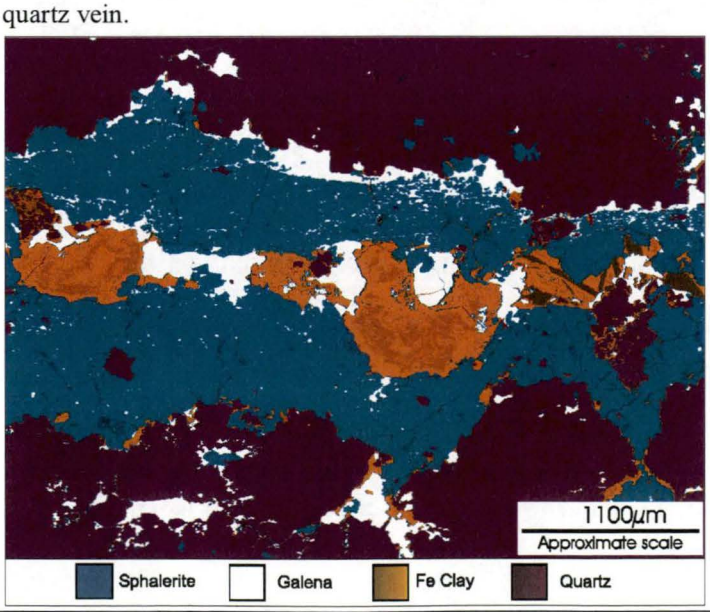

Figure 145 Continued.

b) Late stage sub-horizontal extensional sphalerite - galena - pyrrhotite vein cross-cutting a Stage 2 quartz vein breccia and late-stage coarse-grained chalcopyrite vein.

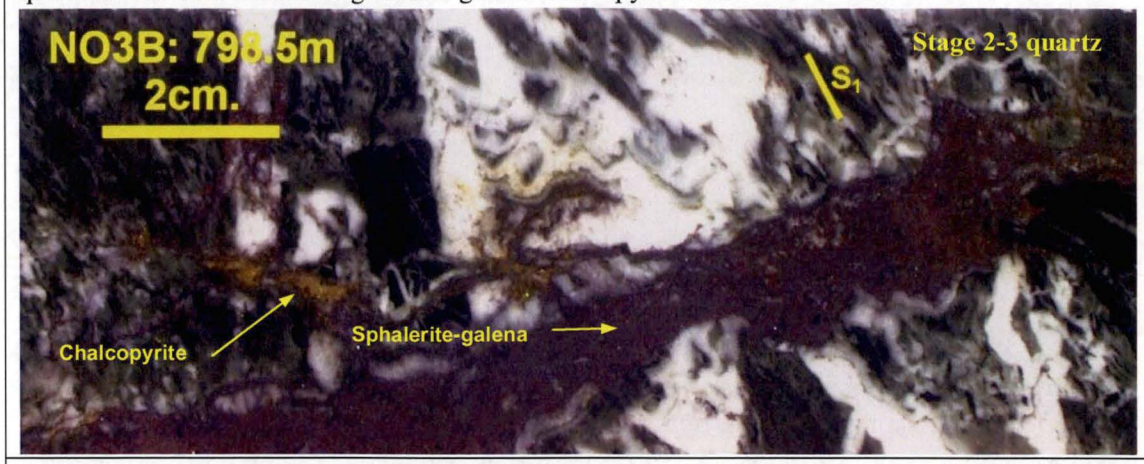

c) Narrow cleavage-parallel vein of galena - sphalerite developed along a fracture in a boudinaged Stage 4 vein that cross-cuts variably crustiform-banded Stage 2–3 quartz veins.

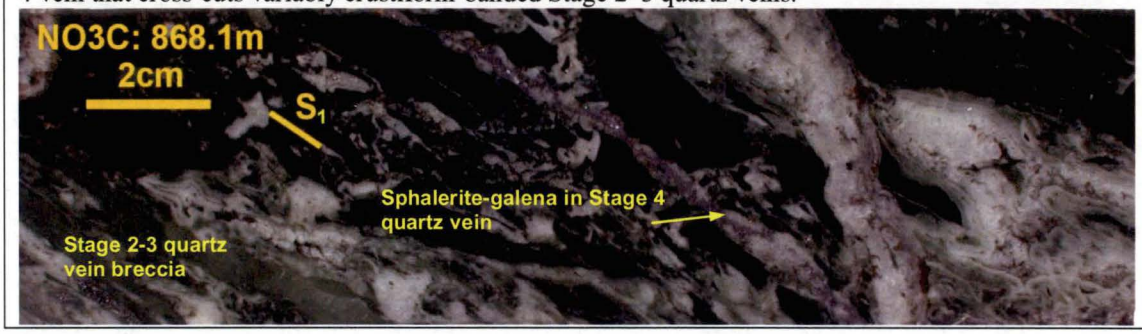

6.4.8 Peripheral Pyrite

Pyrite forms the last ore mineral stage within the New Occidental deposit. It occurs at the margins of the Main Lode, locally within the Main Lode and is strongly developed throughout the Albion Lode (Figure 135). Pyrite occurs as:

1. Partial to complete replacement of magnetite in the hanging wall of the New Occidental deposit. Coarse-grained euhedral to subhedral pyrite replaces cleavage-parallel magnetite seams associated with Stage 1 quartz veins (Figure 146a). Replacive pyrite may also mimic the folded nature of the sub-horizontal magnetite veins. Pyrite replacement of magnetite typically begins along sub-horizontal fractures in the magnetite.

2. Sub-horizontal pyrite veins occur sporadically throughout the core the New Occidental deposit overprinting Stage 2–4 quartz vein breccias, including stilpnomelane-altered quartz breccias (Figure 146b).

3. Pyrrhotite (associated with both early stage gold-bismuth and the late stage chalcopyrite and sphalerite-galena ore assemblages) is variably replaced by pyrite in both the Main and Albion Lodes of the New Occidental deposit (Figure 146c). Pyrrhotite associated with chalcopyrite mineralisation in the Albion Lode is replaced by distinctive porous aggregates of pyrite. Minor Fe-rich clay is often associated with the pyrite

and is usually developed along grain boundaries and cleavage planes in the pyrite (Figure 146c).

4. Disseminated coarse euhedral (cubic) pyrite grains in chlorite-rich parts of the orebody (Figure 146d). Pyrite euhedra contain fine-grained inclusions of chlorite aligned parallel to cleavage and parallel to similar chlorite grains in the surrounding quartz-rich matrix, indicating the pyrite mostly postdates S_1 cleavage development.

There is no evidence gold is associated with late-stage pyrite.

Figure 146: Examples of late-stage pyrite mineralisation.

a) Late stage pyrite partially replacing magnetite in a Stage 1 quartz vein breccia.

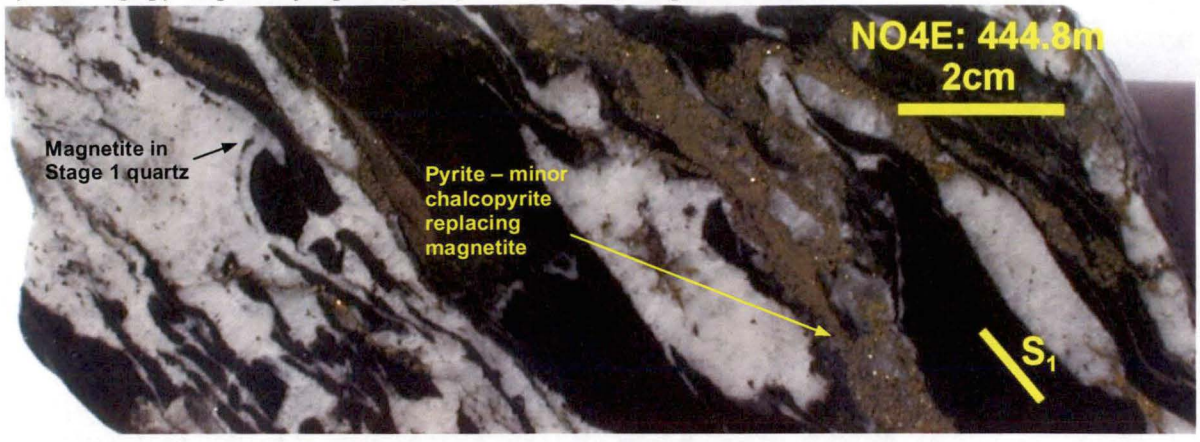

b) Late stage sub-horizontal pyrite veins cross-cutting stilpnomelane-altered Stage 2–3 quartz vein breccia.

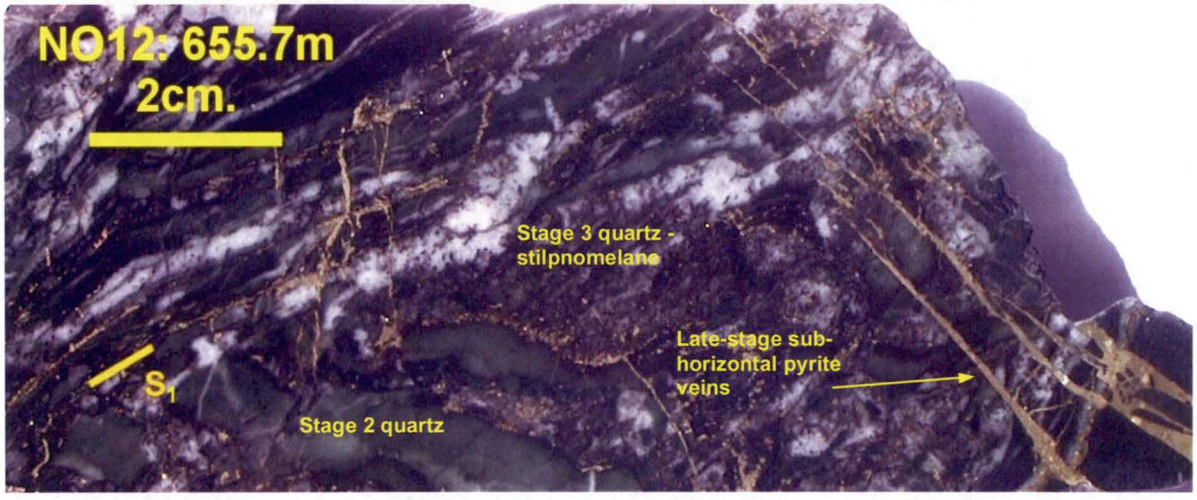

c) NO12A - 708.4m: False colour backscattered electron images of pyrite replacing pyrrhotite intergrown with chalcopyrite and stilpnomelane. Fe-rich clay lines pyrite cleavage plane/grain boundaries.

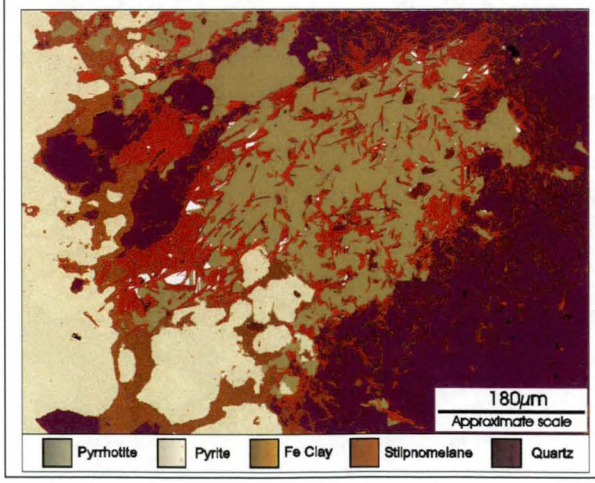

d) NO12A - 708.4m: False colour backscattered electron image of pyrite euhedra in vein quartz that contains numerous tiny inclusions of chlorite that have the same orientation as chlorite grains in the surrounding quartz.

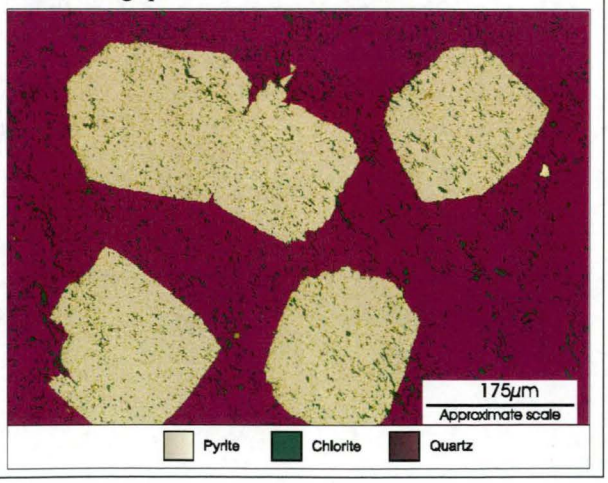

6.4.9 Pyrrhotite Replacement of Syngenetic Pyrite

Pyrrhotite replacement of syngenetic pyrite is widespread throughout the eastern margin of the Cobar Basin. Pyrrhotite flakes form stratabound layers that mimic the original bedding-parallel distribution of syngenetic pyrite. However, individual pyrrhotite flakes are oriented parallel to the strong penetrative S_1 cleavage and $L_1{}^1$ stretching lineation (Figure 147). Pyrrhotite (after syngenetic pyrite) is abundant in upper Chesney Formation, Great Cobar Slate and CSA Siltstone immediately south of the New Occidental deposit about the trace of the Great Chesney Fault. Another large zone of replacive pyrrhotite is also present in fine-grained sandstones and siltstones of the Chesney Formation immediately east of the Peak deposit. These pyrrhotite accumulations occur in zones of strongly developed cleavage, metamorphic chlorite and white mica. Pyrrhotite accumulations are manifested as prominent elongate magnetic anomalies that either parallel the trend of cleavage and major faults (like the Great Chesney Fault and Peak Shear), or parallel bedding (Figure 148). The magnetic data indicate the pyrrhotite accumulations are up to several kilometres long and 100–200m wide.

Pyrrhotite replacement of syngenetic pyrite has occurred during development of S_1 cleavage and formation of the metamorphic chlorite-white mica assemblage. However, its timing relative to the main stages of mineralisation in the New Occidental deposit is less well constrained. This pyrrhotite does not exhibit a spatial or genetic association with any of the quartz vein, alteration or mineralisation stages in the New Occidental deposit. In a number of places, the chalcopyrite - pyrrhotite - pyrite assemblage overprints cleavage-parallel pyrrhotite flakes in footwall Great Cobar Slate and thus postdates pyrrhotite replacement of syngenetic pyrite. It is most likely pyrrhotite replacement of pyrite occurred over an extended time interval coincident with the main period of S_1 cleavage development and encompasses several mineralisation stages.

Figure 147: Pyrrhotite replacement of syngenetic pyrite.

Thinly interbedded siltstone from CSA Siltstone in the New Occidental South area showing stratabound cleavage-parallel pyrrhotite flakes formed by replacement of bedding-parallel pyrite.

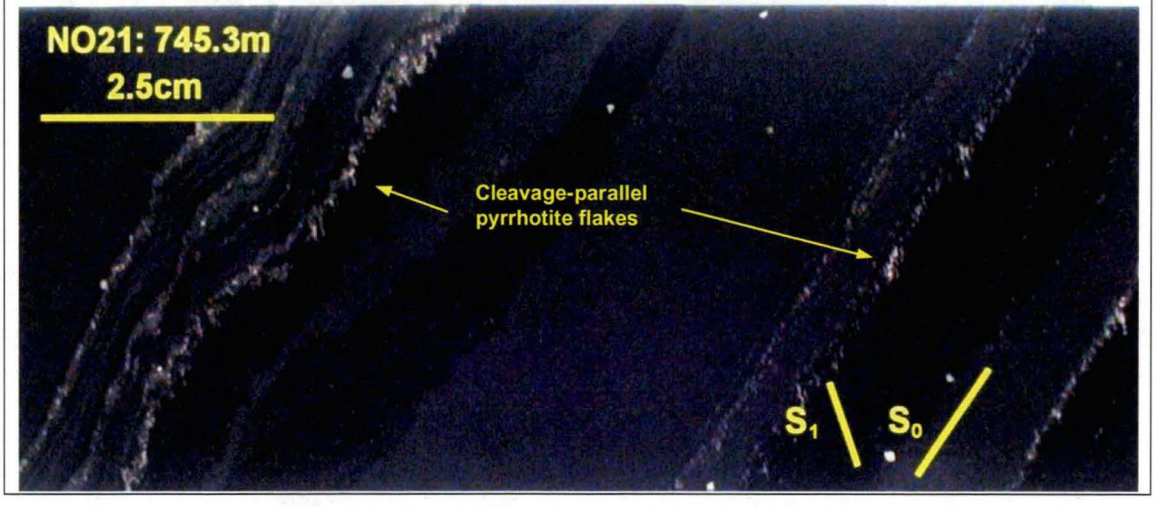

Figure 148: Airborne magnetics of the Cobar Goldfield

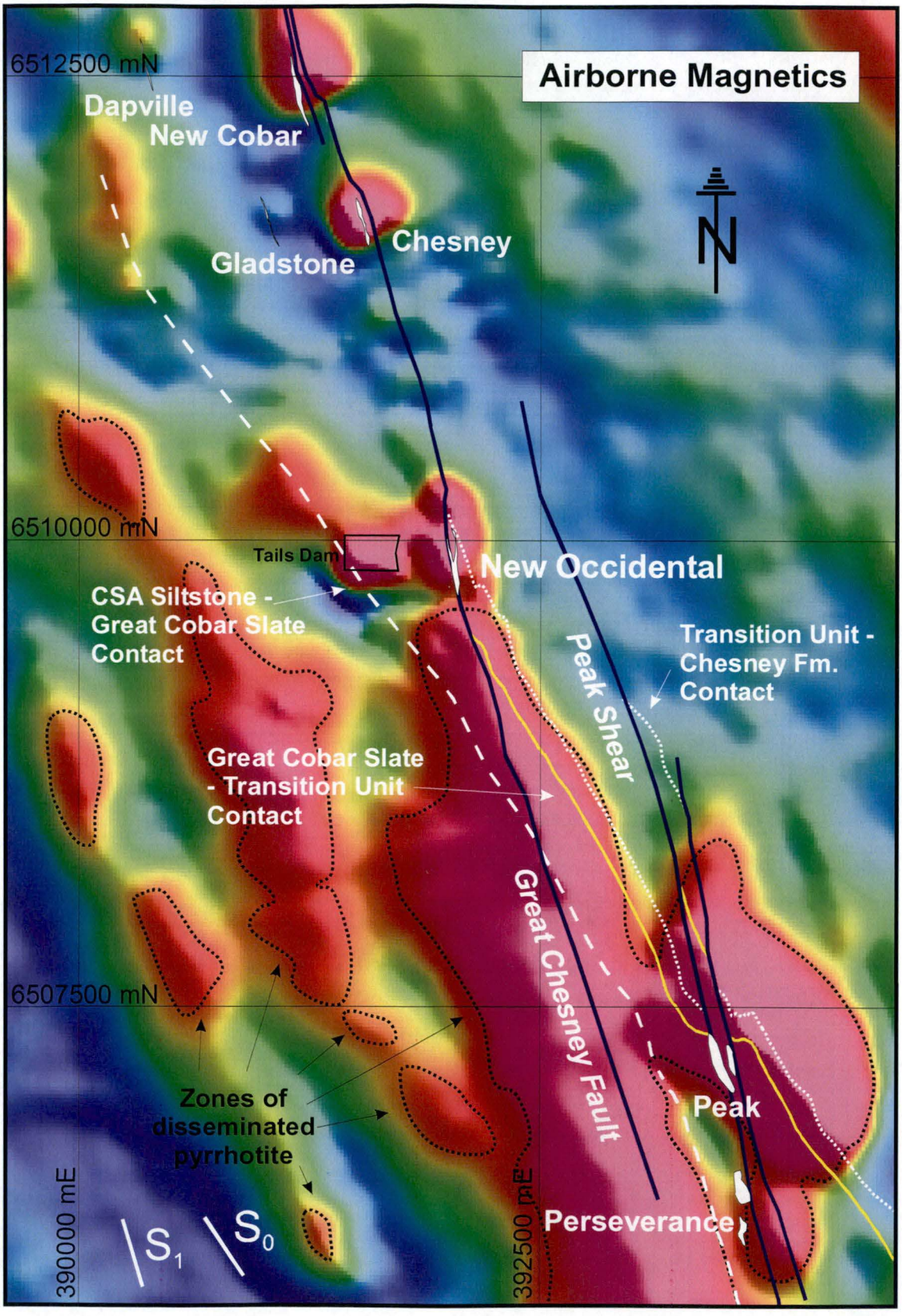

6.5 Timing and Controls on Metal Deposition in the New Occidental Deposit Inferred from Ore Mineral Paragenesis - And Unresolved Aspects!

6.5.1 Timing of Gold Deposition and Potential Controls on Deposition

Much of the gold at the New Occidental was introduced at a relatively early stage in the paragenetic sequence prior to deposition of the bulk of base metal sulfides. $Gold_{(760-990\,fine)}$ deposited concurrently with Stage 2 colloform-banded crystalline and cryptocrystalline quartz veins, indicating gold deposition in the deposit was coincident with maximum slip and dilation on the Great Chesney Fault and the most intense period of fault valve activity along the fault. As such, it is reasonable to conclude initial gold deposition in the deposit resulted from, or at least was significantly influenced by, the physiochemical changes associated with the rapid and large-scale pressure fluctuations in the hydrothermal fluid, including potentially phase separation.

$Gold_{(820-900\,fine)}$ deposited during Stage 3 (bismuthinite-"newoccidentallite"-gold) represents ongoing gold deposition under conditions of higher aH_2S, as evidenced by coeval bismuthinite replacement of native bismuth and "newoccidentallite" replacement of maldonite and gold. Fault valve activity continued along the Great Chesney Fault, although it was less intense, as indicated by the transition from colloform banded cryptocrystalline and crystalline quartz veins to mainly crystalline quartz veins and quartz vein breccias (Stage 3). Gold was potentially deposited in response to ongoing phase separation, or desulfidisation reactions coupled with sulfide replacement of native metals.

$Gold_{(450-820\,fine)}$ deposited during Stage 5 (chalcopyrite - pyrrhotite - electrum) represents a very different style of gold deposition in the New Occidental deposit compared to the previous stages. Stage 5 ore minerals represent the onset of significant base metal sulfide deposition in the New Occidental deposit, which was accompanied by a change in alteration mineralogy from dominantly Fe-phyllosilicates to sericite-minor chlorite. In addition, Stage 5 ore minerals were deposited in the waning stages of fault zone dilation (and onset of local contractional slip) and after deformation along the Great Chesney Fault had transitioned from brittle to ductile (Table 24). Concurrent deposition of base metal sulfides suggests gold was transported as chloride complexes and was deposited in response to cooling of the hydrothermal fluid, increasing *pH* decreasing aCl and/or decreasing oxygen fugacity (e.g. Huston & Large, 1989). The inferred more saline (and possibly more acidic) fluid lends more support for the argument of a second hydrothermal fluid introduced into the New Occidental fluid deposit late in the paragenesis (Section 5.7.6).

In contrast to the New Occidental deposit, studies of other Cobar deposits (e.g. Peak deposit: Hinman, 1992; Peak and Chesney deposits: Jiang, 1996; McKinnons deposit: Forster and Seccombe, 1999) concluded gold was only deposited late in the respective ore mineral parageneses, often coincidental with or later than deposition of base metal sulfides. In the case of the New Occidental deposit, the presence of gold in subsequent ore mineral stages only in those areas where the respective stages overprint original Stage 2 gold and Stage 2 quartz veins, indicates most, if not all, of the later gold, including that associated with base metal sulfides, formed by remobilisation of early-formed high fineness gold. Remnants of early stage high fineness gold (with other early stage minerals) in later stages of lower fineness gold further support this conclusion. Stage 2 gold does not appear to have been

substantially spatially remobilised (generally <0.5m) in during subsequent gold stages and it is common to find later stages of gold intimately intergrown with and even rimming earlier stage gold (Section 6.4.4 and Section 6.4.6). As such, remobilisation processes are more akin to direct replacement of early-stage gold by late-stage gold. It also follows that Stage 3 and 5 ore mineral stages were immediately preceded by periods of retrograde gold solubility. Conversely, lack of appreciable gold associated with the other ore mineral stages (Stage 4, 6 and 7), even where they directly overprint early-stage gold, indicate those stages were not associated with fluids capable of remobilising existing gold.

Progressive Ag-enrichment of metallic gold in successive ore mineral stages in the New Occidental deposit provides only limited constraints on the chemistry of the associated hydrothermal fluid. Gammons & William-Jones (1995) argue a range of physiochemical conditions, including initial $(Au/Ag)_{aq}$ value of the fluid, pH, temperature, aH_2S, aO_2 and aCl^-, influence Au/Ag ratios of metallic gold, depending on whether Au and Ag were transported as similar or dissimilar bisulfide or chloride complexes. In addition, they have also shown primary heterogeneity in electrum composition can be easily destroyed by subsequent re-equilibration processes including metamorphism. Based on the data of Gammons & William-Jones (1995), one possible explanation for the high Au/Ag ratios of early metallic gold, evolving to more Ag-rich gold, in the New Occidental deposit is the initial ore fluids were relatively H_2S-rich and/or Cl-poor and that the fluids became more saline with time. This explanation is consistent with previous suggestions the Stage 5 chalcopyrite - pyrrhotite - electrum assemblage deposited from a more saline (and possibly more acidic) second hydrothermal fluid introduced into the New Occidental fluid deposit late in the ore mineral paragenesis.

Further analysis of controls on the transport and deposition of gold in the New Occidental deposit will be undertaken once data on temperature of metal deposition and ore fluid composition from fluid inclusion studies has been compiled.

6.5.2 Significance of Late-stage Base Metal Deposition and the Role of Sulfur in Ore Deposit Formation

The relatively late timing of deposition of the bulk of base metals in the New Occidental deposit raises a fundamental question about deposit formation. Specifically, were all base metals transported with gold in the initial hydrothermal fluid but failed to deposit in substantial amounts during the early stages of gold-dominated ore mineral deposition due to unfavourable conditions (i.e. low aH_2S or insufficient temperature decrease), or was the initial hydrothermal fluid relatively base metal-poor and the bulk of the base metals introduced via a second later hydrothermal fluid?

Phase relations in the system Fe-S-O suggest evolution from the magnetite-bearing assemblage (Stage 1), through pyrrhotite-bearing assemblages (Stage 2–6), to the final pyrite-bearing assemblage (Stage 7) in the New Occidental deposit was due to progressively increasing S_2-H_2S fugacities in the ore fluids (e.g. Titley & Beane, 1981; Large et al., 1989; Hemley et al., 1992; Figure 149a–b), rather than to a change in the oxidation state of the hydrothermal fluids from oxidised to reduced (e.g. Sharpe and Gemmell, 2000). The pyrrhotite - pyrite transition may also be in part due to decreasing temperature of the hydrothermal fluid (e.g. Large et al., 1989; Figure 149b;

Mikucki, 1998), which is suggested by the corresponding change from higher temperature phyllosilicate alteration assemblages (chlorite - stilpnomelane - sericite) associated with the bulk of ore mineral assemblages (Stage 2–5) to lower temperature assemblages (greenalite - Fe-rich clays) with late-stage sphalerite-galena-pyrrhotite and pyrite ore mineral assemblages (Stage 6–7).

Replacement of native elements/alloys (native bismuth, gold and maldonite) by Au-Bi sulfides (bismuthinite and Bi_5AuS_4), and progressive changes in solid solution series minerals from Se-rich to S-rich Bi-Pb minerals also support an increase in aH_2S in the hydrothermal fluid with time (e.g. Mintser, 1979; Kolonon, 1979; Brookins, 1988; Benchekroun et al., 1996; Figure 149c). Potential causes of increasing aH_2S in the New Occidental ore fluid with time (or lower aH_2S in the early stages of metal deposition) include loss of H_2S during phase separation associated with depressurisation of the hydrothermal fluid during fault valve activity on the Great Chesney Fault, mixing of an early low-sulfur fluid with late sulfur-rich fluids and progressive addition of sulfur to the hydrothermal fluid, either from ongoing reactions between the hydrothermal fluid and syngenetic pyrite or metamorphic pyrrhotite in wallrock to the deposit, or sulfur released during pyrrhotite replacement of syngenetic pyrite (Mikucki, 1998).

Loss of H_2S during phase separation is most likely to have occurred during deposition of Stage 1–3 quartz veins in the New Occidental deposit given those stages reflect the most intense period of fluid depressurisation in the deposit (Section 4.5). Interestingly, native metal and low-sulfur ore mineral assemblages were deposited during deposition of Stage 2–3 quartz veins. However, phase separation is unlikely to explain the oxide ore metal assemblage (magnetite-scheelite-wolframite) associated with Stage 1 quartz veins in the hanging wall of the deposit. Mixing of an initial low-sulfur hydrothermal fluid with a later sulfur-rich fluid is supported by alteration mineral studies which suggest sericite alteration at the New Occidental deposit (corresponding to the main stage of base metal deposition) may reflect the late introduction of a second fluid. Finally, abundant wallrock sulfides are a potential important and relatively accessible source of sulfur for ore mineral deposition in the New Occidental deposit. Alteration studies have already shown that the New Occidental ore fluid was progressively buffered by wallrock (Section 5.7.1), providing a simple mechanism for progressive addition of wallrock sulfur to the hydrothermal fluid. Likewise, pyrrhotite replacement of pyrite, which is interpreted to have occurred over an extended time interval coincident with the main period of S_1 cleavage development (Section 6.4.9), is an equally plausible means by which wallrock sulfur was added to the hydrothermal fluid. Coincidentally, most pyrrhotite replacement of syngenetic pyrite appears to have occurred prior to the main stage of base metal sulfide deposition.

Fluid inclusion studies are required to determine whether phase separation occurred during deposition of the early quartz vein stages or whether fluid compositions indicate a second fluid was involved in deposit formation. The role of wallrock sulfides in deposit formation can likewise be resolved by sulfur isotope studies of wallrock and ore sulfides and Pb isotope studies may be able to distinguish between different generations of lead sulfides (e.g. early galena-clausthalite and late-stage galena).

Figure 149: Interpreted physiochemical conditions of ore formation in the New Occidental deposit in the system Fe-S-O.

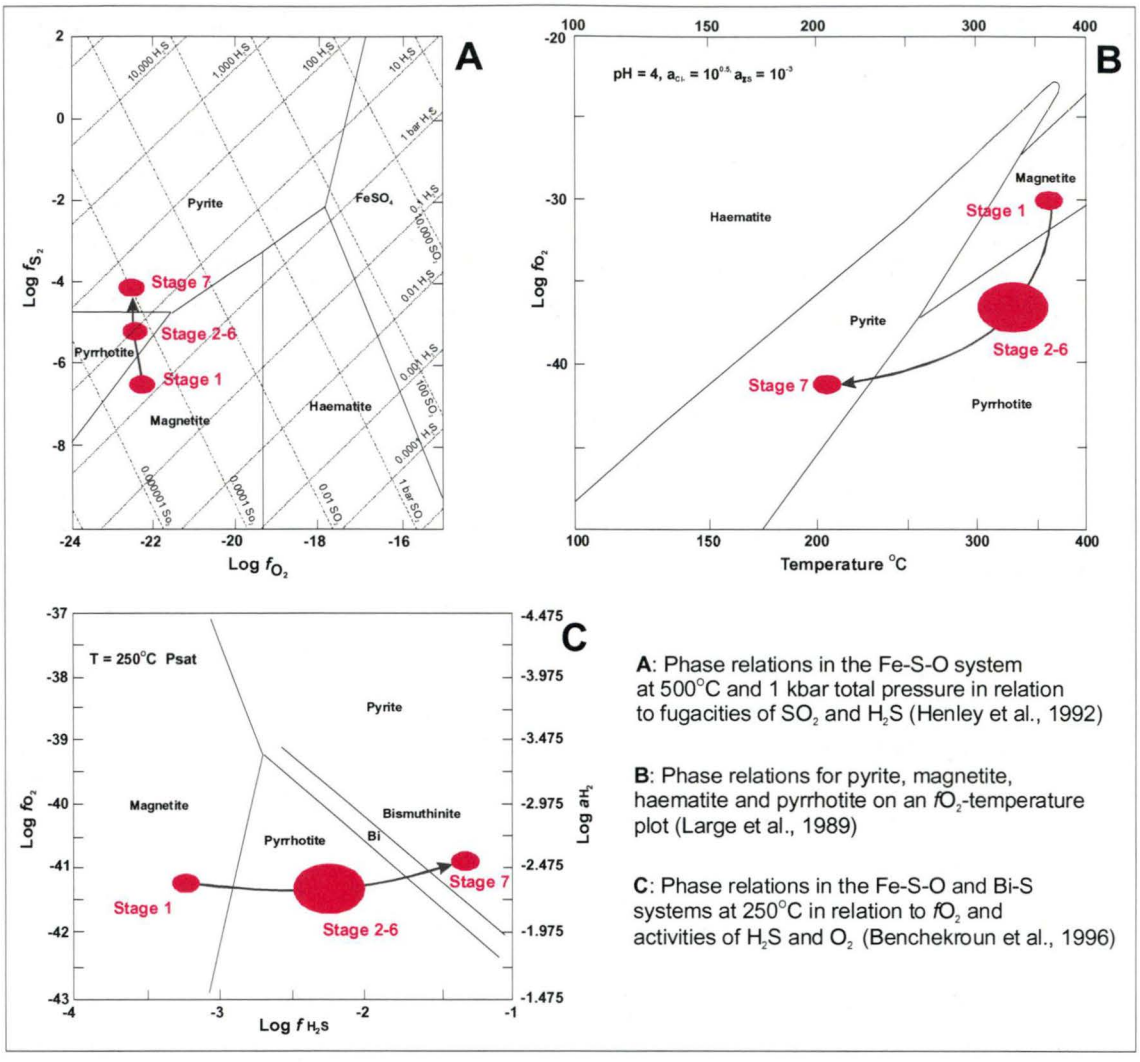

6.6 Comparison with Ore Mineral Paragenetic Sequences in other Cobar Deposits

The paragenesis outlined for the New Occidental deposit has a number of features common to parageneses proposed for other deposits in the Cobar Basin, including:

A paragenetic sequence consisting of early-stage magnetite (where present) → chalcopyrite - pyrrhotite → galena - sphalerite - pyrrhotite → pyrite (e.g. New Cobar, Chesney, Great Cobar, Peak and CSA deposits - Section 6.2.1).

Gold is commonly intimately associated with bismuth mineralisation (e.g. New Cobar and Perseverance deposits) and also with chalcopyrite - pyrrhotite mineralisation (e.g. Peak, New Cobar, Chesney and Perseverance deposits) (Table 23).

In contrast to the New Occidental deposit, studies of other Cobar deposits (e.g. Peak deposit: Hinman, 1992; Peak and Chesney deposits: Jiang, 1996; McKinnons deposit: Forster and Seccombe, 1999) concluded gold was deposited late in the respective ore mineral parageneses, often coincidental with or later than deposition of base metal sulfides.

Of all the Cobar deposits, early-stage bismuth-rich mineralisation is best developed at the New Occidental deposit. It is weak to moderately developed at the Perseverance and New Cobar deposits and relatively poorly developed in the other deposits (Table 26). In contrast, late-stage chalcopyrite - pyrrhotite mineralisation, indicated by average Cu contents, is relatively weakly developed in the New Occidental deposit compared to most other Cobar deposits (Table 26). Similarly, late-stage Pb-Zn-Ag mineralisation, measured by average Pb-Zn contents, is strongly developed in the Peak and CSA deposits, but only weakly developed in most of the other deposits. In terms of metal contents, the New Cobar deposit is most similar to the New Occidental deposit, although the former has a stronger chalcopyrite - pyrrhotite overprint.

Microprobe analyses indicate metallic gold in the New Occidental deposit is of higher average fineness than that at both the Peak and Perseverance deposits (Reynolds, 1998; 1999a, b; 2000a, b; 2001). This is also reflected in whole rock Ag/Au ratios, which are higher for the more base metal rich deposits (Table 26). However, successive stages of gold mineralisation at both the Peak and Perseverance deposits were also progressively more silver-rich.

Table 26: Comparison of metal contents of deposits in the Cobar Goldfield.

	New Occidental	Peak	Perseverance	Chesney	New Cobar	Great Cobar
Au (ppm)	8.8	9.1	11.3	0.8	6.8	1.5
Ag (ppm)	4.0	8.4	8.8		4.1	
Bi (ppm)	450	20–50	60	20	70	20–50
Cu %	0.1	0.7	0.85	1.9	0.6	2.5
Pb %	0.07	1.1	0.14	<0.1	0.02	<0.1*
Zn %	0.07	1.0	0.11	<0.1	0.07	<0.1*
Fe Sulfide %	1–2	5–10	~10	5–10	2–5	5–10
Magnetite %	0.1	Absent	Absent	0.5	1	1–2

* - A galena - sphalerite lode is developed in the footwall of the copper orebodies at Great Cobar.

Early stage of gold - bismuth ore minerals similar to that at the New Occidental, New Cobar and Perseverance deposits has not been recognised at the Peak (Hinman, 1992; Jiang, 1996), Chesney (Jiang, 1996) and McKinnons Tank (Forster & Seccombe, 1999) gold deposits. Gold at the Peak, New Cobar and Chesney deposits is predominantly associated with chalcopyrite - pyrrhotite ± galena ± sphalerite. However, those deposits also typically contain large zones of gold-poor base metal sulfides. This conundrum, that gold in Cobar deposits is almost always associated with base metal sulfides but not all zones of base metal sulfides are gold-mineralised, can be explained if, like the New Occidental deposit, very fine grained gold ± bismuth was introduced into those deposits at an early stage and then remobilised during subsequent stages of base metal sulfides. Zones of base metal sulfides are therefore only appreciably gold-bearing where they have inherited gold from the early stage of gold-bismuth mineralisation. Such early-stage fine-grained gold - bismuth may well

have been completely overprinted during subsequent base metal ore mineral stages, especially where the latter stages of base metal ore minerals are strongly developed (e.g. Peak). This interpretation is supported by detailed mineralogy of the Perseverance deposit (Reynolds, 2000b), which showed Cu-Au mineralisation is localised in zones of pre-existing high fineness gold - bismuth mineralisation (Priestly, 2000), and by the presence of bismuth ore minerals associated with gold in the Chesney (Robertson, 1974) and Peak (Hinman, 1992) deposits.

7 WHOLE-ROCK AND TRACE ELEMENT GEOCHEMISTRY

7.1 Introduction

The geochemistry of orogenic gold deposits is strongly dependent upon host rock composition, chemistry of the ore fluid, ore fluid/wallrock ratio and the physiochemical conditions under which fluid-rock interaction takes place (Kerrich, 1989; McCuaig and Kerrich, 1994; Eilu et al., 2001). Many studies have attempted to determine the chemistry of the ore fluid from ore-element associations and detailed geochemistry of wallrock alteration assemblages surrounding deposits. By characterising the nature of this alteration, including element enrichments and depletions, aspects of the ore fluid composition can be deduced. It may then be possible to infer the source of the fluid(s) based on determined chemistry (Kerrich, 1989; Leitch and Lentz, 1994; Mikucki, 1998; Ridley and Diamond, 2000). Finally, an understanding of the geochemical characteristics of the ore fluid and associated wallrock alteration may assist exploration for additional ore zones in the Cobar Basin. A number of studies have already shown Cobar's base metal deposits possess alteration haloes that provide a vector to ore (e.g. Robertson, 1974; Binns & Appleyard, 1986; Robertson & Taylor, 1987); although deterministic alteration features of gold deposits in the Cobar Basin have not been previously identified.

The key to unravelling ore fluid composition in fault-hosted quartz vein deposits like the New Occidental deposit is distinguishing between the effects of three inter-related processes (e.g. Kerrich, 1989; McCuaig and Kerrich, 1994; Leitch & Lentz, 1994):

1. **Wallrock alteration and replacement** due to interaction between ore fluids and sandstones and siltstones either side of the Great Chesney Fault, causing mobile element enrichment and depletion.

2. **Dilation** along the Great Chesney Fault and emplacement of large volumes of vein quartz into open-spaced fractures and breccias, resulting in dilution of wallrock components and increased wallrock volume.

3. **Selective mineral dissolution** associated with compressive shearing along the Great Chesney Fault. Shortening factors calculated for wallrock around the New Occidental deposit (Section 3.9) indicate potential for significant mass loss in cleavage zones surrounding the deposit.

The three processes can be distinguished by the behaviour of elements/oxides associated with mineral phases not mobilised by wallrock alteration, replacement and/or mineral dissolution. The concentration of immobile elements/oxides will not be significantly modified by wallrock alteration and replacement, whereas fault zone dilation will dilute these elements/oxides and mineral dissolution has the potential to concentrate them (e.g. Leitch & Lentz, 1994; Emsbo et al., 2003). Mobile element enrichments and depletions associated with wallrock-fluid interaction can then be determined once the effects of such volume changes have been accounted for.

Whole rock and trace element geochemical data for the ore zone and surrounding wallrocks in the New Occidental deposit has been analysed to answer the following questions:

2. **What volume changes occurred in wallrock surrounding the New Occidental deposit, either due to dissolution or mass addition associated with deformation and mineralisation processes?**

3. **What is the nature and extent of wallrock-ore fluid interaction surrounding the New Occidental deposit?** Element depletions and enrichments can be determined once the effects of volume change have been accounted for.

4. **What is the inferred composition of the New Occidental ore fluid(s) and can temporal changes in fluid composition be distinguished?** Specifically, are the discrete domains of different alteration types characterised by specific element enrichments/depletions, which can then be related to changing hydrothermal fluid composition?

5. **Can multi-element geochemistry be used to expand the exploration target size for gold deposits in the Cobar Basin?**

Previous geochemical studies of other Cobar deposits highlighted the potential for detailed whole-rock and trace-element geochemistry of the New Occidental deposit to answer these questions. Binns & Appleyard (1986) used immobile element geochemistry to establish that broad siliceous zones in the Western System of the CSA deposit formed by extensive dilational silicification. However, on the basis of systematic whole rock and trace element geochemical studies, Robertson & Taylor (1987) concluded the scale of major element depletions exceeded that expected from simple dilution by quartz. Similar studies of the New Cobar, Chesney, Peak and Queen Bee deposits (Robertson, 1974; Binns & Appleyard, 1986; Robertson & Taylor, 1987) identified extensive alkali and alkaline-earth element (Li, Na, K, Rb, Sr, Ca and Ba) depletion haloes surrounding all of the deposits studied. The depletion haloes relate to destruction of feldspar and white mica around the orebodies and, proximal to ore, an increase in chlorite. Robertson (1974) and Robertson & Taylor (1987) also documented relatively narrow zones of element enrichment around the main ore zones in the deposits, which are significantly smaller than the previously described depletion zones. Chalcophile elements including Cu, Pb, Zn, Fe, Mn, Co, Hg and Se, Sn, Bi and As are enriched. Localised K-enrichment has also been detected in the Cu-rich parts of the CSA deposit where coarse-grained hydrothermal muscovite is developed (Robertson & Taylor, 1987).

7.2 Data Collection

Core from three separate drillholes through the New Occidental deposit were selected for this study. The chosen drillholes contain representative sections of all of the principal styles of quartz veins and ore mineral assemblages. In addition, the three sampled intervals include relatively unaltered and unmineralised wallrock from both the immediate footwall and hanging wall of the New Occidental deposit beyond the limits of visible alteration and mineralisation. The wallrock samples all contain a well-developed cleavage. They are also within the extensive, albeit subtle, alteration halo detected by SWIR spectrometry around the Great Chesney Fault, and therefore contain slightly increased levels of metamorphic chlorite and white mica relative to wallrock located 200–300m from the fault (Section 5.6). Such samples were chosen to be more representative of unaltered wallrock for this study in preference to more distal wallrock samples collected beyond the subtle alteration halo detected by SWIR

spectrometry to ensure a similar protolith for altered and unaltered samples. One of the drillholes is through the centre of the deposit (NO3C), the second intersected the presently deepest known part of the deposit (NO1F) and the third intersected the upper northern margin of the deposit (NO4F). Each of the sampled intervals of drillcore represents true horizontal widths of approximately 100m (Figure 150). Detailed geological logs are also available for the chosen drillholes.

Peak Gold Mines' technicians halved the core with diamond saw and sampled one half of the core in 1-metre intervals. The resultant 4–5kg samples were submitted to Amdel Laboratories in Adelaide, South Australia where they were crushed 25mm and then ground in a mixermill to d_{95} = 110–120μm. Sample pulps were then statistically sub-sampled for assay. Sub-sample pulps on the margins of the ore zones in NO1F and NO4F were composited into 2- and 4-metre wide samples. Samples were assayed for whole rock and trace elements, including rare earth elements (REE) by a variety of analytical methods (Table 27).

Figure 150: Location of whole-rock and trace element assay traverses.

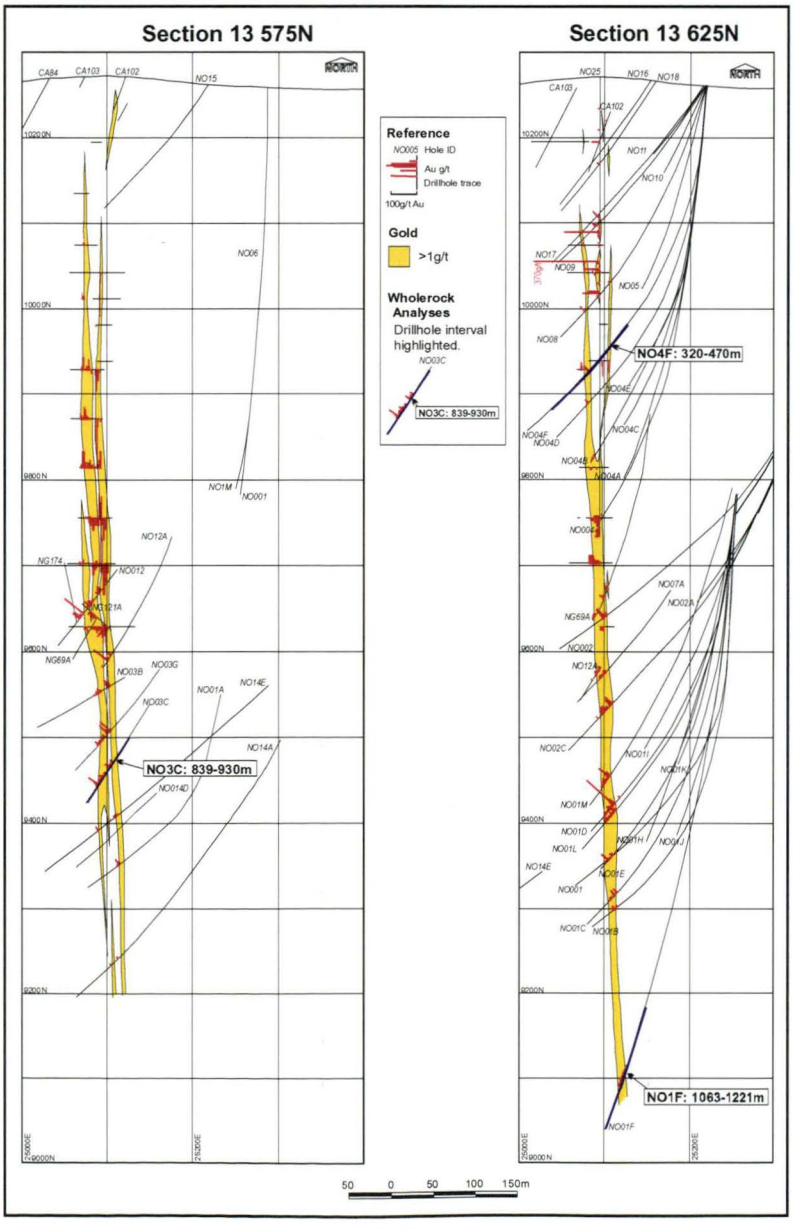

Table 27: Analytical suite for whole-rock and trace element analyses.

Analytical Technique	Assay Suite (Detection Limit)*
Fire Assay (50g)	Au (0.01)
ICP-OES (aqua regia digest)	Ag (0.5), As (1), Bi (5), Co (2), Cu (1), Fe (100), Mn (5), Pb (3), Sb (5), Zn (1)
ICP-OES (mixed acid digest including HF)	Ag (1), As (3), Sc (2), Cr (2)
Whole rock Analysis – ICPOES (whole-rock fusion)	Al_2O_3 (0.01%), CaO (0.01%), K_2O (0.01%), Fe_2O_3 (0.01%), LOI (0.01%), MgO (0.01%), MnO (0.01%), Na_2O (0.01%), P_2O_5 (0.01%), SiO_2 (0.01%), TiO_2 (0.005%), V (20)
ICP-MS (solution from whole-rock fusion)	Ba (10), Be (0.5), Bi (3), Cd (3), Co (15), Cs (3), Ga (1), Hf (1), In (0.5), Mo (2), Nb (10), Rb (0.5), Sb (1), Sn (10), Sr (5), Ta (2), Te (5), Tl (3), Th (0.5), U (0.5), W (3), Y (1), Zr (15)
Rare Earth Suite – ICP-MS (solution from whole-rock fusion)	Ce (1), Dy (0.5), Er (1), Eu (0.5), Gd (1), Ho (0.5), La (1), Lu (0.5), Nd (0.5), Pr (1), Sm (0.5), Tb (0.5), Tm (1), Yb (1)
Chemical Titration	S (0.01%), C (0.02%)
XRF	Se (1)
Detection limits in ppm unless otherwise stated.	

- Analyses below detection limit have been assigned values equal to half the detection limit

7.3 Geochemistry of Core Traverses across the New Occidental Deposit

Major and trace element distributions in all three drillhole traverses reveal consistent patterns of major and trace element increases and decreases across the ore zones in the New Occidental deposit (Figure 151 – Figure 159; sample analyses are tabulated in Appendices 9 and 10).

Hanging wall sandstones (Chesney Formation) and footwall siltstones/mudstones (Great Cobar Slate) are characterised by a relatively consistent and simple whole rock geochemistry. Wallrock is characterised by high levels of SiO_2, moderate concentrations of Al_2O_3 and Fe_2O_3 and $K_2O > CaO >> Na_2O$, which is consistent with their siliclastic and granitic provenance. Similar whole rock geochemistry of the Great Cobar Slate and Chesney Formation supports Glen's (1987a) contention that these two units share the same provenance and that the principal difference between the two is grain size.

Relative to wallrock, ore zones are characterised by:

1. Variable but usually significant increases in SiO_2, S, Au, Ag, As, Bi, Cd, Co, Cr, Cu, In, Mo, Pb, Sb, Se, W and Zn
2. Variable decreases in Al_2O_3, K_2O, TiO_2, P_2O_5, C, CaO, Ba, Be, Rare Earth Elements (REE: Ce, Dy, Er, Eu, Gd, Ho, La, Nd, Pr, Sm, Tb, Y, Yb), Cs, Ga, Hf, Nb, Rb, Sc, Sr, Ta, Th, U, V and Zr
3. Decreases in Fe_2O_3, MgO, MnO and Na_2O in the middle of the deposit and increases at the margins of the deposit.

Figure 151: Major element geochemistry of Drillhole NO1F.

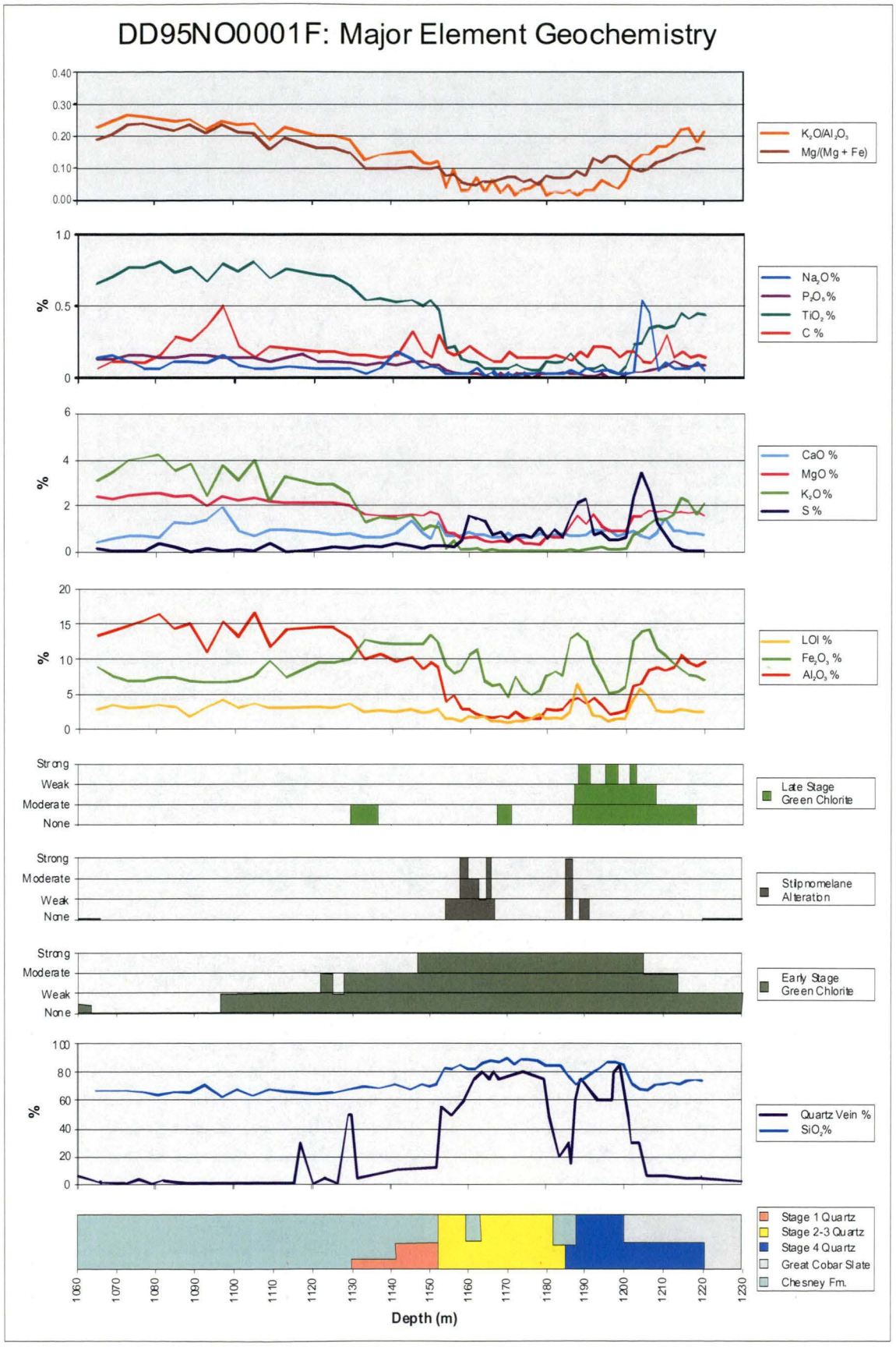

Figure 152: Major element geochemistry of Drillhole NO3C.

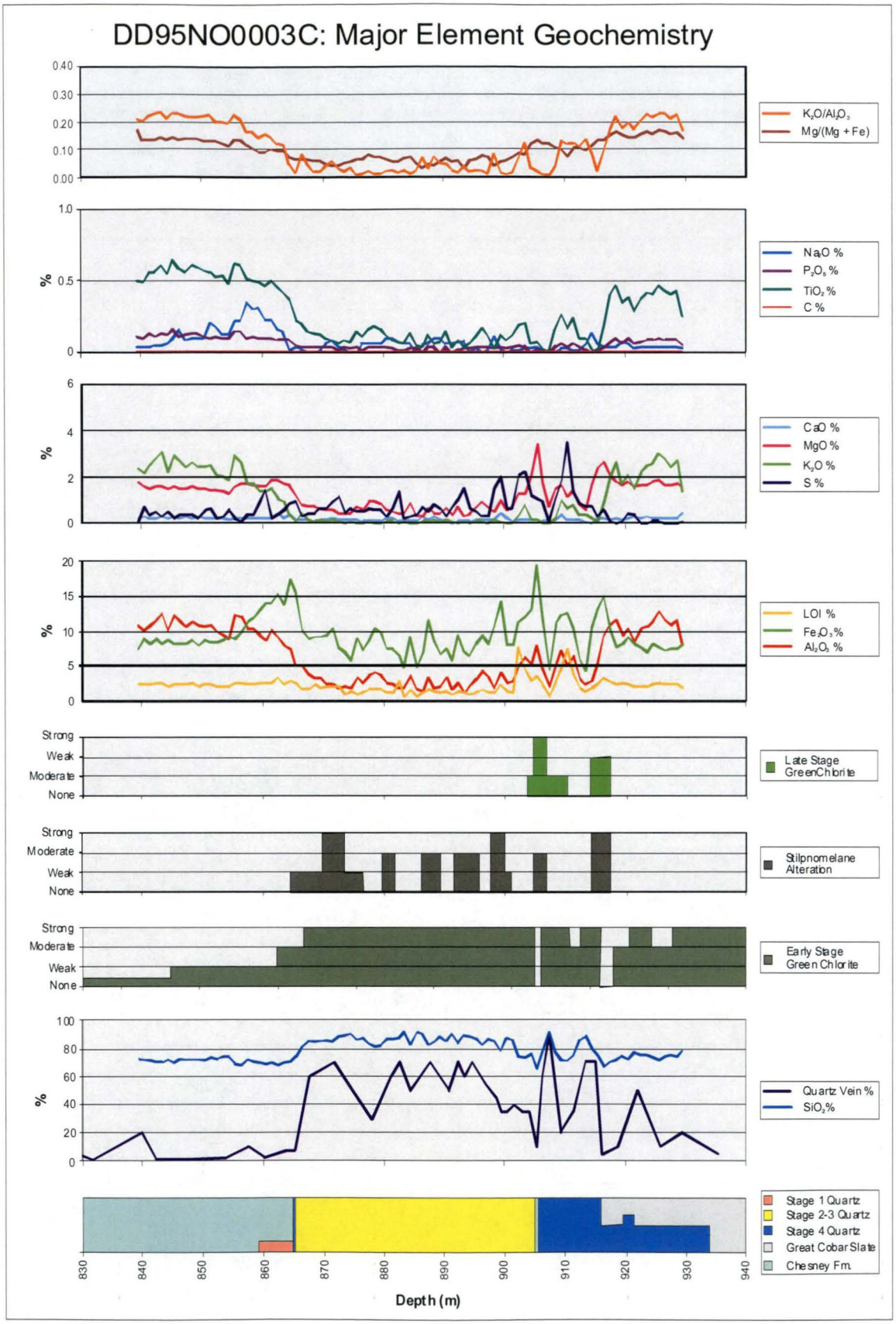

Figure 153: Major element geochemistry of Drillhole NO4F.

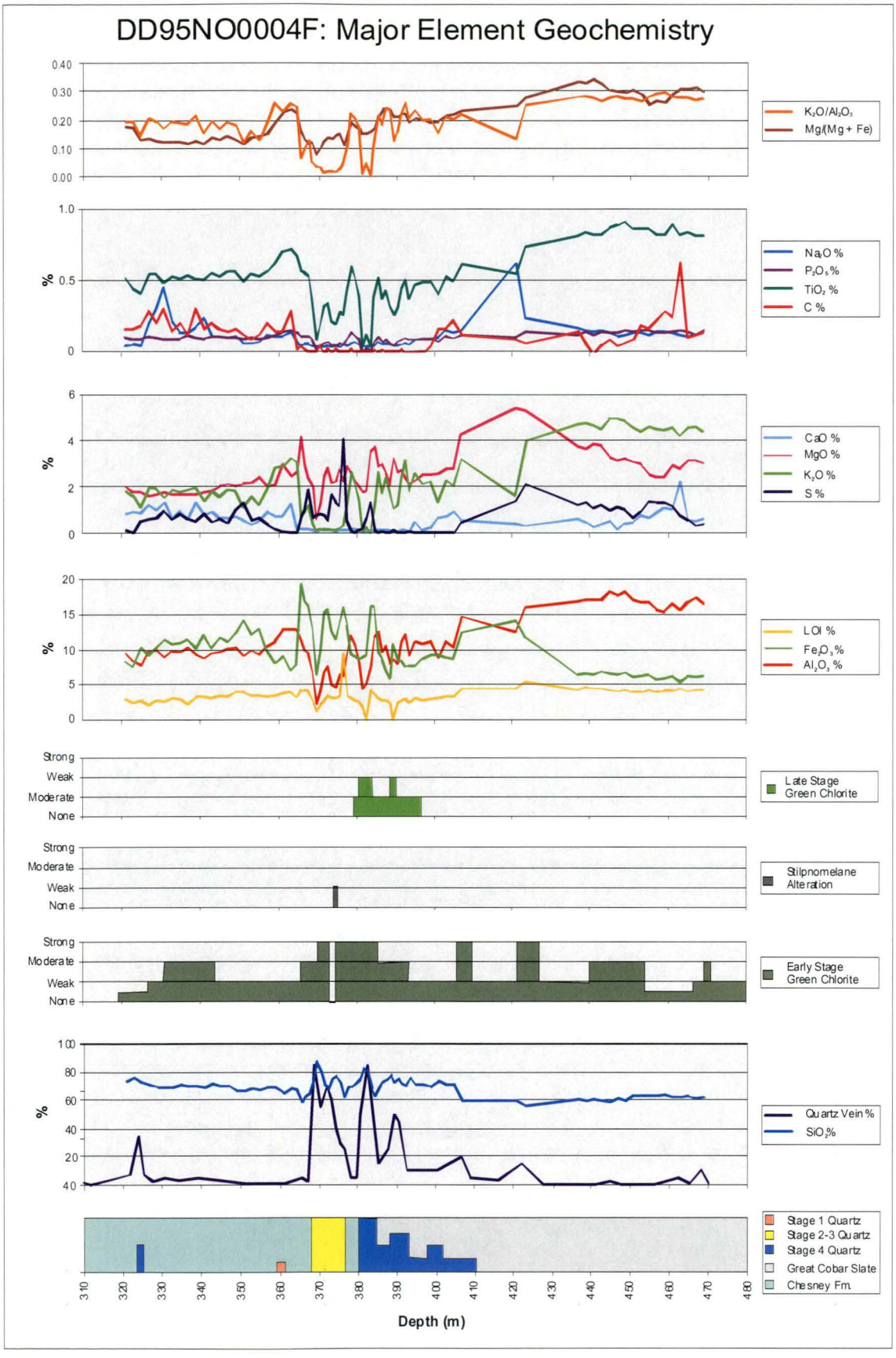

Figure 154: Trace element distributions in Drillhole NO1F.

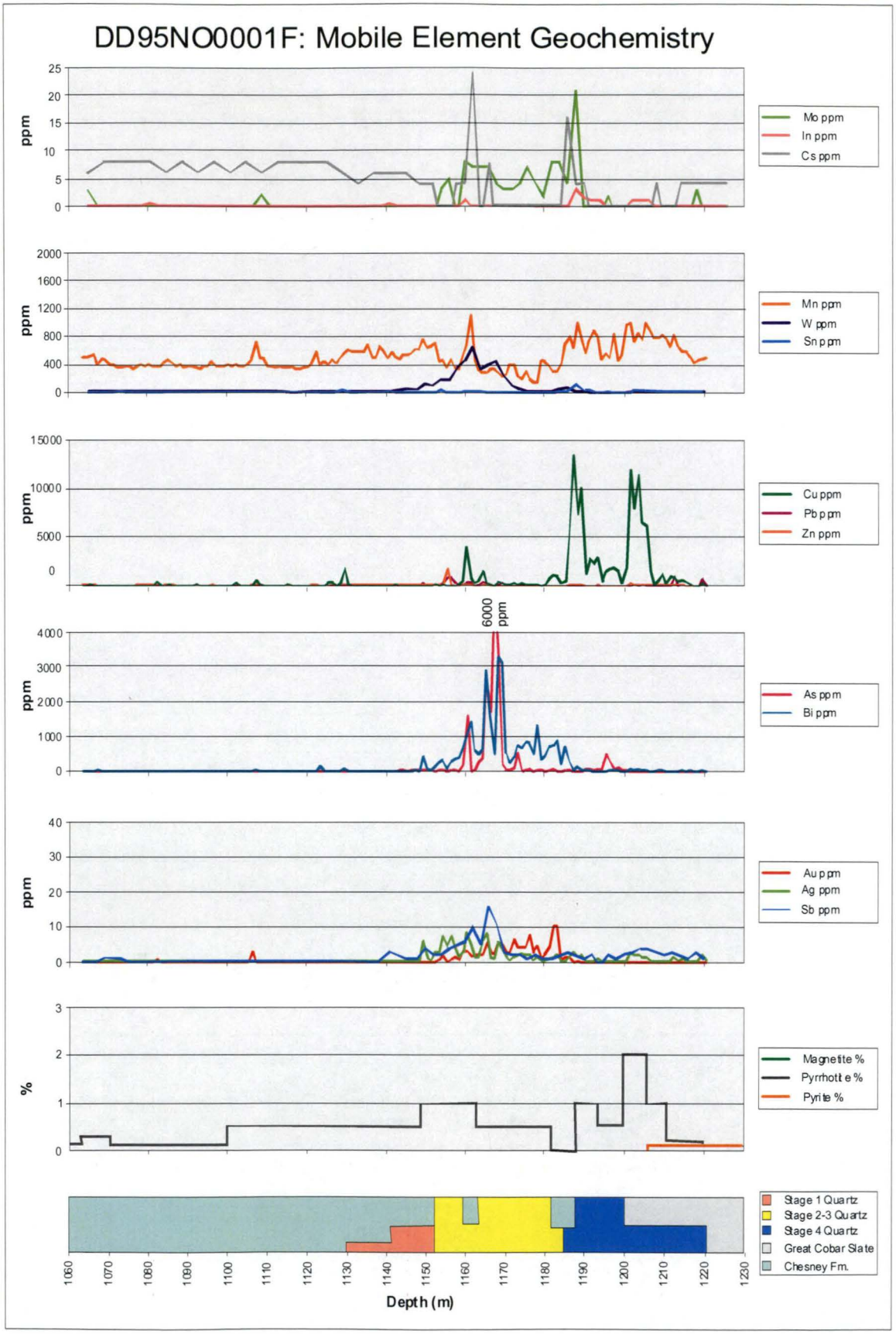

Figure 155: Trace element distributions in Drillhole NO3C.

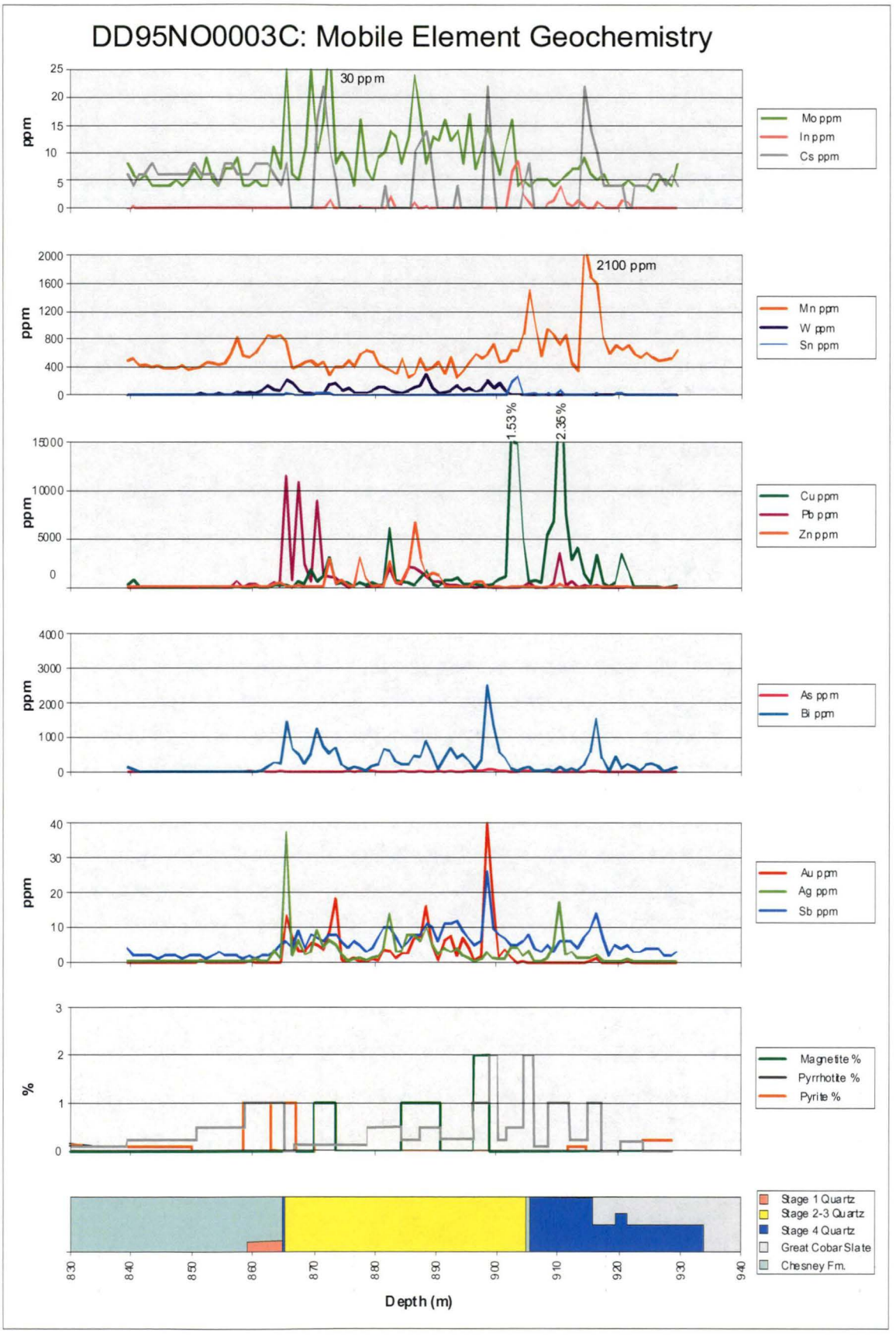

Figure 156: Trace element distributions in Drillhole NO4F.

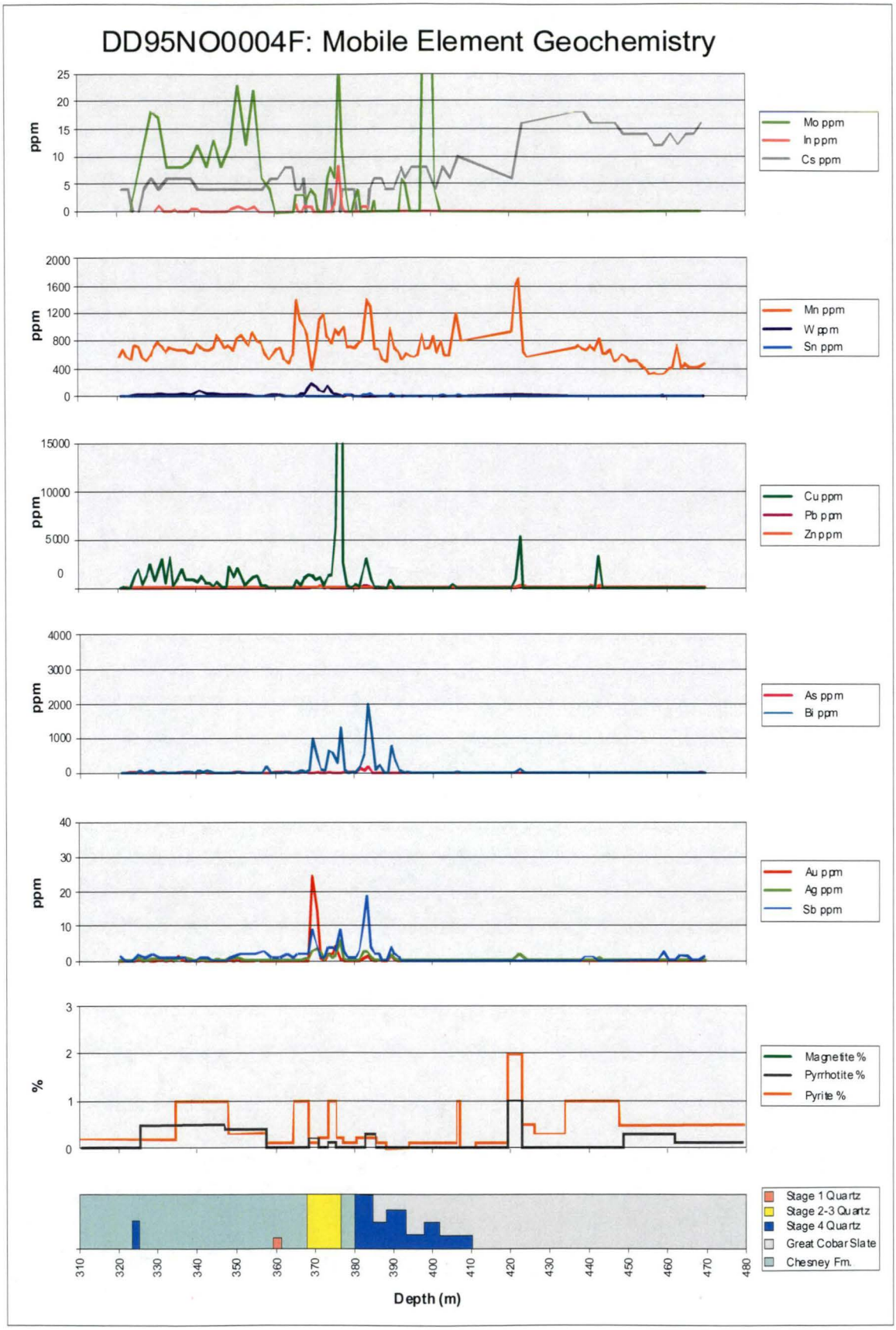

Figure 157: Trace element distributions in Drillhole NO1F.

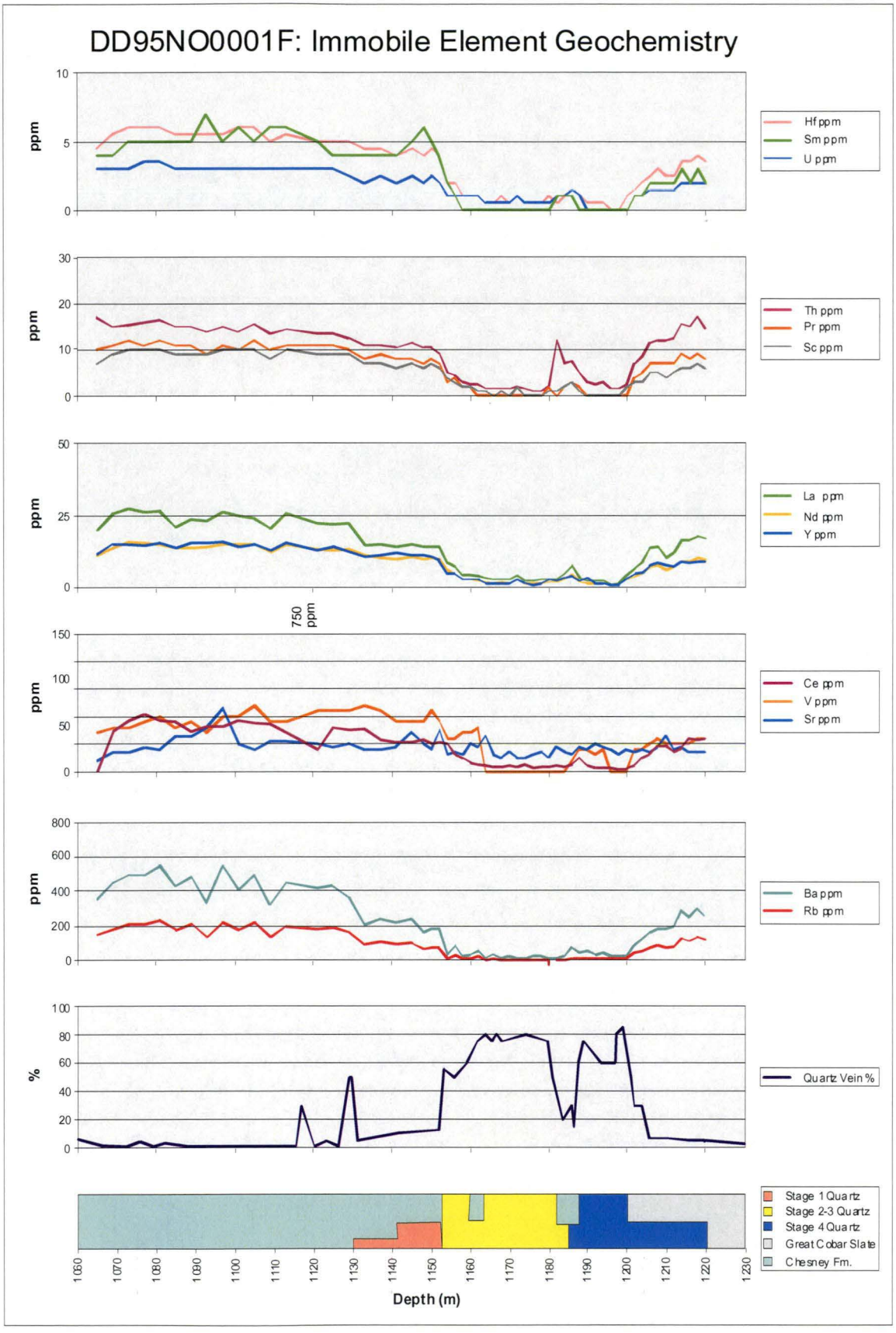

Figure 158: Trace element distributions in Drillhole NO3C.

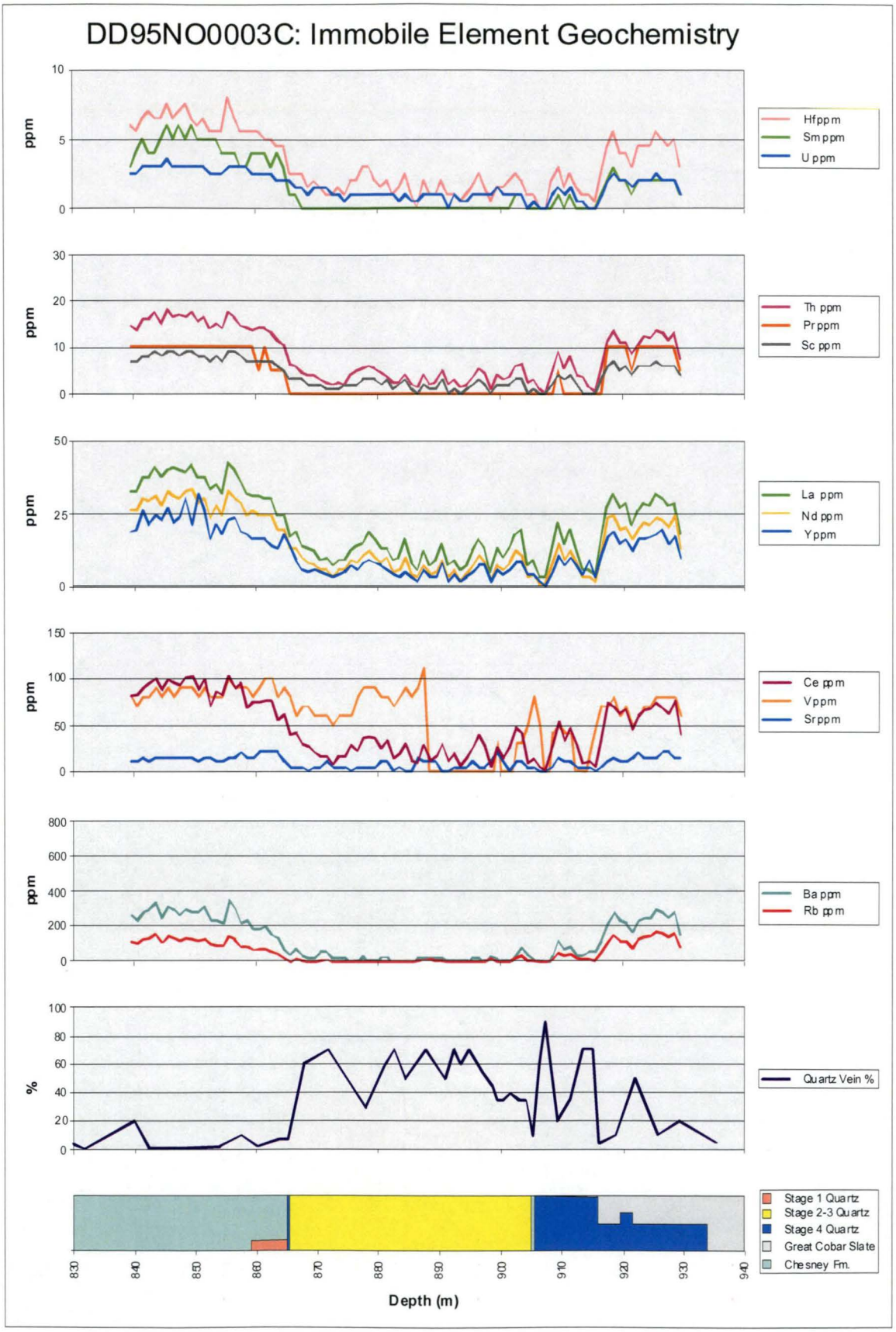

Figure 159: Trace element distributions in Drillhole NO4F.

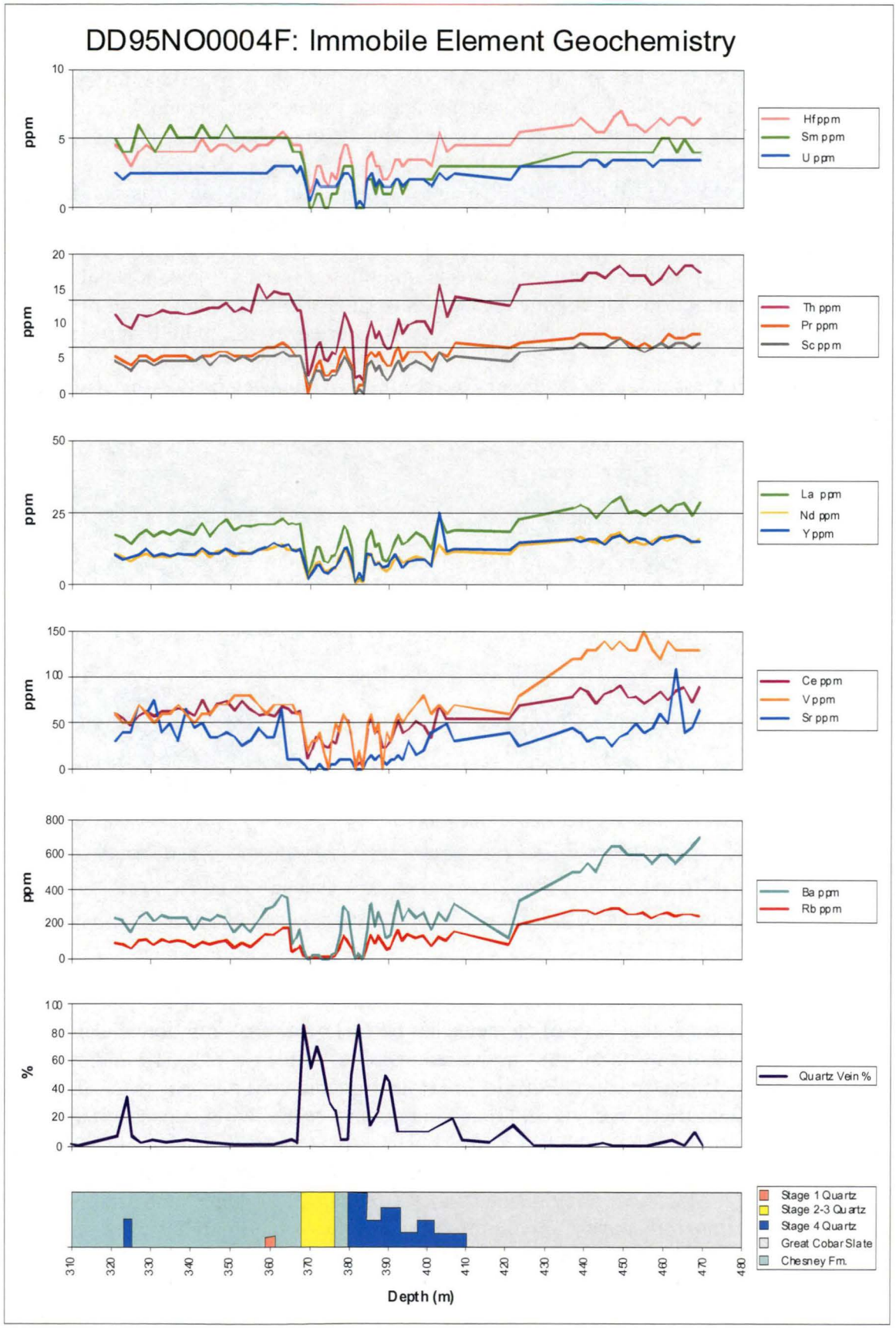

7.4 Effects of Volume Change on Wallrock Geochemistry

7.4.1 Establishing the Basis for Mass Balancing

The impact of dissolution and mass addition on mobile element geochemistry of wallrock surrounding the New Occidental deposit can be systematically determined by evaluating the distribution of immobile elements in deposit wallrock (e.g. Maclean & Barrett, 1993; McCuaig & Kerrich, 1994; Leitch & Lentz, 1994; Stanley & Madeisky, 1994). Provided such elements are immobile during deformation-induced dissolution and hydrothermal alteration and individual immobile elements have a relatively consistent concentration in unaltered (unveined) and unmineralised wallrock, it is possible to use variations in immobile elements to balance mobile element distributions for volume changes associated with deformation and/or hydrothermal alteration (Leitch & Lentz, 1994; Bierlein et al., 2000; Figure 160).

Figure 160: Mass balance calculations to account for volume changes associated with deformation and/or hydrothermal alteration.

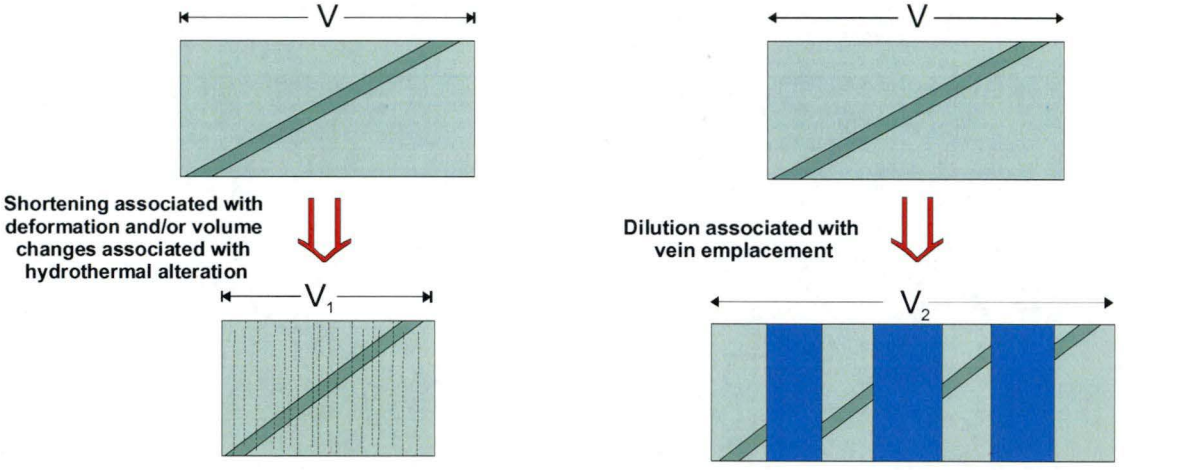

Drillcore sample (volume = V_1) containing element A (concentration = $X_{A\ Post\text{-}shortening}$)

Shortening Factor = $(V - V_1) / V$%

Shortening concentrates immobile elements:

$X_{A\ Pre\text{-}shortening} = X_{A\ Post\text{-}shortening} / (1 - \%\ Shortening)$

Drillcore sample (volume = V_2) containing element A (concentration = $X_{A\ Post\text{-}veining}$)

% Veining = $(V_2 - V) / V_2$ %

Vein emplacement dilutes immobile elements:

$X_{A\ Pre\text{-}veining} = X_{A\ Post\text{-}veining} / (1 - \%\ Veining)$

A relatively consistent suite of elements has been shown to be immobile during hydrothermal alteration in volcanic-hosted massive sulfide deposits (Kranidiotis & MacLean, 1987; Maclean & Barrett; 1993), in orogenic gold deposits (McCuaig & Kerrich, 1994; Bierlein et al., 2000) and in intrusive-related gold deposits (Titley, 1994). The suite of immobile elements consistently comprises Al_2O_3, TiO_2, P_2O_5, Zr, Th, Y, Nb, Ga, Hf and REE. Binns and Appleyard (1986) suggested that Al_2O_3, TiO_2, total Fe, Mg, Mn, V, Cr and Zn, and to a lesser extent, H, P, Ni, Zr and Y were essentially immobile during alteration at the CSA deposit, although Robertson & Taylor (1987) found TiO_2 was locally depleted in certain parts of the orebody.

Most numerical mass balance modelling of alteration systematics has been undertaken with igneous protoliths where immobile element ratios (e.g. Al_2O_3/ TiO_2, TiO_2/Zr, Zr/Y and La/Yb) constrain protolith composition (e.g. Maclean & Barrett; 1993).

Protolith in the New Occidental deposit comprises sandstones in the deposit hanging wall (Chesney Formation) and siltstones/mudstones (Great Cobar Slate) in the footwall of the deposit. Most of the immobile elements/oxides quoted above, with the exception of Al_2O_3, are contained in resistive heavy minerals in deposit wallrock, including ilmenite ($FeTiO_2$), monazite ($[Ce,La,Y,Th]PO_4$), zircon ($ZrSiO_4$) and minor rutile (TiO_2) and apatite ($Ca_5[PO_4]_3[F,Cl,OH]$) (Reynolds, 1998), which will vary in concentration as a result of gravity processes during sedimentation. Comparisons of concentrations of potentially immobile oxides/elements in the least altered and mineralised wallrock in footwall and hanging wall of each drillhole, after applying a correction for quartz vein content (Table 28), show oxide/element concentrations generally vary in a non-systematic way between drillholes and between footwall and hanging wall, but are relatively consistent within each domain (Figure 157 – Figure 159). For example, Al_2O_3 content of hanging wall sandstones increases with depth (NO4F → NO3C → NO1F), which may indicate stratigraphically lower sandstones are less mature (contain more feldspar), whereas the Al_2O_3 content of footwall siltstones/mudstones decreases with depth, which may indicate increasing siltstone (quartz) content with depth in the Great Cobar Slate.

Table 28: Immobile element geochemistry of "least altered" wallrock (corrected for quartz vein content using the approach outlined in Figure 160).

	Average NO1F H'Wall	Average NO1F F'Wall	Average NO3C H'Wall	Average NO3C F'Wall	Average NO4F H'Wall	Average NO4F F'Wall
# Samples	15	5	15	11	21	18
% Qtz veins	1.3	5.8	3.1	10 0	2.3	0.7
Al_2O_3%	14.5	10.1	11 6	12 1	10.5	16.8
Hf (ppm)	5.3	2.5	4.9	2.2	5.2	4.1
P_2O_5%	0.14	0.10	0.13	0.09	0.11	0.14
Sc (ppm)	11.1	8.7	10.3	10.1	8.8	12.0
TiO_2%	0.76	0.44	0.59	0.44	0.57	0.84
Th (ppm)	15	16	17	13	19	26
U (ppm)	3.1	2.0	3.1	2.2	2.7	3.4
Y (ppm)	30	18	25	18	24	32
Zr (ppm)	216	89	140	70	194	162
Ti/Zr	22	30	26	38	18	31
REE:						
Ce (ppm)	87	58	65	49	66	81
Dy (ppm)	4.3	3.0	4.1	3.1	3 5	4.8
Er (ppm)	2.0	1.5	2.1	1.4	1 9	2.2
Eu (ppm)	1.5	1.1	1.5	1.1	1.6	1 7
Gd (ppm)	4.8	3.0	4.5	3.1	3.9	5.3
Ho (ppm)	1.0	0.5	0.8	0.4	0 8	1.1
La (ppm)	49	34	40	31	41	53
Nd (ppm)	29	19	31	24	23	32
Pr (ppm)	9.6	6.4	8.6	6.5	7.7	10.4
Sm (ppm)	5.6	3 6	6.9	5.0	4.5	6.2
Yb (ppm)	2.3	1 5	2.6	1.3	2.0	2.5

Likewise, ratios of immobile elements (TiO_2/Th, TiO_2/Zr, P_2O_5/Th, Ce/La) within each wallrock and footwall domain, inclusive of altered and mineralised zones (Figure 161a–d), are relatively consistent within each domain but differ between domains.

For example, ilmenite/monazite ratios (based on higher TiO_2/Th ratios) are highest in NO1F hanging wall sandstones and decrease up-sequence (NO3C to NO4F). NO1F hanging wall sandstones are also characterised by significantly lower Ce/La ratios (within monazite) compared to other hanging wall domains. In general, hanging wall domains (Chesney Formation) contains more zircon than footwall domains (Great Cobar Slate).

Figure 161: Two-element variation diagrams for selected whole rock and trace elements associated with immobile phases in the New Occidental deposit.

(a) TiO_2-Th

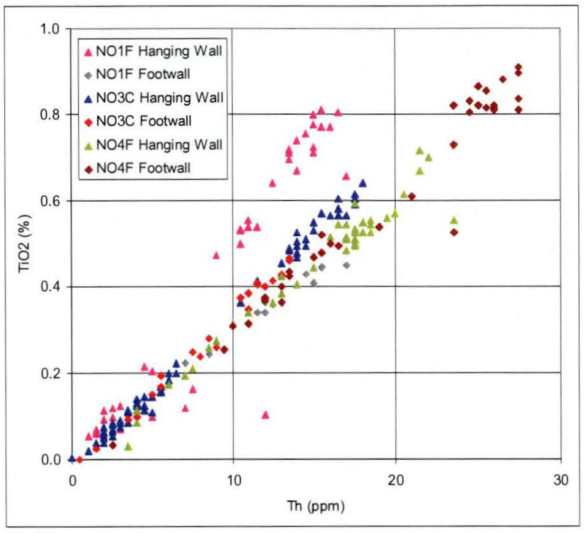

(b) TiO_2-P_2O_5

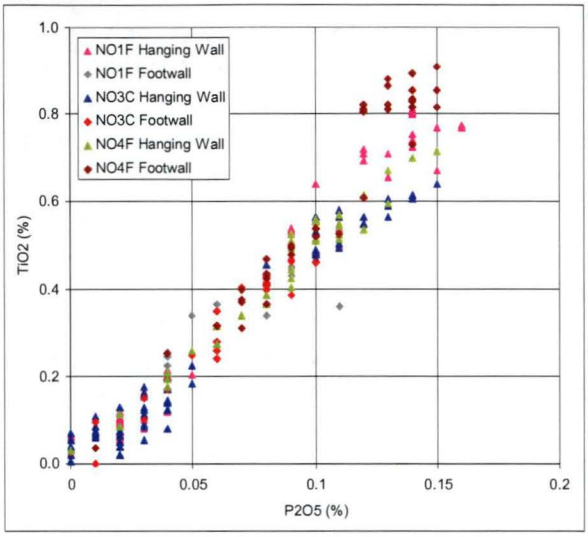

(c) TiO_2-Th

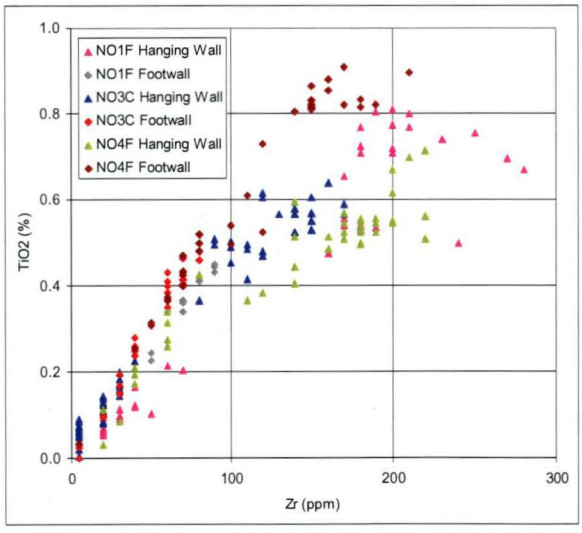

(d) Ce-La

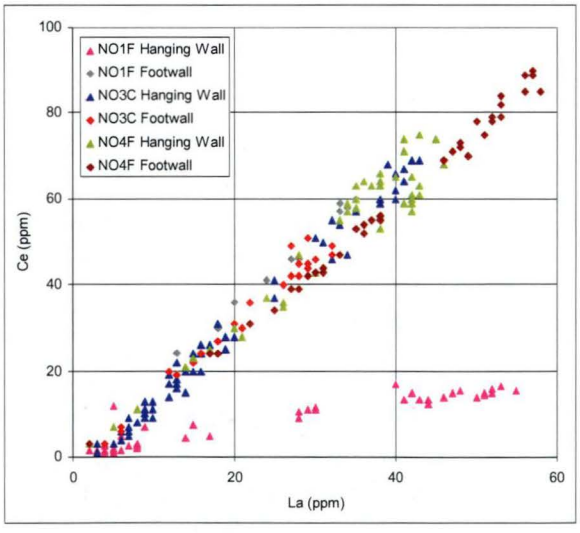

Mass balancing of New Occidental deposit geochemistry is feasible because concentrations of immobile oxides/elements in least altered wallrock are relatively consistent within each wallrock domain, as are immobile element ratios. However, the mass balancing must be based on protolith compositions established for the respective footwall and hanging wall domains in each drillcore traverse. It also highlights the importance of correctly identifying protolith in the highly altered core of the deposit.

7.4.2 Calculation of Correction and Volume Factors

The Gresens method (Gresens, 1967) and its derivatives (e.g. Leith & Lentz, 1994) have been widely used as the basis for mass balance constraints of alteration systems, particularly in unveined rock (Leith & Lentz, 1994). The basis of the standard Gresens method is Gresens's equation:

$$X_n = W^B - W^A = w * (F_v * X^B * S^B / S^A - X^A) \text{ where:}$$

X_n = change in weight proportion of component n

W^B, W^A = weights of component n in parent rock A and altered rock B

w = initial weight of parent rock

F_V = Volume Factor, the ratio of volume of altered rock (V^B) to parent rock (V^A)

X^B, X^A = weight proportions of component n in parent rock A and altered rock B, used directly from chemical analyses

S^B, S^A = specific gravities of parent rock A and altered rock B

Rearrangement of Gresens' equation (Leith & Lentz, 1994) yields:

$$F_V = V^B / V^A = M^B / M^A * S^A / S^B \text{ where:}$$

M^B, M^A = total masses of parent rock A and altered rock B

Where change in specific gravity from parent rock to altered rock is minor (<5%), the equation is further simplified and F_V may be estimated by the inverse immobile element weight ratio (Leith & Lentz, 1994):

$$F_V = M^B / M^A = X^A{}_n / X^B{}_n = R^{A/B} \text{ where:}$$

$R^{A/B}$ = Correction Factor, the ratio of weight proportions of a component (element/oxide) in parent rock A and altered rock B, used directly from chemical analyses

Volume increases are indicated by factors >1 whilst volume decreases give factors <1. However, because New Occidental ore contains appreciable volumes of dilutant vein material (up to 100%) and F_V values are much greater than unity, a modified Gresens approach has been used in this study. Modified Volume and Correction Factors used herein are the inverse of those terms used by Gresens (1967):

$$F_V^* = V^A / V^B \quad \text{and} \quad R^{A/B*} = X^B{}_{Element} / X^A{}_{Element}$$

Modified factors <1 indicate a volume increase whereas factors >1 indicate volume reduction.

Modified Correction Factors ($R^{A/B*}$) were calculated for the previously identified suite of potential immobile oxides/elements in the New Occidental deposit:

1. **Al_2O_3** (metamorphic sericite and chlorite)
2. **TiO_2** (rutile, ilmenite)
3. **U-REE-Th** (monazite)

4. **P_2O_5** (monazite and apatite)

5. **Zr-Hf** (zircon)

Of the REE elements, only Ce, Dy, La, Nd, Pr, Sm and Y exist in sufficient concentration to be used to define Correction Factors.

Each of the three drillhole traverses was subdivided into hanging wall and footwall domains based on the predominant composition of breccia fragments. Modified correction factors were then calculated for each the 13 immobile elements in the three drillhole traverses from the ratio of element concentration and average concentration of the respective immobile element in the "least altered" sections of each protolith domain (shown in Table 28):

$$R^{A/B^{*}\,(Sample\ Interval)}{}_{Element} = X^{B\,(Sample\ Interval)}{}_{Element} / X^{A\,(Protolith\ Domain)}{}_{Element}$$

Specific gravity (SG) measurements of diamond drillcore from the New Occidental deposit (Peak Gold Mines data; Table 29) indicate subtle increases in rock mass density around the deposit that are partly due to Fe-chlorite (SG = 3.0 – 3.1) replacement of metamorphic muscovite (SG = 2.8 – 2.9) but also to addition of various sulfide minerals (SG = 4.0 – 5.5). The data also indicates the strongly quartz-veined ore zones have a lower SG than wallrock, attributable to the lower density of quartz (SG = 2.65) although, again, the relative change in rock mass density is very small.

Table 29: Specific Gravity data for principal rock-types in the New Occidental deposit (Peak Gold Mines data).

Domain	Median Specific Gravity	Change relative to Unaltered Wallrock
Chesney Formation: unmineralised and unaltered interbedded sandstones/siltstones	2.78 – 2.80	
Altered Chesney Formation: moderate-strongly Fe-chlorite-altered weakly veined (<5% quartz veins) sandstones/siltstones	2.80 – 2.81	+1%
Magnetite-mineralised Chesney Formation: strongly Fe-chlorite-altered and magnetite-quartz veined (5–10%) sandstones/siltstones	2.81 – 2.85	+2%
Quartz Breccia: intense quartz-chlorite/stilpnomelane vein breccia (>80% quartz) with minor (<5%) sulfides and wallrock fragments (<10%)	2.71 – 2.75	-2%
Sulfide-mineralised Quartz Breccia: intense quartz-chlorite vein breccia (>50% quartz) with base metal sulfides (>5%) and wallrock fragments (<50%)	2.85 – 3.00	+3–8%
Great Cobar Slate: weakly altered siltstones/mudstones	2.78 – 2 80	

As a consequence, the average of the 13 correction factors calculated for each sample interval can be assumed to be equivalent to the modified Volume Factor (F_V^*) for each sample interval:

$$F_V^{*\,(Sample\ Interval)} = Average\ (R^{A/B^{*}\,(Sample\ Interval)}{}_{Al_2O_3} + R^{A/B^{*}\,(Sample\ Interval)}{}_{TiO_2} + R^{A/B^{*}\,(Sample\ Interval)}{}_{Ce} + R^{A/B^{*}\,(Sample\ Interval)}{}_{Dy} + etc)$$

A worked example using two sample intervals in drillhole NO1F shows how the modified Correction Factor and Volume Factor for each sample interval are calculated:

	Al_2O_3 %	Ce ppm	Dy ppm	La ppm	Nd ppm	P_2O_5 %	Pr ppm	Sm ppm	Th ppm	TiO_2 %	U ppm	Y ppm	Zr ppm	Modified Volume Factor
DD95NO1F: 1083–1087m	14 3	73	4	42	27	0.14	9	5.5	15	0.725	3	27	180	
Average NO1F: H'wall Protolith	14 5	87	4	49	29	0 14	10	5 6	15	0 757	3	30	216	
Modified Correction Factor	0 99	0 84	0 92	0 86	0.93	0.99	0 94	0.97	1.00	0 96	0.96	0.91	0 83	**0.93**
DD95NO1F: 1163–1165m	1.9	8	0	6	4	0 01	1	0 5	2	0.065	1	3	20	
Average NO1F: H'wall Protolith	14 5	87	4	49	29	0 14	10	5 6	15	0 757	3	30	216	
Modified Correction Factor	0 13	0.09	0.00	0.12	0 12	0 07	0 10	0 09	0.10	0.09	0.16	0 10	0.09	**0.10**

Down-the-hole distributions of individual Correction Factors and averaged Volume Factors in each if three drillholes are similar (e.g. NO1F; Figure 162) and consistently <1 in the ore zones, indicating the suite of immobile oxides/elements responded relatively consistently to the volume increases associated with ore formation in each drillhole. Calculated Volume Factors for the different ore zones indicate that volume increase is substantial, particularly in the middle of the ore zones where modified Volume Factors are usually <0.2 (indicating >8-fold volume increase). The consistent profiles for the suite of 13 chosen immobile elements (Figure 162) provides confidence the suite is immobile and can be used to mass balance mobile element geochemistry in the deposit. The use of 13 immobile elements in calculating an averaged Volume Factor has the added advantage of minimising bias from an individual element/oxide that may not be completely immobile. In addition, the suite of immobile elements is sourced from several different resistive minerals. Where elements exhibit different "Correction Factor" profiles (e.g. Th and Ba in NO1F; Figure 162) to the suite of immobile elements, enrichment/depletion of that element is most likely indicated.

Figure 162: Modified Volume Factors (F_V^*) calculated from Correction Factors ($R^{A/B*}$) for Drillhole NO1F.

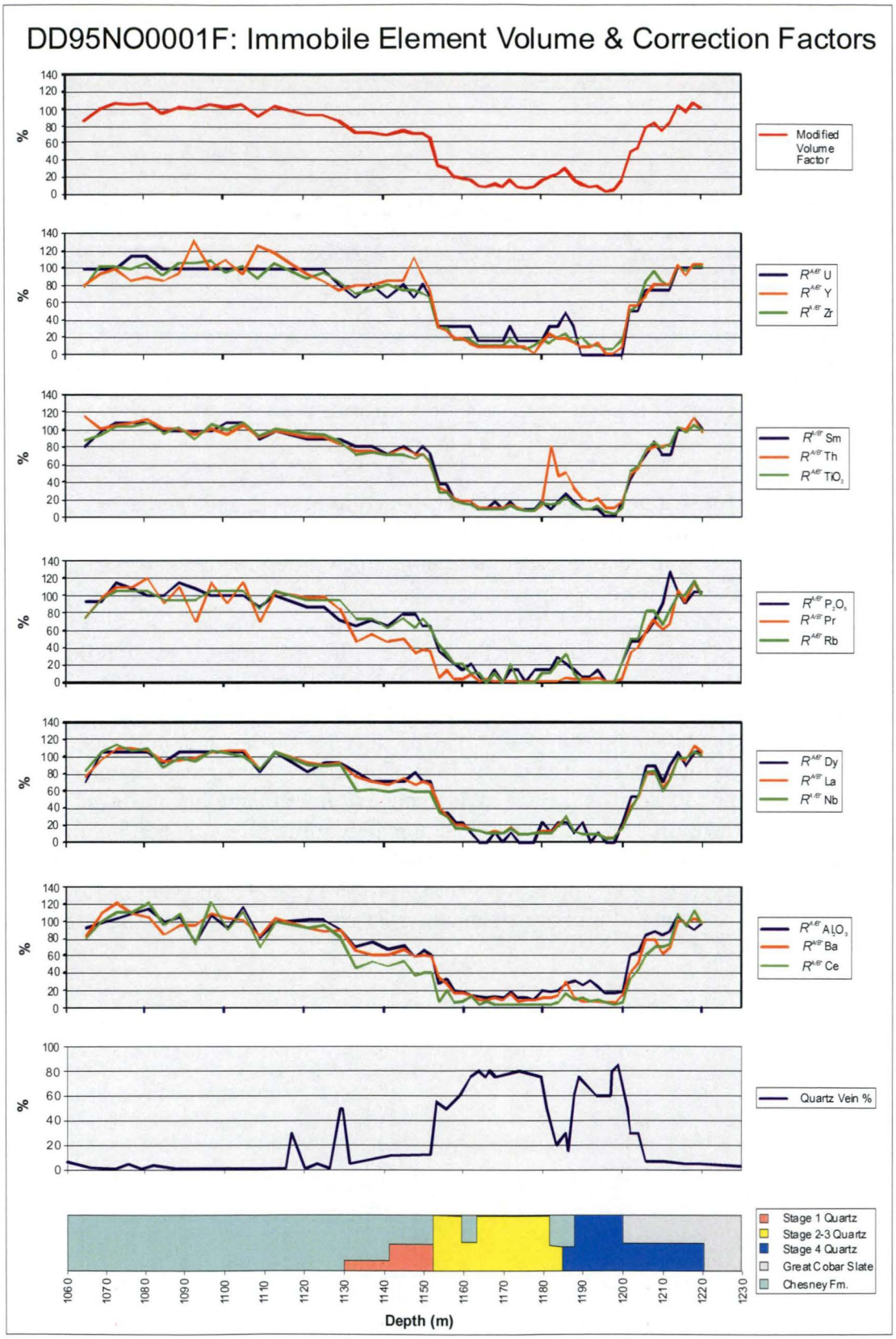

7.4.3 Cause of Volume Changes within the New Occidental Deposit

The extent of volume change associated with the ore zone in each drillhole is determined by summing the Volume Factors (F_V^*) in each drillhole traverse according to the formula:

$$Volume\ Change_{\ True\ Thickness} = [\Sigma\ (1 - F_V^{*(Sample\ Interval)}) * Thickness^{(Sample\ Interval)}] * cosine\ (drillhole\ inclination)$$

The magnitude of the volume changes, which is consistently positive ($F_V^* < 1$), is greatest in the centre of the New Occidental deposit (NO3C) and diminishes towards the deposit margins (NO1F and NO4F) (Table 30), consistent with previous interpretations of the loci of maximum dilation during formation of the New Occidental deposit (Section 4.3.7).

Table 30: Calculation of true thickness of volume change associated with ore zones

Drillhole	Interval Thickness (m)	Down-the-hole Volume Change (m)	Drillhole Dip (Degrees)	True Thickness of Volume Change (m)
NO1F	154	+54.2	-71	+17.7
NO3C	91	+44.2	-52	+27.2
NO4F	127	+23.1	-46	+16.0

The first step to unravelling the cause(s) of the observed volume changes associated with formation of the New Occidental deposit is to determine the component of volume change attributable to dilation associated with vein emplacement. Volume Factors exhibit a strong inverse correlation with volume of quartz veins (e.g. Figure 162) and SiO_2 content in each of the drillhole traverses. Comparison of the relative volume of dilutant ($1 - F_V^*$) % and vein quartz in each of the drillhole traverses (Figure 163) indicates most, if not all, volume change is the result of vein emplacement, especially when the effect of non-quartz vein minerals is considered. Quartz veins in the New Occidental deposit contain appreciable non-quartz minerals including chlorite, stilpnomelane and sulfides, which increases the total volume change attributable to vein emplacement by as much as 30–40%. A small component of the volume change (up to 7%) may be attributed to rock mass density changes associated with quartz veining, wallrock alteration and sulfides associated with deposit formation.

The greatest volume change coincides with zones of Stage 2–3 quartz vein breccias (Table 31). Lesser, but still significant, dilation corresponds to the Stage 4 quartz vein breccia in the footwall of the deposit. In all drillholes, zones of Stage 1 quartz veins are characterised by relatively minor volume increases. The effects of dilation, as measured by Volume Factors < 1 (Figure 162) extends 20–50m beyond the main zone of mineralisation, indicating that even small-scale quartz veins surrounding the deposit formed by infilling dilated fractures/slip planes, rather than as "sweat-out" veins.

Figure 163: Relationship between volume change and quartz veining.

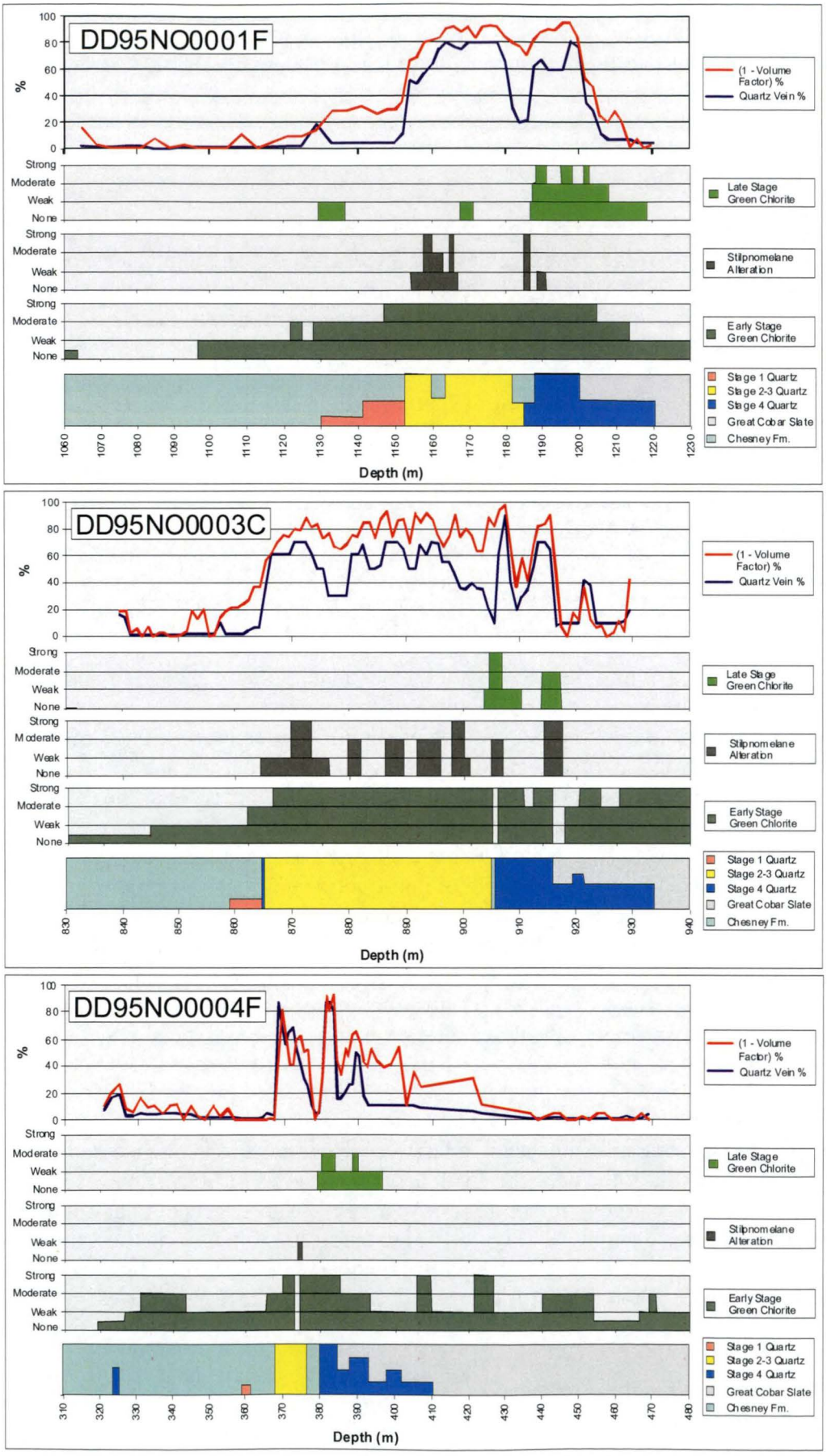

Table 31: Breakdown of volume changes by quartz vein domain.

Domain	Average Quartz Vein Volume (%)	Average Volume Change (%)	True Horizontal Thickness of Volume Change (m)	Total True Horizontal Thickness of Volume Change (m)
NO1F Stage 1	7.6	27.9	2.3	**17.7m**
NO1F Stage 2–3	62.6	84.1	8.7	
NO1F Stage 4	41.8	63.7	5.8	
NO3C Stage 1	4.6	24.8	1.2	**27.2m**
NO3C Stage 2–3	54.5	77.9	17.7	
NO3C Stage 4	42.8	70.8	6.5	
NO4F Stage 1	1.6	0.2	0.0	**16.0m**
NO4F Stage 2–3	49.5	51.7	3.4	
NO4F Stage 4	26.5	47.9	9.5	

Mass balancing of immobile elements/oxides has not identified volume decreases (concentrations of immobile elements) that would highlight mineral dissolution associated with wallrock shortening. This may be because the sample traverses did not extend beyond the zones of strong cleavage development surrounding the New Occidental deposit – that is, the degree of shortening/mineral dissolution is similar in "least altered" wallrock and strongly altered and mineralised wallrock within ore zones.

7.5 Element Enrichments and Depletions in the New Occidental Deposit

7.5.1 Correcting Mobile Element Concentrations for Volume Change

The modified Volume Factors calculated for each drillhole interval have been used to correct the concentration of the remaining elements/oxides in each of the drillhole traverses for the effects of volume change:

$$X^{B\,(Sample\ Interval)}{}_{rc} = X^{B\,(Sample\ Interval)} * F_V{}^{*(Sample\ Interval)} \text{ where:}$$

$X^B rc$ = concentration of element n recalculated for volume change.

Recalculated concentrations ($X^B rc$) of major elements/oxides in the three drillhole traverses across the New Occidental deposit (Figure 164 – Figure 166) reveal markedly different distributions than the equivalent raw (uncorrected) distributions (c.f. Figure 151 – Figure 159), confirming volume increases associated with quart vein deposition has had a significant impact on mobile element concentrations. The corrected element/oxide distributions in each of the three drillhole traverses exhibit similar patterns of depletion and enrichment within the various quartz vein domains, which suggests element/oxide depletion and enrichment changed systematically within the deposit through time. This is best demonstrated by comparing average recalculated concentrations of mobile elements for the different quartz vein domains, which were determined by first calculating average $X^B rc$ values for the three quartz vein domains in each drillhole and then averaging those values (Table 32).

Figure 164: Corrected Major and Trace Elements for Drillhole NO1F.

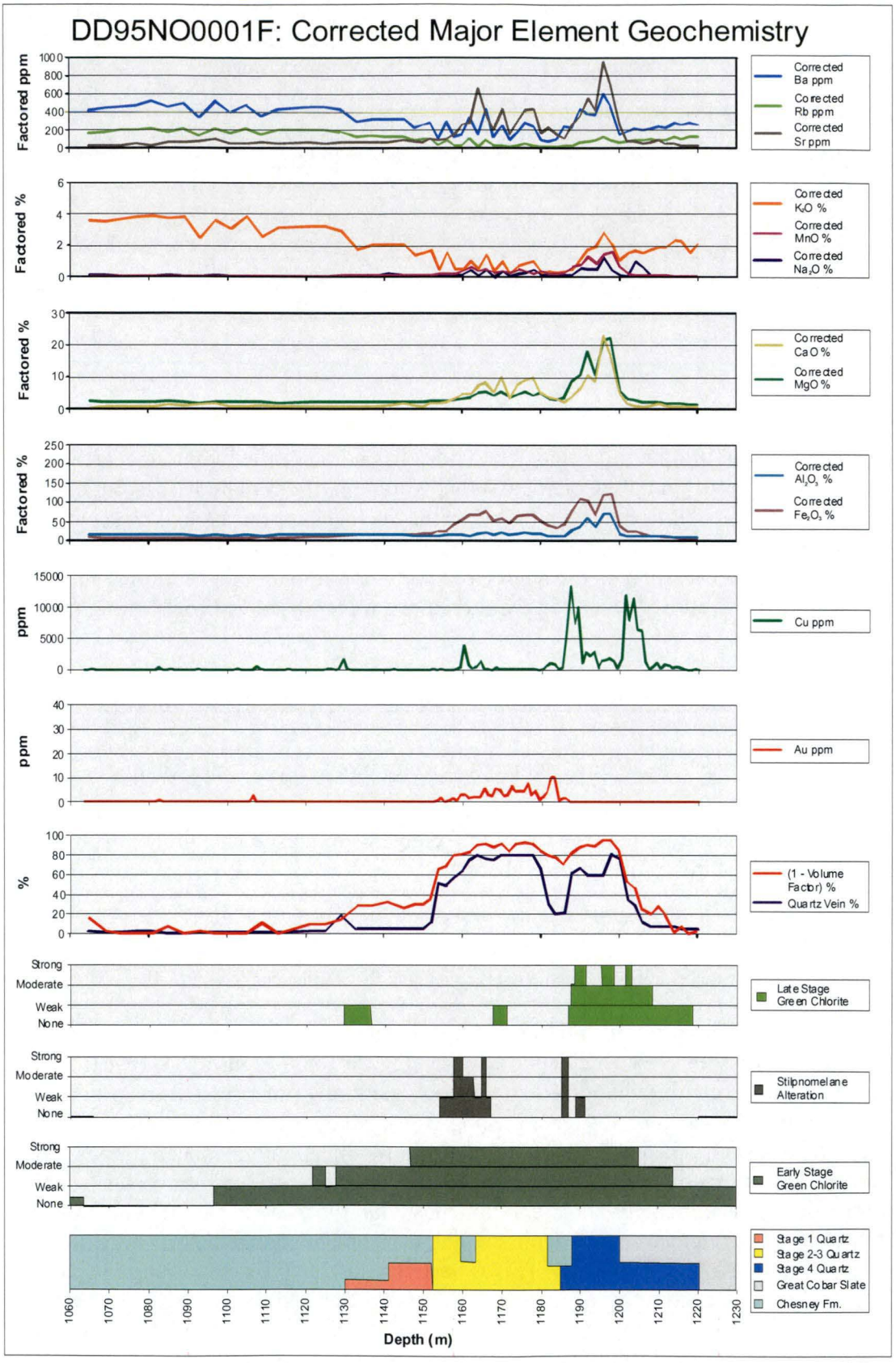

Figure 165: Corrected Major and Trace Elements for Drillhole NO3C.

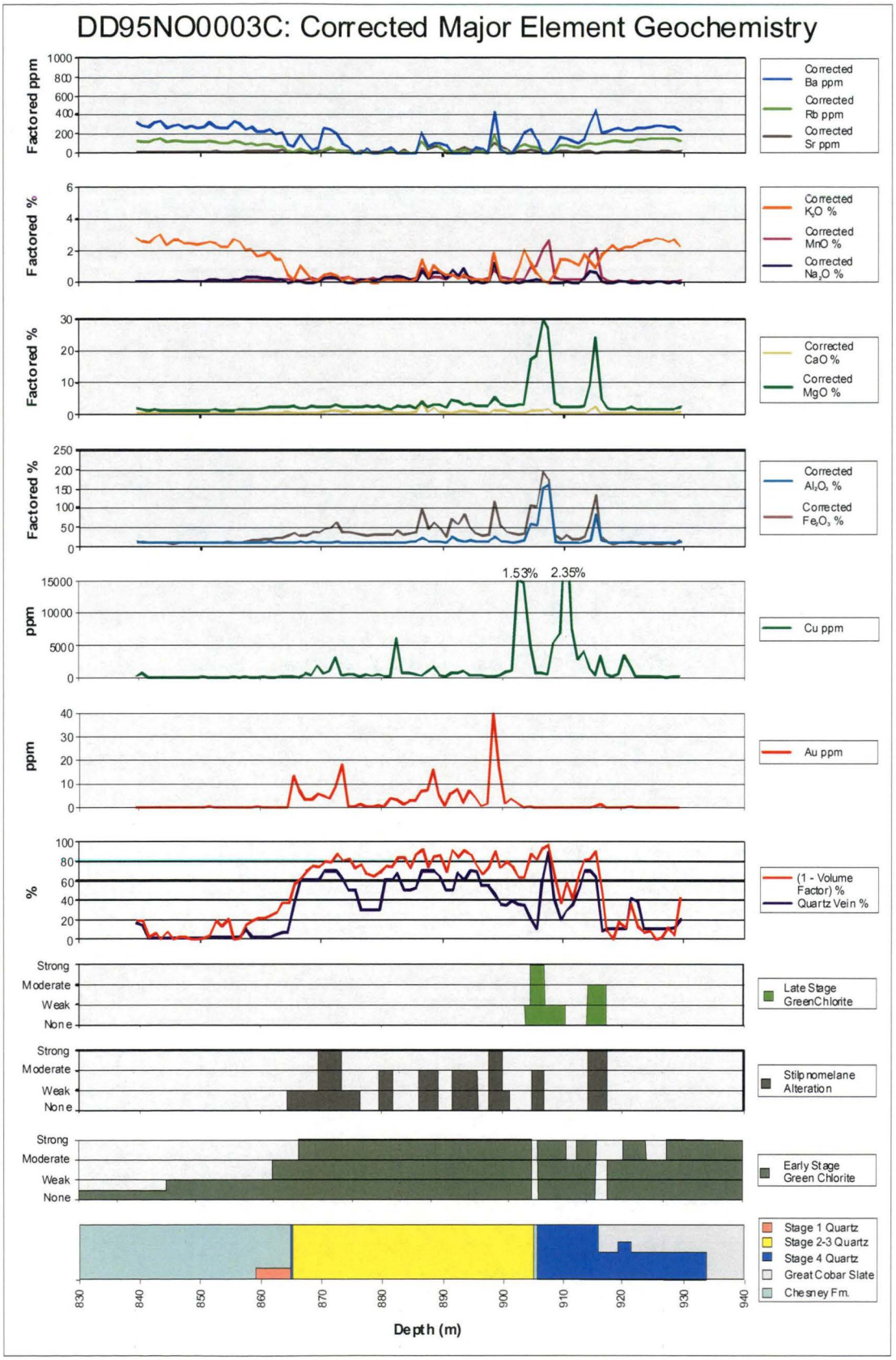

Figure 166: Corrected Major and Trace Elements for Drillhole NO4F.

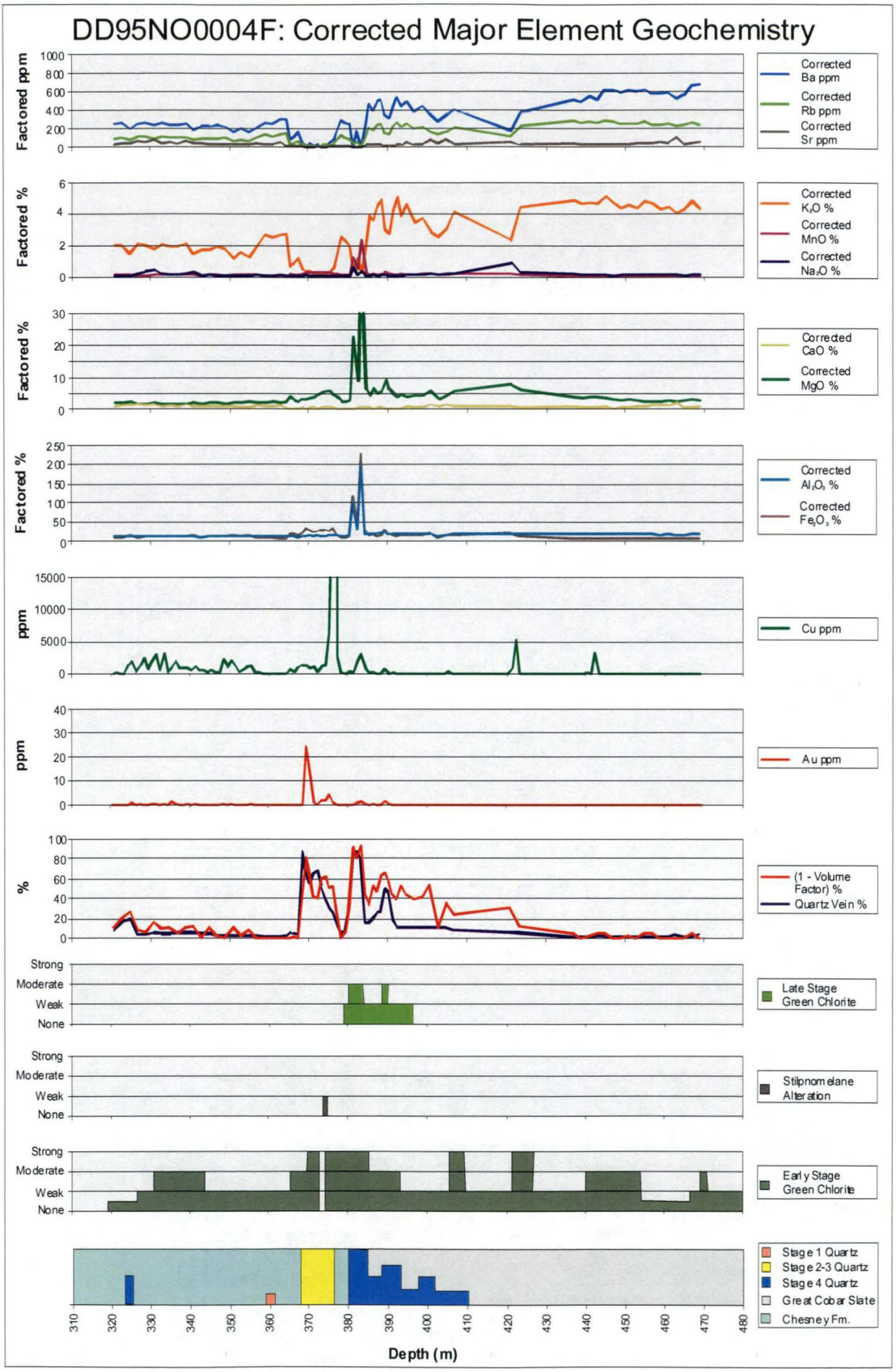

Table 32: Method for determining average $X^B rc$ values for quartz vein domains.

D'hole	NO1F			NO3C			NO4F			Average		
Quartz Vein Stage	1	2–3	4	1	2–3	4	1	2–3	4	**1**	**2–3**	**4**
Ag	0.89	18.18	2.24	1.16	21.07	11.52	0.06	4.87	0.70	**0.70**	**14.70**	**4.82**
Al_2O_3	139,089	153,094	145,620	122,374	129,571	180,059	112,921	119,917	186,601	**124,795**	**134,194**	**170,760**
As	23	3140	129	24	90	62	22	22	50	**23**	**1,084**	**80**
Au	0.0	21.4	0.4	0.1	26.7	0.9	0.0	11.9	0.4	**0.06**	**20.03**	**0.58**
Ba	314	174	245	228	66	168	238	39	381	**260**	**93**	**265**
Be	2.9	8.8	4.5	2.1	2.6	1.7	2.5	3.9	4.6	**2.48**	**5.12**	**3.61**
*All values in ppm												

Log isocon plots of average $X^B rc$ values for the three quartz vein domains versus average concentration in least altered wallrock for each element/oxide (Figure 167 – Figure 169) indicate elements that are neither enriched nor depleted (plot on the line defined by x = y), those that are enriched (plot above the line) and those that are depleted (plot below the line) (Table 33). Element depletions and enrichments are strongest in zones of Stage 2–3 quartz veins, moderately developed in zones of Stage 4 quartz veins, and only weakly developed in zones of Stage 1 quartz veins. Similar elements are enriched and depleted in the different quartz vein stages; the differences between the quartz vein stages being relative intensity of enrichment and depletion.

Table 33: Element/oxide enrichments and depletions by quartz vein stage (bold = major enrichment/depletion).

Quartz Vein Stage	Enrichments	Depletions
1	**SiO_2**, Fe_2O_3, S, Na_2O, C, MnO, Zn, **Pb**, Cr, Be, **W**, Co, **Bi**, **As**, **Se**, Ag, In, Sb	K_2O, Cu, Ba, Rb, Nb
2–3	**SiO_2**, **Fe_2O_3**, S, CaO, MgO, MnO, **Cu**, C, Na_2O, **Pb**, **Zn**, **Bi**, **W**, Cr, V, Sr, Co, Ga, **Mo**, Sn, **Sb**, **Ag**, **Au**, **Cd**, **In**	**K_2O, Ba, Rb,** Hf, Sc
4	**SiO_2**, **Fe_2O_3**, MgO, Al_2O_3, **S**, CaO, **Cu**, MgO, **MnO**, Na_2O, **Pb**, **Be**, Cr, Zn, Co, Sr, Ga, **As**, **Sn**, **Se**, **Sb**, Mo, Cs, **Ag**, Be, **In**, Au	K_2O, Ba, Rb

The most surprising aspect of the element/oxide enrichments/depletions measured for the New Occidental deposit (Table 33) is the apparent enrichment of Al_2O_3 associated with Stage 4 quartz veins. Alumina had previously been interpreted to be immobile based on the similarity between the Correction Factors calculated for Al_2O_3 and Correction Factors determined for the other 12 immobile elements/oxides (Section 7.4.2). The inclusion of Correction Factors for Al_2O_3 in the calculation of averaged Volume Factors does not have any appreciable impact on the Volume Factors on the basis that differences between the different Correction Factors for each sample interval is relatively small and because the weighting on each element is small (<8%).

Figure 167: Log isocon plot of average concentration of elements associated with Stage 1 quartz veins versus unaltered wallrock.

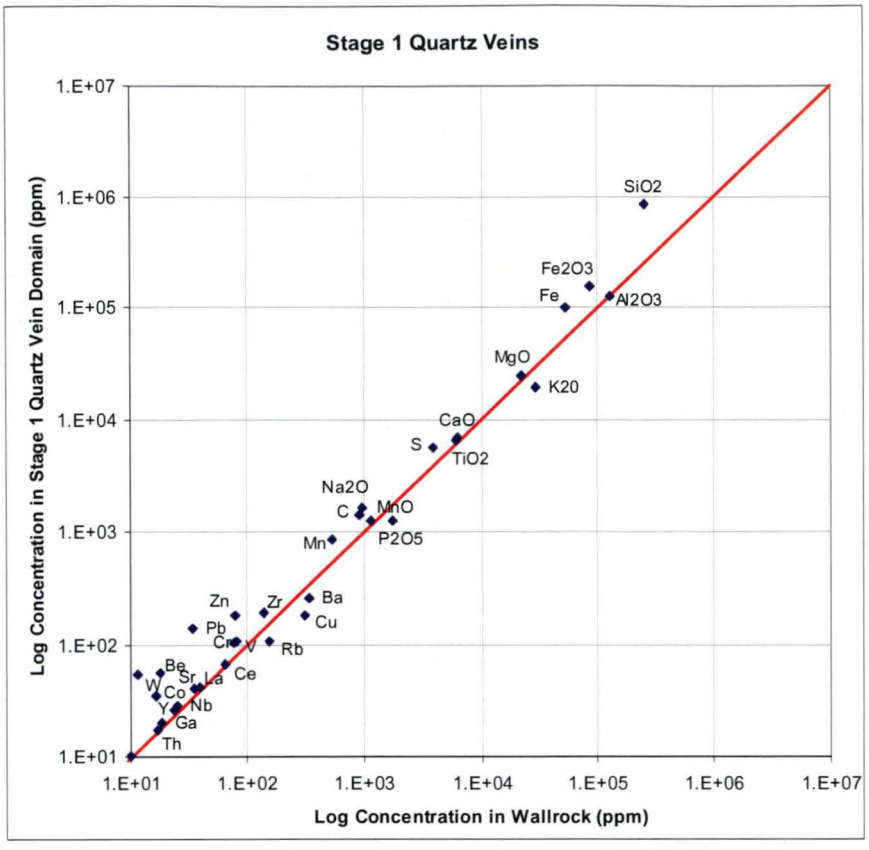

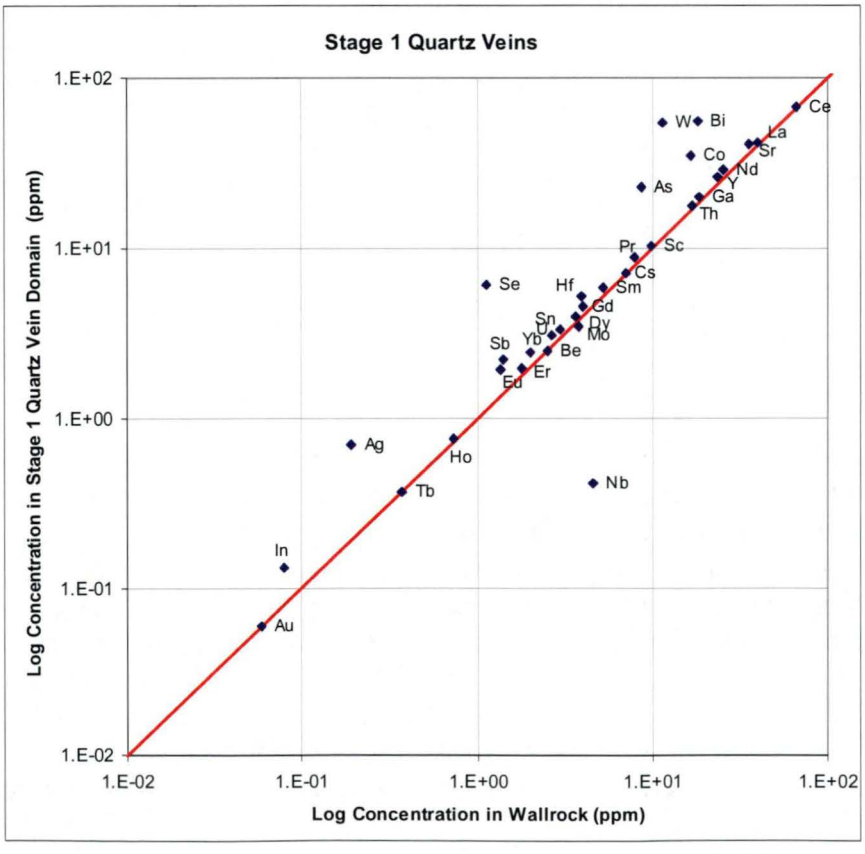

Figure 168: Log isocon plot of average concentration of elements associated with Stage 2–3 quartz veins versus unaltered wallrock.

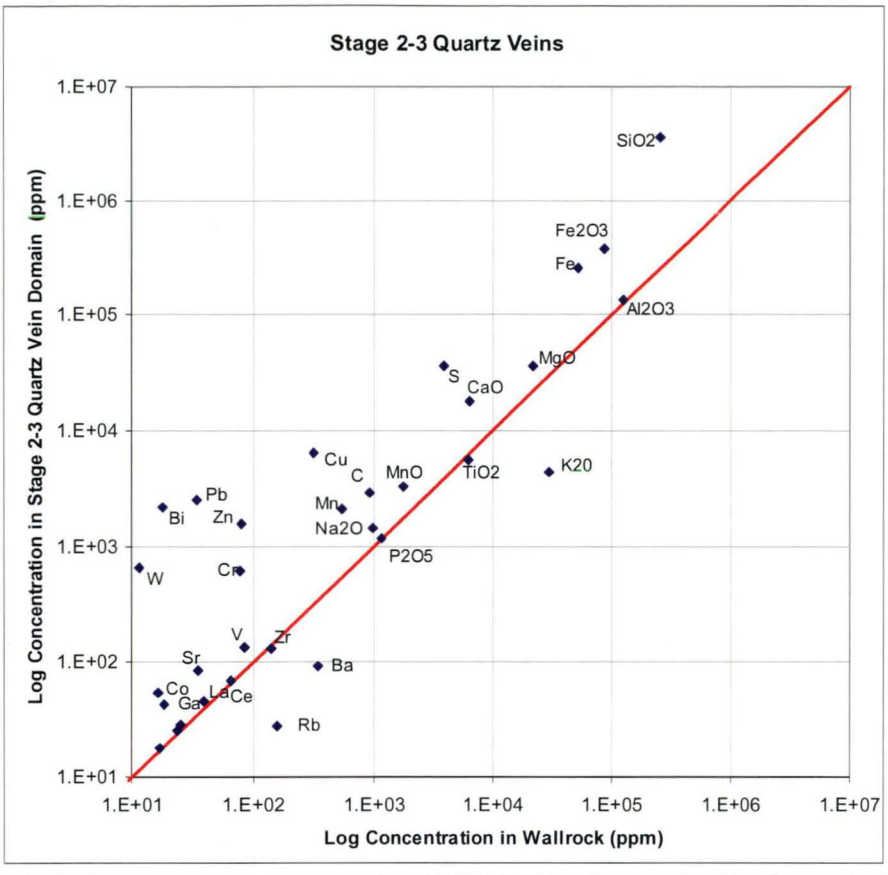

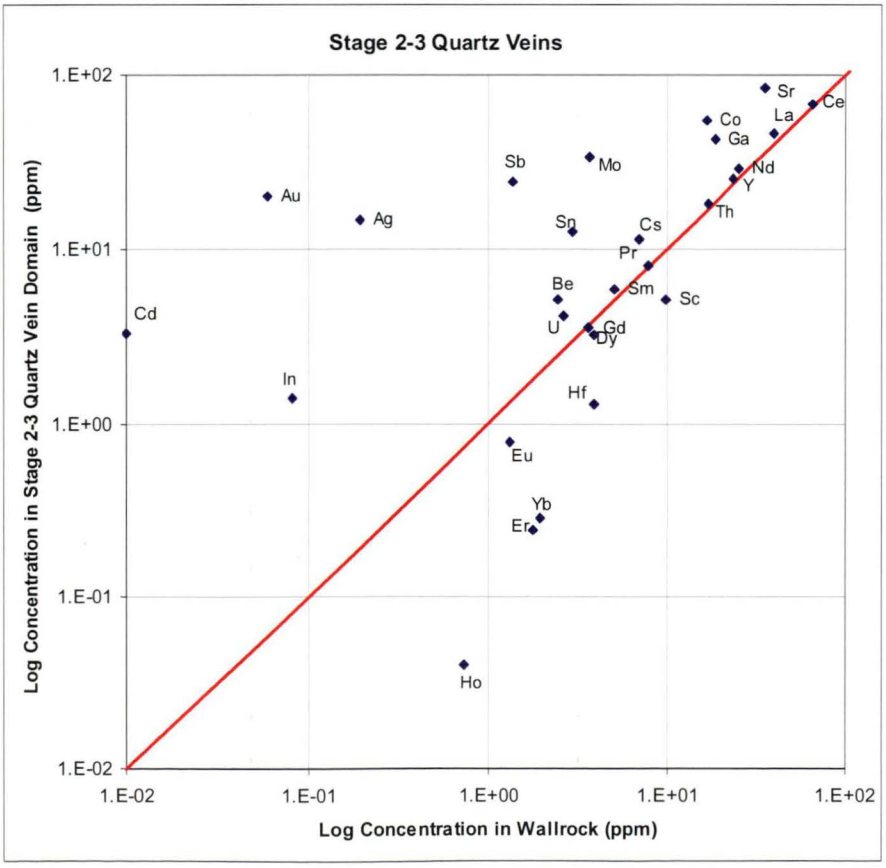

Figure 169: Log isocon plot of average concentration of elements associated with Stage 4 quartz veins versus unaltered wallrock.

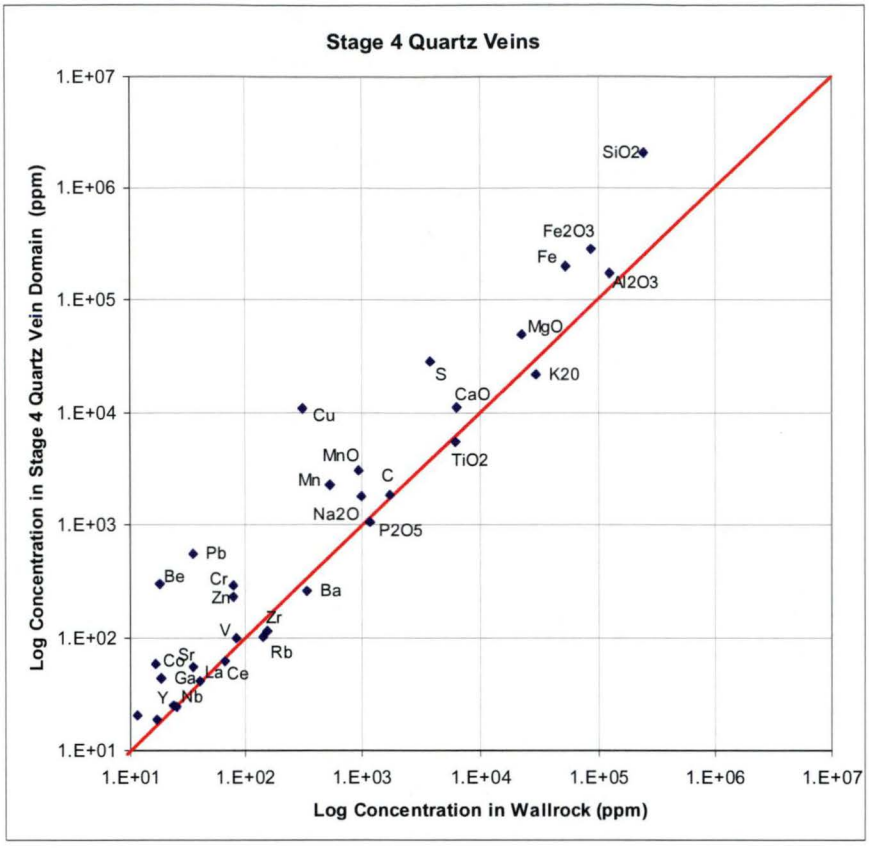

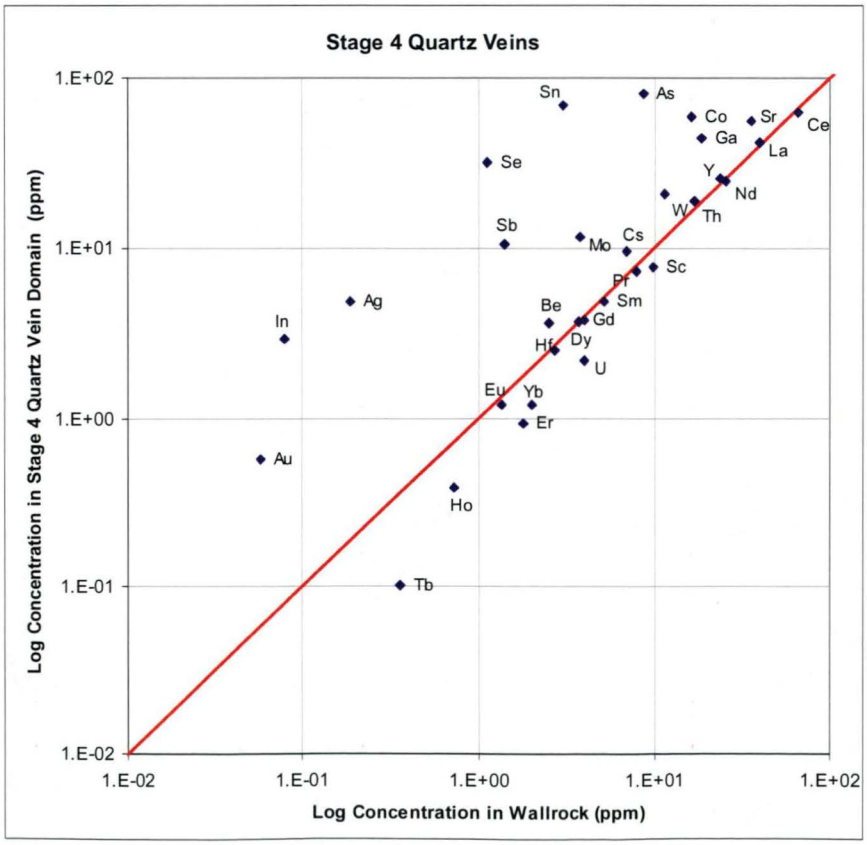

7.5.2 Enrichment/Depletion Associated with Wallrock Alteration

The major changes in wallrock alteration mineralogy in the New Occidental deposit identified in Section 5.4 are:

1. Metamorphic white mica + chlorite → Fe-chlorite
2. Fe-chlorite → stilpnomelane
3. quartz → Mg-Fe chlorite
4. Mg-Fe chlorite → white mica
5. Fe-chlorite, stilpnomelane, Mg-Fe chlorite → greenalite, Fe-clays

Each alteration stage, apart from the last stage which is volumetrically insignificant, is associated with well-defined variations in corrected major element geochemistry.

The broad alteration halo of early-stage Fe-chlorite alteration around the New Occidental deposit is in part outlined by Fe-enrichment (Figure 164 – Figure 166; Figure 170a), although other Fe-rich phyllosilicates (stilpnomelane and, to a lesser extent, greenalite and Fe-rich clays) and Fe-sulfides also contribute to and accentuate iron enrichment within the deposit. In the core of the deposit, quartz vein emplacement has diluted the overall iron content of the rock mass (Figure 170b), although corrected Fe_2O_3 values indicate consistent Fe-enrichment throughout the orebody (Figure 164 – Figure 166).

Figure 170: Variation diagrams of K_2O/Al_2O_3 ratio versus Fe_2O_3 and SiO_2 respectively.

(a) $K_2O/Al_2O_3 - Fe_2O_3$

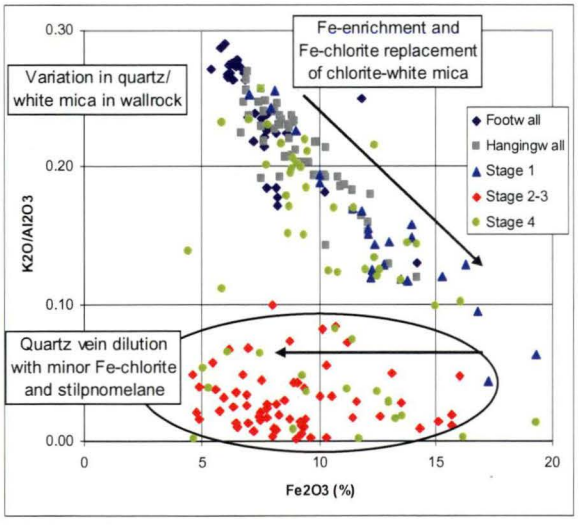

(b) $K_2O/Al_2O_3 - SiO_2$

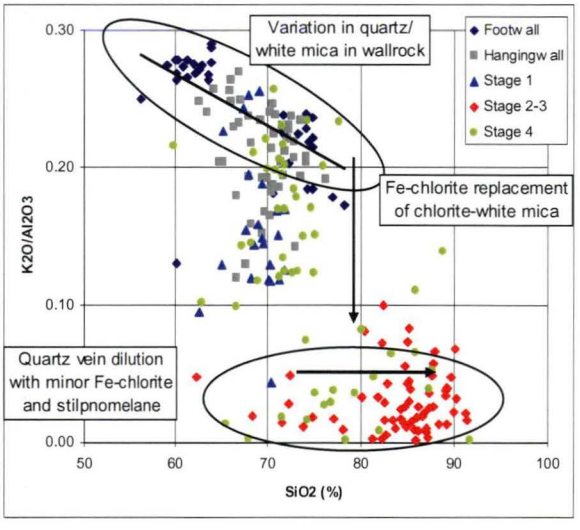

Early-stage Fe-chlorite alteration is associated with progressive destruction of metamorphic white mica in wallrock around the New Occidental deposit, which manifests as K_2O-Ba-Rb depletion (Figure 164 – Figure 166), the onset of which can be distinguished some 10–20m from the orebody margins. Variation diagrams of K_2O/Al_2O_3 versus Fe_2O_3 and SiO_2 (Figure 170a & b respectively) highlight this change. K_2O/Al_2O_3 values decrease with increasing Fe_2O_3 content and constant SiO_2 content (especially for samples containing Stage 4 quartz veins), which corresponds to

destruction of white mica and replacement with Fe-chlorite at the margins of the New Occidental deposit. At very low K_2O/Al_2O_3 values, corresponding to the core of the deposit, white mica is largely absent and the effects of quartz vein dilution are obvious (decreasing Fe_2O_3 and increasing SiO_2 values at constant K_2O/Al_2O_3 values).

Zones of stilpnomelane alteration and veining within the deposit are characterised by K_2O-Ba-Rb-Fe_2O_3-Sr-minor MgO enrichment (Figure 164 – Figure 166). Microbeam analyses indicate stilpnomelane contains up 3.6 wt% K_2O and 3.5 wt% MgO, most likely as impurities in the stilpnomelane lattice (e.g. Deer et al., 1966).

Late-stage Fe-Mg chlorite alteration and veining in the New Occidental deposit are characterised by K_2O-Ba-Rb-Fe_2O_3-MgO-Al_2O_3-Na_2O-Sr and, locally, CaO enrichment (Figure 164 – Figure 166). The suite of enriched elements/oxides corresponds directly to the chemical constituents of late-stage chlorite (Table 19). The strong enrichment in Al_2O_3 coincident with late-stage green chlorite (Figure 169) suggests Al_2O_3 was mobile during that stage of alteration and ore formation (i.e., its concentration has increased relative to the remainder of the suite of recognised immobile elements). For example, Al_2O_3 and TiO_2 are well correlated in wallrock domains and correlate reasonably in zones of Stage 1–3 quartz veins, but Al_2O_3 is enriched relative to TiO_2 (and other immobile elements) in Stage 4 quartz veins and in some footwall samples containing late-stage green chlorite alteration (Figure 171a). A variation diagram of Mg/(Mg+Fe) versus log Al_2O_3/TiO_2 (Figure 171b) highlights the pronounced enrichment of Al_2O_3 at Mg/(Mg+Fe) values in the range 0.10–0.15, which corresponds to late-stage chlorite. It also suggests subtle Al_2O_3-enrichment associated with Stage 2–3 quartz veins associated with Fe-chlorite and/or stilpnomelane alteration.

Figure 171: Two-element variation diagrams for selected major elements in the New Occidental deposit.

(c) Al_2O_3 - TiO_2

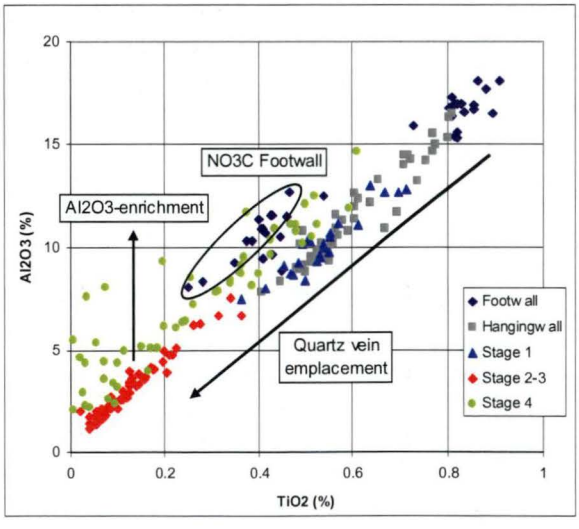

(d) Mg/(Mg+Fe) - Log Al_2O_3/TiO_2

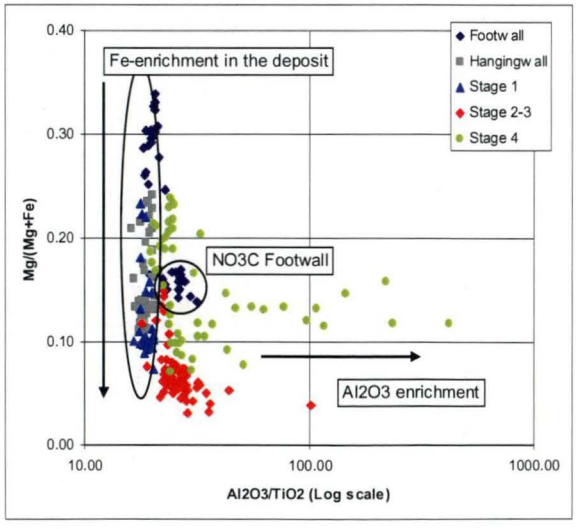

Na_2O-enrichment within the New Occidental deposit contrasts with the laterally extensive Na depletion halos that Robertson & Taylor (1987) noted around many Cobar deposits, including the CSA and Peak deposits. There are no specific Na-rich alteration or vein minerals that account for Na_2O-enrichment within the deposit or

within zones of late-stage chlorite. However, microprobe analyses indicate chlorite and stilpnomelane from the deposit contains up 1.5 wt% Na_2O and 2 wt% Na_2O respectively (Section 5.4.1 and 5.4.2) as impurities in the crystal lattice.

Whilst Na-enrichment is common in certain types of oxide Cu-Au and orogenic Au deposits (Davidson & Large; 1998; Kerrich et al., 2000) alumina normally behaves as an immobile phase (McCuaig and Kerrich, 1994; Eilu and Mikucki, 1998; Ridley and Diamond, 2000; Eilu et al., 2001). The most likely explanation for Al-Na-enrichment in zones of late-stage green chlorite alteration is that formation of late-stage chlorite is associated with localised mineral dissolution. Late-stage green chlorite has aggressively replaced quartz, stilpnomelane and early-formed Fe-chlorite (Section 5.4.3) during relatively intense deformation that immediately followed formation of Stage 4 quartz veins in the New Occidental deposit. Relative to the composition of stilpnomelane, late-stage chlorite contains significantly more Al_2O_3 (19–20 wt% Al_2O_3 compared to 6–7 wt% Al_2O_3 in stilpnomelane), less silica (25 wt% SiO_2 compared to 46–48 wt% SiO_2 in stilpnomelane) and significantly more MgO. Fe-Mg chlorite replacement of a quartz + stilpnomelane assemblage cannot simply be reconciled with retrograde quartz solubility and the disproportionately large volumes of late-stage chlorite relative to stilpnomelane observed in the rock mass. Formation of late-stage chlorite at the expense of quartz + stilpnomelane not only requires removal of appreciable silica but also addition of a number of constituents to the rock volume, most notably Al_2O_3 and MgO.

In contrast, alumina appears to have been relatively immobile during earlier stages of alteration and ore formation in the New Occidental deposit (Figure 167 – Figure 168) albeit, some mobility of Al_2O_3 is suspected during formation of Stage 2–3 quartz veins. Conservation of Al_2O_3 during previous stages of ore formation indicates the bulk of Fe-chlorite and stilpnomelane in the deposit formed by replacement of metamorphic chlorite/white mica and Fe-chlorite respectively.

Narrow zones of white mica alteration associated with late-stage chalcopyrite - pyrrhotite (defined by Cu > 0.5%) in the New Occidental orebody are characterised by discrete zones of K_2O-Ba-Rb enrichment (Figure 164 – Figure 166), similar to localised K-enrichment detected in the Cu-rich parts of the CSA deposit where hydrothermal muscovite is developed (Robertson & Taylor, 1987). Variation diagrams of Cu versus K_2O /TiO_2 and Rb/TiO_2 (effectively K_2O and Rb respectively corrected for quartz vein dilution) highlight a small population of samples characterised by elevated Cu values and moderately enriched K_2O and Rb that contain late-stage hydrothermal white mica alteration (Figure 172). The white mica alteration is developed as an overprint on late-stage chlorite alteration in the footwall of the deposit; hence the apparent association between elevated copper and Stage 4 quartz veins. However, increased K_2O content associated with Stage 4 quartz veins is attributable to white mica alteration; late-stage green chlorite contains on average only 0.25 wt% K_2O, compared to up to 10 wt% K_2O in muscovite (Reynolds, 1999a).

Figure 172: Variation diagrams of K_2O/TiO_2 and Rb/TiO_2 ratios versus Log Cu.

(a) K_2O/TiO_2 - Log Cu

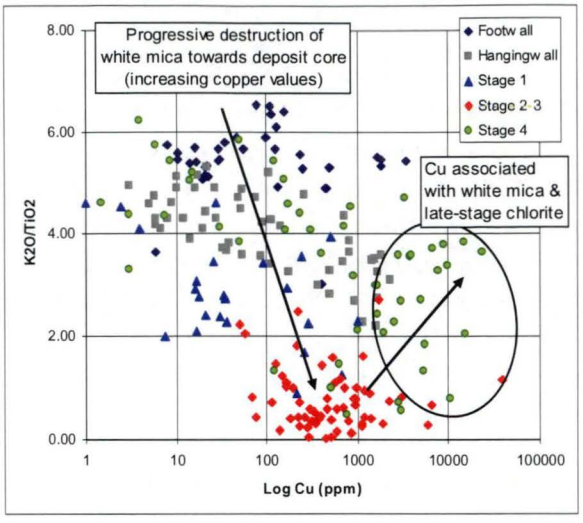

(b) Rb/TiO_2 - Log Cu

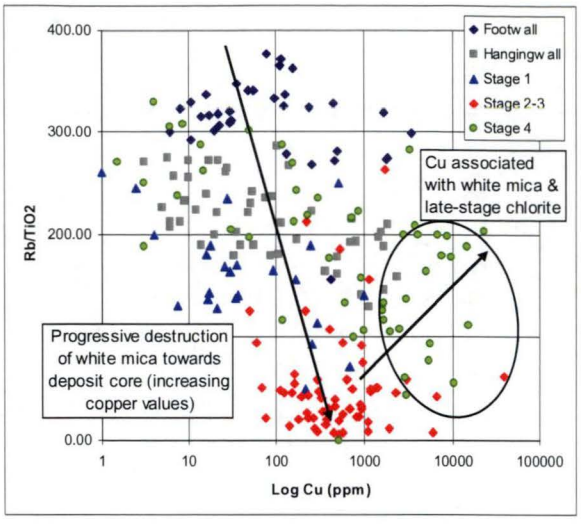

7.5.3 Enrichment/Depletion Associated with Ore Minerals

A wide range of metals are enriched in the New Occidental deposit (Table 33). Enrichment is restricted to the immediate orebody with no apparent enrichment in surrounding altered wallrock. Relatively narrow zones of ore element enrichment within much broader alteration haloes have previously been documented around the New Cobar, Chesney, Peak and Queen Bee deposits (Robertson, 1974; Robertson & Taylor, 1987).

Correlation coefficients calculated for the suite of whole rock and trace elements (Figure 173) highlight the following elemental associations in the New Occidental deposit:

1. **Au-Ag-Bi-Sb-Se-W-As**. Arsenic demonstrates a weak correlation with Bi-Sb-Se-W but is largely uncorrelated with Au-Ag.
2. **Pb-Ag-Se**
3. **Cu-In-S-Sn**
4. **Zn-Cd**. Silver and Mo are weakly correlated with Zn-Cd
5. **Fe_2O_3-Co-MnO-S**
6. **C-CaO-Sr**

The association of **Au-Ag-Bi-Sb-Se-W** reflects early stage gold-bismuth mineralisation associated with Stage 2–3 quartz veins in the New Occidental deposit. Tungsten, in the form of scheelite ($CaWO_4$) and minor wolframite ($[Fe,Mn]WO_4$), is associated with early-stage magnetite and Stage 1 quartz veins. The presence of W in the association most likely reflects the presence early-stage magnetite that has been overprinted by gold-bismuth ore minerals in the centre of the deposit. NO3C, in

particular, is characterised by relatively abundant remnant magnetite within the main zone of gold mineralisation.

The association of **Pb-Ag-Se** is correlated with galena (PbS) - clausthalite (PbSe) associated with the latter stages of gold-bismuth ore minerals in the centre of the deposit. The association of Ag with Pb and Se may reflect silver substitution into the crystal lattice of galena-clausthalite (e.g. Van Hook, 1960; Craig, 1967).

The association of **Cu-In-S-Sn** is related to chalcopyrite ($CuFeS_2$) that is principally developed in the footwall of the New Occidental deposit. Sn in the form of cassiterite (SnO_2) occurs in association with scheelite and wolframite as tiny inclusions within magnetite and as inclusions in chalcopyrite, the latter potentially reflecting chalcopyrite replacement of magnetite. However, Sn and W are poorly correlated, suggesting that the bulk of Sn in the deposit is associated with the main stage of chalcopyrite. The mineral form of indium, which is present in trace levels within the New Occidental deposit, is unknown. However, indium has an atomic weight similar to Sn, which suggests it may occur as an impurity in cassiterite.

The association of **Zn-Cd** reflects late-stage sphalerite in the centre of the New Occidental deposit. Even though galena is commonly observed in association with late-stage sphalerite veins, Pb and Zn correlate poorly, in part due to the lack of Zn-bearing phases in early stage galena-clausthalite.

The association of **Fe_2O_3-Co-MnO-S** is related to Fe-rich silicate alteration minerals including chlorite and stilpnomelane and iron sulfide (pyrrhotite and pyrite) mineralisation. Microprobe analyses have shown that hydrothermal chlorite in the New Occidental deposit contains on average 36 wt% FeO and 0.35 wt% MnO whilst stilpnomelane on average contains 34 wt% FeO and 0.41 wt% MnO. However, the highest levels of MnO and Co correspond to zones of well-developed pyrrhotite in the deposit, indicating Mn and Co occur as impurities in pyrrhotite.

The association of **C-CaO-Sr** appears to relate to calcite ($CaCO_3$). Calcite occurs in relatively minor amounts in barren Stage 4 quartz-chlorite veins in the distal parts of the deposit environs and is also a minor component of Stage 1 quartz veins in the hanging wall of the deposit, in late-stage sphalerite-galena-pyrrhotite veins and in late Stage 5 quartz veins. The strong correlation between C-CaO and Sr indicates that the bulk of Sr in the deposit is associated with calcite rather than with detrital feldspar in unaltered wallrock.

Robertson & Taylor (1987) noted broad subtle base metal depletion in the alkali and alkaline-earth element depletion haloes around the CSA, Tharsis and Queen Bee deposits. There is no evidence of base metal depletion surrounding the New Occidental deposit, although emplacement of early-stage quartz veins, which were not associated with base metal ore minerals, potentially may have diluted overall base metal contents in wallrock.

Figure 173: Correlation co-efficients for wholerock and trace elements in the New Occidental deposit.

	Ag	Al2O3	As	Au	Ba	Be	Bi	C	CaO	Cd	Ce	Co	Cr	Cs	Cu	Dy	Er	Eu	Fe2O3	Ga	Gd	Hf	Ho	In	K2O	La	LOI
Ag	1.00	-0.37	0.07	0.36	-0.34	-0.31	0.40	-0.07	-0.19	0.31	-0.35	-0.01	0.27	-0.04	0.29	-0.33	-0.38	-0.30	0.12	-0.27	-0.33	-0.35	-0.35	0.24	-0.35	-0.35	-0.01
Al2O3		1.00	-0.17	-0.41	0.94	0.83	-0.47	0.08	0.28	-0.24	0.92	0.13	-0.49	0.52	-0.19	0.92	0.87	0.81	-0.03	0.69	0.91	0.79	0.86	-0.16	0.95	0.94	0.55
As			1.00	0.08	-0.13	-0.05	0.46	-0.01	0.06	-0.02	-0.16	-0.13	0.11	-0.07	-0.03	-0.17	-0.14	-0.16	-0.10	-0.17	-0.18	-0.14	-0.12	-0.03	-0.13	-0.18	-0.14
Au				1.00	-0.33	-0.32	0.50	-0.14	-0.18	0.18	-0.39	-0.13	0.20	0.07	-0.02	-0.40	-0.37	-0.37	-0.03	-0.15	-0.40	-0.36	-0.33	-0.01	-0.34	-0.38	-0.31
Ba					1.00	0.84	-0.43	0.22	0.38	-0.18	0.90	-0.08	-0.40	0.60	-0.23	0.88	0.83	0.74	-0.28	0.56	0.85	0.75	0.83	-0.21	0.98	0.91	0.44
Be						1.00	-0.26	0.11	0.45	-0.24	0.80	-0.01	-0.36	0.46	-0.20	0.79	0.75	0.72	-0.12	0.45	0.77	0.70	0.78	-0.21	0.82	0.82	0.44
Bi							1.00	-0.19	-0.13	0.03	-0.50	-0.02	0.26	-0.05	0.11	-0.50	-0.46	-0.44	0.08	-0.24	-0.51	-0.47	-0.42	0.06	-0.46	-0.51	-0.20
C								1.00	0.98	0.02	0.23	-0.26	-0.06	0.07	-0.12	0.17	0.23	0.26	-0.25	-0.16	0.17	0.35	0.19	-0.14	0.15	0.15	-0.07
CaO									1.00	-0.12	0.39	-0.21	-0.18	0.12	-0.11	0.31	0.36	0.37	-0.13	-0.01	0.30	0.43	0.37	-0.14	0.31	0.32	0.16
Cd										1.00	-0.22	-0.14	0.14	0.05	0.01	-0.23	-0.20	-0.22	-0.11	-0.15	-0.22	-0.20	-0.18	0.08	-0.18	-0.21	-0.17
Ce											1.00	0.07	-0.45	0.45	-0.21	0.96	0.91	0.87	-0.05	0.50	0.95	0.90	0.89	-0.18	0.89	0.98	0.47
Co												1.00	-0.31	0.03	0.14	0.11	0.09	0.20	0.75	0.37	0.14	0.14	0.03	0.16	-0.08	0.08	0.34
Cr													1.00	-0.30	0.12	-0.44	-0.40	-0.41	-0.26	-0.48	-0.46	-0.37	-0.38	0.10	-0.39	-0.45	-0.32
Cs														1.00	-0.21	0.46	0.43	0.42	-0.05	0.45	0.43	0.35	0.47	-0.20	0.58	0.48	0.25
Cu															1.00	-0.21	-0.28	-0.20	0.29	-0.14	-0.18	-0.22	-0.25	0.88	-0.22	-0.20	0.58
Dy																1.00	0.91	0.89	-0.02	0.52	0.97	0.87	0.90	-0.19	0.88	0.97	0.47
Er																	1.00	0.86	-0.03	0.50	0.90	0.88	0.91	-0.24	0.83	0.92	0.39
Eu																		1.00	0.10	0.43	0.89	0.85	0.82	-0.20	0.74	0.87	0.42
Fe2O3																			1.00	0.26	0.01	0.04	-0.07	0.30	-0.30	-0.05	0.40
Ga																				1.00	0.52	0.38	0.51	-0.08	0.58	0.54	0.46
Gd																					1.00	0.87	0.88	-0.16	0.86	0.96	0.49
Hf																						1.00	0.83	-0.19	0.74	0.87	0.36
Ho																							1.00	-0.23	0.83	0.91	0.42
In																								1.00	-0.21	-0.18	0.54
K2O																									1.00	0.91	0.44
La																										1.00	0.49
LOI																											1.00

	MgO	MnO	Mo	Na2O	Nb	Nd	P2O5	Pb	Pr	Rb	S	Sb	Sc	Se	SiO2	Sm	Sn	Sr	Ta	Tb	Th	TiO2	U	V	W	Y	Yb	Zn	Zr
Ag	-0.32	-0.12	0.32	-0.17	-0.18	-0.34	-0.35	0.75	-0.35	-0.34	0.30	0.40	-0.42	0.65	0.28	-0.34	0.14	-0.23	-0.09	-0.25	-0.36	-0.36	-0.28	-0.11	0.36	-0.34	-0.34	0.32	-0.34
Al2O3	0.79	0.21	-0.36	0.38	0.63	0.92	0.92	-0.23	0.94	0.95	-0.23	-0.60	0.94	-0.43	-0.90	0.88	-0.09	0.44	0.35	0.74	0.91	0.96	0.89	0.74	-0.46	0.92	0.86	-0.27	0.78
As	-0.15	-0.14	-0.01	-0.10	-0.06	-0.18	-0.17	-0.02	-0.17	-0.13	0.05	0.25	-0.16	0.35	0.18	-0.17	-0.02	0.02	-0.03	-0.09	-0.17	-0.16	-0.17	-0.19	0.47	-0.16	-0.14	-0.03	-0.13
Au	-0.38	-0.24	0.25	-0.15	-0.16	-0.39	-0.37	0.22	-0.39	-0.33	0.16	0.61	-0.42	0.44	0.41	-0.38	-0.04	-0.22	-0.08	-0.23	-0.38	-0.39	-0.30	-0.31	0.41	-0.38	-0.36	0.17	-0.35
Ba	0.62	-0.04	-0.35	0.34	0.73	0.87	0.88	-0.20	0.90	0.99	-0.23	-0.57	0.88	-0.38	-0.76	0.84	-0.12	0.53	0.40	0.77	0.87	0.94	0.86	0.74	-0.38	0.89	0.82	-0.22	0.76
Be	0.69	0.08	-0.36	0.34	0.52	0.74	0.80	-0.18	0.80	0.82	-0.19	-0.63	0.81	-0.27	-0.75	0.68	-0.12	0.56	0.31	0.69	0.83	0.85	0.77	0.56	-0.27	0.82	0.73	-0.28	0.74
Bi	-0.29	-0.13	0.17	-0.26	-0.24	-0.51	-0.50	0.30	-0.51	-0.44	0.21	0.61	-0.48	0.79	0.39	-0.51	0.01	-0.21	-0.13	-0.32	-0.48	-0.49	-0.43	-0.43	0.56	-0.47	-0.46	0.02	-0.45
C	-0.26	-0.31	-0.07	0.19	0.18	0.18	0.20	-0.06	0.16	0.17	-0.07	-0.20	0.08	-0.07	-0.01	0.19	-0.07	0.92	0.17	0.22	0.06	0.19	0.15	0.25	0.04	0.19	0.20	-0.07	0.35
CaO	0.11	-0.09	-0.25	0.24	0.16	0.24	0.35	-0.16	0.31	0.33	-0.04	-0.39	0.29	-0.14	-0.28	0.20	-0.07	0.95	0.27	0.38	0.29	0.37	0.27	0.20	-0.01	0.37	0.31	-0.16	0.50
Cd	-0.25	-0.18	0.31	-0.07	-0.09	-0.21	-0.24	0.16	-0.22	-0.18	0.04	0.23	-0.23	0.04	0.28	-0.21	-0.03	-0.14	-0.04	-0.12	-0.22	-0.22	-0.19	0.04	0.16	-0.22	-0.20	0.97	-0.21
Ce	0.64	0.12	-0.29	0.40	0.60	0.96	0.96	-0.21	0.98	0.88	-0.24	-0.64	0.91	-0.43	-0.83	0.92	-0.11	0.52	0.41	0.79	0.90	0.97	0.94	0.73	-0.39	0.95	0.92	-0.23	0.90
Co	0.34	0.62	0.07	0.22	-0.16	0.11	0.08	0.03	0.10	-0.08	0.22	0.06	0.10	-0.02	-0.38	0.13	0.06	-0.18	-0.17	-0.03	0.13	0.07	0.11	0.17	-0.19	0.09	0.12	-0.08	0.09
Cr	-0.47	-0.37	0.08	-0.22	-0.18	-0.42	-0.43	0.26	-0.44	-0.40	0.08	0.25	-0.43	0.28	0.53	-0.39	0.08	-0.24	-0.14	-0.30	-0.43	-0.44	-0.41	-0.35	0.21	-0.44	-0.39	0.13	-0.38
Cs	0.42	0.12	-0.07	0.29	0.47	0.45	0.45	0.03	0.46	0.60	0.00	-0.08	0.44	0.00	-0.46	0.44	-0.13	0.25	0.13	0.50	0.49	0.50	0.50	0.54	0.03	0.48	0.45	0.01	0.35
Cu	-0.05	0.11	0.21	-0.06	-0.15	-0.23	-0.22	0.06	-0.21	-0.22	0.70	0.20	-0.23	0.11	-0.04	-0.24	0.46	-0.13	-0.08	-0.19	-0.19	-0.22	-0.22	-0.18	-0.06	-0.21	-0.28	0.02	-0.21
Dy	0.66	0.16	-0.31	0.39	0.60	0.97	0.95	-0.19	0.97	0.87	-0.24	-0.63	0.92	-0.41	-0.83	0.94	-0.11	0.44	0.30	0.78	0.91	0.96	0.94	0.75	-0.40	0.98	0.93	-0.25	0.86
Er	0.63	0.16	-0.30	0.38	0.54	0.91	0.90	-0.24	0.92	0.82	-0.30	-0.59	0.89	-0.43	-0.78	0.88	-0.14	0.48	0.28	0.79	0.88	0.91	0.88	0.67	-0.38	0.93	0.92	-0.22	0.86
Eu	0.60	0.24	-0.26	0.49	0.44	0.87	0.86	-0.17	0.88	0.73	-0.23	-0.59	0.84	-0.36	-0.78	0.85	-0.16	0.50	0.21	0.70	0.84	0.86	0.85	0.67	-0.35	0.90	0.87	-0.24	0.82
Fe2O3	0.27	0.74	0.11	0.16	-0.35	-0.04	-0.04	0.07	-0.04	-0.30	0.37	0.10	-0.05	0.09	-0.35	-0.04	0.17	-0.14	-0.15	-0.14	-0.03	-0.07	0.00	0.00	0.00	-0.04	-0.01	-0.07	0.03
Ga	0.76	0.46	-0.25	0.21	0.40	0.51	0.49	-0.21	0.52	0.59	-0.09	-0.16	0.54	-0.34	-0.72	0.48	-0.01	0.10	0.17	0.46	0.55	0.54	0.48	0.47	-0.42	0.53	0.48	-0.16	0.37
Gd	0.67	0.19	-0.30	0.39	0.58	0.96	0.95	-0.21	0.97	0.85	-0.22	-0.62	0.91	-0.43	-0.84	0.94	-0.10	0.43	0.30	0.77	0.90	0.95	0.93	0.73	-0.40	0.96	0.91	-0.23	0.86
Hf	0.50	0.14	-0.23	0.41	0.47	0.88	0.90	-0.22	0.89	0.72	-0.26	-0.60	0.84	-0.42	-0.74	0.87	-0.13	0.53	0.30	0.71	0.82	0.89	0.88	0.64	-0.35	0.87	0.90	-0.23	0.96
Ho	0.65	0.13	-0.30	0.39	0.57	0.87	0.88	-0.21	0.89	0.82	-0.23	-0.57	0.84	-0.39	-0.77	0.83	-0.13	0.49	0.33	0.82	0.87	0.90	0.85	0.64	-0.36	0.93	0.89	-0.20	0.84
In	-0.03	0.13	0.22	-0.10	-0.15	-0.20	-0.20	0.02	-0.20	-0.21	0.60	0.19	-0.22	0.09	-0.05	-0.21	0.72	-0.14	-0.06	-0.17	-0.17	-0.20	-0.20	-0.15	-0.05	-0.19	-0.25	0.08	-0.18
K2O	0.66	-0.02	-0.35	0.34	0.72	0.88	0.88	-0.22	0.90	0.99	-0.23	-0.57	0.90	-0.41	-0.77	0.85	-0.12	0.46	0.36	0.75	0.88	0.93	0.86	0.72	-0.40	0.89	0.82	-0.22	0.73
La	0.68	0.13	-0.28	0.40	0.62	0.96	0.96	-0.20	0.99	0.90	-0.23	-0.63	0.92	-0.43	-0.85	0.93	-0.11	0.47	0.35	0.80	0.94	0.98	0.95	0.74	-0.41	0.96	0.91	-0.22	0.88
LOI	0.65	0.39	-0.11	0.29	0.25	0.43	0.44	-0.07	0.47	0.45	0.51	-0.29	0.45	-0.17	-0.76	0.38	0.35	0.26	0.11	0.39	0.52	0.49	0.43	0.37	-0.36	0.48	0.38	-0.17	0.39
MgO	1.00	0.55	-0.33	0.34	0.33	0.61	0.64	-0.22	0.66	0.66	-0.04	-0.46	0.70	-0.36	-0.87	0.55	-0.01	0.25	0.18	0.56	0.73	0.69	0.59	0.45	-0.44	0.69	0.59	-0.26	0.52
MnO		1.00	-0.07	0.17	-0.19	0.12	0.12	-0.10	0.13	-0.02	0.08	-0.07	0.17	-0.16	-0.48	0.10	0.06	-0.08	-0.06	0.02	0.16	0.11	0.08	0.06	-0.25	0.16	0.14	-0.16	0.13
Mo			1.00	-0.07	-0.24	-0.28	-0.30	0.21	-0.30	-0.34	0.15	0.31	-0.33	0.22	0.29	-0.26	0.03	-0.26	-0.17	-0.29	-0.26	-0.32	-0.22	-0.15	0.15	-0.32	-0.29	0.33	-0.25
Na2O				1.00	0.16	0.40	0.39	-0.11	0.40	0.32	0.16	-0.26	0.41	-0.22	-0.44	0.39	-0.11	0.35	0.05	0.29	0.44	0.41	0.39	0.30	-0.16	0.40	0.41	-0.07	0.37
Nb					1.00	0.64	0.60	-0.11	0.61	0.72	-0.09	-0.29	0.55	-0.22	-0.45	0.65	-0.10	0.27	0.34	0.62	0.56	0.63	0.61	0.57	-0.20	0.59	0.56	-0.11	0.45
Nd						1.00	0.96	-0.19	0.98	0.87	-0.27	-0.61	0.93	-0.42	-0.81	0.99	-0.13	0.38	0.29	0.74	0.90	0.96	0.96	0.76	-0.39	0.94	0.93	-0.22	0.84
P2O5							1.00	-0.19	0.97	0.86	-0.27	-0.64	0.92	-0.42	-0.82	0.94	-0.13	0.47	0.35	0.75	0.91	0.97	0.95	0.70	-0.38	0.94	0.92	-0.25	0.89
Pb								1.00	-0.20	-0.21	0.08	0.23	-0.27	0.73	0.20	-0.18	0.01	-0.19	-0.06	-0.16	-0.22	-0.22	-0.12	0.01	0.14	-0.20	-0.20	0.18	-0.22
Pr									1.00	0.89	-0.25	-0.64	0.94	-0.43	-0.84	0.96	-0.13	0.45	0.32	0.77	0.93	0.98	0.96	0.76	-0.39	0.96	0.92	-0.24	0.87
Rb										1.00	-0.22	-0.56	0.88	-0.39	-0.77	0.83	-0.12	0.48	0.36	0.76	0.87	0.93	0.84	0.73	-0.39	0.88	0.80	-0.21	0.72
S											1.00	0.27	-0.30	0.22	-0.05	-0.29	0.32	-0.04	-0.16	-0.10	-0.16	-0.23	-0.22	-0.15	0.15	-0.23	-0.29	0.05	-0.23
Sb												1.00	-0.64	0.56	0.53	-0.58	0.07	-0.46	-0.21	-0.45	-0.64	-0.66	-0.58	-0.43	0.47	-0.63	-0.60	0.24	-0.62
Sc													1.00	-0.48	-0.84	0.90	-0.16	0.43	0.28	0.66	0.90	0.94	0.90	0.67	-0.42	0.91	0.89	-0.27	0.81
Se														1.00	0.37	-0.41	0.10	-0.20	-0.12	-0.28	-0.44	-0.43	-0.33	-0.25	0.54	-0.41	-0.41	0.04	-0.41
SiO2															1.00	-0.77	-0.03	-0.41	-0.26	-0.65	-0.84	-0.86	-0.80	-0.65	0.43	-0.84	-0.77	0.29	-0.74
Sm																1.00	-0.14	0.34	0.27	0.70	0.87	0.92	0.94	0.76	-0.37	0.91	0.92	-0.22	0.81
Sn																	1.00	-0.06	-0.05	-0.10	-0.11	-0.13	-0.15	-0.13	-0.04	-0.12	-0.15	-0.03	-0.15
Sr																		1.00	0.29	0.50	0.44	0.51	0.41	0.34	-0.05	0.50	0.44	-0.18	0.60
Ta																			1.00	0.32	0.16	0.36	0.31	0.23	-0.11	0.32	0.26	-0.06	0.37
Tb																				1.00	0.75	0.79	0.73	0.61	-0.27	0.83	0.76	-0.14	0.76
Th																					1.00	0.94	0.91	0.68	-0.42	0.92	0.87	-0.24	0.81
TiO2																						1.00	0.95	0.76	-0.39	0.96	0.91	-0.24	0.89
U																							1.00	0.74	-0.32	0.93	0.90	-0.21	0.86
V																								1.00	-0.22	0.72	0.69	0.05	0.63
W																									1.00	-0.39	-0.36	0.15	-0.31
Y																										1.00	0.92	-0.24	0.88
Yb																											1.00	-0.23	0.85
Zn																												1.00	-0.23
Zr																													1.00

7.5.4 Inferred Ore-fluid Composition

The distribution of major and trace elements in the New Occidental deposit is the function of two interrelated processes involving fault zone dilation/quartz vein deposition and hydrothermal wallrock alteration. Although wallrock alteration extends beyond the main zone of dilation and quartz veining, the strong spatial association between wallrock alteration and fault zone dilation, as evidenced by relatively strong correlations between elements/oxides associated with each of these two processes, clearly indicates wallrock alteration is intimately associated with quartz vein formation.

Fault zone dilation associated with deposition of large volumes of quartz veins has diluted a wide range of elements, including both mobile (Al_2O_3-K_2O-C-CaO-Na_2O-Fe_2O_3-Ba-Be-Cs-Ga-Rb-Sr-Ta-V) and immobile elements (Hf-Nb-P_2O_5-REE-Sc-Th-TiO_2-U-Zr), although most chalcophile elements (Au-Ag-Bi-Sb-Se-W-Pb-Cu-In-Sn-Zn-Cd-Mo), S and SiO_2 exhibit net enrichment. Corrections for the effects of volume change during deposit formation, which is largely related to vein emplacement, have allowed the geochemistry of individual stages of wallrock alteration in the New Occidental deposit to be characterised (Table 34). In particular, such corrections have revealed where elements are enriched (or are immobile) even though their uncorrected concentration decreases within the deposit. The pattern of element enrichments and depletions in the deposit can then be used to characterise how the composition of the New Occidental hydrothermal fluid changed with time.

The gross geochemical changes in deposit geochemistry identified in this part of the study confirm aspects of hydrothermal fluid composition inferred from alteration and ore mineralogy studies (Section 5.7 and 6.4 respectively). Element enrichments and depletions (Table 34) indicate the early hydrothermal fluid was extremely Fe-rich and characterised by high $a(Fe^{2+})$ but low $a(K^{+})$. Corrected Na and Mg concentrations appear unchanged or only slightly depleted in the zones of metamorphic white mica destruction, suggesting those elements were incorporated into the early-stage Fe-chlorite. However, corrected major element geochemistry clearly shows progressive enrichment of K, Mg and, to a certain extent, Na and Ca in subsequent alteration stages. For example, subtle enrichment of K-Mg-Na is evident during stilpnomelane alteration and is stronger again in the subsequent stage of Fe-Mg chlorite alteration. Such trends suggest a degree of wallrock buffering of the original hydrothermal fluid as inferred in Section 5.7.

The cause of the peculiar Al-enrichment (accompanied by enrichment of K, Mg and Na) during late-stage Fe-Mg chlorite alteration coincident with retrograde quartz solubility during the later stages of, or immediately post, deposition of Stage 4 quartz veins cannot be adequately explained. The retrograde quartz solubility has previously been tentatively attributed to pressure increases at relatively constant temperature during the waning stages of fault valve activity on the Great Chesney Fault and the transition from brittle to ductile deformation in the deposit (Section 5.7.5). It is possible this also triggered Al-mobility, although no net depletion of Al has been identified elsewhere in the deposit. However, if Al-depletion was relatively minor but widespread in the deposit (e.g. associated with the broad zones of early Fe-chlorite wallrock alteration) then it would not easily be detected. It is therefore suggested that Al mobility may be due to physical changes to the ore fluid rather than to any changes in fluid composition.

Table 34: Element enrichments and depletions in the New Occidental vein, ore mineral and alteration paragenesis.

Stage	Location	Quartz Vein Stage	Ore Mineralogy		Geochemistry		Gangue Minerals (Alteration + Vein)
			Major	Minor	Enrichments	Depletions	
1	Hanging wall	Stage 1: Strongly deformed coarsely crystalline quartz veins and breccia	Magnetite	Scheelite, wolframite	Fe-Mn-W	K-Be-Ba-Cs-Nb-Rb	Fe-rich chlorite, calcite
2	Deposit core	Stage 2: Moderately-strongly deformed crystalline to cryptocrystalline crustiform and colloform-banded quartz veins and breccias	Gold, maldonite (Au_2Bi), native bismuth, Se-rich ikunolite (Bi_4Se_3-Bi_4S_3 solid solution series), clausthalite-galena (PbSe-PbS solid solution series)	Rare species of bismuth selenides, pyrrhotite, chalcopyrite	Fe-Mn-Au-Se-Bi-As-Ag-Sb		Fe-rich chlorite
3	Deposit core	Stage 3: Moderately-strongly deformed crystalline crustiform and colloform-banded quartz veins and breccias	Bismuthinite (Bi_2S_3), "newoccidentallite" (Bi_5AuS_4)	Gold	Fe-Mn-Au-Se-Bi-As-Ag-Sb-K-Ba-Rb-Sr minor Mg		Stilpnomelane, minor biotite
4	Immediate Footwall and lesser Hanging wall	Stage 4: Weakly to moderately deformed microcrystalline quartz veins and breccias	Arsenopyrite		Mg-Fe-Mn-As-Ca-Sr-K-Ba-Rb-Al-Na and, locally, Ca	Locally Si	Mg-rich iron chlorite
5	Footwall + local Hanging wall		Chalcopyrite, pyrrhotite	Silver-rich gold or electrum - cassiterite	Fe-Cu-Sn-In K-Ba-Rb		Sericite
6	Deposit core		Sphalerite, galena, pyrrhotite		Fe-Zn-Pb-Ag-Cd	Insignificant	Greenalite, Fe-rich clay, calcite
7	Deposit core	Stage 5: Sparse undeformed quartz veins	Pyrite		Fe	Insignificant	Fe-rich clay

Geochemical studies completed herein provide some further evidence that a second hydrothermal fluid was introduced into the New Occidental deposit during the latter stages of deposit formation. Although the small volume of white mica developed in the deposit limits analysis of its geochemistry, K, Rb and Ba are enriched in the zones of white mica alteration and late-stage chalcopyrite - pyrrhotite (Table 34). This trend is different to the one of progressive K-Mg-Na-Ca enrichment previously attributed to wallrock buffering of the hydrothermal fluid. In addition, ore element geochemistry suggests two different (but related) associations in the deposit that correspond to the two stages of hydrothermal fluid activity:

1. Early stage gold-rich (Au-Ag-Bi-Sb-Se-W-Pb-As)

2. Late stage base metal rich (Cu-In-S-Sn, Zn-Cd±Mo and Fe-Co-Mn-S).

However, the presence of granitophile ore elements in both associations (Bi-W in the first stage and Sn-In±Mo in the second stage) suggest the two stages are potentially related through a common source. The sources of metals in the New Occidental deposit will be discussed in detail in Chapter 10 following analysis of lead and sulfur isotopes in Chapter 9.

7.5.5 Multi-Element Geochemistry as an Exploration Tool

Alteration studies have already demonstrated the extensive alteration haloes around the New Occidental deposit, including those subtle haloes detected by SWIR spectrometry, provide a vector to ore and can also be used to distinguish between gold-bearing and barren alteration systems. In contrast, ore element enrichment has been shown herein to be restricted to a relatively narrow zone around the deposit. Similarly, Robertson & Taylor (1987) have also identified narrow zones of ore element enrichment around other Cobar deposits, indicating the exploration target size of Cobar deposits will not be significantly enlarged through the use of multi-element geochemistry. However, the geochemical signatures of the two different ore-types in the New Occidental deposit established in this study can be used to assist exploration in the Cobar region in other ways.

The ore-element suites can be used to discriminate between gold and base metal systems. A key aspect of exploring for gold deposits in the Cobar Basin is determining whether there is a gold-rich component to the numerous zones of base metal mineralisation in the Cobar Basin (base metal deposits are not only more widespread than gold deposits but many gold deposits occur within broader zones of base metals). Therefore, identifying ore elements normally associated with early-stage gold (Au-Ag-Bi-Sb-Se-W-Pb-As) within base metal zones provides a positive indication that the system contains early-stage gold mineralisation. The early-stage ore elements may be remobilised by the over-printing base metal stage (e.g. Au, Ag, Sb, Se and Bi) or occur as remnants in within base metal mineralisation (e.g. W and As). For example, silver-rich gold and bismuth minerals associated with late stage chalcopyrite - pyrrhotite in the New Occidental deposit represent remobilised early-stage Au-Bi, whereas scheelite and wolframite inclusions in pyrrhotite constitute replaced W-bearing magnetite.

The larger and more diverse suite of elements identified herein can also be used to help identify potential ore zones, especially in the weathered environment. Gold, Ag,

Cu and Zn have been shown to be extremely mobile in the weathered environment in the Cobar region and may be completely stripped from weathered ore zones (Cohen et al., 1996). However, the extended suites contain elements that are immobile or relatively immobile in the extensive regolith overlying much of the Cobar Basin. These immobile elements may be retained in the weathered zone immediately above ore zones or in transported iron oxide lags lateral to ore zones (e.g. Peak Gold Mines data; McQueen et al., 2000; McQueen & Spry, 2000; Rutherford, 2000, Scott, 2000). For example, W and Bi associated with early-stage gold are retained in the weathering profile above many of the gold deposits in the Cobar Basin (McQueen et al., 2000; Peak Gold Mines data). Bismuth is also concentrated in iron oxide lags downstream from the New Occidental deposit (Peak Gold Mines data). Arsenic likewise has been shown to concentrate in lags (e.g. Elura deposit; Lorrigan, 2000). Lead, Sn and In also are largely immobile in the weathered environment and can be used to indicate the presence of late-stage base metal sulfide mineralisation.

7.6 Comparisons with Major Gold - Base Metal Deposit Types

The New Occidental deposit and other Cobar deposits are readily distinguished from the major gold - base metal deposit-types on the basis of mineralogy and geochemistry, although they have many of the characteristics of orogenic gold deposits and gold-rich volcanic-hosted massive sulfide deposits (Table 35).

The distinctive Fe-rich phyllosilicate alteration mineralogy of the New Occidental deposit contrasts with the generalised alteration mineralogy indicated for most major gold-base metal deposit types (Table 35). The predominance of chlorite - stilpnomelane over sericite and the absence of appreciable carbonates in the New Occidental deposit indicates the New Occidental ore fluid is characterised by higher $a(Fe^{2+})/ a(H^{+})$ values and lower Xco_2 compared to ore fluids associated with most other deposit types. Fe-chlorite - stilpnomelane - greenalite alteration minerals have, however, been reported from orogenic gold deposits hosted in iron-rich rock-types (e.g. Agnico-Eagle deposit, Quebec, Wyman et al. 1986) and from metamorphosed magnetite-bearing volcanic hosted massive sulfide deposits (e.g. Phelps Dodge deposit, Quebec - Kranidiotis & MacLean, 1987; Currawong deposit, Benambra, Victoria - Bodon & Valenta, 1995). Studies have shown the composition of host rocks plays an important role in determining the composition of alteration minerals in these deposits, with Fe-rich alteration minerals directly correlated with precursor Fe-rich host rocks (e.g. Phillips, 1986; Zhao et al., 1994; McCuaig & Kerrich, 1994; Ridley & Diamond, 2000; Eilu et al., 2001). In contrast, the sedimentary host rocks to the New Occidental deposit (and other Cobar deposits) are not particularly Fe-rich, indicating the deposit's Fe-rich character is, in large part, attributable to Fe-rich nature of hydrothermal fluids.

The initial stage of pre-gold ore minerals in the New Occidental deposit is characterised by a trace element association typical of granitic intrusive-related deposits (W-Bi-Te), the main gold ore mineral stage by trace elements typical of orogenic gold deposits (Au-Ag-As-Sb-Te-Sb-Se) whereas the later base metal-rich ore mineral stages have element associations more typical of volcanic-hosted massive sulfide deposits (Cu-Pb-Zn-Ag-Sn). In fact, base metals in many orogenic deposits are considered immobile (McCuaig and Kerrich, 1994; Eilu and Mikucki, 1998; Arne et al., 1999; Bierlein et al., 2000; Ridley & Diamond, 2000; Eilu et al., 2001).

Conversely, whilst gold-bearing volcanic-hosted massive sulfide deposits and to a lesser extent, intrusion-related gold-base metal deposits contain both gold and base metal mineralisation, those deposit-types usually do not contain the precious metal and trace element enrichments that characterise the New Occidental deposit (Table 35).

The overall tonnage and grade of the New Occidental deposit are typical of a number of gold deposit types, including epithermal and orogenic types (Figure 174a), whereas the Au/Ag ratio of the deposit is most similar to orogenic gold deposits, although the more silver-rich base metal stage in the New Occidental deposit (characterised by Ag/Au ratios >1) is most similar to volcanogenic massive sulfide deposits (Figure 174b).

Figure 174: Gold grade - deposit tonnage - silver grade plots showing predominance fields for major gold deposit types in relation to the New Occidental deposit.

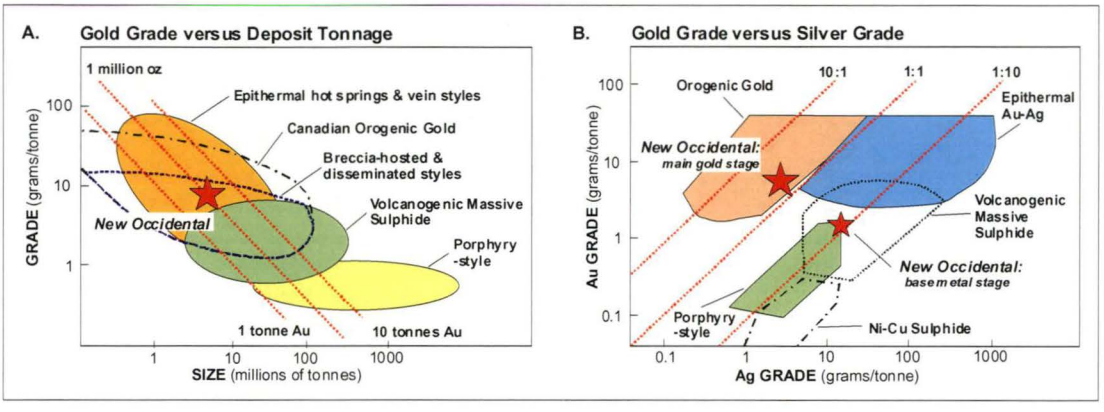

Major element enrichment/depletion patterns in the New Occidental deposit do not by themselves indicate a particular deposit-type affiliation. Major elements (Fe, Mg, Ca and Na) are variably enriched or depleted in orogenic gold deposits and other major deposit-types depending on the bulk composition of the host lithology (Kerrich, 1989; McCuaig and Kerrich, 1994; Ridley & Diamond, 2000).

Table 35: Geochemistry of major gold and base metal deposit-types.

Deposit Type	High or Enriched Elements	Associated Alteration	Low or Depleted Elements	Source
New Occidental deposit	Au, Ag, As, Sb, Te, S, Se, Bi, W, Mo, Sb, Sn, Cu, Pb, Zn, In, Cd, Co, Be, SiO_2, MgO, FeO	Quartz, Fe-chlorite, stilpnomelane, minor white mica, carbonate and greenalite - Fe-rich clays	K_2O, Rb, Ba ± Na_2O	This study
Orogenic Au deposits	Au, Ag, As, Sb, Te, S ±Se, ±Bi, ±W, ±Mo ±B, ±Sb, K_2O, Rb, Ba, Li, Cs, Tl, CH_4, H_2S. Variable MgO, FeO, CaO	Quartz, sericite, carbonate, chlorite	Na_2O, Sr, Y, Cu, Pb, Zn	McCuaig and Kerrich (1994); Robert & Poulsen, 1997; Eilu and Mikucki, (1998); Arne et al. (1999); Bierlein et al. (2000); Kerrich et al. (2000); Eilu et al. (2001)
Intrusion-related gold deposits associated with W-Sn provinces	Au, Bi, W, As, Sn, Mo, Te and Sb ±Cu	Quartz, K-feldspar, albite, carbonate and/or sericitic alteration assemblages		Groves et al., (1998); Thompson et al., (1999); Kerrich et al. (2000)
Sediment-hosted Zn-Pb-Ag deposits (SEDEX)	Zn, Pb, Tl, Mn, Fe ±As, ±Ba, ±Cu, ±Mo ±B	Carbonate alteration		McGoldrick and Large (1998); Large et al. (2000)
Low Sulfidation Epithermal deposits	Au, Ag, As, Sb, Zn, Pb, Hg, Se, K_2O and high Ag/Au ratios	Quartz (chalcedony), adularia, carbonate, sericite and illite-smectite	Cu and Te/Se ratios	White and Hedenquist (1995)
High Sulfidation Epithermal deposits	Au, Ag, As, Sb, Bi, Cu, Pb, Hg, Te, Sn, Mo and Te/Se ratios	Quartz, alunite, kaolinite, pyrophyllite, diaspore, illite	K_2O, Zn and Ag/Au ratios	White and Hedenquist (1995)
Porphyry Cu-Au deposits	Cu, Au, Mo, Ag, Zn, Pb, As, Sb, Hg, Te, Sn, S ±K	Quartz, biotite, magnetite, k-feldspar, actinolite → chlorite, epidote, calcite, albite, sericite, kaolinite with lesser variable argillic, advanced argillic and calc-silicate assemblages	CaO, MgO, Na_2O in deposit cores	Cooke et al. (1998); Kerrich et al. (2000)
Gold-rich Volcanic-Hosted Massive Sulfide deposits (VHMS)	Zn, Pb, Ag, Cu, Au, Mn, Ba, S, K_2O, MgO, CaO, FeO, Cd, Sn, Se, Co. Tl, Sb, Bi, Mo, As, Rb	Quartz, Fe-Mg chlorite, carbonate, sericite	Na_2O, Al_2O_3, Y, Nb, Sc, V, Sr	Galley (1995); Large et al., (1989); Huston (2000); Kerrich et al. (2000); Sharpe and Gemmell (2000); Large et al. (2001); Gemmell and Fulton (2001)
Iron Oxide Cu-Au deposits	Fe, Cu, Au, lesser Ag, As, Co, Fe, Mo, Nb, Ni, P, REE, U	Na-Ca feldspar to K-feldspar, sericite, fayalite-grunerite, actinolite, carbonate		Kerrich et al. (2000); Davidson & Large (1998); Hitzman & Valenta (2005)

8 FLUID INCLUSION STUDIES

8.1 Introduction

Paragenetically constrained fluid inclusion studies of the New Occidental deposit potentially resolve several key aspects of deposit formation, including the temperature and composition of the hydrothermal fluids and the physiochemical processes associated with mineral deposition (e.g. Roedder, 1984; Brown, 1998). However, several previous studies of mineral deposits in the Lachlan Orogen, including the nearby CSA deposit, have concluded fluid inclusions have been extensively modified by metamorphism and deformation and are largely unsuited to meaningful microthermometric analysis (e.g. Wilkins & Balkans, 1978; Marshall et al., 2000; Giles & Marshall, 2004). Cathelineau et al. (1991) and Ridley & Diamond (2000) highlighted additional problems associated with microthermometric analysis of fluid inclusions in orogenic gold deposits, including:

1. Difficulty visually identifying phase changes and estimating liquid/vapour ratios in the typically small inclusions;
2. Distinguishing mineralisation-related inclusion populations when multiple generations of fluid inclusions are present; and
3. Post-entrapment modification of fluid inclusions.

Therefore, the purpose of fluid inclusion studies of the New Occidental deposit is firstly to determine:

1. **Whether fluid inclusions in the New Occidental deposit are reliable indicators of main stage ore fluids?** Marshall et al. (2000) and Giles & Marshall (2004) argued the presence of recrystallised grain boundaries, widespread decrepitated and leaked inclusions and inconsistent liquid/vapour ratios of liquid+vapour inclusions indicate many quartz-sulfide veins in the CSA deposit have been extensively recrystallised. Similarly, Wilkins and Barkas (1978) suggested the majority of inclusions in syntectonic quartz from deformed granitic rocks in the Lachlan Orogen were introduced during deformation and recovery of the rocks. In contrast, other studies of Cobar deposits concluded fluid inclusion populations are representative of syn-deformational hydrothermal fluids (e.g. Seccombe, 1990; Hinman, 1992, Jiang, 1996; Forster, 1997; Sun & Seccombe, 2000).

Provided fluid inclusions in the New Occidental deposit are found to be representative of main-stage ore deposition, then:

2. **What are the temperatures and compositions of ore fluids associated with New Occidental deposit formation?** The detailed paragenesis established for the New Occidental deposit allows fluid inclusion data from vein quartz to be related to deformation, alteration and mineralisation stages and can provide independent constraints on formation temperatures and fluid compositions inferred from alteration mineralogy.

3. **Are changes in mineralogy of veins and associated alteration assemblages reflected in the chemistry of the fluids, and is there evidence for a second compositionally distinct ore fluid associated with the main stage of chalcopyrite mineralisation?** Analysis of fluid inclusions trapped in successive stages of quartz veins in the deposit may help explain the various trends in alteration and ore mineral deposition evident in the deposit, including changes from early-stage precious metal deposition to late-stage base metal deposition.

8.2 Previous Fluid Inclusion Studies of Cobar Deposits

Fluid inclusion studies have not previously been undertaken on the New Occidental deposit. However, fluid inclusions from several of the other Cobar deposits have been analysed (Table 36).

The studies acknowledged the relatively small size (<20 μm) of fluid inclusions, the dominance of secondary fluid inclusion populations and the relative scarcity of remnant populations of undeformed "primary" inclusions (Brill, 1998a; Seccombe, 1990; Jiang, 1996). Studies also noted the presence of abundant deformation textures, including sub-grain boundaries and deformation bands. Non-planar anhedral to euhedral inclusions in relatively undeformed sections of minerals have been regarded as primary inclusions (Brill, 1998a; Seccombe, 1990; Jiang, 1996; Forster, 1997). Seccombe (1990) suggested the best primary inclusions from the Elura deposit occurred in clear equigranular quartz aggregates adjacent to sulfides. However, Giles & Marshall (2004) argued clear quartz adjacent to sulfides in the CSA deposit was "recrystallised" and are therefore unrepresentative of ore fluids. Secondary inclusions are typically arranged in planar arrays around healed microfractures or associated with grain boundaries. Many inclusions, including probable primary inclusions, are strongly deformed (necked, stretched and flattened) and exhibit variable liquid/vapour ratios, suggesting they have leaked (Brill, 1998a; Seccombe, 1990; Jiang, 1996; Forster, 1997, Giles & Marshall, 2004). Marshall et al. (2000) identified decrepitated inclusions in quartz veins in the CSA deposit. They attribute decrepitation of fluid inclusions to fluctuating fluid pressures during vein formation, with explosive decrepitation occurring in inclusions entrapped during fluid over-pressuring that were subsequently exposed to lower fluid pressures and implosive decrepitation when inclusions forming during periods of low fluid pressure were subjected to over-pressuring.

Fluid inclusions from all of the deposits studied had very simple compositions comprising only liquid (L) and vapour (V) phases. Daughter minerals are extremely rare, with Jiang (1996) recognising minor solid phases in Stage 3 fluid inclusions from the main part of the Peak orebody. The bulk of inclusions homogenised to the liquid phase although vapour-rich inclusions have been recognised in the CSA deposit (Brill, 1998a) and Peak deposit (Hinman, 1992; Jiang, 1996). Inclusions are generally water-rich, although CO_2 and CH_4- bearing inclusions have been recognised in the CSA (Brill, 1988a; Giles & Marshall, 2004), Elura (Seccombe, 1990) and Peak deposits (Hinman, 1992; Jiang, 1996).

Table 36: Results of Previous Fluid Inclusion Studies on Cobar Deposits.

Deposit	Inclusion Types	Inclusion Composition L= Liquid V = Vapour	Inclusion Size (average μm)	Homogenisation Temperature (T_h)	Inclusion Salinity (wt% NaCl)
Peak (Hinman, 1992)	Quartz· Stage 3 (qtz-galena-sphalerite)	L + V (CH_4-CO_2)		$T_{h(L)}$ = 140–360°C	2–5 wt% NaCl
(Lawrie & Hinman, 1998)	Quartz Stage 4 (qtz-pyrrhotite-chalcopyrite-Au-chlorite-sericite)	L + V (CH_4)		$T_{h(L)}$ = 300–350°C	4–6 wt% NaCl (max)
Peak Jiang, 1996)	Quartz· Stage 1	L + V (V/L = <0 1)	2–5μm diam.	$T_{h(L)}$ = 232–317°C	0 8–4 3 wt% NaCl
	Quartz-Chalcopyrite Stage 2 Cu-Au mineralisation (based on secondary inclusions in Stage 1 quartz)	L + V (V/L = <0 1)	1–8μm diam	$T_{h(L)}$ = 283–364°C	3–23 wt% NaCl
	Quartz Stage 3	L + V V/L = 0 05–0 7	2–10μm diam.	$T_{h(L)}$ = 205–393°C	1 9–12 4 wt% NaCl
	Quartz-Sphalerite: Stage 4 Pb-Zn mineralisation (based on secondary inclusions in Stage 1–3 quartz)	L + V V/L = 0.03–0.15	2–9μm diam	$T_{h(L)}$ = 300–393°C	6–41 wt% NaCl (max)
	Quartz: Stage 5	L + V V/L = 0.05–0.15	2–10μm diam.	$T_{h(L)}$ = 190–355°C	2.7–6 4 wt% NaCl
	Quartz· Stage 7	L + V V/L = 0.05–0 10	2–10μm diam	$T_{h(L)}$ = 197–300°C	1.4–4.2 wt% NaCl
Chesney (Jiang, 1996)	Quartz Stage 2	L + V V/L = 0 1–1.0	≤10μm diam	$T_{h(L)}$ = 179–317°C	2 5–6.3 wt% NaCl
	Quartz Stage 3	L + V V/L = 0 1–1 0	≤10μm diam.	$T_{h(L)}$ = 151–243°C	5 2–6 9 wt% NaCl
	Quartz· Stage 4	L + V (liquid-rich)	≤4μm diam	$T_{h(L)}$ = 285–381°C	4 6–9 1 wt% NaCl
	Quartz Stage 5	L	≤4μm diam		6 7–7 6 wt% NaCl
CSA (Brill, 1988a)	Quartz· Type A (often fibred quartz and mainly associated with Pb-Zn mineralisation or chlorite shear zones)	L + V (CH_4) V/L = 0 5–2	≤15μm diam	$T_{h(L)}$ = 199–389°C (3 inclusions homogenised to V)	1.8–2.2 wt% NaCl
	Quartz-Calcite. Type B (all quartz types)	L + V (CH_4-CO_2) V/L ratios constant	≤15μm diam	As above	As above
	Quartz Type C (secondary)	L ± V	≤5μm	Not analysed	Not analysed
CSA (Giles & Marshall, 2004)	Quartz Syn-mineralisation			$T_{decrepitation}$ = 350–380°C	
	Quartz. Stage 2 post-mineralisation)	L (CH_4)		T_t = 350°C	
	Quartz· Stage 3 post-mineralisation	L + V (CH_4)		$T_{h(L)}$ = 196–326°C T_t = 330–350°C	<5 wt% NaCl
	Quartz: Stage 4 post-mineralisation	L+ V (H_2O only)		$T_{h(L)}$ = 127–305°C T_t = 275–350°C	<7 wt% NaCl
Elura (Seccombe, 1990)	Quartz (fibred quartz from pyritic and siliceous ores)	L + V (CH_4-CO_2) V/L = 0 1–0 4	≤20μm diam	$T_{h(L)}$ = 298–354°C & $T_{h(L)}$ = 150–231°C	1.4 wt% NaCl
	Quartz (extension veins in wallrock)	L + V (CH_4–CO_2) V/L = low	≤20μm diam.	$T_{h(L)}$ = 170–225°C	
Elura (Lawrie & Hinman, 1998)	Quartz Stage 2 (qtz-carbonate)	L + V (H_2O-n-alkanes)		$T_{h(L)}$ = 120–160°C	
	Quartz Stage 3 (qtz-pyrite)	L + V (H_2O- CH_4-C_2H_6-CO_2)		$T_{h(L)}$ < 220°C	
(Sun and Seccombe, 2000)	Quartz-Sphalerite. Stage 5 (qtz-sphalerite-galena-pyrrhotite-sericite-chlorite-dolomite)	L + V (H_2O- CH_4-CO_2)		$T_{h(L)}$ = 220–270°C	13 wt% NaCl (max)
	Quartz? Stage 6 (qtz-tetrahedrite-tennantite-enargite-chalcopyrite-galena-pyrite- Ba-feldspar-chlorite-albite)	L + V (H_2O- CH_4-CO_2) (more vapour-rich)		$T_{h(L)}$ = 330–380°C (Lawrie & Hinman, 1998) $T_{h(L)}$ = 130–423°C (Sun & Seccombe, 2000)	6 wt% NaCl (max) (Lawrie & Hinman, 1998) 1.5–63 wt% NaCl (max) (Sun & Seccombe, 2000)
McKinnons (Forster, 1997)	Quartz-Calcite Stage 4 (qtz-carbonate-sphalerite-galena)	L + V (CO_2)	≤15μm diam	$T_{h(L)}$ = 297–307°C	4–8 wt% NaCl
(Forster &	Quartz Stage 5 (qtz-	L + V (CO_2)	≤15μm diam	$T_{h(L)}$ = 220–269°C	5–6 wt% NaCl

Deposit	Inclusion Types	Inclusion Composition L= Liquid V = Vapour	Inclusion Size (average μm)	Homogenisation Temperature (T_h)	Inclusion Salinity (wt% NaCl)
Seccombe, 1999)	carbonate-base metals-pyrite)				
	Quartz. Stage 6 (qtz-chlorite-k-feldspar)	L + V (CO_2)	≤12μm diam.	$T_{h(L)}$ = 157–240°C	4–5 wt% NaCl
	Quartz Stage 7	L + V (CO_2?)		$T_{h(L)}$ = 112–173°C	1–4 wt% NaCl

A common issue with the fluid inclusion studies undertaken to date on Cobar deposits is that quartz vein paragenetic sequences are poorly defined and relationships between quartz veins and gold-sulfide minerals are ambiguous. Paragenetic sequences used to constrain fluid inclusion studies of the Peak, CSA, Elura and Chesney deposits (e.g. Brill, 1988a; Seccombe, 1990; Hinman, 1992; Jiang 1996; Giles & Marshall, 2004) rely on stages of quartz veins distinguished on the basis of either mineralogy of the spatially associated sulfide minerals and/or the orientation and internal textures of quartz veins. Firstly, as has been shown in the New Occidental deposit, sulfide minerals may post-date associated quartz or may not even be directly associated with a quartz vein stage. Most previous studies have not adequately established the relative timing of quartz vein formation and spatially associated gold/sulfide ore minerals. Secondly, a quartz vein stage may comprise veins with multiple orientations, including both sub-horizontal and steeply dipping orientations, and contain a range of textures including open-space infill, comb, breccia and laminated forms. Based on descriptions of the different quartz vein stages cited in those studies (e.g. Brill, 1988a; Seccombe, 1990; Jiang, 1996; Giles & Marshall, 2004) and the author's own observations (Section 4.6), many quartz vein stages identified in those studies are poorly constrained and most likely part of the same stage.

8.3 Data Collection & Analytical Techniques

Detailed fluid inclusion petrography of 24 samples of quartz vein material from the four main quartz veins stages in the New Occidental deposit was undertaken by the author to determine the character and distribution of fluid inclusion populations and their relationship to primary and secondary deformational and metamorphic fabrics. Semi-quantitative estimates of fluid inclusion size and liquid/vapour ratios in fluid inclusions were also made.

Microthermometric measurements of suitable fluid inclusions in 8 of the 24 samples were subsequently collected (Figure 175), including homogenisation temperatures (T_h), melting temperatures of ice and occasionally of clathrate (Tm), and rarely, eutectic temperatures (T_e). In addition, decrepitation temperatures (T_d) were also measured. These measurements provide non-pressure corrected trapping temperatures and fluid inclusion salinities. Microthermometry was undertaken in the Fluid Inclusion laboratory, University of Tasmania with a Linkam MDS600 heating/freezing stage. The stage has an upper temperature limit of 600°C and was calibrated using synthetic fluid inclusions supplied by Synflinc Inc. Fluid inclusions were initially frozen and, where possible, the temperature of first melting (T_e), final melting (T_m) and clathrate melting (T_c) were recorded. Fluid inclusions were then heated and temperatures of homogenisation (T_h) measured. The precision of measured temperatures are ± 1.0°C for heating and ± 0.3°C for freezing. Salinities

were calculated as NaCl equivalent weight percent (eq. wt.% NaCl) from freezing point depression temperatures and applying a linear least squares regression method (Potter et al., 1978).

Figure 175: Location of fluid inclusion samples used for microthermometric analysis.

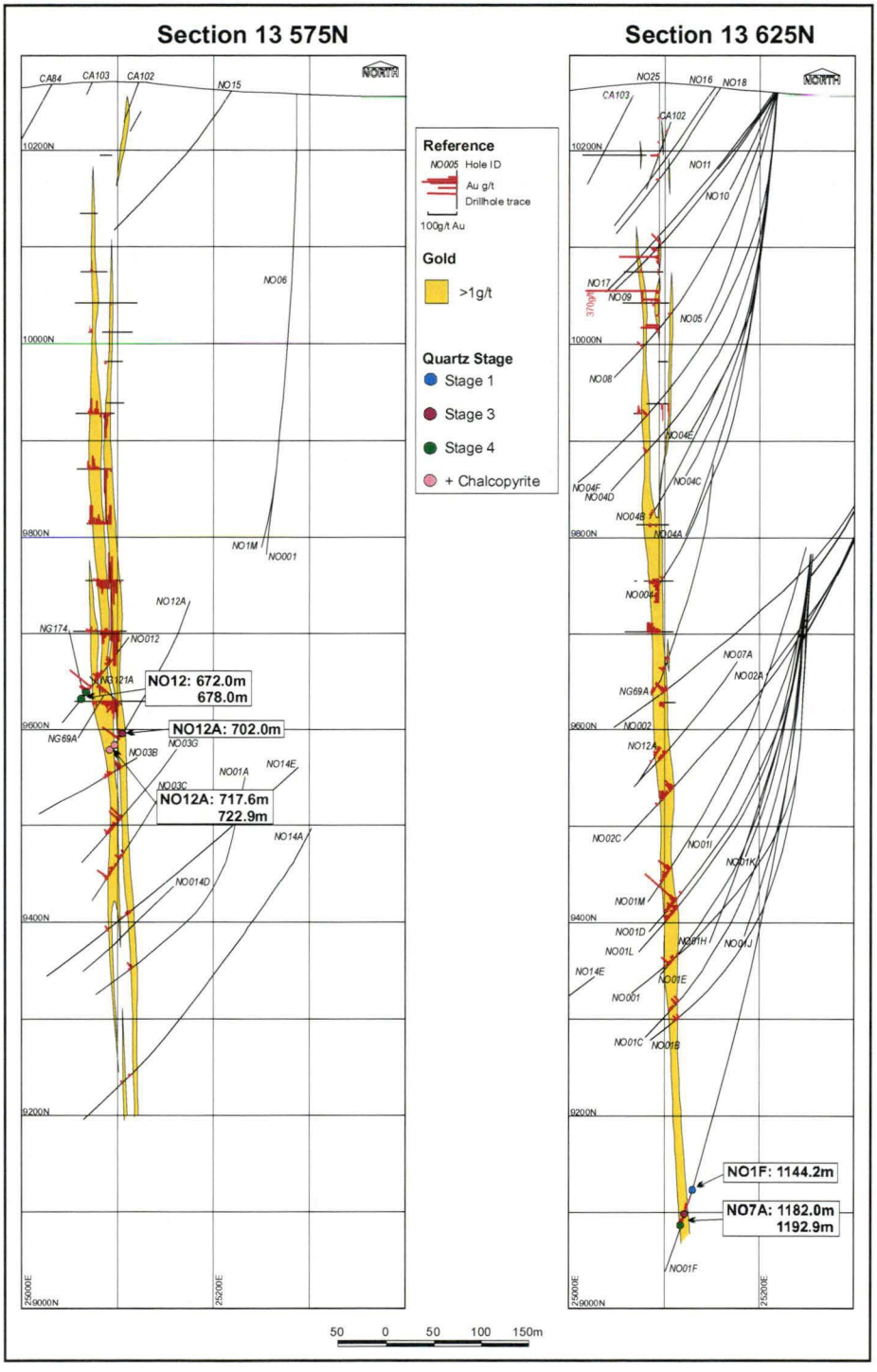

Thermal-decrepitation mass spectrometric analysis was performed on 14 quartz samples from the New Occidental deposit by CODES SRC staff at the request of the author to provide semi-quantitative information on the bulk compositions of fluid

inclusions in the New Occidental deposit. Samples of quartz were drilled out, washed with 6M HCl overnight, dried and then washed with analytical grade acetone. The procedure was designed to remove sulfides and any organic contaminants existing on the surface of the sample. Samples were then heated to 550°C in a mass spectrometer at the Central Science Laboratory, University of Tasmania and the bulk composition of gases released during rupturing of the contained fluid inclusions was analysed. The technique, although unable to discriminate between different stages of fluid inclusions, offered a simple method of identifying the presence of four gases, H_2S, CH_4, CO_2 and N_2, in the fluid inclusions. This approach was considered valid because most of the two-phase fluid inclusions in the New Occidental deposit are either primary or psuedosecondary inclusions. Unfortunately, the methodology as applied was not entirely successful, as the acetone treatment did not completely remove organic contamination, which was detected in all samples analysed and was reflected in low-temperature NH_2 absorption features. Furthermore, the presence of organic contaminants prevents detection of small quantities of CO_2 in the samples. The results of the analysis are summarised in a report prepared by Zaw and Dedenczuk (2000).

8.4 Petrography of New Occidental Fluid Inclusions

Fluid inclusions are relatively common in quartz from the New Occidental deposit. However, most inclusions are extremely small (<1–2μm diameter) with only 1–2% of all inclusions being >5μm in diameter. Of the 24 samples selected for fluid inclusion examination (on the basis of transparency and apparent absence of deformation effects), only 8 samples contained fluid inclusions of sufficient size for microthermometric analysis (>5μm in diameter). Largest fluid inclusions were located in Stage 1 (Figure 177a–c) and 3 (Figure 177d–f) quartz and some Stage 4 quartz (Figure 177g–v), whereas fluid inclusions could not be identified in the Stage 2 cryptocrystalline quartz and those in Stage 5 quartz were too small for analysis. A minor but distinctive phase of late-Stage 4 quartz developed around clusters of chalcopyrite - pyrrhotite, forming relatively undeformed overgrowths on pre-existing Stage 3 and 4 quartz crystals, yielded relatively abundant fluid inclusions (Figure 177o–r).

Much of the vein quartz vein in the New Occidental deposit is highly fractured and clouded with multiply oriented microfissures filled with very fine-grained often decrepitated fluid inclusions and inclusions of chlorite, stilpnomelane and other phyllosilicate phases. Even relatively undeformed quartz crystals exhibit undulose extinction. However, there is little evidence of significant recrystallisation of quartz or resetting of quartz grain boundaries (c.f. descriptions of the CSA deposit in Marshall et al., 2000). Where quartz is strongly deformed (recognised by the presence of deformation bands and increased density of cross-cutting microfissures), fluid inclusions are often flattened parallel to cleavage and stretched and necked along cleavage. Deformed inclusions are also characterised by overall lower concentrations of vapour phase, suggesting some leakage of inclusion contents. Deformation effects are clearly strongest in earlier quartz vein stages (Stage 1 and 3 quartz) and weakest in Stage 4 quartz veins, although Stage 4 quartz is also locally strongly deformed. Relatively undeformed quartz occurs predominantly in areas of open-space filling Stage 3 quartz vein breccias from the centre of the deposit and in the main footwall

Stage 4 quartz vein breccia. The late-Stage 4 quartz overgrowths associated with chalcopyrite - pyrrhotite are also relatively undeformed.

Three types of fluid inclusions were identified in the New Occidental deposit (Figure 176):

1. **Primary** - Primary inclusions that formed concurrently with host quartz were only observed in relatively undeformed crystalline quartz (typically Stage 3 and 4 quartz, with rare examples in Stage 1 quartz), either weakly aligned parallel to well-developed primary growth bands in the host quartz crystal crystals (Figure 177a-c) and/or randomly oriented throughout cores of euhedral zoned quartz (Figure 177d-e). Primary inclusions were also observed in late-Stage 4 quartz overgrowths associated with chalcopyrite – pyrrhotite (Figure 177f-g). Primary fluid inclusions comprise of relatively rare small to large (maximum 20μm diameter), equant to rounded two-phase (liquid + vapour: 5–50% vapour) fluid inclusions (Figure 177h-p). The equant negative crystal shapes infer relatively rapid cooling, and therefore limited recrystallisation of the host minerals (e.g. Roedder, 1997). No solid phases were observed in this inclusion type.

   Vapour-rich inclusions were identified in Stage 3 quartz within cores or along growth bands in relatively undeformed quartz crystals (Figure 177h-k). The inclusions are typically interspersed with liquid-rich inclusions. Vapour-rich and liquid-rich inclusions both occur in the same growth band or crystal core indicating they are part of the same fluid inclusion population. Dark rims on vapour bubbles in some vapour-rich inclusions suggest thin liquid CO_2 rims may be present (Figure 177i-l).

2. **Pseudo-secondary** – Trails of pseudo-secondary fluid inclusions occur in discordant planes that cross-cut primary vein fabrics including growth bands. The planes are often perpendicular or oriented at high angles to growth bands, terminate within the quartz crystal and may be terminated at growth zones in crystals, indicating they formed during crystal growth (Figure 177b, c, q). They often occur in close proximity to primary inclusions and have equivalent or slightly lower vapour concentrations. Such inclusions are interpreted to represent entrapment of primary hydrothermal fluid in micro-fissures formed during growth of the host crystal (c.f. Roedder, 1984). Pseudo-secondary fluid inclusions are typically small to medium-sized (<5μm diameter), equant and two-phase (liquid + vapour: 1–10% vapour).

3. **Secondary** – Secondary fluid inclusions are located along planar healed microfractures that crosscut both growth bands and quartz grain boundaries (Figure 177b, c, g). They are small (<1–2μm diameter) thin and relatively flat, mainly single phase (liquid only) with lesser two-phase (liquid + vapour: <5% vapour) fluid inclusions (Figure 177r).

Figure 176: Schematic representation of types of fluid inclusions in the New Occidental deposit.

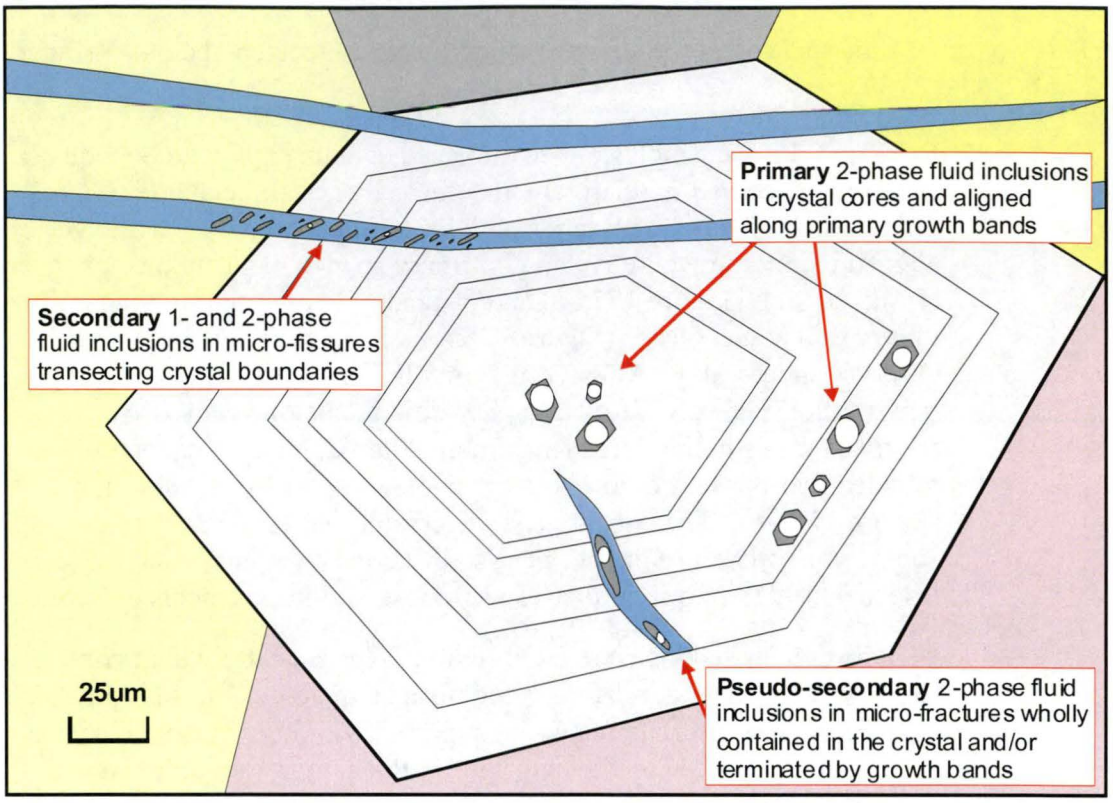

Figure 177: Examples of fluid inclusions in the New Occidental deposit.

a) NO1F-1144.2m: Stage 1 comb quartz containing growth bands nucleated on wallrock (left) with calcite in core of vein (right). Primary two-phase (L+V) inclusions occur in the zoned cores (plane light).

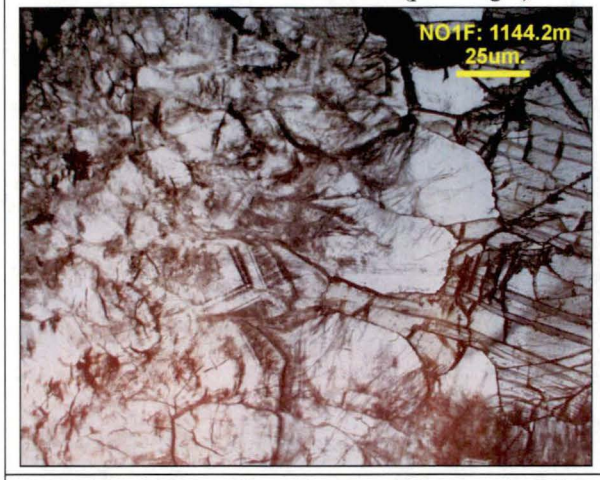

b) NO1F-1182.0m: Stage 3 quartz with growth bands defined by chlorite inclusions. Zoned cores contain primary two-phase inclusions and cross-cutting trails of pseudo-secondary inclusions (plane light).

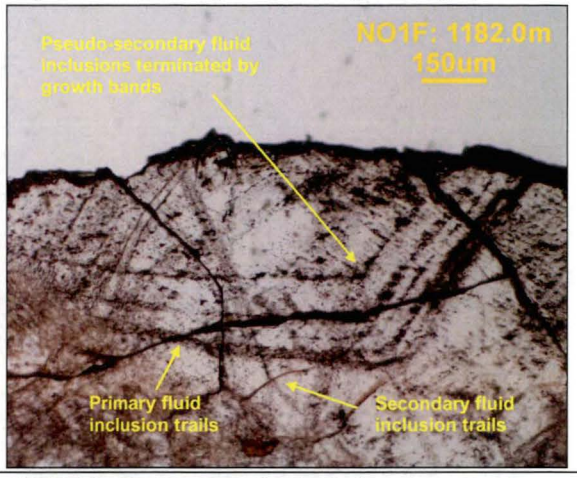

c) NO12A-702.0m: Stage 3 quartz vein breccia with trails of primary inclusions defining growth bands and perpendicular trails of pseudosecondary and secondary inclusions (plane light)

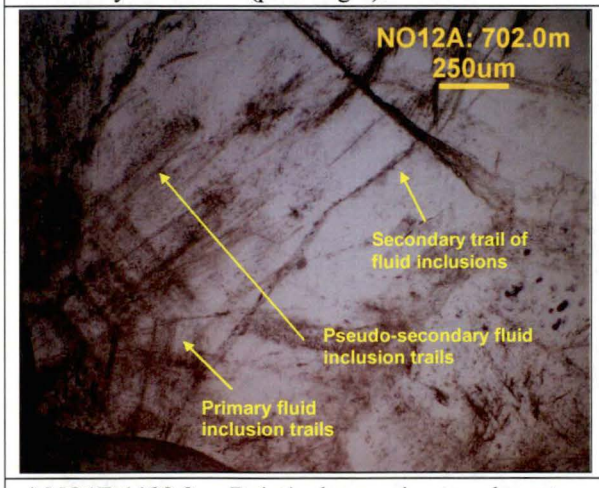

d) NO12-672.0m: zoned euhedral quartz crystal, containing abundant primary two-phase (L+V) fluid inclusions, rimmed by quartz-chlorite in Stage 4 open-space fill quartz vein breccia (plane light).

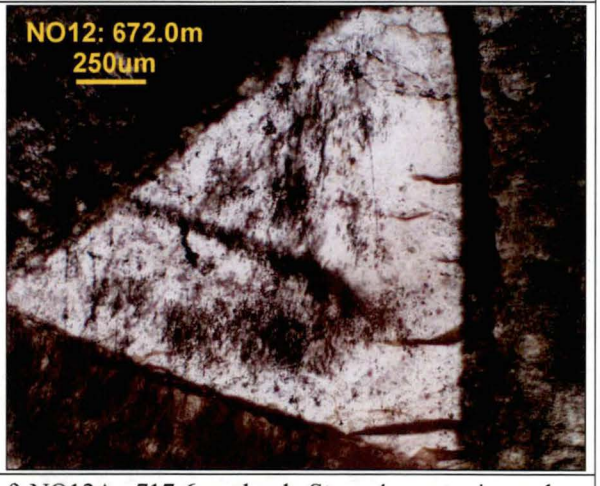

e) NO1F-1192.9m: Relatively massive translucent quartz core surrounded by cloudy quartz-chlorite intergrowth in open-space fill Stage 4 footwall quartz breccia (plane light).

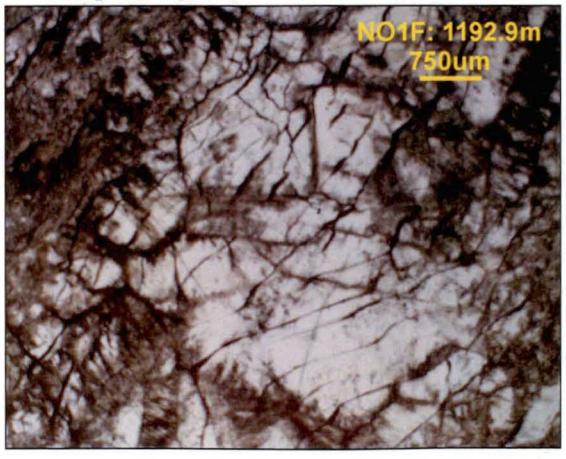

f) NO12A - 717.6m: cloudy Stage 4 quartz rimmed by clear quartz and chalcopyrite (grey). The clear quartz contains numerous small primary two-phase (L+V) inclusions (reflected light).

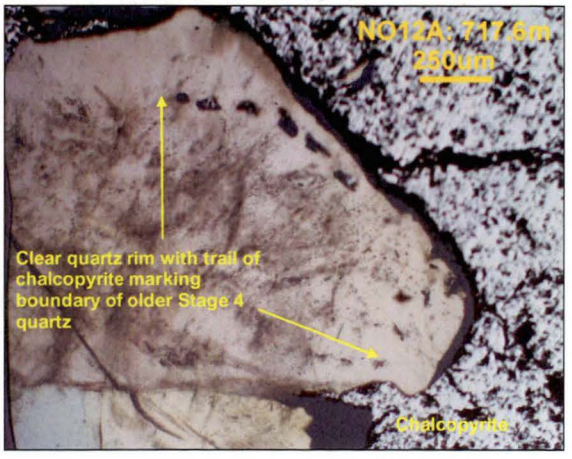

g) NO12A - 722.9m: clear Stage 4 quartz overgrowths around opaque chalcopyrite in Stage 3 comb quartz containing primary two-phase (L+V) inclusions and trails of secondary single phase (L) fluid inclusions (plane light). The core of the quartz crystal contains common decrepitated inclusions.

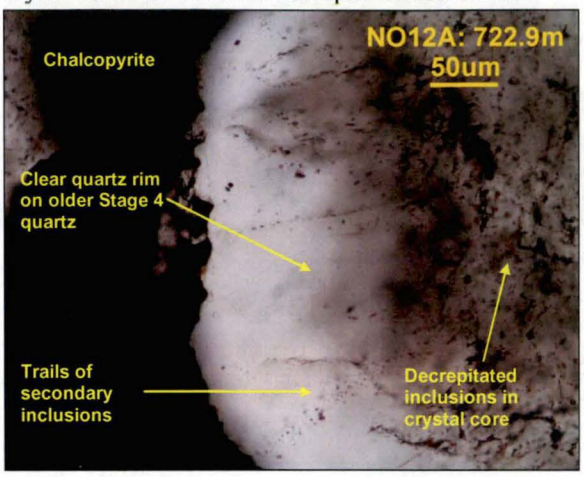

h) NO12A-702.0m: primary vapour-rich two phase (L+V) inclusions from the growth bands in the crystal centre in c) (plane light). Note decrepitated inclusions at right.

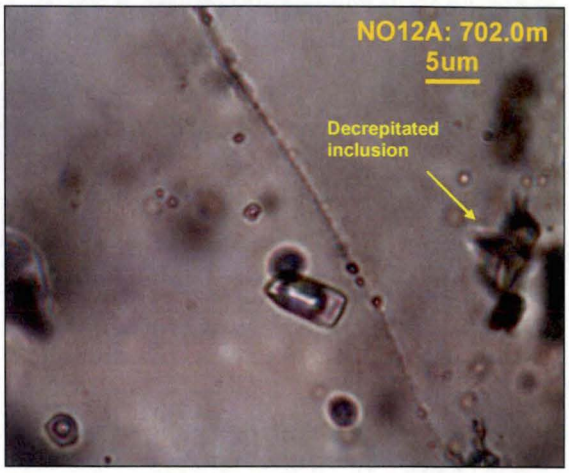

i) NO1F-1182.0m: Primary two-phase vapour-rich (L+V) inclusions from the centre of b) (plane light). The smaller of the two equant inclusions contains a possible CO_2 bubble.

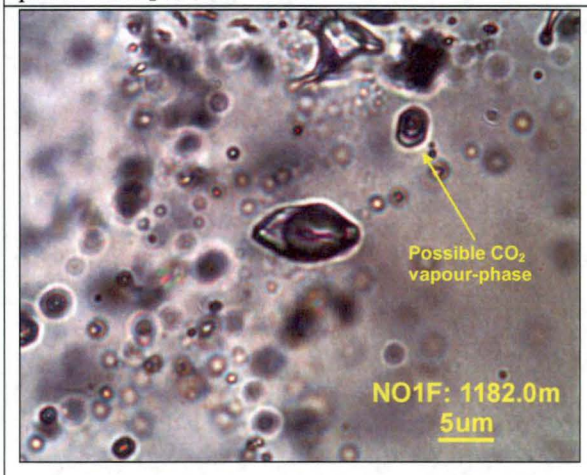

j) NO1F-1182.0m: large primary two-phase vapour-rich (L+V) inclusion with possible liquid CO_2 rim around the vapour bubble (plane light).

k) NO12A - 717.6m: equant primary two-phase (L+V) vapour-rich inclusion with possible liquid CO_2 rim around the vapour bubble (plane light).

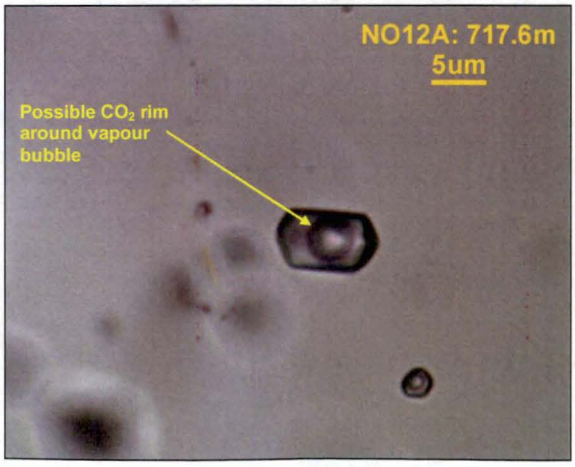

l) NO12A - 717.6m: large flattened primary two phase (L+V) inclusion with possible liquid CO_2 rim around the vapour bubble (plane light).

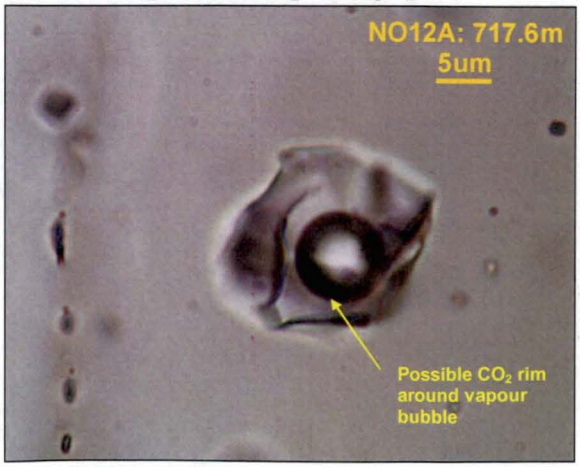

m) NO1F-1192.9m: trail of generally equant primary two-phase (L+V) inclusions with some larger flattened primary inclusions (plane light).

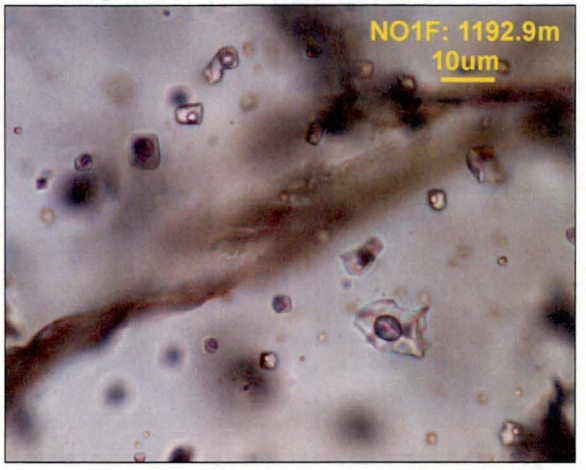

n) NO12A-702.0m: large necked and flattened primary two-phase (L+V) inclusions from the growth bands in the crystal centre in c) (plane light).

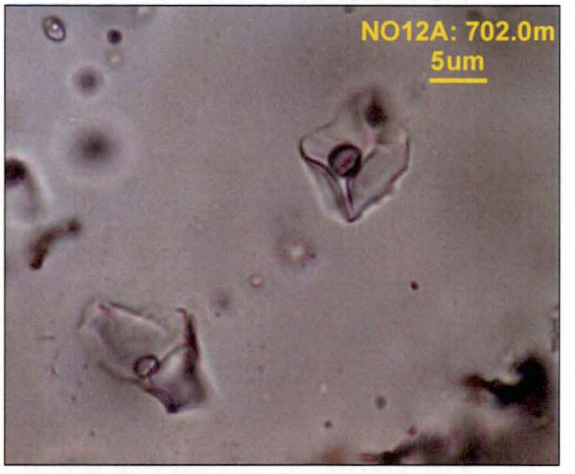

o) NO1F-1182.0m: trails of elongate primary two-phase (L+V) inclusions defining growth bands in the core of the quartz crystal (plane light).

p) NO12-672.0m: scattered small two-phase (L+V) primary inclusions and one large vapour-rich flattened inclusion the core of the quartz crystal in d) (plane light).

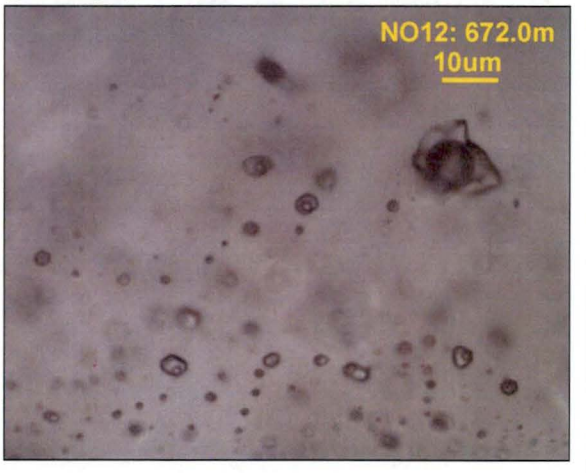

q) NO1F-1144.2m: trails of pseudosecondary inclusions cross-cut growth bands in a zoned quartz crystal (plane light).

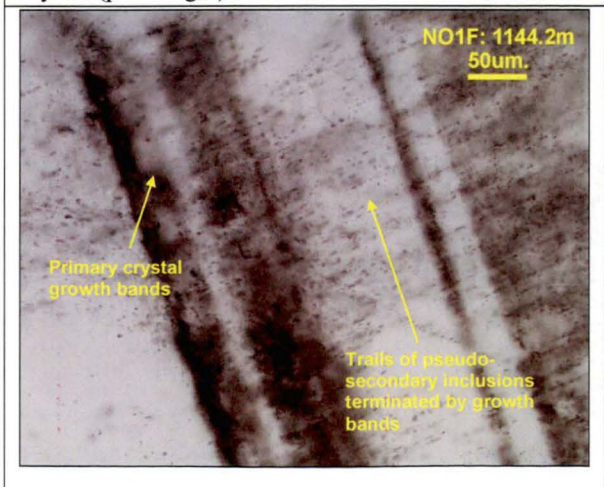

r) NO1F-1144.2m: trails of small secondary two-phase (L+V) inclusions (plane light).

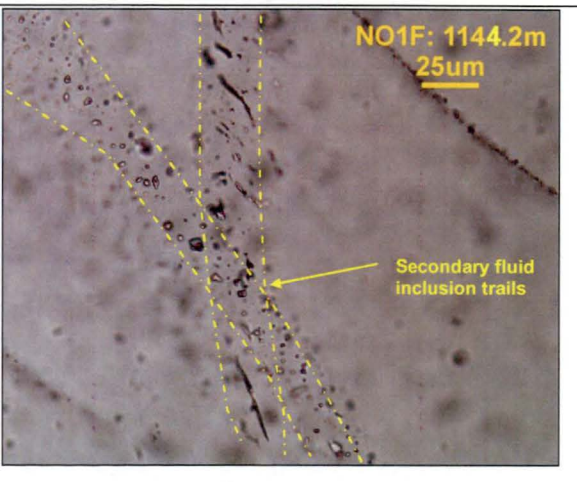

8.5 Microthermometric & Mass Spectrometric Analysis of Fluid Inclusions

8.5.1 Results of Microthermometric & Mass Spectrometric Analysis

Microthermometric data were mainly derived from primary and pseudosecondary fluid inclusions in Stage 3 and 4 quartz, including late Stage 4 quartz associated with chalcopyrite - pyrrhotite. Limited data was obtained from Stage 1 quartz (Table 37).

Table 37: Numbers of microthermometric measurements collected from the New Occidental deposit.

Sample No.	Host	Inclusion Type	$n_{(Th)}$	$n_{(Tm)}$	$n_{(Te)}$	$n_{(Tc)}$
NO1F-1144.2m	Stage 1 Quartz	Liquid-rich	22	24	1	
NO1F-1182.0m – Core	Stage 3 Quartz	Liquid-rich	55	8	4	1
		Vapour-rich	7	1	1	
NO1F-1182.0m – Rim	Stage 3 Quartz	Liquid-rich	11	5	-	3
		Vapour-rich	2			1
NO12A-702.0m	Stage 3 Quartz	Liquid-rich	64	15	7	4
		Vapour-rich	5	3	2	1
NO1F-1192 9m	Stage 4 Quartz	Liquid-rich	38	16		
NO12-672.0m	Stage 4 Quartz	Liquid-rich	15	15		
NO12-678.0m	Stage 4 Quartz	Liquid-rich	16	17	2	
NO12A-717.6m	Stage 4 Quartz with chalcopyrite	Liquid-rich	37	11	11	6
NO12A-722 9m	Stage 4 Quartz with chalcopyrite	Liquid-rich	15	16	-	-
TOTAL			**287**	**131**	**28**	**16**

Temperatures of final melting and clathrate melting were only recorded for a few larger fluid inclusions as such measurements are extremely difficult where inclusions are <5μm in diameter). In a number of instances, final melting was recognised by sudden bubble mobility or bubble expansion. Upon heating, a significant number of both small and large irregular-shaped two-phase fluid inclusions decrepitated at temperatures in the range 200–300°C. As a result, only final melting temperatures were recorded for some fluid inclusions. Homogenisation experiments were repeated up to three times in order to determine whether results are reproducible.

New Occidental samples display a range of final melting temperatures (T_m = -0.2 to -6.8°C) with samples of Stage 3 quartz and late Stage 4 quartz associated with chalcopyrite yielding lowest values (Figure 178; Table 38). Two samples (NO1F-1144.2m; NO12-678.0m) yielded first melting temperatures (T_e) in the range of -20 to -21°C. Fluid inclusions in three samples (NO1F-1182.0m; NO12-702.0m; NO12A-717.6m), including vapour-rich inclusions, yielded significantly lower first melting temperatures (minimum -61.5°C). Those samples also contained clathrate (gas hydrate $CO_2.5¾H_2O$) and yielded clathrate melting temperatures (T_c) of +1 to +12°C (Figure 178; Table 38). Although liquid CO_2 was tentatively identified in some of the larger vapour-rich inclusions at room temperature, homogenisation of liquid CO_2 was not observed. None of the inclusions changed colour upon freezing.

Homogenisation temperatures (T_h) of fluid inclusions in the New Occidental deposit exhibit a significant range (122–411°C), with many samples containing multiple

populations of inclusions with different ranges of homogenisation temperatures (Figure 178; Figure 179; Table 38).

Figure 178: Summary of microthermometric data for New Occidental deposit.

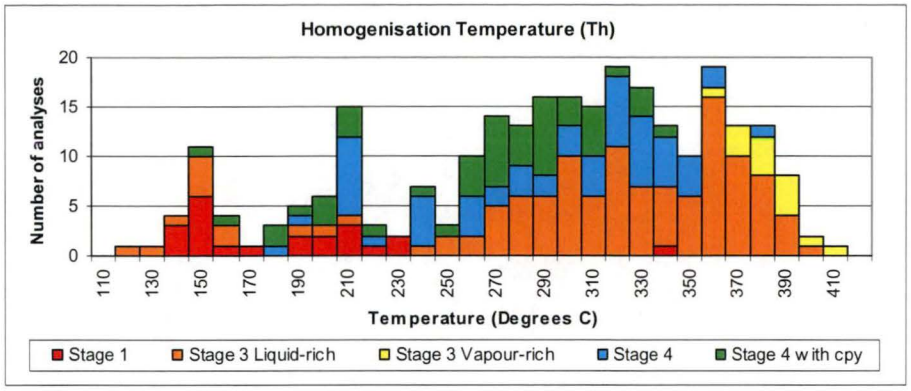

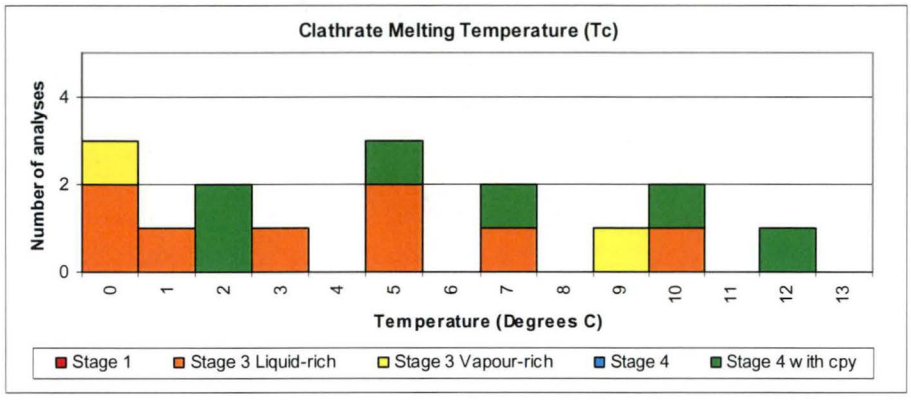

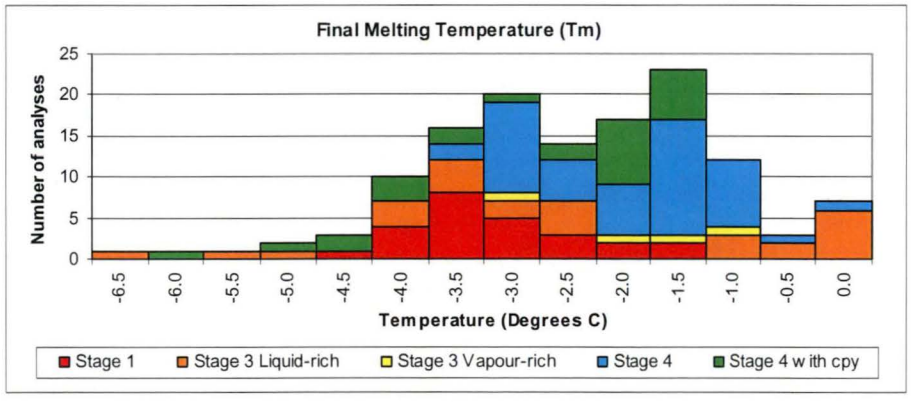

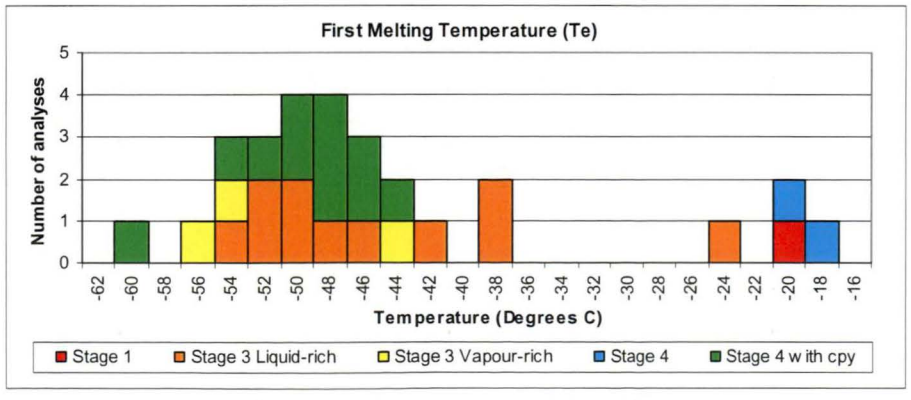

Figure 179: Homogenisation temperatures (T_h) for New Occidental fluid inclusions.

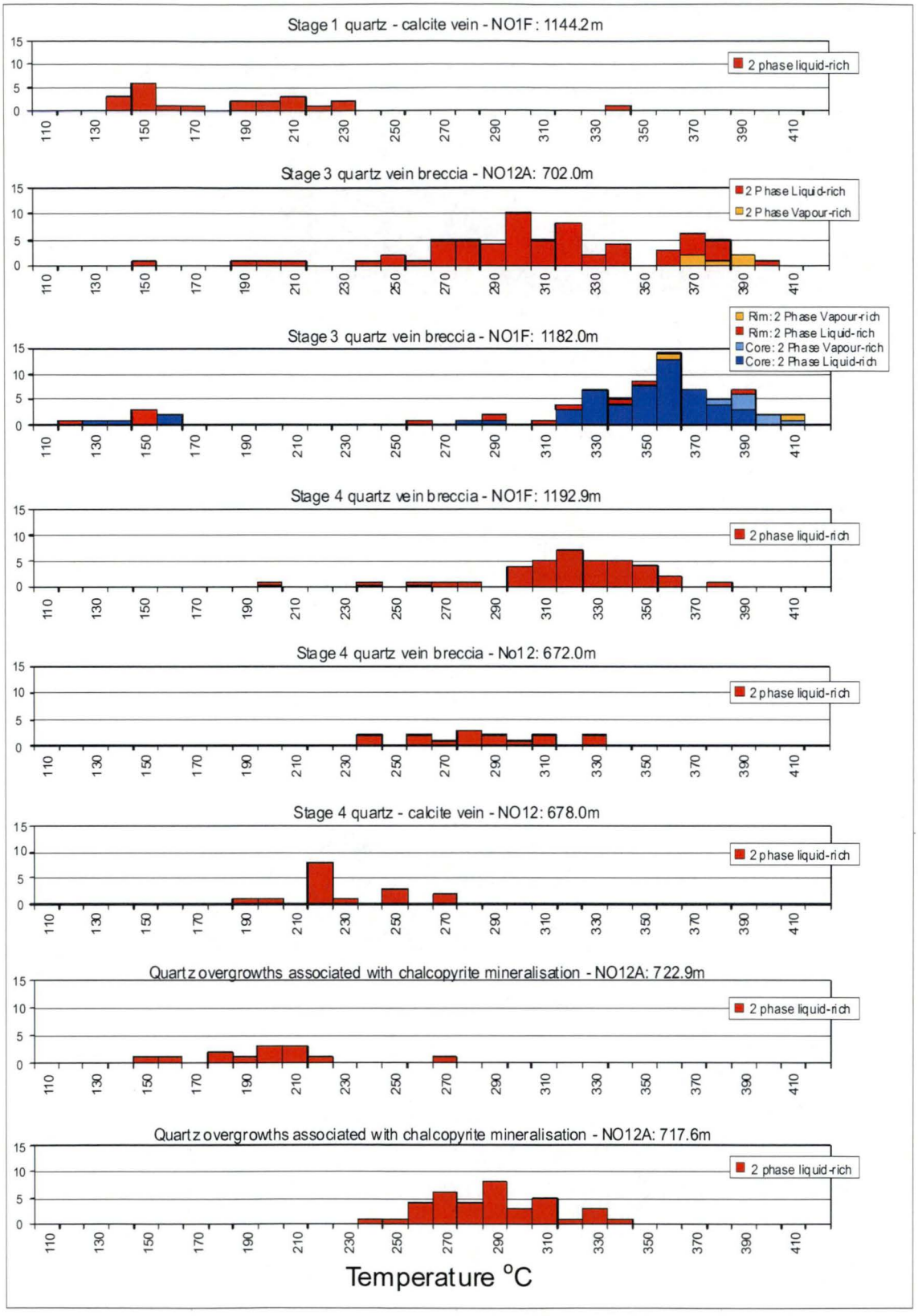

Table 38: Summary of results of microthermometric and mass spectrometric analysis of New Occidental fluid inclusions.

Sample No.	Type	Size	V/L Ratio	T_h (°C)	T_e (°C)	T_m (°C)	Salinity (eq. wt.% NaCl)	T_c (°C)	Vapour Composition*
NO1F-1144 2m Stage 1 Quartz	2-Phase (L+V), homogenise to L	5–15μm	5–20%	(1) = 344°C (2) = 140 to 232°C	— -20.4°C	-4.6°C -1 2 to -4.4°C	7 3% 2 1 to 7 0%	— —	H_2S = major CH_4 = minor
NO7-964 4m Stage 1 Quartz	2-Phase (L+V)	5μm	<10%	Not analysed due to highly brecciated and cloudy nature of quartz and small size of inclusions					H_2S = major CH_4 = minor
NO13-544 6m Stage 1 Quartz	2-Phase (L+V)	5–20μm	<10%	Not analysed due to highly brecciated and cloudy nature of quartz and small size of inclusions					H_2S = major CH_4 = minor
NO1F-1155 9m Stage 2-3 Quartz	2-Phase (L+V)	5–15μm	<10%	Not analysed due to highly brecciated and cloudy nature of quartz and small size of inclusions					H_2S = major CH_4 = minor
NO1F-1182 0m Stage 3 Quartz	2-Phase (L+V), approx 10% homogenise to V	5–20μm	5–50%	Core = 122 to 411°C Rim = 132 to 402°C	— -49 4 to -55.8°C	-0 4 to -3 8°C -0 2 to -3.4°C	0 7 to 6 1% 0.4 to 5 5%	0 8 to 5 2°C 3.8°C	H_2S = major CO_2 = major CH_4 = minor
NO12A-702 0m Stage 3 Quartz-cpy	2-Phase (L+V) , approx 10% homogenise to V	5–20μm	5–50%	151 to 399°C	-24 2 to -56.9°C	-1 3 to -6 8°C	3 1 to 10 2%	1.2 to 10 2°C	H_2S = major CO_2 = major CH_4 = minor
NO1F-1192.9m Stage 4 Quartz	2-Phase (L+V), homogenise to L	5–15μm	5–30%	222 to 388°C	—	-0 5 to -2 3°C	0.9 to 3 9%	—	H_2S = major CH_4 = minor
NO12-672.0m Stage 4 Quartz	2-Phase (L+V), homogenise to L	5–15μm	5–30%	240 to 334°C	—	-2 9 to -3.7°C	4.6 to 6 0%	—	Not Analysed
NO12-678 0m Stage 4 Quartz	2-Phase (L+V), homogenise to L	5–15μm	5–20%	177 to 264°C	-19.7 to -20 7°C	-1 2 to -0.8°C	2 1 to 4.6%	—	Not Analysed
NO12A-747 7m Stage 4 Quartz	Minor 2-Phase (L+V)	5–20μm	<10%	Not analysed due to highly brecciated and cloudy nature of quartz and small size of inclusions					H_2S = major CH_4 = minor
NO14E-1012 8m Stage 4 Quartz	Minor 2-Phase (L+V)	<5μm	<10%	Not analysed due to highly brecciated and cloudy nature of quartz and small size of inclusions					H_2S = moderate CH_4 = minor
NO12A-717 6m Stage 4 Quartz-cpy	2-Phase (L+V), homogenise to L	5–20μm	5–30%	242 to 338°C	-44 3 to -61 5°C	-3.2 to -6 1°C	5 2 to 9 3%	2 6 to 12 3°C	H_2S = major CO_2 = major CH_4 = minor
NO12A-722 9m Stage 4 Quartz-cpy	2-Phase (L+V), homogenise to L	5–10μm	5–10%	154 to 275°C	—	-1.8 to -2 7°C	3 1 to 4.5%	—	H_2S = major CH_4 = minor
NO12A-732.6m Stage 4 Quartz-cpy	2-Phase (L+V) in clear quartz around cpy	5–20μm	<20%	Not analysed due to small size of inclusions					H_2S = major CH_4 = minor
NO14E-992.0m Stage 4 Quartz-cpy	Minor 2-Phase (L+V) in clear quartz around cpy	5–10μm	<10%	Not analysed due to small size of inclusions					H_2S = moderate CH_4 = minor

* H_2S and CH_4 contents based on mass spectrometric analysis of gaseous phases released as inclusions ruptured upon heating CO_2 inferred from T_e and T_c values

Stage 1 quartz predominantly yielded low homogenisation temperatures, with a single significantly higher homogenisation temperature of 344°C.

Stage 3 quartz homogenisation temperatures are mostly in the range of 350–410°C. Both Stage 3 quartz samples (NO1F-1182.0m and NO12A-702.0m) contained approximately 10% vapour-rich inclusions that homogenised to the vapour phase (Table 38) and yielded relatively high homogenisation temperatures (average T_h = 384°C) equivalent to those derived from co-existing liquid-rich inclusions. In the NO1F-1182.0m sample, homogenisation temperatures were recorded from the core and rim of a relatively large zoned quartz crystal (Figure 177b). Both the rim and core contained co-existing liquid- and fluid-rich inclusions, although the proportion of vapour-rich inclusions was lower in the rim. Homogenisation temperatures are on average 10°C higher in the core than in the rim. Sample NO12A-702.0m also yielded a second lower temperature population of T_h values in the range 250–350°C associated with clear quartz surrounding chalcopyrite grains. The clear quartz is interpreted to be a late-Stage 4 quartz overgrowth associated with chalcopyrite-pyrrhotite.

A small but consistent population of high temperature fluid inclusions (T_h = 330–388°C) were identified in the main footwall Stage 4 quartz vein breccia. However, fluid inclusions in the remaining samples of Stage 4 quartz, including Stage 4 quartz associated with chalcopyrite, generally have lower homogenisation temperatures (T_h = 250–330°C). One sample of Stage 4 quartz intergrown with calcite, which is interpreted to have formed in the waning stages of Stage 4 quartz deposition, yielded relatively low homogenisation temperatures (T_h = 177–264°C).

Most samples also yielded a scatter of much lower homogenisation temperatures in the range 110–230°C. These values were mainly recorded from smaller fluid inclusions.

Mass spectrometric analysis of gas phases in fluid inclusions from the New Occidental deposit revealed H_2S is the dominant gas phase, CH_4 is a consistent but minor phase, and N_2 was not detected (Table 38). The presence or otherwise of CO_2 in fluid inclusions could not be ascertained because organic material was not completely removed in the sample preparation stage. In both samples from drillhole NO14E, H_2S is less abundant than in the other drillhole samples (Zaw & Dedenczuk, 2000).

Zaw & Dedenczuk (2000) noted the shape of absorption spectra for H_2S and CH_4 in the New Occidental samples is quite different; H_2S absorption peaks are generally sharp and well defined, and occur at higher rupture temperatures whereas CH_4 absorption peaks are broader, less well defined and extend over a larger temperature range. Zaw & Dedenczuk suggested absorption spectra indicate H_2S and CH_4 occur in different fluid inclusion populations, with CH_4 present as a minor component in most fluid inclusions in the New Occidental deposit, whilst H_2S is present only in inclusions that rupture at relatively higher temperatures. However, fluid inclusion petrography and microthermometry undertaken by the author indicates a more complex pattern of fluid inclusion decrepitation in the deposit. Widespread decrepitation of two-phase (L+V) fluid inclusions in the New Occidental samples were observed during heating at temperatures between 200–300°C, with the larger vapour-rich inclusions more prone to decrepitation relative to the smaller and liquid-rich inclusions. This suggests high partial pressures of contained gases (e.g. Shepherd et al., 1985). Deformed (necked) primary and some secondary inclusions also ruptured relatively easily. Fluid inclusion decrepitation in the New Occidental deposit is therefore likely to be a function of the composition of contained gases, the strength of the host quartz and the presence of nearby defects. The presence of H_2S and CH_4 in all twelve samples analysed

by mass spectrometry, which represent a range of quartz stages (Stage 1–4), suggests those gas phases are not restricted to a particular quartz vein stage in the New Occidental deposit, but are a common constituent of two-phase fluid inclusions in all quartz vein stages in the deposit (Table 38).

8.6 Interpretation of Fluid Inclusion Data

8.6.1 Representiveness of Fluid Inclusion Populations

Marshall et al. (2000) and Giles & Marshall (2004) argued fluid inclusions in the CSA deposit do not allow direct determination of fluids associated with mineralisation, due mainly to deformation and/or decrepitation of primary and oldest secondary fluid inclusions by near-isobaric heating. As described previously (Section 8.4), fluid inclusions in the New Occidental deposit commonly record the effects of widespread and relatively intense deformation. Decrepitated inclusions are relatively common in deformed quartz and many two-phase fluid inclusions, and especially vapour-rich inclusions decrepitated when heated to temperatures in excess of >200°C.

However, scarce relatively undeformed primary fluid inclusions in the New Occidental deposit yielded consistent T_h populations and fluid/vapour ratios that are interpreted to be representative of main stage ore fluids. Maximum homogenisation temperatures are equivalent to deposition temperatures estimated from alteration mineralogy in the New Occidental deposit (Section 5.7.3) and other Cobar deposits (Table 36), including peak metamorphic temperatures estimated by Giles & Marshall (2004) for the CSA deposit. The CSA deposit also contains a significantly stronger base metal sulfide overprint compared to the New Occidental deposit. In the case of the CSA deposit, both the quartz-poor chalcopyrite - pyrrhotite - pyrite and late-stage quartz-free galena - sphalerite - pyrrhotite - pyrite overprints are associated with major deformation and recrystallisation of precursor quartz and are likely responsible for the bulk of deformation effects observed in fluid inclusions in that quartz. In comparison, chalcopyrite - pyrrhotite is only weakly developed in the New Occidental deposit and only overprints the footwall of the deposit, whilst the galena - sphalerite overprint is extremely weak. The primary fluid inclusions identified in the New Occidental deposit were recorded from parts of the deposit characterised by low base metal sulfide contents.

Based on the microthermometric data collected during this study, all but one T_h measurement from **Stage 1 quartz** (NO1F-1144.2m) are likely to be from secondary inclusions, or have been modified by processes accompanying subsequent deformation. Associated alteration and ore minerals (Fe-chlorite – magnetite) suggest the primary ore fluid associated with Stage 1 quartz deposition was higher temperature and more likely similar to the single high-temperature T_h measurement of 344°C recorded from the sample (Sections 5.7 and 6.5).

Both samples of **Stage 3 quartz** (NO1F-1182.0m; NO12A-702.0m) yielded equivalent high-temperature T_h populations of fluid inclusions with relatively high vapour contents and similar fluid compositions. However, sample NO12A-702.0m also contained a second population of inclusions with lower T_h. Homogenisation temperatures from the higher temperature population are consistent with inferred temperatures for associated stilpnomelane alteration (Section 5.7.3) and are thus interpreted to provide reliable physiochemical constraints on the primary ore fluid associated with Stage 3 quartz veins. The lower temperature T_h population in sample NO12A-702.0m is attributed to fluid inclusions associated with overprinting coarse-grained chalcopyrite equivalent to late Stage

4 quartz. The inclusions appear spatially related to chalcopyrite grains in the sample and are interpreted to represent secondary fluid inclusions in Stage 3 quartz that have the same composition of primary inclusions in the Stage 4 quartz veins. Such relationships have been observed in a number of orogenic gold deposits (e.g., Robert et al., 1995; Wilkinson & Johnston, 1996; Dugdale & Hagemann, 2001).

The three samples of **Stage 4 quartz** (NO1F-1192.9m; NO12-672.0m; NO12-678.0m) yielded different T_h populations but a single T_m population. However, T_h values appear consistent with the different styles of Stage 4 quartz in each sample. Sample NO1F-1192.9m, which is from the core of the major Stage 4 footwall quartz vein breccia, provided the highest temperatures. Sample NO12-672.0m comprises Stage 4 quartz veins on the immediate margin of the footwall quartz vein breccia and provided intermediate T_h values, whereas Sample NO12-678.0m, which comprises Stage 4 quartz intergrown with late-stage calcite on the outer margins of the major Stage 4 footwall breccia, yielded lowest T_h values. All three samples are interpreted to be reliable indicators of the range of physiochemical conditions under which Stage 4 quartz was deposited in the New Occidental deposit.

The two samples of **late Stage 4 quartz associated with chalcopyrite** (NO12A-702.0m; NO12A-717.6m) yielded similar T_h populations and consistent fluid compositions, whilst the third sample (NO12A-722.9m) and generally lower T_h values and a different fluid composition. Whilst fluid inclusions in samples NO12A-702.0m and NO12A-717.6m are considered to be representative of fluids associated with deposition of late Stage 4 quartz and cogenetic chalcopyrite, sample NO12A-722.9m contains fluid inclusions that yielded only much lower T_h values, indicating either entrapment of later lower temperature fluids or that inclusions were modified by subsequent deformation processes.

8.6.2 Inferred Ore Fluid Compositions

First melting temperatures measured from fluid inclusions in Stage 1 and Stage 4 quartz in the New Occidental deposit approximate the eutectic temperature (T_e = -20.8°C) in the aqueous H_2O-NaCl system, indicating fluids associated with those stages of quartz comprise relatively simple but relatively pure H_2O-NaCl solutions (e.g. Shepherd et al., 1985). In comparison, hydrothermal fluids associated with deposition of Stage 3 quartz and late Stage 4 quartz associated with chalcopyrite are inferred to contain appreciable CO_2 based on the observation of clathrate during freezing experiments and T_e values of the order -57.0°C measured from vapour-rich fluid inclusions. Similarly, decrepitation of many of the vapour-rich inclusions in those quartz samples during heating experiments is also consistent with the presence of CO_2; Shepherd et al. (1985); Dugdale & Hagemann (2001) and Mernagh (2001) attribute widespread decrepitation of fluid inclusions in orogenic gold deposits to the high internal partial pressures of CO_2. Depression of T_e values below -57.0°C and clathrate melting temperatures greater than +10°C in fluid inclusions indicate additional gaseous phases, including CH_4, N_2 and/or H_2S, are present (Shepherd et al., 1985). Some inclusions from Stage 3 and late Stage 4 quartz associated with chalcopyrite yielded T_e <-57.0°C and T_c >10°C, therefore indicating the presence of additional gas phases. Mass spectrometry undertaken in this study indicates those additional gas phases are mainly H_2S and CH_4 but not N_2. Other salts including $CaCl_2$ and $MgCl_2$ are unlikely to be present, based on the apparent lack of colour change of inclusions upon freezing.

Final melting temperatures (T_m) indicate New Occidental ore fluids are typically weakly saline (0.4–10.2 eq. wt.% NaCl; average 4.5 eq. wt.% NaCl), assuming fluids are simple aqueous H_2O-NaCl solutions (Figure 180).

Figure 180: Calculated salinities for New Occidental deposit fluid inclusions.

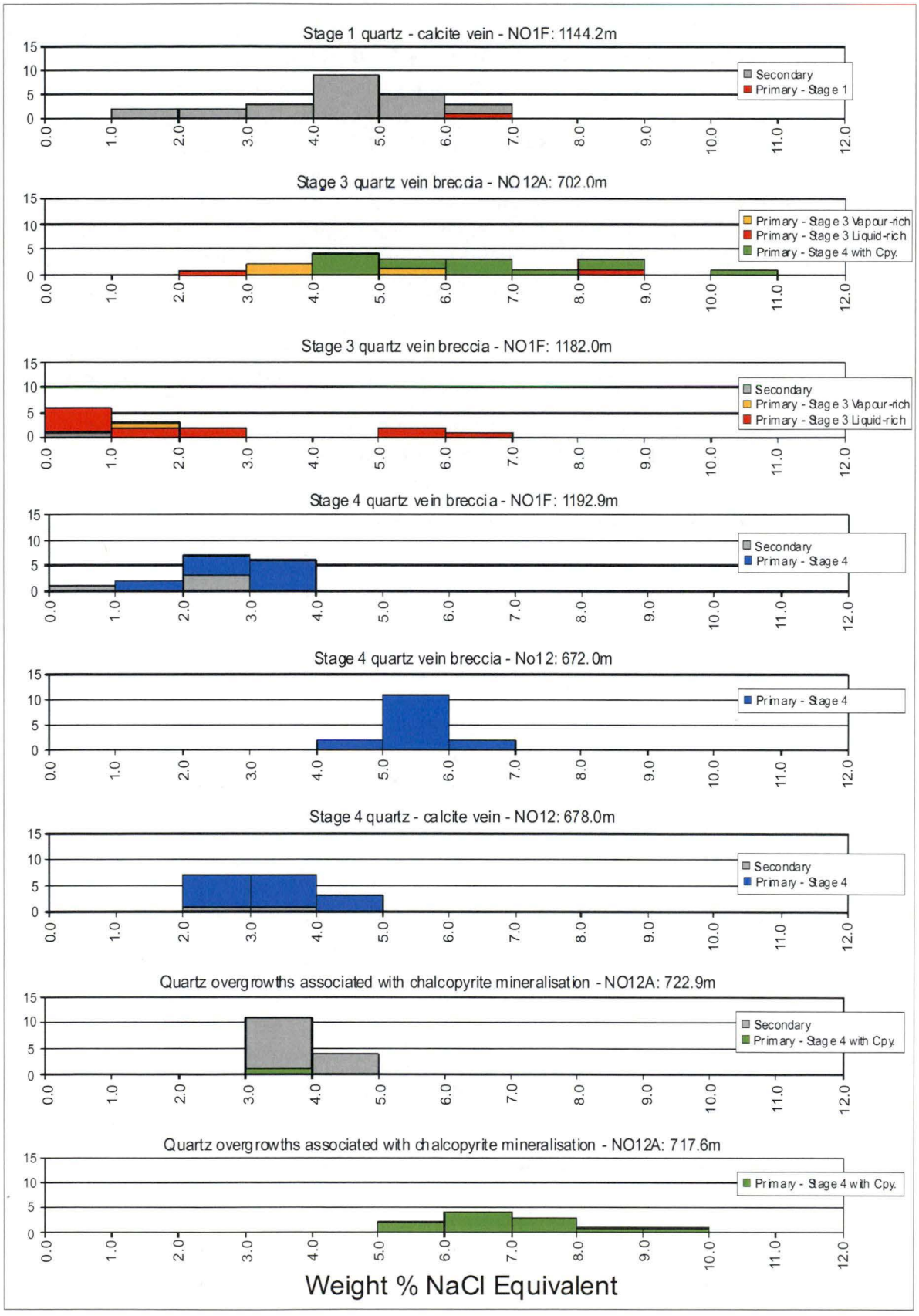

However, Shepherd et al. (1985) indicate the presence of CO_2 in fluid inclusions can result in anomalously high calculated salinities because clathration can result in water being removed from the aqueous phase, thereby increasing the salinity of the residual solution. Shepherd et al. (1985) showed clathrate melting temperatures (T_c) in H_20-NaCl- CO_2 aqueous solutions are a function of the salinity, thereby allowing fluid salinity to be calculated from depression of values below the nominal 10°C for H_20-NaCl- CO_2 aqueous solutions. Shepherd et al. (1985) also noted that CH_4 raises the upper temperature limit of clathrate melting (T_c >10°C), thereby countering the effect of NaCl. Salinities estimated from depression of T_c values in samples from the New Occidental deposit that contain appreciable CO_2 (samples of Stage 3 quartz and Stage 4 quartz associated with chalcopyrite) are consistent with salinities calculated from T_m values. For example, sample NO12A-717.6m yielded T_m/T_c pairs of -4.3/5.1°C, -3.7 /2.6°C, -3.8/2.8°C and -5.1/7.4°C. Those T_m values indicate salinities in the range of 6–8% eq. wt.% NaCl, whereas the T_c values indicate salinities of 5–10% eq. wt.% NaCl (Figure 181). Therefore, salinities estimated from T_m values appear reasonable and have not been unduly influenced by CO_2.

Figure 181: Comparison of estimated fluid salinity for T_m/T_c pairs measured in sample NO12A-717.6m using ice and clathrate melting curves (from Shepherd et al., 1985).

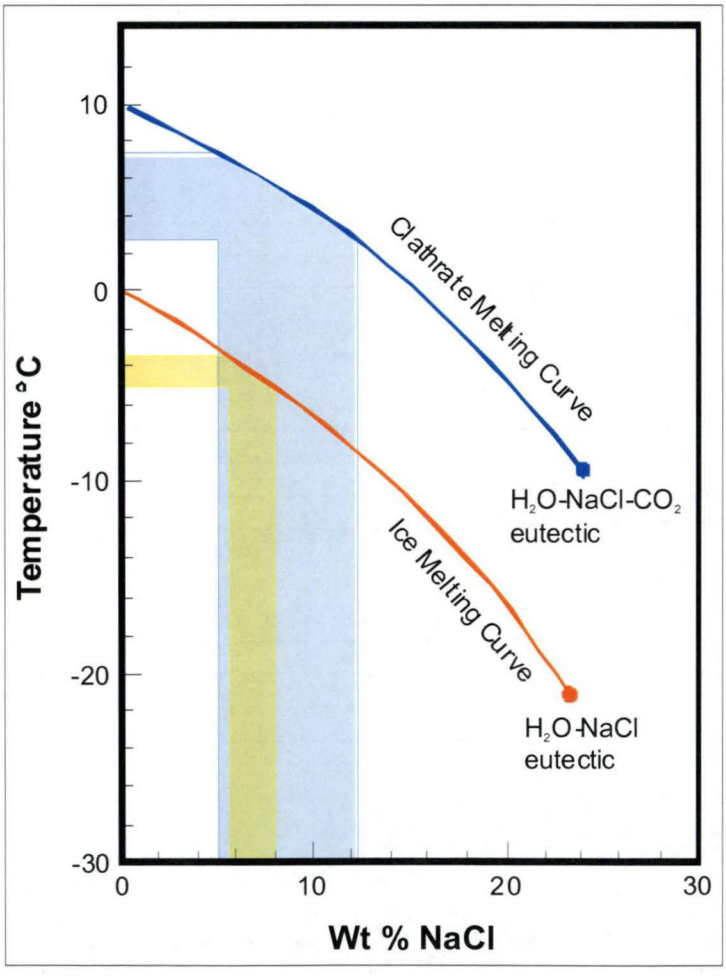

Overall, New Occidental hydrothermal fluids are weakly saline H_2O-H_2S-CO_2-CH_4 fluids with low to moderate CO_2 contents (CO_2 was not identified in Stage 4 quartz but was identified in late Stage 4 quartz associated with chalcopyrite). Stage 3 quartz contained mixtures of H_2S-CO_2 ± CH_4 -rich fluids and low-moderate salinity CO_2-free aqueous fluids. Fluids associated with late Stage 4 quartz-chalcopyrite appear to have slightly higher

salinity than other fluids (Figure 182 and Table 39), which provides further evidence that the main stage of chalcopyrite-pyrrhotite in the New Occidental deposit was associated with introduction of a second, compositionally distinct hydrothermal fluid.

Abundant secondary fluid inclusions characterised by low vapour/liquid ratios and lower T_h values (100–300°C) throughout the New Occidental deposit indicate the deposit was flooded by weakly saline H_2O-minor CH_4 fluids under decreasing temperature conditions following the main mineralisation event(s). The presence of CH_4 in the fluids is indicated by mass spectrometric analysis, which showed CH_4 was also detected in samples containing predominantly secondary fluid inclusions (Section 8.5.1). Giles & Marshall (2004) also identified widespread entrapment of lower temperature H_2O-CH_4 fluids in the CSA deposit.

Figure 182: Plot of fluid inclusion salinity and homogenisation temperature for New Occidental fluid inclusions.

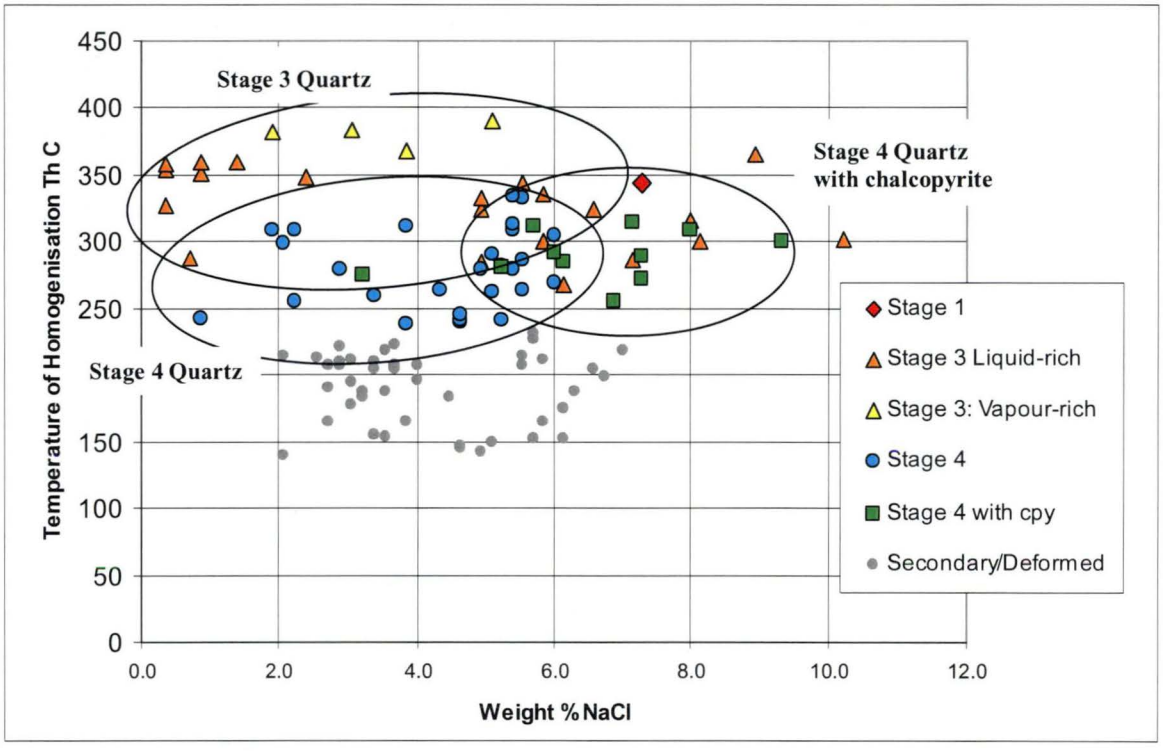

Table 39: Inferred fluid compositions for quartz stages in the New Occidental deposit.

Quartz Vein Stage	Fluid Composition	Salinity
Stage 1 Quartz	Insufficient data	Insufficient data
Stage 3 Quartz	Mixtures of H_2O-NaCl liquid-rich fluids and H_2O-H_2S-CO_2 and minor CH_4 gas-rich fluids	1–6 eq. wt.% NaCl
Stage 4 Quartz	H_2O-NaCl-H_2S-minor CH_4	2–6 eq. wt.% NaCl
Late Stage 4 Quartz associated with chalcopyrite	H_2O-NaCl-CO_2-H_2S-minor CH_4	5–10 eq. wt.% NaCl
Post-mineralisation (trapped as secondary inclusions in all quartz vein stages)	H_2O-NaCl-minor CH_4	2–6 eq. wt.% NaCl

8.6.3 Evidence for Phase Separation in Stage 3 Quartz

Fluid inclusions in Stage 3 quartz yielded consistently higher homogenisation temperatures than other vein stages and homogenised to either vapour or liquid phase. Such behaviour can reflect fluid immiscibility in response to phase separation but may also result from mixing of different fluids, as proposed by Hinman (1992) for the Peak deposit. Alternatively, such behaviour may indicate variable P-T conditions during entrapment, or crystallisation and deformation effects that have altered the volume and/or composition of inclusions, including necking down or leakage (e.g. Shepherd et al., 1985; Roedder, 1997; Brown, 1998). Phase separation in the New Occidental hydrothermal fluid during deposition of Stage 3 quartz best explains the data presented herein. In addition, the criteria used by Ramboz et al. (1982) to confirm phase separation in the parent hydrothermal fluid at the time of fluid inclusion entrapment are reasonably satisfied.

The high-temperature (T_h >350°C) vapour-rich and liquid-rich inclusions in both samples of Stage 3 quartz represent primary inclusions that occur within the same growth bands in zoned quartz crystals. The inclusions also homogenise to the vapour or liquid phase at similar T_h values (350–390°C), thereby demonstrating contemporaneous entrapment of both inclusion types at similar temperature ranges and confirming the first two criteria for phase separation listed by Ramboz et al. (1982). The final criterion for phase separation, that bulk molar volumes of the vapour- and liquid-rich fluid inclusions are compatible with equilibrium coexistence at a unique homogenisation temperature, appears to be satisfied in the case of the New Occidental deposit, although it cannot be confirmed because fluid compositions have not been adequately quantified. Fluids associated with deposition of Stage 3 quartz are known to comprise mixtures of H_2O-NaCl-H_2S-CO_2-CH_4 (Section 8.6.2). Phase separation in such a system is expected to partition CO_2-CH_4-H_2S to the vapour phase and H_2O-NaCl to the liquid phase (Shepherd et al., 1985; Brown, 1998; Dugdale & Hagemann, 2001). New Occidental fluid inclusions that homogenise to a vapour-phase are clearly CO_2-rich whereas those that homogenise to a liquid phase are H_2O-rich and contain less CO_2. The relative proportions of H_2S and CH_4 in the two inclusion types was not established in this study, although their presence was confirmed. Fluid inclusions homogenising to the vapour phase also tend to have lower salinities than inclusions homogenising to the liquid phase, although the dataset is relatively small (Figure 180). It is important to note that, at the temperatures inferred for fluid inclusion entrapment during deposition of Stage 3 quartz in the New Occidental deposit, phase separation is unlikely to result in vapour- and liquid-rich inclusions with markedly different salinities. For example, based on isotherms in the system H_2O-NaCl (Figure 183), a fluid at 400°C containing 2-3 wt.% eq. NaCl decompressed to 250–300 bars (point A in Figure 183) would undergo phase separation to yield a vapour phase containing <1 wt.% eq. NaCl (point A') and a liquid phase containing approximately 5–6 wt.% eq. NaCl (A"). At lower temperatures (e.g. 350°C) phase separation would produce an even smaller spread of salinity values. The salinities recorded for fluid inclusions in Stage 3 quartz are consistent with those theoretical values and, in the case of sample NO1F-1182.0m, exhibit a bimodal distribution.

Mixing of two different, partially immiscible hydrothermal fluids (a CH_4-rich saline fluid and a more oxidised, higher temperature H_2O-CO_2-rich low salinity fluid) has been proposed at the Peak and Elura deposits (Hinman, 1992; Lawrie et al., 1999 respectively). Much of the evidence cited by Hinman (1992) and Lawrie et al. (1999) for fluid mixing, including variable fluid inclusion densities and contrasting fluid compositions, could be equally well explained by phase separation in a single parent fluid. In the case of the New Occidental deposit, there is little or no evidence for the introduction of a second

hydrothermal fluid during deposition of Stage 3 quartz. The relatively consistent homogenisation temperatures for the two different inclusion types (vapour- and liquid-rich) preclude mixing of fluids with different temperatures. Compositional differences, whilst potentially indicative of different fluid compositions, can be accounted for by phase separation. Likewise, alteration and ore mineral assemblages and wholerock geochemistry (Sections 5.4, 6.4 and 7) do not indicate a sudden or dramatic change in ore fluid composition or character associated with deposition of Stage 3 quartz.

Figure 183: Selected isotherms in the system H_2O–NaCl showing the composition of coexisting vapour and liquid phases (from Shepherd et al. 1985).

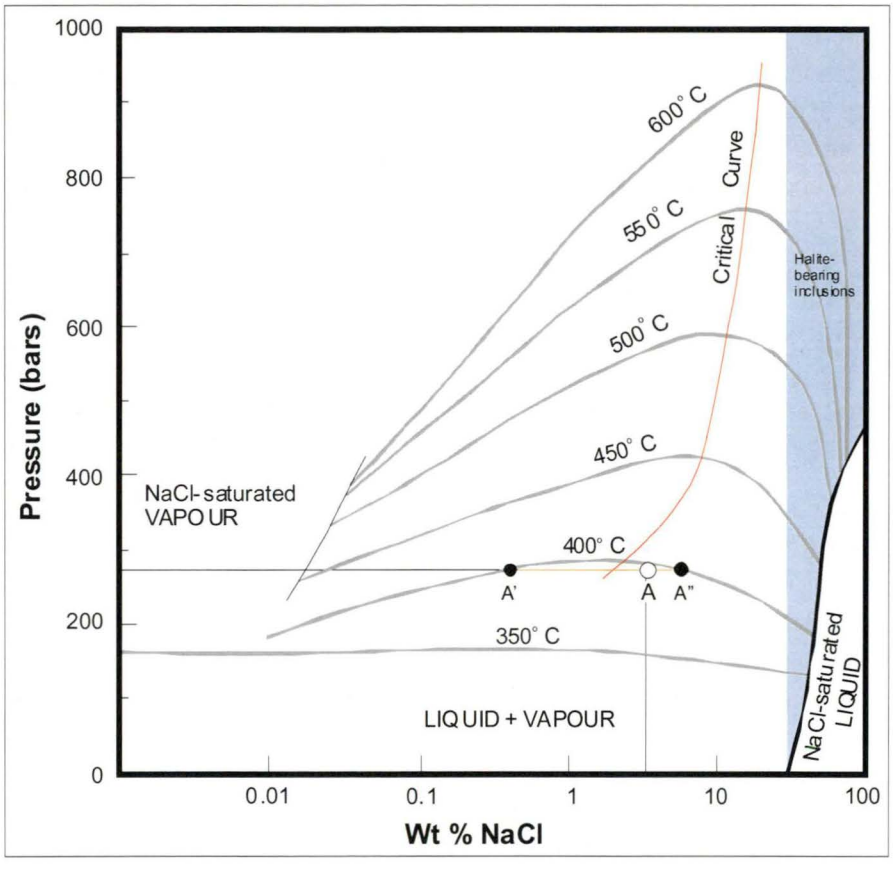

Pressure-temperature variations alone do not explain the full extent of density and compositional variations in fluid inclusions from the New Occidental deposit, unless pressure fluctuations triggered phase separation. Quartz vein textures in the deposit indicate significant variations in pressure (between lithostatic and near-hydrostatic) during quartz vein deposition in the deposit (Section 4.4), with greatest variations indicated during deposition of Stage 2–3 quartz (e.g. crustiform and colloform banded crystalline to cryptocrystalline quartz deposited in alternating sub-horizontal extensional veins and steeply dipping fault-fill veins). Such pressure variations have likely contributed to variations in fluid inclusion density in the New Occidental deposit, in much the same way as inferred in a number of orogenic gold deposits (e.g. Robert et al., 1995; Mernagh, 2001; Dugdale & Hagemann, 2001), but are unlikely to account for the observed differences in inclusion composition. The relatively consistent homogenisation temperatures for the two different inclusion types (vapour- and liquid-rich) indicates significant temperature fluctuations are unlikely to have occurred during deposition of Stage 3 quartz.

A range of fluid inclusion deformation effects has been observed in the New Occidental deposit, including coalescence, necking down and leakage of inclusions, indicating early

stages of quartz in the deposit have undergone substantive deformation. Such effects are probably responsible for the scatter evident in the microthermometric data from the deposit (e.g. Roedder, 1997). Coalescence, necking down and leakage of fluid inclusions produce random variations in fluid inclusion data (Roedder, 1997, Shepherd et al., 1985). The systematic compositional variations of fluid inclusions in Stage 3 quartz from the New Occidental deposit are therefore interpreted to be primary features unaffected by post-deposition processes. Likewise, fluid inclusions homogenising to opposite modes in Stage 3 quartz often have equant euhedral shapes and appear relatively undeformed, consistent with limited recrystallisation of the host quartz (e.g. Roedder, 1997).

8.6.4 Inferred Trapping Temperatures

Homogenisation temperatures for Stage 3 quartz should approximate trapping temperatures because conditions of fluid inclusion formation in Stage 3 quartz were at the H_2O-CO_2-NaCl solvus (e.g. Shepherd et al. 1985; Roedder, 1997; Brown, 1998). Fluid inclusions formed from a fluid undergoing phase separation generally skew T_h histograms towards higher temperatures (Bodnar et al., 1989; Roedder, 1997). T_h histograms for Stage 3 quartz are not overly skewed (Figure 179), suggesting trapping temperatures for Stage 3 quartz are most likely centred on the peak of the T_h histogram (Table 40).

Homogenisation temperatures for the other stages of quartz in the New Occidental deposit require correction to compensate for confining pressure, given there is no evidence of phase separation in inclusions from those stages of quartz. Assuming a depth of formation of approximately 5–7km for the New Occidental deposit (Section 4.4.10), lithostatic pressure during deposit formation was likely to have been 1.5–2.0kbar. T_h values of 250–350°C for fluids with 5 eq. wt.% NaCl (comparable to the bulk of New Occidental deposit data) require a correction of approximately +100°C (e.g. Figure 10 in Brown, 1998). Pressure corrections are greater for more saline fluids (Roedder, 1997). However, much of the quartz in the New Occidental deposit (Stage 2–3 quartz in the deposit centre and Stage 4 quartz in the main footwall breccia) formed during periods of significant fluid pressure fluctuation (lithostatic towards near-hydrostatic) during fault zone slip and dilation. Robert et al. (1995) estimated fluid pressure reductions of 200–350 bars during cyclic stress reversals during vein formation in orogenic gold deposits in the Val d'Or district, Canada, which formed under lithostatic pressures of 2.3–3.0 kbars. Dugdale & Hagemann (2001) calculated fluid pressure reductions of up to 500 bars in fluids at 300°C and 1.5 kbars in the Bronzewing gold deposit, Western Australia. Hagemann & Lüders (2003) suggested fluid pressures varied between 700 bars to 1.7 kbars during fault zone movement in the Wiluna gold deposit, Western Australia. As a consequence, fluid pressures may have been as low as 500–700 bars during quartz deposition in the New Occidental deposit, assuming near-hydrostatic fluid pressures. Therefore, temperature corrections of only +50°C would be required under such conditions (e.g. Figure 10 in Brown, 1998). However, pressure fluctuations may have been progressively smaller with increasing distance from the fault zone and during the waning stages of seismic activity along the fault. Therefore, larger pressure corrections could reasonably be applied to T_h values in samples distal to the main zones of fault dilation (Stage 1 quartz and Stage 4 quartz from quartz breccias and smaller veins peripheral to the footwall breccia) and in samples formed after the main periods of fault zone dilation (e.g. late-Stage 4 quartz associated with chalcopyrite).

Because confining pressure has not been quantified during this study, only semi-quantitative estimates of trapping temperatures can be made for fluids where phase separation has not been observed. However, if temperature corrections of the order of +50°C are applied to homogenisation temperatures from samples of Stage 4 quartz, then

trapping temperatures for Stage 4 quartz in the footwall quartz breccia are of a similar magnitude to trapping temperatures measured for Stage 3 quartz, whereas trapping temperatures for late-Stage 4 quartz associated with chalcopyrite and peripheral Stage 4 quartz breccias and veins are slightly lower than for Stage 3 quartz. A similar pressure correction applied to the single high temperature T_h value recorded for the sample of Stage 1 quartz suggests this quartz vein stage was trapped as similar temperatures to other quartz vein stages.

The inferred trapping temperatures for the various quartz vein stages in the New Occidental deposit are consistent with formation temperatures estimated from alteration studies. Stage 2-3 quartz is characterised by the highest temperature alteration assemblages with subsequent quartz stages corresponding to progressively lower temperature alteration assemblages (Section 5.7).

Table 40: Inferred fluid inclusion homogenisation and trapping temperatures for quartz in the New Occidental deposit.

Quartz Vein Stage	T_h	Pressure Correction*	Trapping Temperature
Stage 1 Quartz	Insufficient data		
Stage 3 Quartz	350–410°C	0°C	350–410°C
Stage 4 Quartz in main footwall breccia	310– 350°C	+50°C	360– 400°C
Stage 4 Quartz in smaller quartz vein breccias and veins peripheral to the main footwall breccia	210–330°C	+50°C	260–380°C
Late Stage 4 Quartz associated with chalcopyrite	270–340°C	+50°C	320–390°C

* Semi-quantitative temperature corrections estimated from data presented in Figure 10, Brown (1998).

8.6.5 Depth of Deposit Formation Inferred from Fluid Inclusions

The recognition of phase separation during deposition of Stage 2–3 quartz in the New Occidental provides some additional constraints on the depth of deposit formation, although pressure determinations depend on constraining the fluid inclusion compositions (e.g. Roedder, 1997; Brown, 1998). Assuming a simple H_2O-NaCl system, a formation temperature for Stage 2–3 quartz of approximately 350–400°C and fluid salinities of 3-5 wt% NaCl, the hydrothermal fluid would have had to have been decompressed to approximately 200–250 bars in order to trigger phase separation (Figure 183). Assuming phase separation occurred under purely lithostatic pressures, depth of deposit formation would have been <1km (based on a lithostatic pressure gradient of 300bar/km; e.g. Hinman, 1992). Alternatively, if phase separation occurred under near-hydrostatic conditions, which is considered more likely given the evidence for significant reductions in fluid pressure associated with fault zone rupture during deposition of Stage 2-3 quartz, the depth of formation would be of the order of 2km (assuming a hydrostatic pressure gradient of 100bar/km). Such depths are clearly inconsistent with other geological evidence (Section 4.4.10).

The addition of CO_2 and CH_4 has been shown to significantly increase the pressure and decrease the temperature at which phase separation is initiated in a fluid (Parry, 1986; Roedder, 1997; Brown, 1998; Hageman & Lüders, 2003). Phase relations in the system H_2O-NaCl-CO_2-CH_4 are also significantly more complex than in the simpler H_2O-NaCl system, with the solvus being particularly sensitive to CO_2 content (Roedder, 1997; Brown, 1998). Brown (1998) indicates mesothermal deposits in medium grade metamorphic rocks typically contain between 5-15 mol% CO_2. Assuming the temperatures of the New

Occidental fluid was 350–400°C and the fluid contained approximately 10 mol% CO_2, approximately 6 wt% NaCl and negligible CH_4, phase separation would occur at fluid pressures of 600-700 bars (Figure 184a,b). This translates to depths of 2km (assuming purely lithostatic pressures) and 6-7km (assuming hydrostatic fluid pressures), the latter depths being deeper than the formation depths previously estimated from quartz textures present in the New Occidental deposit (Section 4.4.10). A higher CO_2 content of approximately 20 mol% CO_2 more than doubles the pressure at which phase separation occurs (Figure 184b). This suggests the CO_2 content of the New Occidental fluid was <10 mol% and/or that fluid pressures were >hydrostatic.

Figure 184: Phase diagrams for the H_2O-CO_2-NaCl system showing estimated fluid pressures during deposition of Stage 3 quartz in the New Occidental deposit.

a) Solvi for the H_2O-CO_2-NaCl system for 6 wt% NaCl from Parry (1986). The shaded area shows fluid pressures corresponding to homogenisation temperatures of Stage 3 quartz assuming XCO_2 values typical of mesothermal deposits (e.g. Brown, 1998).

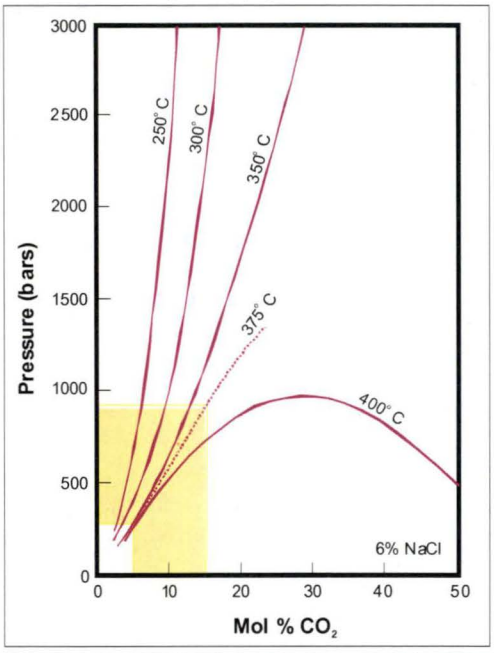

b) Solvi for the H_2O-CO_2-NaCl system (concentrations specified) after Hagemann & Lüders (2003). Shaded areas show fluid pressures corresponding to the average homogenisation temperature of Stage 3 quartz in the New Occidental deposit based on the two solvi.

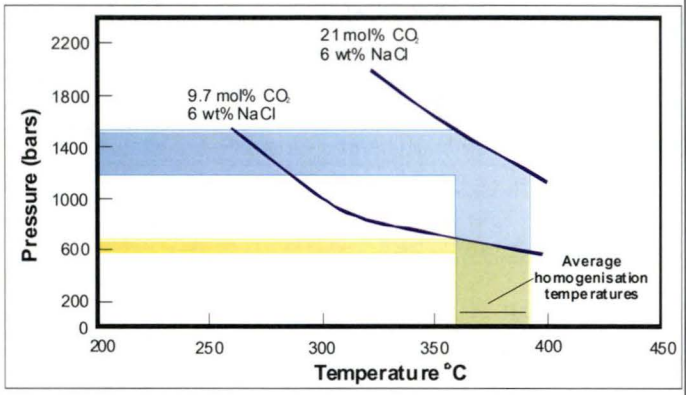

8.7 Significance of New Occidental Fluid Inclusion Data in the Context of Cobar deposits and Orogenic Gold Deposits

Fluid inclusion studies of the New Occidental deposit were limited by the scarcity of primary inclusions, reflecting the effects of deformation associated with deposit formation, and their relatively small size. As a consequence, reliable fluid inclusion data could only be obtained from two of the five stages of quartz in the deposit (Stages 2 and 4). However, the data obtained from samples of those quartz stages has provided some important constraints on formation of the New Occidental deposit.

The New Occidental deposit was formed from similar H_2O-CO_2-NaCl-CH_4 hydrothermal fluids to those at other Cobar deposits (Table 36). However, to date the New Occidental deposit is the only deposit where H_2S has been detected. The recognition of H_2S in New Occidental fluid inclusions suggests gold was transported as bisulfide complexes and that gold deposition may have been triggered by H_2S partitioning to the vapour phase during

phase separation. Some studies have identified significantly more saline hydrothermal fluids associated with sulfide mineralisation in the Peak and Elura deposits (Table 36), which is consistent with increased capacity to transport Pb, Zn and Cu in more saline fluids and the higher fluid salinities of fluids associated with late-stage base metal sulfide mineralisation at New Occidental. However, some of the calculated salinities (e.g. 20–60 eq. wt.% NaCl: Jiang, 1996; Sun & Seccombe, 2000) seem anomalously high given the absence of salt daughter minerals in inclusions. The New Occidental deposit also yielded highest homogenisation temperatures of any Cobar deposit, although trapping temperatures may have been comparable once pressure corrections are applied to T_h data from the other deposits.

Compositions and temperatures of hydrothermal fluids associated with the New Occidental deposit are also typical of orogenic gold deposits. The majority of world orogenic gold deposits formed from H_2O-NaCl-CO_2 ±CH_4 fluids with low to moderate CO_2 contents and salinities (Ho et al., 1990; Ridley & Diamond, 2000). Kerrich et al. (2000) noted fluid inclusions in many orogenic gold deposits also contain variable amounts of CH_4 and minor amounts of N_2 and H_2S. Orogenic gold deposits formed at similar temperatures (T_h = 200–500°C with most in the range 250–400°C) (Ridley & Diamond, 2000; Kerrich et al., 2000).

The most likely explanation for vapour-rich and liquid-rich fluid inclusions in Stage 3 quartz in the New Occidental deposit homogenising to either liquid or vapour phases at similar T_h values is that the hydrothermal fluid underwent phase separation. Phase separation is also inferred during deposition of Stage 2 quartz on the basis of similar quartz vein textures, even though fluid inclusion data could not be obtained for this stage. Phase separation during deposition of Stage 2–3 quartz, and not in other quartz stages in the deposit, is consistent with the paragenesis and structural history determined for the deposit. Stage 2–3 quartz is characterised by the highest temperature alteration assemblage (stilpnomelane - Fe-chlorite ± biotite). Vein characteristics and overprinting criteria indicate deposition during cyclic decompression of the hydrothermal fluid from lithostatic to near hydrostatic values in response to large-scale slip and dilation along the Great Chesney Fault, conditions ideal for initiating phase separation.

The New Occidental deposit is the only Cobar deposit where phase separation has been identified, although fluid inclusion data from the Peak deposit (Hinman, 1992; Jiang, 1996) suggests phase separation may have occurred in that deposit. Hinman (1992) identified low density CO_2-CH_4-rich and high density fluid inclusions homogenising to the vapour and liquid phases respectively at >350°C in his Stage 2–4. Hinman argued CO_2 partitions to the liquid phase and CH_4 partitions to the vapour phase during phase separation; inclusion compositions at the Peak therefore being inconsistent with equilibrium coexistence at a unique homogenisation temperature. However, most studies indicate phase separation in the system H_2O-NaCl-CO_2-CH_4 will partition CO_2-CH_4-H_2S to the vapour phase and H_2O-NaCl to the liquid phase (e.g. Shepherd et al., 1985; Brown, 1998; Dugdale & Hagemann, 2001), indicating the presence of CO_2-CH_4 vapour-rich inclusions in the Peak deposit does not preclude the possibility of phase separation during deposit formation. Phase separation is expected to be very difficult to confirm for the Peak deposit, especially during deposition of any early-stage gold, given the intense deformation and multiple stages of over-printing base metal mineralisation in the deposit.

Phase separation is also suspected in the other gold-rich deposits in the Cobar Goldfield, in particular at the New Cobar and Chesney deposits. Both deposits are hosted by fault splays off the Great Chesney Fault and contain abundant quartz vein breccias, colloform and crustiform banded cryptocrystalline to crystalline quartz and high-temperature alteration

mineral assemblages including stilpnomelane and Fe-rich chlorite. Those features indicate hydrothermal fluids in the New Cobar and Chesney deposits were relatively high temperature and were subjected to large-scale cyclic decompression in response to slip and dilation along the Great Chesney Fault, conditions likely to trigger phase separation. In contrast, although the base metal deposits in the Cobar Basin probably formed from similar or slightly lower temperature hydrothermal fluids compared to the gold-rich deposits (Table 36), there is no evidence fluids in the base metal deposits were subjected to large-scale cyclic decompression. For example, the base metal deposits typically do not contain the range of quartz vein textures that indicate large-scale and relatively violent fault zone dilation. Rather, they are characterised by more ductile deformation fabrics (Section 4.6).

Phase separation is interpreted to be associated with the main stage of gold deposition in numerous orogenic gold deposits (e.g. Golden Mile, Mt Charlotte and Lancefield, Yilgarn Craton, Ho et al., 1990; Sigma, Abitibi Belt, Canada, Robert et al., 1995; Wattle Gully, Victoria, Cox, 1995; Croagh Patrick in western Ireland, Wilkinson & Johnston, 1996; Fosterville, Victoria, Mernagh, 2001; Bronzewing and Wiluna, Yilgarn Craton, Western Australia, Dugdale & Hagemann, 2001 and Hagemann & Lüders, 2003). The general consensus is that the vapour-rich ($CO_2 \pm CH_4$) and low-moderate salinity liquid-rich inclusion populations represent end members of phase separation resulting from changing physiochemical conditions in the veins (Ridley and Diamond, 2000). Whilst phase separation in orogenic gold deposits is thought to have occurred in response to a number of mechanisms, including decreases in temperature (Ho et al., 1990; Ridley and Diamond, 2000), or in response to CH_4 production during fluid-wallrock interaction (Ho et al., 1990), cyclic fluid decompression at relatively constant temperatures during seismic activity along host shear zones appears to be the dominant control (Robert et al., 1995; Cox, 1995; Cox et al., 1995; Wilkinson & Johnston, 1996; Ridley and Diamond, 2000; Dugdale & Hagemann, 2001).

Fluid inclusion homogenisation temperatures for each quartz vein stage exhibit considerable variability, which is unlikely to be caused by deformation effects (e.g. leakage and necking) or entrapment of secondary fluids alone. Temperature variability is also a function of the thermal structure of the Great Chesney Fault and patterns of fluid flow within the fault. Peak temperatures measured for the New Occidental hydrothermal fluid (350–400°C) are considerably hotter than the temperature of wallrock at the inferred depth of deposit formation (150–200°C, assuming a relatively high local geothermal gradient of +30°C/km and a deposit depth of 5–7km). The inferred wallrock temperature is consistent with the temperature of widespread secondary fluid inclusions in the New Occidental deposit (Figure 182). In addition, the New Occidental deposit extends over a vertical interval of at least 1.2km. The deepest known part of the deposit is therefore expected to be of the order of 30–50°C hotter than the deposit top. Based on the same geothermal gradient, hydrothermal fluids were potentially sourced from depths of >12km, although shallower depths are possible if fluids were magmatically derived.

Cyclic fault rupture triggered advection of pulses of hotter temperature hydrothermal fluids to higher structural levels in the Great Chesney Fault zone. The efficiency of fluid flow in the fault was dependent on the complexity of fluid pathways within the fault zone and its overall permeability. Large-scale fault slip and dilation (e.g. during deposition of Stage 2–3 quartz) is interpreted to have created large-scale and continuous vertical pathways within the fault zone and triggered rapid ascent of deeper-sourced (hence hotter) fluids up the fault zone. Pressure reductions accompanying fault zone dilation, which were associated with formation of implosion breccias in the deposit, also enhanced fluid flow along the fault, with fluids migrating to zones of lower pressure (e.g. Sibson, 1992). In contrast, smaller-

scale fault slip associated with limited fault zone dilation (e.g. during deposition of late Stage 4 and Stage 5 quartz) more likely created relatively torturous fluid pathways, resulting in slow advection of shallower (hence less hot) hydrothermal fluids within the fault zone.

The degree to which the hotter hydrothermal fluids equilibrated with cooler wallrock within the Great Chesney Fault during deposit formation is dependent on the permeability of the fault zone and the frequency of rupture events. Rapid fluid flow and frequent fault zone ruptures have the effect of maintaining a steady flow of hotter fluids along the fault (e.g. Stage 2–3 quartz) and limiting fluid-wallrock equilibration, whereas slower fluid flow and less frequent fault ruptures allow more time for the hydrothermal fluid to both thermally and chemically equilibrate with wallrock (Stage 1, 4 and 5 quartz). Ascending fluids were also cooled as they mixed with earlier fluids that have already begun to equilibrate to ambient wallrock temperatures. Cox et al. (1991) proposed a mechanism for fluid-wallrock interaction that is applicable to the formation of the New Occidental deposit; fluids infiltrated wallrock along an extensive network of sub-horizontal extensional fractures formed about the Great Chesney Fault during the initial stages of fluid over-pressuring in the fault. Further increases in fluid pressure in the fault eventually triggered fault zone rupture, initiating quartz (and other mineral) deposition in the extensional fractures. Residual fluids that were either partly of fully thermally equilibrated with wallrock were drawn out of the sub-horizontal fractures by the negative pressure associated with fault rupture and mixed with new pulses of ascending hotter hydrothermal fluid. Fluid-wallrock interaction also has the effect of at least locally warming wallrock about the Great Chesney Fault. The New Occidental hydrothermal fluid may have also undergone adiabatic cooling during phase separation, which, depending on the degree of unmixing, may have caused cooling of the order of 2.5°C per 1% unmixing (e.g. Drummond & Ohmoto, 1985; Hagemann & Lüders, 2003).

In summary, fluid inclusion studies of the New Occidental deposit have provided further evidence that the early-stage gold-rich mineralisation and late-stage base metal mineralisation in the deposit formed under different physiochemical conditions. Gold was deposited from relatively high temperature weakly saline H_2O-NaCl-CO_2-CH_4 fluids that underwent phase separation in response to cyclic decompression associated with large-scale fault zone slip and dilation. In contrast, base metals were deposited from slightly more saline hydrothermal fluids that did not undergo phase separation during a period of more ductile deformation along the host fault zone. Studies have also confirmed the broad similarities between gold mineralisation in the deposit and orogenic gold deposits around the world, both in terms of fluid compositions and mechanisms of deposit formation.

9 LEAD AND SULFUR ISOTOPIC STUDIES

9.1 Introduction

Lead isotopes have been used to constrain both the age and source of lead-bearing minerals in hydrothermal deposits (Faure, 1986). In the case of the New Occidental deposit, lead isotopes potentially provide useful information on the genesis of the deposit, especially as distinctive Pb-bearing minerals are intimately associated with a number of ore mineral stages in the deposit paragenesis (galena-clausthalite with early stage gold and galena in the late base metal stage). In addition, the plumbo-tectonic framework established by Carr et al. (1995) for the Lachlan Orogen provides a means by which the source(s) of lead, and hence co-genetic metals, in the New Occidental deposit (and in other Cobar deposits) and the age of deposit formation can be constrained relative to other ore deposits in the Lachlan Orogen.

Sulfur isotope systematics of paragenetically constrained sulfur-bearing minerals in the New Occidental deposit, host rocks and, more generally, base metal deposits in the Lachlan Orogen, can be used to help characterise the source of sulfur in hydrothermal fluids and infer temperatures of ore mineral deposition (e.g. Rye & Ohmoto, 1974; Ohmoto & Rye, 1979; Faure, 1986; Ohmoto, 1986).

Unfortunately, lead and sulfur isotope studies cannot be used to investigate the genesis of the earliest ore mineral stage in the New Occidental deposit (magnetite-scheelite-wolframite stage) and potentially may have limited application to the study of the early stages of low-sulfur gold-bismuth ore minerals in the deposit. In this latter case, the lead-bearing phases are extremely fine-grained and often intergrown with other mineral phases, which make selective analysis difficult. Furthermore, the sulfur isotopic fractionation of bismuth sulfides is not well understood (Faure, 1986).

Specifically, lead and sulfur isotope studies were undertaken on the New Occidental deposit in order to:

1. **Improve constraints on the likely source(s) of metals in the New Occidental deposit.** On the basis of lead isotope data, metal source(s) for Cobar deposits have variously been proposed as homogenous Palaeozoic crust (Carr et al., 1995), a combination of metamorphosed sedimentary and volcanic basement and basin sediments undergoing thermal maturation (Lawrie & Hinman, 1998) and pre-Cobar Basin granites (Jiang & Seccombe, 2000). Although relatively homogenous, the lead isotope signatures of Cobar deposits exhibit subtle differences from each other (Suppel et al., 1990; Dean, 1991; Lawrie & Hinman, 1998), which relate to source rock.

2. **Determine the Pb-model age of Cobar mineralisation.** The detailed plumbo-tectonic model established for the Lachlan Orogen, including for the Cobar deposits, can yield model ages for ore deposits with a precision generally better than ±15 Ma (Carr et al., 1995). Such ages may help resolve confusion over the age of Cobar mineralisation (c.f. $^{40}Ar/^{39}Ar$ ages of 401.5 Ma and 384.0 Ma for sericite associated with early- and late-stage ore minerals respectively in the Peak deposit cited by Perkins et al. [1994] and the ca. 340 Ma age inferred by Jiang and Seccombe [1995] from a combination of a Rb-Sr isochron age from the Peak Rhyolite and K-Ar age of feldspar in veins overprinting the Peak Rhyolite).

3. **Improve constraints on the source(s) of sulfur in the New Occidental deposit.** Initial sulfur isotope studies of Cobar deposits (Sun, 1983; Seccombe, 1985; 1990; Brill, 1988a; Forster, 1997) suggest sulfur in Cobar deposits was derived from Cobar Basin sediments. More recently, an exotic source of orebody sulfur with minor local contamination from basin sulfur has been proposed on the basis of differences between $\delta^{34}S$ values for syngenetic/metamorphic pyrite and pyrrhotite and orebody sulfides (Jiang et al., 1995a,b; Jiang, 1996; Seccombe, 1998; Sun et al., 2000b; Jiang & Seccombe, 2000).

4. **Use sulfur isotopes to provide independent constraints on formation temperatures for mineralisation in the New Occidental deposit.** Galena - sphalerite and pyrrhotite - pyrite mineral pairs from the New Occidental deposit may potentially constrain sulfide mineral formation temperatures. Sulfur isotope fractionation temperatures from a range of different sulfide mineral pairs have been cited for the Elura (Seccombe, 1985; Sun & Seccombe, 1998), Peak (Jiang et al., 1995; Jiang & Seccombe, 2000) and McKinnons deposits (Forster, 1997). In contrast, Brill (1988a) concluded the bulk of the sulfides in the CSA deposit are not in isotopic equilibrium and therefore $\delta^{34}S$ fractionation temperatures are unreliable.

9.2 Previous Isotope Studies of Cobar Deposits

9.2.1 Lead Isotope Studies

Joint CSIRO, NSW Geological Survey and exploration company studies during the 1970s and 80s established a comprehensive lead isotope database for mineral deposits in the Lachlan Orogen (Suppel et al., 1990; Carr et al., 1995; Dean, 1991). Additional Pb isotope data was subsequently collected at the Peak (Hinman, 1992; Jiang, 1996) and Elura (Sun and Seccombe, 2000) deposits. The database, however, does not contain samples from the New Occidental and Perseverance deposits. Although the resultant database is relatively comprehensive in that it contains data for most of the major deposits in the Cobar Basin, with the exception of the Peak and Elura deposits, paragenetic constraints on much of the lead isotope data is lacking.

Carr et al. (1995) argue lead isotope systematics (e.g. model ages and tectonic associations) can be interpreted in terms of variable degrees of mixing between crustal and mantle-derived lead. They devised a plumbo-tectonic model for the eastern Lachlan Orogen in which end-member mantle and crustal lead reservoirs evolved along distinct growth curves. The mantle growth curve is single-stage growth curve with μ=10 and passing through lead isotope values from the Goonumbla (Northparkes E22, E26 and E27) orebodies at an age of 440 Ma. This curve represents a long-lived relatively homogenous Palaeozoic reservoir containing mantle-derived Pb. The crustal growth curve is a modified late-stage Cumming and Richards (1975) global crustal growth curve defined by a μ=13.3 and which passes through the average Pb isotope values for the Woodlawn Pb-Zn mineralisation at an age of 420 Ma. This curve reflects Pb that has had a long crustal residence time (Carr et al., 1995).

Variations in Pb isotope composition of lead-bearing minerals are resolved in terms of mixing isochrons between the two growth curves. The isochrons, which are defined by negative slopes on $^{207}Pb/^{204}Pb$ - $^{206}Pb/^{204}Pb$ ratio plots, reflect hydrothermal, magmatic or metamorphic-driven mixing of crustal-dominated Pb and Pb derived from rocks with mantle heritage, the latter principally being Ordovician igneous rocks. Carr et al. (1995)

also suggested the mixing model yields ages with a precision generally less than ± 15 m.y. based on comparisons with independent K-Ar and $^{40}Ar/^{39}Ar$ age dates for Palaeozoic granites in the Lachlan Orogen. In contrast, Carr et al. showed the original Cumming and Richard (1975) growth curve yields model ages that differ by up to 36 m.y. from those independent ages.

Cobar deposits and other deposits in the Lachlan Orogen have relatively homogenous lead isotope ratios, plotting on the crustal growth curve of Carr et al. (1995) (Figure 11), which reflects metals sourced from isotopically homogenous crust or, less likely, the homogenising effect of large-scale magmatic and hydrothermal processes (Carr et al., 1995). Suppel et al. (1990) and Dean (1991) recognised subtle differences in the lead isotope composition of Cobar deposits. Deposits hosted in Ordovician Girilambone Group (Gunderbooka and Mulga King) and Cobar Supergroup equivalent rocks in the Canbelego-Mineral Hill trend (Mt Boppy and Mineral Hill) are characterised by slightly lower $^{207}Pb/^{204}Pb$ and $^{208}Pb/^{204}Pb$ values than deposits within the Cobar Basin and the Mount Hope and Rast Troughs to the south (Gilgunnia, Nymagee, Mt Hope).

Lawrie and Hinman (1998) noted Au-rich deposits (Peak and New Cobar) in the Cobar Basin tend to be less radiogenic than the base metal-rich deposits (CSA and Elura) and concluded the less radiogenic lead represents an ore fluid derived from unspecified metamorphic basement whilst the more radiogenic lead represents a basinal fluid. They argued mixing of these two fluids has produced intermediate lead isotope compositions. Jiang and Seccombe (2000), however, argued differences between basement and basinal ore-lead isotope signatures proposed by Lawrie and Hinman (1998) is within the analytical error of the measurements. They argued the lead isotope signatures of the host sediments and basement rocks preclude these units from being the source of ore lead. Jiang and Seccombe (2000) determine a 420 Ma Pb-model age for the Peak deposit using the Cumming and Richards (1975) growth curve, which corresponds to the age of granitic intrusions in Girilambone Group basement flanking the Cobar Basin. They proposed ore-lead was pre-concentrated in the pre-Cobar Basin granites and then remobilised by later hydrothermal fluids into the Cobar Basin sequences, whilst preserving the original isotopic signature of the source granites. Sun & Seccombe (2000) have likewise suggested Pb in the Elura deposit is leached from basement granites by hydrothermal fluids associated with deposit formation.

9.2.2 Sulfur Isotope Studies

A large number of sulfur isotope studies have been performed on Cobar deposits (Table 41).

Table 41: Sulfur Isotope studies of Cobar deposits

Deposit:	Studies:
CSA	Rayner (1969); Sun (1983); Brill (1988a)
Great Cobar	Rayner (1969); Sun (1983);
Peak	Jiang et al. (1995); Jiang (1996); Jiang & Seccombe (2000)
Central Area, Cobar Goldfield	Seccombe & Brill (1989); Seccombe (1991)
Elura	Sun (1983); Seccombe (1990); Sun & Seccombe (2000)
McKinnons	Forster (1997)
Canbelego (Mt Boppy)	Sun (1983)

Cobar deposits yield relatively consistent $\delta^{34}S$ values in the range of +4 to +12‰ (Figure 185) consistent with sulfur isotope values obtained from Silurian VMS deposits in the eastern part of the Lachlan Orogen (Woodlawn and Captain's Flat; Sun, 1983). Some variation is evident in the data, with the Peak, New Occidental and New Cobar deposits returning on average lighter $\delta^{34}S$ values than other Cobar deposits (Seccombe & Brill, 1989; Seccombe; 1991).

Studies have shown sulfide $\delta^{34}S$ values do not exhibit significant isotopic compositional variations between ore-types, different vein systems within the one ore-type, or between different levels in the deposits. Likewise, only relatively subtle variations have been noted between different paragenetic stages within the one deposit (Brill, 1988a; Seccombe, 1990; Jiang et al., 1995; Forster, 1997). Seccombe and Brill (1989) and Seccombe (1991) concluded there is no systematic difference in isotopic composition of Cobar deposits.

Cobar's Cu-Au deposits are characterised by sulfur isotopic disequilibria (Seccombe, 1985; Brill, 1988a), which Brill argued reflects the different sulfide minerals having formed at different stages in the deposit paragenesis under sulfur-deficient conditions. Seccombe (1985) and Sun & Seccombe (1998) concluded galena - sphalerite in the Elura deposit is isotopically equilibrated and obtained $\delta^{34}S$ isotope fractionation temperatures for galena - sphalerite mineral pairs of 220–449°C, consistent with fluid inclusion homogenisation temperatures. Jiang et al. (1995) obtained fractionation temperatures of 300–350°C from galena-chalcopyrite mineral pairs in the Peak deposit, consistent with fluid inclusion temperatures estimated for that stage of mineralisation, suggesting isotopic equilibrium between some sulfide minerals. However, galena - sphalerite mineral pairs yielded unrealistic temperatures of formation, suggesting these minerals were not in sulfur-isotopic equilibrium.

Jiang et al. (1995) and Sun & Seccombe (1998) determined distal disseminated pyrite and pyrrhotite in the Peak and Elura deposits are characterised by more positive $\delta^{34}S$ values (+16.3 to +20.1‰) than orebody sulfides (+5.4 to +10.2‰). They argue the distal pyrite and pyrrhotite have $\delta^{34}S$ values equivalent to that of Early Devonian seawater sulfate, having formed by reduction of Early Devonian seawater sulfate (+19‰) within a closed system in relatively deep impermeable marine sediments that prevented significant isotopic fractionation. Jiang et al. (1995) suggested that subsequent metamorphism was associated with significant isotopic fractionation, producing metamorphic pyrite/pyrrhotite with much lower $\delta^{34}S$ values (-4.7 to +5.9‰) compared to orebody sulfides and their "sedimentary" sulfides. However, the compositional range for metamorphic sulfides in the Peak deposit cited by Jiang et al. (1995) is based on a single outlier value (-4.7‰) and the remainder of values cluster with orebody $\delta^{34}S$ values.

The ultimate source of sulfur in Cobar deposits remains uncertain, although most authors propose a homogenous source (Jiang et al. 1995; Jiang & Seccombe, 2000). Brill (1988a) concluded the isotopic signature of the CSA deposit is consistent with ore fluids derived by metamorphic dehydration reactions in the underlying sedimentary pile. Jiang et al (1995a) suggested that ore sulfur in the Peak deposit was derived from a mixed igneous and metasedimentary source homogenised by magmatism at deeper levels within the Cobar Basin. Sun and Seccombe (1998) proposed ore fluid $\delta^{34}S$ values associated with the Elura deposit indicate a deeper source for the majority of the sulfur in the deposit, most likely basin or basement rocks at a higher metamorphic grade than the deposit host-rocks.

Figure 185: Sulfur Isotope Signatures of Cobar Deposits

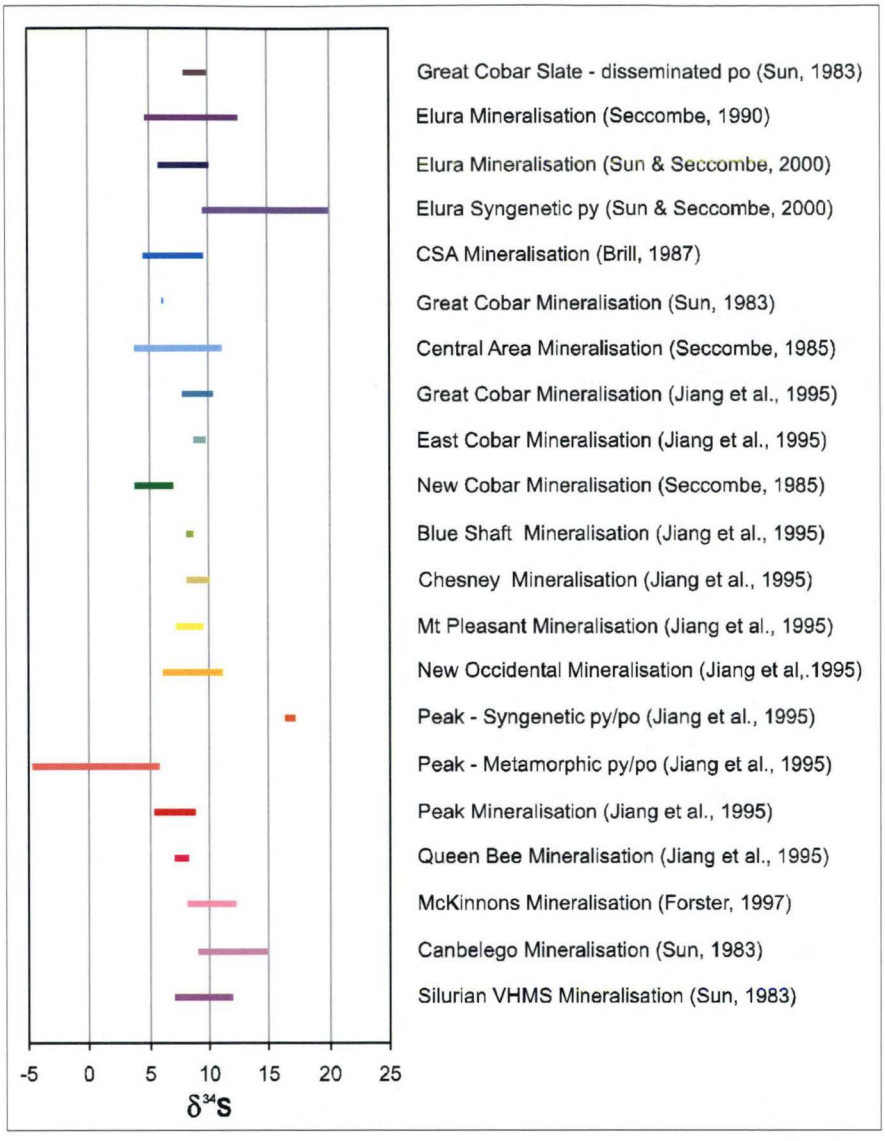

9.3 Data Collection and Analytical Techniques

9.3.1 Lead Isotope Samples

A total of 13 samples (Figure 186) were selected from New Occidental deposit to characterise the Pb isotopic signature of the two stages of Pb-bearing ore minerals in the deposit; the galena-clausthalite (Pb-Bi)(S-Se) solid solution series minerals associated with early-stage gold and galena associated with late stage galena - sphalerite - pyrrhotite.

Samples of fine-grained early-stage galena - clausthalite were selected on the basis of positive identification of early-stage galena - clausthalite minerals by Reynolds (1998; 1999a), elevated Pb-Bi assays, the absence of appreciable Zn and the presence of well-developed Stage 2–3 quartz veins (Table 42). Elevated Zn was interpreted to indicate the presence of late-stage galena - sphalerite. Late-stage galena was sufficiently coarse-grained to be directly sampled.

Figure 186: Location of lead isotope samples from the New Occidental deposit.

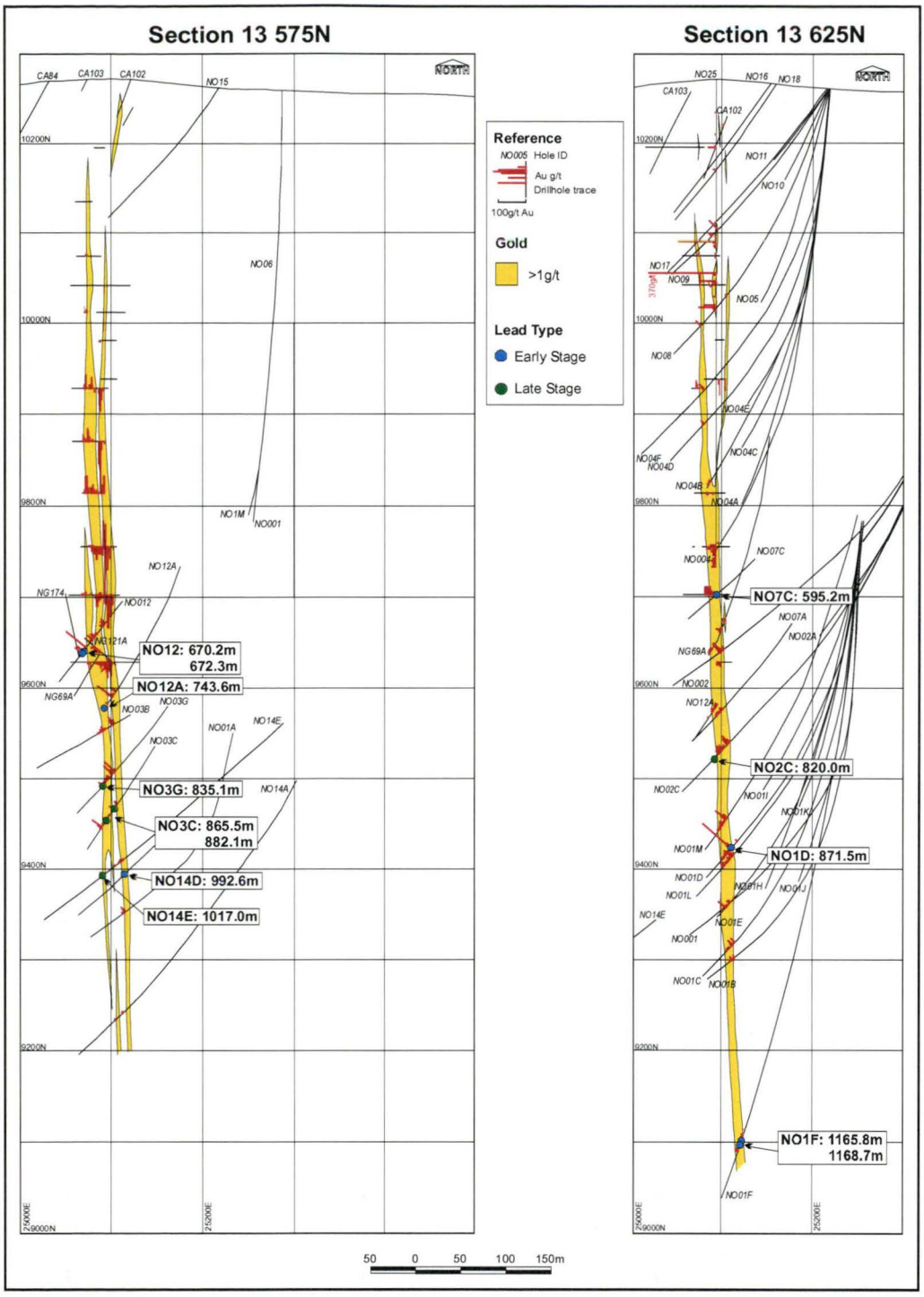

In addition, two samples of disseminated pyrite from near the Peak deposit were chosen to characterise the isotopic composition of stratiform pyrite and six samples of galena were collected from the Perseverance deposit to provide initial indications of its isotopic signature.

Samples were submitted to Sirotope at the CSIRO Division of Exploration and Mining, North Ryde for analysis by Thermal Ionisation Mass Spectrometry (TIMS). Coarse-grained galena was handpicked from the samples of the late-stage galena - sphalerite in the New Occidental deposit and from all of the Perseverance samples. For the remainder of samples, which are all low-Pb, a 50–100mg pulped sub-sample was digested with aqua

regia, evaporated and solubilised Pb was dissolved in HBr. Samples containing less than 1500ppm Pb were spiked with ^{202}Pb.

Pb isotope data for other Cobar deposits, which are contained within the Lachlan Orogen Pb isotope database, were provided to the author by CSIRO. A number of data points within this database were excluded from the subsequent analysis undertaken as part of this study on the basis they are both low Pb and contain radiogenic Pb.

Table 42: Samples submitted for Pb isotope analysis

Holeid	Depth (m)	Deposit	Type	Au ppm	Cu ppm	Pb ppm	Zn ppm	Ag ppm	Bi ppm
NO1D	871 5	New Occidental	Early-stage Pb with Bi	26	216	561	23	5	660
NO7C	595.2	New Occidental	Early-stage Pb with Bi	72.7	400	680	57	17.5	2800
NO1F	1165.8	New Occidental	Early-stage Pb with Bi	5.84	280	240	98	8	2900
NO1F	1168.7	New Occidental	Early-stage Pb with Bi	5.73	400	170	27	5 5	3300
NO12A	743.6	New Occidental	Early-stage Pb with Bi	1.22	195	240	100	3	1250
NO14D	992.6	New Occidental	Early-stage Pb with Bi	45 4	155	160	36	4	2050
NO12	670.2	New Occidental	Early-stage Pb with Bi	32	1600	660	88	8.5	5650
NO12	672 3	New Occidental	Early-stage Pb with Bi	33.2	1500	1200	93	15	12800
NO3G	835.1	New Occidental	Late Pb-Zn	9.01	1550	6650	135	38.5	6700
NO14E	1017 0	New Occidental	Late Pb-Zn	15 9	38500	57100	24100	96	550
NO2C	820.0	New Occidental	Late Pb-Zn	0 14	4200	20000	50	21	460
NO3C	865.5	New Occidental	Late Pb-Zn	13.2	230	11500	160	37.5	1450
NO3C	882.1	New Occidental	Late Pb-Zn	3.24	6050	1950	2700	14	580
PK64	229.4	Peak	Disseminated stratiform pyrite	0.005	87	27	132	0.1	5
PK64	443.4	Peak	Disseminated stratiform pyrite	0.005	30	52	77	0.1	5
PE34	279.5	Perseverance	Early-stage Pb with Au-Cu	0.4	55500	10400	668	54	125
PE60A	510.5	Perseverance	Early-stage Pb with Au-Cu	1.48	2580	68900	212	121	331
PE60	567.0	Perseverance	Early-stage Pb with Au-Cu	4.94	4930	108000	4340	56	13
PP971	769 7	Perseverance	Late Pb-Zn	0.01	573	36600	12200	5.2	55
PP971	864 0	Perseverance	Late Pb-Zn	0.04	1950	31200	79000	3.4	0 5
PP971	868.8	Perseverance	Late Pb-Zn	0.08	421	19800	126000	3.2	0.5

9.3.2 Sulfur Isotope Samples

A total of 18 samples containing a mixture of sulfides including pyrite, pyrrhotite, galena, sphalerite and chalcopyrite were selected from the New Occidental deposit for sulfur isotope analysis (Figure 187). In addition, a sample of stratiform pyrite with overprinting metamorphic pyrrhotite from near the Peak deposit was sampled in an attempt to characterise the isotopic composition of those sulfides (Table 43).

Samples were submitted to the Central Science Laboratory at the University of Tasmania, Hobart, Tasmania for analysis using a Nd:YAG laser ablation sulfur isotope microprobe. Polished sections approximately 150 μm thick were prepared for each sample. The sections were polished with 1 μm diamond paste to reduce isotopic fractionation caused by rough surfaces. The polished section was loaded into the laser system in an oxygen atmosphere and burned with a laser to produce SO_2 and other contaminant gases. The current of ablation initiation depended on the sulfide species. Laser ablation pits were approximately 150-200 μm in diameter and up to 150 μm deep, which limited the grainsize of individual sulfide phases to 200 μm and greater. The gas sample was then passed through a system of

traps to remove various contaminant species such as H_2O and CO_2. Once a relatively gas-pure sample was obtained it was drawn into a VG Isogas Sira II mass spectrometer where the isotopic ratios of the sample and standard gases were compared. Results are corrected for laboratory dependent fractionation factors (Huston et al., 1995). All sulfur isotope measurements are reported in standard notation relative to the Canyon Diablo Troilite (CDT; Faure, 1986). In order to assess the isotopic homogeneity of the samples, up to three different grains of the same mineral within each sample were analysed.

Figure 187: Location of sulfur isotope samples from the New Occidental deposit.

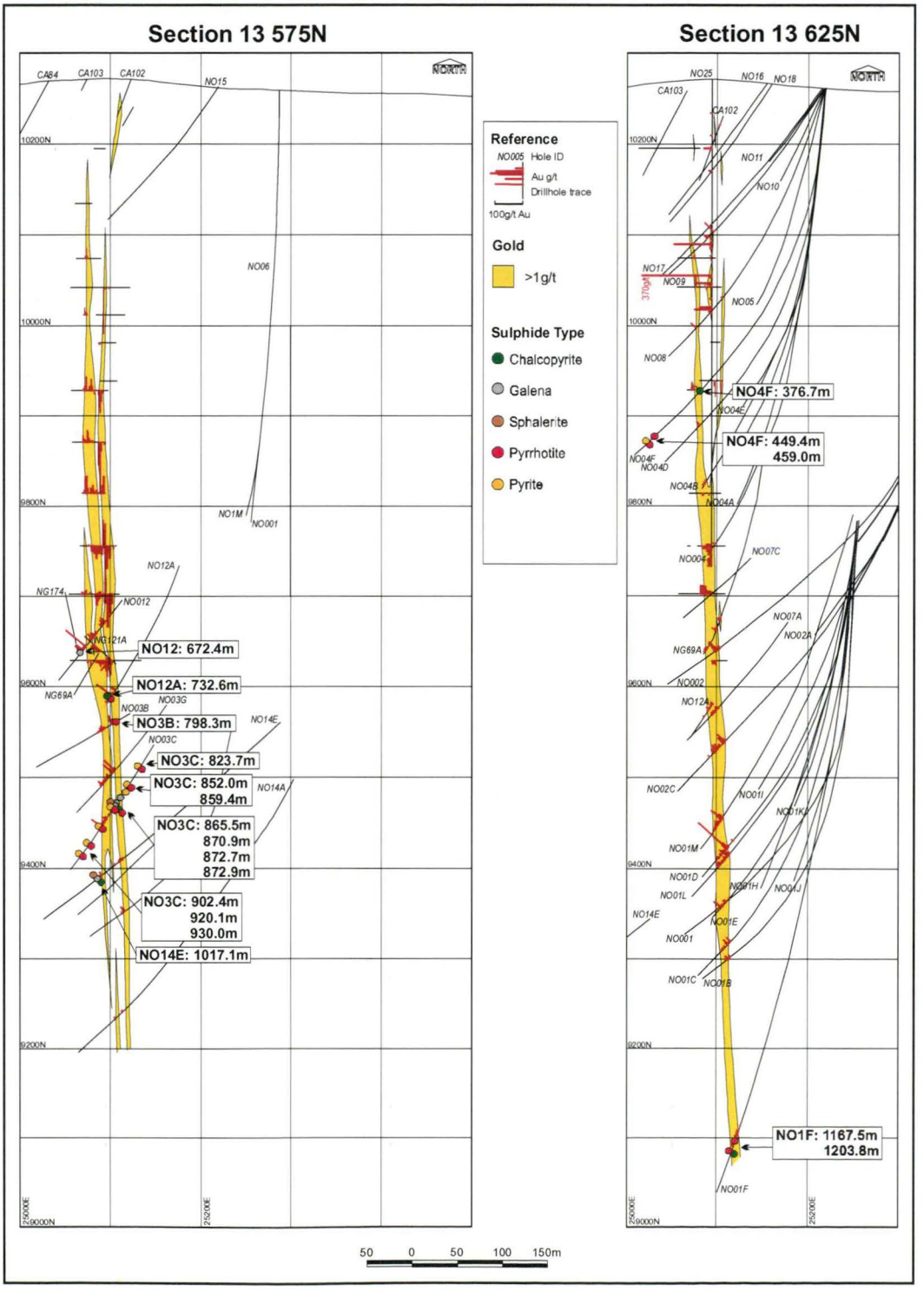

Table 43: Samples submitted for sulfur isotope analysis.

Holeid	Depth	Sulfides	Comments
NO01F	1167.5m	Po	Coarse-grained pyrrhotite in Stage 4 quartz breccia containing Stage 2/3 quartz vein fragments
NO01F	1203.8m	Cpy - Po	Stringer chalcopyrite-pyrrhotite in brecciated Stage 4 quartz veins
NO03C	823.7m	Cpy - Po	Minor chalcopyrite in stringer Stage 4 quartz veins
NO03C	852.0m	Po	Coarse-grained pyrite in vein replacing magnetite
NO03C	859.4m	Py	Coarse-grained pyrite in vein replacing magnetite
NO03C	865.5m	Gn	Galena-sphalerite in fractures in brecciated Stage 4 quartz veins
NO03C	870.9m	Gn	Galena in cross-cutting veinlets in Stage 2/3 quartz breccia
NO03C	872.7m	Gn - Sp	Galena-sphalerite in cross-cutting veinlets in Stage 2/3 quartz breccia
NO03C	872.9m	Cpy - Po	Coarse-grained chalcopyrite-pyrrhotite in cross-cutting veinlets in Stage 2/3 quartz breccia
NO03C	902.4m	Cpy - Po	Coarse-grained chalcopyrite-pyrrhotite in cross-cutting veinlets in Stage 2/3 quartz breccia
NO03C	920.1m	Cpy - Po	Coarse-grained chalcopyrite-pyrrhotite in stringer Stage 4 quartz veins
NO03C	930.0m	Cpy - Po	Coarse-grained chalcopyrite-pyrrhotite in stringer Stage 4 quartz veins
NO04F	376.7m	Cpy	Chalcopyrite as splashes in brecciated Stage 2 quartz veins
NO04F	449.4m	Po	Disseminated stringers of pyrrhotite in sheared sandstone
NO04F	459.0m	Py - Po	Bedding parallel pyrite aggregates partly replaced by cleavage-parallel pyrrhotite flakes
NO12	672.4m	Gn	Fine grained disseminated bismuth minerals in late chlorite-altered Stage 4 quartz breccia
NO12A	732.6m	Cpy - Po	Chalcopyrite-pyrrhotite replacing magnetite in colloform Stage 1 quartz-magnetite vein
NO14E	1017.1m	Cpy - Gn - Sp	Coarse-grained chalcopyrite-galena-sphalerite on footwall margin of Stage 4 quartz vein breccia
PK64 (Peak)	451.7m	Py - Po	Bedding-parallel pyrite aggregates partly replaced by cleavage-parallel pyrrhotite flakes

Cpy - chalcopyrite, Gn - galena, Po - pyrrhotite, Py - pyrite, Sp - sphalerite

9.4 Lead Isotopic Composition of the New Occidental Deposit

9.4.1 Results of Lead Isotope Analyses

Lead mineralisation in the New Occidental deposit is characterised by a narrow range of Pb isotopic ratios comparable to ratios recorded from galena samples from the Perseverance deposit during this study. Low-Pb samples, including some samples of mineralisation from the Peak deposit and pyrite from near the Peak deposit generated higher $^{206}Pb/^{204}Pb$ and $^{207}Pb/^{204}Pb$ ratios (Table 44). Precision of lead isotopic analyses undertaken in this study, as indicated by analysis quality, is largely very good, with the exception of sample NO12 - 672.3m, which suffered some fractionation during analysis and was repeated.

Table 44: Lead Isotope Analyses for Samples from the New Occidental and Perseverance deposits and for Pyrite samples from the Peak deposit environs.

Sample No	$^{206}Pb/^{204}Pb$	$^{207}Pb/^{204}Pb$	$^{208}Pb/^{204}Pb$	Pb Conc ppm	Quality High=0 Low=9
New Occidental Deposit - Early Stage Galena-Clausthalite					
NO1D - 871.5	18.107	15.632	38.267	1950	2
NO7C - 595.2m	18.084	15.600	38.157	517	2
NO 1F - 1165.7m	18.115	15.620	38.228	244	2
NO 1F - 1168.6m	18.110	15.614	38.217	202	2
NO 12A - 743.6m	18.174	15.649	38.300	8.4	0
NO 14D - 992.3m	18.134	15.654	38.333	266	1
NO12 - 670.2	18.109	15.626	38.250	189	3
NO12 - 672.3	18.122	15.638	38.228	3330	9
New Occidental Deposit - Late Stage Galena					
NO3G - 835.1m	18.080	15.605	38.174	Galena	3
NO14E - 1017.0m	18.084	15.623	38.234	Galena	1
NO2C - 820.3m	18.060	15.596	38.157	Galena	2
NO3C - 865.5m	18.070	15.593	38.127	Galena	4
NO3C - 882.1m	18.071	15.593	38.153	Galena	4
Stratiform pyrite from Peak area					
PK64 - 229.4m	18.492	15.664	39.056	22.9	4
PK64 - 443.4m	18.463	15.660	38.972	25.6	6
Perseverance Deposit - Early Galena (with gold - chalcopyrite)					
PE34 - 279.5m	18.073	15.612	38.193	Galena	2
PE60A - 508.5m	18.079	15.625	38.239	Galena	2
PE60 - 567.0m	18.068	15.599	38.159	Galena	2
Perseverance Deposit - Late Galena (with sphalerite and black chlorite alteration)					
PP971 - 769.7m	18.063	15.600	38.150	Galena	2
PP971 - 864.0m	18.070	15.606	38.160	Galena	2
PP971 - 868.4m	18.083	15.612	38.188	Galena	3

9.4.2 New Occidental Deposit Isotopic Signature

Lead isotope initial ratios from the New Occidental deposit define two partially overlapping groups. Early stage galena-clausthalite, which is typically low-Pb, is characterised by slightly higher and more variable $^{206}Pb/^{204}Pb$, $^{207}Pb/^{204}Pb$ and $^{208}Pb/^{204}Pb$ ratios compared to late-stage galena in the deposit, although such differences are largely within the calculated experimental error or the measurements. Collectively, data lie along apparent trends centred on or above the Lachlan Orogen crustal growth curve of Carr et al. (1995), and yield model ages between 400 and 430 Ma (estimated for the weighted average of the two sample groups based on $^{207}Pb/^{204}Pb$ versus $^{206}Pb/^{204}Pb$ primary isochrons derived by Carr et al., 1995; Figure 188). New Occidental deposit samples plot above the Lachlan Orogen crustal growth curve on $^{208}Pb/^{204}Pb$ versus $^{206}Pb/^{204}Pb$ ratio plots, suggesting a higher initial ω value ($^{232}Th/^{204}Pb$ ratio) in the New Occidental deposit source reservoir compared to the ω value used by Carr et al. (1995) in their formulation of the Lachlan Orogen crustal growth curves.

Figure 188: Lead isotopic ratios of sulfide minerals from the New Occidental deposit plotted in relation to the Lachlan Fold Belt crustal and mantle growth curves of Carr et al. (1995).

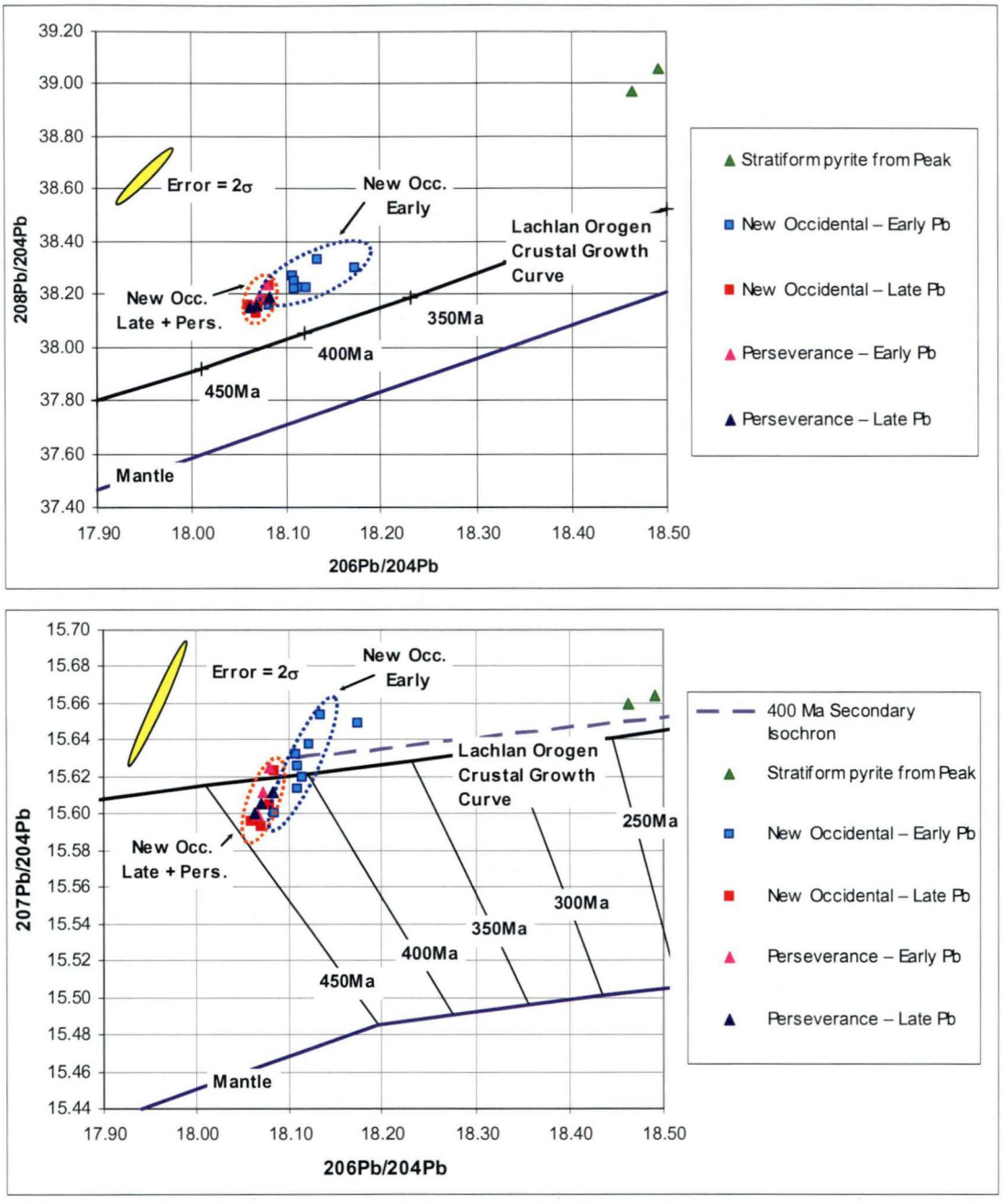

9.4.3 The Impact of ^{238}U Radiogenic Decay

Whole-rock samples of early-stage galena-clausthalite mineralisation in the New Occidental deposit are characterised by relatively low Pb contents (8–3580 ppm Pb), as are the samples of syngenetic pyrite from near the Peak deposit (23–26 ppm Pb), and therefore ^{206}Pb derived from the decay of ^{238}U may constitute a significant component of the total ^{206}Pb in the samples. Calculated $^{206}Pb/^{204}Pb$ ratios, assuming initial Pb isotope ratios equivalent to the average of galena samples from the New Occidental deposit ($^{206}Pb/^{204}Pb$ = 18.073, $^{207}Pb/^{204}Pb$ = 15.602, $^{208}Pb/^{204}Pb$ = 38.169), a Devonian (0.40 Ga) age for mineralisation and initial U contents in the range 0.2–2 ppm, reveal sample NO12A - 743.6m from the New Occidental deposit and the two pyrite samples from near the Peak

deposit are affected by appreciable $^{238}U/^{206}Pb$ decay (Figure 189). Based on these calculations, the relatively high $^{206}Pb/^{204}Pb$ ratio of sample NO12A - 743.6m is attributable to radiogenic decay of only 0.2 ppm ^{238}U, whereas the $^{206}Pb/^{204}Pb$ ratios of the two Peak pyrite samples can be accounted for by the radiogenic decay of 2 ppm U. Such uranium contents are consistent with wholerock analyses of the New Occidental deposit and surrounding wallrock (Section 7.3), which indicate New Occidental deposit wallrock is characterized by uranium contents of the order of 2–3 ppm (principally contained in detrital monazite and zircon) whilst the deposit itself contains less than 0.5ppm U. The other samples of early-stage galena-clausthalite in the New Occidental deposit comprise largely hydrothermal quartz and are therefore also expected to contain only minor amounts of U. The samples containing >200 ppm Pb, and especially those samples containing >1000 ppm Pb, should therefore yield initial isotopic compositions (Figure 189).

Figure 189: Pb Content against present day $^{206}Pb/^{204}Pb$ ratios for Devonian (0.42Ga) Mineralisation assuming an initial $^{206}Pb/^{204}Pb$ ratio of 18.07 and a range of initial U contents.

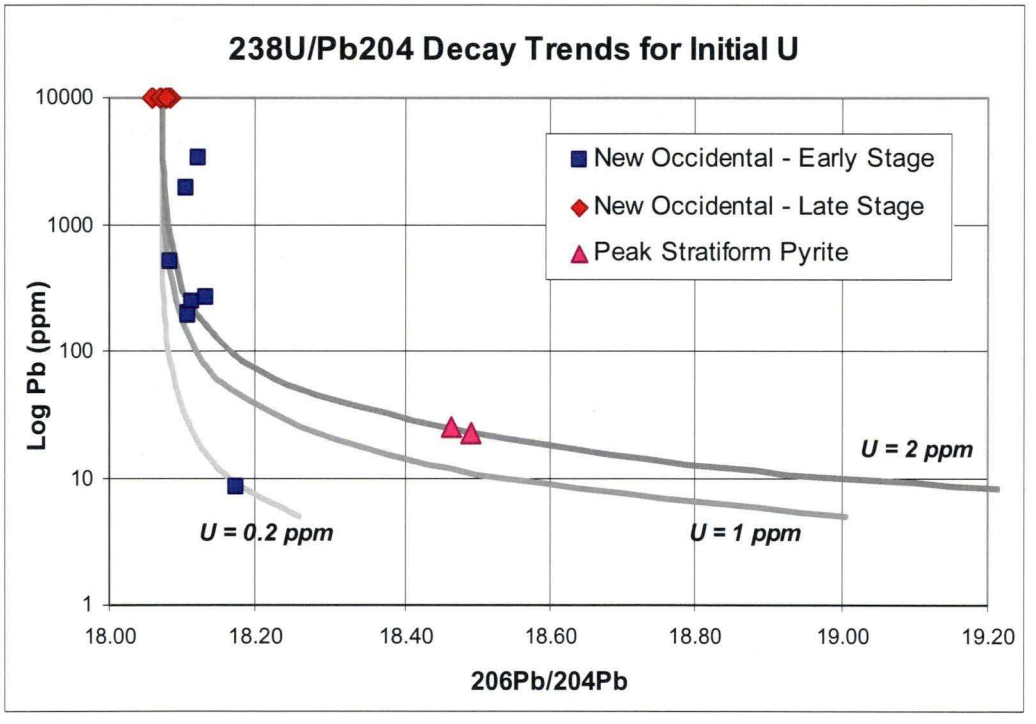

9.5 Plumbo-tectonics of the Cobar Basin and Lachlan Orogen

9.5.1 Lead Isotope Signatures of Cobar and Lachlan Orogen Deposits

Deposits in the Cobar Basin and adjacent basement are characterised by relatively homogenous Pb isotopic ratios (Figure 190). Subtle differences in isotopic composition exist between the various deposits and three main groupings are herein recognised:

1. **Cobar Basement:** including the Gunderbooka, Harts Tank, Mt Boppy and Mulga King deposits, but also including the McKinnons deposit and Mrangelli prospect, which are located in the western part of the Cobar Basin.

2. **Cobar Basin Group 1A:** incorporating the bulk of the lead isotope data for deposits in the Cobar Goldfield, including Great Cobar, New Cobar, Gladstone,

Wood Duck, New Occidental (late stage only), Peak, Perseverance and Queen Bee deposits, but also Mt Drysdale (a small gold deposit northeast of the CSA located on the edge of the Cobar Basin).

3. **Cobar Basin Group 1A:** including early-stage lead mineralisation from the New Occidental deposit and some Wood Duck and New Cobar data.

4. **Cobar Basin Group 2:** including the Elura and CSA deposits.

Figure 190: Lead isotope ratios of Cobar deposits (all data from CSIRO database apart from data collected from the New Occidental and Perseverance deposits in this study).

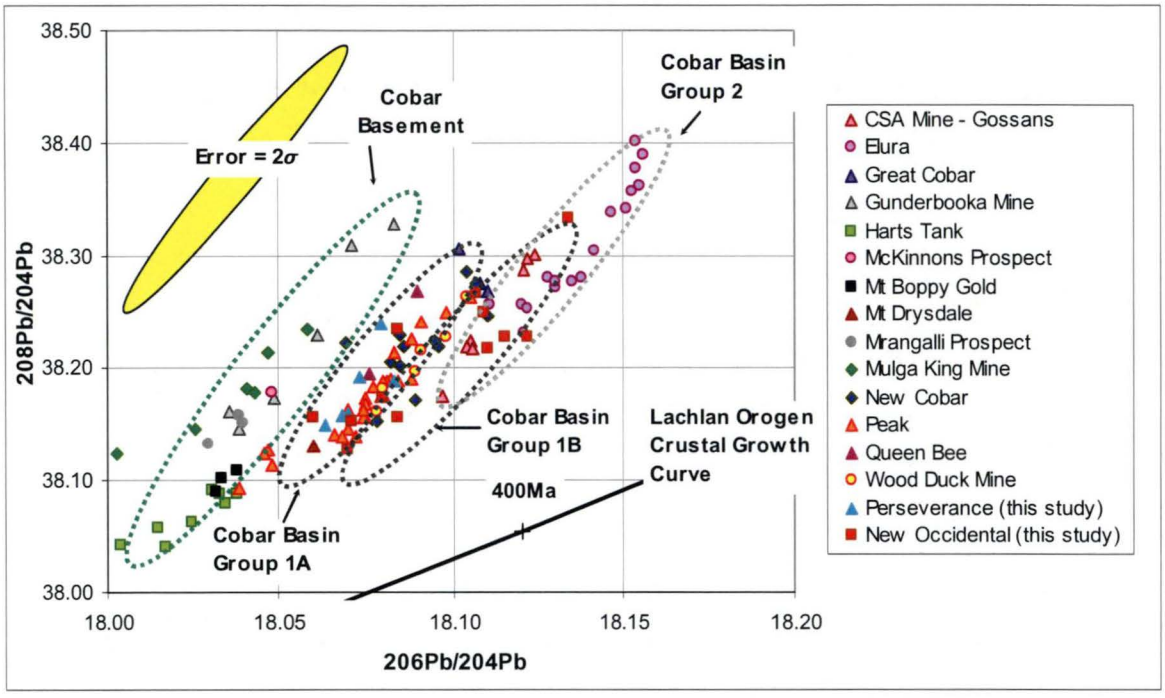

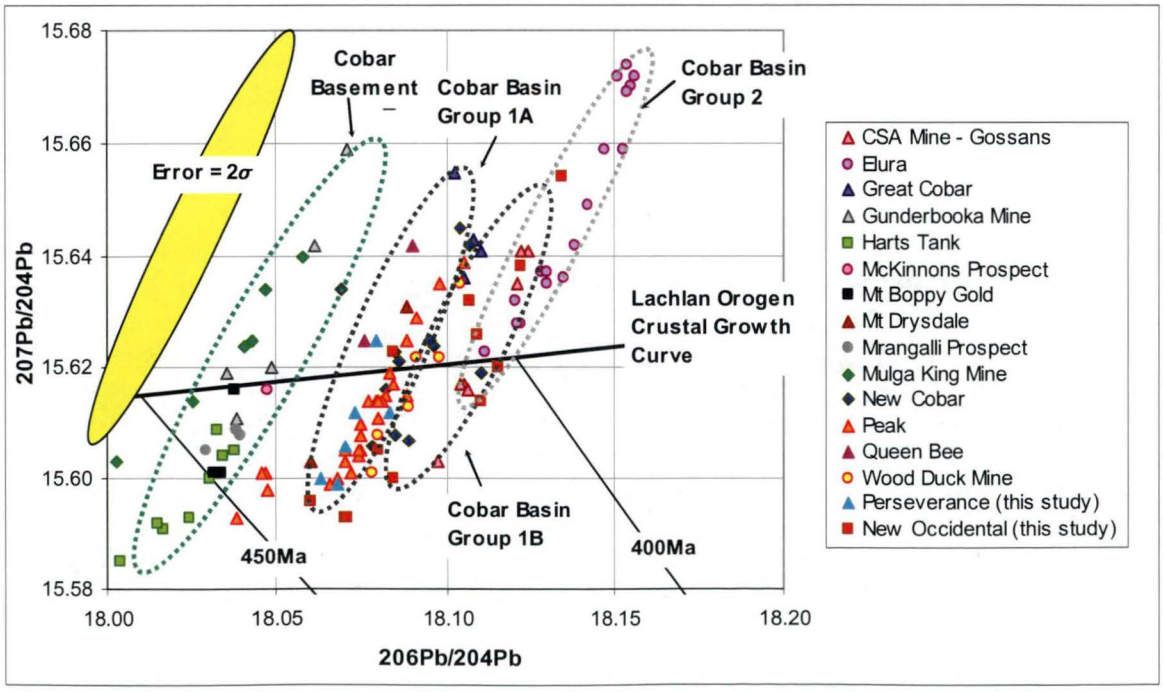

On $^{208}Pb/^{204}Pb$ versus $^{206}Pb/^{204}Pb$ plots, the four groupings outline a fractionation trend that is parallel to but higher than the Lachlan Orogen crustal growth curve, suggesting a source reservoir with a consistently higher ω value than used by Carr et al. (1995) to formulate the Lachlan Orogen crustal growth curve. On $^{207}Pb/^{204}Pb$ versus $^{206}Pb/^{204}Pb$ plots, the same four distinct groups successively plot on or about the Lachlan Orogen crustal growth curve. The Cobar Basement and Cobar Basin Group 2 deposits both lie slightly above the Lachlan Orogen crustal growth curve whereas the Cobar Basin Group 1 deposits plot on or slightly below the growth curve. This suggests Cobar Basement and Cobar Basin Group 2 deposits have a common source reservoir which has a slightly higher μ value that that used to define the crustal growth curve, whilst Cobar Basin Group 1 deposits were derived from a reservoir with similar or slightly lower μ values than used to define the crustal growth curve.

Several samples from the Peak deposit, described by Lawrie and Hinman (1998) as including high-temperature pyrite, yielded significantly lower $^{206}Pb/^{204}Pb$ ratios than the bulk of the Peak deposit samples. Those samples plot nearer the Cobar Basement group. Similarly, samples from the Mrangelli prospect and McKinnons deposit, which are located in the centre and western part of the Cobar Basin respectively, have isotopic compositions equivalent to the Cobar Basement signature. Samples from the CSA (gossan samples) plot in the overlap between the Cobar Basin 1B and 2 groups. However, the gold-poor, base metal-rich nature of the CSA deposit suggests it is more likely grouped with Elura in the Cobar Basin 2 group.

The fourfold classification outlined herein is an expansion of the classification previously proposed by Suppel et al. (1990) and Dean (1991) and encapsulates the differences in isotopic signature between Cobar Basin deposits described by Lawrie and Hinman (1998). Jiang and Seccombe (2000) argued the distinction between the Cobar Basin groups proposed by Lawrie and Hinman (1998) is within the analytical error of the Pb isotope measurements. However, the consistent differences in isotopic composition (principally $^{206}Pb/^{204}Pb$ ratio) between the different mineralisation styles in the Cobar Basin appear meaningful and are clearly in excess of variations expected from analytical error (as indicated by error ellipses shown in Figure 190).

Lead isotope data from deposits located to the south of the main part of the Cobar Basin also match the groupings established herein for the Cobar deposits (Figure 191). The deposits, which include deposits located on the southern margin of the Cobar Basin (Nymagee and Shuttleton), within the Mt Hope Trough (Gilgunnia, May Day and Wagga Tank) and in the southern extension of the Canbelego-Mineral Hill trend (Mineral Hill), all yield lead isotopic compositions consistent with the Cobar Basin Group 1 deposits. The deposits all contain mixed gold-base metal mineralisation and are regarded as having had a similar genesis to Cobar-type deposits (Suppel & Gilligan; 1993).

Carr et al. (1995) recognised Cobar deposits have a similar isotopic signature to Silurian stratabound and VHMS deposits including the Woodlawn, Captains Flat, Currawang and Currawong deposits. In contrast, Devonian stratabound and VHMS deposits, which are predominantly from the Buchan Basin in eastern Victoria, typically have lower $^{207}Pb/^{204}Pb$ and $^{208}Pb/^{204}Pb$ ratios than the Cobar deposits. Siluro-Devonian intrusion-related mineralisation, including mineralisation associated with the Devonian Bega batholith and Early Devonian Boggy Plain Supersuite, have higher $^{206}Pb/^{204}Pb$ ratios and slightly lower $^{207}Pb/^{204}Pb$ and $^{208}Pb/^{204}Pb$ ratios than Cobar deposits (Carr et al., 1995) (Figure 192). Carr et al. (1995) suggest the Silurian stratabound and VHMS deposits are sourced from predominantly crustal rock-types, whereas the Devonian stratabound and VHMS deposits

and Siluro-Devonian and Permo-Carboniferous intrusion-related deposits are derived from a source comprising some rock-types containing lead with a mantle affinity. The latter deposits are also gold-bearing, whereas the Silurian stratabound and VHMS deposits contain little or no appreciable gold.

Figure 191: Lead isotope ratios of deposits from the southern part of the Canbelego-Mineral Hill Trend and Mt Hope Trough relative to Cobar deposits (all data from CSIRO database apart from data collected from the New Occidental and Perseverance deposits in this study).

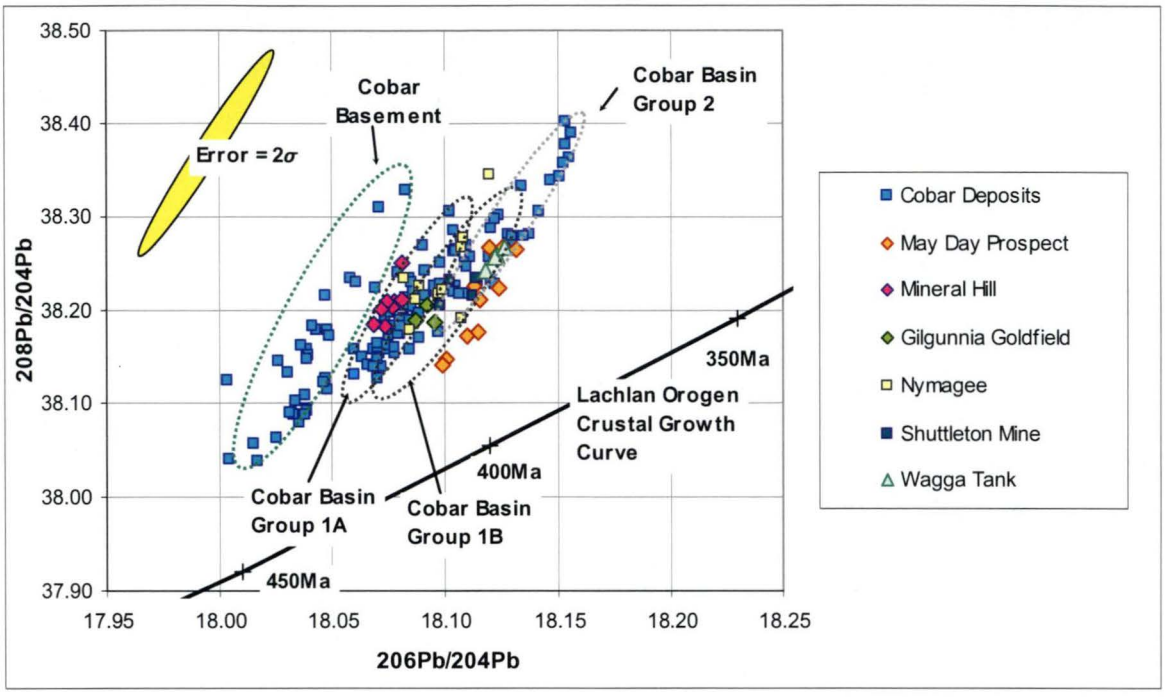

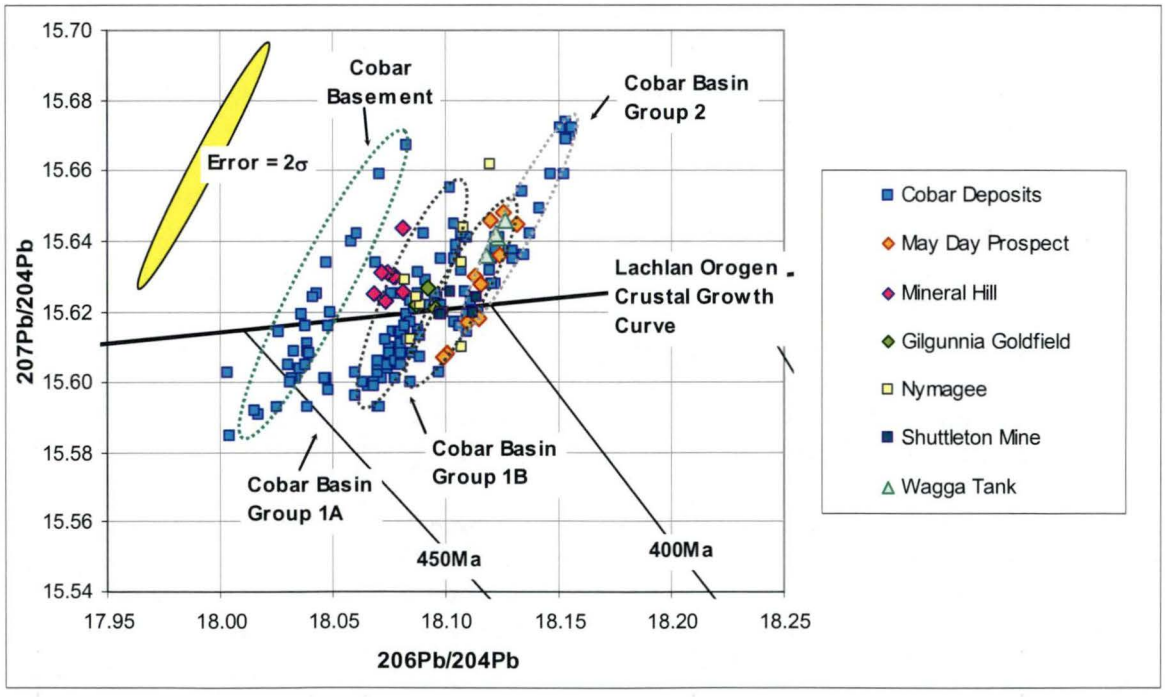

Figure 192: Lead isotope ratios of Lachlan Orogen deposits (modified after Carr et al., 1995).

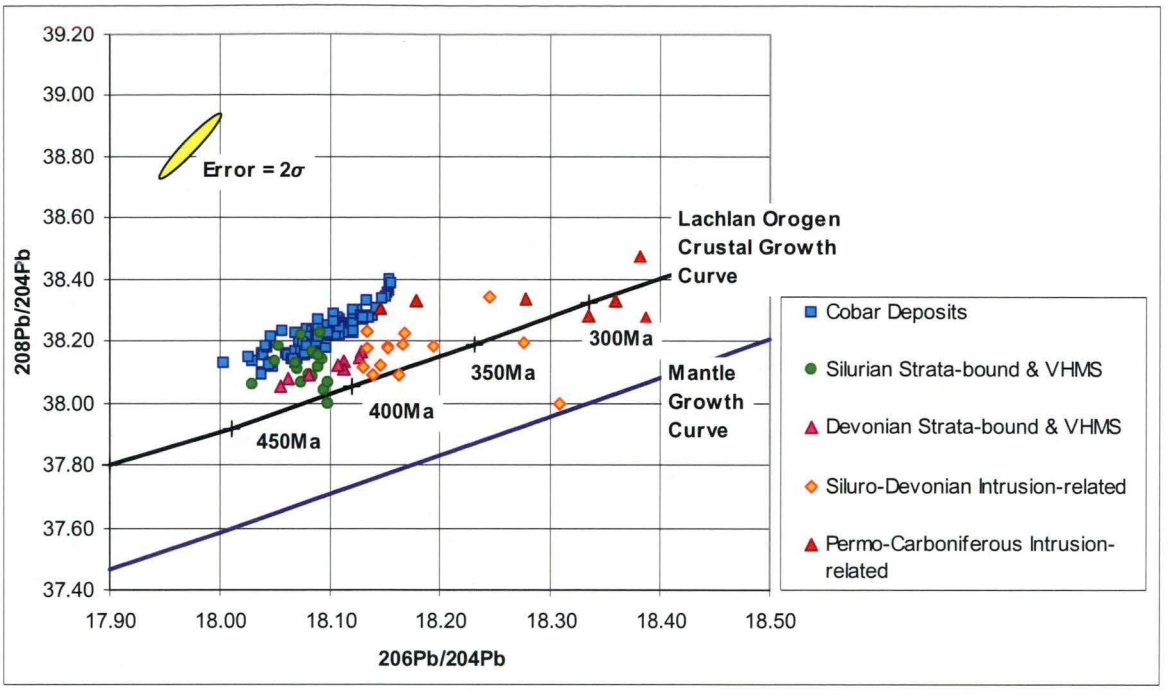

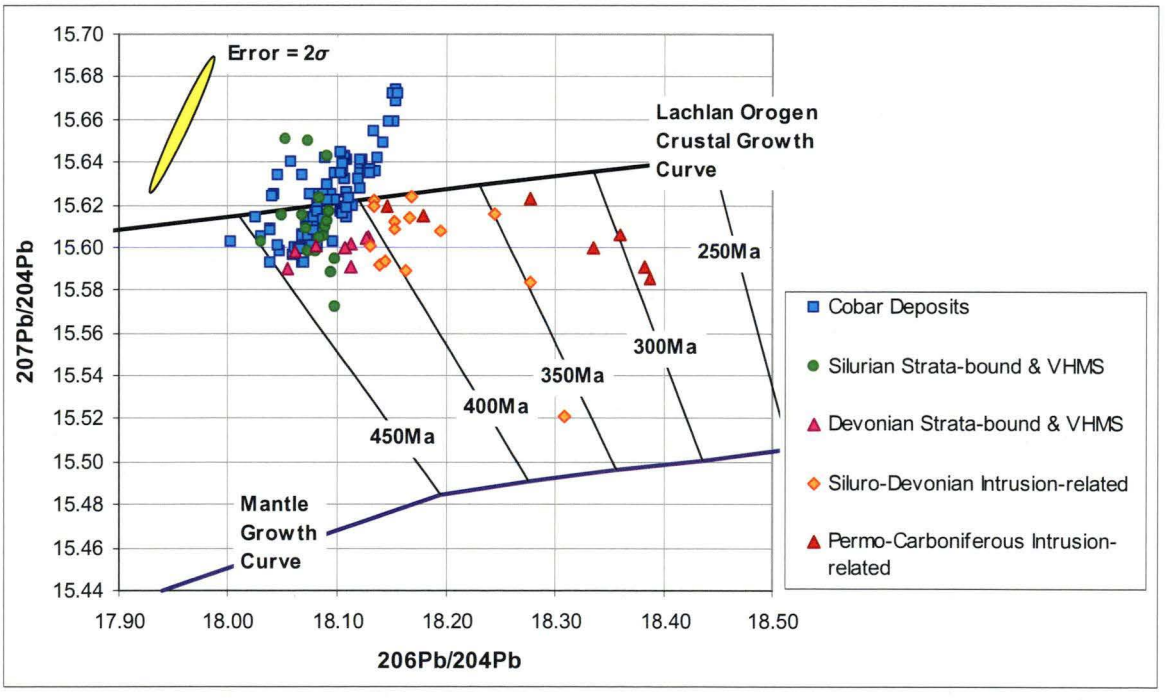

9.5.2 Source of Lead in Cobar Deposits

The relatively consistent patterns in lead isotopic signatures of deposits across the Lachlan Orogen, from Cobar Basin deposits in the northern part of the Central Belt to deposits in the Mt Hope Trough to the south, stratabound and VHMS deposits in the Eastern Belt of the Lachlan Orogen and I-type and S-type granitoids scattered throughout the Lachlan Orogen (Suppel et al., 1990; Dean, 1991), indicates a relatively homogenous reservoir that extended across the Lachlan Orogen (e.g. Carr et al., 1995). The only minor difference between the Cobar source-rock reservoir and that of the remainder of the eastern Lachlan

Orogen is that the Cobar source-rock reservoir appears to be characterised by slightly higher μ and ω values, that is, a more "crustal" signature, which could reflect the greater proportion of S-type granitoids and quartz-rich sedimentary rocks and relative paucity of mafic igneous rock-types in the Cobar reservoir compared to that of the remainder of the Lachlan Orogen.

The origin of subtle differences in lead isotopic signature of Cobar deposits (Section 9.5.1) has been a point of conjecture. Lawrie and Hinman (1998) proposed Cobar Basin Group 1 deposits formed by mixing of a basement-derived Cu-Au ore fluid with a lead isotope composition equivalent to the Cobar Basement deposits and a basin-derived Pb-Zn ore fluid with a lead isotope composition equivalent to the Cobar Basin Group 2 deposits. This model fails to account for the lower μ value of Cobar Basin Group 1 deposits compared to the other two groupings and that the lead isotope signatures of individual Cobar Basin deposits are not consistent with the metal endowments of the different deposits. For example, the Peak deposit, which contains appreciable lead-zinc, has relatively low $^{206}Pb/^{204}Pb$ ratios whereas the coeval New Cobar deposit, which contains little or no lead-zinc and therefore is expected to have relatively low $^{206}Pb/^{204}Pb$ ratios, has the most radiogenic lead isotope signature of all of the Cobar Basin Group 1 deposits. Likewise, early-stage gold-galena-clausthalite in the New Occidental deposit is characterised by lower $^{206}Pb/^{204}Pb$ ratios than the late-stage galena - sphalerite, whereas the opposite would be expected based on the mixing model of Lawrie and Hinman (1998). Finally, the underlying premise of Lawrie and Hinman (1998), that Cobar deposits are Cu-Au-rich, Pb-Zn-rich or simple mixtures of the two, is incorrect. Deposits range from Cu-Pb-Zn-rich, Au-poor deposits (Queen Bee and CSA) to Cu-rich with minor Au (Great Cobar, Chesney, Gladstone and Wood Duck) to Au-Cu-rich (New Cobar and Perseverance) to Au-rich base metal-poor (New Occidental) to Au-Cu-Pb-Zn rich (Peak).

Alternatively, the variation in lead isotope signature of Cobar deposits may simply reflect differences in age of mineralisation, with the three groupings (Cobar Basement, Cobar Basin Group 1A/1B and Cobar Basin Group 2) yielding model ages of 430–440Ma, 420Ma, 410Ma and 380Ma respectively based on the Lachlan Orogen crustal growth curve (Figure 190). However, it is unlikely age differences are the sole cause of variations in isotopic composition of Cobar deposits. Age differences alone do not account for the apparently different μ values of the Cobar Basin Group 1 and Cobar Basement and Group 2 deposits, or the scatter in lead isotope ratios observed within individual deposits and between deposits of equivalent age, including the more radiogenic signature of early-stage galena-clausthalite compared to that of late-stage galena in the New Occidental deposit. Carr et al. (1995) also urged caution when using model ages derived from the Lachlan Orogen plumbo-tectonic model, citing a ±15 m.y. precision for model ages determined for Palaeozoic lead sources because of the contribution of local terrane compositional differences to data scatter. It is, however, possible Cobar Basin Group 2 deposits, including the Elura deposit, are younger than Cobar Basin Group 1 deposits, especially given independent $^{40}Ar/^{39}Ar$ ages for deformation and alteration assemblages in the Elura deposit of 376–389 Ma (Sun et al., 2000) compared to the 400 Ma age quoted for Group 1 deposits (Glen et al., 1992).

Another possible explanation of variation in lead isotope signatures of Cobar deposits is differences in host-rock composition. Suppel et al. (1990) and Dean (1991) demonstrated isotopic signatures of Cobar deposits can in part be sub-divided by host-rock and their sub-division can be extended to define host-rock associations for the three Cobar deposit groupings:

1. **Cobar Basement** - hosted in Ordovician-Silurian sedimentary rocks and granitoids or in relatively thin sequences of Cobar Basin-equivalent strata underlain by more extensive sequences of Ordovician-Silurian sedimentary rocks and granitoids.

2. **Cobar Basin Group 1** - hosted in the lowermost unit of the Cobar Basin sedimentary sequence (Nurri Group), which has a provenance comprising largely Ordovician-Silurian sedimentary rocks and granitoids exposed to the east and north of the Cobar Basin (Glen, 1985).

3. **Cobar Basin Group 2** - hosted in the uppermost unit of the Cobar Basin sedimentary sequence (Amphitheatre Group) which was sourced from predominantly quartz-rich sedimentary rock-types exposed to the west and northwest of the Cobar Basin (Glen, 1985).

Implicit in this proposed grouping of Cobar deposits is the assumption the various host-rocks in the Cobar area have different Pb isotope signatures, which has not yet been determined. Secondly, it assumes the lead isotope signature of deposits in the Canbelego-Mineral Hill trend is inherited from the underlying basement strata and not the immediate host-rock sequence, which is time-equivalent to Cobar Basin strata. Other contradictory evidence includes both the CSA and Queen Bee deposits yielding Cobar Basin Group 1 lead isotopic signatures even though both deposits are hosted in lower Amphitheatre Group (CSA Siltstone) and could reasonably be expected to yield Cobar Basin Group 2 signatures, and the dissimilar μ values for Cobar Basement and Cobar Basin Group 1 deposits, even though host rocks for the Cobar Basin Group 1 deposits are sourced from Ordovician-Silurian sedimentary rocks and granitoids in the Cobar Basement (Glen, 1985).

Jiang (1996) argued lead in the Peak deposit could not have been derived from the host-rocks, including the Peak Rhyolite, Nurri Group and underlying Girilambone Group. However, there are a number of questions surrounding the quality of data presented by Jiang, including issues of significant ^{206}Pb addition from the decay of ^{238}U and incoherent groupings that do not demonstrate any consistent relationship to the Lachlan Orogen crustal or mantle growth curves (Figure 193), including samples of the same rock-type that have been subjected to different sample preparation techniques designed to remove hydrothermal lead (which is likely to represent the bulk of lead in the strongly altered Peak Rhyolite). Such data is also at odds with the isotopic signature determined for stratiform pyrite from near the Peak deposit in this study (Figure 193). Although the samples of Peak pyrite contain appreciable ^{206}Pb addition from the decay of ^{238}U, they have similar $^{207}Pb/^{204}Pb$ ratios to Cobar deposits. Assuming the Pb isotope signature of the stratiform pyrite is representative of the isotopic composition of host Nurri Group strata, Cobar Basin and basement strata could indeed have contributed Pb to Cobar deposits.

Jiang & Seccombe (2000) and Sun & Seccombe (2000) proposed lead in Cobar deposits was remobilised from pre-Cobar Basin granitoids by saline hydrothermal fluids capable of transporting high levels of Pb and that the resultant mineralisation preserved the original isotopic signature of the source granitoids. Their model implies there has not been any further isotopic fractionation during remobilisation or addition of lead from other compositionally distinct sources. Much of their argument is based on a 420 Ma model age derived for the Peak and Elura deposits using the Cumming and Richards (1975) growth curve, which is equivalent to the age of granitoids within basement flanking the Cobar Basin (Glen et al., 1983; Lawrie & Hinman, 1998) but is much older than independent ages of mineralisation in the Peak (400 Ma) and Elura (370–390 Ma) deposits (Section 2.7). Such conclusions are difficult to sustain given Carr et al. (1995) have demonstrated model

ages derived for Lachlan Orogen deposits using the Cumming and Richards (1975) growth curve differ by ± 16–35 m.y. from independent K-Ar and $^{40}Ar/^{39}Ar$ age dates. Clearly, the Cumming and Richards growth curve is not sufficiently precise to distinguish between a 420 Ma and 400 Ma age for lead in Cobar deposits. Secondly, the Peak and Elura deposits do not have identical Pb-isotopic signatures, as would be expected had they shared a common source. Finally, there is no evidence basement granitoids contain elevated concentrations of lead. The lead isotopic signature of Silurian granitoids in the Cobar basement has not been determined, although similar I- and S-type granitoids in the Lachlan Orogen have crustal isotopic compositions (e.g. Carr et al., 1995).

Figure 193: Lead isotope ratios of Cobar deposit host rocks (data from Jiang, 1996) compared to Cobar deposit data (CSIRO database + this study) and Peak stratiform pyrite (this study).

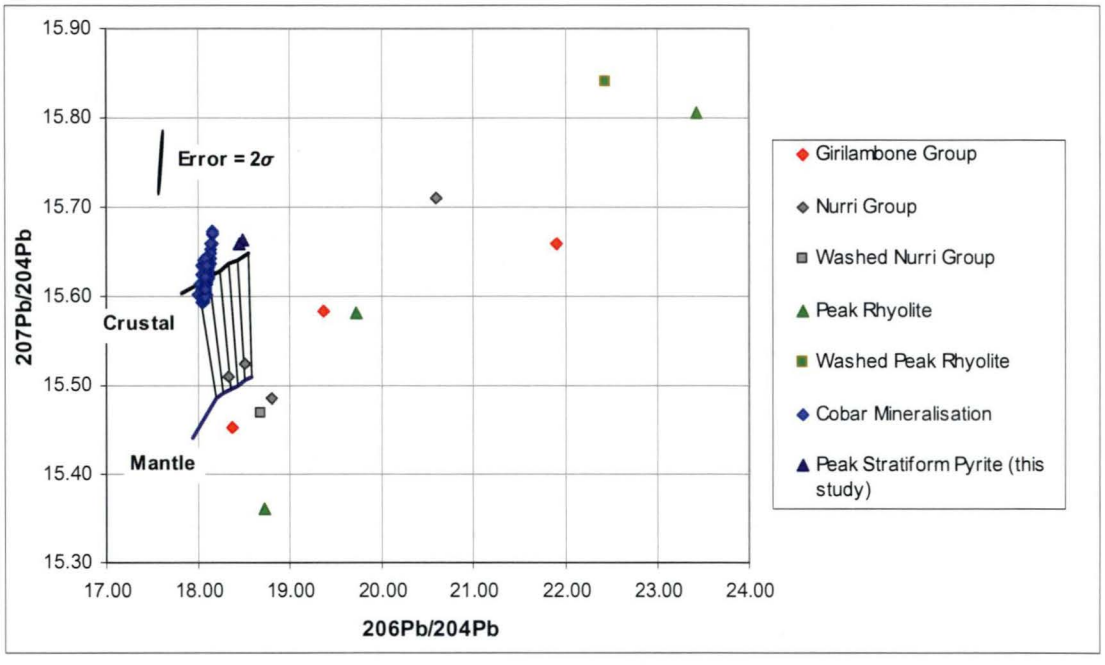

Based on the data presented herein, lead in Cobar deposits was largely derived from a large-scale, relatively homogenous Palaeozoic crustal lead reservoir that extended across the Lachlan Orogen (e.g. Carr et al., 1995). The subtle variations in lead isotope signature identified between the different groupings of Cobar deposits cannot be explained entirely by age differences or differences in host rock composition. Rather, the variations must reflect subtle differences in metal source(s). Based on the composite mixing model developed by Carr et al. (1995) to explain variations in lead isotopic composition of Lachlan Orogen deposits, variations in lead isotopic composition of Cobar deposits are herein explained in terms of differences in age of deposit formation (compositional variations parallel the Lachlan Orogen crustal growth curve) and mixing with mantle-derived lead (compositional variations parallel to Lachlan Orogen mixing isochrons) (Figure 194). Cobar Basement and Cobar Group 2 deposits appear to share a common lead source, based on their similar μ and ω values (herein the Cobar Crustal growth curve). However, Cobar Basement deposits plot on or about the 430 Ma Lachlan Orogen mixing isochron, whereas Cobar Basin Group 2 deposits plot on a 390 Ma mixing isochron (Figure 194). As noted previously, a younger age for Cobar Basin Group 2 deposits is consistent with independent $^{40}Ar/^{39}Ar$ ages for deformation and alteration assemblages in the Elura deposit of 376–389 Ma (Sun et al., 2000). The source reservoir for Cobar Basin Group 1 deposits is characterised by lower $^{207}Pb/^{204}Pb$ ratios and exhibits a weaker "crustal" signature, suggesting these deposits may have contained a small component of mantle-derived lead. A Pb-model age of 410–420Ma is estimated for Cobar Basin Group 1

deposits (Figure 194), which suggests the deposits are marginally younger than Cobar Basement deposits, although the age difference between the two deposit groups is within the accuracy indicated by Carr et al. (1995) for Pb-model ages estimated from the Lachlan Orogen growth curves. Glen (1991) and Glen et al. (1992) argue Cobar Basement and Cobar Basin Group 1 deposits formed during the same period of deformation and metamorphism. Therefore, Cobar Basin Group 1 deposits are considered to be of a similar of slightly younger age than Cobar Basement deposits.

Figure 194: Interpretation of Cobar lead isotope signatures.

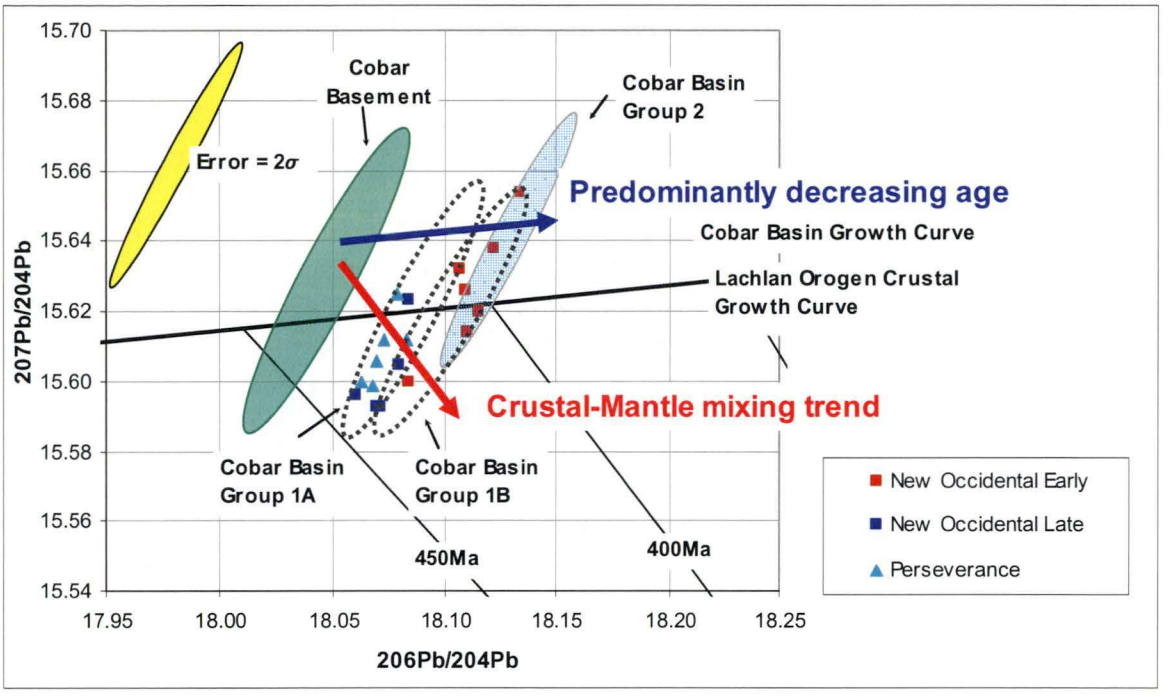

Carr et al. (1995) noted the Au-rich Silurian-Devonian VHMS deposits in the Lachlan Orogen are often characterised by lower $^{207}Pb/^{204}Pb$ ratios, which they attribute to a mantle metal source. This mantle input may reflect reworking of mantle lead contained in Ordovician mafic volcanics and intrusions (e.g. sources of mantle lead in Northparkes deposits; Carr et al., 1995) localised in basement beneath the Cobar Basin or, alternatively, that the hydrothermal systems responsible for Cobar Basin Group 1 deposits tapped deeper crustal levels compared to the systems that formed Cobar Basement and Cobar Basin Group 2 deposits.

Lead isotopes also offer a means by which potentially gold-bearing base metal deposits in the Cobar Basin can be distinguished from base metal-only deposits. Deposits with lead isotope compositions that plot within the Cobar Basin Group 1 fields on or below the Lachlan Orogen Growth Curve on $^{207}Pb/^{204}Pb$ versus $^{206}Pb/^{204}Pb$ plots (e.g. Figure 190) are more likely to be gold-bearing, whereas deposits characterised by higher $^{207}Pb/^{204}Pb$ values (plotting above the Lachlan Orogen Growth Curve) are more likely to be base metal-rich.

9.5.3 Significance of Lead Isotope Model Ages for Cobar Deposits

Whilst the Pb isotope model age for mineralisation in the Cobar Goldfield based on the Lachlan Orogen Crustal growth curve is relatively imprecise, it does provide sufficient resolution to suggest the age of Cobar mineralisation is more likely to be in the 395–405 Ma range proposed by Glen et al. (1992), rather than the younger 385–389 Ma range

proposed by Sun et al. (2000), although Elura is potentially younger than the deposits in the Cobar Goldfield. Likewise, the lead isotope data for Cobar deposits indicates mineralisation in the various Cobar Basin Group 1 deposits is of a similar age. In the case of the Peak deposit, the model age of Cobar deposits is clearly at odds with the 362 ± 25 Ma whole-rock Rb-Sr isochron age Jiang (1996) determined for the Peak Rhyolite and, by inference, his Carboniferous age inferred for the Peak deposit. Similarly, there is no evidence late-stage Pb-Zn-black chlorite in the Peak deposit is appreciably younger than the early-stage Pb in the deposit, as proposed by Perkins et al., (1994).

9.6 Sulfur Isotopic Composition of the New Occidental Deposit

9.6.1 Results of Sulfur Isotope Analyses

Laser ablation microprobe analyses of sulfide minerals from the New Occidental deposit (Table 45) demonstrate acceptable laboratory precision with replicate analyses typically within a relatively tight range of 0.5‰ to 2‰. The variation may in part be due to fine-grained inclusions of other sulfide phases within analysed sulfide grains. Carbonate was a minor problem in some of the samples whilst galena-bearing samples in a number of instances yielded relatively small quantities of SO_2.

Ore sulfides in the New Occidental deposit have a relatively wide range of $\delta^{34}S$ values (+4.2‰ to +11.4‰; mean ± 1 SD: 9.4 ± 1.7‰). Individual sulfide minerals in the deposit have different compositional ranges (Table 46); with chalcopyrite and sphalerite showing the widest variation in $\delta^{34}S$ values. The order of ^{34}S enrichment in sulfide minerals from the New Occidental deposit is sphalerite/pyrrhotite > chalcopyrite > pyrite > galena. This does not conform to the general ^{34}S enrichment pattern of pyrite > sphalerite/pyrrhotite > chalcopyrite > galena (e.g. Rye and Ohmoto, 1974), indicating sulfide minerals in the New Occidental deposit are not in isotopic equilibrium. Co-existing sulfide pairs, sphalerite-galena and pyrrhotite-galena, yield unreasonable formation temperature estimates (Table 47) using the fractionation factors developed by Ohmoto & Rye (1979), providing further indication the sulfide minerals are not in isotopic equilibrium.

Disseminated sulfides (pyrrhotite and pyrite) in the footwall of the New Occidental deposit have distinctly heavier $\delta^{34}S$ values (+16.4‰ to +18.6‰; mean ± 1 SD: 17.2 ± 0.9‰) than orebody sulfides (Table 46).

Table 45: Sulfur isotope analyses for samples from the New Occidental deposit and for pyrite-pyrrhotite samples from the Peak deposit environs.

Sample No.	Point No.	Chalcopyrite $\delta^{34}S$ w.r.t. CDT	Galena $\delta^{34}S$ w.r.t. CDT	Sphalerite $\delta^{34}S$ w.r.t. CDT	Pyrite $\delta^{34}S$ w.r.t. CDT	Pyrrhotite $\delta^{34}S$ w.r.t. CDT
N01F-1167.5	1					+10.10
	2					+8.50
N01F-1203.8	1	+7.64				+7.95
	2	+9.56				+9 28
	3	+8 60				
NO3B-798.3	1			+9 91		+10 2
	2			+12.83		
NO3C-823.7	1	+9 19				+9.99
	2	+11 54				+11.01
NO3C-852.0	1					+9 36
	2					+9 53
N03C-859.4	1				+7.87	
	2				+9.70	
	3				+8 21	
N03C-865.5	1		+7.75			
	2		+8.56			
	3		+6.75			
N03C-870 9	1		+7.99			
	2		+8.48			
	3		+8.80			
N03C-872 7	1			+10 48		
	2		+7.76	+11 10		
	3			+11 08		
NO3C-872 9	1	+10.73				+10.22
	2	+10.79				+10.73
NO3C-902.4	1	+10.95				+10.88
	2	+11.26				+11.23
	3					+13.61
NO3C-920 1	1	+9.53				+9.66
	2	+10.51				+9.79
NO3C-930 0	1	+10.6				+10.09
	2	+11.02				
N04F-376.7	1	+4.16				
	2	+4.98				
	3	+6.33				
N04F-449.4	1					+16.57
	2					+16.65
	3					+17.00
N04F-459.0	1				+18.42	+16.79
	2				+18.60	+16.40
N012-672 4	1 & 2		+5.64#			
N012A-732.6	1	+10 77**				+11.08
	2	+10.38**				+9 41
	3	+8 09				+9.06
NO14E-1017.1	1	+9.97	+8.91	+7 28		
	2	+10.17	+9.17	+8.46		
PK64-451.7 (Peak)	1				+10.13	+9.31
	2				+9.66	+10.36

* Insufficient SO_2 yield for analysis

SO_2 yields from points 1 and 2 combined for analysis

** CO_2 separation

Table 46: $\delta^{34}S$ compositions of sulfide minerals in the New Occidental deposit

	Range $\delta^{34}S$ w.r.t. CDT	Mean $\delta^{34}S$ w.r.t. CDT	Standard Deviation $\delta^{34}S$ w.r.t. CDT
Chalcopyrite (ore)	+4.2 to +11.5‰	+9.4‰	2.1‰
Galena (ore)	+5.6 to +9.2‰	+8.0‰	1.1‰
Sphalerite (ore)	+7.3 to 12.8‰	+10.2‰	1.8‰
Pyrite (ore)	+7.9 to +10.1‰	+8.6‰	1.0‰
Pyrite (disseminated)	+18.4 to 18.6‰	18.5‰	0.1‰
Pyrrhotite (ore)	+8.0 to +13.6‰	+10.1‰	1.2‰
Pyrrhotite (disseminated)	+16.4 to +17.0‰	+16.7‰	0.2‰

Table 47: Sulfur Isotope Fractionation Temperatures from Mineral Pairs

Sample	Galena $\delta^{34}S$‰	Sphalerite/Pyrrhotite $\delta^{34}S$‰	Pyrite $\delta^{34}S$‰	$\Delta_{mineral\ pairs}$ ‰	Temperature °C
N03C-872.7	8.01	11.09		3.08	212
N04F-459.0		16.60	18.51	1.91	124

Samples of orebody sulfides (mainly chalcopyrite and pyrrhotite) from a traverse across the New Occidental deposit were analysed in order to determine whether sulfur in the deposit was in part derived from isotopically heavier sulfur in host Cobar Basin sediments. However, they do not exhibit heavier $\delta^{34}S$ values on the margins of the deposit (Figure 195). In fact, no systematic variation in $\delta^{34}S$ values is evident either across the deposit or up/down dip. Likewise, $\delta^{34}S$ values do not vary between the different ore mineral stages; Stage 5 chalcopyrite - pyrrhotite, Stage 6 galena - sphalerite - pyrrhotite and Stage 7 pyrite have similar isotopic compositions.

Figure 195: Distribution of $\delta^{34}S$ values in the New Occidental deposit.

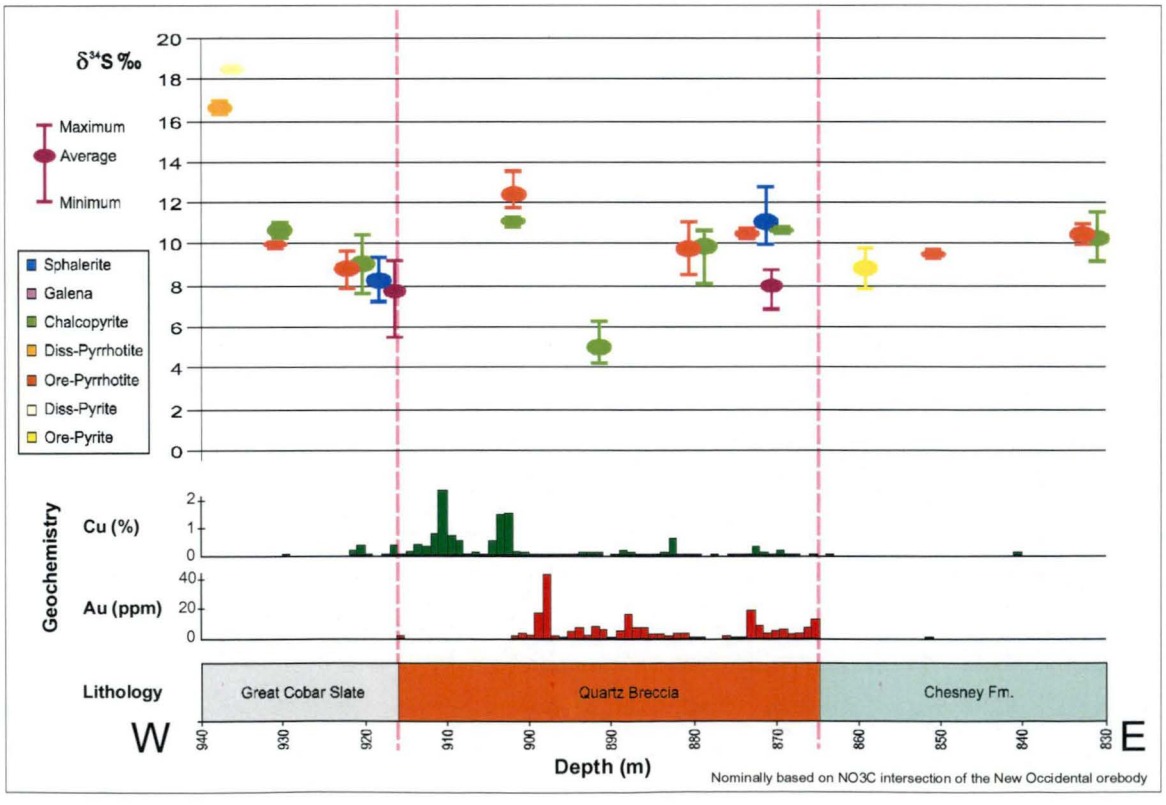

9.6.2 Comparison with Sulfur Isotopes from other Cobar deposits and Lachlan Orogen VHMS deposits

The sulfur isotope signature of the New Occidental deposit (mean ± 1 SD: 9.4 ± 1.7‰) is very similar to the signature of other Cobar deposits for which comprehensive sulfur isotope data exists, including the Peak (7.1 ± 1.4‰), CSA (7.5 ± 0.8‰), Elura (8.1 ± 2.0‰) and McKinnons (10.4 ± 1.3‰) deposits. The McKinnons deposit is compositionally closer to the New Occidental deposit than either the Peak or CSA deposits (Figure 196).

Figure 196: Comparison of the overall variation in $\delta^{34}S$ values for selected Cobar deposits.

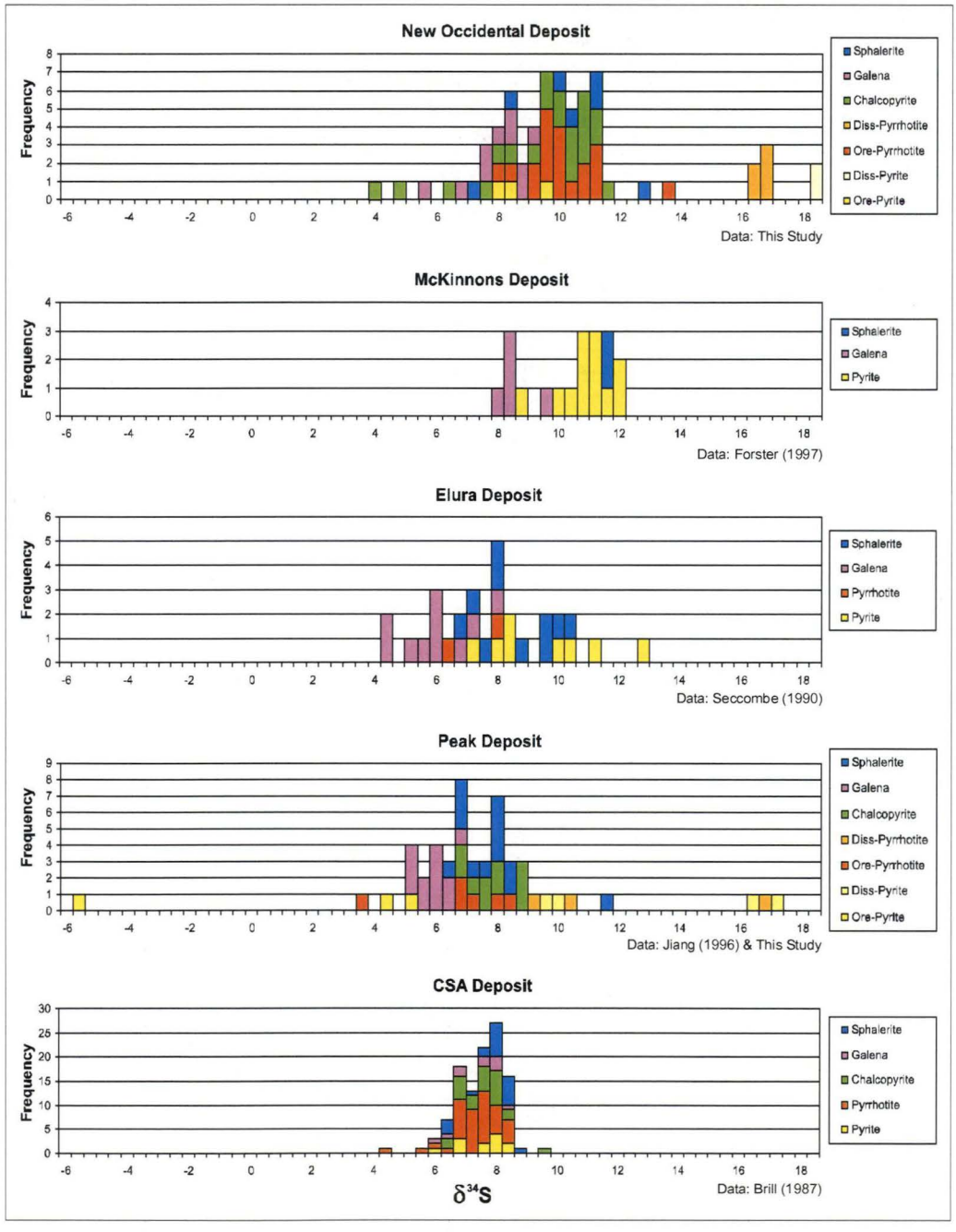

The New Occidental deposit also yielded $\delta^{34}S$ values broadly similar to those Cobar deposits for which only limited $\delta^{34}S$ values are available, including the Great Cobar, New Cobar, Chesney, Mount Pleasant and Queen Bee deposits (Figure 185). Enriched $\delta^{34}S$ values determined for disseminated stratiform pyrite and coexisting but overprinting cleavage-parallel pyrrhotite peripheral to the New Occidental deposit are similar to $\delta^{34}S$

values (+16.3 to +20.1‰) obtained by Jiang et al. (1995) and Sun & Seccombe (1998) for sedimentary pyrite/pyrrhotite in the Peak and Elura deposits respectively.

Silurian VHMS deposits in the Eastern Belt of the Lachlan Orogen possess very similar isotopic compositions to those of the Cobar deposits, including Woodlawn (7.4 ± 2.3‰), Captain's Flat (8.4 ± 0.9‰), Sunny Corner (7.4 ± 2.7‰) and Hill End Trough (6.4 ± 5.5‰) deposits (Ayres et al., 1979; Stanton & Rafter, 1966; Seccombe et al., 1984; Downes & Seccombe, 2004 respectively).

Figure 197: Comparison of $\delta^{34}S$ values for Lachlan Orogen VHMS deposits.

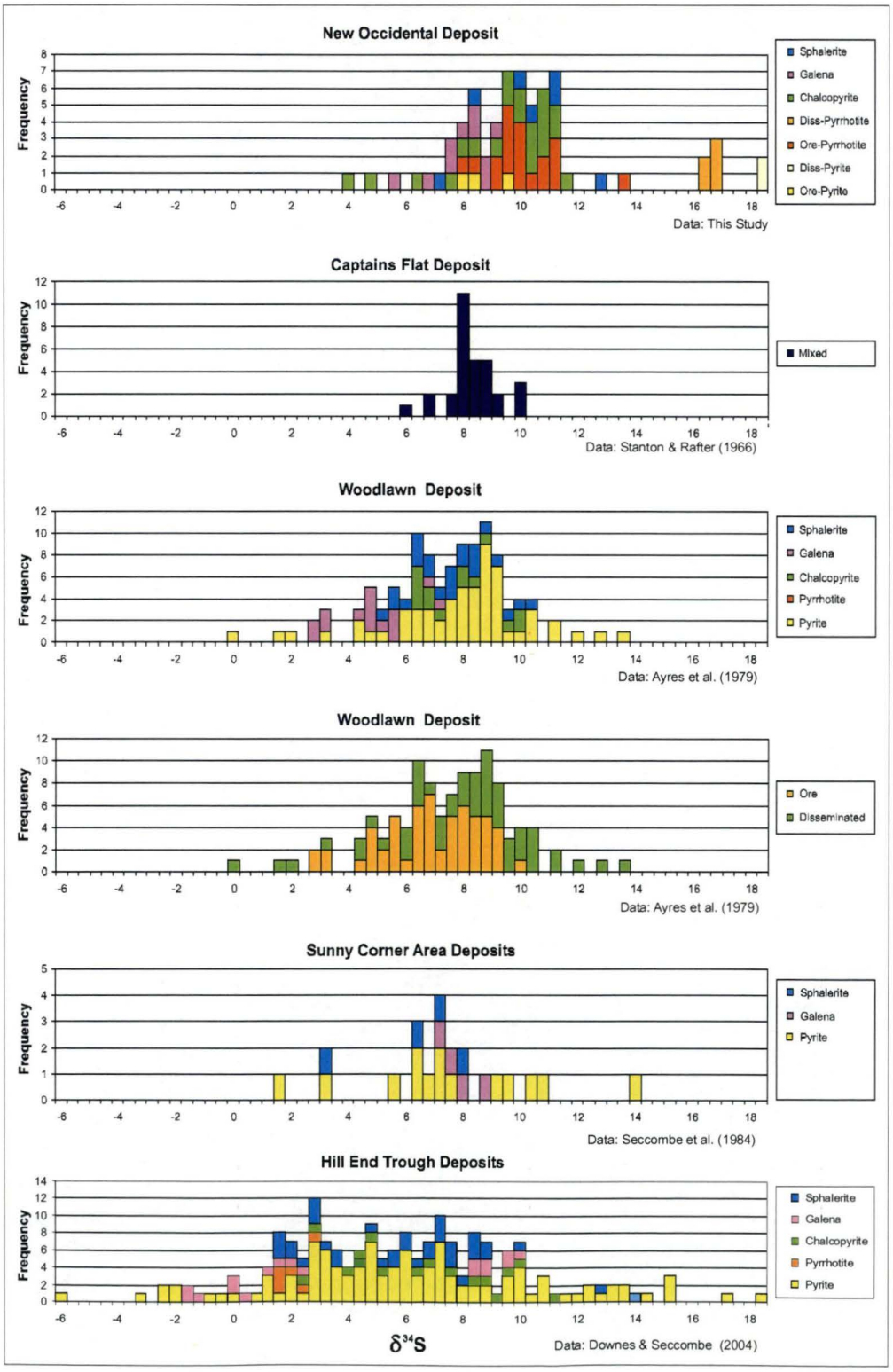

9.7 Sulfur Isotope Systematics

9.7.1 Source of Sulfur in Cobar Basin Sediments

Stratiform disseminated syngenetic pyrite and overprinting cleavage-parallel disseminated pyrrhotite in Cobar Basin sediments peripheral to several New Occidental deposits (New Occidental deposit: this study; Peak deposit: Jiang et al., 1995; Elura deposit: Sun & Seccombe, 1998) have consistently isotopically heavier $\delta^{34}S$ values than orebody sulfides, suggesting sulfur in the stratiform pyrite/metamorphic pyrrhotite has a different origin to sulfur in orebody sulfides. Enriched $\delta^{34}S$ values determined for disseminated pyrite and coexisting pyrrhotite are broadly similar to the $\delta^{34}S$ value of Late Silurian - Early Devonian seawater sulfate (approximately 20‰; Claypool et al., 1980), suggesting sulfide sulfur was derived from reduction of coeval seawater sulfate. Potential mechanisms include biogenic (e.g. Ohmoto and Rye, 1979; Jiang et al. 1995) or inorganic closed-system reduction of seawater sulfate (e.g. Claypool et al., 1980; Jiang et al., 1995; Cross et al., 2004). Alternatively, sulfate-bearing fluids were organically reduced as a consequence of circulating through organic-rich sedimentary sequences at elevated temperatures (e.g. Ohmoto and Rye, 1979)

Biogenic or inorganic closed system reduction of Devonian seawater sulfate most likely produces a spread of $\delta^{34}S$ values that range from slightly to strongly negative (Ohmoto and Rye, 1979; Jiang et al., 1995). The relatively narrow and consistent range of $\delta^{34}S$ values for disseminated pyrite/pyrrhotite at the three different Cobar deposits and the small difference between the $\delta^{34}S$ values of those sulfides and coeval seawater sulfate appears to preclude both processes.

Eastoe & Gustin (1996) regarded the period from the Late Cambrian to Devonian as being characterised by widespread marine anoxia, with anoxia most probable in restricted basins of limited size. The deepwater Cobar Basin potentially satisfies those criteria, being both small and isolated within the broader tectonic framework of the Palaeozoic Lachlan Orogen (Scheibner, 1976; Glen, 1990). However, the presence of pyrite in Cobar Basin shales indicates sulfate was present in the overlying water column (e.g. Eastoe & Gustin, 1996) and that the Cobar Basin was not anoxic.

Organic reduction of sulfate-bearing fluids as they circulate through organic-rich (methane-bearing) sedimentary sequences at elevated temperatures (>100°C) can produce sulfides with essentially the same $\delta^{34}S$ values of sulfates in the parent strata or fluid (Ohmoto & Rye, 1979). Cobar Basin sediments have been metamorphosed to lower greenschist facies not long after deposition (Brill, 1988b; Glen et al., 1992) and methane and other hydrocarbons have been shown to be a common constituent in hydrothermal fluids associated with mineralisation (Lawrie & Hinman, 1998; Lawrie et al., 1999; this study).

Jiang et al. (1995a) claimed metamorphism of sedimentary sulfides ($\delta^{34}S$ values of +16.3‰ to +17.2‰) at the Peak deposit was associated with significant isotopic fractionation, producing metamorphic pyrite/pyrrhotite with significantly lower $\delta^{34}S$ values of the order -4.7‰ to +5.9‰. Jiang et al.'s (1995a) classification of pyrite/pyrrhotite as sedimentary, metamorphic or hydrothermal appears somewhat arbitrary, especially given the widespread hydrothermal alteration surrounding the Peak deposit. For example, fine-grained pyrite and pyrrhotite on cleavage planes on the margins of the Peak deposit, which they interpret to be of a metamorphic origin, could equally be part of the Peak deposit and of hydrothermal origin. Furthermore, if the single negative $\delta^{34}S$ value in Jiang et al.'s (1995a)

metamorphic pyrite/pyrrhotite grouping is ignored, the remaining $\delta^{34}S$ values are in the range +3.6‰ to +7.4‰, which is equivalent to $\delta^{34}S$ values of orebody sulfides.

Rye and Ohmoto (1974) concluded the original isotopic composition of large-scale sulfur distributions is generally preserved during metamorphism, arguing metamorphism causes only minor changes in sulfur isotope systematics. For example, the stratigraphic variation in $\delta^{34}S$ values throughout the Woodlawn deposit, which has been metamorphosed to greenschist facies, indicates there has not been any large-scale re-equilibration of sulfur isotope composition during to metamorphism of that deposit (Ayres et al., 1979).

The most likely source of sulfur in Cobar Basin sediments is coeval Devonian seawater sulfate. Organic reduction of the sulfate, probably during diagenesis or the early stages of deformation of the sedimentary sequence, produced pyrite with similar $\delta^{34}S$ values to the precursor sulfate. Subsequent metamorphism of the early-stage pyrite produced pyrrhotite with a very similar $\delta^{34}S$ value to that of the original pyrite. Pyrite and pyrrhotite with much lower $\delta^{34}S$ values are most likely part of the hydrothermal sulfide halo surrounding the various deposits.

9.7.2 Source of Sulfur in Cobar Deposits

The consistent $\delta^{34}S$ composition of Cobar deposits, including across or up and down the deposits, between lodes/lenses, or between different stages of mineralisation, and the similarity to $\delta^{34}S$ values of Silurian-Devonian VHMS deposits, suggests a common homogenous sulfur source for Cobar deposits and/or common sulfur fractionation processes (e.g. Ohmoto & Rye, 1979). Potential sources of sulfur in Cobar deposits include:

1. Assimilation of sulfur from syngenetic or metamorphosed syngenetic sulfides in Cobar Basin sediments
2. Sulfur leached from homogenous source rocks other than Cobar Basin sediments and/or
3. Reduction of coeval seawater sulfate at elevated temperatures.

The systematic differences in sulfur isotope composition between orebody sulfides and syngenetic or metamorphosed syngenetic sulfides in the Cobar Basin indicate sulfur in orebody sulfides was not directly sourced from Cobar Basin sedimentary sulfides. Some mixing of the two types of sulfur seems likely given the extent and intensity of wallrock alteration haloes surrounding each of the Cobar deposits, although the absence of any systematic variation in $\delta^{34}S$ values in orebody sulfides from the footwall of the New Occidental deposit across the deposit into the hanging wall indicates such mixing has been minimal.

Lead isotope data infers metals in Cobar deposits were sourced from a relatively homogenous crustal lead reservoir (including S-type granitoids) containing a minor component of mantle-derived material most likely derived from Ordovician mafic igneous rock-types. However, the sulfur isotopic signature of Cobar deposits is inconsistent with derivation of a significant component of orebody sulfur from such igneous rock-types given they would contribute sulfur with a $\delta^{34}S$ value of 0 ± 3‰ (Ohmoto & Rye, 1979), which is substantially lower than the average $\delta^{34}S$ value of sulfides in Cobar deposits; e.g., granitoid-related gold mineralisation in the Lucky Draw deposit in the Eastern Lachlan Orogen yield $\delta^{34}S$ values of -2 – 0‰ (McQueen & Perkins, 1995). Therefore, whilst a

component of orebody sulfur derived from leaching of sulfides in igneous rock-types cannot be precluded, its contribution is likely to be minor. Similarly, based on the typical range of $\delta^{34}S$ values for sedimentary sulfides (Ohmoto & Rye, 1979), sulfur in Cobar deposits is also unlikely to be sourced from basement-derived sedimentary sulfides (sedimentary sulfides in Cobar Basin strata having already been precluded).

It is more likely the bulk of sulfur in Cobar deposits was derived from contemporaneous seawater. Sangster (1968), Large (1992) and Eastoe & Gustin (1996) highlighted $\delta^{34}S$ values of VHMS deposits around the world vary with time in a parallel fashion to the $\delta^{34}S$ values of contemporaneous seawater, indicating the sulfur isotope composition of seawater sulfate exerts a major control on the sulfur isotope composition of that deposit type. This is consistent with studies of Lachlan Orogen VHMS deposits (Ayres et al., 1979; Stanton & Rafter, 1966; Seccombe et al., 1984; Downes & Seccombe, 2004), which concluded orebody sulfur in those deposits was largely derived from seawater sulfate that was partially reduced at relatively high temperatures of the order of 300°C, or directly from a mixture of seawater sulfate and lighter sulfur derived from a volcanic source. For example, Downes & Seccombe (2004) measured $\delta^{34}S$ values predominantly in the range 23.4–30.6‰ for barite in Hill End Trough deposits, which they argued is equivalent to interpreted composition of seawater sulfate during Late Silurian to earliest Devonian times.

A number of processes produce significant isotopic fractionation and modification of the isotopic signature of seawater sulfur (Rye & Ohmoto, 1974; Ohmoto & Rye, 1979; Eastoe & Guston, 1996), including:

1. The mechanism by which seawater sulfate is reduced, including by biogenic, organic or inorganic reduction in closed or open systems
2. The temperature of seawater sulfate reduction, which determines fractionation between sulfate and reduced sulfur species
3. The degree of mixing of seawater sulfur with other sulfur sources as the ore-fluid leaches sulfur-bearing minerals in the rock mass through which it is circulating
4. The temperature, pH and f_{O_2} of the hydrothermal fluid during mineral precipitation, which determine isotopic fractionations between the ore fluid and hydrothermal minerals and between the various sulfur-bearing minerals
5. The extent to which hydrothermal mineral deposition is associated with replacement of pre-existing hydrothermal minerals
6. Whether isotopic equilibrium is maintained during mineral formation.

The most important of those processes is the mechanism of seawater sulfate reduction, which can result in $\delta^{34}S$ values for reduced sulfur species that are 0–60‰ lower than the $\delta^{34}S$ value of seawater sulfate (Ohmoto & Rye, 1979). Based on a sulfur isotope composition of Cobar hydrothermal fluids of the order of 8–11‰, sulfate reduction produced a negative fractionation of approximately 10‰, based on a $\delta^{34}S$ value of Devonian seawater sulfate of 20‰. Biogenic reduction and closed system inorganic reduction typically produces large negative fractionations (>20–25‰), whilst organic reduction produces negligible fractionation (Ohmoto and Rye, 1979), thereby eliminating those mechanisms as the prime method of sulfate reduction. The range of $\delta^{34}S$ values of the orebody sulfides are, however, consistent with the bulk of the orebody sulfur being

derived from partial inorganic reduction of seawater sulfate at relatively high temperatures as it circulated through the upper crust. If it assumed the hydrothermal fluid was initially H_2S-rich, then $\delta^{34}S_{fluid} = \delta^{34}S_{H_2S}$ and an apparent fractionation of -10‰ between sulfates and H_2S equates to a temperature of reduction of >400°C (using the equilibrium isotope fractionation factors of Ohmoto and Rye, 1979). Such temperatures are consistent with independent fluid inclusion temperatures of formation derived for a number of Cobar deposits, including the New Occidental deposit (this study).

Under ore-forming temperatures of >400°C, where H_2S and SO_2 are considered to be the dominant sulfur-bearing species, $\delta^{34}S_{minerals}$ can potentially deviate considerably from $\delta^{34}S_{fluid}$ in response to changes in the temperature, *pH* and f_{O_2} of the hydrothermal fluid, especially when the redox state of the hydrothermal fluid is near the SO_4^{2-}/ H_2S boundary (Ohmoto & Rye, 1979). As a consequence, Ohmoto and Rye suggested sulfide minerals formed in equilibrium with magnetite and/or haematite can have $\delta^{34}S$ values much lower than $\delta^{34}S_{fluid}$. With respect to the New Occidental deposit, sulfide minerals analysed in this study were deposited much later in the paragenetic sequence than magnetite from a hydrothermal fluid that was H_2S-rich and remained so during all stages of sulfide mineral deposition. As a result, $\delta^{34}S_{H_2S}$ is unlikely to have changed in response to decreasing temperature such that $\delta^{34}S_{H_2S} = \delta^{34}S_{fluid}$.

Finally, significant sulfur isotope fractionation does not appear to have taken place during sulfide deposition in the Cobar deposits. Isotopic fractionation temperatures for co-existing sulfide mineral pairs from the New Occidental deposit indicate sulfur isotope disequilibria within the deposit (Table 47). Sulfur isotopic disequilibria are apparent at most of the Cobar deposits (Brill, 1988a; Jiang et al., 1995a, b; Forster, 1997) except Elura (Seccombe, 1990; Sun & Seccombe, 1998). Isotopic disequilibria between the sulfide minerals in the New Occidental deposit and in other Cobar deposits most likely reflects the rapid rate of hydrothermal mineral precipitation in those deposits (e.g. Rye & Ohmoto, 1974; Ohmoto & Rye, 1979).

In conclusion, the sulfur isotope composition of the New Occidental deposit and of other Cobar deposits is interpreted to reflect inorganic reduction of contemporaneous seawater sulfate at elevated temperatures (>400°C) as seawater circulated through the crust. Whilst a component of igneous sulfur cannot be precluded, sourced either directly from contemporaneous magmatic activity or by leaching of sulfides in igneous rock-types, it is considered to have been a relatively minor component. Although a range of hydrothermal processes could have potentially modified the sulfur isotope signature of those deposits, it appears unlikely the sulfur isotope composition of the deposits has been significantly influenced by variations in the temperature, *pH* and/or f_{O_2} of the hydrothermal fluid. Furthermore, isotopic disequilibria during mineral deposition has also ensured $\delta^{34}S_{minerals} = \delta^{34}S_{fluid}$. It is possible the ore fluid has been locally contaminated with isotopically heavier sulfur derived from sedimentary sulfides in the country rock at the margins of the deposits. However, this effect appears to be insignificant.

10 A GENETIC MODEL FOR ORE FORMATION IN THE NEW OCCIDENTAL DEPOSIT: SOURCE, TRANSPORT AND PEPOSITIONAL PROCESSES

10.1 Introduction

Results documented in the previous chapters of this thesis raise the following questions about the genesis of the New Occidental deposit:

1. **What was the composition and source of hydrothermal fluid(s) that formed the New Occidental deposit?** Lead and sulfur isotopes and deposit geochemistry place a number of important constraints on metal and sulfur sources (Section 9.5.2 and 9.7.2 respectively), whilst the composition and temperature of the ore fluids inferred from alteration mineralogy, wholerock geochemistry and fluid inclusion studies also imply aspects of ore fluid provenance and metal complexing (Sections 5.7, 8.6 and 8.7 respectively).

2. **How were orebody components (metals + sulfur) transported from their interpreted sources to the site of deposit formation?** Possible transport mechanism(s) must be consistent with both the inferred source(s) of metals and sulfur and the structural controls on formation of the Cobar deposits (Chapter 3).

3. **What were the dominant controls on ore mineral deposition in the New Occidental deposit?** Triggers for ore mineral deposition identified so far include destabilisation of gold bisulfide complexes in response to phase separation initiated by rapid depressurisation of the hydrothermal fluid and mixing of hydrothermal fluids during fault-valve behaviour along the Great Chesney fault (Section 8.7). Other potential controls on metal deposition include hydrothermal fluid-wallrock interaction (e.g. Hinman, 1992), mixing of different fluid types (e.g. Lawrie & Hinman, 1998; Stegman, 2000), cooling of fluids (e.g. Hinman, 1992) and desulfidisation associated with sulfide mineral replacement of magnetite, chlorite and stilpnomelane (e.g. Stegman, 2000).

4. **How was early-stage gold in the New Occidental deposit remobilised during subsequent stages of base metal-rich ore mineralisation and what caused gold to become progressively more silver-rich with time?** The latter conflicts with the reported trend to higher fineness gold in the Peak deposit (Hinman, 1992).

5. **What caused metal zonation at the New Occidental deposit and could these processes explain district-scale metal zonation patterns at Cobar?** Metal zonation in Cobar deposits has been ascribed to differing degrees of mixing of basinal Pb-Zn rich fluids with basement-derived Cu-Au rich fluids (Lawrie & Hinman, 1998), differences in thrust geometry tapping different sources (Glen, 1991) and variations in temperature and depth of formation (Gilligan, 1974). Alternatively, metal zonation may reflect superposition of temporarily and genetically distinct stages of mineralisation (e.g. Perkins et al., 1994). However, these models do not adequately account for *all* of the observed variations within Cobar deposits, especially the presence or absence of gold (Section 2.8.3).

6. **What are the implications of this work for future exploration in the Cobar Basin?** The detailed quartz vein, alteration and ore mineral paragenesis identified at the New Occidental deposit, together with the results of geochemical, fluid inclusion and lead and sulfur isotope studies, allow metal and sulfur sources, transport mechanisms and depositional processes for Cobar deposits to be critically re-assessed. Understanding the mechanisms by which the New Occidental deposit formed not only unravels the cause(s) of metal zonation at the New Occidental deposit and potentially explains district-scale zonation in the Cobar Basin but also provides the focus for renewed exploration in the region.

10.2 Origin of Hydrothermal Fluids

10.2.1 Fluid Compositions and Evidence for a Second Hydrothermal Fluid

Fluid inclusion studies (Chapter 8), coupled with studies of deposit mineralogy and geochemistry (Chapters 5, 6 and 7), indicate the New Occidental hydrothermal fluid was moderate to high temperature (350–400°C) with fluid temperature only decreasing markedly in later stages of deposit formation corresponding to the galena - sphalerite - greenalite - Fe-clay - carbonate mineral assemblage. Fluid temperatures on the periphery of the deposit during deposition of Stage 4 quartz were up to 50–100°C lower than in the core of the deposit, that is, more typical of average greenschist metamorphic temperatures, indicating hydrothermal fluids were much hotter than deposit wallrocks and therefore were rapidly advected from much deeper structural levels during faulting. Fluids were characterised by near-neutral *pH* (chlorite-stable) and low salinities, although fluids associated with the main stage of base metal deposition (chalcopyrite-pyrrhotite-sericite assemblage) were slightly more saline and more acidic. Fluid sulfur fugacity (f_S) was low during the main stage of gold deposition but increased substantially during the latter stages of deposit formation coincident with the main stage of base metal deposition (Table 48).

The evolution in the composition of the New Occidental fluid identified in this study is interpreted to be the product of two over-lapping processes: hydrothermal fluid-wallrock interaction and introduction of a second compositionally distinct hydrothermal fluid in the latter stages of deposit formation. Fluid-wallrock interaction best explains the initial strong Fe-enrichment and K-Rb-Ba-depletion associated with Fe-chlorite alteration and white mica destruction in wallrock around the deposit and the subsequent and progressively stronger K-Na-Rb-Ba-Mg-enrichment associated with stilpnomelane and then Fe-Mg chlorite alteration in the middle stages of deposit formation (Section 7.5). However, the change in fluid composition between the main stage of gold deposition and later stage of base metal deposition does not appear to simply reflect progressive evolution of the New Occidental hydrothermal fluid as it interacted with host rocks. Rather, it is interpreted to reflect fundamental changes in the composition of the hydrothermal fluid. For example, sulfur isotope systematics indicate sulfur in the New Occidental deposit is not sourced from wallrock, as might be expected if the observed increases in sulfur fugacity were attributable to ongoing fluid-wallrock interaction, but has an external source. Likewise, increasing fluid salinity, decreasing fluid pH, change in trace element geochemistry and onset of sericite alteration cannot easily be explained by fluid-wallrock interaction, but rather point to the introduction of a second hydrothermal fluid. Ongoing interaction between the second fluid and wallrock, including previously deposited hydrothermal minerals (e.g. Fe-rich phyllosilicates) during the latter stages of hydrothermal activity in the New Occidental

deposit resulted in a return to deposition of chlorite and other Fe-Mg-rich silicate alteration minerals in the wall rocks at the expense of sericite. This change is also accompanied by an overall reduction in temperature of the hydrothermal fluid. Deposition of Mg-rich chlorite, and occasionally talc, with late-stage galena - sphalerite - pyrrhotite - pyrite in the base metal-rich Cobar deposits (especially the Peak, Great Cobar and CSA deposits) also suggest the second fluid was Mg-rich.

Table 48: Composition of the New Occidental hydrothermal fluid.

	Gold Stage (Early)	Base Metal Stage (Late)	Post-Mineralisation
Fluid Temperature	350–400°C	350–400°C reducing during Pb-Zn stage to 200–300°C	150–200°C
pH	Neutral	Slightly acidic	Neutral
Salinity	1–6 eq. wt.% NaCl	5–10 eq. wt.% NaCl	2–6 eq. wt.% NaCl
Composition	H_2O-CO_2-H_2S-minor CH_4	H_2O-CO_2-H_2S-minor CH_4	H_2O-minor CH_4
Chemistry	• Au-Bi-Se-Pb-W-As-Fe-Sb (minor Cu) • High Fe/(Fe+Mg) • Low f_S • Low X_{CO_2}	• Cu-Pb-Zn-Ag-Fe-Mo (minor Sn-In-Cd) • Lower Fe/(Fe+Mg) • Higher aK^+ • Higher f_S • Higher X_{CO_2}	
Mineral Assemblages	1. Magnetite-minor scheelite-wolframite-Fe-rich chlorite-calcite 2. Gold-maldonite-native bismuth-Se-rich ikunolite-clausthalite-galena-Fe-rich chlorite-minor pyrrhotite-chalcopyrite 3. Bismuthinite-"newoccidentallite"-gold-stilpnomelane-minor biotite 4. Arsenopyrite-Mg-rich iron chlorite	5. Chalcopyrite-pyrrhotite-minor electrum-cassiterite-sericite 6. Sphalerite-galena-pyrrhotite-greenalite-Fe-rich clay-calcite 7. Pyrite-Fe-rich clay	

10.2.2 Evidence for a Metamorphic Fluid Source

The New Occidental deposit is the product of significant fluid flow localised along the steeply dipping Great Chesney Fault during intense deformation and low-grade (greenschist facies) metamorphism of the eastern margin of the Cobar Basin. The interpreted architecture of the fault zone in relation to the basin margin (Figure 26) and fault-length-displacement scaling relations indicate the fault penetrates substantial distances into basement and was therefore capable of tapping fluids from deep beneath the Cobar Basin. Maximum fluid inclusion temperatures of 350–400°C recorded from the New Occidental deposit indicate hydrothermal fluids were potentially sourced from depths >12km (assuming a relatively high geothermal gradient of +30°C/km), significantly deeper than the inferred 5–7km depth of deposit formation and interpreted 5km pre-deformational thickness of basin sediments (Section 8.7). However, the fluid source may have been shallower if fluids were wholly or partially magmatically derived (e.g. exsolved from moderate- to high-level intrusions).

A number of previous studies concluded hydrothermal fluids associated with formation of Cobar deposits were at least in part magmatically derived (Jiang, 1996; Lawrie & Hinman,

1998), based largely on metal associations. However, there is no conclusive evidence of magmatic input to the New Occidental hydrothermal fluid or to fluids associated with formation of other Cobar deposits and, on balance of the evidence available, large-scale magmatic input appears unlikely. Intrusion-related gold deposits around the world are typically proximal to or located within the genetically related igneous intrusions and often zoned about those intrusions (Groves et al., 1998; Thompson et al., 1999). However, to date, no syn-mineralisation igneous rocks have been identified in the Cobar Basin. Felsic porphyries near the Queen Bee deposit and the intrusive rhyolite at the Peak deposit unequivocally pre-date deformation and mineralisation (Stegman, 1998; 2001a; Section 2.6.5). Rather, Cobar deposits exhibit an intimate association with fault zones and zones of deformation (Section 2.6.2). Fluid compositions are somewhat ambiguous. Groves et al. (1998), Sillitoe & Thompson (1998) and Thompson et al. (1999) have indicated magmatically derived fluids are generally moderate-strongly saline (>20 wt. % eq. NaCl) and acidic and do not contain appreciable CH_4, although they described a number of intrusion-related gold deposits from around the world that formed from low salinity CO_2-rich fluids (e.g. Yukon deposits, Alaska and Timbarra in New South Wales, Australia). Some of these gold deposits also exhibit trends to higher fluid salinities during deposit formation (similar to that observed in the New Occidental hydrothermal fluid), which Sillitoe & Thompson (1998) and Thompson et al. (1999) attributed to phase separation at deeper structural levels; the initial low-salinity CO_2-rich fluids represent the exsolved vapour phase and subsequent more saline aqueous fluids represent the residual liquid phase (Thompson et al., 1999). The sulfur isotope signature of Cobar deposits potentially precludes a magmatic input to hydrothermal fluids associated with formation of Cobar deposits, indicating at most only a very minor magmatic sulfur component (Section 9.7.2), although the source of deposit sulfur is not necessarily the same as other fluid components.

Abundance of base metals (Pb-Zn-Ag) in Cobar deposits, the hydrocarbon-rich nature of hydrothermal fluids (Lawrie & Hinman, 1998; Lawrie et al., 1999a,b) and the presence of carbonate replacement-style Pb-Zn mineralisation in carbonates beneath the Elura deposit (Leevers, 2000) and on the Winduck Shelf immediately west of the Cobar Basin has prompted many authors (e.g. Hinman, 1992; Gilligan & Byrnes, 1995; Lawrie & Hinman, 1998; Lawrie et al., 1999a, b; David, 2000) to conclude the bulk of Pb-Zn-Ag in Cobar deposits was sourced from basin sediments. However, this is at odds with the lead isotope systematics of Cobar deposits, which suggest a deeper crustal source for lead, and the relatively high temperature of hydrothermal fluids associated with formation of base metal sulfides in Cobar deposits (>300°C; Table 36). Although such formation temperatures are slightly lower than temperatures associated with earlier gold deposition, they are still substantially higher than the maximum temperatures expected based on the interpreted depth of deposit formation (e.g. 150–200°C assuming depth of formation of 5-7km and a geothermal gradient of 30°C/km; Section 8.7). The generally low salinity of fluid inclusions in Cobar deposits (<10 wt% NaCl equivalent) also appears inconsistent with involvement of basinal brines, although hydrothermal fluids in the base metal-rich Cobar deposits (Peak and Elura) are locally more saline (Jiang, 1996, Lawrie & Hinman, 1998; Sun & Seccombe, 2000; Table 36).

Spatial (fault-/shear-hosted) and temporal (syn-deformational/metamorphic) features of the New Occidental deposit (and other deposits at the eastern Cobar Basin margin) clearly favours a metamorphic fluid source. The inferred composition of New Occidental hydrothermal fluids is typical of metamorphic fluids associated with orogenic gold deposits (e.g. Ho et al., 1990; McCuaig & Kerrich, 1994; Eilu & Mikucki, 1998; Arne et al., 1999; Bierlain et al., 2000; Kerrich et al., 2000; Eilu et al., 2001 Ridley & Diamond, 2000), a conclusion already drawn in a number of previous studies of Cobar deposits (Glen, 1987;

de Roo, 1989; Jiang et al., 1995; Lawrie & Hinman, 1998; Solomon et al., 2000; Heinrich et al., 2000). Fluid compositions and temperatures indicate fluids were largely sourced from basement underlying the Cobar Basin, most likely from rocks undergoing amphibolite facies metamorphism at temperatures of 400–500°C. Lead isotope studies indicate the likely source of metals in the New Occidental deposit (and for Cobar deposits) is deeper crustal basement to the Cobar Basin, which is generally interpreted to be homogenous at the scale of the Lachlan Orogen (Section 9.5.2). Likewise, the large difference and abrupt transition between $\delta^{34}S$ values for orebody sulfides and syngenetic/diagenetic pyrite and metamorphic pyrrhotite in the footwall of the New Occidental deposit indicates a local (Cobar Basin) sulfur source in the deposit is unlikely. Rather, the consistent sulfur isotopic signature of Cobar deposits and Silurian-Devonian volcanic-hosted massive sulfide deposits in the eastern Lachlan Orogen indicates a common sulfur source for the deposits, which is interpreted to be contemporaneous late Silurian-Early Devonian seawater sulfate that has been inorganically reduced at elevated temperatures (300–400°C) as it circulated through the middle crust (Section 9.7).

10.2.3 Inferred Source Rock Composition

Immediate basement to the Cobar Basin is interpreted to consist of Cambro-Silurian quartz-rich metasediments and minor mafic metavolcanics of the Girilambone Group and extensive pre-Cobar Basin Silurian-Devonian S-type, lesser I-type granites and rare ultramafic intrusions (Gilligan & Byrnes, 1995). Basement to the Cobar Basin can reasonably be assumed to have a predominantly felsic igneous composition on the basis of:

1. A granitic provenance for Girilambone Group metasediments (Gilligan & Byrnes, 1995)
2. The western and southeastern flanks of the Cobar Basin contain areally extensive S-type granites (Glen, 1990). Granites along the western margin of the Cobar Basin form inliers in upper Cobar Supergroup sediments whereas granites to the southeast of the Cobar Basin have intruded Girilambone Group metasediments.
3. Lesser magnetite-bearing I-type granitoids (Wild Wave Granodiorite and other small un-named intrusives identified in mapping by Peak Gold Mines' geologists) are also present along the eastern margin of the Cobar Basin (Glen et al., 1983; PGM company data).
4. Sediments in the Cobar Basin have a quartz-rich continental or granitic provenance and basal basin sediments (Nurri Group) contain abundant granitic detritus (Glen, 1987a; 1994).
5. Detrital zircons in Cobar Basin sediments have similar age groupings to inherited and detrital zircons in granites and sedimentary rocks in the Eastern Lachlan Orogen, implying a similar ultimate provenance of all of these units (Perkins et al., 1994).
6. Southern parts of the Cobar Basin and the Rast and Mt Hope Troughs contain abundant felsic volcanics (Gilligan & Byrnes, 1995), interpreted to be derived from partial melting of basement granites and sediments. Felsic intrusives like the Peak Rhyolite contain zircons which have undergone prolonged recycling in the crust (U/Pb dates to 1500Ma; Perkins et al., 1994). Similarly complex zircons occur in the Queen Bee Porphyry (20km south of New Occidental deposit) (Mark Fanning pers. comm. 2001).

The geochemical signature of the New Occidental deposit, particularly its W-Bi-Sn-Mo endowment, support derivation of metals from a felsic igneous source rock, particularly as there is ample evidence of this association in felsic igneous rocks in the Lachlan Orogen. Alternatively, these elements could have been directly sourced from rocks similar to those that melted to form the granites. Numerous small W-Bi-Sn-Mo deposits are associated with Silurian S-type granitoids in the southern parts of the Central Lachlan Orogen (Gilligan & Byrnes, 1995) and minor Bi-Mo has also been identified in the nearby I-type Wild Wave Granodiorite (Peak Gold Mines data). Bismuth is also a common constituent of gold deposits in the Lachlan Orogen, including Cobar Basin deposits, deposits in the Mt Hope Trough and within the Canbelego-Mineral Hill trend (e.g. Cobar-Lucknow, Mineral Hill, Nymagee and Mt Hope deposits; McClatchie, 1973; Suppel & Gilligan, 1993; Gilligan & Byrnes, 1994) and deposits associated with Silurian, early Devonian and Carboniferous I-type granitoids in the Eastern Belt of the Lachlan Orogen (McClatchie, 1973) including the Lucky Draw deposit (Sheppard et al., 1995) and Major Creek deposit (McQueen & Perkins, 1995). The presence of elevated bismuth in deposits throughout the Lachlan Orogen is further evidence of a homogenous large-scale metal reservoir in the Lachlan Orogen during the Palaeozoic.

A minor component of mantle-derived Pb in early ore mineral stages in the New Occidental deposit is also inferred from lead isotope studies (Section 9.5.2). Although not widespread, mafic igneous rocks are a component of Cobar Basin basement and are inferred to be associated with formation of the Girilambone copper deposits to the east of the Cobar Basin (Gilligan & Byrnes, 1995). The widespread presence of CH_4 in the New Occidental deposit (and other more complex hydrocarbons in other Cobar deposits; Lawrie et al., 1999) suggests carbonaceous rock-types were also present in the basement.

10.2.4 Origin of Early-Stage Gold-Rich and Late-Stage Gold-Poor Base Metal-Rich Hydrothermal Fluids

A key unresolved aspect of New Occidental deposit formation is the relationship between early-stage gold-rich and late-stage gold-poor base metal-rich hydrothermal fluids in the deposit, and what the two fluids imply about fluid sources and transport processes. It is also unclear whether the two fluids represent separate fluid pulses of a single evolving fluid system or two (or more) unrelated fluid systems.

The similarity between inferred temperatures and composition of New Occidental hydrothermal fluids and hydrothermal fluids associated with orogenic gold deposits (e.g. Ho et al., 1990; McCuaig & Kerrich, 1994; Eilu & Mikucki, 1998; Mikucki, 1998; Arne et al., 1999; Bierlain et al., 2000; Kerrich et al., 2000; Ridley & Diamond, 2000; Eilu et al., 2001) provides a basis for analysing metal sources and transport mechanisms associated with formation of the New Occidental deposit. Gold is relatively soluble at temperatures of 400–500°C, equivalent to amphibolite facies metamorphic grades, is characterised by relatively high solubility (e.g., Mikucki, 1998; Bastakov et al., 2000). Accordingly, genesis under such conditions could readily account for the gold-rich nature of early-stage fluids associated with the New Occidental deposit.

Most studies have concluded gold (and silver) in orogenic gold deposits were transported as bisulfide complexes rather than as chloride complexes, with chloride complexes ($AuCl_2^-$) only becoming important at significantly higher temperatures and fluid salinities (Seward, 1973; Huston & Large, 1989; Benning & Seward; 1996; Benchekroun et al., 1996; Mikucki, 1998) or when reduced sulfur content of the fluid is very low and *pH* is higher (Gibert et al., 1998). Gibert et al. (1998) also argued bisulfide complexes ($AuHS^0$ and

$Au(HS)_2^-$) predominate over chloride compounds except where aH_2S is high at near neutral to acidic conditions. Most studies (Seward, 1973; Benning & Seward; 1996; Mikucki, 1998) concluded gold in orogenic deposits is predominantly transported as $Au(HS)_2^-$, whereas the $Au(HS)^0$ complex dominates at lower temperatures (<270°C) characteristic of epithermal deposits. In contrast, Gibert et al. (1998) concluded $AuHS^0$ is the dominant gold-bearing species under physiochemical conditions similar to those estimated for orogenic gold deposits (350–450°C, P = 500 bars, low salinity near-neutral *pH* fluids in chemical equilibrium with oxygen-sulfur buffers Py-Po-Mt or Py-Po-Hm and the quartz-K-feldspar-muscovite *pH* buffer).

Based on the interpreted fluid composition of the early-stage gold-rich New Occidental hydrothermal fluid and the corresponding predominance fields of the major gold-transporting ligands cited by Huston & Large (1989), Mikucki (1998) and Gibert et al. (1998) (Figure 198a–f), gold in the New Occidental fluid appears most likely to have been transported as bisulfide complexes, either $Au(HS)_2^-$ or $Au(HS)^0$. The Huston & Large (1989) predominance fields (Figure 198b) yield somewhat ambiguous results, due in part to the fact that these were constructed for slightly more acidic fluids (*pH* = 4) than inferred for the New Occidental fluids (*pH* = 5-6). Nonetheless, the predominance fields of Huston & Large (1989) and Micucki (1998) indicate the dominant gold bisulfide complex in early-stage New Occidental fluids was most likely $Au(HS)_2^-$, whereas those of Gibert et al. (1998) suggest it was $Au(HS)^0$. The fluid compositions inferred for the late-stage base metal-rich New Occidental fluids also plot within the predominance fields for bisulfide gold complexes (Figure 198a–f), although gold chloride complexes may have been important with higher salinity and aH_2S (e.g. Gibert et al., 1998). Compared to early-stage New Occidental fluids, late-stage fluids are characterised by higher gold solubilities (Figure 198e–f), which potentially explains why late-stage fluids readily remobilised early-stage gold in the deposit.

The minor amounts of base metals deposited with the early-stage gold in the New Occidental deposit indicate either low overall abundance of base metals in the early hydrothermal fluids and/or that base metal deposition was not triggered by processes leading to deposition of early-stage gold. Hydrothermal fluids with low base metal content suggest either that source rocks did not contain appreciable base metals and/or early-stage fluids were unable to transport them. The low salinity of the early-stage New Occidental hydrothermal fluids would have limited significant base metal transport (e.g. McCuaig and Kerrich, 1994; Eilu et al., 2001), with only minor base metals transported as bisulfide complexes and Bi transported as thio-hydroxy complexes (e.g. Wood et al., 1987; Törmänen and Koski, 2005). Wood et al. (1987) indicate the potential for Bi chloride complexing appears low.

The late-stage base metal-rich hydrothermal fluid identified at the New Occidental deposit had a slightly different origin to the earlier gold-rich fluid. The absence of gold and relative abundance of base metals in the late-stage fluid implies interaction with either (i) a gold-poor, base metal-rich source (i.e. different source to the one from which the early-stage fluid was derived) or (ii) the same or similar source region but that the late-stage fluid was unable to mobilise gold but could transport base metals. The later scenario could be a function of fluid composition, or indicate that most of the accessible gold in the source region was removed during the earlier fluid interaction. Components common to both early- and late-stage fluids in the New Occidental deposit (e.g. CO_2 and CH_4) and metals of felsic igneous association in both fluids (e.g. Bi-W in gold-rich fluids and Sn-In-Mo in late-stage base metal-rich fluids; Section 7.5.3) suggests potential interaction with a common source region.

Figure 198: Predominance fields for major gold complexes under a variety of physiochemical conditions, showing interpreted conditions under which the New Occidental deposit formed.

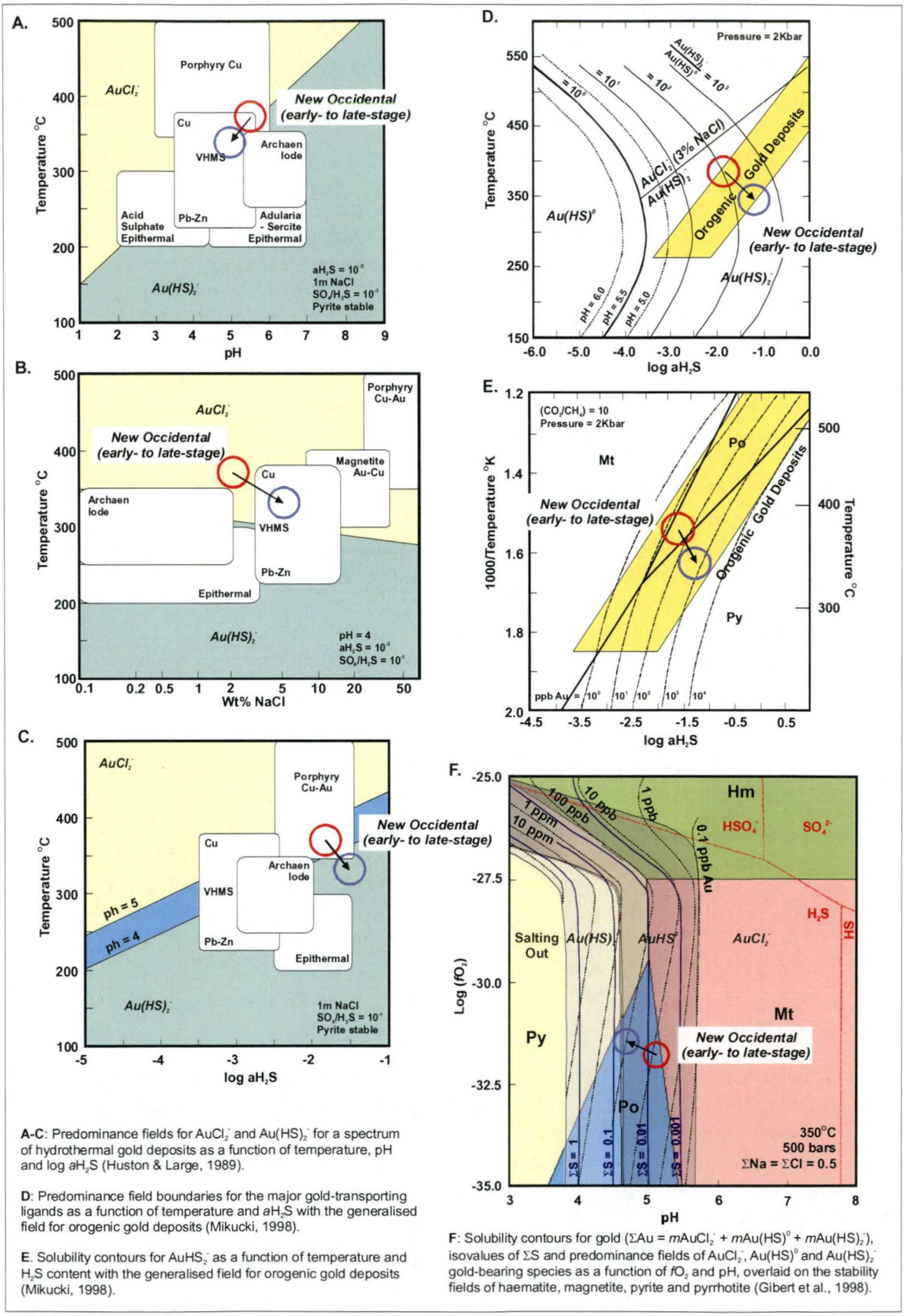

A-C: Predominance fields for $AuCl_2^-$ and $Au(HS)_2^-$ for a spectrum of hydrothermal gold deposits as a function of temperature, pH and log aH_2S (Huston & Large, 1989).

D: Predominance field boundaries for the major gold-transporting ligands as a function of temperature and aH_2S with the generalised field for orogenic gold deposits (Mikucki, 1998).

E. Solubility contours for $AuHS_2^-$ as a function of temperature and H_2S content with the generalised field for orogenic gold deposits (Mikucki, 1998).

F: Solubility contours for gold ($\Sigma Au = mAuCl_2^- + mAu(HS)^0 + mAu(HS)_2^-$), isovalues of ΣS and predominance fields of $AuCl_2^-$, $Au(HS)^0$ and $Au(HS)_2^-$ gold-bearing species as a function of fO_2 and pH, overlaid on the stability fields of haematite, magnetite, pyrite and pyrrhotite (Gibert et al., 1998).

Ore-metals associated with early-stage fluids in the New Occidental deposit (e.g. Au-Bi-As-W) are interpreted to have been mainly transported as bisulfide and other non-chloride complexes, whilst those associated with the late-stage fluids (e.g. Cu-Pb-Zn-Ag-Sn) were most likely transported as chloride complexes (e.g. Wood et al., 1987; Huston & Large 1989; McCuaig and Kerrich, 1994; Ridley & Diamond, 2000; Eilu et al., 2001). These differences in metal transport may be caused by:

- Increased fluid salinity, with higher salinities favouring transportation of base metals and some remobilised gold as chloride complexes (e.g. Huston & Large 1989; Eilu et al., 2001). The increased fluid salinity could reflect the influx of evolved (deeply circulated) seawater during the later stages of deposit formation (as argued based on S-isotopic data). This would also account for increased f_S from early- to late-stage fluids in the deposit.
- Phase separation in the deposit, similar to the process described by Thompson et al. (1999) in a number of intrusion-related gold deposits, with early-stage CO_2-rich low salinity fluids representing exsolved vapour-dominated fluids that preferentially moved up the Great Chesney Fault relative to the higher salinity aqueous liquid phase.
- Decreasing source region temperatures during deposit formation. The lower temperatures of late-stage fluids relative to early-stage fluids may indicate a lower temperature source, which favoured base metal transport instead of gold (e.g. Huston & Large, 1989; Large et al., 1989; Huston, 1998: Huston, 2000).

Localised remobilisation of earlier formed gold in the New Occidental deposit by late-stage fluids indicates late-stage fluids were most likely relatively under-saturated with respect to gold, consistent with the trend to higher gold solubilities (from early- to late-stage fluids) predicted from gold solubility curves of Mikucki (1998) and Gibert et al. (1998) (Figure 198e–f). Therefore, unless there was a pronounced increase in the solubility of gold during transport from source to site of deposition (not predicted by those gold solubility contours, Figure 198d–f), the general lack of gold in late-stage fluids suggests a gold-poor source. This may indicate that gold had already been mobilised from source rocks by the early-stage fluids or alternatively that a new source region did not contain appreciable accessible gold (e.g. lacked easily altered, mantle-derived mafic rock types). Lead isotope systematics indicate lead deposited from the second base metal-rich fluid had a stronger crustal signature (higher μ value) than lead associated with the initial gold-rich ore mineral stage, that is, there is no evidence of a mantle lead component in the late-stage galena.

Controls on the compositional differences between early-stage gold-rich and the late-stage base metal-rich hydrothermal fluids associated with New Occidental deposit formation cannot be conclusively resolved on the basis of evidence so far collected. Whilst at least a partial difference in metal sources is suggested by the subtle differences in Pb isotopic signature of lead-bearing minerals deposited from the respective fluids, other compositional similarities between the two fluids suggest differences may reflect either evolution or modification of a dominant fluid, interacting with similar crust, rather than to two (unrelated) fluid systems. Influx of reduced seawater during the latter stages of deposit formation, phase separation (producing a more NaCl-rich residual fluid) and/or decreasing temperature of fluid systems are all potential explanations for the differences in fluid types associated with formation of the New Occidental deposit. However, phase separation is unlikely to have been a major factor in the formation of the base metal-rich deposits in the Cobar Basin (e.g. Elura and CSA; Section 8.7). Firstly, fluid inclusion studies undertaken

at these deposits provide no evidence that phase separation occurred in these deposits and phase separation does not explain the trends to both substantially higher fluid salinities and sulfur fugacity (reflecting the H_2S content of the fluid) in those deposits. Similarly, differences in apparent formation temperatures for gold-rich and base metal-rich mineralisation stages do not appear large enough (Table 36) to solely account for the differences in fluid composition and metal content. They certainly do not explain increases in fluid salinity. In particular, the increasing salinity and f_S of New Occidental hydrothermal fluids from early- to late-stage appears to have played an important role in modifying the metal suite hydrothermal fluids both leached and transported.

10.3 An Integrated Fluid Flow Model

Isotopic evidence suggests the source of sulfur in the New Occidental and other Cobar deposits was coeval seawater circulated to at least mid-crustal levels (i.e. T > 300–400°C), whereas metals were sourced from the mid to lower crust at depths equivalent to amphibolite facies conditions (400–500°C). Both sulfur and metal sources indicate deposit formation was a function of large-scale fluid flow. Structural analysis of the New Occidental deposit (this study) and other Cobar deposits (Glen, 1991; this study), indicate the deposits formed during a period of intense deformation, concentrated at the eastern margin of the Cobar Basin and that fluid flow was intimately associated with fault development during basin deformation. Such circulation and chemical evolution of fluids has been proposed in a number of geological environments wherever hydraulic pressure gradients have been established, including in syntectonic (collisional or transpressive) metamorphic belts (Etheridge et al., 1983; 1984; Cox et al., 1986; Nesbitt et al., 1986; Nesbitt & Muehlenbachs, 1989; Bastrakov et al., 2000; Kerrich et al., 2000; Sibson, 2001; Craw & Campbell, 2004) and in rift and other extensional basins (Simms & Garven, 2004). The scale of fluid flow varies and depends on several factors including the spacing of faults, the hydraulic properties of the faults and basin sediments and intensity of deformation (Kerrich et al., 2000; Cox et al., 2001; Simms & Garven, 2004).

Many of the faults bounding and dissecting the Cobar Basin are herein interpreted to maintain their steep dips evident at surface, cutting across basin-basement contacts and penetrating substantial depths into basement (Section 3.9; c.f. the listric geometries of major faults within and bounding the Cobar Basin modelled by Glen, 1990; 1991; Glen et al., 1994). Some of the faults at the basin margin are interpreted to have been active during basin formation and, by definition, must originally have cut underlying basement. In the case of the Cobar Basin, the complex anastomosing network of steeply-dipping reverse faults along the eastern basin margin induced by basin deformation, including re-activated basin-forming faults (Figure 199; Structural Zone 1 of Glen, 1985) provide transient high permeability pathways, facilitating vertical fluid flow (e.g. Simms & Garven, 2004). The steep dipping faults, oriented at low angles to the maximum regional gradient in hydraulic head shorten the pathways between lower crust and surface environments and maximise potential flow rates.

The two hydrothermal fluids associated with the formation of the New Occidental deposit may in part represent evolution of a single fluid system, although two completely separate fluid systems using the same upper crustal fluid pathways (faults or high strain zones) cannot be ruled out. The early-stage gold-bearing fluid was most likely at least partly sourced from the base of the seismogenic zone under amphibolite facies conditions where solubility of gold is high (e.g. Mikucki, 1998). Such fluids were probably also under-saturated with gold in their source regions and, provided the fluids were effectively channelled and not extensively modified through fluid-wallrock interaction, would remain

under-saturated and be able to effectively transport gold from the source region to the site of deposition (e.g. Mikucki, 1998). The absence of appreciable sulfur in the early fluid suggests hydrothermal fluids initially did not contain a significant component of meteoric water, but were most likely derived from regional metamorphic dehydration reactions (e.g. Groves et al., 1987). The late-stage fluid exhibits many similarities to the early-stage fluid, although sulfur isotope systematics and inferred composition of late-stage fluids associated with base metal deposition suggest late-stage fluids contained a component of connate or meteoric water derived from Silurian-Devonian seawater, which increased the salinity, $a\mathrm{Mg}^{2+}$ and f_S of the hydrothermal fluid. As a result, the early hydrothermal fluid evolved from gold-bearing low salinity fluids to more saline gold-poor, base metal-bearing fluids as seawater was introduced into the fluid system.

The seawater was either trapped in sediments at the time of deposition and/or surface meteoric water drawn down during initial extension and formation of the Cobar Basin at around 400–420Ma (e.g. Kerrich, 1989) or during basin deformation (390–400Ma), driven by hydraulic fluid pressure gradients between contractional and dilational zones or by topographic effects (e.g. Guha et al., 1983; Sibson, 2001). The key question is how meteoric/connate water was drawn down to substantial depths (>10km assuming sulfate reduction occurred at 300–400°C)? It is possible extension during formation of the Cobar Basin triggered convective circulation beneath the Cobar Basin with draw down of meteoric water along basin-forming faults (e.g. Simms & Garven, 2004). Draw-down during Cobar Basin deformation is more problematic given clear evidence of up-flow along most, if not all, faults along the highly deformed *eastern margin* of the Cobar Basin (Structural Zone 1 of Glen, 1985). However, contemporaneous downflow may have occurred in the less-deformed areas such as along basin-bounding faults at the western margin of the Cobar Basin or along basement faults on the Kopyje Shelf to the east of the Cobar Basin. Alternatively, seawater may have been trapped by reverse (thrust) faulting during deformation of the eastern basin margin.

The build-up of supra-lithostatic fluid pressures in zones of more intense deformation along the eastern margin of the Cobar Basin and cyclic decompression of those hydrothermal fluids in response to slip on major faults like the Great Chesney Fault appears to have been the major driver of fluid flow. As previously shown (Section 4.4.8), conditions along the eastern margin of the Cobar Basin during D_1 basin deformation were ideal for fault-valve activity; the steeply-dipping major faults were extremely unfavourably oriented for slip with respect to the principal stress direction, no favourably oriented faults were present, and the Great Cobar Slate, which forms a stratigraphic top to many of the gold deposits, provided a relatively impermeable barrier to fluid flow. Prior to fault rupture, fluid pressures within the fault zone exceeded the fluid pressures in the adjacent country rock. As a consequence, hydrothermal fluids migrated out of the fault and into the adjacent wallrocks beneath the pressure seal (Great Cobar Slate). This process continued until rising fluid pressures in the wallrocks lead to the formation of sub-horizontal extensional hydraulic fractures. Immediately after fault slip and rupture of the seal, fluids migrated back into the fault zone, resulting in closure of the sub-horizontal fractures in the wallrocks with fluid flow focussed into dilational zones along the fault zone (e.g. Cox, 1995). Meteoric water in basement and basin sediments would have also been drawn into the fault at the same time under near-hydrostatic conditions (Kerrich, 1989). Resealing of the pressure seal in response to precipitation of hydrothermal minerals reduced fluid pressure along the fault and fault-normal compression reinitiated the fault-valve cycle (Sibson, et al., 1988; Fournier, 1999).

Figure 199: Idealised fluid convection during extension and inversion of the Cobar Basin.

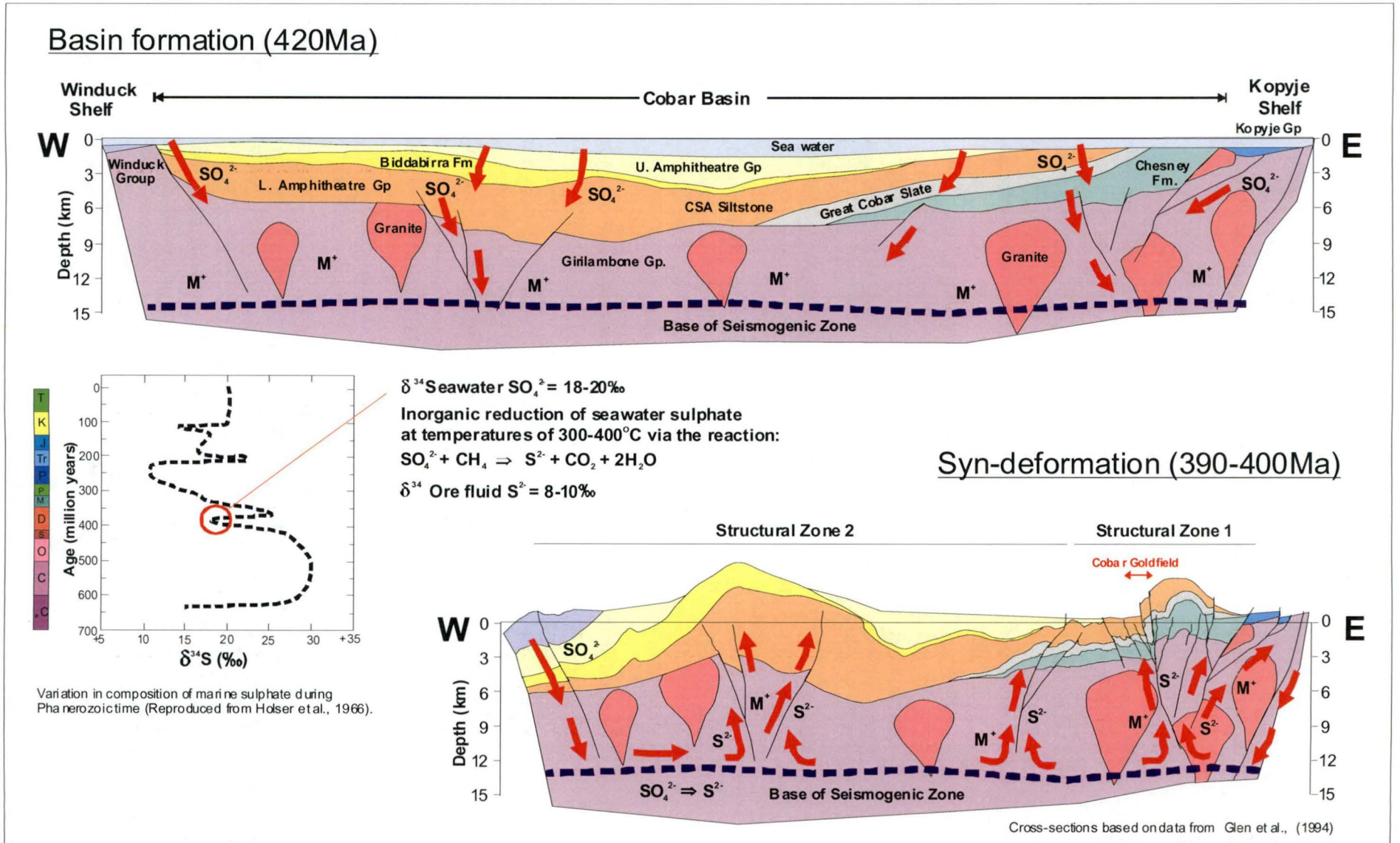

The influx of late-stage base metal-rich fluids in the New Occidental deposit corresponds to a change from dominantly brittle to more ductile deformation in the deposit. In part, this can be attributed to reduced fault-valve activity in the fault zone as a consequence of lower fluid pressures associated and decreasing intensity of deformation. Ongoing formation of sub-horizontal extensional veins during base metal deposition indicates fluid pressures continued to exceed σ_3 (= σ_v). However, the predominance of fibrous extensional veins and the absence of implosive breccia textures in those veins indicates incremental vein growth in a much lower fluid flux, lower strain-rate regime than had previously existed previously. Decreased strain rates and lower fluid fluxes are interpreted to have facilitated more ductile deformation resulting in less episodic and more continuous fluid flow (albeit at lower flow rates) along multiple shear zones and slip planes within the fault zone.

The predominance of deposits along the eastern margin of the Cobar Basin, compared to the western basin margin and the coeval Rast and Mt Hope Troughs to the south, potentially reflects source rocks with locally enhanced metal endowment (e.g. an increased portion of mantle-derived mafic volcanics in basement beneath the Cobar Basin). Alternatively and more likely, it indicates greater discharge of deeply-sourced (+ circulated) fluids, at the more intensely deformed eastern margin of the Cobar Basin. The greater depth-integrated permeability or connectivity to deeper fluid sources of faults in this area is also likely to have promoted more effective trapping of metals at the site of metal deposition by increasing the pressure, temperature and chemical disequilibria between source and site of deposition.

10.4 Controls on Metal Deposition

A range of mechanisms are potentially responsible for ore deposition and remobilisation within the New Occidental deposit including:

1. Phase separation associated with rapid depressurisation of the ore fluid during deposition of Stage 2–3 quartz in the early stages of deposit formation
2. Collection of gold in liquid bismuth during deposition of Stage 2–3 quartz (e.g. Douglas et al., 2000; Törmänen & Koski, 2005)
3. Mixing between two or more fluids, especially between meteoric water and early-stage gold-rich and the late-stage base metal-rich hydrothermal fluids
4. Fluid-rock interaction, including between ore fluids and wallrock and/or earlier formed alteration and ore minerals
5. Adiabatic or conductive cooling of ore fluids throughout the paragenetic sequence (e.g. Mikucki & Groves, 1990; McCuaig & Kerrich, 1994; Mikucki, 1998, Hagemann. & Lüders, 2003).

Gold deposition during the early stages of formation of the New Occidental deposit requires destabilisation of gold bisulfide complexes. Subsequent gold remobilisation and re-precipitation with late-stage chalcopyrite - pyrrhotite most likely indicates gold-bisulfide complexes reformed and were again destabilised, although gold-chloride complexes may have also been involved with formation of late-stage base metal mineralisation in response to increasing fluid salinity (Section 10.2). The late stage deposition of base metal sulfides requires breakdown of base metal chloride complexes. In the case of gold-bisulfide complexes, a reduction in sulfur fugacity (or aH_2S) of the hydrothermal fluid is likely the dominant control on gold precipitation, whereas increases in fluid pH, decreases in fluid temperature and oxidation of the fluid all destabilise gold-chloride complexes (Seward,

1973; Benning & Seward; 1996; McCuaig & Kerrich, 1994; Mikucki, 1998; Gibert et al., 1998). The key reactions governing gold deposition from bisulfide and chloride complexes are:

$AuHS^0 + ½H_{2\,(aq)} = Au_{(s)} + H_2S_{\,(aq)}$ (Gibert et al., 1998)

$Au(HS)_2^- + ½H_{2\,(aq)} = Au_{(s)} + H_2S_{\,(aq)} + HS^-$ (Mikucki & Groves, 1990)

$AuCl_2^- + ½H_{2\,(aq)} = Au_{(s)} + 2Cl^- + H^+$ (Mikucki & Groves, 1990)

The trend to increasingly sulfur-rich ore minerals through the New Occidental paragenetic sequence, from the initial stage of oxide minerals to native metals, low-sulfur selenides, pyrrhotite-bearing assemblages and a final pyrite-rich assemblage, indicates a progressive increase in S_2-H_2S fugacities in the New Occidental hydrothermal fluid (e.g. Titley & Beane, 1981; Large et al., 1989; Henley et al., 1992), rather than a change in the oxidation state of the hydrothermal fluids from oxidised to reduced (e.g. Sharpe and Gemmell, 2000). In simple terms, increasing aH_2S in the New Occidental hydrothermal fluid corresponds to an increase in gold bisulfide solubility throughout the paragenetic sequence, suggesting early-formed gold would have been relatively easily remobilised during successive stages of ore mineral deposition (Figure 200). This is corroborated by the presence of gold in subsequent ore mineral stages (e.g. Stage 3 gold - Bi_5AuS_4 – bismuthinite, Stage 4 arsenopyrite and Stage 5 silver-rich gold with late-stage chalcopyrite - pyrrhotite), only in those areas where subsequent ore mineral stages overprint gold-bearing Stage 2 quartz veins. Deposition of those stages of gold in the New Occidental deposit immediately after the periods of gold solubility therefore indicates localised reversals of that trend. Conversely, lack of appreciable gold associated with late-stage (Stage 6) galena – sphalerite and Stage 7 pyrite, even where these ore minerals directly overprint gold-bearing Stage 2 quartz veins, indicates the associated hydrothermal fluids were not capable of remobilising existing gold.

The intimate association of gold with Stage 2-3 colloform-banded cryptocrystalline quartz breccias and close correlation between increasing gold grade and intensity of quartz vein brecciation and colloform banding in Stage 2–3 quartz suggests phase separation is the most likely process to have triggered initial gold deposition in the New Occidental deposit. As has been shown previously (Sections 4.4.8 and 8.6.3), phase separation most likely occurred in response to catastrophic drops in fluid pressure associated with seismic faulting along the Great Chesney Fault. However, this may also have been caused by advective cooling of the hydrothermal fluid as it moved to higher crustal levels (Hagemann. & Lüders, 2003) or by expansion of the solvus due to mixing of the ore fluid with CH_4-rich fluids (e.g. Mikucki, 1998). Exsolution of H_2S and partitioning of that and other reduced gas phases to the vapour phase during phase separation reduced gold solubility in the remaining fluid (e.g. Mikucki & Groves, 1990; Mikucki, 1998; Mernagh & Bastrakov, 2000), which, in the case of the New Occidental deposit, is consistent with detection of H_2S in the gaseous phase of fluid inclusions (Section 8.5.1). The absence of associated sulfides indicates gold deposition in the early stages of deposit formation was unlikely to have been initiated by sulfidation of wallrock or alteration minerals. Similarly, fluid inclusions and alteration systematics indicate fluid composition was relatively homogenous during the early stages of deposit formation, indicating fluid mixing is unlikely to have been a depositional mechanism.

Figure 200: Solubility contours for Au complexes under a range of physiochemical conditions, overlaid on the stability fields of pyrrhotite, magnetite, haematite and pyrite.

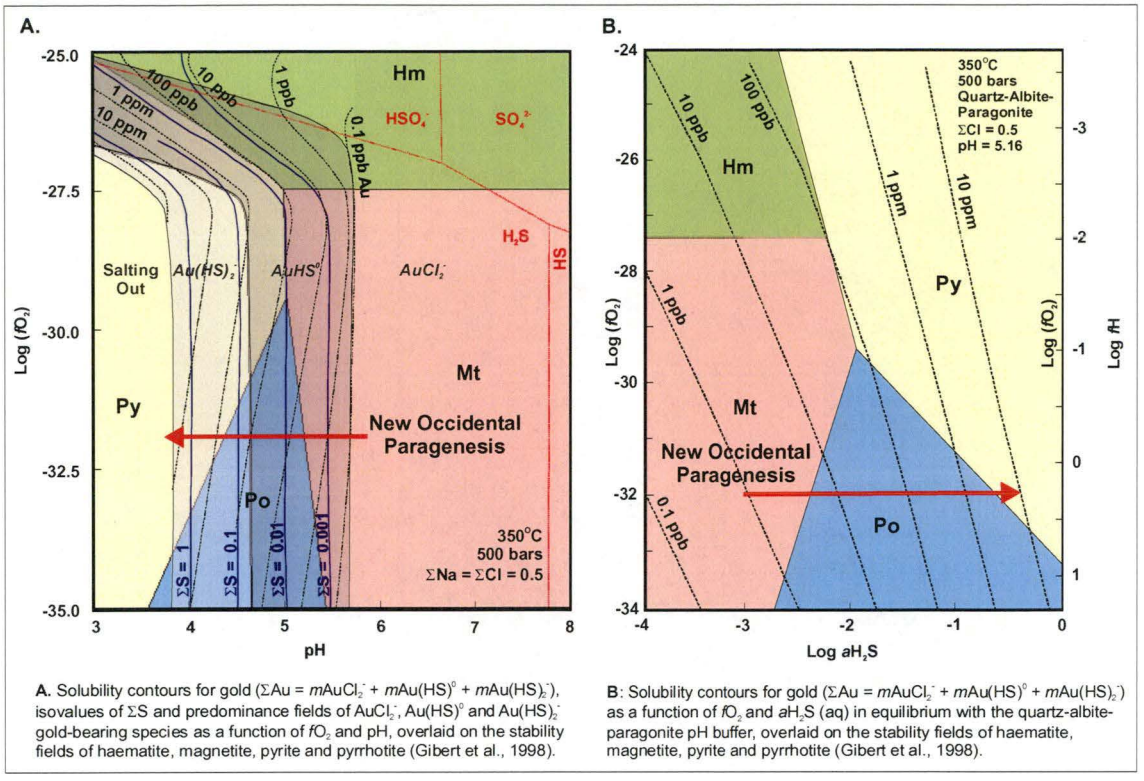

A. Solubility contours for gold ($\Sigma Au = mAuCl_2^- + mAu(HS)^0 + mAu(HS)_2^-$), isovalues of ΣS and predominance fields of $AuCl_2^-$, $Au(HS)^0$ and $Au(HS)_2^-$ gold-bearing species as a function of fO_2 and pH, overlaid on the stability fields of haematite, magnetite, pyrite and pyrrhotite (Gibert et al., 1998).

B: Solubility contours for gold ($\Sigma Au = mAuCl_2^- + mAu(HS)^0 + mAu(HS)_2^-$) as a function of fO_2 and aH_2S (aq) in equilibrium with the quartz-albite-paragonite pH buffer, overlaid on the stability fields of haematite, magnetite, pyrite and pyrrhotite (Gibert et al., 1998).

Another probable mechanism for deposition of gold with Stage 2 quartz veins involves gold collection by liquid bismuth. Whilst the aqueous solubility of Bi is poorly constrained from experimental data, Törmänen and Koski (2005) argued thio-hydroxy complexes such as $Bi_2S_2(OH)^0_2$ can transport appreciable Bi in reduced, weakly acidic fluids in the temperature range consistent with formation of the New Occidental deposit (up to 350°C) and that relatively small decreases in temperature (10–20°C) can trigger precipitation of native bismuth. Liquid bismuth persists as a discrete phase down to relatively low temperatures (<250°C) and, due to the very high partition co-efficient of gold between hydrothermal fluids and liquid bismuth, is capable of preferentially scavenging gold from fluids undersaturated with respect to gold (Douglas et al., 2000). Törmänen and Koski (2005) suggested liquid bismuth trapped in void space between main-stage mineral grains can scavenge gold from ambient hydrothermal fluid to a greater extent than bismuth isolated as inclusions within early-formed minerals. Gold-bearing native bismuth is expected to precipitate when the gold content is <13 wt% Au, whereas native bismuth and maldonite co-precipitate at higher gold contents (Figure 201). Subsequent exsolution of gold occurs during cooling, to produce the mixed assemblage of native bismuth, gold and maldonite, as observed in the New Occidental deposit. Gold collection by liquid bismuth during deposition of early-stage gold in the New Occidental deposit is indicated by the intimate association of gold with bismuth minerals in the New Occidental deposit, the common occurrence of composite grains and intergrowths of gold-bismuth-maldonite interstitial to other gangue and ore minerals, and deposition of gold from a hydrothermal fluid that was increasingly undersaturated with respect to gold (Figure 200). As such, it offers an alternate or additional mechanism to phase separation for early-stage gold deposition in the deposit.

Figure 201: Au-Bi alloy phase diagram modified from Okamoto & Massalski (1983).

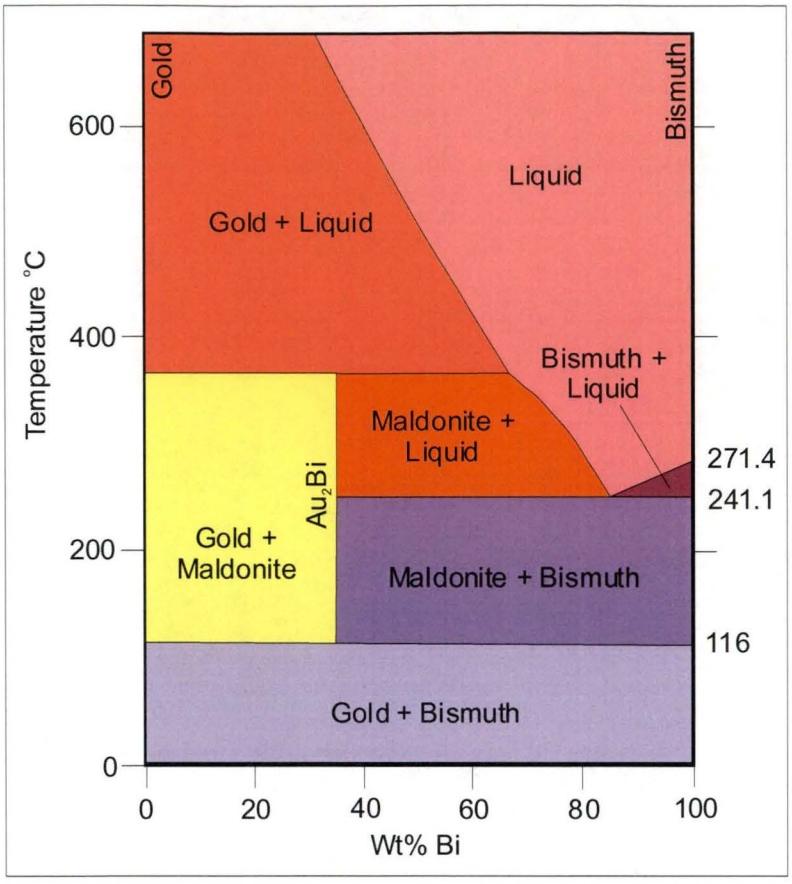

Replacement of native elements/alloys (native bismuth, gold and maldonite) by Au-Bi sulfides (bismuthinite and Bi_5AuS_4), and progressive changes in solid solution series minerals from Se-rich to S-rich Bi-Pb minerals also indicate an increase in aH_2S in the hydrothermal fluid with time (e.g. Mintser, 1979; Kolonon, 1979; Benchekroun et al., 1996; Figure 149c; Törmänen & Koski, 2005; Paar et al., 2006). For example, replacement of native bismuth by bismuthinite is controlled by the following reaction:

$$2Bi + 3H_2S + {}^3/_2O_2 = Bi_2S_3 + 3H_2O$$ (Benchekroun et al., 1996)

Sulfidation of the early-formed low-sulfur ore minerals (native bismuth, maldonite, Se-rich ikunolite and clausthalite) and also of Fe-rich silicates (Fe-chlorite and stilpnomelane) would have subsequently caused gold precipitation in response to a decrease in H_2S activity and oxygen fugacity (e.g. Groves & Phillips, 1987; McCuaig & Kerrich, 1994; Benchekroun et al., 1996; Mikucki, 1998) by the following reaction (unbalanced):

$$AuHS^0 + FeO_{(silicates,\ oxides)} = Au_{(s)} + H_2S_{(aq)} + FeS_{2\ (pyrite/pyrrhotite)}$$ (McCuaig & Kerrich, 1994)

Such reactions are indicated by the intimate spatial association between early formed Fe-chlorite, stilpnomelane, gold, native bismuth, maldonite, Se-rich ikonolite and clausthalite with overprinting bismuthinite, pyrrhotite, Bi_5AuS_4, S-rich ikunolite and galena and highlight the essential role of iron silicates in controlling sulfur fugacity, and hence gold solubility in the New Occidental deposit (e.g. Benchekroun et al., 1996). Likewise, increases in the Fe^{3+}/Fe^{2+} ratio of wallrock alteration chlorite identified by PIMA spectrometry associated with sulfide mineral (pyrite/pyrrhotite) haloes around the New Occidental deposit also suggest concomitant reduction of the ore fluids and H_2S loss from

the infiltrating ore fluid during wallrock sulfidisation. Sulfidation reactions that triggered gold precipitation in the New Occidental deposit, however, appear to have largely involved low-sulfur ore minerals as opposed to Fe-rich silicates like Fe-chlorite and stilpnomelane. Gold in the New Occidental deposit is predominantly located with remnants of low-sulfur ore minerals within quartz veins rather than in the wallrock associated with Fe-sulfides (c.f. Mt Charlotte and the Golden Kilometre mines, Western Australia; Groves & Phillips, 1987). This is probably due to initial gold deposition (Stage 2 gold-bismuth-maldonite) occurring almost exclusively within quartz veins in the New Occidental deposit, in response to phase separation (veins representing dilational low-pressure zones) and/or to scavenging of gold by liquid bismuth, and because the gold was intimately intergrown with low-sulfur ore minerals. Precipitation of remobilised early-stage gold in the New Occidental deposit appears to have occurred in close proximity to the original site of deposition and this is interpreted to have occurred rapidly.

The final stage of gold deposition during deposition of late stage chalcopyrite - pyrrhotite most likely reflects ongoing destabilisation of gold bisulfide complexes by desulfidation reactions with low-sulfur ore minerals and destabilisation of gold chloride complexes triggered by temperature reduction of the hydrothermal fluid (e.g. Huston & Large, 1989; Mikucki, 1998; Gibert et al., 1998; Figure 202). Fluid inclusion studies suggest an overall temperature reduction during base metal deposition from early-stage gold deposition, which is also indicated by the transition from pyrrhotite-stable to pyrite-stable ore mineral assemblages (e.g. Large et al., 1989; Mikucki, 1997; Figure 149b) and by the corresponding change from higher temperature phyllosilicate alteration assemblages (chlorite - stilpnomelane) associated with early-stage gold to lower temperature assemblages (sericite and greenalite - Fe-rich clays) associated with base metal deposition.

Deposition of base metal sulfides in the latter stages of formation of the New Occidental deposit appears to reflect decreasing temperature of the hydrothermal fluids in the later stages of deposit formation, with Cu-rich assemblages being deposited prior to lower temperature lead-zinc-rich assemblages (e.g. Huston & Large, 1989; Figure 198a–c). Decreasing fluid temperatures were most likely a function of lower flow rates and greater fluid-wallrock interaction (the wallrock being significantly cooler than the hydrothermal fluids) resulting from decreasing fluid supply and strain rates in the waning stages of deposit formation.

Progressive silver enrichment of gold deposited in the New Occidental deposit, especially during deposition of late-stage chalcopyrite-pyrrhotite, may be driven by a range of physiochemical changes in the ore fluid (e.g. Gammons & Williams-Jones, 1995). However, the simplest explanation is that silver content of the hydrothermal fluid increased over time as fluid salinity increased, thereby allowing formation of silver-chloride complexes. Deposition of silver during the latter stages of deposition formation also most likely reflected destabilisation of Ag chloride complexes in response to the reduction in fluid temperature.

Figure 202: Fields of gold and copper transport and deposition in fO_2 - temperature spacing showing Fe-S-O stability fields, predominance fields for $AuCl^{2-}$ and $Au(HS)_2^-$ and $AuCl^{2-}$ solubility curves (Huston & Large, 1989).

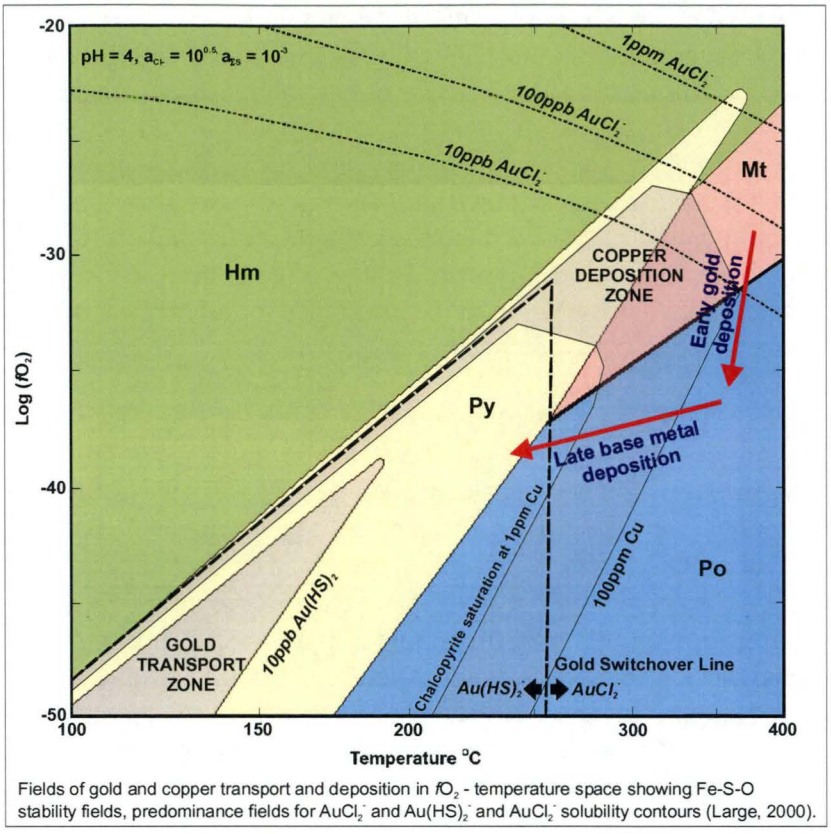

Fields of gold and copper transport and deposition in fO_2 - temperature space showing Fe-S-O stability fields, predominance fields for $AuCl_2^-$ and $Au(HS)_2^-$ and $AuCl_2^-$ solubility contours (Large, 2000).

10.5 Metal Zonation in Cobar Deposits – a Function of Evolving Fluid Composition and Fluid Flow Pathways in the Cobar Basin

The evolution of hydrothermal fluids in the New Occidental deposit, beginning with an initial gold-rich high temperature, weakly saline hydrothermal fluid that was subjected to repeated cyclic decompression during intense fault-valve activity along the Great Chesney Fault, which was followed by a late-stage more saline lower temperature base metal-rich, gold-poor hydrothermal fluid in the latter stages of deposit formation, provides the basis for an alternate explanation of the distinct district and deposit-scale metal zonation in Cobar deposits. In essence, the difference in metal endowment of Cobar deposits is explained by the degree to which individual deposit settings were exposed to the two temporally and compositionally distinct hydrothermal fluids. For example, gold-bearing Cobar deposits (New Occidental, Peak and New Cobar deposits) formed from the early-stage fluid whereas base metal deposits containing little or no gold (CSA and Elura deposits) formed from the late-stage gold-poor base metal-rich hydrothermal fluid. Deposits containing gold and late-stage base metals, which include most gold deposits to a limited extent but especially the Peak deposit, formed from mixtures of the two fluids, with Au-base metal ratios potentially reflecting the relative proportion of the two hydrothermal fluids present during deposit formation (Figure 203).

Figure 203: Bulk metal ratios of Cobar deposits.

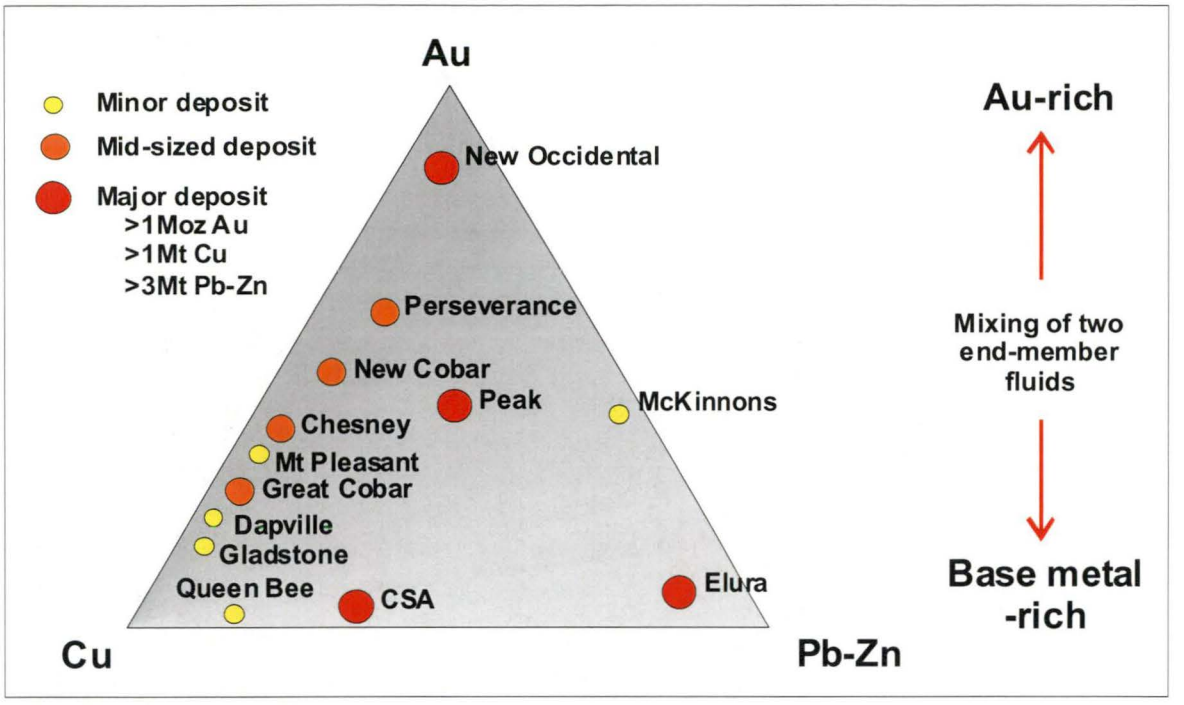

The degree to which deposits were exposed to the two different hydrothermal fluids depended to a large extent upon the evolution of fluid pathways within the Cobar Basin, which ultimately was a function of the deformational history of the basin. For example, fault zones active in the early stages of basin deformation (e.g. Great Chesney Fault and Peak Shear) provided fluid pathways for early-stage gold-bearing fluids, base metal-rich fluids focussed along fault zones active during the latter stages of basin deformation, whereas both fluid types infiltrated fault zones active over the life of basin deformation. The presence of base metal overprints in all gold-rich deposits in the Cobar Basin indicates the early-formed fault zones remained at least partially accessible to hydrothermal fluids for the duration of hydrothermal activity in the Cobar Basin.

The efficiency of fluid transport and metal deposition mechanisms were also important factors influencing the size of Cobar deposits and metal zonation within deposits. The gold endowment of gold-rich deposits is a function of the volume of gold-bearing hydrothermal fluid transported to the deposit environs and the efficiency of gold deposition within the deposit. Formation of large, gold-rich deposits in the Cobar Basin most likely occurred along the most active and deep-seated faults which focussed large-scale fluid flow and initiated gold deposition in response to phase separation during repeated rupture events. The Great Cobar Slate appears to have played a very important role as a local- to district-scale seal, promoting over-pressuring of hydrothermal fluids within fault zones and the Chesney Formation. In the case of base metal deposits, transport efficiency would likewise have been maximised along major faults and other high strain zones, although, at least at the New Occidental, less intense cyclic decompression during fault zone rupture accompanied late-stage base metal deposition. For example, late-stage base metal-rich fluids do not appear to have undergone phase separation and quartz vein textures in the New Occidental deposit change from brittle and open-space filling to incremental crack-seal and brittle-ductile shear types (Section 4.5). In contrast to the larger gold-rich deposits in the Cobar Basin, most of the major base metal deposits that contain little or no gold (CSA and Elura deposits) are hosted in relatively high strain zones of intense cleavage development but are not immediately associated with obvious large-displacement faults, although such faults are inferred to underlie these deposits (Table 6). Metal deposition was

controlled by other mechanisms, most likely decreasing temperature associated with fluid-wallrock interaction and mixing of hydrothermal fluids with meteoric waters. The zonation from Cu-rich to Pb-Zn-rich deposits can also be attributed to decreasing fluid temperature (Figure 204), but may also reflect ongoing evolution of the hydrothermal fluid at its source.

Figure 204: Schematic cross-section showing potential transport and trapping mechanisms for Cobar deposits.

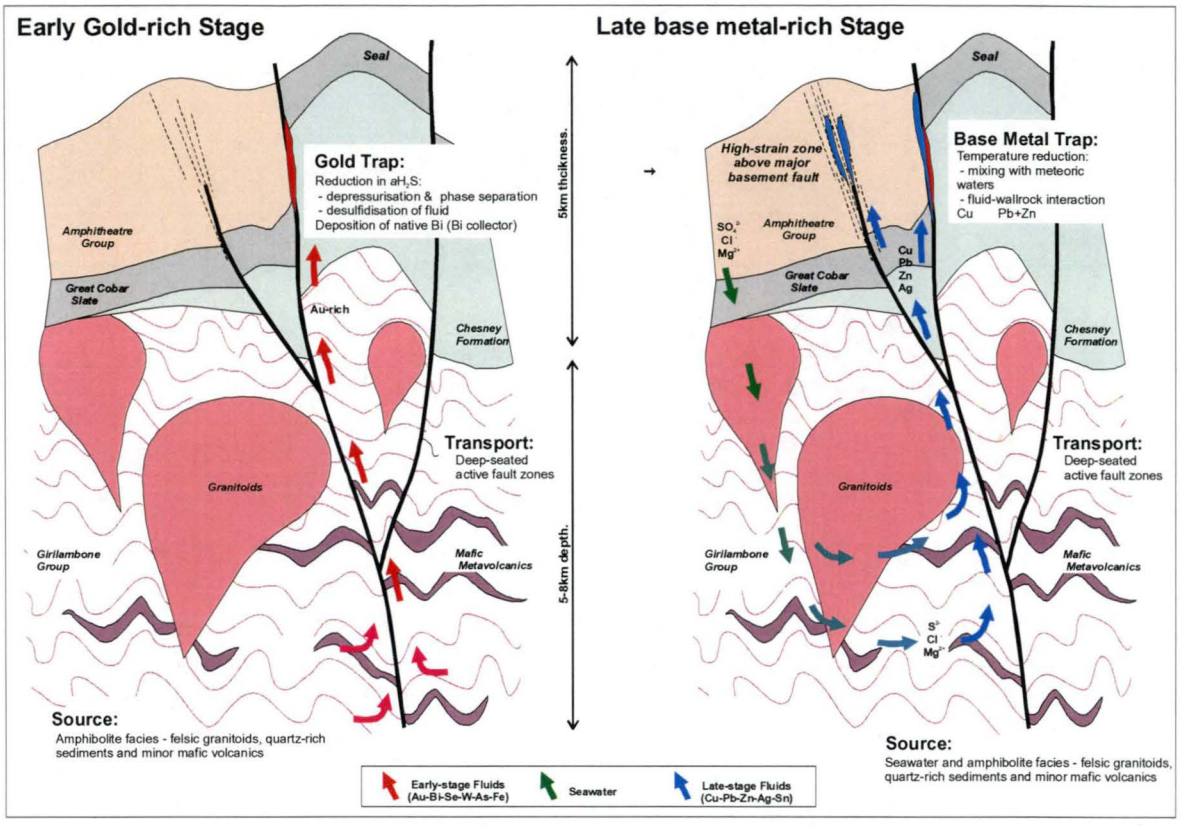

10.6 Implications for Exploration of the Cobar Basin

This study has identified a number of factors critical to formation of gold and base metal deposits in the Cobar Basin that provide a focus for renewed exploration in the Cobar region:

1. Deposits are associated with major deep-seated fault systems that penetrate basement beneath the Cobar Basin and which were active during basin deformation. In some cases, the faults may be reactivated syn-sedimentary faults that controlled the architecture and initial subsidence of the Cobar Basin. The faults tapped and then focussed discharge of deep-derived or circulated (i.e. >10km depth) hydrothermal fluids. Such faults can generally be identified by large-scale offsets of basin stratigraphy. Otherwise, they can also be identified by reconstructing the structural framework and deformational history of the basin. The most prospective faults are the long strike-length north-northwest trending reverse faults that are aligned in en echelon arrangement along the eastern margin of the basin, although shorter subsidiary structures may also host mineralisation.

2. Larger Cobar deposits are characterised by a steep-dipping pipe-like geometry that parallels the strong steep northerly plunging stretching lineation on the S_1 cleavage. Deposits are generally relatively narrow (10-30m), of moderate strike length (100-200m) but have significant vertical extents (500-1500m), making them relatively difficult exploration targets. Deposits are located within short strike-length dilational sites created by reverse movement on the steeply dipping faults, the size of deposit being chiefly a function of the magnitude of syn-mineralisation fault zone displacement. Dilational sites are often located at suitably oriented competency contrast boundaries (e.g. New Occidental, Peak, Perseverance and Chesney deposits) or on subtle changes in the dip of the fault zones (New Cobar deposit). Where fault displacement was <250m, individual lenses within deposits exhibit gentle to moderate southerly plunges, either perpendicular to the stretching lineation or parallel to the intersection of bedding and cleavage. However, where large-scale fault displacement has occurred, ore lenses are typically vertically elongate, as in the case of the New Occidental deposit. The vertical elongation reflects the repeated focussing of strain, dilation and fluid flow along relatively discrete (short strike-length) segments of the fault zones. Initial vein deposition at these sites may serve to enhance existing competency contrasts, promoting further localised dilation during subsequent fault activity. Direction of deposit growth and hence elongation parallels the strong stretching lineation on cleavage.

3. Fault-valve behaviour along the major faults is a key determinant in formation of gold-rich deposits in the Cobar Basin, with gold deposition intimately linked to cyclic decompression of the hydrothermal fluid. The richest gold deposits are therefore predicted to occur in structural settings where the intensity of fault-valve behaviour is greatest, that is:

   - Along steeply-dipping major faults that were unfavourably oriented for slip, e.g. faults oriented at high angles to σ_1 that require very high fluid pressures ($P_f \geq \sigma_3 = \sigma_v$) to slip.
   - Absence of more favourably oriented faults that would fail at much lower fluid pressures and therefore prevent significant over-pressuring of hydrothermal fluids.
   - Fault zones beneath or within relatively impermeable units like the Great Cobar Slate that promote over-pressuring of the hydrothermal fluids in the underlying rocks.
   - Dilational sites along or within fault zones that focus fluid flow and allow large P_f drops from supra-lithostatic to near hydrostatic during fault rupture events.
   - Transient high fluid flux and fault zone permeability, which supports large-scale fluid flow from sources in basement beneath the Cobar Basin.

   The southern extensions of the Peak Shear (south of Perseverance deposit) and Great Chesney Fault (south of New Occidental deposit) represent immediate, albeit much deeper, analogues of the settings hosting major gold deposits in the Cobar Basin (Figure 205). The Coronation-Beechworth Fault on the eastern flank of the Chesney-Narri Anticline and the Queen Bee Fault further to the south (Figure 205) are also prospective on this basis.

Evidence for fault-valve activity in a deposit includes the presence of:

- Arrays of sub-horizontal fibred quartz extension veins (indicating $P_f \geq \sigma_3 = \sigma_v$).
- Multiple sets of sub-horizontal quartz veins exhibiting complex over-printing relationships with steeply dipping fault-fill veins (indicating cyclic fluid pressure fluctuations from supra-lithostatic to near-hydrostatic).
- Crystalline to cryptocrystalline crustiform and colloform-banded quartz textures (indicating large-scale pressure drops in the fault zone)
- Implosive-style brittle vein breccias (indicating large-scale pressure drops at dilational sites)
- Two-phase fluid inclusions that homogenise at similar temperatures to the gas or liquid states (indicating phase separation due to decompression of hydrothermal fluids).

A major implication of these conclusions is that the eastern margin of the Cobar Basin is far more prospective for gold deposits than the western margin of the basin on the basis the bulk of Late Devonian deformation was focussed in Glen's (1990) Structural Zone 1 (e.g. eastern and northeastern basin margin), which is borne out by the current known distribution of gold deposits in the Cobar Basin.

4. Recognition of two temporally and compositionally distinct hydrothermal fluids associated with formation of the New Occidental deposit (an early gold-rich fluid and a late-stage base metal-rich fluid that was capable of remobilising early-formed gold but did not contribute any further gold) provides an explanation for the district and deposit-scale metal zonation in the Cobar region. Features indicating the first gold-bearing fluid was involved in deposit formation include:

   - Elevated levels of Bi-Se-W-As-Sb in the ore. Whilst these elements do not appear to extend beyond the immediate ore zones, Bi, W and As are usually present in concentrations that are orders of magnitude higher than gold contents. Therefore, the suite can be used to discriminate between gold-mineralised systems and gold-poor base metal-rich systems. In addition, those elements are readily concentrated in resistate phases in the secondary environment, providing enlarged exploration targets.
   - Au/Ag ratios in the range 1–2. Lower ratios are indicative of late-stage base metal-rich mineralisation.
   - Higher temperature Fe-rich alteration mineral assemblages including Fe-chlorite ± stilpnomelane ± biotite. Whilst stilpnomelane and biotite are usually confined to the immediate ore zones, visible Fe-rich chlorite alteration haloes may extend up to 30m either side of the ore zones.
   - Subtle but distinctive trends of increasing chlorite and white mica content, increasing white mica crystallinity and phengite content (i.e. increasing Fe/Mg/Si and decreasing Al content of white mica) and increasing Fe/(Fe+Mg) ratio and Fe^{3+}/Fe^{2+} ratio of chlorite in wallrock,

which can readily be detected by SWIR spectrometry to 100m from ore zones.

- ❖ Lead isotopic signatures characterised by similar $^{207}Pb/^{204}Pb$ and $^{208}Pb/^{204}Pb$ ratios but slightly higher $^{206}Pb/^{204}Pb$ ratios compared to late-stage galena mineralisation.

In contrast, late-stage base metal rich hydrothermal fluids produced Mg-chlorite ± talc and sericite alteration and ores containing elevated Cu-In-Pb-Zn-Cd-Ag-Sn-Co-Mn-S and Au/Ag ratios <1.

5. The presence of elevated Bi in a deposit not only indicates the first gold-bearing ore fluid was involved in deposit formation but also suggests the deposit may be more gold-rich (on the basis liquid bismuth can preferentially scavenge and concentrate gold from a hydrothermal fluid).

Figure 205: Exploration targets in the Cobar Goldfield.

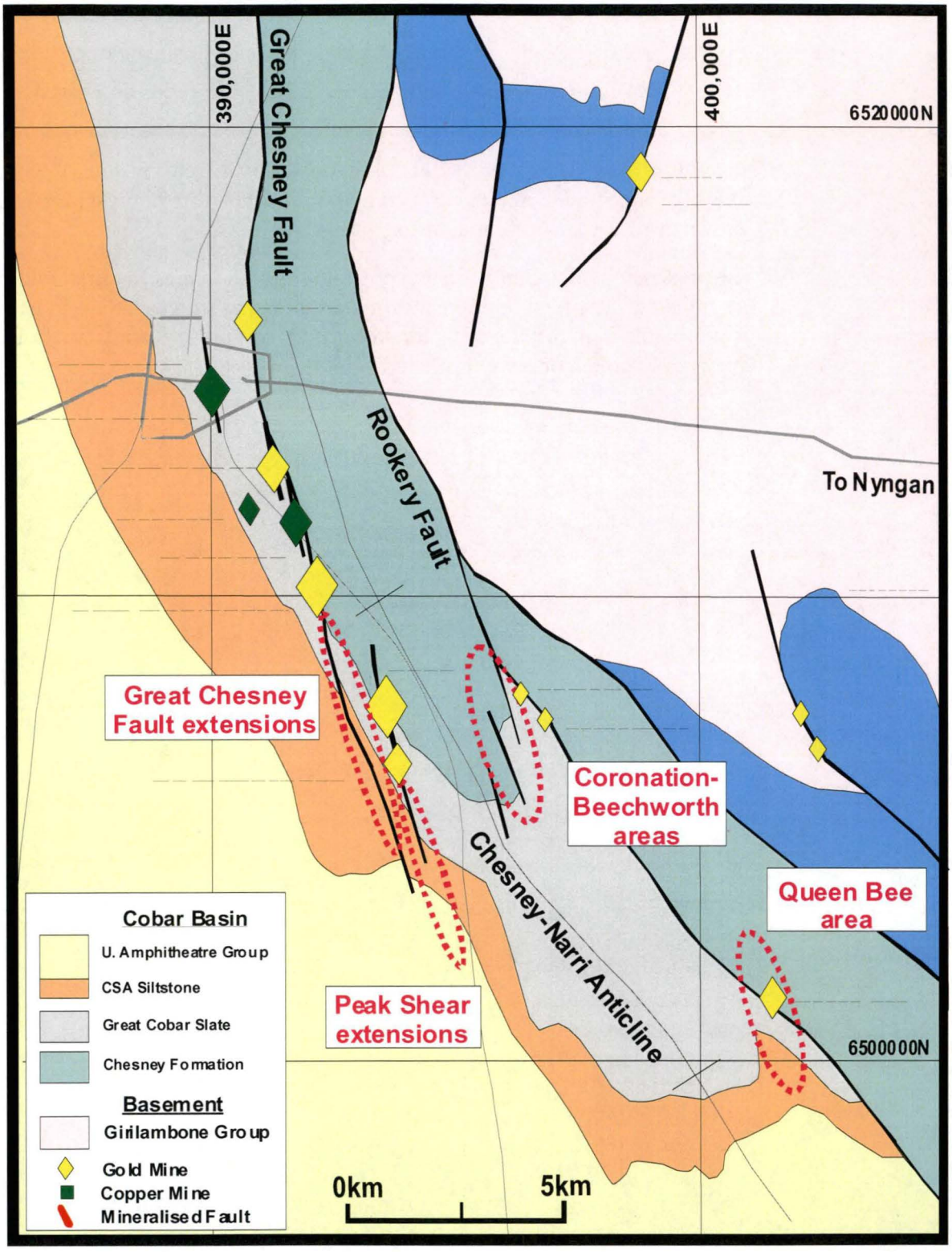

REFERENCES

Andrews, E.C., 1913. Report on the Cobar Copper and Gold Field, Part 1. *Mineral Resources No. 17*: Sydney, New South Wales Dept. of Mines, 207pp.

Arne, D., Bierlein, F., McKnight, S. & Mernagh, T., 1999. Recognition of wallrock alteration in sediment-hosted mesothermal gold deposits: examples from Central Victoria. Exploration Geochemistry for the New Millenium, *AIG Bulletin*, 30: 89–96.

AusSpec, 2000. Analysis of PIMA Spectral data from Peak Gold Mines. Analysis Report (unpubl.), 5pp.

Ayres, D.E., Burns, M.S. & Smith, J.W. 1979. Sulfur-isotope study of the massive sulfide orebody at Woodlawn, New South Wales. *Journal of the Geological Society of Australia.* 26: 197–201.

Bastrakov, E.N., Cassidy, K.F. & Shvarov, Y.V., 2000. Gold transport at Archaean lode gold deposits: gold solubility along rock-buffered pathways. Geological Society of Australia Abstracts No 59, *15th Australian Geological Convention, Sydney, July 2000*, p 75.

Beane, R.E., 1994. A graphic view of hydrothermal mineral stability relations. In Lentz, J.R. (editor) Alteration Processes Associated with Ore-forming systems. Geological Association of Canada, Short Course Notes, 11: 1–30.

Beane, R.E. & Titley, S.R., 1981. Porphyry copper deposits. Part II. Hydrothermal alteration and mineralisation. *Economic Geology, 75th Anniversary Volume*, p 235–263.

Benchekroun, F., Berger, G. & Moine, B., 1996. A mineralogical and chemical model for gold precipitation in the Salsigne deposit, (Montagne-Noire). Comptes Rendus, Academie des Sciences, Serie II: *Sciences de la Terre et des Planetes*. 323/3: 129–136.

Benning, L.G. & Seward, T.M., 1996. Hydrosulfide complexing of Au(I) in hydrothermal solutions from 150–400°C and 500–1500 bar. *Geochimica et Cosmochimica Acta*, 60: 1849–1871.

Bierlein, F.P., Arne, D.C., McKnight, S., Lu, J., Reeves, S., Besanko, J., Marek, J. & Cooke, D., 2000. Wall-rock petrology and geochemistry in alteration halos associated with mesothermal gold mineralisation, Central Victoria, Australia, *Economic Geology*, 95: 283–312.

Binns, R.A., 1983. The nature and origin of Cobar 'elvan'. [Abstract]: *Geological Society of Australia Abstracts*, 9:315–316.

Binns, R.A. and Appleyard, E.C., 1986. Wallrock alteration in the western system of the C.S.A. mine, Cobar, New South Wales, Australia. *Applied Geochemistry*, 1:2111–225.

Bodnar, R.J., Binns, P.R. & Hall, D.L., 1989. Synthetic fluid inclusions – VI. Quantitative evaluation of the decrepitation behaviour of fluid inclusions in quartz at one atmosphere confining pressure. *Metamorphic Geology*, 7: 229–242.

Bodon, S.B. & Valenta, R.K., 1995. Primary and tectonic features of the Currawong Zn-Cu-Pb(-Au) massive sulfide deposit, Benambra, Victoria: implications for ore genesis. *Economic Geology*, 90: 1694–1721.

Boullier, A. & Robert, F., 1992. Palaeoseismic events recorded in Archaean gold-quartz vein networks, Val d'Or, Abitibi, Quebec, Canada. *Journal of Structural Geology*, 14 (2): 161–179.

Brill, B.A., 1988a. The geochemistry and genesis of the CSA Cu-Pb-Zn deposit, NSW, Australia: Unpublished Ph.D. thesis, Newcastle University, Australia.

Brill, B.A., 1988b. Illite crystallinity, b_0 and Si content of K-white mica as indicators of metamorphic conditions in low-grade metamorphic rocks at Cobar, New South Wales. *Australian Journal of Earth Sciences*, 35: 295–302.

Brill, B.A., 1989. Deformation and recrystallisation microstructures in deformed ores from the CSA mine, Cobar N.S.W., Australia. *Journal of Structural Geology*, 11: 591–601.

Brooke, W.J.L., 1975. Cobar mining field. In: Knight, C.L., (Editor) *Economic Geology of Australia and New Guinea, I Metals*: Australasian Institute of Mining and Metallurgy, Monograph 5, pp 683–694.

Brown, E.H., 1971. Phase relations of biotite and stilpnomelane in the greenschist facies. *Contributions to Mineralogy & Petrology*, 31: 275–299.

Brown, E.H., 1975. A petrogenetic grid for reactions producing biotite and Al-Fe-Mg silicates in the greenschist facies. *Journal of Petrology*. Volume 16: 258-271.

Brown, P.E., 1998. Fluid inclusion modelling for hydrothermal systems. Techniques in Hydrothermal Ore Deposits Geology, *Reviews in Economic Geology*, Volume 10, pp 151–169.

Caritat, P. de, Hutcheon, I. & Walshe, J.L., 1993. Chlorite geothermometry: A review. *Clays and Clay Minerals*, 41: 219–239.

Carr, G.R., Dean, J.A., Suppel, D.W. and Heithersay, P.S., 1995. Precise Lead Isotope Fingerprinting of Hydrothermal Activity Associated with Ordovician to Carboniferous Metallogenic Events in the Lachlan Fold Belt of New South Wales. *Economic Geology*. 90: 1467–1505.

Cathelineau, M., 1988. Cation site occupancy in chlorites and illites as a function of temperature. *Clay Minerals*, 23: 471–485.

Cathelineau, M., Boiron, M.C., Essarraj, S., Lespinasse, M., Poty, B. & Sellier, E., 1991. Fluid density changes and gold deposition in gold quartz veins: the role of pressure fluctuations linked to multistage deformation. In Pagel & Leroy (editors) *Source, Transport and Deposition of Metals*, Balkema, Rotterdam, 656pp.

Cathelineau, M. & Nieva, D., 1985. A chlorite solid solution geothermometer. The Los Azufres (Mexico) geothermal system. *Contributions to Mineralogy and Petrology*, 91:235–244.

Claypool, G.E., Holser, W.T., Kaplan, I.R., Sakai, H. & Zak, I. 1980. The age curves of sulfur and oxygen isotopes in marine sulfate and mutual interpretation. *Chemical Geology*, 28: 199–260.

Clout, J.M.F., Cleghorn, J.H. & Eaton, P.C., 1990. Geology of the Kalgoorlie Gold Field. In: Hughes, F.E., (Editor) *Geology of the Mineral Deposits of Australia and Papua New Guinea*. The Australasian Institute of Mining and Metallurgy: Melbourne, 1: 411–431.

Coller, D., 1998. Cobar Structural Review. Unpublished report prepared for Peak Gold Mines Pty Limited by ERA-Maptek Limited.

Cohen, D.R., Rutherford, N.F., Dunlop, A.C. & Alipour, S., 1996. Geochemical exploration in the Cobar region. In: Cook, W.G., Ford, A.J.H., McDermott, J.J., Standish, P.N., Stegman, C.L. & Stegman, T.M. (editors), *The Cobar Mineral Field – A 1996 Perspective*. Australasian Institute of Mining and Metallurgy, Spectrum Series, 3/96, pp 125–155.

Conolly, H.J.C., 1946. Cobar exploration (1943–1946). New Occidental Gold Mines N.L. Internal report, November 1946 (unpubl.).

Cook, W.G., Pocock, J.A. & Stegman, C.L., 1998. Peak gold-copper-lead-zinc-silver deposit, Cobar. In: Berkman, D.A. & Mackenzie, D.H. (Editors) *Geology of Australian and Papua New Guinean Mineral Deposits.* The Australasian Institute of Mining and Metallurgy, pp 609–614.

Cooke, D.R., Heithersay, P.S., Wolfe, R. & Calderon, A.L., 1998. Australian and western Pacific porphyry Cu-Au deposits. *AGSO Journal of Australian Geology and Geophysics*, 17:97–104.

Cox, S.F., 1987. Antitaxial crack seal microstructures and their relationship to displacement paths. *Journal of Structural Geology*, 9: 779–787.

Cox, S.F., 1995. Faulting processes at high fluid pressures: - An example of fault behaviour from the Wattle Gully Fault, Victoria, Australia. *Journal of Geophysical Research*, 100 (B7): 12841–859.

Cox, S.F., 2000. Breccias in mineralised fault systems. In: Breccias, lode gold and skarn deposits. Ore Deposit Models and Exploration Strategies, CODES Short Course Manual, June 2000. Centre for Ore Deposit Research, University of Tasmania.

Cox, S.F., Knackstedt, M.A. & Braun, J., 2001. Principals of Structural Control on Permeability and Fluid Flow in Hydrothermal Systems. In: Richards, J.P. & Tosdal, R.M. (Editors) *Structural Controls on Ore Genesis: Reviews in Economic Geology, Volume 14* Society of Economic Geologists. pp 1–24.

Cox, S.F. & Etheridge, M.A. 1983. Crack-seal and fibre growth mechanisms and their significance in the development of layer silicate microstructures. *Tectonophysics*, 92: 147–170.

Cox, S.F., Etheridge, M.A.& Wall, V.J. 1986. The role of fluids in syntectonic mass transport, and the localisation of metamorphic vein-type ore deposits. *Ore Geology Reviews*, 2: 65–86.

Cox, S.F., Wall, V.J., Etheridge, M.A. & Potter, T.F., 1991. Deformation and metamorphic processes in the formation of mesothermal vein-hosted gold deposits – Examples from the Lachlan fold belt in Central Victoria, Australia. *Ore Geology Reviews*, 6: 391–423.

Cox, S.F., Sun, S.F., Etheridge, M.A., Wall, V.J. & Potter, T.F., 1995. Structural and geochemical controls on the development of turbidite-hosted gold quartz vein deposits, Wattle Gully Mine, Central Victoria, Australia. *Economic Geology*, 90:1722–1746.

Craig, J.R., 1967. Phase Relations and Mineral Assemblages in the Ag - Bi - Pb – S System. *Mineralium Deposita* 1:278–306.

Craw, D. & Campbell, J.R., 2004. Tectonic and structural setting for active mesothermal gold vein systems, Southern Alps, New Zealand. *Journal of Structural Geology*, 26: 995–1005.

Cross, M.M., Manning, A.C., Bottrell, S.H. & Worden, R.H., 2004. Thermochemical sulfate reduction (TSR): experimental determination of reaction kinetics and implications of the observed reaction rates for petroleum reservoirs. *Organic Geochemistry*, 35: 393–404.

Cumming, G.L. & Richards, J.R., 1975. Ore lead isotope ratios in a continuously changing earth. *Earth Planetary Science Letters*, 28: 155–171.

David, V., 2000. Structural setting of the Elura Zn-Pb-Ag deposit Cobar, NSW, Australia. In: McQueen, K.G. & Stegman, C.L. (editors). *Central West Symposium Cobar 2000. Geology, Landscapes and Mineral Exploration. Extended Abstracts*, pp 15–20.

Davidson, G.J. & Large, R.R., 1998. Proterozoic copper-gold deposits. *AGSO Journal of Australian Geology and Geophysics*, 17: 105–114.

Dean, J.A., 1991. Lead isotope signatures of the Lachlan fold belt: New South Wales. Department of Mineral Resources, Minfo 33, p 1–5.

Deer, W.A., Howie, R.A. & Zussmann, J., 1966. *An introduction to the rock-forming minerals.* Longman Group Limited, London, 528p.

de Roo, J.A., 1989a Mass transfer and preferred orientation development during extensional microcracking in slate-belt folds, Elura Mine, Australia. *Journal of Metamorphic Geology*, 7: 311–322

de Roo, J.A., 1989b. The Elura Ag-Pb-Zn Mine in Australia – Ore genesis in a slate belt by syndeformational metasomatism along hydrothermal conduits. *Economic Geology*, 84: 256–278.

Douglas, N., Mavrogenes, J., Hack, A. & England, R., 2000. The liquid bismuth collector model: An alternative gold deposition mechanism. Geological Society of Australia, Abstracts No. 59, *15th Australian Geological Convention, Sydney, 2000*, p 135.

Dowling, K., 1989. The discrimination of gold-bearing and barren quartz in North Queensland Vein deposits. Unpublished PhD thesis, James Cook University of North Queensland, Townsville.

Dowling, K. & Morrison, G.W., 1988. Application of Quartz textures to the classification of gold deposits using North Queensland examples. In: Skinner, B. (editor) Economic Geology Monograph 6, *The Geology of Gold Deposits: The Perspective in 1988*: 334–347. Economic Geology Publishing Company.

Downes, P.M. & Seccombe, P.K., 2004. Sulfur isotope distribution in the Late Silurian volcanic-hosted massive sulfide deposits of the Hill End trough, eastern Lachlan fold belt, New South Wales. *Australian Journal of Earth Sciences*, 51: 123–139.

Drummond, B.J., Goleby, B.R., Wake-Dyster, K.D., Glen, R.A. and Palmer, D., 1992. New tectonic model for the Cobar Basin, NSW, points to new exploration targets in the Lachlan Fold Belt. *BMR Research Newsletter 16*

Drummond, B.J., Glen, R.A., Goleby, B.R., Wake-Dyster, K.D. and Palmer, D., 1992. Deep Seismic of the Cobar Basin II: A ramp Basin Controlled by Mid-Crustal Detachment [Abs]. *Geological Society of Australia, Abstracts*, 32: 44.

Dugdale, A.L. & Hagemann, S.G., 2001. The Bronzewing lode-gold deposit, Western Australia: *P-T-X* evidence for fluid immiscibility caused by cyclic decompression in gold-bearing quartz veins. *Chemical Geology*, 173: 59–90.

Eastoe, C.J. & Gustin, M.M., 1996. Volcanogenic massive sulfide deposits and anoxia in the Phanerozoic oceans. *Ore Geology Reviews*, 10: 179–197.

Eggleton, R.A. & Chappell, B.W., 1978. The crystal structure of stilpnomelane. Part III: chemistry and physical properties. *Mineralogical Magazine*, 42: 361–368.

Eilu, P. & Mikucki, E.J., 1998. Alteration and primary geochemical dispersion associated with the Bulletin lode-gold deposit, Wiluna, Western Australia. *Journal of Geochemical Exploration*, 63: 73–103.

Eilu, P., Mikucki, E.J. & Dugdale, A.L., 2001. Alteration zoning and primary geochemical dispersion at the Bronzewing lode-gold deposit, Western Australia. *Mineralium Deposita*, 36: 13–31.

Emsbo, P., Hofstra, A.H., Lauha, E.A., Griffin, G.L. & Hutchinson, R.W., 2003. Origin of High-Grade Gold Ore, Source of Ore Fluid Components, and Genesis of the Meikle and Neighbouring Carlin-Type Deposits, Northern Carlin Trend, Nevada. *Economic Geology*, 98:1069–1106.

Etheridge, M.A., Wall, V.J. and Vernon, R.H., 1983. The role of the fluid phase during regional metamorphism and deformation. *Journal of Metamorphic Geology*, 1:205–226.

Etheridge, M.A., Cox, S.F., Wall, V.J. and Vernon, R.H., 1984. High fluid pressures during regional metamorphism and deformation: Implications for mass transport and deformation mechanisms. *Journal of Geophysical Research*, 89 (No. B6):4344–358.

Faure, G., 1986. *Principles of Isotope Geology*. J Wiley and Sons. Toronto. 589pp.

Fergusson C.L. & Phillips D., $^{40}Ar/^{39}Ar$ and K-Ar age constraints on the timing of regional deformation, south coast of New South Wales, Lachlan Fold Belt: problems and implications. *Australian Journal of Earth Sciences* (2001) 48: 395–408.

Fischer, M., Roller, K., Kuster, M., Stockhert, B. & McConnell, V.S., 2003. Open fissure mineralisation at 2600m depth in Long Valley exploratory well (California) – insight into the history of the hydrothermal system. *Journal of Volcanology and Geothermal Research*, 127: 347–363.

Forde, A., 1991. The late orogenic timing of mineralisation in some slate belt gold deposits, Victoria, Australia. *Mineralium Deposita*, 26: 257–266.

Forde, A. & Bell, T.H., 1994. Late structural control of mesothermal vein-hosted gold deposits in Central Victoria, Australia: mineralisation mechanisms and exploration potential. *Ore Geology Reviews*, 9: 33–59.

Forster, D.B., 1997. McKinnons gold deposit, Cobar, NSW. BSc (Hons) Thesis, Newcastle University, Australia (unpubl.).

Forster, D.B. & Seccombe, P.K., 1999. Syntectonic base-metal mineralisation with an epithermal gold overprint: McKinnons gold deposit, Cobar, NSW, Australia. In: Weber, G. (editor), *Proceedings, International Conference on Earth Science, Exploration around the Pacific Rim. AusIMM Publication Series* 4: 235–242.

Fournier, R.O., 1985. The behaviour of silica in hydrothermal solutions. *Reviews in Economic Geology*, 2: 45–61.

Fournier, R.O., 1999. Hydrothermal processes related to movement of fluid from plastic into brittle rock in the magmatic-epithermal environment. *Economic Geology*, 94: 1193–1211.

Fredericksen, D.C. & Gane, M., 1998. Stawell gold deposits. In: Berkman, D.A. & Mackenzie, D.H. (Editors), *Geology of Australian and Papua New Guinean mineral deposits*, Australasian Institute of Mining and Metallurgy, Melbourne, pp 535–542.

Galley, A.G., 1993. Characteristics of semi-conformable alteration zones associated with volcanogenic massive sulfide districts. *Journal of Geochemical Exploration*, 48: 175–200.

Gammons, C.H. & Williams-Jones, A.E., 1995. Hydrothermal geochemistry of electrum: thermodynamic constraints. *Economic Geology*, 90: 420–432.

Gemmell, J.B. & Fulton, R., 2001. Geology, genesis, and exploration implications of the footwall and hanging-wall alteration associated with the Hellyer volcanic-hosted massive sulfide deposit, Tasmania, Australia. *Economic Geology*, 96:1003–1036.

Gibert, F., Pascal, M.L. & Pichavant, M., 1998. Gold solubility and speciation in hydrothermal solutions: Experimental study of the stability of bisulfide complex of gold ($AuHS^0$) at 350 to 450°C and 500 bars. *Geochimica et Cosmochimica Acta*, No 62, 17: 2931–2947.

Giles, A.D. & Marshall, B., 2004. Genetic significance of fluid inclusions in the CSA Cu-Pb-Zn deposit, Cobar, Australia. *Ore Geology Reviews*, 24: 241–266.

Gilligan, L.B., 1974. Cobar and Mineral Hill Synclinorial Zones. In: Markham, N.L. & Basden, H. (editors) *The Mineral Deposits of New South Wales*. Dept. of Mines, Geological Survey of New South Wales, pp 148–171.

Gilligan L.B. & Byrnes J.G., 1994. *Cobar 1:250 000 Metallogenic Map SH/55-14: Metallogenic Study and Mineral Deposit Data Sheets.* Geological Survey of New South Wales, Sydney.

Gilligan L.B. & Suppel, D.W., 1978. Mineral deposits in the Cobar Super-Group and their structural setting. *Geological Survey of New South Wales, Quarterly Notes,* 33: 15–22.

Glen, R.A., 1985. Basement control on the deformation of cover basins: an example from the Cobar district in the Lachlan Fold Belt, Australia. *Journal of Structural Geology*, 7: 301–315.

Glen, R.A., 1987a. *Geology of the Wrightville 1:100,000 sheet 8034.* Geological Survey of New South Wales, Department of Mineral Resources.

Glen, R.A., 1987b. Copper and Gold Deposits in Deformed Turbidites at Cobar, Australia: Their Structural Control and Hydrothermal Origin. *Economic Geology*, 82: 124–140

Glen, R.A., 1990. Formation and inversion of transtensional basins in the western part of the Lachlan Fold Belt, with emphasis on the Cobar Basin. *Journal of Structural Geology*, 12: 601–620.

Glen, R.A., 1991. Inverted transtensional basin setting for gold and base metal deposits at Cobar, New South Wales. *BMR Journal of Geology and Geophysics*, 120: 13–24.

Glen, R.A., 1992. Thrust, extensional and strike-slip tectonics in an evolving Palaeozoic orogen - a synthesis of the Lachlan Orogen of southeastern Australia. *Tectonophysics*, 214: 341–380.

Glen, R.A., 1994. *Geology of the Cobar 1:100,000 sheet 8035.* Second Edition. Geological Survey of New South Wales, Department of Mineral Resources.

Glen, R.A., 1995. Thrusts and thrust-associated mineralisation in the Lachlan Orogen. *Economic Geology*, 90: 1402–1429.

Glen, R.A., Clare, A. and Spencer, R., 1996. Extrapolation of the Cobar Basin Model to the Regional Scale: Devonian Basin-Formation and Inversion in Western New South Wales. In: Cook, W.G., Ford, A.J.H., McDermott, J.J., Standish, P.N., Stegman, C.L. & Stegman, T.M. (editors), *The Cobar Mineral Field – A 1996 Perspective.* Australasian Institute of Mining and Metallurgy, Spectrum Series, 3/96, pp 43–83.

Glen, R.A., Dallmeyer, R.D. & Black, L.P., 1992. Isotopic dating of basin inversion – the Palaeozoic Cobar Basin, Lachlan Orogen, Australia. *Tectonophysics*, 214: 249–268.

Glen, R.A., Drummond, B.J., Goleby, B.R., Palmer, D. and Wake-Dyster, K.D., 1994. Structure of the Cobar Basin, New South Wales, based on seismic reflection profiling. *Australian Journal of Earth Sciences*, *41*: 341–352.

Glen, R.A., Lewington, G.L.D. & Shaw, S.E., 1983. Basement/cover relations and a Silurian I-type intrusion from the Cobar-Lucknow area, Cobar, New South Wales. *Journal and Proceedings of the Royal Society of New South Wales*, 116: 25–32.

Gresens, R.L., 1967. Composition-volume relationships of metasomatism. *Chemical Geology*, 2: 47–55.

Groves, D.I. & Phillips, G.N., 1987. The genesis and tectonic controls on Archaean lode gold deposits of the Western Australian shield: a metamorphic –replacement model. *Ore Geology Reviews*, 2: 287–322.

Groves, D.I., Phillips, G.N., Ho, S.E., Houstoun, S.M. & Standing, C.A., 1987. Craton-scale distribution of Archaean greenstone gold deposits: predictive capacity of the metamorphic model. *Economic Geology,* 82: 2045–2058.

Groves, D.I., Ridley, J.R., Bloem, E.M.J., Gebre-Mariam, M., Hagemann, S.G., Hronsky, J.M.A., Knight, J.T., McNaughton, J.T., Ojala, J., Vielricher, R.M., McCuaig, T.C., & Holyland, P.W., 1995. Lode gold deposits of the Yilgarn block: Products of Late Archaean crustal-scale over-pressured hydrothermal systems, In: Coward, M.P. and Ries, A.C. (editors) Early Precambrian processes: *Geological Society Special Publication*, 95: 155–172.

Groves, D.I., Goldfarb, R.J., Gebre-Mariam, M., Hagemann, S.G., & Robert, F., 1998. Orogenic gold deposits: A proposed classification in the context of their crustal distribution and relationships to other gold deposits. *Ore Geology Review*, 13: 7–27.

Guha, J., Archambault, G. and Leroy, J., 1983. A correlation between the evolution of mineralising fluids and the geomechanical development of a shear zone as illustrated by the Henderson 2 Mine, Quebec. *Economic Geology*, 78: 1605–1618.

Hagemann, S.G., & Cassidy, K.F., 2000. Archaean orogenic gold deposits. *Reviews in Economic Geology*, 13: 9–68.

Hagemann, S.G., Groves, D.I., Ridley, J.R. & Vearncombe, J.R., 1992. The Archaean Lode Gold Deposits at Wiluna, Western Australia: High-level Brittle-Style Mineralisation in a Strike-Slip Regime. *Economic Geology*, 87: 1022–1053.

Hagemann, S.G. & Lüders, V., 2003. P-T-X conditions of hydrothermal fluids and precipitation mechanism of stibnite-gold mineralisation at the Wiluna lode-gold deposits, Western Australia: conventional and infrared microthermometric constraints. *Mineralium Deposita*, 38: 936-952.

Heinrich, C.A., Andrew, A.S. & Knill, M.D., 2000. Regional metamorphism and ore formation: evidence from stable isotopes and other fluid tracers. *Reviews in Economic Geology*, 11: 97–117.

Hemley, J.J., Cygan, G.L., Fein, J.B., Robinson, G.R. & D'Angelo, M., 1992. Hydrothermal ore-forming processes in the light of studies in rock-buffered systems: I. Iron-copper-zinc-lead sulfide solubility relations. *Economic Geology*, 87: 1–22.

Hillier, S. & Velde, B., 1991. Octahedral occupancy and the chemical composition of diagenetic (low-temperature) chlorites. *Clay Mineralogy*, 26: 149–168.

Hinman, M.C., 1992. The structural and geochemical genesis of the Peak base and precious metal deposit, Cobar, New South Wales, Australia. Unpublished PhD thesis, James Cook University of North Queensland, Townsville.

Hemley, J.J., Cygan, G.L., Fein, J.B., Robinson, G.R. & D'Angelo, W.M., 1992. Hydrothermal ore-forming processes in the light of studies in rock-buffered systems: 1. Iron-copper-zinc-lead sulfide solubility relations. *Economic Geology*, 87: 1–22.

Hitzman, M.W. & Valenta, R.K., 2005. Uranium iron oxide-copper-gold (IOGG) systems. *Economic Geology*, 100: 1657–1661.

Ho, S.E., Bennett, J.M., Cassidy, K.F., Hronsky, J.M.A., Mikucki, E.J. & Sang, J.H., 1990. Section 2.1.1: Fluid Inclusion Studies. In Ho, S.E., Groves, D.I. & Bennett, J.M., (Editors) *Gold deposits of the Yilgarn Block, Western Australia: nature, genesis and exploration*

guides. Geology Department (Key Centre) & University Extension, the University of Western Australia, Publication No. 20, p198–211.

Hobb, B.E., Means, W.D. & Williams, P.F., 1976. *An Outline of Structural Geology*. John Wiley & Sons, Inc. New York pp 571.

Hodgson, C.J., 1989. The structure of shear-related, vein-type gold deposits: A review. *Ore Geology Reviews*. 4:231–237.

Hornibrook, M., 1998a. Preliminary outcomes - PIMA mineralogy of gold and copper mineralisation at the New Occidental and New Cobar deposits - Cobar Mineral District, NSW. Peak Gold Mines Report PGM0403 (unpubl.) 7pp.

Hornibrook, M., 1998b. PIMA mineralogy of selected drill holes at the Peak Au-Cu deposit and the Mt Pleasant and Comstock prospects, Cobar Gold Field, NSW. Peak Gold Mines Report PGM0564 (unpubl.) 7pp.

Huston, D.L., 1998. The hydrothermal environment. *AGSO Journal of Australian Geology and Geophysics*. 17(4): 15–30.

Huston, D.L., 2000. Gold in volcanic-hosted massive sulfide deposits: distribution, genesis and exploration. *Society of Economic Geology Reviews*, Volume 13, p401–426.

Huston, D.L. & Large, R.R., 1989. A chemical model for the concentration of gold in volcanogenic massive sulfide deposits. *Ore Geology Reviews*, 4: 171–200.

Huston, D.L., Power, M., Gemmell, J.B. & Large, R.R., 1995. Design, calibration and geological application of the first operational Australian laser ablation sulfur isotope microprobe. *Australian Journal of Earth Sciences*, 42: 549–555.

Hutcheon, I., de Caritat, P. & Abercrombie, H.J., 1994. Clay minerals – equilibrium models and temperature indicators. In: Lentz, D.R. (editor). *Alteration and Alteration Processes Associated with Ore-Forming Processes. Short Course Notes Volume 11*, Geological Association of Canada, p43–68.

Jenkins, D.M. & Chernosky, J.V., 1986. Phase equilibria and crystallochemical properties of Mg-chlorite. *American Mineralogist*, 71: 924–936.

Jiang, W.T., Peacor, D.R. & Buseck, P.R., 1994. Chlorite geothermometry? – contamination and apparent octahedral vacancies. *Clays and Clay Minerals*, 42(5) 593–605.

Jiang, Z., 1996. Geochemical studies of the Peak and Chesney Gold Deposits, Cobar, NSW, Australia. Unpublished PhD Thesis, University of Newcastle.

Jiang, Z., Seccombe, P.E., Andrew, A.S. & Todd, A., 1995. Sulfur and carbon isotope variations in the Peak Gold Mine, Cobar, NSW: Implications for a mixed source of components. In: Seccombe, P.K. & Ashley, P.M. (editors) *Centre for Isotope Studies, Research Report 1993–94*, pp 61–70.

Jiang, Z. & Seccombe, P.E., 1995. Pb and Sr isotope characteristics of mineralisation and host rocks, and new ages for igneous activity and mineralisation, Peak mine, Cobar, NSW. In: Seccombe, P.K. & Ashley, P.M. (editors) *Centre for Isotope Studies, Research Report 1993–94*, pp 76–81.

Jiang, Z., Seccombe, P.E., Andrew, A.S. & Todd, A., 1995. Stable isotope signature of the Chesney Cu-Au vein deposit, Cobar, NSW. In: Seccombe, P.K. & Ashley, P.M. (editors) *Centre for Isotope Studies, Research Report 1993–94*, pp 82–87.

Jiang, Z. & Seccombe, P.K., 2000. Source of ore-forming components at the Peak mine, Cobar, NSW: evidence from isotope studies. In: McQueen, K.G. & Stegman, C.L. (editors). *Central West Symposium Cobar 2000. Geology, Landscapes and Mineral Exploration. Extended Abstracts*, pp 41–45.

Kavalieris, I., Walshe, J.L., Halley, S. & Harrold, B.P., 1990. Cone-related gold mineralisation in the Pani Volcanic Complex, North Sulawesi, Indonesia: A study of geologic relations, fluid inclusions and chlorite composition. *Economic Geology*, 85: 1208–1225.

Kelso, I.J., 1982. The geology of the Queen Bee copper mine, Cobar, New South Wales. Unpublished B. Appl. Sci. thesis, Sydney, New South Wales Institute of Technology.

Kerrich, R., 1989. Geodynamic setting and hydraulic regimes: shear zone hosted mesothermal gold deposits. In: Burstall, J.T. (Editor), *Mineralisation and Shear Zones, Geological Society of Canada, Short Course Notes Volume 6*: 89–128.

Kerrich, R., Goldfarb, R., Groves, D. & Garwin, S., 2000. The geodynamics of world-class gold deposits: characteristics, space-time distribution, and origins. *SEG Reviews,* 13: 501–551.

Kolonin, G.R., 1979. Native bismuth as a geological thermometer IV. The existence of a stability field of metallic bismuth at temperatures above its boiling point. In Angino, E.E. & Long, D.T., (editors) *Geochemistry of Bismuth*. Dowden, Hutchinson & Ross, Pennsylvania, p 401–407.

Kranidiotis, P. & MacLean, W.H., 1987. Systematics of chlorite alteration at the Phelps Dodge massive sulfide deposit, Matagami, Quebec. *Economic Geology*, 82: 1898–1911.

Large, R.R., 1992. Australian volcanic-hosted massive sulfide deposits: features, styles and genetic models. *Economic Geology,* 87: 471–510.

Large, R.R., Bull, S.W. & McGoldrick, P.J., 2000. Lithogeochemical halos and geochemical vectors to stratiform sediment hosted Zn-Pb-Ag deposits, Part 2. HYC deposit, McArthur River, Northern Territory. *Journal of Geochemical Exploration*, 68: 105–126.

Large, R.R., Huston, D.L., McGoldrick, P.J., Ruxton, P.A. & McArthur, G., 1989. Gold distribution and genesis in Australian volcanogenic massive sulfide deposits and their significance for gold transport models. *Economic Geology Monograph No. 6*, p 520–536.

Large, R.R., McPhie, J., Gemmell, J.B., Hermann, W. & Davidson, G.J., 2001. The spectrum of ore deposit types, volcanic environments, alteration halos, and related exploration vectors in submarine volcanic successions: some examples from Australia. 2001. *Economic Geology,* 96: 913–938.

Lawrie, K.C., 1991a. The Cobar base metal deposits, N.S.W. In: Lawrie, H.F.C. (editor), *Base metals symposium. James Cook University, Economic Geology Research Unit, Contribution 38*, 137–143.

Lawrie, K.C., 1991b. Metal zoning and fluids in the Elura orebodies, N.S.W.: Implications for formation of syntectonic massive sulfide orebodies. *Bureau of Mineral Resources, Australia, Record 1990/95*, 52 (Abstract).

Lawrie, K.C. & Hinman, M.C., 1998. Cobar-style polymetallic Au-Cu-Ag-Pb-Zn deposits. *AGSO Journal of Geology & Geophysics*, 17(4), pp 169–187.

Lawrie, K.C., Mernagh, T.P., Boreham, C.J. & Logan, G.A., 1999. Evidence for possible zinc transport in hydrocarbon-bearing (C_1–C_9) fluids in the formation of Cobar-style deposits. *AGSO Research Newsletter*, 31:17–19.

Lawrie, K.C., Mernagh, T.P. & Hinman, M.C., 1999. Hydrocarbons and fluid mixing in the formation of Cobar-style deposits. In: Stanley et al. (editors). Mineral Deposits: Processes to Processing – Proceedings of the 5th biennial SGA meeting and the 10th quadrennial IACOD meeting, London, 22–25 August, 1999. A.A. Balkema, Rotterdam, pp 243–246.

Leevers, P., 2000. Stratigraphy and controls on mineralisation in the Elura orebody. In: McQueen, K.G. & Stegman, C.L. (editors). *Central West Symposium Cobar 2000. Geology, Landscapes and Mineral Exploration. Extended Abstracts*, pp 46–47.

Lorrigan, A.N., 2000. Distribution of the Elura lag anomaly. In: McQueen, K.G. & Stegman, C.L. (editors). *Central West Symposium Cobar 2000. Geology, Landscapes and Mineral Exploration. Extended Abstracts*, pp 51–54.

Leitch, C.H.B. & Lentz, D.R., 1994. The Gresens Approach to Mass Balance Constraints of Alteration Systems. In: Lentz, D.R. (editor). *Alteration and Alteration Processes Associated with Ore-Forming Processes. Short Course Notes Volume 11*, Geological Association of Canada, pp161–192.

MacLean, W.H. & Barrett, T.J., 1993. Lithogeochemical techniques using immobile elements. *Journal of Geochemical Exploration*, 48: 109–133.

Marshall, B., Giles, A.D. & Hagemann, S.G., 2000. Fluid inclusions in metamorphosed and synmetamorphic (including metamorphogenic) base and precious metal deposits, indications of ore-forming conditions and/or ore-modifying histories? In Spry, P.G, Marshal, B. & Vokes, F.M. (editors), Metamorphosed and Metamorphogenic Ore Deposits, *Reviews in Economic Geology*, 11: 119–148.

McClatchie, L., 1973. The occurrence of Bi in the Lachlan Fold Belt in New South Wales. AusIMM Proceedings. *AusIMM Proceedings*. 28: 27–36.

McCuaig, T.C. & Kerrich, R., 1998. P-T-t-deformation-fluid characteristics of lode gold deposits: evidence from alteration systematics. *Ore Geology Reviews,* 12: 381–453.

McGoldrick, P. & Large, R.R., 1998. Proterozoic stratiform sediment-hosted Zn-Pb-Ag deposits. *AGSO Journal of Geology & Geophysics*, 17(4), pp 189–196.

McQueen, K.G. and Perkins, C., 1995. The nature and origin of granitoid-related gold deposit at Dargue's reef, Major's Creek, New South Wales. *Economic Geology*, 90: 1646–1662.

McQueen, K.G., Cairns, C. & Leah, P.A., 2000. Mineralogical controls on element dispersion in regolith in the Cobar Goldfield, NSW. In: McQueen, K.G. & Stegman, C.L. (editors). *Central West Symposium Cobar 2000. Geology, Landscapes and Mineral Exploration. Extended Abstracts*, pp 55–59.

McQueen, K.G. & Spry, M.J., 2000. Landscape-regolith controls on mineral exploration in the Cobar region of NSW. In: McQueen, K.G. & Stegman, C.L. (editors). *Central West Symposium Cobar 2000. Geology, Landscapes and Mineral Exploration. Extended Abstracts*, pp 65–67.

Mernagh, T.P., 2001. A fluid inclusion study of the Fosterville mine: a turbidite-hosted gold field in the western Lachlan Fold Belt, Victoria, Australia. *Chemical Geology*, 173: 91–106.

Mernagh, T.P. & Bastrakov, E.N., 2000. The source of gold in the western Lachlan Fold Belt: constraints from mass transfer modelling. Geological Society of Australia Abstracts No 59, *15th Australian Geological Convention, Sydney, July 2000*, p 344.

Mikucki, E.J., 1998. Hydrothermal transport and depositional processes in Achaean lode-gold systems: A review. *Ore Geology Reviews,* 13: 307–321.

Mikucki, E.J. and Groves, D.I., 1990. Gold transport and depositional models, In: Ho, S.E, Groves, D.I. and Bennett, J.M. (editors). *Gold deposits of the Archaean Yilgarn Block, Western Australia: Nature, Genesis and Exploration Guides*. Geology Department and University Extension, University of Western Australia Publication No. 20, pp 60–78.

Minster, E.F., 1979. The geochemical properties of the behaviour of bismuth in hypogenic processes. In Angino, E.E. & Long, D.T., (editors) *Geochemistry of Bismuth*. Dowden, Hutchinson & Ross, Pennsylvania, p 268–327.

Miyano, T. & Klein, C., 1989. Phase equilibria in the system K_2O-FeO-Al_2O_3-SiO_2-H_2O-CO_2 and the stability limit of stilpnomelane in metamorphosed Precambrian iron-formations. *Contributions to Mineralogy and Petrology*, 102: 478–491.

Mulholland, C.St.J, and Rayner, E.O., 1961. The Gold-Copper Deposits of Cobar, New South Wales: Central Section (Great Cobar to New Occidental). *New South Wales Department of Mines Technical Report 6 for 1958*, pp 28–48.

Neall, F.B. & Phillips, G.N., 1987. Fluid – wall rock interaction in an Achaean hydrothermal deposit: a thermodynamic model for the Hunt mine, Kambalda. *Economic Geology*, 82: 1679–1694.

Nesbitt, B.E., Murowchick, J.B. and Muehlenbachs, K., 1986. Dual origins of lode gold deposits in the Canadian Cordillera. *Geology*, 14: 506–509.

Nesbitt, B.E. and Muehlenbachs, K., 1989. Geology, geochemistry, and genesis of mesothermal lode gold deposits of the Canadian Cordillera: Evidence for ore formation from evolved meteoric water. In: Skinner, B. (editor) *Economic Geology Monograph 6, The Geology of Gold Deposits*: The Perspective in 1988: 553–563. Economic Geology Publishing Company.

Neumayr, P., Hagemann, S.G. & Couture, J.F., 2000. Structural setting, textures, and timing of hydrothermal vein systems in the Val d'Or camp, Abitibi, Canada: implications

for the evolution of transcrustal, second- and third-order fault zones and gold mineralisation. *Canadian Journal of Earth Sciences*, 37: 95–114.

Nguyen, P.T., Cox, S.F., Harris, L.B. & Powell, C.McA., 1998. Fault-valve behaviour in optimally oriented shear zones: an example at the Revenge gold mine, Kambalda, Western Australia. *Journal of Structural Geology*, 20 (12): 1625–1640.

Okamoto, H. & Massalski, T.B., 1983. The Au-Bi (gold-bismuth) system. *Bulletin of Alloy Phase Diagrams*, 4: 401–407.

Ohmoto, H., (1986). Stable isotope geochemistry of ore deposits. *Reviews in Mineralogy* 16: 551–578.

Ohmoto, H. & Rye, R.O. 1979. Isotopes of sulfur and carbon. In Barnes, H.L. (editor) *Geochemistry of hydrothermal ore deposits*, Wiley, New York, p 509–567.

Oliver, N.H.S., Ord, A., Valenta, R.K. & Upton, P., 2001. Deformation, fluid flow, and ore genesis in heterogeneous rocks, with examples and numerical models from the Mount Isa district, Australia. In: Richards, J.P. & Tosdal, R.M. (Editors) *Structural Controls on Ore Genesis: Reviews in Economic Geology, Volume 14* Society of Economic Geologists. pp 51–74.

Paar, W.H., Putz, H., Topa, D., Roberts, A.C., Stanley, C.J. and Culetto, F.J., 2006. Jonassonite Au(Bi,Pb)5S4, a new mineral species from Nagybörszsöny, Hungary. *The Canadian Mineralogist*, 44: 1127–1136.

Parry, W.T., 1986. Estimation of X_{C0_2}, P and fluid inclusion volume from fluid inclusion temperature measurements in the system NaCl-CO_2-H_2O. *Economic Geology*, 81:1009-1013.

Perkins, C., Hinman, M.C., and Walshe, J.L., 1994. Timing of mineralisation and deformation, Peak Au mine, Cobar, New South Wales. *Australian Journal of Earth Sciences*, 41:509–522.

Perkins, C., Walshe, J.L., and Morrison, G., 1995. Metallogenic Episodes of the Tasman Fold Belt System, Eastern Australia. *Economic Geology*. 90: 1443–1466.

Philips, G.N., 1986. Geology and alteration in the Golden Mile, Kalgoorlie. *Economic Geology*, 81: 779–808.

Potter, R.W., Clynne, M.A. & Brown, D.L., 1978. Freezing point depression of aqueous sodium chloride solutions. *Economic Geology* 73, 284–285.

Priestly, M., 2000. The Perseverance deposit, Cobar Goldfield. Internal Peak Gold Mines report (unpubl.).

Ramboz, C., Pichavant, M., Weisbrod, A., 1982. Fluid immiscibility in natural processes: use and misuse of fluid inclusion data: II. Interpretation of fluid inclusion data in terms of immiscibility. *Chemical Geology*, 37: 29–48.

Ramsay, J.G., 1980a. The crack-seal mechanism of rock deformation. *Nature*, 284: 135–139.

Ramsay, J.G., 1980b. Shear zone geometry: a review. *Journal of Structural Geology*, 2(1–2): 83–99.

Ramsay, J.G., Bierlein, F.P., Arne, D.C. & VandenBerg, A.H.M., 1998. Turbidite-hosted gold deposits of Central Victoria, Australia: their regional setting, mineralisation styles, and some genetic constraints. *Ore Geology Reviews*, 13: 131–151.

Ramsay, J.G. & Huber, M.I., 1983. *The Techniques of Modern Structural Geology*. Academic Press, London, 307pp.

Rayner, E.O., 1969. The copper ores of the Cobar region. New South Wales Geological Survey Memorandum, 10, 131pp.

Reuter, A. & Dallmeyer R.D., 1989. K-Ar and $^{40}Ar/^{39}Ar$ dating of cleavage formed during very low-grade metamorphism: a review. *In:* Daly J.S., Cliff, R.A. & Yardley B.W.D. eds. *Evolution of Metamorphic Belts*, pp. 161–171. Geological Society of London Special Publication 43.

Reynolds, I.M., 1998. Mineralogy and Ore Petrography of Gold-Bismuth Ores in the New Occidental Gold Deposit, Cobar, New South Wales, Australia. Unpublished Rio Tinto Technology Development Limited Report (BR2823).

Reynolds, I.M., 1999a. New Occidental Deposit: Mineralogy and Ore Petrography of a Second Suite of Complex Gold-Bismuth Ores. Unpublished Rio Tinto Technology Development Limited Report (R2864).

Reynolds, I.M., 1999b. Mineralogy and Ore Petrography of a Suite of Samples from the Perseverance Gold Deposit, Cobar, New South Wales, Australia. Unpublished Rio Tinto Technology Development Limited Report (BR2885).

Reynolds, I.M., 2000a. Peak Gold Mine: Mineralogy and Ore Petrography of Five Gold Ore Types. Unpublished Rio Tinto Technology Development Limited Report (BR2918).

Reynolds, I.M., 2000b. Mineralogy and Ore Petrography of a Second Suite of Samples from the Perseverance Gold Deposit, Cobar, New South Wales, Australia. Unpublished Rio Tinto Technology Development Limited Report (BR2974).

Reynolds, I.M., 2001. Mineralogy of Four Ore Samples from the New Occidental Gold Deposit, Cobar, New South Wales, Australia. Unpublished Rio Tinto Technology Development Limited Report.

Ridley, J.R. & Diamond, L.W., 2000. Fluid chemistry of orogenic lode gold deposits and implications for genetic models. *SEG Reviews* 13: 141–162.

Robert, F., 1990. Structural setting and control of gold-quartz veins of the Val D'Or area, southeastern Abitibi Subprovince. In: Ho, S.E., Robert, F. & Groves, D.I., (compilers) Gold and Basemetal Mineralisation in the Abitibi Subprovince, Canada, with Emphasis on the Quebec Segment. Short Course Notes, Geology Key Centre and University Extension, The University of Western Australia, Publication No. 24: 167–210.

Robert, F., Boullier, A. & Firdaous, K., 1995. Gold-quartz veins in metamorphic terranes and their bearing on the role of fluids in faulting. *Journal of Geophysical Research*, 100 (B7): 12,861–12,879.

Robert, F & Brown, A.C., 1986. Achaean gold-bearing quartz veins at the Sigma Mine, Abitibi Greenstone Belt, Quebec: Part II. Vein paragenesis and hydrothermal alteration. *Economic Geology*, 81: 593–616.

Robert, F. & Poulsen, K.H., 1997. World-class Archaean gold deposits in Canada: An overview. *Australian Journal of Earth Sciences*, 44: 329–351.

Robert, F. & Poulsen, K.H., 2001. Vein Formation and Deformation in Greenstone Gold Deposits. In: Richards, J.P. & Tosdal, R.M. (Editors) *Structural Controls on Ore Genesis: Reviews in Economic Geology, Volume 14* Society of Economic Geologists. pp 111–152.

Robertson, I.D.M., 1974. The Environmental Features and Petrogenesis of the Mineral Zones of Cobar, N.S.W. Unpublished Ph.D. Thesis, Uni New England.

Robertson, I.D.M. & Taylor, G.F., 1987. Depletion haloes in fresh rocks surrounding the Cobar orebodies, N.S.W., Australia: Implications for exploration and ore genesis. *Journal of Geochemical Exploration*, 27: 77–101

Roedder, E., 1997. Fluid inclusion studies of hydrothermal ore deposits. In: Barnes, H.L. (editor), *Geochemistry of hydrothermal ore deposits*, New York, Wiley, pp 657–698.

Rutherford, N.F., 2000. Geochemistry in the weathered profile, Cobar, NSW. In: McQueen, K.G. & Stegman, C.L. (editors). *Central West Symposium Cobar 2000. Geology, Landscapes and Mineral Exploration. Extended Abstracts*, pp 87–93.

Rye, R.O. & Ohmoto, H., 1974. Sulfur and carbon isotopes and ore genesis: a review. *Economic Geology*, 69:826–842.

Sangster, D.F., 1979. Evidence of an exhalative origin for deposits of the Cobar district, New South Wales. *BMR Journal,* 4 (1): 15–24.

Scheibner, E., 1976. Explanatory notes on the tectonic map of New South Wales. Geological Survey New South Wales., Sydney.

Schmidt, B.L., 1980. Geology of the Elura Ag-Pb-Zn deposit, Cobar district, N.S.W. Unpublished M.Sc. thesis, Australian National University, Canberra.

Schmidt, B.L., 1990. Elura zinc-lead-silver deposit, Cobar, in (Editor F.E. Hughes) *Geology of the Mineral Deposits of Australia and Papua New Guinea*, pp 1329–1336, The Australasian Institute of Mining and Metallurgy, Melbourne.

Schmidt, D., Livi, K.J.T. & Frey, M., 1999. Reaction progress in chloritic material: an electron microbeam study of the Taveyanne greywake, Switzerland. *Journal of Metamorphic Geology*, 17: 229–241.

Scott, A.K. & Phillips, K.G., 1990. C.S.A copper-lead-zinc deposit, Cobar, in Editor F.E. Hughes) *Geology of the Mineral Deposits of Australia and Papua New Guinea*, pp 1337–1343, The Australasian Institute of Mining and Metallurgy, Melbourne.

Scott, K.M., 2000. Element mobilities during the weathering of the Elura Zn-Pb-Ag orebody – the influence of mineralogy. In: McQueen, K.G. & Stegman, C.L. (editors). *Central West Symposium Cobar 2000. Geology, Landscapes and Mineral Exploration. Extended Abstracts*, pp 94–97.

Scott, R.J. & Berry, R.E., 2004. A new method for obtaining and quantifying the reliability of structural data from axially-oriented drill core using a fabric of known orientation. *Journal of Structural Geology*, 26: 643–658.

Seccombe, P.K., 1985. Sulfur isotopes and ore genesis at the CSA and Elura mines, Cobar N.S.W. Second Australian Stable Isotope Conference (Abstracts Volume) Macquarie University, North Ryde, 26–27 August, 1985.

Seccombe, P.K., 1990. Fluid Inclusion and sulfur isotope evidence for syntectonic mineralisation at the Elura Mine, southeastern Australia. *Mineralium Deposita*, 25: 304–313.

Seccombe, P.K. & Brill, B.A., 1989. Fluid inclusion and S, O, H and C isotopic evidence for metamorphic Cu, Zn, Pb and Au formation at Cobar, NSW, Australia. *28th International Geological Congress, Abstracts* 3: 66.

Seccombe, P.K., Lau, J.L., Lea, J.F. & Offler, R., 1984. Geology and ore genesis of silver-lead-zinc-copper sulfide deposits, Sunny Corner, N.S.W. *Proceedings of the Australasian Institute of Mining and Metallurgy*, 289: 51–57.

Seward, T.M., 1973. Thio complexes of gold and the transport of gold in hydrothermal ore solutions. *Geochimica et Cosmochhimica Acta*, 37: 370–399.

Sharpe, R. & Gemmell, J.B., 2000. Sulfur isotope characteristics of the Achaean Cu-Zn Gossan Hill VHMS deposit, Western Australia. Mineralium Deposita, 35: 533–550.

Shepherd, T.J., Rankin, A.H. & Alderton, D.H.M., 1985. A practical guide to fluid inclusion studies. Blackie, London, 239 pp.

Sheppard, S., Walshe, J.L. and Pooley, G.D., 1995. Noncarbonate, skarnlike Au-Bi-Te mineralisation, Lucky Draw, New South Wales, Australia. *Economic Geology*, 90: 1553–1569.

Shi, B.L. & Reed, G.C., 1998. CSA copper-lead-zinc deposit, Cobar. In: Berkman, D.A. & Mackenzie, D.H. (editors) *Geology of Australian and Papua New Guinean Mineral Deposits.* The Australasian Institute of Mining and Metallurgy, pp 601–608.

Sibson, R.H., 1986. Brecciation processes in fault zones: Inferences from earthquake rupturing. *Pure Applied Geophysics*, 124: 159–175.

Sibson, R.H., 1992. Implications of fault-valve behaviour for rupture nucleation and recurrence. *Tectonophysics*, 211: 283–293.

Sibson, R.H., 1993. Load-strengthening versus load-weakening faulting. *Journal of Structural Geology*, 15: 123–128.

Sibson, R.H., 2001. Seismogenic Framework for Hydrothermal Transport and Ore Deposition. In: Richards, J.P. & Tosdal, R.M. (Editors) *Structural Controls on Ore Genesis: Reviews in Economic Geology, Volume 14* Society of Economic Geologists. pp 25–47.

Sibson, R.H., Robert, F, & Poulsen, K.H., 1988. High angle reverse faults, fluid pressure cycling, and mesothermal gold deposits. *Geology*, 16: 551–555.

Simms, M.A. & Garven, G., 2004. Thermal convection in faulted extensional sedimentary basins: theoretical results from finite-element modelling. *Geofluids*, 4: 109–130.

Sheppard, S., Walshe, J.L. & Pooley, G.D., 1995. Non-carbonate, skarnlike Au-Bi-Te mineralisation, Lucky Draw, New South Wales, Australia. Economic Geology. 90: 1553–1569.

Smith, J.V., 1992. Experimental kinematic analysis of en-echelon structures in relation to the Cobar Basin, Lachlan Fold Belt. *Tectonophysics*, 214: 269–276.

Solomon, M., Groves, D.I. & Jaques, A.L., 2000. *The Geology and Origin of Australia's Mineral Deposits.* Centre of Ore Deposit Research, University of Tasmania and Centre for Global Metallogeny, University of Western Australia, Printing Authority of Tasmania, Hobart, Australia, 1002pp.

Stanley, C.R. & Madeisky, H.E., 1994. Lithogeochemical exploration for hydrothermal ore deposits using Pearce Element Ratio analysis. In: Lentz, D.R. (editor). *Alteration and Alteration Processes Associated with Ore-Forming Processes. Short Course Notes Volume 11*, Geological Association of Canada, pp193–212.

Stanton, R.L. & Rafter, T.A., 1966. The isotopic constitution of sulfur in some stratiform lead-zinc sulfide ores. Mineralium Deposita, 1:16–19.

Stegman, C.L., 1998. It's all a Matter of Competency – Exploring in the Cobar Gold Field, NSW. *Australian Institute of Geoscientists, Bulletin 23*: 75–82.

Stegman, C.L., 2000. The New Occidental deposit: variation on a theme. In: McQueen, K.G. & Stegman, C.L. (editors). *Central West Symposium Cobar 2000. Geology, Landscapes and Mineral Exploration. Extended Abstracts*, pp 107–112.

Stegman, C.L., 2001a. Cobar Deposits: Still defying classification.

Stegman, C.L., 2001b. How domain boundaries impact on the Resource Estimate – Case Studies based on advanced Projects in the Cobar Gold Field.

Stegman, C.L. and Pocock, J.A., 1996. The Cobar Gold Field – A geological perspective. In: Cook, W.G., Ford, A.J.H., McDermott, J.J., Standish, P.N., Stegman, C.L. & Stegman, T.M. (editors), *The Cobar Mineral Field – A 1996 Perspective.* Australasian Institute of Mining and Metallurgy, Spectrum Series, 3/96, pp 229–264.

Stegman, C.L. and Stegman, T.M., 1996. History of Mining in the Cobar Region. In: Cook, W.G., Ford, A.J.H., McDermott, J.J., Standish, P.N., Stegman, C.L. & Stegman, T.M. (editors), *The Cobar Mineral Field – A 1996 Perspective.* Australasian Institute of Mining and Metallurgy, Spectrum Series, 3/96, pp 3–42.

Sullivan, C.J., 1947. The Geology of the Cobar Mineral Field and its bearing on Prospecting. Dept. of Supply and Shipping, BMR. Geol. and Geophys. Unpublished Report No. 1947/74.

Sullivan, C.J., 1951. Geology of the New Occidental, New Cobar and Chesney mines, Cobar, New South Wales. Bureau of Mineral Resources, Report 6, 45 p.

Sun, S.S., 1983. Implications of Sulfur and Pb isotope data to genesis of massive sulfide in the Cobar area. CSIRO Div. Mineralogy Res. Rev. pp 33–34.

Sun, Y., Jiang, Z., Seccombe, P.K. & Feng, Y., 2000. New dating and a review of previous data for the development, inversion and mineralisation in the Cobar Basin. In: McQueen, K.G. & Stegman, C.L. (editors). *Central West Symposium Cobar 2000. Geology, Landscapes and Mineral Exploration. Extended Abstracts*, pp 113–116.

Sun, Y., Seccombe, P.K., Andrew, A.S. & Todd, A., 2000. Sulfur and carbon isotopic characteristics of the Elura Zn-Pb deposit, Cobar. In (editors): Andrew A.S. & Seccombe, P.K., Centre for Isotopic studies, Research Report 1995–2000, pp59–65.

Sun, Y. & Seccombe, P.K., 2000. Fluid evolution and stable isotope constraints on component sources at the Elura deposit, Cobar. In: McQueen, K.G. & Stegman, C.L. (editors). *Central West Symposium Cobar 2000. Geology, Landscapes and Mineral Exploration. Extended Abstracts*, pp 117–121.

Suppel, D.W. and Gilligan, L.B., 1993. *Nymagee 1:250 000 Metallogenic Map SI/55-2: Metallogenic Study and Mineral Deposit Data Sheets.* 171pp. Geological Survey of New South Wales, Sydney.

Suppel, D.W., Lewis, P.G., Carr, G.R., Dean, J.A. & Glen, R.A., 1990. Gold deposit associations of the Lachlan Fold Belt in New South Wales. Pacific Rim 90 Congress, p 523–532.

Taylor, R.G., 1992. *Ore Textures, Recognition and Interpretation, 1 - Infill textures.* Townsville, James Cook University, Economic Geology Research Unit, 24pp.

Taylor, R.G. & Pollard, P.J., 1993. *Mineralised Breccia Systems: Methods of Recognition and Interpretation.* Townsville, James Cook University, Economic Geology Research Unit, Contribution 46, 32pp.

Thompson, B.P., 1953. Geology and ore occurrence in the Cobar district. In: *Geology of Australian Ore Deposits.* 5th Empire Mining and Metallurgy Congress of Australia and New Zealand, 1:863–896.

Thompson, J.F.H., Sillitoe, R.H., Baker, T., Lang, J.R. & Mortensen, J.K., 1999. Intrusion-related gold deposits associated with tungsten-tin provinces. *Mineralium Deposita*, 34: 323–334.

Titley, S.R., 1994. Evolutionary habits of hydrothermal and supergene alteration in intrusion-centred ore systems: southwestern North America. In Lentz, J.R. (editor) Alteration Processes Associated with Ore-forming systems. Geological Association of Canada, Short Course Notes, 11: 237–260.

Törmänen, T.O. & Koski, R.A., 2005. Gold enrichment and the Bi-Au association in pyrrhotite-rich massive sulfide deposits, Encanaba Trough, Southern Gorda Ridge. *Economic Geology*, 100: 1135–1150.

Van Hook, H.J., 1960. The Ternary System Ag_2S – Bi_2S_3 – PbS. *Economic Geology* 55:759–788.

Vearncombe, J.R., 1993. Quartz vein morphology and implications for formation depth and classification of Archaean gold-vein deposits. *Ore Geology Reviews*, 8: 407–424.

Vearncombe, J.R., 1998. Shear zones, fault networks and Archaean gold. *Geology*, 26: 855–858.

Vidal, O., Parra, T. & Trotet, F., 2001. A thermodynamic model for Fe-Mg aluminous chlorite using data from phase equilibrium experiments and natural pelitic assemblages in the 100°C to 600°C, 1 to 25kb range. *American Journal of Science*, 301: 557–592.

Walshe, J.L., 1986. A six-component chlorite solid solution model and the condition of chlorite formation in hydrothermal and geothermal systems. *Economic Geology*, 81: 681–703.

Walshe, J.L., Heithersay, P.S., and Morrison, G.W., 1995. Toward an Understanding of the Metallogeny of the Tasman Fold Belt System. *Economic Geology*. 90: 1382–1401.

Webster, N.B., 1999. Polaris at Peak. BSc (Hons) Thesis, University of New England, Armidale (unpub).

White, N.C. & Hedenquist, J.W., 1995. Epithermal gold deposits: styles, characteristics and exploration. *Society of Economic Geologists Newsletter*, 23 (1): 9–13.

Wilkinson, J.J. & Johnston, J.D., 1996. Pressure fluctuations, phase separation, and gold precipitation during seismic fracture propagation. *Geology*, 24(5): 395–398.

Wilson, T.C., 1996. Structural Controls on Mineralisation at the New Cobar and Chesney Mine Areas, Cobar, N.S.W. Unpublished BSc (Hons) Thesis, School of Earth Sciences, Flinders University of South Australia.

Wood, S.A., Crerar, D.A. & Borcsik, M.P., 1987. Solubility of the assemblage pyrite-pyrrhotite-magnetite-sphalerite-galena-gold-stibnite-bismuthinite-argentite-molybdenite in H_2O-NaCl-CO_2 solutions from 200 to 350°C. *Economic Geology*, 82: 1864–1887.

Wyman, W.F., 2001. Cambrian granite-related hydrothermal alteration and Cu-Au mineralisation in the southern Mt Read Volcanics, Western Tasmania, Australia. PhD Thesis, University of Tasmania (unpubl.).

Wyman, D.A., Kerrich, R. & Fryer, B.J., 1986. Gold mineralisation overprinting iron formation at the Agnico-Eagle deposit, Quebec, Canada: Mineralogical, microstructural and geochemical evidence. In: Macdonald, A.J. (editor), *Proceedings of Gold '86, an International Symposium on the Geology of Gold.* Konsult International Inc., Toronto. pp. 108–123.

Wilkins, R.W.T & Barkas, J.P., 1978. Fluid inclusions, deformation and recrystallisation in granite tectonites. *Contributions to Mineralogy and Petrology*, 65: 293–299.

Wilkinson, J.J., and Johnstone, J.D., 1996. Pressure fluctuations, phase separation, and gold precipitation during seismic fracture propagation, *Geology*, 24: 395–398.

Xie, X., Byerly, G.R. & Ferrell, R.E., 1997. IIb trioctahedral chlorite form the Barberton greenstone belt: crystal structure and rock composition constraints with implications to geothermometry. *Contributions to Mineralogy and Petrology*, 126: 275–291.

Zane, A., Sassi, R. & Guidotti, C., 1998. New data on metamorphic chlorite as a petrogenetic indicator mineral, with special regard to greenschist-facies rocks. *The Canadian Mineralogist*, 36: 713–726.

Zaw, K. & Dedenczuk, D., 2000. Preliminary mass spectrometric analysis of volatiles in fluid inclusions from the New Occidental deposit, Cobar Gold Field. Report prepared for Peak Gold Mines Pty Limited, CODES SRC, University of Tasmania, Hobart (unpubl.).

Zhao, B., Meyer, F.M., Robb, L.J. & McWha, M., 1994. A preliminary study of alteration associated with the Ventersdorp Contact reef at Western Deep Levels South Mine, Witswatersrand Basin, South Africa. *South African Journal of Geology*, 97(3): 348–356.

Zobak, M.D. & Beroza, G.C., 1993. Evidence for near-frictionless faulting in the 1989 (M 6.9) Loma Prieta, California, earthquake and its aftershocks. *Geology*, 21: 181–185.

Appendix 1: Raw and Calculated Drillhole Structural Data

Appendix 2: Stereographic Nets

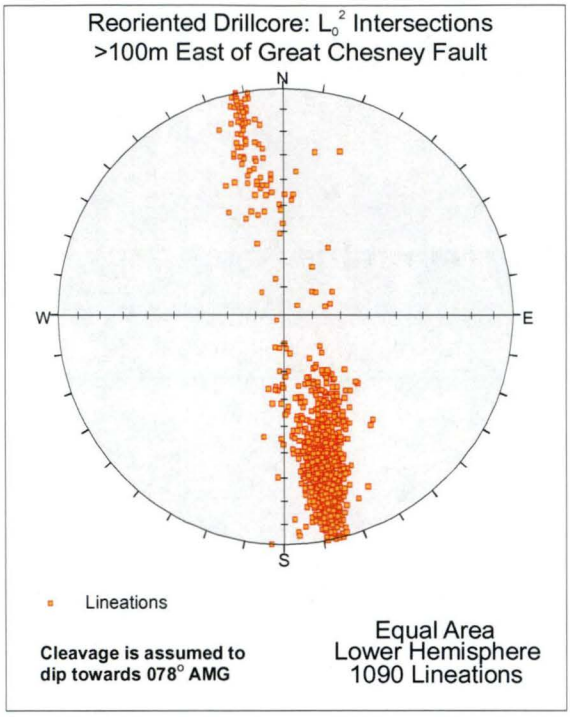
Reoriented Drillcore: L_0^2 Intersections
>100m East of Great Chesney Fault
N
W
E
S
Lineations
Cleavage is assumed to dip towards 078° AMG
Equal Area
Lower Hemisphere
1090 Lineations

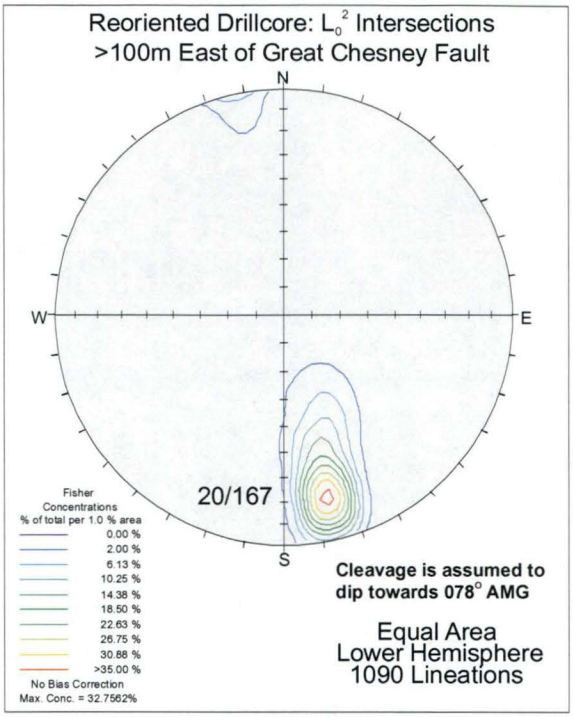
Reoriented Drillcore: L_0^2 Intersections
>100m East of Great Chesney Fault
N
W
E
S
20/167
Fisher Concentrations
% of total per 1.0 % area
0.00 %
2.00 %
6.13 %
10.25 %
14.38 %
18.50 %
22.63 %
26.75 %
30.88 %
>35.00 %
No Bias Correction
Max. Conc. = 32.7562%
Cleavage is assumed to dip towards 078° AMG
Equal Area
Lower Hemisphere
1090 Lineations

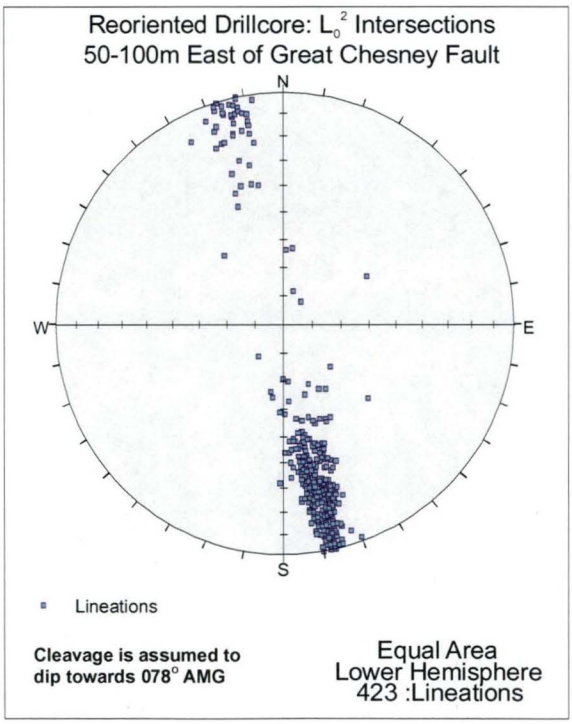
Reoriented Drillcore: L_0^2 Intersections
50-100m East of Great Chesney Fault
N
W
E
S
Lineations
Cleavage is assumed to dip towards 078° AMG
Equal Area
Lower Hemisphere
423 :Lineations

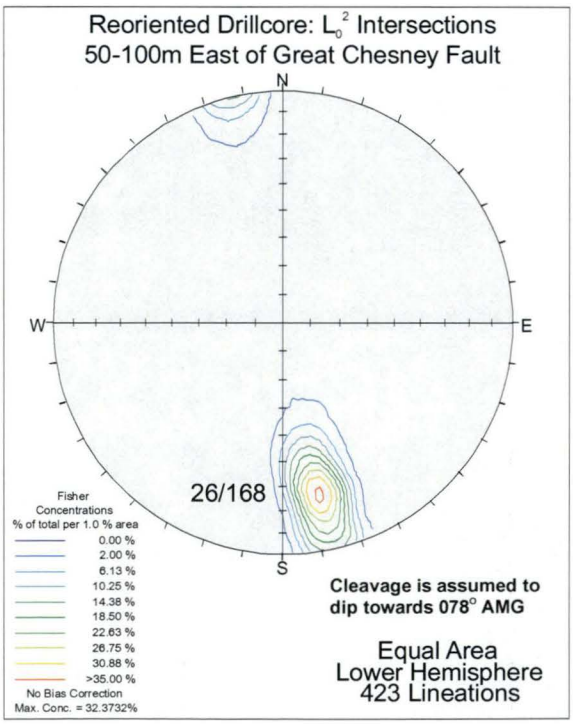
Reoriented Drillcore: L_0^2 Intersections
50-100m East of Great Chesney Fault
N
W
E
S
26/168
Fisher Concentrations
% of total per 1.0 % area
0.00 %
2.00 %
6.13 %
10.25 %
14.38 %
18.50 %
22.63 %
26.75 %
30.88 %
>35.00 %
No Bias Correction
Max. Conc. = 32.3732%
Cleavage is assumed to dip towards 078° AMG
Equal Area
Lower Hemisphere
423 Lineations

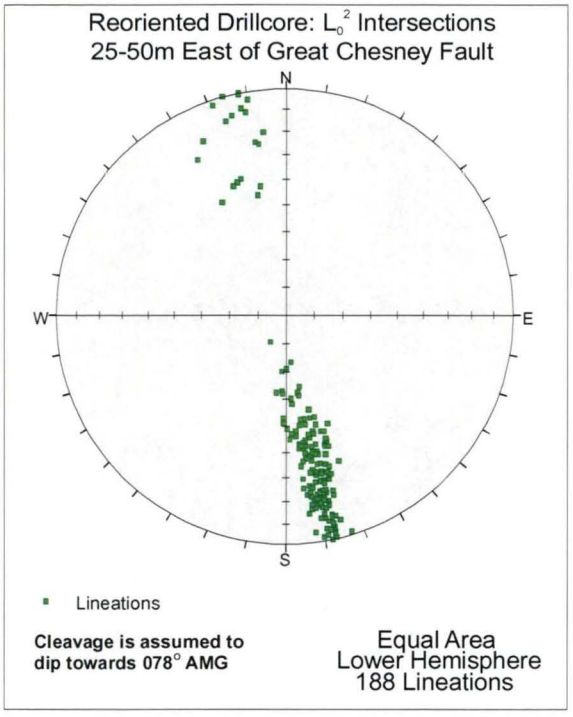
Reoriented Drillcore: L_0^2 Intersections
25-50m East of Great Chesney Fault
N
W
E
S
Lineations
Cleavage is assumed to dip towards 078° AMG
Equal Area
Lower Hemisphere
188 Lineations

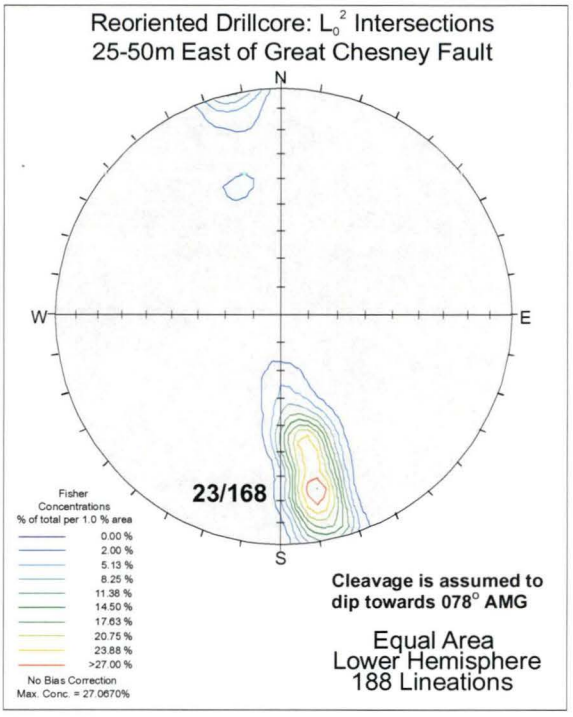
Reoriented Drillcore: L_0^2 Intersections
25-50m East of Great Chesney Fault
N
W
E
S
23/168
Fisher
Concentrations
% of total per 1.0 % area
0.00 %
2.00 %
5.13 %
8.25 %
11.38 %
14.50 %
17.63 %
20.75 %
23.88 %
>27.00 %
No Bias Correction
Max. Conc. = 27.0670%
Cleavage is assumed to dip towards 078° AMG
Equal Area
Lower Hemisphere
188 Lineations

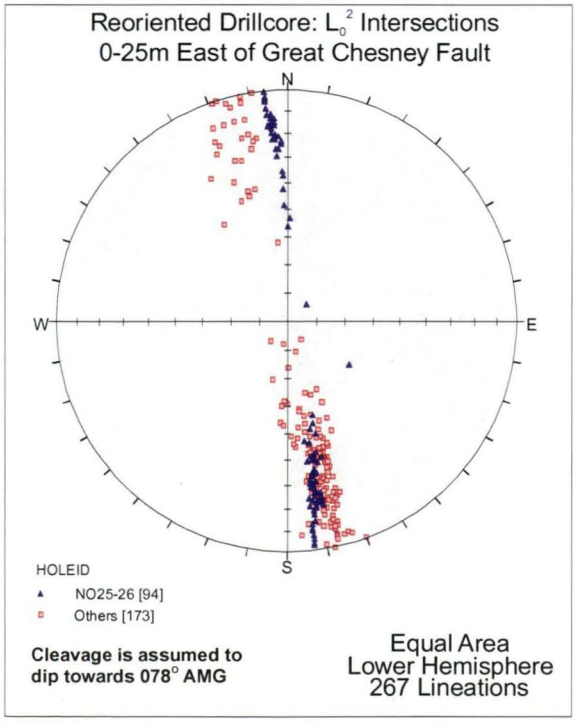
Reoriented Drillcore: L_0^2 Intersections
0-25m East of Great Chesney Fault
N
W
E
S
HOLEID
NO25-26 [94]
Others [173]
Cleavage is assumed to dip towards 078° AMG
Equal Area
Lower Hemisphere
267 Lineations

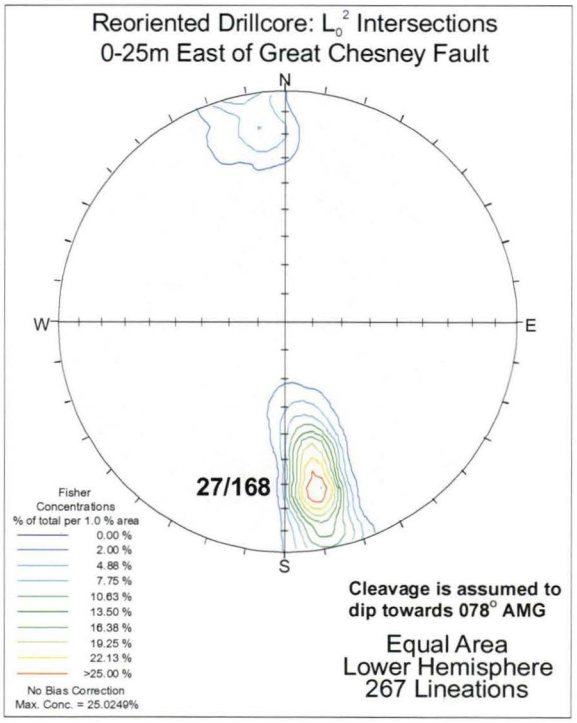
Reoriented Drillcore: L_0^2 Intersections
0-25m East of Great Chesney Fault
N
W
E
S
27/168
Fisher
Concentrations
% of total per 1.0 % area
0.00 %
2.00 %
4.88 %
7.75 %
10.63 %
13.50 %
16.38 %
19.25 %
22.13 %
>25.00 %
No Bias Correction
Max. Conc. = 25.0249%
Cleavage is assumed to dip towards 078° AMG
Equal Area
Lower Hemisphere
267 Lineations

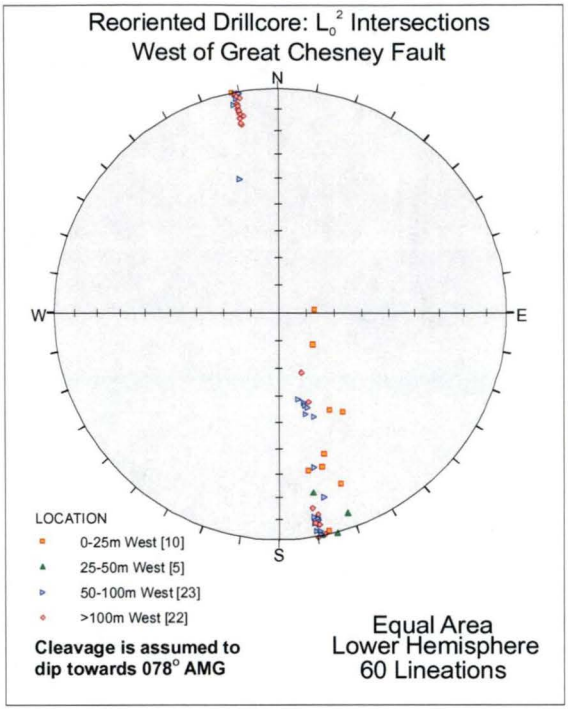
Reoriented Drillcore: L_0^2 Intersections
West of Great Chesney Fault
N
W
E
S
LOCATION
0-25m West [10]
25-50m West [5]
50-100m West [23]
>100m West [22]
Cleavage is assumed to dip towards 078° AMG
Equal Area
Lower Hemisphere
60 Lineations

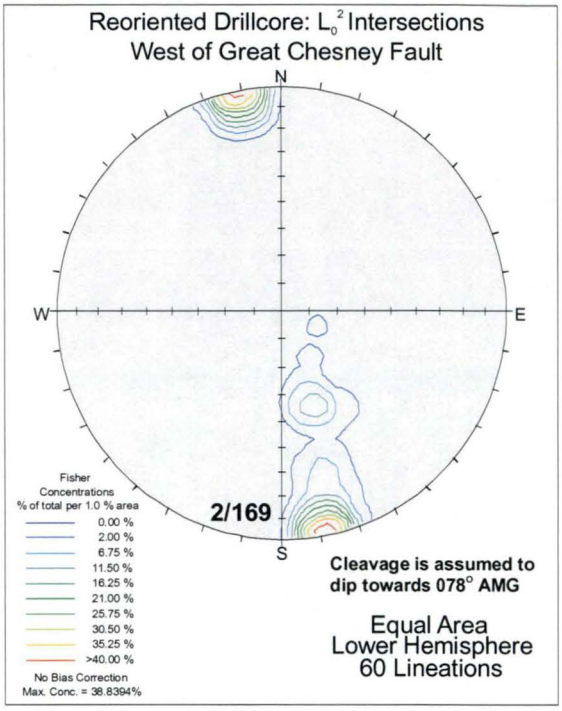
Reoriented Drillcore: L_0^2 Intersections
West of Great Chesney Fault
N
W
E
S
Fisher
Concentrations
% of total per 1.0 % area
0.00 %
2.00 %
6.75 %
11.50 %
16.25 %
21.00 %
25.75 %
30.50 %
35.25 %
>40.00 %
No Bias Correction
Max. Conc. = 38.8394%
2/169
Cleavage is assumed to dip towards 078° AMG
Equal Area
Lower Hemisphere
60 Lineations

Stereonets of reoriented vein measurements from the New Occidental Project drillcore.

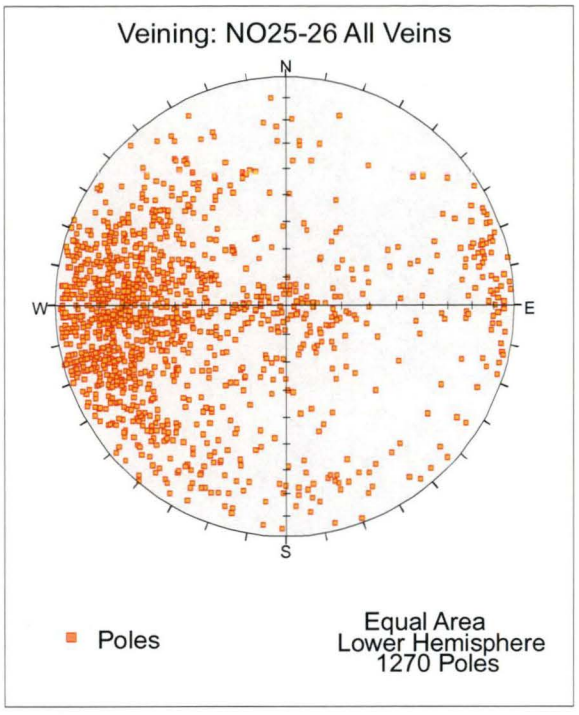

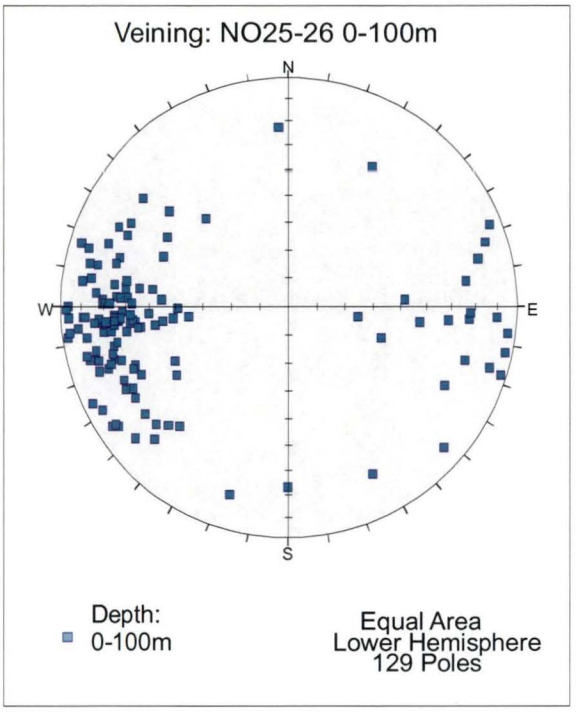

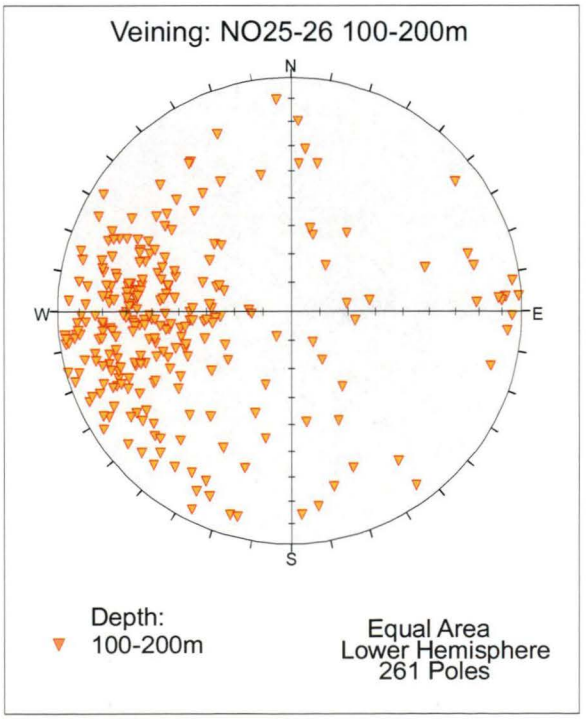

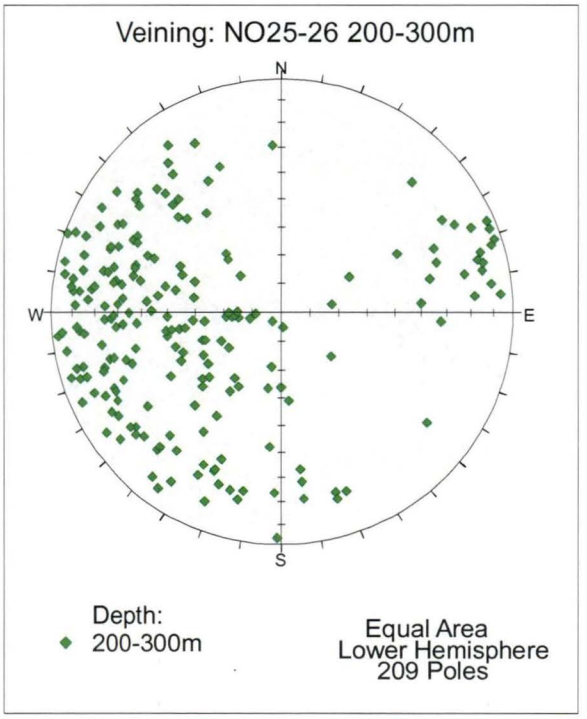

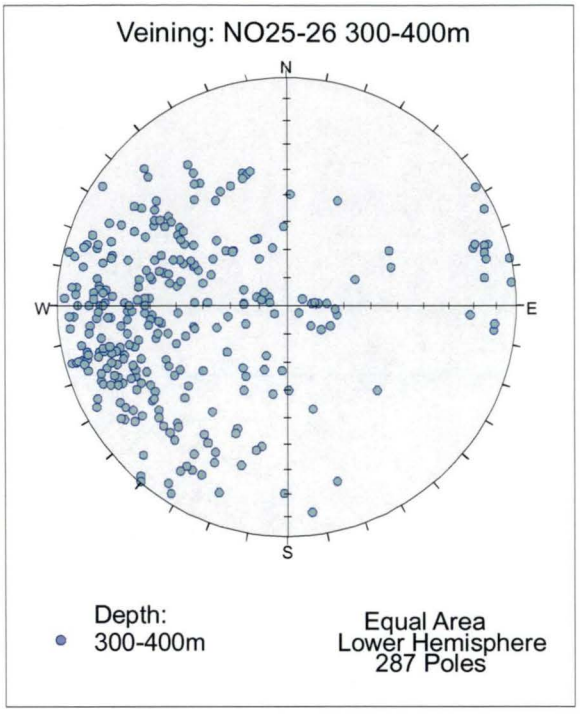
Veining: NO25-26 300-400m
N
W
E
S
Depth:
300-400m
Equal Area
Lower Hemisphere
287 Poles

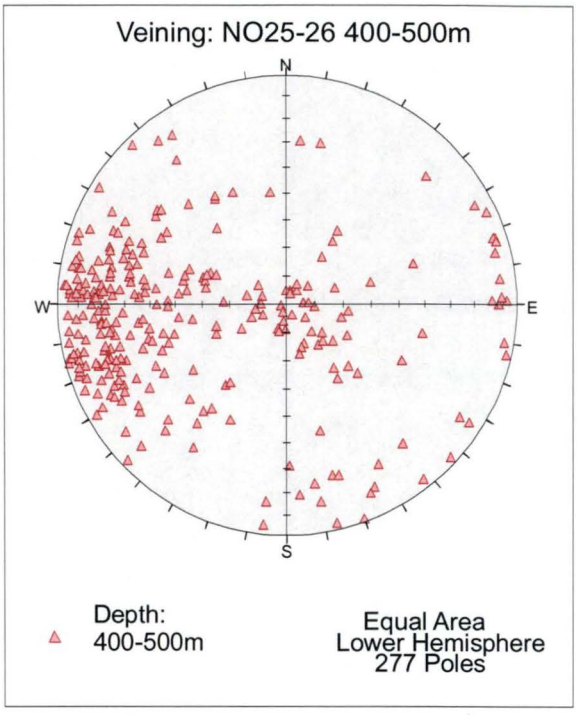
Veining: NO25-26 400-500m
N
W
E
S
Depth:
400-500m
Equal Area
Lower Hemisphere
277 Poles

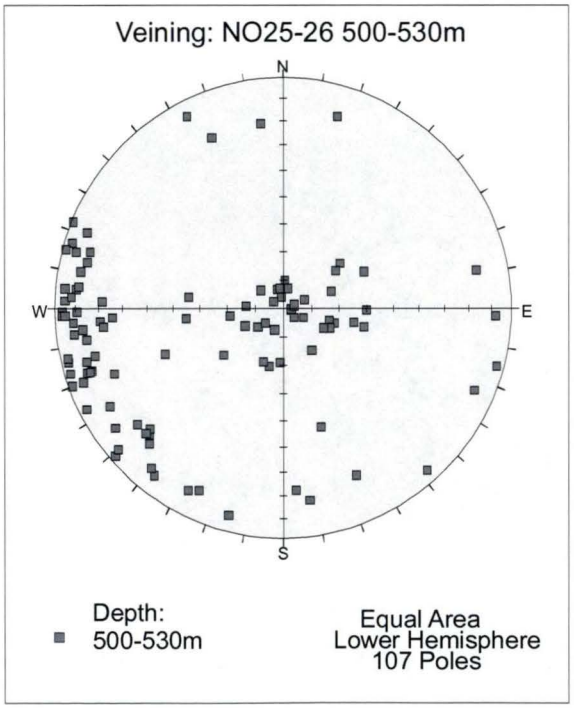
Veining: NO25-26 500-530m
N
W
E
S
Depth:
500-530m
Equal Area
Lower Hemisphere
107 Poles

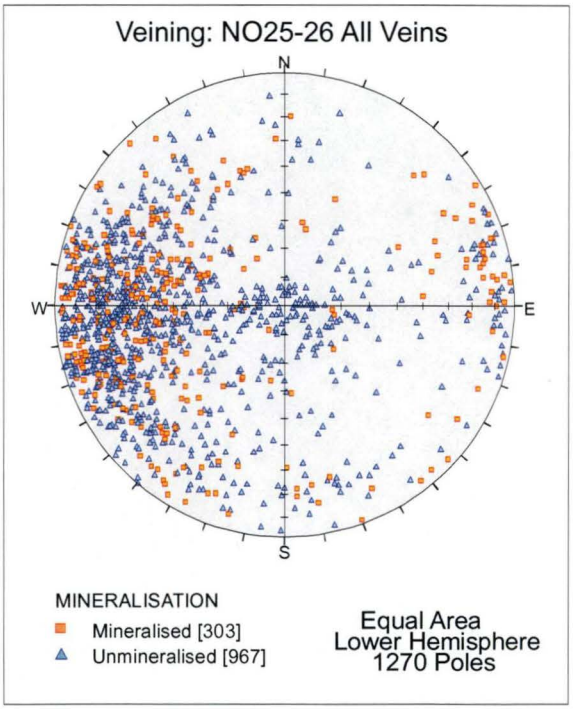
Veining: NO25-26 All Veins
N
W
E
S
MINERALISATION
Mineralised [303]
Unmineralised [967]
Equal Area
Lower Hemisphere
1270 Poles

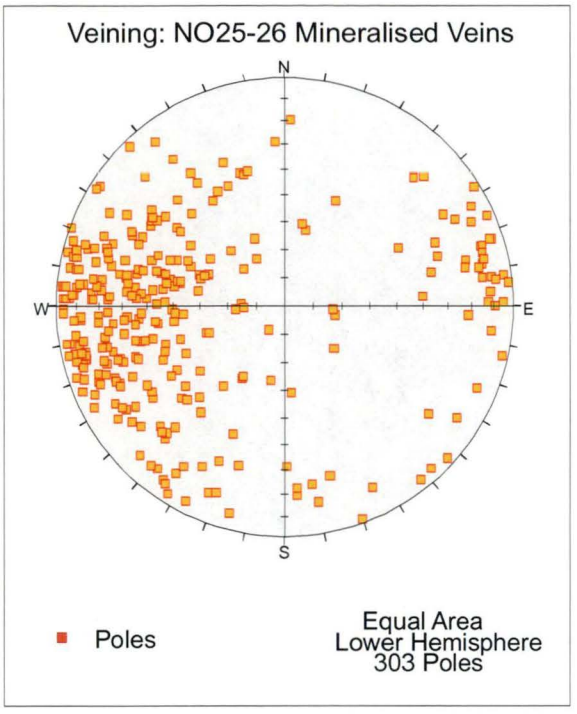
Veining: NO25-26 Mineralised Veins
N
W
E
S
Poles
Equal Area
Lower Hemisphere
303 Poles

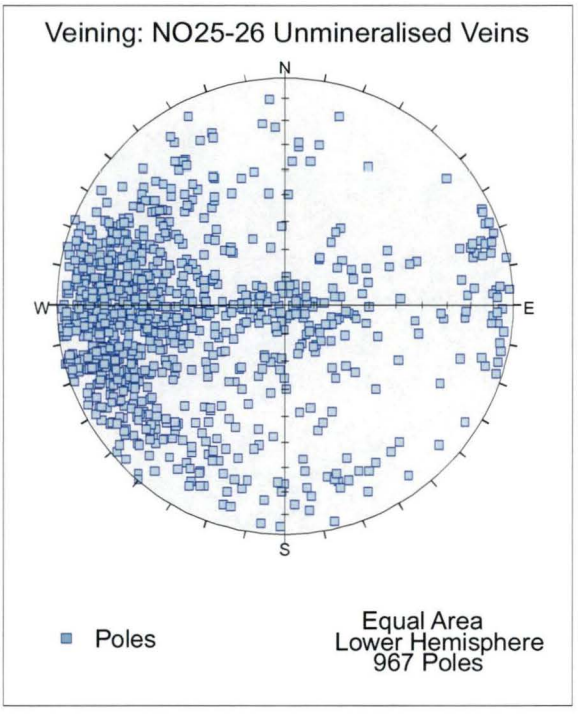
Veining: NO25-26 Unmineralised Veins
N
W
E
S
Poles
Equal Area
Lower Hemisphere
967 Poles

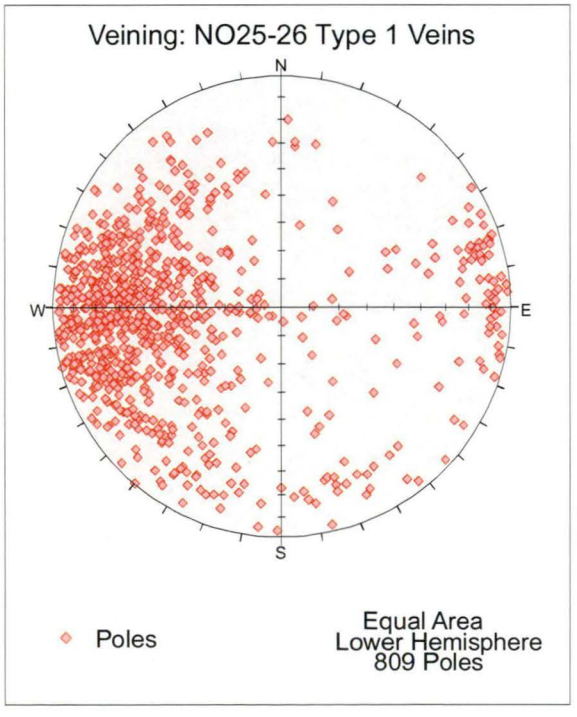
Veining: NO25-26 Type 1 Veins
N
W
E
S
Poles
Equal Area
Lower Hemisphere
809 Poles

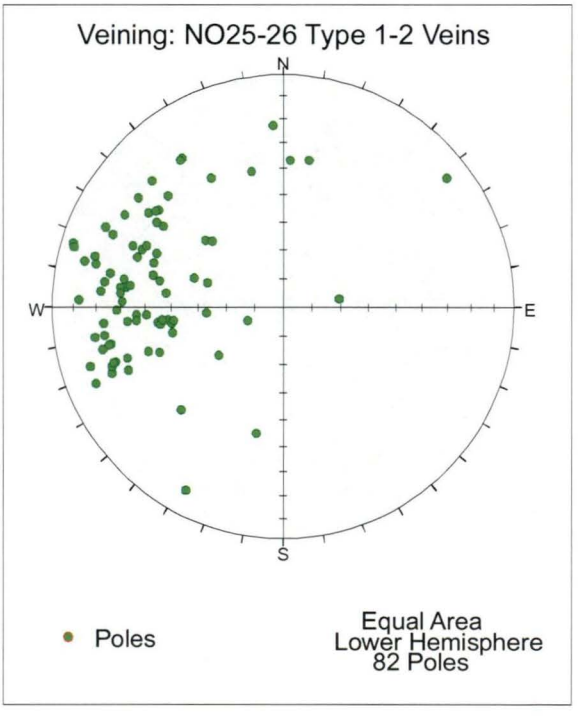
Veining: NO25-26 Type 1-2 Veins
N
W
E
S
Poles
Equal Area
Lower Hemisphere
82 Poles

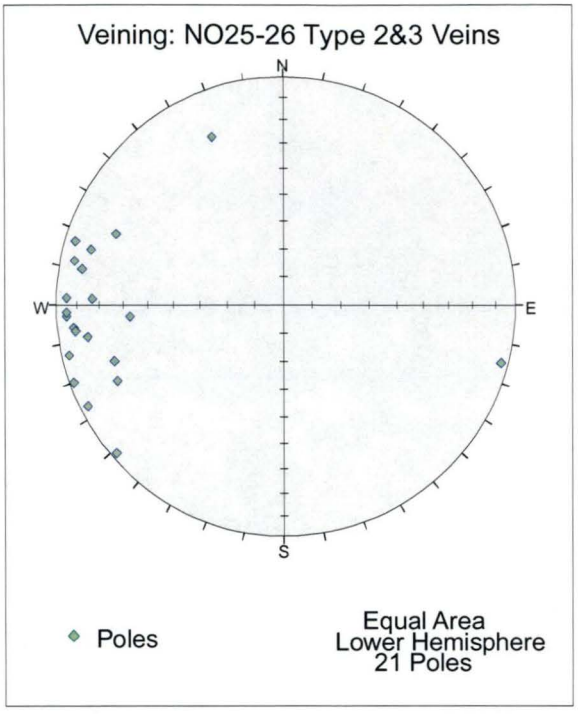
Veining: NO25-26 Type 2&3 Veins
N
W
E
S
Poles
Equal Area
Lower Hemisphere
21 Poles

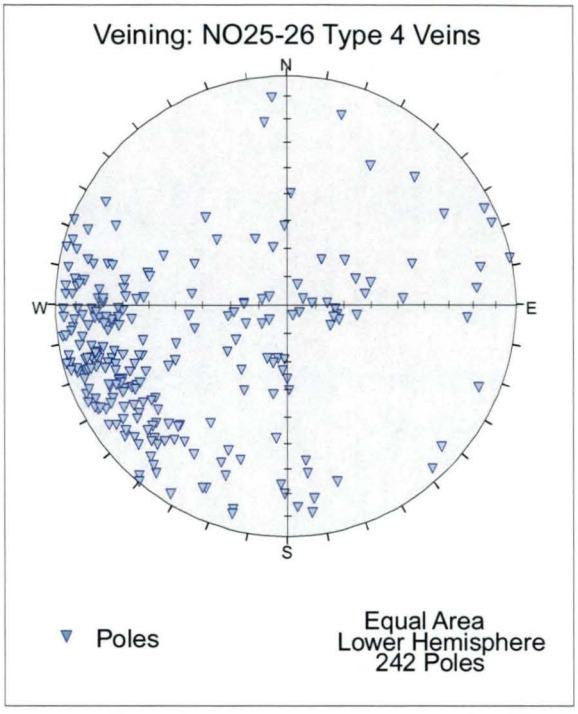
Veining: NO25-26 Type 4 Veins
N
W
E
S
Poles
Equal Area
Lower Hemisphere
242 Poles

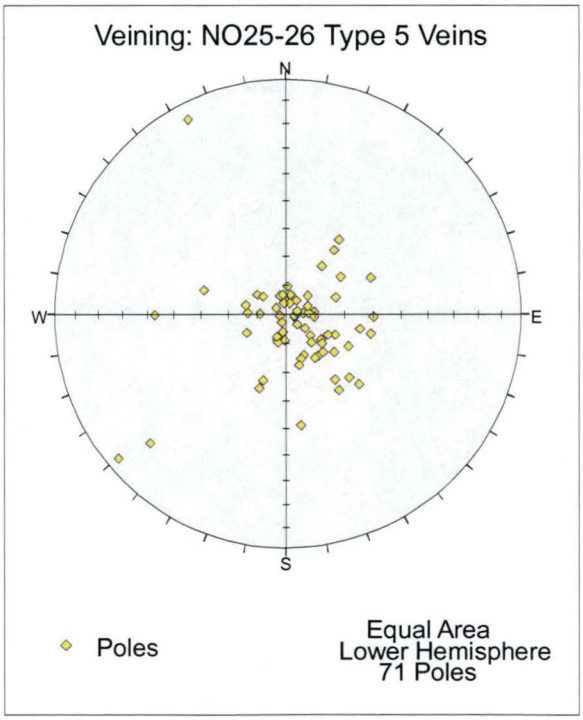
Veining: NO25-26 Type 5 Veins
N
W
E
S
Poles
Equal Area
Lower Hemisphere
71 Poles

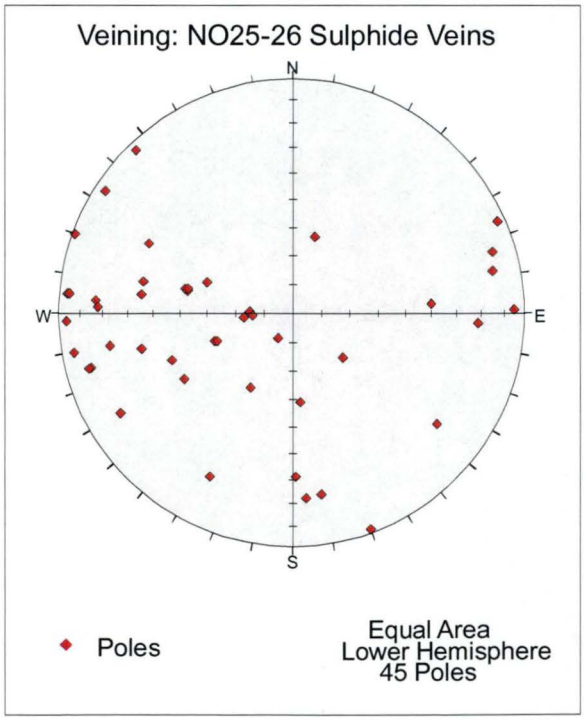
Veining: NO25-26 Sulphide Veins
N
W
E
S
Poles
Equal Area
Lower Hemisphere
45 Poles

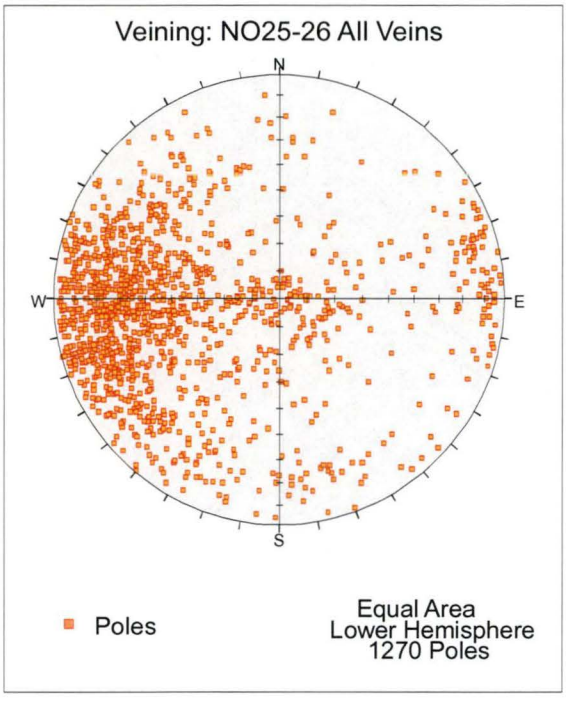
Veining: NO25-26 All Veins
N
W
E
S
Poles
Equal Area
Lower Hemisphere
1270 Poles

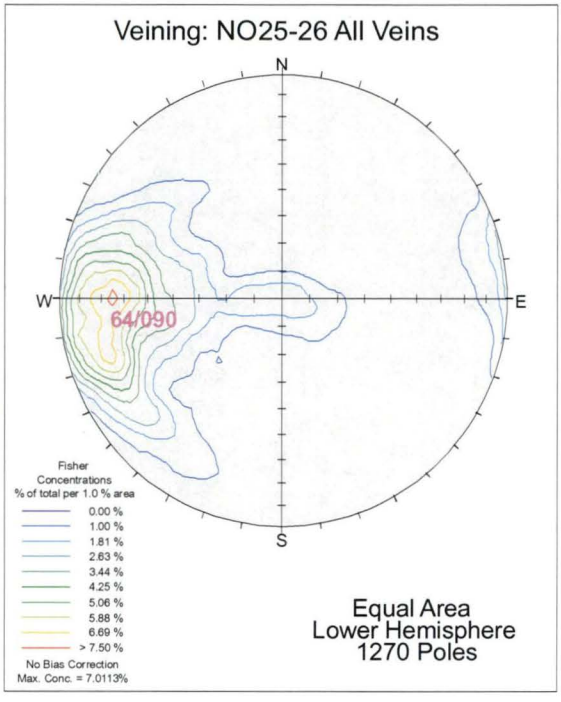
Veining: NO25-26 All Veins
N
W
E
S
64/090
Fisher
Concentrations
% of total per 1.0 % area
0.00 %
1.00 %
1.81 %
2.63 %
3.44 %
4.25 %
5.06 %
5.88 %
6.69 %
> 7.50 %
No Bias Correction
Max. Conc. = 7.0113%
Equal Area
Lower Hemisphere
1270 Poles

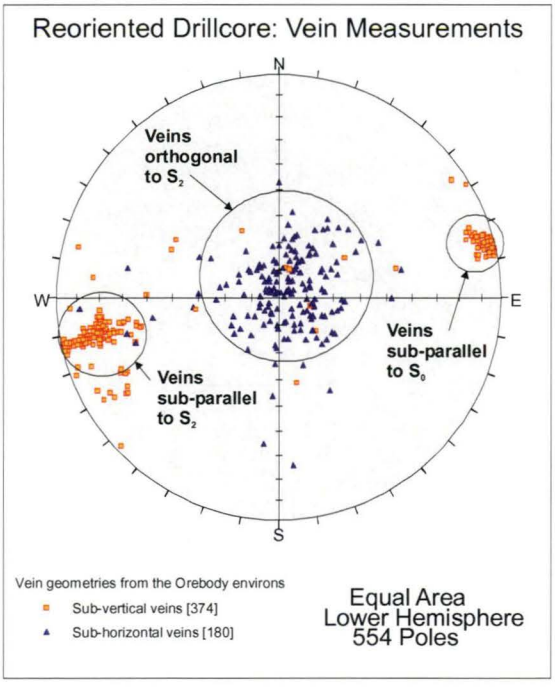
Reoriented Drillcore: Vein Measurements
N
W
E
S
Veins
orthogonal
to S2
Veins
sub-parallel
to S2
Veins
sub-parallel
to S0
Vein geometries from the Orebody environs
Sub-vertical veins [374]
Sub-horizontal veins [180]
Equal Area
Lower Hemisphere
554 Poles

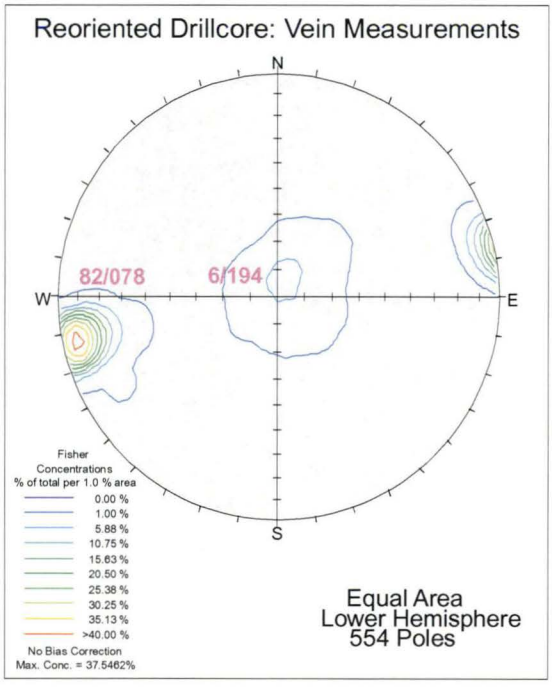
Reoriented Drillcore: Vein Measurements
N
W
E
S
82/078
6/194
Fisher
Concentrations
% of total per 1.0 % area
0.00 %
1.00 %
5.88 %
10.75 %
15.63 %
20.50 %
25.38 %
30.25 %
35.13 %
>40.00 %
No Bias Correction
Max. Conc. = 37.5462%
Equal Area
Lower Hemisphere
554 Poles

Stereonets of reoriented measurements of D_2 shears and related structures from the New Occidental Project drillcore.

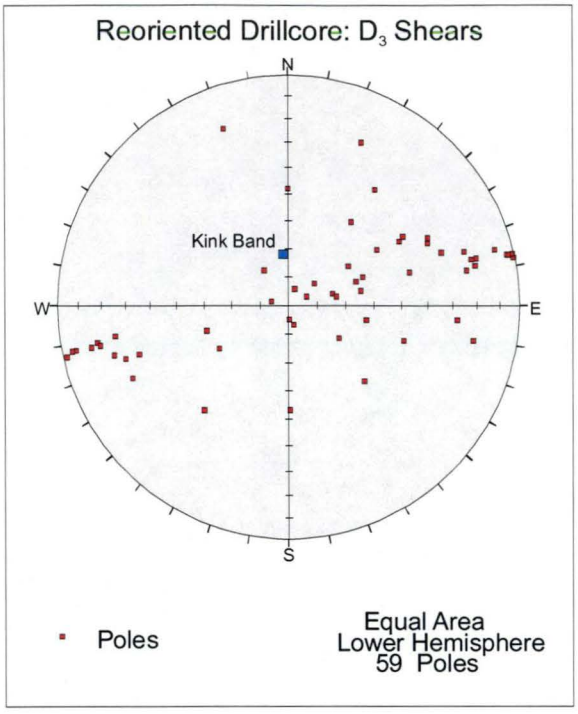

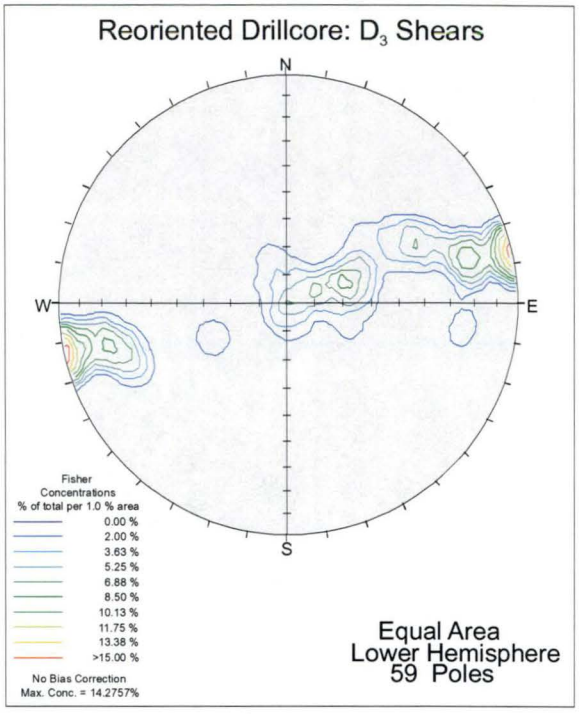

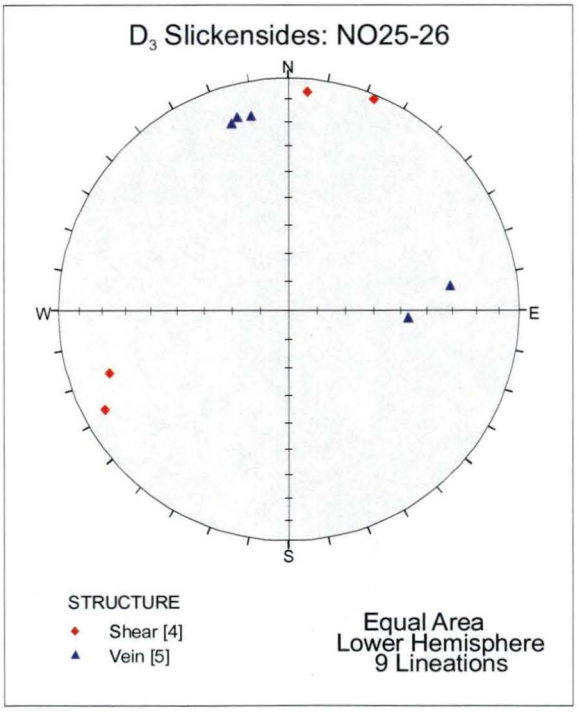

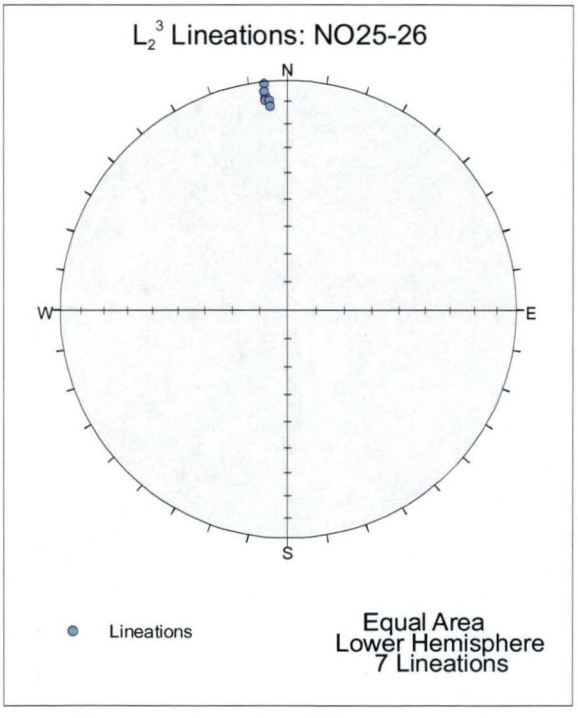

Appendix 3: Qualitative Energy Dispersive Electron Microbeam Analyses – Chlorite

Microprobe Analyses

				Weight Percents							
Drillhole	**Depth**	**Mineral**	**Description**	**SiO_2**	**Al_2O_3**	**FeO**	**MnO**	**MgO**	**Na_2O**	**K_2O**	**TOTAL**
NO07A	728 7	Early Chlorite	Fine grained	24 78	20.37	36.88	0.22	5.70	0 00	0.60	88 55
NO07A	728.7	Early Chlorite	Fine grained	24 43	20.68	36 68	0 11	5.78	0.00	0.80	88.48
NO07A	728 7	Early Chlorite	Fine grained	24.09	21 65	36 90	0 14	5 51	0 00	0 50	88.79
NO07A	728.7	Early Chlorite	Fine grained	23 95	20.85	36.72	0 13	6.42	0.00	0 25	88.32
NO07A	728.7	Early Chlorite	Fine grained	25 22	20.55	37 37	0 15	5 89	0 00	0 80	89 98
NO07A	728 7	Early Chlorite	Fine grained	24.81	21 86	36 68	0 22	5.09	0 00	0.60	89 26
NO07A	728 7	Early Chlorite	Fine grained	24 23	20 37	37 59	0 13	6.11	0 00	0 60	89 03
NO07A	728 7	Early Chlorite	Fine grained	25 05	21.00	36 77	0 16	5 99	0 00	0 60	89 57
NO07A	728.7	Early Chlorite	Fine grained	24.66	21.33	37 62	0 14	5.87	0.00	0 70	90 32
NO07A	728.7	Early Chlorite	Fine grained	24 61	21 86	37 72	0 12	5 61	0 00	0 25	90 17
NO14D	992 7	Early Chlorite	Fine grained	24 50	20 62	40 00	0 24	3 33	0 50	0 25	89.44
NO14D	992 7	Early Chlorite	Fine grained	24 59	20 60	39.99	0 50	3 15	1 00	0 25	90 08
NO14D	992 7	Early Chlorite	Fine grained	24.35	20 91	38 82	0.47	3.92	1 20	0 25	89 92
NO14D	992.7	Early Chlorite	Fine grained	24.84	20 15	39 22	0.54	3 90	1 10	0.25	90.00
NO14D	992 7	Early Chlorite	Fine grained	24 15	20.02	39 29	0 45	4 30	1 20	0 25	89 66
NO14D	992.7	Early Chlorite	Fine grained	23 86	20 91	39.40	0 20	3 85	0.60	0.25	89 07
NO14D	992 7	Early Chlorite	Fine grained	24.88	20.57	38 75	0.37	4 22	1.10	0.25	90 14
NO14D	992.7	Early Chlorite	Fine grained	24 23	21 09	38.96	0 29	4.36	1 30	0 25	90.48
NO14D	992.7	Early Chlorite	Fine grained	24.43	20 65	39 52	0.28	3 77	1 00	0 25	89 90
NO14D	992 7	Early Chlorite	Fine grained	24 65	21.19	39.61	0 20	3.38	0 90	0 25	90.18
NO07A	736.4	Early Chlorite	Fine grained in rock fragments	23 24	20 12	38 93	0 39	5 56	0 25	1 50	89 99
NO07A	736 4	Early Chlorite	Fine grained in rock fragments	23.81	20 09	38 30	1.02	5 36	0 25	0 50	89 33
NO07A	736.4	Early Chlorite	Fine grained in rock fragments	24.04	19.94	38.96	0 57	5 02	0 25	0.00	88.78
NO07A	736 4	Early Chlorite	Fine grained in rock fragments	23.94	19 94	38 67	0.36	5 50	0 50	0.50	89.41
NO07A	736 4	Early Chlorite	Fine grained in rock fragments	23 64	19 85	38 22	1.07	4.90	1 00	0.00	88.68
NO07A	736 4	Early Chlorite	Fine grained in rock fragments	23.96	19.58	38 57	0 53	6 43	1 00	0 00	90.07
NO07A	736.4	Early Chlorite	Fine grained in rock fragments	24 59	19 53	39 25	0.12	5 80	0.80	0.00	90 09
NO07A	736 4	Early Chlorite	Fine grained in rock fragments	25.00	19 84	38 67	0.39	5.55	1 00	0.00	90.45
NO07A	736 4	Early Chlorite	Fine grained in rock fragments	24 83	19 63	38.02	0 49	5 21	0 90	0.50	89 58
NO07A	736 4	Early Chlorite	Fine grained in rock fragments	24.89	19.97	38 94	0.34	5 57	0 50	0.00	90.21
NO12	630.8	Early Chlorite	Fine grained in rock fragments	24.66	21.74	36 70	0 11	6.16	0 70	0 25	90.32
NO12	630 8	Early Chlorite	Fine grained in rock fragments	24 56	21.12	37.01	0 12	6 14	0 80	0 25	90 00
NO12	630.8	Early Chlorite	Fine grained in rock fragments	24 41	20 82	37 46	0.24	5 98	1.00	0 25	90 16
NO12	630.8	Early Chlorite	Fine grained in rock fragments	24.82	21 50	37 51	0.17	5 76	0 25	0.25	90 26
NO12	630 8	Early Chlorite	Fine grained in rock fragments	24 35	21 25	37 52	0 11	6.53	0 25	0 25	90.26
NO12	630.8	Early Chlorite	Fine grained in rock fragments	24 87	21 49	36 73	0.12	6.16	1.00	0 25	90.62
NO12	630 8	Early Chlorite	Fine grained in rock fragments	25.32	20 96	37.47	0.05	5 69	0 00	0.25	89 74
NO12	630.8	Early Chlorite	Fine grained in rock fragments	24 89	21.00	37 65	0 10	5.79	0 70	0.25	90 38
NO12	630 8	Early Chlorite	Fine grained in rock fragments	25.46	20 49	36 83	0 10	6.35	0.50	0 25	89.98
NO12	630.8	Early Chlorite	Fine grained in rock fragments	25 20	21 39	36 80	0.28	5.39	0 70	0 25	90 01
NO12A	708.4	Early Chlorite	Fine grained in rock fragments	24 64	20.57	39 24	0.14	5 25	0.50	0 25	90 59
NO12A	708 4	Early Chlorite	Fine grained in rock fragments	24.39	20 52	39.73	0 25	4.92	0.90	0.25	90.96
NO12A	708 4	Early Chlorite	Fine grained in rock fragments	24 83	19 75	39.52	0.19	5 25	0 50	0.25	90 29
NO12A	708 4	Early Chlorite	Fine grained in rock fragments	24 10	19.89	39 01	0 10	5 69	1.00	0 25	90 04
NO12A	708.4	Early Chlorite	Fine grained in rock fragments	24 85	19.71	39.89	0 10	5.39	0.80	0.25	90 99
NO12A	708 4	Early Chlorite	Fine grained in rock fragments	24.67	19.92	38 39	0.19	6 63	0 70	0 25	90 75
NO12A	708 4	Early Chlorite	Fine grained in rock fragments	24 49	19.98	39 87	0 10	5 03	0 60	0 25	90.32
NO12A	708.4	Early Chlorite	Fine grained in rock fragments	24 75	19 65	39 74	0.10	5.81	0.70	0 25	91.00
NO12A	708 4	Early Chlorite	Fine grained in rock fragments	25.09	20 20	38 82	0 21	5 36	0 60	0 25	90 53
NO12A	708 4	Early Chlorite	Fine grained in rock fragments	24 53	20.38	39.42	0 19	5.63	0 50	0 25	90 90
NO03C	873 1	Chlorite with Stilpn	Coarse grained	23.60	19.59	41.28	0 27	3.94	0.25	0 50	89.43
NO03C	873.1	Chlorite with Stilpn.	Coarse grained	23 09	19 89	41 44	0.14	3.99	0 25	0.25	89 05
NO03C	873.1	Chlorite with Stilpn	Coarse grained	22 43	20 00	41.39	0 17	4 46	0 25	0 80	89 50
NO03C	873 1	Chlorite with Stilpn.	Coarse grained	23 29	19 20	41 54	0 00	4.04	0 25	0.60	88.92
NO03C	873.1	Chlorite with Stilpn	Coarse grained	23 15	19 81	41.33	0 20	4 38	0 25	1.00	90 12

Microprobe Analyses

				Weight Percents							
Drillhole	**Depth**	**Mineral**	**Description**	**SiO_2**	**Al_2O_3**	**FeO**	**MnO**	**MgO**	**Na_2O**	**K_2O**	**TOTAL**
NO03C	873.1	Chlorite with Stilpn.	Fine grained	24 48	19 07	41.51	0.11	4.20	0.25	1 20	90 82
NO03C	873 1	Chlorite with Stilpn	Fine grained	24.05	20.04	40.28	0 17	3 72	0.25	0 50	89.01
NO03C	873.1	Chlorite with Stilpn.	Fine grained	24.45	18 55	40 77	0 30	4.36	0 25	0.50	89 18
NO03C	873 1	Chlorite with Stilpn	Fine grained	24 28	19 39	40.27	0.23	4.42	0 25	0 60	89 44
NO03C	873 1	Chlorite with Stilpn	Fine grained	23 82	20 27	41 61	0 10	4.64	0 25	0 80	91 49
NO03C	889.0	Chlorite with Stilpn	Fine grained in rock fragments	25.05	19 41	42 19	0 19	2.96	0 90	0.25	90 95
NO03C	889.0	Chlorite with Stilpn	Fine grained in rock fragments	23.85	18 75	42 07	0 27	3 74	1 50	0.25	90 43
NO03C	889.0	Chlorite with Stilpn.	Fine grained in rock fragments	23.95	18 23	42 59	0 13	3 11	1 20	0.25	89.46
NO03C	889 0	Chlorite with Stilpn.	Fine grained in rock fragments	23 96	19 98	42 38	0 14	3 89	0 50	0.25	91 10
NO03C	889 0	Chlorite with Stilpn	Fine grained in rock fragments	24 85	20 16	42 40	0.18	3 75	0 70	0 25	92 29
NO03C	889 0	Chlorite with Stilpn.	Fine grained in rock fragments	24 01	20 22	43 13	0 15	2.15	1.40	0 25	91 31
NO03C	889 0	Chlorite with Stilpn.	Fine grained in rock fragments	23.24	19.02	42.59	0.14	3 02	1.50	0.25	89.76
NO03C	889.0	Chlorite with Stilpn	Fine grained in rock fragments	24.66	19.70	42.33	0.17	2 56	1 20	0 25	90 87
NO03C	889 0	Chlorite with Stilpn	Fine grained in rock fragments	24 90	19 54	42.46	0.18	2 35	1 10	0 25	90.78
NO03C	889.0	Chlorite with Stilpn.	Fine grained in rock fragments	24 61	19 04	42 83	0.15	3.96	1.50	0.25	92.34
NO12A	707.7	Chlorite with Stilpn	Fine grained	23 72	21.64	40 87	0 19	4 01	0 25	0.25	90 93
NO12A	707.7	Chlorite with Stilpn	Fine grained	23 94	21.22	41.11	0.22	3 75	0.50	0 25	90 99
NO12A	707.7	Chlorite with Stilpn.	Fine grained	24.59	20.62	40 36	0 24	4 06	0.70	0 25	90 82
NO12A	707.7	Chlorite with Stilpn	Fine grained	23 94	20.30	40 75	0 33	3 82	0.90	0.25	90 29
NO12A	707.7	Chlorite with Stilpn	Fine grained	23.41	20 61	40.89	0 27	3 59	1 00	0.25	90 02
NO12A	707 7	Chlorite with Stilpn	Fine grained	23 75	20 52	40.80	0 18	3 60	0.60	0 25	89.70
NO12A	707 7	Chlorite with Stilpn	Fine grained	24 13	20 45	40.49	0 20	4.42	0 70	0 25	90 64
NO12A	707 7	Chlorite with Stilpn.	Fine grained	24 11	20 77	40.04	0 31	3.96	0 50	0 25	89 94
NO12A	707.7	Chlorite with Stilpn.	Fine grained	24.85	20.20	40 56	0 22	4.58	0.60	0 25	91 26
NO12A	707 7	Chlorite with Stilpn.	Fine grained	23.52	20 69	40 86	0 26	4 25	0 25	0 25	90 08
NO14D	999 5	Chlorite with Stilpn	Fine grained	24 94	19 79	40 26	0 20	3 86	1.30	0 25	90 60
NO14D	999 5	Chlorite with Stilpn	Fine grained	24 78	19 62	39 18	0 25	4 51	0 60	0 25	89 19
NO14D	999.5	Chlorite with Stilpn.	Fine grained	25.18	19 76	39 54	0 18	4.28	0.70	0 25	89 89
NO14D	999.5	Chlorite with Stilpn	Fine grained	25 23	18 99	39.70	0 30	4 49	0.90	0 25	89.86
NO14D	999 5	Chlorite with Stilpn	Fine grained	24.91	19 83	38 61	0 33	5 12	1.10	0 25	90.15
NO14D	999.5	Chlorite with Stilpn	Fine grained	24.81	19 23	40.09	0 29	4 34	1 00	0 25	90 01
NO14D	999.5	Chlorite with Stilpn	Fine grained	24.35	19 40	39.49	0.24	4 70	0.90	0 25	89.33
NO14D	999.5	Chlorite with Stilpn	Fine grained	24.69	19 55	39.46	0.17	4 67	0 60	0 25	89.39
NO14D	999 5	Chlorite with Stilpn	Fine grained	25 09	19 70	39 38	0.33	3 97	0 80	0 25	89.52
NO14D	999 5	Chlorite with Stilpn	Fine grained	24 56	20.42	40 23	0 20	3 40	1 00	0 25	90.06
NO12	665 2	Late Chlorite	Coarse grained	25.04	21.68	33.80	0 60	8 80	0 25	0.25	90 42
NO12	665.2	Late Chlorite	Coarse grained	24 54	21 88	34.22	0.43	8.57	0.25	0 25	90.14
NO12	665 2	Late Chlorite	Coarse grained	24 07	21 84	34 74	0 36	8 55	0 25	0 25	90.06
NO12	665 2	Late Chlorite	Coarse grained	24.58	22 75	33 98	0 52	8 09	0 25	0 25	90.42
NO12	665.2	Late Chlorite	Coarse grained	24 87	21 42	34.24	0 46	8 46	0 25	0 25	89.95
NO12	665 2	Late Chlorite	Fine grained	24 97	21 25	33 40	0.58	9.11	0 25	0.25	89.81
NO12	665 2	Late Chlorite	Fine grained	24 59	21 38	34.01	0.46	9 14	0 25	0.25	90.08
NO12	665 2	Late Chlorite	Fine grained	24 65	21 89	34.42	0 50	8 13	0 25	0 25	90 09
NO12	665.2	Late Chlorite	Fine grained	25.08	22.01	34 42	0 50	9.14	0 25	0 25	91 65
NO12	665 2	Late Chlorite	Fine grained	24 56	21 61	34.41	0.54	9.01	0 25	0 25	90 63
NO12	666.0	Late Chlorite	Coarse grained	24.81	20 81	35.38	0.38	9.08	0 25	0.25	90 96
NO12	666 0	Late Chlorite	Coarse grained	24.49	20 95	32.63	0.40	10 47	0 50	0 25	89 69
NO12	666 0	Late Chlorite	Coarse grained	24 80	21 22	34 02	0 30	9.13	0 50	0 25	90 22
NO12	666.0	Late Chlorite	Coarse grained	24 82	20 54	33 46	0 45	9 32	0 70	0 25	89 54
NO12	666 0	Late Chlorite	Coarse grained	25.13	20.87	33 78	0 34	9.95	0 25	0 25	90 57
NO12	666 0	Late Chlorite	Coarse grained	24 06	21 53	34 42	0.41	9.01	0.50	0.25	90 18
NO12	666 0	Late Chlorite	Coarse grained	24 81	20.88	34 55	0 32	9 53	0 25	0 25	90 59
NO12	666 0	Late Chlorite	Coarse grained	24 85	21.60	34 57	0 34	8 41	0.25	0 25	90 27
NO12	666.0	Late Chlorite	Coarse grained	24 08	21.12	34 98	0 42	8.49	0 50	0 25	89.84
NO12	666.0	Late Chlorite	Coarse grained	24 85	20 55	34 56	0 38	8.57	0 25	0.25	89.41

Microprobe Analyses

				Weight Percents							
Drillhole	**Depth**	**Mineral**	**Description**	**SiO_2**	**Al_2O_3**	**FeO**	**MnO**	**MgO**	**Na_2O**	**K_2O**	**TOTAL**
NO12A	743.5	Late Chlorite	Fine grained in quartz aggregates	25 82	20.44	34 46	0.46	7 60	1 20	0 25	90.23
NO12A	743 5	Late Chlorite	Fine grained in quartz aggregates	25 43	20 43	34.82	0 33	7.46	1.10	0.25	89 82
NO12A	743 5	Late Chlorite	Fine grained in quartz aggregates	25.34	20 49	34 72	0 23	7 85	0 50	0.25	89.38
NO12A	743.5	Late Chlorite	Fine grained in quartz aggregates	25.36	20 51	34.58	0 44	7 67	0.60	0.25	89.41
NO12A	743.5	Late Chlorite	Fine grained in quartz aggregates	25.00	21 22	34.74	0 40	7.72	0 70	0 25	90.03
NO12A	743.5	Late Chlorite	Fine grained in quartz aggregates	25 45	20 41	35.40	0.30	7 41	0.90	0 25	90 12
NO12A	743.5	Late Chlorite	Fine grained in quartz aggregates	24.95	21 14	35.41	0 31	6.90	1 10	0 25	90.06
NO12A	743 5	Late Chlorite	Fine grained in quartz aggregates	25 34	20.91	35 87	0.61	6 46	0 25	0 25	89.69
NO12A	743.5	Late Chlorite	Fine grained in quartz aggregates	24.84	20.37	34 76	0 41	7.47	1.20	0 25	89 30
NO12A	743.5	Late Chlorite	Fine grained in quartz aggregates	24.90	21 31	35.33	0 63	6.64	0.60	0 25	89.66
NO14	543.9	H/W Chlorite	In veins and immediate wallrock	25 72	21 21	30 62	0 33	10 94			88.82
NO14	543 9	H/W Chlorite	In veins and immediate wallrock	25.16	21.50	31 07	0 51	10.82			89 06
NO14	543.9	H/W Chlorite	In veins and immediate wallrock	24 85	22 00	30 94	0 39	10 54			88 72
NO14	543 9	H/W Chlorite	In veins and immediate wallrock	24 92	21.41	30.81	0.36	10.41			87.91
NO14	543 9	H/W Chlorite	In veins and immediate wallrock	24 72	21 16	30 70	0 26	9.70			86.54
NO14	543 9	H/W Chlorite	In veins and immediate wallrock	25.24	20.68	29 87	0.33	10 58			86 70
NO14	543.9	H/W Chlorite	In veins and immediate wallrock	25 14	20.60	29 99	0 24	10 46			86.43
NO14	543.9	H/W Chlorite	In veins and immediate wallrock	25.63	21 16	31.04	0 23	10 24			88 30
NO14	543 9	H/W Chlorite	In veins and immediate wallrock	24 85	21 33	30.73	0.19	10 16			87 26
NO14	543.9	H/W Chlorite	In veins and immediate wallrock	25.09	21.40	30 31	0 23	10 77			87 80
NO14	543 9	H/W Chlorite	In veins and immediate wallrock	24.96	21 08	30.92	0 38	10 17			87.51
NO14	543 9	H/W Chlorite	In veins and immediate wallrock	24 63	21 38	30.92	0 32	10 10			87 35
NO14	543 9	H/W Chlorite	In veins and immediate wallrock	24 46	20.65	31 16	0 23	9.76			86 26
NO14	543.9	H/W Chlorite	In veins and immediate wallrock	24 50	20.50	30 71	0.36	10.02			86 09
NO14	543 9	H/W Chlorite	In veins and immediate wallrock	25 00	20.72	30.36	0 46	10.94			87 48
NO14	543.9	H/W Chlorite	In veins and immediate wallrock	24 46	20 32	30.64	0 23	10.09			85 74
NO14	543 9	H/W Chlorite	In veins and immediate wallrock	23 83	20 64	30 84	0 32	9.72			85 35
NO14	543 9	H/W Chlorite	In veins and immediate wallrock	25 08	20.62	30.21	0 33	10.06			86 30
NO14	543 9	H/W Chlorite	In veins and immediate wallrock	24 25	20.40	30.62	0 34	10 13			85 74
NO14	543.9	H/W Chlorite	In veins and immediate wallrock	24.80	20.66	30 84	0 41	9.94			86 65
N0O3G	807 4	Gossan Chlorite	In colloform qtz-chlorite veins	23 55	20 58	36 04	0 55	5.55			86 27
N0O3G	807.4	Gossan Chlorite	In colloform qtz-chlorite veins	23 09	20 58	36.15	0 61	5 99			86.42
N0O3G	807 4	Gossan Chlorite	In colloform qtz-chlorite veins	23.22	20.18	36 52	0.65	5 79			86 36
N0O3G	807 4	Gossan Chlorite	In colloform qtz-chlorite veins	23.23	20 77	36 45	0.48	5.99			86 92
N0O3G	807.4	Gossan Chlorite	In colloform qtz-chlorite veins	23 39	20 86	35 83	0 33	5 76			86 17
N0O3G	807 4	Gossan Chlorite	In colloform qtz-chlorite veins	23.81	21.04	36.42	0 45	5.58			87.30
N0O3G	807.4	Gossan Chlorite	In colloform qtz-chlorite veins	23 50	20.72	37.44	0 61	5.39			87 66
N0O3G	807 4	Gossan Chlorite	In colloform qtz-chlorite veins	23 40	20 71	37 04	0 45	5 40			87 00
N0O3G	807.4	Gossan Chlorite	In colloform qtz-chlorite veins	23 99	20.19	35 90	0 54	6.11			86.73
N0O3G	807 4	Gossan Chlorite	In colloform qtz-chlorite veins	23 73	19.76	37.55	0 40	5 72			87 16
N0O3G	807 4	Gossan Chlorite	In colloform qtz-chlorite veins	23 85	20.39	37.68	0 66	5 03			87.61
N0O3G	807 4	Gossan Chlorite	In colloform qtz-chlorite veins	23.45	20 53	37 85	0.29	5.06			87 18
N0O3G	807 4	Gossan Chlorite	In colloform qtz-chlorite veins	24.29	20 77	37 95	0.55	4.80			88 36
N0O3G	807 4	Gossan Chlorite	In colloform qtz-chlorite veins	23 40	20.19	37 44	0 42	4 71			86 16
N0O3G	807.4	Gossan Chlorite	In colloform qtz-chlorite veins	23 20	20 30	37.47	0 61	4 85			86 43
N0O3G	807 4	Gossan Chlorite	In colloform qtz-chlorite veins	23 66	20.71	37 97	0 48	4.91			87 73
N0O3G	807.4	Gossan Chlorite	In colloform qtz-chlorite veins	23.39	20.73	37 87	0 46	4.86			87 31
N0O3G	807 4	Gossan Chlorite	In colloform qtz-chlorite veins	23 15	20 72	37.81	0 42	5 09			87 19
N0O3G	807 4	Gossan Chlorite	In colloform qtz-chlorite veins	22 57	20 41	37.81	0 55	4 97			86.31
N0O3G	807.4	Gossan Chlorite	In colloform qtz-chlorite veins	23.48	20 46	37 79	0 39	5.15			87 27
NO14E	1157 6	F/W Chlorite	In veins and immediate wallrock	25 70	21 69	27.51	0.28	11 84			87 02
NO14E	1157.6	F/W Chlorite	In veins and immediate wallrock	24 85	21 51	27 73	0.28	12 25			86.62
NO14E	1157 6	F/W Chlorite	In veins and immediate wallrock	25.75	21.12	27 43	0 36	12.17			86 83
NO14E	1157.6	F/W Chlorite	In veins and immediate wallrock	25 11	20.98	27 30	0.26	11 79			85.44
NO14E	1157.6	F/W Chlorite	In veins and immediate wallrock	25.17	22.44	27 97	0 33	12 10			88.01

Microprobe Analyses

				Weight Percents							
Drillhole	**Depth**	**Mineral**	**Description**	**SiO_2**	**Al_2O_3**	**FeO**	**MnO**	**MgO**	**Na_2O**	**K_2O**	**TOTAL**
NO14E	1157.6	F/W Chlorite	In veins and immediate wallrock	24.75	21 58	28.19	0.32	11 83			86.67
NO14E	1157.6	F/W Chlorite	In veins and immediate wallrock	24 96	21.42	27.50	0.39	11 94			86.21
NO14E	1157.6	F/W Chlorite	In veins and immediate wallrock	24 60	21.77	27 83	0 34	11 61			86 15
NO14E	1157 6	F/W Chlorite	In veins and immediate wallrock	25 36	21.68	27.02	0.27	12 22			86.55
NO14E	1157 6	F/W Chlorite	In veins and immediate wallrock	24 82	21 86	27 66	0 39	11.78			86 51
NO14E	1157.6	F/W Chlorite	In veins and immediate wallrock	24 89	20.96	28 32	0 50	11.53			86 20
NO14E	1157.6	F/W Chlorite	In veins and immediate wallrock	24 73	21 42	27.65	0 26	11.56			85 62
NO14E	1157.6	F/W Chlorite	In veins and immediate wallrock	25.15	21 54	27.83	0.44	12 27			87 23
NO14E	1157 6	F/W Chlorite	In veins and immediate wallrock	25.70	21 47	26 45	0.46	12 72			86 80
NO14E	1157 6	F/W Chlorite	In veins and immediate wallrock	25 91	21 22	27 57	0.12	11 72			86.54
NO14E	1157.6	F/W Chlorite	In veins and immediate wallrock	25.16	21 70	27 78	0.27	11 27			86.18
NO14E	1157.6	F/W Chlorite	In veins and immediate wallrock	25.36	21 68	28 21	0 20	11 92			87.37
NO14E	1157.6	F/W Chlorite	In veins and immediate wallrock	25 32	21 35	27 47	0 26	11.93			86.33
NO14E	1157 6	F/W Chlorite	In veins and immediate wallrock	24 72	21 58	27 82	0 42	11 91			86 45
NO14E	1157 6	F/W Chlorite	In veins and immediate wallrock	24.99	21 49	27 85	0 49	12 42			87.24
NO25	179.8	Albion Chlorite	In veins and immediate wallrock	22.71	19.73	38 44	0 38	5.11			86 37
NO25	179 8	Albion Chlorite	In veins and immediate wallrock	23 63	20 21	38.54	0 68	5.32			88 38
NO25	179.8	Albion Chlorite	In veins and immediate wallrock	23.13	20.44	37.77	0 42	5.02			86 78
NO25	179 8	Albion Chlorite	In veins and immediate wallrock	23.30	20.65	37 60	0 45	4.90			86.90
NO25	179.8	Albion Chlorite	In veins and immediate wallrock	23 25	21.02	38 49	0 52	5 09			88 37
NO25	179 8	Albion Chlorite	In veins and immediate wallrock	23 38	20.62	37.76	0.49	4 86			87 11
NO25	179 8	Albion Chlorite	In veins and immediate wallrock	22 92	20 14	37.62	0.36	5 09			86.13
NO25	179.8	Albion Chlorite	In veins and immediate wallrock	22 95	20 72	38 42	0.62	5 00			87.71
NO25	179 8	Albion Chlorite	In veins and immediate wallrock	23.64	21 04	38 28	0 65	5.33			88.94
NO25	179.8	Albion Chlorite	In veins and immediate wallrock	23.67	20 45	38 33	0 42	5.05			87.92
NO25	223 8	Albion Chlorite	In veins and immediate wallrock	23 89	20 69	36 20	0 44	6 18			87.40
NO25	223 8	Albion Chlorite	In veins and immediate wallrock	23 92	21 11	36 51	0.30	6 34			88 18
NO25	223 8	Albion Chlorite	In veins and immediate wallrock	23 92	20.94	35 74	0.49	6 70			87.79
NO25	223.8	Albion Chlorite	In veins and immediate wallrock	24.14	20 70	35 91	0 51	6 59			87 85
NO25	223.8	Albion Chlorite	In veins and immediate wallrock	23 63	21.00	36.34	0 45	6.40			87 82
NO25	223.8	Albion Chlorite	In veins and immediate wallrock	24.39	20.49	36 27	0 53	6.55			88.23
NO25	223.8	Albion Chlorite	In veins and immediate wallrock	24.03	20.39	36 22	0 46	7 01			88 11
NO25	223.8	Albion Chlorite	In veins and immediate wallrock	23 86	21.26	35.73	0 28	6 34			87.47
NO25	223 8	Albion Chlorite	In veins and immediate wallrock	23 47	20 51	35.78	0 28	6 54			86 58
NO25	223 8	Albion Chlorite	In veins and immediate wallrock	24 12	20 18	35 41	0.53	6.56			86.80
NO25	214.7	Albion Chlorite	In veins and immediate wallrock	23.05	20 54	36 39	0 49	6 24			86.71
NO25	214 7	Albion Chlorite	In veins and immediate wallrock	23 76	21 10	36.08	0.55	6 32			87.81
NO25	214 7	Albion Chlorite	In veins and immediate wallrock	22 91	20 95	36 33	0 54	6.14			86.87
NO25	214 7	Albion Chlorite	In veins and immediate wallrock	23.33	20.38	36 01	0 46	6 09			86.27
NO25	214.7	Albion Chlorite	In veins and immediate wallrock	23 59	21.07	35.72	0 74	6.30			87 42
NO25	214 7	Albion Chlorite	In veins and immediate wallrock	23 60	20 28	36.03	0.31	6.61			86 83
NO25	214.7	Albion Chlorite	In veins and immediate wallrock	23 03	21 16	36.36	0.38	5 97			86 90
NO25	214.7	Albion Chlorite	In veins and immediate wallrock	22 87	21.56	36.14	0.51	6 23			87 31
NO25	214 7	Albion Chlorite	In veins and immediate wallrock	23.58	21 45	35 89	0.49	6 46			87.87
NO25	214 7	Albion Chlorite	In veins and immediate wallrock	23 32	20 41	36 09	0.43	6 39			86 64
NO26	327 6	Albion Chlorite	In veins and immediate wallrock	24 15	20 81	35 91	0.60	7 00			88 47
NO26	327.6	Albion Chlorite	In veins and immediate wallrock	23 55	20 21	35.90	0 53	6 17			86 36
NO26	327 6	Albion Chlorite	In veins and immediate wallrock	23 20	20 75	35 99	0 54	6 22			86 70
NO26	327 6	Albion Chlorite	In veins and immediate wallrock	23 35	20 56	35 76	0 43	6 25			86 35
NO26	327 6	Albion Chlorite	In veins and immediate wallrock	24.04	20 70	35 74	0 54	6 19			87.21
NO26	327 6	Albion Chlorite	In veins and immediate wallrock	23 87	19 84	36 19	0.42	6.35			86.67
NO26	327 6	Albion Chlorite	In veins and immediate wallrock	24.50	20 12	36.01	0 33	6.67			87.63
NO26	327.6	Albion Chlorite	In veins and immediate wallrock	23 79	20.40	36 05	0 46	6 31			87 01
NO26	327.6	Albion Chlorite	In veins and immediate wallrock	23.53	20 40	36 34	0 48	6 09			86 84
NO26	327.6	Albion Chlorite	In veins and immediate wallrock	23.90	19 89	36 46	0.38	6 37			87.00

Microprobe Analyses

		Normalised Cation Distribution										Site Occupancy					
Drillhole	Depth	Si	Al	Al	Fe	Mn	Mg	Ca	Na	K	Total	Si + Al	Balance	Total	Fe/(Fe+Mg) Cation Ratio	Tetrahedral Al Cations
NO07A	728 7	5.56	2 44	2.95	6.92	0 04	1 91	0 00	0 00	0 17	20 00	8.00	12.00	20 00	0.78	2 44
NO07A	728 7	5 48	2.52	2 94	6 88	0 02	1.93	0 00	0.00	0 23	20.00	8 00	12.00	20.00	0 78	2.52
NO07A	728 7	5.39	2 61	3 09	6.90	0.03	1 84	0 00	0 00	0 14	20 00	8 00	12.00	20 00	0 79	2 61
NO07A	728 7	5.37	2 63	2 88	6.88	0.02	2 14	0 00	0 00	0 07	20 00	8 00	12.00	20 00	0.76	2 63
NO07A	728 7	5 57	2 43	2 91	6 90	0 03	1.94	0.00	0.00	0 23	20 00	8 00	12.00	20.00	0 78	2.43
NO07A	728 7	5 53	2 47	3 27	6.83	0.04	1.69	0 00	0 00	0.17	20 00	8 00	12 00	20 00	0 80	2.47
NO07A	728 7	5 41	2 59	2.76	7 01	0.02	2.03	0.00	0.00	0 17	20.00	8.00	12 00	20.00	0.78	2 59
NO07A	728 7	5.54	2 46	3 02	6 80	0.03	1.98	0 00	0.00	0.17	20 00	8 00	12 00	20.00	0 77	2.46
NO07A	728 7	5.42	2 58	2 94	6.91	0.03	1.92	0 00	0 00	0 20	20 00	8.00	12 00	20.00	0 78	2 58
NO07A	728 7	5.43	2.57	3 11	6 96	0.02	1 84	0.00	0 00	0.07	20 00	8.00	12 00	20 00	0 79	2 57
NO14D	992 7	5.52	2 48	3.00	7 54	0 05	1 12	0.00	0.22	0.07	20 00	8 00	12.00	20 00	0 87	2 48
NO14D	992 7	5 48	2 52	2 90	7.46	0 09	1.05	0.00	0.43	0 07	20 00	8 00	12.00	20.00	0 88	2.52
NO14D	992 7	5.39	2.61	2 85	7 19	0 09	1 29	0 00	0 52	0 07	20.00	8 00	12.00	20 00	0.85	2.61
NO14D	992 7	5 51	2 49	2.78	7 28	0.10	1 29	0.00	0.47	0.07	20 00	8.00	12.00	20.00	0 85	2.49
NO14D	992 7	5.36	2.64	2.61	7 30	0 08	1.42	0 00	0 52	0 07	20 00	8 00	12 00	20 00	0 84	2.64
NO14D	992 7	5 37	2 63	2.92	7.42	0.04	1 29	0 00	0.26	0 07	20 00	8.00	12 00	20 00	0.85	2 63
NO14D	992 7	5 49	2.51	2.85	7.15	0 07	1 39	0.00	0 47	0 07	20.00	8.00	12.00	20 00	0 84	2 51
NO14D	992.7	5.31	2 69	2.76	7 14	0.05	1 42	0 00	0 55	0.07	20 00	8.00	12 00	20.00	0.83	2.69
NO14D	992 7	5 43	2 57	2 85	7.35	0.05	1 25	0 00	0.43	0 07	20.00	8.00	12 00	20.00	0 85	2 57
NO14D	992 7	5 48	2.52	3 03	7.36	0.04	1 12	0.00	0.39	0 07	20.00	8 00	12 00	20 00	0 87	2.52
NO07A	736.4	5 13	2.87	2 37	7 19	0.07	1.83	0 00	0 11	0.42	20 00	8 00	12 00	20 00	0 80	2.87
NO07A	736 4	5 32	2.68	2.61	7.16	0.19	1.79	0 00	0 11	0.14	20 00	8 00	12.00	20 00	0 80	2 68
NO07A	736 4	5.43	2.57	2 73	7 36	0 11	1.69	0 00	0.11	0 00	20 00	8 00	12.00	20 00	0 81	2 57
NO07A	736 4	5.33	2.67	2 56	7 20	0 07	1 82	0 00	0 22	0 14	20 00	8 00	12 00	20 00	0 80	2 67
NO07A	736.4	5 30	2 70	2.55	7 17	0 20	1 64	0.00	0.43	0 00	20.00	8 00	12 00	20.00	0.81	2 70
NO07A	736.4	5 25	2.75	2 31	7 07	0 10	2 10	0.00	0.42	0 00	20.00	8 00	12.00	20.00	0.77	2.75
NO07A	736 4	5.42	2.58	2.49	7 24	0 02	1 91	0 00	0 34	0 00	20.00	8 00	12.00	20 00	0 79	2.58
NO07A	736 4	5 48	2.52	2.60	7 09	0 07	1.81	0.00	0 42	0 00	20 00	8 00	12.00	20 00	0 80	2 52
NO07A	736 4	5.50	2.50	2 62	7 04	0.09	1.72	0 00	0 39	0.14	20 00	8.00	12 00	20 00	0.80	2.50
NO07A	736.4	5.50	2 50	2 70	7 19	0.06	1.83	0 00	0.21	0.00	20 00	8.00	12 00	20.00	0 80	2 50
NO12	630 8	5 37	2 63	2 94	6 68	0.02	2 00	0 00	0.30	0 07	20 00	8 00	12 00	20.00	0.77	2 63
NO12	630 8	5 37	2.63	2 81	6 76	0 02	2 00	0.00	0.34	0 07	20.00	8 00	12.00	20 00	0 77	2 63
NO12	630.8	5 33	2.67	2.68	6.84	0.04	1 95	0.00	0.42	0 07	20.00	8 00	12.00	20.00	0 78	2 67
NO12	630 8	5.45	2.55	3.02	6.89	0 03	1 89	0 00	0.11	0 07	20 00	8 00	12 00	20 00	0 79	2 55
NO12	630.8	5.33	2 67	2.81	6 87	0.02	2 13	0 00	0 11	0.07	20 00	8 00	12 00	20.00	0 76	2.67
NO12	630 8	5.38	2.62	2.86	6 64	0 02	1.99	0.00	0 42	0.07	20 00	8 00	12 00	20 00	0.77	2 62
NO12	630 8	5.61	2 39	3.09	6 95	0 01	1.88	0 00	0 00	0 07	20.00	8 00	12.00	20.00	0 79	2 39
NO12	630 8	5 44	2 56	2 85	6 88	0 02	1.89	0.00	0.30	0.07	20 00	8 00	12 00	20 00	0 78	2 56
NO12	630 8	5 58	2 42	2 87	6 75	0 02	2 07	0 00	0 21	0 07	20 00	8.00	12 00	20 00	0.76	2.42
NO12	630 8	5.53	2.47	3 06	6.75	0 05	1 76	0 00	0 30	0.07	20 00	8.00	12 00	20.00	0.79	2 47
NO12A	708 4	5 42	2.58	2.75	7 22	0 03	1 72	0 00	0 21	0.07	20 00	8 00	12.00	20.00	0 81	2 58
NO12A	708.4	5.34	2 66	2.63	7 27	0.05	1.60	0.00	0 38	0.07	20.00	8 00	12.00	20 00	0 82	2.66
NO12A	708.4	5 49	2.51	2.64	7 31	0.04	1 73	0 00	0 21	0.07	20 00	8.00	12 00	20 00	0.81	2.51
NO12A	708 4	5.30	2 70	2 45	7 17	0 02	1.86	0 00	0 43	0 07	20.00	8.00	12.00	20.00	0 79	2 70
NO12A	708.4	5.44	2 56	2 52	7 30	0.02	1 76	0.00	0 34	0 07	20.00	8 00	12 00	20 00	0.81	2.56
NO12A	708 4	5.36	2 64	2 47	6.98	0 03	2 15	0 00	0.30	0 07	20 00	8 00	12 00	20 00	0.76	2 64
NO12A	708 4	5 42	2.58	2 62	7.37	0 02	1 66	0 00	0 26	0.07	20.00	8 00	12.00	20.00	0 82	2.58
NO12A	708 4	5 41	2 59	2 46	7 26	0.02	1.89	0 00	0 30	0.07	20.00	8 00	12 00	20 00	0.79	2 59
NO12A	708 4	5 51	2.49	2 75	7.13	0.04	1.76	0 00	0 26	0 07	20.00	8.00	12 00	20.00	0 80	2 49
NO12A	708 4	5 37	2 63	2 63	7 22	0 04	1 84	0 00	0.21	0 07	20 00	8.00	12 00	20.00	0 80	2.63
NO03C	873 1	5.34	2.66	2.56	7.81	0 05	1.33	0 00	0.11	0 14	20.00	8 00	12.00	20 00	0.85	2.66

Microprobe Analyses

		Normalised Cation Distribution										Site Occupancy				
Drillhole	Depth	Si	Al	Al	Fe	Mn	Mg	Ca	Na	K	Total	Si + Al	Balance	Total	Fe/(Fe+Mg) Cation Ratio	Tetrahedral Al Cations
NO03C	873 1	5.24	2 76	2 57	7.87	0.03	1 35	0 00	0.11	0 07	20 00	8 00	12 00	20.00	0 85	2.76
NO03C	873 1	5 05	2 95	2.35	7 79	0 03	1 50	0.00	0 11	0 23	20 00	8 00	12 00	20.00	0 84	2 95
NO03C	873 1	5 30	2 70	2.44	7 90	0 00	1.37	0 00	0 11	0 17	20.00	8 00	12 00	20.00	0 85	2 70
NO03C	873.1	5.17	2.83	2 39	7.72	0.04	1 46	0 00	0.11	0 28	20 00	8 00	12 00	20.00	0.84	2.83
NO03C	873.1	5.44	2 56	2 43	7 71	0 02	1.39	0 00	0.11	0 34	20 00	8.00	12.00	20 00	0 85	2 56
NO03C	873 1	5 46	2 54	2 81	7 64	0 03	1 26	0 00	0 11	0 14	20.00	8 00	12 00	20.00	0 86	2 54
NO03C	873.1	5 54	2.46	2 49	7 72	0.06	1.47	0 00	0.11	0 14	20 00	8 00	12 00	20.00	0.84	2.46
NO03C	873 1	5.47	2.53	2 61	7.58	0 04	1.48	0.00	0 11	0 17	20 00	8 00	12.00	20 00	0.84	2 53
NO03C	873 1	5.23	2 77	2 48	7.65	0 02	1.52	0 00	0 11	0.22	20 00	8.00	12.00	20 00	0 83	2 77
NO03C	889.0	5 58	2 42	2 67	7.85	0.04	0.98	0 00	0.39	0 07	20 00	8.00	12 00	20 00	0.89	2.42
NO03C	889 0	5 29	2 71	2.19	7 80	0 05	1 24	0.00	0 65	0 07	20 00	8 00	12 00	20 00	0.86	2 71
NO03C	889.0	5 42	2.58	2 27	8 05	0 02	1 05	0.00	0 53	0 07	20 00	8.00	12.00	20 00	0 88	2 58
NO03C	889.0	5.32	2 68	2 54	7 86	0.03	1.29	0 00	0.22	0 07	20 00	8.00	12 00	20 00	0.86	2 68
NO03C	889.0	5 43	2 57	2.63	7 75	0.03	1 22	0.00	0 30	0 07	20.00	8 00	12 00	20.00	0.86	2.57
NO03C	889 0	5.32	2.68	2 60	7.99	0 03	0.71	0 00	0 60	0.07	20 00	8 00	12.00	20 00	0 92	2.68
NO03C	889.0	5 22	2 78	2 25	7.99	0 03	1.01	0 00	0.65	0 07	20 00	8 00	12 00	20 00	0 89	2.78
NO03C	889.0	5 49	2 51	2.65	7 88	0 03	0 85	0.00	0 52	0 07	20 00	8 00	12 00	20.00	0.90	2 51
NO03C	889 0	5 56	2.44	2.71	7 93	0.03	0.78	0 00	0 48	0 07	20.00	8 00	12 00	20.00	0 91	2 44
NO03C	889 0	5.34	2 66	2.21	7.78	0 03	1 28	0.00	0 63	0 07	20.00	8.00	12 00	20 00	0 86	2.66
NO12A	707.7	5 25	2 75	2.90	7 57	0.04	1 32	0.00	0.11	0 07	20 00	8 00	12 00	20 00	0 85	2 75
NO12A	707.7	5 30	2 70	2 83	7 61	0 04	1 24	0 00	0 21	0 07	20 00	8 00	12 00	20.00	0 86	2 70
NO12A	707.7	5.43	2 57	2 80	7.45	0 04	1.34	0 00	0 30	0.07	20 00	8 00	12 00	20 00	0 85	2 57
NO12A	707 7	5 32	2 68	2 64	7 57	0 06	1 27	0 00	0.39	0 07	20 00	8 00	12 00	20 00	0 86	2 68
NO12A	707 7	5 22	2.78	2 63	7 62	0 05	1 19	0.00	0 43	0.07	20 00	8 00	12.00	20 00	0.86	2.78
NO12A	707 7	5.33	2 67	2.77	7 66	0 03	1 21	0 00	0 26	0 07	20.00	8 00	12 00	20.00	0.86	2 67
NO12A	707 7	5 33	2 67	2.66	7 48	0.04	1 46	0.00	0 30	0 07	20 00	8 00	12.00	20 00	0 84	2 67
NO12A	707.7	5 39	2.61	2.85	7 48	0 06	1.32	0.00	0.22	0 07	20 00	8.00	12 00	20.00	0 85	2 61
NO12A	707.7	5 46	2 54	2 69	7.45	0 04	1.50	0 00	0.26	0 07	20 00	8 00	12 00	20.00	0 83	2 54
NO12A	707.7	5 26	2 74	2 71	7.64	0.05	1.42	0 00	0.11	0 07	20.00	8 00	12 00	20.00	0 84	2 74
NO14D	999 5	5.50	2.50	2.64	7 42	0 04	1.27	0 00	0 56	0 07	20 00	8.00	12 00	20.00	0 85	2 50
NO14D	999.5	5 56	2 44	2.75	7 36	0 05	1 51	0 00	0 26	0 07	20 00	8 00	12.00	20 00	0 83	2.44
NO14D	999 5	5 61	2 39	2 80	7.37	0.03	1 42	0 00	0 30	0.07	20 00	8.00	12 00	20.00	0.84	2 39
NO14D	999 5	5.62	2.38	2.60	7 39	0 06	1 49	0 00	0.39	0.07	20 00	8 00	12 00	20 00	0 83	2.38
NO14D	999 5	5 48	2 52	2.62	7 10	0 06	1 68	0 00	0 47	0 07	20 00	8 00	12.00	20 00	0.81	2 52
NO14D	999 5	5.51	2 49	2 55	7.45	0.05	1 44	0 00	0 43	0.07	20 00	8.00	12 00	20.00	0.84	2 49
NO14D	999 5	5.44	2 56	2 55	7 38	0 05	1 57	0 00	0.39	0 07	20 00	8 00	12 00	20 00	0 82	2 56
NO14D	999.5	5 53	2 47	2 69	7 39	0 03	1.56	0 00	0.26	0 07	20 00	8.00	12 00	20 00	0 83	2.47
NO14D	999.5	5 62	2 38	2.82	7 38	0.06	1.33	0 00	0.35	0 07	20.00	8 00	12.00	20 00	0.85	2.38
NO14D	999 5	5 47	2 53	2 83	7.50	0 04	1.13	0 00	0 43	0.07	20 00	8 00	12 00	20.00	0 87	2.53
NO12	665.2	5 37	2 63	2 85	6.06	0 11	2 81	0 00	0 10	0 07	20 00	8 00	12 00	20 00	0 68	2 63
NO12	665 2	5 28	2 72	2 84	6.16	0 08	2 75	0.00	0 10	0.07	20 00	8 00	12.00	20 00	0.69	2 72
NO12	665 2	5 19	2 81	2 74	6.27	0 07	2 75	0 00	0 10	0 07	20 00	8.00	12 00	20.00	0.70	2 81
NO12	665.2	5 28	2 72	3 04	6.10	0 09	2 59	0 00	0 10	0 07	20 00	8 00	12.00	20 00	0 70	2 72
NO12	665 2	5 37	2.63	2.83	6 19	0.08	2 72	0 00	0 10	0.07	20 00	8 00	12.00	20 00	0 69	2 63
NO12	665 2	5.38	2 62	2 78	6 02	0.11	2 93	0 00	0.10	0 07	20 00	8 00	12 00	20.00	0.67	2 62
NO12	665 2	5.29	2 71	2 70	6.11	0 08	2 93	0 00	0 10	0 07	20.00	8.00	12 00	20 00	0 68	2 71
NO12	665.2	5 33	2 67	2.90	6 22	0 09	2.62	0 00	0.10	0 07	20 00	8 00	12 00	20.00	0 70	2.67
NO12	665 2	5.30	2 70	2 78	6 08	0 09	2 88	0 00	0 10	0 07	20 00	8 00	12.00	20.00	0.68	2 70
NO12	665 2	5 25	2.75	2 70	6.16	0.10	2 87	0 00	0 10	0 07	20.00	8 00	12.00	20 00	0 68	2 75
NO12	666.0	5 30	2 70	2 54	6.32	0 07	2 89	0.00	0 10	0.07	20 00	8 00	12 00	20 00	0 69	2 70
NO12	666 0	5 23	2.77	2 50	5 82	0.07	3 33	0 00	0 21	0 07	20 00	8 00	12.00	20.00	0.64	2 77

Microprobe Analyses

		Normalised Cation Distribution										Site Occupancy				
Drillhole	Depth	Si	Al	Al	Fe	Mn	Mg	Ca	Na	K	Total	Si + Al	Balance	Total	Fe/(Fe+Mg) Cation Ratio	Tetrahedral Al Cations
NO12	666.0	5 31	2 69	2 66	6 09	0 05	2.91	0 00	0 21	0 07	20 00	8.00	12 00	20 00	0 68	2 69
NO12	666.0	5.34	2.66	2 55	6 02	0.08	2 99	0.00	0 29	0.07	20.00	8 00	12 00	20 00	0.67	2.66
NO12	666.0	5 35	2 65	2 59	6.02	0 06	3.16	0 00	0.10	0 07	20 00	8.00	12.00	20 00	0.66	2 65
NO12	666.0	5.16	2.84	2.60	6.17	0.07	2.88	0 00	0 21	0 07	20 00	8.00	12.00	20 00	0 68	2.84
NO12	666 0	5.30	2.70	2.56	6 17	0.06	3.04	0.00	0 10	0 07	20.00	8 00	12 00	20.00	0 67	2.70
NO12	666.0	5 35	2 65	2 84	6.23	0 06	2.70	0 00	0.10	0 07	20 00	8.00	12.00	20.00	0 70	2 65
NO12	666.0	5.21	2 79	2 59	6 32	0 08	2 74	0 00	0 21	0.07	20 00	8 00	12 00	20 00	0.70	2 79
NO12	666 0	5 41	2 59	2 68	6.29	0 07	2 78	0.00	0 11	0 07	20.00	8 00	12 00	20.00	0 69	2 59
NO12A	743 5	5 55	2 45	2 72	6 19	0 08	2.43	0.00	0.50	0.07	20 00	8 00	12 00	20 00	0 72	2.45
NO12A	743 5	5 50	2 50	2 71	6 30	0 06	2 40	0 00	0.46	0.07	20 00	8 00	12 00	20 00	0.72	2.50
NO12A	743 5	5 53	2 47	2 79	6.33	0 04	2 55	0.00	0 21	0 07	20.00	8 00	12.00	20.00	0 71	2 47
NO12A	743 5	5.53	2.47	2 80	6 30	0.08	2.49	0.00	0 25	0 07	20 00	8 00	12 00	20.00	0.72	2.47
NO12A	743 5	5 40	2.60	2 80	6.28	0 07	2 49	0 00	0 29	0.07	20 00	8.00	12 00	20.00	0.72	2 60
NO12A	743 5	5.50	2 50	2.71	6.40	0 05	2 39	0.00	0 38	0 07	20.00	8 00	12.00	20 00	0 73	2 50
NO12A	743.5	5 40	2 60	2.78	6 40	0.06	2 22	0 00	0.46	0 07	20 00	8.00	12.00	20.00	0.74	2.60
NO12A	743 5	5 57	2.43	2 99	6 60	0 11	2 12	0.00	0.11	0 07	20.00	8 00	12 00	20 00	0.76	2.43
NO12A	743 5	5 40	2.60	2.61	6.32	0 08	2 42	0 00	0.51	0.07	20 00	8.00	12.00	20 00	0 72	2 60
NO12A	743.5	5 44	2 56	2.94	6.46	0 12	2 16	0.00	0 25	0 07	20.00	8 00	12 00	20 00	0.75	2 56
NO14	543.9	5 54	2.46	2 92	5 51	0 06	3.51	0.00	0.00	0 00	20.00	8 00	12 00	20 00	0.61	2.46
NO14	543.9	5.41	2 59	2 86	5.59	0.09	3 47	0 00	0.00	0.00	20 00	8.00	12.00	20.00	0 62	2.59
NO14	543 9	5 36	2 64	2.96	5 58	0 07	3 39	0 00	0 00	0 00	20 00	8.00	12.00	20.00	0 62	2 64
NO14	543 9	5.43	2 57	2.93	5 62	0 07	3.38	0.00	0.00	0 00	20 00	8 00	12 00	20 00	0.62	2 57
NO14	543 9	5.49	2 51	3 03	5 70	0 05	3 21	0 00	0 00	0.00	20 00	8 00	12 00	20.00	0 64	2.51
NO14	543 9	5.57	2.43	2 95	5.51	0 06	3 48	0 00	0 00	0.00	20 00	8 00	12 00	20.00	0.61	2 43
NO14	543 9	5 57	2 43	2.95	5 56	0.05	3.45	0.00	0.00	0.00	20.00	8 00	12 00	20 00	0.62	2 43
NO14	543 9	5 57	2 43	2 99	5 64	0 04	3 32	0 00	0 00	0.00	20 00	8 00	12 00	20.00	0.63	2 43
NO14	543 9	5.46	2 54	2 99	5.65	0 04	3 33	0 00	0 00	0 00	20.00	8 00	12 00	20 00	0.63	2 54
NO14	543 9	5.46	2 54	2.95	5.52	0 04	3.49	0.00	0.00	0.00	20.00	8 00	12 00	20.00	0.61	2.54
NO14	543.9	5 48	2 52	2 93	5.67	0 07	3 33	0.00	0 00	0 00	20.00	8 00	12 00	20 00	0 63	2.52
NO14	543.9	5.41	2.59	2 95	5.68	0.06	3 31	0.00	0.00	0 00	20 00	8.00	12.00	20 00	0.63	2 59
NO14	543 9	5 46	2 54	2.89	5 82	0 04	3 25	0 00	0 00	0.00	20 00	8 00	12.00	20 00	0.64	2 54
NO14	543 9	5.47	2 53	2 86	5 73	0 07	3 33	0.00	0 00	0 00	20.00	8 00	12 00	20 00	0.63	2.53
NO14	543 9	5.46	2.54	2 80	5.55	0 09	3 56	0.00	0.00	0 00	20 00	8 00	12.00	20.00	0 61	2 54
NO14	543 9	5.48	2 52	2.85	5.74	0.04	3.37	0.00	0 00	0.00	20.00	8 00	12 00	20 00	0 63	2.52
NO14	543.9	5 37	2 63	2 86	5 82	0.06	3 27	0 00	0.00	0 00	20 00	8 00	12.00	20.00	0.64	2.63
NO14	543 9	5 58	2.42	2 98	5.62	0 06	3.34	0.00	0 00	0.00	20.00	8 00	12 00	20 00	0 63	2 42
NO14	543 9	5 43	2 57	2.82	5 74	0 06	3 38	0 00	0 00	0 00	20 00	8 00	12 00	20.00	0.63	2 57
NO14	543 9	5.50	2.50	2.91	5 72	0 08	3 29	0.00	0.00	0 00	20 00	8 00	12.00	20.00	0 64	2.50
N0O3G	807 4	5.43	2 57	3.03	6.95	0 11	1.91	0 00	0 00	0.00	20 00	8.00	12 00	20 00	0.78	2 57
N0O3G	807 4	5 31	2 69	2 88	6 95	0.12	2 05	0 00	0 00	0 00	20 00	8.00	12 00	20 00	0.77	2 69
N0O3G	807 4	5.35	2.65	2 84	7.04	0 13	1 99	0.00	0.00	0 00	20.00	8.00	12.00	20 00	0.78	2 65
N0O3G	807 4	5 31	2 69	2 90	6 97	0 09	2 04	0.00	0 00	0 00	20 00	8 00	12 00	20 00	0 77	2 69
N0O3G	807.4	5 39	2 61	3 05	6.90	0 06	1 98	0 00	0.00	0 00	20 00	8.00,	12.00	20 00	0 78	2 61
N0O3G	807 4	5 43	2.57	3 08	6 94	0.09	1 90	0.00	0 00	0.00	20 00	8 00	12 00	20 00	0.79	2.57
N0O3G	807.4	5 35	2 65	2 92	7 13	0 12	1.83	0.00	0.00	0 00	20.00	8 00	12.00	20.00	0 80	2 65
N0O3G	807.4	5.37	2 63	2.96	7 10	0 09	1 85	0.00	0.00	0 00	20.00	8 00	12 00	20 00	0 79	2 63
N0O3G	807 4	5.49	2.51	2 94	6 87	0 10	2.08	0 00	0 00	0 00	20 00	8.00	12 00	20.00	0.77	2 51
N0O3G	807.4	5.44	2 56	2 77	7.20	0 08	1 95	0.00	0 00	0.00	20 00	8.00	12.00	20 00	0 79	2 56
N0O3G	807.4	5.45	2 55	2.95	7 21	0 13	1 71	0.00	0.00	0.00	20 00	8 00	12 00	20 00	0.81	2.55
N0O3G	807.4	5.39	2 61	2 94	7 27	0.06	1.73	0.00	0 00	0 00	20 00	8 00	12.00	20 00	0 81	2 61
N0O3G	807 4	5.51	2 49	3.07	7 20	0 11	1 62	0.00	0.00	0.00	20 00	8 00	12 00	20.00	0.82	2 49

Microprobe Analyses

		Normalised Cation Distribution										Site Occupancy				
Drillhole	Depth	Si	Al	Al	Fe	Mn	Mg	Ca	Na	K	Total	Si + Al	Balance	Total	Fe/(Fe+Mg) Cation Ratio	Tetrahedral Al Cations
N0O3G	807.4	5 45	2 55	2 99	7 29	0 08	1.63	0 00	0 00	0.00	20.00	8 00	12 00	20 00	0 82	2 55
N0O3G	807 4	5.38	2 62	2 93	7 27	0 12	1 68	0 00	0.00	0.00	20.00	8 00	12 00	20 00	0 81	2 62
N0O3G	807 4	5.41	2 59	2 98	7 25	0 09	1 67	0.00	0.00	0 00	20.00	8 00	12.00	20.00	0 81	2 59
N0O3G	807 4	5.37	2 63	2 98	7.27	0.09	1 66	0 00	0 00	0 00	20 00	8 00	12 00	20 00	0 81	2.63
N0O3G	807.4	5.31	2 69	2 92	7 26	0 08	1.74	0 00	0 00	0.00	20 00	8 00	12 00	20 00	0 81	2.69
N0O3G	807.4	5.24	2.76	2.83	7 34	0 11	1 72	0 00	0 00	0 00	20 00	8 00	12.00	20.00	0.81	2 76
N0O3G	807.4	5 39	2 61	2.92	7 25	0 08	1.76	0.00	0 00	0.00	20 00	8.00	12.00	20 00	0 80	2 61
NO14E	1157 6	5 58	2.42	3.13	4 99	0 05	3.83	0 00	0 00	0 00	20 00	8 00	12 00	20 00	0 57	2 42
NO14E	1157 6	5 41	2.59	2.93	5.05	0.05	3 97	0 00	0 00	0 00	20 00	8 00	12.00	20 00	0 56	2 59
NO14E	1157.6	5 60	2 40	3 01	4.99	0.07	3.94	0.00	0 00	0.00	20 00	8 00	12 00	20 00	0 56	2 40
NO14E	1157.6	5.55	2 45	3 02	5.05	0 05	3 89	0 00	0.00	0.00	20 00	8.00	12 00	20 00	0 57	2 45
NO14E	1157 6	5 39	2.61	3.06	5 01	0 06	3 87	0 00	0 00	0 00	20 00	8 00	12 00	20.00	0 56	2 61
NO14E	1157 6	5 40	2 60	2 95	5.14	0 06	3 85	0.00	0 00	0 00	20 00	8 00	12 00	20 00	0 57	2.60
NO14E	1157 6	5.47	2 53	2 99	5 04	0 07	3 90	0 00	0.00	0.00	20 00	8.00	12.00	20 00	0 56	2 53
NO14E	1157 6	5 40	2 60	3.03	5.11	0.06	3 80	0 00	0 00	0 00	20 00	8 00	12.00	20.00	0 57	2 60
NO14E	1157.6	5 52	2 48	3 07	4 91	0 05	3 96	0.00	0 00	0 00	20 00	8 00	12 00	20 00	0 55	2 48
NO14E	1157.6	5 42	2 58	3 04	5 05	0 07	3 83	0.00	0.00	0 00	20 00	8 00	12.00	20 00	0 57	2 58
NO14E	1157 6	5.48	2 52	2 91	5 21	0 09	3 78	0 00	0 00	0 00	20.00	8.00	12 00	20 00	0 58	2 52
NO14E	1157 6	5.46	2 54	3 04	5 11	0 05	3 81	0 00	0 00	0 00	20 00	8 00	12 00	20 00	0.57	2 54
NO14E	1157.6	5.44	2 56	2 93	5 03	0 08	3 96	0 00	0.00	0 00	20 00	8 00	12 00	20 00	0 56	2 56
NO14E	1157 6	5.56	2 44	3 03	4 78	0 08	4 10	0.00	0.00	0.00	20 00	8.00	12 00	20 00	0 54	2 44
NO14E	1157 6	5.66	2 34	3 12	5 04	0 02	3.82	0.00	0 00	0 00	20 00	8 00	12 00	20 00	0 57	2 34
NO14E	1157 6	5.53	2 47	3 15	5 11	0.05	3 69	0 00	0 00	0 00	20 00	8 00	12 00	20 00	0 58	2 47
NO14E	1157 6	5.49	2.51	3 02	5 10	0 04	3 84	0 00	0 00	0 00	20 00	8 00	12.00	20 00	0.57	2 51
NO14E	1157 6	5 54	2 46	3 04	5 02	0 05	3 89	0 00	0 00	0.00	20 00	8 00	12.00	20.00	0.56	2 46
NO14E	1157.6	5 40	2.60	2 96	5 08	0 08	3 88	0 00	0 00	0 00	20 00	8 00	12 00	20 00	0 57	2 60
NO14E	1157 6	5 40	2 60	2 88	5 03	0 09	4.00	0.00	0 00	0 00	20 00	8 00	12 00	20 00	0 56	2 60
NO25	179.8	5 28	2.72	2.68	7 47	0.07	1.77	0.00	0 00	0.00	20 00	8.00	12 00	20 00	0.81	2 72
NO25	179 8	5 36	2 64	2 76	7 31	0 13	1.80	0.00	0 00	0.00	20.00	8.00	12 00	20 00	0.80	2 64
NO25	179 8	5 34	2.66	2 90	7 29	0.08	1 73	0.00	0 00	0 00	20 00	8.00	12 00	20 00	0.81	2.66
NO25	179.8	5.37	2.63	2 98	7 25	0 09	1 68	0 00	0.00	0.00	20.00	8 00	12.00	20.00	0 81	2 63
NO25	179 8	5 27	2.73	2.88	7.30	0.10	1.72	0 00	0 00	0 00	20 00	8 00	12 00	20 00	0 81	2 73
NO25	179 8	5 38	2 62	2 97	7.27	0 10	1.67	0 00	0 00	0 00	20 00	8 00	12 00	20 00	0.81	2.62
NO25	179 8	5 33	2 67	2 85	7.32	0 07	1.76	0 00	0 00	0 00	20 00	8 00	12 00	20.00	0 81	2 67
NO25	179 8	5 25	2.75	2.83	7.35	0 12	1 70	0 00	0 00	0 00	20 00	8 00	12.00	20 00	0 81	2.75
NO25	179 8	5 32	2 68	2.89	7.20	0 12	1 79	0 00	0 00	0 00	20 00	8 00	12 00	20 00	0.80	2.68
NO25	179 8	5 40	2 60	2 89	7 31	0.08	1 72	0.00	0 00	0 00	20.00	8.00	12 00	20 00	0 81	2 60
NO25	223.8	5.42	2 58	2 96	6 87	0 08	2 09	0.00	0.00	0.00	20 00	8 00	12 00	20.00	0 77	2 58
NO25	223.8	5 37	2 63	2 96	6.86	0.06	2 12	0 00	0 00	0 00	20 00	8 00	12 00	20 00	0.76	2.63
NO25	223 8	5 38	2 62	2 93	6 72	0 09	2 25	0 00	0 00	0 00	20 00	8 00	12.00	20.00	0 75	2 62
NO25	223 8	5 44	2 56	2 93	6 76	0 10	2 21	0 00	0 00	0 00	20.00	8 00	12 00	20 00	0 75	2 56
NO25	223 8	5 33	2 67	2.91	6 85	0 09	2 15	0 00	0 00	0 00	20 00	8 00	12.00	20.00	0 76	2.67
NO25	223 8	5.48	2 52	2 90	6 81	0 10	2 19	0.00	0 00	0 00	20.00	8 00	12 00	20.00	0.76	2 52
NO25	223.8	5 39	2 61	2.78	6 79	0 09	2 34	0 00	0 00	0 00	20 00	8 00	12.00	20 00	0 74	2 61
NO25	223 8	5.39	2 61	3.06	6 75	0 05	2 14	0 00	0 00	0 00	20 00	8 00	12.00	20.00	0 76	2 61
NO25	223 8	5 36	2 64	2.88	6 84	0 05	2 23	0 00	0.00	0 00	20 00	8 00	12.00	20.00	0 75	2 64
NO25	223 8	5 50	2 50	2 92	6.75	0 10	2 23	0 00	0 00	0 00	20 00	8 00	12 00	20.00	0 75	2 50
NO25	214 7	5 27	2 73	2 81	6.96	0 09	2.13	0.00	0 00	0 00	20.00	8 00	12 00	20.00	0.77	2 73
NO25	214 7	5 36	2.64	2 97	6 80	0 11	2 12	0 00	0 00	0 00	20 00	8 00	12.00	20 00	0 76	2 64
NO25	214 7	5 23	2 77	2 87	6 94	0 10	2 09	0 00	0 00	0 00	20 00	8.00	12 00	20.00	0.77	2 77
NO25	214.7	5 37	2 63	2.89	6 93	0 09	2.09	0 00	0 00	0 00	20 00	8.00	12 00	20.00	0.77	2 63

Microprobe Analyses

		Normalised Cation Distribution										Site Occupancy				
Drillhole	**Depth**	**Si**	**Al**	**Al**	**Fe**	**Mn**	**Mg**	**Ca**	**Na**	**K**	**Total**	**Si + Al**	**Balance**	**Total**	**Fe/(Fe+Mg) Cation Ratio**	**Tetrahedral Al Cations**
NO25	214.7	5 34	2 66	2.97	6.77	0.14	2.13	0 00	0.00	0 00	20.00	8 00	12.00	20 00	0.76	2 66
NO25	214 7	5 38	2 62	2 83	6 87	0 06	2 25	0 00	0 00	0 00	20 00	8 00	12.00	20.00	0 75	2 62
NO25	214.7	5 26	2 74	2 95	6.94	0 07	2.03	0 00	0 00	0 00	20.00	8 00	12 00	20 00	0.77	2.74
NO25	214.7	5 18	2 82	2 95	6.85	0.10	2 11	0 00	0.00	0.00	20.00	8 00	12 00	20 00	0 76	2.82
NO25	214 7	5 30	2.70	2.99	6.75	0.09	2 17	0 00	0 00	0 00	20.00	8 00	12 00	20 00	0.76	2.70
NO25	214.7	5 33	2 67	2.84	6.90	0.08	2 18	0.00	0 00	0.00	20.00	8 00	12 00	20 00	0 76	2 67
NO26	327 6	5.39	2 61	2.86	6.70	0.11	2 33	0.00	0 00	0 00	20.00	8 00	12 00	20 00	0 74	2 61
NO26	327 6	5 41	2 59	2 88	6.90	0 10	2 11	0.00	0 00	0 00	20.00	8 00	12 00	20 00	0.77	2.59
NO26	327.6	5.30	2.70	2 89	6 88	0 10	2 12	0.00	0 00	0.00	20.00	8 00	12 00	20 00	0 76	2.70
NO26	327 6	5 36	2 64	2 92	6 86	0 08	2 14	0.00	0 00	0.00	20.00	8 00	12 00	20 00	0 76	2 64
NO26	327.6	5.46	2.54	3 01	6 79	0 10	2 10	0.00	0 00	0.00	20 00	8 00	12.00	20.00	0.76	2 54
NO26	327 6	5 47	2 53	2.82	6 93	0 08	2 17	0.00	0 00	0.00	20 00	8.00	12 00	20 00	0 76	2 53
NO26	327.6	5.53	2.47	2 89	6 80	0 06	2 25	0.00	0.00	0.00	20.00	8 00	12 00	20 00	0 75	2.47
NO26	327 6	5 42	2 58	2 90	6 87	0 09	2.14	0.00	0 00	0.00	20 00	8.00	12 00	20 00	0 76	2 58
NO26	327.6	5 38	2.62	2 88	6 95	0 09	2 08	0.00	0.00	0.00	20 00	8 00	12 00	20 00	0 77	2.62
NO26	327 6	5 45	2 55	2 80	6 96	0.07	2.17	0.00	0 00	0.00	20 00	8 00	12.00	20.00	0 76	2 55

Appendix 4: Qualitative Energy Dispersive Electron Microbeam Analyses – Stilpnomelane

Microprobe Analyses

				Weight Percents								
Drillhole	**Depth**	**Mineral**	**Description**	**SiO_2**	**Al_2O_3**	**FeO**	**MnO**	**MgO**	**Na_2O**	**K2O**	**Total**	**FeO/(FeO+MgO)**
NO3C	873 1	Stilpnomelane	Coarse grained	46 74	6 40	35 20	0.31	2.58	1 12	2.54	94 89	0 93
NO3C	873.1	Stilpnomelane	Coarse grained	46 09	6 64	34 36	0 29	2 81	1 15	2 54	93.88	0.92
NO3C	873 1	Stilpnomelane	Coarse grained	46 59	6 57	33 99	0 37	2 20	0 81	1.78	92 31	0.94
NO3C	873.1	Stilpnomelane	Coarse grained	45 84	7 14	34.49	0 26	2 59	0 90	2.27	93 49	0.93
NO3C	873.1	Stilpnomelane	Coarse grained	45 90	6 65	35 19	0.38	1.96	1.44	2 84	94.36	0 95
NO3C	873 1	Stilpnomelane	Fine grained	46 26	6 80	34.51	0 39	2 58	0 95	2.61	94 10	0.93
NO3C	873 1	Stilpnomelane	Fine grained	45.78	6 44	33 20	0.30	2 71	1 46	3.01	92 90	0 92
NO3C	873.1	Stilpnomelane	Fine grained	47 16	5 79	33 37	0.34	2.66	1.23	2 55	93.10	0 93
NO3C	873 1	Stilpnomelane	Fine grained	45 87	6.04	33.35	0 20	2 09	1.33	3 17	92 05	0 94
NO3C	873 1	Stilpnomelane	Fine grained	46.46	5.79	33 69	0 35	2 44	0.99	2 80	92 52	0.93
NO3C	889 1	Stilpnomelane	Coarse grained	46 68	6 45	36 09	0 13	1.84	1.50	2 26	94.95	0 95
NO3C	889 1	Stilpnomelane	Coarse grained	46 47	7.06	36.28	0 17	1 51	1 70	2 25	95 44	0 96
NO3C	889 1	Stilpnomelane	Coarse grained	46.42	6.84	35.69	0.10	1.63	0 80	2 26	93.74	0.96
NO3C	889 1	Stilpnomelane	Coarse grained	46.33	6 02	36 14	0 11	1.88	1.10	2 98	94 56	0 95
NO3C	889.1	Stilpnomelane	Coarse grained	46 56	5 32	37 17	0 17	1 66	1 30	2.54	94 72	0 96
NO3C	889 1	Stilpnomelane	Fine grained	46 74	6 55	36 47	0 22	1 29	1.50	2 16	94 93	0 97
NO3C	889 1	Stilpnomelane	Fine grained	46 49	5.97	36.48	0 17	2 32	1 30	2.09	94 82	0.94
NO3C	889 1	Stilpnomelane	Fine grained	46 53	5 95	36 95	0.18	1.71	1 60	2.72	95 64	0 96
NO3C	889 1	Stilpnomelane	Fine grained	46.52	5 80	36 91	0 22	1 45	1.70	1 57	94 17	0 96
NO3C	889.1	Stilpnomelane	Fine grained	46 44	6.56	36.31	0 20	1 78	1 40	2 23	94 92	0 95
NO7A	736.4	Stilpnomelane	Fine grained replacing chlorite	46 83	5 40	34 33	0.64	2 99	0 50	2 64	93.33	0.92
NO7A	736.4	Stilpnomelane	Fine grained replacing chlorite	47.80	5 19	33 59	0.91	3.32	0 00	3 11	93 92	0.91
NO7A	736 4	Stilpnomelane	Fine grained replacing chlorite	46 94	5 75	34 90	0.68	2 48	0 50	2.85	94 10	0.93
NO7A	736 4	Stilpnomelane	Fine grained replacing chlorite	46 37	5 19	35.16	0.33	2 33	1 00	3 24	93.62	0.94
NO7A	736.4	Stilpnomelane	Fine grained replacing chlorite	46 81	5 53	34.68	1.31	2.42	1 00	1.95	93 70	0.93
NO7A	736.4	Stilpnomelane	Fine grained replacing chlorite	47 01	5 74	34 02	0.73	3 13	0 50	3 63	94 76	0.92
NO7A	736.4	Stilpnomelane	Fine grained replacing chlorite	46 45	4.92	34 69	0.51	2.66	1 00	2 76	92 99	0.93
NO7A	736.4	Stilpnomelane	Fine grained replacing chlorite	46 79	5 29	34.90	0.90	3 02	1 00	2 06	93 96	0 92
NO7A	736 4	Stilpnomelane	Fine grained replacing chlorite	46 47	4 91	34 42	0.79	3.04	1.00	3 53	94.16	0 92
NO7A	736 4	Stilpnomelane	Fine grained replacing chlorite	46.39	6 14	34 72	1.10	2 53	0.50	2 15	93 53	0 93
NO12A	708.4	Stilpnomelane	Fine grained replacing chlorite	46 48	6 58	32.29	0 30	3 35	1 78	2.54	93 32	0.91
NO12A	708.4	Stilpnomelane	Fine grained replacing chlorite	46.87	6.37	32 46	0.33	3 47	1 37	2 56	93 43	0.90
NO12A	708 4	Stilpnomelane	Fine grained replacing chlorite	47.51	5 95	32 58	0 36	3.15	1.32	2.49	93 36	0.91
NO12A	708.4	Stilpnomelane	Fine grained replacing chlorite	47 39	6 36	32 47	0 23	3.01	1 19	2.66	93.31	0 92
NO12A	708 4	Stilpnomelane	Fine grained replacing chlorite	46.62	6 11	33 00	0.18	3 47	1 10	3 14	93 62	0 90
NO12A	708.4	Stilpnomelane	Fine grained replacing chlorite	46 45	6 97	33.14	0 16	3.52	1.89	2 78	94.91	0 90
NO12A	708 4	Stilpnomelane	Fine grained replacing chlorite	46.41	6.67	33 82	0.25	3 53	1 32	2 32	94 32	0 91
NO12A	708 4	Stilpnomelane	Fine grained replacing chlorite	47.44	6 60	32 20	0.12	3 46	1.36	2.52	93.70	0 90
NO12A	708.4	Stilpnomelane	Fine grained replacing chlorite	46.93	6.67	32 95	0.19	2 84	1 28	3.43	94 29	0 92
NO12A	708.4	Stilpnomelane	Fine grained replacing chlorite	46 90	7.14	32 85	0 10	3 33	1.34	2 55	94 21	0.91
NO14D	999 5	Stilpnomelane	Fine grained replacing chlorite	46.84	6 82	32 68	0 56	2.54	1 94	2 52	93 90	0 93
NO14D	999.5	Stilpnomelane	Fine grained replacing chlorite	46.37	6 42	32.83	0.54	2 99	1.33	2 62	93.10	0.92
NO14D	999 5	Stilpnomelane	Fine grained replacing chlorite	46 54	5 95	32.91	0 48	3 15	2.10	3 24	94 37	0 91
NO14D	999 5	Stilpnomelane	Fine grained replacing chlorite	46.08	6.40	33 74	0.43	2 80	1 77	2 74	93.96	0 92
NO14D	999 5	Stilpnomelane	Fine grained replacing chlorite	46 33	6.56	33 42	0 55	2 44	1.56	2.20	93 06	0.93
NO14D	999 5	Stilpnomelane	Fine grained replacing chlorite	46 52	5 99	32.88	0 66	2 74	1.40	3.13	93.32	0 92
NO14D	999 5	Stilpnomelane	Fine grained replacing chlorite	46 09	6.96	32.90	0 69	2 72	1 93	2 54	93.83	0 92
NO14D	999 5	Stilpnomelane	Fine grained replacing chlorite	46.49	6 23	33.24	0 43	2 68	1 31	2 49	92 87	0.93
NO14D	999 5	Stilpnomelane	Fine grained replacing chlorite	46.11	6 44	33.12	0 67	2 91	1.60	2 69	93.54	0 92
NO14D	999 5	Stilpnomelane	Fine grained replacing chlorite	46 78	6 40	32 83	0 33	2.81	1.82	2 44	93 41	0.92

Appendix 5: SWIR Spectral Parameters and Profiles

Table 49: PIMA Spectral Parameters.

Parameter:	Mineralogical Feature:
Wavelength of Al-OH absorption feature	The wavelength of the main Al-OH absorption band at 2190–2230nm indicates the composition of white mica. The wavelength of the Al-OH absorption band increases with increasing Fe/Mg/Si and decreasing Al content of white mica from tending to paragonitic (2194nm–2198nm), muscovitic (2198–2208nm), tending to phengitic (2208–2216nm) and to phengitic (>2216nm).
Depth of Al-OH absorption feature	The depth of the main Al-OH absorption band at 2190–2230nm can indicate the relative abundance of white mica in the sample.
Area of Al-OH absorption feature	The area of the main Al-OH absorption band at 2190–2230nm can indicate the relative abundance of white mica in the sample.
Wavelength of Fe-OH absorption feature	The wavelength of the main Fe-OH absorption band at 2230–2245nm is related to chlorite Fe/(Fe+Mg) ratio. The wavelength of Fe-OH absorption band increases with increasing Fe/(Fe+Mg) ratio. The Fe-OH absorption wavelengths of Fe-chlorites are >2258nm and those of intermediate chlorites vary from 2254–2258nm.
Depth of Fe-OH absorption feature	The depth of the main Fe-OH absorption band at 2230–2245nm can indicate the relative abundance of chlorite in the sample.
Area of Fe-OH absorption feature	The area of the main Fe-OH absorption band at 2230–2245nm can indicate the relative abundance of chlorite in the sample.
Wavelength of Mg-OH absorption feature	The wavelength of the main Mg-OH absorption band at 2300–2350nm is related to the presence of carbonate with chlorite and/or sericite.
Depth of Mg-OH absorption feature	The depth of the main Mg-OH absorption band at 2300–2350nm is related to the presence of carbonate with chlorite and/or sericite.
Ratio of the depth of the Al-OH and Fe-OH absorption features	The ratio of the depth of the main Al-OH absorption feature at 2190–2230nm to the depth of main Fe-OH absorption band at 2230–2245nm is related to the sericite versus chlorite ratio. Values of >1 indicate the dominance of sericite whilst values of <1 indicate the dominance of chlorite. Null values are reported where chlorite or sericite only are present.
Ratio of the depth of the Al-OH and Mg-OH absorption features	The ratio of the depth of the main Al-OH absorption feature at 2190–2230nm to the depth of main Mg-OH absorption band at 2300–2350nm is related to the sericite versus chlorite ratio. Values of >1 indicate the dominance of sericite whilst values of <1 indicate the dominance of chlorite (and/or carbonate). The ratio is influenced by variations in carbonate proportions.
Normalised reflectance value at 1350nm	Normalised reflectance at 1350nm is inversely proportional to abundance of Fe^{2+} minerals and can therefore indicate the presence of strongly Fe^{2+} minerals and/or variations in Fe^{2+} content of minerals like chlorite. Values of <0 indicate the presence of abundant Fe^{2+}-bearing minerals.
Stipnomelane Abundance Index (Ausspec, 2000)	Ratio of the depth of water absorption features around 1914nm to the depth of the deepest feature in the 2150–2450nm range. Spikes of high values can indicate the presence of stilpnomelane but is influenced by the presence of smectite, "wet" samples or water in fluid inclusions.
Sericite Crystallinity Index	The ratio of the depth of the main Al-OH absorption feature at 2190–2230nm to the depth of main water absorption band at around 1914nm is related to the crystallinity of white mica. Values of <1 indicate the presence of smectite, which potentially influence the stilpnomelane abundance index. Increasing values indicate increasing white mica crystallinity.

Figure 206: Comparison of Stilpnomelane and Fe-chlorite corrected and smoothed Hull Quotient Spectra.

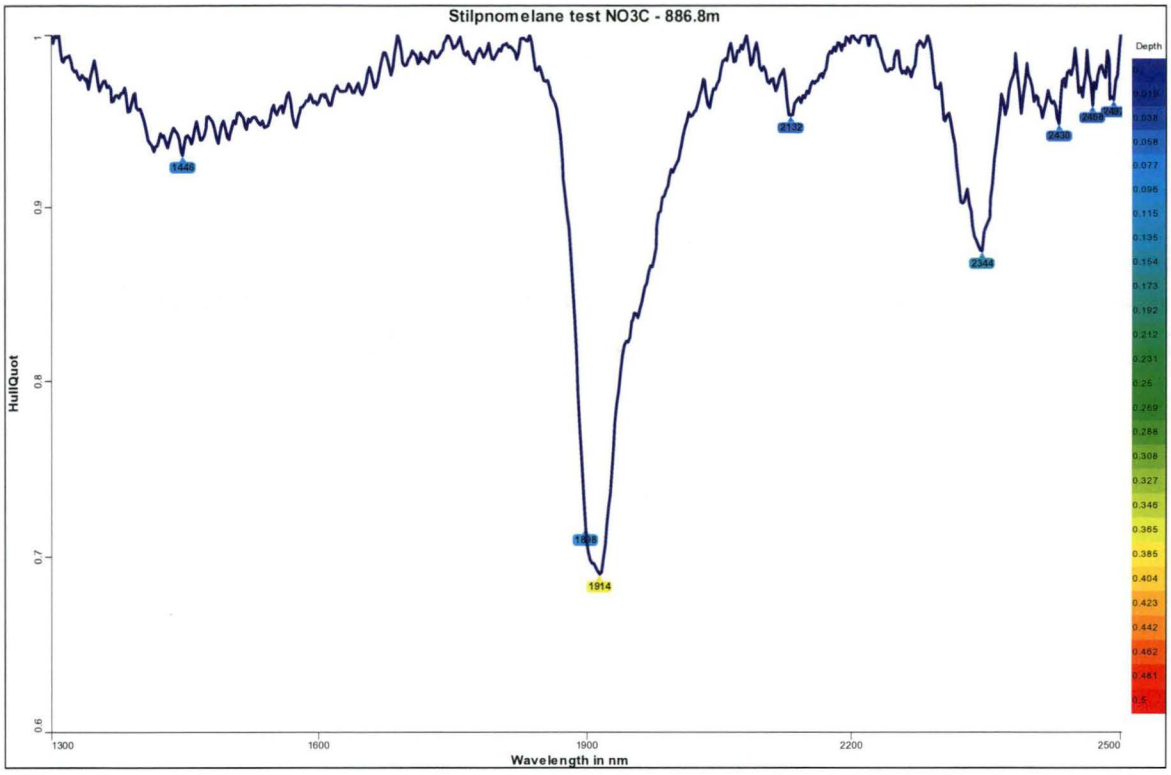

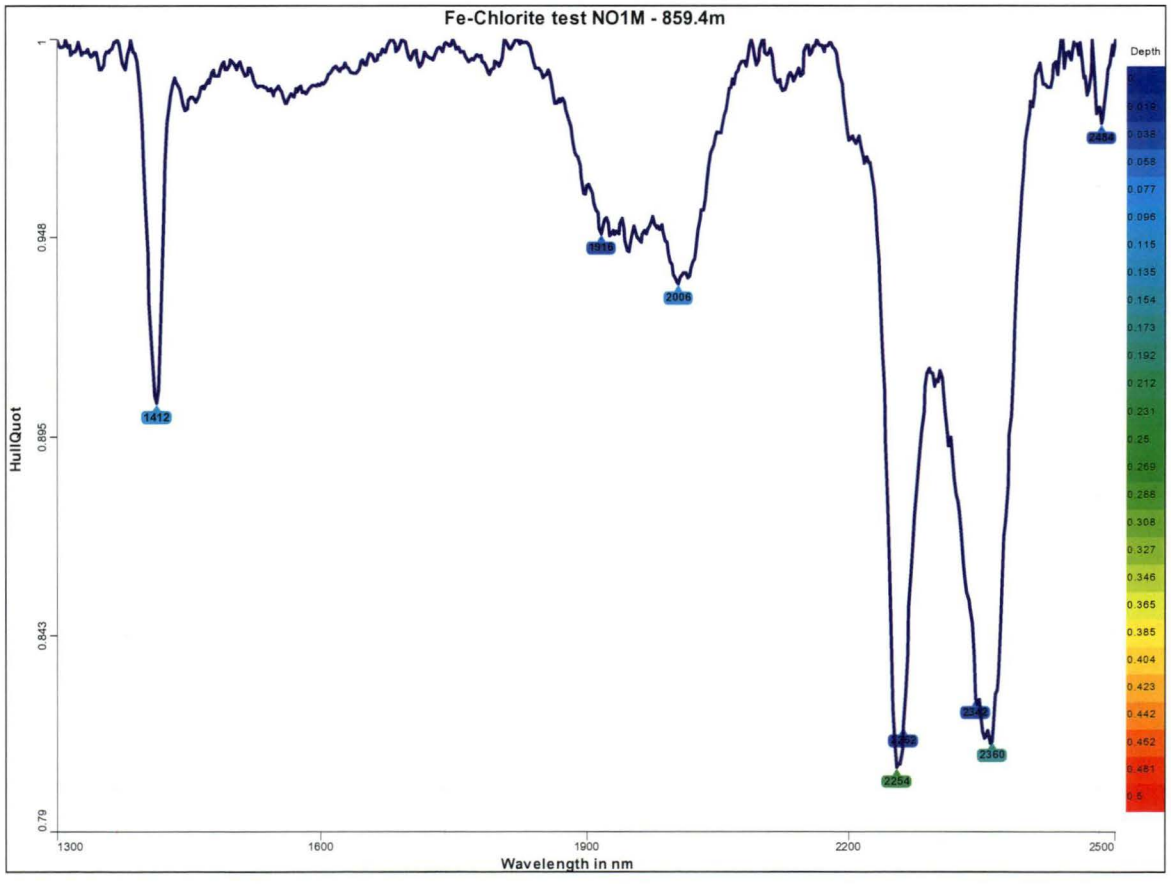

Appendix 6: Qualitative Energy Dispersive Electron Microbeam Analyses – Gold

				Wt%			Au(Ag+Au)	Normalised Atomic %		
Drillhole	**Depth**	**Mineral**	**Description**	**Au%**	**Ag%**	**Total**	**%**	**Au%**	**Ag%**	**Total**
NO07A	734 6	Gold	Au in chalcopyrite	51 25	48.22	99.47	51.5%	36 79	63.21	100.00
NO07A	734.6	Gold	Au in chalcopyrite	70.32	29.34	99.66	70.6%	56 76	43.24	100.00
NO07A	734.6	Gold	Au with ikunolite	84.10	16 03	100 13	84 0%	74 18	25.82	100.00
NO07A	734 6	Gold	Au with ikunolite	84 43	15 33	99 76	84.6%	75 10	24 90	100 00
NO07A	734.6	Gold	Au with ikunolite	84.73	15.26	99 99	84 7%	75.25	24 75	100 00
NO07A	734 6	Gold	Au with ikunolite	84 74	15 31	100.05	84 7%	75.19	24 81	100 00
NO07A	734.6	Gold	Au with ikunolite	84 95	14 34	99 29	85 6%	76.44	23.56	100 00
NO07A	734 6	Gold	Au with ikunolite	84.97	14.64	99 61	85.3%	76.07	23 93	100 00
NO07A	734 6	Gold	Au with ikunolite	86.47	13 92	100 39	86 1%	77 28	22 72	100 00
NO07A	734.6	Gold	Discrete metallic gold	91.02	9 05	100 07	91.0%	84 63	15 37	100.00
NO07A	734.6	Gold	Discrete metallic gold	97.15	2 36	99 51	97.6%	95 75	4 25	100.00
NO07A	734 6	Gold	Discrete metallic gold	97 17	3 20	100 37	96.8%	94 33	5 67	100.00
NO12	630 8	Gold	Au in chalcopyrite	44 70	54 86	99 56	44 9%	30.85	69 15	100 00
NO12	630 8	Gold	Au with chalcopyrite	80 49	19 08	99 57	80.8%	69 79	30.21	100 00
NO12	630 8	Gold	Au with chalcopyrite	81 53	18 11	99.64	81 8%	71.14	28 86	100.00
NO12	630 8	Gold	Au with bismuthinite	82 04	18 40	100.44	81 7%	70.95	29 05	100 00
NO12	630.8	Gold	Au with bismuthinite	83.03	16 84	99 87	83.1%	72 97	27 03	100 00
NO12	630 8	Gold	Au with bismuthinite	83.93	15 75	99 68	84 2%	74.48	25.52	100.00
NO12	630 8	Gold	Au with bismuthinite	87.38	12.83	100.21	87 2%	78.86	21 14	100 00
NO12	630 8	Gold	Au with ikunolite	85.69	14 42	100.11	85 6%	76.49	23.51	100 00
NO12	630 8	Gold	Au with ikunolite	86 13	13 88	100.01	86 1%	77 26	22 74	100 00
NO12	665 2	Gold	Au in bismuthinite	96 71	3 31	100 02	96.7%	94.12	5.88	100 00
NO12	665 2	Gold	Au in bismuthinite	96 98	5 11	102 09	95.0%	91 22	8.78	100 00
NO12	665.2	Gold	Au in bismuthinite	98.38	0 89	99 27	99 1%	98 37	1 63	100 00
NO12	665.2	Gold	Au in bismuthinite	99 05	1 28	100 33	98.7%	97 69	2 31	100 00
NO12	665.2	Gold	Ag-rich patch in Au	93 19	6 27	99.46	93 7%	89 06	10 94	100.00
NO12	665 2	Gold	Au in maldonite	99 93	0.35	100.28	99 7%	99 36	0 64	100.00
NO12	665 2	Gold	Au in metallic bismuth	100.13	0.00	100 13	100 0%	100 00	0.00	100.00
NO12	665 2	Gold	Au in metallic bismuth	100.39	0.00	100 39	100 0%	100.00	0.00	100 00
NO12A	707.7	Gold	Au in newoccidentallite	80.52	9.09	89 61	89 9%	84.50	15 50	100 00
NO12A	707 7	Gold	Au in quartz + newoccidentallite	89 68	10 57	100 25	89 5%	82.29	17.71	100.00
NO12A	707 7	Gold	Au in newoccidentallite	89 92	9 70	99.62	90.3%	83.54	16.46	100 00
NO12A	707.7	Gold	Au in bismuthinite	91 32	7 95	99 27	92.0%	86 28	13.72	100 00
NO12A	707.7	Gold	Au in newoccidentallite	91.46	8 53	99 99	91 5%	85.45	14.55	100.00
NO12A	707 7	Gold	Au in quartz + newoccidentallite	91 50	8 12	99.62	91 8%	86 06	13 94	100 00
NO12A	707 7	Gold	Au in quartz + galena	88.74	11 28	100 02	88 7%	81.16	18.84	100.00
NO12A	707 7	Gold	Au in quartz + ikunolite	90.42	8.76	99 18	91 2%	84 97	15.03	100 00
NO12A	707 7	Gold	Au in quartz	89 60	10.39	99.99	89 6%	82 53	17 47	100.00
NO12A	707 7	Gold	Au in quartz	96 36	3.47	99 83	96 5%	93 83	6 17	100.00
NO12A	707 7	Gold	Au in quartz	99.09	0 31	99 40	99 7%	99 43	0.57	100.00
NO14D	992.7	Gold	Au in galena	75 52	24 55	100 07	75.5%	62.75	37.25	100.00
NO14D	992 7	Gold	Au in galena	79 92	20.15	100 07	79 9%	68.48	31 52	100.00
NO14D	992 7	Gold	Au in galena	81.64	18 40	100 04	81 6%	70 84	29 16	100 00
NO14D	992.7	Gold	Au in galena	83.24	16 89	100 13	83 1%	72.97	27 03	100.00
NO14D	992 7	Gold	Au in bismuth + ikunolite	89.11	10 45	99 56	89 5%	82 36	17 64	100.00
NO14D	992 7	Gold	Au in bismuth + ikunolite	89 68	10.76	100 44	89 3%	82 03	17.97	100 00
NO14D	992 7	Gold	Au in quartz	91 00	9 18	100.18	90 8%	84 44	15.56	100 00
NO14D	992.7	Gold	Au in quartz	91 19	9 25	100 44	90 8%	84 37	15 63	100 00
NO14D	992 7	Gold	Au in quartz	93.27	7 07	100 34	93 0%	87 84	12 16	100 00
NO14D	992.7	Gold	Au in quartz	94 30	6 02	100 32	94.0%	89 56	10 44	100 00
NO14D	992 7	Gold	Au in quartz	98 61	1 12	99.73	98 9%	97.97	2 03	100.00

				Wt%			Au(Ag+Au)	Normalised Atomic %		
Drillhole	**Depth**	**Mineral**	**Description**	**Au%**	**Ag%**	**Total**	**%**	**Au%**	**Ag%**	**Total**
NO14D	992 7	Gold	Au in quartz	99.09	0.77	99.86	99.2%	98.60	1 40	100.00
NO25	223.8	Gold	Au with bismuthinite	88 67	10 74	99 41	89 2%	81 89	18.11	100 00
NO25	223.8	Gold	Au with bismuthinite	90 41	9.56	99 97	90 4%	83 82	16.18	100 00
NO25	223.8	Gold	Au with bismuthinite	90 10	10 22	100 32	89 8%	82.84	17 16	100.00
NO25	223 8	Gold	Au with bismuthinite	90 63	10 39	101 02	89 7%	82 69	17 31	100.00
NO25	223 8	Gold	Au with bismuthinite	92.37	6 94	99 31	93 0%	87 94	12.06	100.00
		Gold	Au with chalcopyrite	86 20	13 83	100 03	86 2%	77 34	22.66	100 00
		Gold	Au with chalcopyrite	85 99	13 89	99.88	86 1%	77.22	22 78	100.00
		Gold	Au with chalcopyrite	86.31	13.95	100 26	86 1%	77 21	22 79	100 00
		Gold	Au with chalcopyrite	84 95	14 63	99 58	85.3%	76 08	23.92	100 00
		Gold	Au with chalcopyrite	85 05	14 81	99.86	85.2%	75.87	24.13	100.00
		Gold	Au with chalcopyrite	85 85	15 15	101.00	85.0%	75 63	24.37	100 00
		Gold	Au with chalcopyrite	84.53	15.22	99 75	84 7%	75 26	24.74	100 00
		Gold	Au with chalcopyrite	84 72	15.22	99.94	84 8%	75.30	24.70	100.00
		Gold	Au with chalcopyrite	84 87	15 32	100.19	84.7%	75 21	24 79	100 00
		Gold	Au with chalcopyrite	84.40	15 39	99 79	84 6%	75 02	24 98	100 00
		Gold	Au with chalcopyrite	82 44	16 86	99.30	83.0%	72 81	27.19	100.00
		Gold	Au with chalcopyrite	83 84	17 07	100 91	83 1%	72.90	27.10	100 00
		Gold	Au with chalcopyrite	82 52	17 42	99.94	82.6%	72 18	27 82	100.00
		Gold	Au with chalcopyrite	81.77	17.65	99.42	82.2%	71 73	28.27	100 00
		Gold	Au with chalcopyrite	80 82	18 68	99.50	81 2%	70.32	29.68	100 00
		Gold	Au with chalcopyrite	80 62	10 20	90.82	88 8%	81 23	18 77	100 00
		Gold	Au with chalcopyrite	78.03	21.89	99 92	78 1%	66 13	33 87	100.00
		Gold	Au with chalcopyrite	77.22	22 25	99.47	77 6%	65.53	34 47	100 00
		Gold	Au with chalcopyrite	75 09	24.08	99.17	75.7%	63 07	36 93	100.00
		Gold	Au with chalcopyrite	74.88	24.41	99 29	75 4%	62.69	37.31	100 00
		Gold	Au with chalcopyrite	73.79	26 25	100.04	73.8%	60 62	39 38	100 00
		Gold	Au with chalcopyrite	71 32	28.09	99 41	71.7%	58 17	41 83	100.00
		Gold	Au with chalcopyrite	71.13	28.79	99 92	71 2%	57.50	42.50	100.00
		Gold	Au with chalcopyrite	67 99	32.32	100.31	67.8%	53 53	46 47	100.00
		Gold	Au with chalcopyrite	67 02	32 43	99 45	67.4%	53.09	46 91	100 00
		Gold	Au with chalcopyrite	67.02	33.10	100.12	66 9%	52.58	47.42	100.00
		Gold	Au with chalcopyrite	66.93	33.52	100 45	66 6%	52 23	47 77	100.00
		Gold	Au with chalcopyrite	62.27	36 96	99 23	62 8%	47.99	52.01	100.00
		Gold	Au with chalcopyrite	52.56	47.36	99 92	52 6%	37 80	62 20	100 00
		Gold	Au with chalcopyrite	51 17	48 03	99.20	51 6%	36 85	63 15	100 00
		Gold	Au with chalcopyrite	46.75	53 35	100 10	46 7%	32 43	67 57	100.00
		Gold	Au with bismuth minerals	91 70	8.02	99.72	92 0%	86 23	13 77	100 00
		Gold	Au with bismuth minerals	90 95	8.18	99 13	91 7%	85.89	14.11	100.00
		Gold	Au with bismuth minerals	91 28	8 20	99 48	91.8%	85 91	14 09	100 00
		Gold	Au with bismuth minerals	91 33	8 70	100 03	91.3%	85 18	14.82	100 00
		Gold	Au with bismuth minerals	90 64	8.72	99 36	91.2%	85.06	14.94	100 00
		Gold	Au with bismuth minerals	91 01	8 90	99 91	91.1%	84 85	15 15	100 00
		Gold	Au with bismuth minerals	90 91	9 08	99 99	90 9%	84 58	15.42	100 00
		Gold	Au with bismuth minerals	90.74	9 13	99.87	90 9%	84 48	15 52	100 00
		Gold	Au with bismuth minerals	91.15	9 15	100 30	90.9%	84 51	15 49	100.00
		Gold	Au with bismuth minerals	91 42	9 39	100 81	90 7%	84 21	15.79	100 00
		Gold	Au with bismuth minerals	90 07	9.46	99 53	90 5%	83.91	16 09	100.00
		Gold	Au with bismuth minerals	89.73	9 96	99.69	90 0%	83 15	16 85	100 00
		Gold	Au with bismuth minerals	90 65	10.09	100 74	90 0%	83 11	16 89	100 00
		Gold	Au with bismuth minerals	89 89	10.10	99 99	89.9%	82.98	17.02	100 00
		Gold	Au with bismuth minerals	89 85	10.15	100 00	89 9%	82.90	17.10	100 00

			Wt%			Au(Ag+Au)	Normalised Atomic %		
Drillhole Depth	**Mineral**	**Description**	**Au%**	**Ag%**	**Total**	**%**	**Au%**	**Ag%**	**Total**
	Gold	Au with bismuth minerals	89.18	10 31	99.49	89 6%	82.57	17.43	100 00
	Gold	Au with bismuth minerals	90 27	10 37	100.64	89.7%	82.66	17.34	100.00
	Gold	Au with bismuth minerals	89.23	10 66	99 89	89.3%	82 09	17 91	100.00
	Gold	Au with bismuth minerals	89.12	11 03	100.15	89.0%	81 57	18 43	100.00
	Gold	Au in quartz	99 96	0.25	100 21	99 8%	99 55	0 45	100.00
	Gold	Au in quartz	99 49	1 18	100 67	98.8%	97 88	2.12	100.00
	Gold	Au in quartz	99.69	1 42	101 11	98.6%	97 46	2 54	100 00
	Gold	Au in quartz	98.99	1 54	100 53	98.5%	97.24	2 76	100 00
	Gold	Au in quartz	98 75	1.59	100 34	98 4%	97 14	2 86	100 00
	Gold	Au in quartz	98.32	1.74	100 06	98 3%	96.87	3 13	100.00
	Gold	Au in quartz	98 85	2 19	101 04	97 8%	96 11	3 89	100.00
	Gold	Au in quartz	98 40	2 31	100.71	97 7%	95.89	4 11	100 00
	Gold	Au in quartz	96 48	2 98	99.46	97 0%	94 66	5 34	100 00
	Gold	Au in quartz	96.83	3 67	100 50	96 3%	93 53	6.47	100.00
	Gold	Au in quartz	95.48	4 05	99.53	95.9%	92 81	7 19	100.00
	Gold	Au in quartz	95 90	4 16	100 06	95.8%	92.66	7.34	100.00
	Gold	Au in quartz	95 14	4 49	99 63	95.5%	92 07	7.93	100.00
	Gold	Au in quartz	95 67	4 59	100 26	95 4%	91.95	8.05	100.00
	Gold	Au in quartz	95 32	4 62	99 94	95 4%	91.87	8 13	100 00
	Gold	Au in quartz	96 16	4 71	100.87	95 3%	91 79	8 21	100 00
	Gold	Au in quartz	94 57	4.84	99.41	95 1%	91 45	8 55	100 00
	Gold	Au in quartz	95 68	5.11	100 79	94 9%	91 11	8 89	100 00
	Gold	Au in quartz	94 49	5.13	99 62	94.9%	90.98	9 02	100 00
	Gold	Au in quartz	95 70	5 48	101 18	94.6%	90.53	9 47	100 00
	Gold	Au in quartz	94.92	5.52	100 44	94 5%	90 40	9 60	100.00
	Gold	Au in quartz	93 81	5 85	99 66	94.1%	89 78	10 22	100.00
	Gold	Au in quartz	93 37	5 93	99 30	94.0%	89 61	10 39	100 00
	Gold	Au in quartz	93 92	5 95	99.87	94 0%	89 63	10.37	100 00
	Gold	Au in quartz	93 51	6 35	99.86	93.6%	88 97	11.03	100 00
	Gold	Au in quartz	93 23	6 59	99.82	93 4%	88 57	11.43	100.00
	Gold	Au in quartz	93 14	6.83	99.97	93 2%	88 19	11 81	100.00
	Gold	Au in quartz	92.99	7 21	100.20	92 8%	87.60	12.40	100.00
	Gold	Au in quartz	93.26	7 21	100 47	92.8%	87.63	12.37	100.00
	Gold	Au in quartz	91 63	7.75	99 38	92.2%	86 62	13.38	100.00
	Gold	Au in quartz	91 29	7 91	99.20	92.0%	86 34	13 66	100.00
	Gold	Au in quartz	91.57	7.96	99 53	92.0%	86.30	13 70	100.00

Appendix 7: Qualitative Energy Dispersive Electron Microbeam Analyses – Ikunolite & Galena-Clausthalite

	Wt%					Normalised Atomic %					Number of Ions in Ikunolite Structure				
Mineral	**Pb%**	**Bi%**	**Se%**	**S%**	**Total**	**Pb**	**Bi**	**Se**	**S**	**Total**	**Pb**	**Bi**	**Se**	**S**	**Total**
Galena-clausthalite	82 32	0.36	6.8	10.22	99 70	49.43%	0 21%	10.71%	39 65%	100 00%	0 989	0.004	0 214	0 793	2.00
Galena-clausthalite	80 58	1 59	7 27	9 75	99.19	49 07%	0 96%	11 62%	38.36%	100 00%	0 981	0.019	0 232	0 767	2.00
Galena-clausthalite	80 05	1 61	8.94	9.84	100.44	47 46%	0 95%	13.91%	37 69%	100.00%	0 949	0.019	0 278	0.754	2.00
Galena-clausthalite	81.5	0.64	9 11	8 88	100.13	49.87%	0 39%	14 63%	35 11%	100.00%	0 997	0 008	0.293	0 702	2.00
Galena-clausthalite	79 77	1 26	9.45	8.85	99.33	48 94%	0.77%	15 21%	35 08%	100.00%	0.979	0 015	0.304	0.702	2 00
Galena-clausthalite	80.27	0 24	12 36	7.39	100.26	49.95%	0 15%	20 18%	29.72%	100.00%	0 999	0 003	0.404	0 594	2 00
Galena-clausthalite	72.91	1 11	22.68	2.22	98.92	49 31%	0 74%	40 25%	9.70%	100.00%	0.986	0.015	0.805	0.194	2.00

			Wt%				Normalised Atomic %				Number of Ions in Ikunolite Structure			
Mineral	**Drillhole**	**Depth**	**Bi%**	**Se%**	**S%**	**Total**	**Bi**	**Se**	**S**	**Total**	**Bi**	**Se**	**S**	**Total**
Ikunolite	NO14D	992.7	84.2	10 3	5 69	100 19	56 68%	18.35%	24 97%	100 00%	3 97	1 28	1 75	7 00
Ikunolite	NO14D	992.7	84.28	11.38	5.14	100 80	56.98%	20 37%	22 65%	100 00%	3 99	1.43	1 59	7 00
Ikunolite	NO14D	992.7	83 21	12 79	4 33	100.33	57 27%	23.30%	19.43%	100 00%	4 01	1 63	1 36	7 00
Ikunolite	NO14D	992 7	83 11	13 14	4.38	100 63	56.75%	23 75%	19 49%	100 00%	3 97	1 66	1.36	7.00
Ikunolite	NO14D	992.7	84.43	10 16	5.56	100 15	57 22%	18.22%	24 56%	100 00%	4 01	1.28	1 72	7 00
Ikunolite	NO14D	992 7	82.39	13.19	4 13	99.71	57 13%	24.21%	18 66%	100 00%	4 00	1.69	1 31	7 00
Ikunolite	NO14D	992 7	83.95	9 81	6 04	99 80	56 24%	17.39%	26.37%	100 00%	3.94	1.22	1 85	7.00
Ikunolite	NO14D	992 7	84 66	7.42	6.64	98 72	57 37%	13 31%	29 33%	100.00%	4.02	0 93	2 05	7 00
Ikunolite	NO14D	992 7	81 38	17 41	1.79	100.58	58 49%	33.12%	8 39%	100 00%	4.09	2 32	0.59	7 00
Ikunolite	NO14D	992 7	80 97	17 72	1 96	100 65	57.57%	33 35%	9 08%	100 00%	4.03	2.33	0.64	7 00
Ikunolite	NO12A	707.7	84.53	9 13	6.06	99 72	57.04%	16.31%	26 65%	100 00%	3 99	1 14	1.87	7.00
Ikunolite	NO12A	707.7	82.97	11.9	4 87	99.74	56 75%	21.54%	21 71%	100 00%	3 97	1.51	1 52	7.00
Ikunolite	NO12A	707 7	84.8	10.58	5 38	100 76	57 35%	18.94%	23.71%	100.00%	4 01	1.33	1.66	7.00
Ikunolite	NO12A	707.7	83.2	12.09	5.07	100 36	56.12%	21 59%	22 29%	100 00%	3 93	1.51	1.56	7.00
Ikunolite	NO12A	707.7	82.73	13.56	4 01	100.30	57 15%	24.79%	18 06%	100 00%	4.00	1 74	1.26	7 00
Ikunolite	NO12A	707.7	83.93	10 61	5.3	99.84	57.27%	19 16%	23 57%	100 00%	4.01	1 34	1 65	7.00
Ikunolite	NO12A	707 7	83 39	10.84	5.36	99.59	56.72%	19 52%	23.76%	100.00%	3 97	1.37	1 66	7.00
Ikunolite	NO12A	707.7	83 65	11.2	5 15	100.00	56 96%	20.19%	22 86%	100 00%	3.99	1 41	1.60	7 00
Ikunolite	NO12A	707.7	83 66	11.46	4.96	100 08	57.18%	20 73%	22.09%	100.00%	4 00	1 45	1 55	7.00
Ikunolite	NO12A	707 7	84 4	9.65	6.24	100 29	56 04%	16 96%	27.00%	100.00%	3 92	1 19	1.89	7.00

Appendix 8: Qualitative Energy Dispersive Electron Microbeam Analyses – Sphalerite

				Weight %					Normalised Atomic %				
Drillhole	**Depth**		**Grain**	**Zn**	**Fe**	**Cd**	**S**	**Total**	**Zn**	**Fe**	**Cd**	**S**	**Total**
NO3C	889	Fine grained with cpy	1	58 53	8 18		32 81	99 52	43.35	7.09	0.00	49 55	100 00
NO3C	889	Fine grained with cpy	2	57 7	8 46		33 59	99 75	42 40	7 28	0 00	50 32	100 00
NO3C	889	Fine grained with cpy	3	58.15	8.56		33.57	100 28	42.56	7 33	0 00	50 10	100 00
NO3C	889	Fine grained with cpy	4	57.83	8 93		33 67	100.43	42.23	7.63	0.00	50.13	100.00
NO3C	889	Fine grained with cpy	5	57 88	8 81		33 48	100 17	42 42	7 56	0 00	50 03	100 00
NO3C	889	Fine grained with cpy	6	59	7 7		33.25	99.95	43.44	6 64	0 00	49.92	100.00
NO12A	708 4	Coarse grained with gn	1	57.41	9 06	0 13	33 61	100 21	42 02	7.76	0 06	50 16	100 00
NO12A	708 4	Coarse grained with gn	2	57.38	9.31	0 13	33 75	100 57	41 83	7.95	0 06	50.17	100.00
NO12A	708.4	Coarse grained with gn	3	57 55	8.68	0.15	33 42	99 8	42.34	7.47	0.06	50 13	100 00
NO12A	708 4	Coarse grained with gn	4	57.51	8 51	0 12	33.67	99.81	42 23	7.31	0.05	50.41	100.00
NO12A	708.4	Coarse grained with gn	5	58.04	8.56	0 14	33.47	100.21	42.56	7 35	0 06	50.04	100.00
NO12A	708.4	Coarse grained with gn	6	58 21	8.34	0.16	33 41	100.12	42 74	7 17	0.07	50 02	100 00
NO12A	Gravity	Coarse grained with gn	1	59 11	7.58		33 3	99.99	43 50	6.53	0.00	49 97	100 00
NO12A	Gravity	Coarse grained with gn	2	58 9	7.74		33.8	100.44	43.03	6 62	0 00	50 35	100.00
NO12A	Gravity	Coarse grained with gn	3	59 28	6.97		33 48	99 73	43 68	6.01	0 00	50 30	100.00
NO12A	Gravity	Coarse grained with gn	4	57.87	8 72		33 83	100.42	42.22	7.45	0.00	50 33	100 00
NO12A	Gravity	Coarse grained with gn	5	58.06	8 6		33.8	100.46	42.37	7 35	0 00	50.29	100 00
NO12A	Gravity	Coarse grained with gn	6	59 08	7 09		33.57	99.74	43.50	6 11	0 00	50 39	100.00
NO12A	Gravity	Coarse grained with gn	7	57.09	8.94		33.74	99 77	41.87	7.68	0.00	50.45	100.00
NO12A	Gravity	Coarse grained with gn	8	57.1	9 29		33 81	100.2	41.71	7 94	0 00	50 35	100 00
NO12A	Gravity	Coarse grained with gn	9	57.08	8 97		33 92	99.97	41.74	7 68	0 00	50.58	100.00
NO12A	Gravity	Coarse grained with gn	10	57.97	7 88		33 65	99 5	42 69	6.79	0.00	50 52	100 00

Appendix 9: Ore Element Analyses

Hole ID	From	To	Ag ppm	As ppm	Au ppm	Bi ppm	Co ppm	Cu ppm	Fe %	Mn ppm	Pb ppm	Sb ppm	Zn ppm
DD95NO0001F	848	849	<0 5	<1	0.02	<5	17	3	4 38	420	<3	<5	63
DD95NO0001F	849	850	<0.5	<1	0 02	<5	20	8	5 26	500	<3	<5	67
DD95NO0001F	850	851	<0 5	<1	0 01	<5	16	<1	3.87	380	<3	<5	54
DD95NO0001F	851	852	<0 5	<1	0 01	<5	18	<1	4 56	440	<3	<5	62
DD95NO0001F	852	853	<0.5	<1	0.01	<5	21	1	5 29	520	<3	<5	68
DD95NO0001F	853	854	<0 5	<1	<0 01	<5	17	1	4 42	420	<3	<5	58
DD95NO0001F	854	855	<0.5	<1	<0.01	<5	18	1	4 41	400	<3	<5	57
DD95NO0001F	855	856	<0 5	<1	0 03	<5	17	<1	4 39	420	4	<5	60
DD95NO0001F	856	857	<0 5	<1	<0 01	<5	20	2	4.80	480	<3	<5	68
DD95NO0001F	857	858	<0.5	<1	0.01	<5	20	3	4 98	520	<3	<5	67
DD95NO0001F	858	859	<0.5	2	<0 01	<5	21	1	5 27	540	<3	<5	70
DD95NO0001F	859	860	<0 5	<1	0 02	10	17	460	4.74	520	<3	<5	53
DD95NO0001F	860	861	<0.5	<1	0.01	<5	20	105	5.50	580	<3	<5	64
DD95NO0001F	861	862	<0 5	<1	0 01	<5	19	3	4 95	480	<3	<5	61
DD95NO0001F	1063	1064	<0.5	<1	0 01	10	22	57	5.70	500	4	<5	67
DD95NO0001F	1064	1065	<0 5	<1	0.01	5	20	24	5.33	500	<3	<5	67
DD95NO0001F	1065	1066	<0.5	<1	<0.01	<5	22	74	5 83	520	<3	<5	72
DD95NO0001F	1066	1067	<0.5	<1	<0 01	<5	22	40	5 86	540	<3	<5	72
DD95NO0001F	1067	1068	<0 5	<1	0 05	40	16	31	4 15	400	14	<5	54
DD95NO0001F	1068	1069	<0 5	<1	0 01	<5	19	26	5 00	480	4	<5	62
DD95NO0001F	1069	1070	<0 5	<1	0.01	5	21	42	5.30	460	4	<5	64
DD95NO0001F	1070	1071	<0 5	<1	0 01	<5	17	8	4 44	400	<3	<5	60
DD95NO0001F	1071	1072	<0 5	<1	<0 01	<5	19	21	4 59	400	<3	<5	63
DD95NO0001F	1072	1073	<0.5	<1	0 04	<5	16	15	4.02	360	4	<5	62
DD95NO0001F	1073	1074	<0.5	1	<0.01	<5	15	<1	3 80	360	<3	<5	64
DD95NO0001F	1074	1075	<0.5	<1	<0 01	<5	17	32	3 97	380	<3	<5	63
DD95NO0001F	1075	1076	<0 5	<1	<0.01	<5	17	39	4 26	380	<3	<5	61
DD95NO0001F	1076	1077	<0 5	<1	<0 01	<5	13	3	3 62	340	<3	<5	60
DD95NO0001F	1077	1078	<0.5	<1	<0 01	<5	14	40	4 05	380	4	<5	69
DD95NO0001F	1078	1079	<0 5	<1	<0 01	<5	13	7	4 00	400	4	<5	73
DD95NO0001F	1079	1080	<0 5	<1	<0 01	<5	14	16	4 06	380	<3	<5	71
DD95NO0001F	1080	1081	<0 5	<1	<0.01	<5	15	14	4 35	400	<3	<5	71
DD95NO0001F	1081	1082	<0 5	<1	0.01	5	15	32	4 25	380	<3	<5	68
DD95NO0001F	1082	1083	<0.5	<1	0.59	15	17	360	4.62	380	14	<5	71
DD95NO0001F	1083	1084	<0 5	3	<0 01	<5	14	7	3 72	380	<3	<5	63
DD95NO0001F	1084	1085	<0 5	3	<0 01	<5	16	34	4.38	440	<3	<5	68
DD95NO0001F	1085	1086	<0 5	<1	<0.01	5	22	160	5 76	460	6	<5	75
DD95NO0001F	1086	1087	<0.5	<1	<0.01	<5	16	14	4 39	420	4	<5	69
DD95NO0001F	1087	1088	<0.5	<1	<0 01	<5	14	3	4.01	380	4	<5	65
DD95NO0001F	1088	1089	<0 5	<1	<0 01	<5	16	2	4 15	400	4	<5	66
DD95NO0001F	1089	1090	<0 5	<1	<0 01	<5	14	4	3 71	360	4	<5	58
DD95NO0001F	1090	1091	<0.5	<1	<0.01	<5	14	3	3.89	380	14	<5	60
DD95NO0001F	1091	1092	<0 5	<1	<0 01	<5	17	20	4 06	380	4	<5	57
DD95NO0001F	1092	1093	<0.5	<1	<0 01	<5	14	74	3 76	360	<3	<5	57
DD95NO0001F	1093	1094	<0 5	<1	<0.01	<5	15	15	3.96	340	4	<5	55
DD95NO0001F	1094	1095	<0 5	<1	<0 01	<5	20	35	4 46	380	4	<5	61
DD95NO0001F	1095	1096	<0 5	5	<0 01	<5	18	4	4.14	380	4	<5	63
DD95NO0001F	1096	1097	<0 5	<1	<0.01	<5	18	2	4 58	440	4	<5	68
DD95NO0001F	1097	1098	<0 5	<1	<0 01	<5	22	14	4 24	380	4	<5	62
DD95NO0001F	1098	1099	<0 5	4	0 01	<5	14	3	3.84	380	4	<5	58
DD95NO0001F	1099	1100	<0 5	<1	0.01	5	13	5	3 79	380	4	<5	55
DD95NO0001F	1100	1101	<0 5	2	0.01	5	18	21	4 19	400	4	<5	56

Hole ID	From	To	Ag ppm	As ppm	Au ppm	Bi ppm	Co ppm	Cu ppm	Fe %	Mn ppm	Pb ppm	Sb ppm	Zn ppm
DD95NO0001F	1101	1102	<0.5	<1	0 01	<5	15	11	3.90	380	<3	<5	56
DD95NO0001F	1102	1103	<0 5	<1	0 01	<5	18	320	4 55	400	<3	<5	77
DD95NO0001F	1103	1104	<0.5	<1	<0.01	5	15	9	4 15	380	4	<5	61
DD95NO0001F	1104	1105	<0 5	2	<0 01	<5	14	4	3.97	380	4	<5	59
DD95NO0001F	1105	1106	<0 5	<1	<0.01	<5	15	2	4 18	400	6	<5	63
DD95NO0001F	1106	1107	<0 5	<1	2.69	<5	16	25	4 94	480	<3	<5	69
DD95NO0001F	1107	1108	<0 5	<1	0 13	50	31	560	9 32	720	18	5	115
DD95NO0001F	1108	1109	<0 5	<1	0.02	5	19	100	5 83	500	6	<5	77
DD95NO0001F	1109	1110	<0.5	<1	<0.01	<5	16	29	4.97	480	<3	<5	62
DD95NO0001F	1110	1111	<0 5	<1	<0 01	<5	16	14	4.65	380	<3	<5	60
DD95NO0001F	1111	1112	<0 5	<1	0 02	<5	16	14	4 74	380	6	<5	61
DD95NO0001F	1112	1113	<0 5	3	<0 01	<5	15	8	4.12	360	4	<5	53
DD95NO0001F	1113	1114	<0 5	1	<0 01	<5	16	2	4.37	380	<3	<5	58
DD95NO0001F	1114	1115	<0 5	2	<0 01	<5	16	<1	4 62	360	4	<5	58
DD95NO0001F	1115	1116	<0.5	<1	0 01	<5	21	96	5 69	360	4	<5	62
DD95NO0001F	1116	1117	<0 5	3	<0.01	<5	19	5	5 35	380	<3	<5	63
DD95NO0001F	1117	1118	<0.5	3	<0.01	<5	18	4	4 78	340	4	<5	62
DD95NO0001F	1118	1119	<0 5	4	0.01	<5	19	6	5.14	340	<3	<5	62
DD95NO0001F	1119	1120	<0.5	<1	0.02	<5	19	4	5 29	360	4	<5	63
DD95NO0001F	1120	1121	<0 5	<1	0.01	<5	18	7	5 38	380	<3	<5	62
DD95NO0001F	1121	1122	<0 5	4	0 01	10	20	9	5.99	420	<3	<5	67
DD95NO0001F	1122	1123	<0 5	1	0.01	10	19	7	6 85	580	4	5	75
DD95NO0001F	1123	1124	<0.5	5	0 09	140	19	33	5 78	400	22	<5	61
DD95NO0001F	1124	1125	<0.5	5	0 03	<5	19	40	5.69	440	4	<5	65
DD95NO0001F	1125	1126	<0 5	1	0.01	<5	17	240	5 29	400	4	<5	64
DD95NO0001F	1126	1127	<0.5	3	0 01	5	21	260	6 02	480	4	<5	75
DD95NO0001F	1127	1128	<0.5	5	0 01	<5	16	23	4.84	420	<3	<5	60
DD95NO0001F	1128	1129	<0.5	<1	0.03	10	19	260	5 82	500	4	<5	73
DD95NO0001F	1129	1130	<0.5	<1	0 07	70	16	1700	5 74	560	20	<5	135
DD95NO0001F	1130	1131	<0.5	<1	<0 01	10	19	94	6.76	620	6	<5	135
DD95NO0001F	1131	1132	<0 5	<1	0 02	10	24	37	7 65	600	8	<5	78
DD95NO0001F	1132	1133	<0 5	4	0.03	<5	24	29	7 80	600	4	<5	88
DD95NO0001F	1133	1134	<0.5	7	<0 01	<5	27	17	7.95	580	<3	5	140
DD95NO0001F	1134	1135	<0 5	3	0.05	5	27	38	8 41	580	6	<5	86
DD95NO0001F	1135	1136	<0 5	<1	0.04	5	27	43	8.25	680	8	<5	98
DD95NO0001F	1136	1137	<0 5	9	0 02	<5	23	10	6.82	500	6	<5	88
DD95NO0001F	1137	1138	<0 5	7	0.02	<5	22	13	7.12	500	8	5	83
DD95NO0001F	1138	1139	<0.5	12	0 01	<5	28	5	8.60	660	4	5	100
DD95NO0001F	1139	1140	<0 5	14	0 02	<5	28	18	8 27	600	6	5	96
DD95NO0001F	1140	1141	<0 5	9	0.02	<5	27	24	7 56	500	20	<5	85
DD95NO0001F	1141	1142	<0 5	11	<0 01	<5	25	24	7 44	580	6	5	89
DD95NO0001F	1142	1143	<0 5	14	0 03	<5	27	74	8 08	520	10	5	95
DD95NO0001F	1143	1144	<0 5	18	<0.01	<5	24	5	7 46	480	6	<5	91
DD95NO0001F	1144	1145	<0 5	19	0.02	<5	24	5	7.30	540	10	<5	85
DD95NO0001F	1145	1146	<0 5	16	0 05	<5	28	36	8 66	540	8	5	105
DD95NO0001F	1146	1147	<0 5	18	0.03	<5	25	18	8.14	560	4	<5	105
DD95NO0001F	1147	1148	<0 5	22	0.03	25	26	5	8 29	620	12	5	105
DD95NO0001F	1148	1149	<0 5	22	0.01	5	29	10	8 29	620	4	5	110
DD95NO0001F	1149	1150	6.0	19	0 08	440	29	29	8 96	760	300	10	105
DD95NO0001F	1150	1151	1 0	25	<0 01	55	29	4	8 25	640	40	5	120
DD95NO0001F	1151	1152	<0 5	19	<0 01	35	27	6	8 28	660	20	5	125
DD95NO0001F	1152	1153	3.0	16	0 16	140	23	67	8.23	700	91	5	125

Hole ID	From	To	Ag ppm	As ppm	Au ppm	Bi ppm	Co ppm	Cu ppm	Fe %	Mn ppm	Pb ppm	Sb ppm	Zn ppm
DD95NO0001F	1153	1154	3 0	31	0 76	260	13	66	5 36	440	120	<5	86
DD95NO0001F	1154	1155	7.5	18	1 72	320	18	71	6.83	460	300	<5	195
DD95NO0001F	1155	1156	4.5	15	0.11	70	17	44	4.98	360	840	<5	1700
DD95NO0001F	1156	1157	7 5	24	0 77	280	15	56	5 74	480	860	<5	185
DD95NO0001F	1157	1158	4.0	29	1.30	360	12	51	5 28	360	240	<5	65
DD95NO0001F	1158	1159	1.5	12	0 57	380	12	175	5 45	340	96	<5	54
DD95NO0001F	1159	1160	3 0	180	3 14	660	19	580	8 21	540	120	5	71
DD95NO0001F	1160	1161	8.5	1600	3.18	980	22	4000	7.78	660	240	10	160
DD95NO0001F	1161	1162	5 0	8	1 87	1400	16	860	9 94	1100	260	15	81
DD95NO0001F	1162	1163	1.5	18	2 08	600	9	200	5 81	480	52	<5	28
DD95NO0001F	1163	1164	1 5	240	2 26	500	10	480	5.92	340	80	<5	36
DD95NO0001F	1164	1165	6 0	400	2 04	640	7	1400	4 10	280	380	<5	97
DD95NO0001F	1165	1166	8.0	2700	5.84	2900	9	280	5.35	280	240	20	98
DD95NO0001F	1166	1167	1 5	1700	2 85	1600	14	150	3 40	340	72	15	26
DD95NO0001F	1167	1168	1.0	6300	2.41	500	9	59	4.04	340	24	15	32
DD95NO0001F	1168	1169	5.5	3500	5 73	3300	10	400	5.14	280	170	10	27
DD95NO0001F	1169	1170	4 0	175	4 83	3100	7	220	3 88	240	220	<5	20
DD95NO0001F	1170	1171	1.5	51	2.54	520	7	81	2 97	260	68	<5	21
DD95NO0001F	1171	1172	<0 5	47	2 97	240	15	81	5 07	400	8	<5	34
DD95NO0001F	1172	1173	1 5	89	6.30	400	15	280	5 44	400	26	<5	40
DD95NO0001F	1173	1174	2.0	540	4.39	740	9	110	3 29	240	46	<5	36
DD95NO0001F	1174	1175	2.5	11	4.41	680	9	280	3 76	200	125	<5	25
DD95NO0001F	1175	1176	2 0	44	4.13	840	9	180	4 07	300	40	<5	29
DD95NO0001F	1176	1177	2 0	55	7 62	820	8	150	3 59	190	44	<5	52
DD95NO0001F	1177	1178	0 5	8	2 84	500	7	120	4.04	145	36	<5	21
DD95NO0001F	1178	1179	1 5	20	4.45	1300	8	130	3 72	140	50	<5	22
DD95NO0001F	1179	1180	<0.5	18	0 96	340	15	38	5 23	460	20	<5	47
DD95NO0001F	1180	1181	0.5	11	1.97	440	16	115	5 88	440	18	<5	39
DD95NO0001F	1181	1182	1.0	26	4.17	720	14	780	5 27	380	30	<5	41
DD95NO0001F	1182	1183	1 5	57	10.20	760	14	1100	5.50	300	36	<5	39
DD95NO0001F	1183	1184	2.0	16	10.10	900	14	940	5 34	300	48	<5	35
DD95NO0001F	1184	1185	<0 5	14	0 77	220	14	220	5 44	420	16	<5	41
DD95NO0001F	1185	1186	<0.5	20	1 52	720	21	380	9 07	680	26	<5	57
DD95NO0001F	1186	1187	1.5	27	1 35	300	33	5400	9 85	800	10	5	70
DD95NO0001F	1187	1188	3.0	15	0.16	50	21	13400	8 21	640	34	5	91
DD95NO0001F	1188	1189	1 5	15	0 23	145	28	7400	11.00	1000	6	5	73
DD95NO0001F	1189	1190	2 0	<1	0 13	35	27	10100	12 50	800	8	<5	125
DD95NO0001F	1190	1191	<0 5	62	0.17	40	13	1200	4 32	560	8	<5	39
DD95NO0001F	1191	1192	0.5	66	0.08	20	18	2800	5 46	740	8	<5	61
DD95NO0001F	1192	1193	0.5	48	0.06	10	20	2300	6 31	880	10	<5	65
DD95NO0001F	1193	1194	1.0	61	0.04	5	22	2900	6.57	800	<3	<5	89
DD95NO0001F	1194	1195	<0 5	22	0 04	5	10	400	3 16	480	4	<5	23
DD95NO0001F	1195	1196	<0.5	500	0.06	15	16	1500	4 34	560	8	<5	45
DD95NO0001F	1196	1197	<0 5	280	0 07	20	10	1700	3.61	500	4	<5	29
DD95NO0001F	1197	1198	<0.5	87	0.07	25	19	1900	5 55	840	8	<5	46
DD95NO0001F	1198	1199	<0.5	110	0.05	20	9	1400	3 20	460	12	<5	25
DD95NO0001F	1199	1200	<0 5	35	0 06	15	8	220	3 14	540	14	<5	14
DD95NO0001F	1200	1201	<0.5	26	0 05	10	13	1800	5 16	960	12	<5	44
DD95NO0001F	1201	1202	3 0	<1	0 05	65	36	11900	11 70	1000	42	10	200
DD95NO0001F	1202	1203	2 0	<1	0.02	25	20	8000	7 08	720	135	5	72
DD95NO0001F	1203	1204	2 0	<1	0 09	60	32	11400	10.10	840	46	10	83
DD95NO0001F	1204	1205	1.5	<1	0 07	35	34	6500	10.20	760	105	<5	85

Hole ID	From	To	Ag ppm	As ppm	Au ppm	Bi ppm	Co ppm	Cu ppm	Fe %	Mn ppm	Pb ppm	Sb ppm	Zn ppm
DD95NO0001F	1205	1206	1 5	<1	0.04	25	41	6300	12.40	1000	59	10	89
DD95NO0001F	1206	1207	<0 5	<1	<0 01	15	32	1400	9.89	880	20	5	88
DD95NO0001F	1207	1208	<0.5	<1	<0.01	15	27	100	8 32	780	14	5	79
DD95NO0001F	1208	1209	<0.5	<1	<0 01	20	26	520	8.10	780	18	10	79
DD95NO0001F	1209	1210	<0.5	4	<0 01	30	26	1200	7.99	820	14	5	86
DD95NO0001F	1210	1211	<0 5	8	<0.01	10	24	240	7 56	780	12	<5	75
DD95NO0001F	1211	1212	<0.5	8	0 03	15	21	900	6 83	660	59	5	79
DD95NO0001F	1212	1213	1 5	6	<0 01	5	21	800	7 77	820	980	10	88
DD95NO0001F	1213	1214	<0 5	6	<0.01	<5	18	420	6.16	660	10	<5	77
DD95NO0001F	1214	1215	1.0	11	0.05	20	16	580	5 64	600	150	<5	67
DD95NO0001F	1215	1216	<0.5	14	0.06	15	15	420	5 58	580	22	<5	63
DD95NO0001F	1216	1217	<0 5	10	<0.01	25	15	94	5 25	520	22	<5	58
DD95NO0001F	1217	1218	<0.5	<1	<0 01	10	13	9	4 42	420	16	<5	50
DD95NO0001F	1218	1219	<0 5	7	<0.01	<5	14	3	4 90	460	12	<5	57
DD95NO0001F	1219	1220	2 0	8	<0 01	25	14	260	4.82	480	660	<5	73
DD95NO0001F	1220	1221	<0 5	2	0 17	<5	14	7	4 94	500	8	<5	57
DD95NO0003C	839	840	<0.5	5	<0.01	120	15	260	4.75	490	10	<5	63
DD95NO0003C	840	841	<0 5	<1	0.03	65	20	720	5 84	520	4	<5	71
DD95NO0003C	841	842	<0.5	1	<0 01	<5	18	21	5.14	420	<3	<5	62
DD95NO0003C	842	843	<0.5	2	<0.01	<5	22	16	5.48	430	<3	<5	68
DD95NO0003C	843	844	<0 5	<1	<0 01	<5	16	10	4 74	400	<3	<5	63
DD95NO0003C	844	845	<0 5	1	<0 01	<5	19	20	5 29	420	4	<5	68
DD95NO0003C	845	846	<0 5	2	<0.01	<5	16	5	4.69	390	<3	<5	65
DD95NO0003C	846	847	<0 5	2	<0 01	<5	17	9	4.77	390	<3	<5	65
DD95NO0003C	847	848	<0.5	3	0.02	<5	18	8	4.82	390	6	<5	63
DD95NO0003C	848	849	<0 5	2	0 02	<5	16	12	5.09	420	4	<5	68
DD95NO0003C	849	850	<0 5	4	<0 01	<5	14	6	4 49	370	<3	<5	63
DD95NO0003C	850	851	<0 5	6	0 09	<5	18	115	5.11	390	8	<5	65
DD95NO0003C	851	852	<0 5	4	0 64	<5	19	53	4 94	400	10	<5	65
DD95NO0003C	852	853	<0 5	4	<0.01	<5	16	14	5.15	470	14	<5	92
DD95NO0003C	853	854	<0.5	5	<0.01	<5	17	33	5 20	450	<3	<5	97
DD95NO0003C	854	855	<0 5	3	<0 01	<5	22	39	5.54	440	10	<5	110
DD95NO0003C	855	856	<0 5	9	<0 01	<5	18	77	5.06	450	10	<5	100
DD95NO0003C	856	857	<0 5	14	<0.01	<5	19	6	5.66	580	<3	<5	93
DD95NO0003C	857	858	0 5	7	0 07	5	20	93	6 83	820	560	<5	150
DD95NO0003C	858	859	<0.5	10	0 02	<5	22	26	7.01	560	32	<5	155
DD95NO0003C	859	860	<0.5	17	0 28	<5	28	34	7 69	540	420	<5	150
DD95NO0003C	860	861	1.0	10	0 09	5	22	170	8.64	600	340	<5	190
DD95NO0003C	861	862	<0 5	18	0.02	30	24	17	8.43	720	36	<5	180
DD95NO0003C	862	863	0 5	14	0 03	125	30	21	10 30	860	76	<5	180
DD95NO0003C	863	864	3.5	16	0.13	260	29	290	9 27	820	500	<5	370
DD95NO0003C	864	865	1 5	27	0 06	238	33	215	10 94	861	184	3	505
DD95NO0003C	865	866	37 5	16	13 20	1450	24	230	10 30	760	11500	<5	160
DD95NO0003C	866	867	2 0	6	7.43	640	20	59	6.52	390	720	<5	115
DD95NO0003C	867	868	6 5	6	3 37	500	18	640	5.89	420	10900	<5	210
DD95NO0003C	868	869	2 5	10	3 19	230	19	360	6 10	470	2500	<5	155
DD95NO0003C	869	870	3 0	11	5.75	520	19	1900	6.44	480	620	<5	165
DD95NO0003C	870	871	9.2	14	5 05	1245	17	575	6 11	414	8885	<5	102
DD95NO0003C	871	872	4 4	14	3.67	708	18	1155	6.78	464	1191	<5	132
DD95NO0003C	872	873	6.5	11	8 76	540	19	3050	5.30	290	1150	<5	2950
DD95NO0003C	873	874	5.0	9	18 40	700	12	310	4.60	400	1050	<5	420
DD95NO0003C	874	875	2 5	13	0 74	190	11	470	3 85	400	490	<5	760

Hole ID	From	To	Ag ppm	As ppm	Au ppm	Bi ppm	Co ppm	Cu ppm	Fe %	Mn ppm	Pb ppm	Sb ppm	Zn ppm
DD95NO0003C	875	876	0.5	18	0.36	70	20	450	5 85	490	46	<5	200
DD95NO0003C	876	877	1 0	15	1 41	135	16	140	5 15	410	84	<5	82
DD95NO0003C	877	878	1.5	18	0 30	110	21	520	6 26	580	450	<5	3050
DD95NO0003C	878	879	0.7	38	0 24	45	38	293	7.51	633	121	<5	906
DD95NO0003C	879	880	1.5	20	0 89	175	24	520	6.84	620	94	<5	130
DD95NO0003C	880	881	1 8	15	0.52	203	19	265	5 43	440	161	<5	194
DD95NO0003C	881	882	4 0	13	3 81	660	18	300	5 45	410	430	<5	84
DD95NO0003C	882	883	14.0	12	3 24	580	16	6050	4 71	360	1950	<5	2700
DD95NO0003C	883	884	2 9	15	1 43	301	12	685	3.45	295	501	<5	556
DD95NO0003C	884	885	3 5	27	2 83	190	24	580	6 72	520	410	<5	520
DD95NO0003C	885	886	8.0	14	2 75	195	14	460	3 13	260	2150	<5	2100
DD95NO0003C	886	887	8.0	14	6 81	450	17	220	4 55	300	2000	<5	6650
DD95NO0003C	887	888	6.0	26	7.49	420	24	940	7.70	520	1550	<5	3000
DD95NO0003C	888	889	10 0	16	16.10	880	15	1750	5.95	360	1100	<5	1150
DD95NO0003C	889	890	5 0	13	5 05	500	14	400	4 95	410	640	<5	1450
DD95NO0003C	890	891	2 5	19	0.78	75	17	165	5 36	470	640	<5	1200
DD95NO0003C	891	892	4 0	12	5.96	380	13	720	4 10	310	390	<5	160
DD95NO0003C	892	893	3 0	47	7.58	680	19	800	6 77	540	240	<5	120
DD95NO0003C	893	894	4.0	10	1 98	400	17	960	4.82	260	250	<5	115
DD95NO0003C	894	895	2.0	12	6.95	480	13	390	4 59	340	105	<5	84
DD95NO0003C	895	896	1 5	18	3 96	340	18	330	5 81	460	70	<5	87
DD95NO0003C	896	897	0.5	28	0 72	80	22	380	6 59	580	34	<5	640
DD95NO0003C	897	898	1 0	21	1 51	320	17	280	5 66	520	89	<5	560
DD95NO0003C	898	899	3 0	80	43 70	2500	17	220	7 66	580	135	10	44
DD95NO0003C	899	900	1 5	72	17.50	1350	30	340	10 20	720	46	<5	85
DD95NO0003C	900	901	1 0	22	1.81	580	14	860	5 63	470	42	<5	84
DD95NO0003C	901	902	1 0	19	3.51	380	19	1100	5.59	480	40	<5	61
DD95NO0003C	902	903	4.5	14	1 64	100	19	15300	8.16	640	14	<5	90
DD95NO0003C	903	904	4.5	1	0 16	20	17	14900	8 45	640	42	<5	125
DD95NO0003C	904	905	2.0	30	0 32	85	40	5050	9.27	880	70	<5	88
DD95NO0003C	905	906	3.5	34	0 04	115	47	620	13 20	1500	460	<5	125
DD95NO0003C	906	907	<0 5	32	0 07	45	28	760	8.22	980	16	<5	71
DD95NO0003C	907	908	<0.5	26	0.09	25	6	520	3 20	560	6	<5	28
DD95NO0003C	908	909	1 5	24	0 08	70	22	5400	7 92	940	50	<5	140
DD95NO0003C	909	910	4 5	14	0 07	30	29	6850	8 78	860	540	<5	135
DD95NO0003C	910	911	17.5	8	0.08	115	27	23500	8 96	720	3550	<5	390
DD95NO0003C	911	912	2 5	14	<0.01	35	22	7700	7.19	860	270	<5	88
DD95NO0003C	912	913	3 0	4	<0.01	85	13	2850	4.19	450	680	<5	45
DD95NO0003C	913	914	1 5	3	0 03	45	10	4050	3.20	350	54	<5	35
DD95NO0003C	914	915	1 5	9	0 03	195	17	1500	6.95	2100	290	<5	46
DD95NO0003C	915	916	1 5	26	0.17	560	31	380	9 43	1700	99	<5	69
DD95NO0003C	916	917	2.5	21	1.19	1550	37	3350	11 00	1600	230	10	110
DD95NO0003C	917	918	0 5	6	<0 01	380	22	470	6 87	840	36	<5	78
DD95NO0003C	918	919	<0 5	2	<0 01	5	17	125	5 10	580	<3	<5	65
DD95NO0003C	919	920	0 5	5	0 02	430	17	450	5 30	700	58	<5	65
DD95NO0003C	920	921	0 5	2	0 12	90	17	3500	5 95	660	10	<5	73
DD95NO0003C	921	922	1 0	10	0 19	230	18	1850	5.74	700	75	<5	63
DD95NO0003C	922	923	<0.5	13	0.08	125	22	98	4 98	580	6	<5	58
DD95NO0003C	923	924	<0 5	11	<0.01	20	15	130	4 42	540	<3	<5	51
DD95NO0003C	924	925	<0.5	16	<0 01	195	19	160	5 31	600	18	<5	61
DD95NO0003C	925	926	<0 5	10	<0 01	220	18	110	4 97	540	10	<5	61
DD95NO0003C	926	927	<0 5	12	<0 01	170	15	78	4 36	490	14	<5	53

Hole ID	From	To	Ag ppm	As ppm	Au ppm	Bi ppm	Co ppm	Cu ppm	Fe %	Mn ppm	Pb ppm	Sb ppm	Zn ppm
DD95NO0003C	927	928	<0.5	7	<0.01	20	16	48	4.68	500	<3	<5	54
DD95NO0003C	928	929	<0.5	7	<0 01	65	16	115	4 57	520	6	<5	55
DD95NO0003C	929	930	<0 5	6	<0.01	140	19	240	5.42	640	6	<5	62
DD95NO0004F	225	226	<0 5	4	<0 01	<5	24	280	6.23	700	4	<5	75
DD95NO0004F	226	227	<0.5	3	<0 01	<5	22	190	6 05	780	4	<5	80
DD95NO0004F	320	321	<0.5	11	0.02	<5	19	3	5 21	560	4	<5	60
DD95NO0004F	321	322	<0 5	15	0.01	15	19	170	5 85	660	4	<5	71
DD95NO0004F	322	323	<0.5	20	0 01	<5	17	57	5 16	560	<3	<5	62
DD95NO0004F	323	324	<0 5	20	0 01	15	17	53	4.83	540	<3	<5	52
DD95NO0004F	324	325	0 5	19	0 08	15	23	1400	7 11	740	6	<5	99
DD95NO0004F	325	326	1 0	16	0 59	65	25	1900	7 47	720	38	<5	98
DD95NO0004F	326	327	<0 5	6	0 04	5	22	340	5.80	560	14	<5	87
DD95NO0004F	327	328	<0.5	6	0.20	40	24	1300	5 85	520	34	<5	105
DD95NO0004F	328	329	0.5	6	0 07	60	26	2400	6.47	580	48	<5	150
DD95NO0004F	329	330	0 5	5	0 15	10	27	700	7.01	700	22	<5	120
DD95NO0004F	330	331	0 5	9	0.33	10	27	1800	7 82	780	12	<5	160
DD95NO0004F	331	332	1 0	7	0 26	40	33	2900	8.42	740	34	<5	160
DD95NO0004F	332	333	<0.5	10	0 05	<5	24	540	6 85	640	8	<5	115
DD95NO0004F	333	334	1.0	10	0 24	10	25	3200	7.70	700	18	<5	150
DD95NO0004F	334	335	<0 5	13	0 04	<5	28	300	7 17	680	10	<5	110
DD95NO0004F	335	336	0.5	17	1 24	15	27	1100	7 51	660	28	<5	115
DD95NO0004F	336	337	1 0	14	0 27	40	27	2000	7 16	660	42	<5	110
DD95NO0004F	337	338	1.0	10	0 07	35	25	900	7.41	660	58	<5	125
DD95NO0004F	338	339	0.5	13	0 11	25	25	840	7.15	640	44	<5	125
DD95NO0004F	339	340	<0 5	16	0 18	10	25	800	6 95	640	24	<5	105
DD95NO0004F	340	341	<0 5	11	0.06	75	26	660	8.55	760	34	<5	105
DD95NO0004F	341	342	0 5	24	0.25	20	28	1200	8 08	700	30	<5	100
DD95NO0004F	342	343	<0 5	7	<0 01	75	22	540	6.74	660	24	<5	87
DD95NO0004F	343	344	<0 5	13	0 10	25	22	460	7.08	660	12	<5	93
DD95NO0004F	344	345	<0 5	7	0 02	10	24	145	6.88	700	6	<5	87
DD95NO0004F	345	346	0 5	14	0 16	10	30	580	9.18	880	20	<5	110
DD95NO0004F	346	347	<0 5	14	0 02	<5	24	110	7 64	800	6	<5	96
DD95NO0004F	347	348	<0.5	15	0.01	5	25	105	6 99	700	10	<5	93
DD95NO0004F	348	349	1 0	15	0 25	15	27	2200	8.57	740	18	<5	130
DD95NO0004F	349	350	0 5	26	0.07	5	36	1100	7 40	660	12	<5	86
DD95NO0004F	350	351	1.0	47	0 27	25	31	2100	9 82	840	34	<5	110
DD95NO0004F	351	352	0.5	39	0.07	15	34	1100	9 37	880	16	<5	115
DD95NO0004F	352	353	<0 5	16	0 02	5	30	240	8 24	820	8	<5	96
DD95NO0004F	353	354	<0.5	9	0 04	5	26	740	7 29	740	6	<5	89
DD95NO0004F	354	355	<0 5	8	0 07	5	33	1100	8.86	920	12	<5	130
DD95NO0004F	355	356	<0 5	4	0 21	15	31	1200	8 36	800	24	<5	120
DD95NO0004F	356	357	<0 5	5	0.06	5	25	240	7.22	760	8	<5	94
DD95NO0004F	357	358	<0.5	6	<0 01	185	19	260	5 52	620	26	<5	76
DD95NO0004F	358	359	<0 5	6	<0.01	<5	17	45	5.01	540	4	<5	63
DD95NO0004F	359	360	<0 5	20	<0 01	<5	20	11	5.25	600	<3	<5	75
DD95NO0004F	360	361	<0 5	23	<0 01	<5	21	6	5.76	680	<3	<5	83
DD95NO0004F	361	362	<0.5	24	<0 01	<5	21	2	5 67	700	<3	<5	91
DD95NO0004F	362	363	<0.5	20	<0 01	40	17	2	4.39	540	4	<5	74
DD95NO0004F	363	364	<0.5	24	<0.01	<5	20	3	4 21	480	<3	<5	72
DD95NO0004F	364	365	<0.5	15	<0 01	<5	18	1	4.90	600	<3	<5	81
DD95NO0004F	365	366	<0 5	15	<0.01	35	39	680	13 20	1400	18	10	150
DD95NO0004F	366	367	<0.5	27	0 04	55	31	260	11 40	1100	28	5	135

Hole ID	From	To	Ag ppm	As ppm	Au ppm	Bi ppm	Co ppm	Cu ppm	Fe %	Mn ppm	Pb ppm	Sb ppm	Zn ppm
DD95NO0004F	367	368	0 5	34	0 06	25	32	1000	10 90	1000	34	<5	120
DD95NO0004F	368	369	0 5	13	0.07	54	24	1361	8 87	888	22	<5	100
DD95NO0004F	369	370	3 0	10	24.40	960	14	1200	4 33	380	96	5	68
DD95NO0004F	370	371	3 5	19	14 60	420	23	900	6 84	680	175	<5	150
DD95NO0004F	371	372	2 5	9	0.91	95	30	1100	10 00	1100	260	<5	200
DD95NO0004F	372	373	<0.5	15	0 16	50	33	220	10.70	1200	22	<5	135
DD95NO0004F	373	374	2 0	22	2.05	648	30	1172	9.10	873	83	<5	109
DD95NO0004F	374	375	1 0	11	1 87	580	26	1400	7.96	760	57	<5	88
DD95NO0004F	375	376	1 5	10	4.17	300	29	6700	9.30	960	20	<5	115
DD95NO0004F	376	377	6 0	5	0.69	1300	30	39300	10 90	900	59	10	160
DD95NO0004F	377	378	0 5	20	0.03	60	35	3000	9.30	1000	8	<5	100
DD95NO0004F	378	379	<0 5	28	0.10	10	23	235	6.29	721	4	<5	79
DD95NO0004F	379	380	<0.5	18	<0 01	25	22	31	6.18	720	6	<5	73
DD95NO0004F	380	381	<0.5	18	<0 01	5	22	400	6.14	700	<3	<5	70
DD95NO0004F	381	382	<0 5	145	0.03	200	26	120	6.48	780	12	<5	62
DD95NO0004F	382	383	2.5	70	0 71	560	21	2000	6 58	820	200	<5	100
DD95NO0004F	383	384	2.5	200	1 28	2000	48	3000	12.00	1400	200	10	120
DD95NO0004F	384	385	1 0	15	0 37	1164	40	912	11.43	1294	88	10	124
DD95NO0004F	385	386	<0 5	3	0 06	85	23	160	6.39	680	8	<5	80
DD95NO0004F	386	387	<0 5	2	0 25	240	21	175	5.96	680	42	<5	82
DD95NO0004F	387	388	<0 5	7	<0 01	15	17	6	4.70	540	6	<5	67
DD95NO0004F	388	389	<0 5	10	0 05	5	15	50	4 22	500	<3	<5	51
DD95NO0004F	389	390	1 5	15	1.49	780	25	720	7.94	980	135	<5	98
DD95NO0004F	390	391	0 5	9	0 17	360	22	50	6.16	700	51	<5	69
DD95NO0004F	391	392	<0.5	7	<0 01	65	21	120	5 70	640	12	<5	74
DD95NO0004F	392	393	<0 5	3	0 01	<5	17	4	4 91	540	14	<5	64
DD95NO0004F	393	394	<0.5	11	<0 01	25	18	14	5.10	620	34	<5	62
DD95NO0004F	394	395	<0.5	3	<0 01	<5	18	4	5.11	580	<3	<5	65
DD95NO0004F	395	396	<0.5	7	<0.01	<5	17	13	4.77	560	4	<5	65
DD95NO0004F	396	397	<0.5	3	<0 01	<5	17	4	4 97	600	<3	<5	66
DD95NO0004F	397	398	<0 5	13	0.01	<5	23	2	6 83	900	24	<5	86
DD95NO0004F	398	399	<0 5	3	0 01	<5	20	2	5.52	680	4	<5	73
DD95NO0004F	399	400	<0 5	3	0 01	<5	21	1	5.94	700	<3	<5	79
DD95NO0004F	400	401	<0.5	6	<0 01	<5	24	4	6.92	860	6	<5	89
DD95NO0004F	401	402	<0 5	3	<0.01	<5	18	2	5.44	640	<3	<5	71
DD95NO0004F	402	403	<0 5	3	<0 01	<5	20	12	6.45	800	6	<5	82
DD95NO0004F	403	404	<0 5	5	<0 01	<5	16	3	5.11	600	<3	<5	69
DD95NO0004F	404	405	<0 5	11	<0.01	<5	17	8	4.93	580	4	<5	68
DD95NO0004F	405	406	<0 5	9	<0.01	15	22	320	6.88	920	12	<5	100
DD95NO0004F	406	407	<0.5	8	0.02	45	35	28	10.40	1200	28	5	140
DD95NO0004F	407	408	<0.5	2	0.02	<5	26	2	6.89	800	4	<5	98
DD95NO0004F	420	421	<0.5	3	<0 01	<5	20	5	5.89	940	6	<5	89
DD95NO0004F	421	422	1 0	5	0.02	35	50	820	14.50	1600	40	10	165
DD95NO0004F	422	423	2 0	4	0.03	120	56	5400	16.30	1700	89	15	190
DD95NO0004F	423	424	1 0	10	0 02	5	19	30	4.05	640	175	<5	185
DD95NO0004F	424	425	<0 5	9	0.02	<5	18	13	3.76	560	14	<5	115
DD95NO0004F	436	437	<0 5	4	<0 01	<5	24	42	4.19	700	10	<5	130
DD95NO0004F	437	438	<0 5	2	0 02	<5	23	28	4.24	740	10	<5	160
DD95NO0004F	438	439	<0.5	5	0.02	<5	17	10	3.72	680	12	<5	130
DD95NO0004F	439	440	<0 5	6	0 02	<5	18	22	4.30	660	16	<5	155
DD95NO0004F	440	441	<0 5	14	0 05	<5	19	84	4.24	740	26	<5	220
DD95NO0004F	441	442	<0.5	7	0 05	<5	16	29	3 62	660	12	<5	150

Hole ID	From	To	Ag ppm	As ppm	Au ppm	Bi ppm	Co ppm	Cu ppm	Fe %	Mn ppm	Pb ppm	Sb ppm	Zn ppm
DD95NO0004F	442	443	1 0	13	0.03	<5	23	3300	4.91	840	42	<5	220
DD95NO0004F	443	444	<0.5	3	<0 01	<5	17	28	3 90	620	10	<5	115
DD95NO0004F	444	445	<0 5	<1	<0 01	<5	19	9	4 09	620	8	<5	120
DD95NO0004F	445	446	<0 5	<1	0 01	<5	20	7	4.26	660	20	<5	120
DD95NO0004F	446	447	<0.5	<1	<0.01	<5	20	9	4 30	500	20	<5	98
DD95NO0004F	447	448	<0.5	1	0 01	<5	19	12	4 02	540	20	<5	95
DD95NO0004F	448	449	<0.5	2	0 01	<5	19	22	4.44	600	12	<5	99
DD95NO0004F	449	450	<0.5	4	0 01	<5	18	22	4 07	560	6	<5	84
DD95NO0004F	450	451	<0 5	5	<0.01	<5	17	20	3.86	500	4	<5	78
DD95NO0004F	451	452	<0.5	10	<0.01	<5	18	23	3 83	520	6	<5	81
DD95NO0004F	452	453	<0.5	10	<0.01	<5	19	22	3 80	500	8	<5	75
DD95NO0004F	453	454	<0.5	5	<0.01	<5	17	20	3 90	440	10	<5	72
DD95NO0004F	454	455	<0.5	4	<0.01	<5	18	15	3 94	400	12	<5	69
DD95NO0004F	455	456	<0 5	<1	<0.01	<5	17	13	3 85	320	24	<5	61
DD95NO0004F	456	457	<0 5	2	<0.01	<5	16	11	3 81	340	26	<5	69
DD95NO0004F	457	458	<0.5	2	<0 01	<5	16	10	3.63	320	24	<5	79
DD95NO0004F	458	459	<0 5	2	0.01	<5	16	12	3 64	320	24	<5	74
DD95NO0004F	459	460	<0 5	3	<0 01	<5	17	22	3.82	340	20	<5	74
DD95NO0004F	460	461	<0 5	4	0.01	<5	18	23	4 01	400	38	<5	82
DD95NO0004F	461	462	<0.5	5	<0 01	<5	17	17	3.61	420	30	<5	67
DD95NO0004F	462	463	<0.5	4	<0 01	<5	14	22	3.14	740	20	<5	70
DD95NO0004F	463	464	<0 5	10	<0 01	<5	16	23	3.44	400	12	<5	76
DD95NO0004F	464	465	<0 5	10	<0.01	<5	17	30	3 72	460	16	<5	77
DD95NO0004F	465	466	0 5	14	<0.01	<5	17	31	3.73	420	24	<5	90
DD95NO0004F	466	467	<0 5	15	<0 01	<5	16	28	3 67	420	32	<5	94
DD95NO0004F	467	468	<0 5	15	<0.01	<5	17	32	3 74	420	28	<5	100
DD95NO0004F	468	469	<0 5	17	<0.01	<5	17	31	3 80	440	28	<5	100
DD95NO0004F	469	470	<0 5	15	<0.01	<5	18	29	3 70	460	34	<5	95

Appendix 10: Whole-rock and Trace Element Analyses

HoleId	From	To	Ag ppm	Al_2O_3 %	As ppm	Ba ppm	Be ppm	Bi ppm	C %	CaO %	Cd ppm	Ce ppm	Co ppm	Cr ppm	Cs ppm	Dy ppm
DD95NO0001F	1063	1067	<1	13.30	12	360	2.5	6	0 06	0.43	<3	72	20	65	6	3.0
DD95NO0001F	1067	1071	<1	14 00	<3	450	3 0	6	0 12	0 61	<3	93	20	66	8	4.5
DD95NO0001F	1071	1075	<1	14.70	4	500	3.0	<3	0.12	0.69	<3	105	5	67	8	4 5
DD95NO0001F	1075	1079	<1	15 50	4	500	3 0	<3	0 10	0.69	<3	94	5	63	8	4 5
DD95NO0001F	1079	1083	<1	16 30	<3	550	3 5	4	0.16	0 68	<3	91	20	71	8	4 5
DD95NO0001F	1083	1087	<1	14 30	4	430	3.0	<3	0 28	1.30	<3	73	5	65	6	4 0
DD95NO0001F	1087	1091	<1	15.00	8	490	3 0	<3	0.26	1 25	<3	82	5	64	8	4 5
DD95NO0001F	1091	1095	<1	10 90	6	330	2.5	<3	0.36	1.44	<3	82	5	77	6	4.5
DD95NO0001F	1095	1099	<1	15 30	8	550	3 5	<3	0 50	1 99	<3	94	5	60	8	4.5
DD95NO0001F	1099	1103	<1	13 20	8	410	3 0	<3	0 22	0.94	<3	88	5	64	6	4 5
DD95NO0001F	1103	1107	<1	16 50	6	500	3 0	<3	0.14	0.71	<3	87	5	64	8	4 5
DD95NO0001F	1107	1111	<1	11 70	<3	320	2.5	12	0 22	0.99	<3	71	20	67	6	3 5
DD95NO0001F	1111	1115	<1	14 20	4	450	3 0	<3	0 20	0 96	<3	88	5	67	8	4.5
DD95NO0001F	1115	1119	<1	8 47	4	460	2.0	<3	3 96	14.00	<3	40	5	27	<3	3 0
DD95NO0001F	1119	1123	<1	14.50	6	420	3.0	<3	0 18	0.86	<3	79	20	66	8	3.5
DD95NO0001F	1123	1127	<1	14 50	4	430	3 0	30	0 18	0 78	<3	76	20	69	8	4 0
DD95NO0001F	1127	1131	<1	13.00	4	370	2.5	14	0 16	0.82	<3	77	20	86	6	4 0
DD95NO0001F	1131	1135	<1	9 99	8	210	2 0	4	0.16	0 65	<3	57	20	67	4	3 5
DD95NO0001F	1135	1139	<1	10.70	16	240	2 0	<3	0.14	0 64	<3	53	20	61	6	3.0
DD95NO0001F	1139	1143	<1	9 67	18	220	2 0	<3	0 16	0 81	<3	52	20	63	6	3 0
DD95NO0001F	1143	1147	<1	10 20	18	240	2 0	<3	0 32	1 36	<3	58	20	66	6	3 0
DD95NO0001F	1147	1149	<1	8 40	24	165	2 0	10	0 18	0 81	<3	50	20	82	4	3 5
DD95NO0001F	1149	1151	3	9.55	26	185	2.0	165	0.14	0.62	<3	52	60	65	4	3 0
DD95NO0001F	1151	1153	2	8.70	20	180	2.0	77	0.30	1 30	<3	51	20	66	4	3 0
DD95NO0001F	1153	1155	5	3.95	22	35	1.5	220	0 18	0.72	<3	30	5	125	<3	1 5
DD95NO0001F	1155	1157	5	4.80	10	90	1.5	145	0.16	0.71	4	24	5	100	<3	1 5
DD95NO0001F	1157	1159	4	2 95	24	25	1.5	300	0.18	0 71	<3	15	5	145	4	1.0
DD95NO0001F	1159	1161	5	2.73	650	30	1 5	550	0 22	0 85	<3	14	20	125	4	1 0
DD95NO0001F	1161	1163	3	2.20	16	55	1.5	750	0.18	0.75	<3	12	5	115	24	0 5
DD95NO0001F	1163	1165	3	1.87	300	15	1.5	490	0 14	0.74	<3	8	5	165	<3	<0.5
DD95NO0001F	1165	1167	6	1 64	2000	35	1 5	1750	0 12	0 67	<3	8	5	155	8	<0.5
DD95NO0001F	1167	1169	3	1 95	4400	15	1 5	1500	0.12	0 64	<3	10	5	180	<3	0.5
DD95NO0001F	1169	1171	2	1.65	115	20	1.5	1450	0 18	0 81	<3	8	5	190	<3	<0 5
DD95NO0001F	1171	1173	1	2 51	83	15	1 5	370	0 14	0 61	<3	14	5	150	<3	0.5
DD95NO0001F	1173	1175	3	1.56	250	15	1.0	600	0.14	0.65	<3	6	5	185	<3	<0 5
DD95NO0001F	1175	1177	2	1 51	48	20	1 0	600	0 14	0.65	<3	8	5	165	<3	<0 5
DD95NO0001F	1177	1179	1	1.39	12	20	1 0	750	0.14	0 81	<3	8	5	190	<3	<0.5
DD95NO0001F	1179	1181	<1	2 86	18	15	1.5	380	0.14	0.73	<3	10	5	185	<3	1 0
DD95NO0001F	1181	1183	1	2 60	48	15	1 5	750	0 16	0 74	<3	9	5	195	<3	0.5
DD95NO0001F	1183	1185	1	2 89	16	25	1 5	600	0.14	0 81	<3	13	5	110	<3	1 0
DD95NO0001F	1185	1187	1	4 04	26	75	1.5	550	0.12	0 72	<3	25	30	88	16	1.0
DD95NO0001F	1187	1189	3	4 38	16	40	1 5	130	0 18	0 71	<3	10	20	220	4	0.5
DD95NO0001F	1189	1191	2	3 60	36	50	1 5	55	0 14	0.77	<3	7	20	110	4	1 0
DD95NO0001F	1191	1193	1	4.47	46	35	1.5	22	0.22	0.98	<3	7	20	140	<3	<0 5
DD95NO0001F	1193	1195	<1	3.42	51	40	1 5	16	0 22	0 95	<3	7	20	145	<3	0 5
DD95NO0001F	1195	1197	<1	2 25	320	25	1 5	20	0 20	0 96	<3	4	5	175	<3	<0 5
DD95NO0001F	1197	1199	<1	2 32	86	20	1.5	22	0.14	0.72	<3	4	5	230	<3	<0.5
DD95NO0001F	1199	1201	<1	2 60	40	25	1.5	14	0 18	0.80	<3	12	5	130	<3	1 0
DD95NO0001F	1201	1203	2	6 09	6	90	1.5	40	0 18	0.93	<3	24	30	115	<3	1.5
DD95NO0001F	1203	1205	2	6.43	4	120	1 5	46	0.12	0 72	<3	30	30	96	<3	1 5
DD95NO0001F	1205	1207	1	8 43	6	160	2.0	16	0.10	0 60	<3	46	30	63	<3	2.5
DD95NO0001F	1207	1209	<1	8.77	<3	185	2 0	16	0 18	0.87	<3	46	30	66	4	2.5

HoleId	From	To	Ag ppm	Al_2O_3 %	As ppm	Ba ppm	Be ppm	Bi ppm	C %	CaO %	Cd ppm	Ce ppm	Co ppm	Cr ppm	Cs ppm	Dy ppm
DD95NO0001F	1209	1211	<1	8.31	12	185	2.0	18	0.30	1 47	<3	36	20	72	<3	2 0
DD95NO0001F	1211	1213	1	8 83	8	195	2 0	10	0.14	0.94	<3	41	20	66	<3	2 5
DD95NO0001F	1213	1215	<1	10 50	16	290	2.5	10	0.18	0 94	<3	59	20	62	4	3 0
DD95NO0001F	1215	1217	<1	9 48	16	250	2 5	20	0.14	0 83	<3	57	5	65	4	2 5
DD95NO0001F	1217	1219	<1	8 90	8	300	2 5	8	0 16	0 83	<3	60	20	49	4	3.0
DD95NO0001F	1219	1221	1	9.69	8	260	2 5	14	0 14	0 75	<3	58	5	61	4	3 0
DD95NO0003C	839	840		10.80	5	270	2 0	84		0 22	<3	54	20	90	6	3 0
DD95NO0003C	840	841		10.10	5	240	2 5	60		0 26	<3	55	20	80	4	3.5
DD95NO0003C	841	842		10.90	5	280	1 5	4		0.25	<3	60	20	140	6	4 5
DD95NO0003C	842	843		11 60	5	310	2.0	<3		0 19	<3	63	20	90	6	3 5
DD95NO0003C	843	844		12 60	5	340	2 5	<3		0.30	<3	67	20	90	8	4 0
DD95NO0003C	844	845		10.20	5	250	2 0	<3		0 22	<3	59	20	140	6	3 5
DD95NO0003C	845	846		12.20	5	320	1 5	<3		0 29	<3	66	20	90	6	4 0
DD95NO0003C	846	847		11 30	5	300	2.5	<3		0 19	<3	64	20	90	6	4 0
DD95NO0003C	847	848		10 60	5	270	2 0	4		0 31	<3	62	20	160	6	3 5
DD95NO0003C	848	849		11 40	5	310	1.5	<3		0 22	<3	68	20	100	6	5 0
DD95NO0003C	849	850		10 80	5	280	2 0	<3		0 28	<3	69	20	100	6	4.0
DD95NO0003C	850	851		10 60	5	280	2 5	<3		0 21	<3	59	20	170	8	5 0
DD95NO0003C	851	852		10.80	5	320	2 0	<3		0 20	<3	66	20	100	6	4 5
DD95NO0003C	852	853		9.87	5	230	2 0	<3		0 22	<3	47	20	100	6	3 0
DD95NO0003C	853	854		9.47	5	240	1 5	<3		0 18	<3	57	20	170	6	3 5
DD95NO0003C	854	855		8.99	5	220	1 5	<3		0 16	<3	55	20	100	4	3 0
DD95NO0003C	855	856		12 40	5	360	2 5	<3		0 23	<3	69	20	100	8	4 0
DD95NO0003C	856	857		12 00	5	310	2 5	<3		0 23	<3	60	20	120	8	4 0
DD95NO0003C	857	858		10 30	5	220	1 5	6		0 18	<3	64	30	80	6	3 5
DD95NO0003C	858	859		10 40	5	230	2.0	<3		0 19	<3	46	30	90	6	3 0
DD95NO0003C	859	860		9.30	30	180	2 5	<3		0.19	<3	50	40	90	6	3 0
DD95NO0003C	860	861		8.76	5	185	1 5	8		0.19	<3	50	30	150	8	3 0
DD95NO0003C	861	862		10 20	20	200	1 5	24		0 22	<3	51	30	100	8	2 5
DD95NO0003C	862	863		9.17	20	155	1 5	79		0.40	<3	51	30	100	8	2 5
DD95NO0003C	863	864		8 01	20	140	1 0	220		0.18	<3	37	40	90	6	2 0
DD95NO0003C	864	865		7 50	40	65	1 0	250		0 39	<3	41	50	130	4	3 0
DD95NO0003C	865	866		5.10	20	30	2 0	1150		0.16	<3	26	30	70	8	2 5
DD95NO0003C	866	867		5 02	5	75	1.5	550		0.12	<3	28	20	60	<3	1 5
DD95NO0003C	867	868		3 91	5	35	1 5	460		0.12	<3	20	20	290	<3	1 0
DD95NO0003C	868	869		3.47	5	10	<0 5	195		0 08	<3	18	20	70	<3	1.0
DD95NO0003C	869	870		3 31	5	15	1.0	440		0 14	<3	14	20	70	<3	1 0
DD95NO0003C	870	871		2 53	20	55	0 5	1050		0.14	<3	11	20	290	16	0 5
DD95NO0003C	871	872		2 32	20	55	1 5	600		0 20	<3	11	20	90	22	1 0
DD95NO0003C	872	873		1 86	5	25	1 0	460		0 15	10	5	20	70	10	<0 5
DD95NO0003C	873	874		2 16	5	20	1 0	600		0 15	<3	11	20	300	4	0 5
DD95NO0003C	874	875		1 86	20	10	<0.5	180		0.17	<3	11	20	90	<3	1.0
DD95NO0003C	875	876		3.30	20	<10	1 0	67		0 13	<3	19	20	70	<3	1 5
DD95NO0003C	876	877		2.66	5	<10	1 0	61		0 04	<3	15	20	300	<3	1 0
DD95NO0003C	877	878		3 64	20	15	<0 5	40		0 04	8	24	20	90	<3	1 5
DD95NO0003C	878	879		4 06	30	<10	<0 5	18		0.06	<3	25	30	80	<3	1 5
DD95NO0003C	879	880		3 72	20	<10	1 0	78		0 06	<3	24	20	220	<3	1 5
DD95NO0003C	880	881		2 73	20	10	1 0	110		0 24	<3	16	20	90	<3	1.0
DD95NO0003C	881	882		2 37	5	15	<0 5	290		0 23	<3	22	20	80	4	1 0
DD95NO0003C	882	883		1 87	5	<10	1 0	230		0 05	8	10	5	360	<3	0 5
DD95NO0003C	883	884		1 88	5	<10	<0.5	135		0.06	<3	13	5	100	<3	0 5
DD95NO0003C	884	885		3 70	30	<10	1 0	74		0 08	<3	20	20	80	<3	1 0

HoleId	From	To	Ag ppm	Al_2O_3 %	As ppm	Ba ppm	Be ppm	Bi ppm	C %	CaO %	Cd ppm	Ce ppm	Co ppm	Cr ppm	Cs ppm	Dy ppm
DD95NO0003C	885	886		1 76	20	<10	<0 5	85		0 08	6	8	5	380	<3	0.5
DD95NO0003C	886	887		1.46	5	15	0.5	180		0.30	18	6	5	120	10	<0.5
DD95NO0003C	887	888		3 42	30	20	0.5	175		0 16	8	19	30	80	12	1 0
DD95NO0003C	888	889		2 04	20	15	<0 5	360		0.31	4	7	5	280	14	<0 5
DD95NO0003C	889	890		2.06	20	15	<0.5	220		0 11	6	11	5	50	6	<0 5
DD95NO0003C	890	891		3.34	20	25	1 0	42		0 04	<3	20	20	50	<3	1.5
DD95NO0003C	891	892		1.79	5	<10	0.5	175		0 03	<3	7	5	360	<3	<0.5
DD95NO0003C	892	893		2.77	40	<10	<0 5	260		0 09	<3	13	20	50	<3	<0.5
DD95NO0003C	893	894		1 17	5	<10	<0 5	175		0.09	<3	4	5	40	4	<0 5
DD95NO0003C	894	895		2 16	5	<10	<0 5	175		0.08	<3	9	5	270	<3	<0.5
DD95NO0003C	895	896		3 04	20	15	0 5	145		0 15	<3	17	20	60	<3	1 0
DD95NO0003C	896	897		4.22	30	15	0 5	52		0 17	<3	26	20	40	<3	1 0
DD95NO0003C	897	898		3 48	20	<10	0.5	130		0 13	<3	18	20	220	<3	1 0
DD95NO0003C	898	899		2 03	120	40	0 5	1000		0 13	<3	3	20	40	22	<0 5
DD95NO0003C	899	900		4 04	80	10	<0 5	550		0 40	<3	17	20	30	4	1 0
DD95NO0003C	900	901		2.77	5	<10	0.5	250		0.19	<3	9	5	270	<3	1.0
DD95NO0003C	901	902		2 99	20	<10	0 5	165		0 10	<3	17	20	50	<3	1.0
DD95NO0003C	902	903		5.10	5	40	<0 5	50		0.13	<3	31	20	50	<3	1 5
DD95NO0003C	903	904		6 18	5	80	1.0	14		0.11	<3	28	20	210	<3	1 5
DD95NO0003C	904	905		5.37	60	30	0 5	46		0.15	<3	6	50	30	4	0 5
DD95NO0003C	905	906		8 07	30	25	<0 5	58		0.17	<3	9	40	20	8	0 5
DD95NO0003C	906	907		4.69	30	<10	1 0	26		0.08	<3	3	30	30	<3	<0.5
DD95NO0003C	907	908		2 11	20	<10	<0.5	14		0.05	<3	1	5	380	<3	<0 5
DD95NO0003C	908	909		5 20	20	25	1.0	36		0.12	<3	19	20	50	<3	1.0
DD95NO0003C	909	910		7.23	20	110	0.5	20		0.33	<3	36	30	50	<3	1.5
DD95NO0003C	910	911		5 15	5	65	0.5	50		0.16	<3	22	20	230	<3	1 0
DD95NO0003C	911	912		6.39	20	80	1.0	20		0.14	<3	31	20	90	<3	1 5
DD95NO0003C	912	913		3 24	5	35	<0 5	46		0 12	<3	20	5	50	<3	1 0
DD95NO0003C	913	914		2.45	5	30	<0.5	18		0 06	<3	6	5	350	<3	0.5
DD95NO0003C	914	915		2.93	5	55	0.5	70		0 03	<3	7	20	40	22	1.5
DD95NO0003C	915	916		5 54	20	45	<0 5	220		0 25	<3	3	30	20	14	<0 5
DD95NO0003C	916	917		9.31	20	115	1 5	550		0.22	<3	24	40	110	10	2 0
DD95NO0003C	917	918		10 90	5	220	1.5	155		0.17	<3	49	20	70	4	2.5
DD95NO0003C	918	919		11.50	5	280	2.0	10		0 18	<3	47	20	70	4	3 5
DD95NO0003C	919	920		9 28	5	230	1.0	180		0.11	<3	42	20	150	4	2 5
DD95NO0003C	920	921		10 30	5	220	1.0	38		0.18	<3	45	20	70	4	2 5
DD95NO0003C	921	922		8 37	20	160	1 5	82		0.27	<3	30	20	60	<3	1.5
DD95NO0003C	922	923		10 30	5	240	1.5	54		0 22	<3	40	20	150	4	3 0
DD95NO0003C	923	924		10 70	5	260	1 5	12		0 30	<3	44	5	70	4	3 0
DD95NO0003C	924	925		11.40	20	260	1 0	84		0 22	<3	45	20	70	4	3.0
DD95NO0003C	925	926		12.70	5	310	2 0	88		0 21	<3	49	20	110	6	3.0
DD95NO0003C	926	927		11 60	5	290	1.0	73		0 20	<3	46	5	70	6	3.0
DD95NO0003C	927	928		10 90	5	250	1 0	12		0.19	<3	42	20	70	4	2 5
DD95NO0003C	928	929		11.60	5	280	1 5	30		0.21	<3	51	20	120	6	3 0
DD95NO0003C	929	930		8 06	5	145	0 5	55		0.40	<3	27	20	70	4	2 0
DD95NO0004F	320	322	<1	9 49	18	240	2 5	10	0.16	0.79	<3	60	20	99	4	3 0
DD95NO0004F	322	324	<1	8 35	16	220	2 0	8	0 16	0 92	<3	55	20	115	4	3.0
DD95NO0004F	324	326	1	7 80	14	155	2 0	38	0.18	0 85	<3	47	20	115	<3	2 5
DD95NO0004F	326	328	<1	9.78	8	240	2.5	18	0 28	1 20	<3	58	30	86	4	3.0
DD95NO0004F	328	330	1	9 99	6	260	2.5	38	0.20	1.01	<3	63	20	79	6	3 5
DD95NO0004F	330	332	1	8 94	4	210	2 5	24	0.30	1.32	<3	57	30	87	4	2 5
DD95NO0004F	332	334	1	9.82	10	250	2.5	8	0 14	0 59	<3	63	20	76	6	3 0

HoleId	From	To	Ag ppm	Al_2O_3 %	As ppm	Ba ppm	Be ppm	Bi ppm	C %	CaO %	Cd ppm	Ce ppm	Co ppm	Cr ppm	Cs ppm	Dy ppm
DD95NO0004F	334	336	1	9.55	12	230	2 5	10	0 20	0 96	<3	63	30	85	6	2.5
DD95NO0004F	336	338	1	10 20	12	240	2 5	50	0 12	0 61	<3	66	20	79	6	3.5
DD95NO0004F	338	340	<1	9 26	10	240	2.5	20	0.30	1.30	<3	64	20	75	6	3.0
DD95NO0004F	340	342	1	8.80	14	175	2.5	46	0.16	0.75	<3	58	30	80	4	3.0
DD95NO0004F	342	344	<1	9.34	8	230	2.0	48	0.20	0.90	<3	75	20	73	4	4 0
DD95NO0004F	344	346	<1	9.62	12	210	2 5	14	0 16	0.67	<3	59	30	79	4	3 0
DD95NO0004F	346	348	<1	10 10	12	250	2.0	8	0.14	0 64	<3	71	20	71	4	3 5
DD95NO0004F	348	350	1	10 20	18	240	2 5	12	0 16	0.71	<3	74	30	80	4	3 5
DD95NO0004F	350	352	1	9 12	36	155	1.5	22	0.12	0 54	<3	64	30	88	4	3.0
DD95NO0004F	352	354	<1	9 67	14	200	2.0	8	0 08	0 35	<3	74	30	76	4	3 5
DD95NO0004F	354	356	<1	9 29	6	155	2.0	12	0 12	0 49	<3	65	30	75	4	3 0
DD95NO0004F	356	358	<1	10 50	10	220	2.5	70	0.20	0 91	<3	59	20	74	4	3.5
DD95NO0004F	358	360	<1	11 10	18	290	3.0	6	0.14	0.72	<3	60	20	78	6	3.5
DD95NO0004F	360	362	<1	12 70	26	300	3 0	4	0 14	0 69	<3	57	20	88	6	4.0
DD95NO0004F	362	364	<1	12 80	30	370	3 0	10	0.28	1.25	<3	68	20	79	8	4.0
DD95NO0004F	364	365	<1	12.70	18	350	3 0	<3	0.02	0 16	<3	65	20	71	8	4 0
DD95NO0004F	365	366	1	11.20	12	85	2.0	24	0.04	0 15	<3	61	30	84	4	3.5
DD95NO0004F	366	367	1	9.83	24	120	1 5	44	0.02	0 16	<3	61	30	77	4	4.0
DD95NO0004F	367	368	1	9.35	36	165	2 0	30	<0 02	0.16	<3	63	30	72	6	3.5
DD95NO0004F	368	369	1	6 68	12	45	2 0	53	<0.02	0 12	<3	37	20	90	<3	2.0
DD95NO0004F	369	370	4	2.20	12	<10	1 5	800	<0 02	0 03	<3	11	5	210	<3	0 5
DD95NO0004F	370	371	4	4.17	12	15	1 5	380	0.04	0 11	<3	21	20	170	<3	1.5
DD95NO0004F	371	372	3	6.69	8	15	2 0	100	<0.02	0 20	<3	35	30	72	<3	2 0
DD95NO0004F	372	373	<1	7 56	16	20	2 0	68	0.02	0 09	<3	35	30	71	<3	2 0
DD95NO0004F	373	374	2	4 79	18	<10	2.0	550	<0.02	0 09	<3	25	20	110	4	1 5
DD95NO0004F	374	375	1	4.47	8	<10	1 5	500	0.02	0 07	<3	23	20	175	4	1 5
DD95NO0004F	375	376	2	6.31	6	25	2 0	290	<0 02	0 11	<3	30	30	95	<3	1 5
DD95NO0004F	376	377	7	6 28	<3	40	1 5	900	<0 02	0 10	<3	28	30	96	<3	2 0
DD95NO0004F	377	378	1	9 70	12	140	2 5	120	<0.02	0.12	<3	43	30	63	4	2.5
DD95NO0004F	378	379	<1	11 90	18	300	3 0	38	0.02	0 15	<3	59	20	68	4	3 5
DD95NO0004F	379	380	<1	10 50	8	260	2 5	34	<0 02	0.15	<3	53	20	65	4	3 5
DD95NO0004F	380	381	<1	8 15	14	175	2 5	14	<0 02	0.12	<3	36	20	99	4	2 5
DD95NO0004F	381	382	<1	4.38	200	<10	1 5	175	<0 02	<0 01	<3	3	20	93	<3	<0.5
DD95NO0004F	382	383	2	4 97	77	35	2 0	470	<0.02	0 04	<3	7	20	180	<3	1 0
DD95NO0004F	383	384	3	7 64	160	<10	1 5	1700	<0.02	0.02	<3	3	60	96	<3	<0 5
DD95NO0004F	384	385	1	11 70	14	160	2 5	1050	0 02	0 11	<3	44	30	72	4	3 0
DD95NO0004F	385	386	<1	12 50	<3	310	3.5	155	<0.02	0 12	<3	56	20	61	6	3 0
DD95NO0004F	386	387	<1	9 51	<3	190	2.5	220	0.02	0 08	<3	39	20	125	6	2 0
DD95NO0004F	387	388	<1	10 40	6	270	2 5	36	<0 02	0 10	<3	42	5	67	6	2 5
DD95NO0004F	388	389	<1	7 90	12	195	2 5	20	<0.02	0 08	<3	24	5	120	4	1 5
DD95NO0004F	389	390	2	8 58	16	120	2.5	650	<0.02	0.06	<3	24	30	125	4	2 0
DD95NO0004F	390	391	<1	7.86	10	135	2.0	310	<0 02	0 06	<3	31	20	105	4	2 5
DD95NO0004F	391	392	<1	10.90	6	250	2 5	84	0 02	0 09	<3	43	20	57	6	3 0
DD95NO0004F	392	393	<1	12.10	6	330	3.0	18	<0 02	0.10	<3	53	20	59	8	2 5
DD95NO0004F	393	394	<1	9.14	10	210	2.0	22	<0.02	0.06	<3	39	20	93	6	2 0
DD95NO0004F	394	396	<1	11 10	4	280	2 5	6	0 12	0 46	<3	43	5	75	8	2 5
DD95NO0004F	396	398	<1	10 80	<3	240	2 5	4	<0 02	0 12	<3	52	20	59	8	3 0
DD95NO0004F	398	400	<1	11.10	4	260	2 5	<3	0 04	0 21	<3	47	20	67	8	2 5
DD95NO0004F	400	402	<1	8 78	10	165	2.0	<3	0 16	0 64	<3	34	20	83	4	2 0
DD95NO0004F	402	404	<1	11 10	<3	260	2 5	4	0.16	0.71	<3	70	20	67	8	6 0
DD95NO0004F	404	406	<1	10.20	10	220	2.5	4	0.22	0.90	<3	54	20	84	6	3.0
DD95NO0004F	406	408	<1	14.70	6	310	2 5	24	0.12	0.55	<3	55	30	70	10	3 5

HoleId	From	To	Ag ppm	Al_2O_3 %	As ppm	Ba ppm	Be ppm	Bi ppm	C %	CaO %	Cd ppm	Ce ppm	Co ppm	Cr ppm	Cs ppm	Dy ppm
DD95NO0004F	420	422	<1	12 50	6	120	2 0	18	0 08	0.42	<3	55	30	62	6	3 5
DD95NO0004F	422	425	1	15.90	8	340	3.0	40	0.06	0.32	<3	69	30	65	16	4.5
DD95NO0004F	436	438	<1	16 80	8	500	3 5	4	0 14	0.59	<3	79	20	53	18	4 5
DD95NO0004F	438	440	<1	17.00	10	500	3 5	<3	0.06	0.45	<3	89	20	61	18	5 0
DD95NO0004F	440	442	<1	17.00	14	550	3 5	<3	<0 02	0 25	<3	84	20	56	16	4.5
DD95NO0004F	442	444	<1	17.00	12	500	3.5	<3	0 04	0 35	<3	71	20	57	16	4 5
DD95NO0004F	444	446	<1	18 10	4	600	3.5	<3	0.08	0 52	<3	82	20	64	16	4 0
DD95NO0004F	446	448	<1	17 70	<3	650	3.5	<3	0.04	0 17	<3	85	20	68	16	5.0
DD95NO0004F	448	450	<1	18 10	12	650	4 0	<3	0.06	0.41	<3	91	20	64	14	5 5
DD95NO0004F	450	452	<1	16 90	10	600	3 5	<3	0.08	0.45	<3	78	5	60	14	4 5
DD95NO0004F	452	454	<1	16 70	10	600	3 5	<3	0.18	0 78	<3	79	20	61	14	5.0
DD95NO0004F	454	456	<1	16 70	8	600	3 5	<3	0.16	0 67	<3	72	20	63	14	4 5
DD95NO0004F	456	458	<1	15 60	6	550	3 5	<3	0.22	0.86	<3	78	5	65	12	4 5
DD95NO0004F	458	460	<1	15.30	8	600	3 5	<3	0.28	1.06	<3	85	20	66	12	5 0
DD95NO0004F	460	462	<1	16.50	4	600	4 0	<3	0 24	1 01	<3	75	20	67	14	4.5
DD95NO0004F	462	464	<1	15 40	12	550	3 5	<3	0.62	2.21	<3	85	5	68	12	5.0
DD95NO0004F	464	466	<1	16.60	24	600	4 0	<3	0.10	0 54	<3	89	5	65	14	5.0
DD95NO0004F	466	468	<1	17.30	20	650	3 5	<3	0.12	0.48	<3	73	5	67	14	4.5
DD95NO0004F	468	470	<1	16.40	20	700	4.0	<3	0.14	0 62	<3	90	20	61	16	5 0

HoleId	From	To	Er ppm	Eu ppm	Fe_2O_3 %	Ga ppm	Gd ppm	Hf ppm	Ho ppm	In ppm	K_2O %	La ppm	LOI %	Lu ppm	MgO %	MnO %
DD95NO0001F	1063	1067	2	1 0	8 86	18	3	4	0.5	<0 5	3 09	40	2 93	<0.5	2 39	0 09
DD95NO0001F	1067	1071	2	1.5	7 66	20	5	4	1 0	<0 5	3.48	51	3 40	<0 5	2.30	0 08
DD95NO0001F	1071	1075	2	1.5	6 95	21	5	5	1 0	<0 5	3.97	55	3.06	<0 5	2.47	0.08
DD95NO0001F	1075	1079	2	1.5	6.86	21	5	5	1 0	<0 5	4 09	52	3 21	<0 5	2 53	0 08
DD95NO0001F	1079	1083	2	1 5	7 50	22	5	5	1 0	0 5	4 19	53	3.42	<0 5	2.58	0 08
DD95NO0001F	1083	1087	2	1 5	7 39	18	5	5	1 0	<0 5	3.54	42	3.31	<0 5	2 42	0 08
DD95NO0001F	1087	1091	2	1.5	6.85	20	5	5	1 0	<0 5	3.84	47	1 80	<0 5	2 43	0.08
DD95NO0001F	1091	1095	2	1 5	6 67	15	5	7	1.0	<0.5	2 45	46	3.01	<0 5	2.04	0.07
DD95NO0001F	1095	1099	2	1.5	6.77	21	5	5	1 0	<0 5	3 79	52	4.17	<0 5	2 40	0.08
DD95NO0001F	1099	1103	2	1.5	7 00	17	5	6	1 0	<0 5	3.13	50	3 05	<0 5	2 23	0.08
DD95NO0001F	1103	1107	2	1 5	7 59	21	5	5	1 0	<0 5	3 97	48	3 57	<0 5	2.32	0.09
DD95NO0001F	1107	1111	2	1.5	9.80	16	4	6	1 0	<0 5	2.26	41	3 03	<0 5	2 18	0 09
DD95NO0001F	1111	1115	2	1 5	7 50	19	5	6	1.0	<0.5	3 26	51	3.14	<0.5	2 13	0 08
DD95NO0001F	1115	1119	2	1 0	3 53	10	3	6	1.0	<0 5	1 80	23	15.40	<0 5	2 59	0 07
DD95NO0001F	1119	1123	2	1 5	9.52	20	4	5	1 0	<0 5	2 95	44	3.29	<0 5	2.13	0 08
DD95NO0001F	1123	1127	2	1 5	9 46	20	4	4	1.0	<0 5	2 95	43	3 13	<0.5	2 12	0.09
DD95NO0001F	1127	1131	2	1 5	9.99	19	4	4	1 0	<0 5	2 53	44	3 57	<0.5	2 01	0 11
DD95NO0001F	1131	1135	2	2 0	12.80	15	4	4	0 5	<0.5	1 29	29	2.63	<0 5	1.61	0.11
DD95NO0001F	1135	1139	1	2 0	12 40	15	4	4	0 5	<0 5	1 54	30	2 68	<0.5	1 60	0.10
DD95NO0001F	1139	1143	2	1 5	12 10	15	4	4	0 5	0 5	1 46	28	2 46	<0 5	1.58	0.09
DD95NO0001F	1143	1147	2	2.0	12 10	15	4	5	0 5	<0 5	1.58	30	2.83	<0 5	1 65	0.09
DD95NO0001F	1147	1149	2	1 5	12 20	14	4	6	0 5	<0 5	1 00	28	2 39	<0 5	1 59	0 10
DD95NO0001F	1149	1151	2	2 0	13 50	15	4	5	0 5	<0.5	1 13	28	2.63	<0 5	1 72	0 12
DD95NO0001F	1151	1153	1	1.5	12 30	14	3	4	0 5	<0 5	1.09	28	2.94	<0 5	1 63	0 10
DD95NO0001F	1153	1155	<1	1.0	9 01	8	2	2	<0 5	<0 5	0.17	17	1.42	<0 5	0.87	0.07
DD95NO0001F	1155	1157	<1	0 5	7.95	9	2	1	<0 5	<0 5	0 48	14	1 44	<0 5	0 83	0.06
DD95NO0001F	1157	1159	<1	<0 5	8.45	6	<1	<1	<0 5	<0 5	0.09	8	1 18	<0 5	0 61	0 05
DD95NO0001F	1159	1161	<1	<0.5	10 50	7	1	<1	<0 5	1 0	0 09	8	1.88	<0.5	0 67	0.08
DD95NO0001F	1161	1163	<1	<0.5	11.20	6	<1	<1	<0.5	<0.5	0 16	7	1 66	<0 5	0 64	0.10
DD95NO0001F	1163	1165	<1	<0 5	6 85	5	<1	<1	<0 5	<0.5	0.05	6	1 88	<0.5	0 49	0 04
DD95NO0001F	1165	1167	<1	<0.5	6 15	5	<1	<1	<0 5	<0.5	0 11	5	1 13	<0.5	0 44	0 04
DD95NO0001F	1167	1169	<1	<0.5	6.33	6	<1	<1	<0 5	<0 5	0 05	5	1.18	<0.5	0 50	0.04
DD95NO0001F	1169	1171	<1	<0 5	4.62	5	<1	<1	<0 5	<0 5	0.08	5	0.87	<0 5	0 43	0 03
DD95NO0001F	1171	1173	<1	<0.5	7.43	14	<1	<1	<0.5	<0 5	0 04	8	1.11	<0.5	0 66	0.05
DD95NO0001F	1173	1175	<1	<0.5	5 55	6	<1	<1	<0 5	<0.5	0 06	4	1 03	<0.5	0.40	0.04
DD95NO0001F	1175	1177	<1	<0 5	4 87	7	<1	<1	<0 5	<0 5	0.06	4	1.47	<0.5	0 39	0 03
DD95NO0001F	1177	1179	<1	<0 5	5.47	6	<1	<1	<0.5	<0.5	0 08	5	2.19	<0.5	0 34	0 02
DD95NO0001F	1179	1181	<1	<0.5	7 70	9	<1	<1	<0 5	<0 5	0 05	5	1 52	<0.5	0.73	0 06
DD95NO0001F	1181	1183	<1	<0.5	8.15	10	<1	1	<0.5	<0.5	0.07	5	1 68	<0 5	0 67	0 05
DD95NO0001F	1183	1185	<1	<0.5	7 70	9	<1	1	<0.5	<0 5	0 07	9	1.46	<0 5	0 67	0 05
DD95NO0001F	1185	1187	<1	0 5	13 00	13	1	1	<0 5	<0 5	0 12	15	2 34	<0 5	1 15	0 09
DD95NO0001F	1187	1189	<1	<0.5	13.60	16	<1	<1	<0.5	3.0	0.08	6	6 37	<0 5	1.59	0 11
DD95NO0001F	1189	1191	<1	<0 5	12 50	9	<1	<1	<0 5	1 5	0 13	4	4 41	<0 5	1.22	0 09
DD95NO0001F	1191	1193	<1	<0.5	9.42	14	<1	<1	<0 5	1 0	0 16	4	2.06	<0 5	1 65	0 12
DD95NO0001F	1193	1195	<1	<0 5	7.45	8	<1	<1	<0.5	1 0	0 22	4	1 76	<0 5	1 15	0.09
DD95NO0001F	1195	1197	<1	<0.5	5 06	7	<1	<1	<0 5	<0 5	0 12	2	1 17	<0 5	0 91	0.06
DD95NO0001F	1197	1199	<1	<0.5	5.28	8	<1	<1	<0 5	<0 5	0.09	3	1.39	<0 5	0 95	0 07
DD95NO0001F	1199	1201	<1	0 5	6.08	6	<1	<1	<0.5	<0 5	0 17	8	1 39	<0 5	0.94	0.11
DD95NO0001F	1201	1203	<1	0 5	12 60	13	1	1	<0 5	1.0	0 76	13	3 98	<0 5	1 60	0 12
DD95NO0001F	1203	1205	<1	1 0	13.80	12	2	1	<0 5	1 0	0.93	18	5.68	<0 5	1 57	0 10
DD95NO0001F	1205	1207	1	1.0	14 20	15	2	2	0 5	1.0	1 21	27	4 81	<0.5	1.80	0 12
DD95NO0001F	1207	1209	1	1 0	11.50	15	3	2	0 5	<0 5	1 49	28	2.69	<0.5	1 76	0 11

HoleId	From	To	Er ppm	Eu ppm	Fe_2O_3 %	Ga ppm	Gd ppm	Hf ppm	Ho ppm	In ppm	K_2O %	La ppm	LOI %	Lu ppm	MgO %	MnO %
DD95NO0001F	1209	1211	1	0.5	10 60	14	2	2	<0.5	<0.5	1 41	20	2.53	<0.5	1 78	0 11
DD95NO0001F	1211	1213	1	1.0	9 41	14	2	2	0 5	<0 5	1 63	24	2 58	<0 5	1 70	0.10
DD95NO0001F	1213	1215	2	1 0	8.58	17	3	3	0 5	<0.5	2 36	33	2.91	<0 5	1.77	0 10
DD95NO0001F	1215	1217	1	1.0	7 83	16	3	2	0.5	<0 5	2 17	33	2.64	<0 5	1 67	0 09
DD95NO0001F	1217	1219	2	1 0	7.70	18	3	3	0 5	<0.5	1 64	35	2.58	<0 5	1 77	0.09
DD95NO0001F	1219	1221	1	1 0	7.16	15	3	2	0.5	<0.5	2.12	34	2 61	<0 5	1 59	0 08
DD95NO0003C	839	840	2	1 0	7 59	15	4	3	0.5	<0 5	2 36	33	2 47	<0 5	1 79	0 08
DD95NO0003C	840	841	2	1 0	9.00	17	4	4	0.5	0 5	2.14	33	2 49	<0 5	1 58	0.08
DD95NO0003C	841	842	2	1 0	8 29	16	5	5	1 0	<0.5	2.51	38	2 46	<0 5	1 50	0 08
DD95NO0003C	842	843	2	1 5	8 80	18	4	4	0 5	<0 5	2 76	38	2 66	<0 5	1 60	0 07
DD95NO0003C	843	844	2	1 5	8.17	18	4	4	0.5	<0 5	3.10	41	2 65	<0 5	1.59	0.08
DD95NO0003C	844	845	2	1 5	8.72	15	4	5	0 5	<0.5	2 25	38	2 20	<0 5	1.53	0.08
DD95NO0003C	845	846	2	1 5	8 08	17	5	6	1.0	<0.5	2.93	40	2 31	<0 5	1 58	0 08
DD95NO0003C	846	847	2	1.5	8 27	17	4	5	1.0	<0 5	2 68	41	2 40	<0 5	1.48	0.07
DD95NO0003C	847	848	2	1 5	8 25	17	4	6	0 5	<0.5	2 44	40	2 39	<0 5	1 51	0 07
DD95NO0003C	848	849	2	1 5	8.67	17	5	5	1.0	<0.5	2 61	39	2.55	<0 5	1 58	0 08
DD95NO0003C	849	850	2	1 5	8 04	17	4	6	0 5	<0 5	2 46	42	2 20	<0 5	1 52	0 07
DD95NO0003C	850	851	2	1.5	8.66	16	5	5	1.0	<0.5	2 44	38	2 46	<0 5	1 50	0 08
DD95NO0003C	851	852	2	1.5	8 33	17	4	5	1 0	<0 5	2.53	38	2 30	<0.5	1 42	0.08
DD95NO0003C	852	853	1	1 5	8.52	15	3	5	0 5	<0.5	2 04	34	2.26	<0.5	1.43	0 09
DD95NO0003C	853	854	2	1 5	8 79	15	4	5	0 5	<0 5	1 97	35	2 14	<0 5	1.37	0 08
DD95NO0003C	854	855	1	1 5	9 13	14	4	4	0 5	<0 5	1.83	32	2 20	<0.5	1 32	0.08
DD95NO0003C	855	856	2	2.0	8 93	19	5	4	1 0	<0 5	2 90	43	2 56	<0 5	1.58	0 09
DD95NO0003C	856	857	2	1.5	9 81	19	5	4	1 0	<0 5	2.61	40	2 63	<0 5	1 74	0 11
DD95NO0003C	857	858	1	1.5	11 40	17	4	3	0.5	<0 5	1 75	36	2.52	<0.5	1 68	0 14
DD95NO0003C	858	859	1	2.0	11 80	16	3	3	0 5	<0 5	1 75	32	2 51	<0 5	1 64	0 10
DD95NO0003C	859	860	1	1 5	13.00	16	3	4	0 5	<0.5	1.35	31	2 72	<0 5	1 56	0.10
DD95NO0003C	860	861	1	1.5	14 00	14	3	4	0 5	<0 5	1 39	31	2 63	<0 5	1.60	0 10
DD95NO0003C	861	862	2	1.5	14 00	16	3	4	0 5	<0 5	1 52	30	2 67	<0 5	1 85	0 13
DD95NO0003C	862	863	1	1 5	15 30	16	3	3	<0.5	<0.5	1.10	30	3.43	<0.5	1.85	0 13
DD95NO0003C	863	864	1	1 5	13.80	15	3	4	<0.5	<0 5	0 94	25	2.50	<0.5	1 71	0 12
DD95NO0003C	864	865	1	1 0	17 30	13	3	3	0 5	<0 5	0.33	25	2 88	<0 5	1 61	0.13
DD95NO0003C	865	866	<1	1 0	15 70	11	2	1	<0 5	<0 5	0.06	17	2 63	<0 5	1 22	0 11
DD95NO0003C	866	867	<1	0.5	10.10	12	2	1	<0 5	<0.5	0 41	19	1 62	<0 5	0 78	0 06
DD95NO0003C	867	868	<1	0 5	8 86	9	1	<1	<0 5	<0 5	0.17	14	1.59	<0 5	0.69	0 06
DD95NO0003C	868	869	<1	<0 5	9 14	8	<1	<1	<0 5	<0 5	0 05	13	2.36	<0 5	0.69	0 07
DD95NO0003C	869	870	<1	<0 5	9 22	8	1	<1	<0 5	0.5	0 04	12	1.95	<0 5	0.67	0 06
DD95NO0003C	870	871	<1	<0 5	9 30	8	<1	<1	<0.5	<0 5	0.10	9	2.21	<0 5	0 54	0 06
DD95NO0003C	871	872	<1	0 5	10.30	6	<1	<1	<0 5	<0 5	0 13	10	2 25	<0 5	0 54	0 06
DD95NO0003C	872	873	<1	<0 5	7 75	6	<1	<1	<0 5	1 5	0 05	7	2.17	<0 5	0 40	0 04
DD95NO0003C	873	874	<1	<0.5	6 92	6	<1	<1	<0.5	<0 5	0 03	9	1 08	<0 5	0.44	0.05
DD95NO0003C	874	875	<1	<0.5	5.89	5	<1	<1	<0 5	<0.5	0.06	9	1.38	<0.5	0.40	0 06
DD95NO0003C	875	876	<1	<0 5	8 97	10	1	<1	<0 5	<0.5	<0 01	12	0 98	<0 5	0 73	0.07
DD95NO0003C	876	877	<1	<0 5	7 15	11	1	<1	<0 5	<0 5	0 02	14	1.24	<0 5	0 58	0 05
DD95NO0003C	877	878	<1	<0.5	8 68	12	2	<1	<0 5	0 5	0.06	15	1 68	<0 5	0 92	0 08
DD95NO0003C	878	879	<1	0 5	10 30	15	1	<1	<0 5	<0 5	0 01	19	1.68	<0 5	0 96	0 09
DD95NO0003C	879	880	<1	0 5	9 60	14	2	<1	<0 5	<0 5	0 01	16	1 57	<0 5	0.88	0.08
DD95NO0003C	880	881	<1	<0.5	7 39	11	1	<1	<0 5	<0 5	0.05	13	1 16	<0 5	0.57	0.05
DD95NO0003C	881	882	<1	<0 5	7 46	12	2	<1	<0 5	<0 5	0.05	13	1 21	<0 5	0 51	0 05
DD95NO0003C	882	883	<1	<0 5	6.47	7	<1	<1	<0 5	2 0	0.02	9	2 84	<0.5	0.43	0 04
DD95NO0003C	883	884	<1	<0.5	4 79	8	<1	<1	<0 5	<0 5	0 04	10	0 75	<0 5	0 40	0 04
DD95NO0003C	884	885	<1	<0.5	9.20	18	1	<1	<0 5	<0.5	0 02	16	1.64	<0 5	0 85	0 07

HoleId	From	To	Er ppm	Eu ppm	Fe_2O_3 %	Ga ppm	Gd ppm	Hf ppm	Ho ppm	In ppm	K_2O %	La ppm	LOI %	Lu ppm	MgO %	MnO %
DD95NO0003C	885	886	<1	<0 5	4.86	8	<1	<1	<0.5	<0.5	0 03	8	0.71	<0 5	0 30	0.04
DD95NO0003C	886	887	<1	<0 5	6 95	12	<1	<1	<0 5	1.0	0 10	6	1 20	<0 5	0.27	0 06
DD95NO0003C	887	888	<1	<0.5	11 60	17	1	<1	<0 5	<0 5	0.10	12	1 71	<0.5	0 64	0 08
DD95NO0003C	888	889	<1	<0.5	8 71	15	<1	<1	<0.5	0 5	0.15	7	1 42	<0 5	0 43	0 05
DD95NO0003C	889	890	<1	<0.5	6 72	12	<1	<1	<0 5	<0 5	0.10	9	1 10	<0 5	0.44	0.05
DD95NO0003C	890	891	<1	<0 5	7 48	12	2	<1	<0.5	<0.5	0 15	15	1 37	<0 5	0 64	0.07
DD95NO0003C	891	892	<1	<0 5	5.76	14	<1	<1	<0 5	<0 5	0.04	7	0 96	<0 5	0.38	0 04
DD95NO0003C	892	893	<1	<0 5	9.32	17	<1	<1	<0.5	<0 5	0.03	9	1 48	<0.5	0 68	0 07
DD95NO0003C	893	894	<1	<0.5	6 90	5	<1	<1	<0.5	<0.5	0 04	6	1 20	<0 5	0 26	0 03
DD95NO0003C	894	895	<1	<0 5	6 44	11	<1	<1	<0 5	<0 5	0 03	7	1 00	<0 5	0.46	0 05
DD95NO0003C	895	896	<1	<0.5	8 25	13	1	<1	<0.5	<0 5	0.06	12	1 21	<0 5	0.68	0 06
DD95NO0003C	896	897	<1	<0.5	9 40	13	2	<1	<0 5	<0.5	0 07	16	1 58	<0 5	0 95	0 08
DD95NO0003C	897	898	<1	<0.5	8.14	11	1	<1	<0 5	<0 5	0.03	13	1 26	<0 5	0.75	0.07
DD95NO0003C	898	899	<1	<0 5	10 70	23	<1	<1	<0.5	<0.5	0 17	5	1.12	<0 5	0 51	0.07
DD95NO0003C	899	900	<1	<0.5	14 30	31	1	<1	<0 5	<0 5	0 04	13	2.31	<0 5	0 98	0.10
DD95NO0003C	900	901	<1	<0.5	7 95	12	<1	<1	<0 5	<0.5	0 01	10	1 33	<0.5	0.60	0 06
DD95NO0003C	901	902	<1	<0 5	8 01	11	1	<1	<0 5	<0.5	0 03	13	1.28	<0.5	0 75	0 06
DD95NO0003C	902	903	<1	<0 5	11.40	13	2	1	<0 5	6.5	0 38	18	7.72	<0 5	1 27	0.08
DD95NO0003C	903	904	<1	<0.5	12 00	13	2	1	<0.5	8.5	0.77	20	4 51	<0.5	1.26	0 09
DD95NO0003C	904	905	<1	<0.5	13.00	28	<1	<1	<0 5	2.5	0.15	7	2 86	<0 5	2 08	0 11
DD95NO0003C	905	906	<1	<0 5	19.30	48	<1	<1	<0 5	1.0	0 11	9	3.73	<0 5	3 43	0 20
DD95NO0003C	906	907	<1	<0.5	11 70	27	<1	<1	<0 5	<0 5	0 01	3	2 36	<0.5	1.82	0 13
DD95NO0003C	907	908	<1	<0.5	4.65	7	<1	<1	<0.5	<0 5	<0.01	3	0 65	<0 5	0 72	0 07
DD95NO0003C	908	909	<1	<0.5	11.20	14	2	<1	<0 5	1.0	0 20	13	2.86	<0 5	1 53	0.13
DD95NO0003C	909	910	<1	0 5	12 40	14	3	1	<0 5	1 5	0 97	22	4 54	<0 5	1 61	0 12
DD95NO0003C	910	911	<1	<0 5	12.50	11	2	<1	<0.5	4 0	0 62	15	7.59	<0 5	1 13	0.09
DD95NO0003C	911	912	<1	0 5	10 40	12	2	1	<0 5	1.0	0 79	20	3 74	<0 5	1 45	0.12
DD95NO0003C	912	913	<1	<0.5	5 87	8	1	<1	<0 5	0.5	0.36	12	1.89	<0.5	0 80	0 06
DD95NO0003C	913	914	<1	<0.5	4 42	6	<1	<1	<0.5	1.5	0.34	6	1.42	<0 5	0 56	0 04
DD95NO0003C	914	915	<1	0 5	10 70	11	1	<1	<0 5	0.5	0.24	6	2.01	<0.5	1 63	0.31
DD95NO0003C	915	916	<1	<0.5	13.30	32	<1	<1	<0 5	<0 5	0.09	4	2 54	<0.5	2 38	0.21
DD95NO0003C	916	917	<1	1.0	15 00	31	2	1	<0 5	1.0	0.92	16	3.27	<0.5	2 65	0 20
DD95NO0003C	917	918	2	1 0	10 20	21	3	2	0.5	0 5	1 98	27	2 96	<0 5	2 10	0 12
DD95NO0003C	918	919	2	1.0	7 75	18	3	3	0 5	<0 5	2.61	32	2 45	<0 5	1 81	0 09
DD95NO0003C	919	920	1	1.0	8 13	20	2	2	<0 5	<0.5	1.71	27	2 57	<0.5	1 67	0 10
DD95NO0003C	920	921	1	0 5	9 06	18	3	2	<0 5	1 5	2 09	29	2 47	<0 5	1.76	0 10
DD95NO0003C	921	922	<1	1 0	8 20	18	2	1	<0 5	1 0	1.49	21	2.12	<0 5	1 60	0 10
DD95NO0003C	922	923	1	0 5	7 64	17	2	2	<0 5	<0 5	2 21	26	2.27	<0.5	1 67	0.09
DD95NO0003C	923	924	2	1.0	6 93	18	3	2	0 5	<0.5	2 53	29	2 27	<0.5	1.62	0 08
DD95NO0003C	924	925	1	1.0	8.10	19	3	2	0 5	<0.5	2 56	28	2.42	<0 5	1 77	0 09
DD95NO0003C	925	926	1	1.0	7 75	20	3	2	0.5	<0 5	3 03	32	2.63	<0.5	1 85	0 09
DD95NO0003C	926	927	2	1 0	7 22	19	3	2	0 5	<0 5	2.78	30	2 39	<0 5	1.66	0 08
DD95NO0003C	927	928	1	1 0	7 59	19	3	2	<0 5	<0.5	2 42	28	2.29	<0.5	1 65	0 08
DD95NO0003C	928	929	1	1 0	7 52	20	3	2	0 5	<0 5	2 73	29	2 46	<0 5	1 69	0.09
DD95NO0003C	929	930	<1	<0 5	8.19	15	2	1	<0 5	<0 5	1.39	18	2 03	<0 5	1.54	0 09
DD95NO0004F	320	322	2	1.0	8.27	14	4	5	1 0	<0 5	1.83	35	2.82	<0.5	2 03	0 10
DD95NO0004F	322	324	1	1 0	7 49	14	3	4	0 5	<0 5	1 60	33	2 41	<0.5	1 77	0.09
DD95NO0004F	324	326	1	1.0	10 30	14	3	4	0 5	<0.5	1 11	28	2 69	<0 5	1.75	0 11
DD95NO0004F	326	328	2	1 5	9 24	14	4	6	0.5	<0 5	1 99	35	2 09	<0 5	1 61	0.09
DD95NO0004F	328	330	2	1.5	10.30	15	4	5	1 0	<0 5	1.92	38	2 72	<0.5	1 65	0.10
DD95NO0004F	330	332	1	1.5	11 40	16	3	4	0.5	1 0	1 50	34	2.47	<0 5	1 74	0 11
DD95NO0004F	332	334	2	1 5	10 80	16	3	5	0 5	<0 5	1 89	37	3.03	<0 5	1 68	0 10

HoleId	From	To	Er ppm	Eu ppm	Fe_2O_3 %	Ga ppm	Gd ppm	Hf ppm	Ho ppm	In ppm	K_2O %	La ppm	LOI %	Lu ppm	MgO %	MnO %
DD95NO0004F	334	336	1	1 5	10.90	15	3	6	0 5	0.5	1 77	35	2.90	<0 5	1.68	0 10
DD95NO0004F	336	338	2	1 5	11 40	16	4	5	1.0	<0 5	1.86	38	2.19	<0 5	1 68	0.11
DD95NO0004F	338	340	2	1 5	10.30	15	3	5	0 5	0 5	1 98	36	3.16	<0 5	1 66	0 10
DD95NO0004F	340	342	1	1 5	12 10	14	3	5	0.5	0.5	1 34	35	3 18	<0 5	1 76	0 11
DD95NO0004F	342	344	2	2.0	10 20	15	4	6	1 0	<0.5	1.81	43	3 01	<0 5	1.82	0 10
DD95NO0004F	344	346	1	1.5	11.80	16	3	5	0.5	<0.5	1 58	34	3.33	<0.5	2.00	0 12
DD95NO0004F	346	348	2	1 5	11 10	16	4	5	0 5	<0.5	1 89	41	3 21	<0 5	2 10	0 12
DD95NO0004F	348	350	2	1.5	12.20	18	4	6	1.0	0 5	1 83	45	3.81	<0 5	2.02	0 11
DD95NO0004F	350	352	2	1.5	14 20	16	4	5	0.5	1 0	1 09	38	3.86	<0 5	2 11	0 13
DD95NO0004F	352	354	2	1.5	12.10	16	4	5	0.5	0 5	1 54	41	3 34	<0 5	2.15	0.12
DD95NO0004F	354	356	2	1 5	13.00	16	3	5	1 0	1 0	1.20	40	3 28	<0.5	2 43	0.14
DD95NO0004F	356	358	2	1 5	9 99	16	4	5	1 0	<0 5	1.98	42	3 16	<0 5	2 04	0 11
DD95NO0004F	358	360	2	1.5	8 05	17	4	5	1 0	<0 5	2 84	42	3 28	<0 5	2.08	0.09
DD95NO0004F	360	362	2	1 5	9 00	19	4	5	1.0	<0.5	2.88	42	3.62	<0.5	3 00	0 12
DD95NO0004F	362	364	2	2 0	6 99	19	5	5	1 0	<0 5	3 24	46	3 81	<0 5	2 48	0 09
DD95NO0004F	364	365	2	1.5	7.92	18	4	5	1.0	<0.5	3.09	42	3 13	<0 5	2 61	0.10
DD95NO0004F	365	366	2	1 5	19.30	23	4	4	1 0	1 5	0 71	43	4 23	<0.5	4 20	0 21
DD95NO0004F	366	367	2	1 0	16 80	18	4	4	1.0	<0 5	0 93	42	4 11	<0 5	2.97	0 17
DD95NO0004F	367	368	2	1.0	16 30	20	4	4	1 0	1.0	1 21	43	3 96	<0.5	2 35	0 16
DD95NO0004F	368	369	1	1 0	13.10	14	3	3	<0.5	1 0	0 33	24	2 84	<0 5	2 03	0 13
DD95NO0004F	369	370	<1	<0.5	6 41	9	<1	<1	<0.5	1 0	0 08	8	1 24	<0 5	0 63	0 05
DD95NO0004F	370	371	<1	<0 5	9.98	13	2	<1	<0 5	<0 5	0.14	14	1.96	<0 5	1 25	0 10
DD95NO0004F	371	372	1	1 0	15.10	16	3	1	<0 5	0.5	0 10	26	2 72	<0.5	2.41	0.16
DD95NO0004F	372	373	1	1 0	15.70	19	3	1	0.5	<0 5	0.15	26	3 38	<0 5	2 84	0 18
DD95NO0004F	373	374	<1	0 5	12.60	13	2	<1	<0 5	<0 5	0 09	17	3 02	<0.5	2.17	0.12
DD95NO0004F	374	375	<1	0 5	11 40	12	2	<1	<0 5	<0 5	0 08	15	2.98	<0 5	2 22	0 10
DD95NO0004F	375	376	<1	0 5	13.50	15	2	1	<0 5	1.5	0.18	20	3 16	<0.5	2 75	0 14
DD95NO0004F	376	377	<1	1 0	16.00	11	2	1	<0 5	8.5	0.30	21	9 45	<0 5	2 23	0 12
DD95NO0004F	377	378	1	1 0	13 50	17	3	2	0.5	1.0	1 14	30	3 31	<0.5	2 85	0 15
DD95NO0004F	378	379	2	1.0	9.36	20	4	3	1 0	<0 5	2.62	41	3 08	<0 5	2 50	0 11
DD95NO0004F	379	380	2	1 0	9 06	19	4	3	1 0	<0 5	2 12	38	2.63	<0.5	2.25	0 11
DD95NO0004F	380	381	1	0 5	8 70	21	3	3	0 5	<0.5	1.39	26	2 47	<0 5	2 04	0.10
DD95NO0004F	381	382	<1	<0 5	8.89	20	<1	<1	<0 5	<0 5	0 04	2	1 82	<0 5	1 77	0 10
DD95NO0004F	382	383	<1	<0 5	9 25	18	<1	<1	<0 5	1 0	0.24	5		<0.5	1.84	0 11
DD95NO0004F	383	384	<1	<0.5	16.20	33	<1	<1	<0 5	1 0	0 02	2	4 23	<0.5	3.55	0 17
DD95NO0004F	384	385	2	1 0	16 10	29	3	2	1 0	<0.5	1 19	31	3.73	<0 5	3.72	0 18
DD95NO0004F	385	386	2	1 0	9 51	22	3	2	0 5	<0 5	2 64	38	3 02	<0.5	2 86	0 10
DD95NO0004F	386	387	1	0 5	8.56	17	2	1	0 5	<0 5	1 70	27	2 74	<0 5	3.00	0.09
DD95NO0004F	387	388	1	1 0	6 99	17	3	2	0.5	<0 5	2 44	29	2.63	<0 5	2.55	0 08
DD95NO0004F	388	389	<1	0 5	5.84	14	2	1	<0 5	<0 5	1 84	18	2 29	<0 5	2 07	0 07
DD95NO0004F	389	390	<1	0 5	10 80	25	2	1	<0.5	<0 5	1.06	17		<0 5	3.22	0.13
DD95NO0004F	390	391	1	0 5	8 63	15	2	1	0 5	<0 5	1 19	22	2.32	<0.5	2.64	0 10
DD95NO0004F	391	392	1	1.0	8.38	19	3	2	0.5	<0.5	2.36	30	2 64	<0 5	2 72	0 09
DD95NO0004F	392	393	1	1 0	7 49	20	3	2	0.5	<0.5	3.11	35	2 81	<0 5	2 39	0 08
DD95NO0004F	393	394	<1	1 0	7.71	15	2	1	<0 5	<0 5	1 84	28	2 28	<0 5	2 10	0 09
DD95NO0004F	394	396	1	1 0	7 78	17	3	2	0.5	<0 5	2 56	31	2 95	<0.5	2 27	0.09
DD95NO0004F	396	398	1	1 0	8 73	18	3	2	0.5	<0.5	2 11	36	2.73	<0 5	2 52	0 10
DD95NO0004F	398	400	1	1 0	9 22	19	3	2	0 5	<0.5	2 21	33	2 80	<0 5	2.51	0.11
DD95NO0004F	400	402	1	1.0	9 32	15	2	2	<0 5	<0 5	1.32	25	2.96	<0 5	2 58	0 11
DD95NO0004F	402	404	3	4 5	8.88	18	6	3	1 5	<0 5	2 29	49	3 13	<0 5	2.76	0.11
DD95NO0004F	404	406	2	2 0	8 78	16	4	3	0.5	<0 5	2 02	36	3.23	<0 5	2.77	0 11
DD95NO0004F	406	408	2	1 5	12 40	25	4	3	1 0	<0.5	3 17	38	4 33	<0 5	4 28	0.14

HoleId	From	To	Er ppm	Eu ppm	Fe_2O_3 %	Ga ppm	Gd ppm	Hf ppm	Ho ppm	In ppm	K_2O %	La ppm	LOI %	Lu ppm	MgO %	MnO %
DD95NO0004F	420	422	2	1.5	14 20	22	4	3	1 0	<0 5	1 63	37	4.40	<0.5	5 39	0 16
DD95NO0004F	422	425	2	1.5	11.80	26	5	3	1.0	<0.5	3.98	46	5 31	<0 5	5.28	0 13
DD95NO0004F	436	438	2	1.5	6.47	26	5	4	1 0	<0.5	4.67	53	4 24	<0 5	3.72	0 10
DD95NO0004F	438	440	2	2.0	6.48	26	6	4	1 0	<0.5	4 73	56	4.62	<0 5	3.65	0.09
DD95NO0004F	440	442	2	1.5	6.43	27	5	4	1.0	<0.5	4 65	53	4 32	<0.5	3.83	0.10
DD95NO0004F	442	444	2	1 5	6 81	25	5	4	1 0	<0 5	4 49	47	4.41	<0 5	3 78	0 10
DD95NO0004F	444	446	2	1 5	6 57	25	5	4	1 0	<0 5	4 96	53	4 28	<0 5	3 30	0 09
DD95NO0004F	446	448	3	2 0	6 45	26	6	4	1 0	<0.5	4 93	58	4.02	<0.5	3 15	0.07
DD95NO0004F	448	450	3	2.0	6.77	26	6	4	1.5	<0 5	4 86	61	4.18	<0 5	3 25	0 08
DD95NO0004F	450	452	2	1 5	6.07	25	5	4	1 0	<0.5	4.53	50	3.94	<0 5	3 06	0 07
DD95NO0004F	452	454	2	1 5	6 28	25	5	4	1 0	<0.5	4.40	52	3 86	<0 5	2 96	0 07
DD95NO0004F	454	456	2	1.5	6 46	24	5	4	1.0	<0.5	4.61	48	4.15	<0 5	2 53	0 05
DD95NO0004F	456	458	2	1 5	5 79	21	5	4	1 0	<0 5	4.48	52	3.91	<0 5	2.40	0 04
DD95NO0004F	458	460	3	1 5	5 95	22	5	5	1.0	<0.5	4.44	56	4.01	<0 5	2 44	0 05
DD95NO0004F	460	462	2	1 5	6.26	24	5	5	1.0	<0 5	4 54	51	4 10	<0 5	2 93	0 06
DD95NO0004F	462	464	3	2.5	5 42	23	6	4	1.5	<0 5	4 18	56	4.31	<0 5	2.75	0 08
DD95NO0004F	464	466	2	1 5	6 16	25	5	5	1.0	<0 5	4 56	57	3 98	<0 5	3.12	0.06
DD95NO0004F	466	468	2	1.5	6.06	25	5	4	1.0	<0.5	4.60	48	4 14	<0.5	3.13	0.06
DD95NO0004F	468	470	2	2 0	6 19	25	5	4	1 0	<0 5	4 41	57	4 15	<0 5	3.03	0.06

HoleId	From	To	Mo ppm	Na_2O %	Nb ppm	Nd ppm	P_2O_5 %	Pr ppm	Rb ppm	S %	Sb ppm	Sc ppm	Se ppm	SiO_2 %	Sm ppm	Sn ppm
DD95NO0001F	1063	1067	3	0 14	<10	22.0	0 13	7	145 0	0 18	<1	10	<1	67 00	4.5	<10
DD95NO0001F	1067	1071	<2	0.15	10	27 5	0.13	9	185.0	0.07	1	11	<1	67 10	5.5	<10
DD95NO0001F	1071	1075	<2	0 12	10	31 5	0 16	10	210 0	0 08	1	12	<1	67 00	6 0	10
DD95NO0001F	1075	1079	<2	0.07	10	31 0	0 15	10	210.0	0.07	<1	11	<1	66 10	6.0	<10
DD95NO0001F	1079	1083	<2	0 07	10	30 5	0 14	10	230 0	0 40	<1	12	1	64 20	6 0	<10
DD95NO0001F	1083	1087	<2	0 12	<10	27.0	0 14	9	175 0	0 21	<1	11	<1	66 10	5 5	<10
DD95NO0001F	1087	1091	<2	0 11	10	27 5	0.16	9	210.0	<0.01	<1	11	<1	65 90	5.5	<10
DD95NO0001F	1091	1095	<2	0.10	<10	28.0	0 15	9	135 0	0 14	<1	9	<1	70 70	5.5	<10
DD95NO0001F	1095	1099	<2	0 16	10	30 0	0 14	10	220 0	0 05	<1	11	<1	62.60	5 5	<10
DD95NO0001F	1099	1103	<2	0 09	<10	30 5	0 14	10	175 0	0 12	<1	10	<1	67.90	6 0	<10
DD95NO0001F	1103	1107	<2	0.07	10	30.5	0.14	10	220 0	0.05	<1	12	<1	63.50	6 0	<10
DD95NO0001F	1107	1111	2	0 07	<10	24 5	0 12	8	135 0	0 40	<1	10	<1	68 00	5.0	<10
DD95NO0001F	1111	1115	<2	0 08	10	30.0	0 14	10	200 0	0 02	<1	11	<1	66 40	5.5	<10
DD95NO0001F	1115	1119	<2	1.31	<10	17 0	0.17	5	65 0	0.03	<1	7	<1	50 10	3.5	<10
DD95NO0001F	1119	1123	<2	0 06	10	26 5	0 12	9	185 0	0 10	<1	11	<1	64 80	5 0	<10
DD95NO0001F	1123	1127	<2	0 06	<10	26.0	0 12	9	190 0	0 20	<1	11	<1	65 30	5 0	<10
DD95NO0001F	1127	1131	<2	0.07	<10	26 5	0.10	9	160 0	0 16	<1	10	2	67 90	5.0	15
DD95NO0001F	1131	1135	<2	0 03	<10	22.0	0 09	7	88 0	0 27	<1	8	<1	70 20	4 5	<10
DD95NO0001F	1135	1139	<2	0 07	<10	20.5	0.10	7	105.0	0 23	<1	9	<1	68 60	4 5	<10
DD95NO0001F	1139	1143	<2	0.18	<10	19.5	0 09	6	90 0	0 38	3	8	<1	71.10	4.0	10
DD95NO0001F	1143	1147	<2	0 13	<10	21.5	0 11	7	97 0	0 27	1	8	<1	67 70	4.5	<10
DD95NO0001F	1147	1149	<2	0 07	<10	19 5	0.11	6	65.0	0.16	1	7	<1	71 30	4.0	<10
DD95NO0001F	1149	1151	<2	0.08	<10	20 5	0.09	7	73.0	0 30	4	8	43	70 10	4 5	<10
DD95NO0001F	1151	1153	<2	0 06	<10	19 5	0.09	6	67.0	0 25	2	7	6	71 80	4 0	<10
DD95NO0001F	1153	1155	3	0 02	<10	11 5	0 05	4	10.5	0.30	2	3	19	82 90	2 0	30
DD95NO0001F	1155	1157	5	0.02	<10	9 0	0 04	3	27.0	0 23	4	4	25	82 40	2 0	<10
DD95NO0001F	1157	1159	<2	0 03	<10	5.5	0.03	2	6 0	0.51	5	2	29	85 20	1.0	<10
DD95NO0001F	1159	1161	8	0 03	<10	5 5	0.02	2	5 5	1 60	6	2	58	81 90	1.0	15
DD95NO0001F	1161	1163	7	0 07	<10	4 0	0 03	1	18.5	1 47	10	<5	63	82 30	1 0	10
DD95NO0001F	1163	1165	7	0 01	<10	3.5	0 01	1	2 0	1.34	5	<5	50	86 20	0 5	10
DD95NO0001F	1165	1167	7	0 04	<10	3 0	<0 01	<1	7.5	0 76	16	<5	145	87 90	0 5	<10
DD95NO0001F	1167	1169	4	<0.01	<10	3.5	0.02	1	3 0	0.88	11	<5	95	87.40	1 0	<10
DD95NO0001F	1169	1171	3	0 03	<10	3.0	<0.01	<1	3 0	0 50	3	<5	73	89 60	0.5	<10
DD95NO0001F	1171	1173	3	0.01	<10	5 0	0.02	2	2.0	0 70	2	<5	14	85.50	1 0	<10
DD95NO0001F	1173	1175	4	0 02	<10	2.5	0 02	<1	2 5	0 76	2	<5	35	89.10	0.5	<10
DD95NO0001F	1175	1177	7	0 02	<10	2 5	<0.01	<1	3 5	0 65	1	<5	18	89 20	0 5	<10
DD95NO0001F	1177	1179	4	0 04	<10	3.0	0 02	<1	2 5	1 02	2	<5	38	87 80	0.5	<10
DD95NO0001F	1179	1181	2	0 02	<10	3 5	0.02	1	2 5	0 58	1	2	10	84.40	1 0	<10
DD95NO0001F	1181	1183	8	0.03	<10	3 5	0 02	1	3 5	0 99	1	<5	18	84 80	0 5	<10
DD95NO0001F	1183	1185	8	0 02	<10	5 5	0 04	2	3.0	0 65	2	2	16	84 40	1 0	10
DD95NO0001F	1185	1187	4	0 05	<10	8.5	0.03	3	10 0	1.51	3	3	29	76 90	1 5	10
DD95NO0001F	1187	1189	21	0 03	<10	3 5	0 02	1	5 5	2 15	2	2	20	71 50	1 0	100
DD95NO0001F	1189	1191	<2	0 06	<10	2 5	0.01	<1	6 5	2.30	1	<5	16	75 20	0 5	35
DD95NO0001F	1191	1193	<2	0 04	<10	2 5	0 01	<1	7 5	0 78	2	<5	4	79 40	0 5	20
DD95NO0001F	1193	1195	<2	0 05	<10	2 5	0.02	<1	10 5	0 85	<1	<5	6	83.30	0.5	<10
DD95NO0001F	1195	1197	2	0 05	<10	1 5	<0 01	<1	5 0	0.52	2	<5	2	87 60	<0.5	10
DD95NO0001F	1197	1199	<2	0.02	<10	1 5	<0.01	<1	4 0	0 56	1	<5	2	87 30	<0 5	<10
DD95NO0001F	1199	1201	<2	0 03	<10	5 0	0 03	2	8 5	0.67	2	<5	2	85 90	1 0	<10
DD95NO0001F	1201	1203	<2	0 04	<10	7.5	0.04	3	40 0	2 38	3	4	15	71.90	1 5	20
DD95NO0001F	1203	1205	<2	0.54	<10	9 5	0.04	3	48.5	3.44	4	5	20	68 20	2 0	15
DD95NO0001F	1205	1207	<2	0.45	<10	14.5	0 05	5	71 0	2 56	4	7	14	67.30	2.5	15
DD95NO0001F	1207	1209	<2	0 05	<10	15 0	0 06	5	86 0	1 23	3	7	4	71 10	3.0	15

HoleId	From	To	Mo ppm	Na_2O %	Nb ppm	Nd ppm	P_2O_5 %	Pr ppm	Rb ppm	S %	Sb ppm	Sc ppm	Se ppm	SiO_2 %	Sm ppm	Sn ppm
DD95NO0001F	1209	1211	<2	0.10	<10	11 5	0 08	4	73.0	0.74	2	7	3	71.80	2.5	15
DD95NO0001F	1211	1213	<2	0.06	<10	14 0	0 11	5	80 0	0 26	3	7	2	72 80	2.5	15
DD95NO0001F	1213	1215	<2	0.07	<10	18 0	0 09	6	125 0	0 10	2	9	2	71 70	3.5	20
DD95NO0001F	1215	1217	<2	0 06	<10	17 5	0.08	6	110 0	0 07	1	8	<1	74.20	3 5	15
DD95NO0001F	1217	1219	3	0 10	<10	20 5	0.09	7	135 0	0 07	3	9	<1	74.90	4 0	20
DD95NO0001F	1219	1221	<2	0 05	<10	19.0	0 09	6	120.0	0.05	1	8	<1	74 40	3.5	15
DD95NO0003C	839	840	8	0.04	10	26 0	0 11	7	110.0	0 10	4	10	1	72 80	6 0	<10
DD95NO0003C	840	841	6	0.04	<10	26 5	0 10	7	105 0	0.70	2	10	3	71 90	5 5	<10
DD95NO0003C	841	842	5	0 04	10	30 0	0.13	8	125.0	0 39	2	10	<1	71.60	6 5	<10
DD95NO0003C	842	843	6	0.05	10	29 5	0 11	8	135.0	0 51	2	10	<1	70 80	7 0	<10
DD95NO0003C	843	844	4	0.05	15	31 5	0.13	9	155.0	0.30	2	10	<1	70 50	6 5	<10
DD95NO0003C	844	845	4	0.06	10	28 0	0 12	8	110 0	0 51	1	10	<1	72 10	6.5	<10
DD95NO0003C	845	846	4	0.10	10	32 5	0 15	9	145 0	0.23	2	10	<1	70 20	7 5	<10
DD95NO0003C	846	847	4	0.15	10	31 5	0 11	9	135.0	0.37	2	10	<1	72 60	6 5	<10
DD95NO0003C	847	848	5	0 08	10	30 5	0.12	8	120 0	0 38	2	10	<1	72.20	7 0	<10
DD95NO0003C	848	849	4	0 09	10	33.0	0 13	9	135 0	0.37	1	10	<1	72 10	7 5	<10
DD95NO0003C	849	850	5	0 09	10	34.0	0 13	9	125.0	0.19	2	10	<1	72.20	6 5	<10
DD95NO0003C	850	851	7	0.09	<10	29 0	0.11	8	120 0	0 58	2	10	<1	71 50	6 0	<10
DD95NO0003C	851	852	5	0 20	10	30 5	0.10	8	130 0	0.61	2	10	<1	73 60	6 5	<10
DD95NO0003C	852	853	9	0.18	<10	23 5	0.11	7	99 0	0 21	1	10	<1	72 90	5 5	<10
DD95NO0003C	853	854	5	0.12	<10	27 5	0 10	8	95 0	0 26	2	10	<1	74.10	5.5	<10
DD95NO0003C	854	855	4	0 12	<10	25 0	0.10	7	91 0	0.55	3	10	<1	74 20	5 5	<10
DD95NO0003C	855	856	7	0 21	10	33 0	0.14	9	145.0	0.20	2	10	<1	69 30	8 0	<10
DD95NO0003C	856	857	7	0 22	10	30 5	0 14	9	125 0	0 10	2	10	<1	68.30	6.5	<10
DD95NO0003C	857	858	9	0 34	<10	29.0	0 10	8	84 0	0 33	2	10	<1	71 90	5 5	<10
DD95NO0003C	858	859	4	0.30	<10	25 0	0 11	7	85.0	0.37	1	10	<1	71 00	5 5	<10
DD95NO0003C	859	860	4	0 31	<10	26 5	0.10	7	67 0	0.94	2	10	<1	69.50	5.5	<10
DD95NO0003C	860	861	5	0 23	<10	25 0	0.10	7	73 0	1 46	1	5	<1	69.00	5 5	<10
DD95NO0003C	861	862	4	0.23	<10	24 5	0 09	7	71.0	0.24	2	10	<1	69 40	5.0	<10
DD95NO0003C	862	863	4	0 16	<10	25 0	0 08	7	58 0	0 33	2	5	7	68 30	5.0	<10
DD95NO0003C	863	864	11	0.14	<10	19 5	0.08	6	47 0	0.60	3	5	18	70.20	4 5	<10
DD95NO0003C	864	865	7	0.01	<10	20 0	0 08	5	18 0	0 83	5	5	23	70.40	4 5	<10
DD95NO0003C	865	866	25	0 03	<10	13 5	0 05	3	5 0	0.96	6	<5	195	73 90	2 5	10
DD95NO0003C	866	867	6	0.02	<10	13.0	0 04	3	19.0	0.26	4	<5	86	80 40	2 5	10
DD95NO0003C	867	868	5	<0 01	<10	9 5	0 04	3	8.5	0 42	9	<5	195	85.00	2.5	<10
DD95NO0003C	868	869	11	<0 01	<10	8 0	0 03	2	2 0	0.43	4	<5	25	84 60	1 5	10
DD95NO0003C	869	870	26	0 01	<10	7.0	0 03	2	1.5	0 64	8	<5	49	84 90	2 0	<10
DD95NO0003C	870	871	10	0 06	<10	5 5	0 03	2	8.5	0 62	7	<5	130	85.30	1.5	10
DD95NO0003C	871	872	16	0.08	<10	6 0	0 04	1	12.5	0.96	6	<5	62	84 70	1 0	10
DD95NO0003C	872	873	30	0.04	<10	3 5	0 01	1	3 5	1 17	8	<5	51	87 80	1 0	15
DD95NO0003C	873	874	8	0.02	<10	5 5	0 03	1	4.0	0 43	8	<5	32	89 20	1.5	<10
DD95NO0003C	874	875	10	<0 01	<10	5.5	0 02	2	2 5	0.67	6	<5	16	90 20	1 0	<10
DD95NO0003C	875	876	8	<0.01	<10	9 0	0.04	2	1 0	0 47	4	<5	2	85.90	2 0	<10
DD95NO0003C	876	877	4	0 06	<10	8.0	0 01	2	1 5	0 49	6	<5	7	87 00	2.0	<10
DD95NO0003C	877	878	16	0.06	<10	11 0	0.03	3	3 0	0 63	5	<5	5	83 50	3 0	<10
DD95NO0003C	878	879	7	0.06	<10	12 0	0.03	3	1.5	0 55	3	<5	<1	81.30	3 0	<10
DD95NO0003C	879	880	5	0 06	<10	9 5	0.03	3	1 0	0.56	4	<5	5	82.30	2.0	<10
DD95NO0003C	880	881	9	0.09	<10	8.5	0 03	2	2 5	0.26	7	<5	8	86 10	1 5	<10
DD95NO0003C	881	882	10	0 09	<10	10.0	0 02	3	5.0	0.63	10	<5	16	86 80	2 0	<10
DD95NO0003C	882	883	14	0.07	<10	5 0	0.01	1	0 5	1 35	10	<5	35	87 00	1 0	<10
DD95NO0003C	883	884	13	0.06	<10	6.0	0 01	2	2.0	0.20	7	<5	12	91 30	1 5	<10
DD95NO0003C	884	885	8	0.06	<10	9.5	0 02	3	1.0	0.28	4	<5	7	82.70	2.5	<10

HoleId	From	To	Mo ppm	Na_2O %	Nb ppm	Nd ppm	P_2O_5 %	Pr ppm	Rb ppm	S %	Sb ppm	Sc ppm	Se ppm	SiO_2 %	Sm ppm	Sn ppm
DD95NO0003C	885	886	13	<0.01	<10	4 5	0.02	1	2 0	0.38	6	<5	5	91 40	1 0	<10
DD95NO0003C	886	887	24	0 05	<10	3.0	<0 01	<1	8.5	0 73	8	<5	7	90 10	<0 5	<10
DD95NO0003C	887	888	17	0.06	<10	7 5	0.03	2	11 5	0 50	8	<5	7	82 60	2 0	<10
DD95NO0003C	888	889	8	0.09	<10	4 0	0.03	1	14 5	0.79	11	<5	28	85.00	1 0	<10
DD95NO0003C	889	890	13	0 09	<10	5 0	<0.01	1	7 5	0 65	10	<5	19	87 70	1.0	<10
DD95NO0003C	890	891	12	0 06	<10	9.0	0.04	3	8.0	0.27	6	<5	<1	85 20	2 0	<10
DD95NO0003C	891	892	16	0.06	<10	3 5	<0 01	<1	2 0	0.72	11	<5	15	89.90	1 0	<10
DD95NO0003C	892	893	12	0 07	<10	5 5	0 01	1	2.0	1.03	11	<5	16	83 70	1 0	<10
DD95NO0003C	893	894	14	0 07	<10	2.0	0 02	<1	3 0	1 47	12	<5	22	89 10	0 5	<10
DD95NO0003C	894	895	8	<0 01	<10	4 5	0.02	1	2 0	0.63	9	<5	13	88.30	1 0	<10
DD95NO0003C	895	896	17	0 02	<10	7 5	0 03	2	4.5	0 50	7	<5	10	86 60	1.5	<10
DD95NO0003C	896	897	7	<0.01	<10	11.0	0 04	3	3 5	0 31	5	<5	3	82.60	2 5	<10
DD95NO0003C	897	898	10	0 01	<10	8 0	0 04	2	1 5	0.27	6	<5	13	86.20	1 5	<10
DD95NO0003C	898	899	15	0 11	<10	1 5	0 02	<1	17.5	1 50	26	<5	80	85 20	0.5	<10
DD95NO0003C	899	900	10	0.02	<10	7.5	0 03	2	3 5	1.98	10	<5	26	78.20	1 5	<10
DD95NO0003C	900	901	6	<0.01	<10	5 5	0.02	2	2 0	0.67	8	<5	22	87 20	1.5	<10
DD95NO0003C	901	902	11	0 01	<10	8 0	0 03	2	1 0	0.62	7	<5	15	85.80	2 0	<10
DD95NO0003C	902	903	16	0 01	<10	12.5	0.05	3	20.5	2 07	5	<5	26	74 10	2 5	185
DD95NO0003C	903	904	4	0.02	<10	10 5	0 04	3	37 5	2 23	5	<5	33	73 30	2 0	270
DD95NO0003C	904	905	5	0 02	<10	3.0	<0.01	<1	9 0	1 20	6	<5	10	76.10	1 0	20
DD95NO0003C	905	906	4	0 04	<10	4.5	0.01	1	10 0	1 05	8	<5	8	65 50	1 0	15
DD95NO0003C	906	907	5	0.01	<10	1 0	<0 01	<1	2.0	0 90	4	<5	5	78.50	<0.5	10
DD95NO0003C	907	908	5	<0 01	<10	0 5	<0 01	<1	<0 5	0.08	3	<5	1	91 60	<0 5	<10
DD95NO0003C	908	909	5	<0.01	<10	8 5	0.03	2	11.5	1 09	5	<5	13	77 20	2.0	15
DD95NO0003C	909	910	4	0.02	<10	15 0	0 06	4	52 0	1.89	3	5	13	71.70	3.0	<10
DD95NO0003C	910	911	5	0 02	<10	9 0	0.04	3	34 5	3.51	6	<5	40	71 20	1 5	60
DD95NO0003C	911	912	6	0.01	<10	12 5	0 06	4	43.0	1.35	6	<5	9	75.00	2 5	<10
DD95NO0003C	912	913	7	0 01	<10	8 0	0 03	2	20.0	0 83	6	<5	13	85 90	1 5	<10
DD95NO0003C	913	914	7	0 06	<10	3.5	0.01	<1	19.0	0.69	4	<5	4	88.80	1 0	<10
DD95NO0003C	914	915	9	0.13	<10	3 5	<0 01	<1	18 5	0.75	7	<5	10	80 20	1 0	<10
DD95NO0003C	915	916	6	0 06	<10	1 5	0 01	<1	9 5	0.32	9	<5	14	74.30	0 5	<10
DD95NO0003C	916	917	5	0 04	<10	11 5	0 04	3	55 0	0 54	14	<5	56	66 70	2 5	10
DD95NO0003C	917	918	6	0.03	<10	23 5	0 07	6	110 0	0 07	7	10	10	70.60	4 5	<10
DD95NO0003C	918	919	4	0 03	<10	24.5	0.10	7	150 0	0 02	2	10	<1	71 50	5 5	<10
DD95NO0003C	919	920	4	0.07	<10	19 5	0 06	5	115.0	0 07	5	10	21	74.30	4.0	10
DD95NO0003C	920	921	4	0.06	<10	20 5	0.09	6	115 0	0.40	4	10	8	72 20	4.0	10
DD95NO0003C	921	922	5	0.02	<10	16 0	0 06	4	77.0	0 33	5	5	13	77.00	3 0	<10
DD95NO0003C	922	923	4	0 03	<10	19 5	0.07	6	125 0	0.02	3	10	2	74.90	4.5	<10
DD95NO0003C	923	924	4	0 04	<10	22.5	0 08	6	140.0	0 02	3	10	<1	74 90	4.5	<10
DD95NO0003C	924	925	4	0.03	<10	21 0	0.08	6	145.0	0.05	4	10	8	73 30	4 5	<10
DD95NO0003C	925	926	3	0 04	10	23.5	0.09	7	170 0	0.05	4	10	7	71 70	5.5	<10
DD95NO0003C	926	927	5	0 04	10	23 0	0 08	6	160 0	0 02	4	10	6	74 10	5.0	<10
DD95NO0003C	927	928	5	0.03	<10	20.5	0 08	6	140 0	0.01	2	10	<1	74 90	4 5	<10
DD95NO0003C	928	929	4	0 04	<10	24.5	0.08	6	160 0	0 01	2	10	2	73 90	5.0	<10
DD95NO0003C	929	930	8	0 02	<10	13 5	0.05	4	81 0	0.07	3	5	2	78 30	3 0	<10
DD95NO0004F	320	322	<2	0.04	<10	21 5	0 10	7	92 0	0 10	1	8	<1	73 60	4.5	<10
DD95NO0004F	322	324	<2	0 05	<10	19.0	0 09	6	84.0	0 02	<1	7	<1	76 30	4.0	<10
DD95NO0004F	324	326	5	0.04	<10	16.5	0 09	5	59.0	0 50	2	6	4	73.00	3.0	<10
DD95NO0004F	326	328	12	0 20	<10	20.5	0 11	7	105.0	0 59	1	8	2	71 40	4.0	<10
DD95NO0004F	328	330	18	0 31	<10	22 0	0.10	7	110.0	0.64	2	8	<1	69.90	4.5	<10
DD95NO0004F	330	332	17	0.45	<10	19.5	0 09	6	77 0	0 97	1	7	1	69 70	4 0	<10
DD95NO0004F	332	334	8	0 22	<10	20 5	0 09	7	110 0	0.56	1	8	<1	69 40	4 0	<10

HoleId	From	To	Mo ppm	Na_2O %	Nb ppm	Nd ppm	P_2O_5 %	Pr ppm	Rb ppm	S %	Sb ppm	Sc ppm	Se ppm	SiO_2 %	Sm ppm	Sn ppm
DD95NO0004F	334	336	8	0.13	<10	19.5	0.09	7	98 0	0.79	1	8	<1	71.30	4 0	<10
DD95NO0004F	336	338	8	0 13	<10	22 0	0.12	7	105.0	0.58	1	8	3	70.40	4 0	<10
DD95NO0004F	338	340	9	0 17	<10	21 0	0 10	7	98.0	0.52	<1	8	2	70 40	4.0	<10
DD95NO0004F	340	342	12	0 23	<10	20 0	0 09	7	70 0	0.83	1	7	1	69 40	4 0	<10
DD95NO0004F	342	344	8	0 11	<10	24.5	0 11	8	98.0	0 47	1	8	2	71 70	5.0	<10
DD95NO0004F	344	346	13	0 11	<10	19 5	0 11	6	86.0	0 59	<1	8	1	70.20	4 0	<10
DD95NO0004F	346	348	8	0.10	<10	23 0	0.10	8	100 0	0.38	<1	9	<1	70.50	4 5	<10
DD95NO0004F	348	350	12	0 11	<10	24.0	0 10	8	105 0	1 00	1	9	<1	66.60	4 5	<10
DD95NO0004F	350	352	23	0 06	<10	20.5	0 09	7	65.0	1.30	2	8	3	66 60	4 0	<10
DD95NO0004F	352	354	12	0 06	<10	23 5	0.10	8	88 0	0.53	2	8	<1	68 30	4 5	<10
DD95NO0004F	354	356	22	0 07	<10	21.5	0.09	7	68.0	0 68	2	8	<1	67 70	4.0	<10
DD95NO0004F	356	358	6	0.12	<10	24 5	0.10	8	105 0	0 35	3	9	6	69 40	4 5	<10
DD95NO0004F	358	360	4	0 11	<10	24.0	0 12	8	145.0	0 16	1	10	<1	69 10	4 5	<10
DD95NO0004F	360	362	<2	0.11	<10	25 5	0.14	8	140 0	0 03	1	10	<1	65.20	5 0	15
DD95NO0004F	362	364	<2	0 14	10	28.0	0.15	9	175 0	<0.01	2	11	<1	68 00	5.5	<10
DD95NO0004F	364	365	<2	0 07	<10	24.5	0 13	8	175.0	0 02	1	10	<1	67 40	5 0	<10
DD95NO0004F	365	366	3	0.04	<10	24 5	0.11	8	41 0	0 65	2	9	1	58.80	4.5	15
DD95NO0004F	366	367	3	0 05	<10	24 5	0.11	8	51.0	0.99	2	8	3	62 70	4.5	<10
DD95NO0004F	367	368	3	0 05	<10	24 5	0 11	8	74 0	1 88	2	8	3	65 10	4 5	15
DD95NO0004F	368	369	2	0 04	<10	14.0	0 08	5	18.5	0.66	2	5	1	72 40	3 0	<10
DD95NO0004F	369	370	4	0.03	<10	5 0	0 02	2	4 0	0 75	9	<5	37	87 30	1.0	<10
DD95NO0004F	370	371	3	0 03	<10	9.0	0 04	3	6.0	0 79	5	3	19	80 20	1.5	<10
DD95NO0004F	371	372	<2	0 03	<10	15 5	0 06	5	5 5	0.74	1	6	5	71 60	3 0	<10
DD95NO0004F	372	373	<2	0.04	<10	16.0	0 07	5	9 0	0.55	1	7	2	68.40	3 0	<10
DD95NO0004F	373	374	6	0.03	<10	10 0	0.04	3	10 5	1.68	4	4	20	74.90	2.0	<10
DD95NO0004F	374	375	8	0.04	<10	9 5	0 04	3	10 0	1 31	4	4	39	77 20	1 5	<10
DD95NO0004F	375	376	6	0 03	<10	11 5	0 06	4	11.5	1.18	3	5	13	72.30	2 5	<10
DD95NO0004F	376	377	27	0 05	<10	11.5	0 05	4	16.0	4 09	9	5	26	62 30	2.0	<10
DD95NO0004F	377	378	12	0.04	<10	18 0	0 09	6	58 0	0.48	3	8	1	69 00	3.5	10
DD95NO0004F	378	379	3	0 06	<10	24.0	0 13	8	130 0	0 03	1	10	<1	69.80	4.5	20
DD95NO0004F	379	380	<2	0 07	<10	22 5	0 11	7	105 0	0 01	1	8	<1	71 90	4 5	10
DD95NO0004F	380	381	2	0 05	<10	15 5	0.08	5	68 0	0 08	1	6	<1	74 70	3.0	<10
DD95NO0004F	381	382	4	0 05	<10	1 0	<0 01	<1	3 5	0 20	3	<5	8	82 10	<0 5	<10
DD95NO0004F	382	383	<2	0.03	<10	3 0	0.02	1	12 0	0.60	11	2		81 50	0.5	25
DD95NO0004F	383	384	<2	0 03	<10	1 5	0 01	<1	1.5	1.29	19	2		68 00	<0 5	30
DD95NO0004F	384	385	<2	0 04	<10	18.5	0 07	6	59.0	0 12	4	8	61	62.90	3 5	45
DD95NO0004F	385	386	2	0.07	<10	21 5	0 10	7	140.0	0 02	2	9	2	68 50	4 0	15
DD95NO0004F	386	387	<2	0.05	<10	15 5	0.07	5	90 0	0.03	2	8	11	73 20	3.0	15
DD95NO0004F	387	388	<2	0 05	<10	16 5	0 08	6	130 0	0 02	<1	9	<1	74.30	3 0	<10
DD95NO0004F	388	389	<2	0.05	<10	11 0	0.06	4	95 0	<0.01	<1	7	<1	77 70	2 0	<10
DD95NO0004F	389	390	<2	0.04	<10	10 0	0.04	3	55 0	0 12	4	6		72 70	2 0	30
DD95NO0004F	390	391	<2	0.04	<10	12 5	0 07	4	61.0	0 02	2	6	16	75.20	2 5	10
DD95NO0004F	391	392	<2	0 05	<10	17 0	0.08	6	125 0	0.02	1	9	2	71 70	3 5	<10
DD95NO0004F	392	393	6	0 06	<10	19 5	0 09	7	165 0	0 01	<1	10	<1	70.70	3 5	10
DD95NO0004F	393	394	5	0.05	<10	15 5	0.08	5	105 0	0.03	<1	7	<1	76 00	3 0	<10
DD95NO0004F	394	396	<2	0.08	<10	18 0	0.08	6	145.0	0.02	<1	9	<1	71 50	3 5	<10
DD95NO0004F	396	398	<2	0 09	<10	20 0	0 09	7	120 0	<0.01	<1	9	<1	71.60	3.5	15
DD95NO0004F	398	400	73	0 09	<10	18.5	0 09	6	130 0	<0 01	<1	9	<1	69 90	3 5	<10
DD95NO0004F	400	402	4	0 10	<10	14 5	0 07	5	75 0	<0 01	<1	7	<1	73 80	3 0	<10
DD95NO0004F	402	404	<2	0.15	<10	28 5	0.11	9	125 0	<0 01	<1	9	<1	71 20	5.5	20
DD95NO0004F	404	406	<2	0.13	<10	21.5	0 09	7	105 0	0 01	<1	8	<1	70.90	4.0	<10
DD95NO0004F	406	408	<2	0.15	<10	23.0	0 12	8	160.0	0 44	<1	11	<1	59 90	4.5	10

HoleId	From	To	Mo ppm	Na_2O %	Nb ppm	Nd ppm	P_2O_5 %	Pr ppm	Rb ppm	S %	Sb ppm	Sc ppm	Se ppm	SiO_2 %	Sm ppm	Sn ppm
DD95NO0004F	420	422	<2	0 62	<10	22 0	0 10	7	84 0	1 34	<1	10	3	60 20	4 5	<10
DD95NO0004F	422	425	<2	0.23	<10	27.5	0 14	9	200.0	2.10	<1	11	5	56 30	5 5	<10
DD95NO0004F	436	438	<2	0.17	10	31 5	0 12	10	280 0	1.21	<1	12	<1	60 40	6.0	<10
DD95NO0004F	438	440	<2	0 15	10	34 0	0.14	11	280.0	1 33	1	13	6	60 00	6.5	<10
DD95NO0004F	440	442	<2	0 14	10	31 5	0 12	10	280 0	1 06	1	13	2	60 90	6 0	<10
DD95NO0004F	442	444	<2	0.15	10	29 5	0 14	10	260 0	1 23	<1	13	1	60.20	5.5	<10
DD95NO0004F	444	446	<2	0.13	10	30.0	0.13	10	280 0	0.98	<1	13	<1	59 20	5 5	<10
DD95NO0004F	446	448	<2	0 11	10	34 5	0 13	11	290.0	1 13	<1	12	<1	61.30	6.5	<10
DD95NO0004F	448	450	<2	0.12	15	36.0	0 15	12	290.0	0.99	<1	12	<1	60 20	7.0	<10
DD95NO0004F	450	452	<2	0.13	10	29 5	0.14	10	260.0	0 67	<1	11	<1	63 60	6 0	<10
DD95NO0004F	452	454	<2	0.13	10	30 5	0.15	10	260 0	0 89	<1	10	<1	63.60	6.0	<10
DD95NO0004F	454	456	<2	0 12	10	28 0	0 15	9	270.0	1 34	<1	11	<1	63 90	5.5	<10
DD95NO0004F	456	458	<2	0 14	10	30 5	0.13	10	240.0	1.32	<1	10	<1	63 90	6.0	<10
DD95NO0004F	458	460	<2	0.14	10	33 5	0.13	11	260.0	1 29	2	11	<1	64.00	6.5	10
DD95NO0004F	460	462	<2	0 13	10	31.0	0 14	10	270 0	1 17	<1	13	<1	62 10	6 0	<10
DD95NO0004F	462	464	<2	0 12	10	33 5	0 15	11	250.0	0.74	1	12	<1	62.60	6 5	<10
DD95NO0004F	464	466	<2	0 11	10	33.5	0 14	11	260 0	0.54	1	12	<1	62 90	6.5	<10
DD95NO0004F	466	468	<2	0.12	10	29 0	0.12	10	260.0	0 31	<1	13	<1	61 40	6 0	<10
DD95NO0004F	468	470	<2	0 15	10	32.5	0.13	11	250 0	0.35	1	13	<1	62.20	6 5	<10

HoleId	From	To	Sr ppm	Ta ppm	Tb ppm	Te ppm	Th ppm	TiO_2 %	Tl ppm	Tm ppm	U ppm	V ppm	W ppm	Y ppm	Yb ppm	Zr ppm
DD95NO0001F	1063	1067	20	2	0 5	<5	17.0	0 655	<3	<1	3.0	70	12	23	2	170
DD95NO0001F	1067	1071	35	2	0 5	<5	15 0	0.710	<3	<1	3.0	80	8	30	2	200
DD95NO0001F	1071	1075	35	2	1 0	<5	15 5	0 770	<3	<1	3 0	80	8	30	3	210
DD95NO0001F	1075	1079	45	2	1 0	<5	16 0	0 770	<3	<1	3 5	90	8	29	3	180
DD95NO0001F	1079	1083	40	3	0 5	<5	16 5	0.805	<3	<1	3 5	100	10	31	2	190
DD95NO0001F	1083	1087	65	2	0 5	<5	15.0	0 725	<3	<1	3 0	80	12	27	2	180
DD95NO0001F	1087	1091	65	2	0.5	<5	15.0	0.775	<3	<1	3.0	90	8	31	2	200
DD95NO0001F	1091	1095	80	<2	1 0	<5	14 0	0.670	<3	<1	3 0	70	10	31	3	280
DD95NO0001F	1095	1099	115	2	0.5	<5	15 0	0 800	<3	<1	3 0	100	10	32	2	210
DD95NO0001F	1099	1103	50	2	0 5	<5	14 0	0.740	<3	<1	3 0	100	8	28	3	230
DD95NO0001F	1103	1107	40	2	0.5	<5	15 5	0 810	<3	<1	3 0	120	12	30	2	200
DD95NO0001F	1107	1111	55	2	0 5	<5	13 5	0 695	<3	<1	3.0	90	10	26	2	270
DD95NO0001F	1111	1115	55	<2	0 5	<5	14.5	0.755	<3	<1	3 0	90	10	31	2	250
DD95NO0001F	1115	1119	750	<2	0.5	<5	9 0	0 665	<3	<1	2.0	100	<3	24	2	240
DD95NO0001F	1119	1123	50	2	0 5	<5	13 5	0.720	<3	<1	3 0	110	10	26	2	200
DD95NO0001F	1123	1127	45	<2	0.5	<5	13.5	0 710	<3	<1	3.0	110	10	28	2	180
DD95NO0001F	1127	1131	50	<2	0.5	<5	12 5	0 640	<3	<1	2.5	110	10	25	2	160
DD95NO0001F	1131	1135	40	<2	0 5	<5	11 0	0.540	<3	<1	2 0	120	24	21	2	170
DD95NO0001F	1135	1139	40	<2	0 5	<5	11 0	0.555	<3	<1	2 5	110	24	22	2	170
DD95NO0001F	1139	1143	45	<2	0 5	<5	10 5	0.530	<3	<1	2 0	90	26	24	2	180
DD95NO0001F	1143	1147	70	<2	0.5	<5	11.5	0.540	<3	<1	2 5	90	53	22	2	180
DD95NO0001F	1147	1149	50	<2	0 5	<5	10.5	0.500	<3	<1	2 0	90	42	22	2	240
DD95NO0001F	1149	1151	40	<2	0 5	<5	10.5	0 535	<3	<1	2.5	110	115	21	2	190
DD95NO0001F	1151	1153	75	<2	<0 5	<5	9 0	0.475	<3	<1	2 0	90	95	19	2	160
DD95NO0001F	1153	1155	30	<2	<0 5	<5	5 0	0 205	<3	<1	1 0	60	180	9	<1	70
DD95NO0001F	1155	1157	35	<2	<0 5	<5	4 5	0 215	<3	<1	1.0	60	170	9	<1	60
DD95NO0001F	1157	1159	30	<2	<0.5	<5	3 0	0 125	<3	<1	1.0	70	360	5	<1	40
DD95NO0001F	1159	1161	50	<2	<0.5	<5	2.5	0.120	<3	<1	1 0	70	450	5	<1	40
DD95NO0001F	1161	1163	45	<2	<0.5	<5	2 5	0.100	<3	<1	1 0	80	650	5	<1	30
DD95NO0001F	1163	1165	65	<2	<0 5	<5	1 5	0.065	<3	<1	0 5	<20	340	3	<1	20
DD95NO0001F	1165	1167	30	<2	<0.5	<5	1 5	0.060	<3	<1	0.5	<20	390	3	<1	20
DD95NO0001F	1167	1169	25	<2	<0.5	<5	1 5	0.070	<3	<1	0 5	<20	450	3	<1	20
DD95NO0001F	1169	1171	35	<2	<0 5	<5	1.5	0 065	<3	<1	0 5	<20	240	3	<1	20
DD95NO0001F	1171	1173	25	<2	<0 5	<5	2 0	0 095	<3	<1	1 0	<20	100	5	<1	20
DD95NO0001F	1173	1175	25	<2	<0 5	<5	1 5	0.060	<3	<1	0 5	<20	52	3	<1	20
DD95NO0001F	1175	1177	30	<2	<0 5	<5	1.0	0 055	<3	<1	0 5	<20	24	2	<1	20
DD95NO0001F	1177	1179	35	<2	<0.5	<5	1 0	0 055	<3	<1	0 5	<20	18	3	<1	5
DD95NO0001F	1179	1181	25	<2	<0 5	<5	2 0	0 115	<3	<1	0 5	<20	22	5	<1	30
DD95NO0001F	1181	1183	45	<2	<0 5	<5	12.0	0 105	<3	<1	1 0	<20	14	4	<1	50
DD95NO0001F	1183	1185	35	<2	<0.5	<5	7 0	0.120	<3	<1	1 0	<20	57	6	<1	40
DD95NO0001F	1185	1187	30	<2	<0 5	<5	7 5	0 165	<3	<1	1.5	20	60	7	<1	40
DD95NO0001F	1187	1189	45	<2	<0.5	<5	5 0	0 100	<3	<1	1 0	40	26	4	<1	30
DD95NO0001F	1189	1191	40	<2	<0.5	<5	3.0	0.070	<3	<1	<0 5	40	14	6	<1	20
DD95NO0001F	1191	1193	50	<2	<0 5	<5	2 5	0 070	<3	<1	<0.5	30	4	3	<1	20
DD95NO0001F	1193	1195	45	<2	<0.5	<5	3 0	0 090	<3	<1	<0 5	40	4	3	<1	30
DD95NO0001F	1195	1197	40	<2	<0.5	<5	1.5	0.040	<3	<1	<0.5	<20	<3	2	<1	5
DD95NO0001F	1197	1199	30	<2	<0.5	<5	1.5	0 030	<3	<1	<0 5	<20	<3	2	<1	5
DD95NO0001F	1199	1201	40	<2	<0 5	<5	2 5	0 080	<3	<1	<0 5	<20	4	5	<1	20
DD95NO0001F	1201	1203	35	<2	<0 5	<5	7 0	0.225	<3	<1	1 0	40	6	9	<1	50
DD95NO0001F	1203	1205	40	<2	<0.5	<5	8 5	0.245	<3	<1	1 0	40	6	10	<1	50
DD95NO0001F	1205	1207	35	<2	<0 5	<5	11.5	0 340	<3	<1	1 5	50	8	15	1	60
DD95NO0001F	1207	1209	45	<2	<0 5	<5	12.0	0.365	<3	<1	1.5	60	6	17	1	70

HoleId	From	To	Sr ppm	Ta ppm	Tb ppm	Te ppm	Th ppm	TiO_2 %	Tl ppm	Tm ppm	U ppm	V ppm	W ppm	Y ppm	Yb ppm	Zr ppm
DD95NO0001F	1209	1211	65	<2	<0 5	<5	12 0	0 340	<3	<1	1 5	50	6	15	1	70
DD95NO0001F	1211	1213	40	<2	<0.5	<5	12.5	0.360	<3	<1	1.5	50	10	14	1	70
DD95NO0001F	1213	1215	45	<2	<0 5	<5	15 5	0 445	<3	<1	2.0	50	6	18	2	90
DD95NO0001F	1215	1217	35	<2	<0 5	<5	15.0	0 410	<3	<1	2 0	50	6	17	1	80
DD95NO0001F	1217	1219	35	<2	<0 5	<5	17 0	0 450	<3	<1	2.0	60	6	18	2	90
DD95NO0001F	1219	1221	35	<2	<0.5	<5	14 5	0.430	<3	<1	2.0	60	6	18	1	90
DD95NO0003C	839	840	10	<2	<0 5	<5	14.5	0 495	<3	<1	2 5	80	6	19	2	90
DD95NO0003C	840	841	10	<2	<0.5	<5	13.5	0 490	<3	<1	2 5	70	14	20	2	100
DD95NO0003C	841	842	15	<2	0.5	<5	16.0	0 565	<3	<1	3.0	80	20	26	3	140
DD95NO0003C	842	843	10	<2	0.5	<5	16 0	0.565	<3	<1	3 0	80	20	21	2	130
DD95NO0003C	843	844	15	<2	0.5	<5	17.5	0.605	<3	<1	3 0	90	20	25	2	120
DD95NO0003C	844	845	15	<2	0 5	<5	15 0	0 550	<3	<1	3.0	80	18	23	3	150
DD95NO0003C	845	846	15	<2	0 5	<5	18 0	0 640	<3	<1	3.5	90	20	27	3	160
DD95NO0003C	846	847	15	<2	<0 5	<5	16.5	0.580	<3	<1	3 0	80	20	22	3	140
DD95NO0003C	847	848	15	<2	0 5	<5	17 0	0 565	<3	<1	3 0	90	20	24	2	170
DD95NO0003C	848	849	15	<2	0 5	<5	16 5	0.605	<3	<1	3 0	90	18	30	3	150
DD95NO0003C	849	850	15	<2	0 5	<5	17 5	0.590	<3	<1	3 0	90	18	21	2	170
DD95NO0003C	850	851	10	<2	0.5	<5	15 5	0 570	<3	<1	3.0	80	18	32	3	150
DD95NO0003C	851	852	15	<2	0 5	<5	16 5	0.565	<3	<1	3 0	90	28	26	3	130
DD95NO0003C	852	853	15	<2	<0.5	<5	14 0	0.525	<3	<1	2.5	80	16	16	2	140
DD95NO0003C	853	854	10	<2	<0 5	<5	15 0	0 530	<3	<1	2 5	80	22	21	2	150
DD95NO0003C	854	855	10	<2	<0.5	<5	14.0	0.480	<3	<1	2 5	80	34	18	2	120
DD95NO0003C	855	856	15	<2	0 5	<5	17.5	0.615	<3	<1	3 0	100	16	23	3	120
DD95NO0003C	856	857	15	<2	0 5	<5	16.5	0.605	<3	<1	3 0	90	22	24	2	120
DD95NO0003C	857	858	20	<2	<0.5	<5	14 5	0.510	<3	<1	3 0	90	44	19	2	90
DD95NO0003C	858	859	15	<2	<0 5	<5	14 0	0 505	<3	<1	3.0	90	34	18	2	100
DD95NO0003C	859	860	15	<2	<0 5	<5	13.5	0.485	<3	<1	2 5	80	44	16	2	110
DD95NO0003C	860	861	20	<2	<0 5	<5	14.0	0 470	<3	<1	2.5	90	36	16	2	120
DD95NO0003C	861	862	20	<2	<0 5	<5	14 0	0 495	<3	<1	2 5	100	61	16	2	110
DD95NO0003C	862	863	20	<2	<0.5	<5	13 0	0.455	<3	<1	2 5	100	135	14	2	100
DD95NO0003C	863	864	20	<2	<0 5	<5	11 5	0 415	<3	<1	2 0	80	81	13	1	110
DD95NO0003C	864	865	10	<2	<0 5	<5	10 5	0 365	<3	<1	2 0	90	74	18	2	80
DD95NO0003C	865	866	5	<2	<0 5	<5	6 5	0 225	<3	<1	2.0	80	220	14	1	40
DD95NO0003C	866	867	5	<2	<0 5	<5	6 0	0 200	<3	<1	1 5	60	160	9	<1	30
DD95NO0003C	867	868	5	<2	<0.5	<5	4 5	0.145	<3	<1	1.5	70	68	6	<1	20
DD95NO0003C	868	869	<5	<2	<0 5	<5	4.0	0 130	<3	<1	1 0	70	32	5	<1	20
DD95NO0003C	869	870	5	<2	<0 5	<5	4 0	0.125	<3	<1	1.5	60	28	6	<1	20
DD95NO0003C	870	871	5	<2	<0.5	<5	3 0	0 090	<3	<1	1.5	60	24	5	<1	5
DD95NO0003C	871	872	10	<2	<0 5	<5	2 5	0 080	<3	<1	1 5	60	20	4	<1	20
DD95NO0003C	872	873	5	<2	<0.5	<5	2.0	0 060	<3	<1	1.0	50	145	3	<1	5
DD95NO0003C	873	874	5	<2	<0 5	<5	2 5	0 085	<3	<1	1 0	60	160	4	<1	20
DD95NO0003C	874	875	5	<2	<0 5	<5	2 0	0 075	<3	<1	0 5	60	61	5	<1	5
DD95NO0003C	875	876	<5	<2	<0.5	<5	4.0	0.140	<3	<1	1.0	60	97	7	<1	20
DD95NO0003C	876	877	5	<2	<0 5	<5	5 0	0 110	<3	<1	1 0	80	40	6	<1	20
DD95NO0003C	877	878	5	<2	<0 5	<5	5.5	0.155	<3	<1	1.0	90	40	8	<1	30
DD95NO0003C	878	879	5	<2	<0 5	<5	6 0	0.175	<3	<1	1 0	90	42	9	<1	30
DD95NO0003C	879	880	5	<2	<0.5	<5	5 5	0 160	<3	<1	1.0	90	71	8	<1	30
DD95NO0003C	880	881	10	<2	<0.5	<5	4 5	0 115	<3	<1	1 0	80	115	7	<1	20
DD95NO0003C	881	882	10	<2	<0.5	<5	3 5	0 085	<3	<1	1 0	80	120	6	<1	20
DD95NO0003C	882	883	<5	<2	<0 5	<5	2.5	0.070	<3	<1	1.0	70	70	4	<1	5
DD95NO0003C	883	884	5	<2	<0 5	<5	2 5	0 065	<3	<1	0 5	80	51	3	<1	5
DD95NO0003C	884	885	<5	<2	<0.5	<5	4.0	0 130	<3	<1	1.0	90	30	5	<1	20

HoleId	From	To	Sr ppm	Ta ppm	Tb ppm	Te ppm	Th ppm	TiO_2 %	Tl ppm	Tm ppm	U ppm	V ppm	W ppm	Y ppm	Yb ppm	Zr ppm
DD95NO0003C	885	886	<5	<2	<0 5	<5	2.0	0 050	<3	<1	0 5	80	60	3	<1	5
DD95NO0003C	886	887	15	<2	<0 5	<5	1 5	0.040	<3	<1	0 5	90	125	2	<1	5
DD95NO0003C	887	888	10	<2	<0 5	<5	4 0	0 125	<3	<1	1 0	110	135	6	<1	20
DD95NO0003C	888	889	10	<2	<0 5	<5	2 0	0 055	<3	<1	1 0	<20	300	3	<1	5
DD95NO0003C	889	890	10	<2	<0 5	<5	2 5	0 070	<3	<1	1.0	<20	105	3	<1	5
DD95NO0003C	890	891	<5	<2	<0.5	<5	5.0	0 145	<3	<1	1 0	<20	40	8	<1	30
DD95NO0003C	891	892	<5	<2	<0 5	<5	2 0	0 040	<3	<1	<0 5	<20	51	2	<1	5
DD95NO0003C	892	893	5	<2	<0 5	<5	3 0	0 085	<3	<1	1.0	<20	67	4	<1	5
DD95NO0003C	893	894	5	<2	<0 5	<5	1 5	0.040	<3	<1	0 5	<20	130	2	<1	5
DD95NO0003C	894	895	5	<2	<0 5	<5	2 0	0 065	<3	<1	0.5	<20	61	3	<1	5
DD95NO0003C	895	896	10	<2	<0 5	<5	3.5	0 110	<3	<1	1 0	<20	94	5	<1	20
DD95NO0003C	896	897	5	<2	<0 5	<5	5 5	0 170	<3	<1	1.0	<20	54	7	<1	30
DD95NO0003C	897	898	5	<2	<0 5	<5	4 5	0 125	<3	<1	1 0	<20	76	7	<1	20
DD95NO0003C	898	899	10	<2	<0 5	<5	1 0	0 020	<3	<1	1 0	<20	210	2	<1	5
DD95NO0003C	899	900	20	<2	<0 5	<5	4 0	0 125	<3	<1	1 5	30	95	6	<1	20
DD95NO0003C	900	901	10	<2	<0 5	<5	3.0	0 085	<3	<1	1.0	<20	160	4	<1	20
DD95NO0003C	901	902	<5	<2	<0 5	<5	3 5	0.115	<3	<1	1 0	<20	48	6	<1	20
DD95NO0003C	902	903	10	<2	<0 5	<5	6 0	0 185	<3	<1	1 0	30	24	8	<1	30
DD95NO0003C	903	904	10	<2	<0.5	<5	6 5	0 200	<3	<1	1 0	30	20	8	<1	30
DD95NO0003C	904	905	5	<2	<0.5	<5	2 5	0 055	<3	<1	<0 5	50	8	4	<1	5
DD95NO0003C	905	906	5	<2	<0 5	<5	3 0	0 075	<3	<1	0 5	80	6	4	<1	5
DD95NO0003C	906	907	<5	<2	<0 5	<5	1 0	0 020	<3	<1	<0 5	50	4	2	<1	5
DD95NO0003C	907	908	<5	<2	<0 5	<5	<0 5	0 005	<3	<1	<0 5	<20	<3	<1	<1	5
DD95NO0003C	908	909	5	<2	<0.5	<5	5 0	0 150	<3	<1	1 0	40	4	5	<1	30
DD95NO0003C	909	910	15	<2	<0 5	<5	9 0	0 260	<3	<1	1 5	50	6	11	1	40
DD95NO0003C	910	911	10	<2	<0 5	<5	5.5	0 170	<3	<1	1 0	40	4	7	<1	30
DD95NO0003C	911	912	10	<2	<0 5	<5	8 0	0 240	<3	<1	1 5	40	4	10	1	40
DD95NO0003C	912	913	5	<2	<0.5	<5	4 0	0 100	<3	<1	0 5	<20	6	7	<1	20
DD95NO0003C	913	914	5	<2	<0 5	<5	3 5	0 095	<3	<1	0 5	<20	4	4	<1	20
DD95NO0003C	914	915	5	<2	<0 5	<5	1 5	0 025	<3	<1	<0 5	20	<3	9	<1	5
DD95NO0003C	915	916	<5	<2	<0 5	<5	0 5	<0 005	<3	<1	<0 5	50	<3	3	<1	5
DD95NO0003C	916	917	5	<2	<0 5	<5	5 5	0 195	<3	<1	1.0	70	4	11	<1	30
DD95NO0003C	917	918	10	<2	<0 5	<5	11 5	0.405	<3	<1	2 0	70	10	17	1	70
DD95NO0003C	918	919	15	<2	<0 5	<5	13 5	0.460	<3	<1	2 5	80	14	19	1	80
DD95NO0003C	919	920	10	<2	<0 5	<5	11 0	0 350	<3	<1	2 0	60	14	15	1	60
DD95NO0003C	920	921	10	<2	<0 5	<5	11 0	0 385	<3	<1	2 0	70	10	16	1	60
DD95NO0003C	921	922	15	<2	<0 5	<5	8 5	0 280	<3	<1	1 5	50	6	12	<1	40
DD95NO0003C	922	923	20	<2	<0 5	<5	10 5	0 375	<3	<1	2 0	60	6	16	1	60
DD95NO0003C	923	924	15	<2	<0 5	<5	12 5	0 415	<3	<1	2 0	70	12	16	1	70
DD95NO0003C	924	925	15	<2	<0 5	<5	12 0	0 400	<3	<1	2 0	70	12	17	2	60
DD95NO0003C	925	926	15	<2	<0 5	<5	13 5	0 465	<3	<1	2 5	80	10	18	1	70
DD95NO0003C	926	927	20	<2	<0 5	<5	13 0	0 425	<3	<1	2 0	80	8	20	2	70
DD95NO0003C	927	928	20	<2	<0.5	<5	11 5	0 410	<3	<1	2 0	80	8	15	1	60
DD95NO0003C	928	929	15	<2	<0 5	<5	13.0	0.430	<3	<1	2.0	80	10	17	2	60
DD95NO0003C	929	930	15	<2	<0.5	<5	7 5	0 250	<3	<1	1.0	60	6	10	1	40
DD95NO0004F	320	322	30	<2	0.5	<5	17.0	0 515	<3	<1	2.5	60	4	21	2	160
DD95NO0004F	322	324	40	<2	<0 5	<5	15 0	0 445	<3	<1	2 0	50	<3	18	1	140
DD95NO0004F	324	326	40	<2	<0 5	<5	14.0	0.405	<3	<1	2 5	50	12	19	1	140
DD95NO0004F	326	328	70	<2	0 5	<5	17 0	0 545	<3	<1	2 5	70	12	21	2	200
DD95NO0004F	328	330	60	<2	0 5	<5	16 5	0.545	<3	<1	2 5	60	14	25	2	170
DD95NO0004F	330	332	75	<2	<0 5	<5	17.0	0.485	<3	<1	2 5	50	28	20	1	160
DD95NO0004F	332	334	40	<2	0 5	<5	18.0	0 525	<3	<1	2 5	60	24	22	2	170

HoleId	From	To	Sr ppm	Ta ppm	Tb ppm	Te ppm	Th ppm	TiO_2 %	Tl ppm	Tm ppm	U ppm	V ppm	W ppm	Y ppm	Yb ppm	Zr ppm
DD95NO0004F	334	336	50	<2	<0 5	<5	17.5	0 510	<3	<1	2 5	60	24	20	2	220
DD95NO0004F	336	338	30	<2	0 5	<5	17 5	0.535	<3	<1	2.5	70	36	22	2	180
DD95NO0004F	338	340	65	<2	0.5	<5	17.0	0 510	<3	<1	2 5	60	20	21	2	170
DD95NO0004F	340	342	45	<2	<0 5	<5	17 5	0.500	<3	<1	2 5	50	86	21	2	180
DD95NO0004F	342	344	50	<2	0.5	<5	18.0	0 550	<3	<1	2 5	60	32	26	2	200
DD95NO0004F	344	346	35	<2	<0 5	<5	18 5	0 525	<3	<1	2 5	60	26	22	2	170
DD95NO0004F	346	348	35	<2	0 5	<5	18 5	0 555	<3	<1	2.5	70	18	22	2	180
DD95NO0004F	348	350	40	<2	0 5	<5	19 5	0 560	<3	<1	2.5	70	12	25	2	220
DD95NO0004F	350	352	35	<2	0 5	<5	17 5	0.495	<3	<1	2.5	80	18	22	2	180
DD95NO0004F	352	354	25	<2	0 5	<5	18 5	0 545	<3	<1	2.5	80	18	22	2	190
DD95NO0004F	354	356	30	<2	0 5	<5	17 5	0 525	<3	<1	2 5	80	8	22	2	190
DD95NO0004F	356	358	45	<2	0 5	<5	23.5	0 555	<3	<1	2.5	70	8	24	2	190
DD95NO0004F	358	360	35	<2	0.5	<5	20 5	0 615	<3	<1	2 5	60	12	26	2	200
DD95NO0004F	360	362	35	<2	0.5	<5	22 0	0.700	<3	<1	3 0	70	10	29	2	210
DD95NO0004F	362	364	65	<2	0 5	<5	21 5	0.715	<3	<1	3 0	70	8	27	2	220
DD95NO0004F	364	365	10	<2	0.5	<5	21 5	0 670	<3	<1	3 0	70	8	28	2	200
DD95NO0004F	365	366	10	<2	0.5	<5	20 0	0 570	<3	<1	3 0	70	8	24	2	170
DD95NO0004F	366	367	10	<2	0 5	<5	18 0	0 550	<3	<1	2.5	60	28	23	2	180
DD95NO0004F	367	368	10	<2	0.5	<5	18 0	0 525	<3	<1	3 0	60	28	25	2	180
DD95NO0004F	368	369	5	<2	<0 5	<5	12 5	0.365	<3	<1	2 0	40	98	16	1	110
DD95NO0004F	369	370	<5	<2	<0 5	<5	4 0	0 085	<3	<1	0 5	20	180	4	<1	30
DD95NO0004F	370	371	<5	<2	<0 5	<5	6 0	0 175	<3	<1	1 0	30	130	7	<1	40
DD95NO0004F	371	372	<5	<2	<0 5	<5	10.0	0 315	<3	<1	2 0	30	85	13	1	60
DD95NO0004F	372	373	5	<2	<0.5	<5	11 0	0.340	<3	<1	1 5	40	69	14	1	60
DD95NO0004F	373	374	<5	<2	<0 5	<5	7 5	0 210	<3	<1	1 5	20	145	9	<1	40
DD95NO0004F	374	375	<5	<2	<0 5	<5	7.0	0 195	<3	<1	1 5	<20	75	8	<1	40
DD95NO0004F	375	376	5	<2	<0 5	<5	9 0	0 275	<3	<1	1.5	30	30	11	<1	60
DD95NO0004F	376	377	5	<2	<0 5	<5	8 5	0 260	<3	<1	1 5	50	16	12	<1	60
DD95NO0004F	377	378	10	<2	<0 5	<5	13 0	0 425	<3	<1	2 0	40	8	17	1	80
DD95NO0004F	378	379	10	<2	0.5	<5	17 5	0 595	<3	<1	2 5	60	10	25	2	140
DD95NO0004F	379	380	10	<2	0 5	<5	16 0	0.515	<3	<1	2 5	50	14	26	2	140
DD95NO0004F	380	381	10	<2	<0 5	<5	13.0	0 385	<3	<1	2 0	40	6	16	1	120
DD95NO0004F	381	382	<5	<2	<0 5	<5	3 5	0 030	<3	<1	<0 5	<20	<3	2	<1	20
DD95NO0004F	382	383	<5	<2	<0 5	<5	4.0	0.115	<3	<1	0 5	20	4	8	<1	20
DD95NO0004F	383	384	<5	<2	<0 5	<5	2 5	0 035	<3	<1	<0 5	<20	<3	3	<1	5
DD95NO0004F	384	385	10	<2	0 5	<5	12.0	0 375	<3	<1	2 0	50	8	22	2	60
DD95NO0004F	385	386	15	<2	0 5	<5	15.5	0.520	<3	<1	2 5	60	4	21	2	80
DD95NO0004F	386	387	10	<2	<0.5	<5	12 0	0 370	<3	<1	1 5	40	4	14	1	60
DD95NO0004F	387	388	15	<2	<0.5	<5	13 5	0 425	<3	<1	2 0	50	4	15	1	70
DD95NO0004F	388	389	10	<2	<0 5	<5	11 0	0 315	<3	<1	1 5	<20	4	12	<1	50
DD95NO0004F	389	390	5	<2	<0 5	<5	9 5	0 255	<3	<1	1 5	40	4	13	1	40
DD95NO0004F	390	391	10	<2	<0 5	<5	10 0	0 310	<3	<1	1 5	30	6	17	1	50
DD95NO0004F	391	392	10	<2	<0 5	<5	13 5	0 435	<3	<1	2 0	50	6	21	1	70
DD95NO0004F	392	393	15	<2	<0 5	<5	16 0	0 500	<3	<1	2.0	60	6	17	2	80
DD95NO0004F	393	394	10	<2	<0 5	<5	13 0	0 365	<3	<1	1.5	50	4	12	1	60
DD95NO0004F	394	396	30	<2	<0 5	<5	15 0	0.470	<3	<1	2 0	60	4	16	1	70
DD95NO0004F	396	398	15	<2	<0 5	<5	15.5	0 480	<3	<1	2.0	70	6	18	2	80
DD95NO0004F	398	400	20	<2	<0 5	<5	15 5	0 480	<3	<1	2.0	80	6	18	1	80
DD95NO0004F	400	402	40	<2	<0 5	<5	13 0	0 400	<3	<1	1 5	60	4	13	1	70
DD95NO0004F	402	404	45	<2	1 0	<5	23 5	0 525	<3	<1	2 5	70	6	50	3	120
DD95NO0004F	404	406	50	<2	0 5	<5	16.5	0 495	<3	<1	2 0	60	8	23	2	100
DD95NO0004F	406	408	30	<2	0 5	<5	21 0	0 610	<3	<1	2 5	70	8	25	2	110

HoleId	From	To	Sr ppm	Ta ppm	Tb ppm	Te ppm	Th ppm	TiO_2 %	Tl ppm	Tm ppm	U ppm	V ppm	W ppm	Y ppm	Yb ppm	Zr ppm
DD95NO0004F	420	422	40	<2	0 5	<5	19.0	0.540	<3	<1	2.0	60	12	24	2	100
DD95NO0004F	422	425	25	<2	0 5	<5	23 5	0 730	<3	<1	3 0	80	10	30	2	120
DD95NO0004F	436	438	45	<2	1 0	<5	24 5	0 805	<3	<1	3 0	120	8	32	2	140
DD95NO0004F	438	440	40	<2	1 0	<5	24 5	0 830	<3	<1	3 0	120	6	31	3	150
DD95NO0004F	440	442	30	<2	1.0	<5	26 0	0 820	<3	<1	3.5	130	6	32	2	150
DD95NO0004F	442	444	35	<2	0 5	<5	26.0	0 815	<3	<1	3 5	130	6	32	2	150
DD95NO0004F	444	446	35	<2	0 5	<5	25 0	0.865	<3	<1	3 0	140	6	28	2	150
DD95NO0004F	446	448	25	<2	1.0	<5	26 5	0.880	<3	<1	3 5	130	4	33	3	160
DD95NO0004F	448	450	35	2	1 0	<5	27 5	0.910	<3	<1	3 5	140	4	35	3	170
DD95NO0004F	450	452	40	<2	0 5	<5	25 5	0 855	<3	<1	3 5	130	<3	31	3	160
DD95NO0004F	452	454	50	<2	1 0	<5	25 5	0.855	<3	<1	3.5	130	<3	33	3	160
DD95NO0004F	454	456	40	<2	0.5	<5	25 5	0 855	<3	<1	3.5	150	4	32	2	160
DD95NO0004F	456	458	45	<2	0 5	<5	23.5	0 820	<3	<1	3.0	130	<3	28	2	170
DD95NO0004F	458	460	60	<2	1 0	<5	25.0	0 820	<3	<1	3.5	120	4	33	3	190
DD95NO0004F	460	462	50	<2	1 0	<5	27 5	0 895	<3	<1	3.5	140	4	34	2	210
DD95NO0004F	462	464	110	<2	1.0	<5	25.5	0 815	<3	<1	3.5	130	<3	35	3	180
DD95NO0004F	464	466	40	<2	1 0	<5	27 5	0 835	<3	<1	3 5	130	<3	34	3	180
DD95NO0004F	466	468	45	<2	0 5	<5	27 5	0 810	<3	<1	3 5	130	4	31	2	150
DD95NO0004F	468	470	65	<2	1.0	<5	26 0	0 810	<3	<1	3.5	130	4	31	3	150